



**T. Pradeep**

**Publications 2018**



# **Contents**

1. Publications
2. Lectures Delivered
3. Patents/Technology
4. Media Reports

# Journal Papers Published in 2018\*

1. Clathrate hydrates in interstellar environment, Jyotirmoy Ghosh, Rabin Rajan J. Methikkalam, Radha Gobinda Bhuin, Gopi Ragupathy, Nilesh Choudhary, Rajnish Kumar and T. Pradeep, Proc. Natl. Acad. Sci. U.S.A., 2018. (DOI: 10.1073/pnas.1814293116)
2. UPLC and ESI-MS analysis of metabolites of *Rauvolfia tetraphylla* L. and their spatial localization using desorption electrospray ionization (DESI) mass spectrometric imaging, Mohana Kumara P., Uma Shaanker R. and T. Pradeep, Phytochemistry, 159 (2019) 20–29 (DOI: 10.1016/j.phytochem.2018.11.009.)
3. Sustainable and affordable composites built using microstructures performing better than nanostructures for arsenic removal, Sritama Mukherjee, Avula Anil Kumar, Chennu Sudhakar, Ramesh Kumar, Tripti Ahuja, Biswajit Mondal, Srikrishnarka Pillalamarri, Ligy Philip and T. Pradeep, ACS Sustain. Chem. Eng., 2018 (DOI: 10.1021/acssuschemeng.8b05157). (Just Accepted)
4. Metal-ligand interface in the chemical reactions of ligand protected noble metal clusters, Kumaranchira Krishnadas, Ganapati Natarajan, Ananya Bakshi, Atanu Ghosh, Esma Khatun and T. Pradeep, Langmuir, 2018 (DOI: 10.1021/acs.langmuir.8b03493). - Feature article.
5. Rapid isotopic exchange in nanoparticles, Papri Chakraborty, Abhijit Nag, Ganapati Natarajan, Nayanika Bandyopadhyay, Ganesan Paramasivam, Manoj Kumar Panwar, Jaydeb Chakrabarti and T. Pradeep, Science Advances, 5 (2019) eaau7555 (DOI: 10.1126/sciadv.aau7555).
6. Appearance of SERS activity in single silver nanoparticles by laser-induced reshaping, Kamalesh Chaudhari, Tripti Ahuja, Vasanthanarayan Murugesan, Vidhya Subramanian, Mohd. Azhardin Ganayee, Thomas Thundat and T. Pradeep, Nanoscale, 11 (2018) 321–330 (DOI: 10.1039/c8nr06497k).

7. Approaching materials with atomic precision using supramolecular cluster assemblies, Papri Chakraborty, Abhijit Nag, Amrita Chakraborty and T. Pradeep, *Acc. Chem. Res.*, 52 (2019) 2-11 (DOI: 10.1021/acs.accounts.8b00369).
8. Camouflaging structural diversity: Co-crystallization of two different nanoparticles having different cores but the same shell, Mohammad Bodiuzzaman, Atanu Ghosh, Korath Shivan Sugi, Abhijit Nag, Esma Khatun, Babu Varghese, Ganesan Paramasivam, Sudhadevi Antharjanam, Ganapati Natarajan and T. Pradeep, *Angew. Chem. Int. Ed.*, 58 (2018) 189-194 (DOI: 10.1002/ange.201809469R1).
9. Isomerism in supramolecular adducts of atomically precise nanoparticles, Abhijit Nag, Papri Chakraborty, Ganesan Paramasivam, Mohammad Bodiuzzaman, Ganapati Natarajan, and T. Pradeep, *J. Am. Chem. Soc.*, 140 (2018) 13590–13593 (DOI: 10.1021/jacs.8b08767)
10. Thirty-fold photoluminescence enhancement induced by secondary ligands in monolayer protected silver clusters, Esma Khatun, Atanu Ghosh, Papri Chakraborty, Priya Singh, Mohammad Bodiuzzaman, Ganesan Paramasivam, Ganapati Natarajan, Jyotirmoy Ghosh, Samir Kumar Pal, and T. Pradeep, *Nanoscale*, 10 (2018) 20033–20042 (DOI: 10.1039/C8NR05989F).
11. Atomically precise cluster-based white light emitters, Esma Khatun, Sandeep Bose, Madhuri Jash and T. Pradeep, *J. Chem. Sci. (Prof. M. V. George Special Issue)*, 130 (2018) (<https://doi.org/10.1007/s12039-018-1559-4>).
12. Monolayer protected noble metal clusters as potential standards for negative ion mass spectrometry, Ananya Baksi, Papri Chakraborty, Abhijit Nag, Debasmita Ghosh, Shridevi Bhat and T. Pradeep, *Anal. Chem.*, 90 (2018) 11351–11357 (DOI: 10.1021/acs.analchem.8b02280).
13. Holey MoS<sub>2</sub> nanosheets with photocatalytic metal rich edges by ambient electrospray deposition for solar water disinfection, Depanjan Sarkar, Biswajit Mondal, Anirban Som, Swathy Jakka Ravindran, Sourav Kanti Jana, C. K. Manju and T. Pradeep, *Global Challenges*, (2018) 1800052 (<https://doi.org/10.1002/gch2.201800052>). (Accepted as the front cover page of December 2018 issue)

14. Detection of  $[\text{Au}_{25}(\text{PET})_{18}(\text{O}_2)_n]^-$  ( $n=1,2,3$ ) species by mass spectrometry, Shridevi Bhat, Raghu Narayanan, Ananya Bakshi, Papri Chakraborty, Ganesan Paramasivam, Rabin Rajan J. Methikkalam, Abhijit Nag, Ganapati Natarajan and T. Pradeep, *J. Phys. Chem. C.*, 122 (2018) 19455–19462 (DOI: 10.1021/acs.jpcc.8b03220).
15. Preparation of gas phase naked silver cluster cations outside a mass spectrometer from ligand protected clusters in solution, Madhuri Jash, Arthur C. Reber, Atanu Ghosh, Depanjan Sarkar, Md Bodiuzzaman, Pallab Basuri, Ananya Bakshi, Shiv N. Khanna and T. Pradeep, *Nanoscale*, 10 (2018) 15714–15722 (DOI: 10.1039/c8nr04146f).
16. Electrohydrodynamic assembly of ambient ion-derived nanoparticles to nanosheets at liquid surfaces, Depanjan Sarkar, Rajesh Singh, Anirban Som, C. K. Manju, Mohd Azhardin Ganayee, Ronojoy Adhikari and T. Pradeep, *J. Phys. Chem. C.*, 122 (2018) 17777–17783 (DOI: 10.1021/acs.jpcc.8b04169).
17. Bent keto form of curcumin, preferential stabilization of enol by piperine, and isomers of curcumin/cyclodextrin complexes: Insights from ion mobility mass spectrometry, Abhijit Nag, Papri Chakraborty, Ganapati Natarajan, Ananya Bakshi, Sathish Kumar Mudedla, Venkatesan Subramanian and T. Pradeep, *Anal. Chem.*, 90 (2018) 8776–8784 (DOI: 10.1021/acs.analchem.7b05231).
18. Patterned nanobrush nature mimics with unprecedented water harvesting efficiency, Depanjan Sarkar, Anindita Mahapatra, Anirban Som, Ramesh Kumar, Ankit Nagar, Avijit Baidya and T. Pradeep, *Adv. Mater. Interfaces*, (2018) 1800667 (DOI: 10.1002/admi.201800667).
19. Species-specific uptake of arsenic on confined metastable 2-line ferrihydrite: A combined Raman-XPS investigation of the adsorption mechanism, Chennu Sudhakar, Avula Anil Kumar, Radha Gobinda Bhuin, Soujit Sen Gupta, Ganapati Natarajan and T. Pradeep, *ACS Sustain. Chem. Eng.*, 2018 (DOI: 10.1021/acssuschemeng.8b01217). (Article ASAP)
20. Towards atomically precise luminescent  $\text{Ag}_2\text{S}$  clusters separable by thin layer chromatography, C. K. Manju, Jyoti Sarita Mohanty, Depanjan Sarkar, Sudhakar Chennu and T. Pradeep, *J. Mater. Chem. C*, 6 (2018) 5754–5759 (DOI: 10.1039/c7tc05858f).

21. Polymorphism of  $[\text{Ag}_{29}(\text{BDT})_{12}(\text{TPP})_4]^{3-}$  cluster: Interactions of secondary ligands and their effect on solid state luminescence, Abhijit Nag, Papri Chakraborty, Md Bodiuzzaman, Tripti Ahuja, P. K. Sudhadevi Antharjanam and T. Pradeep, *Nanoscale*, 10 (2018) 9851–9855 (DOI: 10.1039/C8NR02629G).
22. Metals in urine in relation to the prevalence of pre-diabetes, diabetes and atherosclerosis in rural India, Ganesan Velmurugan, Krishnan Swaminathan, Ganesh Veerasekar, Jonathan Q Purnell, Sundaresan Mohanraj, Mani Dhivakar, Anil Kumar Avula, Mathew Cherian, Nalla G Palaniswami, Thomas Alexander and T. Pradeep, *Occup. Environ. Med.*, 75 (2018) 661–667 (DOI: 10.1136/oemed-2018-104996).
23. Atomically precise nanocluster assemblies encapsulating plasmonic gold nanorods, Amrita Chakraborty, Ann Candice Fernandez, Anirban Som, Biswajit Mondal, Ganapati Natarajan, Ganesan Paramasivam, Tanja Lahtinen, Hannu Häkkinen, Nonappa and T. Pradeep, *Angew. Chem. Int. Ed.*, 57 (2018) 6522–6526 (DOI: 10.1002/anie.201802420).
24. Synthesis of silicon nanoparticles from rice husk and their use as sustainable fluorophores for white light emission, Sandeep Bose, Mohd Azhardin Ganayee, Biswajit Mondal, Avijit Baidya, Sudhakar Chennu, Jyoti Mohanty and T. Pradeep, *ACS Sustain. Chem. Eng.*, 6 (2018) 6203–6210 (DOI: 10.1021/acssuschemeng.7b04911).
25. Detection of hydrocarbons by laser assisted paper spray ionization mass spectrometry (LAPSI MS), Pallab Basuri, Depanjan Sarkar, Ganesan Paramasivam and T. Pradeep, *Anal. Chem.*, 90 (2018) 4663–4668 (DOI: 10.1021/acs.analchem.7b05213).
26. Fabrication of a waterborne durable superhydrophobic material functioning in air and under oil, Avijit Baidya, Sarit Das, Robin Ras and T. Pradeep, *Adv. Mater. Interfaces*, 5 (2018) 1701523 (DOI: 10.1002/admi.201701523).
27. Fullerene functionalized monolayer protected silver clusters:  $[\text{Ag}_{29}(\text{BDT})_{12}(\text{C}_{60})_n]^{3-}$  ( $n=1-9$ ), Papri Chakraborty, Abhijit Nag, Ganesan Paramasivam, Ganapati Natarajan and T. Pradeep, *ACS Nano*, 12 (2018) 2415–2425 (DOI: 10.1021/acsnano.7b07759).

28. Understanding proton capture and cation-induced dimerization of  $[\text{Ag}_{29}(\text{BDT})_{12}]^{3-}$  clusters by ion mobility mass spectrometry, Papri Chakraborty, Ananya Baksi, Sathish Kumar Mudedla, Abhijit Nag, Ganesan Paramasivam, Venkatesan Subramanian and T. Pradeep, *Phys. Chem. Chem. Phys.*, 20 (2018) 7593–7603 (DOI: 10.1039/C7CP08181B).
29. Probing the mechanical response of luminescent dithiol protected  $\text{Ag}_{29}(\text{BDT})_{12}(\text{TPP})_4$  cluster crystals, Korath Shivan Sugi, Gangapuram Mallikarjunachari, Anirban Som, Pijush Ghosh and T. Pradeep, *ChemNanoMat*, 4 (2018) 401–408 (DOI: 10.1002/cnma.201700371).

## **PUBLICATIONS WITH OTHER GROUPS**

30. Interconversions of structural isomers of  $[\text{PdAu}_8(\text{PPh}_3)_8]^{2+}$  and  $[\text{Au}_9(\text{PPh}_3)_8]^{3+}$  revealed by ion mobility mass spectrometry, Keisuke Hirata, Papri Chakraborty, Abhijit Nag, Shinjiro Takano, Kiichirou Koyasu, T. Pradeep and Tatsuya Tsukuda, *J. Phys. Chem. C.*, 122 (2018) 23123–23128 (DOI: 10.1021/acs.jpcc.8b04722).
31. Self-propagated combustion synthesis of a few layer graphene: An optical properties perspective, Manonmani Mohandoss, Soujit Sen Gupta, Ramesh Kumar, Rabiul Islam Md., Anirban Som, Azhardin Ganayee Mohd., T. Pradeep and Shihabudheen M. Maliyekkal, *Nanoscale*, 10 (2018) 7581–7588 (DOI: 10.1039/C7NR09156G).

\* Some of these may appear in 2019

\*\* "Papers with T. Pradeep as the/a corresponding author are reproduced in the following pages."

## **BOOK CHAPTERS**

32. Capacitive Deionization (CDI): An alternative cost-efficient desalination technique, Soujit Sen Gupta, Md Rabiul Islam and Thalappil Pradeep, *Advances in Water Purification Techniques: Meeting the Needs of Developed and Developing Countries*, Satinder Ahuja (Ed), Elsevier, Amsterdam 1 (2019) 167–204 (eBook ISBN: 9780128147917)

# Journal Papers

# Clathrate hydrates in interstellar environment

Jyotirmoy Ghosh<sup>a</sup>, Rabin Rajan J. Methikkalam<sup>a,1</sup>, Radha Gobinda Bhui<sup>a,2</sup>, Gopi Ragupathy<sup>a</sup>, Nilesh Choudhary<sup>b</sup>, Rajnish Kumar<sup>b,3</sup>, and Thalappil Pradeep<sup>a,3</sup>

<sup>a</sup>Department of Science and Technology (DST) Unit of Nanoscience and Thematic Unit of Excellence (TUE), Department of Chemistry, Indian Institute of Technology Madras, Chennai 600036, India; and <sup>b</sup>Department of Chemical Engineering, Indian Institute of Technology Madras, Chennai 600036, India

Edited by Francois Forget, Laboratoire de Météorologie Dynamique, Paris, France, and accepted by Editorial Board Member Jean Jouzel December 10, 2018 (received for review August 18, 2018)

Clathrate hydrates (CHs) are ubiquitous in earth under high-pressure conditions, but their existence in the interstellar medium (ISM) remains unknown. Here, we report experimental observations of the formation of methane and carbon dioxide hydrates in an environment analogous to ISM. Thermal treatment of solid methane and carbon dioxide–water mixture in ultrahigh vacuum of the order of  $10^{-10}$  mbar for extended periods led to the formation of CHs at 30 and 10 K, respectively. High molecular mobility and H bonding play important roles in the entrapment of gases in the in situ formed 5<sup>12</sup> CH cages. This finding implies that CHs can exist in extreme low-pressure environments present in the ISM. These hydrates in ISM, subjected to various chemical processes, may act as sources for relevant prebiotic molecules.

clathrate hydrate | interstellar medium | ISM | ultra-high vacuum | amorphous solid water

Clathrate hydrates (CHs) are crystalline inclusion compounds in which different guest molecules are encased in H-bonded water cages (1). These trapped molecules are generally small such as CH<sub>4</sub>, CO<sub>2</sub>, N<sub>2</sub>, H<sub>2</sub>, etc. Among several such known CHs, those of CH<sub>4</sub> and CO<sub>2</sub> have drawn close attention of the scientific community due to their use as potential future source of energy (1, 2) and in CO<sub>2</sub> sequestration (3), respectively. Natural methane and carbon dioxide hydrates are found in permafrost and marine sediments on the outer continental shelves (4) at ambient temperatures (<300 K) and moderately high pressures (6 atm) (1). They could also exist in many solar system bodies such as in the Martian permafrost (5–7), on the surface of Titan (8), and on other icy satellites due to the prevalent thermodynamic (high P, low T) conditions (9). The stabilizing conditions (generally high pressures) of methane hydrate suggest that it is nonexistent in ultrahigh vacuum (UHV). Near zero diffusion prevents molecular rearrangements at cryogenic conditions, making the formation of cage structures impossible for water at interstellar temperatures. Therefore, it is not surprising that there is no report of its existence in conditions of relevance to space. Using thermodynamic data of methane hydrate available in the literature, its stability was extrapolated to low T, P region as shown (*SI Appendix*, Fig. S1), which suggests stability up to  $2 \times 10^{-6}$  mbar at 30 K. This temperature and pressure range is very close to nebular pressures, which could reach as high as  $10^{-3}$  mbar, and the temperature range can vary from 4 to 100 K (9). Equilibrium condensation curve of methane hydrate in protostellar nebula also suggests its stability  $\sim 1 \times 10^{-8}$  mbar at 45 K (10).

Experimentally, in situ formation of CHs in UHV, and cryogenic interstellar conditions has not been explored. However, it was proposed that at low pressure, CH may be grown epitaxially on other preformed CHs or by annealing the condensed gas–water mixture (11). CH of CO<sub>2</sub> was obtained in a vacuum of  $10^{-6}$  torr, but at 120 K (12). We have adopted the annealing method to obtain CHs. In experiments conducted in the temperature window of 10–160 K and at  $10^{-10}$  mbar pressure, we observed CH<sub>4</sub> and CO<sub>2</sub> hydrates at temperatures near 30 and 10 K, respectively. Molecular mobility and structural rearrangement observed in these experiments at cryogenic conditions suggest unusual processes in water. The anomalous eruption of CH<sub>4</sub>,

CO<sub>2</sub>, or other volatile gases in cold interstellar clouds or in comets could possibly be explained by the existence of such hydrates in gas-forming regions of the interstellar space (10, 12). Irradiation or annealing leads to the chemical evolution of ice in ISM, forming new species (13). CHs could be one such new chemical system in the ISM, which may be subjected to additional processing.

## Results and Discussion

Fig. 14 displays time-dependent reflection absorption infrared (RAIR) spectra of 300 monolayers (MLs; 1 monolayer is equivalent to  $\sim 1.0 \times 10^{15}$  molecules  $\cdot$  cm<sup>-2</sup>) of a codeposited mixture (1:1) of CH<sub>4</sub> and water at the C–H antisymmetric stretching region at three different temperatures (10, 20, and 30 K) and two different annealing times (0 and 25 h) under UHV. The annealing time is crucial for the success of the experiment. The figure clearly shows no change in peak position for the C–H antisymmetric stretching band of solid CH<sub>4</sub> (3,009 cm<sup>-1</sup>) with time, at 10 and 20 K. This peak is due to the untrapped CH<sub>4</sub>; in other words, CH<sub>4</sub> hydrate was not observed at 10 and 20 K. A completely new IR peak (3,017 cm<sup>-1</sup>) appears alongside the peak at 3,009 cm<sup>-1</sup> after 25 h of annealing at 30 K. This new peak (3,017 cm<sup>-1</sup>) is attributed to the CH<sub>4</sub> hydrate, where CH<sub>4</sub> is trapped in the CH cage. The rest of the untrapped CH<sub>4</sub> remained in the pores of amorphous ice. The experimental blue shift of 8 cm<sup>-1</sup> is due to the entrapment of CH<sub>4</sub> in the hydrate cage. Here, the trapped CH<sub>4</sub> inside the CH cage behaves more

## Significance

Formation of clathrate hydrate (CH) requires high pressures and moderate temperatures, which enable their existence in marine sediments and the permafrost region of earth. The presence of CHs in interstellar medium (ISM) is still in question due to the extreme high vacuum and ultracold conditions present there. Here, we conclusively identified methane and carbon dioxide hydrates in conditions analogous to ISM. We found that molecular mobility and interactions play crucial roles in the formation of CHs, even though there is no external pressure to force cage formation. Various chemical processes on these hydrates in ISM may lead to relevant prebiotic molecules.

Author contributions: J.G. and T.P. designed research; J.G. and R.R.J.M. performed research; J.G., R.R.J.M., and T.P. contributed new reagents/analytic tools; J.G., R.R.J.M., R.G.B., G.R., N.C., R.K., and T.P. analyzed data; and J.G., R.R.J.M., R.G.B., G.R., R.K., and T.P. wrote the paper.

The authors declare no conflict of interest.

This article is a PNAS Direct Submission. F.F. is a guest editor invited by the Editorial Board.

This open access article is distributed under [Creative Commons Attribution-NonCommercial-NoDerivatives License 4.0 \(CC BY-NC-ND\)](#).

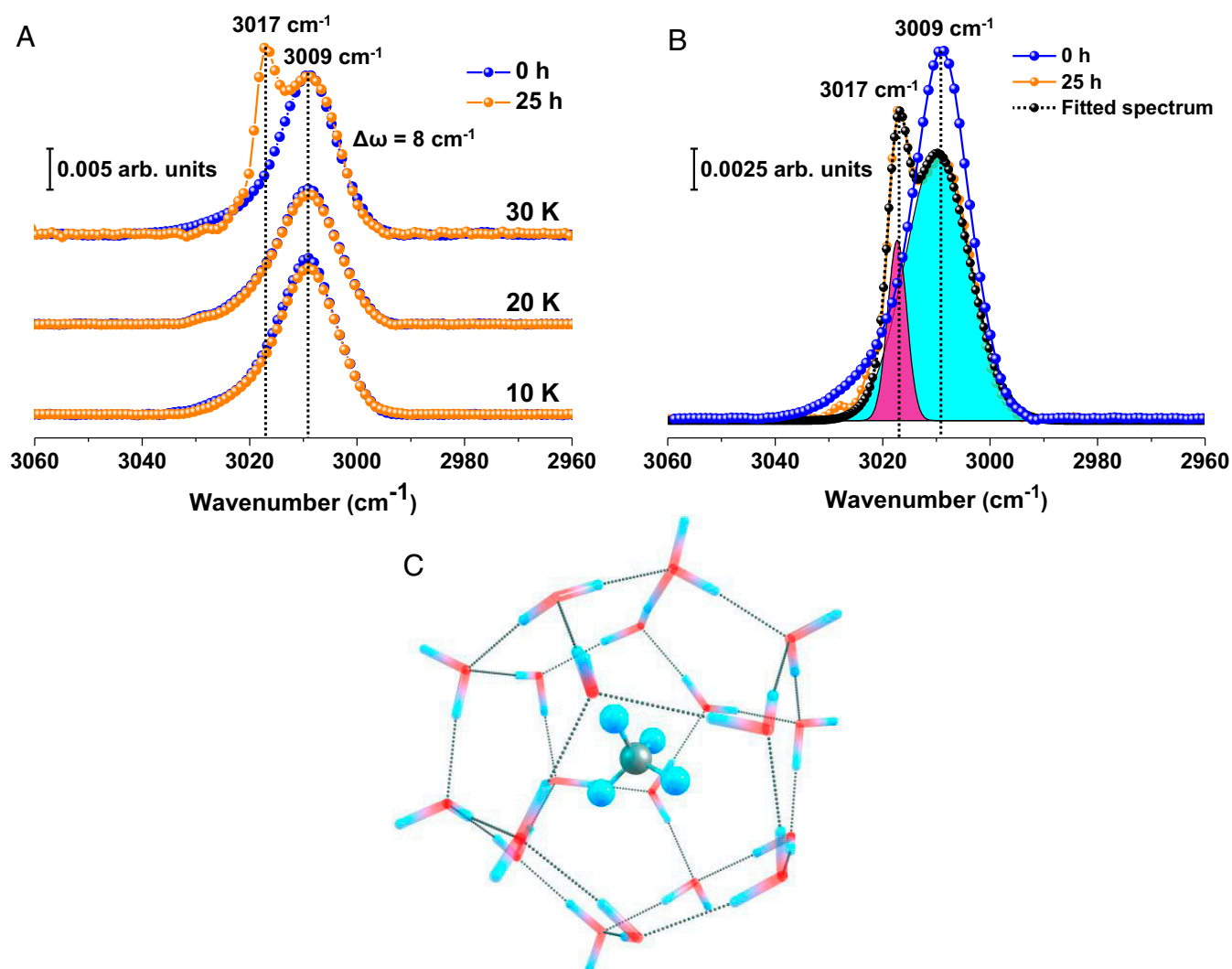
<sup>1</sup>Present address: Institute of Chemistry, The Hebrew University, Jerusalem 91904, Israel.

<sup>2</sup>Present address: Lehrstuhl für Physikalische Chemie II, Friedrich-Alexander-Universität Erlangen-Nürnberg, 91058 Erlangen, Germany.

<sup>3</sup>To whom correspondence may be addressed. Email: rajnish@iitm.ac.in or pradeep@iitm.ac.in.

This article contains supporting information online at [www.pnas.org/lookup/suppl/doi:10.1073/pnas.1814293116/-DCSupplemental](http://www.pnas.org/lookup/suppl/doi:10.1073/pnas.1814293116/-DCSupplemental).





**Fig. 1.** CH<sub>4</sub> hydrate formation as studied by RAIR spectroscopy and quantum chemical calculations. (A) Normalized time-dependent RAIR spectra of 300 MLs CH<sub>4</sub>+H<sub>2</sub>O (1:1) mixed ice at 10, 20, and 30 K at the C–H antisymmetric stretching region. (B) Time-dependent RAIR spectra of the same system at 30 K. Here, the blue trace was divided by a factor of 7 to match the intensity of orange trace. Difference in intensity is due to desorption of CH<sub>4</sub> at 30 K, near its desorption temperature. Deconvoluted IR peaks are shown by cyan (3,009 cm<sup>-1</sup>) and pink shade (3,017 cm<sup>-1</sup>). (C) DFT-optimized structure of CH<sub>4</sub> trapped within CH (5<sup>12</sup> cage). Here, water cage and guest molecule (CH<sub>4</sub>) are shown. Color code used: gray, C; red, O; cyan, H.

like gaseous CH<sub>4</sub> as expected. It is known that vibrational frequency of free guest molecules in CH fall in between their vapor and condensed phase frequencies (14). The IR peak was deconvoluted to show the actual concentration of CH<sub>4</sub> trapped inside the hydrate cages and pores of amorphous solid water (ASW). The peak widths were calculated upon deconvolution, and the values were 14.1 and 4.2 cm<sup>-1</sup> for the peaks at 3,009 and 3,017 cm<sup>-1</sup>, respectively. Note the reduced width (4.2) of 3,017 cm<sup>-1</sup> for the hydrate peak, characteristic of a unique structure. Taking the IR intensity, the extent of CH<sub>4</sub> in the hydrate form was estimated to be 12.71% of the total CH<sub>4</sub> at this condition. As the annealing temperature is close to that of desorption, about 6/7 of the adsorbed CH<sub>4</sub> desorbs during annealing. Furthermore, we confirmed the formation of CH<sub>4</sub> hydrate by quantum chemical calculations. Density functional theory (DFT) calculations of the CH<sub>4</sub> hydrate revealed that the small cage (5<sup>12</sup>) as shown in Fig. 1C is favorable to form at this particular condition. Our computationally determined shift in the C–H antisymmetric mode during hydrate formation closely matches with the experimental value (*SI Appendix, Table S1*). A microsecond molecular dynamics simulation of CH<sub>4</sub> hydrate nucleation

predicts preferential formation of smaller 5<sup>12</sup> cages in the initial stages of CH<sub>4</sub> hydrate nucleation, supporting our observation (2).

Keeping the CH<sub>4</sub> and water ice mixture at 30 K for more than 25 h results in the formation of CH<sub>4</sub> hydrate. The long experimental time scale and the temperature (30 K), very near to the desorption temperature of CH<sub>4</sub>, are two crucial factors for the formation of CH<sub>4</sub> hydrate under UHV conditions. We propose that prolonged subjugation of CH<sub>4</sub>–water mixture at 30 K enhances the mobility of CH<sub>4</sub> molecules and leads to its insertion within the cages formed simultaneously. In a time-dependent study of 150 MLs of pure solid CH<sub>4</sub> at 25 K (*SI Appendix, Fig. S2*), the additional peak (3,017 cm<sup>-1</sup>) was not observed. This is again a piece of evidence that the above peak is due to CH<sub>4</sub> hydrate.

To support our claim of the formation of CH in ISM, we have chosen a more stable hydrate, namely that of CO<sub>2</sub>, which is already known to form CH at 120 K and 10<sup>-6</sup> torr (12). Fig. 2A represents the temperature-dependent RAIR spectra of 300 MLs of the codeposited mixture (1:5 ratio) of CO<sub>2</sub> and water in the C = O antisymmetric stretching region. The figure shows two IR peaks for the C = O antisymmetric stretching band of solid CO<sub>2</sub> at 10 K. The peak at 2,353 cm<sup>-1</sup> is attributed to the untrapped CO<sub>2</sub> that exists





molecular volcano (MV) (18, 19). The intensity of MV peak (at 140 K) increases, upon the formation of CH<sub>4</sub> hydrate. Before the formation of CH<sub>4</sub> hydrate, the MV peak is due to the trapped CH<sub>4</sub> in ASW. The reason for the enhancement of MV peak intensity is the simultaneous release of trapped CH<sub>4</sub> from ASW pores as well as from the CH<sub>4</sub> hydrate cage (Fig. 3C). Note that the amount of gases deposited is the same in both the cases. Slight distortion in the MV peak is attributed to the modification of ASW pores due to CH formation (Fig. 3A). The amount of desorption due to CH is estimated to be 14.53% of the total CH<sub>4</sub> at this condition, and it is correlated to the amount of CH calculated from the IR data (Fig. 1B).

In Fig. 3B, we compared the TPD spectra of 300 MLs of CO<sub>2</sub>+H<sub>2</sub>O at two ratios, 1:1 and 1:5, which were deposited at 10 K. Then, these two systems were annealed at 120 K for the complete formation of CO<sub>2</sub> hydrate. After that, they were cooled back to 10 K, and TPD mass spectra were taken. The heating rate for TPD was 30 K · min<sup>-1</sup>. The peak at 140 K corresponds to MV of CO<sub>2</sub>. Fig. 3B shows that the intensity of MV increased as the ratio of CO<sub>2</sub> and H<sub>2</sub>O was changed from 1:1 to 1:5. Taking the area under the MV peaks, the amount of CH formed was found 1.7 times higher for (1:5) than the former. As previously explained, the extent of formation of CO<sub>2</sub> hydrate is greater for the latter ratio (Fig. 2). Here again, the enhancement agrees with the IR data. No additional desorption of CH<sub>4</sub> and CO<sub>2</sub> above this temperature suggest that the hydrates have been decomposed.

## Conclusion

We have shown that CHs can form in UHV and they can exist in the ISM conditions down to 10 K and 10<sup>-10</sup> mbar. The anomalous eruption of volatile gases in ISM could be explained by the existence of hydrates. Enclathration of these gases and additional processing (e.g., irradiation, heating, etc.) may result in complex organic or prebiotic molecules. We believe that the present report may have an impact on both astronomy and chemistry.

## Materials and Methods

**Experimental Setup.** Experiments were conducted in an ultrahigh vacuum instrument (base pressure ~10<sup>-10</sup> mbar), which was described elsewhere (20, 21). Briefly, the instrument consists of a UHV chamber made of stainless steel, equipped with RAIR spectroscopy and TPD mass spectrometry. The spectrometer can also perform low energy ion scattering and secondary ion mass spectrometry, which have not been used in the present work (20). Vacuum of the order of ~10<sup>-10</sup> mbar is an essential condition for simulating the condition of ISM. Vacuum was maintained by three oil-free Turbo molecular pumps backed by diaphragm pumps (Pfeiffer Vacuum). The system has a collective pumping speed of ~400 L/s. The UHV system is fully covered with a heating jacket, which allows an easy bake out over the weekend. The pressure of the experimental chamber is monitored by a Bayard-Alpert gauge (Pfeiffer Vacuum), controlled by a "MaxiGauge" vacuum gauge controller (Pfeiffer, Model TPG 256 A).

A thin film of ice was grown on top of a Ru(0001) single crystal that was mounted on a copper holder, which in turn was attached at the tip of a closed cycle helium cryostat (Coldedge Technologies). The substrate temperature could be controlled from 8 to 1,000 K. Comprehensive heat shielding and excellent thermal contact between the substrate holder and the cryofinger allowed us to achieve 8 K in 2 h. For the present study, the temperature was measured by a thermocouple sensor attached to the substrate. Repeated heating to 300 K before vapor deposition ensured surface cleanliness, adequate for the present experiments. Temperature ramping was controlled and monitored by a temperature controller (Lakeshore 336) (20).

**Sample Preparation.** For the formation of methane hydrate, ~99.99% pure methane gas, purchased from Rana Industrial Gases & Products, was used. The gas lines were connected to the experimental chamber through a high-precision all-metal leak valve through which the flow rate or deposition pressure of different gases was controlled. These two deposition tubes or gas lines were directed to the center of the substrate. Out of the two sample inlet lines, one was used exclusively for methane or carbon dioxide while the

other line was used exclusively for water vapor deposition. Here, Millipore water (H<sub>2</sub>O of 18.2 MΩ resistivity), taken in a test tube, connected to the sample line through a glass-to-metal seal was used for the experiment. The Millipore water was further purified through several freeze–pump–thaw cycles before introduction into the UHV chamber. During the exposure of different samples into the UHV chamber, mass spectra were recorded with a residual gas analyzer (RGA) attached near to the sample inlet line. Recorded mass spectra were used as an indication of the purity of the samples as well as to measure the ratio of the mixtures. The ratio of the mixed ice was achieved by the proper adjustment of flow or inlet pressure of the sample gas by regulating the leak valves. The substrate was kept at a perpendicular position for the uniform growth of ice. Here, most of the experiments were performed using 300 MLs coverage of the mixed ice. One point to be noted is that all of the experiments were performed under multilayer deposition conditions, and therefore, the substrate does not play any significant role in the formation of CH. The deposition of molecular solids was controlled through leak valves, and ML coverage was calculated (18, 22) assuming that  $1.33 \times 10^{-6}$  mbar · s = 1 ML, which was estimated to contain  $\sim 1.1 \times 10^{15}$  molecules · cm<sup>-2</sup>. Surface coverages mentioned were quantitative by following a similar deposition method adopted elsewhere (23). The inlet pressure during the sample deposition was decided based on the coverage desired at the time of the experiment.

**Typical Experimental Protocol.** For the deposition of 300 MLs of 1:1 mixed methane and ice, the chamber was backfilled at a total pressure of  $\sim 5 \times 10^{-7}$  mbar (where methane pressure was  $2.5 \times 10^{-7}$  mbar and water pressure was  $2.5 \times 10^{-7}$  mbar) and the mixture was exposed to the surface for 10 min. Evacuation of residual water from the experimental chamber is one of the most common issues with UHV experiments, particularly when we deposit large amounts of water. After deposition, we waited for a few minutes to reach the background pressure before starting the spectroscopic measurements. Periodic bake out of the chamber during weekends ensures the cleanliness of the chamber.

This 1:1 mixed methane and ice was slowly (heating rate = 2 K · min<sup>-1</sup>) heated to 30 K, near the desorption temperature of methane. At this temperature, most of the methane sublimed, which was observed in the mass spectra recorded by the residual gas analyzer. After that, the remaining mixed ice was maintained at 30 K for over 25 h. The ice sample was constantly monitored by IR spectroscopy. In other words, time-dependent RAIRS were recorded over a period of 25 h. During such measurements, a few monolayers of additional water could be deposited but this is rather negligible to be reflected in the spectra. Variation of a few monolayers in coverage does not change the observed phenomena. During the time-dependent measurements, we maintained identical conditions from the beginning to the end. The position of the substrate, the external IR detector (mercury cadmium telluride; MCT), and the environment (dry N<sub>2</sub>) in the IR spectrometer were kept constant throughout the experiment. A similar time-dependent RAIR study was carried out at 10 and 20 K also, and the spectra were collected for over 25 h as a separate set of experiments. IR exposure over extended periods did not have an effect on CH formation as revealed by studies at lower temperatures.

For the CO<sub>2</sub> hydrate study, 300 MLs of mixed ice was made by the codeposition of a mixture of CO<sub>2</sub>:H<sub>2</sub>O at 10 K. Different ratios (1:5, 1:10, and 1:90) of CO<sub>2</sub>:H<sub>2</sub>O were used. For each of the ratios, the total inlet pressure was kept at  $\sim 5 \times 10^{-7}$  mbar, whereas the inlet pressures of CO<sub>2</sub> and water were varied according to the desired ratio. For the temperature-dependent measurements, after deposition of 1:5 ratio of CO<sub>2</sub>:H<sub>2</sub>O at 10 K, the sample was slowly heated (heating rate = 2 K · min<sup>-1</sup>) up to 160 K. In another set of experiments, sequential deposition of CO<sub>2</sub> and water was carried out, where at first 150 MLs of CO<sub>2</sub> were deposited, which was followed by the deposition of 150 MLs of water at 10 K. By this way, we generated a sequentially deposited (CO<sub>2</sub>@H<sub>2</sub>O) film of equal coverage. A similar temperature-dependent IR study was carried out as described before, with this sequentially deposited film to observe the formation of CO<sub>2</sub> CH.

**RAIRS Setup.** RAIR spectra were recorded using a Bruker FT-IR spectrometer, Vertex 70. The external IR beam was focused onto the substrate using gold-plated mirrors through ZnSe windows (transparent to IR beam), attached to the vacuum chamber. The reflected IR beam from the substrate was refocused using another gold-plated mirror to a liquid N<sub>2</sub> cooled external MCT IR detector. The spectra were collected in the 4,000–550 cm<sup>-1</sup> range with 2 cm<sup>-1</sup> resolution. Each spectrum was an average of 512 scans to get a better signal-to-noise ratio. The IR beam path outside the UHV chamber was purged with dry N<sub>2</sub>.



**TPD-MS Setup.** The clathrate hydrates were further characterized by TPD-MS analysis. For this, after ice deposition or clathrate hydrate formation (by following the method described earlier), the substrate was moved to a fixed position by using the sample manipulator to ensure that the surface is close to the mass spectrometer inlet. During TPD-MS measurements, the substrate was heated at a constant heating rate ( $30 \text{ K} \cdot \text{min}^{-1}$ ). Suitable mass of the desorbed species was selected by the RGA and the intensity of the desorbed species was plotted as a function of substrate temperature. Mass spectrometers were supplied by Extrel CMS (20). For TPD, the inlet of the mass spectrometer was positioned 50 mm from the center of the Ru substrate.

**Computational Details.** We examined the stability of clathrate hydrate cages and their  $\text{CO}_2$ ,  $\text{CH}_4$  inclusion complexes computationally. All of the considered cages of clathrate hydrates have been fully optimized at the B3LYP/6-311++G (d, p) level of theory using the Gaussian 09 program package (24). Frequency calculations characterize the obtained stationary points as minima on the potential energy surface. We sequentially added  $\text{CO}_2$  and  $\text{CH}_4$  molecules in  $5^{12}$ ,  $5^{12}6^2$ , and  $5^{12}6^4$  clathrate hydrate cages and probed their

cage occupancy. In general, the optimizations of clathrate hydrate cages were found to be quite challenging with the Gaussian programs. Normally, most optimizations of clathrate cages take a large number of steps and it was difficult to reach convergence. The B3LYP/6-311++G (d, p) level of theory was found to be reasonable for optimizations of clathrate hydrates and various other water clusters (14). The quantum theory of atoms in molecules methodology (25) was capable of revealing bonding interactions between individual functional groups and atoms in a molecule by the electron density distribution analysis.

All possible cages were considered in the present study. It was found that the  $5^{12}$  clathrate hydrate cage was more stable; stability also depended on the size of the guest molecule. These results were also compared with the computational studies reported (14).

**ACKNOWLEDGMENTS.** J.G. thanks the University Grants Commission (UGC) for his research fellowship. We thank the Department of Science and Technology, Government of India, for supporting our research.

1. Sloan ED, Jr (2003) Fundamental principles and applications of natural gas hydrates. *Nature* 426:353–363.
2. Walsh MR, Koh CA, Sloan ED, Sum AK, Wu DT (2009) Microsecond simulations of spontaneous methane hydrate nucleation and growth. *Science* 326:1095–1098.
3. Park Y, et al. (2006) Sequestering carbon dioxide into complex structures of naturally occurring gas hydrates. *Proc Natl Acad Sci USA* 103:12690–12694.
4. Boswell R (2009) Engineering. Is gas hydrate energy within reach? *Science* 325: 957–958.
5. Chastain BK, Chevrier V (2007) Methane clathrate hydrates as a potential source for martian atmospheric methane. *Planet Space Sci* 55:1246–1256.
6. Swindle TD, Thomas C, Mousis O, Lunine JI, Picaud S (2009) Incorporation of argon, krypton and xenon into clathrates on Mars. *Icarus* 203:66–70.
7. Thomas C, Mousis O, Picaud S, Ballenegger V (2009) Variability of the methane trapping in martian subsurface clathrate hydrates. *Planet Space Sci* 57:42–47.
8. Tobie G, Lunine JI, Sotin C (2006) Episodic outgassing as the origin of atmospheric methane on Titan. *Nature* 440:61–64.
9. Mousis O, Lunine JI, Picaud S, Cordier D (2010) Volatile inventories in clathrate hydrates formed in the primordial nebula. *Faraday Discuss* 147:509–525, 527–552.
10. Luspai-Kuti A, et al. (2016) The presence of clathrates in comet 67P/Churyumov-Gerasimenko. *Sci Adv* 2:e1501781.
11. Mao WL, et al. (2002) Hydrogen clusters in clathrate hydrate. *Science* 297:2247–2249.
12. Blake D, Allamandola L, Sandford S, Hudgins D, Freund F (1991) Clathrate hydrate formation in amorphous cometary ice analogs in vacuo. *Science* 254:548–551.
13. Allamandola LJ, Bernstein MP, Sandford SA, Walker RL (1999) Evolution of interstellar ices. *Space Sci Rev* 90:219–232.
14. Buch V, et al. (2009) Clathrate hydrates with hydrogen-bonding guests. *Phys Chem Chem Phys* 11:10245–10265.
15. Fleyfel F, Devlin JP (1991) Carbon dioxide clathrate hydrate epitaxial growth: Spectroscopic evidence for formation of the simple type-II carbon dioxide hydrate. *J Phys Chem* 95:3811–3815.
16. Kumar R, Lang S, Englezos P, Ripmeester J (2009) Application of the ATR-IR spectroscopic technique to the characterization of hydrates formed by  $\text{CO}_2$ ,  $\text{CO}_2/\text{H}_2\text{O}$  and  $\text{CO}_2/\text{H}_2\text{O}/\text{C}_3\text{H}_8$ . *J Phys Chem A* 113:6308–6313.
17. Warrier P, Khan MN, Srivastava V, Maupin CM, Koh CA (2016) Overview: Nucleation of clathrate hydrates. *J Chem Phys* 145:211705.
18. Ghosh J, Hariharan AK, Bhui RG, Methikkalam RRR, Pradeep T (2018) Propane and propane-water interactions: A study at cryogenic temperatures. *Phys Chem Chem Phys* 20:1838–1847.
19. Smith RS, Petrik NG, Kimmel GA, Kay BD (2012) Thermal and nonthermal physicochemical processes in nanoscale films of amorphous solid water. *Acc Chem Res* 45: 33–42.
20. Bag S, et al. (2014) Development of ultralow energy (1–10 eV) ion scattering spectrometry coupled with reflection absorption infrared spectroscopy and temperature programmed desorption for the investigation of molecular solids. *Rev Sci Instrum* 85: 014103.
21. Bhui RG, Methikkalam RRR, Sivaraman B, Pradeep T (2015) Interaction of acetonitrile with water-ice: An infrared spectroscopic study. *J Phys Chem C* 119:11524–11532.
22. Eui-Seong M, Heon K, Yasuhiro O, Naoki W, Akira K (2010) Direct evidence for ammonium ion formation in ice through ultraviolet-induced acid-base reaction of  $\text{NH}_3$  with  $\text{H}_3\text{O}^+$ . *Astrophys J* 713:906–911.
23. Kimmel GA, Petrik NG, Dohnálek Z, Kay BD (2005) Crystalline ice growth on PT(111): Observation of a hydrophobic water monolayer. *Phys Rev Lett* 95:166102.
24. Frisch MJ, et al. (2009) *Gaussian 09, Revision A.1* (Gaussian, Inc., Wallingford, CT).
25. Bader RFW (1990) *Atoms in Molecules. A Quantum Theory* (Oxford Univ Press, Oxford).



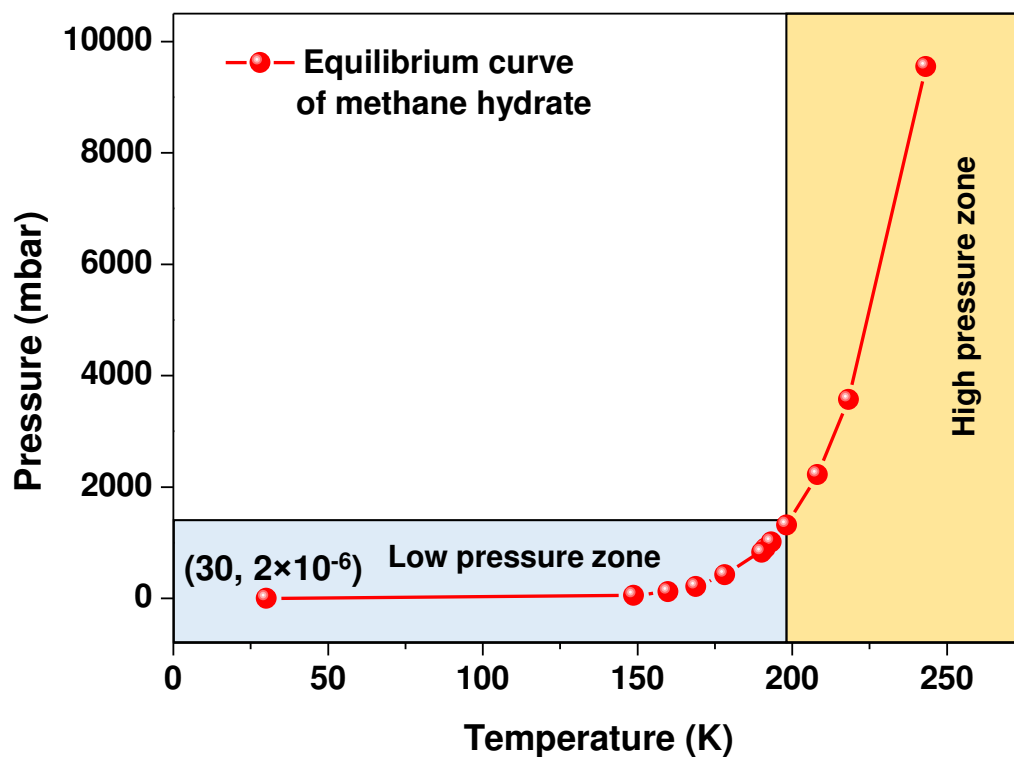
Supplementary Information for  
Clathrate hydrates in interstellar environment

Jyotirmoy Ghosh<sup>a</sup>, Rabin Rajan J. Methikkalam<sup>a</sup>, Radha Gobinda Bhuin<sup>a</sup>, Gopi  
Ragupathy<sup>a</sup>, Nilesh Choudhary<sup>b</sup>, Rajnish Kumar<sup>b,1</sup>, Thalappil Pradeep<sup>a,1</sup>

Corresponding author: Thalappil Pradeep and Rajnish Kumar  
Email: [pradeep@iitm.ac.in](mailto:pradeep@iitm.ac.in), and [rajnish@iitm.ac.in](mailto:rajnish@iitm.ac.in)

**This PDF file includes:**

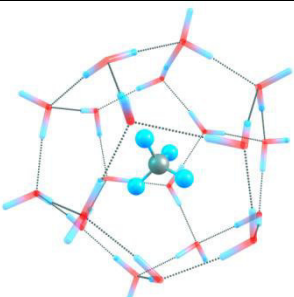
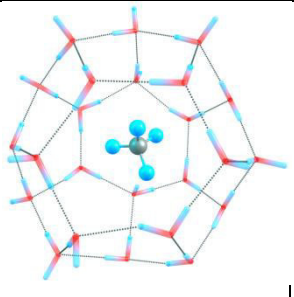
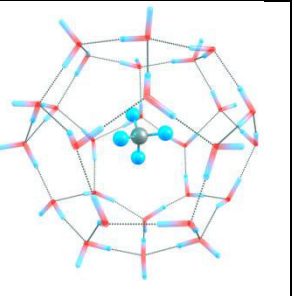
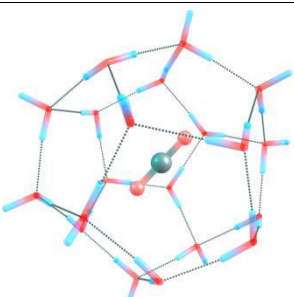
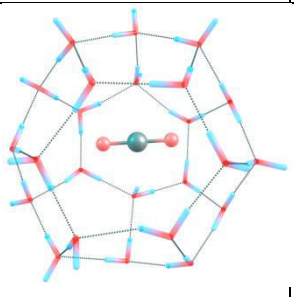
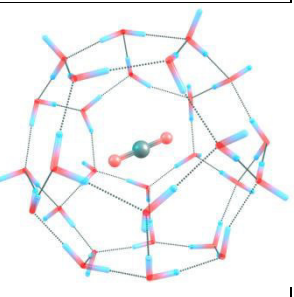
Supplementary text  
Figs. S1 to S6  
Tables S1 to S4



**Fig. S1.** Equilibrium curve for CH<sub>4</sub> clathrate hydrate. The curve depicts the stability of CH<sub>4</sub> clathrate hydrate as a function of temperature and pressure. Extrapolation of the curve to 30 K, denotes that CH<sub>4</sub> hydrate could be stable up to 2×10<sup>-6</sup> mbar pressure. Two different pressure zones of the equilibrium curve are indicated with different colours.

**Table S1**

Comparison of the computational and experimental vibrational shift of CH<sub>4</sub> and CO<sub>2</sub> clathrate hydrate compared to free CH<sub>4</sub> and CO<sub>2</sub> using the B3LYP level of theory with 6-311++G (d, p) basis set. Optimized structures are shown.

	<b>5<sup>12</sup> cage</b>	<b>5<sup>12</sup> 6<sup>2</sup> cage</b>	<b>5<sup>12</sup> 6<sup>4</sup> cage</b>
<b>CH<sub>4</sub> Clathrate hydrate</b>			
<b>Experimental shift</b>	8.0 cm <sup>-1</sup>	-	-
<b>Computational shift</b>	9.3 cm <sup>-1</sup>	-9.2 cm <sup>-1</sup>	-9.1 cm <sup>-1</sup>
<b>CO<sub>2</sub> Clathrate hydrate</b>			
<b>Experimental shift</b>	-36.0 cm <sup>-1</sup>	-	-
<b>Computational al shift</b>	-86.0 cm <sup>-1</sup>	-16.6 cm <sup>-1</sup>	15.8 cm <sup>-1</sup>



**Table S2**

Cartesian coordinates of CH<sub>4</sub> and CO<sub>2</sub> hydrate of 5<sup>12</sup>, 5<sup>12</sup>6<sup>2</sup>, and 5<sup>12</sup>6<sup>4</sup> cages. The structure is optimized by using B3LYP level of theory and 6-311G (d, p) basis set.

**1. Cartesian coordinates of CH<sub>4</sub> hydrate, 5<sup>12</sup> Cage:**

O	-3.113799000	1.008215000	-2.047060000
H	-2.381895000	0.992378000	-2.714133000
H	-3.218239000	0.092361000	-1.737059000
O	0.761157000	-0.854957000	3.737123000
H	1.560278000	-0.913295000	3.191474000
H	0.148218000	-1.525272000	3.382112000
O	-1.002868000	0.947991000	-3.756640000
H	-0.309583000	1.569863000	-3.462264000
H	-0.578668000	0.068649000	-3.767502000
O	3.236217000	-0.955734000	2.135120000
H	3.165067000	-1.629113000	1.426215000
H	3.958821000	-1.235974000	2.706513000
O	-2.887629000	1.244738000	2.323347000
H	-2.864259000	1.802526000	1.528887000
H	-2.060639000	1.440855000	2.816443000
O	3.377885000	1.359687000	-1.664637000
H	3.390890000	1.479109000	-0.669870000
H	4.148373000	1.829781000	-2.000028000
O	-3.128400000	-1.415490000	1.789380000
H	-3.087569000	-0.450695000	2.003609000
H	-3.283298000	-1.476211000	0.831714000

O	2.934977000	-1.253851000	-2.282868000
H	3.114524000	-0.298037000	-2.098165000
H	3.468989000	-1.484359000	-3.050455000
O	-0.392260000	3.941626000	-0.321881000
H	-1.300177000	3.541485000	-0.260272000
H	-0.524169000	4.853345000	-0.602208000
O	-1.315789000	-3.368020000	-1.793775000
H	-0.766874000	-3.555981000	-0.981288000
H	-1.479818000	-4.222051000	-2.206772000
O	1.274060000	3.320629000	1.800109000
H	0.676657000	3.585035000	1.064246000
H	1.488010000	4.128382000	2.278270000
O	0.169003000	-3.814487000	0.364703000
H	-0.238946000	-3.488499000	1.197401000
H	1.064810000	-3.442266000	0.323879000
O	-2.826177000	2.787763000	-0.173036000
H	-2.934327000	2.091445000	-0.898850000
H	-3.618404000	3.333407000	-0.214224000
O	-1.055651000	-2.776069000	2.622687000
H	-1.388378000	-3.388609000	3.286796000
H	-1.855960000	-2.248031000	2.311115000
O	0.248875000	-1.605446000	-3.500857000
H	-0.291977000	-2.196372000	-2.949011000
H	1.080021000	-1.487073000	-3.016487000
O	3.377580000	1.642717000	0.955655000

H	3.325899000	0.801116000	1.444402000
H	2.669365000	2.221709000	1.300892000
O	2.888590000	-2.759494000	0.015226000
H	3.477233000	-3.513445000	-0.097366000
H	2.928022000	-2.253620000	-0.830955000
O	0.935500000	2.696090000	-2.620765000
H	1.742558000	2.253160000	-2.312497000
H	0.528794000	3.081979000	-1.827324000
O	-0.442940000	1.678091000	3.581632000
H	-0.011264000	0.807131000	3.705067000
H	0.163645000	2.190341000	3.026261000
O	-3.430939000	-1.707732000	-1.081963000
H	-2.720572000	-2.319774000	-1.376262000
H	-4.261351000	-2.100719000	-1.369631000
C	0.021699000	0.014389000	-0.004436000
H	0.102928000	-1.071075000	-0.064084000
H	-0.278043000	0.408448000	-0.974906000
H	0.984345000	0.437479000	0.283329000
H	-0.722369000	0.274011000	0.747594000

**2. Cartesian coordinates of CO<sub>2</sub> hydrate, 5<sup>12</sup> Cage:**

O	-0.868021000	3.588583000	-1.062084000
H	0.066218000	3.438070000	-1.408937000
H	-1.430117000	2.919226000	-1.508264000
O	-1.706223000	-2.946539000	2.022264000
H	-0.770471000	-3.035377000	1.755662000

H	-2.171975000	-2.696231000	1.191943000
O	1.596326000	3.122198000	-1.934612000
H	2.186276000	2.918271000	-1.169796000
H	1.624434000	2.318089000	-2.504875000
O	1.040272000	-3.445759000	1.251327000
H	1.080443000	-3.488309000	0.263060000
H	1.111111000	-4.360300000	1.563830000
O	-3.071044000	1.240215000	2.040835000
H	-2.352366000	1.862651000	1.806185000
H	-2.630359000	0.554553000	2.609979000
O	3.820642000	-0.340356000	0.262704000
H	3.423565000	-0.820900000	1.074377000
H	4.775571000	-0.307884000	0.426195000
O	-3.889176000	0.127430000	-0.240429000
H	-3.634618000	0.543466000	0.638883000
H	-3.459546000	0.689488000	-0.919834000
O	2.916361000	-1.388227000	-1.994854000
H	3.314869000	-1.004684000	-1.156094000
H	3.642988000	-1.470212000	-2.630746000
O	1.299069000	2.625576000	2.498043000
H	0.400986000	2.879855000	2.108578000
H	1.586053000	3.384128000	3.028280000
O	-1.096637000	-0.132027000	-3.637858000
H	-1.187205000	-1.051178000	-3.209203000
H	-1.310462000	-0.266456000	-4.573538000

O	1.098934000	0.151735000	3.562278000
H	1.180338000	1.088266000	3.236013000
H	1.116802000	0.201161000	4.529891000
O	-1.340796000	-2.497246000	-2.570136000
H	-1.970098000	-2.436408000	-1.803130000
H	-0.489404000	-2.775385000	-2.172927000
O	-1.038061000	3.174905000	1.441572000
H	-0.949613000	3.321711000	0.415082000
H	-1.488139000	3.970026000	1.766134000
O	-2.952018000	-2.254904000	-0.391508000
H	-3.755968000	-2.794278000	-0.446434000
H	-3.300324000	-1.285945000	-0.316151000
O	1.592742000	0.749874000	-3.423629000
H	0.652483000	0.484801000	-3.511696000
H	1.982256000	0.062811000	-2.849519000
O	2.838088000	-1.586054000	2.308754000
H	2.226577000	-2.283377000	1.979844000
H	2.258337000	-0.965752000	2.813275000
O	1.168056000	-3.356005000	-1.486938000
H	1.409354000	-4.148468000	-1.990155000
H	1.850759000	-2.664779000	-1.716536000
O	3.117526000	2.443550000	0.301684000
H	3.315088000	1.486219000	0.258949000
H	2.488449000	2.526490000	1.047734000
O	-1.694213000	-0.618757000	3.500779000

H	-1.766148000	-1.490403000	3.035732000
H	-0.754396000	-0.372599000	3.401749000
O	-2.559414000	1.650173000	-2.227732000
H	-2.050242000	1.012432000	-2.796781000
H	-3.187348000	2.092683000	-2.818208000
C	-0.236975000	-0.022832000	-0.055102000
O	0.569452115	0.641156553	0.470020419
O	-1.043403816	-0.686813492	-0.580231437

### 3. Cartesian coordinates of CH<sub>4</sub> hydrate, 5<sup>12</sup>6<sup>2</sup> Cage:

O	-1.670912000	-4.226009000	-1.082352000
H	-2.375524000	-3.766957000	-0.603643000
H	-2.959334000	-2.320575000	1.911485000
O	3.529092000	2.803767000	1.029338000
H	-1.351771000	-3.578305000	-1.739442000
H	-2.569391000	-2.645506000	3.386338000
O	-3.825508000	-2.802754000	0.442226000
H	2.929516000	3.374599000	0.509101000
H	-5.468080000	-0.476336000	-1.297831000
O	1.675003000	4.357287000	-0.462631000
H	4.288235000	3.348667000	1.261625000
H	-4.426153000	0.220910000	-0.353308000
O	4.139684000	-1.822405000	0.869087000
H	-4.547179000	-3.439336000	0.475345000
H	-0.981477000	5.165787000	1.386092000
O	-4.100843000	1.509095000	0.645082000

H	-4.152398000	-2.036879000	-0.088426000
H	-1.472644000	4.135872000	0.310204000
O	2.754696000	-3.524800000	-1.148957000
H	0.821835000	4.395381000	0.033043000
H	1.390268000	3.342589000	-2.065515000
O	-2.709958000	3.585579000	-0.704716000
H	1.911470000	5.272815000	-0.647189000
H	1.490020000	3.250005000	-3.612671000
O	-2.744559000	0.731707000	3.040679000
H	3.633583000	-1.680969000	1.697571000
H	-1.998216000	1.501647000	-2.910970000
O	2.229125000	1.390499000	3.194198000
H	4.929342000	-2.315907000	1.112625000
H	-0.744828000	2.479495000	-2.858839000
O	4.353905000	0.558668000	-0.693508000
H	-3.609881000	2.239531000	0.222207000
H	2.223599000	-1.362192000	-3.409527000
O	2.624222000	-1.238043000	3.147085000
H	-3.636143000	1.295966000	1.475066000
H	2.218476000	-2.751014000	-2.703744000
O	-2.471293000	-1.980180000	2.696660000
H	3.194764000	-2.945362000	-0.509959000
H	0.592452000	-4.140968000	1.200296000
O	-4.579206000	-0.571005000	-0.940033000
H	2.062654000	-3.995233000	-0.634114000

H	-0.123889000	-4.625560000	-0.086935000
O	-0.709102000	4.380655000	0.899103000
H	-2.306692000	3.123411000	-1.524305000
H	-0.341601000	-1.612857000	-1.657252000
O	1.122959000	2.810480000	-2.838108000
H	-3.333393000	4.233540000	-1.050255000
H	0.234227000	-2.116329000	-2.985975000
O	-1.711676000	2.439102000	-2.755956000
H	-2.632211000	-0.244876000	2.975008000
H	-1.137195000	1.788790000	3.046958000
O	1.802672000	-2.243961000	-3.435423000
H	-3.253054000	0.885301000	3.844124000
H	-0.512036000	3.000628000	2.303422000
O	0.726252000	-4.665817000	0.391856000
H	1.310371000	1.731422000	3.207575000
H	-1.890831000	-0.791522000	-3.007814000
O	-0.636408000	-1.982559000	-2.497875000
H	2.685233000	1.881333000	2.489575000
H	-3.256373000	-0.341073000	-2.411504000
O	-0.373664000	2.391835000	3.046281000
H	4.094280000	1.264692000	-0.082898000
H	3.437823000	0.428194000	-2.285335000
O	-2.577228000	-0.090461000	-3.057271000
H	4.324432000	-0.265563000	-0.174937000
H	2.208278000	1.072719000	-2.963687000



O	2.862669000	0.369477000	-3.074985000
H	2.459143000	-0.254212000	3.165096000
H	1.068282000	-2.297241000	2.811159000
O	0.330133000	-2.914756000	2.665132000
H	2.970538000	-1.460402000	4.017548000
H	-0.467690000	-2.376841000	2.566654000
C	0.273774000	0.028734000	0.124279000
H	0.247314000	-1.019981000	0.427699000
H	1.075606000	0.172601000	-0.600784000
H	0.463833000	0.641570000	1.005234000
H	-0.680662000	0.318927000	-0.319142000

**4. Cartesian coordinates of CO<sub>2</sub> hydrate, 5<sup>12</sup>6<sup>2</sup> Cage:**

O	0.924327000	-4.271216000	-1.002928000
H	0.117919000	-4.127666000	-0.489932000
H	-1.145871000	-3.412845000	2.055052000
O	1.485002000	4.299181000	0.902052000
H	0.860379000	-3.642443000	-1.746774000
H	-0.618827000	-3.437657000	3.517730000
O	-1.595810000	-4.312127000	0.612579000
H	0.666072000	4.439132000	0.389312000
H	-4.370677000	-3.460119000	-1.063668000
O	-0.918089000	4.510434000	-0.560126000
H	1.796279000	5.172287000	1.162723000
H	-3.810366000	-2.244442000	-0.248867000
O	4.556701000	0.834186000	0.836470000

H	-1.652190000	-5.271066000	0.548338000
H	-3.569920000	3.810540000	1.330457000
O	-4.208194000	-0.945854000	0.721561000
H	-2.330449000	-3.940048000	0.074625000
H	-3.476551000	2.664970000	0.268110000
O	4.397838000	-1.439490000	-1.099305000
H	-1.651706000	4.096084000	-0.048420000
H	-0.651556000	3.378515000	-2.082013000
O	-4.284931000	1.517126000	-0.702504000
H	-1.248593000	5.372562000	-0.835036000
H	-0.127150000	3.105896000	-3.524321000
O	-2.675457000	-0.783823000	3.139978000
H	4.061790000	0.682406000	1.669739000
H	-2.626512000	0.141540000	-2.931559000
O	1.151354000	2.440252000	3.109620000
H	5.486847000	0.891199000	1.077303000
H	-2.114796000	1.621420000	-2.927138000
O	3.371151000	2.829900000	-0.797838000
H	-4.228803000	-0.078109000	0.278439000
H	2.780148000	-0.049862000	-3.413861000
O	2.979907000	0.518745000	3.111220000
H	-3.690206000	-0.835611000	1.540206000
H	3.515440000	-1.175917000	-2.636865000
O	-0.922532000	-2.842374000	2.823957000
H	4.417246000	-0.686008000	-0.490709000

H	2.836439000	-3.029222000	1.236715000
O	-3.548801000	-3.024117000	-0.815092000
H	4.048153000	-2.189809000	-0.570516000
H	2.478621000	-3.804023000	-0.053318000
O	-2.939589000	3.282082000	0.828980000
H	-3.738088000	1.336909000	-1.540270000
H	0.214978000	-1.502215000	-2.331876000
O	-0.661011000	2.737727000	-2.811563000
H	-5.178640000	1.708922000	-1.006373000
H	1.478903000	-1.811849000	-3.163727000
O	-2.912810000	1.071654000	-2.832473000
H	-2.032597000	-1.525377000	3.089947000
H	-1.916372000	0.976551000	3.108154000
O	2.921256000	-1.013355000	-3.403145000
H	-3.242091000	-0.971337000	3.895796000
H	-2.023365000	2.277905000	2.276867000
O	3.230295000	-3.428795000	0.443017000
H	0.196768000	2.212985000	3.129825000
H	-1.449901000	-2.019742000	-3.321833000
O	0.597318000	-2.195804000	-2.880566000
H	1.263372000	3.081360000	2.389559000
H	-2.630423000	-2.186872000	-2.298298000
O	-1.584034000	1.889483000	3.046487000
H	2.792935000	3.329876000	-0.200309000
H	2.673902000	2.143459000	-2.325081000

O	-2.199404000	-1.565376000	-2.908164000
H	3.823983000	2.170298000	-0.243938000
H	1.275135000	1.685598000	-2.748633000
O	2.179542000	1.750217000	-3.075471000
H	2.283661000	1.230852000	3.111445000
H	2.254027000	-1.213976000	2.813420000
O	1.958656000	-2.131674000	2.702163000
H	3.379574000	0.547887000	3.986700000
H	0.998975000	-2.101258000	2.605737000
C	-0.299000000	-0.053692000	0.072084000
O	-0.825551000	1.023644000	-0.532867000
O	0.225129000	-1.130569000	0.675788000

**5. Cartesian coordinates of CH<sub>4</sub> hydrate, 5<sup>12</sup>6<sup>4</sup> Cage:**

O	-1.605874000	4.327345000	1.091007000
H	-0.654904000	4.407629000	0.894300000
H	4.240880000	0.680906000	-1.253611000
O	1.233495000	4.441217000	0.673175000
H	-2.034107000	4.065372000	0.259580000
H	4.480701000	-0.767814000	-0.759697000
O	-2.056668000	2.784311000	3.368236000
H	1.513626000	4.169658000	-0.214507000
H	-4.444734000	-1.192308000	0.417931000
O	2.705554000	2.928418000	2.718463000
H	1.691220000	3.853647000	1.294587000
H	-5.572570000	-0.294812000	0.990577000

O	-2.874993000	3.695924000	-1.473950000
H	-1.163278000	2.570836000	3.676758000
H	-0.987716000	-1.466298000	4.048379000
O	1.895069000	3.860804000	-2.103425000
H	-1.935305000	3.355548000	2.579668000
H	-2.409912000	-0.948528000	3.549798000
O	0.606333000	2.048822000	4.405162000
H	3.264189000	2.163176000	2.446792000
H	3.239813000	-0.849629000	2.774491000
O	-0.745370000	3.468092000	-3.305074000
H	3.315039000	3.605709000	3.030048000
H	2.884539000	-2.358665000	2.721381000
O	-3.398682000	0.421657000	3.080969000
H	-3.397667000	2.847257000	-1.548749000
H	-2.230601000	0.163339000	-3.940207000
O	4.219506000	0.756811000	1.990518000
H	-3.505033000	4.402630000	-1.648458000
H	-2.636723000	-1.076249000	-3.096173000
O	3.469582000	1.595749000	-2.799803000
H	2.467083000	3.109831000	-2.354693000
H	1.962820000	-1.149562000	-3.893241000
O	-4.257056000	1.444682000	-1.756283000
H	2.297519000	4.648681000	-2.483857000
H	1.918542000	-0.261234000	-5.175820000
O	0.544487000	-0.874416000	4.614731000

H	1.345024000	2.393503000	3.866115000
H	-3.187659000	-3.228967000	0.896130000
O	-0.772966000	1.018254000	-4.521579000
H	0.679144000	2.472813000	5.266724000
H	-4.566967000	-3.592812000	0.253793000
O	4.717913000	0.160548000	-0.585984000
H	0.076719000	3.653591000	-2.826103000
H	3.357457000	-2.718420000	-1.839087000
O	-4.722620000	-0.265511000	0.538887000
H	-1.473930000	3.594558000	-2.664691000
H	4.681411000	-3.205331000	-1.185147000
O	-1.875353000	-1.757685000	3.727678000
H	-2.966247000	1.303071000	3.182815000
H	-1.978711000	-2.837672000	2.753840000
O	2.935260000	-1.586080000	3.323035000
H	-3.668930000	0.363306000	2.154304000
H	-2.386425000	-4.376539000	2.643973000
O	-3.001014000	-0.299826000	-3.539573000
H	4.409631000	0.574759000	1.033410000
H	3.100205000	-3.264608000	0.596776000
O	1.933968000	-0.224859000	-4.213202000
H	5.044014000	0.597337000	2.462156000
H	1.901992000	-3.990620000	1.254997000
O	-3.826361000	-2.983336000	0.160478000
H	2.926743000	0.968464000	-3.326700000

H	-3.077576000	-3.004971000	-1.461877000
O	3.961160000	-2.573327000	-1.085948000
H	4.247552000	1.782165000	-3.337163000
H	-3.358176000	-3.237996000	-2.980485000
O	-2.118740000	-3.636620000	2.087794000
H	-3.869394000	0.835977000	-2.420132000
H	1.246287000	-3.243811000	-2.866705000
O	2.798806000	-3.643142000	1.434631000
H	-4.442885000	0.900718000	-0.973779000
H	2.359088000	-3.495501000	-3.917251000
O	-2.657193000	-3.031014000	-2.352912000
H	1.374381000	-1.190133000	4.201493000
H	0.053421000	-4.193386000	-0.205613000
O	2.086042000	-2.871771000	-3.234887000
H	0.583603000	0.093715000	4.565807000
H	-0.517509000	-4.176128000	1.229564000
O	0.223361000	-4.513301000	0.691120000
H	0.042339000	0.616402000	-4.196206000
H	-1.068476000	-3.680186000	-2.349020000
O	-0.160157000	-4.048155000	-2.215880000
H	-0.785060000	1.923773000	-4.127641000
H	-0.237369000	-4.999070000	-2.351085000
C	0.381333000	-0.246902000	-0.139731000
H	0.268241000	-1.056677000	-0.863370000
H	-0.540807000	-0.144842000	0.433693000

H	0.577766000	0.689340000	-0.663475000
---	-------------	-------------	--------------

H	1.199761000	-0.472262000	0.543971000
---	-------------	--------------	-------------

**6. Cartesian coordinates of CO<sub>2</sub> hydrate, 5<sup>12</sup>6<sup>4</sup> Cage:**

C	-0.550460000	0.498600000	-0.096952000
---	--------------	-------------	--------------

O	-1.145201000	-0.417503000	-0.484701000
---	--------------	--------------	--------------

O	0.040166000	1.425588000	0.290450000
---	-------------	-------------	-------------

O	1.082845000	-3.985558000	2.360476000
---	-------------	--------------	-------------

H	1.843465000	-3.387649000	2.473499000
---	-------------	--------------	-------------

H	3.328391000	2.699927000	1.002441000
---	-------------	-------------	-------------

O	3.323752000	-2.196294000	2.509719000
---	-------------	--------------	-------------

H	0.326129000	-3.543707000	2.778462000
---	-------------	--------------	-------------

H	3.035841000	3.327263000	-0.387179000
---	-------------	-------------	--------------

O	0.826312000	-4.812167000	-0.290227000
---	-------------	--------------	--------------

H	3.109558000	-1.345108000	2.921842000
---	-------------	--------------	-------------

H	-3.962353000	-2.146585000	-0.743573000
---	--------------	--------------	--------------

O	4.567539000	-1.785603000	-0.135342000
---	-------------	--------------	--------------

H	3.669184000	-1.996440000	1.626401000
---	-------------	--------------	-------------

H	-4.277706000	-3.636801000	-0.431233000
---	--------------	--------------	--------------

O	-1.139664000	-2.767234000	3.839162000
---	--------------	--------------	-------------

H	1.568986000	-4.376439000	-0.733826000
---	-------------	--------------	--------------

H	-0.025539000	-2.219308000	-3.812846000
---	--------------	--------------	--------------

O	2.639252000	0.163912000	4.067027000
---	-------------	-------------	-------------

H	0.906897000	-4.576584000	0.658940000
---	-------------	--------------	-------------

H	-1.112681000	-3.004221000	-2.955189000
---	--------------	--------------	--------------

O	3.030826000	-3.512784000	-1.778790000
---	-------------	--------------	--------------



H	4.581901000	-0.881471000	-0.529158000
H	3.302119000	0.572848000	-2.889269000
O	-0.146643000	-0.328137000	4.844819000
H	5.482998000	-2.006409000	0.065273000
H	2.308208000	1.247033000	-3.870466000
O	-1.461706000	-4.075461000	-1.600126000
H	-1.985262000	-2.543001000	3.351054000
H	-3.071568000	1.093057000	3.110235000
O	4.544150000	0.707807000	-1.262840000
H	-1.389496000	-3.417766000	4.503116000
H	-3.688675000	1.060709000	1.677818000
O	2.637483000	2.707051000	2.824773000
H	2.678808000	1.059139000	3.677278000
H	-0.201764000	4.067327000	1.813120000
O	-3.350096000	-2.089127000	2.558355000
H	3.205333000	0.178822000	4.845885000
H	-0.268389000	4.356737000	3.343362000
O	1.705636000	-2.044115000	-3.957043000
H	3.608034000	-2.962489000	-1.214814000
H	-3.707321000	-0.564164000	-2.515879000
O	-1.693658000	1.760848000	3.996086000
H	3.581157000	-4.231004000	-2.108399000
H	-5.226665000	-0.758674000	-2.228463000
O	3.712572000	2.844221000	0.121121000
H	0.785251000	-0.262441000	4.587191000

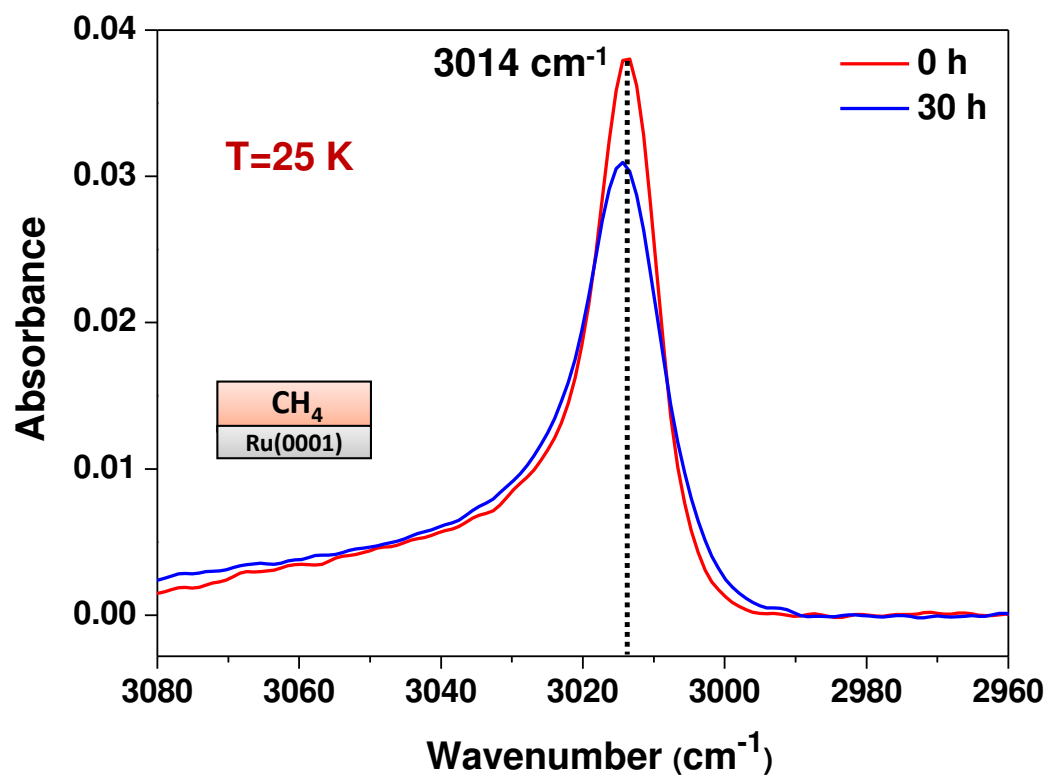
H	0.901983000	4.425392000	-0.849178000
O	-3.723820000	-2.895306000	-0.165832000
H	-0.461812000	-1.196620000	4.522802000
H	1.981672000	5.090096000	-1.747902000
O	-0.994509000	-2.361557000	-3.693403000
H	-0.662814000	-4.378186000	-1.106269000
H	-1.910035000	-1.226475000	-3.723785000
O	2.910870000	0.481866000	-3.769422000
H	-2.019727000	-3.622067000	-0.952441000
H	-3.003083000	-0.555552000	-4.667349000
O	-3.769993000	0.670732000	2.557774000
H	4.245265000	1.484324000	-0.716283000
H	1.308032000	3.153156000	-2.977356000
O	0.070176000	3.732213000	2.692267000
H	5.318336000	1.007483000	-1.751056000
H	0.222056000	2.493160000	-3.852374000
O	-4.386415000	-0.610882000	-1.779895000
H	1.723211000	3.070395000	2.803983000
H	-4.398840000	0.823809000	-0.708806000
O	1.716022000	4.249505000	-1.359645000
H	3.177952000	3.378565000	3.255465000
H	-5.243798000	1.756435000	0.223020000
O	-2.621116000	-0.454904000	-3.788458000
H	-3.546116000	-1.128619000	2.563078000
H	-1.400594000	4.200142000	-0.314769000

O	1.178534000	2.690636000	-3.816980000
H	-3.486148000	-2.399928000	1.647228000
H	-0.961360000	5.610188000	0.154543000
O	-4.366288000	1.640111000	-0.157325000
H	2.104179000	-1.149701000	-3.958760000
H	-1.915402000	2.469763000	-2.752932000
O	-0.669999000	4.691564000	0.134280000
H	2.166162000	-2.532104000	-3.257276000
H	-1.880095000	1.264675000	-3.722875000
O	-1.601040000	2.196055000	-3.625305000
H	-1.086697000	2.239357000	3.415911000
H	-3.372609000	2.878141000	-0.796480000
O	-2.727424000	3.493659000	-1.224271000
H	-1.163910000	1.013200000	4.364138000
H	-3.246424000	4.083672000	-1.781829000

**Table S3**

Comparison of the computational and experimental vibrational frequency of CH<sub>4</sub> and CO<sub>2</sub> Clathrate hydrate using the B3LYP level of theory and 6-311++G(d, p) basis.

<b>B3LYP/6-311++G(d, p) Level</b>	<b>Free CH<sub>4</sub>/CO<sub>2</sub></b>	<b>5<sup>12</sup> cage</b>	<b>5<sup>12</sup> 6<sup>2</sup> cage</b>	<b>5<sup>12</sup> 6<sup>4</sup> cage</b>
<b>CH<sub>4</sub> hydrate</b>	3129.6 (26)	3138.9 (24) 3144.1 (12) 3151.6 (10)	3120.4 (6) 3128.9 (10) 3141.3 (3)	3120.5 (22) 3132.2 (11) 3138.9 (16)
<b>CO<sub>2</sub> hydrate</b>	2420.0 (712)	2333.5 (295)	2403.4 (580)	2435.8 (546)

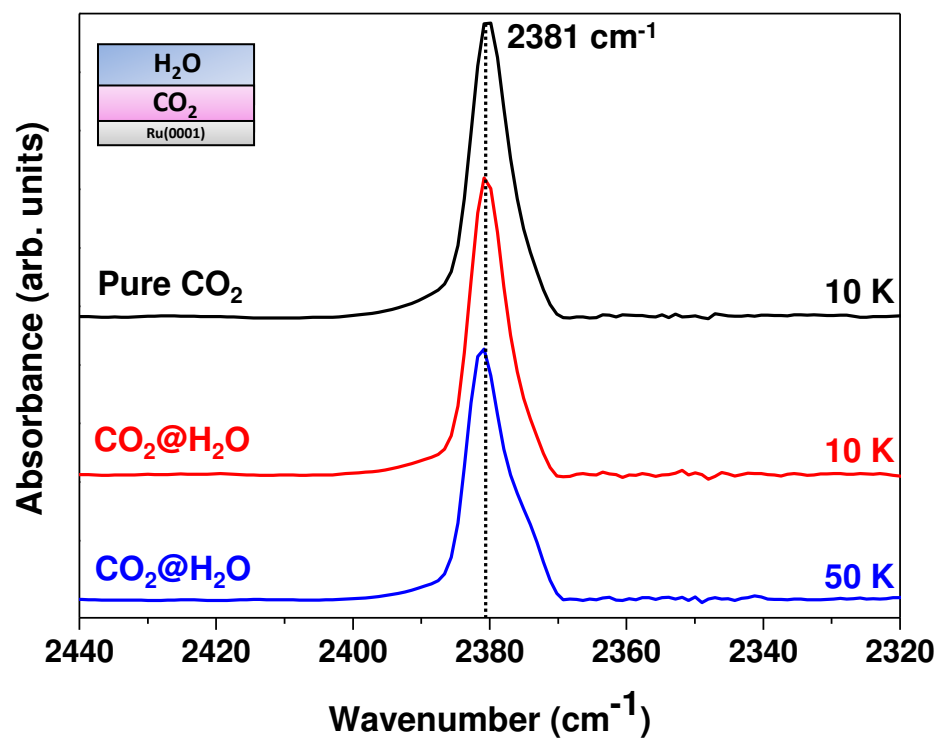


**Fig. S2.** Time dependent RAIR spectra of 150 MLs of solid CH<sub>4</sub> in the C-H antisymmetric stretching region at 25 K. The decrease in the intensity of the IR peak is due to desorption of CH<sub>4</sub> in UHV. This experiment was performed at 25 K instead of 30 K, as at this temperature (30 K), most of the CH<sub>4</sub> desorbed from the surface after 30 hours.

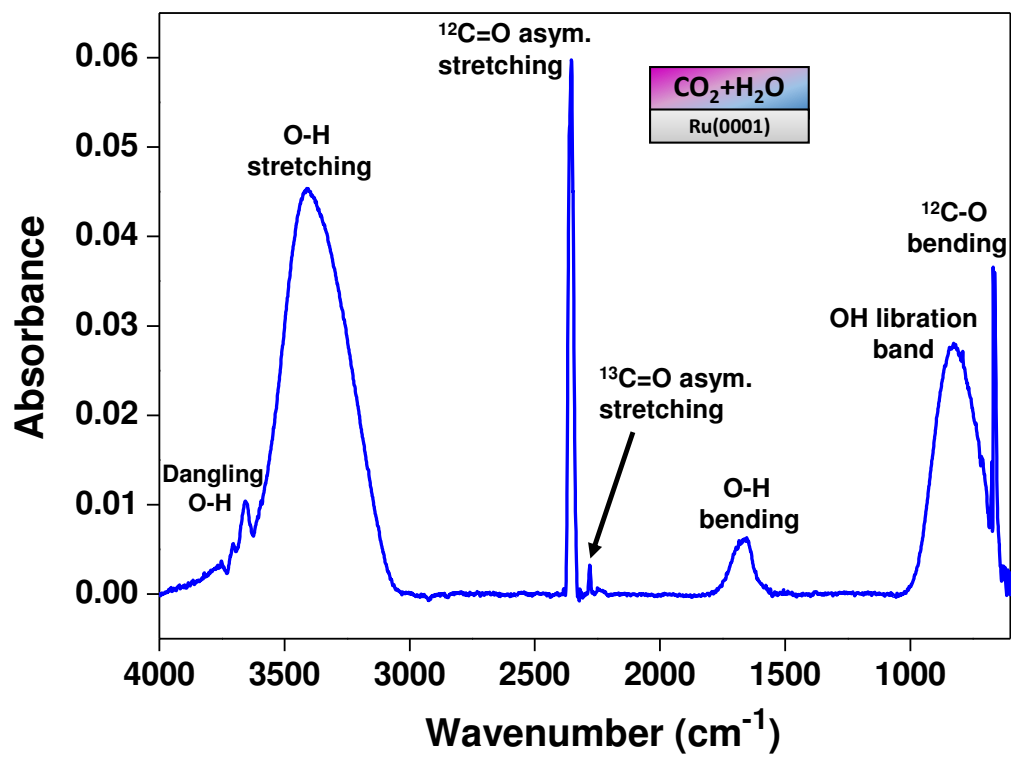
**Table S4**

Properties of (3,-1) bond critical points in CH<sub>4</sub> and CO<sub>2</sub> clathrate hydrate computed at B3LYP level of theory with 6-311++G (d, p) basis set.

Clathrate Hydrate (5 <sup>12</sup> )	Type of bonding	Bonds	$\rho(r_C)$	$\nabla^2\rho(r_C)$
CH <sub>4</sub>	van der Waals interaction	-C-H of free CH <sub>4</sub>	0.27217	-0.89913
		-C-H of CH <sub>4</sub> hydrate	0.27199	-0.89544
		-C-H $\cdots$ H <sub>2</sub> O interaction	0.00598	0.01601
CO <sub>2</sub>	Hydrogen bonding	-C=O of free CO <sub>2</sub>	0.45773	-0.08650
		-C=O of CO <sub>2</sub> hydrate	0.44922	-0.07620
		-C=O $\cdots$ H <sub>2</sub> O interaction	0.01563	0.07161

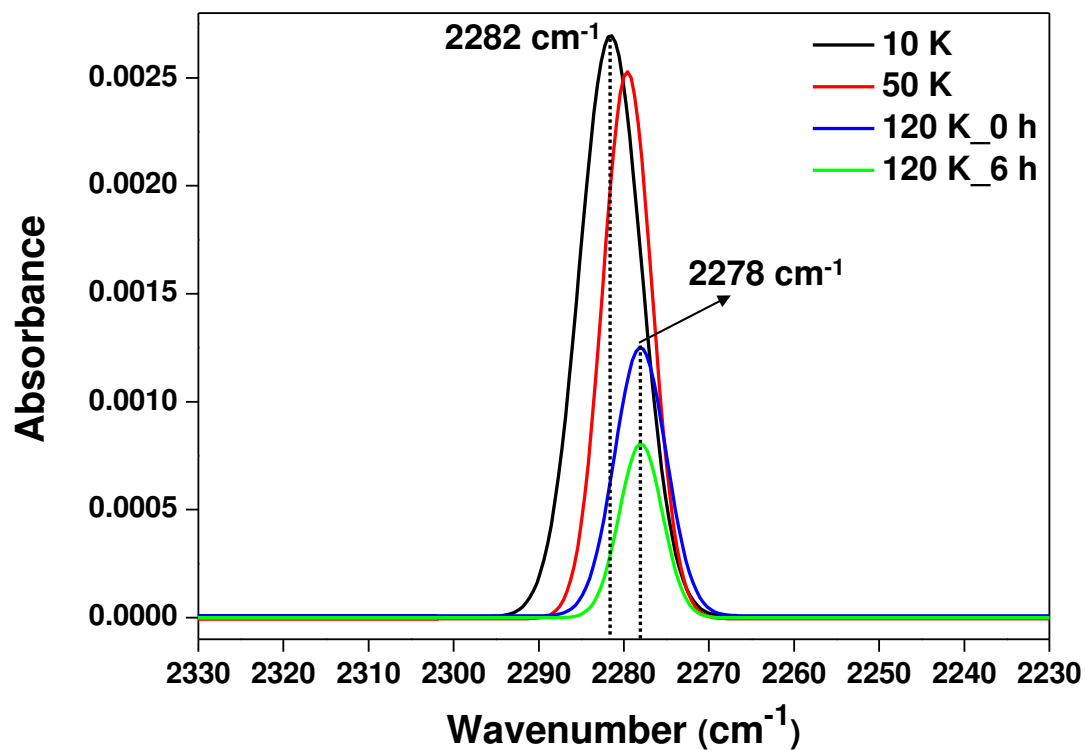


**Fig. S3.** Temperature dependent RAIR spectra of 300 MLs of CO<sub>2</sub>@H<sub>2</sub>O (1:5 ratio) in the C=O antisymmetric stretching region. Spectrum for pure solid CO<sub>2</sub> was added for comparison. The CO<sub>2</sub>@H<sub>2</sub>O symbolism implies that H<sub>2</sub>O was deposited over CO<sub>2</sub>. The spectra were translated vertically for the clarity.

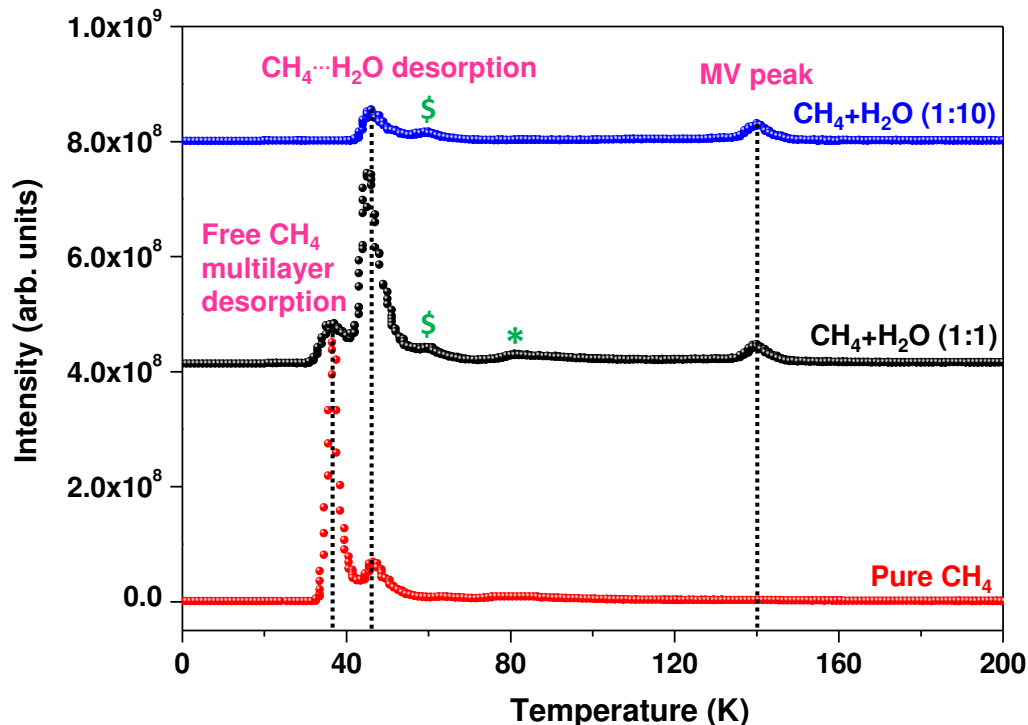


**Fig. S4.** Full scale RAIR spectrum of 300 MLs of  $\text{CO}_2 + \text{H}_2\text{O}$  (1:5 ratio) at 10 K.





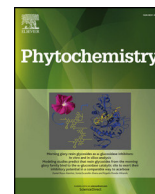
**Fig. S5.** Temperature dependent RAIR spectra of 300 MLs of CO<sub>2</sub>+H<sub>2</sub>O (1:5 ratio) in the <sup>13</sup>C=O antisymmetric region. Reduction in intensity with time is due to partial desorption.



**Fig. S6.** TPD mass spectra of 150 MLs of solid  $\text{CH}_4$  and  $\text{CH}_4+\text{H}_2\text{O}$  co-deposited ice systems at different ratios (heating rate of  $30 \text{ K}\cdot\text{min}^{-1}$ ). Here, the intensities of  $\text{CH}_3^+$  ( $m/z=15$ ) under these conditions are plotted. After the deposition at 10 K, these ice systems were annealed and simultaneously the mass spectra were recorded. The marked desorption (\*, \$) peaks are due to the structural transitions of amorphous ice during annealing (1).

#### References:

1. Jenniskens P & Blake DF (1994) Structural transitions in amorphous water ice and astrophysical implications. *Science* 265(5173):753.



# UPLC and ESI-MS analysis of metabolites of *Rauvolfia tetraphylla* L. and their spatial localization using desorption electrospray ionization (DESI) mass spectrometric imaging

P. Mohana Kumara<sup>a,c,\*</sup>, R. Uma Shaanker<sup>b</sup>, T. Pradeep<sup>a,\*</sup>

<sup>a</sup> DST Unit of Nanoscience and Thematic Unit of Excellence, Department of Chemistry, Indian Institute of Technology Madras, Chennai, 600036, India

<sup>b</sup> School of Ecology and Conservation, Department of Crop Physiology, University of Agricultural Sciences, GKVK, Bengaluru, 560065, India

<sup>c</sup> Center for Ayurveda Biology and Holistic Nutrition, The University of Trans-Disciplinary Health Sciences and Technology (TDU), Bengaluru, 560064, India

## ARTICLE INFO

### Keywords:

*Rauvolfia tetraphylla*  
Apocynaceae  
Indole alkaloids  
DESI-MS  
Ajmaline  
Reserpine  
Yohimbine

## ABSTRACT

*Rauvolfia tetraphylla* L. (family Apocynaceae), often referred to as the wild snakeroot plant, is an important medicinal plant and produces a number of indole alkaloids in its seeds and roots. The plant is often used as a substitute for *Rauvolfia serpentina* (L.) Benth. ex Kurz known commonly as the Indian snakeroot plant or sarphagandha in the preparation of Ayurvedic formulations for a range of diseases including hypertension. In this study, we examine the spatial localization of the various indole alkaloids in developing fruits and plants of *R. tetraphylla* using desorption electrospray ionization mass spectrometry imaging (DESI-MSI). A semi-quantitative analysis of the various indole alkaloids was performed using UPLC-ESI/MS. DESI-MS images showed that the distribution of ajmaline, yohimbine, demethyl serpentine and mitoridine are largely localized in the fruit coat while that for ajmaline is restricted to mesocarp of the fruit. At a whole plant level, the ESI-MS intensities of many of the ions were highest in the roots and lesser in the shoot region. Within the root tissue, except sarpagine and ajmaline, all other indole alkaloids occurred in the epidermal and cortex tissues. In leaves, only serpentine, ajmaline, reserpiline and yohimbine were present. Serpentine was restricted to the petiolar region of leaves. Principal component analysis based on the presence of the indole alkaloids, clearly separated the four tissues (stem, leaves, root and fruits) into distinct clusters. In summary, the DESI-MSI results indicated a clear tissue localization of the various indole alkaloids, in fruits, leaves and roots of *R. tetraphylla*. While it is not clear of how such localization is attained, we discuss the possible pathways of indole alkaloid biosynthesis and translocation during fruit and seedling development in *R. tetraphylla*. We also briefly discuss the functional significance of the spatial patterns in distribution of metabolites.

## 1. Introduction

*Rauvolfia tetraphylla* L. (Family Apocynaceae) (Fig. 1a) is an economically important medicinal plant, often used as a substitute for its conspecific plant, *Rauvolfia serpentina* (L.) Benth. ex Kurz commonly referred to as the Indian snakeroot plant or sarphaganda (Gupta et al., 2012). The latex of both species of plants are used in a variety of cures in folk medicine and several indigenous or traditional medicine systems (Gupta et al., 2012). The white latex is used as emetic, cathartic and expectorant for treating dropsy (Gupta et al., 2012; Kaushik et al., 2013). Both the species of *Rauvolfia* produce a variety of monoterpene indole alkaloids (MIAs) such as reserpine, serpentine,

deserpidine, ajmaline, ajmaline, yohimbine that have been reported to have important pharmaceutical and biological activities. All these compounds originate from strictosidine (Fig. 2), formed by the condensation of tryptamine with secologanin (Hagel et al., 2008; Pan et al., 2015). Little is known about the downstream biosynthetic pathway of these compounds from strictosidine (Fig. 2) (Faisal et al., 2005).

Considering the importance of many of the monoterpene indole alkaloids (MIAs) in pharmaceutical applications, a number of studies have explored to unravel the pathway genes involved in the biosynthesis of these compounds. Using an integrated transcriptomics and proteomics approach for gene discovery, Miettinen et al. (2014) discovered the last four missing steps of the (seco)iridoid biosynthesis pathway in

\* Corresponding author.

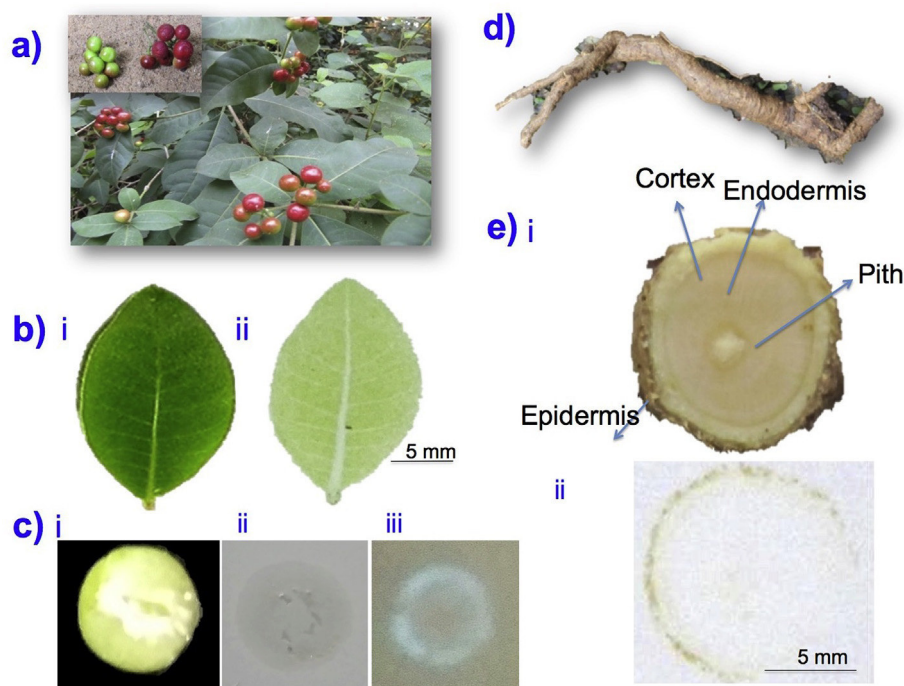
\*\* Corresponding author. DST Unit of Nanoscience and Thematic Unit of Excellence, Department of Chemistry, Indian Institute of Technology Madras, Chennai, 600036, India.

E-mail addresses: [monapatelpgatti@gmail.com](mailto:monapatelpgatti@gmail.com) (P. Mohana Kumara), [pradeep@iitm.ac.in](mailto:pradeep@iitm.ac.in) (T. Pradeep).

<https://doi.org/10.1016/j.phytochem.2018.11.009>

Received 4 June 2018; Received in revised form 15 November 2018; Accepted 16 November 2018

0031-9422/ © 2018 Elsevier Ltd. All rights reserved.



**Fig. 1.** a) Fruit bearing *Rauvolfia tetraphylla* plant. Insert in shows the different stages of fruit b) leaf and its TLC imprint, c) Fruit cross section (i) and its TLC imprint (ii) TLC imprint photo taken with UV light (iii) d) Root and e) Root cross section (i) and its TLC imprint (ii).

*Catharanthus roseus*. More recently, the entire MIA pathway up to strictosidine was engineered in *Nicotiana benthamiana* by heterologous expression of newly identified genes in combination with the previously known biosynthesis genes (Miettinen et al., 2014). Interestingly the biosynthetic pathways of many plant specialised metabolites often involve multiple cell types that are biochemically and morphologically distinct (Hagel et al., 2008; Pan et al., 2015). *In situ* RNA hybridization and immuno-cytochemical studies have shown the localization of MIA pathway enzymes to a number of cell types (St-Pierre et al., 1999). For example, studies in *C. roseus* have shown that secoiridoid metabolism begins in phloem-associated parenchyma cells (IPAP) cells and that loganic acid produced in IPAP cells is transferred to epidermal cells (ECs). Further synthesis involving secologanin and tryptamine occurs in the ECs. Finally, a MIA intermediate, deacetoxyvindoline, moves to the idioblast cells (ICs) and laticifer cells (LCs) and MIAs begin to accumulate in the vacuole of these cells (St-Pierre et al., 1999; Mahroug et al., 2006; Dug   de Bernonville et al., 2015; Burlat et al., 2004).

In a more recent study on a Mediterranean plant, *Thapsia garganica* (dicot, Apiaceae), using MALDI MSI, it was shown that the metabolite, thapsigargin was stored in the secretory ducts in the roots. Transcripts of *TgTPS2* (epikunzeol synthase) and *TgCYP76AE2* in roots were found only in the epithelial cells lining these secretory ducts (Andersen et al., 2017). Similarly, in *Vitex agnuscastus* L, MALDI-MSI analysis showed that the diterpenoids were localized in trichomes on the surface of fruit and leaves. Analysis of a trichome-specific transcriptome database, coupled with expression studies, identified seven candidate genes involved in diterpenoid biosynthesis (Heskes et al., 2018; Boughton et al., 2016).

Unraveling the localization of pathway gene expression and their products or metabolites can profoundly help in understanding, both the regulatory and functional basis of metabolite synthesis in plants (Miettinen et al., 2014). While traditionally, studies have relied on techniques such as *in situ* RNA hybridization and immuno-cytochemical studies, in recent years there has been increasing attempts to use mass spectrometry imaging techniques for localizing plant metabolites. These techniques, such as MALDI-MSI or DESI-MSI are rapid, easy to use and have been used in a number of studies to understand the spatial

context of metabolite accumulation and localization (Bjarnholt et al., 2014; Lee et al., 2012; Ifa et al., 2011; Korte et al., 2012; Hemalatha and Pradeep, 2013; Kueger et al., 2012; Boughton et al., 2016; Andersen et al., 2017; Zifkin et al., 2012). Coupled with tissue-based transcriptomic analysis, the technique can potentially be used in unraveling biosynthetic pathway genes responsible for the synthesis and accumulation of specialised metabolites (Bjarnholt et al., 2014; Zifkin et al., 2012; Andersen et al., 2017).

In this study, using a DESI-MSI approach, we have developed a spatially explicit map of the indole alkaloids in developing fruits and plants of *R. tetraphylla*. We rationalize the results based on both the functional significance of such patterns as well as the possible metabolic regulatory processes that might have resulted in these patterns.

## 2. Results and discussion

ESI MS analysis of the different parts (root, stem, leaf and fruits: Fig. 1) of *R. tetraphylla* showed the presence of prominent metabolites in the range of  $m/z$  300–611 (Table 1). Among the different tissues, by far the roots contained relatively large number of indole alkaloids compared to the stem, leaves and fruits (Fig. S1). Structural characterization of these indole alkaloids were done by both accurate mass measurement and mass fragmentation analysis (Fig. S2) (Smith et al., 2005). Mass fragmentation analysis was done mainly by comparing the observed fragment ions with those retrieved from earlier publications (Fig. S2). Where not available, the patterns were annotated using the fragments core structural features (Supplementary information; Fig. S2). A list of  $m/z$  values of the parent and fragment ions and their chemical formulae are given in Table 1. Based on these masses, the identity and the spatial location of the compounds were established in different parts of the fruit and plant using DESI-MS imaging facility. Principal component analysis (PCA) based on the presence of MIAs clearly separated the four tissues (stem, leaves, root and fruits) in to distinct clusters (Fig. S2). The first and second PC axis respectively explained 66.5% and 30.5% of the variance. The eigenvector contributions for the two axes are: PC1 Leaf-L1 (2.0994) L2 (4.827) L3 (4.827) and PC2 (L1 3.990, Root-R2 0.29, R3- 0.217) (Fig. S3).

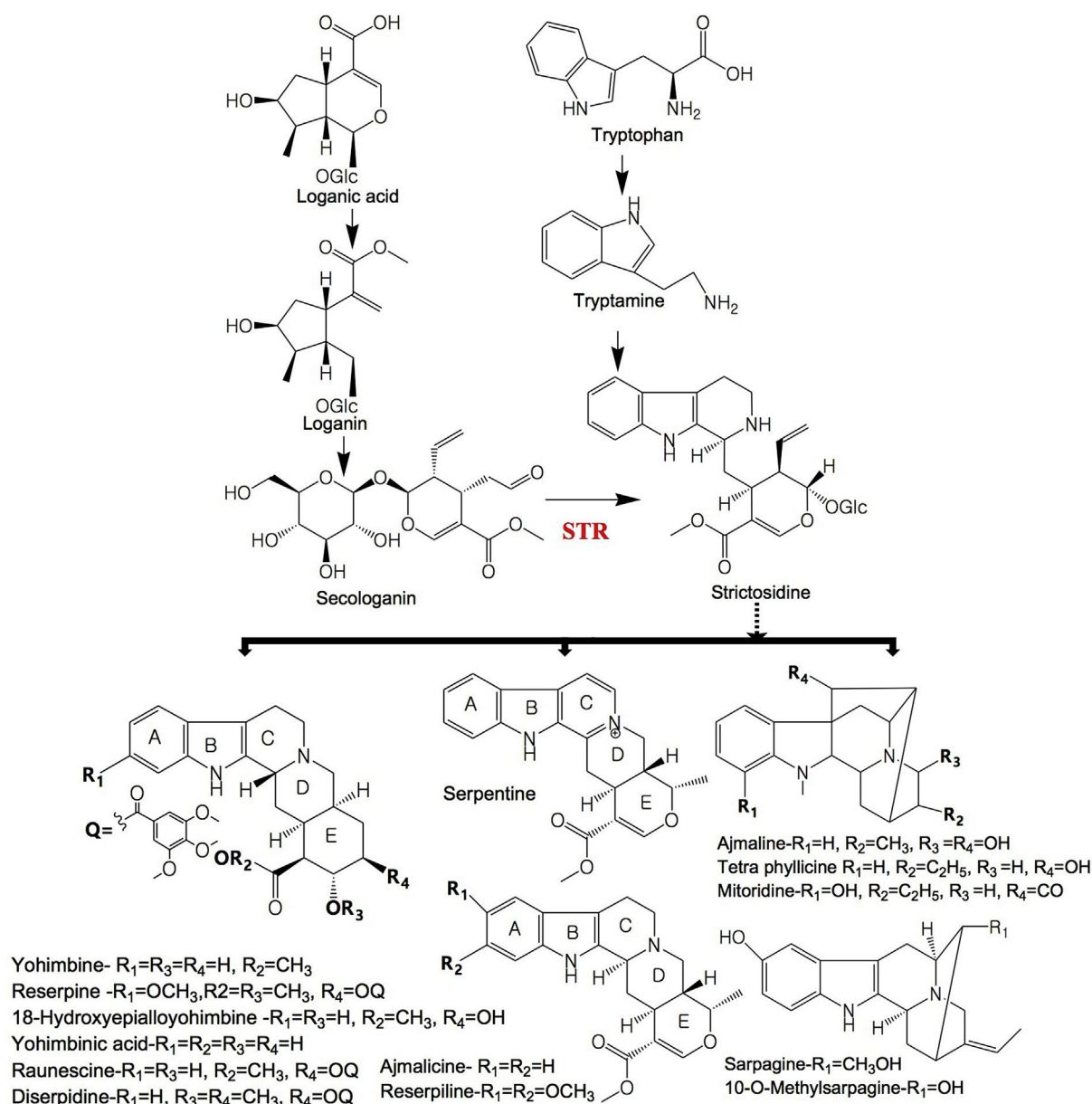


Fig. 2. Pathway of monoterpenoid indole alkaloid biosynthesis. Strictosidine synthase (STR) is a key gene responsible for the biosynthesis of strictosidine. Strictosidine is a major precursor for the biosynthesis of a diversity of MIAs in *Rauvolfia tetraphylla*.

### 2.1. MIAs during fruit development

The spatial locations of different MIAs in cross section of developing fruits were established using DESI-MS. Among the various indole alkaloids, prominent were mitoridine, ajmaline, demethyl serpentine, ajmalicine and yohimbine (Fig. 3). The molecular ion intensities were higher in early stage fruits compared to mature fruit. The alkaloids, mitoridine, 12-methoxyvellosimine, demethyl serpentine, ajmalicine and yohimbine were restricted to the fruit coat (exocarp), while ajmaline was largely restricted to mesocarp of the fruit (Fig. 3). Demethyl serpentine was detected only in fruits and not in other parts of the plant.

### 2.2. MIAs in root and shoot

Cross-sections of root and shoot of the plant showed distinct spatial distribution patterns of the various ions. In roots, most of the indole alkaloids were present and showed tissue specific localization.

Tetraphyllicine, raunescine and deserpidine were present only in epidermis; mitoridine and ajmalicine were present in cortex while reserpine was restricted to the pith region only. Sarpagine, 10-O-methylsarpagine, ajmaline, serpentine, yohimbine and 18-hydroxy-yohimbine were present in higher abundance in epidermis and pith region. Stem contained, sarpagine, ajmaline, serpentine, ajmalicine, yohimbine and 18-hydroxy-yohimbine with a localization pattern similar to that in the root (Fig. 4).

### 2.3. MIAs in leaves

In leaves, only serpentine, ajmalicine, reserpiline and yohimbine were found. Specifically, serpentine was found only in the leaf petiole while the other metabolites were abundant in the leaf blade (Fig. 5).

Intensities of many of these metabolites were highest in the roots upwards to the collar region, representing the transition from the root to the shoot (Figs. 3–5, Fig. S5). For example, reserpine content on dry weight basis, was highest in the main roots ( $0.50\% \pm 0.10$ ) and lateral

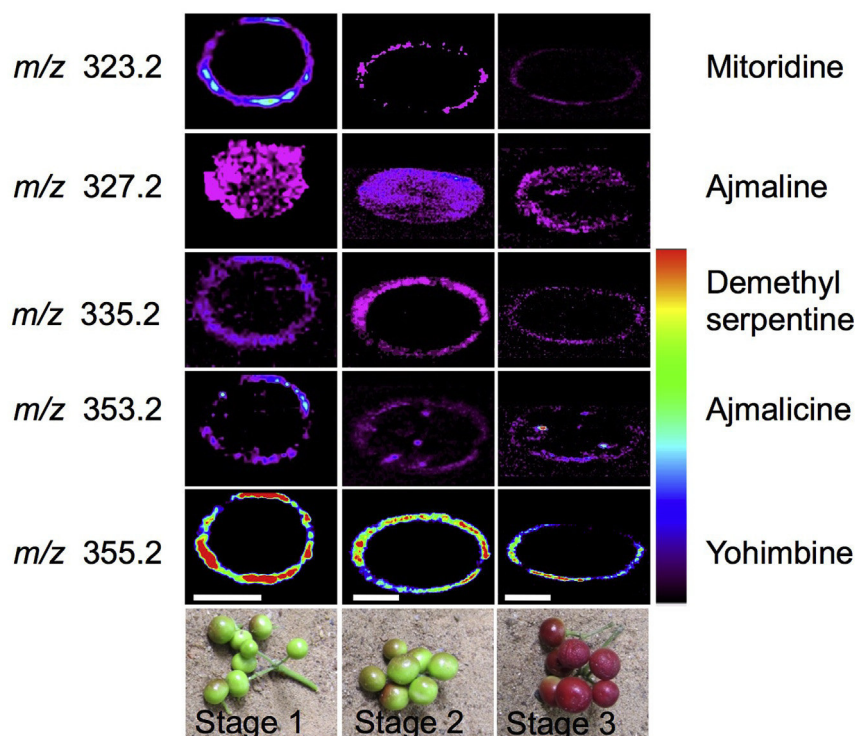
**Table 1**Details of *m/z* values of the ions, fragment ions and chemical formulae of monoterpene alkaloids identified in *Rauvolfia tetraphylla*.

Serial number	Metabolite	Ion type	Exact mass (calculated)	<i>m/z</i> obtained from ESI MS (Orbitrap)	Error (ppm)	Chemical Formula	Mass fragments <sup>a</sup>	Metabolite tissue localization		
								Root/stem	Leaves	Fruit
1	Strictosidine	[M + H] <sup>+</sup>	531.2337	531.2337	0	C <sub>27</sub> H <sub>35</sub> N <sub>2</sub> O <sub>9</sub>	514, 352, 334, 320, 302, 282, 251, 222, 223, 144			
<b>Reserpine type of alkaloids</b>										
2	Yohimbine	[M + H] <sup>+</sup>	355.2016	355.2007	−2.5	C <sub>21</sub> H <sub>27</sub> N <sub>2</sub> O <sub>3</sub>	337, 323, 224, 212, 194, 144	Epidermis and pith	Leaf blade	–
3	Deserpidine	[M + H] <sup>+</sup>	579.2701	579.2698	−0.5	C <sub>32</sub> H <sub>39</sub> N <sub>2</sub> O <sub>8</sub>	547, 448, 367, 335, 195, 144	Epidermis	–	–
4	Reserpine	[M + H] <sup>+</sup>	609.2807	609.2802	−0.8	C <sub>33</sub> H <sub>41</sub> N <sub>2</sub> O <sub>9</sub>	577, 448, 436, 397, 365, 336, 236, 224, 195	Pith	–	–
5	18-Hydroxyepialloyohimbine	[M + H] <sup>+</sup>	371.1965	371.1961	−1.0	C <sub>21</sub> H <sub>27</sub> N <sub>2</sub> O <sub>4</sub>	353, 339, 240, 228, 158, 223, 144	Epidermis and pith	–	–
6	Yohimbic acid	[M + H] <sup>+</sup>	341.1865	341.1862	−0.8	C <sub>20</sub> H <sub>25</sub> N <sub>2</sub> O <sub>3</sub>	32, 32, 11, 19, 61, 58, 144	Epidermis and pith	–	–
7	Raunescine	[M + H] <sup>+</sup>	565.2544	565.2542	−0.3	C <sub>31</sub> H <sub>35</sub> N <sub>2</sub> O <sub>8</sub>	547, 448, 353, 321, 195, 144	Epidermis	–	–
<b>Ajmalicine type of alkaloids</b>										
8	Ajmalicine	[M + H] <sup>+</sup>	353.186	353.1851	−2.5	C <sub>21</sub> H <sub>25</sub> N <sub>2</sub> O <sub>3</sub>	321, 293, 210, 222, 144	Cortex	Leaf blade	Outer part
9	Reserpiline	[M + H] <sup>+</sup>	413.2071	413.2068	−0.7	C <sub>23</sub> H <sub>29</sub> N <sub>2</sub> O <sub>5</sub>	381, 222, 204, 144	–	Leaf blade	–
<b>Ajmaline type of alkaloids</b>										
10	Ajmaline	[M + H] <sup>+</sup>	327.2067	327.2063	−1.2	C <sub>20</sub> H <sub>27</sub> N <sub>2</sub> O <sub>2</sub>	309, 238, 210, 194, 182, 158, 144	Epidermis and pith	–	Endosperm
11	Tetraphyllicine	[M + H] <sup>+</sup>	309.1961	309.1957	−1.3	C <sub>20</sub> H <sub>25</sub> N <sub>2</sub> O	291, 238, 182, 158, 144	Epidermis	–	–
12	Sarpagine	[M + H] <sup>+</sup>	311.176	311.175	−3.2	C <sub>19</sub> H <sub>23</sub> N <sub>2</sub> O <sub>2</sub>	293, 276, 165, 145, 138	Epidermis and pith	–	–
13	Mitoridine	[M + H] <sup>+</sup>	323.176	323.1749	−3.4	C <sub>20</sub> H <sub>23</sub> N <sub>2</sub> O <sub>2</sub>	305, 291, 279, 263, 144	Cortex	–	Outer part
14	10-O-Methylsarpagine	[M + H] <sup>+</sup>	325.1911	325.1907		C <sub>20</sub> H <sub>25</sub> N <sub>2</sub> O <sub>2</sub>	307, 293, 160, 144	Epidermis and pith	–	–
<b>Others</b>										
15	Serpentine	[M + H] <sup>+</sup>	349.1547	349.1537	−2.8	C <sub>21</sub> H <sub>21</sub> N <sub>2</sub> O <sub>3</sub>	317, 293, 277, 263, 235	Epidermis and pith	Leaf petiole	–
16	Demethyl serpentine	[M + H] <sup>+</sup>	335.1396	335.1382	−4.1	C <sub>20</sub> H <sub>19</sub> N <sub>2</sub> O <sub>3</sub>	317, 293, 277, 263, 235	–	–	Outer part

– Below detection threshold.

<sup>a</sup> The mass fragments used to infer the chemical identities of the various compounds are based on published literature provided for each of the alkaloids in the supplementary information.





**Fig. 3.** DESI MS images showing the distribution of indole alkaloids in fruit sections of *R. tetraphylla*. Scale bars correspond to 5 mm and apply to all the images of a row.

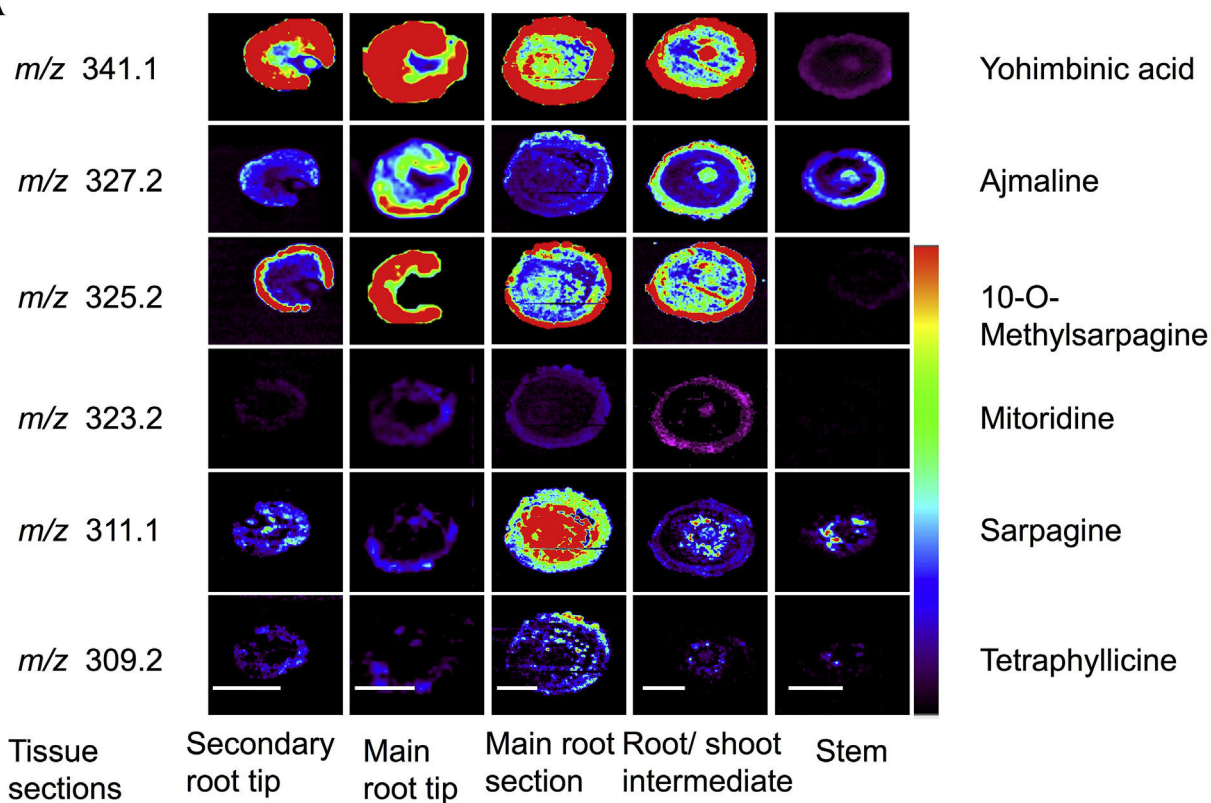
roots ( $0.44\% \pm 0.09$ ), followed by stem ( $0.31\% \pm 0.09$ ), and least in fruits ( $0.02\% \pm 0.02$ ) and absent in leaves (Fig. 6).

In summary, our results show that the MIAs in *R. tetraphylla* exhibit a distinct localization patterns, both, across and within different tissues (Figs. 3 and 4). For example, while roots contained most of the MIAs, the stems contained only sarpagine, ajmaline, serpentine, ajmalicine, yohimbine and 18-hydroxy-yohimbine. Similarly, the leaves had only serpentine, ajmalicine, reserpiline and yohimbine. Within each tissue as well, there were distinct patterns of occurrence. In fruits, several of the MIAs were restricted to the fruit coat, while others were restricted to the mesocarp. Similarly, within roots, there was a clear spatial separation of several of the MIA between the epidermal and cortex tissues. These results add to the now growing literature that suggests there could be spatial patterning of occurrence of specialised metabolites, across and within tissues (Dueñas et al., 2017; Bhandari et al., 2015; Mohana Kumara et al., 2016; Sturtevant et al., 2017). These are now increasingly becoming evident, especially through studies, involving non-invasive, imaging analysis including MALDI MSI and DESI MSI (Bjarnholt et al., 2014; Lee et al., 2012; Ifa et al., 2011; Korte et al., 2012; Hemalatha and Pradeep, 2013; Kueger et al., 2012; Dopstadt et al., 2017; Woodfield et al., 2017). The spatial patterning of MIAs also raises interesting questions, both proximate and ultimate, of such occurrence. Proximately, the patterns are best explained by studying the underlying gene expression patterns, and examining, if there is indeed any spatial correlation between the expression and the occurrence. A few studies have attempted to examine such correlation by analyzing cell and tissue specific transcriptome data. For example, in flaxseed (*Linum usitatissimum*), expression of the key genes involved in the synthesis of pinorensin and the subsequent downstream pathway intermediate were correlated with the spatial distribution of metabolite (Dalisay et al., 2015). Similarly, in highbush blueberry (*Vaccinium corymbosum*), occurrence of major classes of flavonoids was correlated to the transcript abundance. Proanthocyanidins (PAs) and corresponding transcripts encoding anthocyanidin reductase and leucoanthocyanidin reductase were mostly concentrated in young fruits

and localized predominantly to the inner fruit tissue containing the seeds and placentae (Zifkin et al., 2012). In *Calotropis procera*, tissue specific expression analysis of 30 putative transcripts involved in terpenoid, steroid and cardenolide pathways were correlated with metabolite and transcript accumulation (Pandey et al., 2016). In tea leaves, the expression patterns of genes in C2-2-1 and C2-2-2-1 groups were found to be probably responsible for the development-dependent accumulation of phenolic compounds in the leaves (Jiang et al., 2013). In *Sorghum bicolor*, during accumulation was reported to be correlated with transcript abundance of genes involved in biosynthesis of cyanogenic glycosides (Nielsen et al., 2016). It would be interesting to examine such association between the spatial distribution of the metabolites in tissues with the corresponding gene expression in *R. tetraphylla* as well. Where such correlation between spatial localization and gene expression is not evident, it is likely that the spatial patterns could be due to a disconnect between the sites of synthesis and sites of accumulation of the metabolites. For example, in pea and carrot, cytokinins biosynthesized in cambium of the root is finally exported to the shoot (Chen et al., 1985).

While the above studies may help explain the proximate basis of spatial patterning of metabolites, it is also interesting to examine, the ultimate functional significance of such patterning. One of the earliest studies is due to Berenbaum (1995) who proposed the concept of apparency in the synthesis and accumulation of specialised metabolites by plant tissue. According to this theory, plants bet-hedge on deploying defense responses and investing carbon to synthesizing specialised metabolites. Thus, instead of uniformly investing in synthesis and accumulation of specialised metabolites in all leaves, plants may accumulate the compound in only a proportion of the leaves and within a leaf, only in some parts of the leaf (Hansen et al., 2016). In *R. tetraphylla*, it is interesting to note that ajmaline is specifically distributed in the mesocarp of the fruit and increases through the fruit developmental phase. Ajmaline is a potent inhibitor of  $\text{Na}^+/\text{K}^+$  channel (Kiesecker et al., 2004) and it is likely that the accumulation pattern in the mesocarp could help defend the fruit from insect herbivores. On the

A



B

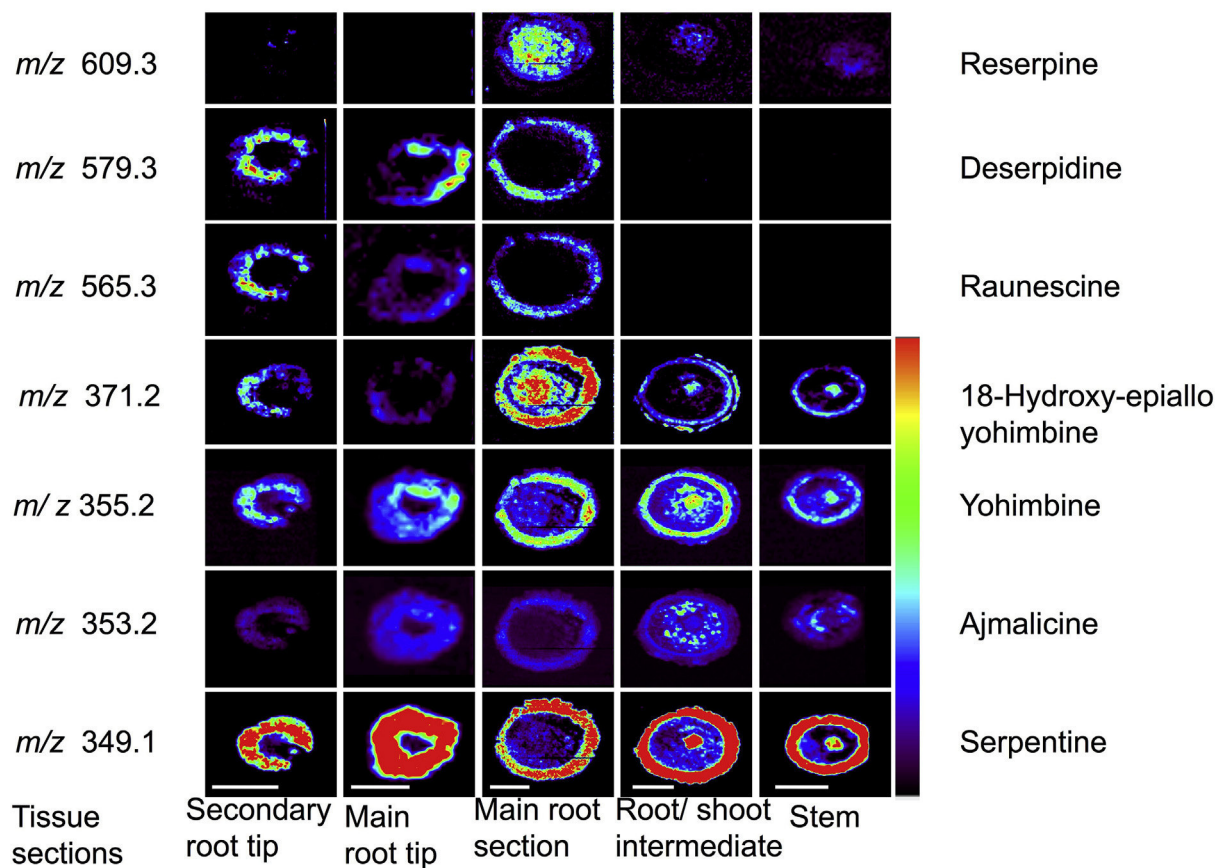


Fig. 4. DESI MS images showing the indole alkaloid distribution in root and stem sections of *R. tetraphylla*. Scale bars correspond to 5 mm and apply to all the images of a row.



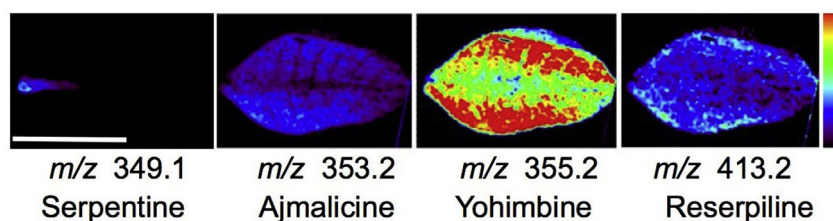


Fig. 5. DESI MS images showing the indole alkaloid distribution in leaf of *R. tetraphylla*. Scale bars correspond to 5 mm and apply to all the images of a row.

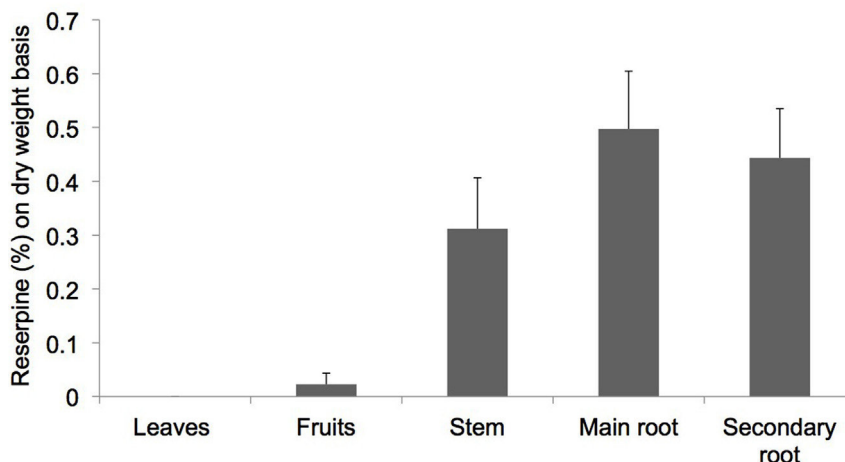


Fig. 6. Reserpine content (on dry weight basis) in different parts of *Rauvolfia tetraphylla* plant. Error bars indicates standard deviation.

other hand, ion intensities of many other compounds such as mitroline, yohimbine that was located in the fruit epidermis decreased with fruit ripening. The functional significance of many of these compounds is unknown, though some of them might serve as intermediates of biosynthesis of indole alkaloids. Yohimbine is an alpha adrenoreceptor inhibitor and could possibly also function in defense. Sarpagine, an ajmaline type monoterpene indole alkaloid, is a  $\text{Na}^+$  channel blocker and is concentrated in the cortex and pith of the root. Reserpine, also abundant in the main root cortex, is a monoamine transport blocker (Mahata et al., 1996). Ajmalicine, an andregnic receptor antagonist, is concentrated in the epidermis and cortex. The functional significance of most of these compounds are yet unknown and clearly more research is required to unravel their significance to plant growth and defense.

Like other terpene alkaloids, the synthesis of MIA begins with the condensation of tryptamine and secologanin to yield strictosidine. Strictosidine is converted into 4,21-dehydrogeissoschizine and thereafter through cyclization and reduction, ajmalicine is formed (KEGG pathway). However, in our study, we failed to recover the primary precursors of the different MIAs. An earlier study (Yamamoto et al., 2016) employing nano-DESI was successful in locating some of the precursors, such as strictosidine, indicating perhaps the need for high-resolution imaging to capture such molecules. It is also likely that our failure to spatially detect them could be due to them not being readily ionized as well as because of their inherently poor stability.

It is now well acknowledged that the primary site of synthesis of the MIAs is the root (Schlutenhofer et al., 2014; O'Connor and Maresh, 2006) and from there perhaps, a few are transported elsewhere in the plant (El-Sayed and Verpoorte, 2007; Liu et al., 2017; Pathania and Acharya, 2016). We have made a preliminary attempt to explore if there exist a tacit relationship between the spatial patterning of the specialised metabolites and their biosynthetic pathway (Figs. 7 and 8). Understandably, the root sections have the largest diversity of MIAs, perhaps representing the pathway intermediaries as well. However there is a clear narrowing of such diversity in the root:stem collar region and thereafter in the stem region, only to be partially restored in

the leaf and fruits. That there is an active transport is supported by the fact that transporters of ajmalicine and other MIAs have been reported (Liu et al., 2017; Zhu et al., 2015; Pathania and Acharya, 2016; Yu and De Luca, 2013).

In conclusion, the study provides a spatial framework of MIAs in different parts of *R. tetraphylla* plants. These results could serve as valuable inputs for further studies to address, both the proximate causes and the ultimate selective advantage of such patterning. Combined with other omics approaches, including transcriptomics/metabolomics, DESI MS imaging of specialised metabolites can offer exciting opportunities to explore tissue specific, and in some cases, cell specific gene expression to validate the spatial occurrences of metabolites.

### 3. Materials and methods

#### 3.1. Plant material

*R. tetraphylla* plants were raised and maintained at IIT Madras Nursery, Chennai (13.0052° N, 80.2420°E). *R. tetraphylla* produces brightly colored fruits, green during early stage, yellowish to red during maturity and shiny black during fully matured stage. The seeds take approximately 30–50 days to mature. Different plant parts were collected from the two-year-old plant during winter season (19-01-2015). Plant was up rooted, segmented into different parts, namely, root, stem and leaves (Fig. 1). Root and stem were further segmented in four different sections, namely, epidermis, cortex endodermis and pith region respectively (Fig. 1e). Different developmental stages of the fruit were collected from the two-year-old plants.

#### 3.2. ESI-MS/MS, orbitrap analysis and assigning the metabolites

Different sections of the root, shoot, and leaves (corresponding to regions that were used for the imaging) were cut into small pieces and soaked in methanol for 12 h. The solution was filtered and centrifuged at 10,000 rpm for 10 min. The supernatant was analyzed by ESI MS/MS

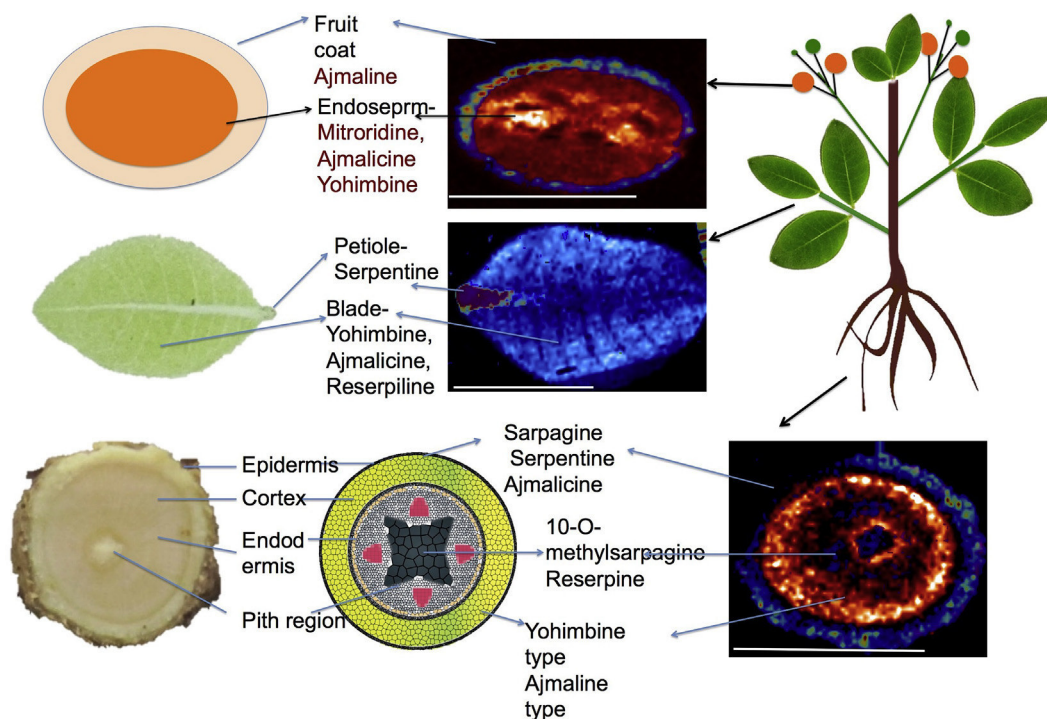


Fig. 7. Superimposed images of root, leaf and fruit sections of *R. tetraphylla* showing the tissue localization of indole alkaloids.

using Thermo Scientific LTQ XL (Thermo Scientific, San Jose, CA, USA) mass spectrometer, and exact mass was analyzed using Thermo Scientific Orbitrap Elite (Thermo Scientific, San Jose, CA, USA) mass spectrometer. The data was acquired in positive ion mode with a spray voltage of 3 kV. Collision induced dissociation (CID) was used for fragmentation of the ions during MS/MS measurements. The identities

of the ions were established based on both, the fragmentation patterns and exact masses of the ions obtained using METLIN and MassBank metabolite database. The mass window tolerance of  $\pm 3$  ppm was used for database search. The MS/MS data was used to infer the compound identity by comparing the fragment ion  $m/z$  with published literature and database. All the spectra were represented in the profile mode.

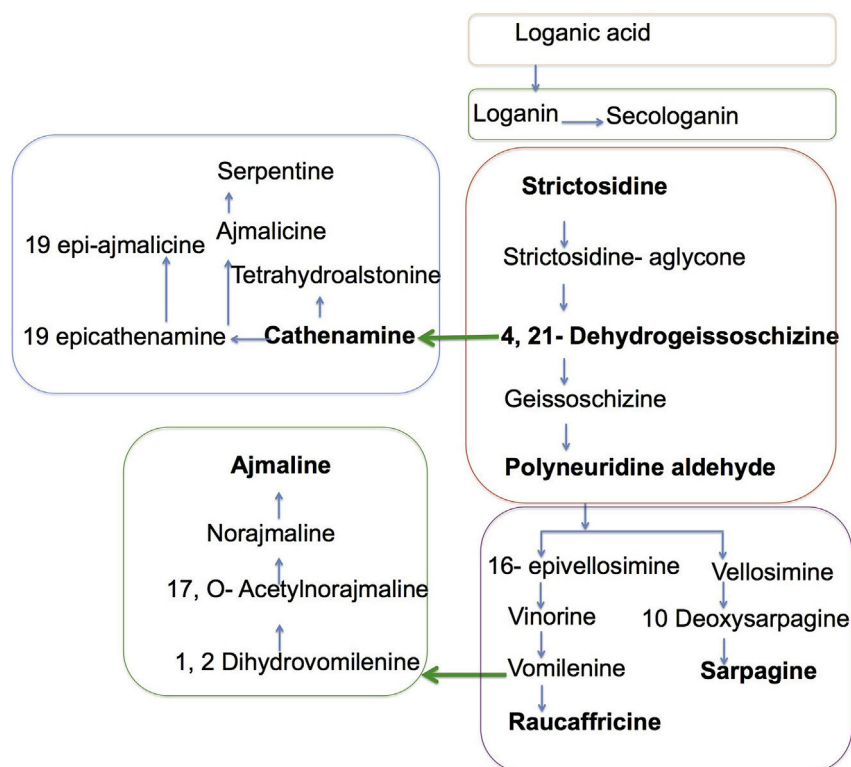


Fig. 8. Schematic illustration of the biosynthesis of monoterpene indole alkaloids (modified from KEGG pathways and Yamamoto et al., 2016).

### 3.3. Extraction and quantification of reserpine using UPLC analysis

Different sections of the root, shoot, and leaves of *R. tetraphylla* were collected from the nursery and oven dried for 3 days at 70 °C (Fig. 1). Tissues were powdered and extracted using 5 mL of methanol (Merck), centrifuged at 10,000 rpm for 5 min and filtered with 0.2 µm filters. Filtered sample (2 µL) was analyzed using UPLC Waters ACQUITY UPLC™ system SYNAPT G2-Si equipped with a binary solvent delivery system, an autosampler, column manager, and a tunable MS detector. Chromatographic separation was performed on a Waters ACQUITY UPLC™ BEH, C18 (130 Å, 1.7 µm, 2.1 mm × 50 mm, 1/pkg) column at 40 ± 5 °C. The mobile phase employed for UPLC analysis consisted of water; methanol (50:50 v/v) in a gradient mode, which was degassed, previously. The flow rate of the mobile phase was kept at 0.50 mL/min and 2 µL of sample solution was injected in each run. The total chromatographic run time was 5 min in resolution mode. The column and autosampler were maintained at 40 ± 5 and 4 ± 5 °C, respectively and pressure of the system was set to 15,000 psi. Care was exercised to ensure that the initial and final volumes of the extract were maintained constant for the sample. Standard curve was developed for the concentration range of 0.125 mg/mL to 1 mg/mL of standard reserpine (Sigma). The best fit ( $R^2 = 0.99$ ) was used in calculating the amount of reserpine in the sample (Fig. S4). All estimates were done on 3 replicates. Semi-quantitative analyses of other indole alkaloids were determined based on the extracted ion chromatogram for the specific ions (Fig. S5).

### 3.4. DESI MS analysis

Plant was uprooted and washed with running tap water and later with distilled water to remove all the debris from the root and other parts (Fig. 1a). Plants were segregated in different parts such as root, stem, leaves and fruits. Stem and roots were cross-sectioned (about 2 mm thick) using surgical blade (Fig. 1e). Fruits were collected at three developmental stages, namely immature (green), mature (green) and ripened (orange to red). Cross sections were made at mid-axis of the fruit and imprinted on flat surface of TLC plate for 10 s to obtain the imprint (TLC Silica gel 60 F<sub>254</sub>, Merck KGaA, Germany). Prior to imprinting, the TLC plates were pre-wetted with methanol and kept on a heating mantle (~70 °C) to obtain molecules present on the cut-end of the sections (Cabral et al., 2013; Mohana Kumara et al., 2015). Young leaves were imprinted on a TLC plate with 2 ton pressure for 15–30 s using a hydraulic pelletizer.

Imaging experiments were conducted using Thermo Scientific LTQ XL (Thermo Scientific, San Jose, CA, USA) mass spectrometer with 2D DESI ion source (Omni Spray Ion Source) from ProSolia, Inc., Indianapolis, IN, USA. The DESI source conditions were as follows; nebulizing gas (dry nitrogen) pressure: 150 psi, spray angle: 60°, tip of spray to surface: 1 mm, tip to inlet distance: 3 mm, spray solvent: methanol, solvent flow rate: 5 µL, spray voltage: 5 kV, and ionization mode: positive (+ve). The image area was chosen according to the sample dimensions and the spatial resolution used was 250 µm × 250 µm. Imaging 1 cm × 1 cm area of tissue sample took approximately 30 min. Imaging time varied with area of the tissue samples. Image files (IMG File) were created using FireFly software from the acquired data and Biomap 3 software was used to process the image files to create images.

### 3.5. Principal component analysis (PCA)

Principal component analysis (PCA) was done based on the exact masses of the compounds ( $m/z$  150–1000 range) recovered from fruits, leaves, and roots to examine if there is a differentiation of the tissues based on their metabolite content. Three representatives mid-point DESI MS spectra corresponding to the different tissues were collected and the masses were extracted for PCA analysis. The analysis was

performed using the statistical software PAST 3.08 (Hammer et al., 2001). The PCA analysis was based on a variance-covariance matrix.

### Conflicts of interest

The authors declare no conflict of interest.

### Acknowledgements

We thank Department of Science and Technology (DST), Government of India for the financial support to carry out this work. P.M.K. thanks IIT Madras, Chennai for a postdoctoral fellowship CY14IPF02 and SERB-DST Fast track grant File No SB/YS/LS-361/2013 for financial support.

### Appendix A. Supplementary data

Supplementary data to this article can be found online at <https://doi.org/10.1016/j.phytochem.2018.11.009>.

### References

- Andersen, T.B., Martinez-Swatson, K.A., Rasmussen, S.A., Boughton, B.A., Jørgensen, K., Andersen-Ranberg, J., Nyberg, N., Christensen, S.B., Simonsen, H.T., 2017. Localization and in-vivo characterization of *Thapsia garganica* CYP76AE2 indicates a role in thapsigargin biosynthesis. *Plant Physiol.* 174, 56–72.
- Berenbaum, M.R., 1995. The chemistry of defense: theory and practice. *Proc. Natl. Acad. Sci. U. S. A.* 92, 2–8.
- Bhandari, D.R., Wang, Q., Friedt, W., Spengler, B., Gottwald, S., Rompp, A., 2015. High resolution mass spectrometry imaging of plant tissues: towards a plant metabolite atlas. *Analyst* 140, 7696–7709.
- Bjarnholt, N., Li, B., D'Alvise, J., Janfelt, C., 2014. Mass spectrometry imaging of plant metabolites - principles and possibilities. *Nat. Prod. Rep.* 31, 818–837.
- Boughton, B.A., Thinakaran, D., Sarabia, D., Bacic, A., Roessner, U., 2016. Mass spectrometry imaging for plant biology: a review. *Phytochemistry Rev.* 15, 445–488.
- Burlat, V., Oudin, A., Courtois, M., Rideau, M., St-Pierre, B., 2004. Co-expression of three MEP pathway genes and geraniol 10-hydroxylase in internal phloem parenchyma of *Catharanthus roseus* implicates multicellular translocation of intermediates during the biosynthesis of monoterpene indole alkaloids and isoprenoid-derived primary metabolites. *Plant J.* 38, 131–141.
- Cabral, E., Mirabelli, M., Perez, C., Ifa, D., 2013. Blotting assisted by heating and solvent extraction for DESI-MS imaging. *J. Am. Soc. Mass Spectrom.* 24, 956–965.
- Chen, C.M., Ertl, J.R., Leisner, S.M., Chang, C.C., 1985. Localization of cytokinin biosynthetic sites in pea plants and carrot roots. *Plant Physiol.* 78, 510–513.
- Dalisy, D.S., Kim, K.W., Lee, C., Yang, H., Rübel, O., Bowen, B.P., Davin, L.B., Lewis, N.G., 2015. Dirigent protein-mediated lignan and cyanogenic glucoside formation in flax seed: integrated omics and MALDI mass spectrometry imaging. *J. Nat. Prod.* 78, 1231–1242.
- Dopstadt, J., Vens-Cappell, S., Neubauer, L., Tudzynski, P., Cramer, B., Dreisewerd, K., Humpf, H.U., 2017. Localization of ergot alkaloids in sclerotia of *Claviceps purpurea* by matrix-assisted laser desorption/ionization mass spectrometry imaging. *Anal. Bioanal. Chem.* 409, 1221–1230.
- Dueñas, M.E., Klein, A.T., Alexander, L.E., Yandean-Nelson, M.D., Nikolau, B.J., Lee, Y.J., 2017. High spatial resolution mass spectrometry imaging reveals the genetically programmed, developmental modification of the distribution of thylakoid membrane lipids among individual cells of maize leaf. *Plant J.* 89, 825–838.
- Dug   de Bernonville, T., Clastre, M., Besseau, S.B., Oudin, A., Burlat, V., Gl  evarec, G.L., Lanoue, A., Papon, N., Giglioli-Guivarc'h, N., St-Pierre, B., Courdavault, V., 2015. Phytochemical genomics of the Madagascar periwinkle: unravelling the last twists of the alkaloid engine. *Phytochemistry* 113, 9–23.
- El-Sayed, M., Verpoorte, R., 2007. *Catharanthus* terpenoid indole alkaloids: biosynthesis and regulation. *Phytochemistry Rev.* 6, 277–305.
- Faisal, M., Ahmad, N., Anis, M., 2005. Shoot multiplication in *Rauwolfia tetraphylla* L. using thidiazuron. *Plant Cell Tissue Organ Cult.* 80, 187–190.
- Gupta, S., Khanna, V.K., Maurya, A., Bawankule, D.U., Shukla, R.K., Pal, A., Srivastava, S.K., 2012. Bioactivity guided isolation of antipsychotic constituents from the leaves of *Rauwolfia tetraphylla* L. *Fitoterapia* 83, 1092–1099.
- Hagel, J.M., Yeung, E.C., Facchini, P.J., 2008. Got milk? The secret life of laticifers. *Trends Plant Sci.* 13, 631–639.
- Hammer, Ø., Harper, D.A.T., Ryan, P.D., 2001. PAST: paleontological statistics software package for education and data analysis. *Palaeontol. Electron.* 4 9pp.
- Hansen, A.C., Glassmire, A.E., Dyer, L.A., Smilanich, A.M., 2016. Patterns in parasitism frequency explained by diet and immunity. *Ecography* 40, 803–805.
- Hemalatha, R.G., Pradeep, T., 2013. Understanding the molecular signatures in leaves and flowers by desorption electrospray ionization mass spectrometry (DESI MS) imaging. *J. Agric. Food Chem.* 61, 7477–7487.
- Heskes, A.M., Sundram, T.C.M., Boughton, A., B.A. Jensen, N.B., Hansen, N.L., Crocoll, C., Cozzi, F., Rasmussen, S., Hamberger, B., Hamberger, B., Staerk, D., Moller, B.L., Pateraki, I., 2018. Biosynthesis of bioactive diterpenoids in the medicinal plant *Vitex*

- agnus-castus*. Plant J. 93, 943–958.
- Ifa, D.R., Srimany, A., Eberlin, L.S., Naik, H.R., Bhat, V., Cooks, R.G., Pradeep, T., 2011. Tissue imprint imaging by desorption electrospray ionization mass spectrometry. Anal. Methods 3, 1910–1912.
- Jiang, X., Liu, Y., Li, W., Zhao, L., Meng, F., Wang, Y., Tan, H., Yang, H., Wei, C., Wan, X., Gao, L., Xia, T., 2013. Tissue-Specific, Development-Dependent Phenolic Compounds Accumulation Profile and Gene Expression Pattern in Tea Plant *Camellia sinensis*. PLoS One 8, e62315.
- Kaushik, N., Kaushik, N., Attri, P., Kumar, N., Kim, C., Verma, A., Choi, E., 2013. Biomedical importance of indoles. Molecules 18, 6620.
- Kiesecker, C., Zitron, E., Lück, S., Bloehs, R., Scholz, E.P., Kathöfer, S., Thomas, D., Kreye, V.A.W., Katus, H.A., Schoels, W., Karle, C.A., Kiehn, J., 2004. Class Ia anti-arrhythmic drug ajmaline blocks HERG potassium channels: mode of action. Naunyn-Schmiedeberg's Arch. Pharmacol. 370, 423–435.
- Korte, A.R., Song, Z., Nikolau, B.J., Lee, Y.J., 2012. Mass spectrometric imaging as a high-spatial resolution tool for functional genomics: tissue-specific gene expression of TT7 inferred from heterogeneous distribution of metabolites in Arabidopsis flowers. Anal. Methods 4, 474–481.
- Kueger, S., Steinhäuser, D., Willmitzer, L., Giavalisco, P., 2012. High-resolution plant metabolomics: from mass spectral features to metabolites and from whole-cell analysis to subcellular metabolite distributions. Plant J. 70, 39–50.
- Lee, Y.J., Perdian, D.C., Song, Z., Yeung, E.S., Nikolau, B.J., 2012. Use of mass spectrometry for imaging metabolites in plants. Plant J. 70, 81–95.
- Liu, J., Cai, J., Wang, R., Yang, S., 2017. Transcriptional regulation and transport of terpenoid indole alkaloid in *Catharanthus roseus*: exploration of new research directions. Int. J. Mol. Sci. 18, 53.
- Mahata, M., Mahata, S.K., Parmer, R.J., O'Connor, D.T., 1996. Vesicular monoamine transport inhibitors. novel action at calcium channels to prevent catecholamine secretion hypertension. 28, 414–420.
- Mahroug, S., Courdavaud, V., Thiersault, M., St-Pierre, B., Burlat, V., 2006. Epidermis is a pivotal site of at least four secondary metabolic pathways in *Catharanthus roseus* aerial organs. Planta 223, 1191–1200.
- Miettinen, K., Dong, L., Navrot, N., Schneider, T., Burlat, V., Pollier, J., Woittiez, L., van der Krol, S., Lugan, R.L., Ilc, T., Verpoorte, R., Oksman-Caldentey, K.M., Martinoia, E., Bouwmeester, H., Goossens, A., Memelink, J., Werck-Reichhart, D.L., 2014. The secoiridoid pathway from *Catharanthus roseus*. Nat. Commun. 5, 3606.
- Mohana Kumara, P., Srimany, A., Ravikanth, G., Uma Shaanker, R., Pradeep, T., 2015. Ambient ionization mass spectrometry imaging of rohitukine, a chromone anti-cancer alkaloid, during seed development in *Dysoxylum binectariferum* Hook.f (Meliaceae). Phytochemistry 116, 104–110.
- Mohana Kumara, P., Srimany, A., Arunan, S., Ravikanth, G., Uma Shaanker, R., Pradeep, T., 2016. Desorption Electrospray Ionization (DESI) Mass Spectrometric Imaging of the Distribution of Rohitukine in the Seedling of *Dysoxylum binectariferum* Hook. F. PLoS One 11 (6), e0158099.
- Nielsen, L.J., Stuart, P., Pičmanová, M., Rasmussen, S., Olsen, C.E., Harholt, J., Møller, B.L., Bjarnholt, N., 2016. Dhurrin metabolism in the developing grain of *Sorghum bicolor* (L.) Moench investigated by metabolite profiling and novel clustering analyses of time-resolved transcriptomic data. BMC Genomics 17, 1021.
- O'Connor, S.E., Maresh, J.J., 2006. Chemistry and biology of monoterpene indole alkaloid biosynthesis. Nat. Prod. Rep. 23, 532–547.
- Pan, Q., Mustafa, N.R., Tang, K., Choi, Y.H., Verpoorte, R., 2015. Monoterpenoid indole alkaloids biosynthesis and its regulation in *Catharanthus roseus*: a literature review from genes to metabolites. Phytochemistry Rev. 15, 221–250.
- Pandey, A., Swarnkar, V., Pandey, T., Srivastava, P., Kanojia, S., Mishra, D.K., Tripathi, V., 2016. Transcriptome and Metabolite analysis reveal candidate genes of the cardiac glycoside biosynthetic pathway from *Calotropis procera*. Sci. Rep. 6, 34464.
- Pathania, S., Acharya, V., 2016. Computational analysis of “-omics” data to identify transcription factors regulating secondary metabolism in *Rauvolfia serpentina*. Plant Mol. Biol. Rep. 34, 283–302.
- Schluttenhofer, C., Pattanaik, S., Patra, B., Yuan, L., 2014. Analyses of *Catharanthus roseus* and Arabidopsis thaliana WRKY transcription factors reveal involvement in jasmonate signaling. BMC Genomics 15, 502.
- Smith, C.A., I'Maille, G., Want, E.J., Qin, C., Trauger, S.A., Brandon, T.R., Custodio, D.E., Abagyan, R., Siuzdak, G., 2005. METLIN: a metabolite mass spectral database. Ther. Drug Monit. 27, 747–751.
- St-Pierre, B., Vazquez-Flota, F.A., De Luca, V., 1999. Multicellular compartmentation of *catharanthus roseus* alkaloid biosynthesis predicts intercellular translocation of a pathway intermediate. Plant Cell 11, 887–900.
- Sturtevant, D., Dueñas, M.E., Lee, Y.J., Chapman, K.D., 2017. Three-dimensional visualization of membrane phospholipid distributions in Arabidopsis thaliana seeds: a spatial perspective of molecular heterogeneity. BBA. Mol. Cell Biol. Lipids 1862, 268–281.
- Woodfield, H.K., Sturtevant, D., Borisjuk, L., Munz, E., Guschina, I.A., Chapman, K., Harwood, J.L., 2017. Spatial and temporal mapping of key lipid species in *Brassica napus* seeds. Plant Physiol. 173, 1998–2009.
- Yamamoto, K., Takahashi, K., Mizuno, H., Aneqawa, A., Ishizaki, K., Fukaki, H., Ohnishi, M., Yamazaki, M., Masujima, T., Mimura, T., 2016. Cell-specific localization of alkaloids in *Catharanthus roseus* stem tissue measured with Imaging MS and Single-cell MS. Proc. Natl. Acad. Sci. U. S. A. 113, 3891–3896.
- Yu, F., De Luca, V., 2013. ATP-binding cassette transporter controls leaf surface secretion of anticancer drug components in *Catharanthus roseus*. Proc. Natl. Acad. Sci. U. S. A. 110, 15830–15835.
- Zhu, J., Wang, M., Wen, W., Yu, R., 2015. Biosynthesis and regulation of terpenoid indole alkaloids in *Catharanthus roseus*. Phcog. Rev. 9 (17), 24–28.
- Zifkin, M., Jin, A., Ozga, J.A., Zaharia, L.I., Scherthaner, J.P., Gesell, A., Abrams, S.R., Kennedy, J.A., Constabel, C.P., 2012. Gene expression and metabolite profiling of developing highbush blueberry fruit indicates transcriptional regulation of flavonoid metabolism and activation of abscisic acid metabolism. Plant Physiol. 158, 200–224.



**UPLC and ESI-MS analysis of metabolites of *Rauvolfia tetraphylla* L. and their spatial localization using desorption electrospray ionization (DESI) mass spectrometric imaging**

P. Mohana Kumara<sup>\*a,c</sup>, R. Uma Shaanker<sup>b</sup> and T. Pradeep<sup>\*a</sup>

<sup>a</sup> *DST Unit of Nanoscience and Thematic Unit of Excellence, Department of Chemistry, Indian Institute of Technology Madras, Chennai, 600036, India,*

<sup>b</sup> *School of Ecology and Conservation, Department of Crop Physiology, University of Agricultural Sciences, GKVK, Bengaluru, 560065, India*

<sup>c</sup> *Center for Ayurveda Biology and Holistic Nutrition, The University of Trans-Disciplinary Health Sciences and Technology (TDU), Bengaluru, 560064*

**Corresponding authors:**

**Prof. T. Pradeep**

[pradeep@iitm.ac.in](mailto:pradeep@iitm.ac.in)

Phone: +91-44-2257 4208

Fax: +91-44-2257 0509/0545

and

**Dr. P. Mohana Kumara**

[monapatelpgatti@gmail.com](mailto:monapatelpgatti@gmail.com)

Mobile: 9790464058, Fax; +91-80-28567926

## Identification of indole alkaloids using exact mass and ESI MS/MS analysis

ESI MS analysis of the different parts (root, stem, leaf and fruits) of *R. tetraphylla* showed the presence of prominent metabolite signatures in the range of  $m/z$  150-1000 (**Table1**). Among the different tissues, roots contained relatively large number of indole alkaloids (Fig S2). Structural characterization of these indole alkaloids were done by both mass fragmentation analysis and accurate mass measurement (**Fig S2**) (Smith et al., 2005). A list of  $m/z$  values of the parent and fragment ions and their chemical formulae are given in **Table 1**.

Based on the masses obtained, we present below the salient results pertaining to exact masses and to the fragmentation ions.

Strictosidine ( $C_{27}H_{34}N_2O_9$ ; exact mass  $m/z$  531.2337), a key metabolic precursor in the synthesis of indole alkaloids was identified by ESI MS analysis in root and leaf. The identity was also confirmed by the characteristic fragmentations: at  $m/z$  514 due to loss of  $H_2O$ ,  $m/z$  499 due to loss of  $CH_3OH$ ,  $m/z$  351 is due loss of glucose,  $m/z$  222, 223 and  $m/z$  144 is due to breakage of C ring. These fragmentations corresponded with the published literatures and metabolite databases (Yamamoto et al., 2016) (**Fig S2a**). Here we present briefly the major alkaloids represented under three broad categories, namely, reserpine type, ajmalcine type and serpentine type of alkaloids.

### Reserpine type of alkaloids

Yohimbine ( $C_{21}H_{26}N_2O_3$ ),  $m/z$  355.2 and exact mass of  $m/z$  355.2007, has a pentacyclic ring system with substitution at C16 and C17. The MS/MS spectrum showed five characteristic fragment ions at  $m/z$  337, 323, 224, 212 and 144. The product ions at  $m/z$  323 and 337 were produced due to the loss of  $CH_3OH$  and  $H_2O$  in terpene moiety, whereas the product ions at  $m/z$  224, 212 and 144 produced due to cleavage of C ring (**Fig S2b**). Correspondingly, the ion at  $m/z$  609.2 and exact mass  $m/z$  609.2802 was identified as reserpine ( $C_{33}H_{41}O_9N_2$ ). ESI MS fragmentation pattern of  $m/z$  609.2 showed the characteristic fragment ions at  $m/z$  397.2 due to loss of trimethoxybenzoic acid moiety and  $m/z$  195.0 due to cleavage of ester bond between trimethoxybenzoic acid from the rest of moiety. Further, fragment ion at  $m/z$  397.2 fragmented to  $m/z$  365.2 due to loss of methanol, and  $m/z$  236.01 due to loss of methanol followed by cleavage of C-ring. Fragment ion at  $m/z$  448.2 was also produced due to cleavage of C ring from the precursor ion (**Fig S2c**). The ion at  $m/z$  144 showed the presence of indole moiety fragmentation, this is one of the characteristic fragment confirming the molecule is the indole group of compounds (Bindu et al., 2014; Kumar et al., 2016a).

Similarly, few other reserpine like molecules  $m/z$  341.2, 371.2, 565.2, 579.2 were identified as yohimbic acid, 18-hydroxyepialloyohimbine, raunescine, deserpidine

respectively based on the exact mass and their mass fragmentation (**Fig S2d-i**). Yohimbinic acid ( $m/z$  341.1862;  $C_{20}H_{25}N_2O_3$ ; **Fig S2d**) mass fragmented to  $m/z$  323 due to the loss of  $H_2O$  in terpene moiety, whereas the product ions at  $m/z$  196, 212 and 144 produced due to cleavage of C ring (**Fig S2b**). 18-hydroxyepialloyohimbine ( $m/z$  371.1961;  $C_{21}H_{26}N_2O_4$ ; **Fig S2e**) fragmented to  $m/z$  353 and 339, were due to the loss of  $CH_3OH$  and  $H_2O$  in terpene moiety, whereas the product ions at  $m/z$  240, 228 and 144 produced due to cleavage of C ring (**Fig S2c**). Deserpidine ( $m/z$  579.2698;  $C_{32}H_{38}N_2O_8$ ; **Fig S2 f-g**) and raunescine ( $m/z$  565.2542;  $C_{31}H_{36}N_2O_8$ ; **Fig S2h-i**) and showed the characteristic mass fragmentations similar to reserpine,  $m/z$  321.2 and  $m/z$  367.2 due to loss of trimethoxybenzoic acid moiety and  $m/z$  195.0 due to cleavage of ester bond between trimethoxybenzoic acid from the rest of moiety. Fragment ion at  $m/z$  448.2 was also produced due to cleavage of C ring from the precursor ion, respectively (**Fig S2 d-i**). Further, fragment ion of deserpidine at  $m/z$  397.2 fragmented to  $m/z$  365.2 due to loss of methanol, and  $m/z$  236.01 due to loss of methanol followed by cleavage of C-ring (**Fig S2d-i**) (Kumar et al., 2016a; Kumar et al., 2016b; Pandey et al., 2016).

### Ajmalcine type of alkaloids

The ion at  $m/z$  353.2 was identified as ajmalcine ( $m/z$  353.1851;  $C_{21}H_{25}N_2O_3$ ; **Fig S2j**). The product ions at  $m/z$  321 was produced due to the loss of  $CH_3OH$  in terpene moiety, whereas the product ions at  $m/z$  210, 222 and 144 were produced due to cleavage of C ring (**Fig S2j-k**). Similarly,  $m/z$  413.2 identified as reserpiline ( $m/z$  413.2068;  $C_{23}H_{29}N_2O_5$ ; **Fig S2k**). The mass fragmentation of  $m/z$  413.2 showed five characteristic fragment ions at  $m/z$  337, 224, 204 and 144. The product ions at  $m/z$  339 produced due to the loss of  $CH_3OH$  in terpene moiety, whereas the product ions at  $m/z$  224, 204 and 144 produced due to cleavage of C ring (**Fig S2i-k**) (Bindu et al., 2014; Kumar et al., 2015; Kumar et al., 2016b; Kumar et al., 2016c; Pandey et al., 2016; Sagi et al., 2016).

### Ajmaline type of alkaloids

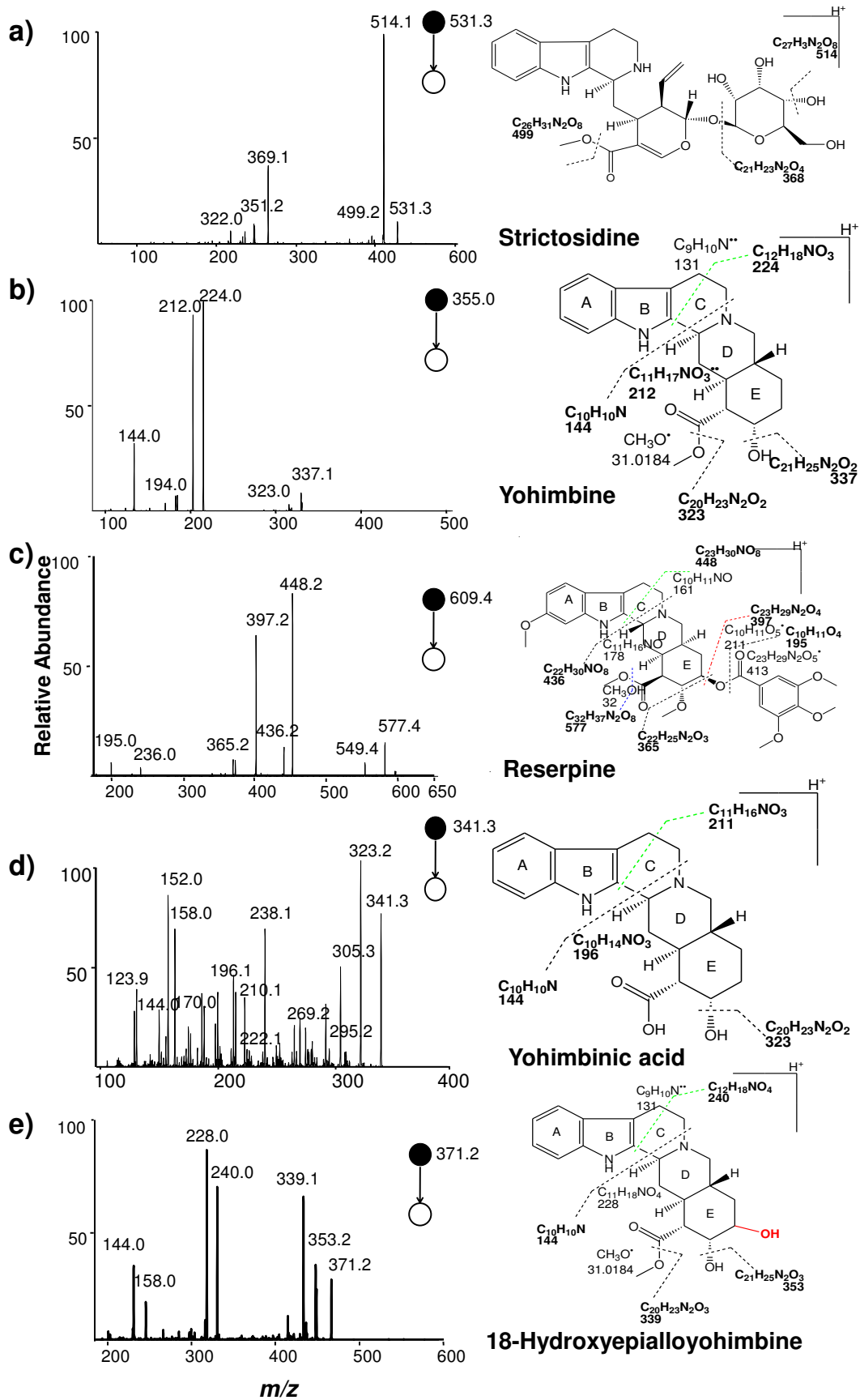
The ion  $m/z$  327.2 at ajmaline ( $m/z$  327.2063;  $C_{20}H_{27}N_2O_2$ ; **Fig S2l**) showed the fragment ions at  $m/z$  309, 238, 210, 194, 182, 158, 144. The product ions at  $m/z$  309 and  $m/z$  291 were produced due to the successive losses of  $H_2O$  in terpene moiety, whereas the product ions at  $m/z$  238, 212, 194 and 144 were produced due to cleavage of C ring. Methyl indole derivative ( $m/z$  158) is formed by ring cleavage at C-ring and further loss of methyl group from nitrogen atom yields the base peak at  $m/z$  144 [ $C_{10}H_{10}N$ ]<sup>+</sup>. Loss of  $C_8H_7NO$  from protonated ion gives  $m/z$  194 [ $C_{12}H_{21}NO$ ]<sup>+</sup> (**Fig S2l-q**). Similarly, ions at  $m/z$  309.2, 311.1, 313.2, 323.2, 325.2 identified as sarpagine ( $m/z$  311.175;  $C_{19}H_{23}N_2O_2$ ; **Fig S2m**), 10-O-methylsarpagine ( $m/z$  325.1907;  $C_{20}H_{25}N_2O_2$ ; **Fig S2n-o**), tetraphyllicine ( $m/z$  309.1957;  $C_{20}H_{25}N_2O$ ; **Fig S2p**), mitoridine ( $m/z$  323.1749;  $C_{20}H_{23}N_2O_2$ ; **Fig S2q**) respectively. Identity of these

molecules was assigned based on the fragmentation patterns at C-ring cleavage (**Fig S2m-q**) (Bindu et al., 2014; Kumar et al., 2015; Kumar et al., 2016b; Kumar et al., 2016c; Pandey et al., 2016).

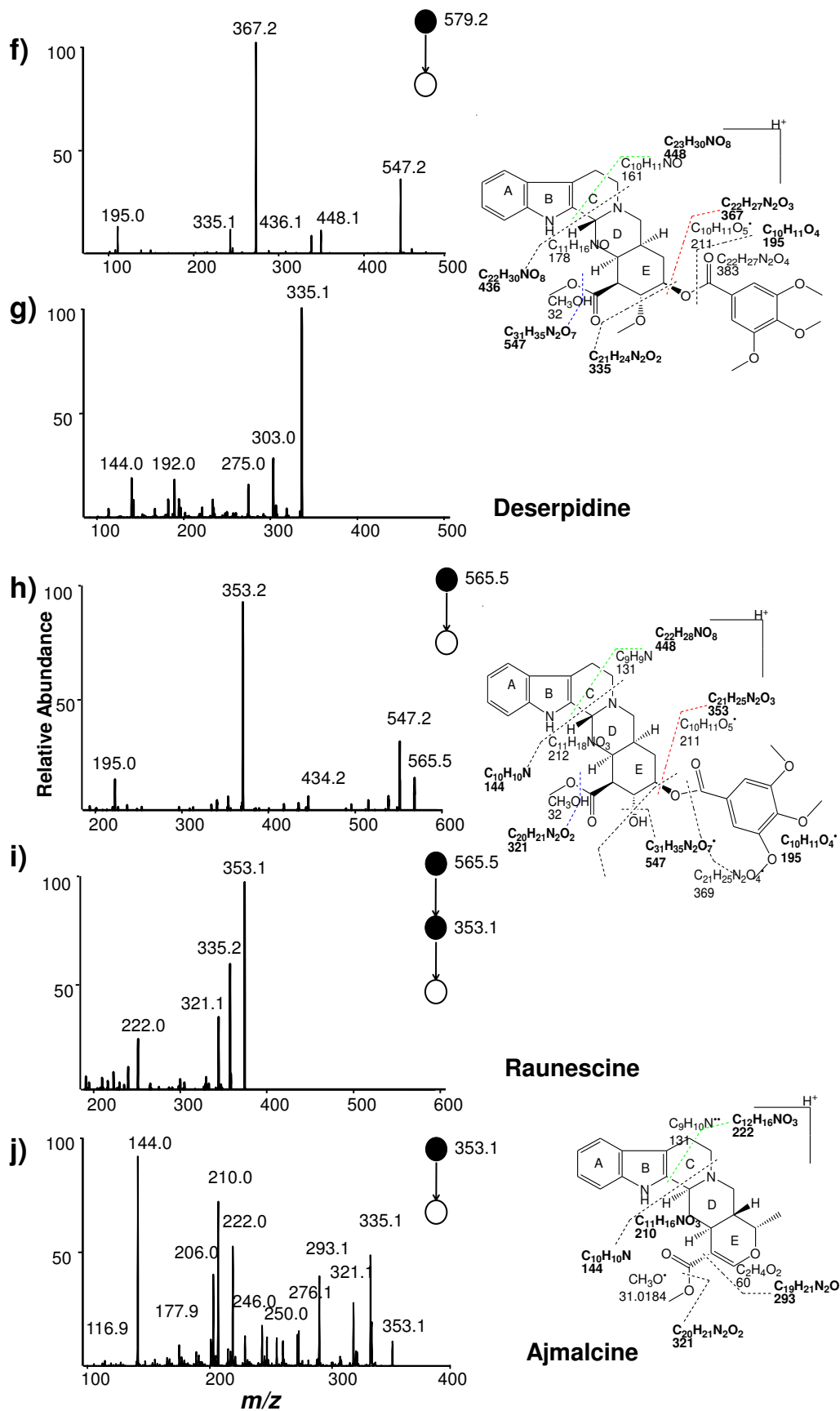
The ions at  $m/z$  349.1 were identified as serpentine ( $m/z$  349.1537;  $C_{21}H_{20}N_2O_3$ ). Serpentine showed the characteristic fragment ions at  $m/z$  317, 289, 277 and 263. The product ions at  $m/z$  317, 289 produced were due to the loss of  $CH_3OH$  and  $CO$  respectively, in terpene moiety, whereas the product ions at  $m/z$  277 and 263 produced were due to cleavage of E ring. One of the derivative of serpentine, demethyl serpentine was identified based on similar fragmentations (**Fig S2s-u**) (Kumar et al., 2016b).



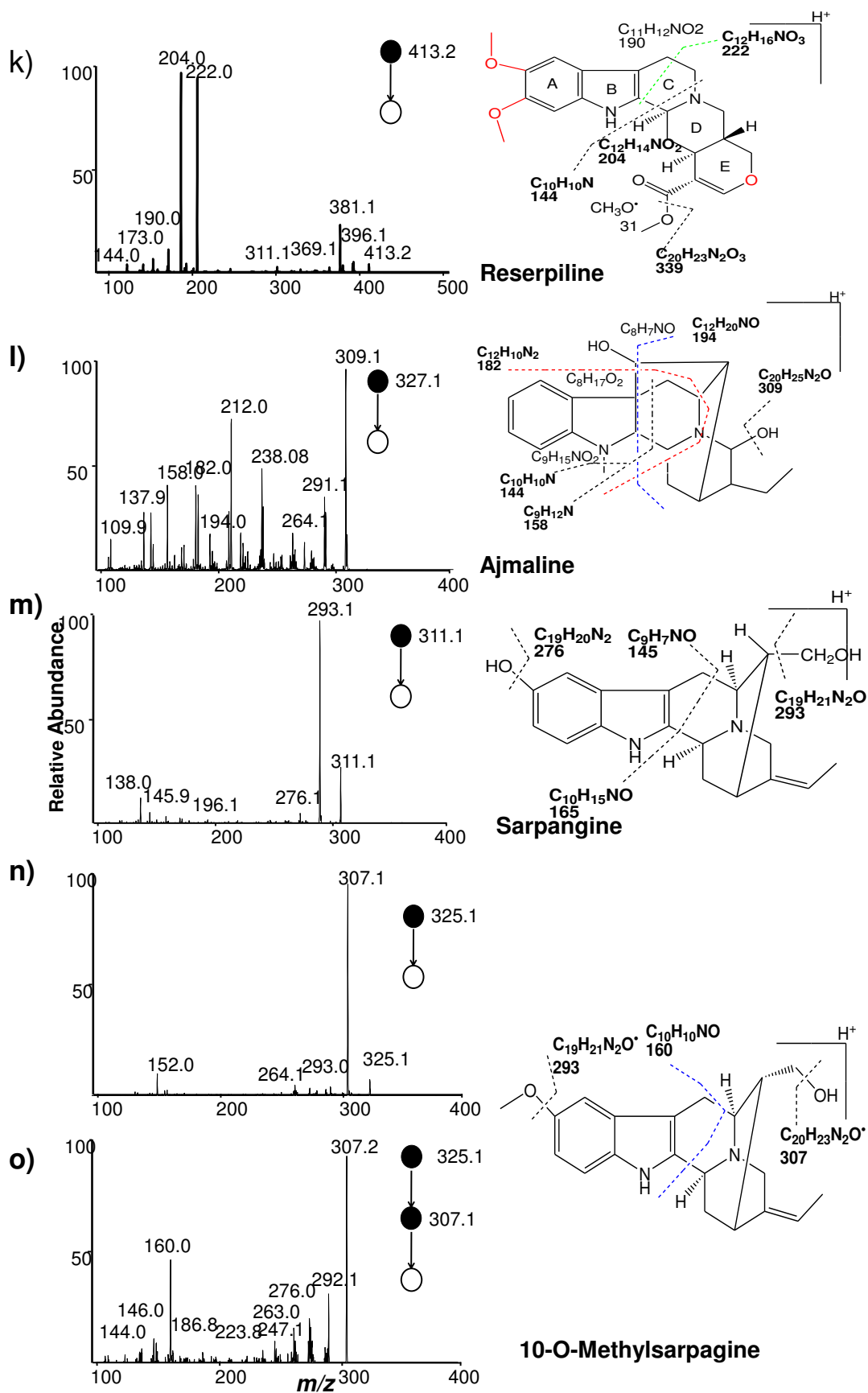
# Supplementary information



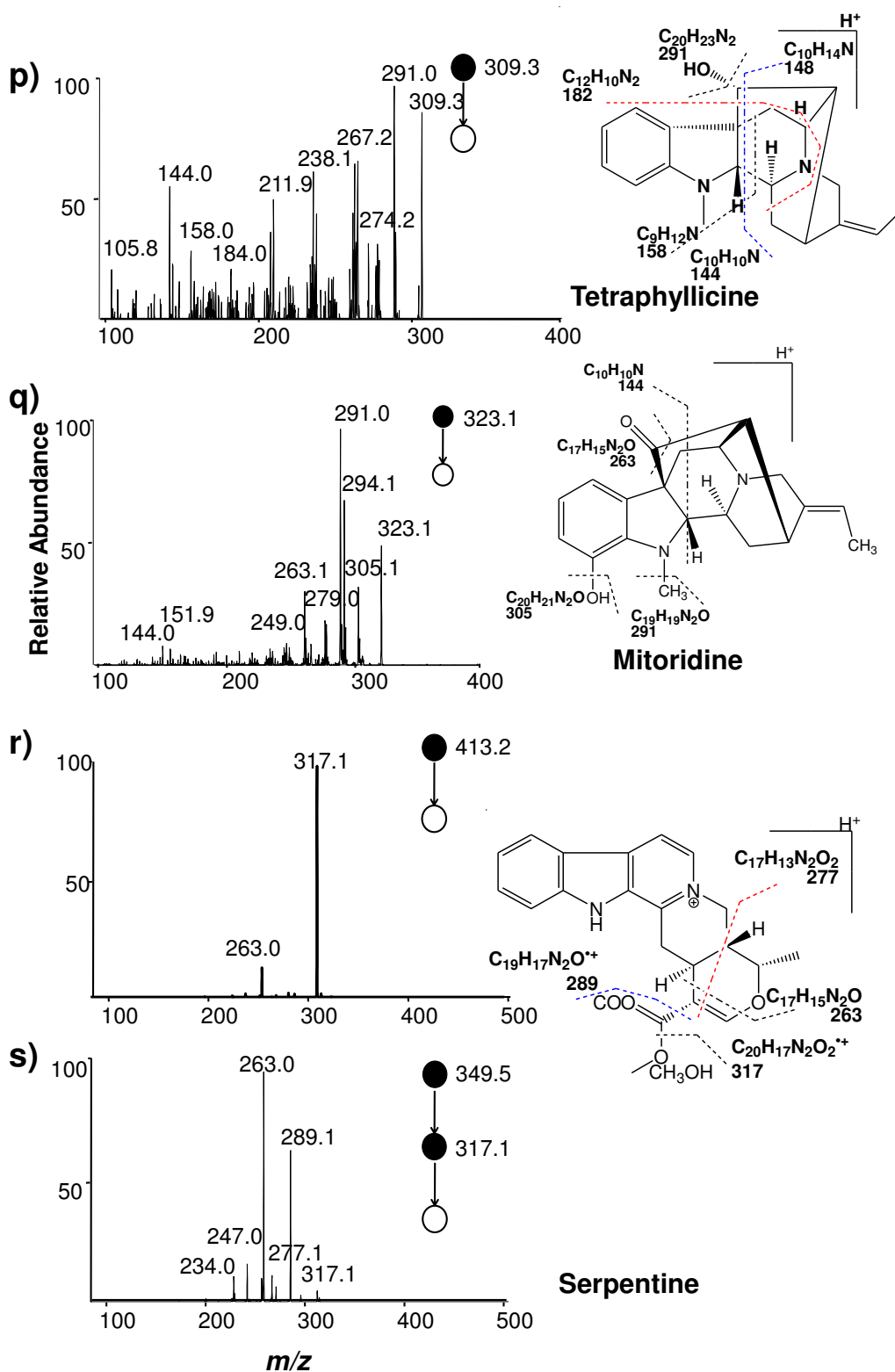
# Supplementary information

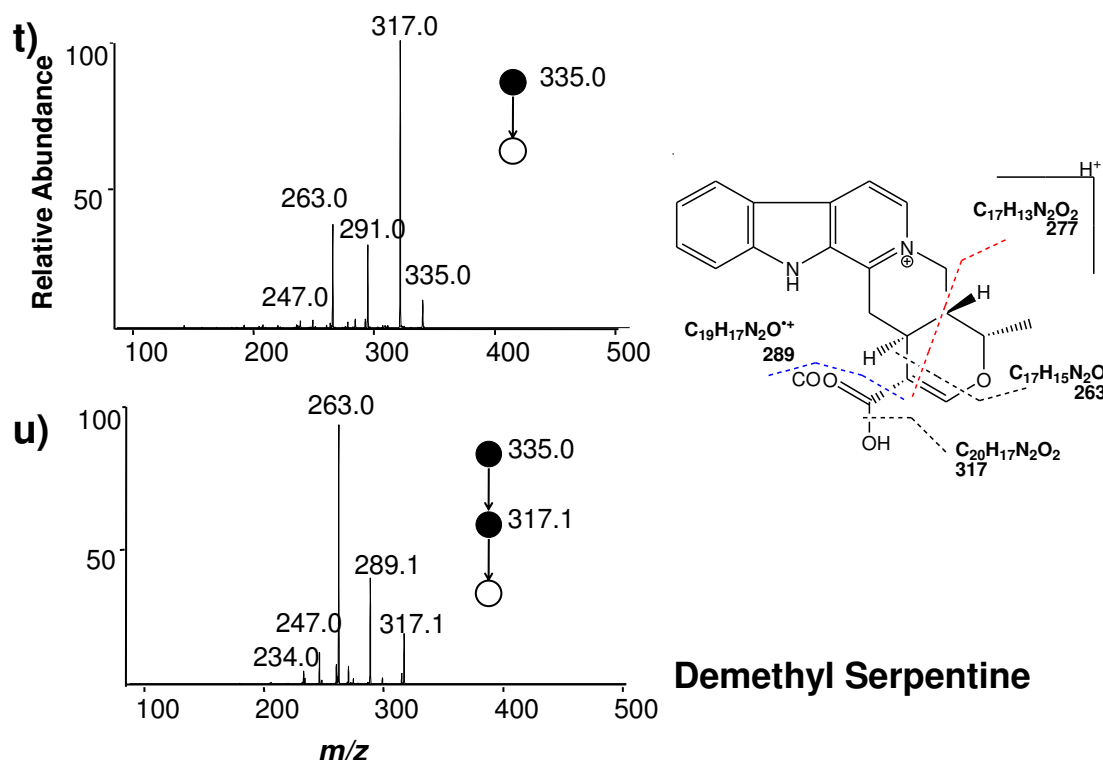


# Supplementary information



# Supplementary information





**Fig S2.** ESI MS/MS analysis of monoterpenoid indole alkaloids and their respective chemical structure and mass fragmentation patterns.

## References

- Bindu, S., Rameshkumar, K.B., Kumar, B., Singh, A., Anilkumar, C., 2014. Distribution of reserpine in *Rauwolfia* species from India“ HPTLC and LC-MS studies. *Ind Crops and Prod.* 62, 430-436.
- Kumar, S., Bajpai, V., Singh, A., Bindu, S., Srivastava, M., Rameshkumar, K.B., Kumar, B., 2015. Rapid fingerprinting of *Rauwolfia* species using direct analysis in real time mass spectrometry combined with principal component analysis for their discrimination. *Anal Methods.* 7, 6021-6026.
- Kumar, S., Singh, A., Bajpai, V., Kumar, B., 2016a. Identification, characterization and distribution of monoterpene indole alkaloids in *Rauwolfia* species by Orbitrap Velos Pro mass spectrometer. *J Pharma Biomed Anal* 118, 183-194.
- Kumar, S., Singh, A., Bajpai, V., Srivastava, M., Singh, B.P., Kumar, B., 2016b. Structural characterization of monoterpene indole alkaloids in ethanolic extracts of *Rauwolfia* species by liquid chromatography with quadrupole time-of-flight mass spectrometry. *J Pharma Anal.*
- Kumar, S., Singh, A., Bajpai, V., Srivastava, M., Singh, B.P., Ojha, S., Kumar, B.C.P.C.A.R., 2016c. Simultaneous Determination of Bioactive Monoterpene Indole Alkaloids in Ethanolic Extract of Seven *Rauwolfia* Species using UHPLC with Hybrid Triple Quadrupole Linear Ion Trap Mass Spectrometry. *Phytochem Anal.* 27, 296-303.

- Pandey, D.K., Radha, Dey, A., 2016. A validated and densitometric HPTLC method for the simultaneous quantification of reserpine and ajmalicine in *Rauwolfia serpentina* and *Rauwolfia tetraphylla*. *Revista Brasileira de Farmacognosia*.
- Sagi, S., Avula, B., Wang, Y.-H., Khan, I.A., 2016. Quantification and characterization of alkaloids from roots of *Rauwolfia serpentina* using ultra-high performance liquid chromatography-photo diode array-mass spectrometry. *Anal Bioanal Chem.*408, 177-190.
- Smith, C.A., I'Maille, G., Want, E.J., Qin, C., Trauger, S.A., Brandon, T.R., Custodio, D.E., Abagyan, R., Siuzdak, G., 2005. METLIN: a metabolite mass spectral database. *Ther Drug Monit.* 27, 747-751.
- Yamamoto, K., Takahashi, K., Mizuno, H., Anegawa, A., Ishizaki, K., Fukaki, H., Ohnishi, M., Yamazaki, M., Masujima, T., Mimura, T., 2016. Cell-specific localization of alkaloids in *Catharanthus roseus* stem tissue measured with Imaging MS and Single-cell MS. *Proc Natl Acad Sci U S A.* 113, 3891-3896.

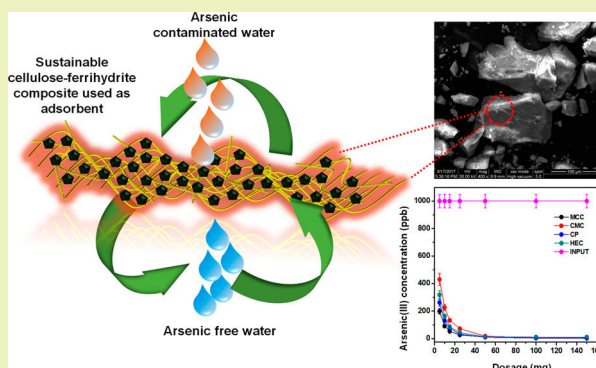
## Sustainable and Affordable Composites Built Using Microstructures Performing Better than Nanostructures for Arsenic Removal

Sritama Mukherjee,<sup>†,‡</sup> Avula Anil Kumar,<sup>†,§</sup> Chennu Sudhakar,<sup>†</sup> Ramesh Kumar,<sup>†</sup> Tripti Ahuja,<sup>†</sup> Biswajit Mondal,<sup>†</sup> Pillalamarri Srikrishnarka,<sup>†</sup> Ligy Philip,<sup>‡,§</sup> and Thalappil Pradeep<sup>\*,†,§</sup><sup>†</sup>DST Unit of Nanoscience (DST UNS) and Thematic Unit of Excellence (TUE), Department of Chemistry, and <sup>‡</sup>EWRE Division, Department of Civil Engineering, Indian Institute of Technology Madras, Chennai 600036, India

## S Supporting Information

**ABSTRACT:** Arsenicosis was recognized over 104 years ago. Elevated arsenic (As) concentrations in water is faced by about 200 million people worldwide and has become one of the biggest challenges in the context of water purification. Providing sustainable and affordable solutions to tackle this menace is a need of the hour. Adsorption on advanced materials is increasingly being recognized as a potential solution. Here, we report various functionalized microcellulose-reinforced 2-line ferrihydrite composites which show outstanding As(III) and As(V) adsorption capacities. Green synthesis of the composite yields granular media with high mechanical strength which show faster adsorption kinetics in a wide pH range, irrespective of the presence of other interfering ions in water. The composites and their interaction with As(III) and As(V) were studied by XRD, HRTEM, SEM, XPS, Raman, TG, and IR spectroscopy. Performance of the media in the form of cartridge reaffirms its utility for point-of-use water purification. We show that cellulose microstructures are more efficient than corresponding nanostructures for the purpose of arsenic remediation. We have also performed an evaluation of several sustainability metrics to understand the “greenness” of the composite and its manufacturing process.

**KEYWORDS:** Arsenic, Cellulose, Nanocomposite, Ferrihydrite, Adsorption, Sustainability metrics



## INTRODUCTION

Arsenic (As), a ubiquitous metalloid occurring across the biosphere (air, soils and rocks, natural waters, and organisms), ranks 20th in the Earth's crust, 14th in seawater, and 12th in the human body in abundance.<sup>1,2</sup> Despite its wide range of utilities in the field of medicine, agriculture, semiconductors, electronics, and metallurgy, As got its reputation as the “king of poisons” as a result of its very high toxicity and easy availability.<sup>3–5</sup> In the natural environment, As is rarely found as the free element but rather in the form of metal arsenites/arsenates or as a part of sulfidic ores (e.g., realgar, orpiment).<sup>6</sup> Mobilization of natural As to groundwater can occur through a combination of natural processes (like volcanic eruption, weathering) and/or anthropogenic activities (like mining, various industrial and agricultural activities).<sup>7,8</sup> The wide impact of As contamination in drinking water and the threat it poses to global health is much more widespread than previously estimated.<sup>9</sup> Arsenic gets ingested mostly through water and also through food.<sup>10</sup> It principally exists in the +3 and +5 oxidation states in water, common species being arsenite ( $\text{AsO}_3^{3-}$ ) and arsenate ( $\text{AsO}_4^{3-}$ ) and their protonated forms, commonly referred to as As(III) and As(V), while the free element As(0) is rarely found naturally.<sup>2</sup> The species existing at pH 7 are  $\text{H}_3\text{AsO}_3$ ,  $\text{H}_2\text{AsO}_4^{1-}$ , and  $\text{HASO}_4^{2-}$ . It is

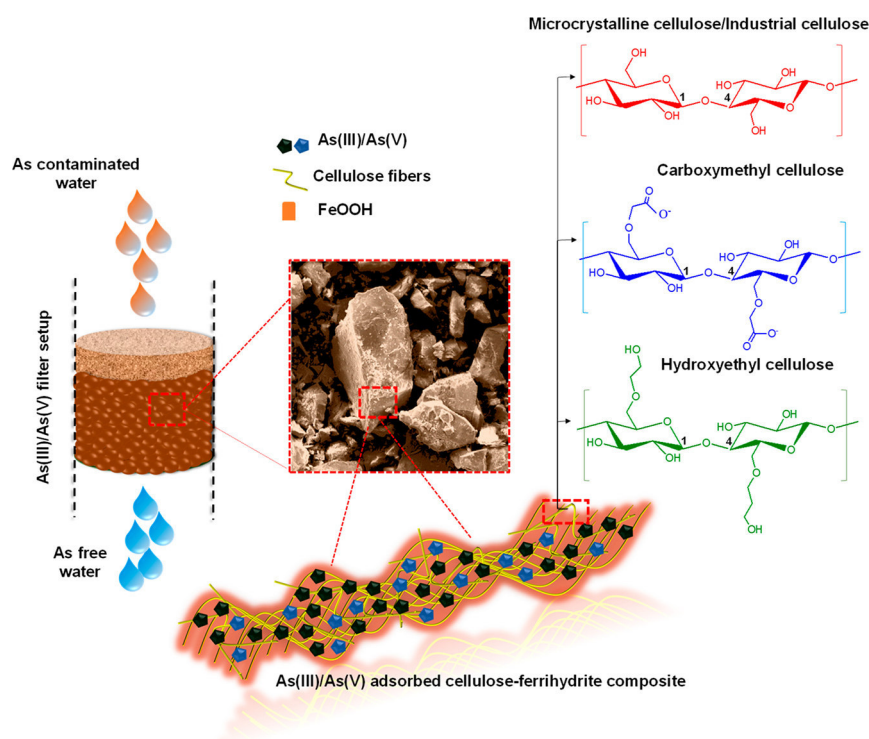
now well recognized that accumulation of As, even at low levels, leads to carcinogenesis and severe dermal hazards like keratosis and neurological disorders.<sup>4,9,11,12</sup> Greater than 200 million people belonging to more than 40 countries worldwide are exposed to concentrations in drinking water exceeding the World Health Organization (WHO) recommended limit of 10  $\mu\text{g/L}$ .<sup>13</sup> Solubility of As in groundwater is influenced by pH, speciation, redox conditions, temperature, and composition of the solution which in turn are governed by geology, climate, drainage, and topography. Desorption and dissolution are two important chemical processes that lead to As mobilization under two different physicochemical conditions. Poorly flushed aquifers having high sulfate and organic content creating highly reducing anaerobic environment are expected to present As in its reduced state, As(III), predominantly, while in alkaline aquifers in arid-to-semiarid climates, As is relatively soluble in its oxidized state, As(V).<sup>2,7</sup> In general, inorganic arsenicals are more toxic than organic ones, and As(III) is 25–60 times more toxic than As(V).<sup>14</sup>

Received: October 7, 2018

Revised: December 5, 2018

Published: December 10, 2018



Scheme 1. Illustration of Cellulose-Templated 2-Line Ferrihydrite Composite Used for Affordable Arsenic Removal from Water<sup>a</sup>

<sup>a</sup>Each of the celluloses were used in making of composites separately.

Several remediation technologies have come up which follow various kinds of approaches like concentration and subsequent removal, dilution and dispersion, conversion to less toxic species, or encapsulation.<sup>15</sup> The most common technologies used previously for As removal have been coagulation with metal salts, lime softening, oxidation techniques, and iron/manganese-based removal processes.<sup>16</sup> These techniques gradually lost their popularity due to their enhanced activity only at higher concentrations of the contaminant and inability to achieve the revised reduced drinking water standards.<sup>17</sup> Adsorption is one of the emerging techniques which has shown high efficiency toward As removal.<sup>18</sup> Adsorption is a phenomenon mainly driven by van der Waals and electrostatic forces causing the contaminants (adsorbate molecules and ions) to attach to the surface of a solid material (adsorbent). Adsorbents like activated carbon, activated alumina, graphene, zerovalent iron filings, zeolites, agricultural/industrial wastes, and iron oxides/hydroxides have been extensively studied and tested.<sup>18–22</sup> Nanomaterials are excellent candidates for water treatment applications due to the preferred characteristics such as large surface area, high specificity, high reactivity, and catalytic potential.<sup>23,24</sup> Nanoscale iron oxides, titania- or zirconia-based nanomaterials, and other metal oxides (like CuO, MgO, etc.) show high removal efficiency and have been researched widely.<sup>25–30</sup> It is recognized that low-cost and simple but effective technologies that can be deployed readily at a household or community level are important.<sup>27,31</sup>

In this context, biopolymers which have the characteristics like nontoxicity, biocompatibility, biodegradability, multifunctionality, and availability of adsorption sites are important to be used as reinforcing agents for nanoparticles which would act as stabilizers and prevent their agglomeration or

disintegration.<sup>32</sup> Chitosan has been studied extensively in the context of biosorbents due to its large numbers of hydroxyl and amino groups, making it chemically reactive and hydrophilic.<sup>32,33</sup> But, from a sustainability viewpoint, we cannot ignore the fact that chitosan is extracted by deacetylation of chitin which is found in the exoskeleton of crustacean shells, making it not so cheap and environmentally less enduring.

In contrast, cellulose is a plant-derived biopolymer available in nature with the highest abundance. It is a polysaccharide consisting of a linear chain of several hundred to many thousands of  $\beta(1 \rightarrow 4)$ -linked D-glucose units arranged in parallel and antiparallel fashion, with a huge number of hydroxyl groups making it reactive and modifiable, apart from being renewable and inexpensive.<sup>34,35</sup> Microcrystalline cellulose (MCC) is porous,  $\sim 10$ – $50 \mu\text{m}$  in diameter, having high cellulose content, with higher crystallinity, and is composed of aggregate bundles of multi-sized cellulose microfibrils that are strongly hydrogen bonded to each other in intra-chain and inter-chain bonding configurations.<sup>36</sup> These intrachain hydrogen bonds, mostly seen as  $\text{O3-H}\cdots\text{O5}$  bonds and interchain hydrogen bonding network between the  $(110)_{\text{triclinic}}$  and  $(200)_{\text{monoclinic}}$  planes, make cellulose a relatively stable polymer and give the cellulose fibrils high axial stiffness.<sup>37</sup> A periodic arrangement of highly ordered (crystalline) structures and disordered (amorphous-like) regions of cellulose chains coexist within the cellulose microfibrils. These smaller crystalline regions contained within the cellulose microfibrils are extracted in the process of producing cellulose nanocrystals (CNCs). The extraction process of the cellulose particles from the cellulose microfibrils may include any pretreatments or disintegration processes either mechanically or chemically. CNC production by mechanical extraction causes increased mechanical damage



leading to lesser percent crystallinity (54–88%) than the parent microfibrils (80–85%) with irregular shape and size (shown in Figure S1).<sup>36</sup> Moreover, imparting additional particle functionalities on CNCs by creating surface charges gives rise to interfibrillar repulsion. Because of all these, MCC is a mechanically and thermally more stable cellulose system for making composites for adsorption-related applications.

In this research, we have introduced micron-sized functionalized cellulose fibers-templated 2-line ferrihydrite nanocomposite for As removal from drinking water (Scheme 1). Four kinds of cellulose precursors with various functionalities, namely, carboxymethyl cellulose (CMC), microcrystalline cellulose (MCC), hydroxyethyl cellulose (HEC), and industrial grade cellulose powder (CP), have been used for making the composites to check the consistency in their adsorption performance for As removal. The individual uptake capacities of each of these composites were compared to that of the nanocellulosic (NC) composite, developed earlier by the group.<sup>38</sup> The composites have been made by a green synthetic process, and all of them show large adsorption capacity for both As(III) as well as As(V) removal. Their stability, in terms of mechanical strength and leaching-resistant properties, over a long period of time suggests the effectiveness of their use as sustainable materials for affordable point-of-use water purifiers. We compared the performance of these microstructures with the corresponding nanostructures and conducted a cost–benefit analysis of their utilization.

## EXPERIMENTAL SECTION

**Materials.** Three types of celluloses, CMC, MCC, and HEC, were purchased from Avantor Performance Materials India Ltd., SRL Pvt. Ltd. (India), and SD Fine Chemicals India Ltd., respectively, while the fourth, CP, was purchased from the local market. Ferric chloride hexahydrate ( $\text{FeCl}_3 \cdot 6\text{H}_2\text{O}$ ), sodium hydroxide (NaOH), and sodium sulfate ( $\text{Na}_2\text{SO}_4$ ) were purchased from RANKEM Glasswares and Chemicals Pvt. Ltd., India. Sodium arsenite ( $\text{NaAsO}_2$ ) and disodium hydrogen arsenate ( $\text{Na}_2\text{HAsO}_4 \cdot 7\text{H}_2\text{O}$ ) were purchased from SD Fine Chemicals Ltd. All chemicals were of laboratory grade and were used without further purification. The porous clay-based particulate and iron filter was developed by CSIR-Institute of Minerals and Materials Technology (IMMT), Bhubaneswar, India, and was purchased from Watsan Envirotech Private Limited, Chennai, India. Deionized (DI) water was used throughout the experiments unless otherwise mentioned.

**Methods: Synthesis of Cellulosic Composites.** Cellulose-templated 2-line ferrihydrite composites were synthesized by a green synthetic route. About 0.05 g of CMC was dissolved in 10 mL of water and sonicated for about 10 min to make it a homogeneous dispersion. The pH was adjusted to 9 by using 0.2 M NaOH. After 5 min of stirring, 0.5 g of  $\text{Na}_2\text{SO}_4$  was added, followed by another 5 min of incubation after which 10 mL of 1 M  $\text{FeCl}_3 \cdot 6\text{H}_2\text{O}$  was added. The mixture was precipitated and brought to pH 8 using 2 M NaOH by dropwise addition. The final reaction mixture was further kept for incubation for about 12 h at ambient temperature. The resulting gel was washed with water to remove soluble salts and was dried at room temperature (around 30 °C). The composite was insoluble in water and appeared like dark brown shiny crystals. The dried solid chunks were crushed mechanically and sieved to get the granular adsorbent media. The product obtained was about 1.2 g.

Similar composites were prepared by changing the cellulose type and keeping the proportions of other reagents and conditions the same. The resulting composites were referred to as CMCFH, MCCFH, HECFH, and CPFH for the precursors CMC, MCC, HEC, and CP, respectively, where the last two letters in the former set (FH) refer to ferrihydrite. The nanocellulose–ferrihydrite composite was referred as NCFH.

**Batch Adsorption Studies.** In a typical batch adsorption experiment, 25 mg of the granular media was shaken with 100 mL of As(III)/As(V) spiked distilled water of 1 mg/L concentration. The water sample was collected to measure the leftover As concentration in treated water as a function of time, using inductively coupled plasma mass spectrometry (ICPMS) after acidification with 5%  $\text{HNO}_3$ .

**pH Effect.** To know the pH effect on As adsorption, 25 mg of granular media was added to 25 mL of As(III)/As(V) spiked water, adjusted to the required pH by 1 M HCl/1 M NaOH, and shaken for 3 h. The treated water sample was analyzed by ICPMS.

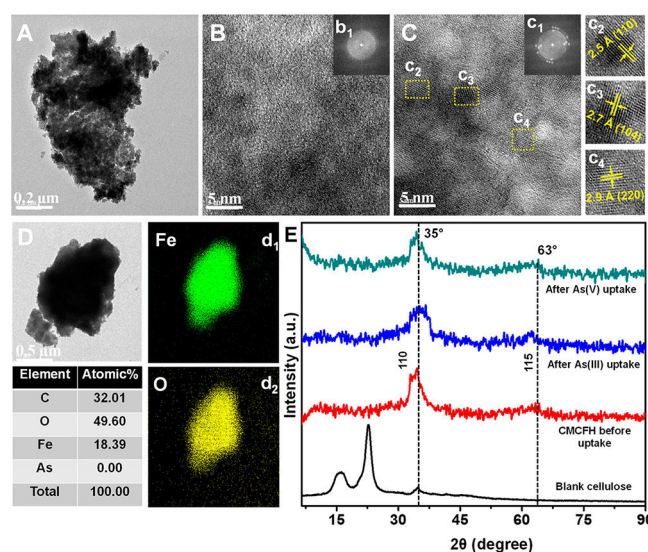
**Interfering Ions.** To understand the effect of interfering ions on As adsorption, the ions of interest which generally exist in groundwater, like calcium ( $\text{Ca}^{2+}$ ), magnesium ( $\text{Mg}^{2+}$ ), potassium ( $\text{K}^+$ ), sodium ( $\text{Na}^+$ ), chloride ( $\text{Cl}^-$ ), carbonate ( $\text{CO}_3^{2-}$ ), bicarbonate ( $\text{HCO}_3^-$ ), nitrate ( $\text{NO}_3^-$ ), silicate ( $\text{SiO}_3^{2-}$ ), sulfate ( $\text{SO}_4^{2-}$ ), fluoride ( $\text{F}^-$ ), and phosphate ( $\text{PO}_4^{3-}$ ), were spiked in 25 mL of distilled water in separate conical flasks, with concentrations relevant to groundwater. This water was treated with 25 mg of CMCFH for 3 h, and ICPMS measurements were conducted. The relevant water quality parameters are listed in Table S1, Supporting Information.

The maximum uptake of As ( $q_e$ ) by cellulosic composites was calculated using eq 1 in the Supporting Information.

Details of instrumentation are presented in the Supporting Information.

## RESULTS AND DISCUSSION

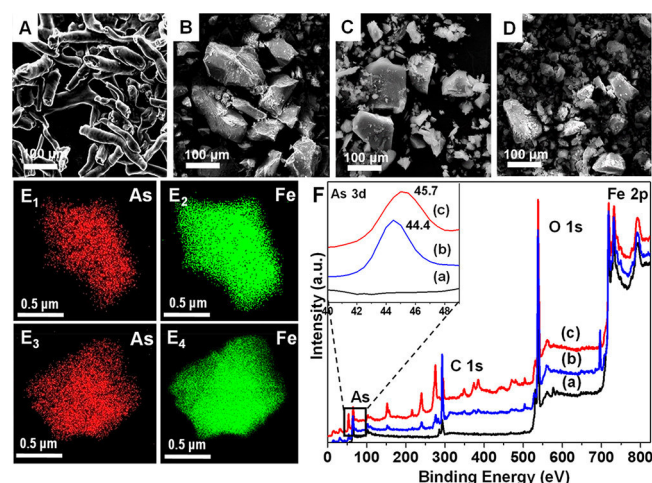
**Characterization of CMCFH, before and after As Uptake.** Figure 1A illustrates the TEM image of the granular CMCFH composite at 0.2  $\mu\text{m}$  scale where homogeneously sized iron oxyhydroxide nanoparticles are embedded in the CMC matrix, confirming composite formation. The structure is largely amorphous. Iron oxyhydroxide nanoparticles are not prominently visible in the large area image due to their small



**Figure 1.** (A) TEM of a CMCFH aggregate. (B) HRTEM of CMCFH along with a fast Fourier-transform of the image (inset b<sub>1</sub>). The material is largely amorphous. (C) Beam-induced crystallization of CMCFH showing crystalline regions along with a fast Fourier-transform of the image (inset c<sub>1</sub>) and lattice-resolved images (insets c<sub>2</sub>, c<sub>3</sub>, and c<sub>4</sub>) showing various crystallographic planes of CMCFH. (D) TEM image, elemental mapping images of Fe and O, respectively, of the initial CMCFH composite before As adsorption (d<sub>1</sub> and d<sub>2</sub>) and their corresponding atomic compositions (C, O, and Fe). (E) Powder XRD patterns of blank cellulose, CMCFH before As adsorption and after As(III), and As(V) adsorption (bottom to top).

size but are present only within the cellulose nanoarchitecture. This analysis is further supported by the determination of surface area (BET isotherm by  $N_2$  adsorption). The specific surface area of parent CMC was  $2.44 \text{ m}^2/\text{g}$  while that of the composite was  $173.31 \text{ m}^2/\text{g}$  with average pore diameter of  $15.51 \text{ \AA}$ . The large increase in surface area is attributed to the confinement of nanoscale iron oxyhydroxide particles in the cellulose matrix which is also responsible for superior As removal performance.<sup>38</sup> To specify the type of iron oxyhydroxide, X-ray diffraction was carried out which gives peaks at  $35^\circ$  (110) and  $63^\circ$  (115), confirming the 2-line ferrihydrite structure.<sup>39</sup> The small grain size of ferrihydrite and its relatively poor crystallinity witnessed in the composites even after As(III) and As(V) adsorption overshadow the slight crystalline nature of blank cellulose before the composite formation. The slight shift in the broad hump at  $63^\circ$  after As(III) adsorption indicated very strong affinity of ferrihydrite toward As(III), which is also evident from adsorption capacities and EDS values. Figure 1B clearly shows the amorphous nature of the composite in ambient conditions at 5 nm scale, with the corresponding fast Fourier-transform (FFT) pattern shown in inset b1. Beam irradiation for a few minutes gives rise to small crystalline domains (Figure 1C) upon gradual conversion of ferrihydrite to hematite (more stable form).<sup>40–43</sup> These nanoscale crystalline features of the irradiated material are shown by HRTEM in the lattice-resolved images of  $c_2$ ,  $c_3$ , and  $c_4$ , where the lattice planes of hematite are observed. The elemental composition of CMCFH has been obtained by TEM-EDS, and mapping is shown in Figure 1D,  $d_1$  and  $d_2$ , which show that O and Fe are the major constituents of the composite apart from carbon present in cellulose. Excess percentage of carbon may be due to the contribution from the grid.

To investigate the morphology of the CMCFH nanocomposite, SEM images of the parent CMC fibers, CMCFH before, and after As(III) and As(V) adsorption were studied (Figure 2A–D). While the parent CMC powder showed



**Figure 2.** (A) SEM of the parent CMC fibers. (B), (C), and (D) SEM of CMCFH before, after As(III), and after As(V) adsorption, respectively.  $E_1$ ,  $E_2$ ,  $E_3$ , and  $E_4$  show the EDS elemental mapping of As and Fe of CMCFH after As(III) ( $E_1$ ,  $E_2$ ) and As(V) ( $E_3$ ,  $E_4$ ) adsorption, respectively. (F) XPS survey spectra of (a) CMCFH before, (b) after As(V), and (c) after As(III) adsorption (bottom to top). Features in the As 3d region for these cases are expanded in the inset.

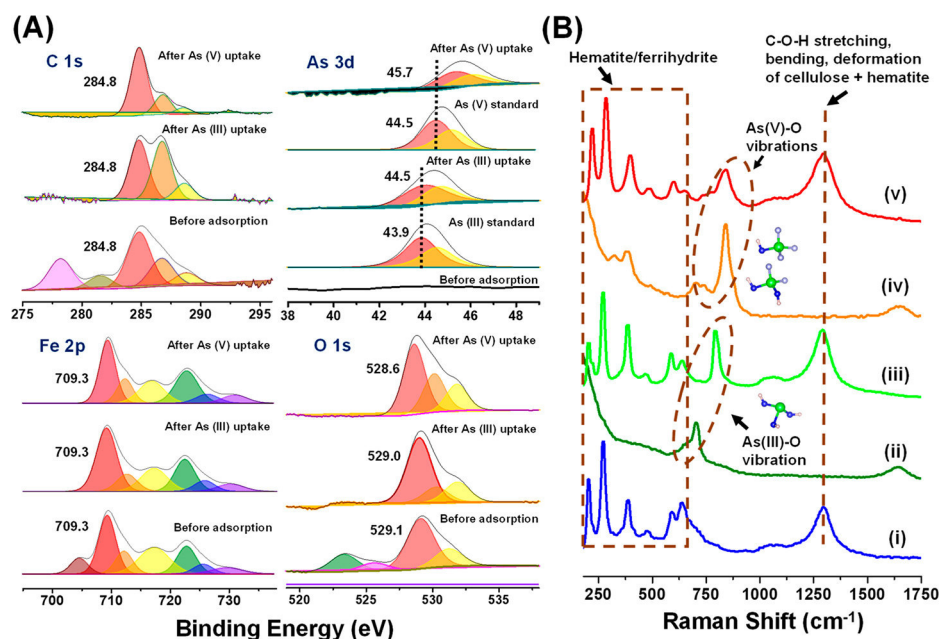
smooth fiberlike branched structures with cracks and visible openings, the composite showed entirely different granular structures, which resulted in a particle size in the range of 50–100  $\mu\text{m}$ . No change in particle morphology was observed upon exposure to various As concentrated solutions which implies that the process of interaction is adsorption. This also implies that the composite possesses very good mechanical strength, which was confirmed by shear stress measurements in dry and wet conditions, shown in Figure S2. For the composite to be suitable in a water purification cartridge, it is important to ensure that it possesses satisfactory wet strength to retain its granular composition so that excessive pressure drop is avoided. Direct shear tests were conducted at various normal stresses to find the shear strength of the granular media. Straight-line approximation of the Mohr–Coulomb failure pattern shown in Figure S3 gave the angle of internal friction ( $\Phi$ ) to be  $38.32^\circ$  and  $39.35^\circ$  for dry and wet media, respectively, showing that the shear strength of prepared granular material is comparable to that of the Indian standard Ennore sand (in the range of  $35$ – $40^\circ$  for  $\Phi$ ).<sup>44</sup> The elemental mapping shown in Figure 2 $E_1$ – $E_4$  illustrates the uniform distribution of As(III) and As(V) over the surface of CMCFH composite upon adsorption.

The components of CMCFH and their interaction with As were also studied by X-ray photoelectron spectroscopy (XPS) as shown by the survey spectra in Figure 2F. The peaks obtained for adsorbed As(III) and As(V) correspond to the uptake during batch studies where it was observed that As(III) had higher tendency to get adsorbed on CMCFH than As(V). This was also confirmed by the TEM-EDS values shown in Figure S4.

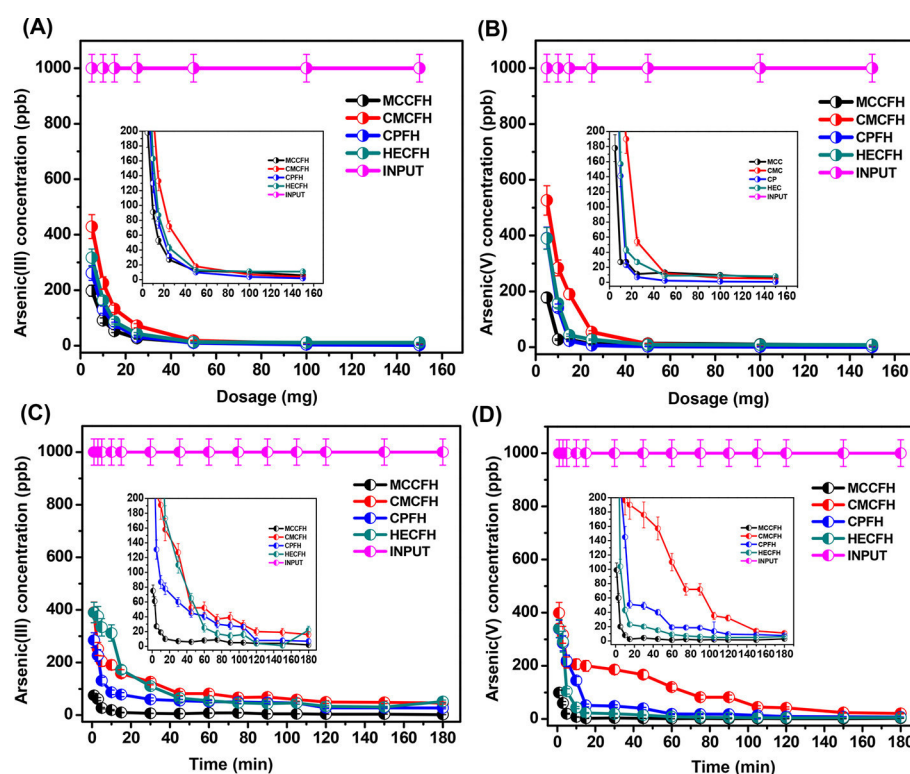
Figure 3A shows the deconvoluted XPS spectra of C 1s, As 3d, Fe 2p, and O 1s of the parent CMCFH and after its interaction with As. The XPS spectrum of C 1s shows a characteristic peak at 284.8 eV for CMCFH which did not show any change after its interaction with As(III) and As(V). Peaks at 286.7 and 288.5 eV denote the presence of hydroxyl C–OH and carboxyl (C=O) bonds in the composite which come from cellulose. The XPS peaks corresponding to As(III) and As(V) standards appeared at 43.9 and 44.5 eV, which showed significant shift toward higher binding energies of 44.5 and 45.7 eV, respectively, after adsorption on CMCFH, suggesting that the adsorption process involves the oxidation of the As(III) species to higher oxidation states or leading to increased stabilization.<sup>45</sup> The shift in As(V) XPS spectra to higher binding energy can be due to the interaction of the electron-rich free arsenate ion with the ferrihydrite group leading to complexation, which may result in reduced availability of electrons in the As center and shortening of As–O bonds. Absence of shift in binding energy for Fe 2p confirms that there is no change in the oxidation state of  $\text{Fe}^{3+}$  of ferrihydrite which shows its characteristic  $\text{Fe}^{3+}$ – $\text{O}^{2-}$  peak at 709.3 eV. This suggests that the As uptake by CMCFH can occur by way of physisorption or by ligand exchange mechanism.<sup>46</sup> There is a slight shift toward lower binding energy in the case of O 1s for the adsorbed samples, when compared to unadsorbed CMCFH. Appearance of additional peaks at 531.9 and 531.8 eV in As(III) and As(V) adsorbed samples may be due to As–O bond formation with hydroxyl groups of cellulose.

The adsorption of As species over CMCFH was further studied by Raman spectroscopy as illustrated in Figure 3B. The Raman spectrum of an aqueous solution As(III) standard at





**Figure 3.** (A) Deconvoluted XPS spectra of C 1s, Fe 2p, O 1s, and As 3d regions of CMCFH before and after As(III) and As(V) adsorption (bottom to top). As 3d data are compared with the standards. (B) Raman spectra of (i) CMCFH solid, (iii) and (v) CMCFH before and after As(III) and As(V) adsorption, respectively; (ii) and (iv) the standard aqueous solutions of As(III) and As(V) at pH 7, respectively. Specific features are labeled. Data have been fitted with their components.



**Figure 4.** Batch study of the comparison of As removal performance of composites made of MCC, CMC, CP, and HEC; residual arsenite (A) and arsenate (B) concentrations as a function of dosage of composites; residual (C) arsenite and (D) arsenate concentrations as a function of contact time with the composites. Insets in each figure show the magnified images in low concentration region, for clarity.

pH 7 gave a characteristic peak due to the  $A_1$  mode of  $H_3AsO_3$  ( $C_{3v}$  symmetry) at  $703\text{ cm}^{-1}$ , while after its adsorption on CMCFH, the peak of interest corresponding to As(III)-O vibrations was shifted to  $789\text{ cm}^{-1}$ . In the case of As(V) adsorption, the characteristic peak corresponding to As(V)=O symmetric stretching vibrations of  $H_2AsO_4^{1-}$  and  $HASO_4^{2-}$

species at  $838\text{ cm}^{-1}$  was shifted to  $842\text{ cm}^{-1}$  in the adsorbed sample. A weak peak at  $588\text{ cm}^{-1}$  and a hump at  $1050\text{ cm}^{-1}$  are due to ferrihydrite ( $FeOOH$ ), while the sharp peaks at 202, 272, 391, and  $637\text{ cm}^{-1}$  are due to the characteristic Raman features of hematite ( $\alpha\text{-Fe}_2\text{O}_3$ ), which were also observed in the Raman spectra of CMCFH in each case. This suggests

thermal transformation of ferrihydrite to more stable hematite (through the maghemite phase, with a peak at 1293 cm<sup>-1</sup>) with increasing laser power.<sup>47,48</sup> This transformation has been confirmed by the XRD pattern of CMCFH, after annealing at 900 °C, shown in Figure S5.<sup>49</sup> The broad peak around 1300 cm<sup>-1</sup> also contains stretching and bending frequencies of C–O–H bonds of the cellulose skeleton.

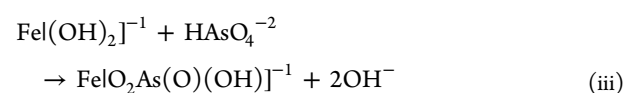
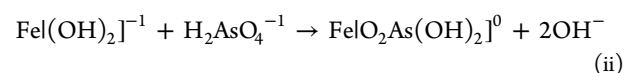
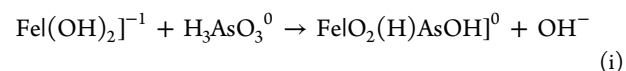
Infrared spectroscopic investigation also provides qualitative insight regarding the As uptake by the composite as shown in Figure S6. Ferrihydrite mainly interacts with the hydroxyl groups of cellulose, which gives the 1420 cm<sup>-1</sup> peak attributed to free –OH bending vibrations of parent cellulose. This gets shifted to 1385 cm<sup>-1</sup> in the composite. The appearance of a distinct peak at 613 cm<sup>-1</sup> in the composite due to ferrihydrite, over the broad feature around 600 cm<sup>-1</sup> in the parent cellulose, assigned to H-bonding of free hydroxyl groups, indicates the interaction between the two. Apart from the characteristic cellulosic peaks shown by CMCFH alone at 3430 (–OH stretching), 2920 (C–H asymmetric stretching and tensile vibration in the pyranoid ring), 1387 (–OH bending), and 1058 cm<sup>-1</sup> (asymmetric C–O–C vibration), As–O stretching peaks were also shown at 785 and 1122 cm<sup>-1</sup> by pristine NaAsO<sub>2</sub>. These latter features were red-shifted to 790 and 1211 cm<sup>-1</sup> after As(III) adsorption on CMCFH. Similarly, Na<sub>2</sub>HAsO<sub>4</sub>·7H<sub>2</sub>O shows peaks at 814 and 1109 cm<sup>-1</sup> due to As–O stretching vibrations, which were also red-shifted to 825 and 1163 cm<sup>-1</sup> after interaction with the composite.<sup>50</sup>

**Batch Studies of As Adsorption on Cellulosic Composites.** Figure 4 represents the comparative performance of various composites prepared with MCC, CMC, HEC, and CP from batch studies, as reported for As(III) and As(V) adsorption, separately. It is observed that MCCFH nano-composite exhibited superior performance where 100 mL of 1 mg/L As spiked water was treated with different dosages of adsorbent composites ranging from 5 to 150 mg, as shown in Figure 4A and B for As(III) and As(V), respectively. Less than 50 mg of any composite is sufficient for bringing down the As concentration below 10 µg/L in 100 mL of water within 3 h of exposure time.

Figure 4C and D show the fast uptake kinetics of the composites where initial 1 mg/L concentration of As(III) and As(V), respectively, was rapidly reduced to 100 µg/L within 60 min of incubation, by virtue of availability of maximum number of free surface sites. At the end of 3 h, the residual concentration of As(III) and As(V) decreased further to 10 µg/L, following a relatively slower kinetics, due to high surface coverage. In order to understand the system better, the kinetic data were initially analyzed using two reaction models: Lagergren's pseudo-first-order and Ho's pseudo-second-order.<sup>51</sup> Mathematical representations of these models and the kinetic plots generated by them are given in the Supporting Information (Figures S7 and S8). The kinetic parameters obtained from these model fits are summarized in Table 1. The plots of  $t/q_t$  against time for adsorption of arsenite and arsenate followed the pseudo-second-order model with the values of the correlation coefficients close to 1 (>0.997), indicating that the availability of number of surface sites for adsorption also plays an important role in overall rate determination. This also suggests that the adsorption of As(III) and As(V) may be occurring in a ligand exchange fashion on the ferrihydrite. At pH ≥ 7, the following equations may be contributing to the overall rate of adsorption.<sup>52</sup>

**Table 1. Estimated Pseudo-First-Order and Second-Order Kinetic Parameters for the Adsorption of As(III) and As(V) by CMCFH**

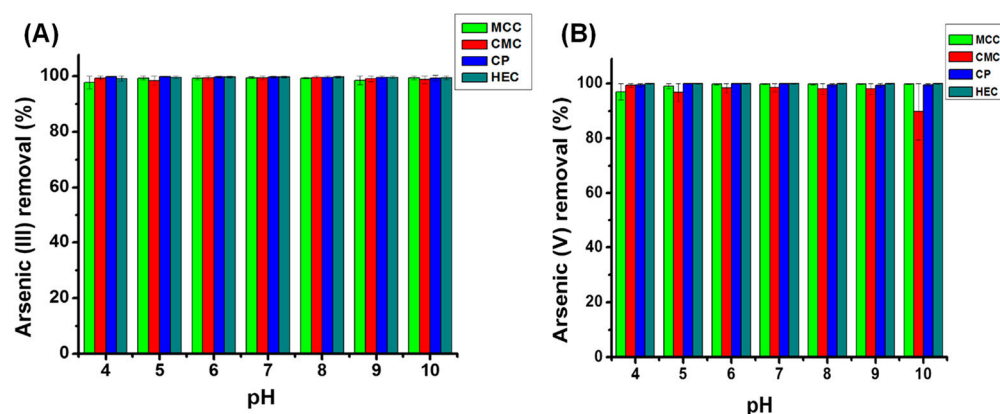
Species	Model	$k$ (1/h) or (g/mg h)	$q_e$ (mg/g)	$R^2$
As(III)	pseudo 1st order	0.0214	3.838	0.9381
As(V)	pseudo 1st order	0.0205	3.946	0.9667
As(III)	pseudo 2nd order	0.4535	3.838	0.9998
As(V)	pseudo 2nd order	0.3965	3.946	0.9979



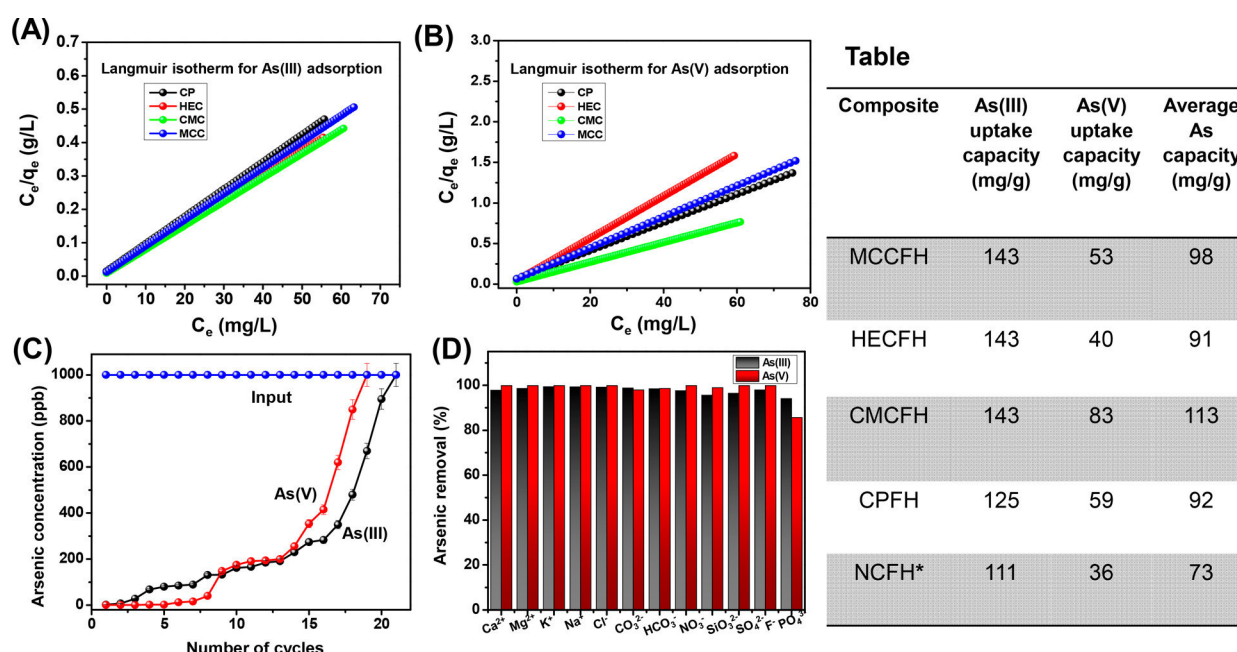
(The symbol “ $]$ ” as in  $\text{Fe}(\text{OH})_2]^{-1}$  used in the chemical equations denote a surface bidentate complex of ferrihydrite.)

The reactions suggest that complexation with iron oxy-hydroxides was driven by the ligand exchange mechanism, which led to the formation of Fe–O–As bonds at neutral pH. As the ferrihydrite composite is exposed to water, it acquires more hydroxyl groups accessible to As species. Two kinds of adsorption geometries are possible in this case.<sup>53,54</sup> 1. Physical adsorption which occurs due to physical interaction of the As species with the surface groups by means of hydrogen bonding, leading to outer sphere complexes. 2. Chemical adsorption of As species to ferrihydrite groups leading to more stable inner sphere complexes. Different kinds of inner sphere complexes are monodentate mononuclear, bidentate binuclear corner sharing, and bidentate mononuclear/binuclear edge sharing. Transformation of outer sphere complex to inner sphere complex is often observed depending upon the pH of the solution.<sup>46</sup> The stabilities of the complexes are in the following order: bidentate binuclear ( $>(\text{FeO})_2\text{AsOH}$ ) > monodentate mononuclear ( $>(\text{FeO})-\text{As}(\text{OH})_2$ ) > physical adsorption. Moreover, to have further insight into the mechanism, various isotherm models like Langmuir, Freundlich, and Dubinin–Radushkevich (D–R) were evaluated (Figure S9).<sup>55,56</sup> While Freundlich showed correlation coefficient ( $R^2$ ) of 0.90, which is lower than the obtained  $R^2$  value of Langmuir fit, D–R isotherm yielded adsorption energy ( $E$ ) value of 3162 kJ/mol. The large  $E$  value and higher correlation with Langmuir isotherm suggest a dominant chemisorption pathway for the As species.

The uptake performance shown by MCCFH in the batch studies was the best among the four composites, attributed to the finer crystalline structure of MCC, as compared to other forms. The uptake efficiencies of the composites prepared by different kinds of celluloses were also tested under different pH conditions. All the composites were found to be working with excellent efficiency in a broad pH region of pH 4–10, as shown in Figure 5A and B. Analysis of the histograms give us insight regarding the possible reasons behind CMCFH showing relatively lesser As(V) uptake than other cellulosic composites in higher pH conditions, like pH 10. To understand this further, zeta potentials of aqueous As(V) solutions at pH 5 and 9 using buffers were studied. As the pH condition was shifted from lower to higher, zeta potential varied from +14 mV (pH



**Figure 5.** Batch study of the comparison of As removal performance of composites made of MCC, CMC, CP, and HEC for (A) arsenite and (B) arsenate removal over a pH window of 4–10.



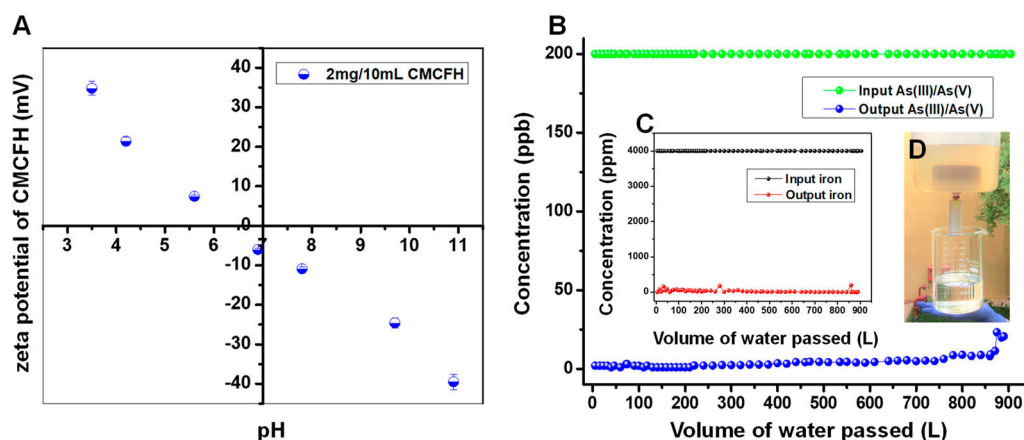
**Figure 6.** Langmuir adsorption isotherms of various composites prepared by MCC, CMC, CP, and HEC for the comparison of maximum uptake capacities of (A) As(III) and (B) As(V). (C) Batch adsorption studies for number of cycles of As(III) and As(V) adsorption by CMCFH. (D) Uptake of As(III) and As(V) in the presence of other competing ions (cations and anions) which are generally present in groundwater by CMCFH; table shows the As uptake capacities of various composites. \*Data from ref 38.

5) to  $-22$  mV (pH 9). Due to the presence of the anionic carboxylate ( $\text{COO}^-$ ) group on CMC skeleton at higher pH and the overall negative surface charge on the solid composite, CMCFH particles experience greater electrostatic repulsion from  $\text{HAsO}_4^{2-}$ , which is the species existing for As(V) at pH 10. This is responsible for lower As(V) adsorption in alkaline medium.<sup>57</sup>

To investigate the maximum adsorption capacity, a series of arsenite and arsenate solutions with initial As concentration from 1 to 200 mg/L were shaken with the composite CMCFH for 24 h at neutral pH. To account for the effect of equilibrium concentration on the adsorption capacity, evaluation was done with the Langmuir isotherm model.<sup>58</sup> The model assumes that localized adsorption occurs at specific homogeneous adsorption sites on the surface of the adsorbent with no lateral interaction between the adsorbed species giving rise to a saturated monolayer at equilibrium. The plots of  $C_e/q_e$  versus  $C_e$  give straight lines using the linearized form of the Langmuir

equation (Supporting Information, eq 2) for various composites, as shown in Figure 6A and B. The values of  $q_{\text{max}}$  and  $b$  can be calculated from the slope and intercept of the plots, respectively. The maximum adsorption capacities for all the composites made of microstructural celluloses were calculated and compared to that of nanocrystalline cellulose templated FeOOH composite (NCFH),<sup>38</sup> as shown in the table. A linear plot of  $C_e/q_e$  versus  $C_e$  along with a high value of correlation coefficient, i.e.,  $R^2 > 0.99$  in each case, indicates that the Langmuir isotherm provides a better fit of the equilibrium data. CMCFH was observed to have the highest average As uptake capacity of 113 mg/g, higher in comparison to other composites, while NCFH showed the lowest adsorption capacity. The higher capacity of microstructured materials over nanostructured materials is unconventional and nonobvious as nanostructured materials are considered superior in the field of adsorption, catalysis, etc., and the origin of this needs architectural investigation. Figure 6C





**Figure 7.** (A) Zeta potential vs pH (pH window 3–11) for CMCFH particles in water (2 mg in 10 mL). (B) As concentration in the water using a 40 g cartridge with the input of 200  $\mu\text{g/L}$  As(III)/As(V) and 4 mg/L 1:1  $\text{Fe}^{2+}/\text{Fe}^{3+}$  mixture. (C) Iron output for the same input. (D) Photograph of the setup used for filtration containing arsenic and iron contaminated water using a cartridge comprised of CMCFH, along with a porous clay prefilter.

illustrates the reuse performance of the CMCFH composite by batch adsorption, as a function of number of cycles. The material was not desorbed, but each time the material was recovered by centrifugation to prevent any weight loss. CMCFH can be reused for greater number of cycles for As(III) removal than As(V) which is in agreement with its higher As(III) uptake than As(V), also shown by SEM-EDS and elemental mapping (Figure S11).

To understand this preference in adsorption, we need to consider the speciation of arsenite and arsenate in water according to varying pH conditions. Depending on the pH, predominant species of arsenate existing in water medium are as follows:  $\text{H}_3\text{AsO}_4$  (pH < 2),  $\text{H}_2\text{AsO}_4^{1-}$  (pH 2–7),  $\text{HAsO}_4^{2-}$  (pH 7–11), and  $\text{AsO}_4^{3-}$  (pH > 12), while those of arsenite are  $\text{H}_3\text{AsO}_3$  (pH < 9),  $\text{H}_2\text{AsO}_3^{1-}$  (pH 9–12),  $\text{HAsO}_3^{2-}$  (pH 12–13), and  $\text{AsO}_3^{3-}$  (pH > 13), respectively. Also, the change in the surface charge of CMCFH particles according to pH variation was studied by zeta potential measurements, shown in Figure 7A. It suggests that the particles possess an overall negative surface charge at pH  $\geq 7$ . Thus, pH is a key factor which influences the speciation of As in solution and the surface charge of the solid particles significantly. Since most of the adsorption procedures were carried out at pH 7 or greater, As(III) species are neutral as compared to negatively charged As(V) species and they do not exhibit as much repulsion, and as a result, As(III) was adsorbed in greater amount by CMCFH at pH 7 and also in a wide pH range. This justification can also be supported by the fact that points of zero charge (PZCs) of iron oxides occur in the pH range 6–8. Hence, the surface of CMCFH particles are expected to be positively charged when the equilibrium pH values are below  $\text{pH}_{\text{PZC}}$ , but the positively charged sites are expected to decrease with increasing pH, making electrostatic interaction with various As species, an important factor explaining higher As(III) removal than As(V).<sup>58</sup>

One of the unique advantages associated with the use of CMCFH as an active adsorbent is that it does not show any significant drop in the performance of As(III) and As(V) removal even when used with water spiked with other interfering ions like calcium ( $\text{Ca}^{2+}$ ), magnesium ( $\text{Mg}^{2+}$ ), potassium ( $\text{K}^+$ ), sodium ( $\text{Na}^+$ ), chloride ( $\text{Cl}^-$ ), carbonate ( $\text{CO}_3^{2-}$ ), bicarbonate ( $\text{HCO}_3^-$ ), nitrate ( $\text{NO}_3^-$ ), silicate ( $\text{SiO}_3^{2-}$ ), sulfate ( $\text{SO}_4^{2-}$ ), phosphate ( $\text{PO}_4^{3-}$ ), and fluoride

( $\text{F}^-$ ) with concentrations relevant to tap water. The removal % of As was calculated using the equation mentioned (eq 3, Supporting Information). While a slight decrease in As(III) uptake (maximum decrease up to 95%) was witnessed in the presence of anions like  $\text{NO}_3^-$ ,  $\text{HCO}_3^-$ ,  $\text{SiO}_3^{2-}$ , and  $\text{SO}_4^{2-}$ , As(V) uptake was fairly consistent (maximum decrease up to 98%) in the presence of most potential interfering ions, as shown in Figure 6D. Interference by phosphate is seen as it competes with arsenate to get adsorbed. Cations hardly showed any effect on the adsorption behavior of CMCFH.<sup>59</sup> Other cellulosic composites (MCCFH, HECFH, and CPFH) also show high As removal efficiency ( $\geq 95\%$ ) in the presence of interfering ions in water as shown in Figure S10.

The toxicity characteristic leaching protocol (TCLP) studies as per the USEPA standard SW-846 Test Method 1311 were conducted using the saturated composite CMCFH to know the possible leaching of adsorbed As. The test showed a leaching of 2.2 mg/L. TCLP regulatory limit set by United States Environmental Protection Agency (USEPA) for As is 5.0 mg/L. For cellulose, the total organic carbon (TOC) detected in the leachate was 1.6 mg/L, while the acceptable USEPA limit for TOC in drinking water is 4.0 mg/L. Deionized water showing a TOC of 0.3 mg/L was used for the experiments.

Thermal stability of CMCFH was checked by thermogravimetric analysis (TGA) in air and in nitrogen atmosphere (Figure S12). The composite loses 23.7% and 27.6% of its initial weight as it was heated from room temperature to 900  $^\circ\text{C}$  in air and nitrogen atmosphere, respectively. The composite begins to lose water loosely adhering to the interior and the exterior of its surface up to 100  $^\circ\text{C}$ , which explains the initial weight loss. By the time the temperature reaches 250–300  $^\circ\text{C}$ , major thermal degradation of the cellulosic skeleton takes place. Beyond 300  $^\circ\text{C}$ ,  $\text{FeOOH}$  starts getting converted to more stable forms of iron oxides after getting dehydrated yielding  $\alpha\text{-Fe}_2\text{O}_3$  at a temperature between 600 and 750  $^\circ\text{C}$ , from XRD analysis (Figure S5).<sup>60–62</sup>

After the performance of the composites in batch experiments was evaluated, a prototype filter consisting of a water purification cartridge (diameter, 35 mm; height, 11 cm) along with an iron remover was developed as shown in Figure 7D. The experiment was done for iron and arsenic together as they coexist in natural environment in the affected regions. About

40 g of CMC FH (72 mesh) was packed, and a porous clay based particulate and iron filter was attached with it, assembled in an antigravity fashion. In Figure 7D, we show the prototype through which over 900 L of water was passed with a flow rate of 8–15 mL min<sup>-1</sup> under gravity. The input water contains 200 µg/L of a mixture of As(III) and As(V) in 1:1 ratio along with 4 mg/L of Fe, keeping the pH at 7.5. The output water samples were tested by ICPMS and were found to have total As and Fe levels well below the WHO permissible limits for drinking water as shown in Figure 7B and C, respectively.

**Microstructures Perform Better than Nanostructures.** As far as the performance and uptake capacity of a material are concerned, they depend not only upon the porosity and the surface area (responsible for physisorption) but also on the chemical functionalization of the material (facilitating chemisorption). In microcellulose fibers with diameter in the micrometer range, maximum available hydroxyl groups may be used for anchoring of ferrihydrite nanoparticles which act as the active adsorption sites, responsible for better interaction with the As species. Microcellulose is subjected to lesser pretreatment and extraction processes which keep the microfibrils more stable mechanically and chemically, as compared to cellulose nanocrystals (CNC). Thus, it gives rise to a more efficient, stable, and stronger composite showing better performance than CNC-based composites. These structural aspects are speculative at present as precise data on the composite structure are not available.

**Economic Analysis.** Arsenic affected population in India is around 70 million.<sup>63</sup> We are aware that the number will differ substantially depending on the tolerance limit chosen. We assumed that 10 L of clean water is needed for cooking and drinking per person per day. Assuming an average As concentration of 200 µg/L in the accessible water in the affected communities,<sup>45</sup> and assuming that all of them are served with this technology for As remediation, it is necessary to have 1.02 million kg of the composite having a removal capacity of 50 mg/g to remove 51100 kg of arsenic from 255.5 billion liters of drinking water needed for a year. The amount of cellulose required to produce this composite media is about 42.5 tons per year. We have considered a reduced adsorption capacity of 50 mg/g in field conditions although the measured capacity is 100 mg/g in the lab. Assuming industrial prices, this quantity of cellulose amounts to \$ 0.09 million. Current industrial production of cellulose in India is about 15 million tons, by paper and pulp industry alone. Since cellulose production and processing are integral parts of the paper and pulp, textile, food processing, and pharmaceutical industries, we can estimate the annual cellulose production by observing output capacities of the aforementioned industries. Hence our cellulose requirement as a raw material can be met easily. Other raw materials are also available in bulk. This evaluation suggests that arsenic menace in India can be handled affordably with such materials.

**Preliminary Sustainability Assessment.** This technology was assessed based on the economic and environmental aspects by qualitatively and quantitatively evaluating some of the relevant sustainability parameters to determine the extent of its “greenness”.<sup>64–66</sup> The formulas referred to for calculating the sustainability metrics are listed as eqs 4–8, Supporting Information.

**Raw Materials.** Major raw materials include cellulose which is renewable and biodegradable. Processing of cellulose usually involves mechanical extrusion and chemical treatment by

strong acid/alkali. Those manufacturers who use mild processing techniques for lignocellulosic fibers should be preferred for supply of the raw material. Iron salts and alkali were used in less quantities which are nontoxic. Water was used as the solvent. The mass intensity (excluding water) was calculated to be 1.9, while the water intensity ( $W_p$ ) came as 29.2. Reaction mass efficiency was 52%. The mass intensity can be brought down to 1 by avoiding loss of the composite during filtration and washing. The method of preparation of the composite is water positive by 2–3 orders of magnitude; i.e., it produces 700 L of clean water for every 1 L of water consumed for its production.

**Energy Consumption.** Electricity was used for stirring, vacuum filtration, and drying. No energy consumption was involved in the operation of the technology. Energy intensity was calculated to be 2.3 kW·h/kg of the composite, according to the lab-scale synthesis setup. The energy intensity can be reduced effectively by increasing the scale of production. Large-scale iron and steel and aluminum industries consume 10 and 15 kW·h/kg of product, respectively.<sup>67,68</sup> However, our energy consumption value is comparable with microfibrillated cellulose manufacturing industries which have an average energy intensity about 2.8 kW·h/kg.<sup>69</sup>

**Resulting Emissions.** No harmful solvents/fumes or side products were discharged during the synthesis of the composite. The *E* factor (environmental factor) was observed to be 0.3, indicating negligible amount of emission of harmful byproducts. The discharged water after washing containing salts can be largely recycled and reused by using a reverse osmosis setup (which will increase energy consumption by 0.8 kW·h/kg).

**Toxicity Potential.** As per European Chemicals Agency (ECHA), FeCl<sub>3</sub> and NaOH have been classified as skin sensitizer and corrosive, respectively. But they are nonflammable and stable at room temperature. FeCl<sub>3</sub> and NaOH show acute oral toxicity (LD<sub>50</sub>) at 900 and 280–680 mg/kg in mice, respectively. Manufacturing process therefore has to be undertaken with some simple precautionary measures.<sup>70</sup>

**Disposal of Waste.** Arsenic-loaded composites were subjected to multiple regenerations for subsequent adsorption cycles by acid/base treatment. They could be finally disposed in leach-free landfills. TCLP suggests safe disposal of the adsorbent after saturation loading.

**Affordability.** This technology can provide arsenic and iron free water under \$ 0.3/1000 L of clear water.

## CONCLUSIONS

We report a green method for preparing highly efficient and sustainable cellulose-based composites for the removal of As(III) and As(V) from drinking water. The 2-line ferrihydrite nanoparticles incorporated in the biopolymeric confinement of microcellulose act as active sites for As(III) and As(V) adsorption. TEM, SEM, and XPS studies ensure that the physical and chemical properties of CMC FH remain intact even after As exposure until saturation, while TCLP and TOC suggest it to be free from leaching. Moreover, the composite works equally well in a wide range of pH with fast kinetics of adsorption. The maximum adsorption capacity of CMC FH by batch studies was 143 and 83 mg/g for As(III) and As(V), respectively. The CMC FH packed cartridge showed arsenic removal (according to WHO standards) for about 1000 L of water with an average flow rate of 12 mL/min without any regeneration of material, confirming it to be an excellent

candidate for an industrially feasible and green material for delivering affordable water in As-affected communities worldwide. Lastly, evaluation of sustainability metrics provided further insights into the socio-economic benefits as well as environmental impact of the manufacturing process of the nanocomposite.

## ■ ASSOCIATED CONTENT

### ■ Supporting Information

The Supporting Information is available free of charge on the ACS Publications website at DOI: 10.1021/acssuschemeng.8b05157.

Instrumentation; equations used in main text; SEM images of cellulose nanocrystals; plot of horizontal shear stress vs horizontal displacement of CMCFH; Mohr–Coulomb failure pattern (shear stress vs normal stress) of CMCFH; HRTEM and EDS of CMCFH after As(III) and As(V) adsorption; XRD of CMCFH annealed up to 900 °C; IR spectra of CMCFH before and after As(III)/As(V) adsorption, corresponding to IR of As standards; pseudo-first-order reaction kinetic plots for the adsorption of As(III) and As(V) on ferrihydrite; pseudo-second-order reaction kinetic plots for the adsorption of As(III) and As(V) on ferrihydrite; As(III) adsorption on MCCFH for Freundlich and Dubinin–Radushkevich isotherm models; effect of interfering ions (cations and anions) for MCCFH, CPFH, and HECFH; SEM-EDS and elemental mapping of CMCFH before and after As(III)/As(V) adsorption; thermogravimetric analysis (TGA) of CMCFH at air and nitrogen atmospheres; physicochemical characteristics of influent natural drinking water (PDF)

## ■ AUTHOR INFORMATION

### Corresponding Author

\*E-mail: [pradeep@iitm.ac.in](mailto:pradeep@iitm.ac.in). Tel.: +91-44 2257 4208. Fax: +91-44 2257 0545/0509.

### ORCID

Avula Anil Kumar: 0000-0001-6878-8736

Ligy Philip: 0000-0001-8838-2135

Thalappil Pradeep: 0000-0003-3174-534X

### Notes

The authors declare no competing financial interest.

## ■ ACKNOWLEDGMENTS

The authors thank Ramprasad and Manjunath for the help in TOC measurements and thermodynamic calculations, EWRE division, Department of Civil Engineering, IIT Madras. The authors also thank Omprakash, S. Manickan, R. G. Robinson, and Manu Santhanam of the Department of Civil Engineering, IIT Madras, for their help in conducting direct shear stress measurements, and the Common facility, Department of Chemistry, IIT Madras is thanked for BET and TGA measurements. Authors thank IIT Madras and the Department of Science and Technology, Government of India for constantly supporting our research program on nanomaterials.

## ■ REFERENCES

- (1) Woolson, E. A. Bioaccumulation of arsenicals. *ACS Symp. Ser.* **1975**, *7*, 97–107.
- (2) Matschullat, J. Arsenic in the geosphere—a review. *Sci. Total Environ.* **2000**, *249*, 297–312.
- (3) Bagla, P.; Kaiser, J. India's spreading health crisis draws global arsenic experts. *Science* **1996**, *274*, 174–175.
- (4) National Research Council. *Arsenic: Medical and Biologic Effects of Environmental Pollutants*; National Academies Press: Washington, DC, 1977; pp 4–15.
- (5) Zhang, S.; Yan, Z.; Li, Y.; Chen, Z.; Zeng, H. Atomically thin arsenene and antimonene: semimetal-semiconductor and indirect-direct band-gap transitions. *Angew. Chem., Int. Ed.* **2015**, *54*, 3112–3115.
- (6) Mandal, B. K.; Suzuki, K. T. Arsenic round the world: a review. *Talanta* **2002**, *58*, 201–235.
- (7) Smedley, P.; Kinniburgh, D. A review of the source, behaviour and distribution of arsenic in natural waters. *Appl. Geochem.* **2002**, *17*, 517–568.
- (8) Bissen, M.; Frimmel, F. H. Arsenic—a review. Part I: occurrence, toxicity, speciation, mobility. *Acta Hydrochim. Hydrobiol.* **2003**, *31*, 9–18.
- (9) Tseng, C. H. Arsenic methylation, urinary arsenic metabolites and human diseases: current perspective. *J. Environ. Sci. Health C* **2007**, *25*, 1–22.
- (10) Meharg, A. A.; Rahman, M. M. Arsenic contamination of Bangladesh paddy field soils: implications for rice contribution to arsenic consumption. *Environ. Sci. Technol.* **2003**, *37*, 229–234.
- (11) Kurzius-Spencer, M.; O'rourke, M. K.; Hsu, C. H.; Hartz, V.; Harris, R. B.; Burgess, J. L. Measured versus modeled dietary arsenic and relation to urinary arsenic excretion and total exposure. *J. Exposure Sci. Environ. Epidemiol.* **2013**, *23* (4), 442–449.
- (12) Kapaj, S.; Peterson, H.; Liber, K.; Bhattacharya, P. Human Health Effects From Chronic Arsenic Poisoning—A Review. *J. Environ. Sci. Health, Part A: Toxic/Hazard. Subst. Environ. Eng.* **2006**, *41*, 2399–2428.
- (13) *Guidelines for Drinking-Water Quality*; WHO Press, World Health Organization: Switzerland, 2011.
- (14) Vahter, M.; Concha, G. Role of metabolism in arsenic toxicity. *Pharmacol. Toxicol.* **2001**, *89*, 1–5.
- (15) Singh, R.; Singh, S.; Parihar, P.; Singh, V. P.; Prasad, S. M. Arsenic contamination, consequences and remediation techniques: a review. *Ecotoxicol. Environ. Saf.* **2015**, *112*, 247–270.
- (16) Litter, M. I.; Alarcón-Herrera, M. T.; Arenas, M. J.; Armienta, M. A.; Avilés, M.; Cáceres, R. E.; Cipriani, H. N.; Cornejo, L.; Dias, L. E.; Cirelli, A. F.; Farfán, E. M.; Garrido, S.; Lorenzo, L.; Morgada, M. E.; Olmos-Márquez, M. A.; Pérez-Carrera, A. Small-scale and household methods to remove arsenic from water for drinking purposes in Latin America. *Sci. Total Environ.* **2012**, *429*, 107–122.
- (17) Sarkar, A.; Paul, B. The global menace of arsenic and its conventional remediation—A critical review. *Chemosphere* **2016**, *158*, 37–49.
- (18) Mohan, D.; Pittman, C. U. Arsenic removal from water/wastewater using adsorbents—A critical review. *J. Hazard. Mater.* **2007**, *142*, 1–53.
- (19) Nicomel, N. R.; Leus, K.; Folens, K.; Van Der Voort, P.; Du Laing, G. Technologies for arsenic removal from water: current status and future perspectives. *Int. J. Environ. Res. Public Health* **2016**, *13*, 62.
- (20) Zhang, Q. L.; Lin, Y.; Chen, X.; Gao, N. Y. A method for preparing ferric activated carbon composites adsorbents to remove arsenic from drinking water. *J. Hazard. Mater.* **2007**, *148*, 671–678.
- (21) Maliyekkal, S. M.; Sreeprasad, T. S.; Krishnan, D.; Kouser, S.; Mishra, A. K.; Waghmare, U. V.; Pradeep, T. Graphene: A Reusable Substrate for Unprecedented Adsorption of Pesticides. *Small* **2013**, *9*, 273–283.
- (22) Sreeprasad, T. S.; Gupta, S. S.; Maliyekkal, S. M.; Pradeep, T. Immobilized graphene-based composite from asphalt: Facile synthesis and application in water purification. *J. Hazard. Mater.* **2013**, *246*, 213–220.
- (23) Wong, W.; Wong, H.; Badruzzaman, A. B. M.; Goh, H.; Zaman, M. Recent advances in exploitation of nanomaterial for arsenic removal from water: a review. *Nanotechnology* **2017**, *28*, 042001.
- (24) Habuda-Stanić, M.; Nuić, M. Arsenic removal by nanoparticles: a review. *Environ. Sci. Pollut. Res.* **2015**, *22*, 8094–8123.



- (25) Chandra, V.; Park, J.; Chun, Y.; Lee, J. W.; Hwang, I. C.; Kim, K. S. Water-dispersible magnetite-reduced graphene oxide composites for arsenic removal. *ACS Nano* **2010**, *4*, 3979–3986.
- (26) Zhang, Y.; Yang, M.; Dou, X. M.; He, H.; Wang, D. S. Arsenate adsorption on an Fe–Ce bimetal oxide adsorbent: Role of surface properties. *Environ. Sci. Technol.* **2005**, *39*, 7246–7253.
- (27) Jing, C.; Cui, J.; Huang, Y.; Li, A. Fabrication, characterization, and application of a composite adsorbent for simultaneous removal of arsenic and fluoride. *ACS Appl. Mater. Interfaces* **2012**, *4*, 714–720.
- (28) Islam, M.; Mishra, P. C.; Patel, R. Arsenate removal from aqueous solution by cellulose-carbonated hydroxyapatite nanocomposites. *J. Hazard. Mater.* **2011**, *189*, 755–763.
- (29) Yang, J.; Zhang, H.; Yu, M.; Emmanuelawati, I.; Zou, J.; Yuan, Z.; Yu, C. High-Content, Well-Dispersed  $\gamma$ -Fe<sub>2</sub>O<sub>3</sub> Nanoparticles Encapsulated in Macroporous Silica with Superior Arsenic Removal Performance. *Adv. Funct. Mater.* **2014**, *24*, 1354–1363.
- (30) Guo, Q.; Cao, Y.; Yin, Z.; Yu, Z.; Zhao, Q.; Shu, Z. Enhanced Removal of Arsenic from Water by Synthetic Nanocrystalline Iowaite. *Sci. Rep.* **2017**, *7*, 17546.
- (31) Sankar, M. U.; Aigal, S.; Maliyekkal, S. M.; Chaudhary, A.; Kumar, A. A.; Chaudhari, K.; Pradeep, T.; Anshup. Biopolymer-reinforced synthetic granular nanocomposites for affordable point-of-use water purification. *Proc. Natl. Acad. Sci. U. S. A.* **2013**, *110*, 8459–8464.
- (32) Crini, G. Recent developments in polysaccharide-based materials used as adsorbents in wastewater treatment. *Prog. Polym. Sci.* **2005**, *30*, 38–70.
- (33) Wang, J.; Chen, C. Chitosan-based biosorbents: modification and application for biosorption of heavy metals and radionuclides. *Bioresour. Technol.* **2014**, *160*, 129–141.
- (34) Carpenter, A. W.; de Lannoy, C. F.; Wiesner, M. R. Cellulose nanomaterials in water treatment technologies. *Environ. Sci. Technol.* **2015**, *49*, 5277–5287.
- (35) Mohammed, N.; Grishkewich, N.; Tam, K. C. Cellulose nanomaterials: promising sustainable nanomaterials for application in water/wastewater treatment processes. *Environ. Sci.: Nano* **2018**, *5*, 623–658.
- (36) Moon, R. J.; Martini, A.; Nairn, J.; Simonsen, J.; Youngblood, J. Cellulose nanomaterials review: structure, properties and nanocomposites. *Chem. Soc. Rev.* **2011**, *40*, 3941–3994.
- (37) Nishiyama, Y.; Johnson, G. P.; French, A. D.; Forsyth, V. T.; Langan, P. Neutron crystallography, molecular dynamics, and quantum mechanics studies of the nature of hydrogen bonding in cellulose I $\beta$ . *Biomacromolecules* **2008**, *9*, 3133–3140.
- (38) Pradeep, T.; Baidya, A.; Rath, B. B.; Kumar, A. A. Cellulose nanocrystals templated iron oxyhydroxide based adsorbent for arsenic removal from water and a device thereof. *Ind. Pat. Appl.* 201641027660, 2016.
- (39) Yu, X.; Tong, S.; Ge, M.; Zuo, J.; Cao, C.; Song, W. One-step synthesis of magnetic composites of cellulose@ iron oxide nanoparticles for arsenic removal. *J. Mater. Chem. A* **2013**, *1*, 959–965.
- (40) Michel, F. M.; Ehm, L.; Antao, S. M.; Lee, P. L.; Chupas, P. J.; Liu, G.; Strongin, D. R.; Schoonen, M. A.; Phillips, B. L.; Parise, J. B. The structure of ferrihydrite, a nanocrystalline material. *Science* **2007**, *316*, 1726–1729.
- (41) Jambor, J. L.; Dutrizac, J. E. Occurrence and constitution of natural and synthetic ferrihydrite, a widespread iron oxyhydroxide. *Chem. Rev.* **1998**, *98*, 2549–2586.
- (42) Zhou, S.; Wang, D.; Sun, H.; Chen, J.; Wu, S.; Na, P. Synthesis, characterization, and adsorptive properties of magnetic cellulose nanocomposites for arsenic removal. *Water, Air, Soil Pollut.* **2014**, *225*, 1945.
- (43) Wirnsberger, G.; Gatterer, K.; Fritzer, H.; Grogger, W.; Pillep, B.; Behrens, P.; Hansen, M.; Koch, C. B. Mesostuctured iron oxyhydroxides. 1. Synthesis, local structure, and magnetism. *Chem. Mater.* **2001**, *13*, 1453–1466.
- (44) Ghosh, A.; Bera, A. K. Effect of geotextile ties on uplift capacity of anchors embedded in sand. *Geotech. Geol. Eng.* **2010**, *28*, 567–577.
- (45) Kumar, A. A.; Som, A.; Longo, P.; Sudhakar, C.; Bhui, R. G.; Gupta, S. S.; Sankar, M. U.; Chaudhary, A.; Kumar, R.; Pradeep, T.; Anshuo. Confined Metastable 2-Line Ferrihydrite for Affordable Point-of-Use Arsenic-Free Drinking Water. *Adv. Mater.* **2017**, *29*, 1604260.
- (46) Sudhakar, C.; Anil Kumar, A.; Bhui, R. G.; Sen Gupta, S.; Natarajan, G.; Pradeep, T. Species-specific uptake of arsenic on confined metastable 2-line ferrihydrite: A combined Raman-XPS investigation of the adsorption mechanism. *ACS Sustainable Chem. Eng.* **2018**, *6* (8), 9990–10000.
- (47) Schwaminger, S. P.; Surya, R.; Filser, S.; Wimmer, A.; Weigl, F.; Fraga-García, P.; Berensmeier, S. Formation of iron oxide nanoparticles for the photooxidation of water: Alteration of finite size effects from ferrihydrite to hematite. *Sci. Rep.* **2017**, *7*, 12609.
- (48) Müller, K.; Ciminelli, V. S.; Dantas, M. S. S.; Willscher, S. A comparative study of As (III) and As (V) in aqueous solutions and adsorbed on iron oxy-hydroxides by Raman spectroscopy. *Water Res.* **2010**, *44*, 5660–5672.
- (49) Pariona, N.; Camacho-Aguilar, K. I.; Ramos-González, R.; Martínez, A. I.; Herrera-Trejo, M.; Baggio-Saitovitch, E. Magnetic and structural properties of ferrihydrite/hematite nanocomposites. *J. Magn. Magn. Mater.* **2016**, *406*, 221–227.
- (50) Goldberg, S.; Johnston, C. T. Mechanisms of arsenic adsorption on amorphous oxides evaluated using macroscopic measurements, vibrational spectroscopy, and surface complexation modeling. *J. Colloid Interface Sci.* **2001**, *234*, 204–216.
- (51) Ho, Y. S. Review of second-order models for adsorption systems. *J. Hazard. Mater.* **2006**, *136*, 681–689.
- (52) Jain, A.; Raven, K. P.; Loeppert, R. H. Arsenite and arsenate adsorption on ferrihydrite: surface charge reduction and net OH-release stoichiometry. *Environ. Sci. Technol.* **1999**, *33*, 1179–1184.
- (53) Maliyekkal, S. M.; Philip, L.; Pradeep, T. As (III) removal from drinking water using manganese oxide-coated-alumina: performance evaluation and mechanistic details of surface binding. *Chem. Eng. J.* **2009**, *153*, 101–107.
- (54) Farrell, J.; Chaudhary, B. K. Understanding arsenate reaction kinetics with ferric hydroxides. *Environ. Sci. Technol.* **2013**, *47*, 8342–8347.
- (55) Manjunath, S. V.; Kumar, M. Evaluation of single-component and multi-component adsorption of metronidazole, phosphate and nitrate on activated carbon from *Prosopis juliflora*. *Chem. Eng. J.* **2018**, *346*, 525–534.
- (56) Inglezakis, V. J.; Zorpas, A. A. Heat of adsorption, adsorption energy and activation energy in adsorption and ion exchange systems. *Desalin. Water Treat.* **2012**, *39*, 149–157.
- (57) Dixit, S.; Hering, J. G. Comparison of arsenic (V) and arsenic (III) sorption onto iron oxide minerals: implications for arsenic mobility. *Environ. Sci. Technol.* **2003**, *37*, 4182–4189.
- (58) Guo, X.; Chen, F. Removal of arsenic by bead cellulose loaded with iron oxyhydroxide from groundwater. *Environ. Sci. Technol.* **2005**, *39*, 6808–6818.
- (59) Meng, X.; Korfiatis, G. P.; Bang, S.; Bang, K. W. Combined effects of anions on arsenic removal by iron hydroxides. *Toxicol. Lett.* **2002**, *133*, 103–111.
- (60) Michel, F. M.; Barrón, V.; Torrent, J.; Morales, M. P.; Serna, C. J.; Boily, J.-F.; Liu, Q.; Ambrosini, A.; Cismasu, A. C.; Brown, G. E. Ordered ferrimagnetic form of ferrihydrite reveals links among structure, composition, and magnetism. *Proc. Natl. Acad. Sci. U. S. A.* **2010**, *107*, 2787–2792.
- (61) Campbell, A.; Schwertmann, U.; Stanjek, H.; Friedl, J.; Kyek, A.; Campbell, P. Si incorporation into hematite by heating Si-ferrihydrite. *Langmuir* **2002**, *18*, 7804–7809.
- (62) Ardizzone, S.; Dioguardi, F.; Mussini, T.; Mussini, P.; Rondinini, S.; Vercelli, B.; Vertova, A. Microcrystalline cellulose powders: structure, surface features and water sorption capability. *Cellulose* **1999**, *6*, 57–69.
- (63) Chakraborti, D.; Rahman, M. M.; Das, B.; Chatterjee, A.; Das, D.; Nayak, B.; Pal, A.; Chowdhury, U. K.; Ahmed, S.; Biswas, B. K.;

et al. Groundwater arsenic contamination and its health effects in India. *Hydrogeol. J.* **2017**, *25*, 1165–1181.

(64) Sheldon, R. A. Metrics of Green Chemistry and Sustainability: Past, Present, and Future. *ACS Sustainable Chem. Eng.* **2018**, *6* (1), 32–48.

(65) Curzons, A. D.; Constable, D. J.; Mortimer, D. N.; Cunningham, V. L. So you think your process is green, how do you know?—Using principles of sustainability to determine what is green—a corporate perspective. *Green Chem.* **2001**, *3*, 1–6.

(66) Jiménez-González, C.; Constable, D. J.; Ponder, C. S. Evaluating the “Greenness” of chemical processes and products in the pharmaceutical industry—a green metrics primer. *Chem. Soc. Rev.* **2012**, *41*, 1485–1498.

(67) International Energy Agency. Iron and steel. <http://www.iea.org/tcep/industry/steel/> (accessed September 18, 2018).

(68) International Energy Agency. Aluminium. <http://www.iea.org/tcep/industry/aluminium/> (accessed September 18, 2018).

(69) Spence, K. L.; Venditti, R. A.; Rojas, O. J.; Habibi, Y.; Pawlak, J. J. A comparative study of energy consumption and physical properties of microfibrillated cellulose produced by different processing methods. *Cellulose* **2011**, *18*, 1097–1111.

(70) European Chemicals Agency. Home Page. <https://echa.europa.eu/> (accessed September 12, 2018).

## Supporting Information

### **Sustainable and affordable composites built using microstructures performing better than nanostructures for arsenic removal**

*Sritama Mukherjee<sup>†</sup>, Avula Anil Kumar<sup>†</sup>, Chennu Sudhakar<sup>†</sup>, Ramesh Kumar<sup>†</sup>, Tripti Ahuja<sup>†</sup>,  
Biswajit Mondal<sup>†</sup>, Srikrishnarka Pillalamarri<sup>†</sup>, Ligy Philip<sup>‡</sup>, Thalappil Pradeep<sup>\*, †</sup>*

<sup>†</sup> DST Unit of Nanoscience (DST UNS) and Thematic Unit of Excellence (TUE), Department of Chemistry, Indian Institute of Technology Madras, Chennai 600036, India.

<sup>‡</sup> EWRE Division, Department of Civil Engineering, Indian Institute of Technology Madras, Chennai 600036, India.

\*Corresponding author

E-mail: [pradeep@iitm.ac.in](mailto:pradeep@iitm.ac.in)

Thalappil Pradeep, DST Unit of Nanoscience (DST UNS) and Thematic Unit of Excellence (TUE), Department of Chemistry, Indian Institute of Technology Madras, Chennai 600036, India.

Tel.: +91-44 2257 4208; Fax: +91-44 2257 0545/0509

### **SUPPORTING INFORMATION CONTENT**

Total number of pages: 18

Total number of figures: 12

Total number of tables: 1

Total number of equations: 8

## TABLE OF CONTENTS

Supporting items	Title	Page no.
	Instrumentation	S3
E1-E8	Equations used in main text	S4-S5
Figure S1	SEM images of Cellulose nanocrystals	S6
Figure S2	Plot of horizontal shear stress vs. horizontal displacement of CMCFH	S7
Figure S3	Mohr-Coulomb failure pattern (Shear stress vs. Normal stress) of CMCFH	S8
Figure S4	HRTEM and EDS of CMCFH after As(III) and As(V) adsorption	S9
Figure S5	XRD of CMCFH annealed up to 900 °C	S10
Figure S6	IR spectra of CMCFH before and after As(III)/As(V) adsorption, corresponding to IR of As standards	S11
Figure S7	Pseudo first-order reaction kinetic plots for the adsorption of As(III) and As(V) on ferrihydrite	S12
Figure S8	Pseudo second-order reaction kinetic plots for the adsorption of As(III) and As(V) on ferrihydrite	S13
Figure S9	As (III) adsorption on MCCFH (a) Freundlich and (b) Dubinin–Radushkevich isotherm models	S14
Figure S10	Interfering ions (cations and anions) studies for (A) MCCFH, (B) CPFH and (C) HECFH, respectively	S15
Figure S11	SEM-EDS and elemental mapping of CMCFH before and after As(III)/As(V) adsorption	S16
Figure S12	Thermogravimetric analysis (TGA) of CMCFH at air and nitrogen atmospheres	S17
Table S1	Physicochemical characteristics of influent natural drinking water	S18

## INSTRUMENTATION

Transmission electron microscopy (TEM) and high-resolution transmission electron microscopy (HRTEM) were performed at an accelerating voltage of 200 kV on a JEOL 3010, 300 kV instrument equipped with a UHR polepiece. The accelerating voltage was kept low to ensure that beam induced damage on the material was low. The samples for HRTEM were prepared as the dispersions which were dropcasted on carbon-coated copper grids and allowed to dry under ambient conditions. Surface morphology, elemental analysis and elemental mapping studies were carried out using a Scanning Electron Microscope (SEM) equipped with energy dispersive spectroscopy (EDS) (FEI Quanta 200). For the SEM and EDS measurements, the samples were spotted on an aluminum sample stub. X-ray Photoelectron Spectroscopy (XPS) measurements were done using an ESCA Probe TPD spectrometer of Omicron Nanotechnology. Polychromatic Mg K $\alpha$  was used as the X-ray source ( $h\nu = 1253.6$  eV). Samples were spotted as drop cast films on a sample stub. Constant analyzer energy of 20 eV was used for the measurements. Binding energy was calibrated with respect to C 1s at 284.8 eV. Raman spectroscopy was performed using a CRM 200 micro Raman spectrometer of WiTec GmbH (Germany). The substrate was mounted on a sample stage of a confocal Raman spectrometer. The spectra were collected at 633 nm laser excitation. For Raman measurements, the corresponding nanomaterial/standard material (as in dried powder form)-coated glass substrates were analyzed keeping the laser and other parameters the same. Total As and iron concentrations in water were detected using PerkinElmer NexION 300X ICPMS (Inductively coupled plasma mass spectrometry) with appropriate standards. It is a type of mass spectrometry that is highly sensitive for analyzing a range of metal ions and capable of distinguishing their isotopic speciation. ICPMS detection systems use electron multipliers, which convert ion currents into electrical signals. The magnitude of the electrical signal is proportional to the number of analyte ions present in the sample. Brunauer–Emmett–Teller (BET) surface area was measured using Micromeritics ASAP 2020. Samples were degassed at 200 °C for 4 h under vacuum and analyzed at 77 K with ultrahigh pure nitrogen gas. Thermogravimetric measurement was done with TA Instruments Q500 Thermogravimetric Analyzer (TGA) under air and N<sub>2</sub> atmosphere from room temperature to 900 °C, with 10 min scan rate. All the uptake capacity studies in batch mode were done in 250 mL polypropylene conical flasks.

**Equation (1):** The maximum uptake of As ( $q_e$ ) by cellulosic composites was calculated using the equation given below:

$$Uptake (qe) = \frac{(C_o - C_e)V}{m}$$

where  $q_e$  is the amount of As(III)/As(V) ions adsorbed per gram of the adsorbent (mg/g) at equilibrium,  $C_e$  is the equilibrium concentration of As(III)/As(V) in the bulk solution (mg/L),  $C_o$  is the initial As(III)/As(V) concentration (mg/L),  $V$  is the volume of solution (L) and  $m$  is the mass of the adsorbent (g).

**Equation (2):** The linearized form of Langmuir equation used in this work is defined as,

$$\frac{C_e}{q_e} = \frac{C_e}{q_{max}} + \frac{1}{bq_{max}}$$

where  $q_e$  is the amount of adsorption at the surface of the adsorbent (mg/g),  $C_e$  is the equilibrium concentration of the solution (mg/L),  $q_{max}$  is the maximum surface density at monolayer coverage and  $b$  is the Langmuir adsorption constant (L/mg) related to the free energy of adsorption and  $1/q_{max}$  and  $1/bq_{max}$  are the Langmuir constants.

**Equation (3):** The removal % of As was calculated using the equation mentioned below:

$$Removal \% = \frac{C_o - C_e}{C_o} \times 100$$

where  $C_o$  and  $C_e$  are the initial and equilibrium concentrations of the metal ions, respectively.

Sustainability metrics equations

**Equation (4):**  $Mass\ intensity = \frac{mass\ of\ all\ products\ used\ excluding\ water}{mass\ of\ product} kg/kg\ product$

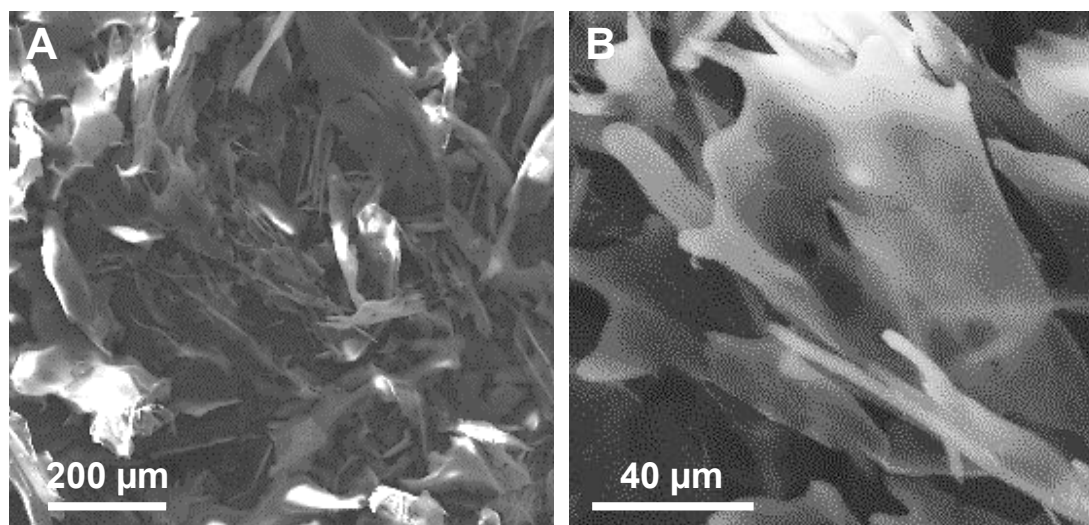
**Equation (5):**  $Water\ intensity\ (W_p) = \frac{mass\ of\ all\ water\ used}{mass\ of\ product} kg/kg\ product$

**Equation (6):**      Reaction mass efficiency (RME) =  $\frac{\text{mass of product}}{\text{mass of all reactants}} \times 100\%$

**Equation (7):**      *Energy Intensity* =  $\frac{\text{amount of non renewable energy used}}{\text{mass of product}} \text{ kW.h/kg}$

**Equation (8):**      *E factor* =  $\frac{[kg(\text{raw materials}) - kg(\text{desired product})]}{kg(\text{total product including water})}$

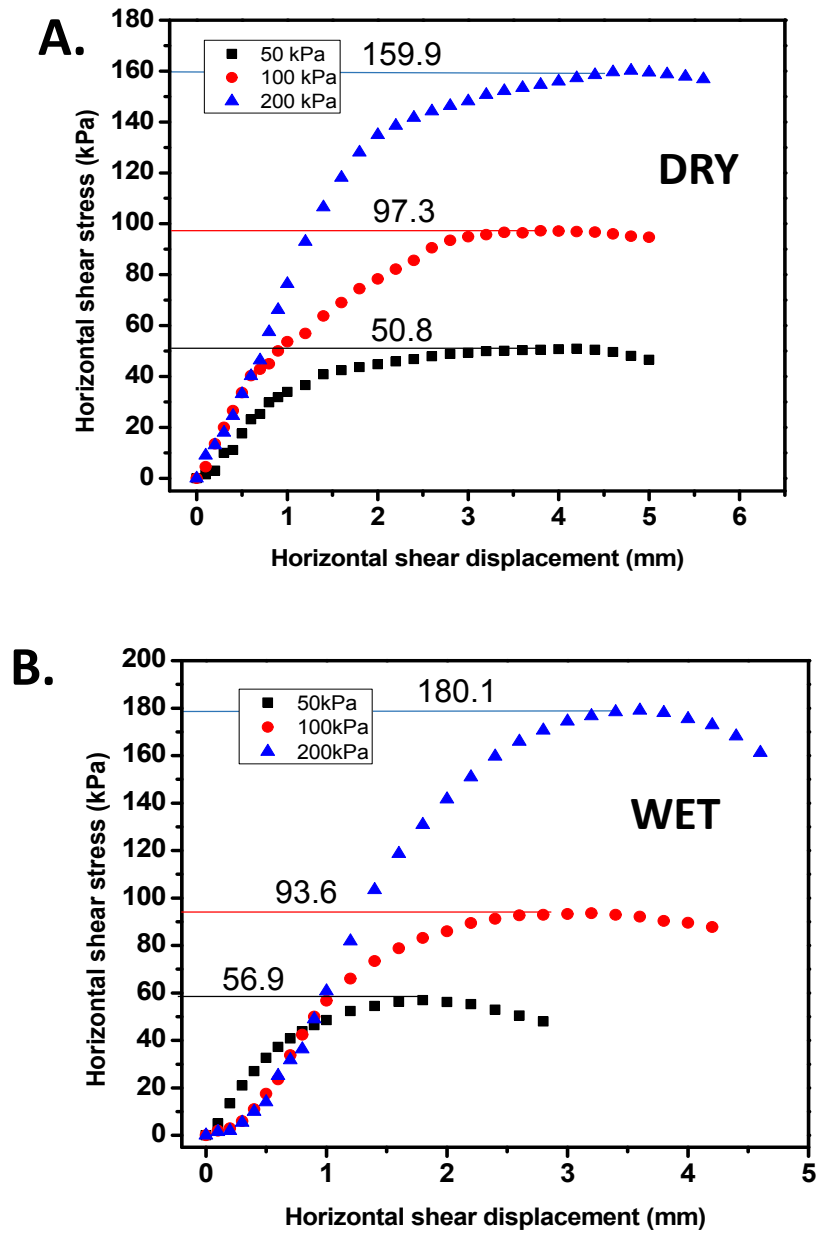
## Supporting Information 1



**Figure S1.** SEM images of cellulose nanocrystals at different length scales.

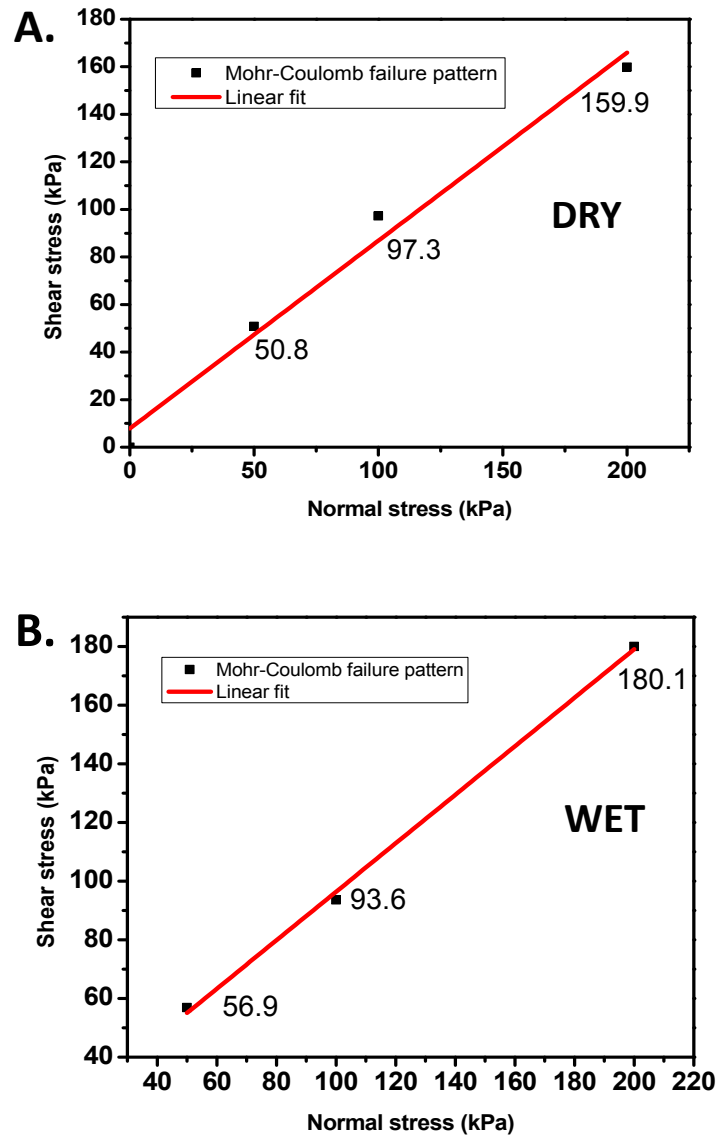


## Supporting Information 2



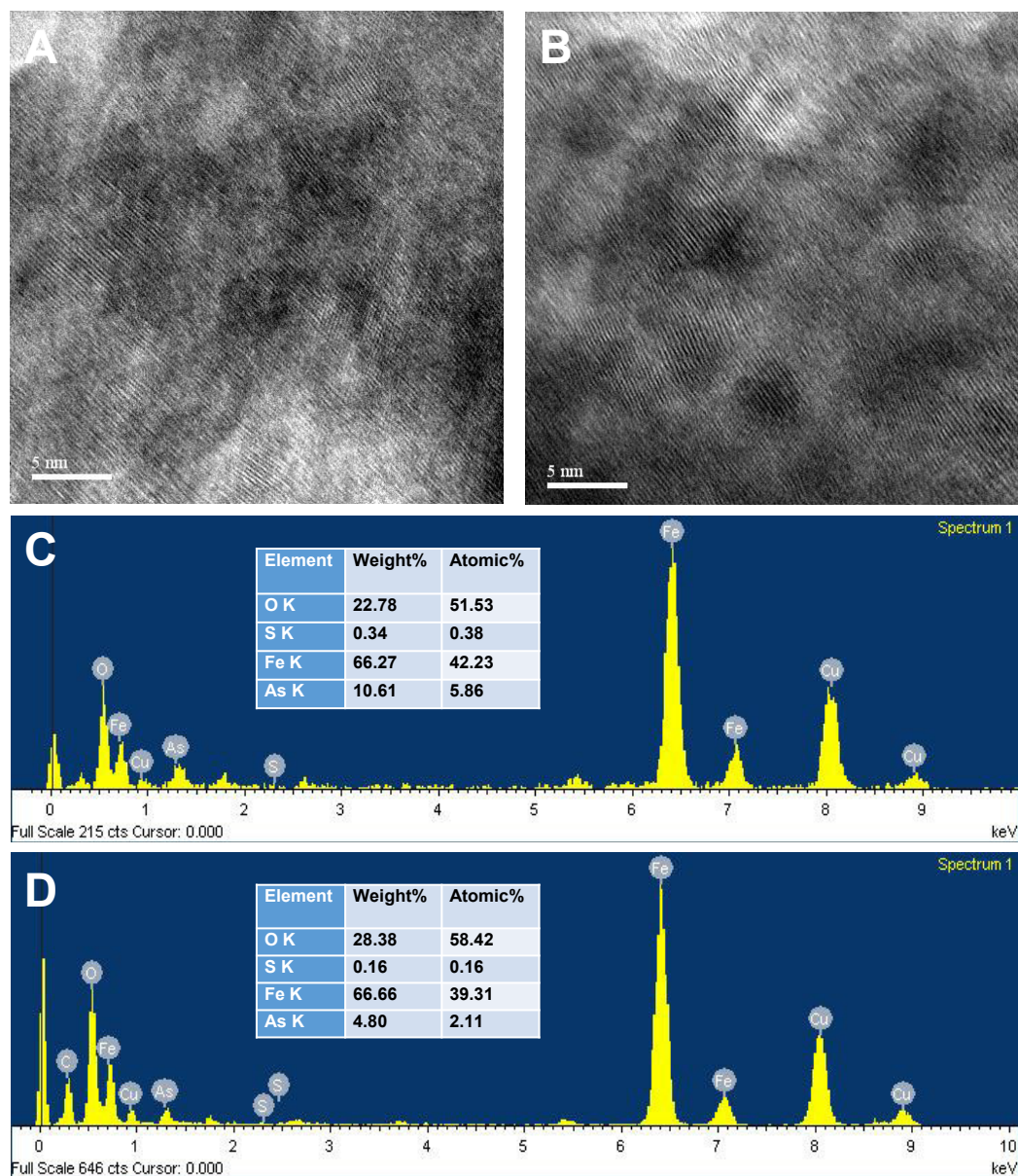
**Figure S2.** Direct shear test (Horizontal shear stress vs. Horizontal displacement). Plot of horizontal shear stress vs. horizontal displacement of loosely packed media obtained from direct shear tests: (A) measured at dry condition and (B) measured at wet condition.

### Supporting Information 3



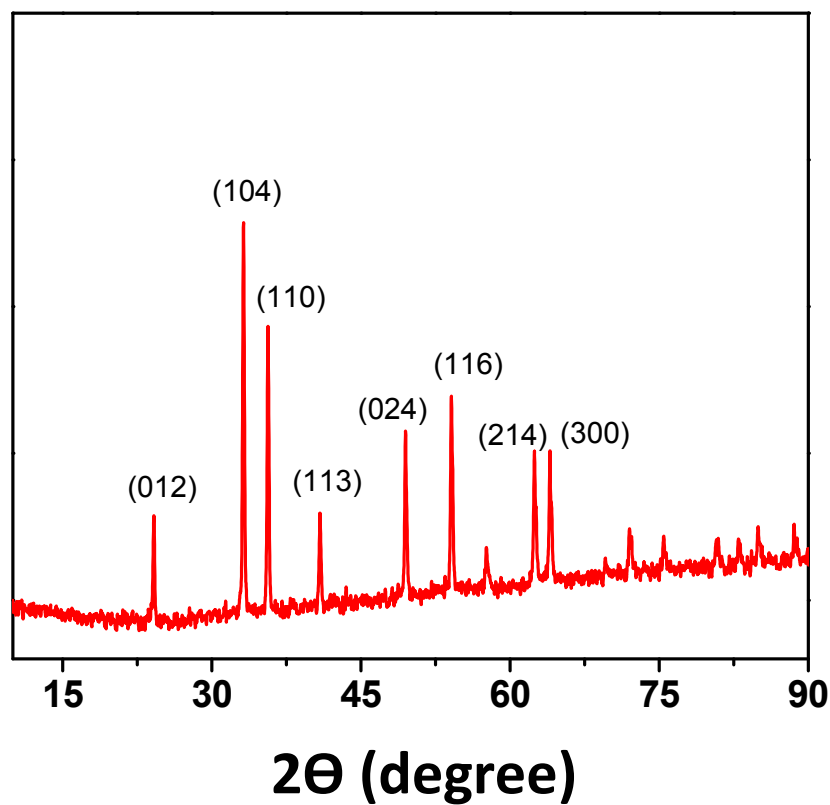
**Figure S3.** Mohr-Coulomb failure pattern (Shear stress vs. Normal stress). Plot of shear stress vs. normal stress of loosely packed media showing the straight-line approximation of the Mohr-Coulomb failure pattern: ( A) measured at dry condition and ( B) measured at wet condition.

## Supporting Information 4



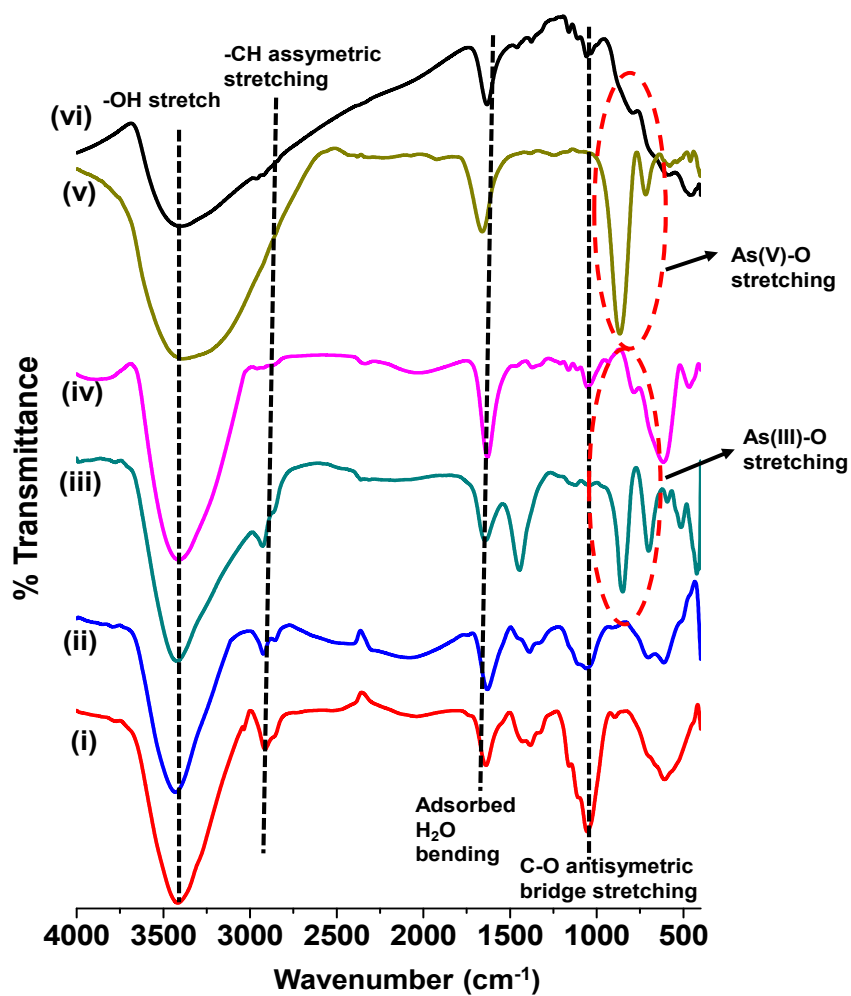
**Figure S4.** HRTEM and EDS of CMCfH after As(III) and As(V) adsorption. (A) and (B) show HRTEM micrograph of As(III) and As(V) adsorbed CMCfH, respectively, after beam induced crystallization. (C) and (D) show EDS of As(III) and As(V) adsorbed CMCfH, respectively.

## Supporting Information 5



**Figure S5.** XRD of CMCFH annealed up to 900 °C showing hematite ( $\alpha$ -Fe<sub>2</sub>O<sub>3</sub>) formation from ferrihydrite content of the composite.

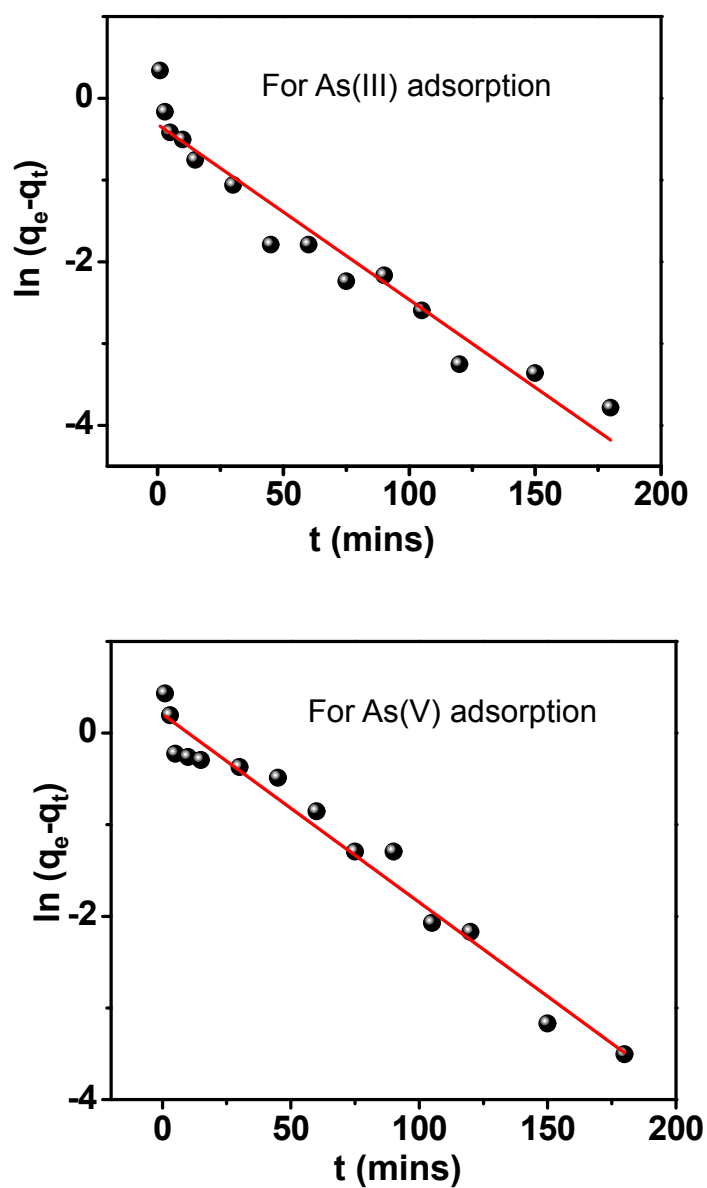
## Supporting Information 6



**Figure S6.** Infrared (IR) spectra of (i) cellulose; (ii) CMCFH solid; (iii) and (v) standard aqueous solutions of As(III) and As(V) at pH 7; (iv) and (vi) CMCFH before and after As(III) and As(V) adsorption, respectively.

## Supporting Information 7

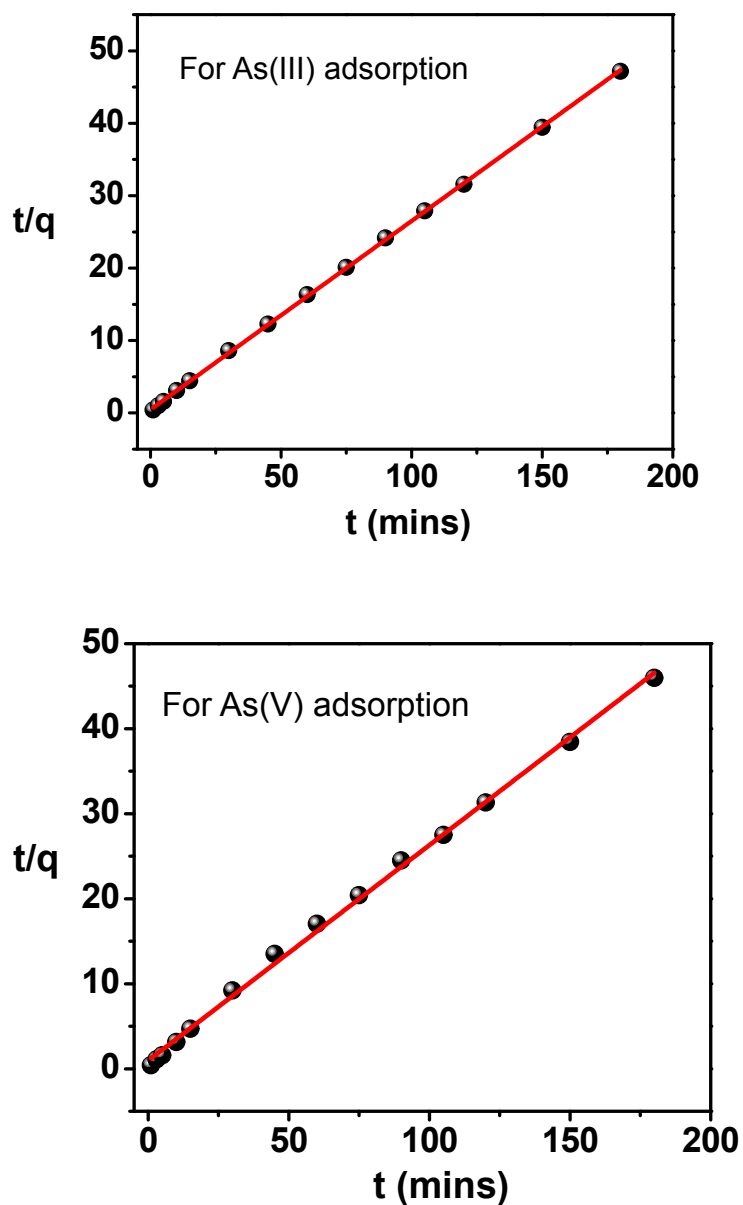
Lagergren pseudo-first-order model:  $\ln(q_e - q_t) = \ln q_e - k_1 t$



**Figure S7.** Pseudo first-order reaction kinetic plots for the adsorption of As(III) and As(V) on ferrihydrite.

## Supporting Information 8

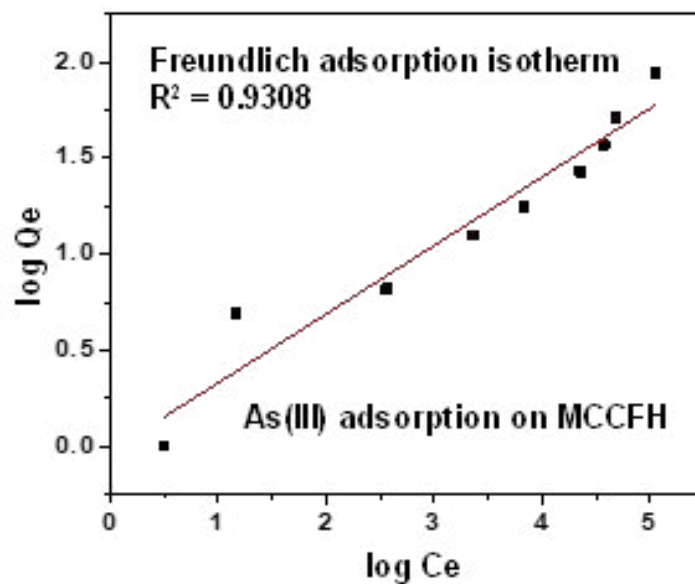
Ho's pseudo-second-order model:  $\frac{t}{q_e} = \frac{1}{k_2 q_e^2} + \frac{1}{q_e} t$



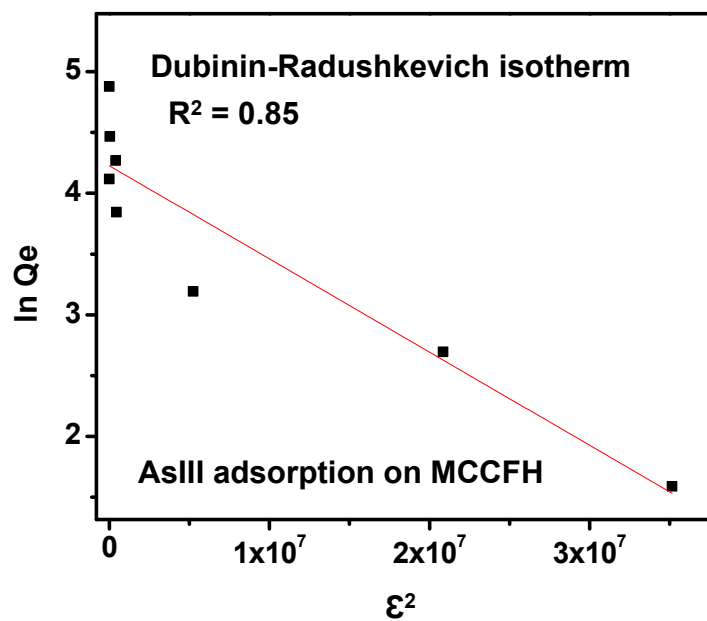
**Figure S8.** Pseudo second-order reaction kinetic plots for the adsorption of As(III) and As(V) on ferrihydrite.

## Supporting Information 9

a. Freundlich adsorption isotherm model:  $\log Q_e = \log K_f + \frac{1}{n} \log C_e$



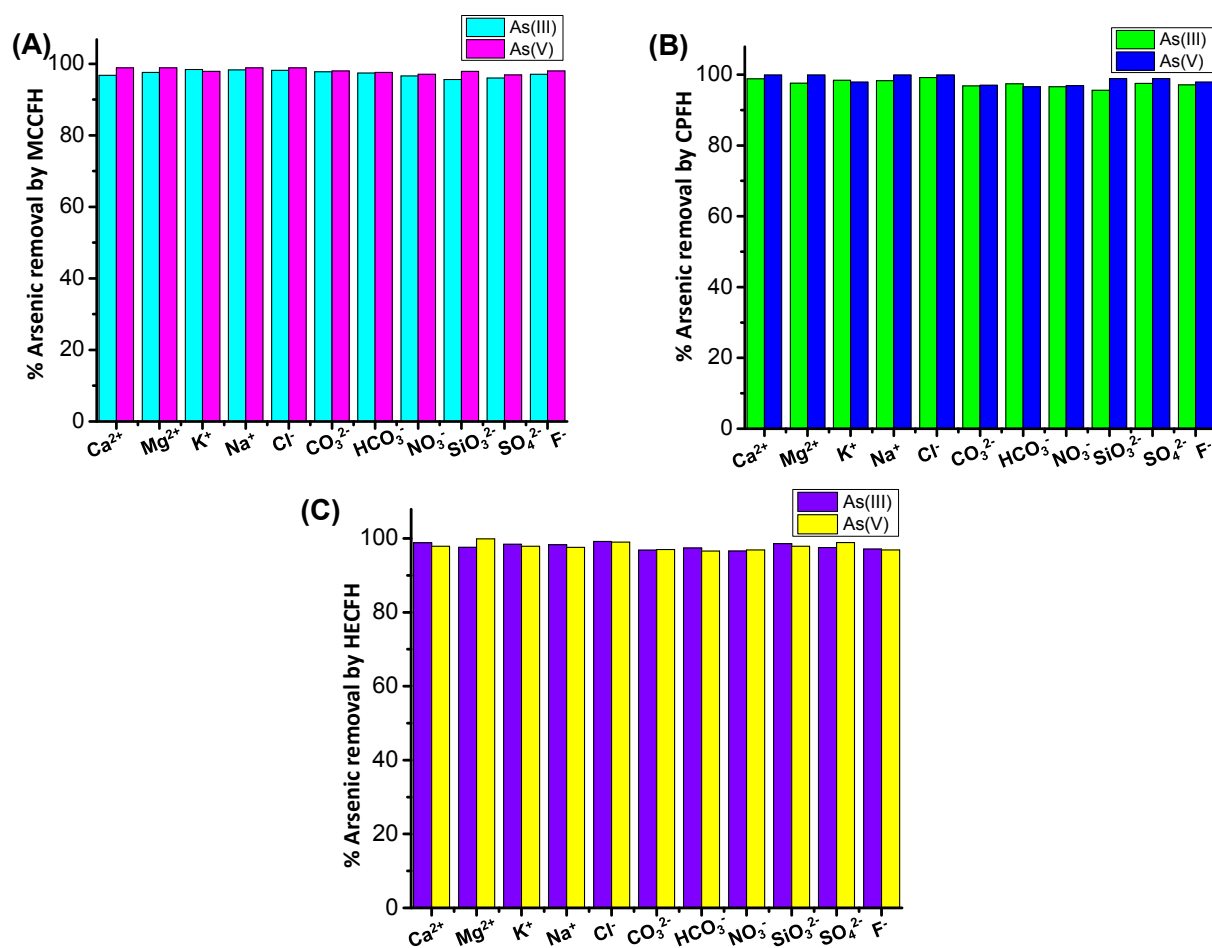
b. Dubinin–Radushkevich isotherm model:  $\ln Q_e = \ln Q_s - K_{ad} \varepsilon^2$



**Figure S9.** Adsorption isotherms showing the correlation coefficients for As (III) adsorption on MCCFH (a) Freundlich and (b) Dubinin–Radushkevich isotherm models, respectively.

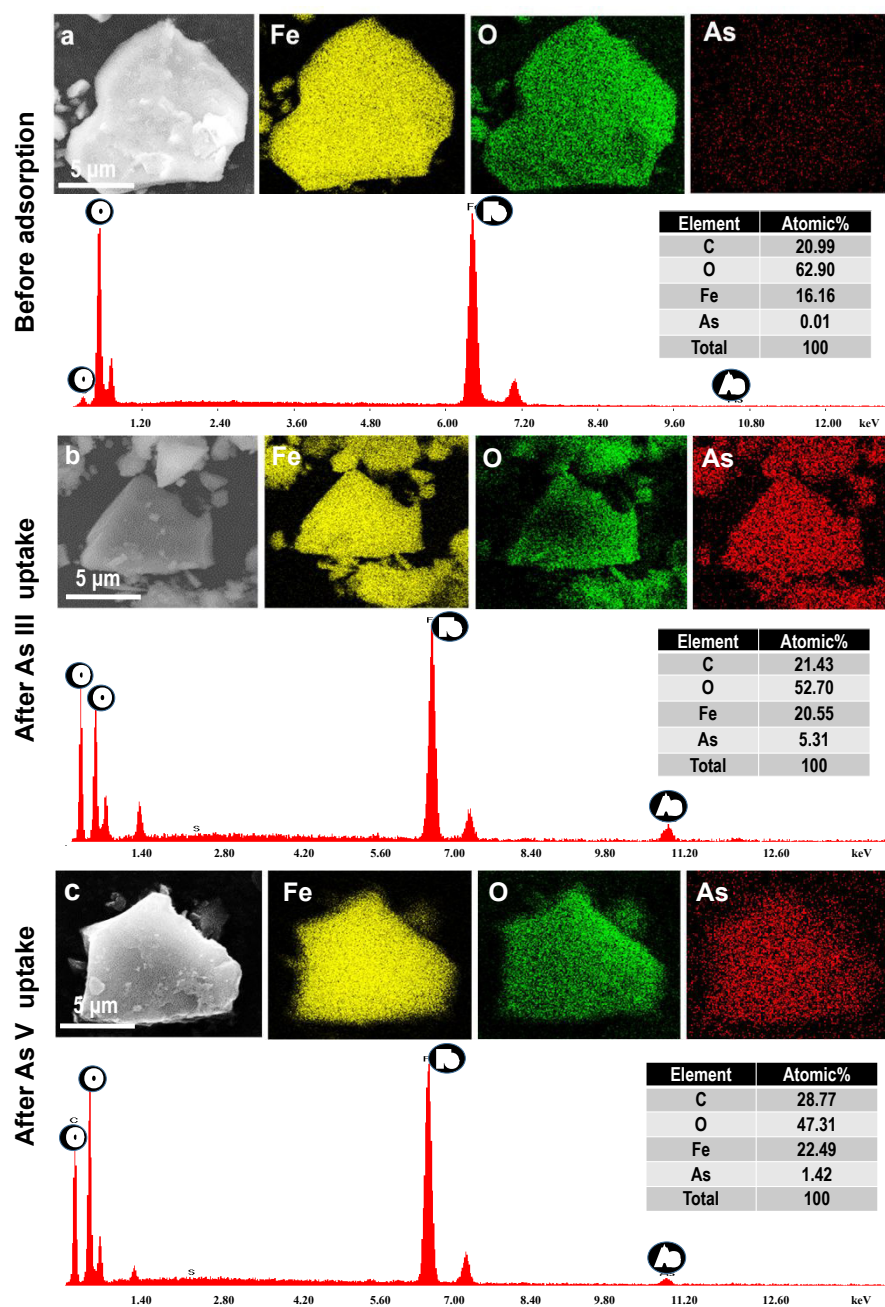


## Supporting Information 10



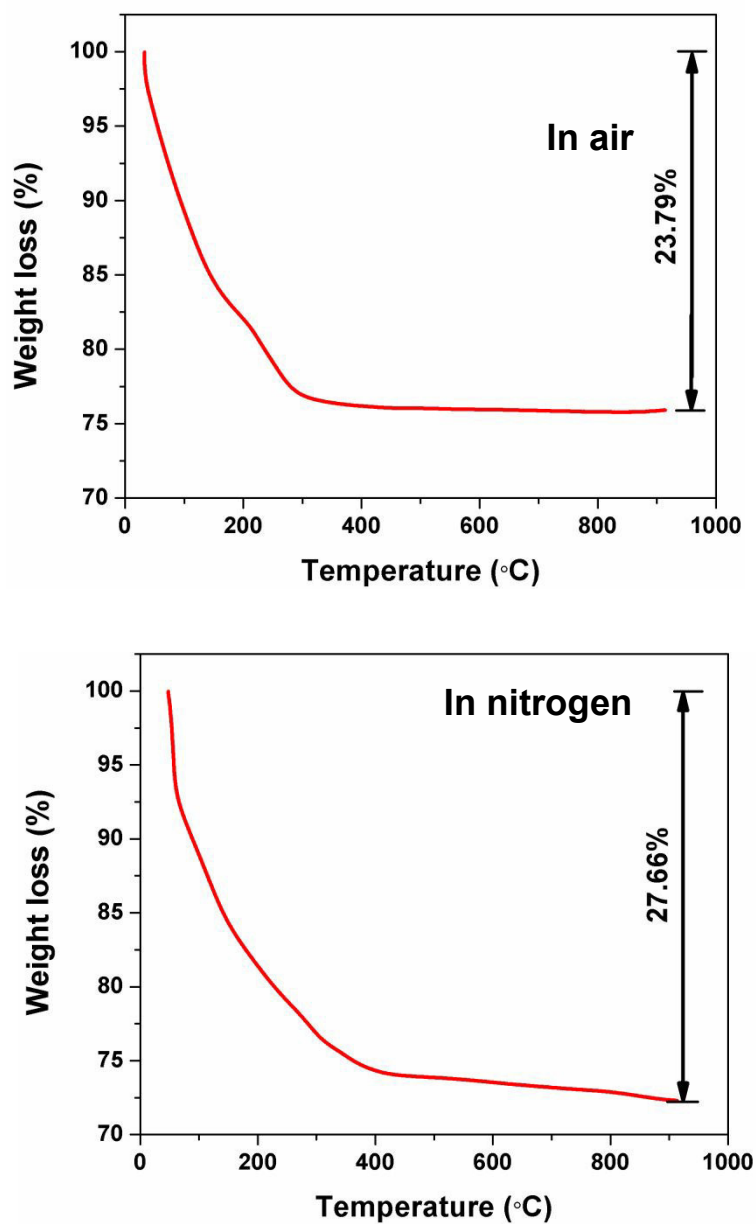
**Figure S10.** Uptake of As(III) and As(V) in presence of other competing ions (cations and anions) which are generally present in groundwater by (A) MCCFH, (B) CPFH and (C) HECFH, respectively.

## Supporting Information 11



**Figure S11.** SEM-EDS and elemental mapping of CMCFH (a) before (b) after As(III) and (c) after As(V) adsorption.

## Supporting Information 12



**Figure S12.** Thermogravimetric analysis (TGA) of CMCFH at air and nitrogen atmospheres from room temperature to 900 °C with 10 min scan rate.

**Table S1.**

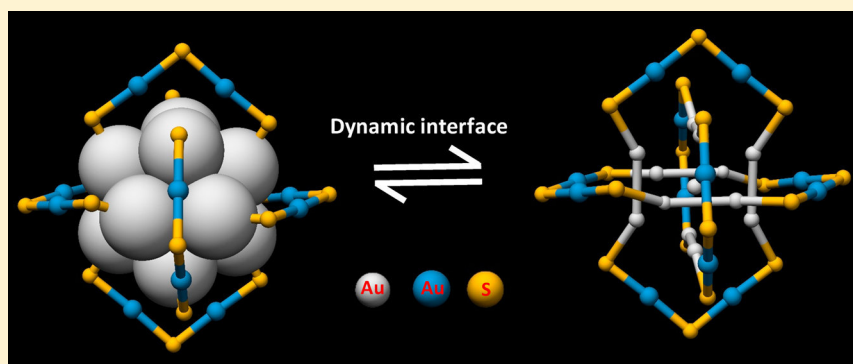
Physicochemical characteristics of influent natural water.

Sl no.	Parameters	Value
1	Total coliforms (CFU/ml)	1-2 * 10 <sup>3</sup>
2	pH at 25°C	7.8
3	Conductivity (µS/cm)	640.0
4	Fluoride (mg/L)	0.57
5	Chloride (mg/L)	86.34
6	Nitrate (mg/L)	1.84
7	Sulfate (mg/L)	32.41
8	Silicate (mg/L)	15.87
9	Phosphate (mg/L)	55.83
10	Sodium (mg/L)	53.74
11	Potassium (mg/L)	2.33
12	Magnesium (mg/L)	14.34
13	Calcium (mg/L)	28.72

## Metal–Ligand Interface in the Chemical Reactions of Ligand-Protected Noble Metal Clusters

Kumaranchira Ramankutty Krishnadas,<sup>†</sup> Ganapati Natarajan, Ananya Bakshi,<sup>‡</sup> Atanu Ghosh,<sup>§</sup> Esma Khatun, and Thalappil Pradeep\*<sup>¶</sup>

Department of Chemistry, DST Unit of Nanoscience (DST UNS) and Thematic Unit of Excellence (TUE), Indian Institute of Technology Madras, Chennai 600 036, India



**ABSTRACT:** We discuss the role of the metal–ligand (M–L) interfaces in the chemistry of ligand-protected, atomically precise noble metal clusters, a new and expanding family of nanosystems, in solution as well as in the gas phase. A few possible mechanisms by which the structure and dynamics of M–L interfaces could trigger intercluster exchange reactions are presented first. How interparticle chemistry can be a potential mechanism of Ostwald ripening, a well-known particle coarsening process, is also discussed. The reaction of  $\text{Ag}_{59}(\text{2,5-DCBT})_{32}$  (DCBT = dichlorobenzenethiol) with 2,4-DCBT leading to the formation of  $\text{Ag}_{44}(\text{2,4-DCBT})_{30}$  is presented, demonstrating the influence of the ligand structure in ligand-induced chemical transformations of clusters. We also discuss the structural isomerism of clusters such as  $\text{Ag}_{44}(\text{SR})_{30}$  ( $-\text{SR}$  = alkyl/aryl thiolate) in the gas phase wherein the occurrence of isomerism is attributed to the structural rearrangements in the M–L bonding network. Interfacial bonding between  $\text{Au}_{25}(\text{SR})_{18}$  clusters leading to the formation of cluster dimers and trimers is also discussed. Finally, we show that the desorption of phosphine and hydride ligands on a silver cluster,  $[\text{Ag}_{18}(\text{TPP})_{10}\text{H}_{16}]^{2+}$  (TPP = triphenylphosphine) in the gas phase, leads to the formation of a naked silver cluster of precise nuclearity, such as  $\text{Ag}_{17}^+$ . We demonstrate that the nature of the M–L interfaces, i.e., the oxidation state of metal atoms, structure of the ligand, M–L bonding network, and so forth, plays a key role in the chemical reactivity of clusters. The structure, dynamics, and chemical reactivity of nanosystems in general are to be explored together to obtain new insights into their emerging science.

### ■ INTRODUCTION

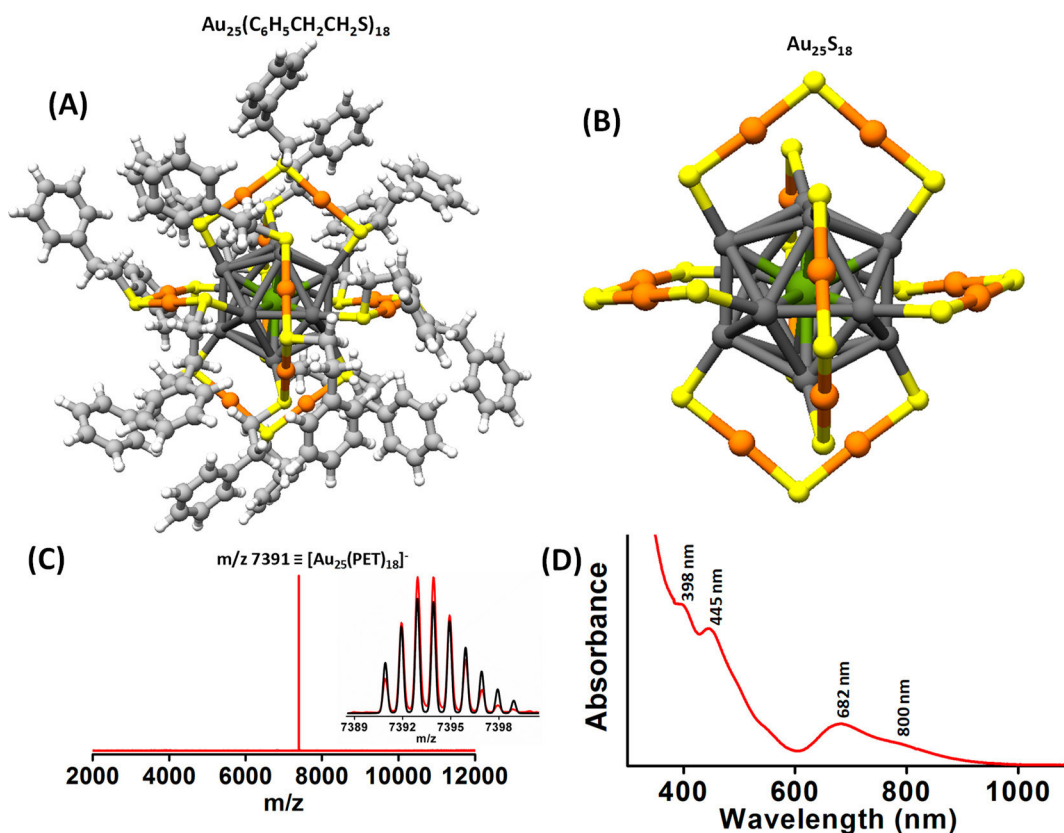
Metal–ligand (M–L) interfaces play key roles in dictating the physical properties, chemical reactivity, and interparticle interactions of ligand-protected metal nanosystems. Atomically precise noble metal clusters,<sup>1,2</sup> such as  $\text{Au}_{102}(\text{SR})_{44}$ ,  $\text{M}_{25}(\text{SR})_{18}$  ( $\text{M} = \text{Ag}/\text{Au}$ ),<sup>4,5</sup> and  $\text{Ag}_{44}(\text{SR})_{30}$ ,<sup>6,7</sup> ( $-\text{SR}$  = alkyl/aryl thiolate), serve as convenient models for investigating the properties of M–L interfaces owing to their well-defined compositions, structures, and molecule-like properties.<sup>8–10</sup> Such clusters have a well-defined metal core protected by a ligand shell. The feasibility of incorporating a variety of ligands such as phosphines,<sup>11–13</sup> thiols,<sup>7,14–19</sup> selenols,<sup>20–22</sup> and alkynes,<sup>23</sup> also makes them suitable systems for studying the M–L interfaces. Early in the literature, these clusters were referred to as “monolayer protected clusters”,<sup>24</sup> assuming that the ligands form an extended ordered layer on particle surfaces,<sup>25</sup> which in turn resemble crystallographic planes of the corresponding metals. Single-crystal X-ray crystallography

revealed that the M–L interfaces in many of these clusters assume well-defined, short  $\text{M}_x\text{L}_y$  oligomeric units. For example,  $\text{Au}_{25}(\text{SR})_{18}$  is composed of a  $\text{Au}_{13}$  core and six  $\text{Au}_2(\text{SR})_3$  units, often referred to as staple motifs. Similarly,  $\text{Ag}_{44}(\text{SR})_{30}$  consists of an  $\text{Ag}_{32}$  core protected by six  $\text{Ag}_2(\text{SR})_5$  mounts. This structural model has been referred to as the “divide and protect” model<sup>26</sup> wherein these clusters are viewed as a core containing a precise number of metal atoms protected by a specific number of  $\text{M}_x\text{L}_y$  oligomeric units. Structural correlations between these clusters and that of M–L complexes and self-assembled monolayers have also been identified.<sup>27</sup> Recently, a few other structural models<sup>28–30</sup> in which these clusters have been considered as interlocked rings,

**Received:** October 19, 2018

**Revised:** December 4, 2018

**Published:** December 6, 2018



**Figure 1.** Crystal structure of  $\text{Au}_{25}(\text{C}_6\text{H}_5\text{CH}_2\text{CH}_2\text{S})_{18}$  (A), schematic showing the icosahedral core and the six  $\text{Au}_2(\text{SR})_3$  staples (B), negative ion ESI MS spectrum (C), and UV/vis absorption spectrum of  $\text{Au}_{25}(\text{C}_6\text{H}_5\text{CH}_2\text{CH}_2\text{S})_{18}$  (D). The  $\text{C}_6\text{H}_5\text{CH}_2\text{CH}_2$  groups of the ligands are omitted in panel B for clarity. The structures are intended to highlight the ligand–core interface. Color codes of atoms: Au atoms at the surface of the  $\text{Au}_{13}$  icosahedron (black), in the center of the  $\text{Au}_{13}$  icosahedron (green), in the staples (orange), sulfur (yellow), carbon (gray), and hydrogen (white). Distinct features in the mass and the UV/vis spectra are also marked in panels C and D. The isotopic resolution of the molecular ion features of  $\text{Au}_{25}(\text{C}_6\text{H}_5\text{CH}_2\text{CH}_2\text{S})_{18}$  at  $m/z$  7391 is shown in the inset of panel C along with a comparison of the theoretical (black) and experimental (red) spectra. The abbreviation PET (phenylethanethiolate) in Figure 1C correspond to the ligand tail group  $\text{C}_6\text{H}_5\text{CH}_2\text{CH}_2\text{S}$ .

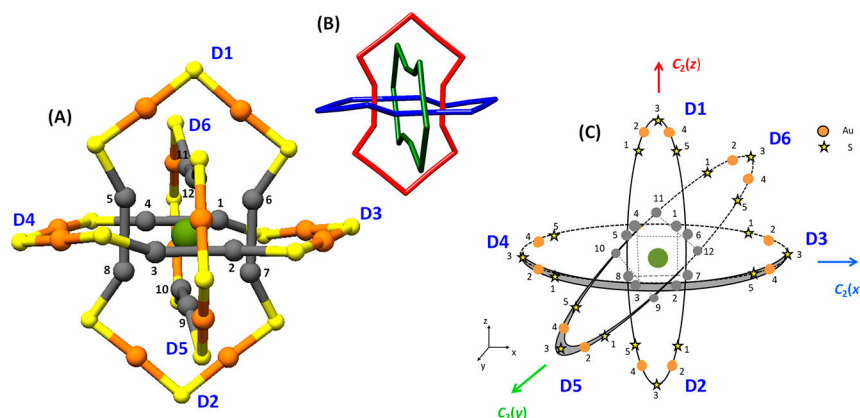
instead of distinct staples or mounts, have been proposed to understand the properties of these clusters. Irrespective of the structural model, the actual structure of the ligands, their spatial distribution on the cluster surface, binding modes of the ligands with the metal atoms, and oxidation states of metal atoms need to be considered in order to understand the M–L interfaces in these clusters.

The nature of ligands such as the types of tail groups (alkyl and aryl) and the positions<sup>31</sup> (ortho, meta, and para) of functional groups ( $-\text{CH}_3$ ,  $-\text{COOH}$ , etc.) in them drastically influence the nuclearity, geometry, solubility, and other properties of clusters.<sup>32,33</sup> Weak van der Waals and/or  $\pi$ – $\pi$  interactions between the ligands is shown to be responsible for their chiroptical properties,<sup>34,35</sup> supramolecular interactions,<sup>36</sup> and cluster assemblies.<sup>37–39</sup> The electronic interaction between the ligands and the metal core influences the optical absorption<sup>40</sup> and luminescence<sup>41,42</sup> features. Metal atoms in the staples serve as the true catalytic sites in such clusters. A variety of chemical transformations of these clusters such as ligand exchange,<sup>43–47</sup> metal atom substitution,<sup>48–53</sup> ligand-induced core etching<sup>54,55</sup> and core transformation,<sup>56–58</sup> were reported in the past few years. Recently, reactions between clusters in the solution phase were also reported.<sup>59–64</sup> These reactions invariably involve the metal atoms and ligands in the staple or mount motifs of these clusters.<sup>65–68</sup> The dynamic nature of the staple motifs or mounts<sup>69–74</sup> and the reactions of these clusters have been studied, mostly in the solution phase.

The stability and the dynamics of these M–L interfaces in gaseous phase, and the resulting chemical reactivity of ligand-protected clusters remain poorly understood. In order to understand the chemical reactivity of these clusters, a better understanding of their M–L interfaces is essential.

In this invited feature article, we discuss the role of M–L interfaces in dictating the solution as well as gas-phase reactions of ligand-protected, atomically precise noble metal clusters. We discuss the role of the staples or mount motifs in such clusters in triggering the intercluster exchange reactions. We propose that interparticle chemistry, as demonstrated between atomically precise clusters, can be helpful in understanding the chemical events behind Ostwald ripening, a well-known particle-coarsening process. Next, we show that the ligand-induced transformation of  $\text{Ag}_{59}(\text{2,5-DCBT})_{32}$  to  $\text{Ag}_{44}(\text{2,4-DCBT})_{30}$  (DCBT = dichlorobenzenethiol) occurs in the solution phase through the dissociation of metal ligand fragments.<sup>75</sup> Then we discuss three examples wherein the gas-phase dynamics and reactivity of M–L interfaces are demonstrated. We present ion mobility mass spectrometric studies showing that ligand-protected clusters such as  $\text{Ag}_{44}(\text{SR})_{30}$  exhibit structural isomerism in the gas phase wherein the isomerism is attributed to the structural rearrangements in the metal–ligand bonding network.<sup>76</sup> Interfacial bonding between  $\text{Au}_{25}(\text{SR})_{18}$  clusters leading to the formation of cluster dimers and trimers is also presented.<sup>77</sup> Finally, we show that the desorption of phosphine and hydride





**Figure 2.** (A) Visualization of  $\text{Au}_{25}\text{S}_{18}$  as the ring structure consisting of three interlocked  $\text{Au}_8\text{S}_6$  rings. (B) Topological configuration of the Borromean rings, with the three  $\text{Au}_8\text{S}_6$  rings being colored red, blue, and green. (C) Two-dimensional schematic diagram of the Borromean rings formed by a planar projection of the  $\text{Au}_{25}\text{S}_{18}$  ring structure shown in panel A, wherein the  $\text{Au}_8\text{S}_6$  rings formed by pairs of coplanar staples are shown as ellipses. In panel C, the gold atoms in the  $\text{Au}_{13}$  icosahedral core are shown by gray circles, and yellow stars represent the positions of S atoms of the thiolate ligand. The orange circles in panel C represent the position of Au atoms in the  $\text{Au}_8\text{S}_6$  rings. The core Au atoms are numbered from 1 to 12, and the staple atoms are numbered clockwise from the end of the staple, from 1 to 5. The lines that join core Au atoms on opposite ends of the same staple are shown by the dotted lines. The three perpendicular  $C_2$  axes are marked with the associated Cartesian axes directions in parentheses. The staple directions are labeled by the six staple locants D1–D6, marked in blue. The  $\text{Au}_8\text{S}_6$  rings in panel C are formed by joining three sets of coplanar staples, i.e., D1–D2, D3–D4, and D5–D6. Color codes of atoms in panel A: Au atoms in the icosahedral core (gray), center of the  $\text{Au}_{13}$  icosahedron (green), staples (orange), and sulfur (yellow). (Adapted with permission from ref 28.)

ligands on a silver cluster,  $[\text{Ag}_{18}(\text{TPP})_{10}\text{H}_{16}]^{2+}$  in the gas phase, leads to the formation of naked silver clusters of specific nuclearity, such as  $\text{Ag}_{17}^+$ .<sup>78</sup> We conclude the article with a summary and brief discussion of future perspectives.

**Intercluster Reactions: What Is the Role of the Metal–Ligand Interface?** As mentioned above, thiolate-protected noble metal clusters have traditionally been viewed as composed of a core consisting of a definite number of metal atoms, protected with a well-defined shell of metal–ligand oligomeric complexes. The single crystal X-ray crystallographic structure of  $\text{Au}_{25}(\text{C}_6\text{H}_5\text{CH}_2\text{CH}_2\text{S})_{18}$ , for example, is shown in Figure 1A,B. This cluster consists of an inner  $\text{Au}_{12}$  icosahedral core (black spheres in Figure 1A,B) encapsulating a central Au atom (green spheres in Figure 1A,B), and the ligands are distributed in six distinct  $\text{Au}_2(\text{SR})_3$  staple motifs (orange and yellow spheres in Figure 1B). The composition and charge state of these clusters are further confirmed through electrospray ionization mass spectrometry (ESI MS) as well, as shown in Figure 1C. The high-resolution mass spectrum (inset of Figure 1C) shows the isotopic features. Although Au has only one isotope, the isotopes of S ( $^{32}\text{S}$ ,  $^{33}\text{S}$ ,  $^{34}\text{S}$ , and  $^{36}\text{S}$ ), C ( $^{12}\text{C}$  and  $^{13}\text{C}$ ), and H ( $^1\text{H}$  and  $^2\text{H}$ ) produce a rich spectrum. Such richness can be used to confirm the composition of the cluster by comparing with the theoretical spectrum. Electronic structure calculations show that the distinct electronic absorption features of these clusters (Figure 1D) originate from various transitions in their discrete electronic energy levels. Thus, crystallography and electronic structure calculations support this structural model of these ligand-protected noble metal clusters. However, in order to understand the chemical reactivity of these clusters, it is necessary to consider other structural models. We discuss some of these aspects in the following sections.

Recently, intercluster reactions, resulting in the exchange of metal atoms, ligands, and metal–ligand fragments between them, have been demonstrated.<sup>59,60,62,63</sup> However, the mechanisms of such reactions, especially how such reactions are triggered, remain unknown. In this section, we discuss a

few possible ways by which the structure and the dynamics of M–L interfaces trigger intercluster reactivity. For this, we consider the reaction between two structurally and compositionally analogous noble metal clusters,  $\text{Ag}_{25}(\text{SR})_{18}$  and  $\text{Au}_{25}(\text{SR})_{18}$ .<sup>59</sup> As mentioned above, these clusters have traditionally been viewed as composed of a distinct  $\text{M}_{13}$  core protected by  $\text{M}_2(\text{SR})_3$  ( $\text{M} = \text{Ag}/\text{Au}$ ) staples. According to the superatom theory,<sup>27</sup> valence electrons of metal atoms in their staples are localized by polar covalent bonds with the sulfur atoms of the ligands. Furthermore, each of the  $\text{M}_2(\text{SR})_3$  staples localizes the valence electron of one of the metal atoms in the  $\text{M}_{13}$  core. Therefore, all of the metal atoms in the six  $\text{M}_2(\text{SR})_3$  staples and six of the metal atoms in the  $\text{M}_{13}$  core are considered to be in the +1 oxidation state. The remaining seven valence electrons of the  $\text{Au}_{13}$  core and an acquired negative charge make the eight-electron superatom,  $[\text{Au}_{25}(\text{SR})_{18}]^-$ . In the crystal structure, charge neutrality is provided by the metal ions or ammonium ions. The studies presented in this article are performed with this  $\text{Au}_{25}(\text{SR})_{18}$  anion in solution, although this may not be mentioned explicitly.

We think that the difference in the oxidation states of metal atoms in the core and the staples, as explained above, plays a crucial role in triggering the intercluster reactions. Because of this difference in oxidation states, redox-like reactions could occur between two clusters. Let us consider two such possibilities, taking the reaction between  $\text{Ag}_{25}(\text{SR})_{18}$  and  $\text{Au}_{25}(\text{SR})_{18}$  as an example. In the first case, an  $\text{Ag}_{25}(\text{SR})_{18}$  molecule reacts with the  $\text{Au}_2(\text{SR})_3$  staples of  $\text{Au}_{25}(\text{SR})_{18}$ , wherein Au of  $\text{Au}_2(\text{SR})_3$  staples is in the +1 oxidation state. Note that redox reactions between silver clusters and Au(I) thioliates are known.<sup>49</sup> Alternatively, an  $\text{Au}_{25}(\text{SR})_{18}$  molecule reacts with the  $\text{Ag}_2(\text{SR})_3$  staples of  $\text{Ag}_{25}(\text{SR})_{18}$ , wherein Ag of the  $\text{Ag}_2(\text{SR})_3$  staple is in the +1 oxidation state. Such reactions between  $\text{Au}_{25}(\text{SR})_{18}$  and Ag(I) thioliates are also known.<sup>48</sup> It remains unclear as to how the difference in oxidation states of metal atoms in the core and the staples contributes to the chemical reactivity of these clusters. Apart from these

possibilities, it has also been intuitively suggested in the reaction between  $\text{Au}_{25}(\text{SR})_{18}$  and  $\text{Ag}_{44}(\text{SR})_{30}$  that the interaction between these two intact clusters could result in the formation of small reactive fragments such as  $\text{Ag}(\text{SR})_2^-$ , which react with the  $\text{Au}_2(\text{SR})_3$  staples of  $\text{Au}_{25}(\text{SR})_{18}$ , resulting in an exchange of metal atoms, ligands, and M–L fragments.<sup>62</sup> In this context, it is important to understand how much the chemistry of these clusters differ from that of the M–L complexes. In other words, do these clusters behave as unique entities in their reactions wherein the overall electronic structures of both of the reacting clusters need to be considered in order to explain their reactivity (rather than attributing their chemistry to the reaction between one of the clusters and the staples or the mounts of the other, as explained earlier)?

A new structural model, namely, the Borromean rings model,<sup>28</sup> has been proposed for the  $\text{Au}_{25}(\text{SR})_{18}$  noble metal cluster by Natarajan et al., wherein  $\text{Au}_{25}(\text{SR})_{18}$  has been considered to be part of three interlocked  $\text{Au}_8(\text{SR})_6$  rings surrounding the central Au atom (Figure 2). In this, all of the metal and sulfur atoms, except the central metal atom, belong to a unique structural component, the  $\text{Au}_8(\text{SR})_6$  ring. This model suggests that disconnecting any ring leads to two unlinked rings, which is a defining characteristic of the Borromean rings bonding topology (Figure 2B). The Borromean rings model also applies to a silver cluster,  $\text{Ag}_{25}(\text{SR})_{18}$ , which is a structural analogue of  $\text{Au}_{25}(\text{SR})_{18}$ . Natarajan et al. also noted that interlocked metal–thiolate ring structures have been found in the core and staple structures of a few gold–thiolate clusters which have crystal structures available, both smaller and larger than  $\text{Au}_{25}(\text{SR})_{18}$ , namely,  $\text{Au}_{10}(\text{SR})_{10}$ ,<sup>79</sup>  $\text{Au}_{20}(\text{SR})_{16}$ ,<sup>80</sup> and  $\text{Au}_{144}(\text{SR})_{60}$ .<sup>30,81</sup> They suggested that the interlocked ring structures form a strong framework for the clusters and may possibly represent a unified viewpoint for the structure of monolayer-protected clusters. According to this interlocked-ring structural model, these clusters being formed out of and stabilized by ring structures are more dynamic in nature than one would expect from the core/staple model because in the latter the  $\text{M}_{13}$  core has been viewed as a distinct, compact structural unit which undergoes structural distortion with difficulty. Furthermore, if the cluster existed in solution as a distinct, structurally rigid  $\text{Au}_{13}$  core and  $\text{Au}_2(\text{SR})_3$  staples, then the exchange of metal atoms into the core would not have been feasible. However, the exchange of metal atoms in the core also occurs during the reaction between  $\text{Ag}_{25}(\text{SR})_{18}$  and  $\text{Au}_{25}(\text{SR})_{18}$ , suggesting that the icosahedral  $\text{Au}_{13}$  core is flexible and dynamic in nature, as experimentally proven by Tsukuda et al.<sup>29</sup> Ghosh et al. have shown that the dynamics of M–L interfaces can be controlled by using dithiolates which bind to the metal core in a bidentate fashion and thereby reduce the flexibility of the metal–ligand bonding network.<sup>82</sup> Hence, we think that an interlocked-ring model of the structure can better explain the enhanced dynamics of M–L interfaces and the reactivity of clusters.

Even though the mechanistic details are not known, it has been suggested that interactions between the M–L interfaces might occur in the initial stages of these reactions. In the reaction between  $\text{Au}_{25}(\text{SR})_{18}$  and  $\text{Ag}_{25}(\text{SR})_{18}$ , we detected a dimeric species,  $[\text{Ag}_{25}\text{Au}_{25}(\text{DMBT})_{18}(\text{PET})_{18}]^{2-}$  (DMBT and PET are 2,4-dimethylbenzenethiolate and 2-phenylethanethiolate, respectively), which could be one of the intermediates of the reaction.<sup>59</sup> Density functional theory (DFT) calculations revealed that this adduct could be formed through weak

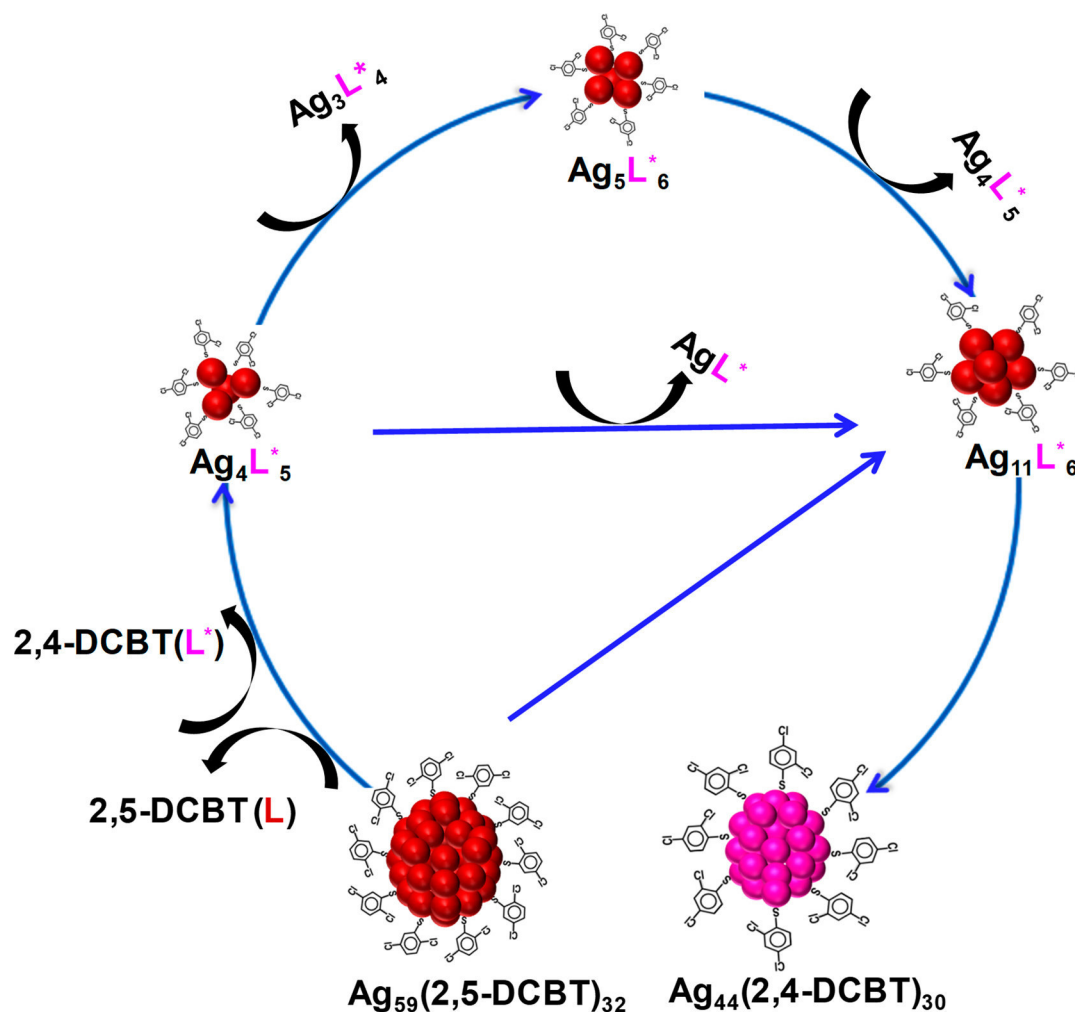
covalent bonding between them via interstaple metal–sulfur bonds.<sup>59</sup> Recently, Zhang et al. attempted to detect such intermediates during the reaction between  $\text{Au}_{38-x}\text{Ag}_x(\text{SR})_{24}$  and  $\text{Au}_{38}(\text{SR})_{24}$  using in situ X-ray absorption fine structure (XAFS) measurements.<sup>66</sup> However, the detection of exchanged Ag atoms in the staples was not successful, possibly due to a shorter residence time of the exchanged Ag atoms in the staples.

**Ostwald Ripening and Interparticle Reactions.** Ostwald ripening is one of the important mechanisms of nanocrystal growth<sup>83</sup> wherein larger particles grow larger at the expense of smaller ones in solution. The thermodynamic driving force behind this process is the difference in surface energies of (smaller and larger) particles in a polydisperse solution/dispersion. Smaller particles possess a higher surface energy, and hence they disappear more easily compared to the larger particles in the same solution/dispersion. Ostwald ripening occurs by the diffusion of the smaller particles toward the larger particles and subsequent reactions between them resulting in the growth of the particle.<sup>83</sup> This makes the larger particles grow larger, consuming or reducing the size of the smaller ones. However, it remains unclear as to how the constituents (atoms, ions, or molecules) of smaller particles are transported to the larger ones, i.e., by a direct interparticle exchange or an exchange of their fragments, in such processes. Details of chemical events in such processes are not known clearly. It was shown that in the case of noble metal clusters, exchanges of metal atoms, ligands, and metal ligand fragments occur through direct interaction or collision between the reacting clusters. How do these two processes i.e., intercluster exchange and Ostwald ripening, differ from each other? Can Ostwald ripening be interpreted or understood as interparticle exchange reactions between larger particles and smaller ones?

Let us discuss this briefly in the context of ligand-protected metal nanosystems. For example, consider a dispersion of thiolate-protected metal nanoparticles, which are typically polydisperse in size. In such a mixture, smaller particles could be more reactive compared to the larger ones for reasons other than the surface energy differences, such as changes in the oxidation states, differences in the redox potentials of (smaller and larger) particles, and differences in metal–ligand binding modes, as mentioned previously in the context of atomically precise clusters. Do such factors contribute to the interparticle reactions (between larger and smaller particles) resulting in Ostwald ripening?

In the intercluster exchange reactions reported so far, the size, structure, composition (i.e., number of metal atoms and ligands), and charge state remain unaltered. This could be due to the tendency of these clusters to retain their compact, highly symmetric, geometrically and electronically stable structures. Furthermore, these clusters are molecule-like and are of comparable sizes, wherein electronic factors, such as shell closing effects rather than geometrical factors, determine the stability. However, in Ostwald ripening, the particle size changes, as mentioned above. In this context, it is interesting to determine whether there is a clear particle size limit at which an intercluster/interparticle exchange reaction and Ostwald ripening can be discriminated by the change or constancy of the particle size? Maran et al. have recently reported the formation of  $\text{Au}_{38}(\text{SR})_{24}$  from a smaller cluster,  $\text{Au}_{25}(\text{SR})_{18}$ , which they referred to as “gold fusion”. However, it remains unclear whether this reaction can be understood as an example of Ostwald ripening of atomically precise clusters.<sup>84</sup> The above





**Figure 3.** Schematic of the ligand-induced conversion pathway of  $\text{Ag}_{59}(\text{2,5-DCBT})_{32}$  to  $\text{Ag}_{44}(\text{2,4-DCBT})_{30}$ . L and L\* denote 2,5-DCBT and 2,4-DCBT, respectively. (Reproduced with permission from ref 75.)

discussion implies that it is important to investigate the (surface/interfacial) chemical events *between* particles in an Ostwald ripening process, at least in the context of ligand-protected nanosystems.

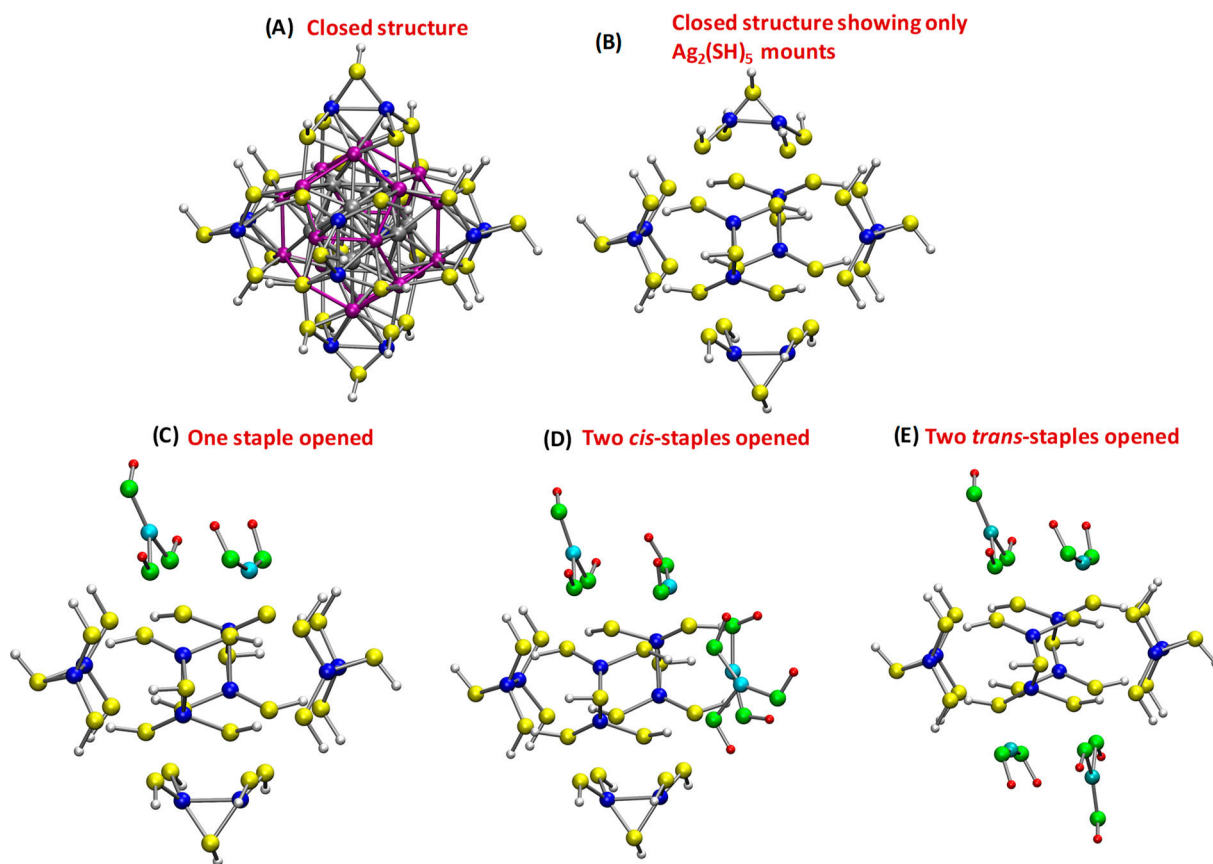
#### Influence of Ligand on Cluster Transformations.

Atomically precise clusters with a wide variety of nuclearity, geometry, and protecting ligands have been reported in the past decade. However, it remains unknown as to how the actual structure of the ligands influences the nuclearity and geometry of the clusters. One of the ways to investigate this aspect is to study the reactions of ligand-protected clusters with free ligands. Often, ligand exchange occurs in these reactions without altering the overall structure and charge states of the clusters.<sup>45–47,85</sup> However, in some cases, reactions of a cluster with a new type of ligand transform the cluster to completely new entities.<sup>86</sup>

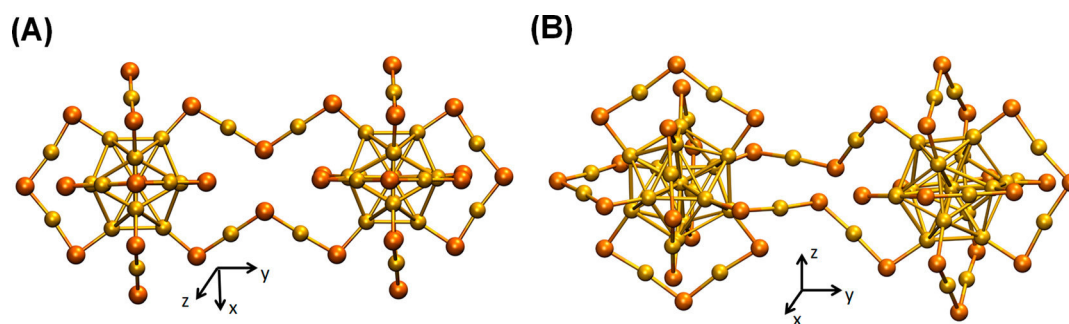
Khatun et al. demonstrated that such a reaction wherein a monothiolate-protected cluster,  $\text{Ag}_{59}(\text{2,5-DCBT})_{32}$ , upon reaction with the 2,4-DCBT ligand slowly converts it to  $\text{Ag}_{44}(\text{2,4-DCBT})_{30}$ .<sup>75</sup> Note that ligands 2,4-DCBT and 2,5-DCBT differ only in the positions of the substituent Cl groups (isomeric thiols). This reaction demonstrates that such minute changes in the structure of the ligands drastically change the nuclearity of the cluster. This could be due to the position-dependent (ortho, para, or meta) changes in the electron-

donating or electron-withdrawing inductive (+I or – I) effects of the methyl groups of the ligands. The  $\pi$ – $\pi$  interactions and steric hindrance between the substituent groups might also play roles in these transformations. Mass spectrometric measurements reveal that the reaction involves the formation of small metal–ligand fragments of clusters (Figure 3). Ligand exchange was proposed to be one of the initial stages of such transformations;<sup>87</sup> however, in this case, no ligand exchanges were observed because the molecular masses of both thiols were the same. The use of different thiols such as FTP (4-fluorothiophenol) and CTP (4-chlorothiophenol) shows ligand-exchanged peaks. Another reason could be the sensitivity of certain structural motifs such as staples and mounts to the structure of the incoming ligands; i.e., a given M–L motif may not be able to accommodate a new type of incoming ligand retaining their geometry and bonding network. Simulations and experimental techniques with better temporal resolution are essential to probing such dynamics of the M–L interfaces.

**Gas-Phase Dynamics and Reactivity of M–L Interfaces.** The dynamics of M–L interfaces have been studied mostly in the solution phase; however, such studies on the structure, dynamics, and reactivity of isolated, ligand-protected metal clusters in the gas phase remain largely unexplored. One of the techniques for probing the gas-phase dynamics of



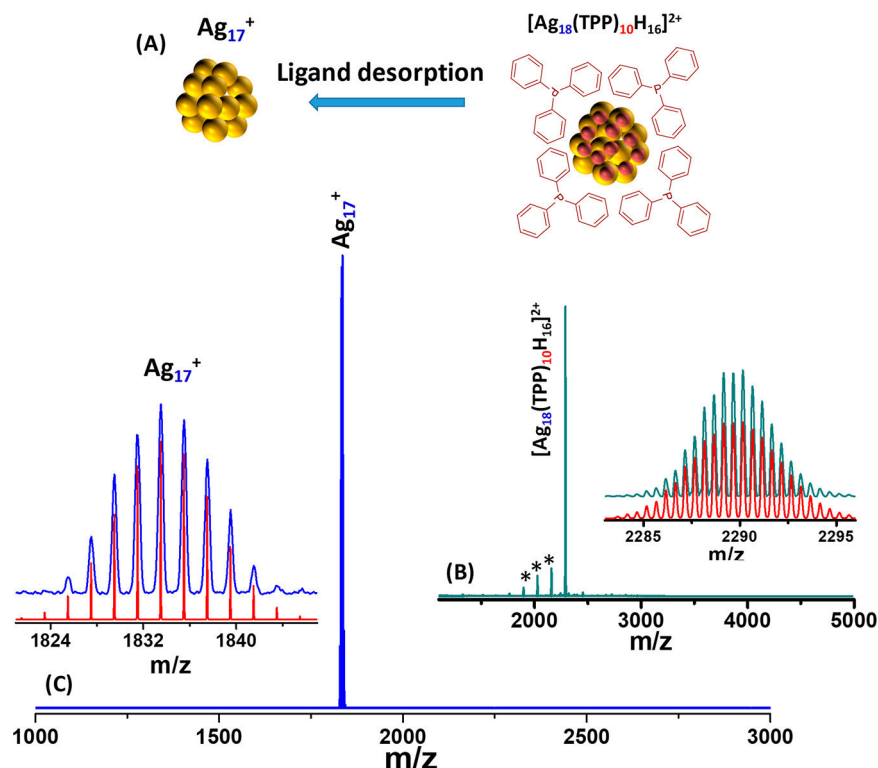
**Figure 4.** Schematic structures of the isomers of  $[\text{Ag}_{44}(\text{SH})_{30}]^{4-}$ . Geometries of  $[\text{Ag}_{44}(\text{SH})_{30}]^{4-}$  with (A) and without (B) the core atoms and its three structural isomers (C–E) with one staple opened structure (C), two cis staple opened structures (D), and two trans staple opened structures (E). Closed  $\text{Ag}_2(\text{SH})_5$  mounts in A–E are shown with blue (silver), yellow (sulfur), and white (hydrogen) colors. Open  $\text{Ag}_2(\text{SH})_5$  mounts in C–E are shown in cyan (silver), green (sulfur), and red (hydrogen). Because the structures of the  $\text{Ag}_{12}$  icosahedron (gray in A) and the  $\text{Ag}_{20}$  dodecahedron (pink in A) are retained in their isomers, these core atoms are not shown in C–E to clearly distinguish the changes in the staple arrangements in its isomers. Because the actual ligands are not shown here, additional structural isomers due to the difference in the ligand conformations are not presented here. (Adapted with permission from ref 76.)



**Figure 5.** Interfacial bonding between two  $[\text{Au}_{25}(\text{SR})_{18}]^-$  clusters resulting in the formation of dimers. (A and B) DFT-optimized structures of possible structural isomers of  $[\text{Au}_{50}(\text{SR})_{36}]^{2-}$  considering intercluster bonding via common  $\text{Au}_2\text{S}_3$  staples. In panel A, there is bonding between the two clusters by two parallel  $\text{Au}_2\text{S}_3$  chains. The view shown is along the negative  $z$  direction (top view). In panel B, a twisted linkage between the  $\text{Au}_2\text{S}_3$  staples of two clusters is shown with the cluster on the right being rotated by  $90^\circ$  anticlockwise about the  $x$  axis and coming out of the paper. Cartesian axes are shown. The ligand R groups have been removed for clarity. Color codes of atoms: gold (yellow) and sulfur (orange). (Adapted with permission from ref 77.)

molecular systems is ion mobility mass spectrometry (IM MS).<sup>88</sup> This technique has been traditionally used for the gas-phase analysis of small molecules<sup>88</sup> and conformational studies of proteins;<sup>76</sup> however, it has recently been utilized to probe the thiolate-protected metal clusters as well.<sup>89</sup> In this technique, molecules are ionized and taken into the gaseous phase using standard mass spectrometric techniques, and then they are separated according to their mobility in the presence

of a buffer gas. The mobility of the molecules depends on their mass to charge ratio, size, and shape. Here we present the results of IM MS measurements of  $\text{Ag}_{44}(\text{SR})_{30}$ . The crystal structure of  $\text{Ag}_{44}(\text{SR})_{30}$  shows that it consists of a  $\text{Ag}_{32}$  core protected by six  $\text{Ag}_2(\text{SR})_5$  mounts.  $\text{Ag}_{44}(\text{SR})_{30}$  is an interesting system in this regard because of its multishell structures and unusual geometry of  $\text{Ag}_2(\text{SR})_5$  mounts (Figure 4B). Furthermore, this cluster occurs in different charge states in



**Figure 6.** Schematic of the desorption of triphenylphosphine (TPP) ligands from  $[\text{Ag}_{18}(\text{TPP})_{10}\text{H}_{16}]^{2+}$ , leading to the formation of naked,  $\text{Ag}_{17}^+$  (A). ESI mass spectra of  $[\text{Ag}_{18}(\text{TPP})_{10}\text{H}_{16}]^{2+}$  (B) and  $\text{Ag}_{17}^+$  (C). The insets of panels B and C show the matching of the theoretical (red) and experimental (blue in C, green in B) isotopic patterns of the corresponding ions. Color codes of atoms in panel A: silver (yellow) and hydrogen (red). (Adapted with permission from ref 78.)

the gas phase. For these experiments,  $\text{Ag}_{44}(\text{SR})_{30}$  clusters were brought into the gas phase using a conventional electrospray ionization (ESI) technique. Ion mobility measurements on these clusters reveal the presence of structural isomers, as depicted in Figure 4.<sup>76</sup> Here we have used a model system,  $\text{Ag}_{44}(\text{SH})_{30}$ , to represent the structure.

DFT calculations suggest that the isomerism arises from the difference in the bonding network of the metal–ligand interface in these clusters. Note that the  $\text{Ag}_2(\text{SR})_5$  mounts have complicated bonding compared to those in the  $\text{Au}_2(\text{SR})_3$  staples; therefore, it is likely that some of the bonds in the  $\text{Ag}_2(\text{SR})_5$  mounts could break, leading to more stable, open structures. However, these isomers possess the same  $\text{Ag}_{32}$  core structure as in the crystal structure. Note that these structures possess exactly the same molecular formulas,  $\text{Ag}_{44}(\text{SR})_{30}$ , and differ from each other only in terms of the structures of a few of their mount motifs and hence are structurally isomeric. Hence, this study reveals that rearrangements in the metal–ligand interface can generate structural isomerism in these clusters. However, if the real ligands are involved, then their conformations also have to be taken into account when their structural isomerism is discussed. However, such an analysis is beyond the scope of this article.

In another example of IM MS experiments, we show that  $\text{Au}_{25}(\text{SR})_{18}$  clusters form dimers,  $[\text{Au}_{50}(\text{SR})_{36}]^{2-}$ , for example, and trimers in gas-phase experiments. DFT calculations show that these dimers were formed by the bonding between  $\text{Au}_2(\text{SR})_3$  staple motifs, as shown in Figure 5.<sup>77</sup> Spectroscopic evidence of such bonding in the gas phase is not available; however, interstaple bonding has been detected in crystals.<sup>38</sup> Note that this type of interstaple bonding has not altered the total number of metal atoms, ligands, and the charge states of

individual clusters in these dimers. Furthermore, the existence of such isomers further supports the dynamic nature of the metal–ligand interface in such clusters. Also, we think that the Borromean rings model is better suited to explaining the formation of such dimers because the longer  $\text{Au}_8(\text{SR})_6$  rings are expected to be more dynamic in nature, compared to the shorter  $\text{Au}_2(\text{SR})_3$  staples, which could facilitate their breaking and reforming, leading to intercluster bonding.

**Desorption of Ligands: A New Route for Naked Metal Clusters.** The strength of the chemical bond between the metal atoms and the anchoring atom of the ligands (Au–S bond in  $\text{Au}_{25}(\text{SR})_{18}$ , for example) largely determines the stability of the clusters. The fragmentation behavior of these clusters was also studied using mass spectrometry<sup>89,90</sup> and computations.<sup>91</sup> For example, phosphines are known to bind to metal atoms less strongly, compared to thiolates, through weak covalent bonds. In this context, it is interesting to test whether it is possible to detach the ligands from phosphine-protected noble metal clusters, in the gaseous or liquid phase, so that naked clusters, with precise nuclearity, are generated. Conventionally, naked metal clusters are generated by techniques such as laser ablation or electrospray ionization which require sophisticated instrumentation for mass selection.

Ghosh et al. demonstrated that it is indeed possible to generate atomically precise naked metal clusters from a silver cluster,  $[\text{Ag}_{18}(\text{TPP})_{10}\text{H}_{16}]^{2+}$ , protected by phosphine and hydride ligands. The ligands on the  $[\text{Ag}_{18}(\text{TPP})_{10}\text{H}_{16}]^{2+}$  can be sequentially desorbed to generate naked silver clusters of specific nuclearity, such as  $\text{Ag}_{17}^+$ .<sup>78</sup> For this,  $[\text{Ag}_{18}(\text{TPP})_{10}\text{H}_{16}]^{2+}$  was introduced into the gas phase using an ESI source. Sequential fragmentation of the ligands was carried out by successively increasing the ionization voltages in

the ESI setup. Figure 6 shows that  $[\text{Ag}_{18}(\text{TPP})_{10}\text{H}_{16}]^{2+}$  initially transforms to  $\text{Ag}_{17}\text{H}_{14}^{+}$ , which finally loses all of the hydride ions, generating  $\text{Ag}_{17}^{+}$ . Note that the desorption of ligands in this case occurred through the breaking of the bond between the metal and the anchoring atom of the ligand, i.e., the Ag–P bond. This is in contrast to the case of thiolate-protected clusters wherein the S–C bond breaks and the metal–sulfur bond is retained. The formation of naked clusters from thiolate-protected clusters has never been observed. This could be attributed to the fact that the Ag/Au–S bond is much stronger than the Ag–P bond. Similarly, ligands such as pyridine and its analogues might also act as weaker ligands for these types of clusters, and such systems also could lead to the formation of naked clusters. However, the example presented above indicates that the desorption of ligands depends on the nature of the ligands as well as the strength of the bond between the metal atom and the anchoring atom of the ligands. Such ligand desorption can occur also in ambient air, leading to naked clusters.<sup>92</sup>

## SUMMARY AND FUTURE PERSPECTIVES

We presented a few examples demonstrating the role of the structure and dynamics of the metal–ligand interface in dictating the chemical reactivity of monolayer-protected noble metal clusters in solution as well as in the gas phase. We suggested that the difference in the oxidation states of metal atoms at the M–L interface could be a key factor triggering intercluster reactions. The structure of the M–L ligand bonding network (staples vs mounts and monodentate vs bidentate) and the dynamics (interlocked (Borromean) rings model vs core-staple model) dictate the type as well as the extent of the exchange processes. Furthermore, these studies imply that a single structural model is inadequate for explaining spontaneous reactions between these clusters; a consideration of multiple structural models is essential to a better understanding of their properties.

We proposed that interparticle chemistry may not be limited to metal clusters, but such reactions might also occur in other nanosystems, which could be a potential mechanism in particle coarsening processes such as Ostwald ripening. We also showed that the nature of the ligands, i.e., their structure and electron-donating and electron-withdrawing properties, is crucial to controlling the geometry and nuclearity of these clusters. The dynamics of the M–L interfaces is not limited to the solution phase; structural rearrangements and interfacial bonding occur in the gas phase as well, leading to the formation of geometrical isomers and cluster assemblies. Finally, we showed that the ligands can be desorbed completely in the gas phase, leading to the formation of atomically precise naked metal clusters. This study indicates that phosphines can be promising ligands for generating naked clusters of other metals as well.

Even though we demonstrated that a number of factors concerning the M–L interfaces, such as oxidation states of metal atoms and the actual structure of the ligands, are important when considering the chemistry of these clusters, the contribution of each of these factors has not been understood in isolation. Among the reasons is the limitation in making many of the clusters by varying only one aspect alone at one time, such as specific ligands.

Probing the interfacial properties of these clusters is essential to creating cluster assembled materials and new types of hybrid materials comprising distinctly different types of nanosystems.

Probing the kinetics and thermodynamics and the real-time monitoring of interfacial phenomena in these clusters have rarely been addressed. The gas-phase dynamics of these clusters remain largely unexplored. Probing the chiroptical properties of these clusters in the gaseous phase could be a potential new direction in this regard. Further efforts are needed to clearly understand the contribution of metal–ligand interfaces in dictating the geometrical structures, dynamics, and chemical reactivity of ligand-protected metal clusters. We think that the dynamic interfacial chemistry is not limited to metal clusters, and hence the structure, dynamics, and chemical reactivity of nanosystems in general are to be explored in greater detail, which might unveil new directions in materials chemistry.

## AUTHOR INFORMATION

### Corresponding Author

\*E-mail: [pradeep@iitm.ac.in](mailto:pradeep@iitm.ac.in). Fax: +91-44-2257-0545.

### ORCID

Thalappil Pradeep: 0000-0003-3174-534X

### Present Addresses

<sup>†</sup>K.R.K.: Postdoctoral fellow at University of Geneva, Switzerland.

<sup>‡</sup>A.B.: Postdoctoral fellow at Karlsruhe Institute of Technology, Germany.

<sup>§</sup>A.G.: Postdoctoral fellow at King Abdullah University of Science and Technology, Kingdom of Saudi Arabia.

### Notes

The authors declare no competing financial interest.

### Biographies



Kumaranchira Ramankutty Krishnadas, after earning a Ph.D. in chemistry from the Indian Institute of Technology Madras in 2016 under the guidance of Prof. T. Pradeep, is currently a postdoctoral researcher at the University of Geneva, Switzerland. He explores chemical reactions of atomically precise noble metal clusters.





Ganapati Natarajan, after earning a Ph.D. in chemistry (2011) from the Department of Chemistry at the University of Cambridge, U.K., is a postdoctoral researcher in Prof. Pradeep's research group. He is a computational materials scientist with interest in the structure and properties of ligand-protected noble metal clusters and nanoparticles, ice, amorphous materials, and materials and nanomaterials in general.



Ananya Bakshi, after earning a Ph.D. in chemistry from the Indian Institute of Technology Madras in 2015 under the guidance of Prof. T. Pradeep, is currently a postdoctoral researcher at Karlsruhe Institute of Technology, Germany. Her research is focused on mass spectrometric investigations of different cluster systems.



Atanu Ghosh, after earning a Ph.D. in chemistry from the Indian Institute of Technology Madras in 2017 under the guidance of Prof. T. Pradeep, is currently a postdoctoral researcher at King Abdullah University of Science and Technology, Kingdom of Saudi Arabia. His research focuses on the synthesis, reactions, and applications of noble metal nanoclusters.



Esma Khatun is a Ph.D. student of Prof. T. Pradeep in the Department of Chemistry, Indian Institute of Technology Madras, India. Her research focuses on the synthesis, reactions, and applications of noble metal nanoclusters.

Thalappil Pradeep is an institute professor and the Deepak Parekh Institute Chair Professor at the Indian Institute of Technology Madras. Prof. Pradeep's research interests are in molecular and nanoscale materials, and he develops instrumentation for such studies. He is involved in the development of affordable technologies for drinking water purification, and some of his technologies have been commercialized.

## ■ ACKNOWLEDGMENTS

K.R.K., A.G., and E.K. thank the UGC for their senior research fellowships. A.B. thanks IIT Madras for an institute postdoctoral fellowship. We thank the Department of Science and Technology for constantly supporting our research program.

## ■ REFERENCES

- (1) Jin, R.; Zeng, C.; Zhou, M.; Chen, Y. Atomically Precise Colloidal Metal Nanoclusters and Nanoparticles: Fundamentals and Opportunities. *Chem. Rev.* **2016**, *116*, 10346–10413.
- (2) Chakraborty, I.; Pradeep, T. Atomically precise clusters of noble metals: Emerging link between atoms and nanoparticles. *Chem. Rev.* **2017**, *117*, 8208–8271.
- (3) Jadzinsky, P. D.; Calero, G.; Ackerson, C. J.; Bushnell, D. A.; Kornberg, R. D. Structure of a thiol monolayer-protected gold nanoparticle at 1.1 Å resolution. *Science* **2007**, *318*, 430–433.
- (4) Heaven, M. W.; Dass, A.; White, P. S.; Holt, K. M.; Murray, R. W. Crystal structure of the gold nanoparticle  $[\text{N}(\text{C}_8\text{H}_{17})_4]\text{[Au}_{25}(\text{SCH}_2\text{CH}_2\text{Ph})_{18}]$ . *J. Am. Chem. Soc.* **2008**, *130*, 3754–3755.
- (5) Joshi, C. P.; Bootharaju, M. S.; Alhilaly, M. J.; Bakr, O. M.  $[\text{Ag}_{25}(\text{SR})_{18}]^-$ : The "Golden" silver nanoparticle. *J. Am. Chem. Soc.* **2015**, *137*, 11578–11581.
- (6) Desireddy, A.; Conn, B. E.; Guo, J.; Yoon, B.; Barnett, R. N.; Monahan, B. M.; Kirschbaum, K.; Griffith, W. P.; Whetten, R. L.; Landman, U.; Bigioni, T. P. Ultrastable silver nanoparticles. *Nature* **2013**, *501*, 399–402.
- (7) Harkness, K. M.; Tang, Y.; Dass, A.; Pan, J.; Kothalawala, N.; Reddy, V. J.; Cliffler, D. E.; Demeler, B.; Stellacci, F.; Bakr, O. M.; McLean, J. A.  $\text{Ag}_{44}(\text{SR})_{30}^{4-}$ : a silver-thiolate superatom complex. *Nanoscale* **2012**, *4*, 4269–4274.
- (8) Zhu, M.; Aikens, C. M.; Hollander, F. J.; Schatz, G. C.; Jin, R. Correlating the crystal structure of a thiol-protected  $\text{Au}_{25}$  cluster and optical properties. *J. Am. Chem. Soc.* **2008**, *130*, 5883–5885.
- (9) Zhu, M.; Aikens, C. M.; Hendrich, M. P.; Gupta, R.; Qian, H.; Schatz, G. C.; Jin, R. Reversible switching of magnetism in thiolate-protected  $\text{Au}_{25}$  superatoms. *J. Am. Chem. Soc.* **2009**, *131*, 2490–2492.
- (10) Antonello, S.; Perera, N. V.; Ruzzi, M.; Gascón, J. A.; Maran, F. Interplay of charge state, lability, and magnetism in the molecule-like  $\text{Au}_{25}(\text{SR})_{18}$  cluster. *J. Am. Chem. Soc.* **2013**, *135*, 15585–15594.
- (11) Bellon, P.; Manassero, M.; Sansoni, M. An octahedral gold cluster: crystal and molecular structure of hexakis[tris-(p-tolyl)-phosphine]-octahedro-hexagold bis(tetraphenylborate). *J. Chem. Soc., Dalton Trans.* **1973**, *22*, 2423–2427.

- (12) Bellon, P. L.; Cariati, F.; Manassero, M.; Naldini, L.; Sansoni, M. Novel gold clusters. Preparation, properties, and X-ray structure determination of salts of octakis(triarylphosphine)enneagold,  $[\text{Au}_9\text{L}_8]\text{X}_3$ . *J. Chem. Soc. D* **1971**, 22, 1423–1424.
- (13) Yao, H.; Iwatsu, M. Water-Soluble Phosphine-Protected Au<sub>11</sub> Clusters: Synthesis, Electronic Structure, and Chiral Phase Transfer in a Synergistic Fashion. *Langmuir* **2016**, 32, 3284–3293.
- (14) Akola, J.; Kacprzak, K. A.; Lopez-Acevedo, O.; Walter, M.; Grönbeck, H.; Häkkinen, H. Thiolate-protected Au<sub>25</sub> superatoms as building blocks: dimers and crystals. *J. Phys. Chem. C* **2010**, 114, 15986–15994.
- (15) Akola, J.; Walter, M.; Whetten, R. L.; Häkkinen, H.; Grönbeck, H. On the structure of thiolate-protected Au<sub>25</sub>. *J. Am. Chem. Soc.* **2008**, 130, 3756–3757.
- (16) Walter, M.; Akola, J.; Lopez-Acevedo, O.; Jadzinsky, P. D.; Calero, G.; Ackerson, C. J.; Whetten, R. L.; Grönbeck, H.; Häkkinen, H. A unified view of ligand-protected gold clusters as superatom complexes. *Proc. Natl. Acad. Sci. U. S. A.* **2008**, 105, 9157–9162.
- (17) Abdul Halim, L. G.; Ashraf, S.; Katsiev, K.; Kirmani, A. R.; Kothalawala, N.; Anjum, D. H.; Abbas, S.; Amassian, A.; Stellacci, F.; Dass, A.; Hussain, I.; Bakr, O. M. A scalable synthesis of highly stable and water dispersible Ag<sub>44</sub>(SR)<sub>30</sub> nanoclusters. *J. Mater. Chem. A* **2013**, 1, 10148–10154.
- (18) AbdulHalim, L. G.; Kothalawala, N.; Sinatra, L.; Dass, A.; Bakr, O. M. Neat and complete: thiolate-ligand exchange on a silver molecular nanoparticle. *J. Am. Chem. Soc.* **2014**, 136, 15865–15868.
- (19) Yang, H.; Wang, Y.; Huang, H.; Gell, L.; Lehtovaara, L.; Malola, S.; Häkkinen, H.; Zheng, N. All-thiol-stabilized Ag<sub>44</sub> and Au<sub>12</sub>Ag<sub>32</sub> nanoparticles with single-crystal structures. *Nat. Commun.* **2013**, 4, 2422.
- (20) Chakraborty, I.; Kurashige, W.; Kanehira, K.; Gell, L.; Häkkinen, H.; Negishi, Y.; Pradeep, T. Ag<sub>44</sub>(SeR)<sub>30</sub>: A Hollow Cage Silver Cluster with Selenolate Protection. *J. Phys. Chem. Lett.* **2013**, 4, 3351–3355.
- (21) Kurashige, W.; Yamaguchi, M.; Nobusada, K.; Negishi, Y. Ligand-Induced Stability of Gold Nanoclusters: Thiolate versus Selenolate. *J. Phys. Chem. Lett.* **2012**, 3, 2649–2652.
- (22) Ossowski, J.; Wächter, T.; Silies, L.; Kind, M.; Noworolska, A.; Blobner, F.; Gnatek, D.; Rysz, J.; Bolte, M.; Feulner, P.; Terfort, A.; Cyganik, P.; Zharnikov, M. Thiolate versus Selenolate: Structure, Stability, and Charge Transfer Properties. *ACS Nano* **2015**, 9, 4508–4526.
- (23) Maity, P.; Takano, S.; Yamazoe, S.; Wakabayashi, T.; Tsukuda, T. Binding motif of terminal alkynes on gold clusters. *J. Am. Chem. Soc.* **2013**, 135, 9450–9457.
- (24) Templeton, A. C.; Wuelfing, W. P.; Murray, R. W. Monolayer-protected cluster molecules. *Acc. Chem. Res.* **2000**, 33, 27–36.
- (25) Häkkinen, H. The gold–sulfur interface at the nanoscale. *Nat. Chem.* **2012**, 4, 443–455.
- (26) Häkkinen, H.; Walter, M.; Grönbeck, H. Divide and Protect: Capping Gold Nanoclusters with Molecular Gold–Thiolate Rings. *J. Phys. Chem. B* **2006**, 110, 9927–9931.
- (27) Walter, M.; Akola, J.; Lopez-Acevedo, O.; Jadzinsky, P. D.; Calero, G.; Ackerson, C. J.; Whetten, R. L.; Grönbeck, H.; Häkkinen, H. A unified view of ligand-protected gold clusters as superatom complexes. *Proc. Natl. Acad. Sci. U. S. A.* **2008**, 105, 9157–9162.
- (28) Natarajan, G.; Mathew, A.; Negishi, Y.; Whetten, R. L.; Pradeep, T. A unified framework for understanding the structure and modifications of atomically precise monolayer protected gold clusters. *J. Phys. Chem. C* **2015**, 119, 27768–27785.
- (29) Yamazoe, S.; Takano, S.; Kurashige, W.; Yokoyama, T.; Nitta, K.; Negishi, Y.; Tsukuda, T. Hierarchy of bond stiffnesses within icosahedral-based gold clusters protected by thiolates. *Nat. Commun.* **2016**, 7, 10414.
- (30) Tlahuice-Flores, A.; Black, D. M.; Bach, S. B. H.; Jose-Yacamán, M.; Whetten, R. L. Structure & bonding of the gold-subhalide cluster I-Au<sub>144</sub>Cl<sub>60</sub><sup>[2]</sup>. *Phys. Chem. Chem. Phys.* **2013**, 15, 19191–19195.
- (31) Chen, Y.; Zeng, C.; Kauffman, D. R.; Jin, R. Tuning the Magic Size of Atomically Precise Gold Nanoclusters via Isomeric Methylbenzenethiols. *Nano Lett.* **2015**, 15, 3603–3609.
- (32) Rambukwella, M.; Sakthivel, N. A.; Delcamp, J. H.; Sementa, L.; Fortunelli, A.; Dass, A. Ligand Structure Determines Nanoparticles' Atomic Structure, Metal-Ligand Interface and Properties. *Front. Chem.* **2018**, 6, 330.
- (33) Zeng, C.; Qian, H.; Li, T.; Li, G.; Rosi, N. L.; Yoon, B.; Barnett, R. N.; Whetten, R. L.; Landman, U.; Jin, R. Total Structure and Electronic Properties of the Gold Nanocrystal Au<sub>36</sub>(SR)<sub>24</sub>. *Angew. Chem., Int. Ed.* **2012**, 51, 13114–13118.
- (34) Dolamic, I.; Knoppe, S.; Dass, A.; Bürgi, T. First enantioseparation and circular dichroism spectra of Au<sub>38</sub> clusters protected by achiral ligands. *Nat. Commun.* **2012**, 3, 798.
- (35) Dolamic, I.; Varnholt, B.; Bürgi, T. Chirality transfer from gold nanocluster to adsorbate evidenced by vibrational circular dichroism. *Nat. Commun.* **2015**, 6, 7117.
- (36) Mathew, A.; Natarajan, G.; Lehtovaara, L.; Häkkinen, H.; Kumar, R. M.; Subramanian, V.; Jaleel, A.; Pradeep, T. Supramolecular functionalization and concomitant enhancement in properties of Au<sub>25</sub> clusters. *ACS Nano* **2014**, 8, 139–152.
- (37) Yoon, B.; Luedtke, W. D.; Barnett, R. N.; Gao, J.; Desiredy, A.; Conn, B. E.; Bigioni, T.; Landman, U. Hydrogen-bonded structure and mechanical chiral response of a silver nanoparticle superlattice. *Nat. Mater.* **2014**, 13, 807–811.
- (38) De Nardi, M.; Antonello, S.; Jiang, D.-e.; Pan, F.; Rissanen, K.; Ruzzi, M.; Venzo, A.; Zoleo, A.; Maran, F. Gold nanowired: a linear (Au<sub>25</sub>)<sub>n</sub> polymer from Au<sub>25</sub> molecular clusters. *ACS Nano* **2014**, 8, 8505–8512.
- (39) Som, A.; Chakraborty, I.; Maark, T. A.; Bhat, S.; Pradeep, T. Cluster-mediated crossed bilayer precision assemblies of 1D nanowires. *Adv. Mater.* **2016**, 28, 2827–2833.
- (40) Gell, L.; Häkkinen, H. Theoretical analysis of the M<sub>12</sub>Ag<sub>32</sub>(SR)<sub>40</sub><sup>4−</sup> and X@M<sub>12</sub>Ag<sub>32</sub>(SR)<sub>30</sub><sup>4−</sup> nanoclusters (M = Au, Ag; X = H, Mn). *J. Phys. Chem. C* **2015**, 119, 10943–10948.
- (41) Wu, Z.; Jin, R. On the ligand's role in the fluorescence of gold nanoclusters. *Nano Lett.* **2010**, 10, 2568–2573.
- (42) Mathew, A.; Varghese, E.; Choudhury, S.; Pal, S. K.; Pradeep, T. Efficient red luminescence from organic-soluble Au<sub>25</sub> clusters by ligand structure modification. *Nanoscale* **2015**, 7, 14305–14315.
- (43) Niihori, Y.; Kikuchi, Y.; Kato, A.; Matsuzaki, M.; Negishi, Y. Understanding ligand-exchange reactions on thiolate-protected gold clusters by probing isomer distributions using reversed-phase high-performance liquid chromatography. *ACS Nano* **2015**, 9, 9347–9356.
- (44) Ni, T. W.; Tofanelli, M. A.; Phillips, B. D.; Ackerson, C. J. Structural basis for ligand exchange on Au<sub>25</sub>(SR)<sub>18</sub>. *Inorg. Chem.* **2014**, 53, 6500–6502.
- (45) Dass, A.; Holt, K.; Parker, J. F.; Feldberg, S. W.; Murray, R. W. Mass spectrometrically detected statistical aspects of ligand populations in mixed monolayer Au<sub>25</sub>L<sub>18</sub> nanoparticles. *J. Phys. Chem. C* **2008**, 112, 20276–20283.
- (46) Song, Y.; Huang, T.; Murray, R. W. Heterophase ligand exchange and metal transfer between monolayer protected clusters. *J. Am. Chem. Soc.* **2003**, 125, 11694–11701.
- (47) Song, Y.; Murray, R. W. Dynamics and extent of ligand exchange depend on electronic charge of metal nanoparticles. *J. Am. Chem. Soc.* **2002**, 124, 7096–7102.
- (48) Wang, S.; Song, Y.; Jin, S.; Liu, X.; Zhang, J.; Pei, Y.; Meng, X.; Chen, M.; Li, P.; Zhu, M. Metal exchange method using Au<sub>25</sub> nanoclusters as templates for alloy nanoclusters with atomic precision. *J. Am. Chem. Soc.* **2015**, 137, 4018–4021.
- (49) Krishnadas, K. R.; Udayabhaskararao, T.; Choudhury, S.; Goswami, N.; Pal, S. K.; Pradeep, T. Luminescent AgAu alloy clusters derived from Ag nanoparticles - Manifestations of tunable Au(I)-Cu(I) metallophilic interactions. *Eur. J. Inorg. Chem.* **2014**, 2014, 908–916.
- (50) Walter, M.; Moseler, M. Ligand-protected gold alloy clusters: doping the superatom. *J. Phys. Chem. C* **2009**, 113, 15834–15837.



- (51) Tian, S.; Yao, C.; Liao, L.; Xia, N.; Wu, Z. Ion-precursor and ion-dose dependent anti-galvanic reduction. *Chem. Commun.* **2015**, 51, 11773–11776.
- (52) Wu, Z. Anti-Galvanic reduction of thiolate-protected gold and silver nanoparticles. *Angew. Chem., Int. Ed.* **2012**, 51, 2934–2938.
- (53) Udayabhaskararao, T.; Sun, Y.; Goswami, N.; Pal, S. K.; Balasubramanian, K.; Pradeep, T.  $\text{Ag}_7\text{Au}_6$ : A 13-atom alloy quantum cluster. *Angew. Chem., Int. Ed.* **2012**, 51, 2155–2159.
- (54) Dreier, T. A.; Ackerson, C. J. Radicals are required for thiol etching of gold particles. *Angew. Chem., Int. Ed.* **2015**, 54, 9249–9252.
- (55) Udaya Bhaskara Rao, T.; Pradeep, T. Luminescent  $\text{Ag}_7$  and  $\text{Ag}_8$  clusters by interfacial synthesis. *Angew. Chem., Int. Ed.* **2010**, 49, 3925–3929.
- (56) Shichibu, Y.; Negishi, Y.; Tsukuda, T.; Teranishi, T. Large-scale synthesis of thiolated  $\text{Au}_{25}$  clusters via ligand exchange reactions of phosphine-stabilized  $\text{Au}_{11}$  clusters. *J. Am. Chem. Soc.* **2005**, 127, 13464–13465.
- (57) Shichibu, Y.; Negishi, Y.; Watanabe, T.; Chaki, N. K.; Kawaguchi, H.; Tsukuda, T. Biicosahedral gold clusters  $[\text{Au}_{25}(\text{PPh}_3)_{10}(\text{SC}_n\text{H}_{2n+1})\text{SCl}_2]^{2+}$  ( $n = 2-18$ ): A stepping stone to cluster-assembled materials. *J. Phys. Chem. C* **2007**, 111, 7845–7847.
- (58) Li, M.-B.; Tian, S.-K.; Wu, Z.; Jin, R. Peeling the core-shell  $\text{Au}_{25}$  nanocluster by reverse ligand-exchange. *Chem. Mater.* **2016**, 28, 1022–1025.
- (59) Krishnadas, K. R.; Bakshi, A.; Ghosh, A.; Natarajan, G.; Pradeep, T. Structure-conserving spontaneous transformations between nanoparticles. *Nat. Commun.* **2016**, 7, 13447.
- (60) Krishnadas, K. R.; Bakshi, A.; Ghosh, A.; Natarajan, G.; Pradeep, T. Manifestation of Geometric and Electronic Shell Structures of Metal Clusters in Intercluster Reactions. *ACS Nano* **2017**, 11, 6015–6023.
- (61) Krishnadas, K. R.; Bakshi, A.; Ghosh, A.; Natarajan, G.; Som, A.; Pradeep, T. Interparticle Reactions: An Emerging Direction in Nanomaterials Chemistry. *Acc. Chem. Res.* **2017**, 50, 1988–1996.
- (62) Krishnadas, K. R.; Ghosh, A.; Bakshi, A.; Chakraborty, I.; Natarajan, G.; Pradeep, T. Intercluster reactions between  $\text{Au}_{25}(\text{SR})_{18}$  and  $\text{Ag}_{44}(\text{SR})_{30}$ . *J. Am. Chem. Soc.* **2016**, 138, 140–148.
- (63) Zhang, B.; Salassa, G.; Burgi, T. Silver migration between  $\text{Au}_{38}(\text{SC}_2\text{H}_4\text{Ph})_{24}$  and doped  $\text{Ag}_x\text{Au}_{38-x}(\text{SC}_2\text{H}_4\text{Ph})_{24}$  nanoclusters. *Chem. Commun.* **2016**, 52, 9205–9207.
- (64) Xia, N.; Wu, Z. Doping  $\text{Au}_{25}$  nanoparticles using ultrasmall silver or copper nanoparticles as the metal source. *J. Mater. Chem. C* **2016**, 4, 4125–4128.
- (65) Bootharaju, M. S.; Sinatra, L.; Bakr, O. M. Distinct metal-exchange pathways of doped  $\text{Ag}_{25}$  nanoclusters. *Nanoscale* **2016**, 8, 17333–17339.
- (66) Zhang, B.; Safonova, O. V.; Pollitt, S.; Salassa, G.; Sels, A.; Kazan, R.; Wang, Y.; Rupprechter, G.; Barrabes, N.; Burgi, T. On the mechanism of rapid metal exchange between thiolate-protected gold and gold/silver clusters: a time-resolved in situ XAFS study. *Phys. Chem. Chem. Phys.* **2018**, 20, 5312–5318.
- (67) Yao, Q.; Feng, Y.; Fung, V.; Yu, Y.; Jiang, D.-e.; Yang, J.; Xie, J. Precise control of alloying sites of bimetallic nanoclusters via surface motif exchange reaction. *Nat. Commun.* **2017**, 8, 1555.
- (68) Wang, S.; Abroshan, H.; Liu, C.; Luo, T.-Y.; Zhu, M.; Kim, H. J.; Rosi, N. L.; Jin, R. Shuttling single metal atom into and out of a metal nanoparticle. *Nat. Commun.* **2017**, 8, 848.
- (69) Varnholt, B.; Oulevey, P.; Lubert, S.; Kumara, C.; Dass, A.; Bürgi, T. Structural Information on the Au–S Interface of Thiolate-Protected Gold Clusters: A Raman Spectroscopy Study. *J. Phys. Chem. C* **2014**, 118, 9604–9611.
- (70) Burgi, T. Properties of the gold-sulphur interface: from self-assembled monolayers to clusters. *Nanoscale* **2015**, 7, 15553–15567.
- (71) Salassa, G.; Sels, A.; Mancin, F.; Bürgi, T. Dynamic Nature of Thiolate Monolayer in  $\text{Au}_{25}(\text{SR})_{18}$  Nanoclusters. *ACS Nano* **2017**, 11, 12609–12614.
- (72) Salorinne, K.; Malola, S.; Wong, O. A.; Rithner, C. D.; Chen, X.; Ackerson, C. J.; Häkkinen, H. Conformation and dynamics of the ligand shell of a water-soluble  $\text{Au}_{102}$  nanoparticle. *Nat. Commun.* **2016**, 7, 10401.
- (73) Ouyang, R.; Jiang, D.-e. Ligand-Conformation Energy Landscape of Thiolate-Protected Gold Nanoclusters. *J. Phys. Chem. C* **2015**, 119, 21555–21560.
- (74) Pradeep, T.; Mitra, S.; Nair, A. S.; Mukhopadhyay, R. Dynamics of alkyl chains in monolayer-protected Au and Ag clusters and silver thiolates: a comprehensive quasielastic neutron scattering investigation. *J. Phys. Chem. B* **2004**, 108, 7012–7020.
- (75) Khatun, E.; Ghosh, A.; Ghosh, D.; Chakraborty, P.; Nag, A.; Mondal, B.; Chennu, S.; Pradeep, T.  $[\text{Ag}_{59}(\text{2,5-DCBT})_{32}]^{3-}$ : a new cluster and a precursor for three well-known clusters. *Nanoscale* **2017**, 9, 8240–8248.
- (76) Bakshi, A.; Ghosh, A.; Mudedla, S. K.; Chakraborty, P.; Bhat, S.; Mondal, B.; Krishnadas, K. R.; Subramanian, V.; Pradeep, T. Isomerism in Monolayer Protected Silver Cluster Ions: An Ion Mobility-Mass Spectrometry Approach. *J. Phys. Chem. C* **2017**, 121, 13421–13427.
- (77) Bakshi, A.; Chakraborty, P.; Bhat, S.; Natarajan, G.; Pradeep, T.  $[\text{Au}_{25}(\text{SR})_{18}]_2^{2-}$ : a noble metal cluster dimer in the gas phase. *Chem. Commun.* **2016**, 52, 8397–8400.
- (78) Ghosh, A.; Bodiuzzaman, M.; Nag, A.; Jash, M.; Bakshi, A.; Pradeep, T. Sequential Dihydrogen Desorption from Hydride-Protected Atomically Precise Silver Clusters and the Formation of Naked Clusters in the Gas Phase. *ACS Nano* **2017**, 11, 11145–11151.
- (79) Wiseman, M. R.; Marsh, P. A.; Bishop, P. T.; Brisdon, B. J.; Mahon, M. F. Homoleptic Gold Thiolate Catenanes. *J. Am. Chem. Soc.* **2000**, 122, 12598–12599.
- (80) Zeng, C.; Liu, C.; Chen, Y.; Rosi, N. L.; Jin, R. Gold-Thiolate Ring as a Protecting Motif in the  $\text{Au}_{20}(\text{SR})_{16}$  Nanocluster and Implications. *J. Am. Chem. Soc.* **2014**, 136, 11922–11925.
- (81) Yan, N.; Xia, N.; Liao, L.; Zhu, M.; Jin, F.; Jin, R.; Wu, Z. Unraveling the long-pursued  $\text{Au}_{144}$  structure by x-ray crystallography. *Science Advances* **2018**, 4, eaat7259.
- (82) Ghosh, A.; Ghosh, D.; Khatun, E.; Chakraborty, P.; Pradeep, T. Unusual reactivity of dithiol protected clusters in comparison to monothiol protected clusters: studies using  $\text{Ag}_{51}(\text{BDT})_{19}(\text{TPP})_3$  and  $\text{Ag}_{29}(\text{BDT})_{12}(\text{TPP})_4$ . *Nanoscale* **2017**, 9, 1068–1077.
- (83) Viswanatha, R.; Sarma, D. D. Growth of Nanocrystals in Solution. In *Nanomaterials Chemistry*; Rao, C. N. R.; Müller, A.; Cheetham, A. K., Eds.; Wiley-VCH Verlag GmbH & Co. KGaA: Weinheim, 2007.
- (84) Dainese, T.; Antonello, S.; Bogialli, S.; Fei, W.; Venzo, A.; Maran, F. Gold Fusion: From  $\text{Au}_{25}(\text{SR})_{18}$  to  $\text{Au}_{38}(\text{SR})_{24}$ , the Most Unexpected Transformation of a Very Stable Nanocluster. *ACS Nano* **2018**, 12, 7057–7066.
- (85) Guo, R.; Song, Y.; Wang, G.; Murray, R. W. Does core size matter in the kinetics of ligand exchanges of monolayer-protected Au clusters? *J. Am. Chem. Soc.* **2005**, 127, 2752–2757.
- (86) Bootharaju, M. S.; Burlakov, V. M.; Besong, T. B. D.; Joshi, C. P.; AbdulHalim, L. G.; Black, D. M.; Whetten, R. L.; Goriely, A.; Bakr, O. M. Reversible Size Control of Silver Nanoclusters via Ligand-Exchange. *Chem. Mater.* **2015**, 27, 4289–4297.
- (87) Bootharaju, M. S.; Joshi, C. P.; Alhilaly, M. J.; Bakr, O. M. Switching a nanocluster core from hollow to nonhollow. *Chem. Mater.* **2016**, 28, 3292–3297.
- (88) Laphorn, C.; Pullen, F.; Chowdhry, B. Z. Ion mobility spectrometry-mass spectrometry (IMS-MS) of small molecules: separating and assigning structures to ions. *Mass Spectrom. Rev.* **2013**, 32, 43–71.
- (89) Angel, L. A.; Majors, L. T.; Dharmaratne, A. C.; Dass, A. Ion mobility mass spectrometry of  $\text{Au}_{25}(\text{SCH}_2\text{CH}_2\text{Ph})_{18}$  nanoclusters. *ACS Nano* **2010**, 4, 4691–4700.
- (90) Chakraborty, P.; Bakshi, A.; Khatun, E.; Nag, A.; Ghosh, A.; Pradeep, T. Dissociation of Gas Phase Ions of Atomically Precise Silver Clusters Reflects Their Solution Phase Stability. *J. Phys. Chem. C* **2017**, 121, 10971–10981.

(91) Liu, C.; Lin, S.; Pei, Y.; Zeng, X. C. Semiring chemistry of  $\text{Au}_{25}(\text{SR})_{18}$ : Fragmentation pathway and catalytic active site. *J. Am. Chem. Soc.* **2013**, *135*, 18067–18079.

(92) Jash, M.; Reber, A. C.; Ghosh, A.; Sarkar, D.; Bodiuzzaman, M.; Basuri, P.; Baksi, A.; Khanna, S. N.; Pradeep, T. Preparation of gas phase naked silver cluster cations outside the mass spectrometer from ligand protected clusters in solution. *Nanoscale* **2018**, *10*, 15714–15722.



## CONDENSED MATTER PHYSICS

## Rapid isotopic exchange in nanoparticles

Papri Chakraborty<sup>1</sup>, Abhijit Nag<sup>1</sup>, Ganapati Natarajan<sup>1</sup>, Nayanika Bandyopadhyay<sup>1</sup>,  
Ganesan Paramasivam<sup>1</sup>, Manoj Kumar Panwar<sup>1</sup>, Jaydeb Chakrabarti<sup>2</sup>, Thalappil Pradeep<sup>1\*</sup>

Rapid solution-state exchange dynamics in nanoscale pieces of matter is revealed, taking isotopically pure atomically precise clusters as examples. As two isotopically pure silver clusters made of <sup>107</sup>Ag and <sup>109</sup>Ag are mixed, an isotopically mixed cluster of the same entity results, similar to the formation of HDO, from H<sub>2</sub>O and D<sub>2</sub>O. This spontaneous process is driven by the entropy of mixing and involves events at multiple time scales.

Copyright © 2019  
The Authors, some  
rights reserved;  
exclusive licensee  
American Association  
for the Advancement  
of Science. No claim to  
original U.S. Government  
Works. Distributed  
under a Creative  
Commons Attribution  
NonCommercial  
License 4.0 (CC BY-NC).

## INTRODUCTION

Since the discovery of deuterium (D) (1) and the isolation of D<sub>2</sub>O (2), isotopic exchange in molecules has served as a characteristic signature of their dynamic chemical bonds (3). The rate of isotopic exchange in water (H<sub>2</sub>O + D<sub>2</sub>O = 2HDO) is fast with an equilibrium constant of  $3.75 \pm 0.07$  at room temperature (4), and it occurs at measurable speeds down to cryogenic temperatures (5). H/D exchange in proteins has been an important tool to understand their surface structure (6). Moreover, isotopic exchange in systems like H<sub>2</sub>/D<sub>2</sub> has high activation barrier and occurs at very high temperatures (~1000 K) or over heated catalytic metal surfaces (7). The existence of nanomaterials of noble metals with precise composition (8, 9) allows the feasibility of their isotopic exchange to be tested. Using high-resolution electrospray ionization mass spectrometry (ESI MS), we show that atomically precise monolayer-protected nanoclusters, made of isotopically pure silver (<sup>107</sup>Ag and <sup>109</sup>Ag), despite their well-defined structures and ligand protection, undergo rapid exchange of the isotopes of the metal atoms. The exchange approaches a dynamic equilibrium within a minute in solution at room temperature. Using two archetypal examples of Ag nanoparticles of precise composition, [Ag<sub>25</sub>(SR)<sub>18</sub>]<sup>−</sup> (10) and [Ag<sub>25</sub>(S<sub>2</sub>R)<sub>12</sub>(TPP)<sub>4</sub>]<sup>3−</sup> (11), where SR, S<sub>2</sub>R, and TPP are protecting ligands, we demonstrate that the rapid isotopic exchange reflects their solution-state dynamics. In addition, we show the ability to control the exchange dynamics by controlling the temperature. Time-resolved measurements further reveal that the mechanism of exchange involves several processes that occur at different time scales. The spontaneity in such reactions is mainly driven by the mixing entropy contribution to the free energy. Such an exchange mechanism, reminiscent of isotopic exchange between H<sub>2</sub>O and D<sub>2</sub>O, presents intriguing insights into the nature of nanoscale matter.

## RESULTS

To study isotopic exchange, we chose [Ag<sub>25</sub>(SR)<sub>18</sub>]<sup>−</sup> clusters (10) initially. Two identical but isotopically different clusters, [<sup>107</sup>Ag<sub>25</sub>(DMBT)<sub>18</sub>]<sup>−</sup> and [<sup>109</sup>Ag<sub>25</sub>(DMBT)<sub>18</sub>]<sup>−</sup> (DMBT = 2,4-dimethyl benzene thiol), were prepared starting from isotopically pure metals and extensively characterized to ensure their chemical purity and isotopic identity.

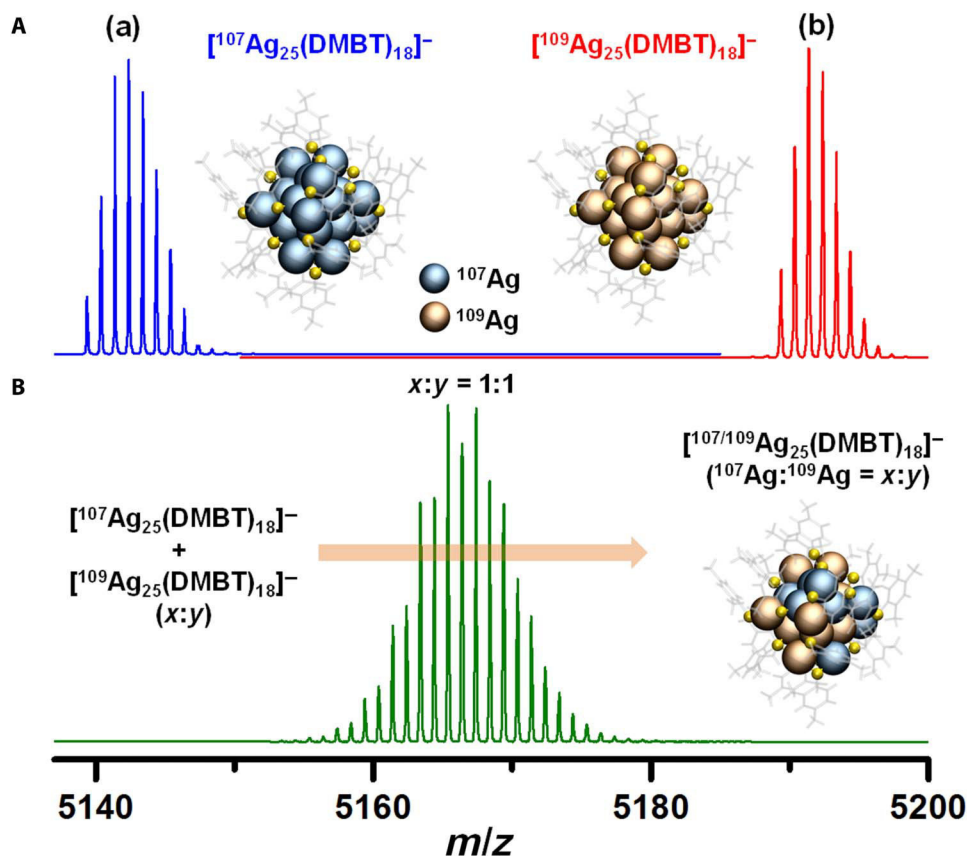
The isotopic clusters showed identical optical absorption spectra (fig. S1A). ESI MS of [<sup>107</sup>Ag<sub>25</sub>(DMBT)<sub>18</sub>]<sup>−</sup> and [<sup>109</sup>Ag<sub>25</sub>(DMBT)<sub>18</sub>]<sup>−</sup> are presented in Fig. 1A, a and b, respectively. The peak maxima of the spectra are separated by *m/z* (mass/charge ratio) 50 because of the interchange of 25 atoms of <sup>107</sup>Ag with <sup>109</sup>Ag. The mass spectral distributions of the isotopic clusters are narrower than those of a sample with natural Ag (fig. S1B). The isotope patterns (fig. S1, C and D) are purely due to the isotopes of S, C, and H in the ligands, and therefore, they are similar to those of the [Au<sub>25</sub>(PET)<sub>18</sub>]<sup>−</sup> cluster (12, 13) [PET (phenyl ethane thiol) has the same atomic composition (C<sub>8</sub>H<sub>10</sub>S) as DMBT], as Au has only one isotope. The minor differences with calculated patterns (fig. S1, C and D) are due to the slight isotopic impurity, as the isotope enrichment was ~98%. Upon mixing an equimolar mixture of [<sup>107</sup>Ag<sub>25</sub>(DMBT)<sub>18</sub>]<sup>−</sup> and [<sup>109</sup>Ag<sub>25</sub>(DMBT)<sub>18</sub>]<sup>−</sup> in solution at room temperature, the spectrum changed instantaneously, and the resulting distribution is shown in Fig. 1B. No peaks due to the parent clusters were observed, indicating that they were totally exchanged in this process. The mass spectral distribution calculated (fig. S2A) considering a system where each isotope of Ag (107/109) has a probability of occupying 50% of the total sites of the cluster is similar to the distribution observed in Fig. 1B. It is nearly identical to that of the ion [Ag<sub>25</sub>(DMBT)<sub>18</sub>]<sup>−</sup>, having the natural isotope distribution (<sup>107</sup>Ag: 51.839%, <sup>109</sup>Ag: 48.161%), and the minor differences arise as the <sup>107</sup>Ag/<sup>109</sup>Ag ratio is not exactly 1:1 in nature (fig. S2B). The two isotopically pure clusters were further mixed at varying molar ratios, and in each case, rapid exchange between the two clusters resulted in a binomial mass spectral distribution (fig. S3), in agreement with the calculated isotope pattern considering the relative abundance of each isotope from their initial molar ratio of mixing (fig. S4). Such an equilibrium statistical distribution is expected for a system where there are nearly equivalent sites that have equal probability of exchange.

Control over the exchange dynamics was achieved by lowering the temperature. The parent solutions were cooled to −20°C and mixed in a 1:1 molar ratio, and ESI MS was measured instantly. The source and desolvation temperatures were lowered to 30°C, and the sample was infused from an external syringe, which was also cooled to −20°C to reduce the effect of temperature during injection. In Fig. 2 (A to D), we presented the intermediate stages involving stepwise exchange of the isotopes of the atoms between the two clusters. Although the reaction kinetics was slower at lower temperatures, the equilibrium distribution was attained in about 30 s. Rapid exchange occurred even in alloys of the cluster (14), such as [Ag<sub>24</sub>Au(SR)<sub>18</sub>]<sup>−</sup> (fig. S5).

To probe how the dynamics of the exchange process is controlled by the inherent structures of the cluster, we performed a similar study

<sup>1</sup>DST Unit of Nanoscience (DST UNS) and Thematic Unit of Excellence (TUE), Department of Chemistry, Indian Institute of Technology Madras, Chennai 600 036, India. <sup>2</sup>Department of Chemical, Biological and Macromolecular Sciences, S. N. Bose National Centre for Basic Sciences, Sector III, Block JD, Salt Lake, Kolkata 700098, India.

\*Corresponding author. Email: pradeep@iitm.ac.in

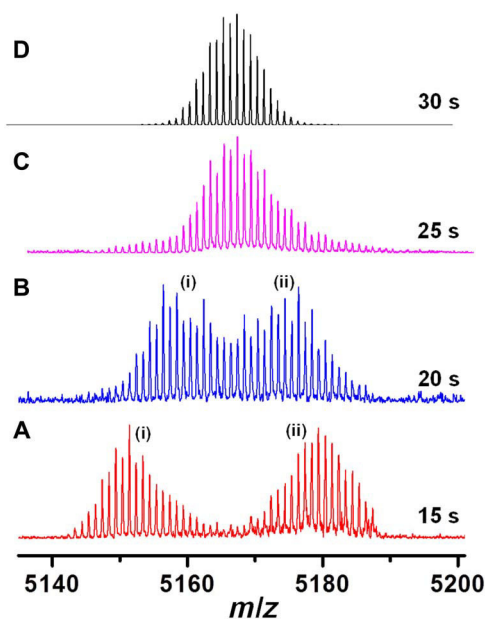


**Fig. 1. Mass spectra of the parent isotope clusters and the product of mixing.** (A) ESI MS of the as-synthesized isotopically pure clusters, (a)  $[^{107}\text{Ag}_{25}(\text{DMBT})_{18}]^-$  and (b)  $[^{109}\text{Ag}_{25}(\text{DMBT})_{18}]^-$ . (B) Mass spectral distribution of the product obtained by mixing the two isotopic clusters at 1:1 molar ratio. The spectrum was collected within 1 min after mixing the solutions of the clusters at room temperature. A representation of the clusters is shown. Comparison with the calculated mass spectrum is presented in figs. S1 and S2. Yellow, S; transparent gray, ligands.

with  $[\text{Ag}_{29}(\text{BDT})_{12}(\text{TPP})_4]^{3-}$ , where the dithiolate protection provides a very different structure (11) as compared to that of  $[\text{Ag}_{25}(\text{DMBT})_{18}]^-$ . Isotopically pure  $[^{107}\text{Ag}_{29}(\text{BDT})_{12}(\text{TPP})_4]^{3-}$  (BDT = benzene dithiol) and  $[^{109}\text{Ag}_{29}(\text{BDT})_{12}(\text{TPP})_4]^{3-}$  clusters were synthesized and characterized using optical absorption (fig. S6C) and ESI MS (fig. S6, A and B). We observed a reduced exchange rate compared to that of  $[\text{Ag}_{25}(\text{DMBT})_{18}]^-$ . At room temperature, an equimolar mixture of the two isotopic  $[\text{Ag}_{29}(\text{BDT})_{12}(\text{TPP})_4]^{3-}$  clusters, at a concentration of  $1.5 \times 10^{-3}$  mM, showed stepwise exchanges reaching a dynamic equilibrium over a period of 3 hours (fig. S7A). Although the labile TPP ligands were lost during ionization, the use of soft ionization conditions enabled us to observe that exchange occurred at a similar rate to that in the intact TPP-protected clusters that exist in solution (fig. S7B). The clusters mixed at any arbitrary molar ratios also attained equilibrium in a similar manner, and in all cases, the relative abundance of the isotopes in the final product was in accordance with their initial molar ratio of mixing (fig. S8).

The slower exchange rates seen here encouraged us to analyze the dynamics in greater detail. A kinetic plot of the percentage of unexchanged parent isotopic cluster ( $C_t$ ) versus time ( $t$ ) is shown in Fig. 3. At a given time, the percentage of exchange on either of the two isotopic clusters was similar when mixed in equimolar quantities. Therefore, monitoring the kinetics with respect to either of them gave identical results. In this plot, we included a hypothetical data point at  $t = 0$  min and  $C_t = 100\%$ , assuming that at 0 min, that is, in an

ideal situation before mixing, the abundance of a particular isotope ( $^{107}\text{Ag}/^{109}\text{Ag}$ ) in the clusters is 100%. Figure 3 shows that at room temperature ( $25^\circ\text{C}$ ), the  $^{107}\text{Ag}/^{109}\text{Ag}$  exchange rate was initially fast, and within 8 to 10 min, about 30% exchange occurred. Later, the exchange progressed slowly, and after about 250 min, the rate slowed down further, approaching an equilibrium corresponding to a state of 50% exchange. A triexponential effectively fitted the data points, suggesting at least three different rates for the exchange process with rate constants of  $5.9 \times 10^{-1} \text{ min}^{-1}$ ,  $1.4 \times 10^{-2} \text{ min}^{-1}$ , and  $7.1 \times 10^{-18} \text{ min}^{-1}$ , respectively. Similar exchange was studied at higher temperatures of  $40^\circ$  and  $60^\circ\text{C}$  (fig. S9, A and B), and the kinetic plots are shown in the inset of Fig. 3. The rate increased substantially at higher temperatures, and the reaction was complete within 60 min, whereas upon cooling the reaction mixture to  $0^\circ\text{C}$  the rate was drastically reduced and the process took around 3 days to attain equilibrium (fig. S9, C and D). Similar features were also observed for H/D exchange in supramolecular polymers in water (15). The three stages of exchange suggest that possibly the isotopic exchange in nanoparticles proceeds through (i) rapid exchange of their surface atoms, (ii) slower diffusion of the exchanged atoms within the core, and (iii) subsequent equilibration in the whole cluster. The reaction rates were dependent on the concentration of the clusters, which was evident from the kinetic studies at lower ( $1.5 \times 10^{-5}$  mM) and higher ( $1.5 \times 10^{-1}$  mM) concentrations compared to the above case ( $1.5 \times 10^{-3}$  mM) (fig. S10). At a given concentration of the parent clusters, we also



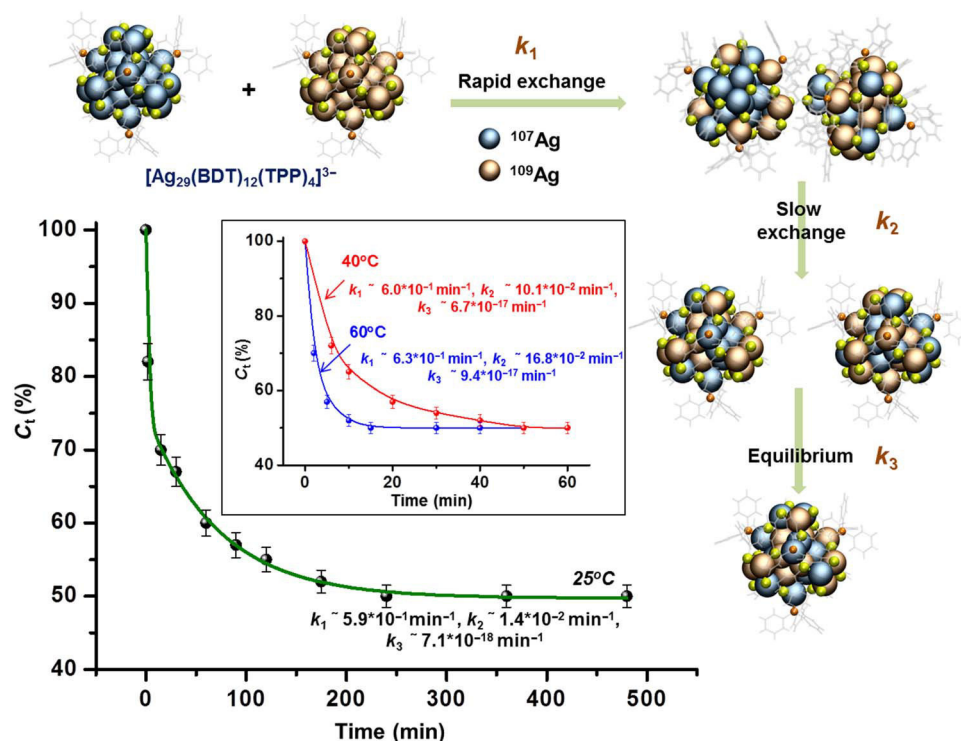
**Fig. 2. Low-temperature reaction showing the intermediate steps of exchange.** Exchange between the two isotopic  $[\text{Ag}_{25}(\text{DMBT})_{18}]^-$  clusters at  $-20^\circ\text{C}$  showing the intermediate stages of exchange (A) to (D) with mixing time (s). Distributions (i) and (ii) denote exchange at the  $^{107}\text{Ag}_{25}(\text{DMBT})_{18}^-$  and  $^{109}\text{Ag}_{25}(\text{DMBT})_{18}^-$  sides, respectively. Noise in the spectrum is due to the short acquisition time.

investigated the reaction rates at different molar ratios of mixing. Keeping the total number of moles of the mixture as constant, and starting from an excess concentration of  $^{107}\text{Ag}_{29}(\text{BDT})_{12}(\text{TPP})_4^{3-}$ , the rate increases with an increase in the concentration of  $^{109}\text{Ag}_{29}(\text{BDT})_{12}(\text{TPP})_4^{3-}$ , reaching a maximum at 1:1 condition. As the relative concentration of  $^{109}\text{Ag}_{29}(\text{BDT})_{12}(\text{TPP})_4^{3-}$  in the reaction mixture increases, the number of effective collisions between the isotopically different entities increases, and hence, the rate of exchange increases. Similar results were obtained starting from an excess concentration of  $^{109}\text{Ag}_{29}(\text{BDT})_{12}(\text{TPP})_4^{3-}$  and slowly increasing the concentration of  $^{107}\text{Ag}_{29}(\text{BDT})_{12}(\text{TPP})_4^{3-}$  in the mixture. Kinetic studies at different molar ratios showing the rate constants (fig. S11) and corresponding time-dependent ESI MS (fig. S12) are included in the Supplementary Materials. Reaction rates were independent of solvents such as dimethyl formamide (DMF), acetonitrile (ACN), and dichloromethane (DCM).

To investigate the mechanism and the driving forces of the isotopic exchange reaction, we carried out molecular docking studies and free-energy calculations. The mechanism of atom exchange is expected to be initiated through intercluster collisions (16), and this expectation is consistent with the temperature dependence of the rate constants. We have carried out molecular docking simulations for studying the interaction between two  $[\text{Ag}_{25}(\text{DMBT})_{18}]^-$  and two  $[\text{Ag}_{29}(\text{BDT})_{12}(\text{TPP})_4]^{3-}$  clusters. In each case, docking generated 10 different possible orientations, and the lowest-energy geometries for the approach of two  $[\text{Ag}_{25}(\text{DMBT})_{18}]^-$  and two  $[\text{Ag}_{29}(\text{BDT})_{12}(\text{TPP})_4]^{3-}$  clusters are represented in Fig. 4 (A and B). However, the other possible geometries were also similar in both cases, where the two clusters approach along the same orientation or along other symmetry equivalent orientations such that they interact at similar sites and generate the same configuration. The other possibilities were also energetically

similar within 0.01 to 0.07 kcal/mol. As all the possible structures obtained from docking were geometrically and energetically equivalent, it is likely that exchange reaction will be more favorable when the clusters approach along this specific geometry. The FFGMG obtained by docking two  $[\text{Ag}_{25}(\text{DMBT})_{18}]^-$  clusters indicates that after collision, the clusters may bind together supramolecularly in the initial steps of the reaction with an interaction energy of  $-23.7$  kcal/mol between the two clusters (Fig. 4A). The rapid exchange and the structural changes in  $[\text{Ag}_{25}(\text{DMBT})_{18}]^-$  can also be viewed from their topologically simplified structure (referred to as the aspicule model) (17), which considers the structure of an  $\text{M}_{25}\text{L}_{18}$  cluster (where  $\text{M} = \text{Au}, \text{Ag}$ ;  $\text{L} = \text{ligand}$ ) as a system of three interlocked Borromean rings of  $\text{M}_8(\text{SR})_6$  around a central  $\text{M}$  atom. Rapid exchange of isolobal  $\text{Ag}_2(\text{SR})_3$  and  $\text{Ag}(\text{SR})_2$  entities may occur. The opening of the rings can also make the core more exposed and facilitate spontaneous exchange of  $\text{Ag}$  or  $\text{Ag-SR}$  units between the core and staples of the two clusters. In comparison,  $[\text{Ag}_{29}(\text{BDT})_{12}(\text{TPP})_4]^{3-}$  does not contain any interlocked rings or chain structures. It has a rigid surface network with cross-linking dithiolates in the outer shell. In the lowest-energy geometry of two  $[\text{Ag}_{29}(\text{BDT})_{12}(\text{TPP})_4]^{3-}$  clusters (Fig. 4B), the proximity of  $\text{Ag}_3\text{S}_6$  or  $\text{AgS}_3\text{P}$  motifs of the two clusters may result in opening up of these staples. Molecular docking reveals an interaction energy of  $-7.8$  kcal/mol between two  $[\text{Ag}_{29}(\text{BDT})_{12}(\text{TPP})_4]^{3-}$  clusters (Fig. 4B). The supramolecular interactions between the clusters mainly include van der Waals and  $\text{C-H}\cdots\pi$  interactions. In the case of  $[\text{Ag}_{25}(\text{DMBT})_{18}]^-$  clusters, the H of the benzene ring and  $-\text{CH}_3$  group of one ligand on a cluster can interact with the  $\pi$ -system of the benzene ring of another cluster to facilitate the binding. These  $\text{C-H}\cdots\pi$  interaction distances are in the range of 2.99 to 4.16 Å, which are comparable with the  $\text{C-H}\cdots\pi$  distances observed in the crystal structures of  $\text{Au}_{246}$  (18) and  $\text{Ag}_{29}$  (19) nanoclusters. Interactions are also similar in the case of  $[\text{Ag}_{29}(\text{BDT})_{12}(\text{TPP})_4]^{3-}$  clusters. The  $\text{C-H}\cdots\pi$  interactions exist between  $-\text{H}$  of BDT of one cluster with benzene ring of BDT of another cluster at a distance of about 3.46 to 4.39 Å. The interactions are greater in the  $[\text{Ag}_{25}(\text{DMBT})_{18}]^-$  cluster, leading to higher binding energy. The interactions between the ligands are indicated in fig. S13. The reduced intercluster interaction energy and higher rigidity in the structure of  $[\text{Ag}_{29}(\text{BDT})_{12}(\text{TPP})_4]^{3-}$  might result in a slower exchange rate as compared to that of  $[\text{Ag}_{25}(\text{DMBT})_{18}]^-$ . However, more detailed computations are required to understand the complete mechanism of the atom exchange process.

We considered the thermodynamics of the reaction to identify the main driving force of the isotopic exchange reaction. The energy barrier for an intercluster isotopic exchange represents the energy cost of breaking and reforming bonds and any intermediate barriers, which must be crossed while the atoms travel along the path from their initial to final positions. We computed the enthalpic [electronic energy, zero-point energy (ZPE), and specific heat] and the entropic (electronic, translational, rotational, and vibrational) contributions to the free energy. Computational details are mentioned in Materials and Methods, and detailed results are presented in table S2. The total electronic energies of the clusters do not vary when different isotopes of the atoms are exchanged and rearranged because their bonding interactions are identical. Hence, any differences in enthalpy will be due to ZPE. Furthermore, the vibrational contribution to enthalpy and entropy will also contribute to the free energy. However, we found that there were only very small differences in the free energy of the clusters ( $\sim 0.01$  eV) due to isotopic exchange, and moreover, these differences cancel out when the reaction free energy  $[\Delta G_{\text{react}} = G(\text{products}) - G(\text{reactants})]$  is computed for the 1:1 ratio. In this calculation, we



**Fig. 3. Kinetic study of isotopic exchange in  $[\text{Ag}_{29}(\text{BDT})_{12}(\text{TPP})_4]^{3-}$  clusters.** Plot of percentage of unexchanged parent isotopic cluster ( $C_t$ ) versus time (min) of reaction at room temperature (25°C). Kinetics at 40° and 60°C are presented in the inset. Average of three kinetic measurements is plotted, and the error bar is indicated at each point. A schematic showing the different stages of isotopic exchange is also shown in the figure. Yellow, S; orange, P; transparent gray, ligands.

have assumed that the parent clusters are the isotopically pure reactants and that the products are the two mixed isotope clusters with the following compositions:  $(m,n) = (12,13)$  and  $(13,12)$  in the case of  $[\text{Ag}_m^{107}\text{Ag}_n^{109}(\text{DMBT})_{18}]^-$  and  $(m,n) = (14,15)$  and  $(15,14)$  in the case of  $[\text{Ag}_m^{107}\text{Ag}_n^{109}(\text{BDT})_{12}(\text{TPP})_4]^{3-}$ . Thus, in the absence of other contributions to the reaction free energy, the contribution from the mixing of isotopic clusters is expected to be of central importance in understanding the driving force of the reaction.

We now describe how we estimated the mixing contribution to the free energy. Application of the concept of entropy to a single cluster is not proper due to the small number of atoms ( $10^2$  to  $10^3$ ) in an individual cluster; however, we may apply it to the macroscopically large ensemble of  $N$  clusters, and the ensemble configuration is defined by the positions of  $^{107}\text{Ag}$  and  $^{109}\text{Ag}$  atoms in  $N$  clusters, where  $N$  is taken to be in the thermodynamic limit. The final equilibrium state of the cluster ensemble will be that in which the number of isotopic substituents is maximum for a given molar ratio so that the whole ensemble of clusters has the highest entropy ( $S$ ), which is defined as  $S = k \log W$ , where  $W$  is the total number of ways of arranging the two isotopes of Ag atoms (microstates) in the total available sites of the clusters, and  $k$  is the Boltzmann constant. For the equimolar composition, this will occur for the half-mixed compositions of each clusters, that is,  $n = (12, 13)$  and  $(13, 12)$  for  $\text{Ag}_{25}$ , and  $(14, 15)$  and  $(15, 14)$  for  $\text{Ag}_{29}$ , where these compositions have the identical maximum degeneracy in positional arrangements.

We approximate the ensemble of clusters with two crystalline lattices, one consisting of  $^{107}\text{Ag}$  and the other of  $^{109}\text{Ag}$ , which are fused together, and then assume random thermal exchanges of atoms in the joint lattice. In this simplification, we considered only the Ag atoms,

neglecting the cluster structure and symmetry and all interatomic interactions, and this situation is identical to the mixing of two ideal gases. Hence, the expression for mixing or configurational entropy is simply that of mixing two different ideal gases, which is known from statistical mechanics, and is given by

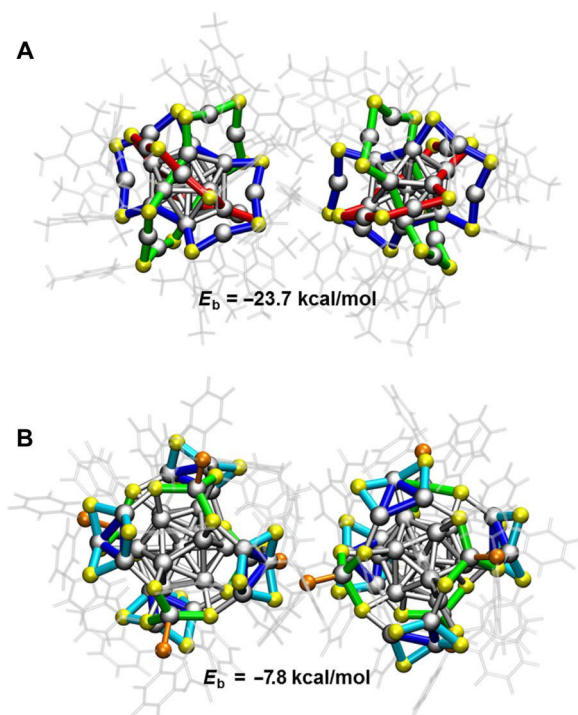
$$\Delta S_{\text{mix}} = -n_{\text{mol}} R [p \ln p + (1 - p) \ln (1 - p)]$$

where  $p$  is the mole fraction of  $^{107}\text{Ag}$ ,  $(1 - p)$  is the mole fraction of  $^{109}\text{Ag}$ , and  $n_{\text{mol}}$  is the total number of moles of the mixture.  $\Delta S_{\text{mix}}$  attains its maximum negative value for the half-and-half mixture, that is,  $p = 0.5$ , for a given total number of moles of the mixture (20). For a 1:1 ratio of mixing,  $\Delta S_{\text{mix}}$  is  $R \ln 2 = 5.76 \text{ J K}^{-1} \text{ mol}^{-1}$ , which is  $1.37 \text{ cal K}^{-1} \text{ mol}^{-1}$ , and  $\Delta G_{\text{mix}} = -T^* \Delta S_{\text{mix}} = -408.26 \text{ cal mol}^{-1}$  ( $T = 298 \text{ K}$  and  $n_{\text{mol}} = 1$ ). Because the calculated reaction free energies are negligible, the mixing entropic contribution to the free energy must be the main driving force of the observed spontaneous reaction. We remark that the mixing entropy term would also be important in spontaneous bimetallic intercluster reactions, where there are larger enthalpic changes due to the bonding interactions such as those between  $\text{Ag}_{25}(\text{DMBT})_{18}$  and  $\text{Au}_{25}(\text{PET})_{18}$  (16).

## DISCUSSION

The results presented establish that spontaneous isotopic exchange can occur between atomically precise silver nanoclusters. While it is rapid in  $[\text{Ag}_{25}(\text{SR})_{18}]^-$ , it is relatively slower in  $[\text{Ag}_{29}(\text{S}_2\text{R})_{12}(\text{TPP})_4]^{3-}$ , reflecting the differences in their chemical structures. Spontaneity in such reactions, driven by their entropy of mixing, reflects the dynamic





**Fig. 4. Molecular docking studies.** Force-field global minimum geometry (FFGMG) of two (A)  $[Ag_{25}(DMBT)_{18}]^{-}$  and (B)  $[Ag_{29}(BDT)_{12}(TPP)_4]^{3-}$  clusters, lying in close proximity. Gray, Ag; yellow, S; orange, P. The overlapping Borromean rings are shown in blue, green, and red in (A); staple units are shown in green and blue in (B); and ligand shell is shown in transparent gray. Atomic diameters were reduced to show the bonding.

nature of nanoparticles in solution. However, our study is restricted only to subnanometer-sized clusters, where exchange is shown to be dependent on their inherent structures. In a similar manner, the study may also be extended to classic nanomaterials of various sizes. Future possibilities include investigating the correlation between the extent of exchange with the size of the nanoparticles and the nature of their ligands or the constituent metal atoms.

The fundamental significance of this study is to understand the dynamics in nanoscale systems, which is comparable to solution-state dynamics of many simpler molecules like  $H_2O$ . This study has the potential to answer questions regarding the rigidity of the structures and rapid interconversions between the subunits that constitute nanosystems. Nanoparticle dynamics contributing to catalysis is of relevance to applications. In homogeneous catalysis involving nanoparticles, the site at which chemistry occurs could be changing continuously. This characteristic implies associated dynamics for the anchored ligands and therefore may contribute to their solution-state availability. This phenomenon may also be important in biology, where nanoparticles are used as carriers of molecular cargo.

Moreover, isotopic exchanges like H/D exchanges in  $H_2O/D_2O$  (21) can alter physical and chemical properties of the materials. Isotopic exchange affects the vibrational modes. In the case of clusters also, there will be changes in the vibrations, although these were found to be very small from our calculations. The change in properties is small in this particular case probably because the mass ratio of the two isotopes of Ag (109/107) is 1.019 (in contrast, the mass ratio for other isotopes like D/H is  $\sim 2$ ), and hence, the effect will be

less compared to the total mass of the cluster. However, the effect of isotopic exchange may become significant to alter the properties with the appropriately chosen cluster system and appropriately chosen metal or ligand isotopes. Isotopic modification can introduce a change in both the spatial distribution of nuclear mass and the nuclear spins in the clusters. Because the x-ray diffraction pattern of mixed isotope clusters and single isotope clusters would be identical, the use of neutron scattering could be useful to probe the structure and dynamics of these clusters. The change in the nuclear spins would affect the nuclear magnetic resonance (NMR) spectrum, and in the case of clusters with an unpaired electronic spin, isotopic modification would change the electron spin resonance properties through the electron-nuclear hyperfine interactions, which depend on the values of the nuclear spins. For example, in the case of isotopes of metals such as Pd ( $^{102}Pd$ ,  $^{104}Pd$ ,  $^{105}Pd$ ,  $^{106}Pd$ ,  $^{108}Pd$ , and  $^{110}Pd$ ),  $^{105}Pd$  has a nuclear spin of  $(5/2)^+$ , while other isotopes have 0 nuclear spin. This is similar in the case for the isotopes of Pt ( $^{192}Pt$ ,  $^{194}Pt$ ,  $^{195}Pt$ ,  $^{196}Pt$ ,  $^{198}Pt$ ), where  $^{195}Pt$  has a nuclear spin of  $(1/2)^-$ , while other isotopes have 0 nuclear spin. Such isotopic modification in clusters and their crystals might have applications in magnetic devices.

## MATERIALS AND METHODS

### Reagents and materials

Isotopically pure Ag foils,  $^{107}Ag$  (98%) and  $^{109}Ag$  (98%), were purchased from Cambridge Isotope Laboratories Inc. 2,4-DMBT, 1,3-BDT, sodium borohydride ( $NaBH_4$ ), and tetraphenyl phosphonium bromide ( $PPh_4Br$ ) were purchased from Sigma-Aldrich. Triphenyl phosphine (TPP) was purchased from Spectrochem, India. All the solvents [DCM, methanol (MeOH), DMF, and ACN] were of the high-performance liquid chromatography grade and were used without further purification.

### Synthesis of isotopically pure silver nitrate ( $^{107}AgNO_3$ and $^{109}AgNO_3$ ) from isotopically pure metal foils ( $^{107}Ag$ and $^{109}Ag$ )

About 50 mg of the metal foils of the isotopes of Ag ( $^{107}Ag$  and  $^{109}Ag$ ) was separately reacted with about 2 ml of concentrated nitric acid (70%) in a 5-ml reaction vessel and heated at  $70^\circ C$  inside a fume hood. The heating was continued until the evolution of nitrogen oxide gases was complete and the solution turned colorless. The solution was then diluted with water, and heating was continued. The process of addition of water was continued for a few times, and lastly, 0.5 ml of a concentrated solution of  $AgNO_3$  was kept for crystallization. For crystallization, the solution was kept inside an airtight dark box in the presence of solid  $P_2O_5$  and NaOH pellets (kept separately in the same box) to enhance the evaporation of water and remove excess acid. Colorless crystals of  $AgNO_3$  were obtained within 5 to 7 days. The yield of the reaction was around 95%.

### Synthesis of isotopically pure $[^{107}Ag_{25}(DMBT)_{18}]^{-}[PPh_4]^{+}$ and $[^{109}Ag_{25}(DMBT)_{18}]^{-}[PPh_4]^{+}$ clusters

Isotopically pure clusters were synthesized using the isotopically pure  $AgNO_3$  salt, which was synthesized according to the above mentioned method. The clusters were synthesized following a reported protocol (9). About 38 mg of  $^{107}AgNO_3$ / $^{109}AgNO_3$  was dissolved in a mixture of 2 ml of methanol and 17 ml of DCM. To this reaction mixture, about 90  $\mu l$  of 2,4-DMBT was added. The mixture was kept under stirring condition at  $0^\circ C$ . About 6 mg of  $PPh_4Br$  in 0.5 ml of methanol was added after about 15 to 20 min. Next, about 15 mg of  $NaBH_4$  in 0.5 ml of ice-cold water was added to the solution in a dropwise fashion. The stirring was continued for about 7 to 8 hours; the solution was then stored at  $4^\circ C$  for about 2 days. For purification, the sample

was centrifuged and DCM was removed by rotary evaporation. The precipitate was washed twice with methanol. Then, the cluster was redissolved in DCM and centrifuged to remove any further insoluble impurities. Further removal of DCM by rotary evaporation led to the formation of the purified clusters ( $[^{107}\text{Ag}_{25}(\text{DMBT})_{18}]^{-}[\text{PPh}_4]^{+}$  /  $[^{109}\text{Ag}_{25}(\text{DMBT})_{18}]^{-}[\text{PPh}_4]^{+}$ ) in their powder form.

#### Synthesis of isotopically pure $[^{107}\text{Ag}_{29}(\text{BDT})_{12}(\text{TPP})_4]^{3-}$ and $[^{109}\text{Ag}_{29}(\text{BDT})_{12}(\text{TPP})_4]^{3-}$ clusters

Isotopically pure clusters were synthesized using the isotopically pure  $\text{AgNO}_3$  salt following a reported method (10). About 20 mg of  $^{107}\text{AgNO}_3$  /  $^{109}\text{AgNO}_3$  was dissolved in a mixture of 5 ml of MeOH and 10 ml of DCM. To this solution, about 13.5  $\mu\text{l}$  of 1,3-BDT ligand was added, and the reaction mixture was kept under stirring condition. Addition of the thiol immediately resulted in a turbid yellow solution, which turned clear upon addition of about 200 mg of  $\text{PPh}_3$ . After about 15 min, a freshly prepared solution of 10.5 mg of  $\text{NaBH}_4$  in 500  $\mu\text{l}$  of water was added. The stirring was continued under dark conditions for 3 to 5 hours. During the course of the reaction, the dark brown color of the solution changed to orange. After completion of the reaction, the mixture was centrifuged and the supernatant was discarded. The precipitate consisting of the  $\text{Ag}_{29}$  cluster was washed repeatedly with methanol. The sample was dissolved in DMF and again centrifuged to remove any further insoluble contaminants. The supernatant was vacuum dried, and the purified clusters ( $[^{107}\text{Ag}_{29}(\text{BDT})_{12}(\text{TPP})_4]^{3-}$  /  $[^{109}\text{Ag}_{29}(\text{BDT})_{12}(\text{TPP})_4]^{3-}$ ) were obtained in powder form.

#### Synthesis of isotopically pure $[^{107}\text{Ag}_{24}\text{Au}(\text{DMBT})_{18}]^{-}$ and $[^{109}\text{Ag}_{24}\text{Au}(\text{DMBT})_{18}]^{-}$ clusters

Isotopically pure  $[^{107}\text{Ag}_{25}(\text{DMBT})_{18}]^{-}$  and  $[^{109}\text{Ag}_{25}(\text{DMBT})_{18}]^{-}$  clusters were used as the precursor to which  $\text{Au}^{+}$  was added in a controlled manner such that galvanic replacement of a Ag atom with Au resulted in the formation of  $[^{107}\text{Ag}_{24}\text{Au}(\text{DMBT})_{18}]^{-}$  and  $[^{109}\text{Ag}_{24}\text{Au}(\text{DMBT})_{18}]^{-}$  clusters (13), respectively.

#### Reaction of the isotopically pure clusters

In each case, stock solutions of parent isotopically pure clusters were prepared at a concentration of  $1.5 \times 10^{-3}$  mM. Then, they were mixed in different molar ratios, and their reaction was monitored by ESI MS.

#### Instrumentation

The optical absorption spectra were measured in PerkinElmer Lambda 25 ultraviolet-visible spectrophotometer. All the mass spectrometric measurements were done in a Waters SYNAPT G2-Si instrument. The instrument is well equipped with ESI, and all spectra were measured in the negative ion and resolution mode. The instrument is capable of measuring ESI MS with high-resolution touching orders of 50,000 ( $m/\Delta m$ ). The instrument was calibrated using NaI. An optimized condition involving a capillary voltage of 3 kV, a cone voltage of 20 V, a desolvation gas flow of 400 liters/hour, a source temperature of 100°C, a desolvation temperature of 150°C, and a sample infusion rate of 30  $\mu\text{l}$ /hour was used for all measurements. For low-temperature measurements, the source and desolvation temperatures were lowered to 30°C, and the sample was infused by an external syringe, which was also cooled at  $-20^\circ\text{C}$ .

#### Computational methods

##### Free-energy calculations

The exchange effect of silver isotopes ( $^{107}\text{Ag}$  and  $^{109}\text{Ag}$ ) was computationally studied in  $[\text{Ag}_{25}(\text{DMBT})_{18}]^{-}$  and  $[\text{Ag}_{29}(\text{BDT})_{12}(\text{PPh}_3)_4]^{3-}$  clusters by calculating free energy and thermochemistry parameters such as ZPE, enthalpy (H), and entropy (S) using density functional theory (DFT), as implemented in real-space grid-based projector

augmented wave (PAW) package (22). The PAW setup  $\text{Ag}(4d^{10}5s^1)$ ,  $\text{S}(3s^23p^4)$ ,  $\text{P}(3s^23p^3)$ ,  $\text{C}(2s^22p^2)$ , and  $\text{H}(1s^1)$  was considered to include only the valence electronic structure for the constituent atoms including the scalar-relativistic effects for Ag. Further, a reduced model was used considering  $-\text{CH}_3$  instead of the benzene rings in DMBT, BDT, and TPP ligands to reduce the high computational time of frequency calculations. The real-space calculation in finite difference mode, along with Perdew-Burke-Ernzerhof (PBE) functional, was applied for the geometry optimizations with a grid spacing of 0.2 Å, and the minimization criterion was the residual forces of 0.05 eV/Å, without considering any symmetry constraints. The atomic masses of Ag isotopes were taken as 106.905 and 108.905 for  $^{107}\text{Ag}$  and  $^{109}\text{Ag}$ , respectively. The vibrational modes were calculated only for Ag, S, and P atoms using the finite difference approximation of the Hessian matrix by considering the two displacements ( $+\Delta$  and  $-\Delta$ ) per atom in each Cartesian coordinate. Further, the calculated vibrational energies were used to calculate the thermodynamic quantities like H, S, and Gibbs free energy (G).

The calculation of G is made in the ideal gas approximation. It includes the electronic energy ( $E_{\text{pot}}$ ), ZPE ( $E_{\text{ZPE}}$ ), translational, rotational, and vibrational components of H and S, which are based on DFT calculations. An additional entropy of mixing component was calculated separately from statistical mechanics.

Enthalpy (H) is calculated within the atomistic simulation environment as

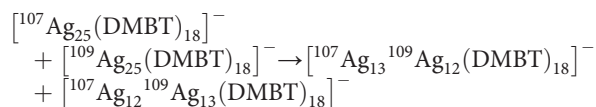
$$H = E_{\text{pot}} + E_{\text{ZPE}} + C_{\text{v\_trans}} + C_{\text{v\_rot}} + C_{\text{v\_vib}}, \text{ and entropy is } S = S_{\text{trans}} + S_{\text{rot}} + S_{\text{elec}} + S_{\text{vib}}$$

Hence, the Gibbs free energy at temperature  $T$  and pressure  $P$  is calculated as

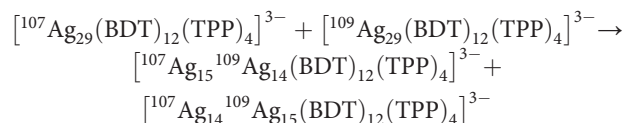
$$G = H - T^*S$$

The structural isomers of each isotopically substituted cluster arising from the different possible ways of arranging  $n$  Ag isotopic substituent atoms among the total number of Ag atoms are all degenerate as far as their total electronic energy is concerned, with a small difference of only 0.01 eV for both  $\text{Ag}_{29}$  and  $\text{Ag}_{25}$  in the value of G of the parent and isotopic substituent clusters, in terms of their enthalpic and the vibrational entropic components (see table S2).

We may write the reaction equations for the 1:1 ratio of mixing as follows, and in doing so, we assume that both products,  $(m,n) = (12,13)$  and  $(13,12)$  for  $\text{Ag}_{25}$  and  $(m,n) = (14,15)$  and  $(15,14)$  for  $\text{Ag}_{29}$ , are equally likely to form.



For the case of  $[\text{Ag}_{29}(\text{BDT})_{12}(\text{TPP})_4]^{3-}$



For  $(m,n) = (12,13)$ ,  $(13,12)$  in  $[\text{Ag}_{25}(\text{DMBT})_{18}]^{-}$  and  $(m,n) = (14,15)$ ,  $(15,14)$  in  $[\text{Ag}_{29}(\text{BDT})_{12}(\text{TPP})_4]^{3-}$  substituent cases (1:1 molar ratio), we have computed the reaction molar Gibbs free energy ( $\Delta G_{\text{react}}$ ) at standard temperature (298 K) and pressure (1 atm). The reaction free

energies ( $\Delta G_{\text{react}}$ ) are zero for both  $\text{Ag}_{29}$  and  $\text{Ag}_{25}$  clusters (see table S2), and the overall free energy of reaction is given by

$$\Delta G = \Delta G_{\text{react}} + \Delta G_{\text{mix}} = G(\text{products}) - G(\text{reactants}) + \Delta G_{\text{mix}}$$

For  $[\text{Ag}_{25}(\text{DMBT})_{18}]^-$ ,

$$G(\text{products}) = G \text{ of } {}^{107}\text{Ag}^{109}\text{Ag}(12, 13) + G \text{ of } {}^{107}\text{Ag}^{109}\text{Ag}(13, 12)$$

$$G(\text{reactants}) = G \text{ of parent } {}^{107}\text{Ag}_{25} + G \text{ of parent } {}^{109}\text{Ag}_{25}$$

and similarly for  $\text{Ag}_{29}$ .

The expression for mixing or configurational entropy is simply that of mixing two different ideal gases, which is known from statistical mechanics, and is given by

$$\Delta S_{\text{mix}} = -n_{\text{mol}} R [p \ln p + (1 - p) \ln (1 - p)]$$

where  $p$  is the mole fraction of  ${}^{107}\text{Ag}$ ,  $(1 - p)$  is the mole fraction of  ${}^{109}\text{Ag}$ , and  $n_{\text{mol}}$  is the total number of moles of the mixture (17). We note that the mixing entropy is independent of the cluster size and only depends on the mixing ratio; hence, we expect the half-and-half-mixture to have the largest mixing free energy. For the 1:1 mixture, we have  $p = 0.5$ , and hence,  $\Delta S_{\text{mix}}$  is  $R \ln 2$  ( $n_{\text{mol}} = 1$ ) and  $\Delta G_{\text{mix}} = -T \Delta S_{\text{mix}} = -RT \ln 2$ , where  $R$  is the gas constant in joules per mole and  $n_{\text{mol}} = 1$ . This analysis reveals that the entropy of isotopic mixing is the largest and most significant contribution to the Gibbs free energy. Because of the fractional mixing ratio, the mixing entropy is always positive, and therefore,  $\Delta G_{\text{mix}}$  is always negative and is larger than the other terms in the free energy. Hence,  $\Delta G_{\text{mix}}$ , being the largest contribution to the overall reaction, causes  $\Delta G$  to be always negative, which makes the reaction spontaneous.

The mixing ratio  $x = 0.5$  corresponds to the nearest integer numbers of exchanged Ag atoms to half of the total number of Ag atoms in the cluster, because both clusters have an odd number of Ag atoms, for example,  $(25/2) = 12.5$ , hence, (13,12) or (12,13), where these compositions both have the identical maximum degeneracy in arrangements as a function of the number of substituents  $n$  in the  $\text{Ag}_{25}$  cluster. Similarly, for the  $\text{Ag}_{29}$  cluster,  $(29/2) = 14.5$  and, hence, (14,15) or (15,14) are the most entropically favorable compositions in  $\text{Ag}_{29}$ .

### Molecular docking

To understand the intermolecular interactions in  $[\text{Ag}_{25}(\text{SR})_{18}]^-$  clusters, molecular docking studies were performed using AutoDock4.2 and its associated tools (23). DFT-optimized geometry and partial charges of  $[\text{Ag}_{25}(\text{SR})_{18}]^-$  were used for this study. We used  $[\text{Ag}_{25}(\text{SR})_{18}]^-$  as both “ligand” and “receptor.” Receptor grids were generated using  $126 \times 126 \times 126$  grid points in  $xyz$ , with a grid spacing of 0.375 Å, and map types were created using AutoGrid-4.2. The grid parameter file (.gpf) was saved using MGL Tools-1.4.6.50. The docking parameter files (.dpf) were generated using MGLTools-1.4.6.50. The results of AutoDock generated an output file (.dlg), and the generated conformers were scored and ranked as per the interaction energy. Ten lowest-energy conformers were obtained. We used the Lamarckian genetic algorithm for the output file using MGLTools-1.4.6. The binding free energy of the FFGMG of the dimeric cluster adduct was  $-23.7$  kcal/mol. Similar study was done with  $[\text{Ag}_{29}(\text{S}_2\text{R})_{12}(\text{TPP})_4]^{3-}$  clusters, where  $[\text{Ag}_{29}(\text{S}_2\text{R})_{12}(\text{TPP})_4]^{3-}$  was used as both ligand and receptor. In this case, the binding free energy of FFGMG of the dimeric adduct was  $-7.8$  kcal/mol.

### Calculation of theoretical isotope patterns with varying composition of ${}^{107}\text{Ag}/{}^{109}\text{Ag}$

We calculated the theoretical isotope patterns of  $[\text{Ag}_{25}(\text{DMBT})_{18}]^-$  and  $[\text{Ag}_{29}(\text{BDT})_{12}(\text{TPP})_4]^{3-}$  by varying the abundance of each isotope ( ${}^{107}\text{Ag}/{}^{109}\text{Ag}$ ) in them by 1% change so that the composition is  $(x,y)$ , that is,  $\{(100,0), (99,1), (98,2), \dots, (0,100)\}$ , where  $x$  and  $y$  are the abundance of  ${}^{107}\text{Ag}$  and  ${}^{109}\text{Ag}$ , respectively. The experimental spectra were compared with the calculated spectra to find the best match and hence confirm the composition.

### Details of fitting the kinetic data

The triexponential fitting in Fig. 3 was performed using the Origin 8.5 software package. The equation  $y = k_1 \exp(-t^*a) + k_2 \exp(-t^*b) + k_3 \exp(-t^*c)$  was used for the triexponential fits. The parameters  $k_1$ ,  $k_2$ ,  $k_3$ ,  $a$ ,  $b$ , and  $c$  were varied during the fitting, and  $t$  was used as the independent variable. Both monoexponential and biexponential fits were inadequate, and only a triexponential fit could successfully fit the data points.

### SUPPLEMENTARY MATERIALS

Supplementary material for this article is available at <http://advances.sciencemag.org/cgi/content/full/5/1/eaau7555/DC1>

Fig. S1. Characterization of isotopically pure  $[\text{Ag}_{25}(\text{DMBT})_{18}]^-$  and  $[\text{Ag}_{25}(\text{DMBT})_{18}]^-$  clusters.

Fig. S2. Isotope patterns of the product obtained by reaction of  $[\text{Ag}_{25}(\text{DMBT})_{18}]^-$  and  $[\text{Ag}_{25}(\text{DMBT})_{18}]^-$  at 1:1 molar ratio.

Fig. S3. ESI MS of reaction product obtained by mixing the two isotopic  $[\text{Ag}_{25}(\text{DMBT})_{18}]^-$  and  $[\text{Ag}_{25}(\text{DMBT})_{18}]^-$  clusters at various molar ratios.

Fig. S4. Comparison of the experimental and calculated isotope patterns of the products obtained by mixing  $[\text{Ag}_{25}(\text{DMBT})_{18}]^-$  and  $[\text{Ag}_{25}(\text{DMBT})_{18}]^-$  at various molar ratios.

Fig. S5. Isotope exchange in  $[\text{Ag}_{24}\text{Au}(\text{DMBT})_{18}]^-$  clusters.

Fig. S6. Characterization of isotopically pure  $[\text{Ag}_{29}(\text{BDT})_{12}(\text{TPP})_4]^{3-}$  and  $[\text{Ag}_{29}(\text{BDT})_{12}(\text{TPP})_4]^{3-}$  clusters.

Fig. S7. Reaction between  $[\text{Ag}_{29}(\text{BDT})_{12}(\text{TPP})_4]^{3-}$  and  $[\text{Ag}_{29}(\text{BDT})_{12}(\text{TPP})_4]^{3-}$  clusters in 1:1 molar ratio at room temperature.

Fig. S8. ESI MS of reaction product obtained by mixing the two isotopic  $[\text{Ag}_{29}(\text{BDT})_{12}(\text{TPP})_4]^{3-}$  and  $[\text{Ag}_{29}(\text{BDT})_{12}(\text{TPP})_4]^{3-}$  clusters at various molar ratios.

Fig. S9. Time-dependent study of reaction between  $[\text{Ag}_{29}(\text{BDT})_{12}(\text{TPP})_4]^{3-}$  and  $[\text{Ag}_{29}(\text{BDT})_{12}(\text{TPP})_4]^{3-}$  in 1:1 molar ratio at various temperatures.

Fig. S10. Kinetic study of isotopic exchange at different concentrations of  $[\text{Ag}_{29}(\text{BDT})_{12}(\text{TPP})_4]^{3-}$  clusters.

Fig. S11. Kinetic study of isotopic exchange in  $[\text{Ag}_{29}(\text{BDT})_{12}(\text{TPP})_4]^{3-}$  clusters at different molar ratios of mixing.

Fig. S12. Time-dependent study of reaction between  $[\text{Ag}_{29}(\text{BDT})_{12}(\text{TPP})_4]^{3-}$  and  $[\text{Ag}_{29}(\text{BDT})_{12}(\text{TPP})_4]^{3-}$  at various molar ratios.

Fig. S13. Molecular docking studies.

Table S1. Abundance of  ${}^{107}\text{Ag}$  in product =  $\{x/(x + y)\} \times 100$  and  ${}^{109}\text{Ag}$  in product =  $\{y/(x + y)\} \times 100$ .

Table S2. Table showing ZPE and Gibbs free energy ( $G$ ) values of the isotopic clusters.

### REFERENCES AND NOTES

1. H. C. Urey, F. G. Brickwedde, G. M. Murphy, A hydrogen isotope of mass 2. *Phys. Rev.* **39**, 164–165 (1932).
2. G. N. Lewis, R. T. Macdonald, Concentration of  $\text{H}^2$  isotope. *J. Chem. Phys.* **1**, 341–344 (1933).
3. A. Thibblin, P. Ahlberg, Reaction branching and extreme kinetic isotope effects in the study of reaction mechanisms. *Chem. Soc. Rev.* **18**, 209–224 (1989).
4. J. W. Pyper, R. S. Newbury, G. W. Barton Jr., Study of the isotopic disproportionation reaction between light and heavy water using a pulsed-molecular-beam mass spectrometer. *J. Chem. Phys.* **46**, 2253–2257 (1967).
5. S.-C. Park, K.-H. Jung, H. Kang, H/D isotopic exchange between water molecules at ice surfaces. *J. Chem. Phys.* **121**, 2765–2774 (2004).
6. L. Konermann, J. Pan, Y.-H. Liu, Hydrogen exchange mass spectrometry for studying protein structure and dynamics. *Chem. Soc. Rev.* **40**, 1224–1234 (2011).
7. G. Pratt, D. Rogers, Homogeneous isotope exchange reactions.  $\text{H}_2/\text{D}_2$ . *J. Chem. Soc. Faraday Trans. 1* **72**, 1589–1600 (1976).

8. I. Chakraborty, T. Pradeep, Atomically precise clusters of noble metals: Emerging link between atoms and nanoparticles. *Chem. Rev.* **117**, 8208–8271 (2017).
9. R. Jin, C. Zeng, M. Zhou, Y. Chen, Atomically precise colloidal metal nanoclusters and nanoparticles: Fundamentals and opportunities. *Chem. Rev.* **116**, 10346–10413 (2016).
10. C. P. Joshi, M. S. Bootharaju, M. J. Alhilaly, O. M. Bakr,  $[\text{Ag}_{25}(\text{SR})_{18}]^-$ : The “Golden” silver nanoparticle. *J. Am. Chem. Soc.* **137**, 11578–11581 (2015).
11. L. G. AbdulHalim, M. S. Bootharaju, Q. Tang, S. Del Gobbo, R. G. AbdulHalim, M. Eddaoudi, D.-E. Jiang, O. M. Bakr,  $\text{Ag}_{25}(\text{BDT})_{12}(\text{TPP})_4$ : A tetravalent nanocluster. *J. Am. Chem. Soc.* **137**, 11970–11975 (2015).
12. M. Zhu, C. M. Aikens, F. J. Hollander, G. C. Schatz, R. Jin, Correlating the crystal structure of a thiol-protected  $\text{Au}_{25}$  cluster and optical properties. *J. Am. Chem. Soc.* **130**, 5883–5885 (2008).
13. M. W. Heaven, A. Dass, P. S. White, K. M. Holt, R. W. Murray, Crystal structure of the gold nanoparticle  $[\text{N}(\text{C}_6\text{H}_{17})_4][\text{Au}_{25}(\text{SCH}_2\text{CH}_2\text{Ph})_{18}]$ . *J. Am. Chem. Soc.* **130**, 3754–3755 (2008).
14. M. S. Bootharaju, C. P. Joshi, M. R. Parida, O. F. Mohammed, O. M. Bakr, Templated atom-precise galvanic synthesis and structure elucidation of a  $[\text{Ag}_{24}\text{Au}(\text{SR})_{18}]^-$  nanocluster. *Angew. Chem. Int. Ed.* **55**, 922–926 (2016).
15. X. Lou, R. P. M. Lafleur, C. M. A. Leenders, S. M. C. Schoenmakers, N. M. Matsumoto, M. B. Baker, J. L. J. van Dongen, A. R. A. Palmans, E. W. Meijer, Dynamic diversity of synthetic supramolecular polymers in water as revealed by hydrogen/deuterium exchange. *Nat. Commun.* **8**, 15420 (2017).
16. K. R. Krishnadas, A. Baksi, A. Ghosh, G. Natarajan, T. Pradeep, Structure-conserving spontaneous transformations between nanoparticles. *Nat. Commun.* **7**, 13447 (2016).
17. G. Natarajan, A. Mathew, Y. Negishi, R. L. Whetten, T. Pradeep, A unified framework for understanding the structure and modifications of atomically precise monolayer protected gold clusters. *J. Phys. Chem. C* **119**, 27768–27785 (2015).
18. C. Zeng, Y. Chen, K. Kirschbaum, K. J. Lambright, R. Jin, Emergence of hierarchical structural complexities in nanoparticles and their assembly. *Science* **354**, 1580–1584 (2016).
19. A. Nag, P. Chakraborty, M. Bodiuzzaman, T. Ahuja, S. Antharjanam, T. Pradeep, Polymorphism of  $\text{Ag}_{29}(\text{BDT})_{12}(\text{TPP})_4^{3-}$  cluster: Interactions of secondary ligands and their effect on solid state luminescence. *Nanoscale* **10**, 9851–9855 (2018).
20. P. Atkins, J. De Paula, *Atkins’ Physical Chemistry* (Oxford Univ. Press, 2006).
21. J. D. Bernal, G. Tamm, Zero point energy and physical properties of  $\text{H}_2\text{O}$  and  $\text{D}_2\text{O}$ . *Nature* **135**, 229–230 (1935).
22. J. J. Mortensen, L. B. Hansen, K. W. Jacobsen, Real-space grid implementation of the projector augmented wave method. *Phys. Rev. B* **71**, 035109 (2005).
23. G. M. Morris, R. Huey, W. Lindstrom, M. F. Sanner, R. K. Belew, D. S. Goodsell, A. J. Olson, AutoDock4 and AutoDockTools4: Automated docking with selective receptor flexibility. *J. Comput. Chem.* **30**, 2785–2791 (2009).

**Acknowledgments:** P.C. thanks the Council of Scientific and Industrial Research (CSIR) for a research fellowship. A.N. thanks IIT Madras for an Institute Doctoral fellowship. G.P. thanks IIT Madras for an Institute Postdoctoral fellowship. We thank the Department of Science and Technology (DST), Government of India for continuous support of our research program. We thank D. Frenkel, University of Cambridge, UK, for useful discussions on the computational part of the work. **Funding:** This work was supported by the Council of Scientific and Industrial Research (CSIR), Indian Institute of Technology Madras and Department of Science and Technology (DST), Government of India. **Author contributions:** P.C. carried out the synthesis and designed and conducted the experiments. P.C. and A.N. carried out the ESI MS measurements. A.N. carried out the molecular docking studies. G.N. and G.P. carried out the DFT calculations. N.B. participated in the experiments. M.K.P. calculated the theoretical mass spectral distributions. G.N. and J.C. supervised the computational part. T.P. proposed the project and supervised the progress. The manuscript was written through contributions of all the authors. **Competing interests:** P.C., A.N., G.N., G.P., and T.P. are inventors of an Indian patent application related to this work (no. 201741037349, filed on 23 October 2017). The other authors declare that they have no competing interests. **Data and materials availability:** All data needed to evaluate the conclusions in the paper are present in the paper and/or the Supplementary Materials. Additional data related to this paper may be requested from the authors.

Submitted 12 July 2018  
Accepted 27 November 2018  
Published 4 January 2019  
10.1126/sciadv.aau7555

**Citation:** P. Chakraborty, A. Nag, G. Natarajan, N. Bandyopadhyay, G. Paramasivam, M. K. Panwar, J. Chakrabarti, T. Pradeep, Rapid isotopic exchange in nanoparticles. *Sci. Adv.* **5**, eaau7555 (2019).



## Rapid isotopic exchange in nanoparticles

Papri Chakraborty, Abhijit Nag, Ganapati Natarajan, Nayanika Bandyopadhyay, Ganesan Paramasivam, Manoj Kumar Panwar, Jaydeb Chakrabarti and Thalappil Pradeep

*Sci Adv* **5** (1), eaau7555.  
DOI: 10.1126/sciadv.aau7555

### ARTICLE TOOLS

<http://advances.sciencemag.org/content/5/1/eaau7555>

### SUPPLEMENTARY MATERIALS

<http://advances.sciencemag.org/content/suppl/2018/12/21/5.1.eaau7555.DC1>

### REFERENCES

This article cites 22 articles, 1 of which you can access for free  
<http://advances.sciencemag.org/content/5/1/eaau7555#BIBL>

### PERMISSIONS

<http://www.sciencemag.org/help/reprints-and-permissions>

Use of this article is subject to the [Terms of Service](#)

---

*Science Advances* (ISSN 2375-2548) is published by the American Association for the Advancement of Science, 1200 New York Avenue NW, Washington, DC 20005. 2017 © The Authors, some rights reserved; exclusive licensee American Association for the Advancement of Science. No claim to original U.S. Government Works. The title *Science Advances* is a registered trademark of AAAS.

## Supplementary Materials for Rapid isotopic exchange in nanoparticles

Papri Chakraborty, Abhijit Nag, Ganapati Natarajan, Nayanika Bandyopadhyay, Ganesan Paramasivam, Manoj Kumar Panwar, Jaydeb Chakrabarti, Thalappil Pradeep\*

\*Corresponding author. Email: pradeep@iitm.ac.in

Published 4 January 2019, *Sci. Adv.* **5**, eaau7555 (2019)  
DOI: 10.1126/sciadv.aau7555

### This PDF file includes:

Fig. S1. Characterization of isotopically pure  $[^{107}\text{Ag}_{25}(\text{DMBT})_{18}]^-$  and  $[^{109}\text{Ag}_{25}(\text{DMBT})_{18}]^-$  clusters.

Fig. S2. Isotope patterns of the product obtained by reaction of  $[^{107}\text{Ag}_{25}(\text{DMBT})_{18}]^-$  and  $[^{109}\text{Ag}_{25}(\text{DMBT})_{18}]^-$  at 1:1 molar ratio.

Fig. S3. ESI MS of reaction product obtained by mixing the two isotopic  $[^{107}\text{Ag}_{25}(\text{DMBT})_{18}]^-$  and  $[^{109}\text{Ag}_{25}(\text{DMBT})_{18}]^-$  clusters at various molar ratios.

Fig. S4. Comparison of the experimental and calculated isotope patterns of the products obtained by mixing  $[^{107}\text{Ag}_{25}(\text{DMBT})_{18}]^-$  and  $[^{109}\text{Ag}_{25}(\text{DMBT})_{18}]^-$  at various molar ratios.

Fig. S5. Isotope exchange in  $[\text{Ag}_{24}\text{Au}(\text{DMBT})_{18}]^-$  clusters.

Fig. S6. Characterization of isotopically pure  $[^{107}\text{Ag}_{29}(\text{BDT})_{12}(\text{TPP})_4]^{3-}$  and  $[^{109}\text{Ag}_{29}(\text{BDT})_{12}(\text{TPP})_4]^{3-}$  clusters.

Fig. S7. Reaction between  $[^{107}\text{Ag}_{29}(\text{BDT})_{12}(\text{TPP})_4]^{3-}$  and  $[^{109}\text{Ag}_{29}(\text{BDT})_{12}(\text{TPP})_4]^{3-}$  clusters in 1:1 molar ratio at room temperature.

Fig. S8. ESI MS of reaction product obtained by mixing the two isotopic  $[^{107}\text{Ag}_{29}(\text{BDT})_{12}(\text{TPP})_4]^{3-}$  and  $[^{109}\text{Ag}_{29}(\text{BDT})_{12}(\text{TPP})_4]^{3-}$  clusters at various molar ratios.

Fig. S9. Time-dependent study of reaction between  $[^{107}\text{Ag}_{29}(\text{BDT})_{12}(\text{TPP})_4]^{3-}$  and  $[^{109}\text{Ag}_{29}(\text{BDT})_{12}(\text{TPP})_4]^{3-}$  in 1:1 molar ratio at various temperatures.

Fig. S10. Kinetic study of isotopic exchange at different concentrations of  $[\text{Ag}_{29}(\text{BDT})_{12}(\text{TPP})_4]^{3-}$  clusters.

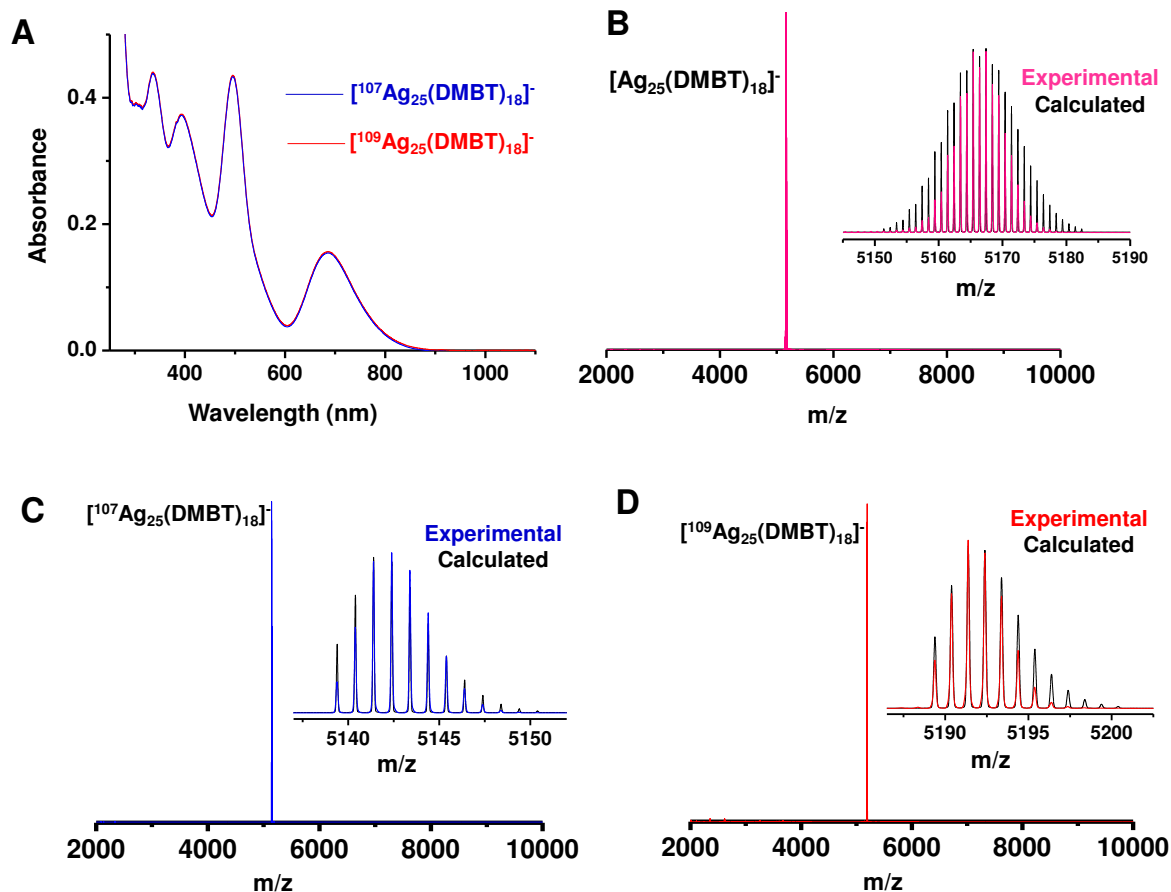
Fig. S11. Kinetic study of isotopic exchange in  $[\text{Ag}_{29}(\text{BDT})_{12}(\text{TPP})_4]^{3-}$  clusters at different molar ratios of mixing.

Fig. S12. Time-dependent study of reaction between  $[^{107}\text{Ag}_{29}(\text{BDT})_{12}(\text{TPP})_4]^{3-}$  and  $[^{109}\text{Ag}_{29}(\text{BDT})_{12}(\text{TPP})_4]^{3-}$  at various molar ratios.

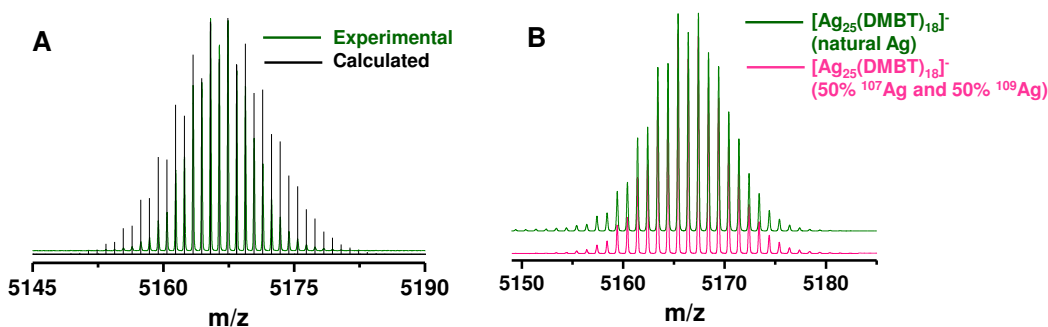
Fig. S13. Molecular docking studies.

Table S1. Abundance of  $^{107}\text{Ag}$  in product =  $\{x/(x+y)\} \times 100$  and  $^{109}\text{Ag}$  in product =  $\{y/(x+y)\} \times 100$ .

Table S2. Table showing ZPE and Gibbs free energy ( $G$ ) values of the isotopic clusters.



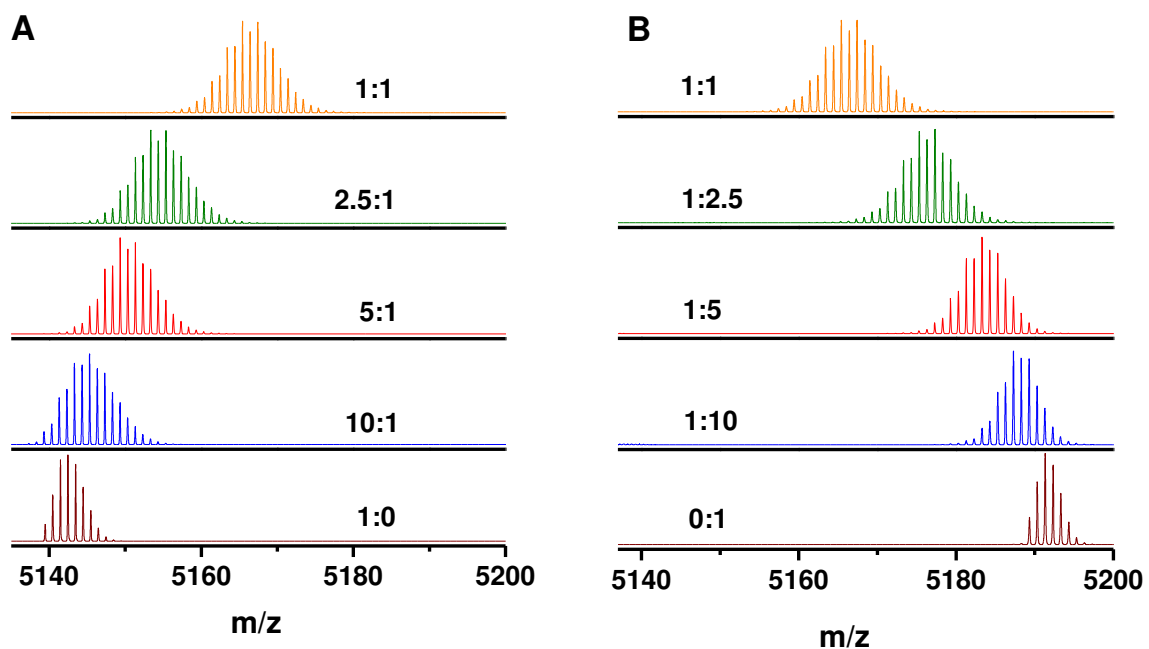
**Fig. S1. Characterization of isotopically pure  $[^{107}\text{Ag}_{25}(\text{DMBT})_{18}]^-$  and  $[^{109}\text{Ag}_{25}(\text{DMBT})_{18}]^-$  clusters.** (A) UV-vis spectra of  $[^{107}\text{Ag}_{25}(\text{DMBT})_{18}]^-$  and  $[^{109}\text{Ag}_{25}(\text{DMBT})_{18}]^-$  clusters showing identical features. ESI MS of (B)  $[\text{Ag}_{25}(\text{DMBT})_{18}]^-$  made from natural Ag, (C)  $[^{107}\text{Ag}_{25}(\text{DMBT})_{18}]^-$  and (D)  $[^{109}\text{Ag}_{25}(\text{DMBT})_{18}]^-$ . Insets show the comparison of the experimental and calculated isotope patterns of the peaks. The minor differences in the experimental spectra (in C and D) in comparison to the calculated spectra are due to the slight contribution of the other isotope in each sample as the isotope enrichment was 98%.



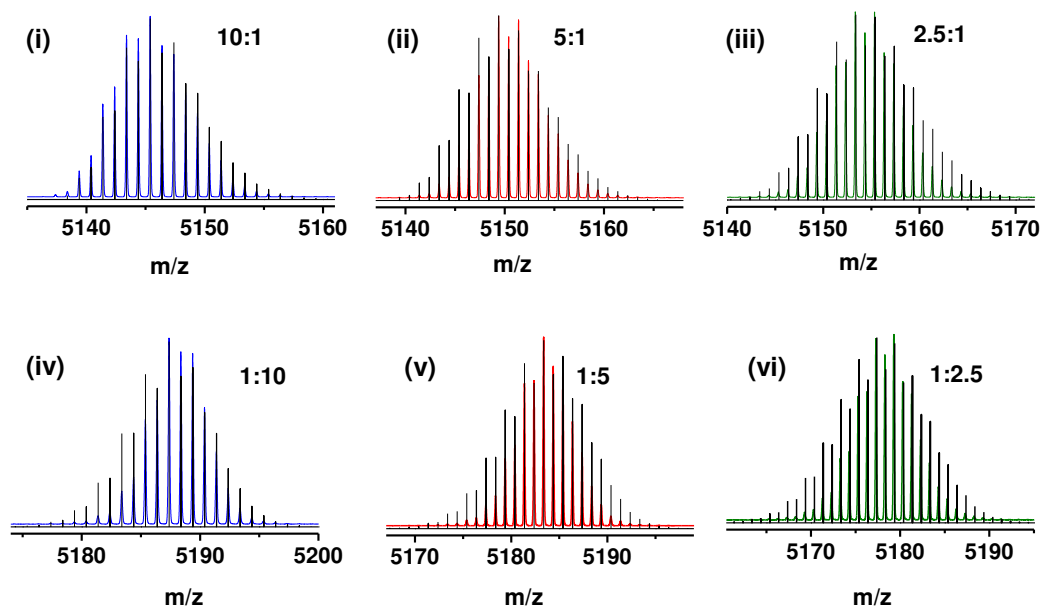
**Fig. S2. Isotope patterns of the product obtained by reaction of  $[^{107}\text{Ag}_{25}(\text{DMBT})_{18}]^-$  and  $[^{109}\text{Ag}_{25}(\text{DMBT})_{18}]^-$  at 1:1 molar ratio.** Experimental isotope distribution of the product obtained by mixing  $[^{107}\text{Ag}_{25}(\text{DMBT})_{18}]^-$  and  $[^{109}\text{Ag}_{25}(\text{DMBT})_{18}]^-$  at 1:1 molar ratio. The isotope pattern is compared with (A) the distribution computed considering 50% abundance of each isotope in  $[\text{Ag}_{25}(\text{DMBT})_{18}]^-$  and (B) experimental isotope patterns of  $[\text{Ag}_{25}(\text{DMBT})_{18}]^-$  synthesized from natural Ag.

**N.B.** In this case, the overall isotope distribution has contribution from the isotopes of the metal Ag and also C, H and S in the ligands. For the two parent clusters (Fig. 1 and S1) which are isotopically pure there is only one isotope of Ag. However, the product, which is a 1:1 mixture of the two isotopic clusters, has an isotope abundance of  $^{107}\text{Ag}$ :  $\frac{1}{2}$  and  $^{109}\text{Ag}$ :  $\frac{1}{2}$  and the isotope pattern for Ag will follow the binomial distribution and as a result will be broader compared to the monoisotopic case. This contribution from the isotopic abundance of Ag will be reflected in the overall isotope distribution and thus the product distribution is obviously broader than the two parent clusters.

Moreover natural abundance of Ag is  $^{107}\text{Ag}$  (51.84%) and  $^{109}\text{Ag}$  (48.16%). Hence the ratio of their abundances is 1.08, i.e.  $\sim 1$ , hence product distribution is similar to the cluster made of naturally abundant Ag.



**Fig. S3. ESI MS of reaction product obtained by mixing the two isotopic  $^{107}\text{Ag}_{25}(\text{DMBT})_{18}^-$  and  $^{109}\text{Ag}_{25}(\text{DMBT})_{18}^-$  clusters at various molar ratios.** Product obtained by mixing  $^{107}\text{Ag}_{25}(\text{DMBT})_{18}^-$  and  $^{109}\text{Ag}_{25}(\text{DMBT})_{18}^-$  at varying molar ratios where in (A)  $^{107}\text{Ag}_{25}(\text{DMBT})_{18}^-$  cluster is kept in higher concentration and in (B)  $^{109}\text{Ag}_{25}(\text{DMBT})_{18}^-$  cluster is kept in higher concentration. The initial molar ratio of mixing the two clusters ( $^{107}\text{Ag}_{25}(\text{DMBT})_{18}^- : ^{109}\text{Ag}_{25}(\text{DMBT})_{18}^-$ ) is indicated for each product observed.

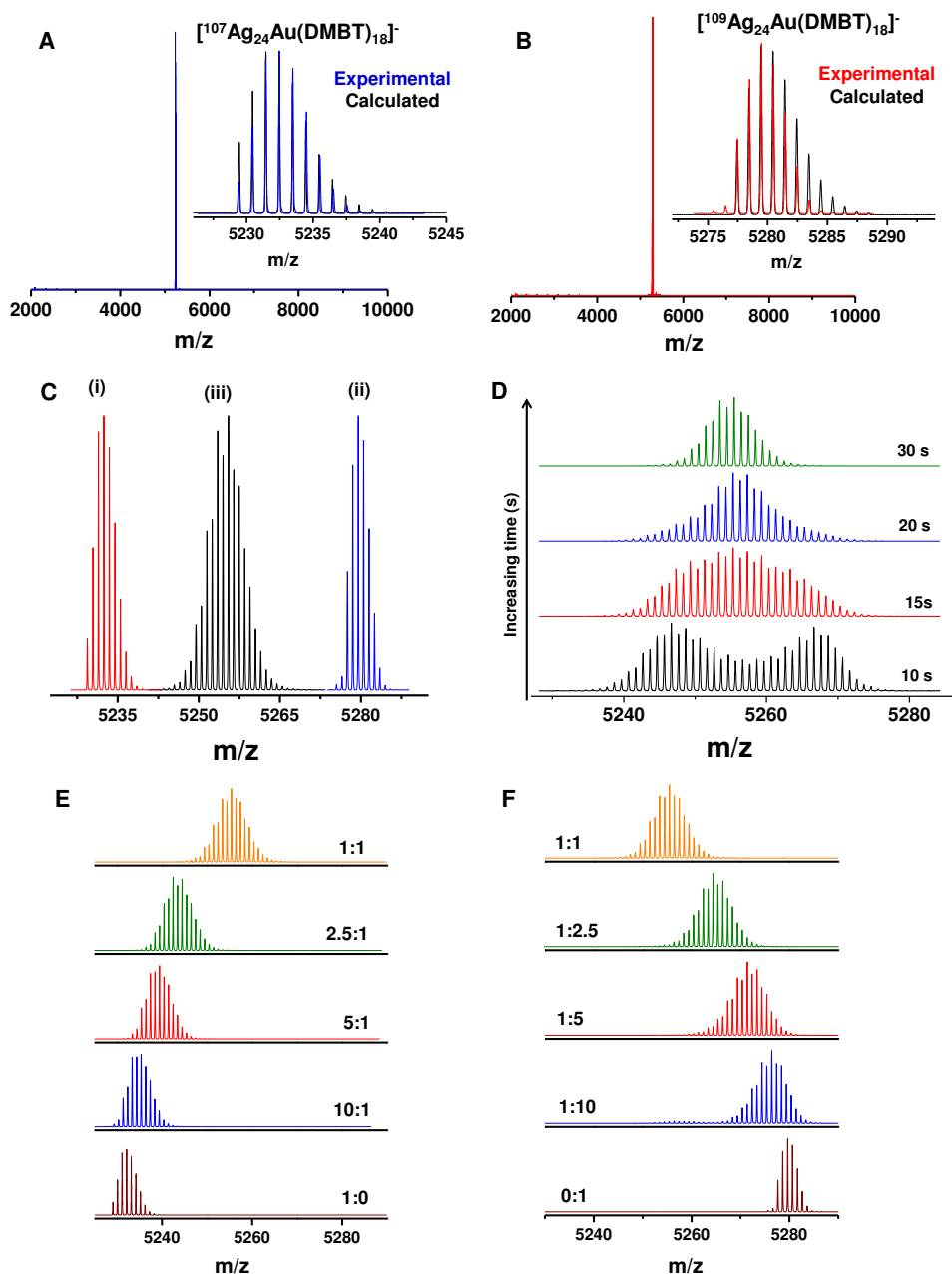


**Fig. S4. Comparison of the experimental and calculated isotope patterns of the products obtained by mixing  $[^{107}\text{Ag}_{25}(\text{DMBT})_{18}]^-$  and  $[^{109}\text{Ag}_{25}(\text{DMBT})_{18}]^-$  at various molar ratios.** Comparison of the experimental isotope patterns of the products obtained at different molar ratios of mixing the two isotopic clusters ( $[^{107}\text{Ag}_{25}(\text{DMBT})_{18}]^- : [^{109}\text{Ag}_{25}(\text{DMBT})_{18}]^-$ ) with the calculated patterns. The experimental patterns showed best match with the calculated patterns considering the abundances of each isotope in the cluster from their initial molar ratio of mixing.

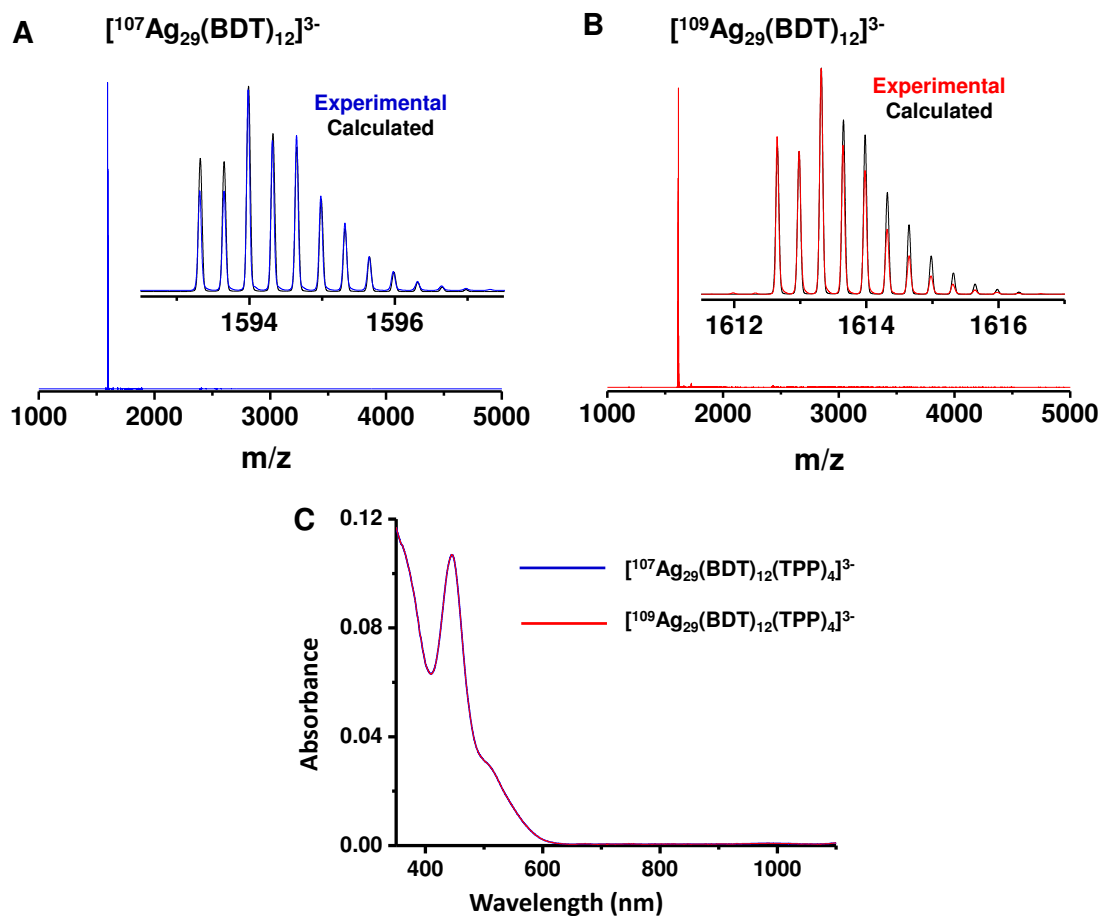
Note. Molar ratio of mixing ( $[^{107}\text{Ag}_{25}(\text{DMBT})_{18}]^- : [^{109}\text{Ag}_{25}(\text{DMBT})_{18}]^-$ ) = x:y

**Table S1. Abundance of  $^{107}\text{Ag}$  in product =  $\{x/(x + y)\} \times 100$  and  $^{109}\text{Ag}$  in product =  $\{y/(x + y)\} \times 100$ .**

Sl. No.	x:y	Abundance ( $^{107}\text{Ag}$ : $^{109}\text{Ag}$ )	Sl. No.	x:y	Abundance ( $^{107}\text{Ag}$ : $^{109}\text{Ag}$ )
1	10:1	90.909:9.091	5	1:10	9.091:90.909
2	5:1	83.333:16.667	6	1:5	16.667:83.333
3	2.5:1	71.428:28.571	7	1:2.5	28.571:71.428
4	1:1	50:50	8	1:1	50:50

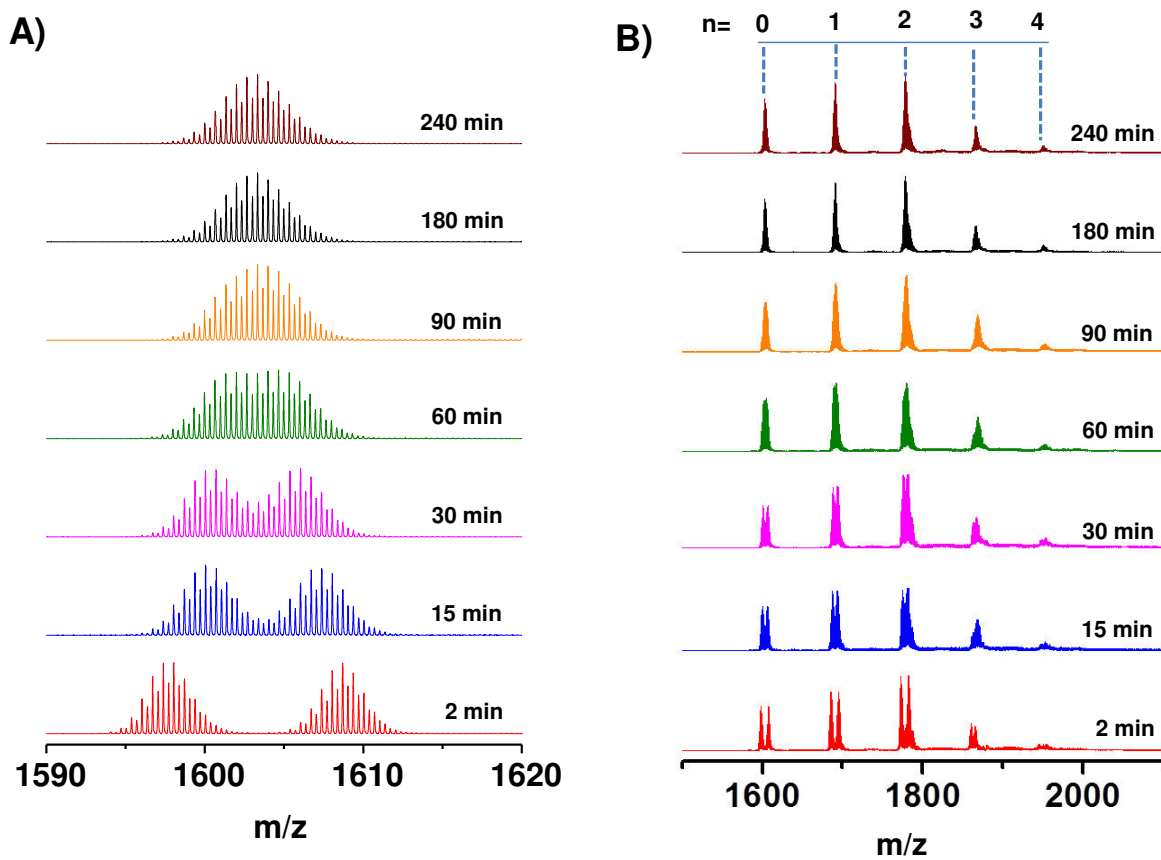


**Fig. S5. Isotope exchange in  $[\text{Ag}_{24}\text{Au}(\text{DMBT})_{18}]^-$  clusters.** ESI MS of (A)  $[\text{}^{107}\text{Ag}_{24}\text{Au}(\text{DMBT})_{18}]^-$  and (B)  $[\text{}^{109}\text{Ag}_{24}\text{Au}(\text{DMBT})_{18}]^-$ . Insets show the comparison of the experimental and calculated isotope patterns. (C) Reaction of  $[\text{}^{107}\text{Ag}_{24}\text{Au}(\text{DMBT})_{18}]^-$  and  $[\text{}^{109}\text{Ag}_{24}\text{Au}(\text{DMBT})_{18}]^-$  in 1:1 molar ratio at room temperature, where (i), (ii) and (iii) denotes ESI MS of  $[\text{}^{107}\text{Ag}_{24}\text{Au}(\text{DMBT})_{18}]^-$ ,  $[\text{}^{109}\text{Ag}_{24}\text{Au}(\text{DMBT})_{18}]^-$  and the product (50% abundance of each isotope), respectively. All the spectra are shown in the same scale. (D) Intermediates stages of reaction in 1:1 molar ratio at  $-20^\circ\text{C}$ . (E) and (F) Reaction at various molar ratios,  $[\text{}^{107}\text{Ag}_{24}\text{Au}(\text{DMBT})_{18}]^-$  :  $[\text{}^{109}\text{Ag}_{24}\text{Au}(\text{DMBT})_{18}]^-$  ratio is indicated in the figure.

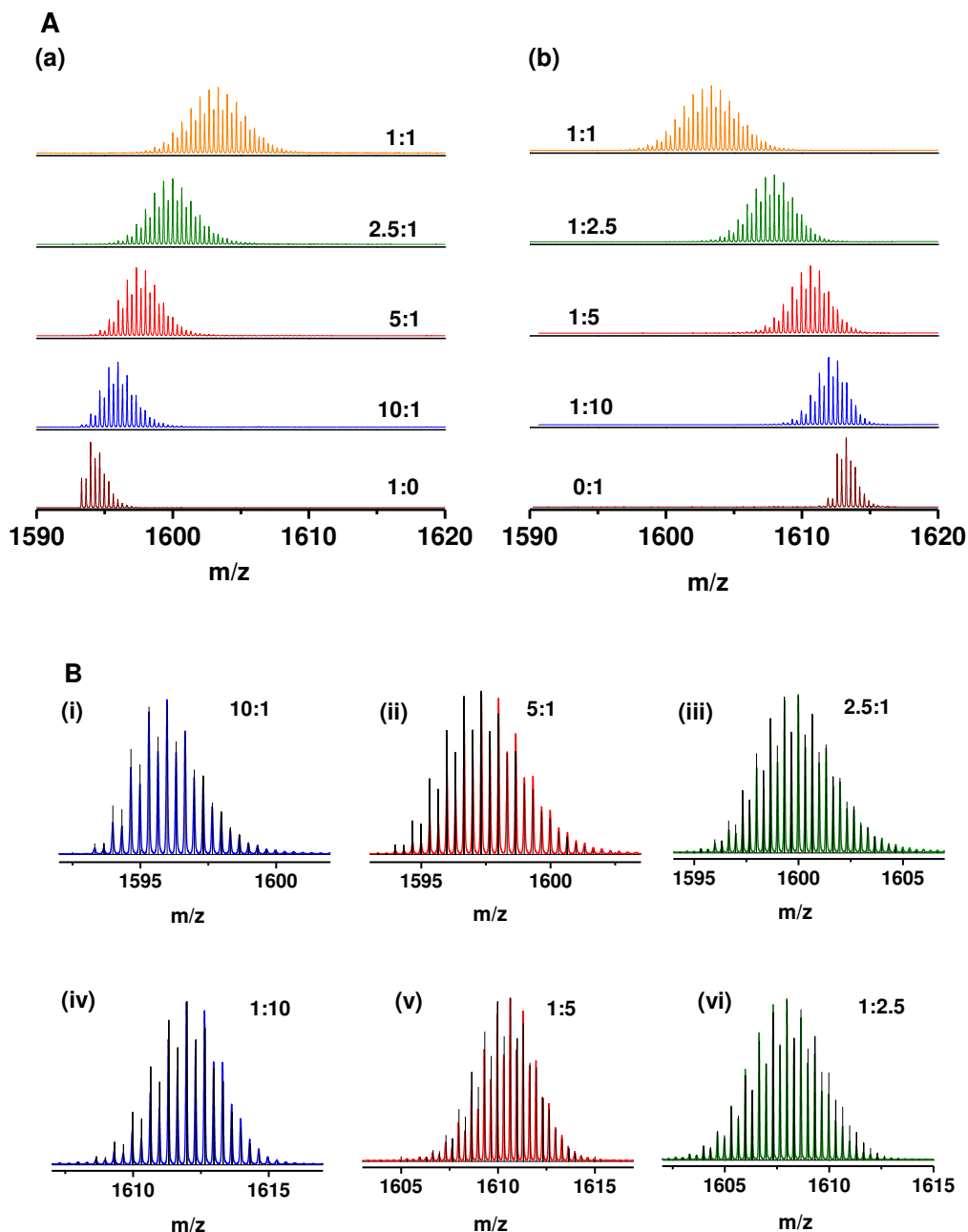


**Fig. S6. Characterization of isotopically pure  $[^{107}\text{Ag}_{29}(\text{BDT})_{12}(\text{TPP})_4]^{3-}$  and  $[^{109}\text{Ag}_{29}(\text{BDT})_{12}(\text{TPP})_4]^{3-}$  clusters.** ESI MS of (A)  $[^{107}\text{Ag}_{29}(\text{BDT})_{12}]^{3-}$  and (B)  $[^{109}\text{Ag}_{29}(\text{BDT})_{12}]^{3-}$  clusters. The labile TPP ligands were lost during ionization. Insets show the comparison of the experimental and calculated isotope patterns of the peaks. The minor differences in the experimental spectra in comparison to the calculated spectra are due to the slight contribution of the other isotope in each sample as the isotope enrichment was 98%. (C), UV-vis spectra of  $[^{107}\text{Ag}_{29}(\text{BDT})_{12}(\text{TPP})_4]^{3-}$  and  $[^{109}\text{Ag}_{29}(\text{BDT})_{12}(\text{TPP})_4]^{3-}$  clusters showing identical features.

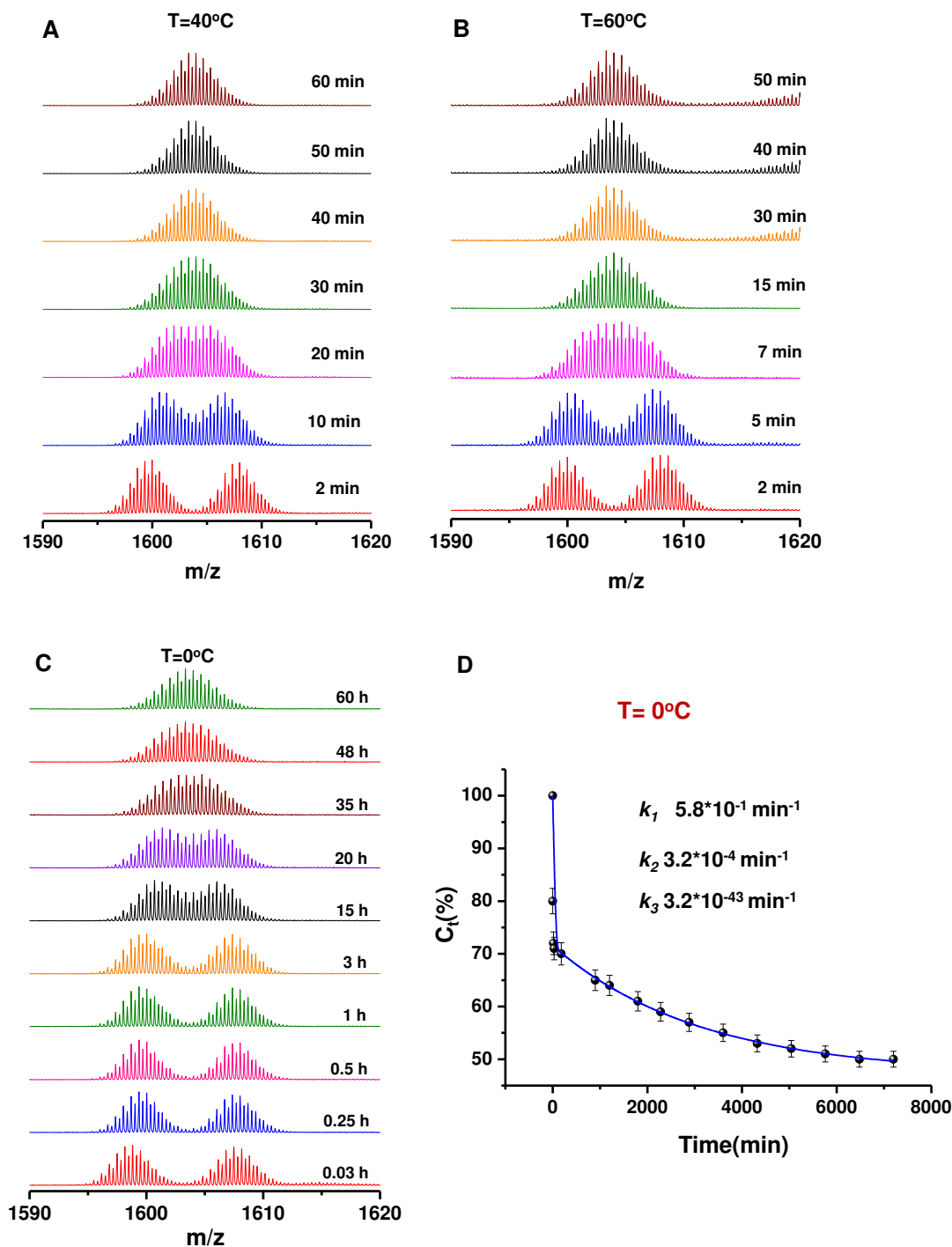




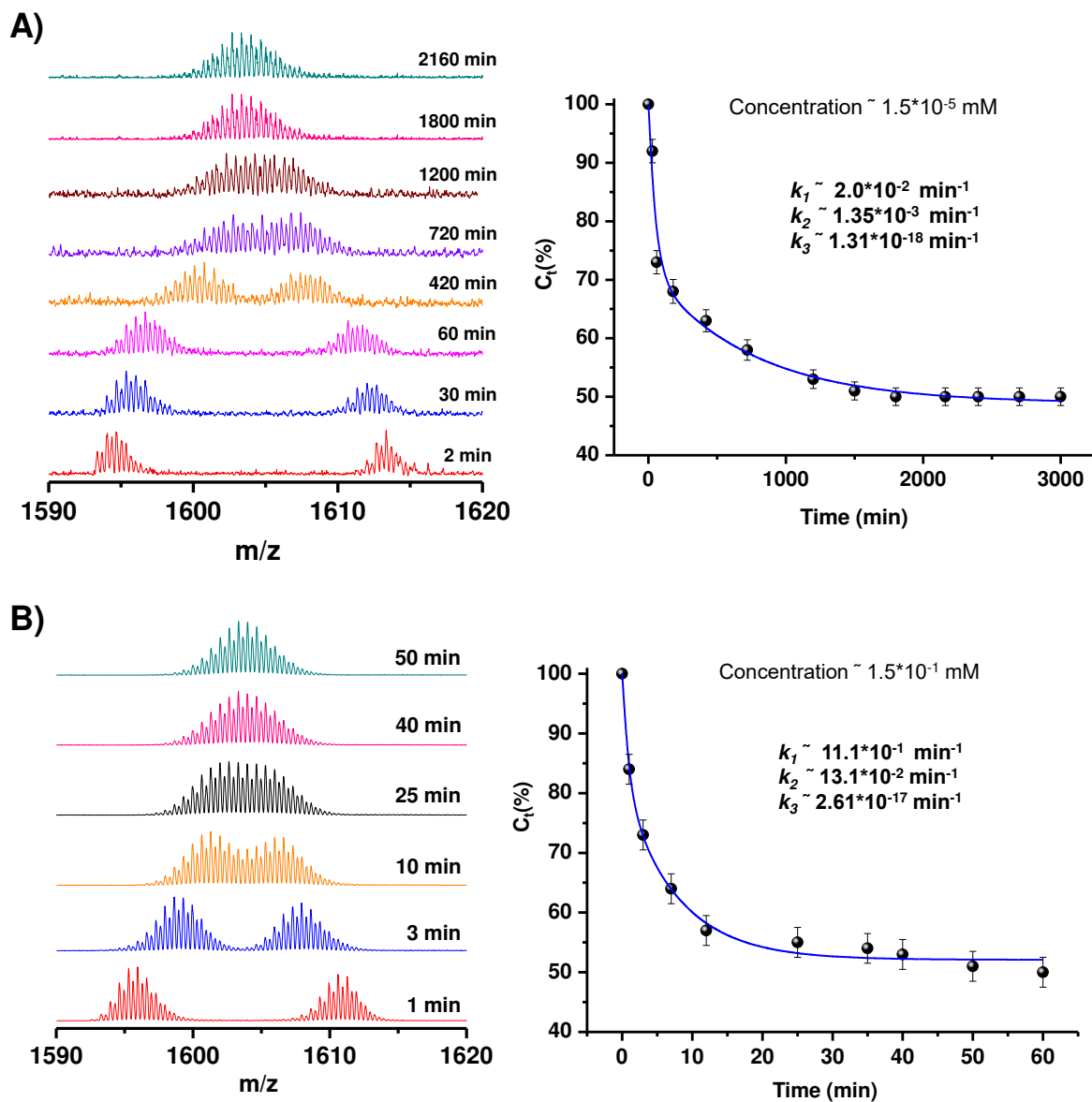
**Fig. S7. Reaction between  $[^{107}\text{Ag}_{29}(\text{BDT})_{12}(\text{TPP})_4]^{3-}$  and  $[^{109}\text{Ag}_{29}(\text{BDT})_{12}(\text{TPP})_4]^{3-}$  clusters in 1:1 molar ratio at room temperature.** (A) Intermediates stages of reaction between  $[^{107}\text{Ag}_{29}(\text{BDT})_{12}]^{3-}$  and  $[^{109}\text{Ag}_{29}(\text{BDT})_{12}]^{3-}$  in 1:1 molar ratio at room temperature. The mixture reaches equilibrium over a period of 2 h. (B) Intermediates stages of reaction between  $[^{107}\text{Ag}_{29}(\text{BDT})_{12}(\text{TPP})_n]^{3-}$  ( $n=0-4$ ) and  $[^{109}\text{Ag}_{29}(\text{BDT})_{12}(\text{TPP})_n]^{3-}$  ( $n=0-4$ ) in 1:1 molar ratio at room temperature, showing the intact TPP attached clusters in ESI MS. The mixture reaches equilibrium at similar time scales.



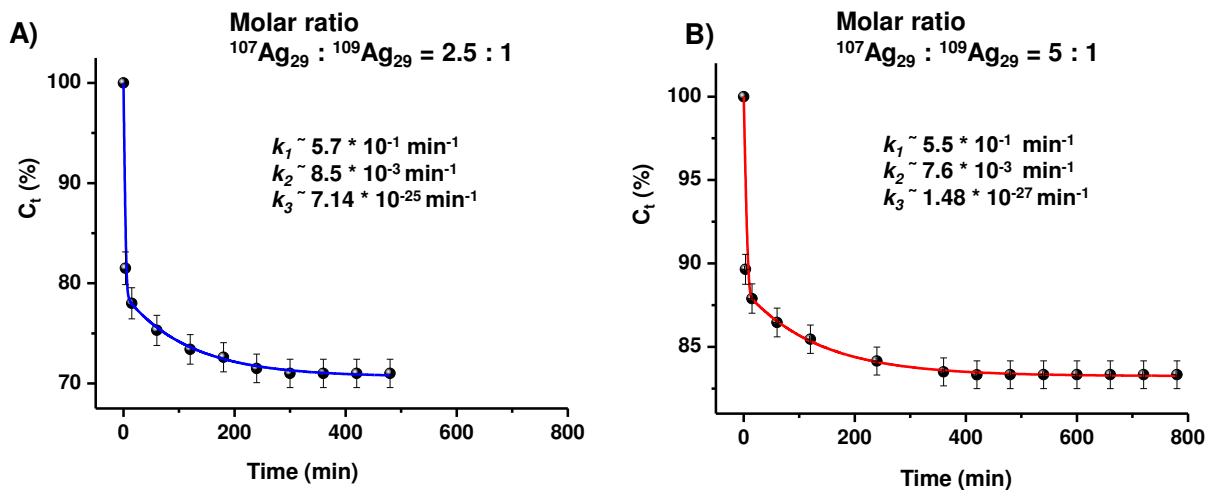
**Fig. S8. ESI MS of reaction product obtained by mixing the two isotopic  $[^{107}\text{Ag}_{29}(\text{BDT})_{12}(\text{TPP})_4]^{3-}$  and  $[^{109}\text{Ag}_{29}(\text{BDT})_{12}(\text{TPP})_4]^{3-}$  clusters at various molar ratios. (A)** Product obtained by mixing the two isotopic clusters  $[^{107}\text{Ag}_{29}(\text{BDT})_{12}]^{3-}$  and  $[^{109}\text{Ag}_{29}(\text{BDT})_{12}]^{3-}$  at varying molar ratios where in (a)  $[^{107}\text{Ag}_{29}(\text{BDT})_{12}]^{3-}$  is kept in higher concentration and in (b)  $[^{109}\text{Ag}_{29}(\text{BDT})_{12}]^{3-}$  is kept in higher concentration. The initial molar ratio of mixing the two clusters ( $[^{107}\text{Ag}_{29}(\text{BDT})_{12}]^{3-} : [^{109}\text{Ag}_{29}(\text{BDT})_{12}]^{3-}$ ) is indicated for each product observed. **(B)** Comparison of the experimental isotope patterns of the products with the calculated isotope patterns considering the abundances of each isotope from their initial molar ratio of mixing.



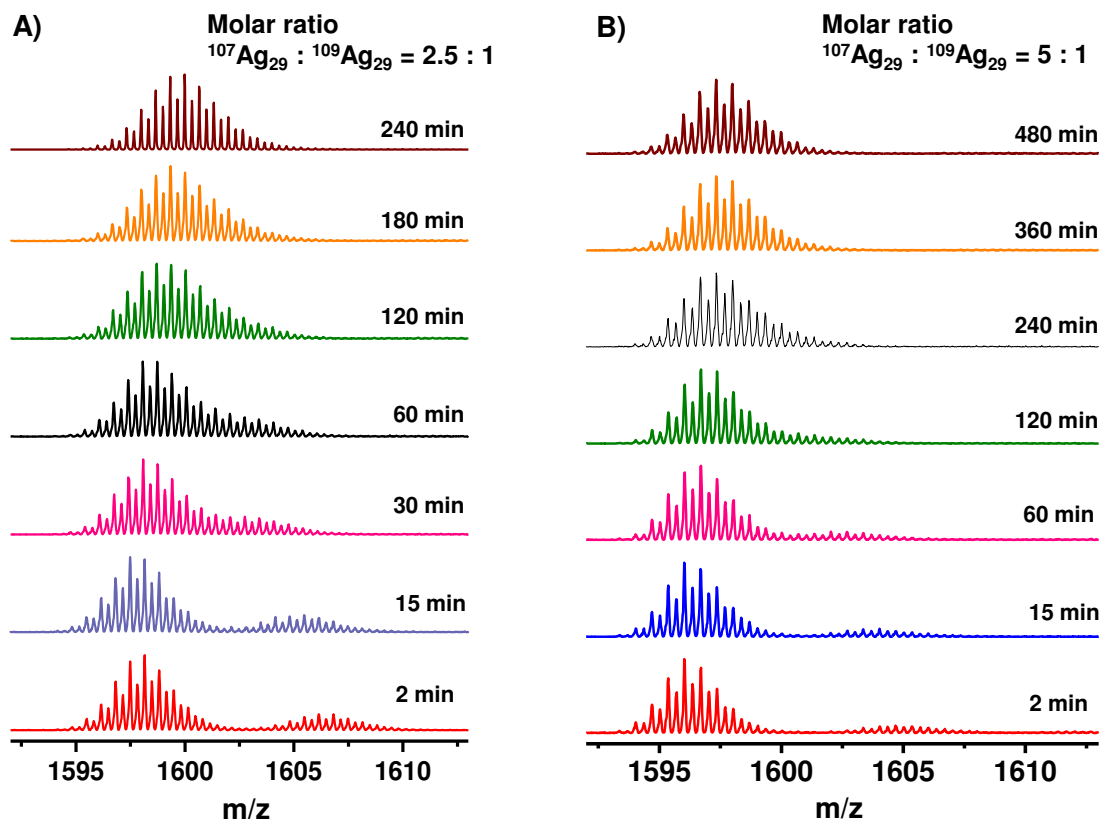
**Fig. S9. Time-dependent study of reaction between  $[\text{}^{107}\text{Ag}_{29}(\text{BDT})_{12}(\text{TPP})_4]^{3-}$  and  $[\text{}^{109}\text{Ag}_{29}(\text{BDT})_{12}(\text{TPP})_4]^{3-}$  in 1:1 molar ratio at various temperatures.** Time-dependent study showing the intermediates stages of reaction between  $[\text{}^{107}\text{Ag}_{29}(\text{BDT})_{12}]^{3-}$  and  $[\text{}^{109}\text{Ag}_{29}(\text{BDT})_{12}]^{3-}$  in 1:1 molar ratio at (A)  $40^{\circ}\text{C}$ , (B)  $60^{\circ}\text{C}$  and (C)  $0^{\circ}\text{C}$ . (D) Kinetic plot of the percentage of unexchanged parent cluster ( $C_i$ ) versus time at  $0^{\circ}\text{C}$ . The rate constants obtained from tri-exponential fitting are indicated in the figure.



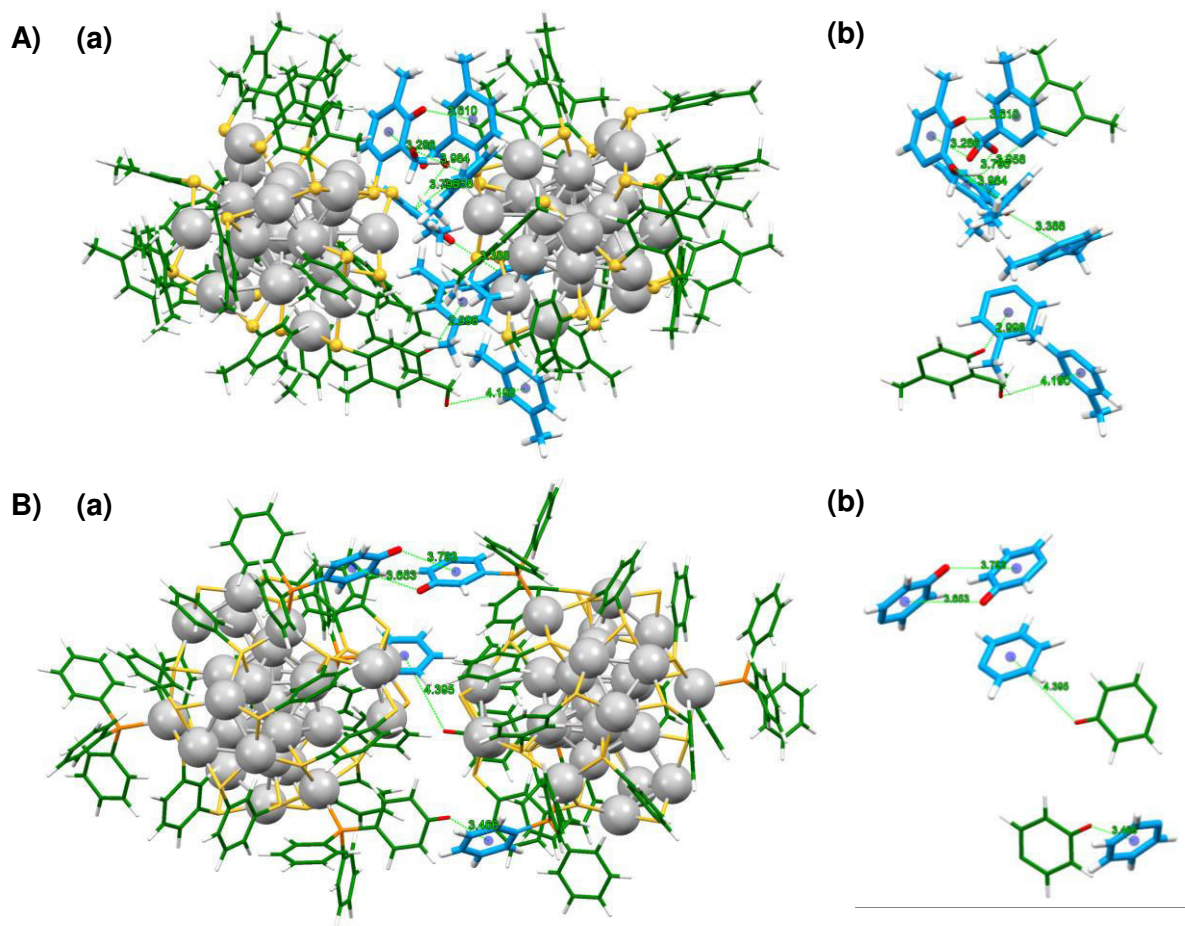
**Fig. S10. Kinetic study of isotopic exchange at different concentrations of  $[\text{Ag}_{29}(\text{BDT})_{12}(\text{TPP})_4]^{3-}$  clusters.** Time-dependent ESI MS and corresponding kinetic study showing the rate constants of the reaction at **A)**  $1.5 \times 10^{-5}$  mM and **B)**  $1.5 \times 10^{-1}$  mM concentration.



**Fig. S11. Kinetic study of isotopic exchange in  $[\text{Ag}_{29}(\text{BDT})_{12}(\text{TPP})_4]^{3-}$  clusters at different molar ratios of mixing.** Kinetic study of isotopic exchange at molar ratios of mixing of  $^{107}\text{Ag}_{29} : ^{109}\text{Ag}_{29}$  clusters, (A) 2.5:1 and (B) 5:1. The rate constants of the three stages of exchange in each case are denoted in the figure.



**Fig. S12. Time-dependent study of reaction between  $[\text{}^{107}\text{Ag}_{29}(\text{BDT})_{12}(\text{TPP})_4]^{3-}$  and  $[\text{}^{109}\text{Ag}_{29}(\text{BDT})_{12}(\text{TPP})_4]^{3-}$  at various molar ratios.** Time-dependent study showing the intermediate stages of reaction at  $^{107}\text{Ag}_{29} : ^{109}\text{Ag}_{29}$  molar ratios of (A) 2.5:1 and (B) 5:1.



**Fig. S13. Molecular docking studies.** Lowest energy geometry obtained from docking two **A)**  $[\text{Ag}_{25}(\text{DMBT})_{18}]^{-}$  and **B)**  $[\text{Ag}_{29}(\text{BDT})_{12}(\text{TPP})_4]^{3-}$  clusters. C-H $\cdots\pi$  interactions are indicated in the figure. Color codes: grey: Ag, yellow: S, orange: P, green: ligands. The H atoms involved in these interactions are shown in red and the benzene rings involved are shown in blue. Expanded view of the ligands involved in these C-H $\cdots\pi$  interactions are shown in the insets b.



**Table S2. Table showing ZPE and Gibbs free energy (*G*) values of the isotopic clusters.**

(a) For  $[\text{Ag}_{29}(\text{BDT})_{12}(\text{TPP})_4]^{3-}$  clusters

(i) Isotopically pure reactants

Cluster	ZPE (eV)	G (eV)
$[\text{}^{107}\text{Ag}_{29}(\text{BDT})_{12}(\text{TPP})_4]^{3-}$	2.400	-1262.250
$[\text{}^{109}\text{Ag}_{29}(\text{BDT})_{12}(\text{TPP})_4]^{3-}$	2.394	-1262.271

(ii) Mixed isotope product clusters with composition (m,n) = (15,14) and (14,15) in  $[\text{}^{107}\text{Ag}_m\text{}^{109}\text{Ag}_n(\text{BDT})_{12}(\text{TPP})_4]^{3-}$ .

(m,n) = (15,14)				(m,n) = (14,15)			
Position of $^{107}\text{Ag}$ atoms	Position of $^{109}\text{Ag}$ atoms	ZPE (eV)	G (eV)	Position of $^{107}\text{Ag}$ atoms	Position of $^{109}\text{Ag}$ atoms	ZPE (eV)	G (eV)
C-1 I-12 S-2	S-14	2.397	-1262.260	S-14	C-1 I-12 S-2	2.397	-1262.261
S-15	C-1 I-12 S-1	2.397	-1262.260	C-1 I-12 S-1	S-15	2.397	-1262.261
C-1 I-6 S-8	I-6 S-8	2.397	-1262.260	I-6 S-8	C-1 I-6 S-8	2.397	-1262.261

(b) For  $[\text{Ag}_{25}(\text{DMBT})_{18}]^-$  clusters

(i) Isotopically pure reactants

Cluster	Zero-point energy (ZPE) (eV)	Free Energy (G) (eV)
$[\text{}^{107}\text{Ag}_{25}(\text{DMBT})_{18}]^-$	1.655	-502.919
$[\text{}^{109}\text{Ag}_{25}(\text{DMBT})_{18}]^-$	1.650	-502.938

- (ii) Mixed isotope product clusters with composition (m,n) = (13,12) and (12,13) in  $[^{107}\text{Ag}_m^{109}\text{Ag}_n(\text{DMBT})_{18}]^-$



(m,n) = (13,12)				(m,n) = (12,13)			
Position of $^{107}\text{Ag}$ atoms	Position of $^{109}\text{Ag}$ atoms	ZPE (eV)	G (eV)	Position of $^{107}\text{Ag}$ atoms	Position of $^{109}\text{Ag}$ atoms	ZPE (eV)	G (eV)
C-1 I-12	S-12	1.652	-502.928	S-12	C-1 I-12	1.652	-502.929
S-12 C/I-1	C/I-12	1.652	-502.928	C/I-12	S-12 C/I-1	1.652	-502.929
C-1 I-6 S-6	I-6 S-6	1.652	-502.928	I-6 S-6	C-1 I-6 S-6	1.652	-502.929

**N.B.** C, I and S refers to centre, icosahedron and staple positions, respectively.



Cite this: *Nanoscale*, 2019, **11**, 321

## Appearance of SERS activity in single silver nanoparticles by laser-induced reshaping†

Kamalesh Chaudhari,<sup>‡a</sup> Tripti Ahuja,<sup>‡a</sup> Vasanthanarayan Murugesan,<sup>a</sup> Vidhya Subramanian,<sup>a</sup> Mohd Azhardin Ganayee,<sup>a</sup> Thomas Thundat <sup>\*b</sup> and Thalappil Pradeep <sup>\*a</sup>

We report simultaneous plasmonic scattering and Raman spectroscopic observations of single citrate capped silver nanoparticles (AgNPs) which exhibit surface enhanced Raman scattering (SERS) upon meeting specific conditions induced by laser (532 nm) exposure. We show that nanoparticles which are not initially SERS active become SERS active by laser-induced reshaping/reorientation. A set-up developed for these observations enabled *in situ* high speed time-lapse characterization using plasmonic and Raman spectroscopies in conjunction with dark-field microscopy (DFM). Changes in the AgNPs were confirmed by monitoring plasmonic scattering spectra and DFM images. Time-lapse observations have shown that laser-induced changes in the plasmonic properties of AgNPs resulted in the appearance of SERS. Spectral matching between plasmon resonance and downward molecular vibronic transitions for molecules adsorbed on the surface of plasmonic nanomaterials is attributed to the nanoparticle SERS. We have further shown that the release of silver ions by silver nanoparticles can be the probable reason for their plasmonic changes. Gold nanoparticles inert to such mild (850  $\mu$ W, 532 nm) laser-induced changes do not exhibit the appearance of SERS.

Received 12th August 2018,  
Accepted 14th November 2018

DOI: 10.1039/c8nr06497k

rscl.li/nanoscale

## Introduction

The development of new nanosensors with multiplexed properties requires spatial and temporal correlation.<sup>1–4</sup> Such correlation is necessary for dual confirmation of sensing signals.<sup>5,6</sup> Each signal provides specific information about the analyte and its interaction with the sensing element. Multiple signals from the same system can be used to assure the detection of the analyte with high specificity. For example, due to the recent advances in photothermal cantilever deflection spectroscopy, multiple properties of analytes (mass, electrical and optical properties) can be measured simultaneously.<sup>7,8</sup> Other examples include electroluminescence or chemi-resistance based sensors.<sup>9,10</sup> Such sensors can provide electri-

cal readout along with other physico-chemical parameters. At various stages in material characterization, it is necessary to find correlation between multiple properties of the material. For example, imaging of nanoparticles by diffraction-limited optical techniques cannot provide information about their actual size but on correlating the optical data with high resolution imaging techniques such as scanning electron microscopy,<sup>11</sup> transmission electron microscopy<sup>12</sup> or atomic force microscopy,<sup>13</sup> structural information of the nanoparticles has been obtained. Such complementary techniques are helpful in correlating optical properties of nanomaterials with their size, shape and structural arrangements. Various integrated techniques and instruments have been developed for such applications in the past.<sup>1,2,14</sup> In such applications, when it comes to visualizing plasmonic nanoparticles in native environments, spectroscopic observations are usually combined with DFM.<sup>1,2,6</sup> It allows the observation of single nanoparticles with a high signal to noise ratio, in real-time, in a native environment where interactions between the particles and analyte molecules take place. Observations with scanning electron microscopy<sup>11</sup> or transmission electron microscopy<sup>12</sup> can provide high resolution images for correlation studies but these observations are possible only under high vacuum which is not suitable for many studies and particles do not remain in their native state. Considering the difficulties in the use of microcantilevers in liquid media, such experiments are

<sup>a</sup>DST Unit of NanoScience (DST UNS) and Thematic Unit of Excellence (TUE), Department of Chemistry, Indian Institute of Technology Madras, Chennai 600 036, India. E-mail: pradeep@iitm.ac.in; Tel: +91044-2257-4208

<sup>b</sup>Department of Chemical and Materials Engineering, University of Alberta, Edmonton, Alberta, T6G 2 V4, Canada. E-mail: thundat@ualberta.ca

†Electronic supplementary information (ESI) available: FESEM and HSI images of AgNPs for spacing correlation, DFM montage of time-lapse images, intensity profiles for noise correction, citrate SERS band assignment, temporal and plasmonic colormaps for AuNPs with their characterization by UV-Vis and HRTEM, ICP-MS data for Ag ion quantification and time-lapse video showing plasmonic and Raman variations at the single particle level. See DOI: 10.1039/c8nr06497k

‡These authors contributed equally.

tedious in terms of obtaining good resolution for every sample and it is difficult to couple the same with molecular identification techniques such as confocal Raman microspectroscopy (CRM). Hence a combination of DFM with CRM can be considered as an efficient combination for the observation of samples in real-time, and in native-environments with enhanced spatial and temporal resolution.<sup>1,2,4,6,15</sup> Examples from the past include demonstrations by the El-Sayed group where they have shown applications of such combined Rayleigh and Raman scattering spectroscopy to monitor live cell division and concomitant molecular changes due to drug delivery to the cells.<sup>16–18</sup> In the recent past, our group has demonstrated a combination of DFM and CRM for the localization of molecules in bacterial and mammalian cells with silver<sup>4</sup> and gold<sup>6</sup> nanoparticles. The set-ups reported in the aforementioned studies were able to do measurements only on fixed samples without single particle tracking and repositioning. For the kind of study reported in the present manuscript, we have modified the set-up such that it can be used for *in situ* time dependent plasmonic and Raman scattering spectroscopic measurements with particle tracking capabilities, on single nanoparticles.

The effect of temperature and laser excitation on SERS has been studied in the past.<sup>19,20</sup> In these studies, either laser heating or changes in the substrate temperature were used as control parameters which can affect SERS blinking in single nanoparticles. However, the real-time fate of nanoparticles and the corresponding nanoplasmonic property effect on SERS blinking were not studied. In our study, we have periodically exposed nanoparticles to a Raman excitation laser where plasmonic changes after each Raman spectrum collection were monitored *in situ*. In the present work, we focus on the appearance of laser-induced SERS activity in citrate capped AgNPs without the aid of aggregating agents. Briefly, we call this technique Particle Dynamics Induced-Plasmon Enhanced Raman Scattering (PDI-PERS).

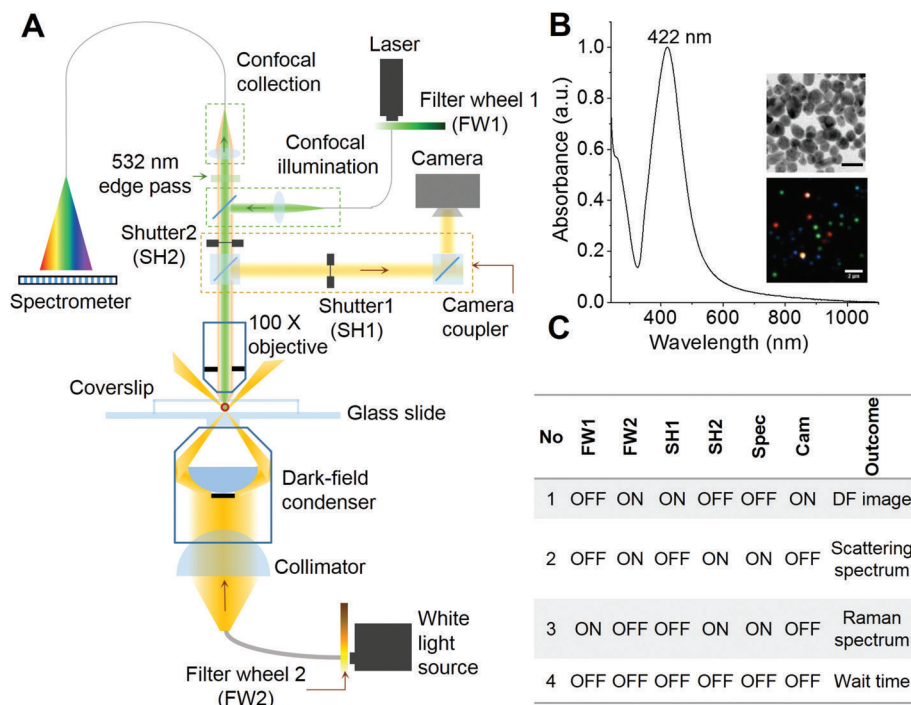
Various routes have been explored to control the SERS activity of nanoparticles in the past.<sup>21–27</sup> These routes are mainly based on controlling the plasmonic nanocavity<sup>14</sup> by changing the gap between nanoparticles such as aggregation, using linker molecules of different lengths<sup>23</sup> *etc.* We report our observations on the possibility of appearance of SERS activity in single AgNPs by laser-induced changes that can help particles to reshape/reorient resulting in SERS favorable on-resonance situations. This supports previously reported steady state observations by Zhang *et al.* which have shown that whenever there is spectral matching between plasmon resonance and downward molecular vibronic transitions, such situations are favorable for SERS and are called on-resonance situations.<sup>14</sup> To observe this effect, we have performed PDI-PERS measurements on immobilized single AgNPs. With the help of immobilization, the translational motion of particles was ceased but it allowed monitoring *in situ* shape and orientation related changes in the particles with the help of DF imaging and spectroscopic measurements. We have also demonstrated the release of silver ions<sup>28</sup> as a probable reason

for the appearance of SERS. Details of the data obtained are discussed in the next section.

## Results and discussion

### Set-up for PDI-PERS

A preliminary form of the set-up for combined plasmonic and Raman scattering microspectroscopy was reported previously by our group.<sup>6</sup> In the previous set-up, plasmonic and Raman spectroscopic measurements were possible with a conventional optical microscopy camera and fixed samples, in the absence of particle tracking, which required manual positioning of the samples during measurements. Also, the absence of automated shutters made it difficult to reposition samples for repetitive measurements. In the set-up developed for the present study (schematic shown in Fig. 1A), we have incorporated a high resolution camera coupler with two automated shutters (SH1 & SH2). These shutters control the signal passing towards the camera and the CCD spectrometer. The intensity of light used to expose the sample is controlled using automated ND filter wheels (FW1 & FW2). Fig. 1B shows the UV-Vis spectrum, TEM image and DFM image of AgNPs used in this study. The AgNPs are polydisperse in size and shape which is also reflected in the DFM image. The existence of single nanoparticles immobilized on an ITO coated glass slide was verified by field emission scanning electron microscopy (FESEM) (Fig. S1†). Single particles as well as small aggregates composed of 2–3 nanoparticles were observed in such images. DFM images on a similar length scale show mostly well separated single nanoparticles, supporting their immobilization (Fig. S1†). Some of the high magnification FESEM images at different locations of the sample are also shown in Fig. S2† which clearly depicts different morphologies of immobilized nanoparticles such as spheres, rods and faceted spheres. The table in Fig. 1C shows the sequence of shutters and ND filter wheels along with their outcomes that were followed during the time-lapse measurements of the immobilized AgNPs. Briefly, the sample was first exposed to white light and a DF image was collected (Sr no. 1, Fig. 1C). This step was followed by position correction using a particle tracking software (if necessary) and then the scattering spectrum was collected (Sr no. 2, Fig. 1C). Then the camera shutter was closed to prevent exposure of CCD to high intensity laser light and the sample was exposed to the Raman excitation laser to collect the spectrum (Sr no. 3, Fig. 1C). After that, all the shutters and ND filter wheels were brought to a close position before opening the camera shutter for the next cycle of measurements (Sr no. 4, Fig. 1C). Repeating this sequence periodically exposes AgNPs under observation to the laser of ~850  $\mu$ W intensity. The particle of interest was brought to the confocal volume by manual positioning before starting the measurement sequence and particle tracking was turned on. We observed from initial measurements that, upon exposure to periodic laser pulses, the plasmonic scattering spectrum and the color of the particle in the DFM image exhibited changes. These changes were



**Fig. 1** (A) Schematic of the set-up for PDI-PERS. Set-up also facilitates high resolution dark field imaging and real-time tracking of single nanoparticles for continuous monitoring of the same nanoparticle. Filter wheels (FW1 and FW2) and shutters (SH1 and SH2) control the intensity of light sources and exposure of spectrometer/camera, respectively. (B) UV-Vis spectrum of the AgNPs used in this study. Insets show TEM (scale bar – 20 nm, top) and hyperspectral dark field image (scale bar – 2  $\mu$ m, bottom) of AgNPs. (C) Time-lapse sequence of neutral density (ND) filter wheels, shutters and the outcomes of such combinations.

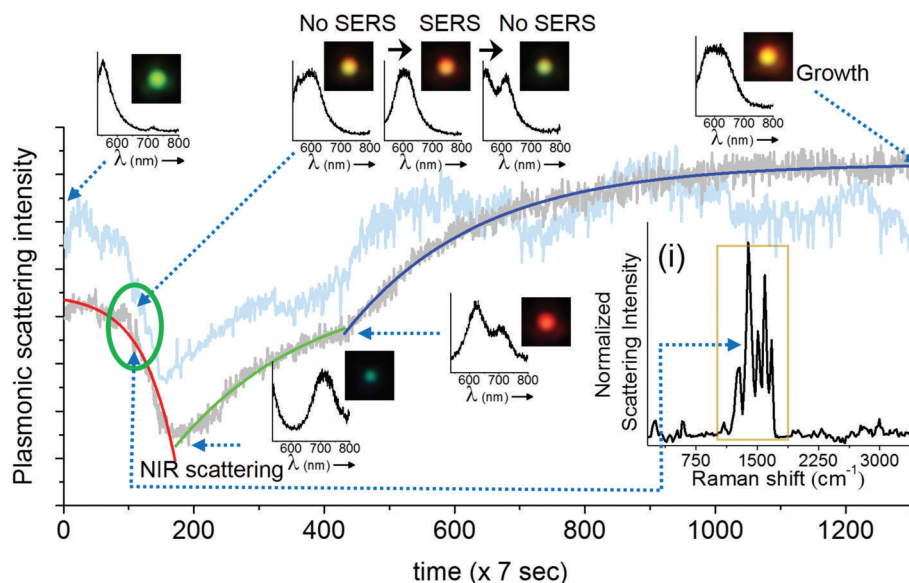
attributed to the laser-induced reshaping/reorientation of AgNPs. In the confocal set-up, the particle under observation alone was exposed to the laser. Hence, photoreduction and heating induced Ostwald ripening was seen only in the particle under observation. As the nanoparticles were linked to the substrate through mercaptopropyltrimethoxy silane, the linker allowed limited movement. Due to the lower power of the white light source in contrast to the laser, even if particles were exposed for long, they did not exhibit any change in color. These data along with the corresponding changes in the SERS activity of AgNPs are discussed in the next section.

#### Observing changes in plasmonic scattering and SERS activity of AgNPs using PDI-PERS

In this section, we demonstrate the PDI-PERS set-up to account for the observed dynamic changes in the shape and size of single nanoparticles and correlate the same with SERS activity. We also discuss the importance and necessity of DFM and plasmonic scattering spectroscopic measurements over the other. We have used water as the medium in these experiments as the refractive index of water (1.33) is close to that of glass (1.5) and this helps the use of a high magnification oil immersion 100 $\times$  objective for the same. But the use of water as a surrounding medium and an oil immersion objective for real-time observations limits the verification of changes in size and shape of AgNPs by other techniques such as AFM or SEM. Hence, we have discussed our observations of shape and size

changes in AgNPs with DFM and plasmonic scattering spectra alone which have been performed *in situ*.

Fig. 2 shows the temporal changes in the plasmonic scattering intensity (gray curve, integrated over DFM images) of a silver nanoparticle monitored with the aforementioned sequence of measurements (Fig. 1C). The scattering intensity of the particle decreases initially and then it increases gradually in two exponential steps. Previously reported simulations<sup>29</sup> of plasmonic nanoparticles have shown that the red shift in the plasmon is mainly a function of the aspect ratio or plasmon length of a nanoparticle, whereas particles with a small aspect ratio exhibit plasmonic scattering in the green region. Along these lines, it has been also shown that particles with a larger volume exhibit a larger scattering intensity as compared to smaller particles. This suggests that in our observations, while there was red shift in the plasmon (time unit 100–200), the particle volume did not change as corroborated by a decrease in the plasmonic scattering but later when its volume started increasing, growth was mostly lateral which resulted in the blue shift and broadening of the plasmonic scattering spectrum along with an increase in the scattering intensity. Fig. S3† shows a montage of all the particle images captured during the observation. Changes in the scattering intensity and plasmon resonance can be seen clearly in this montage. It has been reported previously that changes in the plasmon resonance wavelength are due to changes in the plasmonic length (the length over which oscillations take place),<sup>30</sup>



**Fig. 2** Variations in the plasmonic scattering intensity of a single isolated AgNP are plotted as a function of time (time-lapse interval –  $\times 7$  s). The gray curve shows intensity determined from DF images and the cyan curve shows the intensity integrated over temporal plasmonic spectra. The corresponding DF images and plasmonic scattering spectra of the particles are shown at the time points of interest. The green circle highlights the region where SERS activity of the particle was observed. Inset (i) shows the SERS spectrum of the citrate ligand on AgNPs, measured at the 108<sup>th</sup> time step. Beyond 900 seconds in the time axis, growth was saturated, thereafter no SERS was observed.

and the aspect ratio of the nanostructure, whereas changes in the scattering intensity are mainly related to the volume of the nanoparticle.<sup>29</sup> Such changes are highly dependent and directed by the nature of the ligand but in the context of this paper, we have not studied such details. The possible reason behind the exponential nature of changes is that the increase in the length and volume (lateral growth) of the particle can be complementary and once the changes in length saturate, then only changes in volume begin as indicated in the reported simulations.<sup>29,30</sup> This suggests step by step changes in the shape of the particle upon laser exposure. Similar kinds of changes were observed when the plasmonic scattering intensity was integrated over a complete spectrum of particles (cyan curve, Fig. 2). A better correlation between DFM images and scattering spectral intensities can also be visualized in ESI Video S1.† This video shows that the blue shift observed in DFM images (in the time window of 120–200) is actually due to the NIR shift in the plasmonic scattering spectrum which was not observable in DFM due to lower quantum efficiency of the CCD camera in the NIR region as it responded well only to the blue part of the scattering spectrum. However, in prolonged PDI-PERS measurements, there can be minor changes in the position due to heating of the substrate and the particle may move away from the confocal volume. Hence, DFM of the particle is necessary to monitor and track the position of the particle to facilitate undisturbed and prolonged measurements. Other benefit of DFM based intensity monitoring is that the CCD device can capture images over large areas of the sample and other nanoparticles can be monitored as a control. The minor intensity variations due to occasional auto positioning create similar intensity variations in other particles which can

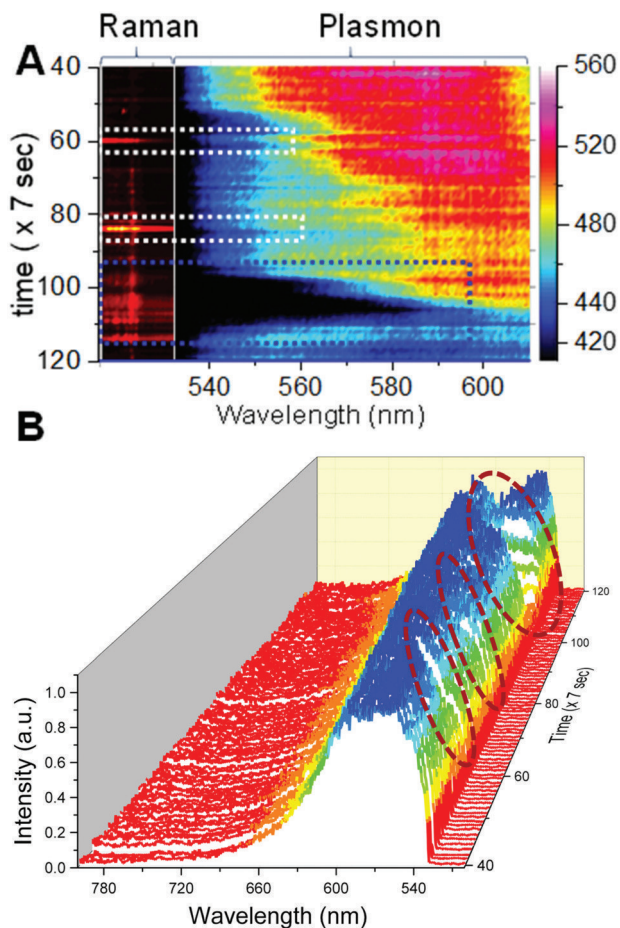
be used for noise correction. Details on noise correction are explained in Fig. S4.† To conclude, DFM in conjunction with the information provided by scattering spectroscopy can be used to interpret smooth RGB channel-based changes resulting from the reshaping of the particle. Inset (i) of Fig. 2 shows a resolved SERS spectrum of the citrate ligand anchored on a AgNP. Assignments for the observed Raman bands are provided in Fig. S5† and corresponding Table S1.†

#### Correlation between plasmonic scattering and SERS activity of AgNPs in time-lapse measurements

When the temporal intensity map of Raman spectra was correlated with the color map of plasmonic spectra (Fig. 3A), it was clear that the particle exhibited surface enhanced Raman activity whenever there was a red shift in the plasmon of AgNPs. The region of interest was expanded from the temporal plasmonic colormap shown in Fig. 3A.

Dotted white and blue squares in the spectral maps show the temporal region when SERS was observed. Complete temporal maps of Raman and plasmonic spectra are shown in Fig. S6.† Correlated plasmonic and Raman scattering spectra corresponding to the time points of interest are provided in Fig. S8.† SERS activity is highly specific to the structure of the plasmonic particle and the position of the vibrating molecule with respect to the particle, hence all the red shifts in the plasmon do not give rise to the SERS spectrum but SERS occurs only when all the favorable conditions are met. Although in this case, only a weak correlation was observed, we conclude that laser-induced changes in plasmons resulted in spectral matching between plasmon resonance and molecular vibronic transitions<sup>14</sup> responsible for maximum SERS activity observed at





**Fig. 3** (A) A selected portion of intensity and color map showing correlated changes in the Raman and plasmonic scattering of AgNPs, respectively made with the help of Matlab algorithm. Dotted squares show that SERS activity was observed upon red shift in the plasmonic scattering of the particle. (B) A temporal plasmonic scattering waterfall plot of AgNPs shows the region (navy blue colored dotted box in (A) and wine colored circles in (B)) when SERS activity of the nanoparticle was observed.

specific times. This phenomenon has been reported previously for plasmon enhanced Raman spectroscopy measurements performed on single molecules adsorbed on a silver substrate with spectrally matching and unmatched plasmons.<sup>14,31</sup> Changes in the scattering spectra can be seen clearly from the temporal 3D waterfall plot (Fig. 3B) for the nanoparticle under observation, and a more prominent correlation between the red shift of the plasmon and SERS can be seen. This is shown by the wine colored circles in Fig. 3B. The RGB profile for the particle is shown in Fig. S7† which was calculated from the time dependent DFM images of the nanoparticle. However, this was not the case when the plasmon was shifted to the NIR region and it finally became broad with a span over both green and red regions, supporting the high specificity of SERS to the particle structure and the position of the analyte with respect to the hot spots in addition to the plasmonic scattering in a specific region. Single nanoparticles exhibited SERS only when an on-resonance condition is fulfilled in which (a) laser exci-

tation and a high energy shoulder of sharp plasmon resonance match with the upward molecular vibronic transitions and (b) the plasmon resonance matches with the downward molecular vibronic transitions.<sup>14</sup> The aforementioned condition was not fulfilled when there was broad plasmonic scattering and hence it led to an off-resonance situation. A major conclusion from these overall data is that although the nanoparticle did not exhibit SERS activity initially, upon laser-induced changes, reshaping/reorientation made it into a SERS-active state. Conclusions made from these data were verified by repeating similar measurements on multiple single silver nanoparticles. Results of the same are discussed in the next section.

#### Laser-induced appearance of the SERS activity in single AgNPs

Fig. 4 shows further measurements performed on single AgNPs. Fig. 4A, B, and C show a Raman intensity map, correlation between the integrated intensity profiles of the Raman intensity and plasmon colormap and a temporal plasmonic colormap (Raman – 1000–2000  $\text{cm}^{-1}$ , plasmon – 562–595 nm) for single AgNPs. Time-lapse Raman and plasmonic spectra corresponding to the Raman and plasmonic colormaps in Fig. 4A and C are shown in Fig. 4D and E respectively. The region of 1000–2000  $\text{cm}^{-1}$  was selected because the most prominent vibrational features of citrate are in this region (refer to the inset of Fig. 2 and Table S1†). The corresponding region of plasmonic scattering is 562–595 nm. Data in Fig. 4B support the fact that SERS activity appeared whenever spectral matching between plasmon resonance and molecular vibronic transitions took place.<sup>14,31</sup>

Reproducibility was checked on various single AgNPs and similar correlation between colormaps and spectra is shown for other particles in Fig. S9.†

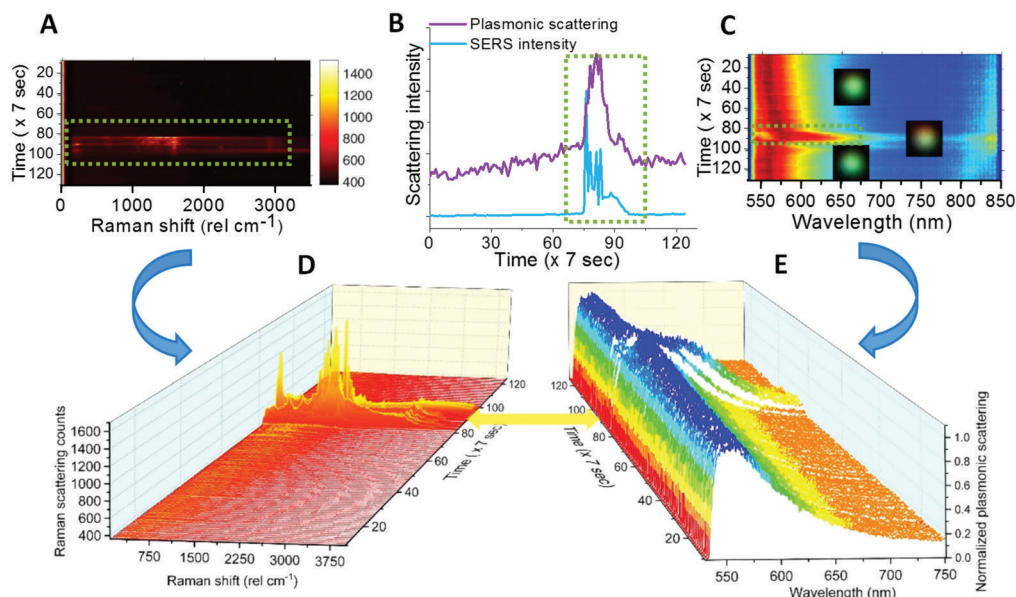
The SERS favorable situations of spectral matching can be called on-resonance situations and others correspond to off-resonance.<sup>14</sup> Plasmonic colormaps (Fig. 4C) justify that particles in the off-resonance situation can undergo laser-induced changes in structure and shape leading to on-resonance.

Temporal intensity profiles suggest that the on-resonance situation implies the possibility of SERS activity. As mentioned previously, fluctuations in the Raman intensity can be the outcome of high specificity of SERS to the position and orientations of molecules with respect to the hot spots on AgNPs. Despite the aforementioned fact, the appearance of SERS by laser-induced changes in single AgNPs is evident. It can be observed that due to intense periodic exposure to the laser, the particles keep reorienting and reshaping and because of this, the on-resonance situation cannot last for a long time. Hence, we have tried to control the intensity of the Raman excitation laser such that the SERS favorable on-resonance situation can be maintained for a longer period. These results are discussed in the next section.

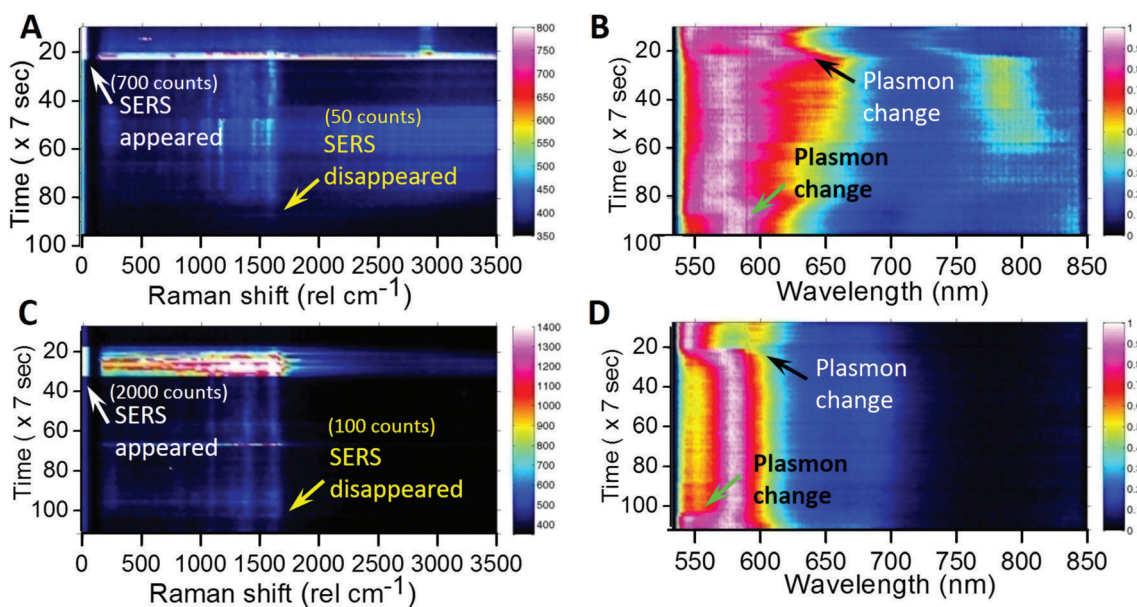
#### Maintaining SERS activity for a longer time by controlling the laser intensity

Temporal maps of Raman intensity (Fig. 5A and C) and plasmonic scattering (Fig. 5B and D) for two single AgNPs are





**Fig. 4** (A) Raman intensity map, (B) correlating integrated intensity profiles for Raman and plasmonic spectral match and (C) plasmonic scattering colormap and their corresponding time-lapse Raman and plasmonic scattering spectra (D&E) for single AgNPs. All the figures show that abrupt changes occurred during time 70 to 100 ( $\times 7$  s), the whole spectra are presented in D & E.



**Fig. 5** Raman intensity map (left) and plasmonic scattering colormap (right) for AgNP-3 (top, A, B) and AgNP-4 (bottom, C, D). White arrows show the point in time when laser intensity was decreased from 850  $\mu$ W to 85  $\mu$ W after the appearance of SERS. Yellow arrows show the point in time when SERS disappeared. The corresponding Raman intensity counts for the 1590  $\text{cm}^{-1}$  peak are also shown within brackets. Black and green arrows show the corresponding points in time of plasmonic colormaps when SERS appeared and disappeared respectively.

shown in Fig. 5. During these measurements, the particle was excited with a laser at 850  $\mu$ W intensity initially. As soon as SERS activity was observed, the excitation laser intensity was reduced to 85  $\mu$ W. White arrows (marked as SERS appeared) in Fig. 5A and C show the point in time when the laser intensity was reduced, and this can be seen by reduction in the intensity and width of the Rayleigh peak in the Raman spectrum. The

corresponding changes in the plasmonic spectrum (black arrows, marked as Plasmon change) can be seen in the plasmonic color maps (Fig. 5B and D). In this way, we were able to slow down the changes in the plasmon position of AgNPs as well as orientation, so as to maintain the SERS activity for a longer time. However, this only slows down changes but does not stop them completely. Hence after sometime, upon

changes in the plasmon (green arrows, marked as the plasmon change) back to the off-resonance situation, SERS activity of the AgNPs diminishes (yellow arrows, marked as SERS disappeared).

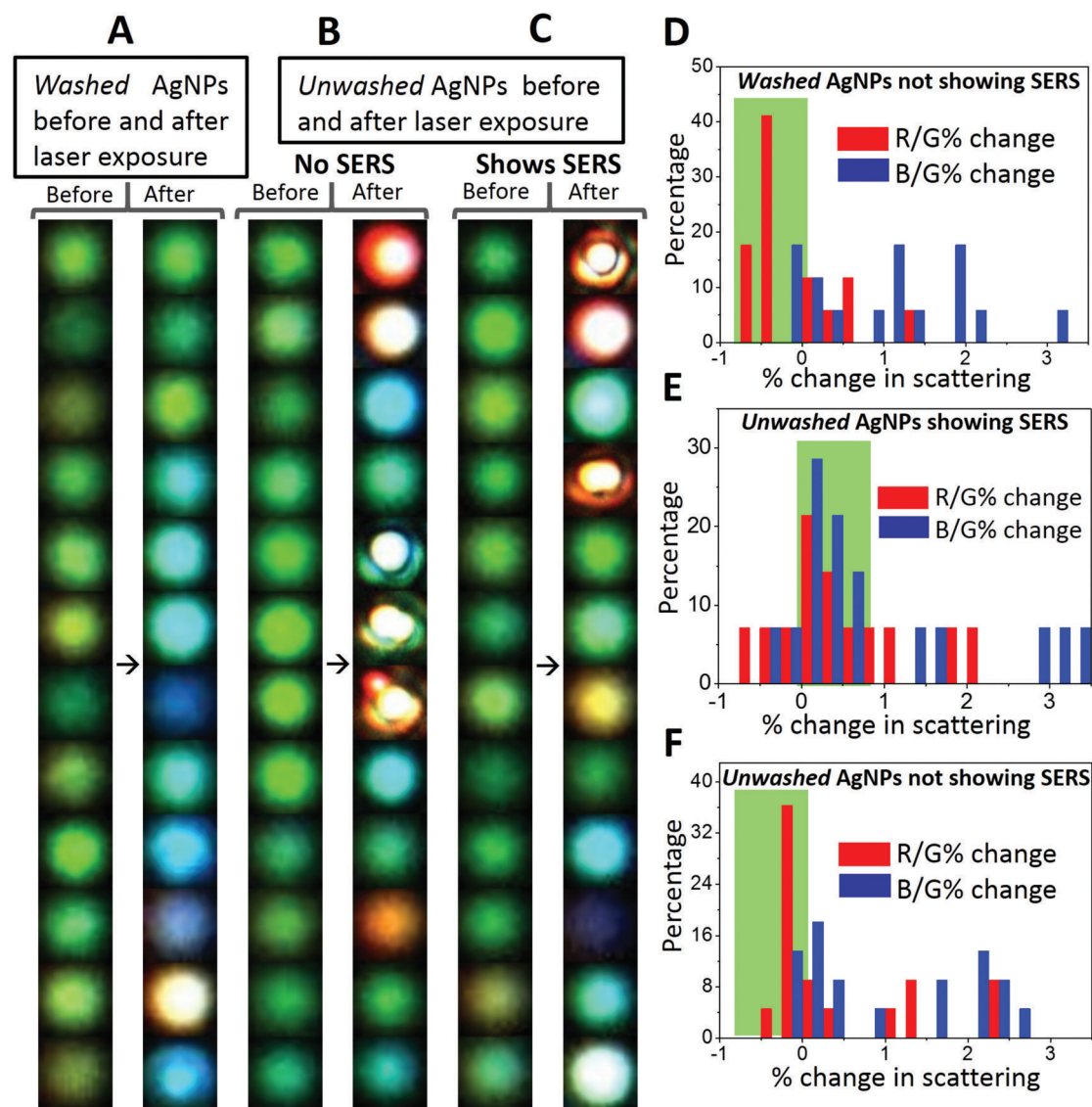
This proves the possibility of controlling SERS activity by slowing down the laser-induced changes in the SERS favorable on-resonance plasmon of AgNPs.

We have also performed such observations on single gold nanoparticles (Fig. S10†). For them, even after performing measurements for a long time, no laser-induced changes were observed due to better stability of AuNPs over AgNPs (Fig. S10†). Only constant luminescence instead of SERS was detected. In order to understand laser-induced changes, we have performed various control experiments by performing

prolonged observations in the absence of laser exposure. In those cases, no such appearance of SERS was seen in AgNPs.

#### Role of silver ions released from AgNPs in the appearance of laser-induced SERS

In control observations, it was found that the growth and reshaping of AgNPs is assisted by the release of silver ions from nanoparticles in the surrounding region. To study this, time-lapse experiments were performed on the AgNPs washed extensively with DI water (four times at an interval of six hours ( $4 \times 6$  hours – 24 hours) after sample immobilization). These particles were referred to as *washed* particles. To prove the decrease in the release of silver ions with time and repeated washing steps, ICP-MS (inductively coupled plasma mass



**Fig. 6** Stacks of single particle images for (A) *washed* AgNPs before and after laser exposure which did not exhibit SERS, (B) *unwashed* AgNPs before and after laser exposure which did not exhibit SERS and (C) *unwashed* AgNPs before and after laser exposure which exhibited SERS. Changes in the red (R) and blue (B) channel scattering intensities relative to the green channel (R/G and B/G) were calculated. Distributions of the percentage change in the aforementioned relative scattering intensities before and after laser exposure are plotted for AgNPs, (D) *washed* AgNPs, (E) *unwashed* AgNPs showing SERS, and (F) *unwashed* AgNPs not showing SERS.

spectrometry) of the collected water was performed. These data are provided in Table S2.† The content of silver ions decreased after successive washing steps. Based on the ICP-MS data of release of silver ions, detailed calculations were performed corresponding to the number of atoms and nanoparticles formed and their effect on the increment of the volume of the nanoparticles. From calculations, it was found that the effective concentration of silver ions released (3.47 ppb) after 6 h is enough to form  $2.5 \times 10^{11}$  new nanoparticles of 50 nm diameter by photoreduction. The same quantity of ions is also enough to increase the diameter of  $1.4 \times 10^{11}$  nanoparticles to 70 nm from 50 nm. Therefore, an increase in the number and growth of nanoparticles is possible from the ions released. As photoreduction is limited to the confocal volume, we haven't observed an increase in the plasmonic particles elsewhere on the substrate.

*Washed* AgNPs were almost inert to the laser-induced changes and no SERS was observed (Fig. 6A). A total of seventeen (twelve are shown here) particles were monitored and only one exhibited laser-induced SERS. The probability of appearance of SERS in *washed* AgNPs was as low as ~6%. AgNPs which were *washed* once with DI water after immobilization exhibited good probability of the laser-induced SERS (~44%). To differentiate from the *washed* AgNPs, these were referred to as *unwashed* AgNPs. The images of *unwashed* particles before and after laser exposure are shown in Fig. 6B which did not exhibit SERS. Fig. 6C shows images of *unwashed* particles before and after laser exposure which exhibited SERS. A total of thirty-six particles (twenty-four shown here) were monitored and fourteen exhibited laser-induced SERS. It can be seen from the images of *washed* and *unwashed* AgNPs before and after laser exposure that *unwashed* particles are more prone to changes in scattering as compared to *washed* particles. For *unwashed* particles, in some cases, drastic changes in the scattering images can be seen. Time dependent changes in the size and shape of nanoparticles can occur due to the Ostwald ripening process. Ostwald ripening of silver nanoparticles in a synthetic mixture has been reported in the past where excess silver ions assist a controlled growth of specific morphologies.<sup>32</sup> In our observations, we have immobilized silver nanoparticles and no excess silver ions were added. Hence, Ostwald ripening is limited to the presence of silver ions released from the surrounding silver nanoparticles. To simplify these observations, changes in the red (R) and blue (B) channel scattering intensities relative to the green channel (R/G and B/G) were calculated and distributions of the percentage change in these quantities before and after laser exposure were plotted.

Details of the calculations are provided in the end of the ESI.† Direct changes in the RGB intensity were not a good parameter to group particles because RGB intensities vary for individual particles. These percentage changes are shown in Fig. 6D, E and F. For the AgNPs which do not exhibit SERS, %R/G change is mostly negative, whereas for the AgNPs which exhibit SERS, %R/G change is mostly positive. Negative and positive % changes are shaded in green color for proper identi-

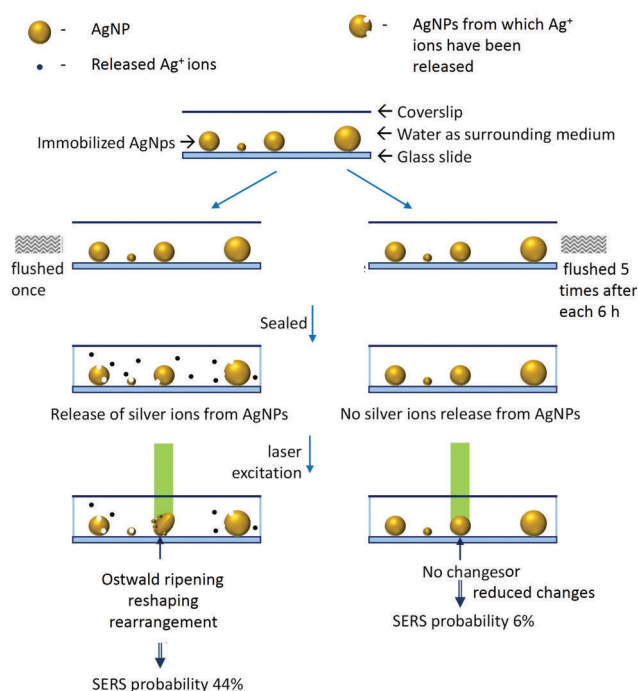


Fig. 7 Schematic to explain the effect of laser irradiation and silver ion release from AgNPs on the appearance of SERS.

fication. This suggests that laser-induced appearance of SERS is assisted by silver release. We conclude our study with certain observations as below.

## Conclusions

We have developed a set-up which enables multispectral, high speed (8–10 s) time-lapse characterization of single nanoparticles by plasmonic and Raman scattering spectroscopy. Observations using this set-up have shown that AgNPs which are initially in the off-resonance situation can change into the on-resonance situation upon exposure to a Raman excitation laser. We note that effects of temperature and laser excitation on SERS blinking have been studied in the past.<sup>19,20</sup> The real-time fate of nanoparticles and consequence of nanoplasmonic properties on SERS blinking are our contributions to this literature. We have also shown that once favorable conditions (like reshaping/reorientation) are obtained, the on-resonance situation can be maintained for longer times by lowering the intensity of the excitation laser from 850  $\mu$ W to 85  $\mu$ W. Supporting experiments<sup>28</sup> have shown that such changes in AgNPs are assisted by the release of silver ions from the surrounding nanoparticles whereas gold nanoparticles are completely inert to such changes due to their relatively less reactivity. We have also performed experiments to correlate the release of silver ions from AgNPs with the probability of the appearance of SERS. It was found that *washed* AgNPs exhibited ~6% SERS probability while *unwashed* AgNPs exhibited ~44%. We have simplified these observations with the help of a schematic shown in Fig. 7.



This study opens up the possibility of multispectral observations of intermolecular, interparticle reactions in real-time at the single-particle/single-molecule level. In the presented study, although measurements with water as a surrounding medium open up various possibilities for investigating biological samples, the limitation was that one needs to rely on dark-field spectroscopy for inference on the morphology of nanoparticles and direct correlation with FESEM was not possible. Such observations will be able to provide new insights into the behavior of molecules on the surface of SERS active nanoparticles. We speculate that many temporal changes with SERS active nanoparticles may involve intermittent states of molecules/particles which may be revealed by studies using the presented strategy.

## Experimental

### Materials

Tetrachloroauric acid trihydrate ( $\text{HAuCl}_4 \cdot 3\text{H}_2\text{O}$ ) (99.9%) was made and purified in lab using pure gold purchased from the local market. Trisodium citrate (>99%) was purchased from Qualigens. 3-(Mercaptopropyl)trimethoxysilane was purchased from Sigma Aldrich. Silver nitrate (99.9%) was purchased from RANKEM, India. Deionized water (DI) ( $\sim 18.2 \text{ M}\Omega$ ) obtained from Millipore was used throughout the experiments.

### Synthesis of citrate capped silver nanoparticles

The synthesis of AgNPs was done by the Turkevich method.<sup>33</sup> Briefly,  $\text{AgNO}_3$  (17 mg in 100 mL DI water) solution was heated to boil and then trisodium citrate (40 mg) was added. Once the color of the solution changed to pale yellow, it was quenched under tap water. The synthesis of AgNPs was confirmed by UV-Vis spectroscopy and transmission electron microscopy (TEM) imaging. A strong localized surface plasmon resonance (LSPR) peak was observed at  $\sim 422 \text{ nm}$  in the UV-Vis spectrum (Fig. 1B). Synthesized AgNPs were polydisperse in size and their shape was studied by TEM.

### Synthesis of citrate capped gold nanoparticles

The synthesis of AuNPs was done by the Turkevich method.<sup>33</sup> Briefly, 100 mL of  $\text{HAuCl}_4$  (1.25 mM in DI water) solution was heated to boil in a round bottom flask and stirred at 400 rpm. Upon boiling, 2 mL trisodium citrate (1%) solution was added. Gradually, the color of the solution changed to wine red. Then the solution was cooled at room temperature. The synthesis of AuNPs was confirmed by UV-Vis spectroscopy and TEM imaging (Fig. S11†). A strong LSPR peak was observed at  $\sim 535 \text{ nm}$  in the UV-Vis spectrum. Synthesized AuNPs were almost uniform with a diameter of  $\sim 25\text{--}35 \text{ nm}$  as observed under TEM.

### UV-Visible extinction spectroscopy

UV-Visible spectroscopic measurements were performed using a PerkinElmer Lambda 25 spectrophotometer in the range of 200–1100 nm.

### Transmission electron microscopy

Transmission electron microscopic (TEM) measurements were performed using a JEOL 3010, 300 kV instrument. Samples were spotted on carbon coated copper grids by drop casting followed by drying in ambient air.

### Field emission scanning electron microscopy (FESEM)

FESEM measurements were performed using an Inspect F50 from FEI, with 1.2 nm resolution at 30 kV in SE (Fig S1A†). Later, FESEM experiments were done using a Tescan-Mira 3 LMH instrument (Fig S2†). Samples were prepared by immobilizing AgNPs on ITO coated glass slides.

### Particle dynamics induced-plasmon enhanced Raman scattering (PDI-PERS)

The PDI-PERS set-up was built by integrating three separate instruments namely a Cytoviva™ high resolution dark field condenser, WiTec GmbH confocal Raman microscope and Dage Excel M cooled CCD camera. The core part of the integration was a coupler comprised of two automatic shutters and two automated ND filter wheels (Thorlabs) as shown in the schematic (Fig. 1A). These automated shutters and ND filter wheels were controlled using a home built controller and LABVIEW software. Particle tracking abilities were included in the LABVIEW software to take care of changes in the position of the sample, if any during measurements. Samples were mounted on a piezo stage for real-time positioning using a tracking software. The piezo stage can correct the position of the particle with  $\sim 27 \text{ nm}$  resolution. A frequency doubled Nd:YAG diode laser (532 nm) was used for Raman excitation of the sample. An L1090 halogen lamp from International Light Technologies Inc., USA was used for white light illumination (400–1000 nm) required for DFM. Samples were focused using a 100 $\times$  oil immersion objective (UPLFLN, Olympus). The scattering signal after passing through a 535 nm edge pass filter was dispersed using a grating (150 grooves per mm) onto a 1024 pixel charge coupled device (CCD) spectrometer.

### Immobilization of nanoparticles

Immobilization of AgNPs and AuNPs on a glass slide was done by the pinpoint immobilization method.<sup>3</sup> Briefly, an ultrasonically cleaned 1 mm thick glass slide (SCHOTT) was flushed with a 0.2  $\mu\text{M}$ , 5 mL solution of (3-mercaptopropyl)trimethoxysilane (in ethanol). Then it was washed extensively with DI water followed by dropping of 10  $\mu\text{L}$  (10 fold diluted) solution of nanoparticles over it and covering it with a clean glass coverslip. After incubation for 30 minutes, the coverslip was removed and the glass slide was washed extensively with DI water to remove unbound nanoparticles. Then 10  $\mu\text{L}$  DI water was dropped on the immobilized region and covered with a 0.145 mm thick Nexterion® clean room cleaned coverslip. It was sealed with nail polish on its sides to avoid drying of the samples. In the overall procedure, care was taken to expose only one side of the slide to chemicals.

## Conflicts of interest

There are no conflicts to declare.

## Acknowledgements

We thank the Department of Science and Technology, Government of India for constantly supporting our research program on nanomaterials. We thank the University of Alberta and the Canada Excellence Research Chairs (CERC) for supporting our research program.

## Notes and references

- 1 X. Shi, H. W. Li, Y. L. Ying, C. Liu, L. Zhang and Y. T. Long, *Chem. Commun.*, 2016, **52**, 1044–1047.
- 2 M. Aioub and M. A. El-Sayed, *J. Am. Chem. Soc.*, 2016, **138**, 1258–1264.
- 3 K. Chaudhari and T. Pradeep, *Sci. Rep.*, 2014, **4**, 27–29.
- 4 S. Vishnupriya, K. Chaudhari, R. Jagannathan and T. Pradeep, *Part. Part. Syst. Charact.*, 2013, **30**, 1056–1062.
- 5 V. Subramanian, S. Jena, D. Ghosh, M. Jash, A. Baksi, D. Ray and T. Pradeep, *ACS Omega*, 2017, **2**, 7576–7583.
- 6 K. Chaudhari and T. Pradeep, *J. Biomed. Opt.*, 2015, **20**, 046011.
- 7 K. Prashanthi, A. Phani and T. Thundat, *Nano Lett.*, 2015, **15**, 5658–5663.
- 8 D. Lee, S. Kim and T. Thundat, *Nano-Bio Sensing, Imaging, Spectrosc.*, 2013, **8879**, 88790Q.
- 9 C. Larson, B. Peele, S. Li, S. Robinson, M. Totaro, L. Beccai, B. Mazzolai and R. Shepherd, *Science*, 2016, **351**, 1071–1074.
- 10 F. J. Ibañez and F. P. Zamborini, *Small*, 2012, **8**, 174–202.
- 11 M. Hu, C. Novo, A. Funston, H. Wang, H. Staleva, S. Zou, P. Mulvaney, Y. Xia and G. V. Hartland, *J. Mater. Chem.*, 2008, **18**, 1949.
- 12 C. Rosman, S. Pierrat, A. Henkel, M. Tarantola, D. Schneider, E. Sunnick, A. Janshoff and C. Sönnichsen, *Small*, 2012, **8**, 3683–3690.
- 13 Y. Song, P. D. Nallathamby, T. Huang, H. E. Elsayed-Ali and X.-H. N. Xu, *J. Phys. Chem. C*, 2010, **114**, 74–81.
- 14 R. Zhang, Y. Zhang, Z. C. Dong, S. Jiang, C. Zhang, L. G. Chen, L. Zhang, Y. Liao, J. Aizpurua, Y. Luo, J. L. Yang and J. G. Hou, *Nature*, 2013, **498**, 82–86.
- 15 K. Ock, W. Il Jeon, E. O. Ganbold, M. Kim, J. Park, J. H. Seo, K. Cho, S. W. Joo and S. Y. Lee, *Anal. Chem.*, 2012, **84**, 2172–2178.
- 16 M. R. K. Ali, Y. Wu, T. Han, X. Zang, H. Xiao, Y. Tang, R. Wu, F. M. Fernández and M. A. El-Sayed, *J. Am. Chem. Soc.*, 2016, **138**, 15434–15442.
- 17 B. Kang, L. A. Austin and M. A. El-Sayed, *ACS Nano*, 2014, **8**, 4883–4892.
- 18 B. Kang, L. A. Austin and M. A. El-Sayed, *Nano Lett.*, 2012, **12**, 5369–5375.
- 19 S. R. Emory, R. A. Jensen, T. Wenda, M. Han and S. Nie, *Faraday Discuss.*, 2006, **132**, 249–259.
- 20 Y. Maruyama, M. Ishikawa and M. Futamata, *J. Phys. Chem. B*, 2004, **108**, 673–678.
- 21 M. F. Cardinal, E. Vander Ende, R. A. Hackler, M. O. McAnally, P. C. Stair, G. C. Schatz and R. P. Van Duyne, *Chem. Soc. Rev.*, 2017, **46**, 3886–3903.
- 22 H. Ko, S. Singamaneni and V. V. Tsukruk, *Small*, 2008, **4**, 1576–1599.
- 23 T. S. Sreeprasad and T. Pradeep, *Langmuir*, 2011, **27**, 3381–3390.
- 24 N. H. Kim, S. J. Lee and M. Moskovits, *Adv. Mater.*, 2011, **23**, 4152–4156.
- 25 X. Yu, H. Cai, W. Zhang, X. Li, N. Pan, Y. Luo, X. Wang and J. G. Hou, *ACS Nano*, 2011, **5**, 952–958.
- 26 N. M. B. Perney, F. J. García De Abajo, J. J. Baumberg, A. Tang, M. C. Netti, M. D. B. Charlton and M. E. Zoorob, *Phys. Rev. B: Condens. Matter Mater. Phys.*, 2007, **76**, 1–5.
- 27 V. K. Rao and T. P. Radhakrishnan, *ACS Appl. Mater. Interfaces*, 2015, **7**, 12767–12773.
- 28 G. Lei, P. F. Gao, T. Yang, J. Zhou, H. Z. Zhang, S. S. Sun, M. X. Gao and C. Z. Huang, *ACS Nano*, 2017, **11**, 2085–2093.
- 29 P. K. Jain, K. S. Lee, I. H. El-Sayed and M. A. El-Sayed, *J. Phys. Chem. B*, 2006, **110**, 7238–7248.
- 30 E. Ringe, M. R. Langille, K. Sohn, J. Zhang, J. Huang, C. A. Mirkin, R. P. Van Duyne and L. D. Marks, *J. Phys. Chem. Lett.*, 2012, **3**, 1479–1483.
- 31 W. Zhu and K. B. Crozier, *Nat. Commun.*, 2014, **5**, 1–8.
- 32 X. Wu, P. L. Redmond, H. Liu, Y. Chen, M. Steigerwald and L. Brus, *J. Am. Chem. Soc.*, 2008, **130**, 9500–9506.
- 33 J. Kimling, M. Maier, B. Okenve, V. Kotaidis, H. Ballot and A. Plech, *J. Phys. Chem. B*, 2006, **110**, 15700–15707.

**Electronic Supplementary Information (ESI) for the paper:**

**“Appearance of SERS activity in single silver nanoparticles by laser-induced reshaping”**

Kamalesh Chaudhari,<sup>a#</sup> Tripti Ahuja,<sup>a#</sup> Vasanthanarayan Murugesan,<sup>a</sup> Vidhya Subramanian,<sup>a</sup> Mohd Azhardin Ganayee,<sup>a</sup> Thomas Thundat,<sup>b\*</sup> and Thalappil Pradeep<sup>a\*</sup>

<sup>a</sup> DST Unit of NanoScience (DST UNS) and Thematic Unit of Excellence (TUE), Department of Chemistry, Indian Institute of Technology Madras, Chennai 600 036, India, Tel: +91044-2257-4208, E-mail: pradeep@iitm.ac.in

<sup>b</sup> Department of Chemical and Materials Engineering, University of Alberta, Edmonton, Alberta, T6G 2V4, Canada, E-mail: thundat@ualberta.ca.

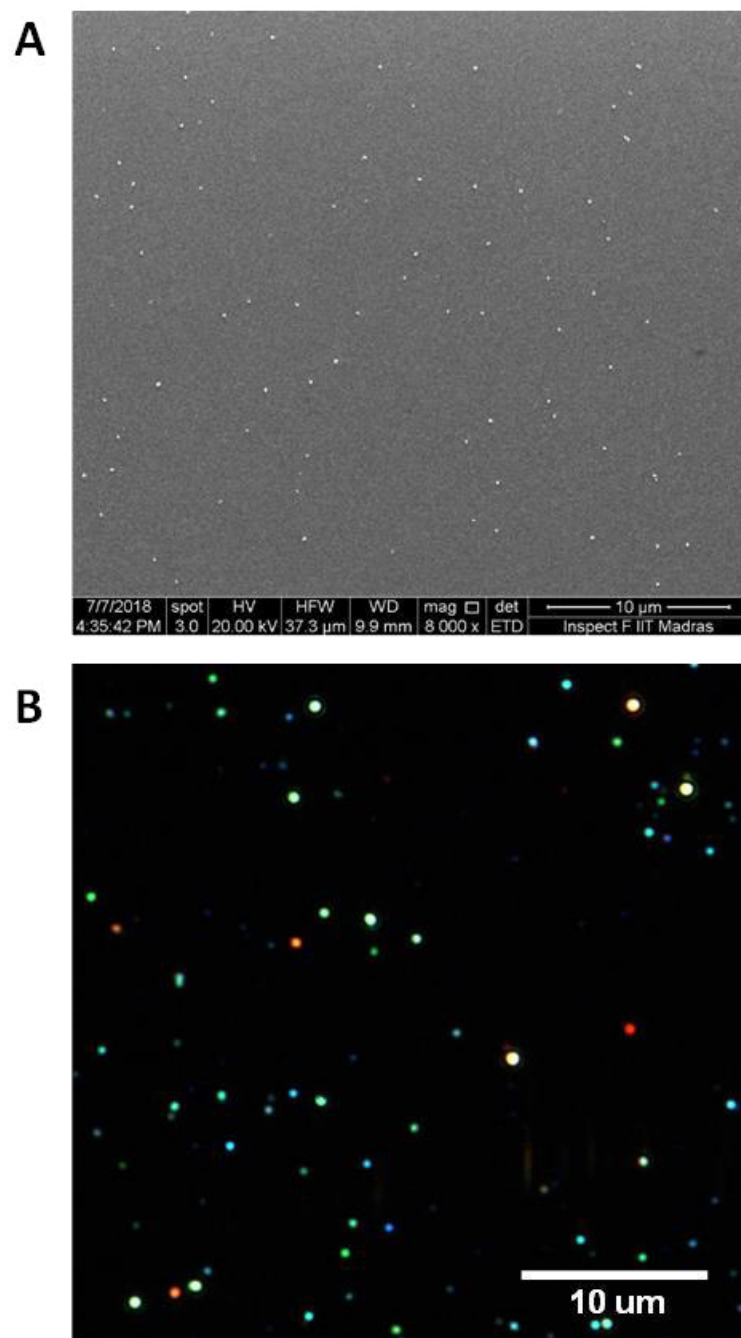
# Equal contribution

\* Corresponding authors

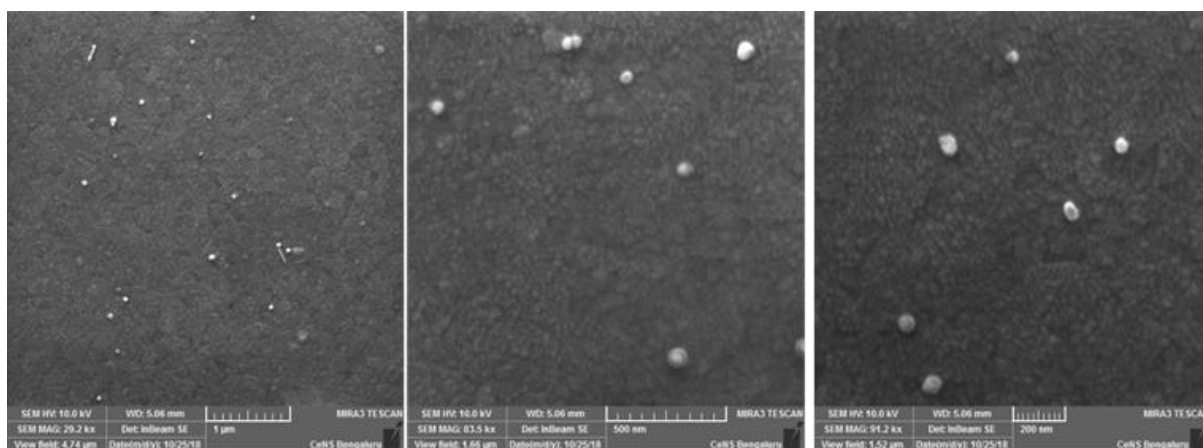
## Table of Contents

S. NO	Title	Page No.
1	Verification of AgNPs immobilization done with FESEM imaging	3
2	High magnification FESEM images for depicting different morphologies of AgNPs	4
3	Montage constructed from DFM images of single AgNP periodically exposed to laser	5
4	Method for the noise correction of temporal intensity profile of AgNP determined using DFM	6
5	Assignments of the Raman bands observed in the SERS spectrum of citrate	7
6	Temporal plasmonic color map and Raman intensity map of AgNP	8
7	RGB profile for the particle calculated from the time-dependent DFM images	9
8	Plasmonic and Raman scattering spectra of AgNP discussed in the main text	10
9	Correlating Raman map, plasmonic colormap and intensity profile with their corresponding time-lapse Raman and plasmonic spectra	11
10	Temporal plasmonic colormap and Raman intensity map of AuNPs	12
11	UV-Vis and TEM characterization of citrate capped gold nanoparticles	12
12	Changes in the silver content in water collected after washing out AgNPs	13
13	Calculations of the number of atoms and nanoparticles formed by Ag ions release and their effect on the increment of the volume of nanoparticles	13
14	Formulas for change in percentage distribution calculation for R/G and B/G channels	13

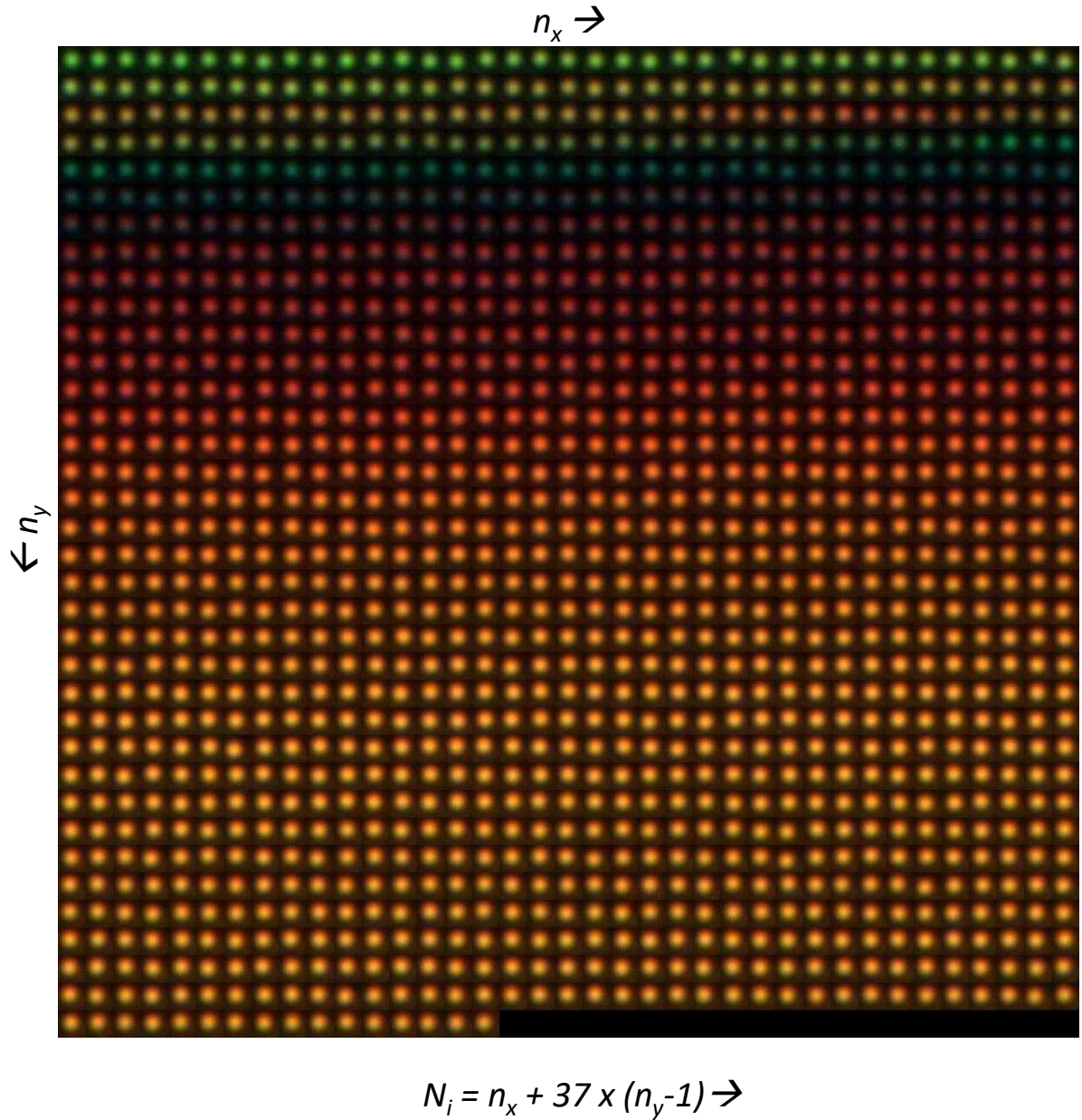




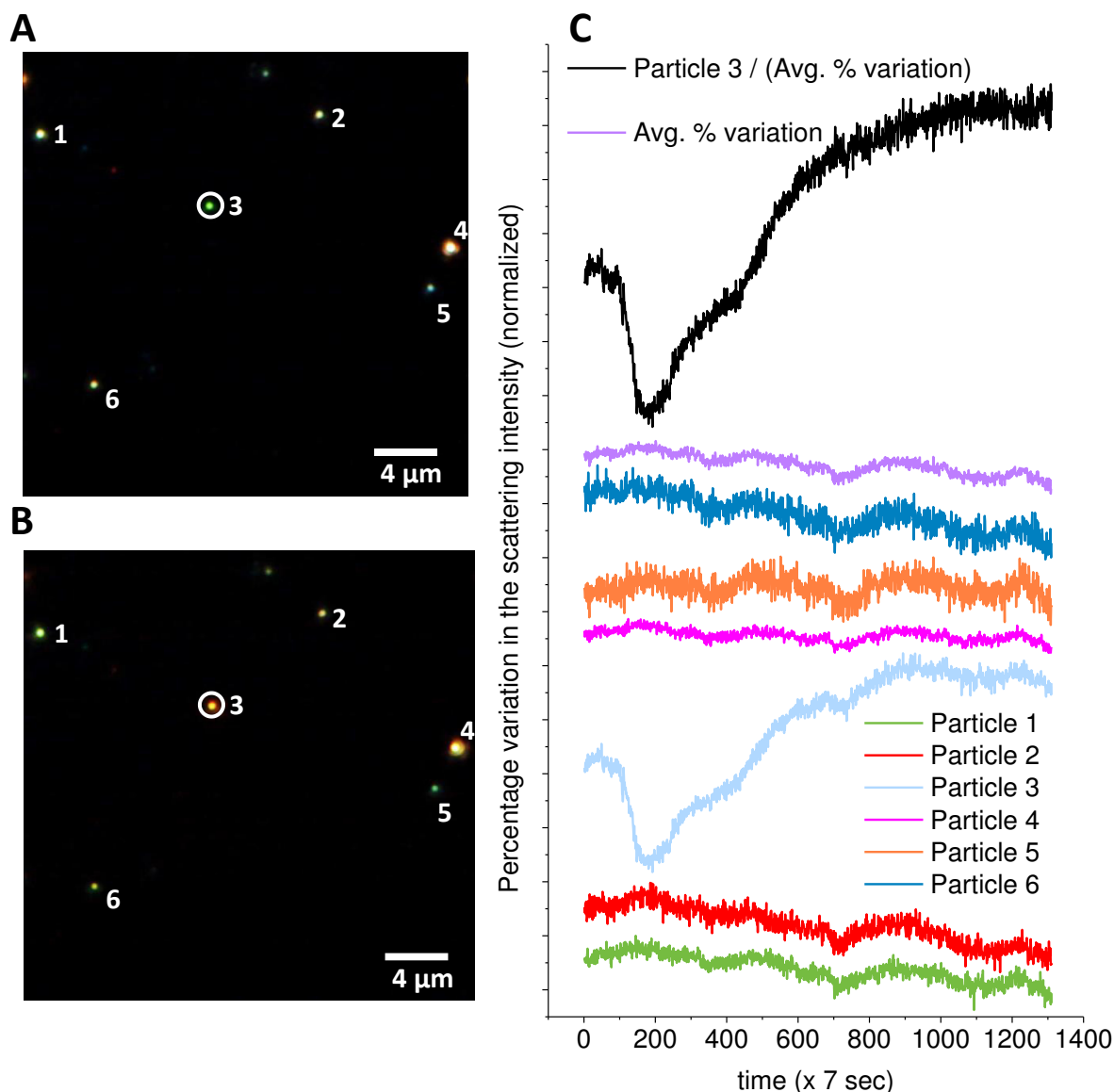
**Fig. S1** Verification of AgNPs immobilization was done using FESEM imaging. It can be seen that interparticle distances are similar in FESEM and DFM images. (A) FESEM image, (B) DFM image of AgNPs immobilized in a given area of  $36 \times 36 \mu\text{m}^2$ .



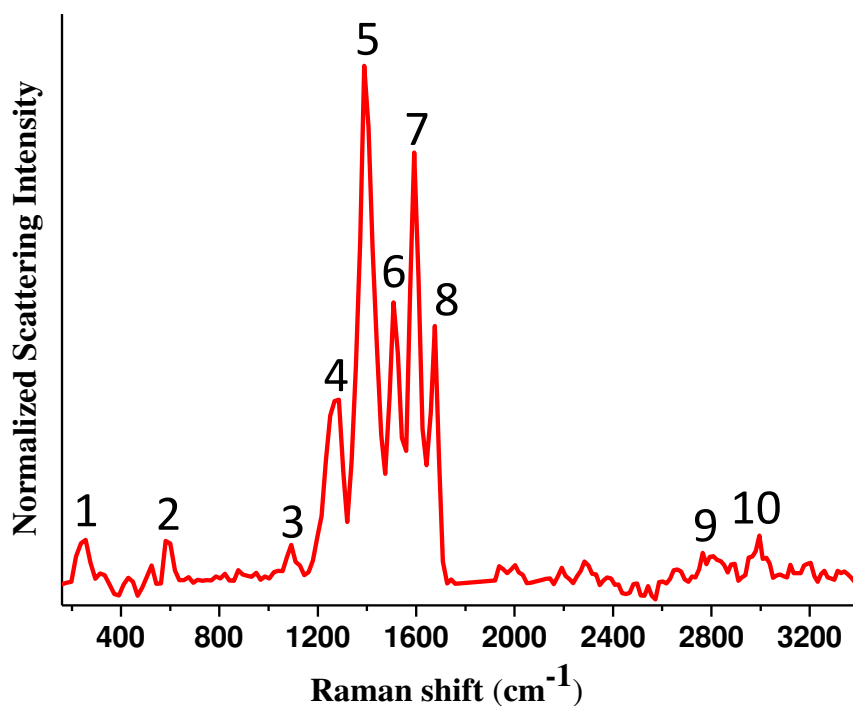
**Fig. S2** High magnification FESEM images depicting different morphologies of the immobilized single AgNPs at various locations. Some aggregates were also seen.



**Fig. S3** Montage of the DFM images for single AgNPs for which intensity profiles are shown in Fig. 2 of the main text. Number of data point shown in Fig. 2 can be correlated to the image by position calculated using the formula given in below image. Here  $N_i$  is data point in time and  $n_x$  and  $n_y$  increase in steps of 1.



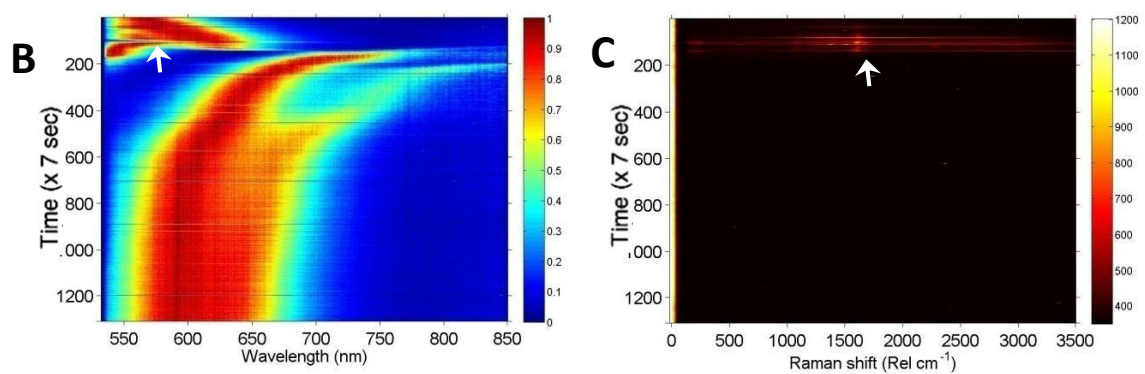
**Fig. S4** Large area dark field images of the region surrounding single AgNP (particle 3) for which intensity profiles are shown in Fig. 2 of the main text. (A) At the beginning of the observation. Monitored particle inside the confocal volume is encircled. (B) At the end of the observation. (C) Graph shows percentage variations in the scattering intensity of particles (1,2,4,5,6) in the surrounding region of particle 3 which were averaged to obtain better correction spectrum (spectrum with purple color). Particle 3 spectrum was corrected by dividing the same with correction spectrum is shown on the top. It can be seen that similar kind of variations were removed after correction.



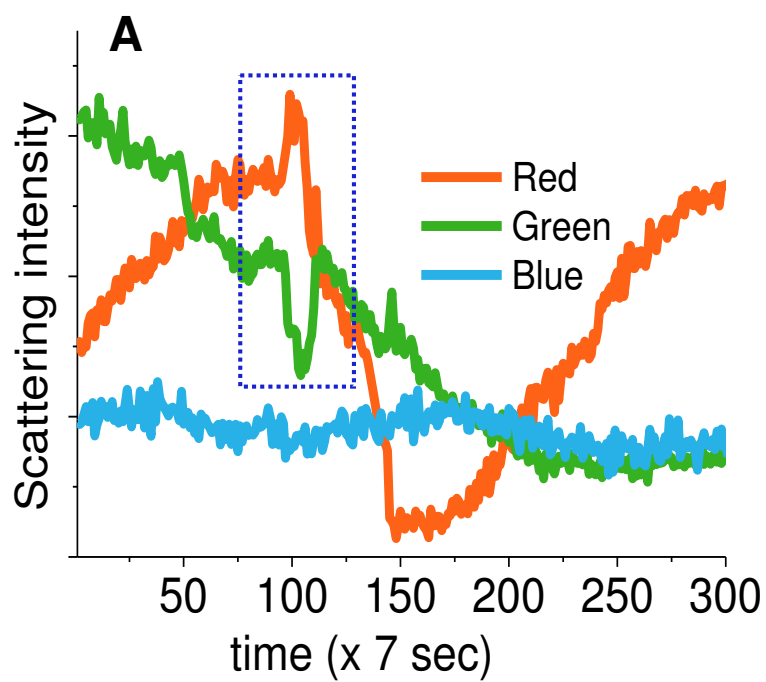
**Fig. S5** SERS spectrum of citrate ligand on the AgNP for which intensity profiles are shown in Fig. 2 of main text. Corresponding Raman band assignments are provided in Table S1 given below.

**Table S1** Citrate SERS band assignments

S.No.	Wavenumber(cm-1)	Band assignments <sup>1-4</sup>
1	246.6	$\nu(\text{Ag-O})$
2	582	$\delta(\text{COO})$
3	1092.2	$\delta(\text{C-O ter. alc})$
4	1285.2	$\delta(\text{CH}_2) + \omega(\text{CH}_2)$
5	1388	$\nu_{\text{sy}}(\text{COO-})$
6	1508.1	$\nu_{\text{as}}(\text{COO-})$
7	1592.3	$\nu_{\text{as}}(\text{COO-})$
8	1675.7	$\nu_{\text{as}}(\text{COO-}) + \delta(\text{OH})$
9	2795.9	$\nu_{\text{sy}}(\text{CH})$
10	3000.1	$\nu_{\text{as}}(\text{CH})$

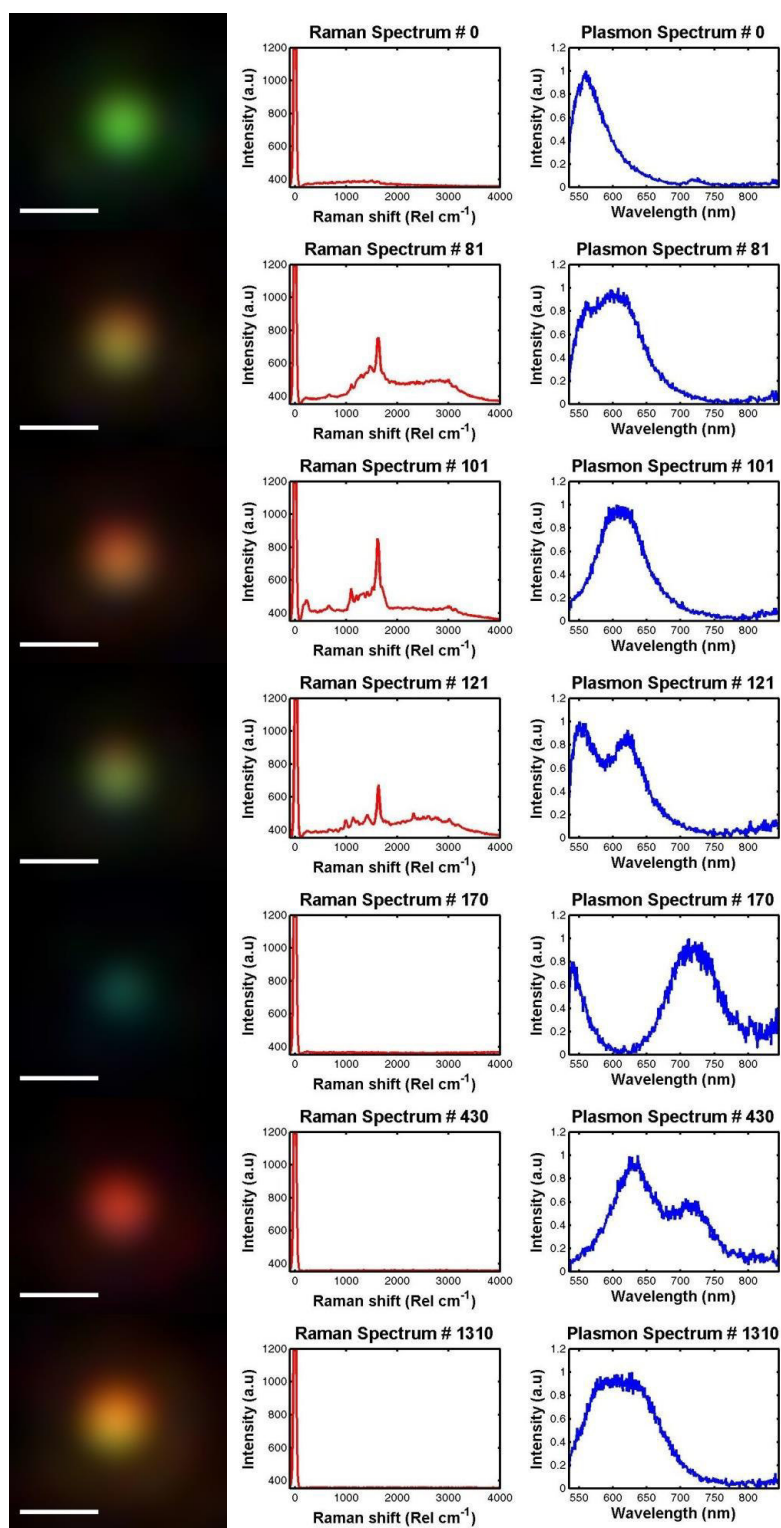


**Fig. S6** Temporal plasmonic colormap and Raman intensity map of changes in the plasmonic and Raman scattering of AgNP for which intensity profiles are shown in the Fig. 3A of the main text.

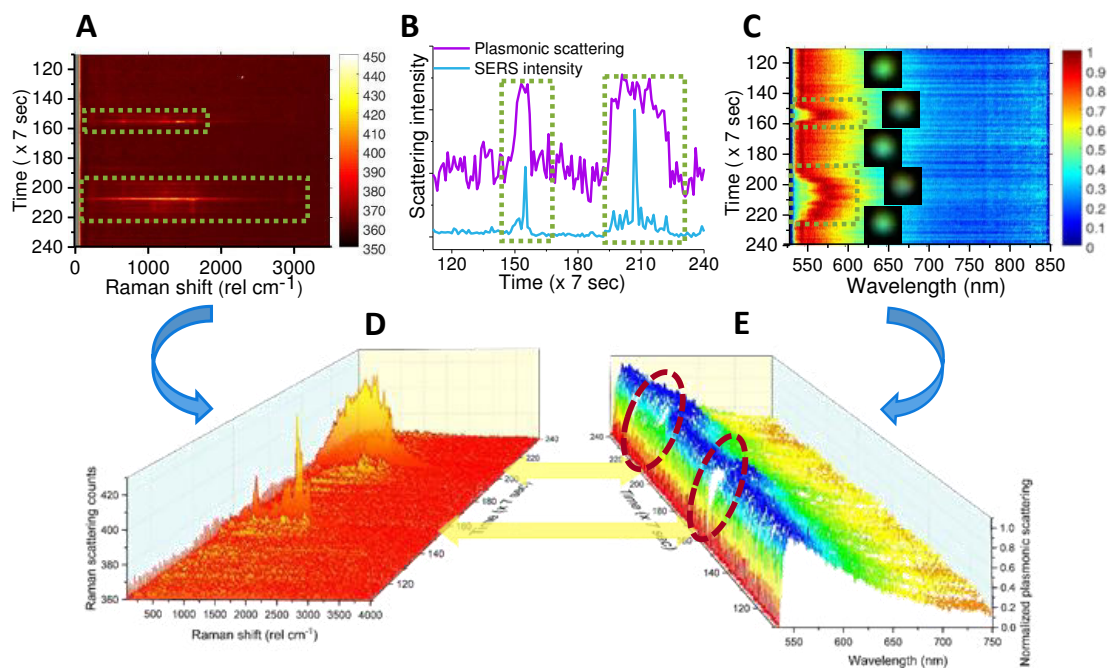


**Fig S7.** RGB profile for the particle calculated from the time-dependent DFM images. Blue color box indicating the time position when SERS activity was observed in the nanoparticle.

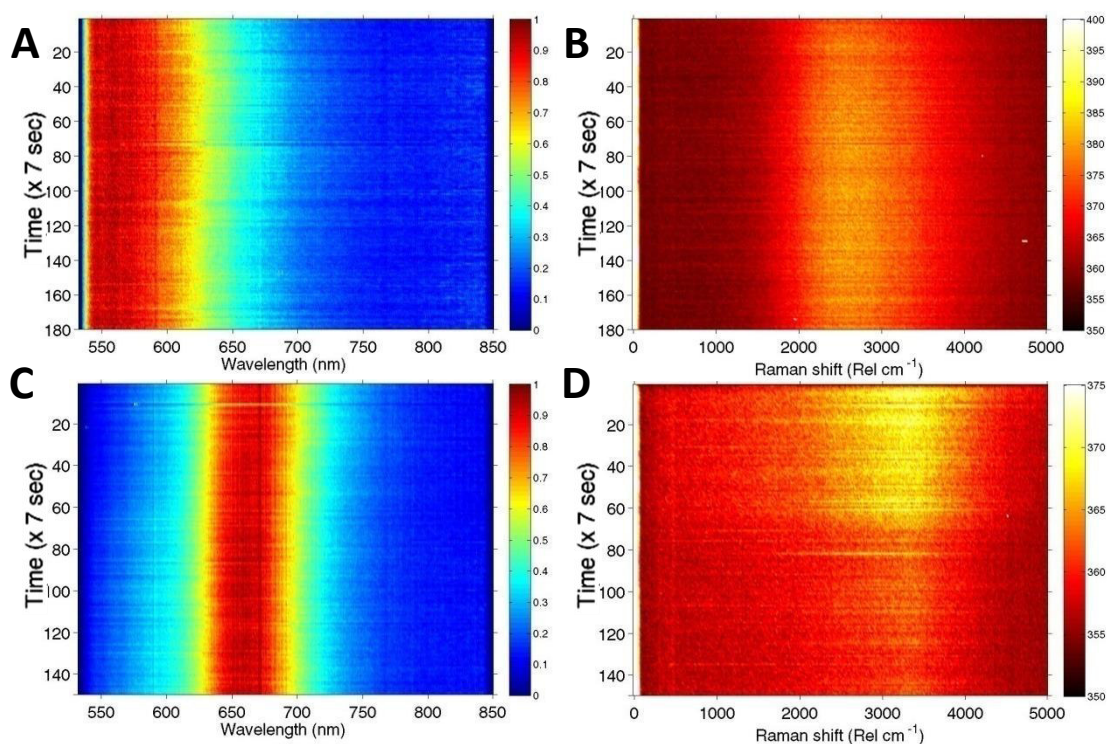




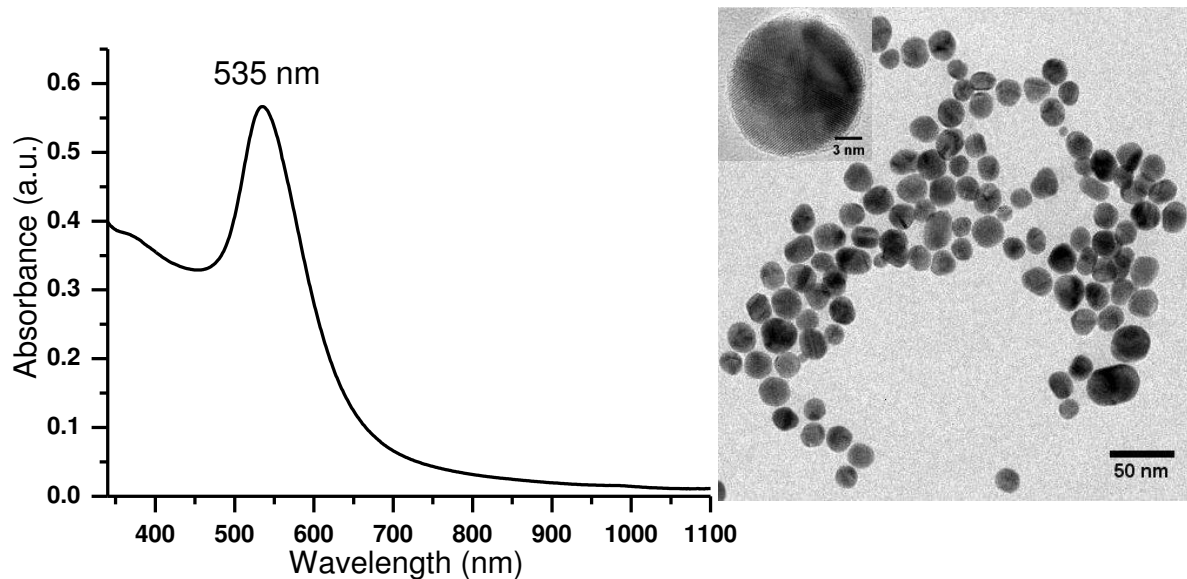
**Fig. S8** Plasmonic and Raman scattering spectra corresponding to the time points of interest of AgNP for which intensity profiles are shown in Fig. 2 of the main text.



**Fig. S9** (A) Raman intensity map, (B) Correlating integrated intensity profiles for Raman and plasmonic spectral match and (C) Plasmonic scattering colormap and their corresponding time-lapse Raman and plasmonic scattering spectra (D&E) for isolated AgNP. All the figures show that abrupt changes occurred during time 145-160 and 190-220 (x 7 sec) shown with wine colored dotted circles, the whole spectra are presented in D & E.



**Fig. S10** A plasmonic scattering colormap (left) and Raman intensity map (right) of two AuNPs.



**Fig. S11** (A) UV-Vis spectrum of the AuNPs used in this study. (B) TEM (scale bar – 50 nm) image of AuNPs. HRTEM (scale bar – 3 nm) of one particle is shown in the inset.

**Table S2** Changes in the Silver content in water collected after washing out immobilized AgNPs in the area of 22 x 22 mm

S. No.	Washing time (hours)	Ag in ppb
1	0	7.14
2	6	3.47
3	12	0.79
4	18	0.32
5	24	0.28

**Calculations of the number of atoms and nanoparticles formed by Ag ions release and their effect on the increment of the volume of nanoparticles**

Silver ion release by ICP-MS (6 h) = 3.47 ppb (3.47 ug/L or 3.47 ng/mL)

For ICP-MS measurements, volume of DI water used for washing immobilized sample = 500 uL, hence, silver ion release = 1.74 ng/500 uL.

Molarity of the silver ions solution with 1.74 ng in 500 uL = 32.3 nM

Applying dilution correction, number of atoms in the 32.3 nM =  $32.3 \times 10^{-9} \times 50 \times 6.02 \times 10^{23} = 0.97 \times 10^{18}$  atoms (Note: 10 uL AgNP volume used for immobilization was washed with 500 uL milliQ water)

No. of atoms present in 50 nm diameter AgNP =  $3.9 \times 10^6$

∴ Total no. of NPs which could be formed =  $0.97 \times 10^{18} / 3.9 \times 10^6 = 2.5 \times 10^{11}$  AgNPs of 50 nm diameter

For 50 nm nanoparticles which could be changed to 70 nm particles =  $1.4 \times 10^{11}$  NPs.

**Calculations of the percentage change in RGB intensity:**

For particle images before and after ( $I_b$  and  $I_a$ , respectively) with RGB intensities  $I_{bR}$ ,  $I_{bG}$ ,  $I_{bB}$  and  $I_{aR}$ ,  $I_{aG}$ ,  $I_{aB}$  following formulae were used to calculate R/G% and B/G% change as given below,

$$\frac{R}{G} \% \text{ change} = \frac{(I_{aR}/I_{aG}) - (I_{bR}/I_{bG})}{(I_{bR}/I_{bG})}$$

$$\frac{B}{G} \% \text{ change} = \frac{(I_{aB}/I_{aG}) - (I_{bB}/I_{bG})}{(I_{bB}/I_{bG})}$$

## References

- 1 E. Vinogradova, A. Tlahuice-Flores, J. J. Velazquez-Salazar, E. Larios-Rodriguez and M. Jose-Yacaman, *J. Raman Spectrosc.*, 2014, **45**, 730–735.
- 2 C. H. Munro, W. E. Smith, M. Garner, J. Clarkson and P. C. White, 1995, 3712–3720.
- 3 J. W. Park and J. S. Shumaker-Parry, *J. Am. Chem. Soc.*, 2014, **136**, 1907–1921.
- 4 D. L. Allara and R. G. Nuzzo, *Langmuir*, 1985, **1**, 52–66.

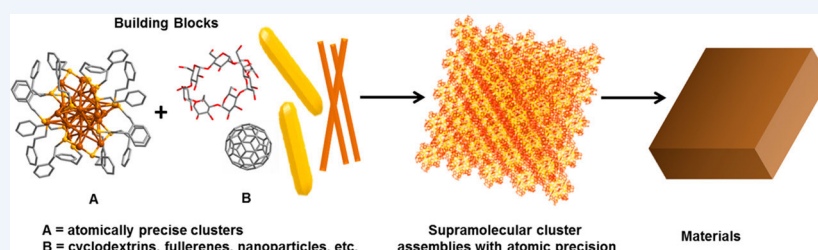


# Approaching Materials with Atomic Precision Using Supramolecular Cluster Assemblies

Published as part of the *Accounts of Chemical Research* special issue “*Toward Atomic Precision in Nanoscience*”.

Papri Chakraborty, Abhijit Nag, Amrita Chakraborty, and Thalappil Pradeep\*

DST Unit of Nanoscience (DST UNS) and Thematic Unit of Excellence (TUE), Department of Chemistry, Indian Institute of Technology Madras, Chennai 600 036, India



**CONSPECTUS:** Supramolecular chemistry is a major area of chemistry that utilizes weaker non-covalent interactions between molecules, including hydrogen bonding, van der Waals, electrostatic,  $\pi \cdots \pi$ , and C–H $\cdots\pi$  interactions. Such forces have been the basis of several molecular self-assemblies and host–guest complexes in organic, inorganic, and biological systems. Atomically precise nanoclusters (NCs) are materials of growing interest that display interesting structure–property correlations. The evolving science of such systems reaffirms their molecular behavior. This gives a possibility of exploring their supramolecular chemistry, leading to assemblies with similar or dissimilar cluster molecules. Such assemblies with compositional, structural, and conformational precision may ultimately result in cluster-assembled hybrid materials. In this Account, we present recent advancements on different possibilities of supramolecular interactions in atomically precise cluster systems that can occur at different length scales. We first present a brief discussion of the aspicule model of clusters, considering  $\text{Au}_{25}(\text{SR})_{18}$  as an example, that can explain various aspects of its atomic precision and distinguish the similar or dissimilar interacting sites in their structures. The supramolecular interaction of 4-*tert*-butylbenzyl mercaptan (BBSH)-protected  $[\text{Au}_{25}(\text{SBB})_{18}]^-$  NCs with cyclodextrins (CD) to form  $\text{Au}_{25}\text{SBB}_{18}\cap\text{CD}_n$  ( $n = 1-4$ ) and that of  $[\text{Ag}_{29}(\text{BDT})_{12}]^{3-}$  with fullerenes to form  $[\text{Ag}_{29}(\text{BDT})_{12}(\text{C}_{60})_n]^{3-}$  ( $n = 1-9$ ) (BDT = 1,3-benzenedithiolate) are discussed subsequently. The formation of these adducts was studied by electrospray ionization mass spectrometry (ESI MS), optical absorption and NMR spectroscopy. In the subsequent sections, we discuss how variation in intercluster interactions can lead to polymorphic crystals, which are observable in single-crystal X-ray diffraction. Taking  $[\text{Ag}_{29}(\text{BDT})_{12}(\text{TPP})_4]^{3-}$  (TPP = triphenylphosphine) clusters as an example, we discuss how the different patterns of C–H $\cdots\pi$  and  $\pi \cdots \pi$  interactions between the secondary ligands can alter the packing of the NCs into cubic and trigonal lattices. Finally, we discuss how the supramolecular interactions of atomically precise clusters can result in their hybrid assemblies with plasmonic nanostructures. The interaction of *p*-mercaptobenzoic acid (*p*-MBA)-protected  $\text{Ag}_{44}(\text{p-MBA})_{30}$  NCs with tellurium nanowires (Te NWs) can form crossed-bilayer precision assemblies with a woven-fabric-like structure with an angle of  $81^\circ$  between the layers. Similar crossed-bilayer assemblies show an angle of  $77^\circ$  when  $\text{Au}_{102}(\text{p-MBA})_{44}$  clusters are used to form the structure. Such assemblies were studied by transmission electron microscopy (TEM). Precision in these hybrid assemblies of Te NWs was highly controlled by the geometry of the ligands on the NC surface. Moreover, we also present how  $\text{Ag}_{44}(\text{p-MBA})_{30}$  clusters can encapsulate gold nanorods to form cage-like nanostructures. Such studies involved TEM, scanning transmission electron microscopy (STEM), and three-dimensional tomographic reconstructions of the nanostructures. The hydrogen bonding interactions of the –COOH groups of the *p*-MBA ligands were the major driving force in both of these cases. An important aspect that is central to the advancement of the area is the close interplay of molecular tools such as MS with structural tools such as TEM along with detailed computational modeling. We finally conclude this Account with a future perspective on the supramolecular chemistry of clusters. Advancements in this field will help in developing new materials with potential optical, electrical, and mechanical properties.

## INTRODUCTION

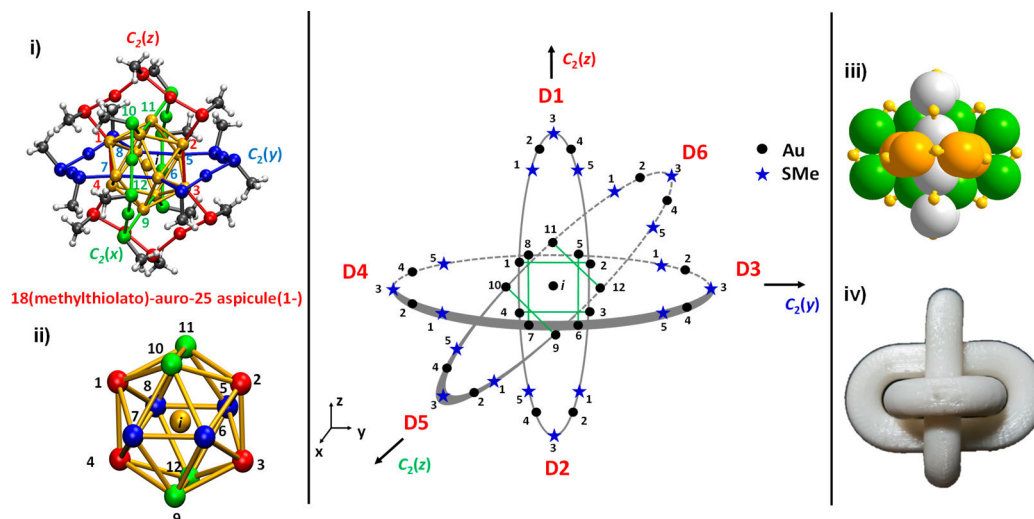
Atomically precise nanoclusters (NCs) present rich diversity in their structures and properties.<sup>1,2</sup> A large variety of clusters made of noble metals like Au, Ag, etc. and protected by ligands<sup>3,4</sup> such as thiols and phosphines are known in the literature, and many of

their structures have been determined from single-crystal studies. Precise composition, precision in molecular structure,

Received: July 28, 2018

Published: December 3, 2018





**Figure 1.** Representation of the  $\text{Au}_{25}(\text{SMe})_{18}$  cluster in the Borromean ring model. Three ellipses encompassing six  $\text{Au}_2(\text{SR})_3$  staples are represented as nearly coplanar rings. These staples are labeled as D1 to D6. The rings include core Au atoms (numbered 1 to 12). The atoms in the staples are numbered 1 to 5 in the clockwise direction. Inset (i) shows these aspicule rings in the standard structure of  $\text{Au}_{25}(\text{SMe})_{18}$ . The three rings are shown in red, green, and blue, while the Au atoms in the icosahedron are shown in gold. Inset (ii) shows an expanded view of the icosahedral core, where the icosahedral central atom alone is shown in gold. A cluster composed of Au (green, orange, and gray) and S (yellow) atoms is shown in inset (iii), and a photograph of a Borromean ring structure is shown in inset (iv). The ring structure enables the cluster to be disassembled completely just by detaching one bond; a break in one ring separates the other two. Reproduced from ref 12. Copyright 2015 American Chemical Society.

electronic energy levels, optical absorption and emission, chemical reactivity,<sup>5,6</sup> catalysis,<sup>3</sup> and an expanding body of emerging properties increasingly reaffirm the molecular nature of such systems. This expanding science makes one wonder about the distinct possibilities of supramolecular chemistry of such molecules. While supramolecular interactions play important roles in cluster crystallization, phase transfer, reaction chemistry, etc., these interactions can also be important for the synthesis of new cluster compounds, e.g., in the formation of cluster assemblies. Recently, Jin and co-workers reported that protecting ligands on clusters can organize in specific patterns that may direct their assembly, which can match the level of atomic precision in biomolecules.<sup>7</sup> The forces guiding the organization of the NCs may vary from weak intermolecular forces like  $\text{C}-\text{H}\cdots\pi$ ,  $\pi\cdots\pi$ , van der Waals, hydrogen bonding, and electrostatic interactions to strong covalent bonding. While molecular interactions between clusters result in their crystallization, interactions with heteromolecules as well as those between clusters forming homomolecular adducts such as dimers,<sup>8</sup> trimers,<sup>8</sup> and polymers<sup>9</sup> can create specific building blocks. Clusters, which have nanometric dimensions, can interact with other systems to form supramolecular architectures of larger dimensions. Such assemblies could also occur in organized biological systems such as viruses and bacteria, leading to bio–nano conjugates or synthetic superstructures of unprecedented diversity.<sup>10,11</sup> This Account briefly illustrates this emerging body of science and projects its growth to suggest future possibilities.

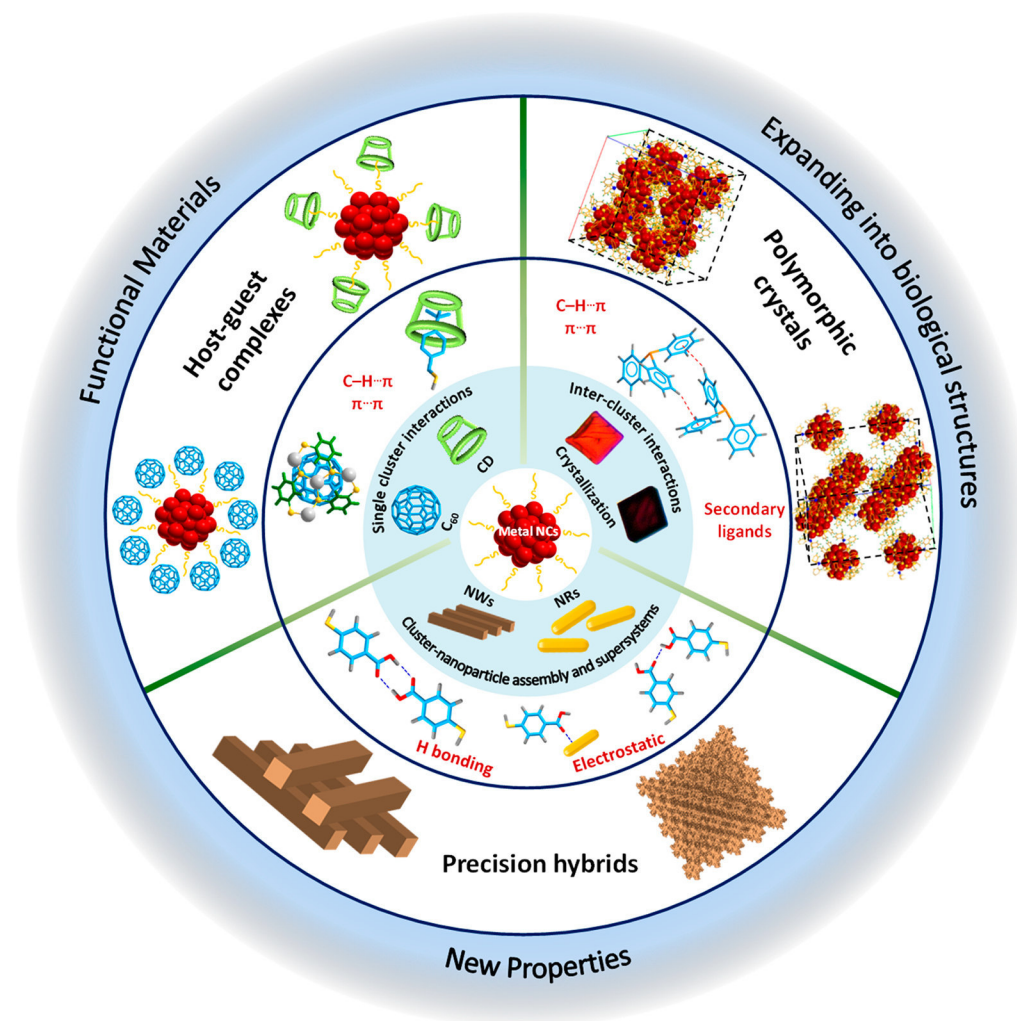
The precision in structures is captured elegantly in the aspicule nomenclature,<sup>12</sup> wherein the cluster is composed of a core and distinct staples having precise labels. The overall structure of  $\text{Au}_{25}(\text{SMe})_{18}$  can be drawn precisely, leading to the name 18(methylthiolato)-auro-25 aspicule(1–) to represent the molecule, as shown in Figure 1. This molecular structure presents symmetry-equivalent sites where interactions are similar or dissimilar. It also indicates the limits or limitations of molecular access and presents the possibilities of interactions

at distinct sites leading to structural transformation, particularly ligand exchange,<sup>13</sup> exchange of core atoms, creation of alloys,<sup>5,14</sup> and supramolecular functionalization.<sup>15</sup> Intercluster interactions between similar or different clusters as well as those with nanoparticles may also be visualized. In this Account, we discuss the different possibilities of supramolecular interactions in the atomically precise clusters and classify them into the following specific categories:

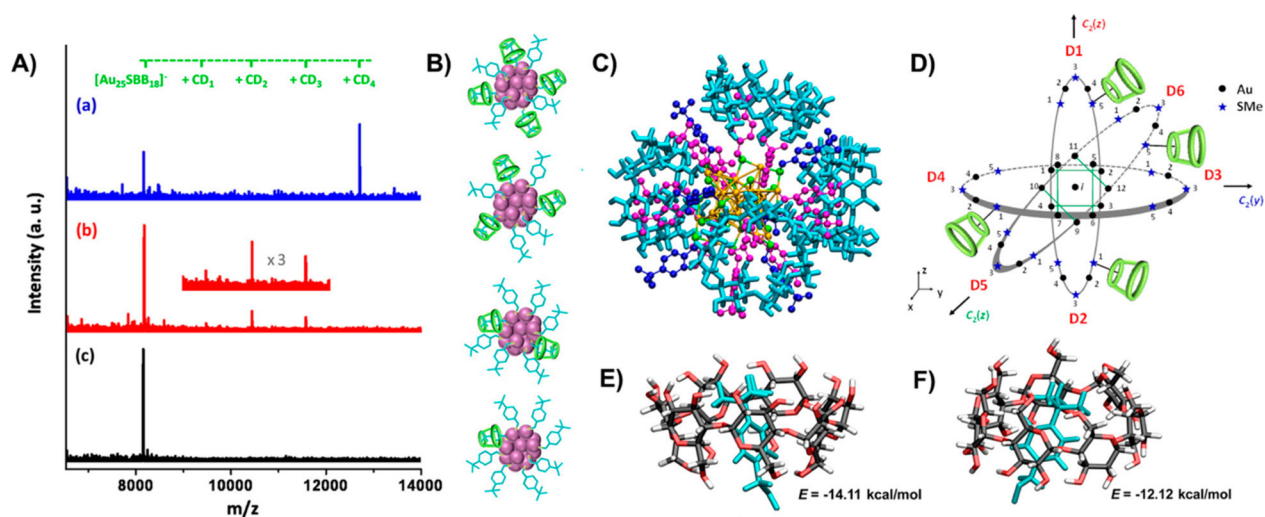
- (A) single cluster interactions (with small molecules)
- (B) intercluster interactions
- (C) cluster–nanoparticle assembly and supersystems

In each of these, the essential interaction is intermolecular in nature, but they occur at different length scales. Consequently, they are explored with different tools. In the first case, single cluster interactions, supramolecular interactions of the clusters with molecules like cyclodextrins (CDs) and fullerenes are studied principally using mass spectrometry (MS). Such results are supplemented by complementary studies using optical and NMR spectroscopy. In the second case, supramolecular interactions lead to intercluster organizations, which are observed by single-crystal diffraction. In the third case, interactions occur on substrates or at surfaces of much larger (bulk-like) phases, so the integrated systems are currently above the limit of regular MS. Here the formation of assemblies around nanostructures such as nanowires and nanorods mediated by supramolecular interactions with NCs is discussed.<sup>16</sup> Such systems are examined with microscopy. All of these systems are examined with computational methods with varying degrees of sophistication. Each of these subclasses is separately presented below, and Scheme 1 presents a schematic of the possible types of supramolecular interactions in the atomically precise clusters, as discussed above. While the interactions and structures derived are atomically precise in detail, a thorough understanding of structural and conformational precision has been possible only for A and B. We hope that more definitive understanding of all three types will be available in the years ahead.



Scheme 1. Schematic Capturing Some of the Supramolecular Interactions Possible in Atomically Precise Clusters<sup>a</sup>

<sup>a</sup>New directions shown at the periphery are not captured in this Account. The size of each component is not to scale.



**Figure 2.** (A) Negative ion ESI MS spectra for the  $\text{Au}_{25}\text{SBB}_{18}$  cluster and its CD adducts. Spectra a, b, and c are at SBB/CD molar ratios of 1:1.2, 1:1, and 1:0, respectively. Part of a spectrum is expanded in (b). (B) Schematic representations of  $\text{Au}_{25}\text{SBB}_{18}/\text{CD}_n$  ( $n = 1-4$ ). (C) Computed structure of  $\text{Au}_{25}\text{SBB}_{18}/\text{CD}_4$  with nearly tetrahedral binding of the four CDs (shown in cyan). H atoms of the SBB ligands have been omitted for clarity. (D) Aspicule representation of  $\text{Au}_{25}\text{SBB}_{18}/\text{CD}_4$ . (E, F) BBSH/CD inclusion complexes where the *tert*-butyl group of BBSH undergoes complexation through the (E) narrower and (F) wider rims of  $\beta$ -CD. In (E) and (F), all of the atoms of BBSH are colored cyan for clarity, whereas atoms of CD are colored differently. Reproduced from ref 15. Copyright 2014 American Chemical Society.

## A. SINGLE CLUSTER INTERACTIONS

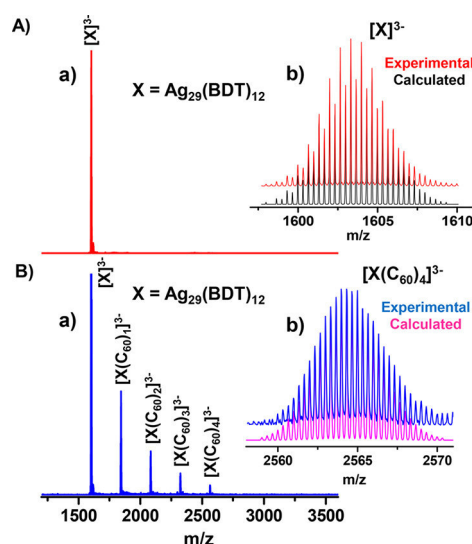
## Supramolecular Interactions of NCs with CDs

The interactions of a cluster with other molecules may be tuned to precisely functionalize the surface of the NCs. We used the 4-*tert*-butylbenzyl mercaptan (BBSH)-protected  $[\text{Au}_{25}(\text{SBB})_{18}]^-$  cluster<sup>15</sup> and studied its supramolecular functionalization with  $\beta$ -CD. CDs are water-soluble cyclic oligosaccharides having hydrophobic cavities that form inclusion complexes with specific molecules.<sup>17</sup> Several host–guest complexes of  $\beta$ -CDs with inorganic complexes containing thiol groups like BBSH have been reported in the literature.<sup>18</sup> We utilized such a molecular recognition process to synthesize  $\text{Au}_{25}\text{SBB}_{18}\cap\text{CD}_n$  ( $n = 1-4$ ), where  $\text{X}\cap\text{Y}$  denotes an inclusion complex between the substrate X and receptor Y.<sup>15</sup> The CD-encapsulated clusters were synthesized from a mixture of the cluster and  $\beta$ -CD in THF/water medium by constant stirring followed by intermittent sonication, and they were characterized using different techniques such as UV–vis, fluorescence, and NMR spectroscopy. The formation of  $\text{Au}_{25}\text{SBB}_{18}\cap\text{CD}_n$  ( $n = 1-4$ ) was observed in electrospray ionization mass spectrometry (ESI MS) (Figure 2A). Schematic structures of  $\text{Au}_{25}\text{SBB}_{18}\cap\text{CD}_n$  ( $n = 1-4$ ) are presented in Figure 2B. Although a mixture of adducts ( $n = 1-4$ ) existed in solution, the amount of  $\text{Au}_{25}\text{SBB}_{18}\cap\text{CD}_4$  was increased by careful control of the SBB/CD molar ratio at 1:1.2. The nature of the interaction was explained using computational studies. In the structure of  $\text{Au}_{25}\text{SBB}_{18}$ , surrounding the icosahedral core there are six  $\text{Au}_2(\text{SR})_3$  staples, corresponding to the six staples D1 to D6 in the aspicule model (Figure 1). In each staple, there are two nonbridging S (positions 1 and 5) joining a core Au to a staple Au and one bridging S (position 3) joining only two exterior Au atoms. The ligands anchored at positions 1 and 5, being less crowded, remain more accessible for encapsulation with CDs. This appears to be counterintuitive, as position 3 appears to be less crowded in the aspicule picture. However, Figure 1(iv) suggests that positions 1 and 5 are indeed accessible. NMR data also revealed the interactions between aromatic protons of SBB and  $\text{H}^3$  and  $\text{H}^5$  (inner protons) of CD. The theoretical structure of  $\text{Au}_{25}\text{SBB}_{18}\cap\text{CD}_4$  (Figure 2C) shows four CDs bound at tetrahedral locations, minimizing the inter-CD interactions. A representation in the aspicule model is shown in Figure 2D. Complexation through the narrower rim of CD facing the cluster core was more favorable than complexation through the wider rim (Figure 2E,F).

The formation of these inclusion complexes was specific to the precise orientation of the SBB ligands, which pointed outward from the core. In the case of  $\text{Au}_{25}(\text{PET})_{18}$  (PET = 2-phenylethyl thiolate),<sup>19,20</sup> which presents a different orientation of the PET ligands, no CD inclusion was observed. CD encapsulation resulted in an enhancement in the luminescence of the cluster and shielded the metal core from incoming ions or ligands and consequently increased its stability. Inclusion complexes of other thiols such as adamantanethiol (SAdm) with CD are also well-known.<sup>21–23</sup> Yan et al.<sup>24</sup> showed the surface functionalization of  $\text{Au}_{38}\text{S}_2(\text{SAdm})_{20}$  NCs with  $\alpha$ -,  $\beta$ -, and  $\gamma$ -CD. This unfolds the possibility of functionalizing other Adm-protected clusters like  $\text{Au}_{30}(\text{SAdm})_{18}$ ,<sup>25</sup>  $\text{Pt}_1\text{Ag}_{28}(\text{SAdm})_{18}(\text{PPh}_3)_4$ ,<sup>26</sup>  $\text{Au}_{24}(\text{SAdm})_{16}$ ,<sup>27</sup> etc. with CDs in a similar fashion. In a recent report, Au NC-grafted CD superstructures were used to develop fluorescence on–off composites.<sup>28</sup> Xie and co-workers used a CD–AuNC– $\text{TiO}_2$  hybrid system to enhance photocatalytic decomposition of organic pollutants.<sup>29</sup>

## Supramolecular Interactions of NCs with Fullerenes

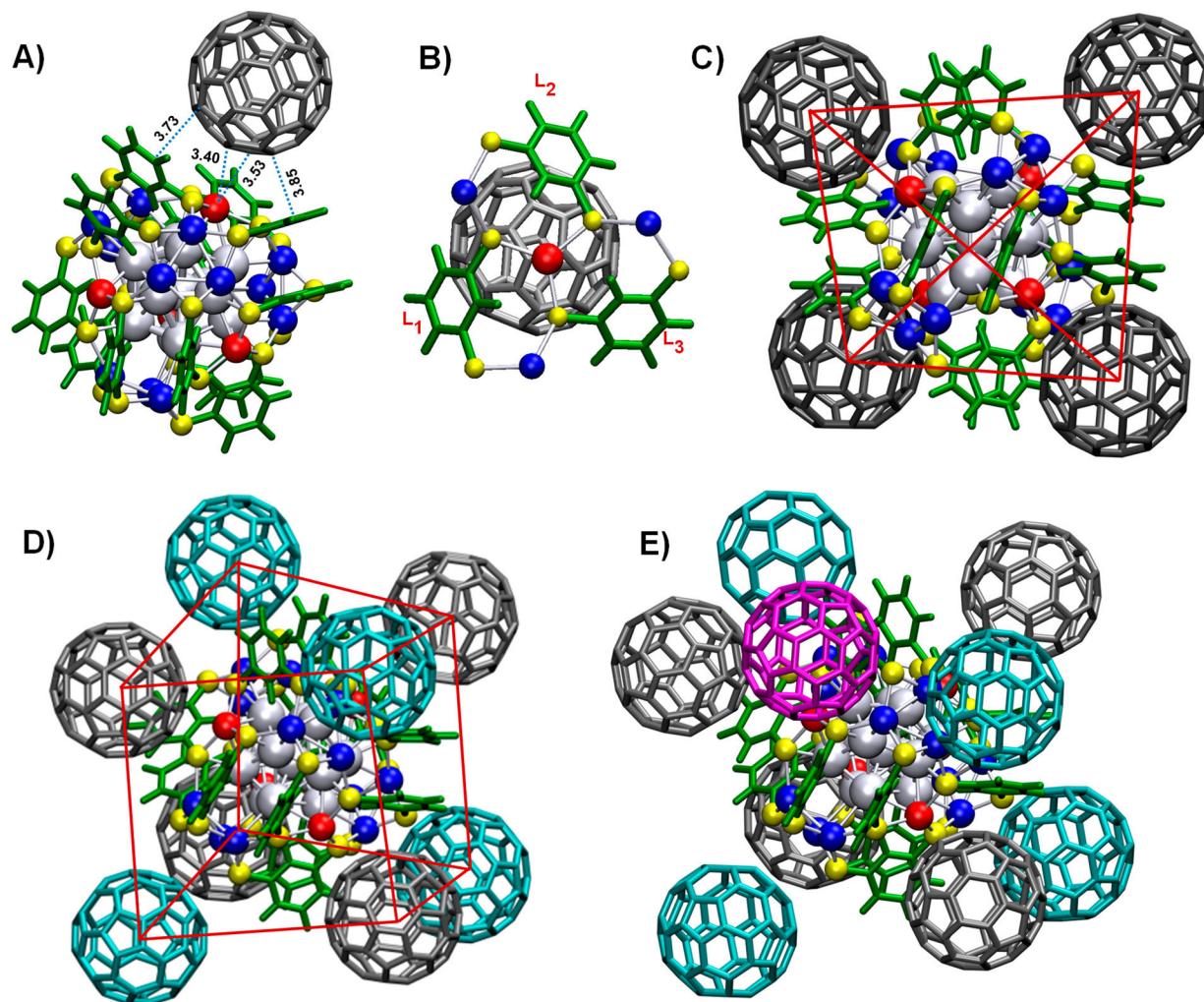
Fullerenes are another important class of molecules for exploration of the supramolecular chemistry of clusters. Fullerenes show electron-accepting properties and form a wide range of supramolecular self-assembled structures.<sup>30</sup> We observed the formation of  $[\text{Ag}_{29}(\text{BDT})_{12}(\text{C}_{60})_n]^{3-}$  ( $n = 1-9$ )<sup>31</sup> (BDT = 1,3-benzenedithiolate) adducts in solution through the interaction of  $[\text{Ag}_{29}(\text{BDT})_{12}]^{3-}$  NCs<sup>32</sup> with  $\text{C}_{60}$ . Twelve Ag atoms cover the icosahedral core, forming four trigonal prisms. The  $\text{Ag}_{13}$  core is further covered by four Ag atoms at tetrahedral positions.<sup>32</sup> Addition of  $\text{C}_{60}$  to the cluster at a cluster: $\text{C}_{60}$  molar ratio of 1:4 resulted in the formation of  $[\text{Ag}_{29}(\text{BDT})_{12}(\text{C}_{60})_n]^{3-}$  ( $n = 1-4$ ) adducts, which were observed by ESI MS (Figure 3). The BDT ligands are arranged



**Figure 3.** ESI MS spectra of (A)  $[\text{Ag}_{29}(\text{BDT})_{12}]^{3-}$  and (B)  $[\text{Ag}_{29}(\text{BDT})_{12}(\text{C}_{60})_n]^{3-}$  ( $n = 1-4$ ). Experimental and theoretical isotopic distributions of the peaks are compared in the insets. Reproduced from ref 31. Copyright 2018 American Chemical Society.

in such a way that they form a cavity, encapsulating the curved surface of fullerenes (Figure 4A,B). This structural compatibility facilitated the supramolecular host–guest complexation. Detailed insights into the structures of  $[\text{Ag}_{29}(\text{BDT})_{12}(\text{C}_{60})_n]^{3-}$  ( $n = 1-4$ ) were obtained from computational studies. In the structure of  $[\text{Ag}_{29}(\text{BDT})_{12}(\text{C}_{60})]^{3-}$  (Figure 4A),  $\text{C}_{60}$  has weak binding interactions with the vertex Ag atom at a distance of about 3.40–3.53 Å and stabilizes the unpassivated Ag atom by  $\eta^2$  interactions. The adduct  $[\text{Ag}_{29}(\text{BDT})_{12}(\text{C}_{60})_4]^{3-}$  (Figure 4C) retains a tetrahedral symmetry in its structure with four  $\text{C}_{60}$  molecules bound at four vertex sites. The primary interactions are  $\pi\cdots\pi$  and van der Waals interactions between the  $\pi$  surface of the fullerene and the aromatic rings of BDT. In the crystal structure of the NC, triphenylphosphine (TPP) ligands are bound at the vertex Ag sites.<sup>32</sup> When TPP was added to  $[\text{Ag}_{29}(\text{BDT})_{12}(\text{C}_{60})_n]^{3-}$  ( $n = 1-4$ ), TPP replaced  $\text{C}_{60}$ , forming  $[\text{Ag}_{29}(\text{BDT})_{12}(\text{TPP})_4]^{3-}$  ( $n = 1-4$ ), which reaffirmed the binding sites of the fullerenes to the cluster. Addition of excess  $\text{C}_{60}$  resulted in an even higher number of  $\text{C}_{60}$  additions to the cluster ( $n > 4$ ). Additional  $\text{C}_{60}$  may bind over the four trigonal faces formed by the  $\text{Ag}_3\text{S}_3$  motifs. The likely structure of  $[\text{Ag}_{29}(\text{BDT})_{12}(\text{C}_{60})_8]^{3-}$  (Figure 4D) shows fullerenes bound at all of the face and vertex positions of the cluster with a slightly distorted cube-like overall geometry. Additional fullerene–





**Figure 4.** (A) Results of DFT calculations on the minimum-energy geometry of  $[\text{Ag}_{29}(\text{BDT})_{12}(\text{C}_{60})]^{3-}$ . Interaction distances (in Å) are marked in the figure. (B) Interactions between the fullerene and the ligands are shown in an expanded view. (C–E) Lowest-energy structures of (C)  $[\text{Ag}_{29}(\text{BDT})_{12}(\text{C}_{60})_4]^{3-}$ , (D)  $[\text{Ag}_{29}(\text{BDT})_{12}(\text{C}_{60})_8]^{3-}$ , and (E)  $[\text{Ag}_{29}(\text{BDT})_{12}(\text{C}_{60})_9]^{3-}$ . Color code: yellow, S; gray, Ag of the icosahedral core; red, tetrahedral sites of four Ag atoms; blue,  $\text{Ag}_3\text{S}_3$  staple motifs composed of 12 Ag atoms making four trigonal planes; green, BDT ligands; black,  $\text{C}_{60}$  at vertex positions; cyan,  $\text{C}_{60}$  at face positions; purple, an additional fullerene located between the face and vertex positions. Reproduced from ref 31. Copyright 2018 American Chemical Society.

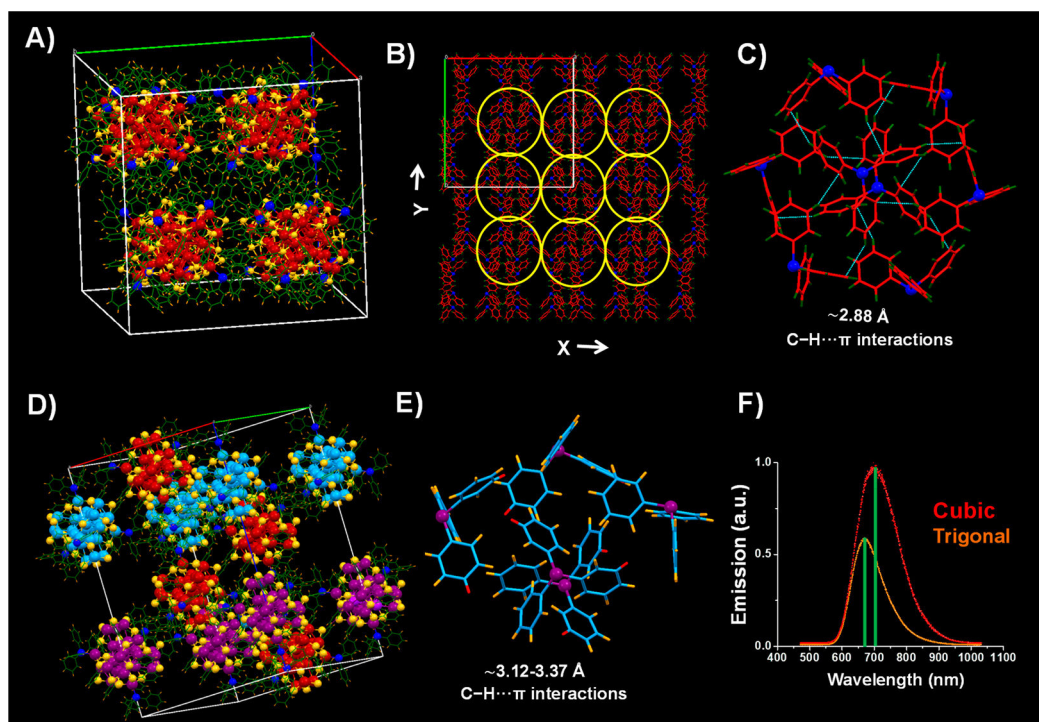
fullerene interactions may also favor further attachment of  $\text{C}_{60}$  (Figure 4E) such that the latter may form a sphere covering the entire cluster surface. Similar results were observed with  $\text{C}_{70}$ , which exhibited stronger  $\pi\cdots\pi$  interactions and closer contacts with the aromatic ligands of the cluster. The importance of intermolecular interactions in the formation of intercluster compounds of fullerides with gold NCs,  $[\text{Au}_7(\text{PPh}_3)_7]\text{C}_{60}\cdot\text{THF}$  and  $[\text{Au}_8(\text{PPh}_3)_8](\text{C}_{60})_2$ , was also demonstrated by Schulz-Dobrick et al.<sup>33</sup> The interactions of a cluster may also be utilized to form atomically precise supramolecular assemblies with other molecules such as catenanes, calixarenes, rotaxanes, porphyrins, etc.

## B. INTERCLUSTER INTERACTIONS

Supramolecular interactions also play a crucial role in arranging the NCs in their crystal lattice. In the crystal lattice of *p*-mercaptobenzoic acid (*p*-MBA)-protected  $\text{Ag}_{44}(\text{p-MBA})_{30}$  NCs, the  $-\text{COOH}$  groups of the *p*-MBA ligands show strong hydrogen bonding between the neighboring NCs.<sup>34</sup> Similar non-covalent interactions have also been observed in the crystal lattices of  $\text{Au}_{102}$ ,<sup>35</sup>  $\text{Au}_{246}$ ,<sup>7</sup>  $\text{Au}_{103}$ ,<sup>36</sup> etc. Interesting packing

patterns such as the 4H phase array of  $\text{Au}_{92}(\text{TBBT})_{44}\text{NCs}$ <sup>37</sup> and the 6H left-handed helical arrangement of  $\text{Au}_{60}\text{S}_6(\text{SCH}_2\text{Ph})_{36}\text{NCs}$ <sup>38</sup> in their crystal lattices were also observed. Considering  $[\text{Ag}_{29}(\text{BDT})_{12}(\text{TPP})_4]^{3-}\text{NCs}$ <sup>32</sup> as an example, we demonstrated how the intercluster interactions may be tuned to create polymorphic crystals. In the structure reported by Bakr and co-workers,<sup>32</sup> evaporation of DMF formed orange crystals in a cubic (C) lattice with space group  $Pa\bar{3}$  (Figure 5A). In our vapor diffusion method (MeOH diffusing into DMF solution of the NCs), dark-red crystals in a trigonal (T) lattice with space group  $R\bar{3}$  were formed (Figure 5D).<sup>39</sup> The difference in packing of the two polymorphic forms is largely due to the difference in the supramolecular interactions of the BDT and TPP ligands. These interactions for the T and C systems may be classified into two categories:

- (i) In a single NC, the C–H groups of the TPP subunits interact with the  $\pi$  system of the aromatic rings of BDT in an intracluster fashion. Moreover, the C–H groups of BDT and the aromatic rings of TPP also interact strongly through intercluster C–H $\cdots\pi$  interactions in both the C



**Figure 5.** (A) Cubic unit cell of  $\text{Ag}_{29}(\text{BDT})_{12}(\text{TPP})_4^{3-}$  NCs. (B) Packing of the TPP subunits viewed from the Z axis in the C system. (C) Strong C-H... $\pi$  interactions (T-shaped) between the eight TPP subunits forming a hexagonal shape in the C system. (D) Trigonal unit cell of the NCs. (E) C-H... $\pi$  interactions between the TPP subunits in the T system. (F) Emission spectra obtained from single crystals of the C and T lattices. The C structure exhibits stronger and slightly red-shifted ( $\sim 30 \text{ nm}$ ) luminescence compared with the T structure. Reproduced with permission from ref 39. Copyright 2018 Royal Society of Chemistry.

and the T systems at distances of  $\sim 3.07\text{--}3.39$  and  $2.92 \text{ \AA}$ , respectively.

- (ii) In the C lattice, the C-H... $\pi$  interactions within the TPP subunits are stronger, forming polymeric chains (Figure 5B) to directly or indirectly connect every NC with others. These distances are comparable to the C-H... $\pi$  distances of  $2.88 \pm 0.42 \text{ \AA}$  seen in  $\text{Au}_{246}$  NCs protected by -SPh-*p*- $\text{CH}_3$  ligands<sup>7</sup> but slightly longer than the interaction distances of  $2.76 \pm 0.05 \text{ \AA}$  in  $\text{Au}_{103}$  NCs protected by -S-Nap.<sup>36</sup> The interaction distances for the TPP subunits are larger in the T system (Figure 5E) compared with the C system, and hence, these interactions are discontinuous and do not form polymeric chains.

It is evident from the crystal packing of the two polymorphs of the clusters that the intercluster interactions of TPP ligands are more favored in C than in T. The C lattice, being more rigid, exhibits a higher luminescence efficiency than the T NCs with a slight red shift ( $30 \text{ nm}$ ) (Figure 5F). This also reveals how the luminescence efficiencies of the NCs in the solid state are controlled by interactions of their secondary ligands.

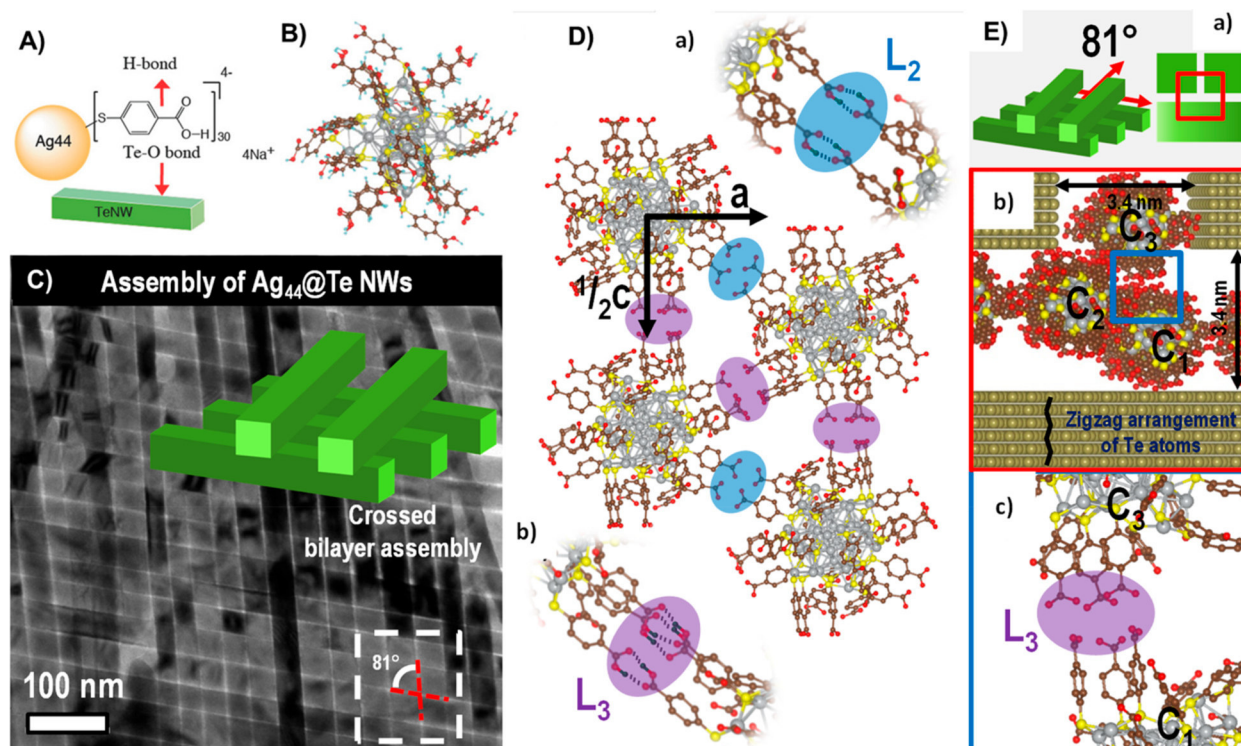
## C. CLUSTER-NANOPARTICLE ASSEMBLY AND SUPERSYSTEMS

### Cluster-Mediated Precision Assemblies of Nanowires

The interactions of NCs are very different from those of nanoparticles or ionic salts of metals.<sup>40</sup> Small thiol-protected clusters like  $\text{Ag}_{32}(\text{SG})_{19}$ <sup>41</sup> tend to coalesce on the surface of one-dimensional (1D) nanomaterials like tellurium nanowires (Te NWs). This finally leads to the decoration of the NWs with Ag nodules, whereas the interactions of Ag(I) ions and Ag NPs lead

to the formation of  $\text{Ag}_2\text{Te}$  NWs.<sup>40</sup> Inspired by this result, in a particular study we modified the surface of Te NWs with  $\text{Ag}_{44}(\text{p-MBA})_{30}$  (abbreviated as  $\text{Ag}_{44}$ ). Next, the  $\text{Ag}_{44}@\text{Te}$  NWs were dispersed in 1-butanol, which was then spread over water, followed by solvent evaporation.<sup>16</sup> The pristine Te NWs formed the usual monolayer assembly when subjected to this process, whereas  $\text{Ag}_{44}@\text{Te}$  NWs led to a crossed-bilayer structure. Upon detailed TEM investigation, the pattern was found to be a woven-fabric-like structure in which NWs in the same layer were parallel but adjacent layers were arranged at an unusual angle of  $81^\circ$  (Figure 6C). To explain the origin of the unusual assembly, we modeled the hydrogen bonding between neighboring  $\text{Ag}_{44}$  units in the cluster superlattice. The *p*-MBA ligands on individual  $\text{Ag}_{44}$  clusters are present in the form of bundles of two ( $L_2$ ) or three ( $L_3$ ) units (Figure 6D). Either two  $L_2$  pairs or two  $L_3$  pairs are known to form hydrogen bonds in the  $\text{Ag}_{44}$  crystal. In  $\text{Ag}_{44}@\text{Te}$  NWs, the clusters attach themselves on the surfaces of the Te NWs via the  $-\text{COO}^-$  groups of some of their *p*-MBA ligands (Figure 6A). Upon solvent evaporation, the  $\text{Ag}_{44}@\text{Te}$  NWs come closer, and hydrogen bonding may occur between free *p*-MBA ligands, which are not bound on the NWs, of two neighboring  $\text{Ag}_{44}$  clusters attached to adjacent NWs. Computational modeling further explained that the greatest number of hydrogen bonds was possible when the two layers were arranged at an angle of  $81^\circ$ , thereby giving the most stable and most symmetrical structure (Figure 6E). When  $\text{Au}_{102}(\text{p-MBA})_{44}$ <sup>35</sup> was used instead of  $\text{Ag}_{44}(\text{p-MBA})_{30}$ , a similar crossed-bilayer structure was observed with an angle of  $77^\circ$  between the two layers, which is due to the difference in the geometrical arrangement of the ligands of the two clusters. Thus, precise angular control between highly ordered Te NW assemblies could be achieved by using atomically precise NCs.





**Figure 6.** (A) Schematic of the bonding of  $\text{Ag}_{44}(\text{p-MBA})_{30}$  clusters to Te NWs. (B) Structure of  $\text{Ag}_{44}(\text{p-MBA})_{30}$  modeled from its crystal structure. (C) TEM image of the crossed bilayer assembly of  $\text{Ag}_{44}@\text{Te NWs}$ . A schematic showing the crossed-bilayer structure of the assembly is presented in the inset. (D) Hydrogen bonding between the  $-\text{COOH}$  groups of the  $\text{p-MBA}$  ligands of neighboring NCs in the  $\text{Ag}_{44}(\text{p-MBA})_{30}$  superlattice. The neighboring clusters interact via hydrogen bonding with  $\text{L}_2$  (inset a) and  $\text{L}_3$  (inset b) types of ligands. (E) (a) Schematic of the crossed bilayer assembly. (b) Expanded view of the region modeled in (a). Further details are shown in (c). Clusters assembled on the surfaces of the Te NWs, which were kept at a distance of 3.4 nm, in three different planes, labeled as  $\text{C}_1$ ,  $\text{C}_2$ , and  $\text{C}_3$ . Reproduced with permission from refs 16 and 45. Copyright 2016 and 2018 Wiley.

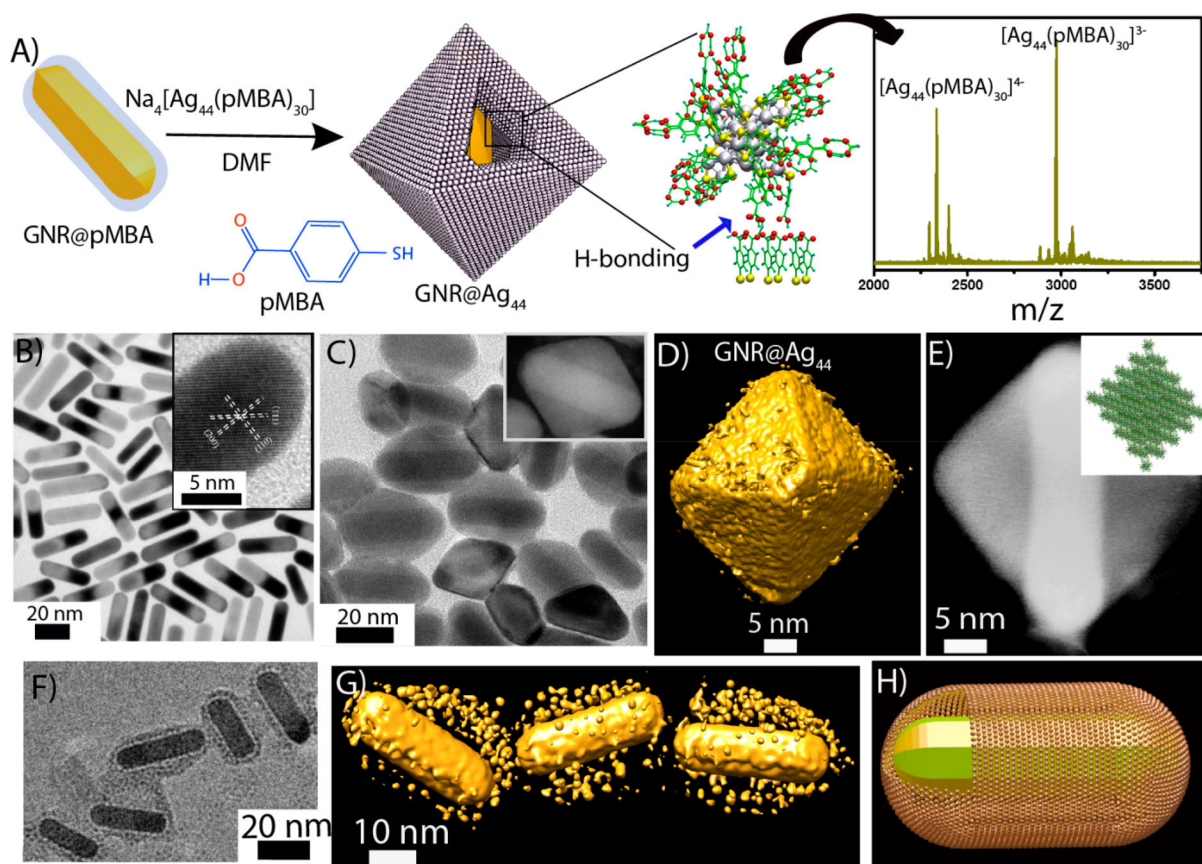
### Nanoparticle-Templated Cluster Supersystems

Once the clusters were known to interact with anisotropic nanoparticles leading to structures of interesting morphology, we expanded the study using similar nanomaterials. Gold nanorods (GNRs) have been at the center of interest for decades because of their unique surface plasmonic properties. Recent studies have revealed that because of their nanometric dimensions, GNRs can accommodate quantum dots on their surfaces and significantly alter the optoelectronic properties of the quantum dots by plasmon–exciton coupling in these systems.<sup>43</sup> Using  $\text{p-MBA}$ -protected gold NCs, Nonappa and co-workers demonstrated the formation of monolayer-thick 2D nanosheets and spherical capsids by tuning the supramolecular interactions such as intercluster hydrogen bonding.<sup>44,45</sup> We placed atomically precise clusters on GNRs to explore the possibility of supramolecular-chemistry-driven hybrid nanostructures.<sup>46</sup> Specifically, GNRs were functionalized with  $\text{p-MBA}$  at neutral pH. These GNRs were then incubated with  $\text{Ag}_{44}(\text{p-MBA})_{30}$  in DMF for 20 h, during which the  $\text{p-MBA}$  groups of the clusters formed hydrogen bonds within themselves as well as with the  $\text{p-MBA}$  groups on the GNR surface (scheme in Figure 7A). This created a multilayer shell encapsulating the individual GNRs within a cage-like nanostructure. Transmission electron microscopy (TEM), scanning transmission electron microscopy (STEM), and 3D tomographic reconstructions of these nanostructures revealed that the final morphology of the hybrid material is octahedral (Figure 7C–E), possibly because of the preferable anchoring of the clusters on the four alternative  $\langle 110 \rangle$  facets over the  $\langle 100 \rangle$  facets on the octagonal GNR

surfaces. Interestingly, the intrinsic properties of the constituent materials, namely, the GNR and  $\text{Ag}_{44}$ , were retained in the final nanostructure which shows remarkable ambient stability. Next, we reacted the  $\text{p-MBA}$ -functionalized GNRs with water-dispersible  $\text{Au}_{102}(\text{p-MBA})_{44}$ <sup>35</sup> and  $\text{Au}_{250}(\text{p-MBA})_{47}$ <sup>47</sup> in a similar fashion to check the generic nature of the scheme in terms of the NCs and the solvents used. Here also we observed encapsulation of the GNRs by the NCs, although in these cases the cluster moieties were less closely packed (Figure 7F). This was attributed to the fact that in the water-soluble state, some of the  $\text{p-MBA}$  ligands of the gold clusters had to be deprotonated, making fewer ligands available for hydrogen bonding and thus making the final structures less compact. We expect that with the rightly chosen NC, this hybrid system can significantly improve the stability and detection limit of cluster-based sensing devices by plasmon-assisted enhancement of cluster properties.

### FUTURE PERSPECTIVES

In this Account, we have presented a glimpse into the various supramolecular interactions possible in atomically precise clusters. While supramolecular functionalization of the NCs with molecules like CD and  $\text{C}_{60}$  highlights the precision in their structures to selectively favor the formation of the host–guest complexes, exploring such composite structures in the solid state would lead to new materials. Although we have observed a mixture of adducts in solution, better control of the polydispersity of the supramolecular adducts to accomplish atomic precision and consequent crystallization are challenging areas. Furthermore, the site of attachment and binding modes of



**Figure 7.** (A) Assembly of  $\text{Ag}_{44}$  NCs on the  $\text{GNR}@p\text{-MBA}$  surface. The ESI MS spectrum of  $\text{Ag}_{44}$  is shown as the inset. (b) TEM image of  $\text{GNR}@p\text{-MBA}$ . HRTEM image of the tip of a GNR is shown in the inset. (C) TEM image of  $\text{GNR}@Ag_{44}$ . A dark-field STEM image is shown in the inset. (D, E) TEM tomographic and dark-field STEM images of  $\text{GNR}@Ag_{44}$ . The image shows that the clusters make a nanocage and encapsulate the GNR. A theoretical model of the assembly of  $\text{Ag}_{44}$  clusters forming an octahedral shape is presented in the inset. (F) TEM image of  $\text{GNR}@Au_{250}$ . (G, H) 3D reconstructed structures and 3D graphical representation of  $\text{GNR}@Au_{250}$ , respectively. Reproduced with permission from ref 46. Copyright 2018 Wiley-VCH.

CD and  $C_{60}$  to the clusters may vary, which may lead to isomerism in the resulting structures. Such isomerism could extend to novel optical properties as well. With an appropriate choice of the host and guest molecules, chirality may also be introduced in supramolecular assemblies of certain clusters. Functionalized fullerenes or CDs may also be used to modify cluster binding. The development of functional cluster-based materials may also include modifying the ligand shell of the cluster with suitable bidentate or multidentate linkers, allowing the creation of cluster-assembled metal–organic frameworks.<sup>48</sup> The observation of polymorphic crystal lattices of NCs also enfold a new area in nanoparticle engineering. Supramolecular interactions may also favor crystallization of dimers or oligomers of clusters. Furthermore, the self-organization of nanostructures with macrostructures leading to architectures of larger dimensions constitutes new types of precision hybrids with diverse possibilities. These derived materials, especially low-dimensional building blocks, may lead to anisotropic solids with unprecedented properties. The self-assembly of NCs leading to spherical capsids<sup>44,45</sup> is a direction toward larger assemblies similar to biological systems. Cluster-assembled hybrid materials may result in a new paradigm of conductive or magnetic luminescent materials.

The choice of supramolecular building blocks presented here has been dominated by the consideration of interactions. However, such building blocks can also be chosen on the basis of

new properties such as magnetism, chirality, energy transfer, etc. that they provide. A unique aspect of clusters is that their size is comparable to the dimensions of biomolecules, which are also building blocks with atomic precision. Thus, structures incorporating biomolecules or synthetic polymers along with clusters is another strategy to create functional materials. In comparison with supramolecular assemblies solely composed of biomolecules, cluster-based assemblies can introduce new optical, magnetic, or electrical properties.

A closer analysis of this area shows that the molecule–materials interface is enriched by MS in its diverse forms. Compositional precision revealed by MS, in conjunction with structural and conformational precision revealed by diffraction and spectroscopy, coupled with computational studies enabling better insights into the properties, are essential components of this area. Several of the finer details of these materials such as the atomistic steps involved in the formation of these assemblies and their time scales are not accessible presently by experimental methods, and therefore, computations become the only credible methodology for exploration. This MS–diffraction–theory combination in the context of novel properties of atomically precise matter is expected to expand into even more larger systems in the years ahead, which should result in a fuller appreciation of materials with atomic precision.



## AUTHOR INFORMATION

### Corresponding Author

\*E-mail: [pradeep@iitm.ac.in](mailto:pradeep@iitm.ac.in).

### ORCID

Thalappil Pradeep: 0000-0003-3174-534X

### Notes

The authors declare no competing financial interest.

### Biographies

**Papri Chakraborty** is a Ph.D. student in the group of Prof. T. Pradeep at Indian Institute of Technology Madras. Her research is focused on mass spectrometric studies of noble metal clusters.

**Abhijit Nag** is a Ph.D. student in the group of Prof. T. Pradeep at Indian Institute of Technology Madras. His research is focused on supramolecular chemistry of clusters and biomolecules.

**Amrita Chakraborty** is a Ph.D. student in the group of Prof. T. Pradeep at Indian Institute of Technology Madras. Her research is focused on cluster–nanoparticle composite systems.

**Thalappil Pradeep** is a Professor at Indian Institute of Technology Madras. He works on molecular and nanoscale materials. Some of his findings have been translated to products through startup companies.

## ACKNOWLEDGMENTS

We thank all of the coauthors of previous publications from our group, who made this Account possible. P.C. and A.C. thank the Council of Scientific and Industrial Research (CSIR) for their research fellowships. A.N. thanks IIT Madras for an Institute Doctoral Fellowship. We acknowledge the financial support of the Department of Science and Technology (DST), Government of India.

## REFERENCES

- (1) Chakraborty, I.; Pradeep, T. Atomically Precise Clusters of Noble Metals: Emerging Link between Atoms and Nanoparticles. *Chem. Rev.* **2017**, *117*, 8208–8271.
- (2) Jin, R.; Zeng, C.; Zhou, M.; Chen, Y. Atomically Precise Colloidal Metal Nanoclusters and Nanoparticles: Fundamentals and Opportunities. *Chem. Rev.* **2016**, *116*, 10346–10413.
- (3) Fang, J.; Zhang, B.; Yao, Q.; Yang, Y.; Xie, J.; Yan, N. Recent Advances in the Synthesis and Catalytic Applications of Ligand-protected, Atomically Precise Metal Nanoclusters. *Coord. Chem. Rev.* **2016**, *322*, 1–29.
- (4) Maity, P.; Xie, S.; Yamauchi, M.; Tsukuda, T. Stabilized Gold Clusters: From Isolation toward Controlled Synthesis. *Nanoscale* **2012**, *4*, 4027–4037.
- (5) Krishnadas, K. R.; Baksi, A.; Ghosh, A.; Natarajan, G.; Som, A.; Pradeep, T. Interparticle Reactions: An Emerging Direction in Nanomaterials Chemistry. *Acc. Chem. Res.* **2017**, *50*, 1988–1996.
- (6) Yao, Q.; Feng, Y.; Fung, V.; Yu, Y.; Jiang, D.-e.; Yang, J.; Xie, J. Precise Control of Alloying Sites of Bimetallic Nanoclusters via Surface Motif Exchange Reaction. *Nat. Commun.* **2017**, *8*, 1555.
- (7) Zeng, C.; Chen, Y.; Kirschbaum, K.; Lambright, K. J.; Jin, R. Emergence of Hierarchical Structural Complexities in Nanoparticles and their Assembly. *Science* **2016**, *354*, 1580.
- (8) Baksi, A.; Chakraborty, P.; Bhat, S.; Natarajan, G.; Pradeep, T.  $[\text{Au}_{25}(\text{SR})_{18}]_2^{2-}$ : A Noble Metal Cluster Dimer in the Gas Phase. *Chem. Commun.* **2016**, *52*, 8397–8400.
- (9) De Nardi, M.; Antonello, S.; Jiang, D.-e.; Pan, F.; Rissanen, K.; Ruzzi, M.; Venzo, A.; Zoleo, A.; Maran, F. Gold Nanowired: A Linear  $(\text{Au}_{25})_n$  Polymer from  $\text{Au}_{25}$  Molecular Clusters. *ACS Nano* **2014**, *8*, 8505–8512.
- (10) Fontana, J.; Dressick, W. J.; Phelps, J.; Johnson, J. E.; Rendell, R. W.; Sampson, T.; Ratna, B. R.; Soto, C. M. Virus-Templated Plasmonic Nanoclusters with Icosahedral Symmetry via Directed Self-Assembly. *Small* **2014**, *10*, 3058–3063.
- (11) Berry, V.; Saraf, R. F. Self-Assembly of Nanoparticles on Live Bacterium: An Avenue To Fabricate Electronic Devices. *Angew. Chem., Int. Ed.* **2005**, *44*, 6668–6673.
- (12) Natarajan, G.; Mathew, A.; Negishi, Y.; Whetten, R. L.; Pradeep, T. A Unified Framework for Understanding the Structure and Modifications of Atomically Precise Monolayer Protected Gold Clusters. *J. Phys. Chem. C* **2015**, *119*, 27768–27785.
- (13) Fernando, A.; Aikens, C. M. Ligand Exchange Mechanism on Thiolate Monolayer Protected  $\text{Au}_{25}(\text{SR})_{18}$  Nanoclusters. *J. Phys. Chem. C* **2015**, *119*, 20179–20187.
- (14) Jin, R.; Nobusada, K. Doping and Alloying in Atomically Precise Gold Nanoparticles. *Nano Res.* **2014**, *7*, 285–300.
- (15) Mathew, A.; Natarajan, G.; Lehtovaara, L.; Häkkinen, H.; Kumar, R. M.; Subramanian, V.; Jaleel, A.; Pradeep, T. Supramolecular Functionalization and Concomitant Enhancement in Properties of  $\text{Au}_{25}$  Clusters. *ACS Nano* **2014**, *8*, 139–152.
- (16) Som, A.; Chakraborty, I.; Maark, T. A.; Bhat, S.; Pradeep, T. Cluster-Mediated Crossed Bilayer Precision Assemblies of 1D Nanowires. *Adv. Mater.* **2016**, *28*, 2827–2833.
- (17) Rekharsky, M. V.; Inoue, Y. Complexation Thermodynamics of Cyclodextrins. *Chem. Rev.* **1998**, *98*, 1875–1918.
- (18) May, B. L.; Gerber, J.; Clements, P.; Buntine, M. A.; Brittain, D. R. B.; Lincoln, S. F.; Easton, C. J. Cyclodextrin and Modified Cyclodextrin Complexes of *E*-4-*tert*-butylphenyl-4'-oxyazobenzene: UV–visible,  $^1\text{H}$  NMR and ab Initio Studies. *Org. Biomol. Chem.* **2005**, *3*, 1481–1488.
- (19) Heaven, M. W.; Dass, A.; White, P. S.; Holt, K. M.; Murray, R. W. Crystal Structure of the Gold Nanoparticle  $[\text{N}(\text{C}_8\text{H}_{17})_4]_4[\text{Au}_{25}(\text{SCH}_2\text{CH}_2\text{Ph})_{18}]$ . *J. Am. Chem. Soc.* **2008**, *130*, 3754–3755.
- (20) Zhu, M.; Aikens, C. M.; Hollander, F. J.; Schatz, G. C.; Jin, R. Correlating the Crystal Structure of a Thiol-Protected  $\text{Au}_{25}$  Cluster and Optical Properties. *J. Am. Chem. Soc.* **2008**, *130*, 5883–5885.
- (21) Park, J. H.; Hwang, S.; Kwak, J. Nanosieving of Anions and Cavity-Size-Dependent Association of Cyclodextrins on a 1-Adamantanethiol Self-Assembled Monolayer. *ACS Nano* **2010**, *4*, 3949–3958.
- (22) Böhm, I.; Isenbügel, K.; Ritter, H.; Branscheid, R.; Kolb, U. Cyclodextrin and Adamantane Host–Guest Interactions of Modified Hyperbranched Poly(ethylene imine) as Mimetics for Biological Membranes. *Angew. Chem., Int. Ed.* **2011**, *50*, 7896–7899.
- (23) Harries, D.; Rau, D. C.; Parsegian, V. A. Solutes Probe Hydration in Specific Association of Cyclodextrin and Adamantane. *J. Am. Chem. Soc.* **2005**, *127*, 2184–2190.
- (24) Yan, C.; Liu, C.; Abroshan, H.; Li, Z.; Qiu, R.; Li, G. Surface Modification of Adamantane-Terminated Gold Nanoclusters using Cyclodextrins. *Phys. Chem. Chem. Phys.* **2016**, *18*, 23358–23364.
- (25) Higaki, T.; Liu, C.; Zeng, C.; Jin, R.; Chen, Y.; Rosi, N. L.; Jin, R. Controlling the Atomic Structure of  $\text{Au}_{30}$  Nanoclusters by a Ligand-Based Strategy. *Angew. Chem., Int. Ed.* **2016**, *55*, 6694–6697.
- (26) Kang, X.; Zhou, M.; Wang, S.; Jin, S.; Sun, G.; Zhu, M.; Jin, R. The Tetrahedral Structure and Luminescence Properties of Bi-metallic  $\text{Pt}_1\text{Ag}_{28}(\text{SR})_{18}(\text{PPh}_3)_4$  Nanocluster. *Chem. Sci.* **2017**, *8*, 2581–2587.
- (27) Crasto, D.; Barcaro, G.; Stener, M.; Sementa, L.; Fortunelli, A.; Dass, A.  $\text{Au}_{24}(\text{SAdm})_{16}$  Nanomolecules: X-ray Crystal Structure, Theoretical Analysis, Adaptability of Adamantane Ligands To Form  $\text{Au}_{23}(\text{SAdm})_{16}$  and  $\text{Au}_{25}(\text{SAdm})_{16}$ , and its Relation to  $\text{Au}_{25}(\text{SR})_{18}$ . *J. Am. Chem. Soc.* **2014**, *136*, 14933–14940.
- (28) Bhunia, S.; Kumar, S.; Purkayastha, P. Gold Nanocluster-Grafted Cyclodextrin Suprastructures: Formation of Nanospheres to Nanocubes with Intriguing Photophysics. *ACS Omega* **2018**, *3*, 1492–1497.
- (29) Zhu, H.; Goswami, N.; Yao, Q.; Chen, T.; Liu, Y.; Xu, Q.; Chen, D.; Lu, J.; Xie, J. Cyclodextrin–Gold Nanocluster Decorated  $\text{TiO}_2$  Enhances Photocatalytic Decomposition of Organic Pollutants. *J. Mater. Chem. A* **2018**, *6*, 1102–1108.
- (30) Diederich, F.; Gomez-Lopez, M. Supramolecular Fullerene Chemistry. *Chem. Soc. Rev.* **1999**, *28*, 263–277.
- (31) Chakraborty, P.; Nag, A.; Paramasivam, G.; Natarajan, G.; Pradeep, T. Fullerene-Functionalized Monolayer-Protected Silver



Clusters:  $[\text{Ag}_{29}(\text{BDT})_{12}(\text{C}_{60})_n]^{3-}$  ( $n = 1-9$ ). *ACS Nano* **2018**, *12*, 2415–2425.

(32) AbdulHalim, L. G.; Bootharaju, M. S.; Tang, Q.; Del Gobbo, S.; AbdulHalim, R. G.; Eddaoudi, M.; Jiang, D.-e.; Bakr, O. M.  $\text{Ag}_{29}(\text{BDT})_{12}(\text{TPP})_4$ : A Tetravalent Nanocluster. *J. Am. Chem. Soc.* **2015**, *137*, 11970–11975.

(33) Schulz-Dobrick, M.; Jansen, M. Intercluster Compounds Consisting of Gold Clusters and Fullerides:  $[\text{Au}_7(\text{PPh}_3)_7]\text{C}_{60}\cdot\text{THF}$  and  $[\text{Au}_8(\text{PPh}_3)_8](\text{C}_{60})_2$ . *Angew. Chem., Int. Ed.* **2008**, *47*, 2256–2259.

(34) Yoon, B.; Luedtke, W. D.; Barnett, R. N.; Gao, J.; Desiredy, A.; Conn, B. E.; Bigioni, T.; Landman, U. Hydrogen-Bonded Structure and Mechanical Chiral Response of a Silver Nanoparticle Superlattice. *Nat. Mater.* **2014**, *13*, 807.

(35) Jadzinsky, P. D.; Calero, G.; Ackerson, C. J.; Bushnell, D. A.; Kornberg, R. D. Structure of a Thiol Monolayer-Protected Gold Nanoparticle at 1.1 Å Resolution. *Science* **2007**, *318*, 430.

(36) Higaki, T.; Liu, C.; Zhou, M.; Luo, T.-Y.; Rosi, N. L.; Jin, R. Tailoring the Structure of 58-Electron Gold Nanoclusters:  $\text{Au}_{103}\text{S}_2(\text{S-Nap})_{41}$  and Its Implications. *J. Am. Chem. Soc.* **2017**, *139*, 9994–10001.

(37) Liao, L.; Chen, J.; Wang, C.; Zhuang, S.; Yan, N.; Yao, C.; Xia, N.; Li, L.; Bao, X.; Wu, Z. Transition-Sized  $\text{Au}_{92}$  Nanoparticle Bridging Non-fcc-structured Gold Nanoclusters and fcc-structured Gold Nanocrystals. *Chem. Commun.* **2016**, *52*, 12036–12039.

(38) Gan, Z.; Chen, J.; Wang, J.; Wang, C.; Li, M.-B.; Yao, C.; Zhuang, S.; Xu, A.; Li, L.; Wu, Z. The Fourth Crystallographic Closest Packing Unveiled in the Gold Nanocluster Crystal. *Nat. Commun.* **2017**, *8*, 14739.

(39) Nag, A.; Chakraborty, P.; Bodiuzzaman, M.; Ahuja, T.; Antharjanam, S.; Pradeep, T. Polymorphism of  $\text{Ag}_{29}(\text{BDT})_{12}(\text{TPP})_4^{3-}$  Cluster: Interactions of Secondary Ligands and their Effect on Solid State Luminescence. *Nanoscale* **2018**, *10*, 9851–9855.

(40) Som, A.; Samal, A. K.; Udayabhaskararao, T.; Bootharaju, M. S.; Pradeep, T. Manifestation of the Difference in Reactivity of Silver Clusters in Contrast to Its Ions and Nanoparticles: The Growth of Metal Tipped Te Nanowires. *Chem. Mater.* **2014**, *26*, 3049–3056.

(41) Udayabhaskararao, T.; Bootharaju, M. S.; Pradeep, T. Thiolate-Protected  $\text{Ag}_{32}$  Clusters: Mass Spectral Studies of Composition and Insights into the Ag–thiolate Structure from NMR. *Nanoscale* **2013**, *5*, 9404–9411.

(42) Desiredy, A.; Conn, B. E.; Guo, J.; Yoon, B.; Barnett, R. N.; Monahan, B. M.; Kirschbaum, K.; Griffith, W. P.; Whetten, R. L.; Landman, U.; Bigioni, T. P. Ultrastable Silver Nanoparticles. *Nature* **2013**, *501*, 399.

(43) Nepal, D.; Drummy, L. F.; Biswas, S.; Park, K.; Vaia, R. A. Large Scale Solution Assembly of Quantum Dot–Gold Nanorod Architectures with Plasmon Enhanced Fluorescence. *ACS Nano* **2013**, *7*, 9064–9074.

(44) Nonappa; Lahtinen, T.; Haataja, J. S.; Tero, T.-R.; Häkkinen, H.; Ikkala, O. Template-Free Supracolloidal Self-assembly of Atomically Precise Gold Nanoclusters: From 2D Colloidal Crystals to Spherical Capsids. *Angew. Chem., Int. Ed.* **2016**, *55*, 16035–16038.

(45) Nonappa; Ikkala, O. Hydrogen Bonding Directed Colloidal Self-Assembly of Nanoparticles into 2D Crystals, Capsids, and Supracolloidal Assemblies. *Adv. Funct. Mater.* **2018**, *28*, 1704328.

(46) Chakraborty, A.; Fernandez, A. C.; Som, A.; Mondal, B.; Natarajan, G.; Paramasivam, G.; Lahtinen, T.; Häkkinen, H.; Nonappa; Pradeep, T. Atomically Precise Nanocluster Assemblies Encapsulating Plasmonic Gold Nanorods. *Angew. Chem., Int. Ed.* **2018**, *57*, 6522–6526.

(47) Lahtinen, T.; Hulkko, E.; Sokolowska, K.; Tero, T.-R.; Saarnio, V.; Lindgren, J.; Pettersson, M.; Häkkinen, H.; Lehtovaara, L. Covalently Linked Multimers of Gold Nanoclusters  $\text{Au}_{102}(\text{p-MBA})_{44}$  and  $\text{Au}_{250}(\text{p-MBA})_n$ . *Nanoscale* **2016**, *8*, 18665–18674.

(48) Huang, R.-W.; Wei, Y.-S.; Dong, X.-Y.; Wu, X.-H.; Du, C.-X.; Zang, S.-Q.; Mak, T. C. W. Hypersensitive Dual-Function Luminescence Switching of a Silver–Chalcogenolate Cluster-Based Metal–Organic Framework. *Nat. Chem.* **2017**, *9*, 689.

# Camouflaging Structural Diversity: Co-crystallization of Two Different Nanoparticles Having Different Cores But the Same Shell

Mohammad Bodiuzzaman<sup>+</sup>, Atanu Ghosh<sup>+</sup>, Korath Shivan Sugi, Abhijit Nag, Esma Khatun, Babu Varghese, Ganesan Paramasivam, Sudhadevi Antharjanam, Ganapati Natarajan, and Thalappil Pradeep\*

**Abstract:** Two ligand-protected nanoscale silver moieties,  $[Ag_{46}(SPhMe_2)_{24}(PPh_3)_8](NO_3)_2$  and  $[Ag_{40}(SPhMe_2)_{24}(PPh_3)_8](NO_3)_2$  (abbreviated as  $Ag_{46}$  and  $Ag_{40}$ , respectively) with almost the same shell but different cores were synthesized simultaneously. As their external structures are identical, the clusters were not distinguishable and become co-crystallized. The occupancy of each cluster was 50 %. The outer shell of both is composed of  $Ag_{32}S_{24}P_8$ , which is reminiscent of fullerenes, and it encapsulates a well-studied core,  $Ag_{14}$  and a completely new core,  $Ag_8$ , which correspond to a face-centered cube and a simple cube, respectively, resulting in the  $Ag_{46}$  and  $Ag_{40}$  clusters. The presence of two entities ( $Ag_{40}$  and  $Ag_{46}$  clusters) in a single crystal and their molecular formulae were confirmed by detailed electrospray ionization mass spectrometry. The optical spectrum of the mixture showed unique features which were in good agreement with the results from time-dependent density functional theory (TD-DFT).

Many molecular clusters of noble metals have been crystallized in the recent past.<sup>[1–17]</sup> All of them can be understood by the divide-and-protect formalism in which metal cores are protected by a composite shell, often formed of staple motifs.<sup>[18]</sup> The molecular architecture providing structural rigidity is also associated with a closed-shell electronic structure, making such cluster systems stable.<sup>[19,20]</sup> A unique possibility in such structures is the existence of a common outer shell with varied inner cores. Nucleation of different cores in the reaction vessel can consequently create such varied structures composed of different cores and same shell simultaneously. Their co-crystallization can lead to new materials.

In this work, we present the complete characterization of such a co-crystal. Upon resolving the structure of such

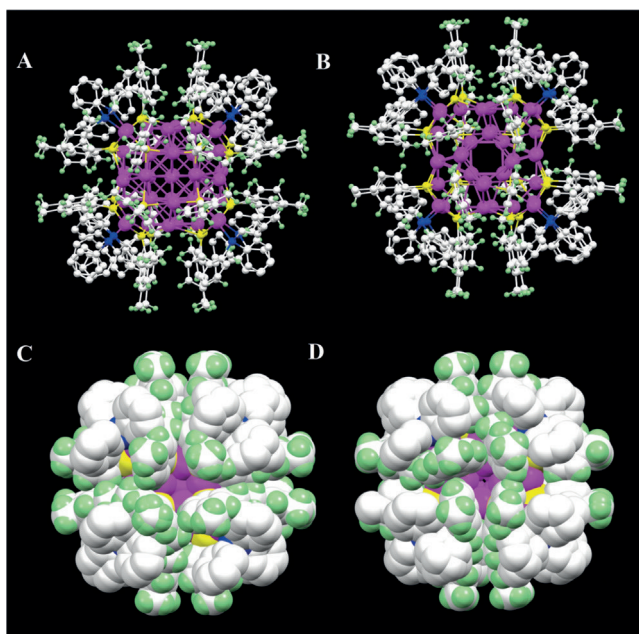
a disordered co-crystal, we obtained the formulae of component clusters as  $[Ag_{46}(SPhMe_2)_{24}(PPh_3)_8](NO_3)_2$  and  $[Ag_{40}(SPhMe_2)_{24}(PPh_3)_8](NO_3)_2$ , also represented as  $Ag_{46}$  and  $Ag_{40}$ , respectively, with 1:1 occupancy in the crystal. Single-crystal X-ray diffraction (SCXRD) shows that the clusters have an almost identical outer shell ( $Ag_{32}S_{24}P_8$ ) with variation only in the inner core ( $Ag_{14}$  and  $Ag_8$ ). Unlike  $Ag_{14}$ , the  $Ag_8$  inner core was not observed before. Existence of the two new clusters in a single crystal and their molecular formulae were confirmed by electrospray ionization mass spectrometry (ESI MS). This identification can open up new avenues of tailoring and elucidating the properties of such well-defined composite materials. The  $Ag_{46}$  and  $Ag_{40}$  units with their ligands are referred to as **I** and **II** in the subsequent discussion.

A mixture of **I** and **II** clusters was synthesized by a ligand-exchange-induced structure transformation (LEIST) process. In this process,  $[Ag_{18}H_{16}(PPh_3)_{10}]^{2+}$  was used as the precursor material and the ligand exchange reaction was performed with 2,4-dimethylbenzenethiol ( $SPhMe_2$ ) (see the Experimental Section in the Supporting Information). The precursor material was synthesized following a method reported by the Bakr group (Figure S1).<sup>[21]</sup> Single crystals were grown by layering hexane onto a dichloromethane solution of pure nanoclusters at 4°C. Dark black crystals were obtained over a period of 5–7 days. A mixture of as-synthesized clusters crystallizes in a C-centered monoclinic system with space group  $C2/m$ .<sup>[22]</sup> From the SCXRD analysis (see the Supporting Information for detailed analysis), it could be unambiguously inferred that there are two types of molecules in the lattice which are nearly isostructural but differing by six silver atoms. In other words, the two molecules are isodimensional and one can replace the position of the other. The total structures of **I** (Figure 1 A,C) and **II** (Figure 1 B,D) are shown in ball-and-stick and space-filling models, which reveal their isodimensionality. Six sites of **II**( $NO_3$ )<sub>2</sub> are vacant in **II**( $NO_3$ )<sub>2</sub>. Owing to their nearly identical outer shell, they are not able to distinguish themselves and crystallize together. Therefore, the six-atom difference does not come into the picture during the growth of the crystals and both the clusters are nucleated in equal proportion in a single crystal. We believe that this arises because of their equal concentration in the solution. A dissection of **I** and **II** was conducted based on the connectivity of silver atoms to ligands to get the inner cores (the metal structures that are not connected to ligands). The structures of inner cores,  $Ag_8$  (in **II**) and  $Ag_{14}$  (in **I**) are presented in Figure 2 A,D, respectively. Both the cores are encapsulated by the  $Ag_{32}S_{24}P_8$  shell (Figure 2 B,E), which is reminiscent of fullerenes. Total structures of  $[Ag_{40}S_{24}P_8]$  and

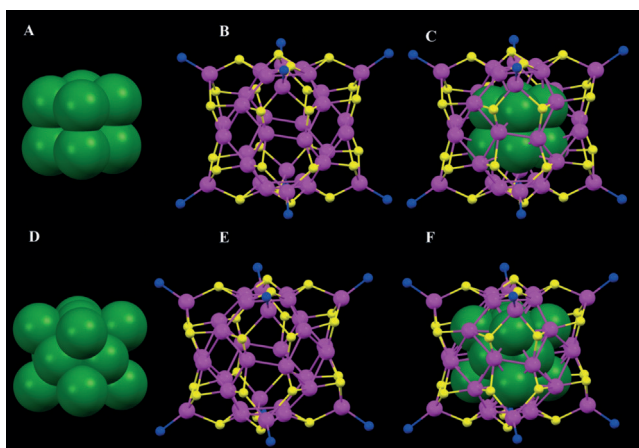
[\*] M. Bodiuzzaman,<sup>[+]</sup> Dr. A. Ghosh,<sup>[+]</sup> K. S. Sugi, A. Nag, E. Khatun, Dr. G. Paramasivam, Dr. G. Natarajan, Prof. T. Pradeep  
Department of Chemistry, DST Unit of Nanoscience (DST UNS) and Thematic Unit of Excellence (TUE)  
Indian Institute of Technology Madras  
Chennai 600036 (India)  
E-mail: pradeep@iitm.ac.in  
Dr. B. Varghese, Dr. S. Antharjanam  
Sophisticated Analytical Instruments Facility  
Indian Institute of Technology Madras  
Chennai 600036 (India)

[+] These authors contributed equally to this work.

Supporting information and the ORCID identification number(s) for the author(s) of this article can be found under:  
<https://doi.org/10.1002/anie.201809469>.



**Figure 1.** A), B) Ball-and-stick models of  $\text{Ag}_{46}$  and  $\text{Ag}_{40}$ , respectively. Note the difference in the center of the cluster. C), D) The same in space-filling model (hydrogens of triphenylphosphines are not fixed). It is clear that the outer shells of the clusters are nearly identical. Counterions are not shown. C white, Ag magenta, S yellow, P blue, H light green.



**Figure 2.** A), D)  $\text{Ag}_8$  and  $\text{Ag}_{14}$  inner-core structures of  $\text{Ag}_{40}$  and  $\text{Ag}_{46}$ , respectively. The inner cores  $\text{Ag}_8$  and  $\text{Ag}_{14}$  correspond to simple cubic and face-centered cubic structures, respectively. B), E)  $\text{Ag}_{32}\text{S}_{24}\text{P}_8$  shell; that is, the structures of the clusters without metal cores. C), F) The structures of  $[\text{Ag}_{40}\text{S}_{24}\text{P}_8]$  and  $[\text{Ag}_{46}\text{S}_{24}\text{P}_8]$ , respectively. Carbon and hydrogen atoms are omitted for clarity. Ag green and magenta, S yellow, P blue.

$[\text{Ag}_{40}\text{S}_{24}\text{P}_8]$  are shown in Figure 2C,F, respectively (carbon and hydrogen atoms are omitted here). The core and shell structures presented for these two clusters (Figure 2) can be viewed in different ways in the context of known structures. A compendium of such known structures is presented in the Supporting Information, Table S1, which brings out unique aspects of the new structures. The first unique aspect is the completely new kind of core  $\text{Ag}_8$  (in **II**) and the well-studied

core  $\text{Ag}_{14}$  (in **I**).<sup>[23–25]</sup> They correspond to perfect simple cubic and face-centered cubic structures, respectively. The face-centered cubic structure ( $\text{Ag}_{14}$ ) can also be visualized as octacapped octahedron,  $\text{Ag}_6@ \text{Ag}_8$  (Figure S2A–C). Here, the  $\text{Ag}_{\text{octahedron}}-\text{Ag}_{\text{cube}}$  distance is 2.70 Å, which indicates the strong interaction between the core atoms. The surface of the octahedral  $\text{Ag}_6$  (Figure S2B) inner core is surrounded by eight equilateral triangle-shaped planes, a fragment of bulk FCC metals.<sup>[24]</sup> The average Ag–Ag bond distance in octahedral  $\text{Ag}_6$  is 2.88 Å, which is almost same as that in bulk (2.89 Å).<sup>[26]</sup> Around the octahedral  $\text{Ag}_6$  core, there are eight Ag atoms, which make a cube (Figure S2A). The average distance between the corners of the cube is 3.8 Å, which is much shorter than that of other reported FCC structures (the same distance is about 4.2 Å).<sup>[23,24]</sup> The surfaces of the  $\text{Ag}_8$  cube are covered by six square-shaped {100} (Figure S3A) facets. Along with this, other facets like rectangular-shaped {110} (Figure S3B) and equilateral triangle-shaped {111} (Figure S3C) are observed. All these facets are shown in ball-and-stick model (Figure S3). In case of **II**, the inner core atoms of the simple cube are bonded very strongly with average Ag–Ag distances of 2.68 Å, which is much shorter than in bulk silver.<sup>[26]</sup>

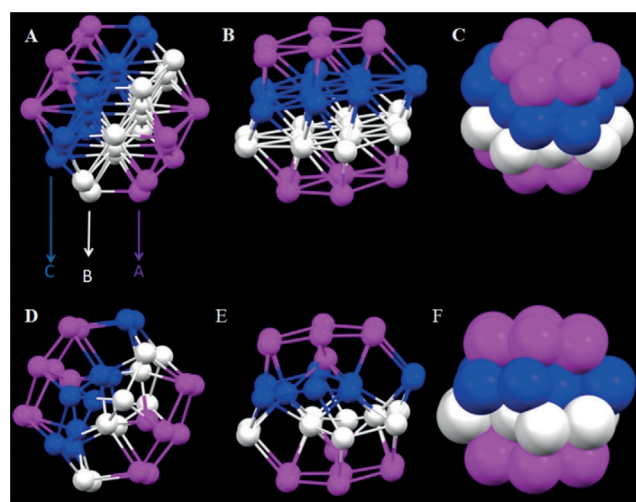
The formation of a common shell,  $\text{Ag}_{32}\text{S}_{24}\text{P}_8$  (Figure S4C) can be described as composed of  $\text{Ag}_{24}$  (Figure S4B) outer core covered by eight units of  $\text{Ag}^{\text{I}}$ -thiolate-phosphine complex ( $\text{AgS}_3\text{P}$ ) (Figure S4A). The  $\text{Ag}_{24}$  outer core can be viewed as it is composed of eight shared hexagonal faces (Figure S4D).  $\text{AgS}_3\text{P}$  units are sitting on the faces of eight hexagons of  $\text{Ag}_{24}$  outer core to form the framework,  $\text{Ag}_{32}\text{S}_{24}\text{P}_8$  (Figure S4F). Each sulfur of  $\text{AgS}_3\text{P}$  bridges the two adjacent silver atoms of a hexagon (Figure S4F). Here the average Ag–Ag distance within the hexagons is 2.92 Å. Another way of looking into the outer core ( $\text{Ag}_{24}$ ) is in terms of six square faces (Figure S5A). The faces are shown in different colors (Figure S5A). Average Ag–Ag distance in the square face is 3.0 Å and square faces are connected by a bond length of 2.86 Å. In this ligand shell, average Ag–S and Ag–P distances are 2.64 Å and 2.45 Å, respectively. It is worth noting that all the Ag–Ag distances in the outer  $\text{Ag}_{24}$  core are exactly same in both the clusters. A summary of Ag–Ag distances is presented in the Supporting Information, Table S2. The bonding between the inner core and outer core are not same in **I** and **II** clusters. In **I** the squares of  $\text{Ag}_{24}$  outer core are connected to the six silver atoms of octahedral  $\text{Ag}_6$  (Figure S5B), forming a six square-pyramid-like architecture (Figure S5C). One such square-pyramid is shown in wireframe model (Figure S5D). In this architecture, Ag–Ag distances between silver atoms on the apex and the square faces are 3.0 Å. Such a square-pyramid-like architecture is not observed in the **II** cluster owing to the absence of an octahedral ( $\text{Ag}_6$ ) inner core. The further differences in bonding between the outer ( $\text{Ag}_{24}$ ) and inner cores in **I** and **II** clusters will be explained later.

A packing diagram of both the clusters is shown in the Supporting Information, Figure S6. Both the clusters are packed in an identical fashion in all the axes and the contribution of each component cluster is 50%. **II** is organized into centered rectangular (Figure S6A) and rectangular (Figure S6C) two-dimensional (2D) lattices along

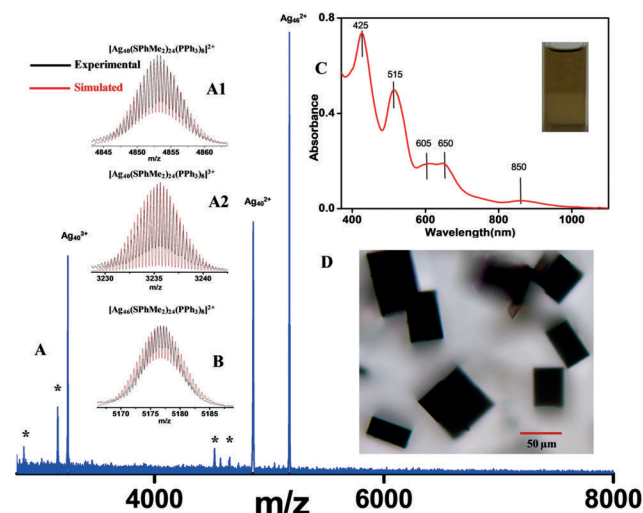


the  $z$  and  $x$  direction, respectively. Similar packing is observed for **I** (Figure S6B,D; along the  $z$  and  $x$  direction, respectively). The crystal structure resolved nitrate as the counter ion and the packing structure clearly indicates the location of two counter ions per cluster (Figure S7). However, the packing is identical for both the molecules (Figure S6), the stacking of silver atoms in their kernels is different. The term kernel refers to the combined unit of outer and inner cores. The construction of  $\text{Ag}_{32}$  (in **II**) and  $\text{Ag}_{38}$  (in **I**) kernels are shown in Figure S8. The  $\text{Ag}_{24}$  outer core (Figure S8A) encapsulates  $\text{Ag}_8$  inner core to form  $\text{Ag}_{32}$  kernel (Figure S8B). Similarly,  $\text{Ag}_{38}$  kernel (Figure S8D) is formed by the combination of  $\text{Ag}_{24}$  outer core and  $\text{Ag}_{14}$  inner core. In  $\text{Ag}_{32}$  kernel (in **II**), atoms of the  $\text{Ag}_8$  core take upward and downward positions of the hexagonal faces of  $\text{Ag}_{24}$  outer core (Figure S8B), and thus the eight silver atoms are not in the same plane of hexagons (Figure S8B,C). In the  $\text{Ag}_{38}$  kernel (in **I**), eight silver atoms that are at the corners of the face-centered cube occupy the center position of the hexagon of the  $\text{Ag}_{24}$  outer core (Figure S8D). Here it is important to note that all the atoms of the hexagon are coordinated to its centered silver atom in  $\text{Ag}_{38}$  kernel (in **I**; Figure S8E) but in  $\text{Ag}_{32}$  (in **II**) only a few atoms of the hexagon are connected to its upward and downward positioned silver atom (Figure S8C). Stacking of the atoms in the  $\text{Ag}_{38}$  and  $\text{Ag}_{32}$  kernels are shown in Figure 3. The  $\text{Ag}_{38}$  kernel (in **I**) exhibits ABC stacking (Figure 3A–C) owing to the in-plane arrangements of the atoms. The stacking planes are shown with three different color arrows in Figure 3A. Such stacking is not observed for  $\text{Ag}_{32}$  kernel (in **II**) as the atoms of inner core ( $\text{Ag}_8$ ) take upward and downward positions of the hexagonal faces of  $\text{Ag}_{24}$  outer core (Figure 3D–F). Space-filling model for both the kernels,  $\text{Ag}_{38}$  and  $\text{Ag}_{32}$  are presented in Figure 3C and F, respectively. Stacking is consistent in other rotations also as shown in Figure 3B and E for  $\text{Ag}_{38}$  and  $\text{Ag}_{32}$  kernels, respectively. The structure of  $\text{Ag}_{38}$  kernel can also be viewed as an inner  $\text{Ag}_6$  octahedron, surrounded by a truncated-octahedral shell of  $\text{Ag}_{32}$  (Figure S9A), which is having close resemble to the predicted structure of  $\text{Au}_{38}(\text{SR})_{24}$ .<sup>[27]</sup> The truncated octahedron shell is shown in wireframe model (Figure S9B) and the  $\text{Ag}_6$  octahedron is presented in space-filling model (Figure S9C).

ESI MS shows the coexistence of those two entities (**I** and **II**) in a single crystal. For this, a single crystal was dissolved in methanol and mass spectral measurement was performed. Sample preparation and instrumental conditions are given in Supporting Information. Full range mass spectrum shows three major peaks at  $m/z$  3235.75, 4853.5, and 5176.25 in positive-ion mode (Figure 4A). Peaks at  $m/z$  5176.25 and 4853.50 are expanded in the Supporting Information, Figures S10A,B. They show the characteristic peak separation of  $m/z$  0.5, which confirm their  $2+$  charge state. Similarly, the separation between peaks centered at  $m/z$  3235.75 is 0.33 which confirms the  $3+$  charge state (Figure S10C). The peaks at  $m/z$  4853.5 and 3235.75 are assigned as  $\text{II}^{2+}$  and  $\text{II}^{3+}$ , respectively. Comparison of isotopic distributions of experimental (black trace) and simulated (red trace) confirm the composition (Figure 4A1,A2). Existence of two charge states in the mass spectrum was also reported previously for the  $[\text{Ag}_{44}(\text{p-MBA})_{30}]^{4-}$  (p-MBA: 4-mercaptobenzoic acid) clus-



**Figure 3.** A),B) The structure of  $\text{Ag}_{38}$  kernel in two different rotations along the  $z$  axis (removing all the carbons, hydrogens, and eight  $\text{AgS}_3\text{P}$  units from total structure of  $\text{Ag}_{46}$ ) in ball-and-stick model. D),E) The structure of  $\text{Ag}_{32}$  kernel in two different rotations along the  $z$  axis (removing all the carbons, hydrogens, and eight  $\text{AgS}_3\text{P}$  units from total structure of  $\text{Ag}_{40}$ ) in ball-and-stick model. C),F) Space-filling model of (B) and (E), respectively. The ABC stacking planes are shown by three different color arrows in  $\text{Ag}_{38}$  kernel (in  $\text{Ag}_{46}$ ). Such stacking is not observed for  $\text{Ag}_{32}$  kernel (in  $\text{Ag}_{40}$ ). All atoms shown are silver.



**Figure 4.** A) Full-range ESI MS of a methanol solution of crystals in positive ion mode. The major peaks are due to  $\text{Ag}_{40}^{2+}$ ,  $\text{Ag}_{40}^{3+}$  and  $\text{Ag}_{46}^{2+}$ . Peaks labeled with an asterisk (\*) correspond to  $\text{PPh}_3$  losses from these ions. Insets A1),A2) Comparison of experimental (black trace) and simulated (red trace) isotopic distributions of  $\text{Ag}_{40}^{2+}$  and  $\text{Ag}_{40}^{3+}$ , respectively. B) The experimental (black) and simulated (red) isotopic distributions of  $\text{Ag}_{46}^{2+}$  are compared. C) UV/Vis absorption spectrum of a solution of crystals in dichloromethane. Inset: Visible light photograph of the cluster solution. D) Optical image of the crystals.

ter.<sup>[8]</sup> Seemingly, population of  $\text{Ag}_{40}^{2+}$  is major in the solution phase and  $\text{Ag}_{40}^{3+}$  might be present in the gas phase. Similarly, the peak at  $m/z$  5176.25 is assigned as  $\text{I}^{2+}$ . The experimental (black trace) and simulated (red trace) isotopic distributions

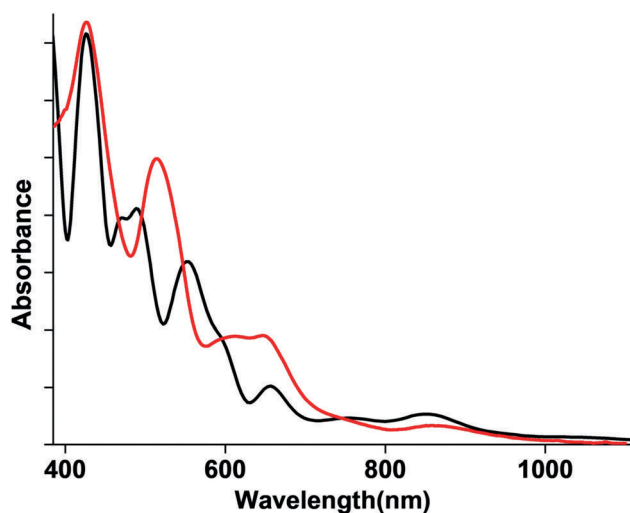
are compared in Figure 4B, which supports the assigned composition. The above observations prove the presence of two species, **I** and **II** in a single crystal. However, one may think whether **II** is formed from **I** by decomposition in the gas phase. To probe this possibility, we performed collision-induced dissociation (CID) experiments on  $\mathbf{I}^{2+}$ , which resulted in systematic triphenylphosphine losses as expected owing to the weaker interaction of the secondary ligands,<sup>[6,28]</sup> yielding  $\mathbf{I}(\text{PPh}_3)_8^{2+}$ ; however no **II** in any charge state was detected (Figure S11). CID mass spectra of **I** and **II** revealed a maximum loss of eight triphenylphosphines in **I** (Figure S12A) and **II** (Figure S12B) clusters, which supports the number of triphenylphosphines present in the cluster formulae. Hence, it is shown that in the gas phase there is no fragmentation of **I** to create **II**, but the possibility of formation of **II** by oxidation of **I** in the solution phase exists. To rule out this possibility, the solution of a mixture of **I** and **II** was heated and stirred in methanol at 50 °C and products were analyzed by UV/Vis and ESI MS as a function of time. Time-dependent UV/Vis spectra showed no significant change with times up to 8 h, only a change in the absorbance was observed. After 8 h, the features of UV/Vis spectra started to disappear, seemingly due to the decomposition of the cluster (Figure S13B). Time-dependent ESI MS exhibited presence of the species, **I** and **II** and no signature of conversion was observed as relative intensities of **I** and **II** were the same. After 8 h, the intensities in the ESI MS started to decrease and the peaks disappeared after 12 h, which confirmed the decomposition of the clusters (Figure S13A). It confirmed that **II** is not the oxidation product of **I**. The UV/Vis spectrum of a mixture of **I** and **II** was measured by dissolving crystals in DCM, which exhibits molecule-like optical absorption that displays three prominent peaks (at 425, 515, and 650 nm) and two shoulder peaks at 605 and 850 nm (Figure 4C). The inset shows a visible-light photograph of the cluster solution. Some of the spectral features are comparable to the clusters,  $[\text{Ag}_{25}(\text{SPhMe}_2)_{18}]^-$ ,  $[\text{Ag}_{44}(\text{FTP})_{30}]^{4-}$  (FTP: 4-fluorothiophenol) and  $[\text{Ag}_{67}(\text{SPhMe}_2)_{32}(\text{PPh}_3)_8]^{3+}$ , but the overall spectrum is very different (Figures S14,S15).<sup>[4-6]</sup> An optical image of the single crystals is shown in Figure 4D.

Thin-layer chromatography (TLC) and high-performance liquid chromatography (HPLC)-based procedures to separate the components of the co-crystals were unsuccessful. We had introduced TLC as a separation technique for gold clusters.<sup>[29]</sup> Seemingly the high charge on the clusters resulted in stronger interactions with the stationary phase and the components were not eluted. In HPLC, the clusters were decomposed after passing through the column. Although HPLC separation is well established for gold clusters, no separation of silver clusters has been accomplished till now and therefore this inability is not surprising. However, to explore the optical properties of individual clusters, we have separately synthesized and characterized both the component clusters. Compound **II** was synthesized with almost complete absence of **I** (Figure S16) by changing the synthetic conditions, while **I** was made by using an isomeric thiol (2,4-SPhMe<sub>2</sub> was changed to 2,5-SPhMe<sub>2</sub>; see the Supporting Information). ESI MS and UV/Vis spectra of pure Ag<sub>46</sub> are presented in the Supporting Information, Figure S17A,C, respectively. Comparison of

experimental isotopic distributions with the simulated one confirms the cluster formula (Figure S17B). One of the components (Ag<sub>46</sub>) has been crystallized and it is having the same structure (Figure S18A,C) as present in the co-crystal (Figure S18B,D). Crystal analysis of 2,5-SPhMe<sub>2</sub> protected Ag<sub>46</sub> is given in the Supporting Information. Unfortunately, we could not grow the single crystal of **II** alone owing to its instability in pure form. The higher stability of **I** can be seen from a time-dependent UV/Vis study. Solutions of Ag<sub>40</sub> and Ag<sub>46</sub> were heated and stirred in methanol at 50 °C and products were analyzed by UV/Vis spectroscopy (Figure S19). UV/Vis spectra revealed the disappearance of highly structured features of **II** after 1.5 h (Figure S19A). In the case of **I**, the spectral features and absorbance were the same up to 3 h, change in absorbance was seen only afterwards (Figure S19B). This observation clearly indicates that Ag<sub>46</sub> is indeed more stable. UV/Vis-NIR spectra of the individual clusters are shown in the Supporting Information, Figure S20 and **II** exhibit an absorption in the NIR region (1279 nm) that is absent in **I** (Figure S20). A unique possibility of mixing the two clusters in different ratios in solution may tune their ratios in the co-crystal and this can open up a new direction in cluster chemistry. However, it may be noted that the mixing ratio may not be the occupancy ratio in the crystal, which is decided by minimum potential energy considerations.

To estimate the HOMO–LUMO gap of **I** and **II**, differential pulse voltammetry (DPV) was performed. DPV results show several peaks in positive and negative potential regions which are assigned as oxidation and reduction peaks, respectively (Figure S21). The HOMO–LUMO gaps of **I** and **II** were determined to be about 1.30 eV and 0.92 eV, respectively (Figure S21). The analysis and experimental details are described in Supporting Information.

The electronic structures of **II** and **I** were analyzed by using the model clusters with reduced ligands,  $[\text{Ag}_{40}(\text{SCH}_3)_{24}(\text{P}(\text{CH}_3)_3)_8]$  (Figure S22A) and  $[\text{Ag}_{46}(\text{SCH}_3)_{24}(\text{P}(\text{CH}_3)_3)_8]$  (Figure S22B), respectively. Here the coordinates of Ag, S, and P atoms were taken from crystal structures and were kept fixed, but C and H atoms were allowed to relax. The electronic structure and optical absorption of the clusters were investigated using density functional theory (DFT) and time-dependent density functional theory (TDDFT) using the projector augmented wave (PAW) method as implemented in GPAW.<sup>[30]</sup> The optical absorption spectra were calculated using linear response TDDFT.<sup>[31]</sup> The theoretical spectrum (black trace) of a 1:1 mixture of both the clusters, constructed from the predictions of individual clusters (Figure S23) is compared with the experimental spectrum (red trace) in Figure 5. The match is particularly good in the higher wavelength region. This further proves the existence of both the structures together in the crystal. Various electronic transitions (Table S3) and the charge density distribution of the frontier orbitals suggest the involvement of most of the atoms. Molecular orbital (MO) transitions to the optical gap of  $[\text{Ag}_{46}(\text{SCH}_3)_{24}(\text{P}(\text{CH}_3)_3)_8]^{2+}$  and  $[\text{Ag}_{40}(\text{SCH}_3)_{24}(\text{P}(\text{CH}_3)_3)_8]^{2+}$  are presented in the Supporting Information, Figures S24 and S25, respectively. The structure of Ag<sub>40</sub><sup>3+</sup> cluster was also optimized to calculate the optical absorption



**Figure 5.** Black trace corresponds to the theoretical spectrum of a 1:1 mixture of both the clusters  $[\text{Ag}_{46}(\text{SCH}_3)_{24}(\text{P}(\text{CH}_3)_3)_8]$  and  $[\text{Ag}_{40}(\text{SCH}_3)_{24}(\text{P}(\text{CH}_3)_3)_8]$  constructed from the theoretical prediction. Red trace indicates the experimental spectrum of mixture of both the clusters.

spectrum and it is compared with that of  $\text{Ag}_{40}^{2+}$  cluster in the Supporting Information, Figure S26. In general, the spectrum of  $\text{Ag}_{40}^{3+}$  cluster is similar to that of the  $\text{Ag}_{40}^{2+}$  cluster. To understand the origin of the optical transitions having the highest oscillator strength ( $f$ ) of  $\text{I}^{2+}$  and  $\text{II}^{2+}$ , density of states (DOS) were calculated and they are plotted in the Supporting Information, Figure S27 and S28. The transitions taking place at 410.03 nm ( $f = 0.373$ ) and 441.49 nm ( $f = 0.225$ ) for  $\text{I}^{2+}$  and  $\text{II}^{2+}$  clusters, respectively are considered here. DOS calculations conclude that in the case of  $\text{I}^{2+}$  the major contributing MOs are HOMO-3 and LUMO + 8. These occupied MOs (as denoted by the dotted vertical lines in the Supporting Information, Figure S27D) are mainly contributed by the 3p atomic orbitals (AOs) of sulfur, 5s, 5p AOs of silver atoms in shell regions, and 5s AOs of Ag atoms in the core, and the unoccupied MOs are formed by 5p AOs of shell silver atoms. In the case of  $\text{II}^{2+}$ , the significant contribution to the transition is from HOMO-1 to LUMO + 11 and these two MOs (as denoted by the dotted vertical lines in the Supporting Information, Figure S27B) are predominantly composed of 5s and 5p AOs of Ag atoms from the shell region of the cluster, respectively. Hence, these optical absorption transitions exhibit a similar characteristic for both **I** and **II** clusters. By using the widely used rule<sup>[19]</sup> to count the free electrons for  $\text{I}^{2+}$  and  $\text{II}^{2+}$  in the metal core, we get 20 and 14 free electrons in them, respectively. Both the clusters could be viewed as superatomic with 20 and 14 electrons distributed in superatomic orbitals as shown in the Supporting Information, Figure S29 and S31, respectively. The isosurfaces of superatomic orbitals of both the clusters are plotted in the Supporting Information, Figures S30 and S32.

In conclusion, we present the possibility of crystallization of structurally similar clusters together leading to new nanocrystal solids. A new category of such crystals is those composed of different cores with the same shell. It is surprising that  $\text{Ag}_8$  and  $\text{Ag}_{14}$  inner cores are nucleated

simultaneously in solution with equal probability. The mechanism of such cluster growth and their encapsulation in shells require additional studies. This observation suggests the possibility of the coexistence of diverse clusters and their co-crystallization. Such nanocluster co-crystals, similar to superlattices will be a way forward to realize cluster assembled materials with new properties. Along with these, it is worthy to mention the observation of a rigid polymeric ligand shell which remains unaltered after removing or adding six silver atoms.

### Acknowledgements

We thank Department of Science and Technology for supporting our research project. We thank the Sophisticated Analytical Instruments Facility, Indian Institute of Technology Madras for SCXRD data collection. M.B., A.G. and K.S.S. thank U.G.C. for their research fellowships. A.N. and E.K. thank IITM for their fellowships. G.P. thanks IITM for an Institute Postdoctoral fellowship. We thank Sourav Kanti Jana for his inputs in performing electrochemical experiments.

### Conflict of interest

The authors declare no conflict of interest.

**Keywords:**  $\text{Ag}_{40}$  ·  $\text{Ag}_{46}$  · co-crystals · nanoclusters

**How to cite:** *Angew. Chem. Int. Ed.* **2019**, 58, 189–194  
*Angew. Chem.* **2019**, 131, 195–200

- [1] I. Chakraborty, T. Pradeep, *Chem. Rev.* **2017**, 117, 8208.
- [2] R. Jin, C. Zeng, M. Zhou, Y. Chen, *Chem. Rev.* **2016**, 116, 10346.
- [3] L. G. AbdulHalim, M. S. Bootharaju, Q. Tang, S. Del Gobbo, R. G. AbdulHalim, M. Eddaoudi, D.-e. Jiang, O. M. Bakr, *J. Am. Chem. Soc.* **2015**, 137, 11970.
- [4] C. P. Joshi, M. S. Bootharaju, M. J. Alhilaly, O. M. Bakr, *J. Am. Chem. Soc.* **2015**, 137, 11578.
- [5] H. Yang, Y. Wang, H. Huang, L. Gell, L. Lehtovaara, S. Malola, H. Häkkinen, N. Zheng, *Nat. Commun.* **2013**, 4, 2422.
- [6] M. J. Alhilaly, M. S. Bootharaju, C. P. Joshi, T. M. Besong, A.-H. Emwas, R. Juárez-Mosqueda, S. Kaappa, S. Malola, K. Adil, A. Shkurenko, H. Häkkinen, M. Eddaoudi, O. M. Bakr, *J. Am. Chem. Soc.* **2016**, 138, 14727.
- [7] R. S. Dhayal, J.-H. Liao, Y.-C. Liu, M.-H. Chiang, S. Kahlal, J.-Y. Saillard, C. W. Liu, *Angew. Chem. Int. Ed.* **2015**, 54, 3702; *Angew. Chem.* **2015**, 127, 3773.
- [8] A. Desireddy, B. E. Conn, J. Guo, B. Yoon, R. N. Barnett, B. M. Monahan, K. Kirschbaum, W. P. Griffith, R. L. Whetten, U. Landman, T. P. Bigioni, *Nature* **2013**, 501, 399.
- [9] M. W. Heaven, A. Dass, P. S. White, K. M. Holt, R. W. Murray, *J. Am. Chem. Soc.* **2008**, 130, 3754.
- [10] P. D. Jadzinsky, G. Calero, C. J. Ackerson, D. A. Bushnell, R. D. Kornberg, *Science* **2007**, 318, 430.
- [11] C. Zeng, H. Qian, T. Li, G. Li, N. L. Rosi, B. Yoon, R. N. Barnett, R. L. Whetten, U. Landman, R. Jin, *Angew. Chem. Int. Ed.* **2012**, 51, 13114; *Angew. Chem.* **2012**, 124, 13291.
- [12] M. S. Bootharaju, C. P. Joshi, M. R. Parida, O. F. Mohammed, O. M. Bakr, *Angew. Chem. Int. Ed.* **2016**, 55, 922; *Angew. Chem.* **2016**, 128, 934.



- [13] G. Soldan, M. A. Aljuhani, M. S. Bootharaju, L. G. AbdulHalim, M. R. Parida, A.-H. Emwas, O. F. Mohammed, O. M. Bakr, *Angew. Chem. Int. Ed.* **2016**, 55, 5749; *Angew. Chem.* **2016**, 128, 5843.
- [14] C. Liu, T. Li, H. Abroshan, Z. Li, C. Zhang, H. J. Kim, G. Li, R. Jin, *Nat. Commun.* **2018**, 9, 744.
- [15] H. Yang, J. Yan, Y. Wang, G. Deng, H. Su, X. Zhao, C. Xu, B. K. Teo, N. Zheng, *J. Am. Chem. Soc.* **2017**, 139, 16113.
- [16] W. Du, S. Jin, L. Xiong, M. Chen, J. Zhang, X. Zou, Y. Pei, S. Wang, M. Zhu, *J. Am. Chem. Soc.* **2017**, 139, 1618.
- [17] L. Ren, P. Yuan, H. Su, S. Malola, S. Lin, Z. Tang, B. K. Teo, H. Häkkinen, L. Zheng, N. Zheng, *J. Am. Chem. Soc.* **2017**, 139, 13288.
- [18] H. Häkkinen, M. Walter, H. Grönbeck, *J. Phys. Chem. B* **2006**, 110, 9927.
- [19] M. Walter, J. Akola, O. Lopez-Acevedo, P. D. Jadzinsky, G. Calero, C. J. Ackerson, R. L. Whetten, H. Grönbeck, H. Häkkinen, *Proc. Natl. Acad. Sci. USA* **2008**, 105, 9157.
- [20] J. U. Reveles, S. N. Khanna, P. J. Roach, A. W. Castleman, *Proc. Natl. Acad. Sci. USA* **2006**, 103, 18405.
- [21] M. S. Bootharaju, R. Dey, L. E. Gevers, M. N. Hedhili, J.-M. Basset, O. M. Bakr, *J. Am. Chem. Soc.* **2016**, 138, 13770.
- [22] CCDC 1842077 contains the supplementary crystallographic data for this paper. These data are provided free of charge by The Cambridge Crystallographic Data Centre.
- [23] H. Yang, J. Yan, Y. Wang, H. Su, L. Gell, X. Zhao, C. Xu, B. K. Teo, H. Häkkinen, N. Zheng, *J. Am. Chem. Soc.* **2017**, 139, 31.
- [24] S. Jin, S. Wang, Y. Song, M. Zhou, J. Zhong, J. Zhang, A. Xia, Y. Pei, M. Chen, P. Li, M. Zhu, *J. Am. Chem. Soc.* **2014**, 136, 15559.
- [25] H. Yang, J. Lei, B. Wu, Y. Wang, M. Zhou, A. Xia, L. Zheng, N. Zheng, *Chem. Commun.* **2013**, 49, 300.
- [26] R. Fournier, *J. Chem. Phys.* **2001**, 115, 2165.
- [27] H. Häkkinen, R. N. Barnett, U. Landman, *Phys. Rev. Lett.* **1999**, 82, 3264.
- [28] A. Ghosh, M. Bodiuzzaman, A. Nag, M. Jash, A. Bakshi, T. Pradeep, *ACS Nano* **2017**, 11, 11145.
- [29] A. Ghosh, J. Hassinen, P. Pulkkinen, H. Tenhu, R. H. A. Ras, T. Pradeep, *Anal. Chem.* **2014**, 86, 1218526.
- [30] J. J. Mortensen, L. B. Hansen, K. W. Jacobsen, *Phys. Rev. B* **2005**, 71, 035109.
- [31] M. Walter, H. Häkkinen, L. Lehtovaara, M. Puska, J. Enkovaara, C. Rostgaard, J. J. Mortensen, *J. Chem. Phys.* **2008**, 128, 244101.

Manuscript received: August 16, 2018

Revised manuscript received: October 14, 2018

Accepted manuscript online: November 8, 2018

Version of record online: November 25, 2018

## Supporting Information

### **Camouflaging Structural Diversity: Co-crystallization of Two Different Nanoparticles having Different Cores but the Same Shell**

*Mohammad Bodiuzzaman<sup>+</sup>, Atanu Ghosh<sup>+</sup>, Korath Shivan Sugi, Abhijit Nag, Esma Khatun, Babu Varghese, Ganesan Paramasivam, Sudhadevi Antharjanam, Ganapati Natarajan, and Thalappil Pradeep\**

anie\_201809469\_sm\_miscellaneous\_information.pdf

**Table of contents:**

Name	Description	Page no.
	Experimental Section	3-4
	Instrumentation	4-6
	Analysis of superatomic orbitals	7
	Analysis of differential pulse voltammetry	8
	X-ray structural analysis	8-9
Table S1	Reported crystal structure and their inner core and shell parameters	9
Table S2	A summary of average Ag-Ag distances in <b>I</b> and <b>II</b> clusters	10
Table S3	A summary of MO transitions of <b>I</b> and <b>II</b>	11
Table S4	Crystal data and structure refinement for co-crystals	12
Table S5	Crystal data and structure refinement for $[\text{Ag}_{46}(\text{2,5-SPhMe}_2)_{24}(\text{PPh}_3)_8]^{2+}$	13
Figure S1	Characterization of $[\text{Ag}_{18}(\text{PPh}_3)_{10}\text{H}_{16}]^{2+}$ by ESI MS and UV-vis absorption spectroscopy	14
Figure S2	Construction of octacapped octahedron ( $\text{Ag}_6@\text{Ag}_8$ )	15
Figure S3	Different facets present in FCC $\text{Ag}_{14}$ core	16
Figure S4	Eight units of $\text{AgS}_3\text{P}$ complexes cover the hexagonal faces of $\text{Ag}_{24}$ outer core	17
Figure S5	Six squares make $\text{Ag}_{24}$ outer core, formation of square pyramid in $\text{Ag}_{46}$	18
Figure S6	Organization of <b>I</b> and <b>II</b> clusters into two-dimensional lattices	19
Figure S7	Packing diagram of <b>I</b> and <b>II</b> clusters	20
Figure S8	Construction of $\text{Ag}_{32}$ and $\text{Ag}_{38}$ kernels	21
Figure S9	Encapsulation of $\text{Ag}_6$ octahedron, by truncated-octahedron shell of $\text{Ag}_{32}$	22
Figure S10	Isotopic distribution of molecular ion peaks of <b>II</b> and <b>I</b> clusters and their peak to peak separations	23
Figure S11	Collision induced dissociation experiments of $\text{I}^{2+}$ to prove the absence of <b>II</b> in any charge state	24
Figure S12	Collision induced dissociation experiments of $\text{I}^{2+}$ and $\text{II}^{2+}$	25
Figure S13	Time dependent ESI MS and UV-vis study of co-crystals in	26

	methanol at 50°C	
Figure S14	Comparison UV-vis spectra of a mixture of <b>I</b> and <b>II</b> with previously reported $[\text{Ag}_{25}(\text{SPhMe}_2)_{18}]^-$ and $[\text{Ag}_{44}(4\text{-FTP})_{30}]^{4-}$	27
Figure S15	Comparison of UV-vis spectra of a mixture of <b>I</b> and <b>II</b> clusters with previously reported $[\text{Ag}_{67}(\text{SPhMe}_2)_{32}(\text{PPh}_3)_8]$	28
Figure S16	Characterization of pure <b>II</b>	29
Figure S17	Characterization of <b>I</b>	30
Figure S18	Comparison of crystal structures of $[\text{Ag}_{46}(2,5\text{-SPhMe}_2)_{24}(\text{PPh}_3)_8]^{2+}$ and $[\text{Ag}_{46}(2,4\text{-SPhMe}_2)_{24}(\text{PPh}_3)_8]^{2+}$	31
Figure S19	Comparison of stability of <b>I</b> and <b>II</b> by time dependent UV-vis study	32
Figure S20	Comparison of optical absorption spectra of <b>I</b> and <b>II</b> clusters	33
Figure S21	Differential pulse voltammetry study of <b>I</b> and <b>II</b> to determine their HOMO-LUMO gap.	34
Figure S22	Reduced model structure of $[\text{Ag}_{40}(\text{SCH}_3)_{24}(\text{P}(\text{CH}_3)_3)_8]^{2+}$ and $[\text{Ag}_{46}(\text{SCH}_3)_{24}(\text{P}(\text{CH}_3)_3)_8]^{2+}$	35
Figure S23	Construction of a predicted optical absorption spectrum from a 1:1 mixture of $[\text{Ag}_{46}(\text{SCH}_3)_{24}(\text{P}(\text{CH}_3)_3)_8]^{2+}$ and $[\text{Ag}_{46}(\text{SCH}_3)_{24}(\text{P}(\text{CH}_3)_3)_8]^{2+}$ clusters	36
Figure S24	MO transitions to the optical gap of $[\text{Ag}_{46}(\text{SCH}_3)_{24}(\text{P}(\text{CH}_3)_3)_8]^{2+}$	37
Figure S25	MO transitions to the optical gap of $[\text{Ag}_{40}(\text{SCH}_3)_{24}(\text{P}(\text{CH}_3)_3)_8]^{2+}$	38
Figure S26	Comparison of predicted (TD-DFT) optical absorption spectrum of $\text{Ag}_{40}^{2+}$ and $\text{Ag}_{40}^{3+}$	39
Figure S27	Comparison of the plot of density of states versus energy of both the clusters, <b>II</b> and <b>I</b>	40
Figure S28	Comparison of the plot of density of states versus energy of both the clusters, <b>II</b> and <b>I</b> of ligands alone and projected density of states of the core and shell by summing over different orbitals of atoms in the core and shell regions	41
Figure S29	Distributions of 20 electrons in $\text{I}^{2+}$	42

Figure S30	Isosurfaces of superatomic orbitals in <b>I</b>	43
Figure S31	Distributions of 14 electrons in <b>II</b> <sup>2+</sup>	44
Figure S32	Isosurfaces of superatomic orbitals in <b>II</b>	45
Figure S33	Ortep representation of [Ag <sub>40</sub> S <sub>24</sub> P <sub>8</sub> ] and [Ag <sub>46</sub> S <sub>24</sub> P <sub>8</sub> ]	46
	References	47

## Experimental Section

### Chemicals

Silver nitrate (AgNO<sub>3</sub>) was purchased from Rankem chemicals. Sodium borohydride (NaBH<sub>4</sub>, 98%), 2,4 & 2,5-dimethylbenzenethiol (DMBT), tetrabutylammonium hexafluorophosphate and triphenylphosphine (TPP) were purchased from Aldrich. All chemicals were used as received without further purification. All the solvents such as dichloromethane (DCM), methanol (MeOH), n-hexane and chloroform (CHCl<sub>3</sub>) were purchased from Rankem chemicals and were of analytical grade. Milli-Q water was used for the synthesis.

### Synthesis and purification of [Ag<sub>18</sub>H<sub>16</sub>(TPP)<sub>10</sub>]<sup>2+</sup>

This cluster was synthesized by a reported procedure.<sup>1-2</sup> 20 mg of AgNO<sub>3</sub> was dissolved in 5 mL methanol (MeOH) and 9 mL of chloroform (CHCl<sub>3</sub>) was added. Then 70 mg of triphenylphosphine, dissolved in 1 mL of chloroform, was added to the above reaction mixture under stirring condition. After 20 minutes of stirring, 6 mg of sodium borohydride in 0.5 mL of ice cold water was added. Upon addition of the reducing agent, color of the solution changed instantly to yellow from colorless. The reaction was continued for three hours under dark condition. The final color of the solution was dark green which indicated the formation of the cluster. Mixture of solvents was removed by evaporation under reduced pressure. The green solid material was washed with water to remove excess silver precursor and the reducing agent. After being cleaned with water, the material was extracted with methanol. This green colored material was characterized by UV-vis and ESI MS (Figure S1) and used for further reaction. The yield of the synthesis was 20% in terms of silver.

### Synthesis and purification of a mixture of **I** and **II**

It was synthesized by a LEIST process. [Ag<sub>18</sub>(TPP)<sub>10</sub>H<sub>16</sub>]<sup>2+</sup> was taken as the precursor in this procedure. 5 mg of the clean precursor cluster was taken in MeOH in a reaction bottle and 0.75 μL of 2,4-dimethylbenzenethiol (DMBT) was added under stirring condition. Just after addition, an instant color change was observed and the reaction was allowed to continue for 12 hours. The final reddish brown color of the reaction mixture indicated the formation of the product cluster. Then the reaction mixture was centrifuged at 5000 rpm for 5 minutes to remove all the insoluble precipitates and the solvent was removed under reduced pressure. Minimum amount (around 1 mL) of MeOH was added to precipitate the material and it was

centrifuged. After centrifugation, the supernatant was discarded and the precipitate was dried under reduced pressure and washed several times with hexane to remove excess triphenylphosphine. This cleaned material was dried under vacuum and dissolved in DCM and methanol which were used for characterization. Yield of the synthesis was 10% in terms of silver.

### **Synthesis and purification of I**

It was synthesized and purified by almost the same procedure as described above. The only difference was in the amount of 2,4 dimethylbenzenethiol used. Here 0.25  $\mu\text{L}$  of thiol was used instead of 0.75  $\mu\text{L}$ . Yield of the synthesis was 5% in terms of silver.

### **Synthesis and purification of $[\text{Ag}_{46}(\text{2,5-SPhMe}_2)_{24}(\text{PPh}_3)_8]^{2+}$**

The synthesis and purification procedures were almost same as described for the mixture. Here an isomeric thiol was used, 2,4-dimethylbenzenethiol was changed to 2,5-dimethylbenzenethiol. Yield of the synthesis was 15% in terms of silver.

### **Crystallization of a mixture of I and II clusters**

Cleaned 40 mg of the solid cluster was dissolved in 2 mL of distilled DCM, filtered by syringe filter of pore size 0.22  $\mu\text{m}$  and layered by distilled hexane at 1:1 (by volume) ratio and kept at 4°C. After approximately one-week, black crystals were observed which were suitable for SCXRD.

### **Crystallization $[\text{Ag}_{46}(\text{2,5-SPhMe}_2)_{24}(\text{PPh}_3)_8]^{2+}$ cluster**

Cleaned 40 mg of the solid cluster was dissolved in 1.5 mL of distilled DCM and 0.5 mL of MeOH, filtered by syringe filter of pore size 0.22  $\mu\text{m}$  and layered by distilled hexane at 1:1 (by volume) ratio and kept at 4°C. After approximately one-week, black hexagonal crystals were observed which were suitable for SCXRD.

## **Instrumentation**

### **UV/Vis spectroscopy:**

UV/Vis spectra were recorded using a Perkin Elmer Lambda 25 instrument in the range of 200 – 1100 nm.

### **ESI MS**

The ESI MS spectra were measured using a Waters Synapt G2Si HDMS instrument. The Synapt instrument is equipped with an electrospray source, quadrupole ion trap, ion mobility cell and time of flight detector. Samples were measured in positive ion mode.

### **X-ray crystallography**

#### **(i) Mixture of $\text{Ag}_{40}$ and $\text{Ag}_{46}$**

Single crystal data were measured using a Bruker Kappa APEX III CMOS diffractometer using  $\text{CuK}\alpha$  ( $\lambda = 1.54178 \text{ \AA}$ ) radiation. Indexing was performed using APEX III. Data integration and reduction were performed using SAINT V8.37A. Absorption correction was



performed by multi-scan method implemented in SADABS (Bruker, 2016). Space group was determined using XPREP implemented in APEX III.

**(ii)  $[\text{Ag}_{46}(\text{2,5-SPhMe}_2)_{24}(\text{PPh}_3)_8]^{2+}$**

Single crystal X-ray diffraction data was collected in a Bruker APEX-III CMOS diffractometer equipped with Mo  $K\alpha$  radiation and photon pixel detector. Unit cell parameters were determined using 36 frames collected from different zones of the reciprocal lattice. The intensity was integrated using SAINT V8.37A software. Multi-scan absorption correction was done using SADABS (Bruker 2016).

**ESI MS conditions**

The conditions for resolved electrospray ionization mass spectra were as follows:

Sample concentration: 10  $\mu\text{g/mL}$

Solvent: MeOH

Flow rate: 30  $\mu\text{L/min}$

Capillary voltage: 3 kV

Cone voltage: 0 V

Source offset: 0 V

Source Temperature: 80-100°C

Desolvation Temperature: 150-200°C

Desolvation gas flow: 400 L/h

Trap gas flow: 10 L/h

**Experimental conditions for differential pulse voltammetry**

Differential Pulse Voltammetry (DPV) was performed using Biologic SP200 potentiostat in 0.1 M tetrabutylammonium hexafluorophosphate ( $\text{Bu}_4\text{NPF}_6$ ) dissolved in dichloromethane at 0-5 °C. Prior to the electrochemical measurements, solutions were degassed for 10 min in five necked reaction vessel which was equipped with three electrodes (both Pt wire used as working and counter electrode and Ag quasi reversible electrode as a reference electrode) and two gas inlet outlet provisions. DPV was performed within a potential window -2V to +2V and the potential was applied to the working electrode (Pt wire) with respect to the reference electrode. In the course of measurements, pulse height and pulse width were maintained as 5 mV and 50 ms, respectively. Solutions of  $\text{Ag}_{40}$  and  $\text{Ag}_{46}$  clusters were taken in an electrolyte solution of  $\text{Bu}_4\text{NPF}_6$  in dry DCM.

## Computational details

The Ag ( $4d^{10}5s^1$ ), S ( $3s^23p^4$ ), P ( $3s^23p^3$ ), C ( $2s^22p^2$ ) and H ( $1s^1$ ) electrons were treated as valence and the inner electrons were included in a frozen core with scalar-relativistic effects being included for Ag. The exchange-correlation functional employed was the generalized gradient approximation of Perdew, Burke and Ernzerhof (PBE) and the basis set was double zeta plus polarization (DZP) in all our calculations. We used a 0.2 Å grid spacing for calculating the electron density and a convergence criterion of 0.05 eV/Å, for the residual forces on atoms was used in all geometry optimizations, without any symmetry constraints. The linear combination of atomic orbitals (LCAO) mode and more accurate finite-difference real-space grid method of GPAW were used to carry out the efficient structure optimization. The optimized structures from the finite-difference real-space grid method were used for the optical absorption calculation using LR-TDDFT.<sup>3</sup> In order to plot the theoretical absorption spectrum for mixture, the amplitude (oscillator strength) of both the clusters was scaled by a factor of 0.5 and then added to each other, to yield the normalized amplitude for the mixture.

The lowest 20 to 50 transitions were considered in order to determine the optical gap of the clusters based on their oscillator strength. The absorption spectra were plotted with a Gaussian broadening of 0.05 eV in the energy range of 0.95-3.3 eV. The distribution of electron density in molecular orbitals corresponding to the optical gap transition was plotted (iso-surface value 0.016-0.018), to analyze the changes in the electronic structure of the clusters. Furthermore, the Bader charge analysis was also carried out to study the charge transfer between the cluster and the ligands. The molecular orbitals were visualised using VESTA software.

For the density of states calculations, the DFT geometry optimization was performed using the crystal structure of the clusters with reduced H ligands,  $[Ag_nS_{24}P_8H_{48}]^{2+}$  ( $n = 46, 40$ ). The hybrid functional, PBE1PBE and LANL2DZ effective core potential (ECP) methodology was used as implemented in Gaussian09 software<sup>4</sup>. Later, the total density of states and projected density of states calculations were analyzed using the Multiwfn3.3.5 package<sup>5</sup>. For all the spectra, the Fermi level ( $E_F$ ) was centred at the middle of HOMO-LUMO gap.

## Analysis of superatomic orbitals

In order to understand further the superatomic orbitals of the atomically-precise monolayer protected  $Ag_{46}$  cluster, the density of states (DOS) spectra were analysed in detail and the configurations of superatomic orbitals ( $1S^2$ ,  $1P^6$ ,  $1D^{10}$  and  $2S^2$ ) identified are shown in Figure S29. A description of our method of identifying the superatomic orbitals is as follows.

It has been shown for bare gold and silver clusters that the superatomic orbitals have a dominant contribution from 6s atomic orbitals in the case of gold and 5s atomic orbitals in the case of silver, compared to the p- and d-atomic orbital contributions (Wanrun Jiang, Yang Gao, Dexuan Xu, Fang Liu, Zhigang Wang; *J. Electron. Mater.* **2017**, *46*, 3938; Takashi Yumura, Mitsuhiro Kumondai, Yasushige Kuroda, Takashi Wakasugi, Hisayoshi Kobayashia, *RSC Adv.* **2017**, *7*, 4950). Therefore, superatomic orbitals in ligand protected clusters may also be expected occur at the energies where there are peaks in the s-orbital

contribution to the DOS, and where this contribution dominates over the p atomic orbital contribution (for the case of P superatomic orbitals), and over the d atomic orbital contribution (for the case of D superatomic orbitals). The superatomic orbitals of any symmetry mainly contain contributions from the metal s atomic orbitals (AOs) because of the greater delocalization of an overlapping system of s-orbitals, which is a necessary requirement for a state describing a free electron.

Hence, the energy level positions of the superatomic orbitals emerge exactly in the regimes where the 5s AOs have the greatest contribution corresponding to peaks in the 5s PDOS. Therefore, the partial DOS (PDOS) spectrum of 5s AOs of Ag<sub>46</sub> cluster was used to identify the configuration of superatomic orbitals and also by comparison of the s-orbital PDOS with the PDOS of the p and d atomic orbitals. We have already shown the PDOS of the Ag s, p and d orbitals in Figure S27. The relative greater contribution of the s atomic orbital compared to p and d can be seen in the regions of energy where the corresponding superatomic orbitals lie.

Based on the above criteria we selected the likely candidates for superatomic orbitals and further checked the symmetry of the overall envelope of the density consistent with the S, P, and D assignment. From the DOS spectrum, it is clear that the frontier orbitals of Ag<sub>46</sub> cluster are mainly dominated by the contribution of 5s atomic orbitals (AOs) of silver atoms. From Figure S29, the highest occupied molecular orbital (HOMO) is the 2S superatomic orbital. The calculated isosurfaces of a selection of MOs, with energies located at 5s peaks, that are most likely to correspond to the superatomic orbitals of Ag<sub>46</sub> cluster are plotted in Figure S30. For Ag<sub>46</sub>, the 2S orbital can be clearly identified by its spherical symmetry. The P and D superatomic orbitals, identified by dominant s-orbital contribution over p- and d-orbital contributions, can be visually distinguished from the S superatomic orbitals by the presence of the nodal planes. It is more difficult, however, to distinguish between the features of the P and D orbitals from the density plots alone. A similar analysis was carried out for Ag<sub>40</sub> which shows that the HOMO level, shown in Figure S31, coincides with the third D-sublevel. The DOS spectrum of Ag<sub>40</sub> cluster clearly shows that there is a splitting in the 1D superatomic orbitals such that three orbitals (1D<sup>6</sup>) lie in the occupied region and another two orbitals exist in the unoccupied region. From the calculations, it is clear that Ag<sub>40</sub> cluster is also a superatom and all their superatomic orbitals are plotted in Figure S32.

Confirmation of nature of the superatomic orbitals is usually made by the computation of the superatomic DOS which is obtained by projection of the Kohn-Sham states onto cluster-centred spherical harmonic functions ( $Y_{lm}(\theta, \varphi)$ ). However, this calculation was beyond our current capabilities. Hence, the superatomic orbital assignments we have presented are approximate, but still reveal the essential superatomic properties of both the clusters.

## Analysis of differential pulse voltammetry

We have performed differential pulse voltammetry (DPV) of Ag<sub>40</sub> and Ag<sub>46</sub> clusters to estimate the highest occupied molecular orbital–lowest unoccupied molecular orbital (HOMO–LUMO) gap. According to earlier studies DPV has been used extensively to determine the HOMO-LUMO gap of atomically precise clusters.<sup>6-10</sup> DPV results show several peaks in positive and negative potential regions which are assigned as oxidation and reduction peaks, respectively. The first reduction peak (R1) and oxidation peak (O1) of Ag<sub>40</sub> cluster are -1.19 V and +0.22 V, respectively (Figure S21). Electrochemical gap of Ag<sub>40</sub> is the difference between the O1 and R1 which is +0.22 - (-1.19) = 1.41 V. The actual HOMO-LUMO gap can be obtained by subtracting the charging energy.<sup>9-10</sup> The charging energy is determined by subtracting the two oxidation potential values (O2-O1=0.71-0.22=0.49 V) (Figure S21A). Hence, the HOMO-LUMO gap for Ag<sub>40</sub> is 0.92 eV (1.41-0.49). Similarly, the HOMO-LUMO gap of Ag<sub>46</sub> was determined to be ~1.30 eV (Figure S21B). The predicted (TDDFT) HOMO-LUMO gaps of Ag<sub>40</sub> and Ag<sub>46</sub> are 1.0 and 1.43 eV, respectively which are close to the experimental results.

### Single crystal X-ray diffraction analysis of a mixture of I and II clusters

Structure was solved using SHELXT-2017 and least-squares refined using SHELXL-2017. Crystal data and refinement conditions are shown in Table S4. Suitable restraints were applied during the least-squares (LS) refinement. The molecule has a crystallographic 2/m symmetry which makes the asymmetric unit as ¼ th of the molecule. The structure solution and refinement clearly indicated the existence of disorder for most of the atoms in the asymmetric unit. Successive jobs of least squares refinement followed by Fourier difference map could finally yield the structure and disorder component. As the refinement proceeded, it became evident that Ag<sub>11</sub> and Ag<sub>12</sub> were not disordered and their actual occupancy refined to 50% of the natural occupancy of the site. The two molecules exist as disorder components in the same site of the X-ray structure, their actual distribution among the unit cells of the crystal cannot be judged from the X-ray as (atomic positions we got from single crystal X-ray structure are only a picture of atom coordinates averaged over all unit cells of the crystal). Apart from disorder caused by the existence of two types of molecules in the same site, there are additional symmetry related disorders in both the molecules. The TPP of P2, P3, P2', P3' are symmetry disordered. Similarly the thiols S6, S7, S6', S7' are also disordered. While some hydrogen atoms could be fixed at geometrically idealized positions, majority of the hydrogen atoms were ignored as the disorder did not allow their fixation. The difference Fourier map towards the end showed the presence of water and hexane molecules in the lattice. The oxygen of water could be located and refined. However, hexane molecules were too disordered to be modeled and hence they were ignored. An ortep representation of Ag<sub>40</sub> and Ag<sub>46</sub> clusters with ellipsoid probability 40% is presented in Figure S27A and B, respectively (carbon and hydrogen atoms are omitted for clarity).

### Single crystal X-ray diffraction analysis of [Ag<sub>46</sub>(2,5-SPhMe<sub>2</sub>)<sub>24</sub>(PPh<sub>3</sub>)<sub>8</sub>]<sup>2+</sup> cluster

Structure was solved using SHELXT-2017 and least-squares refined using SHELXL-2017. The cluster was crystallized in trigonal crystal system with space group P-3.<sup>11</sup> There is one molecule in a unit cell with 1/6<sup>th</sup> of the molecule in the asymmetric unit. Along with the compound there are two molecules of triphenyl phosphino oxide in the unit cell. Triphenyl phosphino oxide is the possibly oxidized product of triphenyl phosphine. The cluster is essentially positively charged and nitrate is balancing the charge. However the anions could not be modeled from the difference Fourier Map due to severe disorder.

**Table S1.** Reported crystal structures of silver clusters and their inner core and shell parameters

Cluster	Inner Core	Shell	Ref
[Ag <sub>67</sub> (SPhMe <sub>2</sub> ) <sub>32</sub> (PPh <sub>3</sub> ) <sub>8</sub> ] <sup>3+</sup>	Ag <sub>23</sub> (centred cuboctahedron)	Ag <sub>44</sub> S <sub>32</sub> P <sub>8</sub>	<sup>12</sup>
[Ag <sub>14</sub> (SPhF <sub>2</sub> ) <sub>12</sub> (PPh <sub>3</sub> ) <sub>8</sub> ]	Ag <sub>6</sub> (octahedron)	Ag <sub>8</sub> S <sub>12</sub> P <sub>8</sub>	<sup>13</sup>
[Ag <sub>38</sub> (SPhF <sub>2</sub> ) <sub>26</sub> (P <sup>n</sup> Bu <sub>3</sub> ) <sub>8</sub> ]	Ag <sub>14</sub> (fcc)	Ag <sub>24</sub> S <sub>26</sub> P <sub>8</sub>	<sup>14</sup>
[Ag <sub>63</sub> (SPhF <sub>2</sub> ) <sub>36</sub> (P <sup>n</sup> Bu <sub>3</sub> ) <sub>8</sub> ] <sup>+</sup>		Ag <sub>49</sub> S <sub>36</sub> P <sub>8</sub>	<sup>14</sup>
[Ag <sub>29</sub> (BDT) <sub>12</sub> (PPh <sub>3</sub> ) <sub>4</sub> ] <sup>3-</sup>	Ag <sub>13</sub> (centred icosahedra)	Ag <sub>16</sub> S <sub>24</sub> P <sub>4</sub>	<sup>15</sup>
[Ag <sub>78</sub> (SPhCF <sub>3</sub> ) <sub>42</sub> (DPPP) <sub>6</sub> ]	Ag <sub>22</sub> (three mutually interpenetrating icosahedra)	Ag <sub>56</sub> S <sub>42</sub> P <sub>6</sub>	<sup>16</sup>
[Ag <sub>50</sub> (DPPM) <sub>6</sub> (TBBM) <sub>30</sub> ]	Ag <sub>12</sub> (hollow icosahedra)	Ag <sub>38</sub> S <sub>30</sub> P <sub>6</sub>	<sup>17</sup>
[Ag <sub>25</sub> (SPhMe <sub>2</sub> ) <sub>18</sub> ] <sup>-</sup>	Ag <sub>13</sub> (centred icosahedra)	Ag <sub>12</sub> S <sub>18</sub>	<sup>18</sup>
[Ag <sub>44</sub> (FTP) <sub>30</sub> ] <sup>4-</sup> [Ag <sub>44</sub> (p-MBA) <sub>30</sub> ] <sup>4-</sup>	Ag <sub>12</sub> (hollow icosahedra)	Ag <sub>32</sub> S <sub>30</sub>	<sup>19, 20</sup>
[Ag <sub>62</sub> S <sub>12</sub> (SBU <sup>t</sup> ) <sub>32</sub> ] <sup>2+</sup>	Ag <sub>14</sub> (fcc)	Ag <sub>48</sub> S <sub>44</sub>	<sup>21</sup>
[Ag <sub>141</sub> X <sub>12</sub> (S-Adm) <sub>40</sub> ] <sup>3+</sup>	Ag <sub>19</sub> (biicosahedra)	Ag <sub>122</sub> S <sub>40</sub> X <sub>12</sub>	<sup>22</sup>
[Ag <sub>23</sub> (SC <sub>2</sub> H <sub>4</sub> Ph) <sub>18</sub> (PPh <sub>3</sub> ) <sub>8</sub> ]	Ag <sub>6</sub> (octahedron)	Ag <sub>12</sub> S <sub>18</sub> P <sub>8</sub>	<sup>23</sup>
[Ag <sub>46</sub> (SPhMe <sub>2</sub> ) <sub>24</sub> (PPh <sub>3</sub> ) <sub>8</sub> ] <sup>2+</sup>	Ag <sub>14</sub> (fcc)	Ag <sub>32</sub> S <sub>24</sub> P <sub>8</sub>	Present work
[Ag <sub>40</sub> (SPhMe <sub>2</sub> ) <sub>24</sub> (PPh <sub>3</sub> ) <sub>8</sub> ] <sup>2+</sup>	Ag <sub>8</sub> (simple cube)	Ag <sub>32</sub> S <sub>24</sub> P <sub>8</sub>	Present work

Acronyms of ligands used:

SPhMe<sub>2</sub>: 2,4 dimethylbenzenethiol

PPh<sub>3</sub>: Triphenylphosphine

SPhF<sub>2</sub>: 3,4-difluoro-benzenethiol

P<sup>n</sup>Bu<sub>3</sub>: Tributylphosphine

BDT: Benzene-1,3-dithiol

SPhCF<sub>3</sub>: 4-(trifluoromethyl)thiophenol  
 DPPP: 1,3-bis(diphenylphosphino)propane  
 p-MBA: 4-mercaptobenzoic acid  
 SBU<sup>t</sup>: *tert*-butyl mercaptan  
 TBBM: 4-*tert*-butylbenzyl mercaptan  
 DPPM: Bis(diphenylphosphino) methane  
 X: Cl, Br and I  
 S-Adm: 1-adamantanethiolate

**Table S2.** A summary of the average Ag-Ag distances in the two clusters reported in this work

Bonds	Bond length in [Ag <sub>46</sub> (SPhMe <sub>2</sub> ) <sub>24</sub> (PPh <sub>3</sub> ) <sub>8</sub> ] (Å)	Bond length in [Ag <sub>40</sub> (SPhMe <sub>2</sub> ) <sub>24</sub> (PPh <sub>3</sub> ) <sub>8</sub> ] (Å)
Ag(P)-Ag(P)	-	2.68
Ag(F)-Ag(F)	3.80	-
Ag(O)-Ag(O)	2.88	-
Ag(F)-Ag(O)	2.70	-
Ag(S)-Ag(S)	3.0	3.0
Ag(P)-Ag(S)	-	3.12
Ag(F)-Ag(S)	2.95	-
Ag(O)-Ag(S)	3.0	-
Ag-S	2.64	2.64
Ag-P	2.45	2.45

The bonds in the table are defined as follows:

Ag-P bond length between Ag and phosphine

Ag-S bond length between Ag and thiolate

Ag(P) refers to the silver atoms of the Ag<sub>8</sub> perfect cube in Ag<sub>40</sub>

Ag(F) refers to the silver atoms of the Ag<sub>8</sub> cube in Ag<sub>46</sub>

Ag(O) refers to the silver atoms of the Ag<sub>6</sub> octahedron in Ag<sub>46</sub>

Ag(S) refers to the silver atoms of the Ag<sub>24</sub> outer core present in both the structures

**Table S3.** A summary of MO transitions to the optical gap of [Ag<sub>46</sub>(SCH<sub>3</sub>)<sub>24</sub>(P(CH<sub>3</sub>)<sub>3</sub>)<sub>8</sub>]<sup>2+</sup> and [Ag<sub>40</sub>(SCH<sub>3</sub>)<sub>24</sub>(PCH<sub>3</sub>)<sub>8</sub>]<sup>2+</sup>



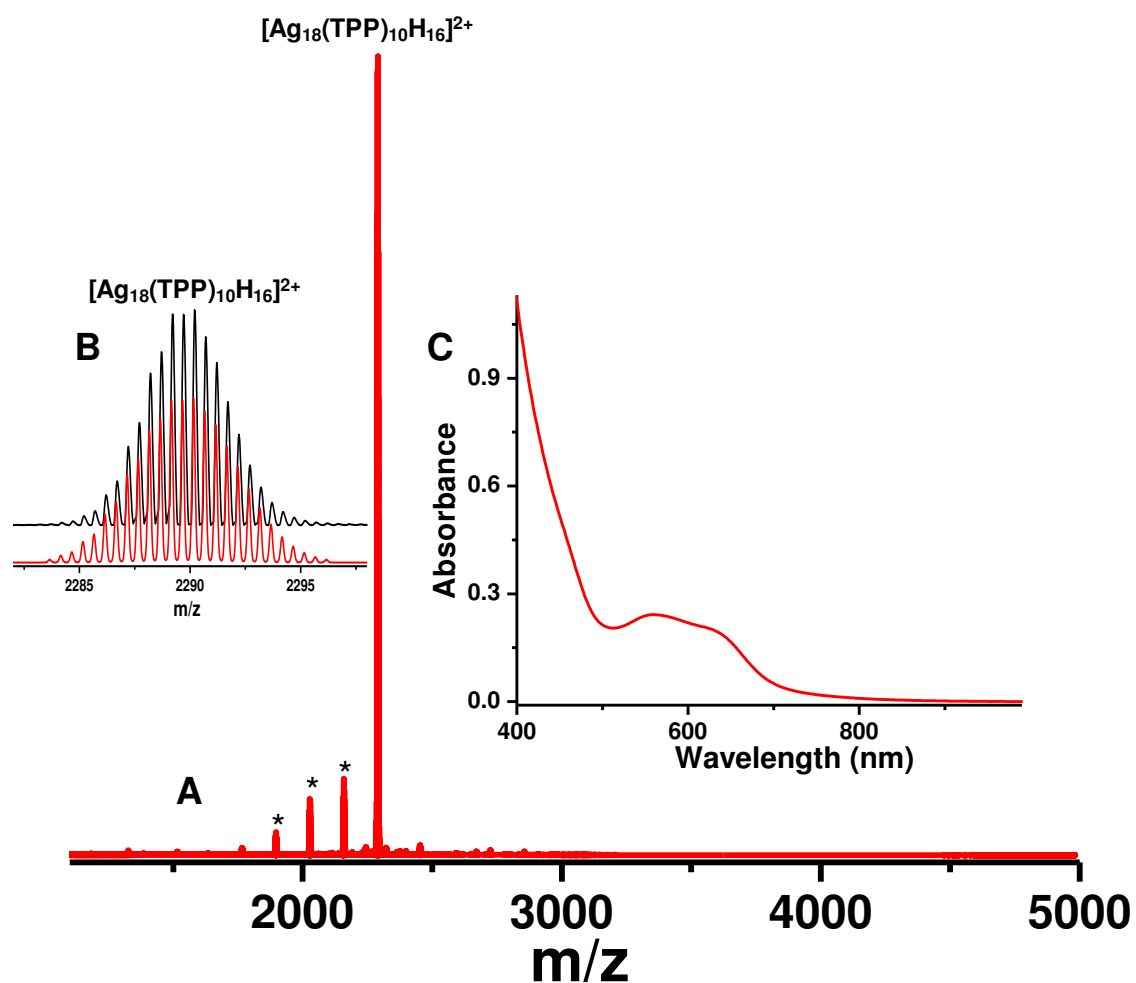
Transition to the optical gap of $[\text{Ag}_{46}(\text{SCH}_3)_{24}(\text{P}(\text{CH}_3)_3)_8]^{2+}$	Transition energy (eV)	Oscillator strength
HOMO-4 $\longrightarrow$ LUMO	1.27	0.183
HOMO-1 $\longrightarrow$ LUMO+3	1.33	0.170
HOMO-6 $\longrightarrow$ LUMO+1	1.34	0.135
HOMO-3 $\longrightarrow$ LUMO+2	1.41	0.119
Transition of the optical gap of $[\text{Ag}_{40}(\text{SCH}_3)_{24}(\text{P}(\text{CH}_3)_3)_8]^{2+}$	Transition energy (eV)	Oscillator strength
HOMO $\longrightarrow$ LUMO+6	0.96	0.390
HOMO-4 $\longrightarrow$ LUMO+4	0.94	0.414

**Table S4.** Crystal data and structure refinement for co-crystal

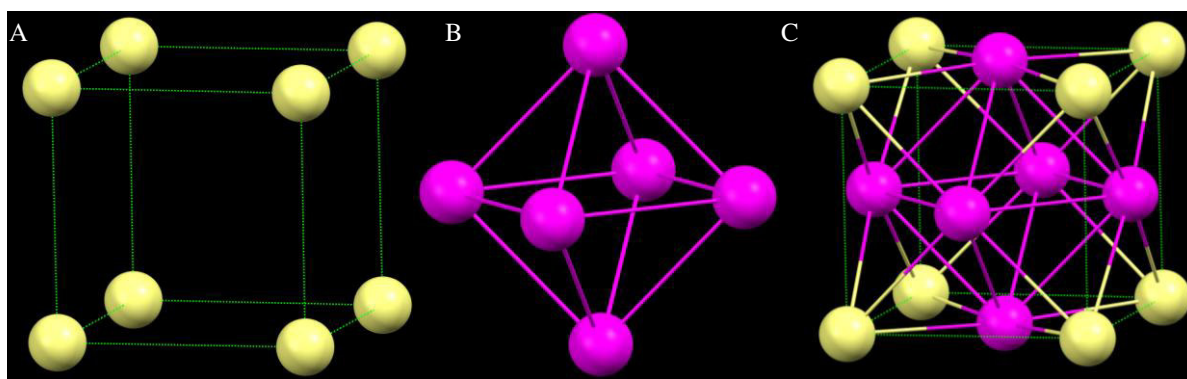
Identification code	SUGI	
Empirical formula	0.5(C <sub>336</sub> H <sub>336</sub> Ag <sub>46</sub> N <sub>2</sub> O <sub>8</sub> P <sub>8</sub> S <sub>24</sub> ) + 0.5(C <sub>336</sub> H <sub>336</sub> Ag <sub>40</sub> N <sub>2</sub> O <sub>8</sub> P <sub>8</sub> S <sub>24</sub> ) + 2H <sub>2</sub> O+2NO <sub>3</sub>	
Formula weight	10189.69	
Temperature	110(2) K	
Wavelength	1.54178 Å	
Crystal system	Monoclinic	
Space group	C2/m	
Unit cell dimensions	a = 28.053(2) Å	α = 90°
	b = 35.669(3) Å	β = 90.6°
	c = 22.5883(16) Å	γ = 90.0°
Volume	22602(3) Å <sup>3</sup>	
Z	2	
Density (calculated)	1.497 g/cm <sup>3</sup>	
Absorption coefficient	16.159 mm <sup>-1</sup>	
F(000)	9918	
Crystal size	0.100 x 0.080 x 0.060 mm <sup>3</sup>	
Theta range for data collection	3.151 to 52.613°	
Index ranges	-28<=h<=28, -36<=k<=36, -23<=l<=23	
Reflections collected	106189	
Independent reflections	13095 [R(int) = 0.1393]	
Completeness to theta = 52.613°	99.0 %	
Absorption correction	Semi-empirical from equivalents	
Max. and min. Transmission	0.36 and 0.24	
Refinement method	Full-matrix least-squares on F <sup>2</sup>	
Data / restraints / parameters	13095 / 3488 / 2035	
Goodness-of-fit on F <sup>2</sup>	1.012	
Final R indices [I>2sigma(I)]	R1 = 0.0785, wR2 = 0.2270	
R indices (all data)	R1 = 0.1475, wR2 = 0.2798	
Extinction coefficient	n/a	
Largest diff. peak and hole	1.170 and -1.141 e Å <sup>-3</sup>	

**Table S5** Crystal data and structure refinement for [Ag<sub>46</sub>(2,5 SPhMe<sub>2</sub>)<sub>24</sub>(PPh<sub>3</sub>)<sub>8</sub>]

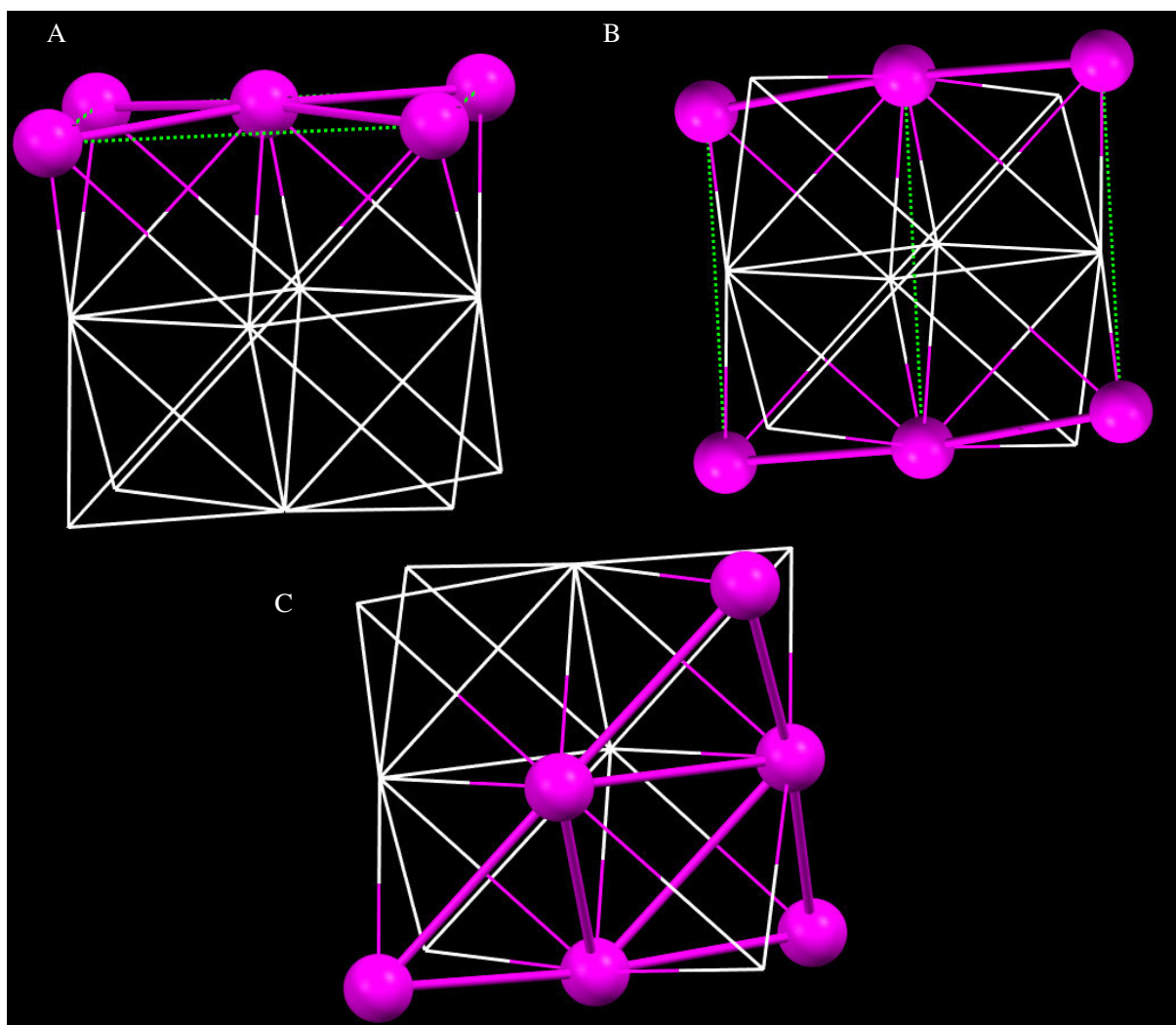
Identification code	1	
Empirical formula	C <sub>372</sub> H <sub>366</sub> Ag <sub>46</sub> O <sub>2</sub> P <sub>10</sub> S <sub>24</sub>	
Formula weight	10909.79	
Temperature	296(2) K	
Wavelength	0.71073 Å	
Crystal system	Trigonal	
Space group	P-3	
Unit cell dimensions	a = 24.7173(5) Å	α = 90°.
	b = 24.7173(5) Å	β = 90°.
	c = 24.6450(6) Å	γ = 120°.
Volume	13039.5(6) Å <sup>3</sup>	
Z	1	
Density (calculated)	1.389 g/cm <sup>3</sup>	
Absorption coefficient	1.844 mm <sup>-1</sup>	
F(000)	5310	
Crystal size	0.100 x 0.100 x 0.050 mm <sup>3</sup>	
Theta range for data collection	2.855 to 24.988°.	
Index ranges	-29 ≤ h ≤ 29, -29 ≤ k ≤ 29, -29 ≤ l ≤ 29	
Reflections collected	229996	
Independent reflections	15300 [R(int) = 0.2081]	
Completeness to theta = 24.988°	99.8 %	
Absorption correction	Semi-empirical from equivalents	
Max. and min. transmission	0.88 and 0.76	
Refinement method	Full-matrix least-squares on F <sup>2</sup>	
Data / restraints / parameters	15300 / 1035 / 845	
Goodness-of-fit on F <sup>2</sup>	1.062	
Final R indices [I > 2σ(I)]	R1 = 0.0600, wR2 = 0.1551	
R indices (all data)	R1 = 0.1782, wR2 = 0.2387	
Extinction coefficient	n/a	
Largest diff. peak and hole	1.487 and -0.829 e.Å <sup>-3</sup>	



**Figure S1.** Characterization of  $[Ag_{18}(PPh_3)_{10}H_{16}]^{2+}$  by UV-vis and ESI MS. (A) Full range ESI MS of a methanol solution of  $[Ag_{18}(PPh_3)_{10}H_{16}]^{2+}$  in positive ion mode. The major peak is for  $[Ag_{18}(PPh_3)_{10}H_{16}]^{2+}$ . (B) Comparison of experimental (red trace) and simulated (black) isotopic distributions of the cluster. Peaks labelled with asterisk (\*) correspond to  $PPh_3$  loss. (C) UV-vis absorption spectrum of the cluster. These data presented here is matching with previous report.<sup>1-2</sup>

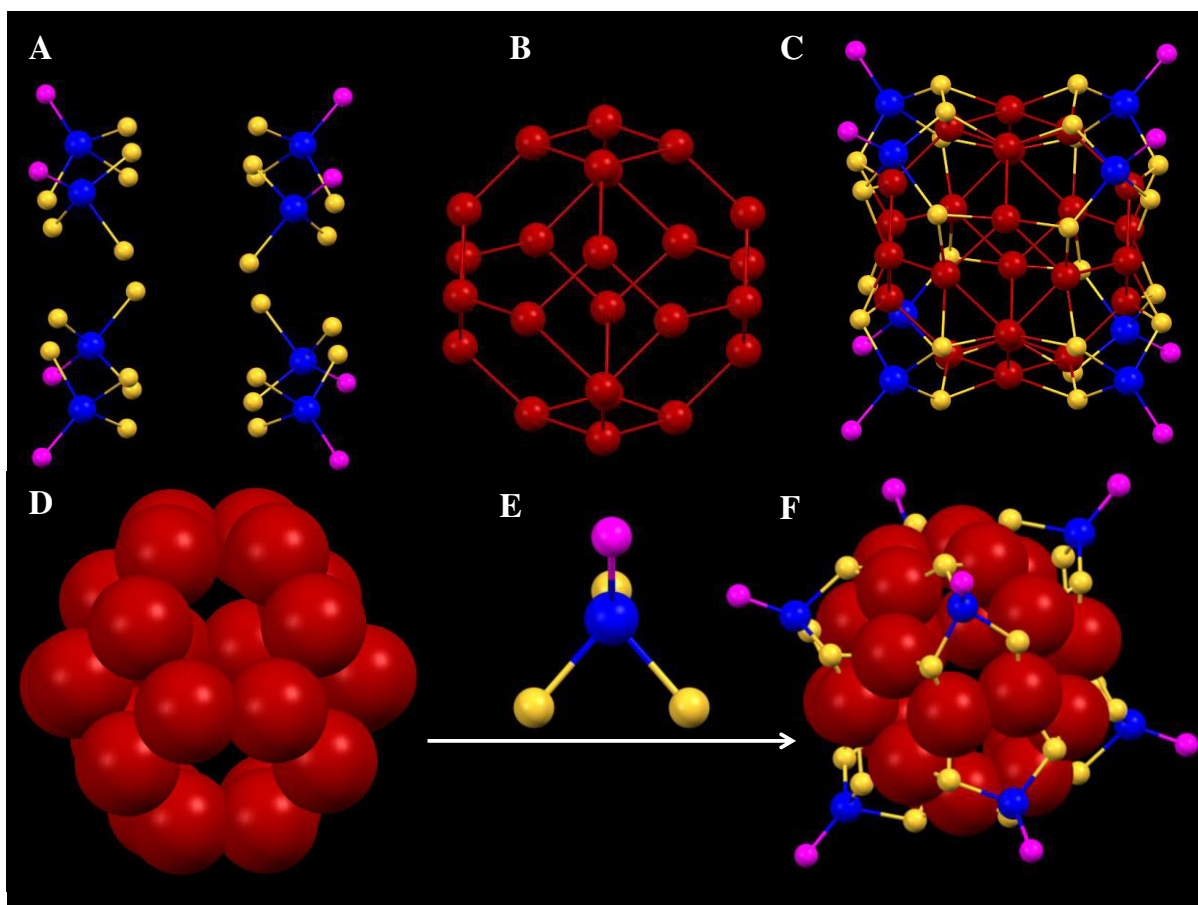


**Figure S2.** Construction of the FCC ( $Ag_{14}$ ) or octacapped octahedron ( $Ag_6@Ag_8$ ). (A)  $Ag_8$  core which caps the  $Ag_6$  octahedron. (B)  $Ag_6$  octahedron which can be viewed also as square bipyramid. (C)  $Ag_{14}$  core which corresponds to FCC or octacapped octahedron. All atoms shown are silver.

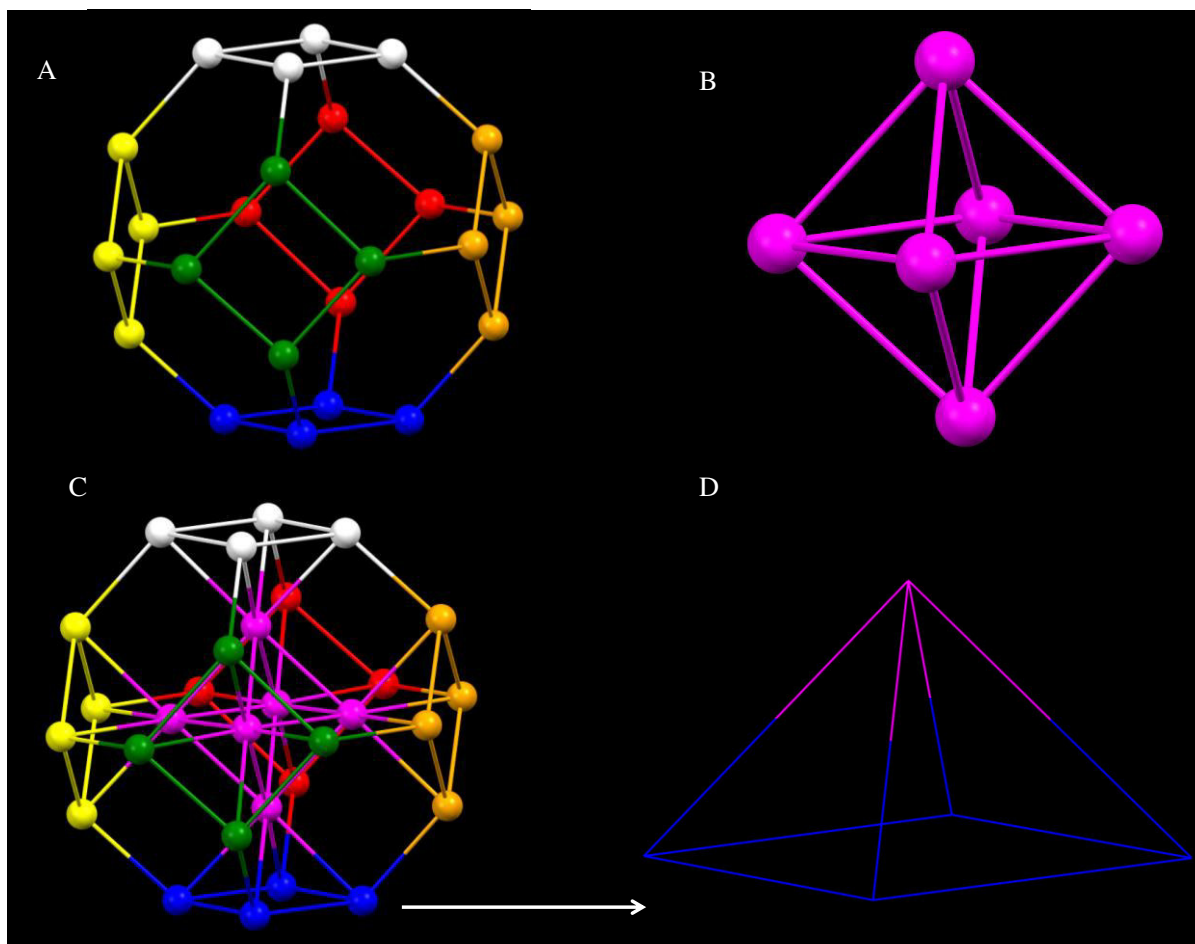


**Figure S3.** Complete crystal facets present in the FCC (Ag<sub>14</sub>). Facets are shown in ball-and-stick model. (A) Square shaped facet {100}. (B) Rectangular shaped facet {110}. (C) Equilateral triangle shaped facet {111}. The atoms other than facets are shown in wireframe model. All atoms shown are silver. All atoms shown are silver.

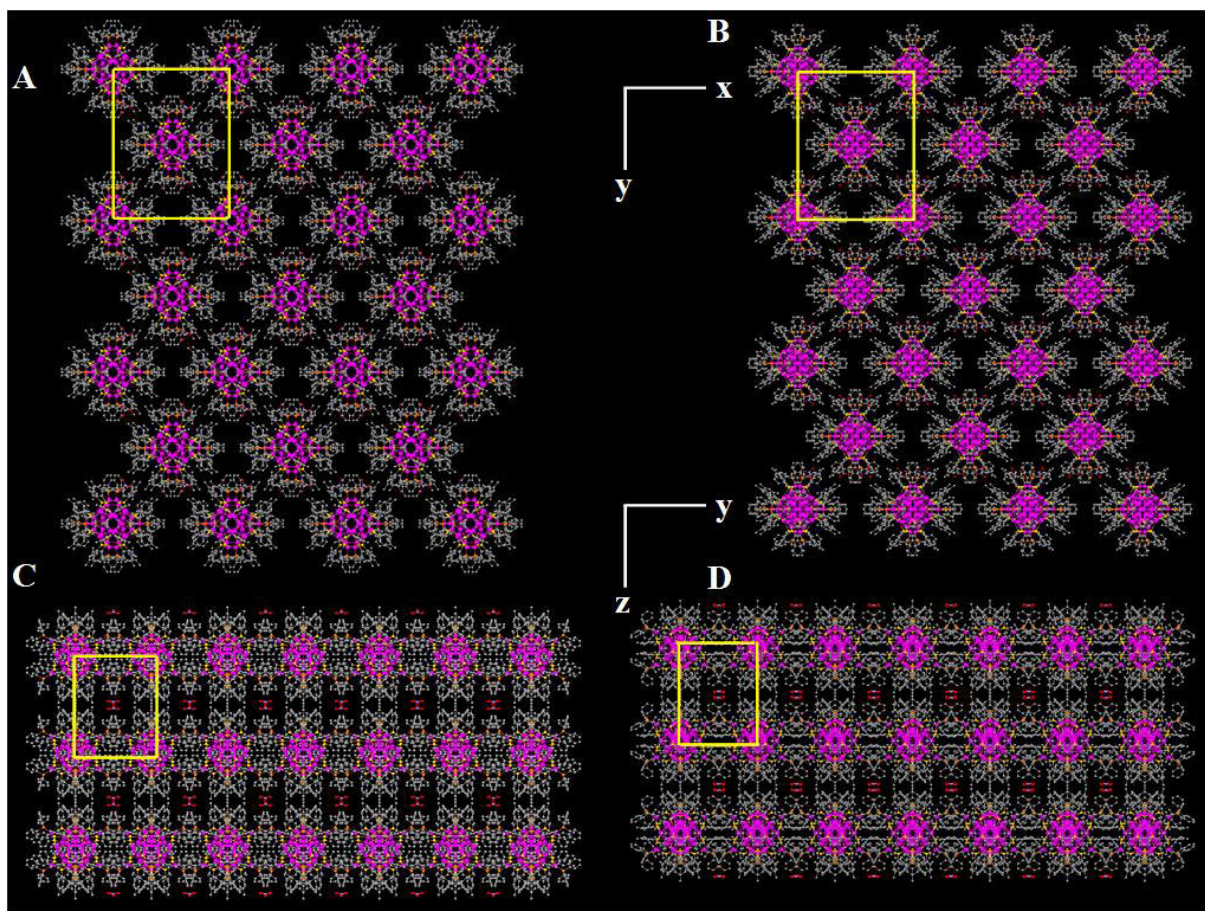




**Figure S4.** Construction of  $\text{Ag}_{32}\text{S}_{24}\text{P}_8$  shell, tetrahedrally oriented silver-thiolate-phosphine complexes ( $\text{AgS}_3\text{P}$ ) are sitting on the faces of eight hexagons of  $\text{Ag}_{24}$  outer core. (A) Eight units of tetrahedrally oriented  $\text{AgS}_3\text{P}$ . (B)  $\text{Ag}_{24}$  outer core in ball-and-stick model. (C)  $\text{Ag}_{24}$  outer core encapsulated by eight units of  $\text{AgS}_3\text{P}$ . (D)  $\text{Ag}_{24}$  outer core in spacefilling model. (E) One  $\text{AgS}_3\text{P}$  unit in ball-and-stick model. (F)  $\text{Ag}_{32}\text{S}_{24}\text{P}_8$  shell. Color legends: yellow, sulphur; blue, red, silver; magenta, phosphorous.

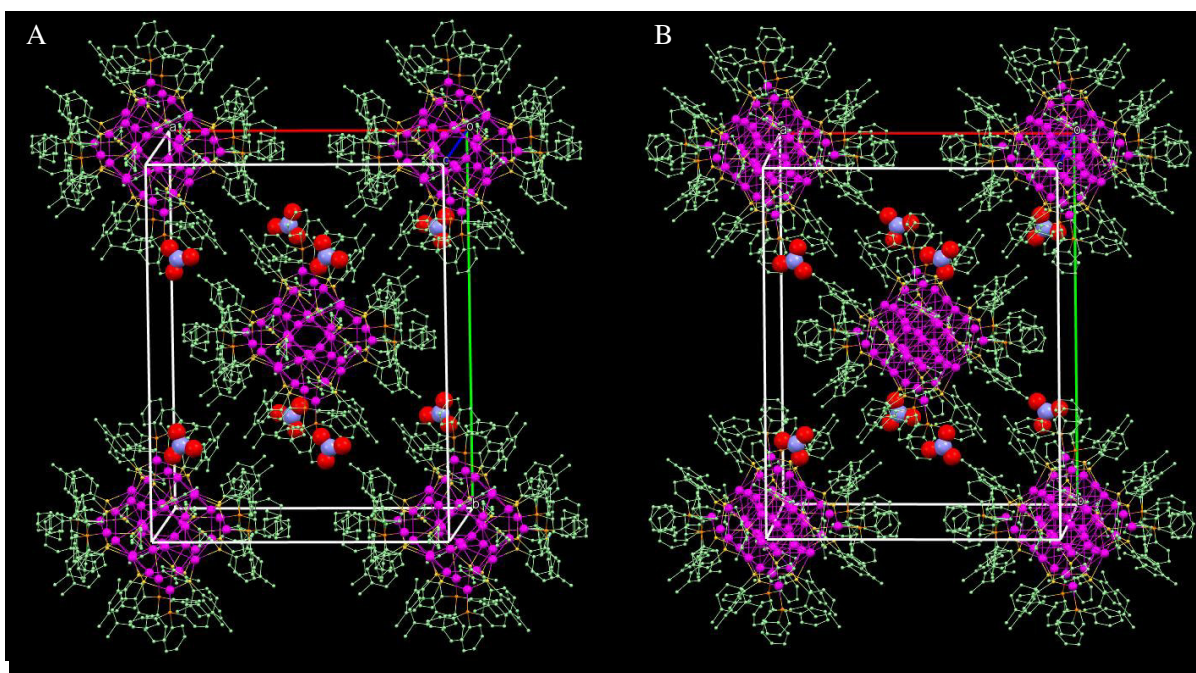


**Figure S5.** Encapsulation of Ag<sub>6</sub> inner core by Ag<sub>24</sub> outer core. (A) Ag<sub>24</sub> outer core consists of six square faces. The faces are shown in six different colours. (B) Ag<sub>6</sub> octahedron. (C) Ag<sub>6</sub> inner core encapsulated by Ag<sub>24</sub> outer core, which resulted in the formation of six square pyramids. (D) One such square pyramid is shown by an arrow in wireframe model. This kind of architecture is not observed in case of **II** cluster. All atoms shown are silver.

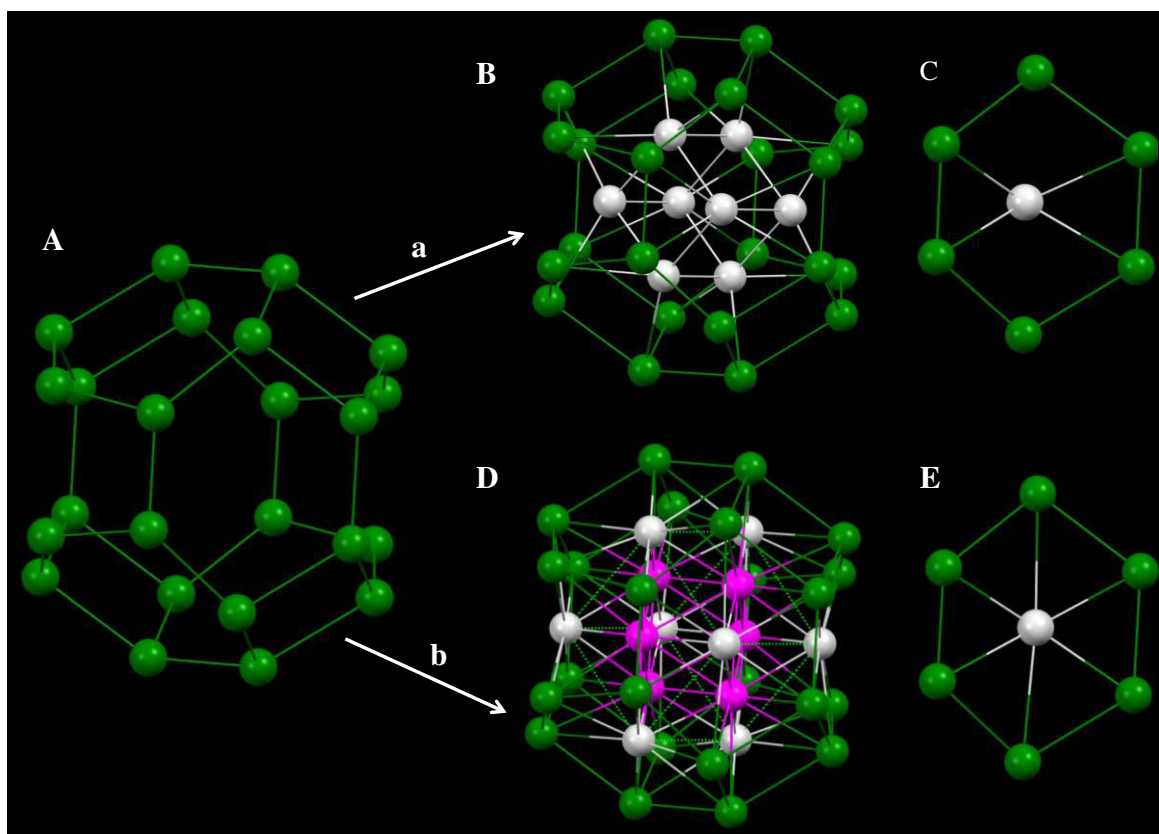


**Figure S6.** (A) and (B) Organization of  $[\text{II}](\text{NO}_3)_2$  and  $[\text{I}](\text{NO}_3)_2$ , respectively in a centred rectangular 2D lattice along z axis. (C) and (D) Packing diagram of the same which exhibits rectangular 2D lattice along x axis. Hydrogen atoms are omitted for clarity. Yellow rectangles correspond to unit cells. Color legends: gray, carbon; magenta, silver; yellow, sulphur; orange, phosphorous; red, oxygen; cyan, nitrogen.

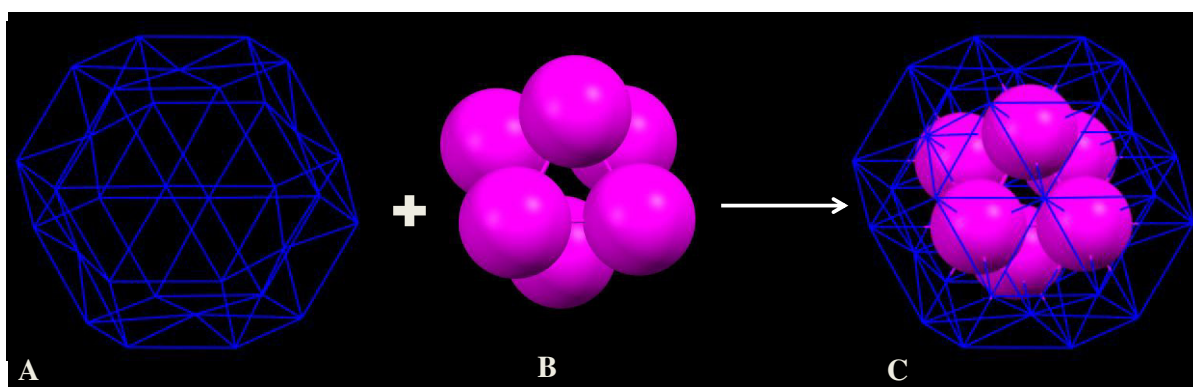




**Figure S7.** The packing diagram of  $[\text{III}](\text{NO}_3)_2$  and  $[\text{I}](\text{NO}_3)_2$  clusters. It clearly reveals the location of counter ions ( $\text{NO}_3^-$ ) in the packing of both the clusters. Each unit cell is having two clusters ( $Z = 2$  in Table S4) and four counter ions (as each counter ion contributes half per cluster). Hence each cluster contains two counter ions ( $\text{NO}_3^-$ ). (A) and (B) Packing of  $[\text{III}](\text{NO}_3)_2$  and  $[\text{I}](\text{NO}_3)_2$  clusters, respectively. Counter ions are shown in spacefilling model. Hydrogen atoms are omitted for clarity. Crystallographic axes a, b and c are shown by red, green and blue colours, respectively. Color legends: light green, carbon; magenta, silver; yellow, sulphur; orange, phosphorous; cyan, nitrogen; red, oxygen.

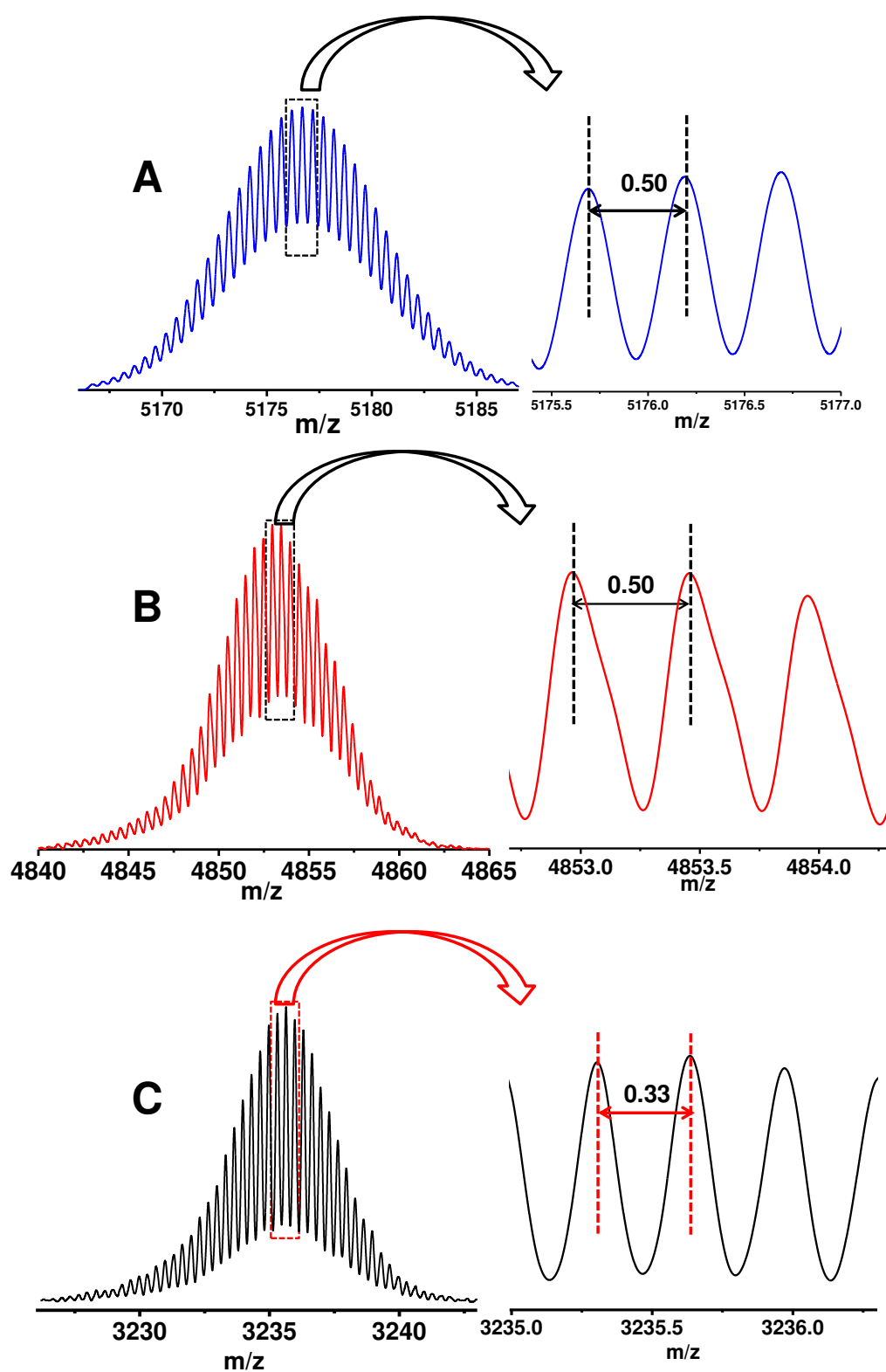


**Figure S8.** The construction of Ag<sub>32</sub> and Ag<sub>38</sub> kernels present in **II** and **I** clusters, respectively. (A) Ag<sub>24</sub> outer core. (B) and (D) Ag<sub>32</sub> and Ag<sub>38</sub> kernels, respectively. (C) and (E) One hexagon from (B) and (D), respectively. (a) Ag<sub>8</sub> inner core of **II**. (b) Ag<sub>14</sub> (Ag<sub>8</sub>@Ag<sub>6</sub>) inner core of **I**. The cubes of simple cubic and face-centred cubic structures are shown in white colour. Ag<sub>6</sub> octahedral inner core is shown in magenta colour. Dotted green lines represent the cube in FCC. All atoms shown are silver.

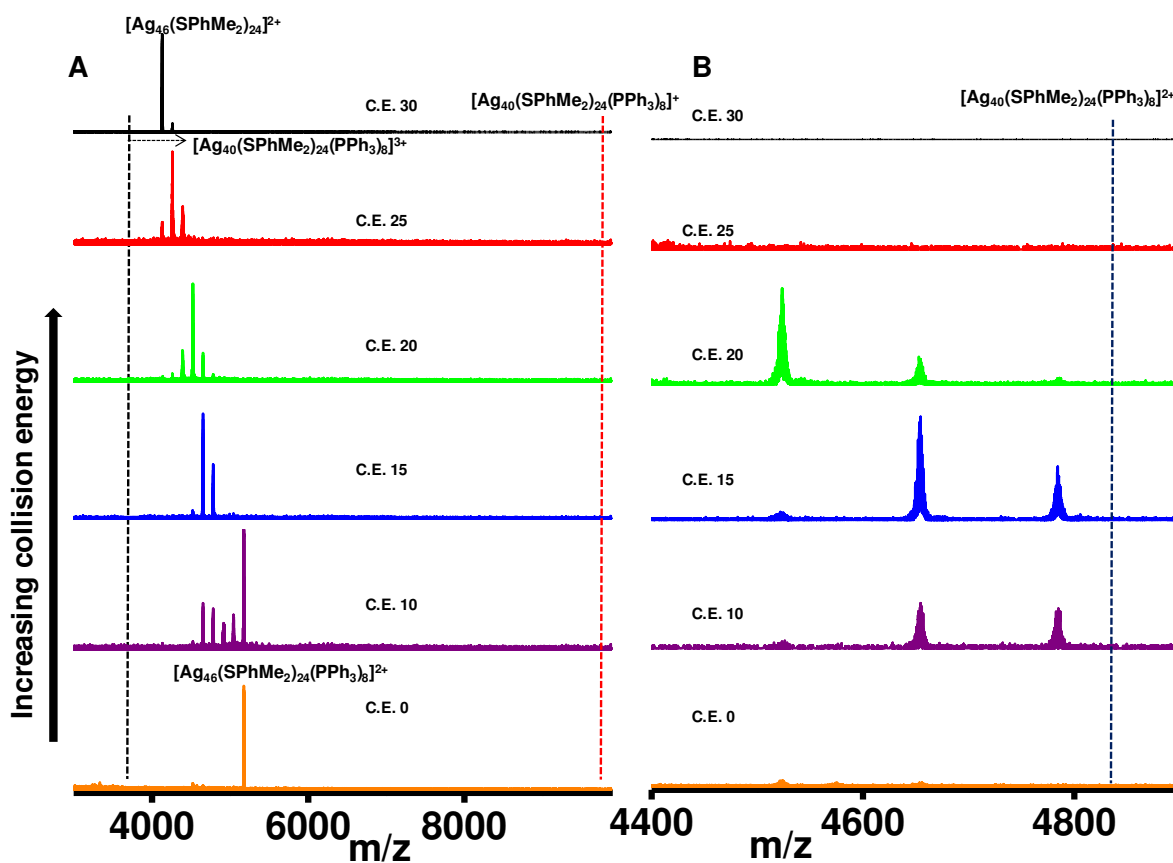


**Figure S9.** (A) Truncated octahedron Ag<sub>32</sub> shell in wireframe model. (B) Inner core Ag<sub>6</sub> octahedron in spacefilling model. (C) Encapsulation of Ag<sub>6</sub> octahedron, by truncated octahedron Ag<sub>32</sub> shell to construct Ag<sub>38</sub>.

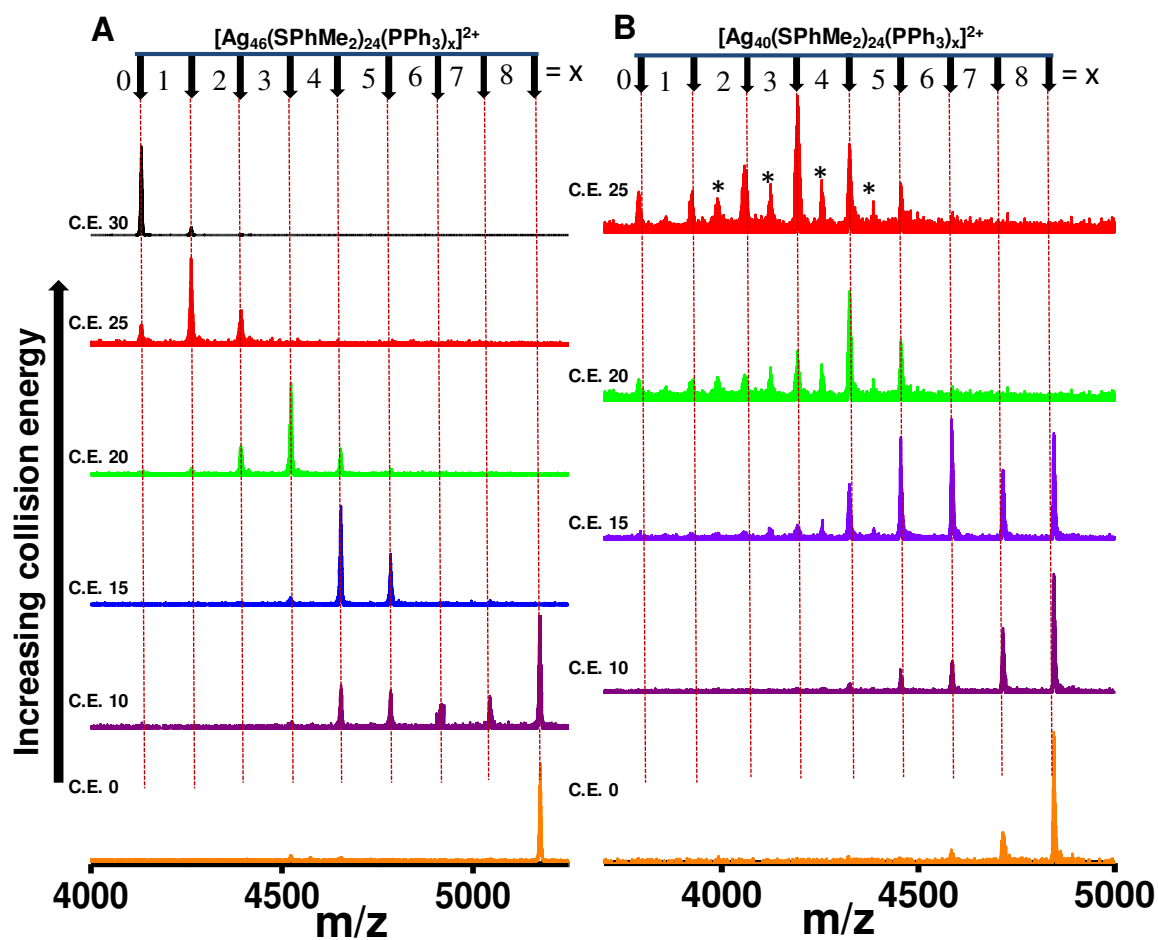




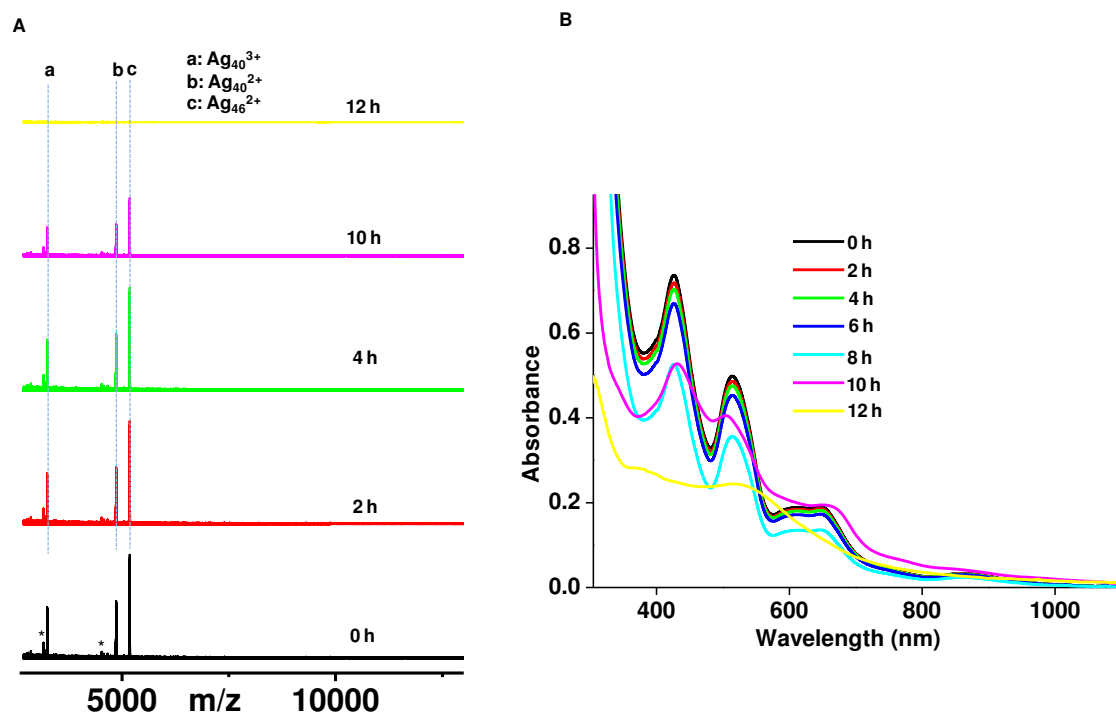
**Figure S10.** Peaks at  $m/z$  5176.25, 4853.5 and 3235.75 are expanded (From main manuscript Figure 4) in A, B and C, respectively. In A and B the characteristic peak separation is  $m/z$  0.5 which confirm +2 charge state. Similarly in C peak separation of  $m/z$  0.33 reveals +3 charge state.



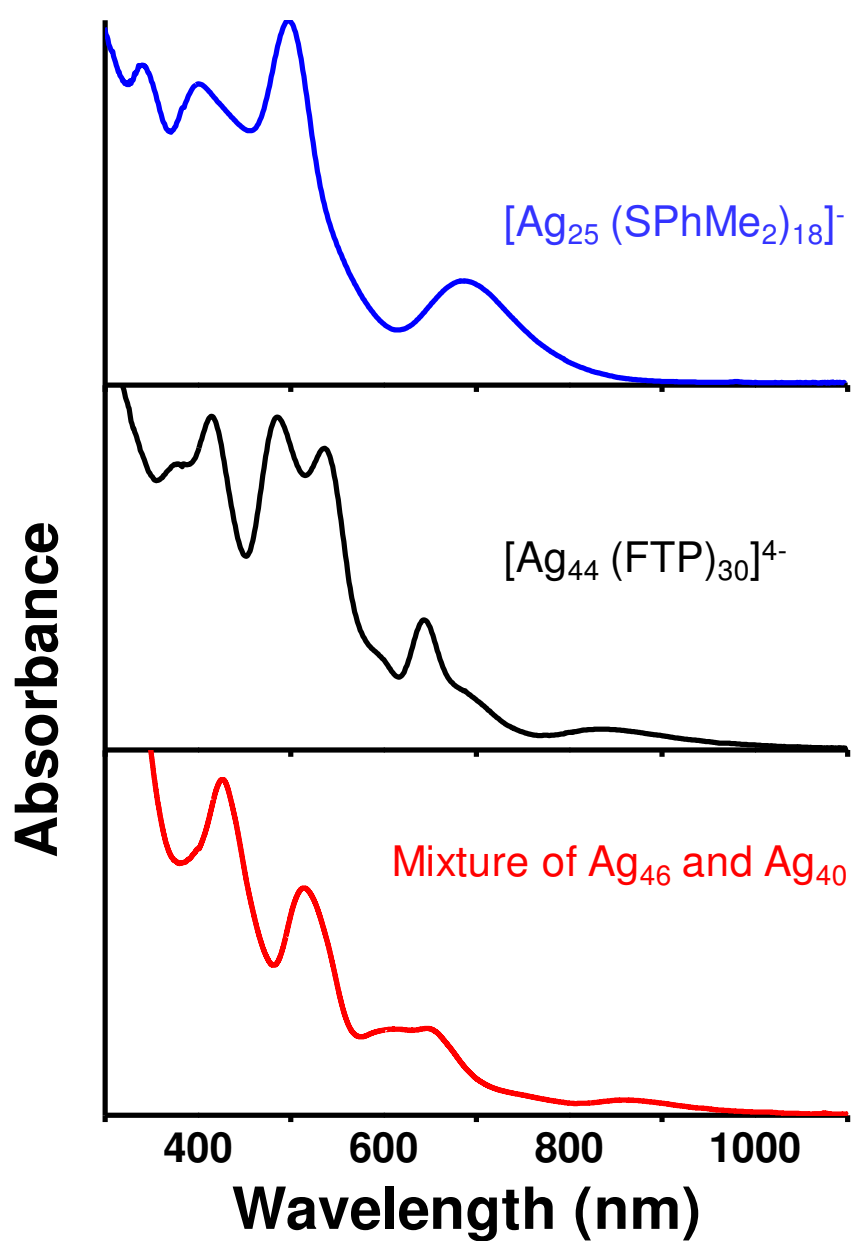
**Figure S11.** Collision energy dependent mass spectra of  $I^{2+}$ . **II** was not detected in any charge state during the collision induced dissociation experiment of  $I^{2+}$ . (A) Full range spectra show the absence of **II** in +3 and +1 charge state. (B) Expanded region from Figure A show the absence of **II** in +2 charge state. Dotted vertical lines of black, red and blue correspond to the  $m/z$  positions of **II** in +3, +1 and +2 charge state, respectively. The collision energy (C.E.) values given are in instrumental units.



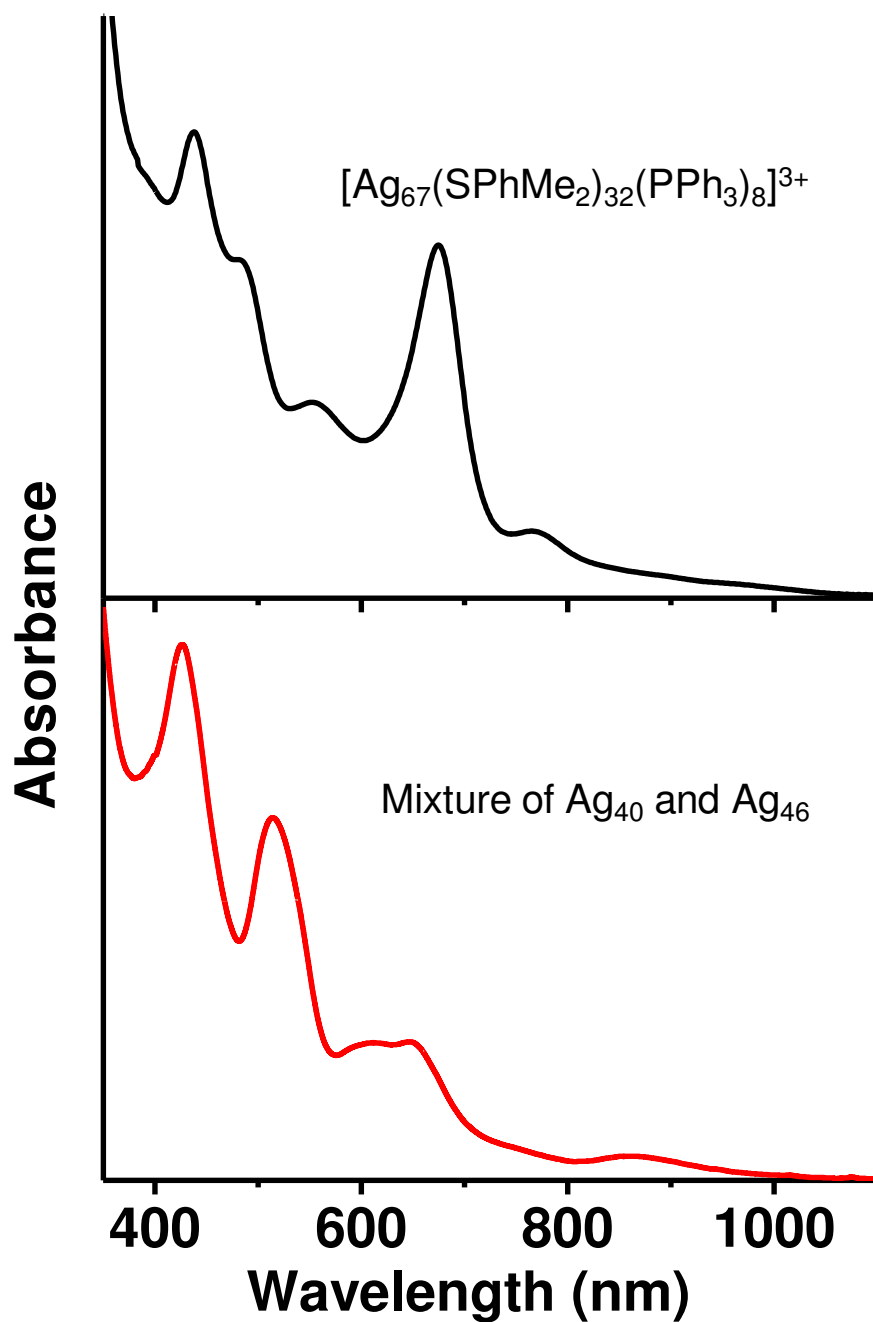
**Figure S12.** Collision-induced dissociation (CID) experiments were performed on both the clusters. (A) and (B) Collision energy dependent mass spectra of  $I^{2+}$  and  $II^{2+}$ , respectively. Systematic losses of secondary ligands (triphenylphosphine) were observed due to weaker binding with the cluster core. CID experiments revealed the maximum loss of eight phosphine ligands which confirm the number of secondary ligands present in the cluster formulae. This observation is consistent with SCXRD results. The symbol asterisk (\*) indicates the loss of thiol ligands ( $SPhMe_2$ ). The collision energy (C.E.) values given are in instrumental units.



**Figure S13.** (A) and (B) Time dependent ESI MS and UV-vis spectra, respectively of a mixture of **II** and **I** clusters, heated in methanol at 50 °C. UV-vis spectra showed no considerable change with time up to 8 h, only change in the absorbance was observed. After 8 h of stirring at 50 °C, the optical absorption spectrum started to change and the highly structured features disappeared after 12 h. This indicates that the cluster was getting decomposed and this is reflected in the ESI MS also. Time dependent ESI MS revealed the presence of the species, **II** and **I** and no interconversion was seen as their relative intensities were same. This observation established that there is no oxidation product of **I** to form **II**. Studies were also conducted on pure clusters also. No interconversion of one cluster to the other was seen. The peaks marked with asterisk indicate the loss of  $\text{PPh}_3$  ligands.

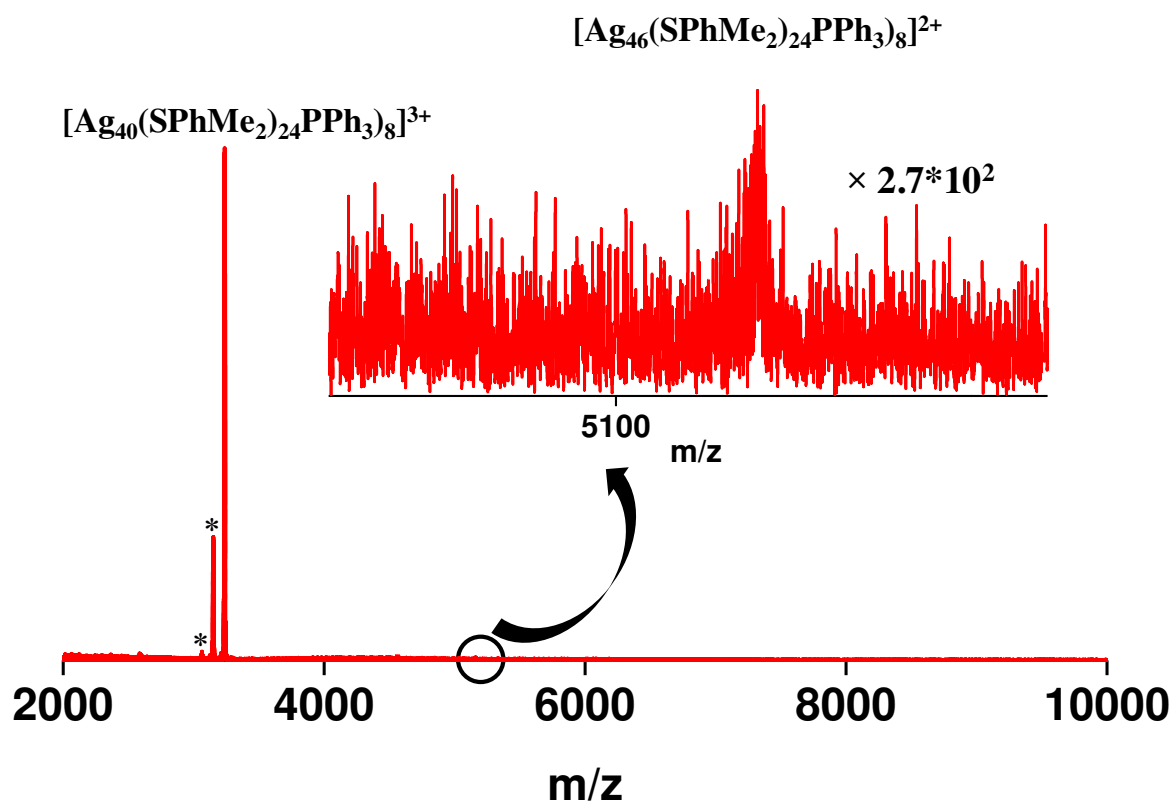


**Figure S14.** Comparison of UV-vis spectra of a mixture of **II** and **I** clusters along with previously reported clusters.<sup>18-19</sup> Some of the features are comparable with the two reported clusters but the overall spectrum is different. FTP refers to 4-fluorothiophenol.

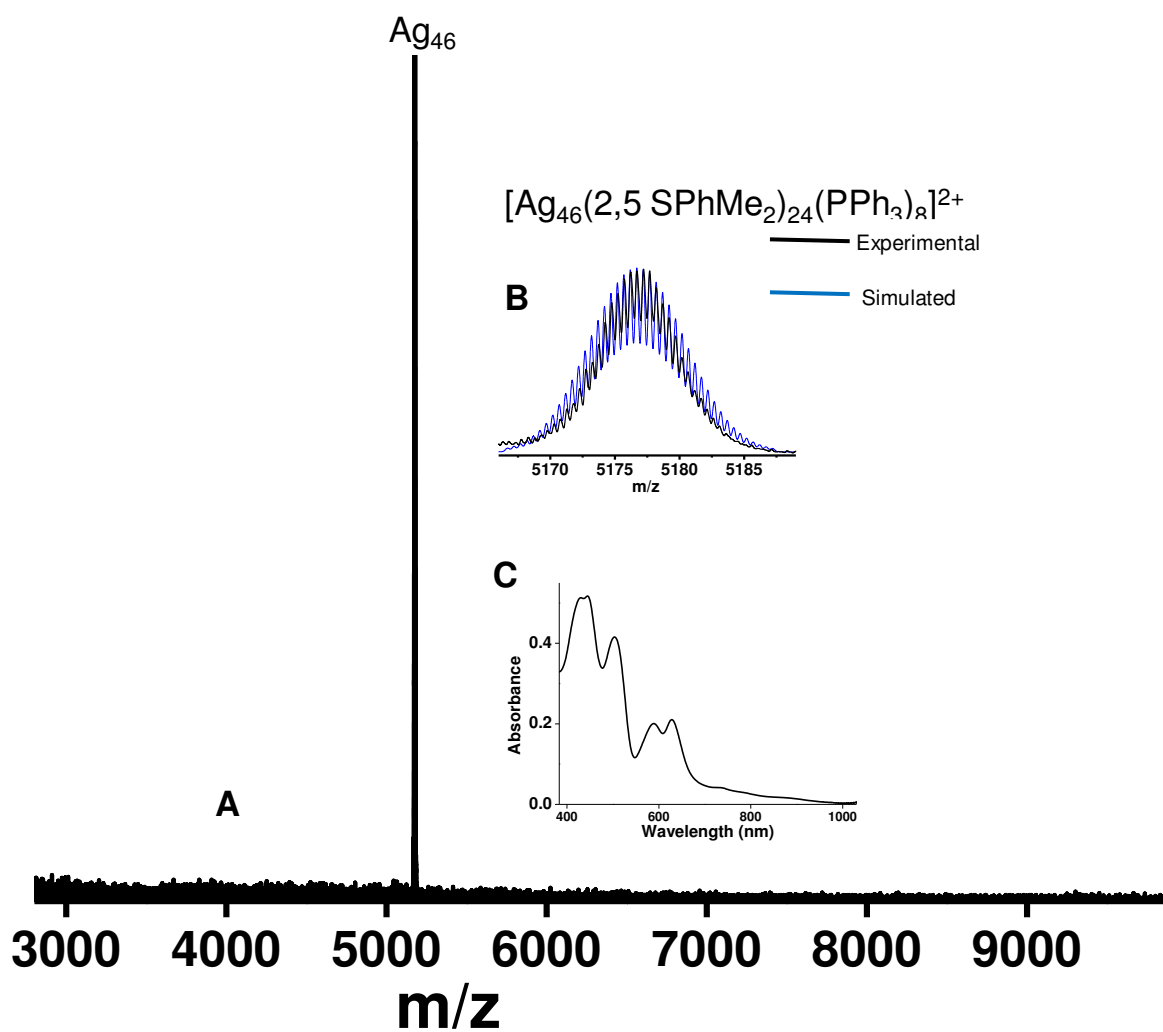


**Figure S15.** Comparison of UV-vis spectra of a mixture of **II** and **I** clusters (red trace) with previously reported  $[Ag_{67}(SPhMe_2)_{32}(PPh_3)_8]^{3+}$  (black trace).<sup>12</sup> Both the clusters are synthesised by using same ligands but UV-vis spectra are very different. This indicates that synthetic methodology plays major role in determining the size and shape of the nanoclusters.

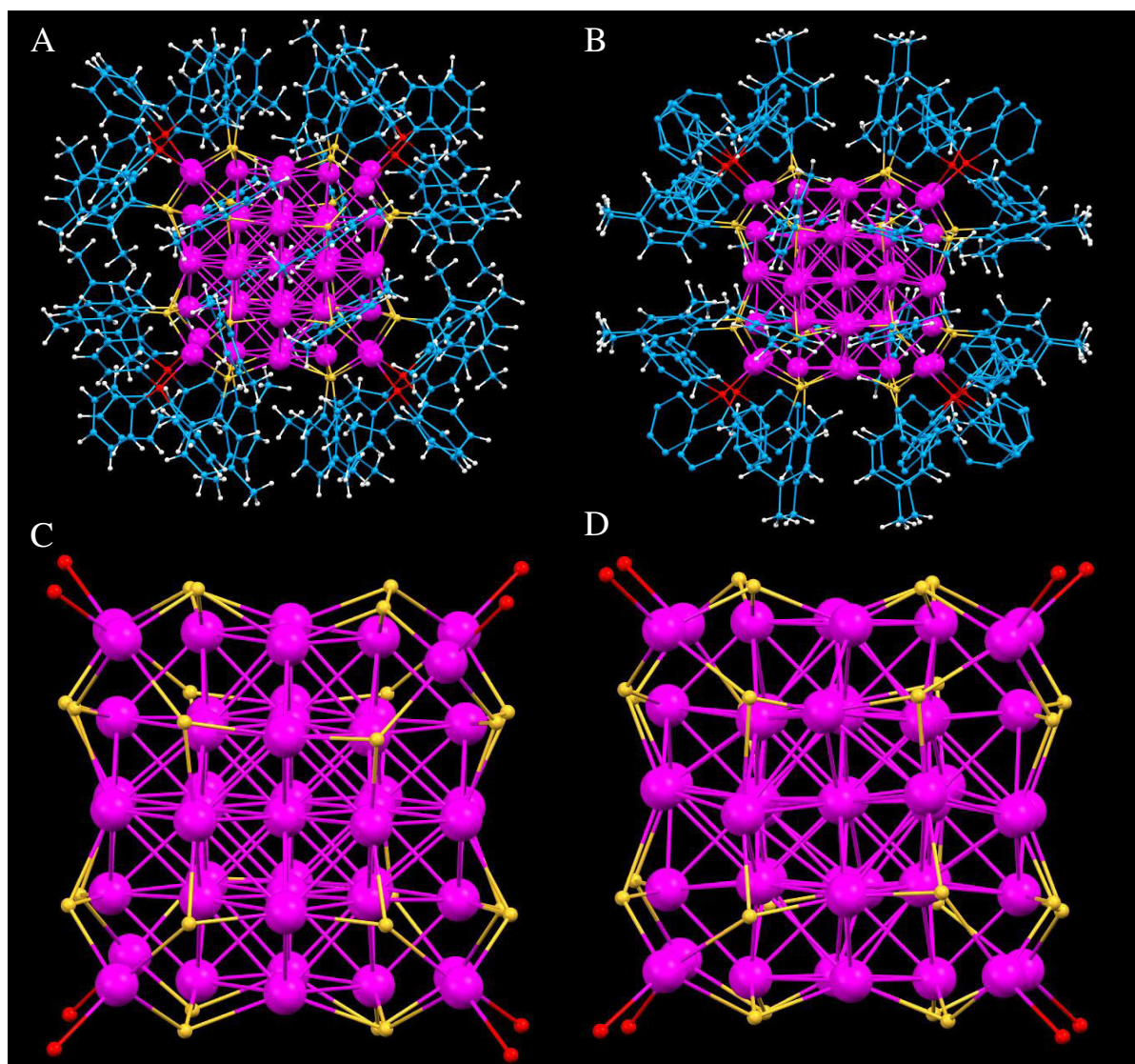




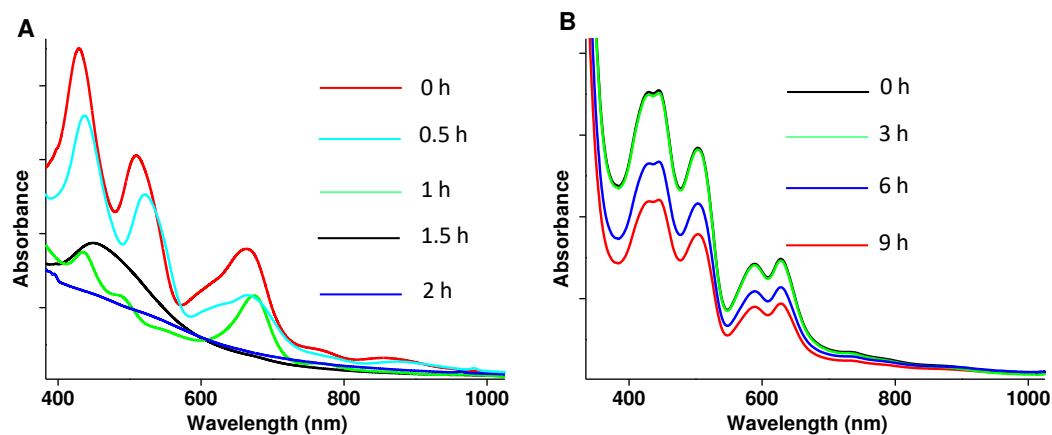
**Figure S16.** (A) Positive ion mode ESI MS. Peaks labelled \* indicate phosphine loses. (B) Expansion of the selected area is shown by an arrow. The peak corresponding to  $\text{Ag}_{46}$  was observable only upon magnification.



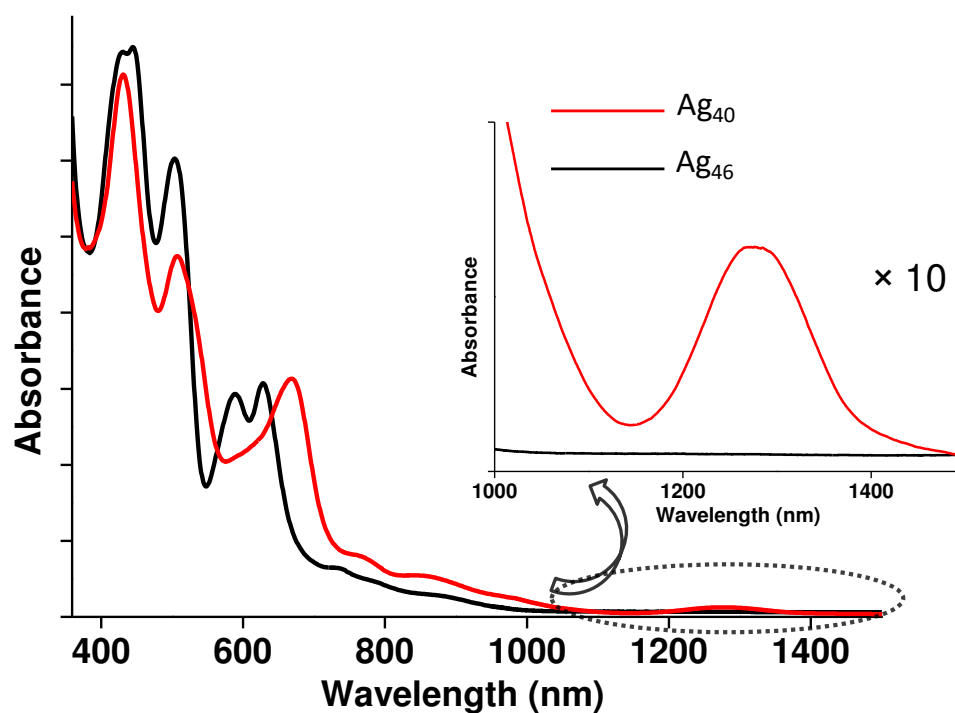
**Figure S17.** (A) Full range ESI MS of a methanol solution of crystals in positive ion mode. The peak is due to  $[\text{Ag}_{46}(\text{2,5-SPhMe}_2)_{24}(\text{PPh}_3)_8]^{2+}$ . (B) The isotopic distribution of experimental spectrum (black) is compared with simulated spectrum (blue). (C) UV-vis absorption spectrum of a solution of crystals in dichloromethane.



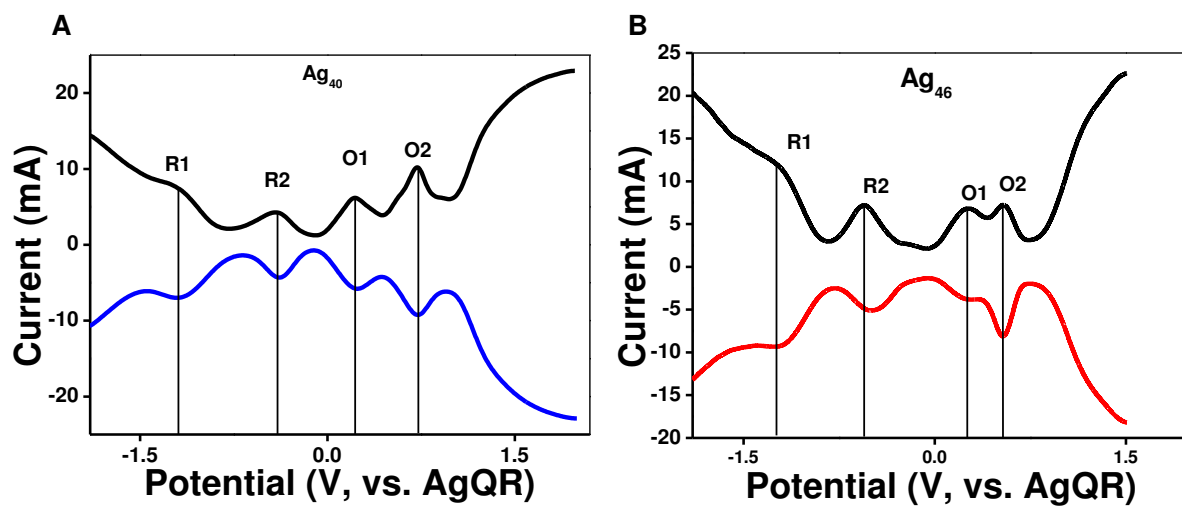
**Figure S18.** Comparison of the crystal structures of  $\text{Ag}_{46}$  cluster present in the co-crystal and the single component crystal. (A) and (B) Full structure of  $[\text{Ag}_{46}(\text{2,5-SPhMe}_2)_{24}(\text{PPh}_3)_8]$  and  $[\text{Ag}_{46}(\text{2,4-SPhMe}_2)_{24}(\text{PPh}_3)_8]$ , respectively. Counter ions are not shown here. Hydrogen atoms of triphenylphosphine for  $[\text{Ag}_{46}(\text{2,4-SPhMe}_2)_{24}(\text{PPh}_3)_8]$  are not fixed. (C) and (D) Structure of  $\text{Ag}_{46}\text{S}_{24}\text{P}_8$  present in multicomponent crystal (co-crystal) and single component crystal, respectively. Carbon and hydrogen atoms are not shown for clarity.



**Figure S19.** Time dependent UV-vis spectra of  $\text{Ag}_{40}$  and  $\text{Ag}_{46}$  clusters, heated at  $50^\circ\text{C}$  in MeOH. (A) and (B) correspond to UV-vis spectra of  $\text{Ag}_{40}$  and  $\text{Ag}_{46}$ , respectively. UV-vis spectra showed the disappearance of highly structured features of  $\text{Ag}_{40}$  after 1.5 h. In the case of  $\text{Ag}_{46}$ , the spectral features and absorbance were the same up to 3 h, only change in absorbance was seen afterwards. This observation reveals that  $\text{Ag}_{40}$  is not thermally very stable as compared to  $\text{Ag}_{46}$ .

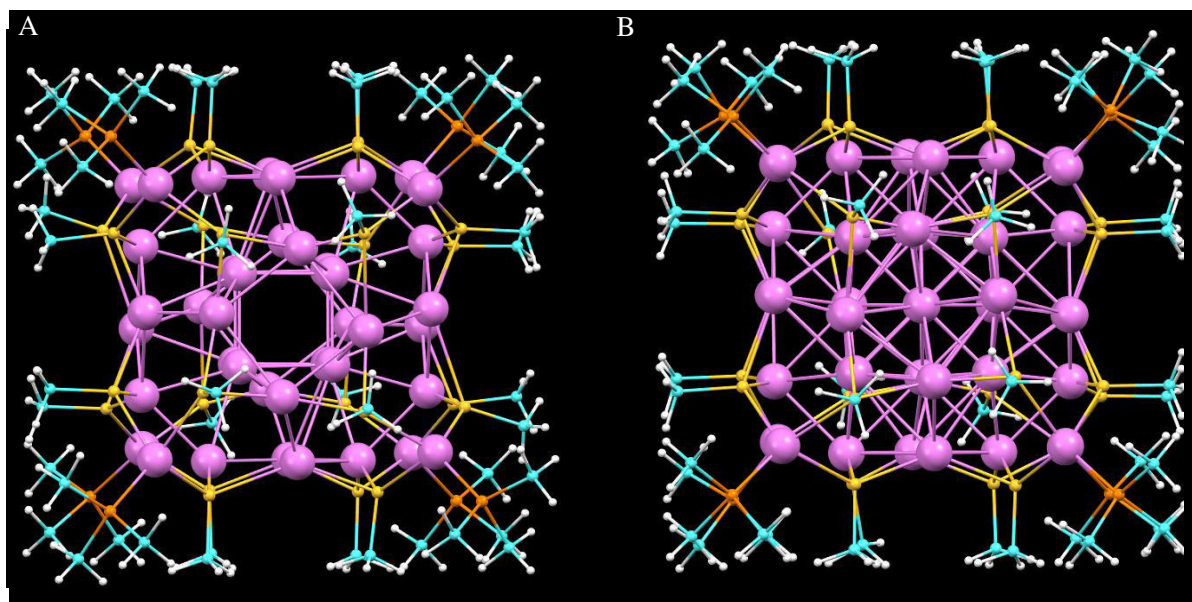


**Figure S20.** Comparison of optical absorption spectra of solutions of  $\text{Ag}_{46}$ ,  $\text{Ag}_{40}$ . UV-VIS-NIR spectra of  $\text{Ag}_{40}$  and  $\text{Ag}_{46}$  clusters in DCM. Red and black spectra correspond to  $\text{Ag}_{46}$  and  $\text{Ag}_{40}$ , respectively. Inset shows the absorption of  $\text{Ag}_{40}$  in the NIR region.

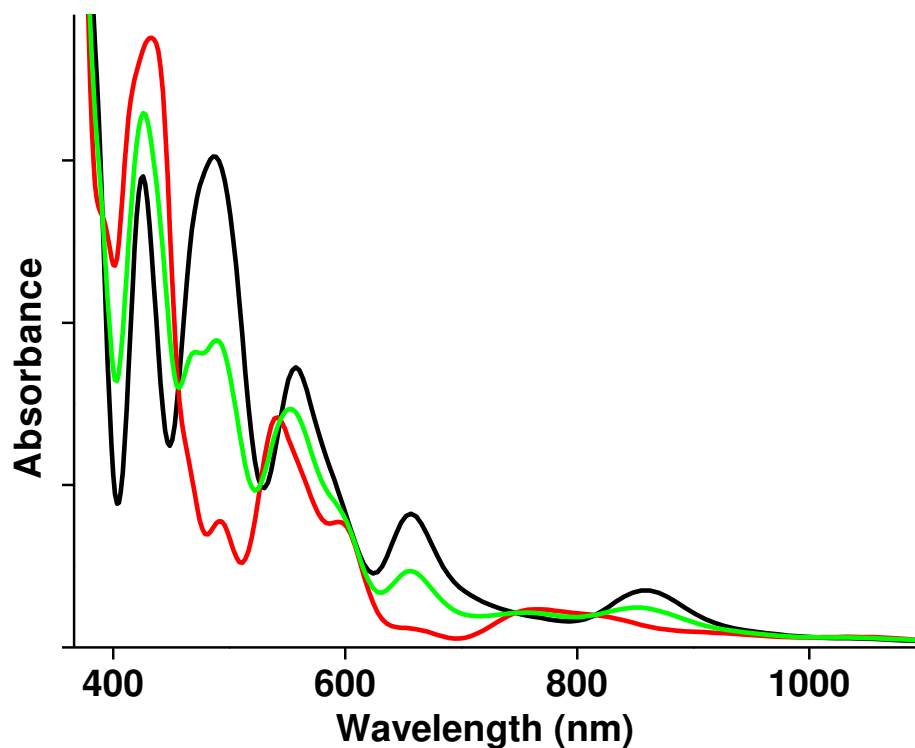


**Figure S21.** (A) and (B) correspond to differential pulse voltammetry (DPV) of  $\text{Ag}_{40}$  and  $\text{Ag}_{46}$  clusters in forward and reverse scan mode. It was carried out to determine the HOMO-LUMO gaps of both the clusters. R1 and R2 indicate the 1<sup>st</sup> and 2<sup>nd</sup> reduction potential values, respectively. O1 and O2 stand for the 1<sup>st</sup> and 2<sup>nd</sup> oxidation potential values.

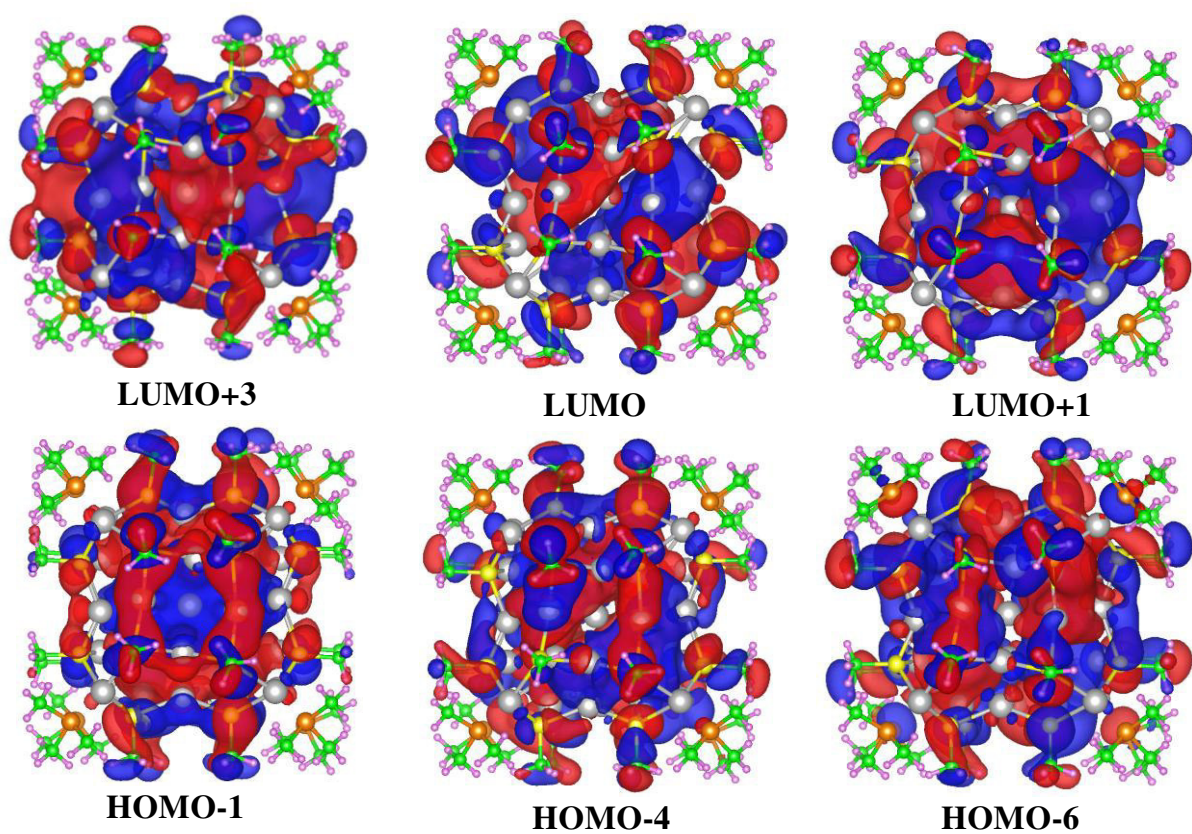




**Figure S22.** Reduced model structure of  $\text{Ag}_{40}$  and  $\text{Ag}_{46}$ . A and B correspond to  $[\text{Ag}_{40}(\text{SCH}_3)_{24}(\text{P}(\text{CH}_3)_3)_8]$  and  $[\text{Ag}_{46}(\text{SCH}_3)_{24}(\text{P}(\text{CH}_3)_3)_8]$ , respectively. Color legends: white, hydrogen; cyan, carbon; yellow, sulphur; orange, phosphorous; magenta, silver.

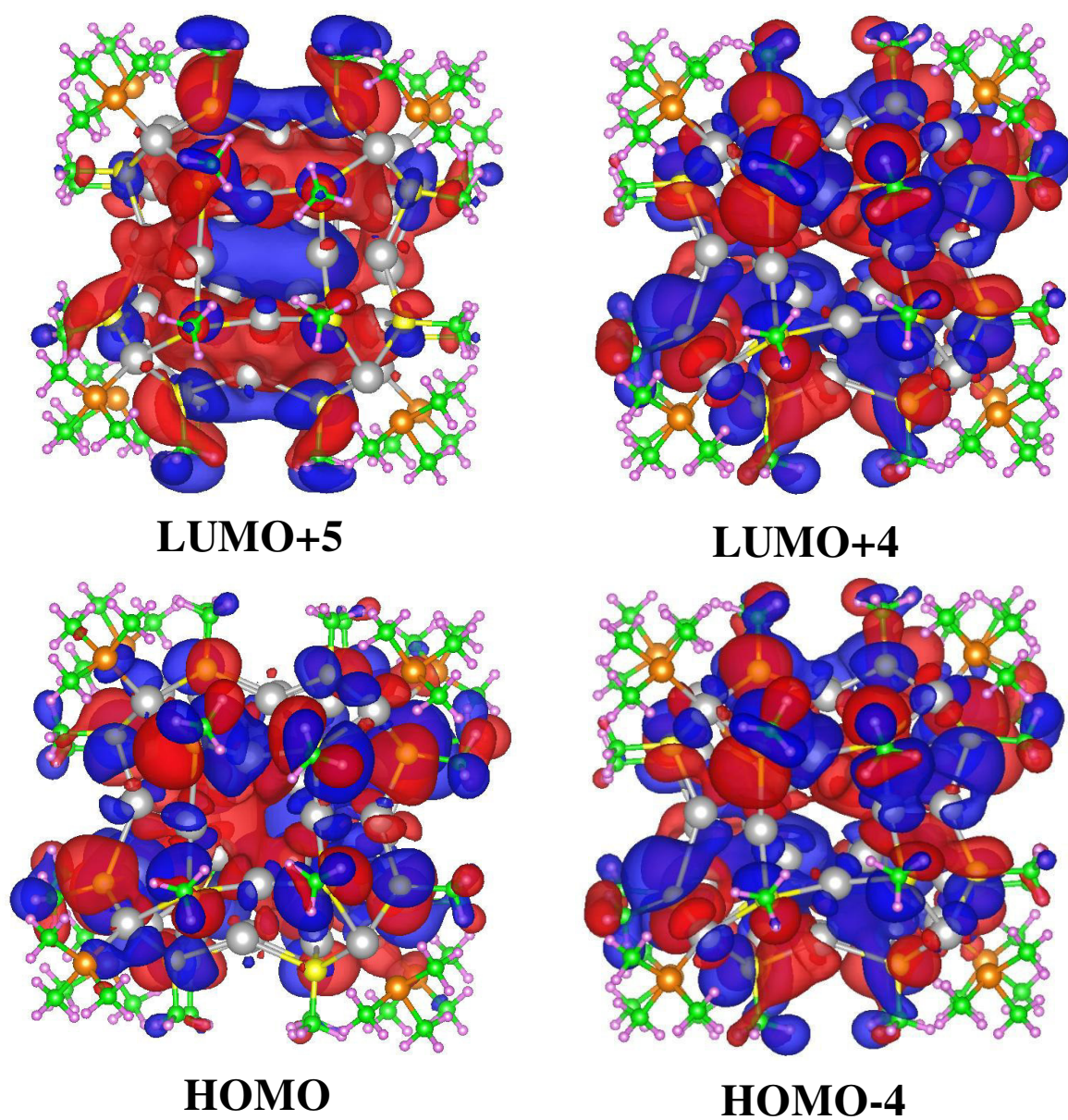


**Figure S23.** Construction of theoretical optical absorption spectrum from a 1:1 mixture of  $\text{Ag}_{40}$  and  $\text{Ag}_{46}$  clusters. Red and black traces indicate the calculated absorption spectrum of  $[\text{Ag}_{40}(\text{SCH}_3)_{24}(\text{P}(\text{CH}_3)_3)_8]$  and  $[\text{Ag}_{46}(\text{SCH}_3)_{24}(\text{P}(\text{CH}_3)_3)_8]$ , respectively. Green trace indicates the mixture of both the clusters in equal proportion.

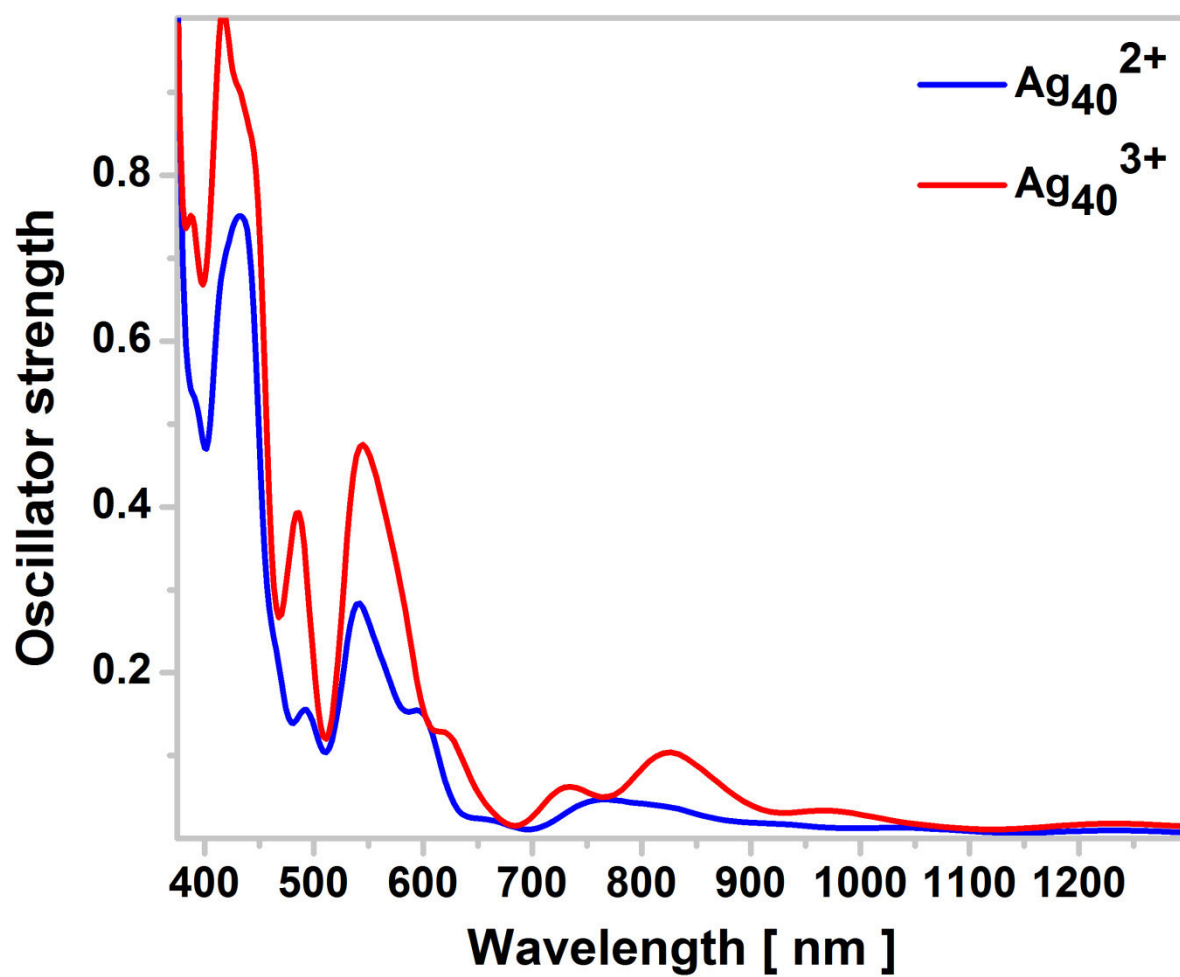


**Figure S24.** Molecular orbital transitions to the optical gap of  $[\text{Ag}_{46}(\text{SCH}_3)_{24}(\text{P}(\text{CH}_3)_3)_8]$ . The calculated HOMO -4, HOMO-1, HOMO-6, LUMO, LUMO+3, LUMO+1 of  $[\text{Ag}_{46}(\text{SCH}_3)_{24}(\text{P}(\text{CH}_3)_3)_8]$  cluster.

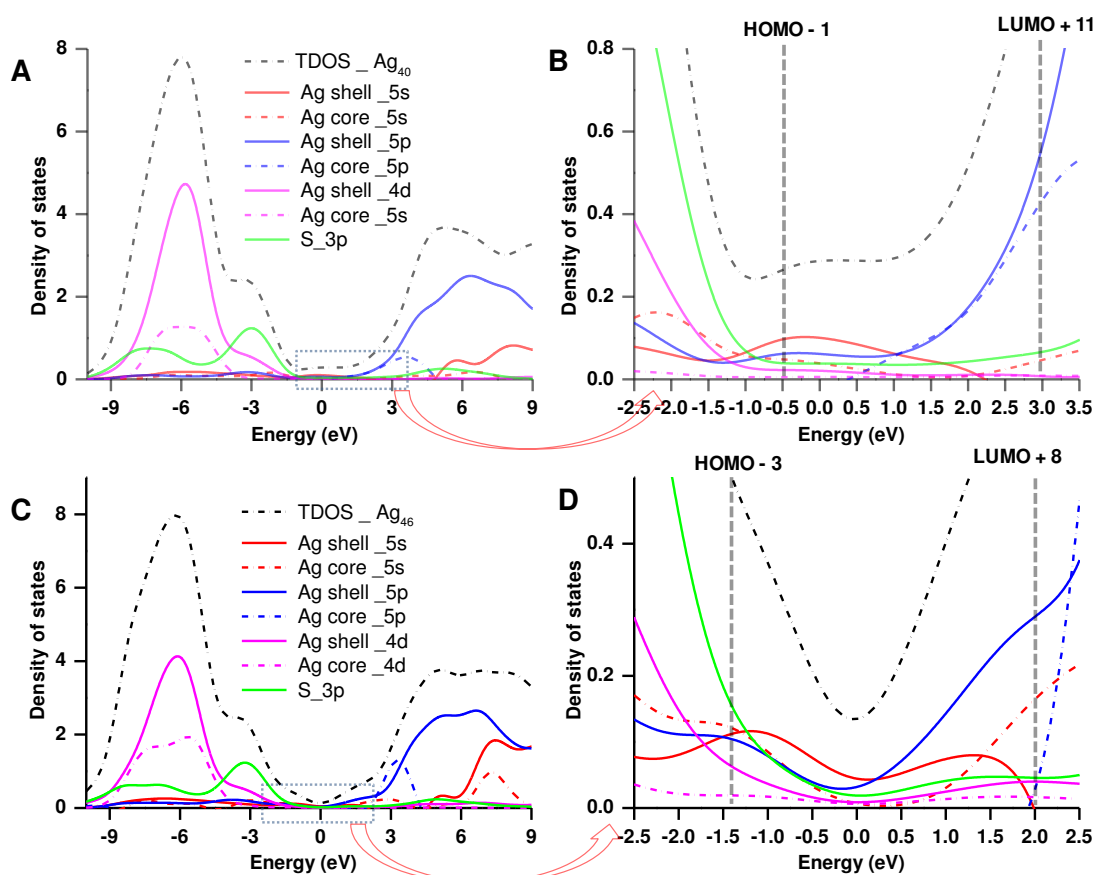




**Figure S25.** Molecular orbital transitions to the optical gap of  $[\text{Ag}_{40}(\text{SCH}_3)_{24}(\text{P}(\text{CH}_3)_3)_8]$ . The calculated HOMO, HOMO-4, LUMO+4 and LUMO+5 of  $[\text{Ag}_{40}(\text{SCH}_3)_{24}(\text{P}(\text{CH}_3)_3)_8]$  cluster.

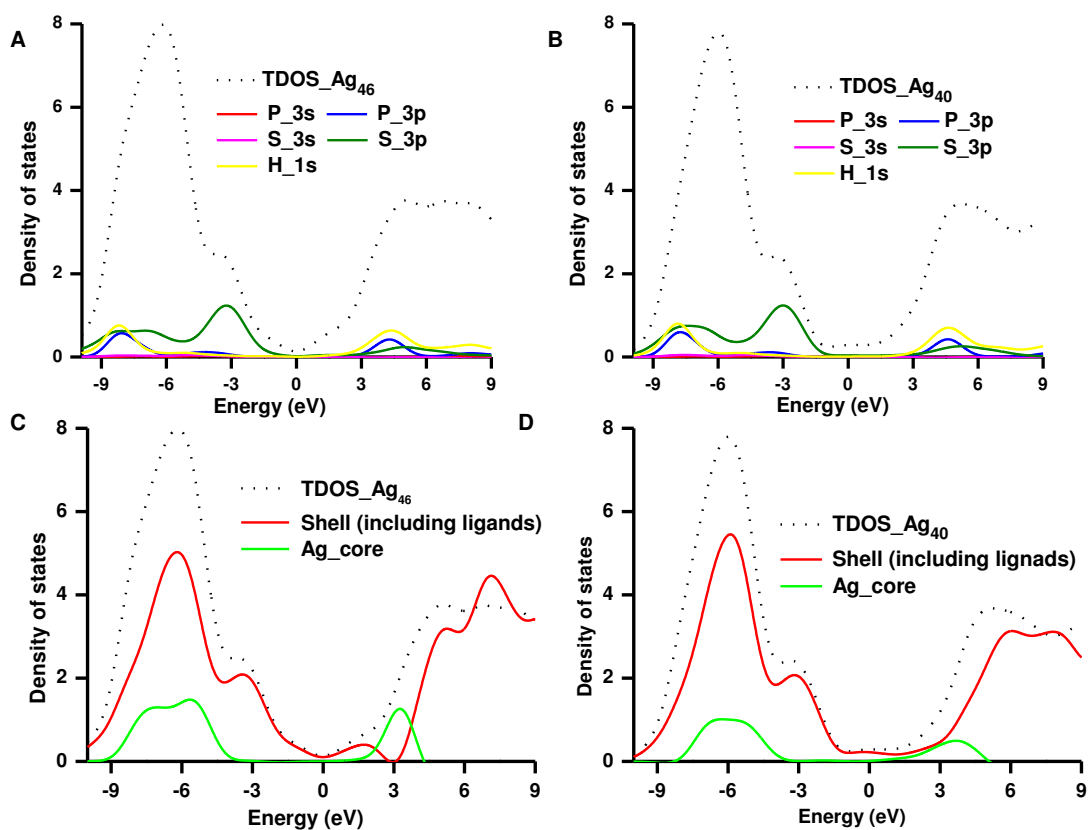


**Figure S26.** Comparison of the predicted optical absorption spectra of  $[\text{Ag}_{40}(\text{SCH}_3)_{24}(\text{P}(\text{CH}_3)_3)_8]$  cluster in its 2+ and 3+ charge states.

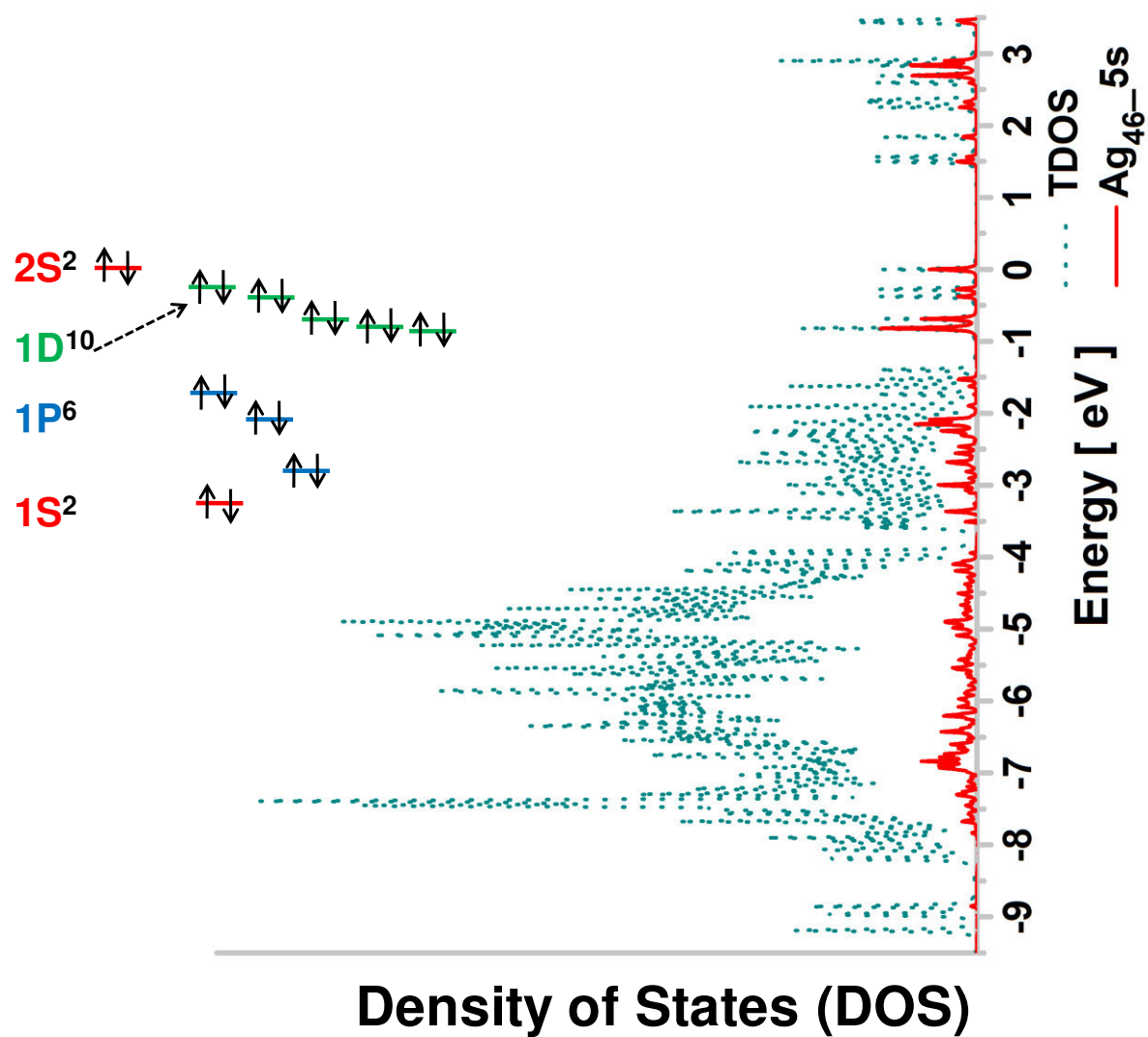


**Figure S27.** Comparison of the plot of density of states versus energy of both the clusters,  $\text{Ag}_{40}$  and  $\text{Ag}_{46}$ . TDOS correspond to total density of states. (A) and (C) correspond to density of states of  $\text{Ag}_{40}$  and  $\text{Ag}_{46}$ , respectively. (B) and (D) correspond to the expansion of (A) and (C), respectively in the specific energy region. The energies of the corresponding molecular orbitals, responsible for major transitions in both the clusters are marked by black dotted lines. Fermi level ( $E_F$ ) was centred at the middle of HOMO-LUMO gap. The optical transitions in both clusters basically have the final state consisting of mainly 5p Ag orbitals. Intraband 5s to 5p, and interband 4d to 5p transitions are expected to occur mainly in these clusters with some contribution from Ag 5p or S 3p to Ag 5s.

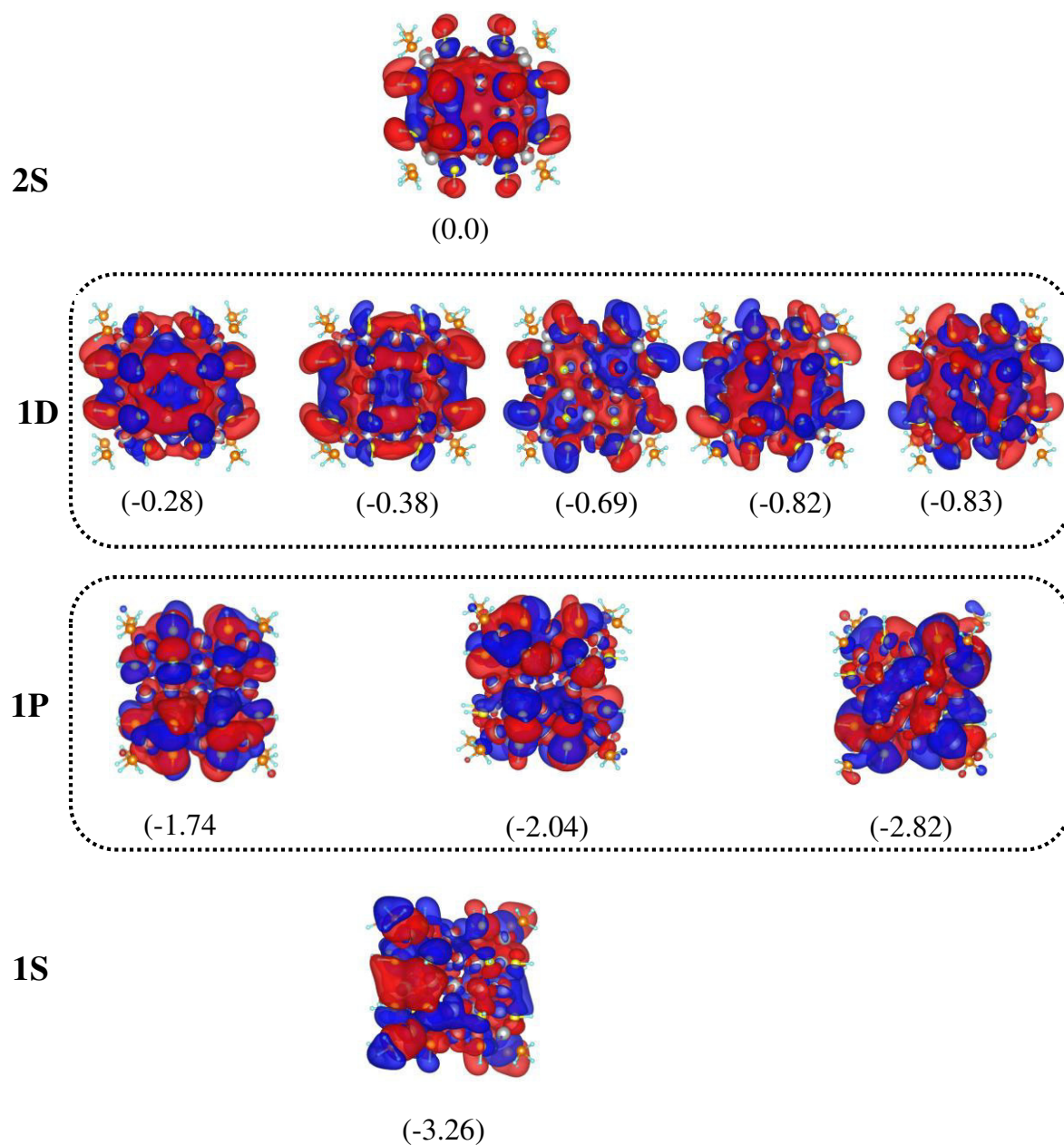




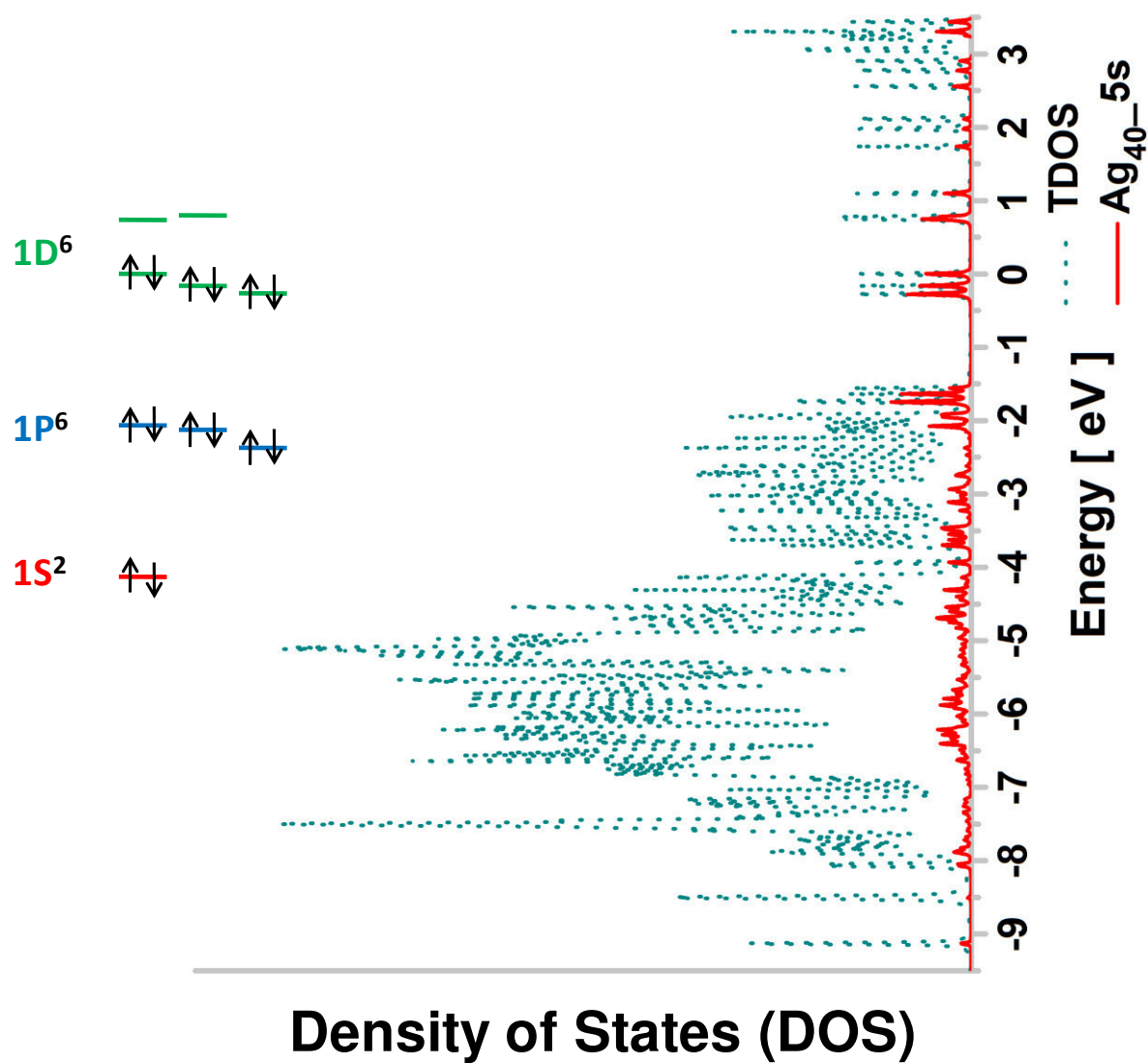
**Figure S28.** (A) and (B) correspond to the density of states of Ag<sub>46</sub> and Ag<sub>40</sub>, respectively for ligands alone. The atomic orbital contributions of ligands other than 3p of sulphur are not significantly influencing near HOMO-LUMO for both the clusters. The total PDOS contribution arising from the core and shell was calculated by summing over different orbitals of atoms in the core and shell regions for Ag<sub>40</sub> (S2 D) and Ag<sub>46</sub> (S2 C).



**Figure S29.** Plot of density of states versus energy in case of  $\text{Ag}_{46}$  and the filling of 20 electrons in the superatomic orbitals. The highest molecular orbital is set to be at zero. Dotted lines correspond to the total density of states and solid red lines indicate the density of states of  $\text{Ag}_{46} 5s$ .

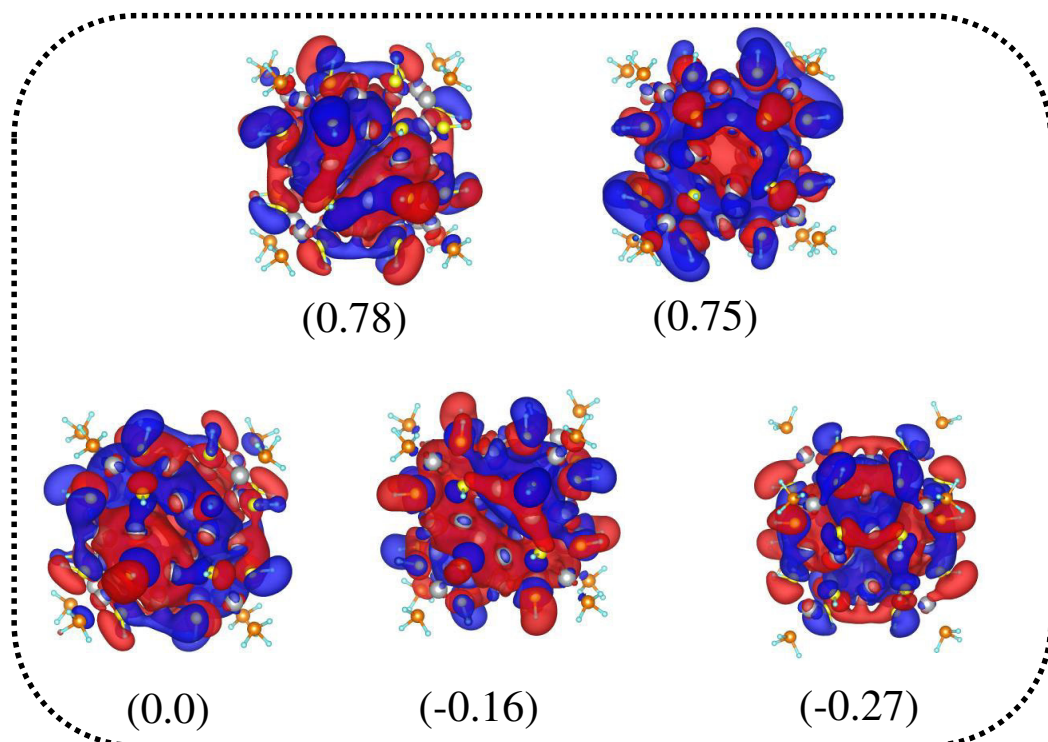


**Figure S30.** Isosurfaces of superatomic orbitals in  $\text{Ag}_{46}$ . The energy values (eV) are shown in the brackets. The highest occupied molecular orbital is set to be at zero.

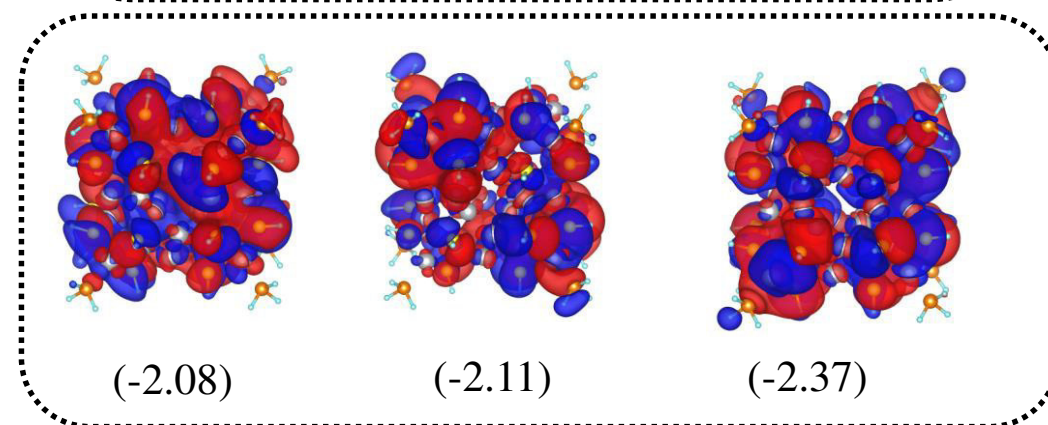


**Figure S31.** Plot of density of states versus energy in case of  $\text{Ag}_{40}$  and the filling of 14 electrons in the superatomic orbitals. The highest molecular orbital is set to be at zero. Dotted lines correspond to the total density of states and solid red lines indicate the density of states of  $\text{Ag}_{40-5s}$ .

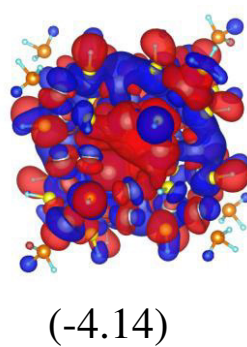
**1D**



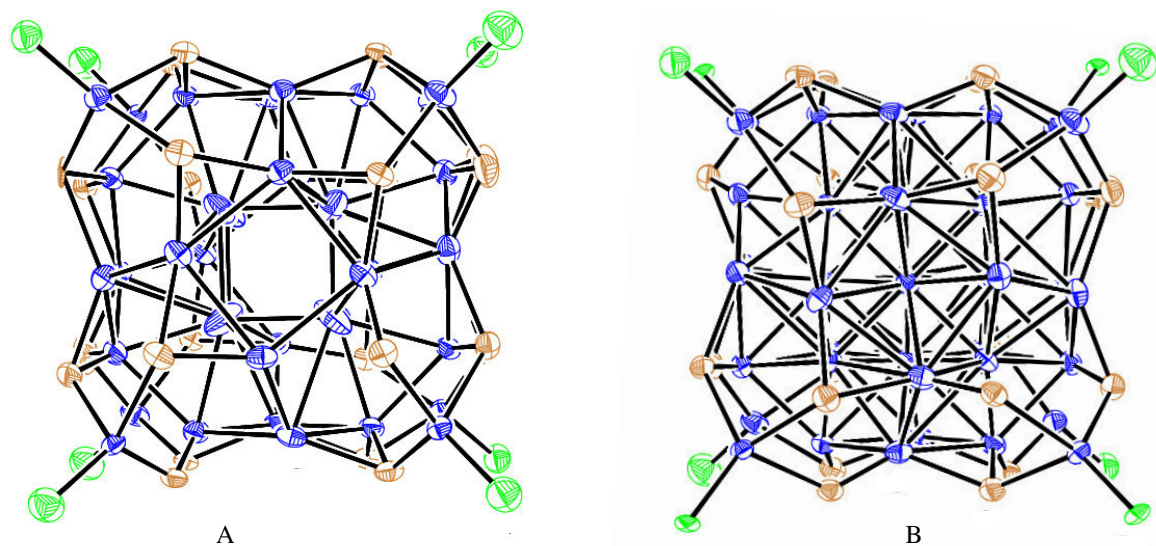
**1P**



**1S**



**Figure S32.** Isosurfaces of superatomic orbitals in  $\text{Ag}_{40}$ . The energy values (eV) are shown in the brackets. The highest occupied molecular orbital is set to be at zero. 1D superatomic orbitals are observed to split such that three orbitals ( $1D^6$ ) lie in the occupied region and another two orbitals are in the unoccupied orbitals.




**Figure S33.** Ortep representation of both the clusters with ellipsoid probability 40%. A and B correspond to  $\text{Ag}_{40}\text{S}_{24}\text{P}_8$  and  $\text{Ag}_{46}\text{S}_{24}\text{P}_8$ , respectively. Color legends: silver, blue; green, phosphorus; brown, sulphur. Carbon and hydrogen atoms are omitted for clarity.



## References

1. Ghosh, A.; Bodiuzzaman, M.; Nag, A.; Jash, M.; Baksi, A.; Pradeep, T., *ACS Nano* **2017**, *11*, 11145.
2. Bootharaju, M. S.; Dey, R.; Gevers, L. E.; Hedhili, M. N.; Basset, J.-M.; Bakr, O. M., *J. Am. Chem. Soc.* **2016**, *138*, 13770
3. Walter, M.; Hakkinen, H.; Lehtovaara, L.; Puska, M.; Enkovaara, J.; Rostgaard, C.; Mortensen, J. J., *J. Chem. Phys.* **2008**, *128*, 244101/1
4. M. Frisch, G. T., H. Schlegel, G. Scuseria, M. Robb, J. Cheeseman, G. Scalmani, V. Barone, B. Mennucci, G. Petersson. Gaussian Inc **2012**.
5. Tian Lu, Feiwu Chen, *J. Comp. Chem.* **2012**, *33*, 580.
6. García-Raya, D.; Madueño, R.; Blázquez, M.; Pineda, T., *J. Phys. Chem. C* **2009**, *113*, 8756-8761.
7. Park, S.; Lee, D., *Langmuir* **2012**, *28*, 7049.
8. Toikkanen, O.; Ruiz, V.; Rönnholm, G.; Kalkkinen, N.; Liljeroth, P.; Quinn, B. M., *J. Am. Chem. Soc.* **2008**, *130*, 11049.
9. Qian, H.; Zhu, Y.; Jin, R., *ACS Nano* **2009**, *3*, 3795.
10. Aljuhani, M. A.; Bootharaju, M. S.; Sinatra, L.; Basset, J.-M.; Mohammed, O. F.; Bakr, O. M., *J. Phys. Chem. C* **2017**, *121*, 10681.
11. CCDC 1841950 contains the supplementary crystallographic data for this paper. These data can be obtained free of charge from The Cambridge Crystallographic Data Centre via [www.ccdc.cam.ac.uk/data\\_request/cif](http://www.ccdc.cam.ac.uk/data_request/cif).
12. Alhilaly, M. J.; Bootharaju, M. S.; Joshi, C. P.; Besong, T. M.; Emwas, A.-H.; Juarez-Mosqueda, R.; Kaappa, S.; Malola, S.; Adil, K.; Shkurenko, A.; Häkkinen, H.; Eddaoudi, M.; Bakr, O. M., *J. Am. Chem. Soc.* **2016**, *138*, 14727.
13. Yang, H.; Lei, J.; Wu, B.; Wang, Y.; Zhou, M.; Xia, A.; Zheng, L.; Zheng, N., *ChemComm* **2013**, *49*, 300.
14. Yang, H.; Yan, J.; Wang, Y.; Su, H.; Gell, L.; Zhao, X.; Xu, C.; Teo, B. K.; Häkkinen, H.; Zheng, N., *J. Am. Chem. Soc.* **2017**, *139*, 31.
15. AbdulHalim, L. G.; Bootharaju, M. S.; Tang, Q.; Del Gobbo, S.; AbdulHalim, R. G.; Eddaoudi, M.; Jiang, De-en.; Bakr, O. M., *J. Am. Chem. Soc.* **2015**, *137*, 11970.
16. Yang, H.; Yan, J.; Wang, Y.; Deng, G.; Su, H.; Zhao, X.; Xu, C.; Teo, B. K.; Zheng, N., *J. Am. Chem. Soc.* **2017**, *139*, 16113.
17. Du, W.; Jin, S.; Xiong, L.; Chen, M.; Zhang, J.; Zou, X.; Pei, Y.; Wang, S.; Zhu, M., *J. Am. Chem. Soc.* **2017**, *139*, 1618.
18. Joshi, C. P.; Bootharaju, M. S.; Alhilaly, M. J.; Bakr, O. M., *J. Am. Chem. Soc.* **2015**, *137*, 11578.
19. Desiredy, A.; Conn, B. E.; Guo, J.; Yoon, B.; Barnett, R. N.; Monahan, B. M.; Kirschbaum, K.; Griffith, W. P.; Whetten, R. L.; Landman, U.; Bigioni, T. P., *Nature* **2013**, *501*, 399.
20. Yang, H.; Wang, Y.; Huang, H.; Gell, L.; Lehtovaara, L.; Malola, S.; Hakkinen, H.; Zheng, N., *Nat. Commun.* **2013**, *4*, 2422.
21. Jin, S.; Wang, S.; Song, Y.; Zhou, M.; Zhong, J.; Zhang, J.; Xia, A.; Pei, Y.; Chen, M.; Li, P.; Zhu, M., *J. Am. Chem. Soc.* **2014**, *136*, 15559.
22. Ren, L.; Yuan, P.; Su, H.; Malola, S.; Lin, S.; Tang, Z.; Teo, B. K.; Häkkinen, H.; Zheng, L.; Zheng, N., *J. Am. Chem. Soc.* **2017**, *139*, 13288.
23. Liu, C.; Li, T.; Abroshan, H.; Li, Z.; Zhang, C.; Kim, H. J.; Li, G.; Jin, R., *Nat. Commun.* **2018**, *9*, 744.

# Isomerism in Supramolecular Adducts of Atomically Precise Nanoparticles

Abhijit Nag, Papri Chakraborty, Ganesan Paramasivam, Mohammad Bodiuzzaman, Ganapati Natarajan, and Thalappil Pradeep\*

DST Unit of Nanoscience and Thematic Unit of Excellence, Department of Chemistry, Indian Institute of Technology Madras, Chennai-600036, India

## Supporting Information

**ABSTRACT:** We present isomerism in a few supramolecular adducts of atomically precise nanoparticles,  $[\text{Ag}_{29}(\text{BDT})_{12} \cap (\text{CD})_n]^{3-}$  ( $n = 1-6$ ), abbreviated as **I** where BDT and CD are 1,3-benzenedithiol and cyclodextrins ( $\alpha$ ,  $\beta$  and  $\gamma$ ), respectively;  $\cap$  symbolizes an inclusion complex. The different host–guest complexes of **I** were characterized in the solution state as well as in the gas phase. The CDs ( $\alpha$ ,  $\beta$  and  $\gamma$ ) encapsulate a pair of BDT ligands protecting the  $\text{Ag}_{29}$  core. This unique geometry of the supramolecular adducts makes the system similar to octahedral complexes of transition metals, which manifest various isomers. These isomers of **I** ( $n = 2-4$ ) were separated by ion mobility mass spectrometry (IM MS). We proposed structures of all the inclusion complexes with the help of IM MS measurements and molecular docking, density functional theory (DFT), and collision cross section (CCS) calculations.

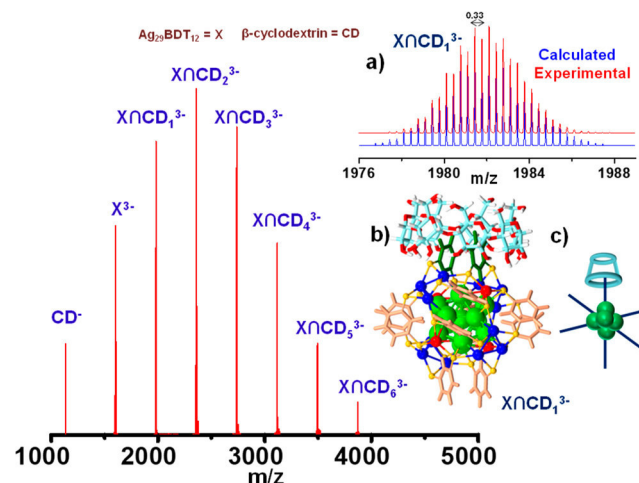
Atomically precise nanoparticles of noble metals with precise composition and structure exhibiting characteristic properties<sup>1–4</sup> are an important class of molecules showing potential applications in energy conversion,<sup>5</sup> sensing,<sup>6</sup> catalysis<sup>7,8</sup> and biomedical applications.<sup>9</sup> Their molecular science is gradually evolving, an important aspect being intercluster reactions.<sup>10–13</sup> Supramolecular chemistry is playing a key role in intercluster interactions to assemble clusters through weak interactions between ligands arising from directed hydrogen-bonding,<sup>14</sup> electrostatic, and C–H $\cdots\pi$  interactions.<sup>15</sup> One of the characteristics of molecular systems is isomerism, which has been important in the evolution of science, especially that of transition metal coordination complexes. Theoretical and experimental efforts to find structural isomerism in nanoclusters<sup>16,17</sup> will provide new insights into designing unique functional materials.

The shape-sensitive hydrophobic cavities of CDs represent a class of receptors that are ideal for the construction of hybrid assemblies.<sup>18,19</sup> The formation of supramolecular adducts of  $\text{Au}_{25}(\text{SBB})_{18}$ , where SBB is 4-(*t*-butyl)benzyl mercaptan, with CD was reported previously.<sup>20</sup>

Here, we establish the occurrence of isomerism in CD adducts of an atomically precise nanoparticle. First, we created supramolecular adducts of  $[\text{Ag}_{29}(\text{BDT})_{12}]^{3-}$  (BDT = 1, 3 benzenedithiol) abbreviated as  $\text{X}^{3-}$ , with CDs. They are labeled as  $\text{X} \cap (\text{CD})_n^{3-}$ ; the symbolism,  $\text{A} \cap \text{B}$  represents an

inclusion complex of **A** in **B**.<sup>21</sup> Isomers were detected for  $n = 2, 3$  and 4 complexes by IM MS, while  $n = 1, 5$  and 6 adducts did not show isomers, as in octahedral complexes. The experimental observations were fully supported by molecular docking, DFT, and CCS calculations.

We prepared  $\text{X} \cap (\text{CD})_{1-6}^{3-}$  clusters in dimethylformamide by careful mixing of  $\text{X}^{22}$  and CDs ( $\alpha$ ,  $\beta$  and  $\gamma$ ) in various proportions and their electrospray ionization mass spectrometry (ESI MS) were performed, as shown in Supporting Information (Figures S2–S6). The cluster,  $\text{X}^{3-}$ , was synthesized following the reported protocol<sup>22</sup> with slight modifications as described in the Experimental Details (Supporting Information) and characterized using optical absorption and ESI MS (Figure S1). The spectrum of 1:6 mixture of  $\text{X}^{3-}$  with  $\beta$ -CD is shown in Figure 1, which exhibited  $n = 1-6$   $\beta$ -CD adducts of the cluster in substantial intensity. Each of these adducts exhibited well-resolved mass spectra showing all the



**Figure 1.** ESI MS of  $[\text{X} \cap (\text{CD})_n]^{3-}$  ( $n = 1$  to 6) (**I**) supramolecular complexes, where **X** and **CD** represent  $\text{Ag}_{29}(\text{BDT})_{12}$  and  $\beta$ -cyclodextrin. (a) Theoretical and experimental isotopic patterns for  $[\text{X} \cap (\text{CD})_n]^{3-}$ . (b) Schematic representation of **I** for  $n = 1$ . Color codes:  $\text{Ag}_{13}$  Core, light green; 4  $\text{Ag}_3$  staples, blue; 4  $\text{Ag}$  tetrahedral positions, red; sulfur, yellow; carbon, brown. Encapsulated BDTs in CD are in dark green. (c) A simple representation of **I** for  $n = 1$ , similar to an octahedral coordination geometry.

Received: August 23, 2018

Published: October 10, 2018



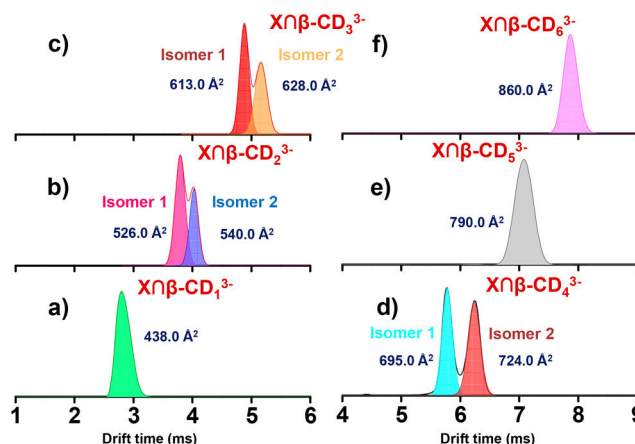
expected isotopologues (Figure 1a). This, along with the fragmentation patterns, confirmed their composition. The adducts lost CD upon collisional activation (Figures S7–S10). Energy threshold needed for the loss increases with the increase in diameter of CDs from  $\alpha$  to  $\gamma$ , suggesting increased interactions with increasing diameter of the cavity (Figure S11). From a comparison of the absorption spectra of the adducts with that of the cluster, it appeared that the absorption features of the adducts were mainly additive with slight changes<sup>19,23</sup> in the absorbances of the constituents indicating that electronic structure of the cluster is almost unaffected by CD complexation (Figure S12). Upon addition of  $\beta$ -CD in  $X^{3-}$  in DMF- $D_7$  (Figure S13),  $^1H$  NMR spectra showed significant changes in the resonances for the H-1, H-3 and H-5 protons.<sup>19</sup> The changing signals of H-1, H-3 and H-5 suggest that the ligands are deeply inserted in the CD cavity.<sup>19</sup> The observation of a maximum of six CD adducts in ESI MS and the NMR results indicated that probably each CD encapsulates a pair of BDT ligands on the cluster surface. Previous study of supramolecular functionalization of  $Au_{25}SBB_{18}^-$  with  $\beta$ -CD showed that each CD encapsulated only one SBB ligand due to their radially outward orientation which were spaced farther apart.<sup>20</sup> We will come back to this aspect when we discuss the computational data.

The attachment of six CDs could imply an octahedral arrangement of CDs on the cluster surface that can result in structural isomers as seen in coordination complexes. If two ligands in an octahedral complex are different from the other four, giving an  $MA_4B_2$  complex, two isomers are possible. The two B ligands can be *cis* or *trans* as shown in Figure S14B. Replacing another A ligand by B gives an  $MA_3B_3$  complex for which there are also two possible isomers. In one, the three ligands of each kind occupy opposite triangular faces of the octahedron; this is called the “*fac*” isomer (for facial) (Figure S14C). In the other, when three ligands are found in a row of an octahedron, it is called “*mer*” isomer (for meridional) (Figure S14C). In contrast, such isomerism is impossible in tetrahedral systems as all the sites are equivalent.

In this discussion, the free and CD included BDTs can be considered as two different ligands, A and B, respectively. For example,  $X\cap CD_2$  can be considered as  $MA_4B_2$  where M corresponds to  $Ag_{29}$ , A corresponds to  $BDT_2$  as the two BDT ligands get included in one CD and B corresponds to  $BDT_2\cap CD$ .

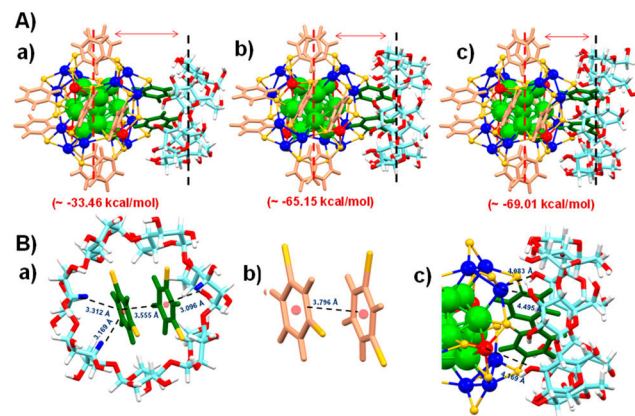
IM MS can effectively separate structural isomers in the gas phase. The drift time profile of various supramolecular adducts shown in Figure 2 reveals the existence of isomers in some of the  $\beta$ -CD adducts. While the adducts for  $n = 1, 5$  and 6 do not reveal isomers, the other adducts,  $n = 2–4$  show two distinct isomers with differing populations. These resemble the situation encountered in octahedral coordination complexes. The mass spectra extracted from the drift time profiles reveal the isomeric nature of the species (Figures S15–S17). The experimental CCS value for each complex is given in Figure 2. It further shows the increasing difference in the CCS with increasing the number of  $\beta$ -CDs. The  $X\cap(\beta\text{-CD})_5$  (Figure 2e) peak is only 13% broader than  $X\cap(\beta\text{-CD})_1$  and  $X\cap(\beta\text{-CD})_6$  peaks (Figure 2a,d). So, there are fewer possibilities to have multiple isomers. In the case of other CD functionalized clusters like  $Au_{25}SBB_{18}\cap CD_n$  ( $n = 2, 3$  and 4), there may be some possibilities for isomerism.

In order to understand the structures of the complexes, we performed molecular docking<sup>24</sup> and DFT calculations. To



**Figure 2.** (a–f) Drift time profile of  $[X\cap(\beta\text{-CD})_n]^{3-}$  ( $n = 1$  to 6) complexes and their corresponding CCS values. (b, c and d) Presence of isomers in the complexes when  $n = 2, 3$  and 4.

verify the lowest energy structure of  $X\cap CD$ , we carried out a global structure search by molecular docking simulations using minimum energy geometry of the adduct. More details about docking and DFT calculations are provided in the computational section of SI. Docking study shows that a pair of BDT ligands gets into the cavity of CDs (Figure S18). The lowest energy docked structures of  $X\cap CD$  ( $\alpha$ ,  $\beta$  and  $\gamma$ ) were used for DFT optimization. The binding energy (BE) values in PBE (Perdew, Burke and Ernzerhof) method for  $X\cap\alpha\text{-CD}$ ,  $X\cap\beta\text{-CD}$  and  $X\cap\gamma\text{-CD}$  were  $-33.46$ ,  $-65.15$  and  $-69.01$  kcal/mol, respectively (Figure 3). With increase of diameter of the CD,



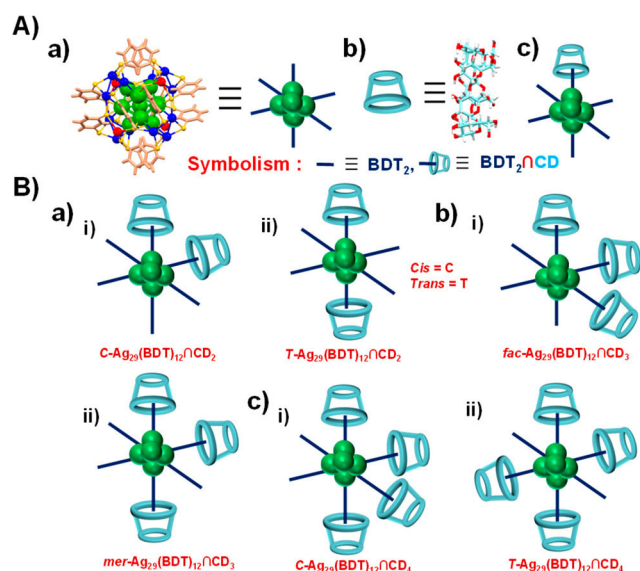
**Figure 3.** (Aa–c) DFT optimized lowest energy structures of  $[X\cap(CD)_n]^{3-}$  complexes where CD stands for  $\alpha$ ,  $\beta$  and  $\gamma$ -CD, respectively. The distance between the CD and the cluster decreases with increasing diameter of the CD. (Ba) The C–H... $\pi$  interactions between BDTs and  $\beta$ -CD. (b) The  $\pi$ – $\pi$  interaction distance between two BDTs. (c) The Ag...O interaction distances with  $\beta$ -CD.

the BE of the adducts is increasing which is in good agreement with the CID experiment shown in Figure S11. As the cavity size increases, a pair of BDT ligands can penetrate more inside the cavity. Here, C–H... $\pi$ , weak ionic  $Ag\cdots O$ , hydrogen bonding and van der Waals (vdWs) interactions are the main reasons for such complexation. For  $\beta$ -CD, the C–H... $\pi$  interaction distances were  $\sim 3.09$  to  $3.31$  Å. The distance between the two BDT ligands decreases when CD encapsulated them (Figure 3Ba,b), which enhances the  $\pi$ – $\pi$  interactions between the BDT ligands in the complex. For  $\beta$ -



CD, the Ag...O interaction distances were  $\sim 4.08$  to  $4.49$  Å. The Ag...O interaction increases from  $\alpha$  to  $\gamma$  CD. Furthermore, Ag–S distance involving core Ag atoms was elongated by  $0.04$  Å whereas the Ag–S distance of the staple was reduced by  $0.06$  Å. Hydrogen bonding interactions are also expected to play a key role in the complexation of a  $\beta$ -CD ligand with X. It is worth noting that the ionic interaction between multiple S atoms on the cluster and H of CD ligand mainly influences the interaction of  $\beta$ -CD with the X cluster. Particularly, the strong ionic interaction of S...H shows a distance of  $2.11$ – $2.80$  Å. On the other hand, hydrogen bonding distances  $3.37$ – $3.86$  Å are found between O of the CD and nearest H of the BDT ligands. To study the effect of vdW interactions, the structures were again reoptimized using a vdW-DF2/DZP methodology and the resulting BEs were compared with those of PBE/DZP methodology (Table S1). We have checked the other encapsulation possibility of CDs from the tail side (Figure S19) also. But in this case, the complex is less stable.

These structures can be drawn in a simpler fashion as shown in Figure 4. We see that the ligand orientation in  $X^{3-}$  displays



**Figure 4.** (Aa–c) Schematic representation of X, CD and  $[X_n(CD)_n]^{3-}$ , respectively. (Ba–c) Simple representation of C/T isomers of  $[X_n(CD)_n]^{3-}$   $n = 2$  and  $4$ , respectively. (Bb) The *fac-mer* isomers of  $[X_n(CD)_n]^{3-}$  ( $n = 3$ ).

an octahedral symmetry, if we consider a pair of BDT as one unit (Figure 4Aa). This simple diagram illustrates the similarity of such complexes with octahedral coordination complexes. At the same time, it confirms the distinct structural possibilities in supramolecular adducts derived from the cluster. The adduct,  $[X_n(CD)_n]^{3-}$  has only one structural isomer as all ligand units are identical (Figure 4Ac) while  $[X_n(CD)_2]^{3-}$  will have two possible isomers, *cis* (C) and *trans* (T) (Figure 4Ba). There are similar possibilities in  $[X_n(CD)_3]^{3-}$ , which can also exhibit *fac-mer* isomerism (Figure 4Bb). Such an analysis presents two isomers for  $[X_n(CD)_4]^{3-}$  also (Figure 4Bc).  $[X_n(CD)_6]^{3-}$  represents an octahedral symmetry by covering the whole cluster with CDs with no isomers (Figure S21). Same is the case with  $[X_n(CD)_5]^{3-}$  also. The IM MS results agree with this (Figure 2).

For  $[X_n\beta\text{-CD}_n]^{3-}$  ( $n > 1$ ) complexes were optimized by using the PBE<sup>25</sup> and vdW-DF2 functionals. PBE functional

results and BEs are presented in Figure S20. The *cis* isomers are more stable compared to the *trans* isomer because of extra hydrogen bonding between the CDs. The DFT optimized structures were further used to calculate the CCSs. The calculated CCSs are in agreement with the experimental CCSs obtained from IM MS allowing accurate assignment (Table S2). The relative populations of the adducts ( $n = 2$ – $4$ ) observed in the mobilogram can be correlated with the stabilization energy as shown in Figure S20. The calculated and experimental CCS values are given in Table S2. DFT optimized structures of  $[X_n\beta\text{-CD}_n]^{3-}$  for  $n = 5$  and  $6$  are given in Figure S21. Now, it is possible to assign isomers 1 and 2 of Figure 2b and d as *cis* and *trans*, respectively. The isomer 1 and isomer 2 of Figure 2c represent the *fac* and *mer* isomers, respectively.

Concerning the implication of the structures, we propose that their isolation in the solid state can result in new kinds of cluster-assembled materials. Supramolecular complexation in such systems may introduce new properties like chirality. Although these are speculative at the moment, we postulate that such supramolecular complexes discussed here may introduce new aspects in the science of atomically precise clusters.

In summary, we synthesized supramolecular complexes of atomically precise clusters with CDs. We proposed isomeric structures of such supramolecular complexes which are reminiscent of coordination complexes. These isomers were separated using IM MS. The obtained CCSs from the experiments were compared with those of the calculated structures. The agreement between the theory and experiment in CCSs and relative populations support the proposed structures. Supramolecular isomerism could be observed for other clusters also depending on the symmetry, orientation and geometry of the ligand surrounding the cluster. We postulate that the discovery of new clusters with amenable ligands would enhance better stabilization of such complexes, allowing the isomers to be used as precursors for new cluster-based materials.

## ■ ASSOCIATED CONTENT

### § Supporting Information

The Supporting Information is available free of charge on the ACS Publications website at DOI: 10.1021/jacs.8b08767.

Experimental details, computational details, ESI MS, NMR results, DFT optimized structures, molecular docking study and CCS calculations (PDF)

Computational data (PDF)

## ■ AUTHOR INFORMATION

### Corresponding Author

\*pradeep@iitm.ac.in

### ORCID

Thalappil Pradeep: 0000-0003-3174-534X

### Notes

The authors declare no competing financial interest.

## ■ ACKNOWLEDGMENTS

We thank the Department of Science and Technology, Government of India for constantly supporting our research program on nanomaterials. A.N. thanks IIT Madras for a doctoral fellowship. P.C. thanks the Council of Scientific and

Industrial Research (CSIR) for her research fellowship. M.B. thanks the University Grants Commission (UGC) for his research fellowship. G.P. thanks IIT Madras for an Institute Postdoctoral fellowship.

## ■ REFERENCES

- (1) Parker, J. F.; Fields-Zinna, C. A.; Murray, R. W. *Acc. Chem. Res.* **2010**, *43*, 1289–1296.
- (2) Maity, P.; Xie, S.; Yamauchi, M.; Tsukuda, T. *Nanoscale* **2012**, *4*, 4027–4037.
- (3) Jin, R.; Zeng, C.; Zhou, M.; Chen, Y. *Chem. Rev.* **2016**, *116*, 10346–10413.
- (4) Chakraborty, I.; Pradeep, T. *Chem. Rev.* **2017**, *117*, 8208–8271.
- (5) Mathew, A.; Pradeep, T. *Part. Part. Syst. Char.* **2014**, *31*, 1017–1053.
- (6) Yuan, X.; Luo, Z.; Yu, Y.; Yao, Q.; Xie, J. *Chem. - Asian J.* **2013**, *8*, 858–871.
- (7) Yamazoe, S.; Koyasu, K.; Tsukuda, T. *Acc. Chem. Res.* **2014**, *47*, 816–824.
- (8) Kurashige, W.; Niihori, Y.; Sharma, S.; Negishi, Y. *Coord. Chem. Rev.* **2016**, 320–321, 238–250.
- (9) Song, X.-R.; Goswami, N.; Yang, H.-H.; Xie, J. *Analyst* **2016**, *141*, 3126–3140.
- (10) Krishnadas, K. R.; Baksi, A.; Ghosh, A.; Natarajan, G.; Pradeep, T. *Nat. Commun.* **2016**, *7*, 13447.
- (11) Krishnadas, K. R.; Ghosh, A.; Baksi, A.; Chakraborty, I.; Natarajan, G.; Pradeep, T. *J. Am. Chem. Soc.* **2016**, *138*, 140–148.
- (12) Krishnadas, K. R.; Baksi, A.; Ghosh, A.; Natarajan, G.; Pradeep, T. *ACS Nano* **2017**, *11*, 6015–6023.
- (13) Krishnadas, K. R.; Baksi, A.; Ghosh, A.; Natarajan, G.; Som, A.; Pradeep, T. *Acc. Chem. Res.* **2017**, *50*, 1988–1996.
- (14) Chakraborty, A.; Fernandez, A. C.; Som, A.; Mondal, B.; Natarajan, G.; Paramasivam, G.; Lahtinen, T.; Häkkinen, H.; Nonappa; Pradeep, T. *Angew. Chem., Int. Ed.* **2018**, *57*, 6522–6526.
- (15) Nag, A.; Chakraborty, P.; Bodiuzzaman, M.; Ahuja, T.; Antharjanam, S.; Pradeep, T. *Nanoscale* **2018**, *10*, 9851–9855.
- (16) Tian, S.; Li, Y.-Z.; Li, M.-B.; Yuan, J.; Yang, J.; Wu, Z.; Jin, R. *Nat. Commun.* **2015**, *6*, 8667.
- (17) Chen, Y.; Liu, C.; Tang, Q.; Zeng, C.; Higaki, T.; Das, A.; Jiang, D.-e.; Rosi, N. L.; Jin, R. *J. Am. Chem. Soc.* **2016**, *138*, 1482–1485.
- (18) Wu, Y.; Shi, R.; Wu, Y.-L.; Holcroft, J. M.; Liu, Z.; Frascioni, M.; Wasielewski, M. R.; Li, H.; Stoddart, J. F. *J. Am. Chem. Soc.* **2015**, *137*, 4111–4118.
- (19) Moussawi, M. A.; Leclerc-Laronze, N.; Floquet, S.; Abramov, P. A.; Sokolov, M. N.; Cordier, S.; Ponchel, A.; Monflier, E.; Bricout, H.; Landy, D.; Haouas, M.; Marrot, J.; Cadot, E. *J. Am. Chem. Soc.* **2017**, *139*, 12793–12803.
- (20) Mathew, A.; Natarajan, G.; Lehtovaara, L.; Häkkinen, H.; Kumar, R. M.; Subramanian, V.; Jaleel, A.; Pradeep, T. *ACS Nano* **2014**, *8*, 139–152.
- (21) Lehn, J.-M. *From Molecular to Supramolecular Chemistry. Supramolecular Chemistry*; Wiley-VCH Verlag GmbH & Co. KGaA: 2006; pp 1–9.
- (22) AbdulHalim, L. G.; Bootharaju, M. S.; Tang, Q.; Del Gobbo, S.; AbdulHalim, R. G.; Eddaoudi, M.; Jiang, D.-e.; Bakr, O. M. *J. Am. Chem. Soc.* **2015**, *137*, 11970–11975.
- (23) Chakraborty, P.; Nag, A.; Paramasivam, G.; Natarajan, G.; Pradeep, T. *ACS Nano* **2018**, *12*, 2415–2425.
- (24) Morris, G. M.; Huey, R.; Lindstrom, W.; Sanner, M. F.; Belew, R. K.; Goodsell, D. S.; Olson, A. J. *J. Comput. Chem.* **2009**, *30*, 2785–2791.
- (25) Perdew, J. P.; Burke, K.; Ernzerhof, M. *Phys. Rev. Lett.* **1997**, *78*, 1396–1396.

## Supporting Information

### Isomerism in Supramolecular Adducts of Atomically Precise Nanoparticles

Abhijit Nag, Papri Chakraborty, Ganesan Paramasivam, Mohammad Bodiuzzaman, Ganapati Natarajan and Thalappil Pradeep\*

DST Unit of Nanoscience and Thematic Unit of Excellence, Department of Chemistry, Indian Institute of Technology Madras, Chennai-600036, India. \*Email: [pradeep@iitm.ac.in](mailto:pradeep@iitm.ac.in)

### Table of Contents

Name	Description	Page No.
	Experimental and computational details	S3-S5
Figure S1	UV-vis and ESI MS of $[\text{Ag}_{29}(\text{BDT})_{12}]^{3-}$	S6
Figure S2	ESI MS of $[\text{X}\cap(\beta\text{-CD})_n]^{3-}$ (n = 1 to 4) supramolecular complexes	S7
Figure S3	ESI MS of $[\text{X}\cap(\alpha\text{-CD})_n]^{3-}$ (n = 1 to 4) supramolecular complexes	S8
Figure S4	ESI MS of $[\text{X}\cap(\gamma\text{-CD})_n]^{3-}$ (n = 1 to 4) supramolecular complexes	S9
Figure S5	ESI MS of $[\text{X}\cap(\alpha\text{-CD})_n]^{3-}$ (n = 1 to 6) supramolecular complexes	S10
Figure S6	ESI MS of $[\text{X}\cap(\gamma\text{-CD})_n]^{3-}$ (n = 1 to 6) supramolecular complexes	S11
Figure S7	Collision induced dissociation (CID) of $[\text{X}\cap(\beta\text{-CD})_4]^{3-}$	S12
Figure S8	Collision induced dissociation (CID) of $[\text{X}\cap(\beta\text{-CD})_3]^{3-}$	S13
Figure S9	Collision induced dissociation (CID) of $[\text{X}\cap(\beta\text{-CD})_2]^{3-}$	S14
Figure S10	Collision induced dissociation (CID) of $[\text{X}\cap(\beta\text{-CD})_1]^{3-}$	S15



Figure S11	Comparison of energy resolved fragmentation of $[X\cap(CD)_1]^{3-}$ with different CDs	S16
Figure S12	UV-vis spectra $[X\cap(\beta\text{-CD})_n]^{3-}$	S17
Figure S13	$^1\text{H}$ NMR spectra of only $\beta\text{-CD}$ and $\beta\text{-CD}$ in the presence of $\text{Ag}_{29}(\text{BDT})_{12}^{3-}$	S18
Figure S14	Isomers of octahedral complexes	S19
Figure S15	IMS MS of $[X\cap(\beta\text{-CD})_2]^{3-}$	S20
Figure S16	IMS MS of $[X\cap(\beta\text{-CD})_3]^{3-}$	S21
Figure S17	IMS MS of $[X\cap(\beta\text{-CD})_4]^{3-}$	S22
Figure S18	Molecular docking lowest energy structures of $[X\cap(CD)_1]^{3-}$ complexes	S23
Figure S19	DFT optimized structure of $[X\cap(\beta\text{-CD})_1]^{3-}$ , where CD encapsulates the cluster from tail side.	S23
Figure S20	DFT optimized structure of $[X\cap(\beta\text{-CD})_n]^{3-}$ ( $n = 2, 3$ and $4$ ) with ccs values and binding energies.	S24
Figure S21	DFT optimized structure of $[X\cap(\beta\text{-CD})_n]^{3-}$ ( $n = 5$ and $6$ ) with ccs values and binding energies.	S25
Table S1	Binding energy values	S26
Table S2	Experimental and Theoretical CCS values	S27

## Experimental Details

### Instrumentation

The UV-vis spectra were measured using a PerkinElmer Lambda 25 UV-vis spectrophotometer. Mass spectrometric measurements were performed in a Waters Synapt G2-Si high-resolution mass spectrometer. NMR measurements were performed using a Bruker 500 MHz NMR spectrometer.

### Chemicals

All the chemicals except the clusters were commercially available and used without further purification. Silver nitrate ( $\text{AgNO}_3$ , 99.9%) was purchased from Rankem, India. Sodium borohydride ( $\text{NaBH}_4$ ), 1,3-benzene dithiol (1,3-BDT), and cyclodextrins ( $\alpha$ ,  $\beta$  and  $\gamma$ ) were purchased from Sigma-Aldrich. Triphenylphosphine (TPP) was purchased from Spectrochem, India. All the solvents, dichloromethane (DCM), methanol (MeOH), ethanol (EtOH), and dimethylformamide (DMF) were of the HPLC grade and were used without further distillation. Deuterated solvents DMF- $d_7$  used for NMR measurements, was purchased from Sigma-Aldrich.

### Synthesis of $[\text{Ag}_{29}(\text{BDT})_{12}]^{3-}$ cluster

$[\text{Ag}_{29}(\text{BDT})_{12}]^{3-}$  clusters were synthesized following a reported protocol with slight modifications<sup>1</sup>. About 20 mg of  $\text{AgNO}_3$  was dissolved in a mixture of 10 mL DCM and 2 mL methanol. To this mixture, about 13.5  $\mu\text{L}$  of the 1,3-BDT ligand was added. The reaction mixture was stirred for about 15 mins. Then, about 10.5 mg of  $\text{NaBH}_4$  dissolved in 500  $\mu\text{L}$  of ice-cold water was added. The stirring was continued under dark conditions for about 5 h. Then, the mixture was centrifuged, the precipitate was discarded. The clusters were obtained as the orange supernatant. The solution was evaporated by rotary evaporation, the orange residue was washed with methanol and finally dissolved in DMF. The solution was characterized by UV-vis and ESI MS, which confirmed the formation of  $[\text{Ag}_{29}(\text{BDT})_{12}]^{3-}$  clusters (Figure S1). However, as the clusters were synthesized without the TPP ligands, they were stable only for a few hours.

## Synthesis of $[\text{Ag}_{29}(\text{BDT})_{12}(\text{CD})_n]^{3-}$ complexes

Immediately after the synthesis of  $[\text{Ag}_{29}(\text{BDT})_{12}]^{3-}$  clusters, CDs ( $\alpha$ ,  $\beta$  and  $\gamma$ ) were added separately to the cluster solution in DMF. The addition of CDs increased the stability of the clusters significantly. The reactivity was monitored using UV-vis and ESI MS studies.

## ESI MS and IM MS measurements

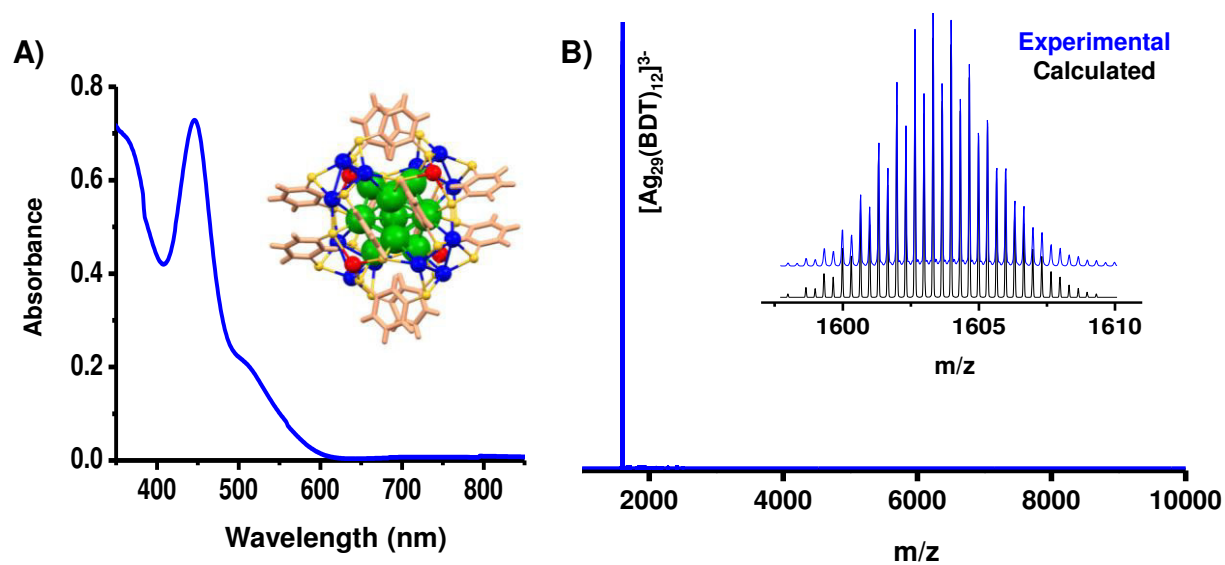
All mass spectrometric measurements were conducted using a Waters Synapt G2Si High Definition Mass Spectrometer equipped with electrospray ionization (ESI) and ion mobility (IM) separation. All samples were measured in the negative electrospray ionization mode. The instrument was calibrated using NaI as the calibrant. All samples were measured keeping almost the same conditions with slight modification wherever required. Typical experimental parameters were: desolvation gas temperature 150°C, Source temperature: 100°C, Desolvation gas flow: 400 L/h, capillary voltage, 3 kV; sample cone, 80 V; source offset, 80 V; trap collision energy, 2 V; trap gas flow, 2 mL/min; helium cell gas flow, 90 mL/min; IMS gas flow, 60 mL/min; trap DC bias, 40 V; IMS wave height, 35 V and IMS wave velocity, 400 m/s. The collision voltage in the transfer cell was raised until fragmentations were seen properly (4-60 V). The concentration of the sample was 1  $\mu\text{g/mL}$  and it was infused at a flow rate of 30  $\mu\text{L/min}$ . CCS values of the CD-cluster complexes were calculated by taking the cluster as a calibrant and using the previous literature<sup>2</sup>.

## Computational Details:

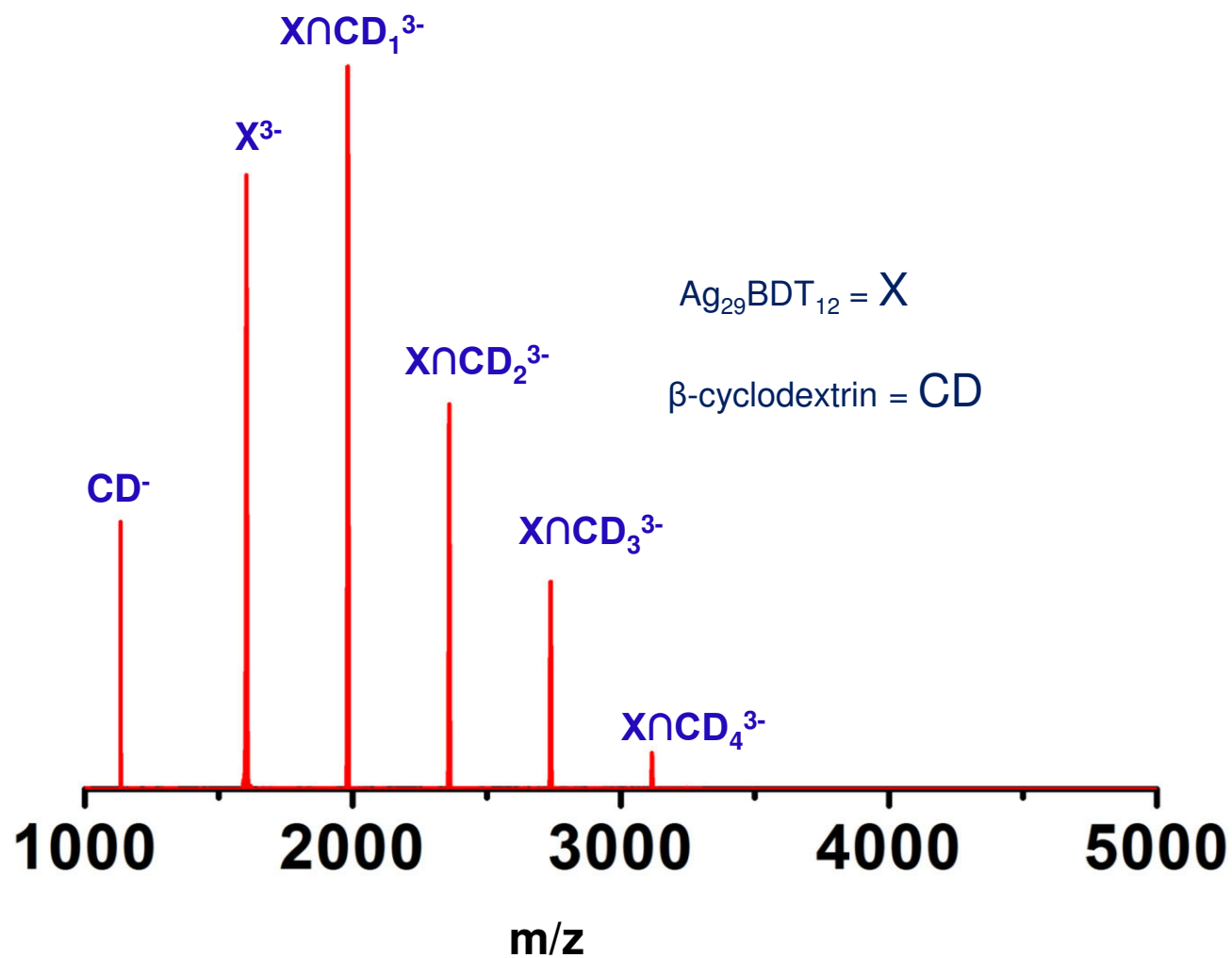
Molecular docking studies have been carried out using AutoDock 4.2 and AutoDock Tools programs<sup>3</sup>. The crystal structures of  $[\text{Ag}_{29}(\text{BDT})_{12}]^{3-}$  and CDs were used for this study. We used CDs as the “ligand” *i.e.* the movable molecule whose rotational and translational degrees of freedom could be varied during the docking. The ‘receptor’ molecule was  $[\text{Ag}_{29}(\text{BDT})_{12}]^{3-}$ , and this was the fixed and completely rigid central molecule. We assigned partial charges from DFT for all atoms of  $[\text{Ag}_{29}(\text{BDT})_{12}]^{3-}$ . Receptor grids were generated using 126  $\times$  126  $\times$  126 grid points with a grid spacing of 0.375 Å and map types for all the ligand atoms were created using AutoGrid 4.6. The van der Waals radius  $\sigma$  (Å) and well depth  $\epsilon$  (kcal/mol) for Ag of 2.63 Å and 4.560 kcal/mol, respectively, were taken from well-tested sources in literature<sup>4-5</sup> and these were

added to the Autodock parameter file which does not contain them by default. The grid parameter file (.gpf) was saved using MGL Tools-1.4.6.50. For docking, the docking parameter files (.dpf) were generated using MGLTools-1.4.6.50 and docking was performed using AutoDock4.2. The results of AutoDock generated an output file (.dlg), and the generated conformers were scored and ranked as per the interaction energy. Ten lowest energy conformers were obtained. The structure showing the lowest binding energy between the interacting molecules was used as an initial structure for DFT optimization. The free energies of binding were calculated subtracting the unbound energies from the sum of the intermolecular and intramolecular energy terms in the adducts, which is a calculation that is performed within the Autodock program.

The PAW set-up was Ag(4d<sup>10</sup>5s<sup>1</sup>), S(3s<sup>2</sup>3p<sup>4</sup>), C(2s<sup>2</sup>2p<sup>2</sup>) and H(1s<sup>1</sup>) with scalar-relativistic effects included for Ag. The initial structure of [Ag<sub>29</sub>(BDT)<sub>12</sub>]<sup>3-</sup> was optimized by taking the crystal structure of [Ag<sub>29</sub>(BDT)<sub>12</sub>(TPP)<sub>4</sub>]<sup>3-</sup>, as reported by Bakr et al. and removing its TPP ligands<sup>1</sup>. The geometric optimizations of the supramolecular complexes were mainly carried out using the PBE exchange functional<sup>6</sup> and a double zeta polarization (DZP) basis set, with a grid spacing of 0.2 Å in LCAO mode<sup>7</sup>, with the convergence criteria as 0.05 eV/Å for the residual forces acting on atoms without any symmetry constraints. Further, the calculated ground state geometry and energy of the complexes were compared with the vdW-DF2 functional<sup>8</sup>. The strength of the interaction between the cyclodextrins and [Ag<sub>29</sub>(BDT)<sub>12</sub>]<sup>3-</sup> cluster was studied by calculating their binding energies by subtracting the sum of energies of isolated [Ag<sub>29</sub>(BDT)<sub>12</sub>]<sup>3-</sup> cluster and CDs from the total energy of the adducts, [Ag<sub>29</sub>(BDT)<sub>12</sub>(CD)<sub>n</sub>]<sup>3-</sup>. All structures were built up using the Avogadro software package<sup>9</sup>.

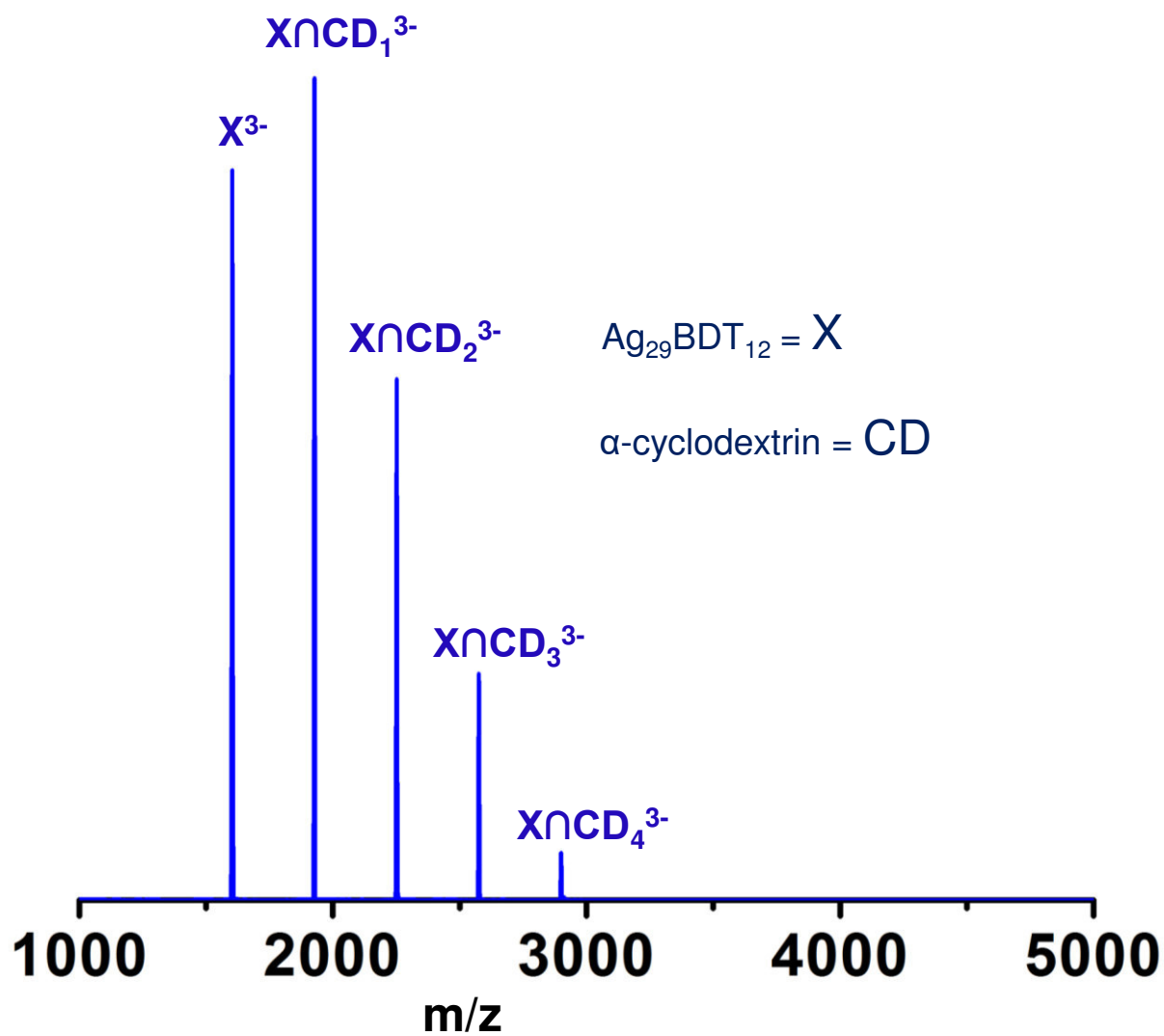


**Figure S1.** A) UV-vis and B) ESI MS of  $[Ag_{29}(BDT)_{12}]^{3-}$ . Inset of A) shows the DFT optimized structure of the cluster and inset of B) shows the experimental and calculated isotope patterns of  $[Ag_{29}(BDT)_{12}]^{3-}$ .

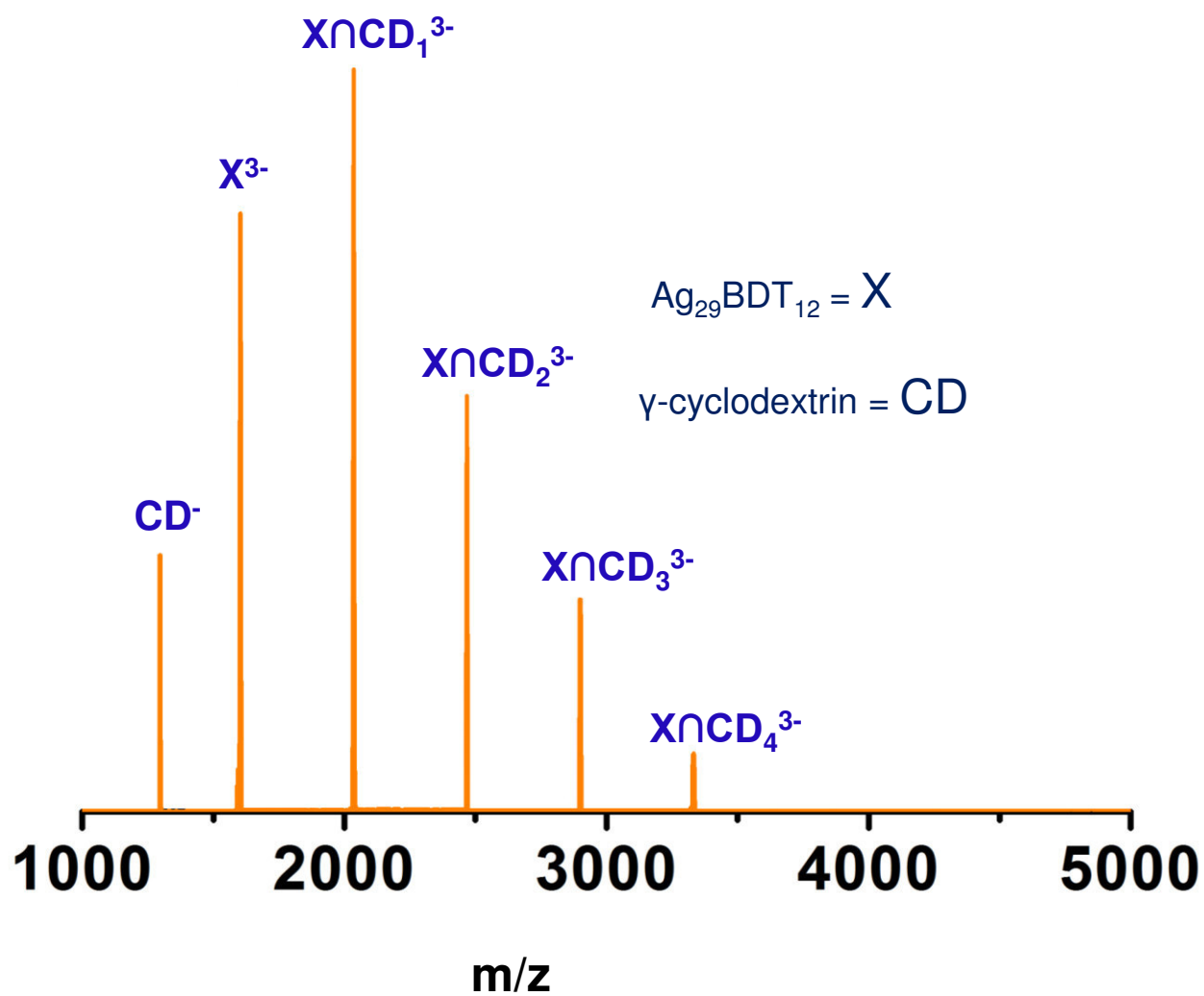


**Figure S2. A)** ESI MS of  $[X\cap(CD)_n]^{3-}$  ( $n = 1$  to  $4$ ) supramolecular complexes when ratio of  $X : CD$  in DMF was  $1:4$ , where  $X$  and  $CD$  represent  $Ag_{29}(BDT)_{12}$  and  $\beta$ -cyclodextrin.

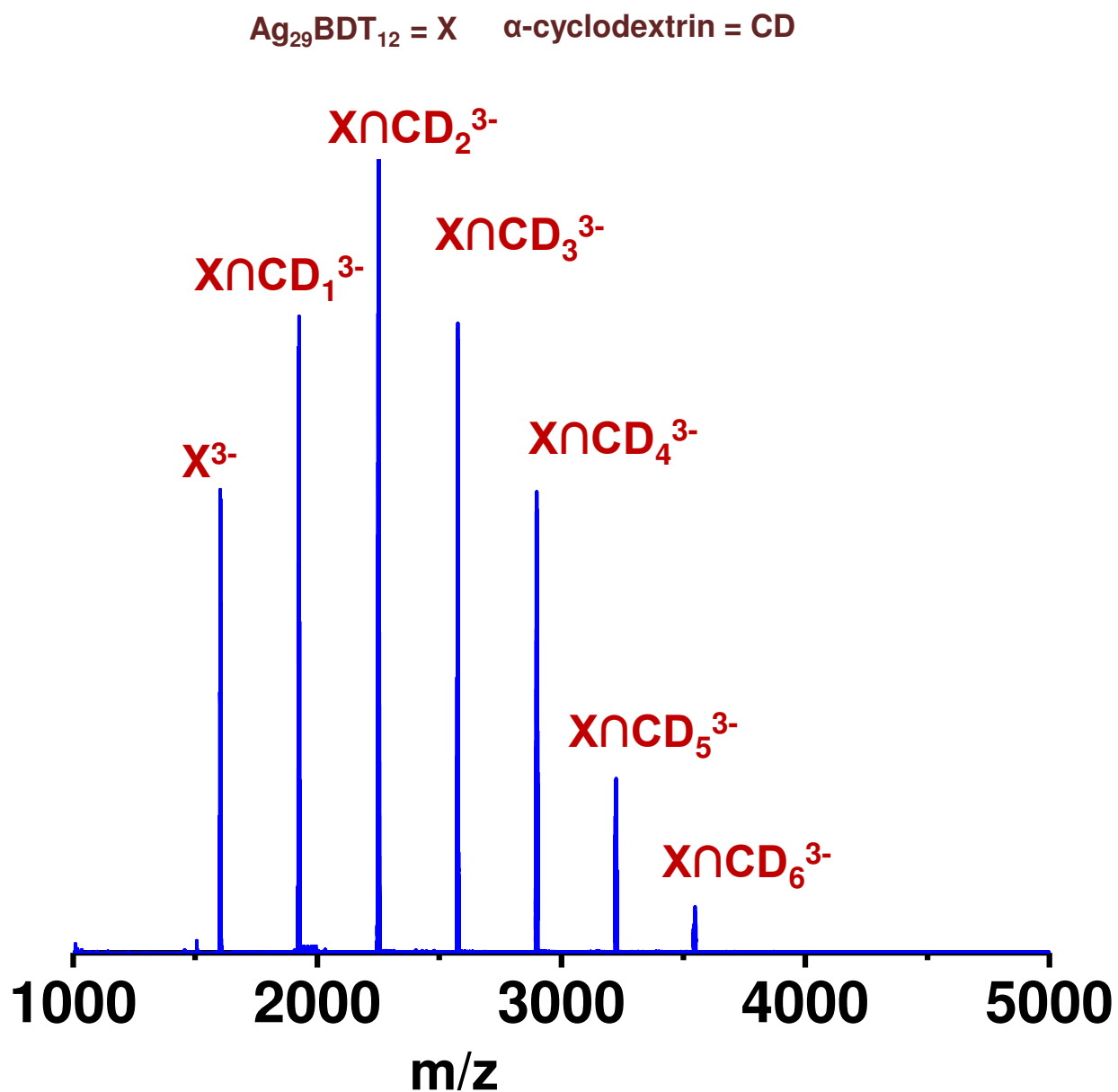




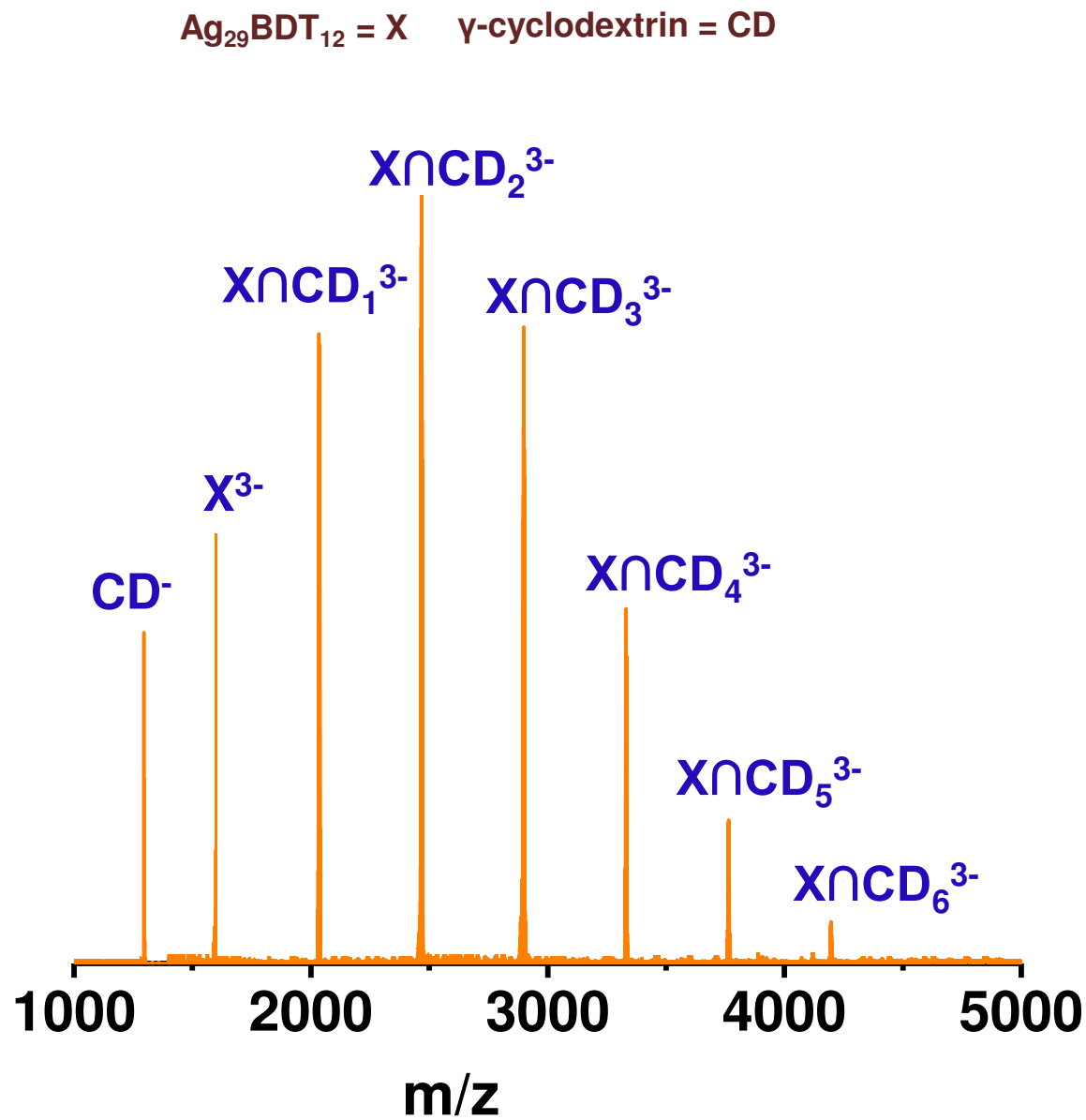
**Figure S3. A)** ESI MS of  $[X_n(CD)_n]^{3-}$  ( $n = 1$  to  $4$ ) supramolecular complexes when the ratio of X : CD in DMF was 1:4, where X and CD represent  $Ag_{29}(BDT)_{12}$  and  $\alpha$ -cyclodextrin.



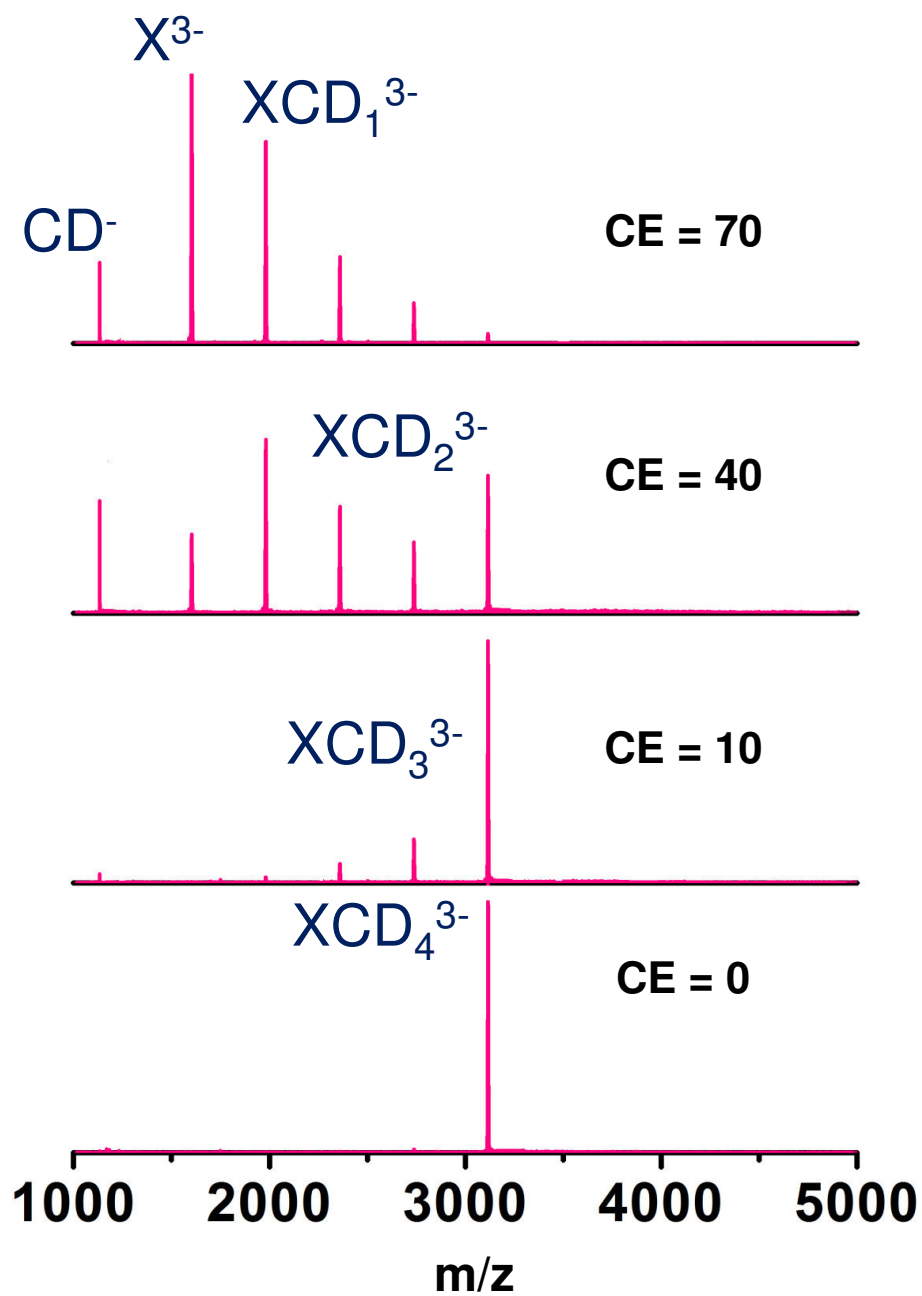
**Figure S4. A)** ESI MS of  $[X\cap(CD)_n]^{3-}$  ( $n = 1$  to  $4$ ) supramolecular complexes when the ratio of  $X : CD$  in DMF was  $1:4$ , where  $X$  and  $CD$  represent  $Ag_{29}(BDT)_{12}$  and  $\gamma$ -cyclodextrin.



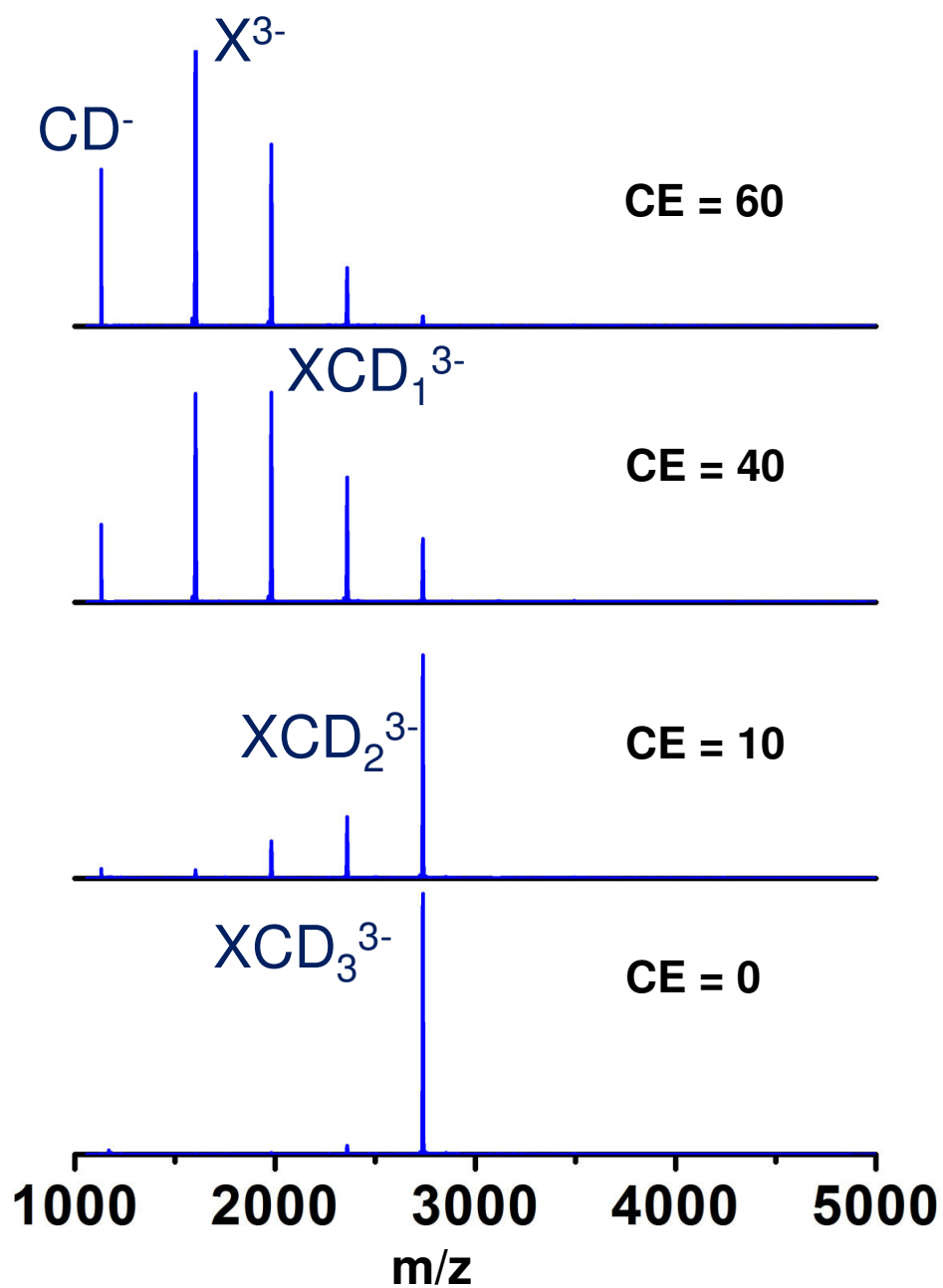
**Figure S5. A)** ESI MS of  $[\text{X}\cap(\text{CD})_n]^{3-}$  ( $n = 1$  to  $6$ ) supramolecular complexes when the ratio of  $\text{X} : \text{CD}$  in DMF was  $1:6$ , where  $\text{X}$  and  $\text{CD}$  represent  $\text{Ag}_{29}(\text{BDT})_{12}$  and  $\alpha\text{-cyclodextrin}$ .



**Figure S6. A)** ESI MS of  $[\text{X}\cap(\text{CD})_n]^{3-}$  ( $n = 1$  to  $6$ ) supramolecular complexes when the ratio of  $\text{X} : \text{CD}$  in DMF was  $1:6$ , where  $\text{X}$  and  $\text{CD}$  represent  $\text{Ag}_{29}(\text{BDT})_{12}$  and  $\gamma\text{-cyclodextrin}$ .

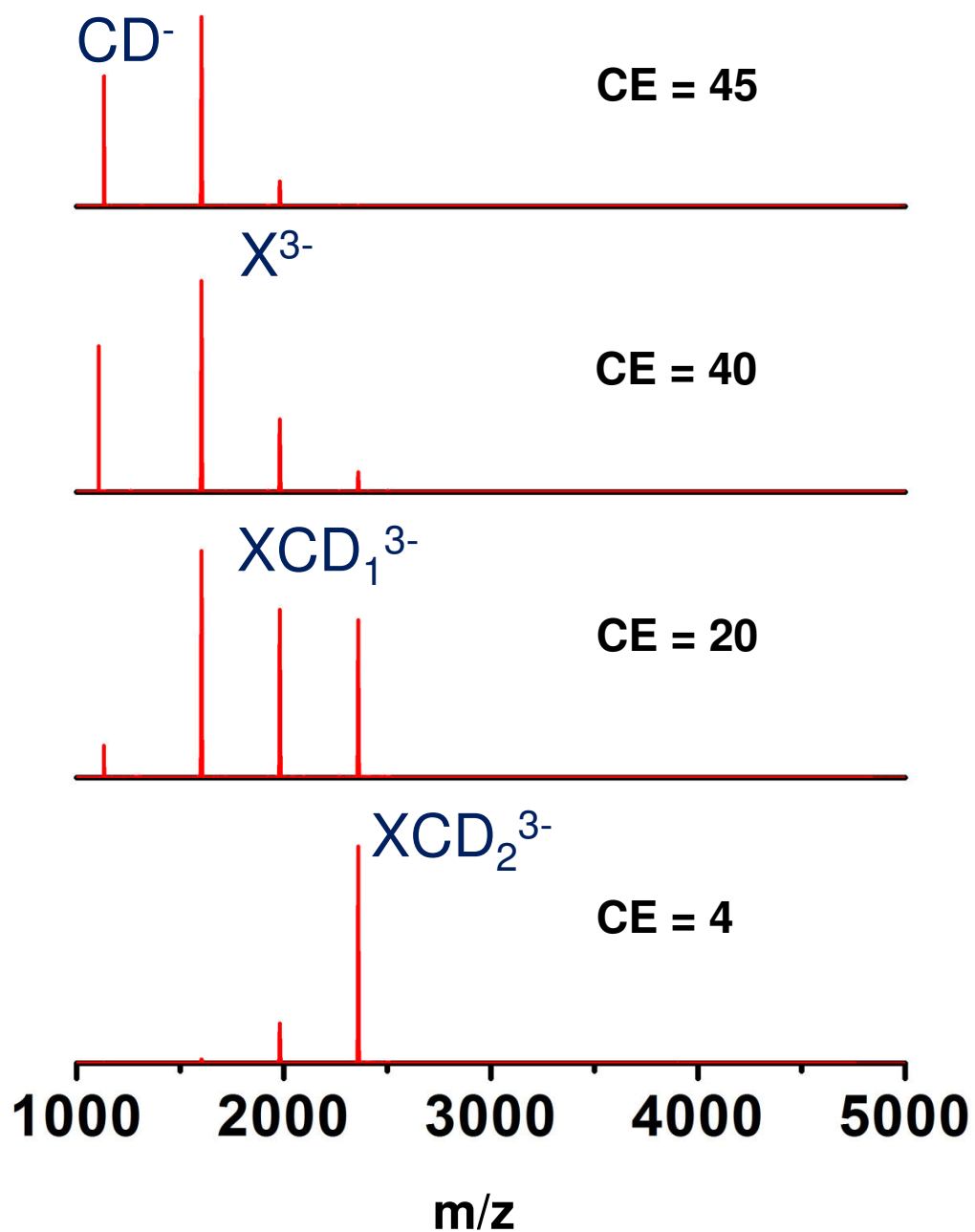


**Figure S7.** Collision induced dissociation (CID) of  $[X\cap(CD)_4]^{3-}$ , where CD is  $\beta$ -cyclodextrin. With the increase of collision of energy (CE), CD lost from the complex. CE is controlled by applied potential (in V).

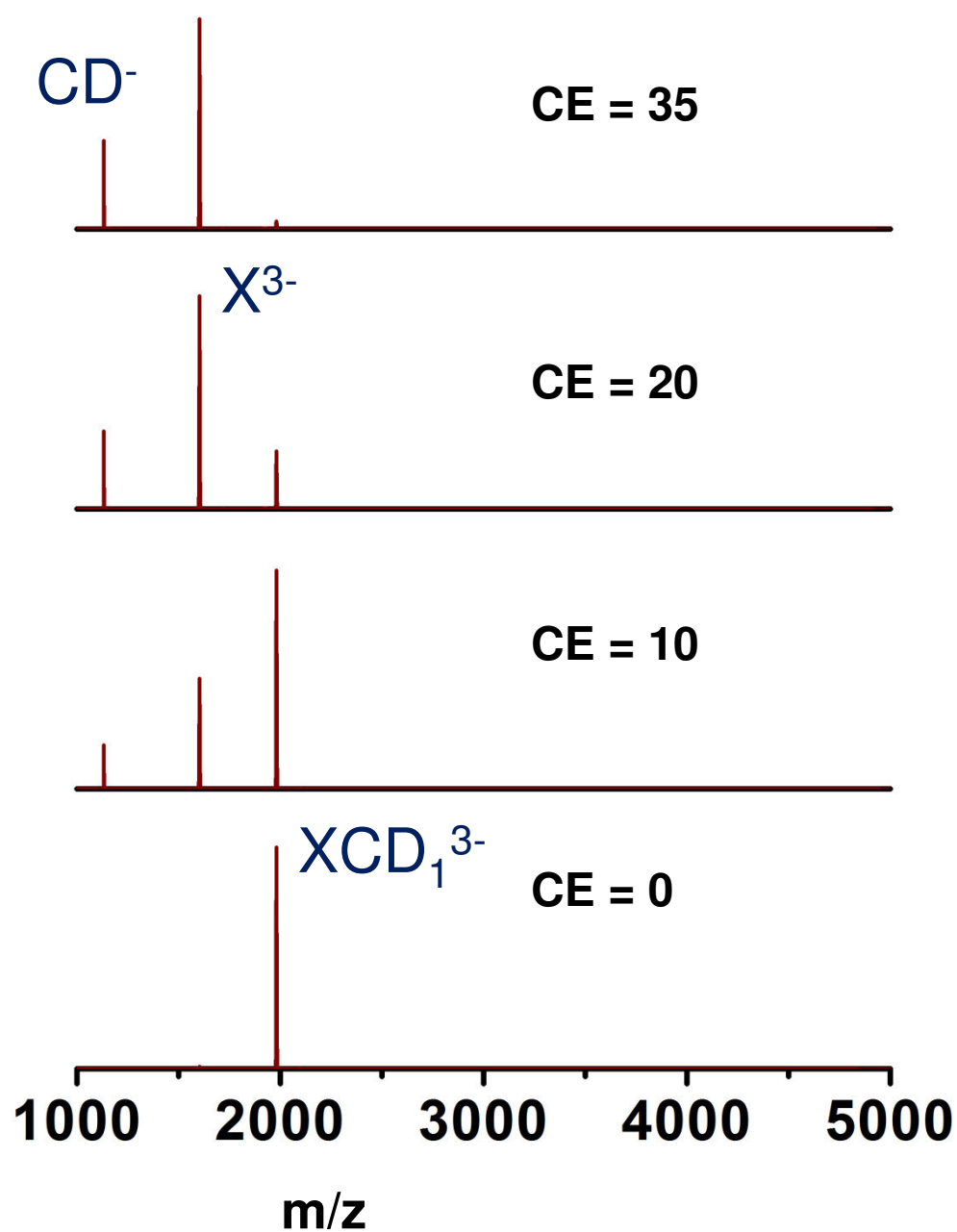


**Figure S8.** Collision induced dissociation (CID) of  $[X\cap(CD)_3]^{3-}$ , where CD is  $\beta$ -cyclodextrin. With the increase of collision of energy (CE), CD was lost from the complex. CE is controlled by applied potential (in V).

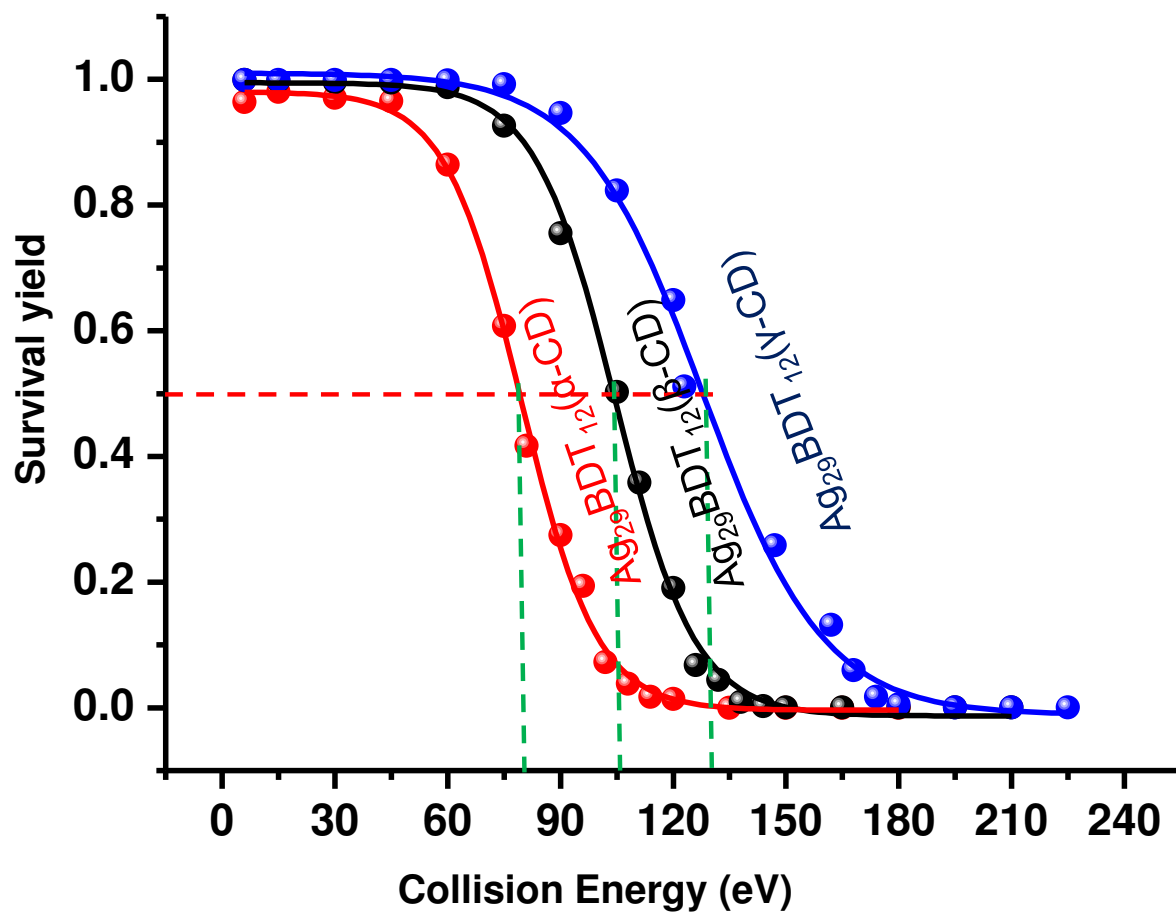




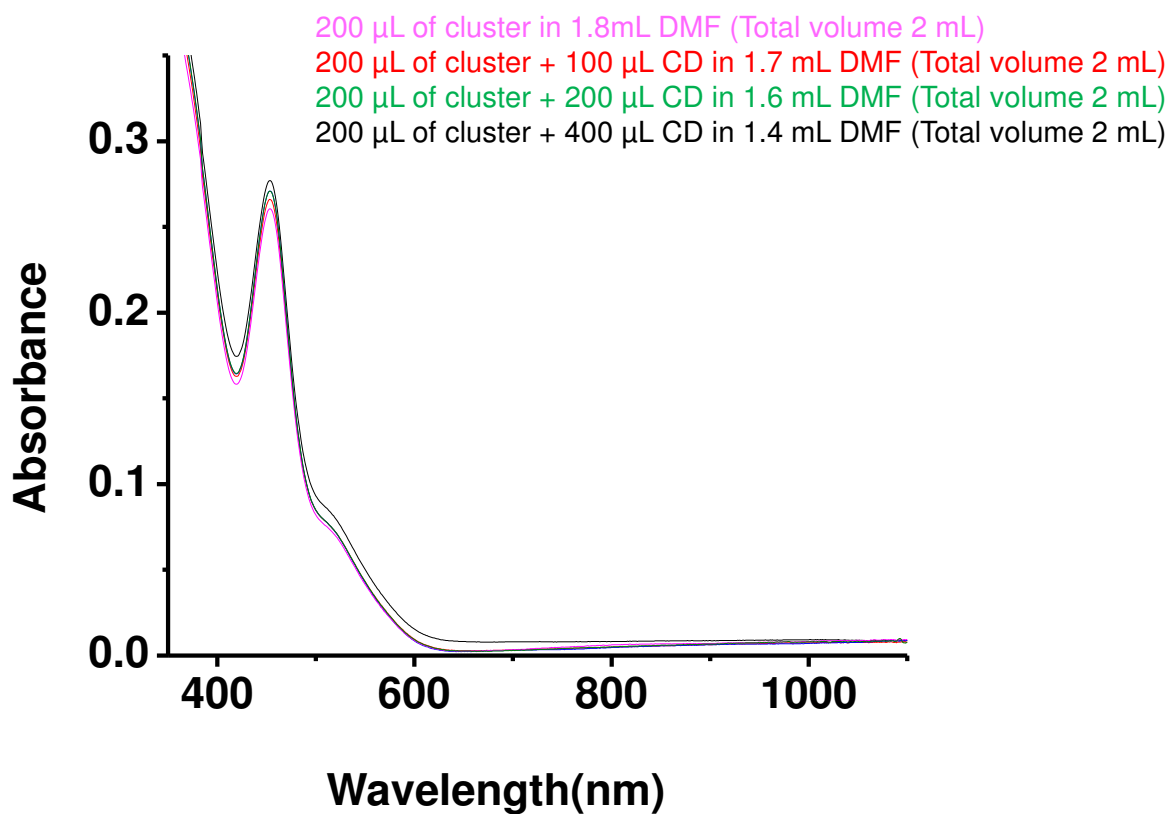
**Figure S9.** Collision induced dissociation (CID) of  $[X\cap(CD)_2]^{3-}$ , where CD is  $\beta$ -cyclodextrin. With the increase of collision of energy (CE), CD was lost from the complex. CE is controlled by applied potential (in V).



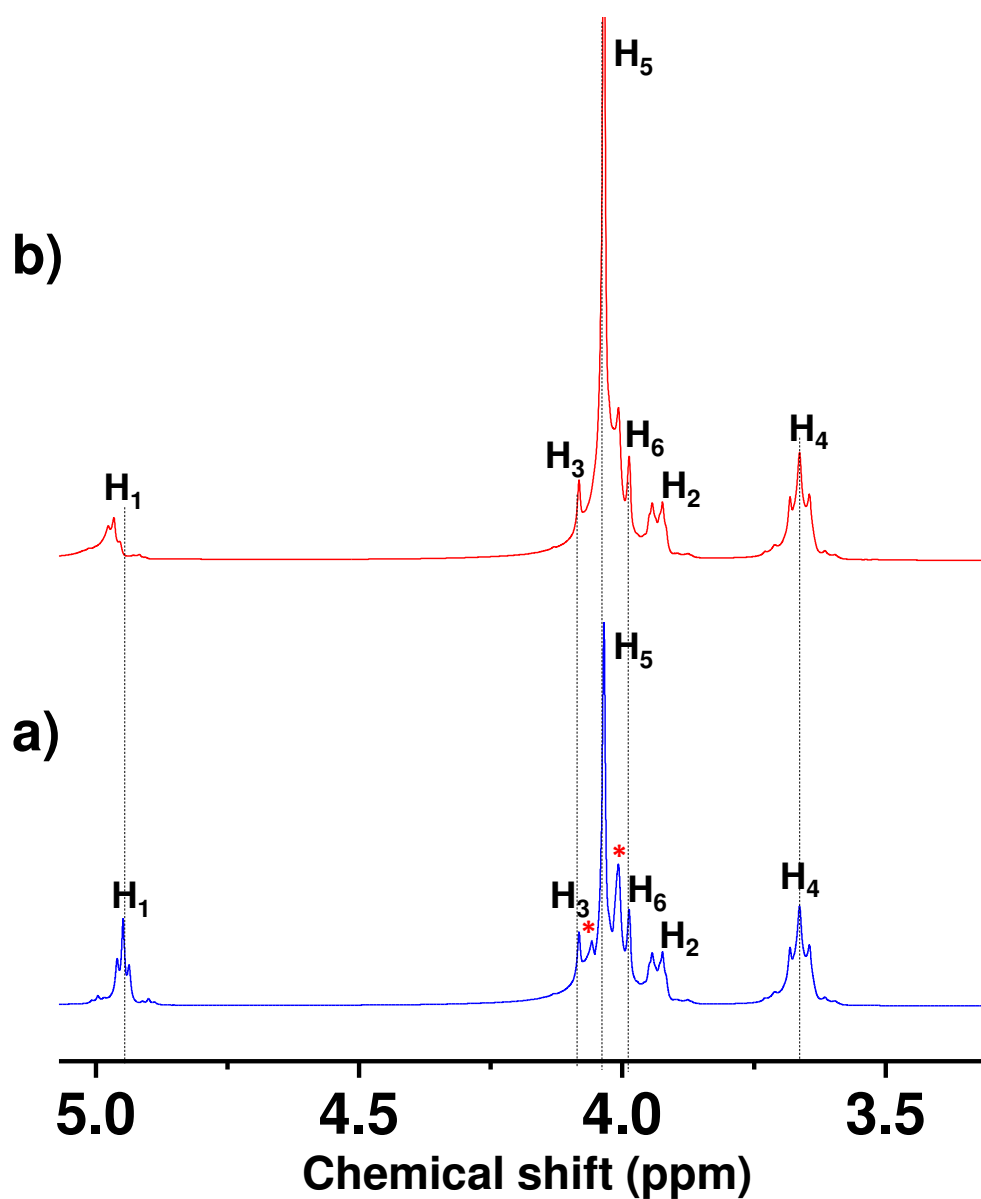
**Figure S10.** Collision induced dissociation (CID) of  $[X\cap(CD)_1]^{3-}$ , where CD is  $\beta$ -cyclodextrin. With the increase of collision of energy (CE), CD was lost from the complex. CE is controlled by applied potential (in V).



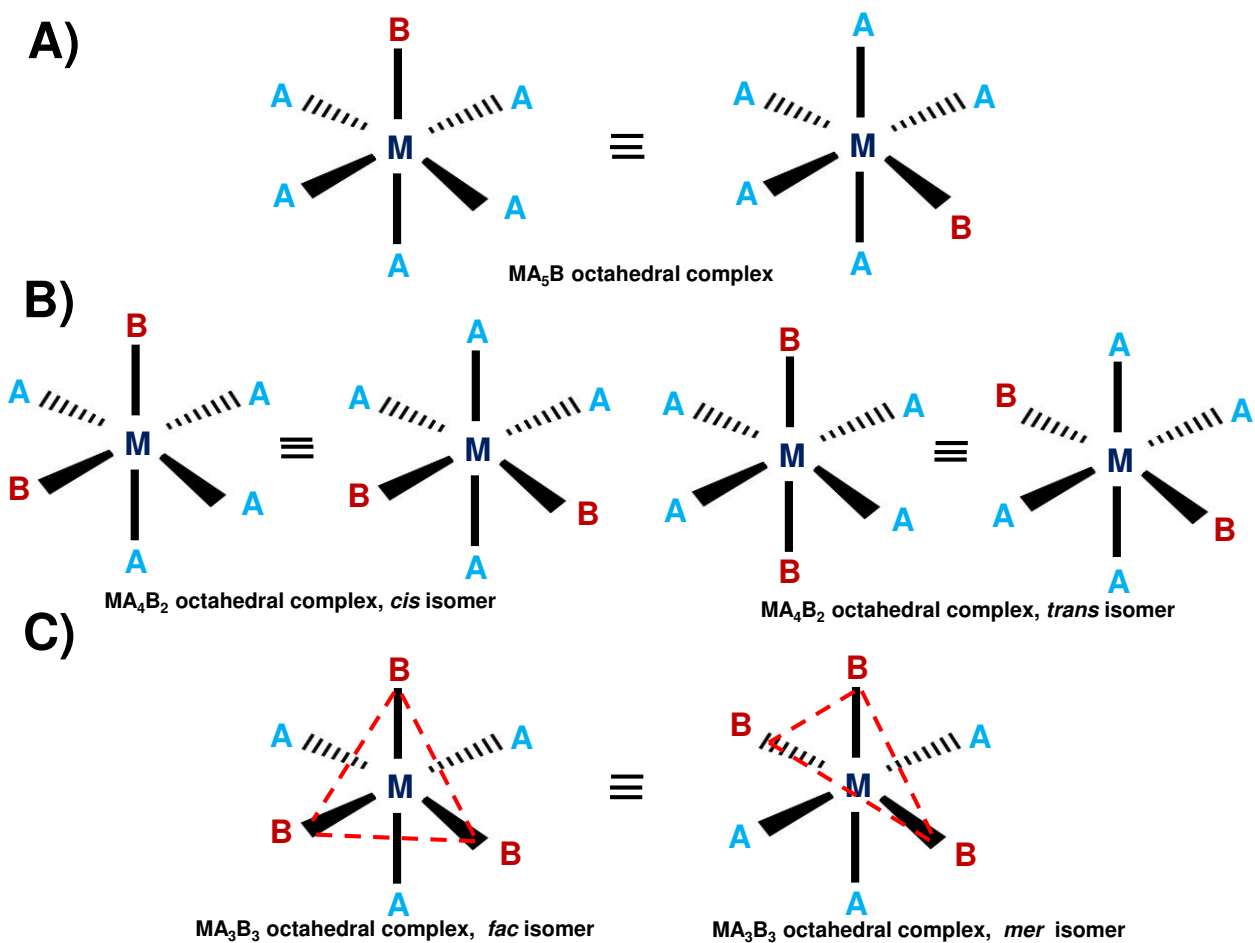
**Figure S11.** Comparison of energy resolved fragmentation of  $[X\cap(CD)_1]^{3-}$  complex with different CDs, where CD stands for  $\alpha$ ,  $\beta$ , &  $\gamma$ -cyclodextrin. With the increase of cavity size, the interaction energy increases.



**Figure S12.** UV-vis spectra showing slight changes upon addition of  $\beta$ -CD to the  $\text{Ag}_{29}(\text{BDT})_{12}^{3-}$  indicating that electronic structure of the cluster is almost unaffected by CD complexation. The concentration of the cluster:CD was varied from 1:1 to 1:4 in room temperature.

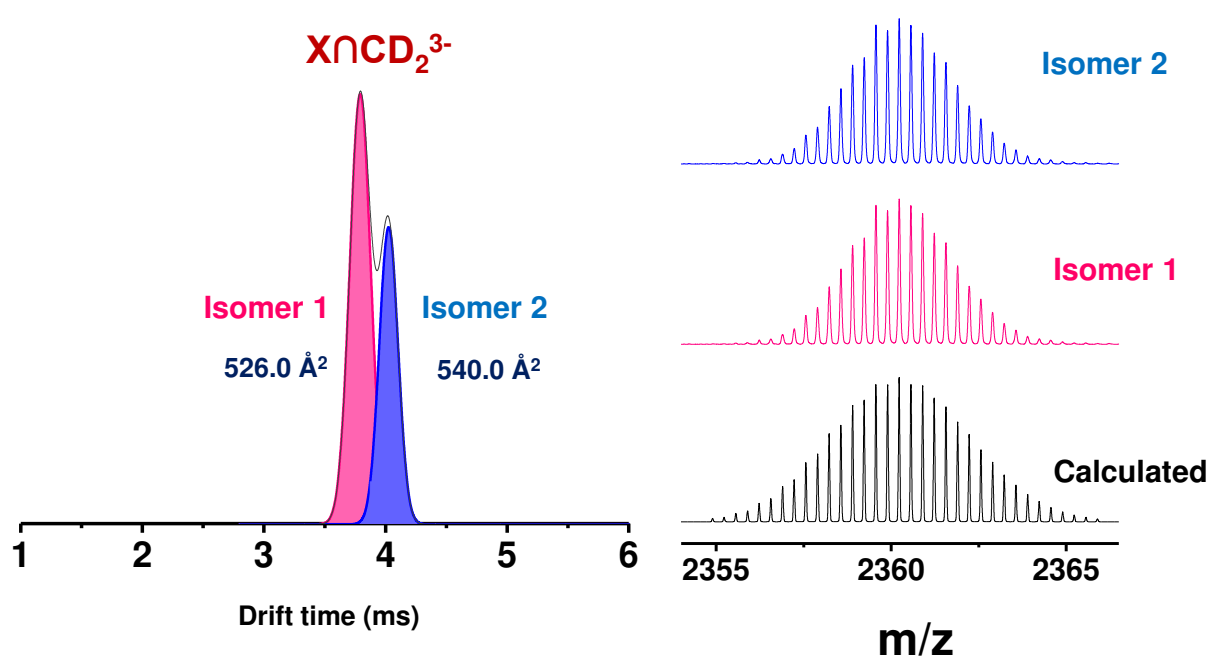


**Figure S13.** <sup>1</sup>H NMR spectra (500 MHz, 298 K, DMF- d<sub>7</sub>) of **a)** only β-CD and **b)** β-CD in the presence of Ag<sub>29</sub>(BDT)<sub>12</sub><sup>3-</sup>. <sup>1</sup>H NMR spectra showed changes in the resonances for the inner-cavity H-5 and H-3 protons. The peaks with the \* marked are also due to H3 and H5 proton and they were showing some changes. The ratio of the concentration of cluster:CD was 1:6. Cyclodextrins are highly symmetric. But when they are encapsulated in a pair of BDT ligands, the symmetry was lost and they were distorted slightly. This will lead to anisotropy in the structure. Because of this anisotropy, H-1 proton could change significantly in NMR after the addition of the cluster.

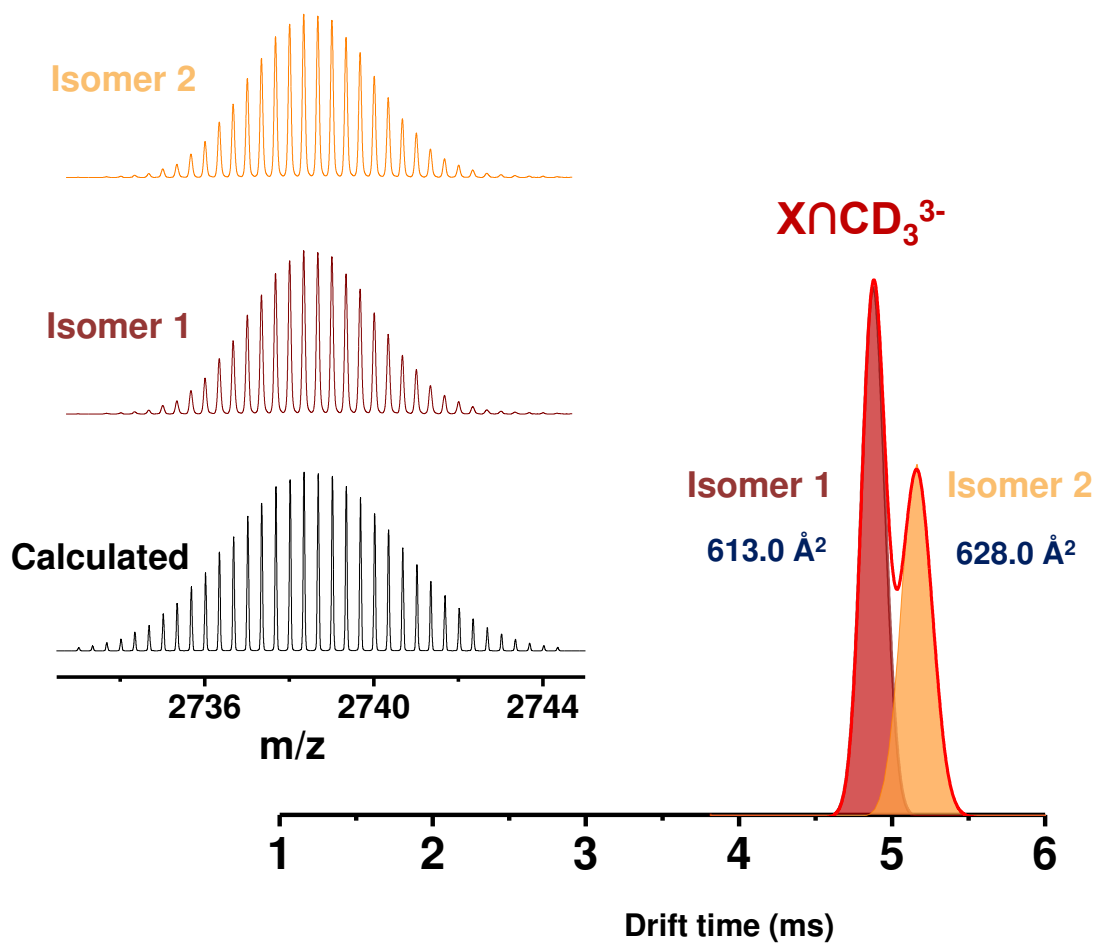


**Figure S14.** Structural isomers of octahedral complexes. A)  $\text{MA}_5\text{B}$  does not show any structural isomerism. B)  $\text{MA}_4\text{B}_2$  shows *cis-trans* isomerism and C)  $\text{MA}_3\text{B}_3$  shows *fac-mer* isomers.

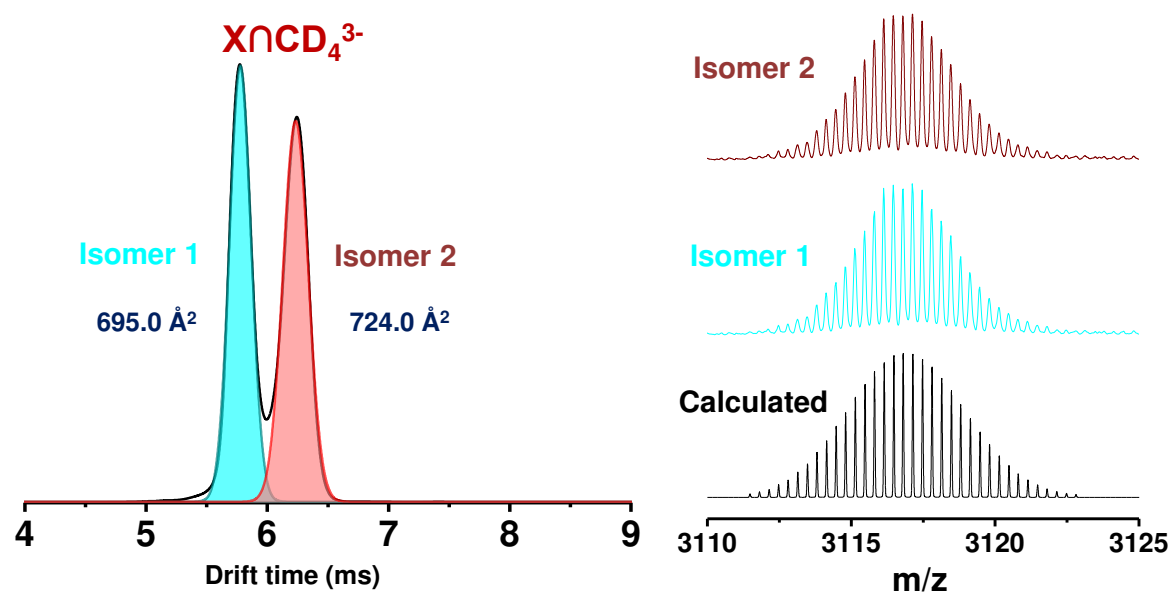




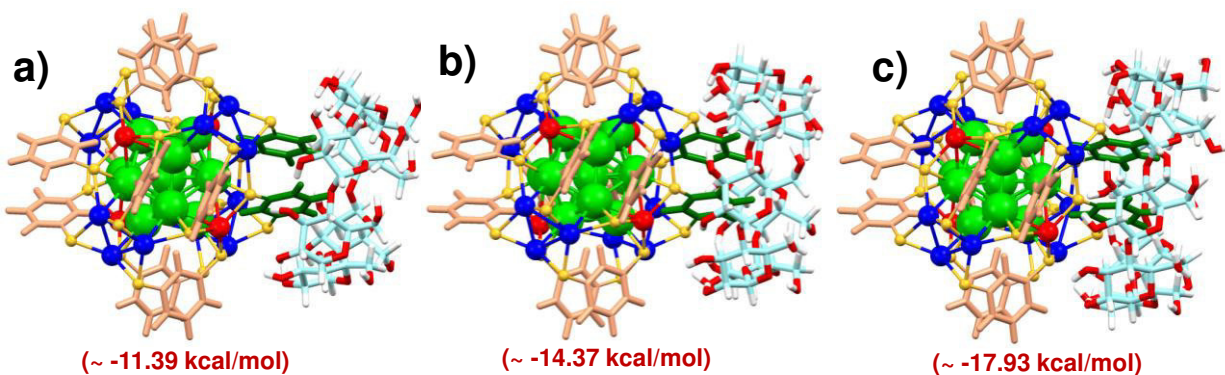
**Figure S15.** Drift time of  $[X\cap(\beta\text{-CD})_2]^{3-}$  showing the presence of two isomeric structures. The isotopic distributions of the isomers are matching with the calculated spectrum. The CCS values are shown.



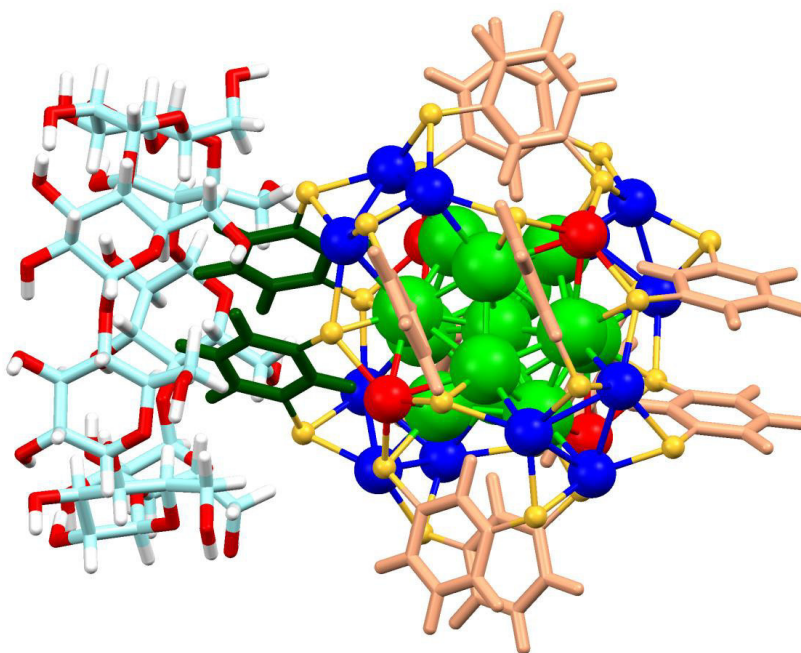
**Figure S16.** Drift time of  $[X\cap(\beta\text{-CD})_3]^{3-}$  showing the presence of two isomeric structures. The isotopic distributions of the isomers are matching with the calculated spectrum. The CCS values are shown.



**Figure S17.** Drift time of  $[X\cap(\beta\text{-CD})_4]^{3-}$  showing the presence of two isomeric structures. The isotopic distributions of the isomers are matching with the calculated spectrum. The CCS values are shown.

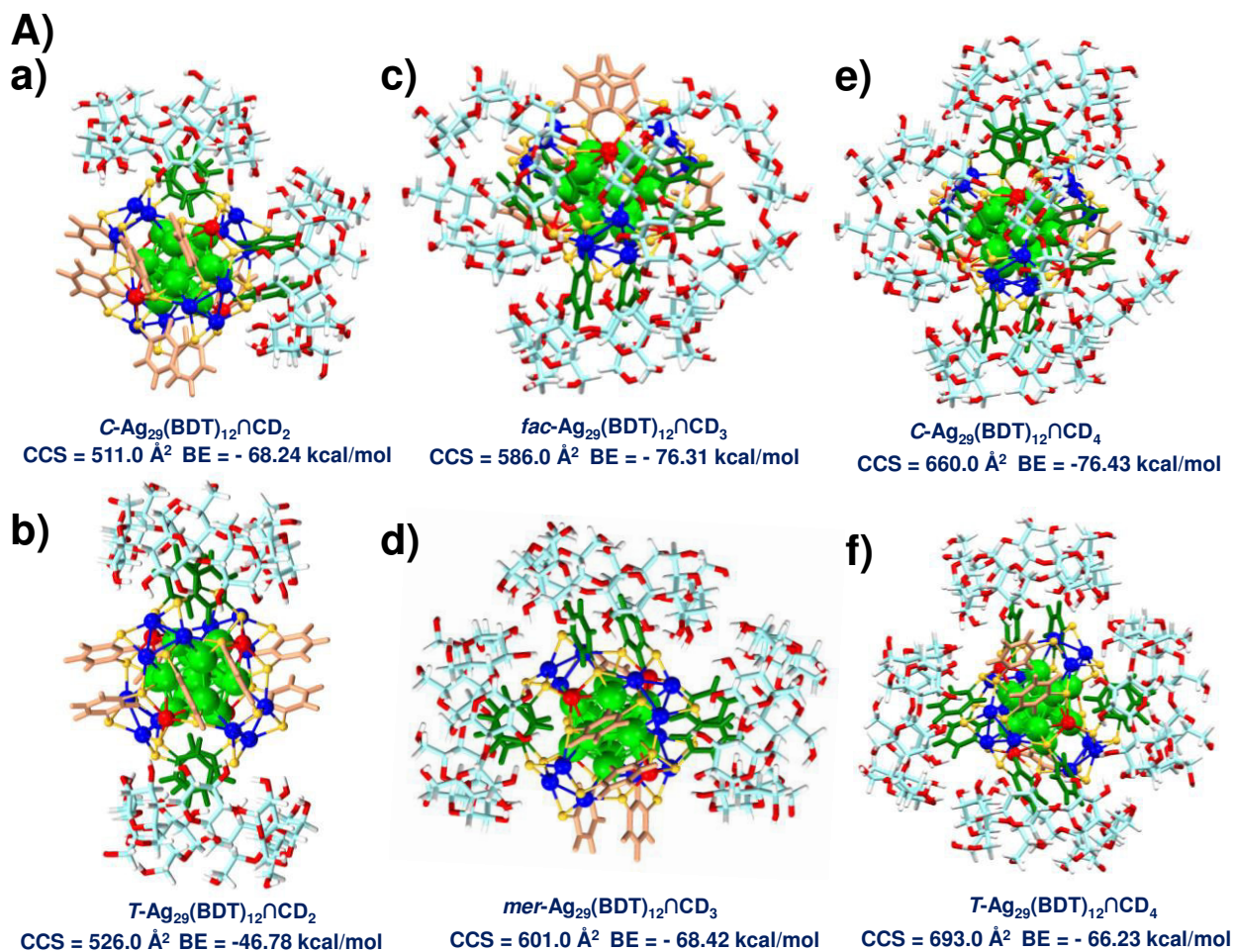


**Figure S18.** a) to c) Molecular docking lowest energy structures of  $[X\cap(\text{CD})_1]^{3-}$  complexes where CD stands for  $\alpha$ ,  $\beta$ , and  $\gamma$ -CD, respectively.

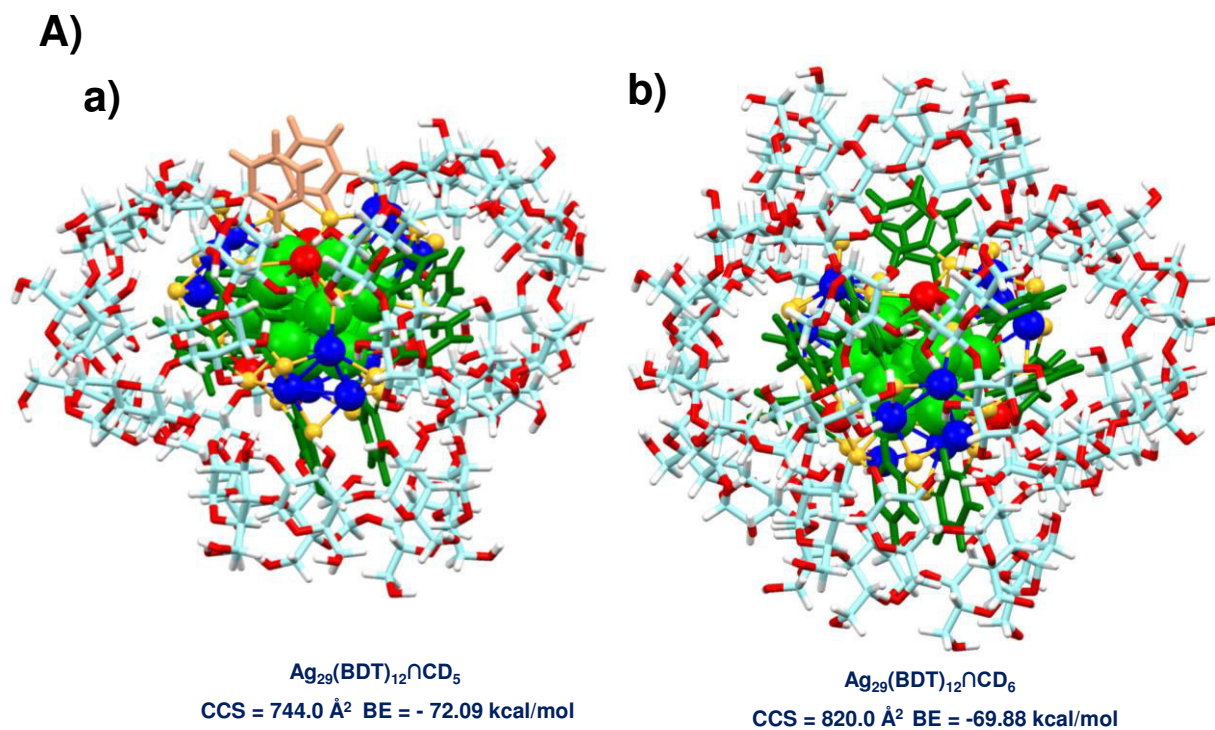


BE = - 27.21 kcal/mol

**Figure S19.** DFT optimized structure of  $[X\cap(\beta\text{-CD})_1]^{3-}$  with binding energy, where CD encapsulates the cluster from the tail side.



**Figure S20.** **A)** **a)**, **b)** and **d)**, **f)** DFT optimised structures of  $C/T$  isomers of  $[\text{X}@\text{(CD)}_n]^{3-}$  for  $n = 2$  and  $4$ , respectively and their corresponding CCS values and binding energies are given below. **c)** and **d)** The DFT optimized  $\text{fac-mer}$  isomers with binding energies and CCS values.



**Figure S21.** A) DFT optimized structure of  $[\text{X}@\text{CD}_n]^{3-}$  where n = 5 **a)** and 6 **b)** with CCS values and binding energies.



**Table S1.** Binding energy values

Systems	(PBE) BE (kcal/mol)	(vdw-DF2) BE (kcal/mol)
$[\text{X}\cap(\alpha\text{-CD})_1]^{3-}$	- 33.46	- 71.74
$[\text{X}\cap(\beta\text{-CD})_1]^{3-}$	- 65.15	- 99.28
$[\text{X}\cap(\gamma\text{-CD})_1]^{3-}$	- 69.01	- 145.82
$C\text{-}[\text{X}\cap(\beta\text{-CD})_2]^{3-}$	- 68.24	- 143.31
$T\text{-}[\text{X}\cap(\beta\text{-CD})_2]^{3-}$	- 46.78	- 101.48
$fac\text{-}[\text{X}\cap(\beta\text{-CD})_3]^{3-}$	- 76.31	- 147.01
$mer\text{-}[\text{X}\cap(\beta\text{-CD})_3]^{3-}$	- 68.42	- 119.02
$C\text{-}[\text{X}\cap(\beta\text{-CD})_4]^{3-}$	- 76.43	- 100.68
$T\text{-}[\text{X}\cap(\beta\text{-CD})_4]^{3-}$	- 66.23	- 86.43
$[\text{X}\cap(\beta\text{-CD})_5]^{3-}$	- 72.09	- 98.23
$[\text{X}\cap(\beta\text{-CD})_6]^{3-}$	- 69.88	- 96.11
$\text{Tail}\text{-}[\text{X}\cap(\beta\text{-CD})_1]^{3-}$	- 27.21	- 63.65

**Table S2.** Experimental and theoretical CCS values

Possible structures	Exp. CCS ( Å <sup>2</sup> )	Calculated CCS by PA ( Å <sup>2</sup> )
$[\text{X}\cap(\beta\text{-CD})_1]^{3-}$	438.0	421.0
$C\text{-}[\text{X}\cap(\beta\text{-CD})_2]^{3-}$	526.0	511.0
$T\text{-}[\text{X}\cap(\beta\text{-CD})_2]^{3-}$	540.0	526.0
$fac\text{-}[\text{X}\cap(\beta\text{-CD})_3]^{3-}$	613.0	586.0
$mer\text{-}[\text{X}\cap(\beta\text{-CD})_3]^{3-}$	628.0	601.0
$C\text{-}[\text{X}\cap(\beta\text{-CD})_4]^{3-}$	695.0	660.0
$T\text{-}[\text{X}\cap(\beta\text{-CD})_4]^{3-}$	724.0	693.0
$[\text{X}\cap(\beta\text{-CD})_5]^{3-}$	790.0	744.0
$[\text{X}\cap(\beta\text{-CD})_6]^{3-}$	860.0	820.0

## References

1. AbdulHalim, L. G.; Bootharaju, M. S.; Tang, Q.; Del Gobbo, S.; AbdulHalim, R. G.; Eddaoudi, M.; Jiang, D.-e.; Bakr, O. M. *J. Am. Chem. Soc.* **2015**, *137*, 11970-11975.
2. Chakraborty, P.; Nag, A.; Paramasivam, G.; Natarajan, G.; Pradeep, T. *ACS Nano* **2018**.
3. M., M. G.; Ruth, H.; William, L.; F., S. M.; K., B. R.; S., G. D.; J., O. A. *J. Comput. Chem.* **2009**, *30*, 2785-2791.
4. Heinz, H.; Vaia, R. A.; Farmer, B. L.; Naik, R. R. *J. Phys. Chem. C* **2008**, *112*, 17281-17290.
5. Pohjolainen, E.; Chen, X.; Malola, S.; Groenhof, G.; Häkkinen, H. *J. Chem. Theory Comput.* **2016**, *12*, 1342-1350.
6. Perdew, J. P.; Burke, K.; Ernzerhof, M. *Phys. Rev. Lett.* **1997**, *78*, 1396-1396.
7. Larsen, A. H.; Vanin, M.; Mortensen, J. J.; Thygesen, K. S.; Jacobsen, K. W. *Phys. Rev. B* **2009**, *80*, 195112.
8. Lee, K.; Murray, É. D.; Kong, L.; Lundqvist, B. I.; Langreth, D. C. *Phys. Rev. B* **2010**, *82*, 081101.
9. Hanwell, M. D.; Curtis, D. E.; Lonie, D. C.; Vandermeersch, T.; Zurek, E.; Hutchison, G. R. *J. Cheminformatics* **2012**, *4*, 17.

Cite this: *Nanoscale*, 2018, **10**, 20033

# A thirty-fold photoluminescence enhancement induced by secondary ligands in monolayer protected silver clusters†

Esma Khatun,<sup>a</sup> Atanu Ghosh,<sup>a</sup> Papri Chakraborty,<sup>a</sup> Priya Singh,<sup>b</sup>  
 Mohammad Bodiuzzaman,<sup>a</sup> Paramasivam Ganesan,<sup>a</sup> Ganapati Natarajan,<sup>a</sup>  
 Jyotirmoy Ghosh,<sup>a</sup> Samir Kumar Pal <sup>b</sup> and Thalappil Pradeep <sup>\*a</sup>

In this paper, we demonstrate that systematic replacement of the secondary ligand PPh<sub>3</sub> leads to an enhancement in the near-infrared (NIR) photoluminescence (PL) of [Ag<sub>29</sub>(BDT)<sub>12</sub>(PPh<sub>3</sub>)<sub>4</sub>]<sup>3-</sup>. While the replacement of PPh<sub>3</sub> with other monophosphines enhances luminescence slightly, the replacement with diphosphines of increasing chain length leads to a drastic PL enhancement, as high as 30 times compared to the parent cluster, [Ag<sub>29</sub>(BDT)<sub>12</sub>(PPh<sub>3</sub>)<sub>4</sub>]<sup>3-</sup>. Computational modeling suggests that the emission is a ligand to metal charge transfer (LMCT) which is affected by the nature of the secondary ligand. Control experiments with systematic replacement of the secondary ligand confirm its influence on the emission. The excited state dynamics shows this emission to be phosphorescent in nature which arises from the triplet excited state. This enhanced luminescence has been used to develop a prototypical O<sub>2</sub> sensor. Moreover, a similar enhancement was also found for [Ag<sub>51</sub>(BDT)<sub>19</sub>(PPh<sub>3</sub>)<sub>3</sub>]<sup>3-</sup>. The work presents an easy approach to the PL enhancement of Ag clusters for various applications.

Received 25th July 2018,  
 Accepted 28th September 2018  
 DOI: 10.1039/c8nr05989f  
 rsc.li/nanoscale

## Introduction

Monolayer protected atomically precise clusters of noble metals with systematic variation in properties belong to a new category of precision materials.<sup>1–3</sup> Their distinct luminescence and characteristic electronic absorption have fascinated the scientific community for the past few years.<sup>4–6</sup> The ability to crystallize them has led to a detailed understanding of their structures and this has promoted in-depth studies of their properties by computational methods.<sup>7–9</sup> Among the properties of such systems, observable luminescence, especially in the near-infrared (NIR) window, has been fascinating due to its chemical and biological applications.<sup>10,11</sup> Depending on the structure, composition and core size of the clusters, luminescence can be observed in different spectral regions (visible, NIR and infrared).<sup>12–14</sup> The electronic structure of the metal–ligand interface is known to be a crucial factor in determining the emission properties.<sup>15,16</sup> Consequently, ligand modification has been shown to result in an enhancement in luminescence.

<sup>17,18</sup> The PL enhancement of Au<sub>25</sub>(PET)<sub>18</sub> (PET: 2-phenylethanethiol) is a good example where ligand modification was done using 4-*tert*-butylbenzyl mercaptan (SBB).<sup>19</sup> Also, Au<sub>22</sub>(SG)<sub>18</sub> (SG: glutathione) displayed high luminescence after surface reconstruction.<sup>20,21</sup> Surface modification can be made *via* the formation of ion pairing which helps in improving the PL intensity as in the case of [Ag<sub>29</sub>(BDT)<sub>12</sub>(PPh<sub>3</sub>)<sub>4</sub>]<sup>3-</sup> (BDT: 1,3-benzenedithiol) which showed more than ten-fold PL increment in the presence of bulky counter ions.<sup>22</sup> The composition of the core also influences the luminescence intensity significantly. The most dramatic aspect of this effect was the observation of a 200-fold enhancement in PL after the addition of 13 Ag atoms in the Au<sub>25</sub> cluster.<sup>23</sup> Also, a huge emission enhancement was observed in [Ag<sub>29</sub>(BDT)<sub>12</sub>(PPh<sub>3</sub>)<sub>4</sub>]<sup>3-</sup> and [Ag<sub>25</sub>(2,4-DMBT)<sub>18</sub>]<sup>-</sup> (DMBT: 2,4-dimethyl benzenethiol) clusters upon doping of Pt and Au atoms.<sup>24–26</sup> [AuAg<sub>24</sub>(DMBT)<sub>18</sub>]<sup>-</sup> and [Au<sub>x</sub>Ag<sub>29-x</sub>(BDT)<sub>12</sub>(PPh<sub>3</sub>)<sub>4</sub>]<sup>3-</sup> exhibited ~25 and ~26 fold higher PL, respectively, compared to that of the corresponding undoped clusters. Doping of the Pt atom in [Ag<sub>29</sub>(BDT)<sub>12</sub>(PPh<sub>3</sub>)<sub>4</sub>]<sup>3-</sup> resulted in a 2.3 fold PL enhancement. The nature of solvent also plays an important role in PL enhancement.<sup>27</sup> An example of this is [PtAg<sub>24</sub>(DMBT)<sub>18</sub>]<sup>2-</sup>, which showed a 100 fold greater QY in acetonitrile compared to that in dichloromethane.<sup>28</sup>

Aggregation-induced luminescence enhancement (AIE) has been proposed to be the driving force for the enhanced luminescence in biological structures, organic luminogens

<sup>a</sup>DST Unit of Nanoscience (DST UNS) and Thematic Unit of Excellence, Department of Chemistry, Indian Institute of Technology Madras, Chennai 600036, India. E-mail: pradeep@iitm.ac.in; Fax: +91-44 2257-0545

<sup>b</sup>Department of Chemical Biological & Macromolecular Sciences, S. N. Bose National Centre for Basic Sciences, Block JD, Sector III, Salt Lake, Kolkata 700098, India

†Electronic supplementary information (ESI) available. See DOI: 10.1039/c8nr05989f

and metal nanoclusters.<sup>21,29–32</sup> In such cases, non-covalent interactions between the molecules restrict the intermolecular motion which affects the luminescence (enhancement or quenching). The AIE is observed in  $\text{Au}_2\text{Cu}_6(\text{S-Adm})_6(\text{PPh}_2\text{Py})_2$  (S-Adm: adamantane thiol),  $\text{Au}_4\text{Ag}_{13}(\text{DPPE})_4(\text{DMBT})_9$  (DPPE: 1,2-bis(diphenylphosphino)ethane),  $\text{Au}_4\text{Ag}_5(\text{DPPM})_2(\text{SR})_6(\text{BPh}_4)$  (DPPM: 1,1-bis(diphenylphosphino)methane), *etc.*<sup>33–35</sup> A recent report by Zhu *et al.* suggested that the addition of excess  $\text{PPh}_3$  in  $[\text{Ag}_{29}(\text{BDT})_{12}(\text{PPh}_3)_4]^{3-}$  can induce aggregation, which resulted in a 13-fold PL improvement (from 0.9% QY to 11.7% QY).<sup>36</sup> The PL intensity can also be tuned by changing the temperature. The lower the temperature, the lower is the molecular motion and hence the higher is the PL intensity.  $[\text{Ag}_{29}(\text{BDT})_{12}(\text{PPh}_3)_4]^{3-}$  displayed an  $\sim 25$  fold greater QY at a lower temperature.<sup>36</sup>

Besides the silver clusters protected with one type of ligand exclusively, such as  $[\text{Ag}_{25}(\text{2,4-DMBT})_{18}]^-$ ,<sup>37</sup>  $[\text{Ag}_{44}(\text{4-FTP})_{30}]^{4-}$  (FTP: 4-fluoro thiophenol),<sup>38</sup>  $[\text{Ag}_{59}(\text{2,5-DCBT})_{32}]^{3-}$  (2,5-DCBT: 2,5-dichloro benzenethiol),<sup>39</sup>  $\text{Ag}_{32}(\text{SG})_{19}$ ,<sup>40</sup> *etc.*, clusters are also known to exist with different types of ligands. Among them, one ligand provides stability to the cluster, called the primary ligand, while the other one enhances the stability and ease of crystallization of the cluster, called the secondary ligand. Such a category of clusters include  $[\text{Ag}_{29}(\text{BDT})_{12}(\text{PPh}_3)_4]^{3-}$ ,<sup>41</sup>  $[\text{Ag}_{51}(\text{BDT})_{19}(\text{PPh}_3)_3]^{3-}$ ,<sup>42</sup>  $[\text{Ag}_{16}(\text{DFBT})_{14}(\text{DPPE})_4]$  (DFBT: difluoro benzenethiol),<sup>43</sup>  $[\text{PtAg}_{28}(\text{S-Adm})_{18}(\text{PPh}_3)_4]^{2+}$ ,<sup>44</sup>  $[\text{Ag}_{67}(\text{2,4-DMBT})_{32}(\text{PPh}_3)_8]^{3+}$ ,<sup>45</sup>  $\text{Ag}_{374}(\text{SR})_{113}\text{Br}_2\text{Cl}_2$ ,<sup>46</sup>  $\text{Ag}_{50}(\text{DPPM})_6(\text{TBBT})_{30}$  (TBBT: *t*-butyl benzenethiol),<sup>47</sup> *etc.* In the experiment here, we have demonstrated that a systematic change in the secondary ligand can lead to an unprecedented PL enhancement, creating a new handle for property modification in this class of materials.  $[\text{Ag}_{29}(\text{BDT})_{12}(\text{PPh}_3)_4]^{3-}$  and  $[\text{Ag}_{51}(\text{BDT})_{19}(\text{PPh}_3)_3]^{3-}$  clusters have been used to demonstrate this effect.  $\text{PPh}_3$  ligands are replaced by *para*-substituted  $\text{PPh}_3$  ligands such as tri(*p*-tolyl)phosphine (TTP), tris(4-fluorophenyl)phosphine (TFPP) and tris(4-chlorophenyl)phosphine (TCPP) as well as diphosphines such as DPPM, DPPE and DPPP (1,3-bis(diphenylphosphino)propane) to prepare the above-mentioned clusters.

In the discussion below, the clusters have been given short labels to simplify the text. The structure, stability, electronic and optical properties of diphosphine-protected  $\text{Ag}_{29}$  have been studied by DFT and time-dependent DFT (TDDFT) calculations. The Kohn–Sham (K–S) molecular orbitals (MOs) have also been calculated to study the contributions of atomic orbitals. A  $\sim 30$  fold enhancement in quantum yield (QY) was observed upon replacement of  $\text{PPh}_3$  by DPPP which makes it possible to develop useful devices. The PL enhancement of the  $\text{Ag}_{29}$  cluster by this method is much higher than that in previous reports.<sup>22,24,25,36</sup> We have also shown the use of enhanced luminescence for the sensing of  $\text{O}_2$  in the solution and solid states. This sensitivity, in turn, is shown to be due to the fact that the luminescence observed is phosphorescent in nature. Though phosphorescence emission has been observed for several gold clusters, it has not been reported for silver clusters to date.<sup>48,49</sup>

## Experimental

### Chemicals and materials

1,3-Benzenedithiol (BDT,  $\geq 99\%$ ), sodium borohydride ( $\text{NaBH}_4$ , 95%) and 1,1-bis(diphenylphosphino)methane (DPPM, 97%) were purchased from Sigma-Aldrich. Silver nitrate ( $\text{AgNO}_3$ ), 1,2-bis(diphenylphosphino)ethane (DPPE), 1,3-bis(diphenylphosphino)propane (DPPP), tri(*p*-tolyl)phosphine (TTP), tris(4-fluorophenyl)phosphine (TFPP) and tris(4-chlorophenyl)phosphine (TCPP) were purchased from Rankem Chemicals. Triphenylphosphine ( $\text{PPh}_3$ , 98%) was purchased from Spectrochem. Dichloromethane (DCM), dimethylformamide (DMF) and methanol (MeOH) were purchased from Rankem and were of HPLC grade. Deuterated solvents, dimethyl sulfoxide- $\text{d}_6$  ( $\text{DMSO-d}_6$ ) and  $\text{CDCl}_3$  were purchased from Sigma-Aldrich. All solvents and chemicals were used without further purification.

**Synthesis of  $[\text{Ag}_{29}(\text{BDT})_{12}]^{3-}$  (**Ia**) and  $[\text{Ag}_{29}(\text{BDT})_{12}(\text{X})_4]^{3-}$ , where X is  $\text{PPh}_3$ , DPPM, DPPE, DPPP, TTP, TFPP and TCPP, labelled as **Ib**, **II**, **III**, **IV**, **V**, **VI** and **VII**, respectively**

The clusters **Ia** and **Ib** were synthesized by a reported method.<sup>41</sup> A similar synthetic methodology was used to synthesize **II**, **III** and **IV** with some modifications, as explained in the ESI.† The addition of DPPM, DPPE and DPPP to **Ia/Ib** also resulted in the formation of these clusters. For the synthesis of **V**, **VI** and **VII**, the ligand exchange (LE) method was followed starting from **Ib**. Details are discussed in the ESI.†

**Synthesis of  $[\text{Ag}_{51}(\text{BDT})_{19}(\text{X})_3]^{3-}$ , where X is  $\text{PPh}_3$ , DPPM, DPPE, DPPP, labeled as **VIII**, **IX**, **X** and **XI**, respectively**

The cluster **VIII** was synthesized by adopting an already reported method which has been discussed thoroughly in the ESI.†<sup>42</sup> The **IX**, **X** and **XI** clusters were synthesized by the LE method starting from **VIII** using DPPM, DPPE and DPPP. Detailed procedures are given in the ESI.†

### Characterization

UV–vis spectra were obtained using a PerkinElmer Lambda 25 spectrometer in the range of 200–1100 nm. Mass spectrometric measurements were done using a Waters Synapt G2-Si high-resolution mass spectrometer. Samples were measured using electrospray ionization (ESI) in the negative mode. PL measurements were performed using a HORIBA JOBIN YVON Nano Log instrument. The bandpass for excitation and emission was set at 3 nm. Dynamic light scattering (DLS) data were measured using the Malvern Zetasizer Nano ZSP instrument using a DMF solution of the clusters. X-ray photoelectron spectroscopic (XPS) measurements were carried out with an Omicron ESCA Probe spectrometer with polychromatic Al K $\alpha$  X-rays ( $h\nu = 1486.7$  eV). The samples (DCM/DMF solution) were drop-casted on an XPS sample stub and dried under ambient conditions. During the measurement, the pass energy for survey scans was kept at 50 eV and changed to 20 eV for specific regions. Binding energies (BE) of the core levels were calibrated with C 1s BE set at 285 eV. NMR spectra were obtained using a Bruker 500 MHz NMR spectrometer (using

DMSO- $d_6$  and  $CDCl_3$  solvents). Time-resolved spectroscopic data were collected by time-correlated single photon counting (TCSPC) with an excitation source of a LifeSpec-ps picosecond diode-laser-pumped fluorescence spectrophotometer from Edinburgh Instruments (Livingston, UK). Picosecond excitation pulses from a picoquant diode laser were used at 409 nm with an instrument response function (IRF) of  $\sim 50$  ps. A micro channel-plate-photomultiplier tube (MCP-PMT; Hamamatsu Photonics, Kyoto, Japan) was used to detect the photoluminescence from the sample after dispersion through a monochromator. The observed fluorescence transients were fitted by using a nonlinear least-squares fitting procedure to a function with F900 software from Edinburgh Instruments.

The quality of the curve fitting was evaluated using reduced  $\chi^2$  and residual data. This time-resolved instrument can resolve at least one-fifth of the instrument response time constants after de-convolution of the IRF. The average lifetime (amplitude-weighted) of a multi-exponential decay is expressed as:

$$\tau_{av} = \sum_{i=1}^N (c_i \tau_i)$$

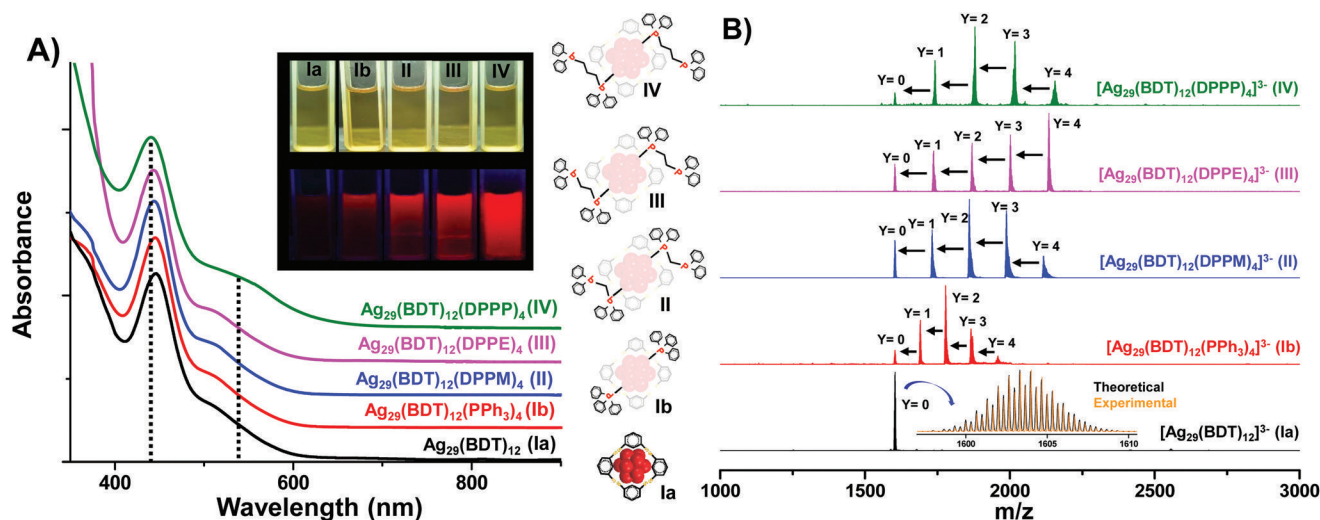
The QYs were measured using dilute solutions of the clusters (0.07 absorbance at  $\sim 446$  nm using the equation given in the ESI†). All computational details are given in the ESI†.

## Results and discussion

### Clusters and their characterization

The luminescence enhancement of  $[Ag_{29}(BDT)_{12}(PPh_3)_4]^{3-}$  (**Ib**), co-protected with thiol (BDT) and phosphine ( $PPh_3$ ), was achieved through substituting the weakly bound  $PPh_3$  (called

the secondary ligand) by other phosphine ligands, such as TTP, TFPP, TCPP, DPPM, DPPE and DPPP (the clusters formed are labelled as **II**, **III**, **IV**, **V**, **VI** and **VII**, respectively). The detailed procedures for their syntheses are given in the ESI†. All clusters were characterized by optical absorption and ESI MS measurements. First, let us discuss the  $Ag_{29}$  clusters synthesized using homologous diphosphines, DPPM, DPPE and DPPP (**II**, **III** and **IV**). The absorption spectra of  $Ag_{29}(BDT)_{12}$  (**Ia**, shown in black) and **Ib** (red) presented in Fig. 1A display a maximum at  $\sim 446$  nm along with an absorption onset at  $\sim 512$  nm. The as-synthesized clusters **II** (blue), **III** (pink) and **IV** (green) show very similar spectra to that of **Ia/Ib**. However, the absorption maxima of **II**, **III** and **IV** are  $\sim 1$ ,  $\sim 2$  and  $\sim 6$  nm blue-shifted compared to that of **Ia/Ib**, respectively, along with the broadening of the absorption bands (see Fig. 1A). The spectra suggest that **II**, **III** and **IV** possess a similar atomic structure to that of **Ib**. To confirm the atomicity of these clusters, ESI MS were obtained as shown in Fig. 1B. The number of phosphines present in the clusters is denoted by  $Y$  (Fig. 1). It is clear from Fig. 1B that all the clusters show a peak at the same position ( $m/z$  1603) for  $Y = 0$  and the maximum value of  $Y$  is 4 (except for **Ia** which does not contain any phosphine). All the cluster ions have  $3^-$  charge state which is validated by the difference between two successive peaks present in the isotopic distributions (Fig. S1A†). The spectrum of **Ia** exhibits only one peak at  $\sim m/z$  1603 which is assigned to  $[Ag_{29}(BDT)_{12}]^{3-}$ , whereas the red spectrum corresponding to **Ib** consists of five peaks. The separation between two successive peaks is  $\sim m/z$  87.3 ( $87.3 \times 3 = 262$ ), the mass of one  $PPh_3$  ligand, in agreement with the composition of **Ib**,  $[Ag_{29}(BDT)_{12}(PPh_3)_4]^{3-}$ . Similarly, the difference between two successive peaks in the blue spectrum is  $\sim m/z$  128 ( $128 \times 3 = 384$ ),



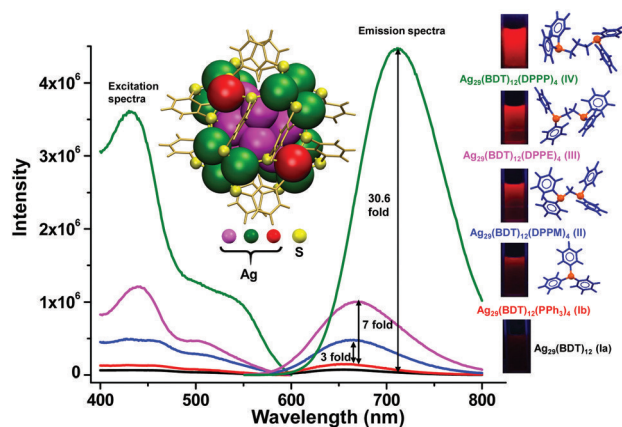
**Fig. 1** UV-vis absorption spectra (A) and ESI MS (B) of **Ia** (black) and **Ib** (red), **II** (blue), **III** (pink) and **IV** (green). The absorption maximum of **IV** is  $\sim 6$  nm blue-shifted compared to that of **Ia/Ib** and the peak at  $\sim 512$  nm is broadened. Inset: Photographs under visible and UV light which show a gradual increase in the PL intensity. Spectra of **Ib**, **II**, **III** and **IV** are vertically shifted for clarity. On the right-hand side, schematic representations of the clusters are presented. All these clusters exhibit  $3^-$  charge state in the ESI MS. The number of phosphines is denoted by  $Y$ . For **II**, **III** and **IV**, the maximum value of  $Y$  is 4 and all of these clusters show systematic phosphine loss. The spectral intensities of all clusters are normalized with respect to the most intense peak. An expanded view of the high-resolution spectrum of **Ia** is shown in the inset.



which matches with the mass of DPPM. For the other spectra, the peak differences are  $\sim m/z$  133 and  $\sim m/z$  137 which match with the masses of DPPE (398) and DPPP (412), respectively. Thus, from the ESI MS, it was clear that the as-synthesized clusters prepared using DPPM, DPPE and DPPP have a similar composition to that of **Ib** and were assigned as  $[\text{Ag}_{29}(\text{BDT})_{12}(\text{X})_4]^{3-}$  where X = DPPM, DPPE and DPPP (**II**, **III** and **IV**). The molecular compositions were further proved by the high resolution spectral features which match with the theoretical spectra. The spectrum corresponding to **Ia** is shown as an inset in Fig. 1B and the spectra of other products are presented in Fig. S1B.† To prove the presence of the Ag–P bond in **Ib**, **II**, **III** and **IV** clusters,  $^{31}\text{P}$  NMR was carried out as presented in Fig. S2.† The NMR spectra were compared with those of the corresponding phosphines.  $\text{PPh}_3$ , DPPM, DPPE and DPPP show  $^{31}\text{P}$  peaks at  $\sim -5.3$ ,  $-26.2$ ,  $-12.7$  and  $-17.2$  ppm, respectively. The corresponding clusters, **Ib**, **II**, **III** and **IV**, display peaks at  $\sim 1.4$ ,  $-3.3$ ,  $-0.1$ , and  $0.4$  ppm, respectively, which affirm the formation of the Ag–P bonds. Elemental characterization of these clusters using XPS was performed (Fig. S3A†). For **Ib**, the Ag  $3d_{5/2}$ , S  $2p_{3/2}$  and P  $2p_{3/2}$  peaks appear at  $\sim 368.5$ ,  $\sim 162.8$  and  $\sim 131.1$  eV, respectively. For **II**, **III** and **IV**, the Ag  $3d_{5/2}$  and S  $2p_{3/2}$  peaks appear at the same positions as that of **Ib**. For P  $2p_{3/2}$ , the peak appears at a higher value of 131.5 eV. Although both Ag(0) and Ag(I) are likely to be present in the spectrum, it is hard to separate them. For diphosphine-protected  $\text{Ag}_{29}$  (**II**, **III** and **IV**), the two P atoms are different but as the energies of the Ag-bound P and the unbound P are nearly the same, it was difficult to differentiate between them. The presence of both the P atoms may be the reason for a shift of P  $2p_{3/2}$  to higher BE in these samples.

## Luminescence

It is well known that cluster **Ib** is extremely stable and also displays a visible luminescence. Though the cluster is weakly luminescent in the solution state, it has high luminescence in the solid state.<sup>41</sup> However, our as-synthesized clusters (**II**, **III** and **IV**) exhibited higher PL intensity even in the solution state as shown in the inset of Fig. 1A. The luminescence profiles of these clusters are presented in Fig. 2. The black, red, blue, pink and green spectra correspond to **Ia**, **Ib**, **II**, **III** and **IV**, respectively. The clusters have almost similar concentrations as their absorbance values were the same and the absorption spectra nearly overlapped with each other. The excitation spectra (at the emission maximum of the clusters) look similar to the absorption spectra. The emission spectra are shown under  $\sim 446$  nm excitation. The data clearly manifest the PL enhancement of **Ia** upon changing the phosphines from  $\text{PPh}_3$  to DPPP (Fig. 2). The PL intensity of **Ib** is  $\sim 2$  times more than that of **Ia**. Among the homologous diphosphines (DPPM, DPPE and DPPP), the long-chain ones show higher PL efficiency than that of the shorter ones and the emission maxima got shifted to a higher wavelength (bathochromic or red-shift). In the case of **Ia**, **Ib**, **II**, **III** and **IV**, emission maxima appeared at  $\sim 655$ ,  $\sim 655$ ,  $\sim 665$ ,  $\sim 670$  and  $\sim 715$  nm, respectively. Cluster **IV** shows the highest luminescence intensity with



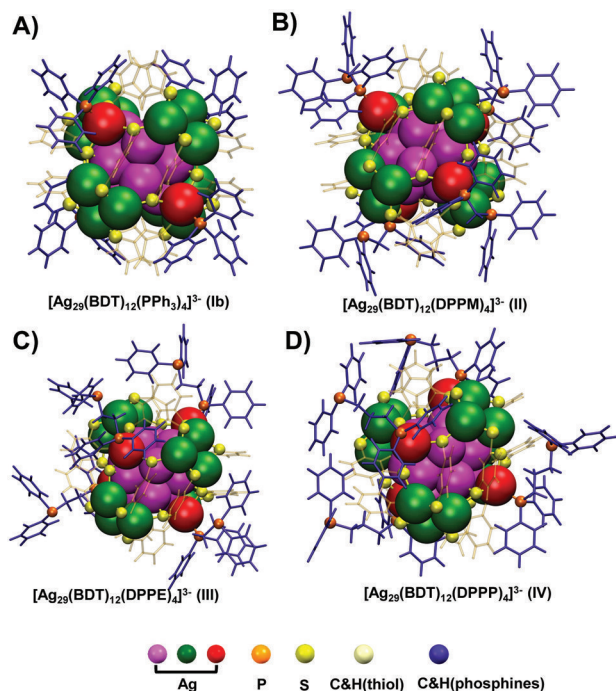
**Fig. 2** Luminescence profiles of **Ia**, **Ib**, **II**, **III** and **IV** which are shown in red, blue, pink and green, respectively. Insets: The DFT calculated structure of the  $\text{Ag}_{29}(\text{BDT})_{12}$  moiety (where pink, green, and red spheres denote Ag atoms; yellow sphere for S atoms; light yellow sphere for the benzene ring of thiols). The phosphine structures are presented on the right-hand side (benzene rings and P atoms are denoted by blue and orange, respectively) of the spectra along with the photographs under UV light which show a gradual increase in PL intensity. With reference to **Ib** (QY = 0.9%), QYs of **Ia**, **II**, **III** and **IV** were calculated as 0.43%, 2.9%, 6.24% and 27.5%, respectively.

the largest shift in the emission maximum. The QYs of all these clusters were calculated using the equation given in the ESI.† Considering **Ib** as a reference (QY is 0.9%),<sup>41</sup> QYs of **II**, **III** and **IV** were 2.9%, 6.24% and 27.5%, respectively. These were enhanced  $\sim 3$ ,  $\sim 7$  and  $\sim 31$  fold in comparison with **Ib**. Cluster **Ia** is less luminescent than **Ib** due to the absence of any phosphine ligand (QY is 0.45%).

## Computational studies

To know the reason behind the luminescence enhancement, a detailed structural investigation was needed. Although **II**, **III** and **IV** were characterized by several experimental tools, any possible changes in their structures were not clear due to the absence of crystal structures. However, theoretical calculations shed light on the structures of these clusters. The energetically most stable structure of **Ib** was derived from DFT calculations as implemented in the grid-based projector augmented wave method (GPAW) using its reported crystal structure (Fig. 3A, B, C and D).<sup>41,50</sup> Then, by replacing  $\text{PPh}_3$  ligands with different diphosphine ligands, the theoretical structures of **II**, **III** and **IV** were obtained. The geometry optimizations of all clusters were performed using the Perdew–Burke–Ernzerhof (PBE) exchange functional in real-space finite difference (FD) mode in GPAW.<sup>51</sup> Detailed descriptions of computational methodologies are presented in the ESI.† The DFT optimized structures of **Ib**, **II**, **III** and **IV** (using the  $3^-$  charge state) with energies of  $-1890.255$  eV,  $-2263.172$  eV,  $-2305.48$  eV and  $-2394.88$  eV are shown in Fig. 3A, B, C and D, respectively. Although the bonding distances of Ag–P (2.499–2.544 Å) for **II**, **III** and **IV** are almost very close to **Ib** (2.491 Å), the magnitude of the calculated phosphine ligand binding energies (the binding energy





**Fig. 3** The DFT calculated energetically most stable structures of **Ib** (A), **II** (B), **III** (C) and **IV** (D). The energies of **Ib**, **II**, **III** and **IV** are  $-1890.255$ ,  $-2263.172$ ,  $-2305.48$  and  $-2394.88$  eV, respectively. The pink, green and red denote Ag atoms; yellow denotes S atoms; orange denotes P atoms; light yellow denotes benzene rings of thiol ligands; blue denotes benzene rings and  $-\text{CH}_2$  units of phosphine ligands.

is the energy difference between the total structure of the cluster and the sum of the energies of the phosphine ligands and  $[\text{Ag}_{29}\text{BDT}_{12}]^{3-}$  unit of **III** ( $-12.25$  kcal mol $^{-1}$ ) and **IV** ( $-10.21$  kcal mol $^{-1}$ ) is higher by  $3.17$  kcal mol $^{-1}$  and  $1.13$  kcal mol $^{-1}$ , respectively than **Ib** ( $-9.03$  kcal mol $^{-1}$ ). Hence, clusters **III** and **IV** are theoretically more stable than **Ib**. Although the time dependent absorption spectra of **Ib** and **IV** did not show much change after 3 weeks (Fig. S3B $^\dagger$ ), the cone voltage dependent fragmentation study from ESI MS (Fig. S3C $^\dagger$ ) revealed that **IV** needed a higher voltage to detach the DPPP ligands (70 V) than those of **Ib** (40 V). This suggests the higher binding energy of DPPP than  $\text{PPh}_3$  with the  $[\text{Ag}_{29}(\text{BDT})_{12}]^{3-}$  unit. Also, the theoretical observation was proved by one more experiment where two bottles were taken and one of them contained **Ib** and the other one was filled with **III**. Then, small amounts of DPPE and  $\text{PPh}_3$  were added to **Ib** and **III**, respectively. The absorption and emission spectra of the cluster solutions before and after phosphine addition are presented in Fig. S4. $^\dagger$  After the addition of DPPE in **Ib**, the absorption spectrum became similar to that of **III** (Fig. S4A $^\dagger$ ). Consequently, a large enhancement in luminescence occurred (Fig. S4B $^\dagger$ ). While in the second case, where  $\text{PPh}_3$  was added to **III**, the absorption and emission spectra showed hardly any change (Fig. S4C and D $^\dagger$ ). This experiment suggested that DPPE can easily substitute  $\text{PPh}_3$  to form cluster **III** but  $\text{PPh}_3$  was unable to replace DPPE. This is due to the

higher binding energy of **III** than that of **Ib**. The calculated binding energy of **II** ( $-6.89$  kcal mol $^{-1}$ ) is lower by  $2.14$  kcal mol $^{-1}$  than **Ib**. However, the above-mentioned experiment was performed using DPPM which shows that the binding energy of **II** is higher than **Ib** (see Fig. S4E, F, G and H $^\dagger$ ) which resulted in the formation of **II** by addition of DPPM in **Ib**, but not the reverse.

The absorption spectra of **Ib**, **II**, **III** and **IV** were calculated using linear-response time-dependent density functional theory (LR-TDDFT) (Fig. S5 $^\dagger$ ). In this regard, the structures of these clusters were simplified by replacing each benzene ring of the phosphines by a reduced  $-\text{CH}_3$  model ligand and the systems were re-optimized. $^{45}$  The solid state structures were considered during the calculation. Thus, the effect of different isomers which can coexist in the solution state was not taken into account. $^{52}$  Due to the above approximations, the theoretical spectra were slightly blue shifted as compared to the experimental ones (Fig. S5 $^\dagger$ ). The two main spectral features, the absorption maximum (peak 1) and the shoulder peak (peak 2), were identified in the theoretical spectra of **Ib**, **II**, **III** and **IV** (Fig. S5 $^\dagger$  and Fig. 4A). In Fig. 4A, the theoretical spectra of **Ib** and **IV** were compared with the experimental spectra. For **Ib**, peak 1 at  $\sim 446$  nm was reproduced exactly in the theoretical spectrum, but peak 2 ( $\sim 512$  nm) appeared at  $\sim 491$  nm which is  $\sim 8$  nm blue-shifted compared to the experimental spectrum. In the case of **II**, **III** and **IV**, peak 1 was blue-shifted by  $\sim 18$  nm ( $\sim 446$ ,  $428$ ,  $425$  and  $423$  nm, respectively). In the lower energy range, except the two main spectral features, a few more weak peaks were observed and these were broadened as we moved from **Ib** to **IV**.

The MO transitions corresponding to peaks 1 and 2 for all clusters are given in Tables S1A and B. $^\dagger$  In the case of **Ib**, the most intense electronic transition related to peak 1 occurred between the deeper lying occupied MO and unoccupied MO (HOMO-13 to LUMO+9). However, the most intense transition corresponding to peak 2 occurred from the frontier occupied MO to unoccupied MO (HOMO-4 to LUMO+9). For **II**, **III** and **IV**, both peak 1 and 2 arise due to the transitions from the deeper occupied MOs to unoccupied MOs (see Tables S1A and B $^\dagger$ ). The shapes of K-S MOs involved in the strongest transitions related to peak 1 and 2 of **Ib**, **II**, **III** and **IV** are shown in Fig. S6 $^\dagger$  and Fig. 4B which confirm that the deeper occupied MOs are made up of more ligand orbitals (2s, 2p), whereas the frontier occupied MOs are having contributions from the 4d orbitals of Ag along with the ligand orbitals. On the other hand, the unoccupied orbitals are mainly composed of the 5sp orbitals of Ag. This suggests that the transitions mainly occurred *via* ligand to metal charge transfer (LMCT) and the extent of LMCT will be higher when transitions occur from the occupied MOs having a higher ligand contribution. As for **II**, **III** and **IV**, both peak 1 and 2 correspond to the transitions occurring from the deeper occupied orbitals and they display more LMCT transitions than **Ib** (here only peak 1 arises from deeper lying occupied MOs). The transitions related to the peaks arising in the lower energy (see Fig. 4A and Fig. S5 $^\dagger$ ) region also occur from the deeper occupied MOs (transitions corresponding to these peaks for **Ib** and **IV** are given in

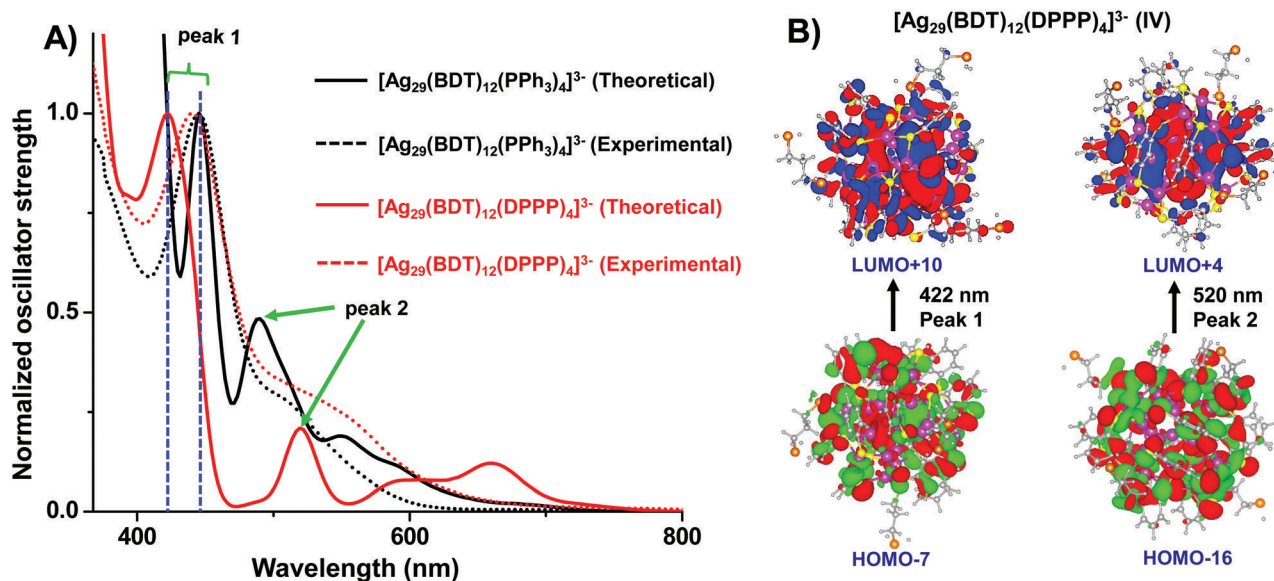


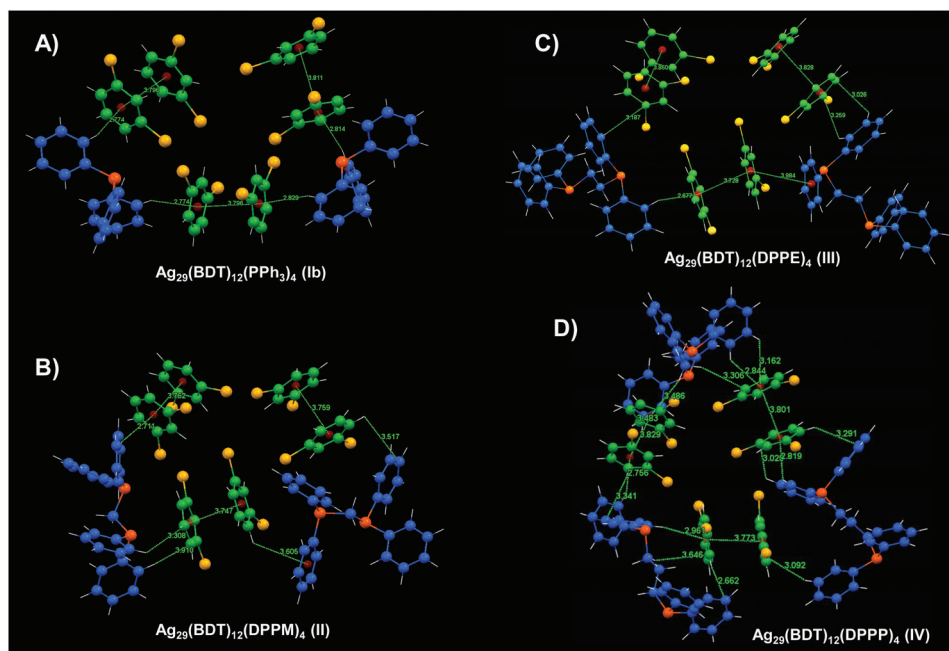
Fig. 4 (A) The theoretical absorption spectra of [Ag<sub>29</sub>(BDT)<sub>12</sub>(P(CH<sub>3</sub>)<sub>3</sub>)<sub>4</sub>]<sup>3-</sup> (black solid line) and [Ag<sub>29</sub>(BDT)<sub>12</sub>(P<sub>2</sub>(CH<sub>2</sub>)<sub>3</sub>(CH<sub>3</sub>)<sub>4</sub>)<sub>4</sub>]<sup>3-</sup> (red solid line) models. The theoretical spectra are compared with the experimental spectra of **1b** and **IV** (black and red dotted line). (B) The shape of the K-S MOs of **IV** which denotes the strongest electronic transitions related to peaks 1 and 2 (422 and 520 nm).

Table S1C†) which are more of ligand character. So, these transitions also contribute to the higher LMCT. From Fig. 4A (and Fig. S5†), we note that the lower energy peak is the most broadened for **IV**. We conclude that the highest LMCT transitions in **IV** result in a 30-fold PL enhancement.

#### The reason behind the luminescence enhancement

Cluster **1b** consists of an Ag<sub>13</sub> icosahedron enclosed by four Ag<sub>3</sub>S<sub>6</sub> motifs which are further capped by four Ag-PPh<sub>3</sub> units.<sup>36,41</sup> There are six  $\pi\cdots\pi$  interactions between the benzene rings of BDT ligands. There are C-H $\cdots\pi$  interactions among the benzene rings of BDT and PPh<sub>3</sub>. The average C-H $\cdots\pi$  distance is  $\sim$ 2.80 Å and  $\pi\cdots\pi$  distance is 3.80 Å (see Fig. 5A). When PPh<sub>3</sub> ligands are substituted by DPPM ligands, the number of C-H $\cdots\pi$  interactions increase (average distance  $\sim$ 3.28 Å) and also the  $\pi\cdots\pi$  interactions become stronger by shortening the distance between the two benzene rings of BDT ligands ( $\sim$ 3.75 Å) (see Fig. 5B). In the case of **III**, the structure becomes more asymmetric and the  $\pi\cdots\pi$  interactions between the benzene rings of BDT are not the same for all the six pairs and the average distance is  $\sim$ 3.79 Å. New  $\pi\cdots\pi$  interactions form between the benzene rings of BDT and DPPE ligands (distance of  $\sim$ 3.98 Å) and several new C-H $\cdots\pi$  interactions are observed in the structure (see Fig. 5C). The average distance of C-H $\cdots\pi$  interactions is  $\sim$ 3.01 Å which is less than that of **II**. In the case of longer-chain diphosphines, the C-H $\cdots\pi$  interaction becomes feasible between sp<sup>2</sup> C-H of diphosphine and the benzene ring of BDT. Also, the distance between the two benzene rings of the neighboring BDT ligand decreases, which strengthens the  $\pi\cdots\pi$  interaction in **IV** (see Fig. 5D). All these non-covalent intramolecular interactions make the diphosphine protected Ag<sub>29</sub> clusters more rigid and energetically

more stable which leads to the suppression of intramolecular vibrational and/or rotational motions (see Fig. 5). The bulkiness of the ligand is another factor which leads to a decrease in the molecular motions. This process is known as restricted intramolecular rotation or motion (RIR or RIM) of protecting ligands which help in increasing the radiative process, reducing the non-radiative processes. Generally, RIR or RIM is more feasible in the solid or crystalline state due to strong intermolecular interactions which result in stronger luminescence. Cluster **1b** also shows high luminescence in the solid state, as mentioned earlier, but the intensity is less than that of **IV** (see photographs in the inset of Fig. S7C†). But in the diluted solution, the clusters are separated from each other by solvent molecules and the emission is weaker. The intermolecular interaction can also be expressed as aggregation which can be quantified by particle size measurement, using DLS. The sizes of **1b** (lowest PL intensity) and **IV** (highest PL intensity) were studied and the data are presented in Fig. S7A and B.† At a higher concentration ( $>0.1$  absorbance), aggregation occurs and thus both the clusters exhibit a larger size (Fig. S7A†). But, at a lower concentration, clusters possess a very small size ( $\sim$ 2 nm) which suggests that under this condition, clusters do not show aggregation (or intermolecular interaction) ( $<0.1$  absorbance). The PL intensities at a lower cluster concentration (shown in Fig. S7C†) reveal that even in a very dilute solution ( $\sim$ 0.05 absorbance), **IV** acquires significant PL intensity while **1b** shows hardly any emission. This suggests that the high PL intensity of **IV** in the solution state is due to the strong non-covalent intramolecular interactions and not due to aggregation or intermolecular interactions. Thus, luminescence enhancement of nanoclusters can be obtained by modifying the ligands which help in the confinement of



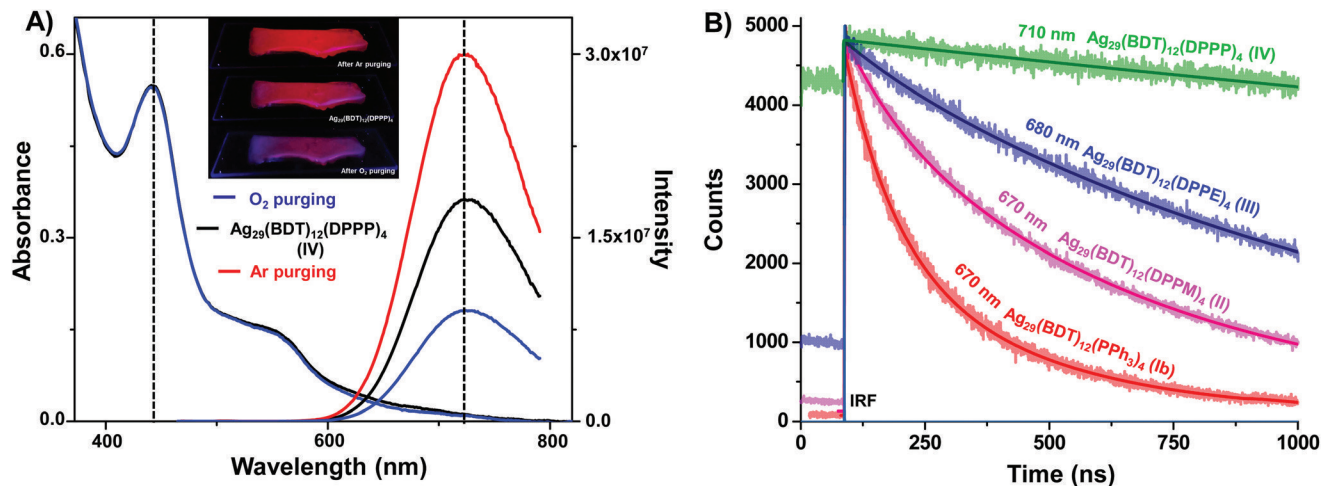
**Fig. 5** Non-covalent intramolecular interactions such as the  $\pi\cdots\pi$  interaction between the benzene rings of BDT ligands and the C–H $\cdots\pi$  interaction between the benzene rings of BDT and phosphine ligands of **Ib** (A), **II** (B), **III** (C) and **IV** (D). The DFT calculated structures of **Ib**, **II**, **III** and **IV** presented in Fig. 3 are considered to demonstrate the interactions. Benzene rings of BDT and phosphine ligands are shown in green and blue, respectively. Yellow and orange correspond to 'S' and 'P' atoms. All 'H' atoms are shown in white. Silver atoms are not shown.

electronic wavefunctions.<sup>15</sup> The computational results propose that the luminescence is due to LMCT. Due to the interaction between the benzene rings of phosphine and BDT ligands, ligand to ligand charge transfer (LLCT) also takes place. As further interaction occurs between the diphosphine and BDT ligands, high charge transfer occurs for diphosphine protected clusters which helps in increasing the PL intensity. The enhanced luminescence in solution is further enhanced in the solid state due to the intercluster interaction. Along with the pronounced emission, cluster **IV** shows a  $\sim 60$  nm red-shifted emission compared to **Ib** (Fig. 2). For **II** and **III**, emission maxima are  $\sim 10$  and  $\sim 15$  nm red-shifted, respectively. Also, small blue-shifts were observed in the absorption maxima of **II**, **III** and **IV** (Fig. 1A). This is mainly due to the distortion in the cluster core ( $\text{Ag}_{13}$ ) arising due to the modifications of phosphine ligands (Fig. S8†). The icosahedral  $\text{Ag}_{13}$  core is highly symmetric in **Ib** (as **Ib** is having a centre of inversion, hence centrosymmetric) which is clearly manifested in Fig. S8A.† The structure looks exactly the same while viewing through the cartesian coordinates, X, Y and Z (*a*, *b* and *c*, respectively). But, the symmetry is disrupted in the case of clusters **II**, **III** and **IV** (see Fig. S8B, C and D†). Cluster **IV** exhibits a highly asymmetric core which resulted in the largest shift in the absorption and emission maxima. Due to the asymmetric metal core and ligands, the total structures of **II**, **III** and **IV** become asymmetric. In the centrosymmetric system, some of the transitions are forbidden (Laporte rule). Therefore, in the asymmetric clusters (**II**, **III** and **IV**), these forbidden transitions become allowed which result in PL enhancement.

### Applications in sensing

Such luminescence has enormous utility in sensing. In the present work, this property was used for the sensing of  $\text{O}_2$  gas which is demonstrated in Fig. 6A. Gaseous  $\text{O}_2$  was purged through the cluster solution for a few seconds and the absorption and emission spectra were obtained which are shown in Fig. 6A (the black spectrum corresponds to **IV**). No change in the absorption spectrum was observed (blue spectrum), but the emission intensity decreased drastically. The solution was then purged with Ar which resulted in PL enhancement keeping the absorption spectrum unchanged (red spectrum in Fig. 6A). Also,  $\text{N}_2$  and  $\text{CO}_2$  gases were used for purging which also showed a similar kind of PL enhancement (Fig. S9A and B†). The cluster showed luminescence quenching even in the solid state upon exposure to  $\text{O}_2$ . The inset of Fig. 6A reveals that cluster coated polystyrene shows an intense luminescence under UV light but when  $\text{O}_2$  was exposed through a balloon, it showed luminescence quenching. With increasing  $\text{O}_2$  concentration, the PL intensity decreased gradually (see Fig. S9C†). An investigation of the reason behind the selective sensing of  $\text{O}_2$  by the cluster led us to the conclusion that the luminescence is actually phosphorescence in nature. Purging of  $\text{N}_2$ ,  $\text{CO}_2$  and Ar gases helped in the removal of dissolved  $\text{O}_2$  from the solution which resulted in PL enhancement.  $d^6$ ,  $d^8$  and  $d^{10}$  heavy metal complexes are known to be triplet emitters (phosphorescent complexes).<sup>53</sup> These metal clusters can also be compared with their metal complexes. Due to the strong metal induced spin-orbit coupling, mixing of singlet-triplet states





**Fig. 6** (A) The optical absorption spectra and PL spectra of IV (black) after oxygenating and deoxygenating the cluster solution by purging O<sub>2</sub> (blue) and Ar (red), respectively. While the absorption spectrum does not show any change, luminescence changes drastically with and without O<sub>2</sub>. (B) Nanosecond resolved decay of Ib, II, III and IV at ( $\lambda_{\text{ex}}$  = 409 nm) for emission maxima i.e., at 670, 670, 680 and 710 nm, respectively.

increased which eliminated the spin-forbidden nature of the radiative relaxation of the triplet state, thus enhancing phosphorescence emission at room temperature. The phosphorescence wavelength, lifetime and quantum yield depend strongly on the nature of ligands. In the present work, the singlet-triplet overlap increases with an increase in carbon chain length, resulting in an enhancement of the PL intensity.

### Lifetime studies

PL lifetimes of the clusters were monitored by using time resolved spectroscopy. Fig. 6B shows the PL decay transients of clusters **Ib**, **II**, **III** and **IV** at their corresponding PL maxima of ~660, ~670, ~680 and ~710 nm, respectively, using excitation at 409 nm. Cluster **Ib** shows bi-exponential fluorescence relaxation with a faster component of 99.65 ns and a slower component of 336.49 ns. The average lifetime of **Ib** is found to be 215 ns. Similarly, clusters **II** (108.44 and 589.95 ns) and **III** (120 and 1133.47 ns) exhibit two lifetime components while **IV** (6196.04 ns) displays only one lifetime component. The average lifetime for the cluster has been observed to be increased gradually from ~215 ns for **Ib** to ~6.2  $\mu$ s for **IV**. Lifetime values of all the clusters are given in Table S2 (see the ESI†). The bi-exponential decay for clusters **Ib**, **II** and **III** indicates that there is some non-radiative process along with the radiative process. As the chain length between the diphosphines increases, the contribution of the faster component decreases (51%, 17% and 4%, respectively) which corroborates that the non-radiative process is decreasing (see Table S2†). The increase in average lifetime upon ligand exchange corroborates the enhanced radiative process (phosphorescence) due to the formation of a rigid and energetically more stable cluster. In the case of phosphorescence, the radiative decay occurs from an excited triplet state back to a singlet state, where the triplet state is formed by non-radiative conversion from the excited singlet state (intersystem crossing). As spin/orbit interactions are feasible in heavy atom containing mole-

cules and thus, a change in spin is more favorable in the metal cluster. Hence, upon substituting PPh<sub>3</sub> by diphosphines, the rate of spin-orbit coupling increases and this leads to a reduction in the non-radiative process. So, the rate of ISC increases as phosphines are substituted by diphosphines. This finding is consistent with the results obtained by our PL and computational studies. The picosecond resolved decay of clusters was measured at their emission maxima.

### PL enhancement in the monophosphine substituted clusters

To compare the PL enhancement of [Ag<sub>29</sub>(BDT)<sub>12</sub>(X)<sub>4</sub>]<sup>3-</sup> in the presence of diphosphines and monophosphines, clusters were synthesized using *para*-substituted PPh<sub>3</sub> ligands such as TTP, TFPP and TCPP (**V**, **VI** and **VII**). The clusters were synthesized following the LE method explained in the ESI.† The absorption spectra of **V**, **VI** and **VII** (red, blue and pink, respectively) are shown in Fig. 7A and the data are comparable to those of **Ib** (black). The PL spectra are shown in Fig. 7B which manifest the increment of the PL intensity of the Ag<sub>29</sub> cluster upon replacing PPh<sub>3</sub> with TTP, TFPP and TCPP. The PL enhancement of **V**, **VI** and **VII** is 3, 5 and 5 times, respectively, with respect to **Ib** (QYs are 2.7%, 4.5% and 4.5%, respectively). The ESI MS of these clusters are shown in Fig. S10,† which show the attachment of four phosphine ligands to each cluster and hence confirm their atomicity. The PL enhancement of **V** can be attributed to the increase in mass which helps in increasing the rate of intersystem crossing (ISC). Halogen atoms are known to increase the rate of the ISC process and hence PL intensities are enhanced in the case of **VI** and **VII**.

### PL enhancement of [Ag<sub>51</sub>(BDT)<sub>19</sub>(PPh<sub>3</sub>)<sub>3</sub>]<sup>3-</sup>

Similar kinds of experiments were done using another known cluster, [Ag<sub>51</sub>(BDT)<sub>19</sub>(PPh<sub>3</sub>)<sub>3</sub>]<sup>3-</sup> (**VIII**), having similar protecting ligands (BDT and PPh<sub>3</sub>). We synthesized three diphosphine (DPPM, DPPE and DPPP) protected Ag<sub>51</sub> clusters, **IX**, **X** and **XI** (detailed synthetic processes are given in the ESI†). The

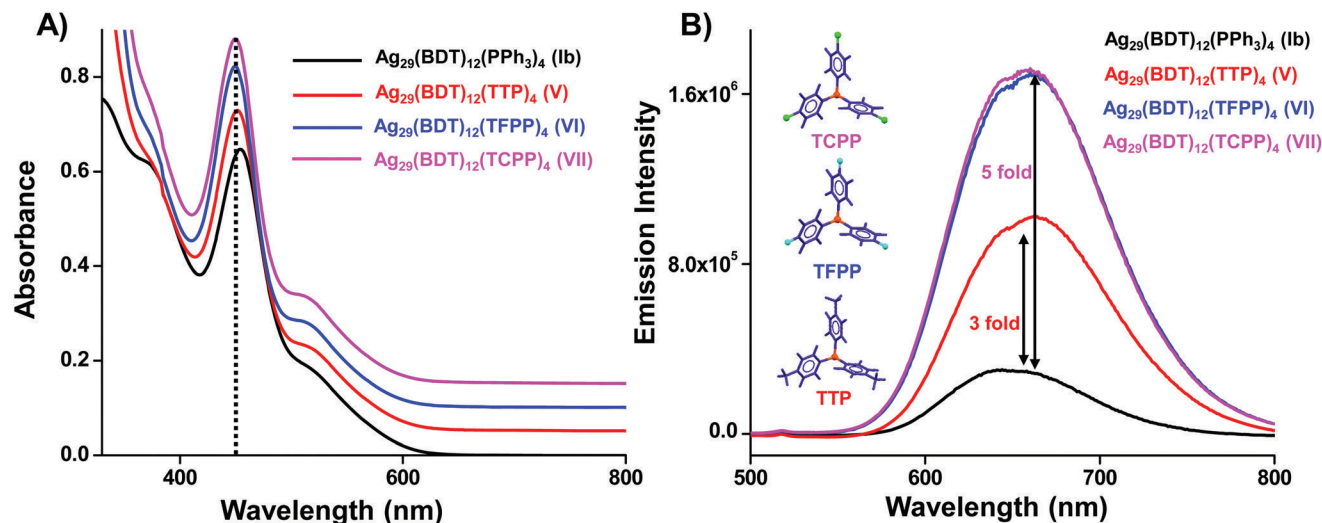


Fig. 7 (A) UV-vis absorption spectra and (B) the excitation-emission spectra (under  $\sim 446$  nm excitation) of Ib, V, VI and VII. Cluster V shows a 3 fold PL improvement compared to that of Ib while a 5 fold enhancement was observed for VI and VII.

absorption and the emission spectra of these clusters are shown in Fig. S11,<sup>†</sup> which are almost similar to VIII proving that the structure and atomicity remained the same in all the clusters. The emission spectra show a 3, 7 and 17 fold PL enhancement for IX, X and XI, respectively (QYs of VIII, IX, X and XI are 0.12%, 0.35%, 0.84% and 2.04%, respectively). Cluster XI also showed PL quenching upon  $O_2$  purging which confirms that the emission process was phosphorescence, similar to that of IV (see Fig. S12<sup>†</sup>).

## Conclusions

In conclusion, we present the synthesis of different phosphine (DPPM, DPPE, DPPP, TTP, TFPP and TCPP) protected  $Ag_{29}$  clusters which are more luminescent than  $[Ag_{29}(BDT)_{12}(PPh_3)_4]^{3-}$ . The luminescence of these clusters can be perceived by the naked eye in the solution state when compared to that of  $[Ag_{29}(BDT)_{12}(PPh_3)_4]^{3-}$ . A detailed analysis is done for  $[Ag_{29}(BDT)_{12}(DPPM)_4]^{3-}$ ,  $[Ag_{29}(BDT)_{12}(DPPE)_4]^{3-}$  and  $[Ag_{29}(BDT)_{12}(DPPP)_4]^{3-}$  using several measurements. Their structures, stability and electronic characteristics are understood from DFT and TD-DFT calculations. Absorption spectra and K-S MOs are calculated. By introducing these diphosphines, the surface rigidity of the clusters is increased *via* the formation of more non-covalent interactions between the ligands ( $\pi \cdots \pi$  and  $C-H \cdots \pi$  interactions). The rigidity of the cluster promotes the radiative transitions by increasing RIR. Hence, these clusters possess longer lifetimes ( $\sim 215$ ,  $\sim 510$ ,  $\sim 1096$  and  $\sim 6196$  ns for  $PPh_3$ , DPPM, DPPE and DPPP protected  $Ag_{29}$ , respectively). The lifetime values for longer chain length phosphines are in the microsecond ( $\mu s$ ) range and also these clusters show PL quenching in the presence of  $O_2$ . Both these observations imply that the PL originates through a phosphorescence process. This process is also enhanced when

heavy ligands are introduced (such as TTP, TFPP and TCPP). A similar kind of PL enhancement is also observed in the case of  $[Ag_{51}(BDT)_{19}(PPh_3)_3]^{3-}$  upon replacing  $PPh_3$  with DPPM, DPPE and DPPP. Selective quenching upon  $O_2$  exposure is used to develop a sensor.

## Conflicts of interest

There are no conflicts to declare.

## Acknowledgements

We thank the Department of Science and Technology, Government of India for supporting our research program. E. K. thanks IIT Madras for an institute doctoral fellowship. P. C. thanks the Council of Scientific and Industrial Research (CSIR) for a research fellowship. A. G., M. B. and J. G. thank the University Grants Commission (UGC) for their fellowships. G. P. thanks the IITM for an Institute Postdoctoral fellowship.

## Notes and references

- 1 R. Jin, C. Zeng, M. Zhou and Y. Chen, *Chem. Rev.*, 2016, **116**, 10346–10413.
- 2 I. Chakraborty and T. Pradeep, *Chem. Rev.*, 2017, **117**, 8208–8271.
- 3 Q. Yao, T. Chen, X. Yuan and J. Xie, *Acc. Chem. Res.*, 2018, **51**, 1338–1348.
- 4 L. Zhang and E. Wang, *Nano Today*, 2014, **9**, 132–157.
- 5 I. Diez and R. H. A. Ras, *Nanoscale*, 2011, **3**, 1963–1970.
- 6 A. Mathew and T. Pradeep, *Part. Part. Syst. Charact.*, 2014, **31**, 1017–1053.

- 7 R. Juarez-Mosqueda, S. Malola and H. Hakkinen, *Phys. Chem. Chem. Phys.*, 2017, **19**, 13868–13874.
- 8 K. L. D. M. Weerawardene, H. Hakkinen and C. M. Aikens, *Annu. Rev. Phys. Chem.*, 2018, **69**, 205–229.
- 9 H. Hakkinen, M. Moseler and U. Landman, *Phys. Rev. Lett.*, 2002, **89**, 033401.
- 10 R. Wang and F. Zhang, *J. Mater. Chem. B*, 2014, **2**, 2422–2443.
- 11 S. Gao, D. Chen, Q. Li, J. Ye, H. Jiang, C. Amatore and X. Wang, *Sci. Rep.*, 2014, **4**, 4384.
- 12 G. Wang, T. Huang, R. W. Murray, L. Menard and R. G. Nuzzo, *J. Am. Chem. Soc.*, 2005, **127**, 812–813.
- 13 M. S. Devadas, J. Kim, E. Sinn, D. Lee, T. Goodson III and G. Ramakrishna, *J. Phys. Chem. C*, 2010, **114**, 22417–22423.
- 14 S. Link, A. Beeby, S. FitzGerald, M. A. El-Sayed, T. G. Schaaff and R. L. Whetten, *J. Phys. Chem. B*, 2002, **106**, 3410–3415.
- 15 B. A. Ashenfelter, A. Desiredy, S. H. Yau, T. Goodson and T. P. Bigioni, *J. Phys. Chem. C*, 2015, **119**, 20728–20734.
- 16 S. H. Yau, B. A. Ashenfelter, A. Desiredy, A. P. Ashwell, O. Varnavski, G. C. Schatz, T. P. Bigioni and T. Goodson, *J. Phys. Chem. C*, 2017, **121**, 1349–1361.
- 17 X. Kang, X. Li, H. Yu, Y. Lv, G. Sun, Y. Li, S. Wang and M. Zhu, *RSC Adv.*, 2017, **7**, 28606–28609.
- 18 Z. Wu and R. Jin, *Nano Lett.*, 2010, **10**, 2568–2573.
- 19 A. Mathew, E. Varghese, S. Choudhury, S. K. Pal and T. Pradeep, *Nanoscale*, 2015, **7**, 14305–14315.
- 20 K. Pyo, V. D. Thanthirige, S. Y. Yoon, G. Ramakrishna and D. Lee, *Nanoscale*, 2016, **8**, 20008–20016.
- 21 K. Pyo, V. D. Thanthirige, K. Kwak, P. Pandurangan, G. Ramakrishna and D. Lee, *J. Am. Chem. Soc.*, 2015, **137**, 8244–8250.
- 22 M. S. Bootharaju, S. M. Kozlov, Z. Cao, A. Shkurenko, A. M. El-Zohry, O. F. Mohammed, M. Eddaoudi, O. M. Bakr, L. Cavallo and J.-M. Basset, *Chem. Mater.*, 2018, **30**, 2719–2725.
- 23 S. Wang, X. Meng, A. Das, T. Li, Y. Song, T. Cao, X. Zhu, M. Zhu and R. Jin, *Angew. Chem., Int. Ed.*, 2014, **53**, 2376–2380.
- 24 G. Soldan, M. A. Aljuhani, M. S. Bootharaju, L. G. AbdulHalim, M. R. Parida, A.-H. Emwas, O. F. Mohammed and O. M. Bakr, *Angew. Chem., Int. Ed.*, 2016, **55**, 5749–5753.
- 25 M. S. Bootharaju, S. M. Kozlov, Z. Cao, M. Harb, M. R. Parida, M. N. Hedhili, O. F. Mohammed, O. M. Bakr, L. Cavallo and J.-M. Basset, *Nanoscale*, 2017, **9**, 9529–9536.
- 26 M. S. Bootharaju, C. P. Joshi, M. R. Parida, O. F. Mohammed and O. M. Bakr, *Angew. Chem., Int. Ed.*, 2016, **55**, 824.
- 27 Y. Li, X. Wang, S. Xu and W. Xu, *Phys. Chem. Chem. Phys.*, 2013, **15**, 2665–2668.
- 28 X. Liu, J. Yuan, C. Yao, J. Chen, L. Li, X. Bao, J. Yang and Z. Wu, *J. Phys. Chem. C*, 2017, **121**, 13848–13853.
- 29 G. Liang, L.-T. Weng, J. W. Y. Lam, W. Qin and B. Z. Tang, *ACS Macro Lett.*, 2014, **3**, 21–25.
- 30 X. Ma, R. Sun, J. Cheng, J. Liu, F. Gou, H. Xiang and X. Zhou, *J. Chem. Educ.*, 2016, **93**, 345–350.
- 31 N. Goswami, Q. Yao, Z. Luo, J. Li, T. Chen and J. Xie, *J. Phys. Chem. Lett.*, 2016, **7**, 962–975.
- 32 Z. Luo, X. Yuan, Y. Yu, Q. Zhang, D. T. Leong, J. Y. Lee and J. Xie, *J. Am. Chem. Soc.*, 2012, **134**, 16662–16670.
- 33 X. Kang, S. Wang, Y. Song, S. Jin, G. Sun, H. Yu and M. Zhu, *Angew. Chem., Int. Ed.*, 2016, **55**, 3611–3614.
- 34 T. Chen, S. Yang, J. Chai, Y. Song, J. Fan, B. Rao, H. Sheng, H. Yu, M. Zhu, T. Chen, S. Yang, J. Chai, Y. Song, J. Fan, B. Rao, H. Sheng, H. Yu and M. Zhu, *Sci. Adv.*, 2017, **3**, e1700956.
- 35 S. Jin, W. Liu, D. Hu, X. Zou, X. Kang, W. Du, S. Chen, S. Wei, S. Wang and M. Zhu, *Chem. – Eur. J.*, 2018, **24**, 3712–3715.
- 36 X. Kang, S. Wang and M. Zhu, *Chem. Sci.*, 2018, **9**, 3062–3068.
- 37 C. P. Joshi, M. S. Bootharaju, M. J. Alhilaly and O. M. Bakr, *J. Am. Chem. Soc.*, 2015, **137**, 11578–11581.
- 38 K. M. Harkness, Y. Tang, A. Dass, J. Pan, N. Kothalawala, V. J. Reddy, D. E. Cliffler, B. Demeler, F. Stellacci, O. M. Bakr and J. A. McLean, *Nanoscale*, 2012, **4**, 4269–4274.
- 39 E. Khatun, A. Ghosh, D. Ghosh, P. Chakraborty, A. Nag, B. Mondal, S. Chennu and T. Pradeep, *Nanoscale*, 2017, **9**, 8240–8248.
- 40 T. Udayabhaskararao, M. S. Bootharaju and T. Pradeep, *Nanoscale*, 2013, **5**, 9404–9411.
- 41 L. G. AbdulHalim, M. S. Bootharaju, Q. Tang, S. Del Gobbo, R. G. AbdulHalim, M. Eddaoudi, D.-E. Jiang and O. M. Bakr, *J. Am. Chem. Soc.*, 2015, **137**, 11970–11975.
- 42 A. Ghosh, D. Ghosh, E. Khatun, P. Chakraborty and T. Pradeep, *Nanoscale*, 2017, **9**, 1068–1077.
- 43 L. Gell, L. Lehtovaara and H. Hakkinen, *J. Phys. Chem. A*, 2014, **118**, 8351–8355.
- 44 X. Kang, M. Zhou, S. Wang, S. Jin, G. Sun, M. Zhu and R. Jin, *Chem. Sci.*, 2017, **8**, 2581–2587.
- 45 M. J. Alhilaly, M. S. Bootharaju, C. P. Joshi, T. M. Besong, A.-H. Emwas, R. Juarez-Mosqueda, S. Kaappa, S. Malola, K. Adil, A. Shkurenko, H. Hakkinen, M. Eddaoudi and O. M. Bakr, *J. Am. Chem. Soc.*, 2016, **138**, 14727–14732.
- 46 H. Yang, Y. Wang, X. Chen, X. Zhao, L. Gu, H. Huang, J. Yan, C. Xu, G. Li, J. Wu, A. J. Edwards, B. Dittrich, Z. Tang, D. Wang, L. Lehtovaara, H. Hakkinen and N. Zheng, *Nat. Commun.*, 2016, **7**, 12809.
- 47 W. Du, S. Jin, L. Xiong, M. Chen, J. Zhang, X. Zou, Y. Pei, S. Wang and M. Zhu, *J. Am. Chem. Soc.*, 2017, **139**, 1618–1624.
- 48 M. Sugiuchi, J. Maeba, N. Okubo, M. Iwamura, K. Nozaki and K. Konishi, *J. Am. Chem. Soc.*, 2017, **139**, 17731–17734.
- 49 K. L. D. M. Weerawardene, E. B. Guidez and C. M. Aikens, *J. Phys. Chem. C*, 2017, **121**, 15416–15423.
- 50 J. J. Mortensen, L. B. Hansen and K. W. Jacobsen, *Phys. Rev. B: Condens. Matter Mater. Phys.*, 2005, **71**, 035109.
- 51 J. P. Perdew, K. Burke and M. Ernzerhof, *Phys. Rev. Lett.*, 1996, **77**, 3865–3868.
- 52 A. Baksi, A. Ghosh, S. K. Mudedla, P. Chakraborty, S. Bhat, B. Mondal, K. R. Krishnadas, V. Subramanian and T. Pradeep, *J. Phys. Chem. C*, 2017, **121**, 13421–13427.
- 53 V. Sathish, A. Ramdass, P. Thanasekaran, K.-L. Lu and S. Rajagopal, *J. Photochem. Photobiol., C*, 2015, **23**, 25–44.

**Electronic Supplementary Information (ESI) for the paper**

**Thirty-fold photoluminescence enhancement induced by secondary ligands  
in monolayer protected silver clusters**

Esma Khatun<sup>a</sup>, Atanu Ghosh<sup>a</sup>, Papri Chakraborty<sup>a</sup>, Priya Singh<sup>b</sup>, Mohammad Bodiuzzaman<sup>a</sup>,  
Ganesan Paramasivam<sup>a</sup>, Ganapati Nataranjan<sup>a</sup>, Jyotirmoy Ghosh<sup>a</sup>, Samir Kumar Pal<sup>b</sup> and  
Thalappil Pradeep<sup>a\*</sup>

a. *Department of Chemistry, DST Unit of Nanoscience (DST UNS) and Thematic Unit of  
Excellence (TUE)*

*Indian Institute of Technology Madras*

*Chennai, 600 036, India*

b. *Department of Chemical Biological & Macromolecular Sciences, S. N. Bose National  
Centre for Basic Sciences, Block JD, Sector III, Salt Lake, Kolkata 700098, India*

E-mail: [pradeep@iitm.ac.in](mailto:pradeep@iitm.ac.in)

**Table of Contents**

<b>Description</b>	<b>Page number</b>
Synthesis of [Ag <sub>29</sub> (BDT) <sub>12</sub> ] and [Ag <sub>29</sub> (BDT) <sub>12</sub> (X) <sub>4</sub> ] where X= PPh <sub>3</sub> , DPPM, DPPE, DPPP, TTP, TFPP and TCPP	<b>3-4</b>
Synthesis of [Ag <sub>51</sub> (BDT) <sub>19</sub> (PPh <sub>3</sub> ) <sub>3</sub> ]	<b>4</b>
Synthesis of [Ag <sub>51</sub> (BDT) <sub>19</sub> (X) <sub>3</sub> ] where X= DPPM, DPPE and DPPP	<b>4</b>
Quantum yield measurements	<b>4-5</b>
Computational methods	<b>5-6</b>



List of figures	Description	Page number
<b>S1</b>	Expanded region of the ESI MS of $[\text{Ag}_{29}(\text{BDT})_{12}]^{3-}$ (A) and other peaks (B)	<b>6-7</b>
<b>S2</b>	The NMR spectra of $[\text{Ag}_{29}(\text{BDT})_{12}(\text{X})_4]$ (where X= PPh <sub>3</sub> , DPPM, DPPE and DPPP)	<b>8</b>
<b>S3</b>	XPS spectra of $[\text{Ag}_{29}(\text{BDT})_{12}(\text{X})_4]$ (where X= PPh <sub>3</sub> , DPPM, DPPE and DPPP) (A), time dependent absorption spectra of <b>Ib</b> and <b>IV</b> (B) and cone voltage dependent ESI MS of <b>Ib</b> and <b>IV</b> (C)	<b>9-10</b>
<b>S4</b>	UV-vis absorption and emission spectra of $[\text{Ag}_{29}(\text{BDT})_{12}(\text{PPh}_3)_4]$ , $[\text{Ag}_{29}(\text{BDT})_{12}(\text{DPPM})_4]$ and $[\text{Ag}_{29}(\text{BDT})_{12}(\text{DPPE})_4]$ before and after DPPM, DPPE and PPh <sub>3</sub> addition	<b>11-12</b>
<b>S5</b>	The theoretical absorption spectra of $[\text{Ag}_{29}(\text{BDT})_{12}(\text{X})_4]$ (where X= PPh <sub>3</sub> , DPPM, DPPE and DPPP)	<b>13</b>
<b>S6</b>	The shape of the K-S MOs of <b>Ib</b> (A), <b>II</b> (B) and <b>III</b> (C) which denote the strongest electronic transitions related to peak 1 and 2.	<b>14</b>
<b>Table S1</b>	The list of MO transitions of $[\text{Ag}_{29}(\text{BDT})_{12}(\text{X})_4]$ (where X= PPh <sub>3</sub> , DPPM, DPPE and DPPP) correspond to the absorption maxima (A) and absorption onset (B). (C) The MO transitions related to lower energy peaks of $[\text{Ag}_{29}(\text{BDT})_{12}(\text{X})_4]$ (X = PPh <sub>3</sub> and DPPP)	<b>15-17</b>
<b>S7</b>	DLS particle size distribution of $[\text{Ag}_{29}(\text{BDT})_{12}(\text{PPh}_3)_4]$ and $[\text{Ag}_{29}(\text{BDT})_{12}(\text{DPPP})_4]$ at higher and lower concentrations and PL spectra observed at lower concentration	<b>17</b>
<b>S8</b>	The Ag <sub>13</sub> icosahedral metal core of $[\text{Ag}_{29}(\text{BDT})_{12}(\text{X})_4]$ (where X= PPh <sub>3</sub> , DPPM, DPPE and DPPP)	<b>18</b>
<b>S9</b>	The emission spectra of $[\text{Ag}_{29}(\text{BDT})_{12}(\text{DPPP})_4]$ after purging N <sub>2</sub> and CO <sub>2</sub>	<b>19</b>

<b>Table S2</b>	The lifetime values of $[\text{Ag}_{29}(\text{BDT})_{12}(\text{X})_4]$ (where X= $\text{PPh}_3$ , DPPM, DPPE and DPPP)	<b>20</b>
<b>S10</b>	ESI MS of $[\text{Ag}_{29}(\text{BDT})_{12}(\text{X})_4]$ where X= $\text{PPh}_3$ , TTP, TFPP and TCPP	<b>20</b>
<b>S11</b>	UV-vis absorption and emission spectra of $[\text{Ag}_{51}(\text{BDT})_{19}(\text{X})_3]$ (where X= $\text{PPh}_3$ , DPPM, DPPE and DPPP)	<b>21</b>
<b>S12</b>	UV-vis absorption (A) and emission (B) spectra of <b>XI</b> before (black) and after (red) $\text{O}_2$ purging.	<b>21</b>

**Synthesis of  $[\text{Ag}_{29}(\text{BDT})_{12}]$  (**Ia**) and  $[\text{Ag}_{29}(\text{BDT})_{12}(\text{X})_4]$  (where, X:  $3\text{PPh}_3$ , DPPM, DPPE, DPPP, TTP, TFPP and TCPP) (**Ib**, **II**, **III**, **IV**, **V**, **VI** and **VII**, respectively)**

For the synthesis of  $[\text{Ag}_{29}(\text{BDT})_{12}(\text{PPh}_3)_4]$  (**Ib**), ~20 mg of  $\text{AgNO}_3$  was dissolved in MeOH (5 mL) and then DCM (~9 mL) was added to the solution.<sup>1</sup> The solution was then kept for stirring. After ~5 min, 13.5  $\mu\text{L}$  of 1,3-BDT was added which resulted in the formation of a yellow colored silver-thiolate complex. Then, ~200 mg of  $\text{PPh}_3$  (in 0.5 mL of DCM) was added to the reaction mixture after 5 min. A colorless silver-thiolate-phosphine complex was formed which was further reduced by ~11 mg of  $\text{NaBH}_4$  (in 0.5 mL of ice-cold  $\text{H}_2\text{O}$ ), turning the color of the solution to dark brown and then bright orange. The reaction mixture was kept at room temperature under stirring for 3 h in dark. After completion of the reaction, the precipitate was collected by centrifuging the mixture, and the supernatant was discarded. The precipitate was then washed thrice with methanol to remove the unreacted by-products and the orange colored cluster was extracted with DMF. The  $[\text{Ag}_{29}(\text{BDT})_{12}]$  (**Ia**) cluster was synthesized following the same synthetic method without the  $\text{PPh}_3$  ligand.

For the synthesis of  $[\text{Ag}_{29}(\text{BDT})_{12}(\text{DPPM}/\text{DPPE}/\text{DPPP})_4]$  (**II**, **III** and **IV**), the above-mentioned procedure was used. In these cases, ~50 mg of DPPM/DPPE/DPPP and ~22.5 mg of  $\text{NaBH}_4$  were used. After 3 h of reaction, clear reddish orange color solutions were formed which were first concentrated under rotavapor and then the clusters were precipitated using MeOH. The precipitates were collected

after centrifugation and washed repeatedly using MeOH. The clusters were then dissolved in DCM, DMF etc.

In spite of direct synthesis method,  $[\text{Ag}_{29}(\text{BDT})_{12}(\text{X})_4]$  where,  $\text{X} = \text{PPh}_3$ , DPPM, DPPE, DPPP (**II**, **III** and **IV**) were also synthesized by ligand addition method from **Ia** and **Ib**. In this case, the absorbance of the stock solution of **Ia**/ **Ib** was kept at  $\sim 0.07$  absorbance (at 450 nm) and 5 mg of  $\text{PPh}_3$ , DPPM, DPPE, DPPP were added in 3 mL of cluster solution, respectively. Following the ligand exchange (LE) method **V**, **VI** and **VII** were synthesized from **Ib**.

#### Synthesis of $[\text{Ag}_{51}(\text{BDT})_{19}(\text{PPh}_3)_3]$ (**VIII**)

The cluster was synthesized adopting an already reported method.<sup>2</sup> About 20 mg of  $\text{AgNO}_3$  was dissolved in 5 mL of methanol and then 9 mL of  $\text{CHCl}_3$  was added. After few mins,  $\sim 13.5 \mu\text{L}$  of BDT (0.5 mL of  $\text{CHCl}_3$ ) was added to the solution. After 5 min of stirring in dark,  $\sim 200$  mg of  $\text{PPh}_3$  (in 0.5 mL of  $\text{CHCl}_3$ ) was added to the mixture. Then, 0.5 mL of an ice-cold aqueous solution containing  $\sim 11$  mg of  $\text{NaBH}_4$  was added which resulted in the immediate color change of the solution from colorless to dark brown. The reaction was kept for 3 h under dark. Then, the supernatant (green color) was collected by centrifugation (for 10 min at high speed) and the concentrated solution was collected by rotary evaporation. The cluster was precipitated using hexane after washing several times with mQ water. Then the precipitate was collected by centrifugation and dissolved in DMF for further characterizations.

#### Ligand exchange (LE) synthesis of $[\text{Ag}_{51}(\text{BDT})_{19}(\text{X})_3]$ (where, $\text{X}$ : DPPM, DPPE, DPPP) (**IX**, **X** and **XI**)

The **IX**, **X** and **XI** clusters were synthesized by ligand exchange method from **VIII** using DPPM, DPPE, and DPPP.

#### Quantum yield (QY) measurements

Luminescence QYs of as-synthesized  $\text{Ag}_{29}$  clusters using different phosphines (**II**, **III**, **IV**, **V**, **VI** and **VII**) were determined by the integrated luminescence intensity method by comparing the PL emission

with the **Ib** (QY is 0.9%). The luminescence of a sample can be written in a formula with related parameters

$$F = K\phi C\sigma lI$$

where ‘F’ is the PL QY of the sample, ‘C’ is the number density of fluorophores (concentration of the sample), ‘ $\sigma$ ’ is the one-photon absorption cross section, ‘l’ is the path length traversed by photons are absorbed, ‘I’ is the flux of incident photons (photons cm<sup>-2</sup> s), ‘F’ is the integrated luminescence signal in the emission region, and ‘K’ is an instrumental parameter. The samples were excited at ~450 nm wavelength and all experimental conditions were kept constant. Then the QY of clusters can be measured using following formula,

$$\phi_s = \frac{F_s}{C_s \sigma_s} \times \frac{C_r \sigma_r}{F_r} \times \phi_r$$

where ‘s’ and ‘r’ refer to clusters and the reference, respectively. ‘C $\sigma$ ’ represents absorption of the sample hence, replaced by ‘A’ where A is the absorbance at excitation wavelength. Thus, the formula can be rewritten as,

$$\phi_s = \frac{F_s}{A_s} \times \frac{A_r}{F_r} \times \phi_r$$

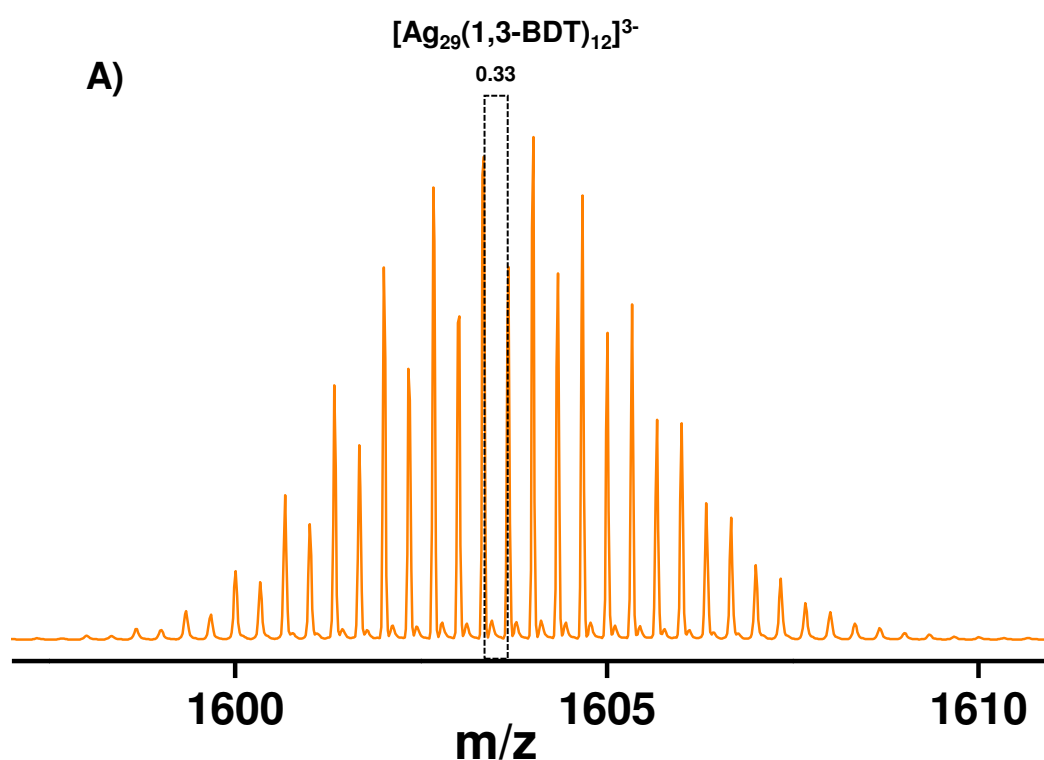
The absorbance of all the samples along with the reference were measured at ~446 nm and were set as 0.07. After that, luminescence intensities of the samples were measured.

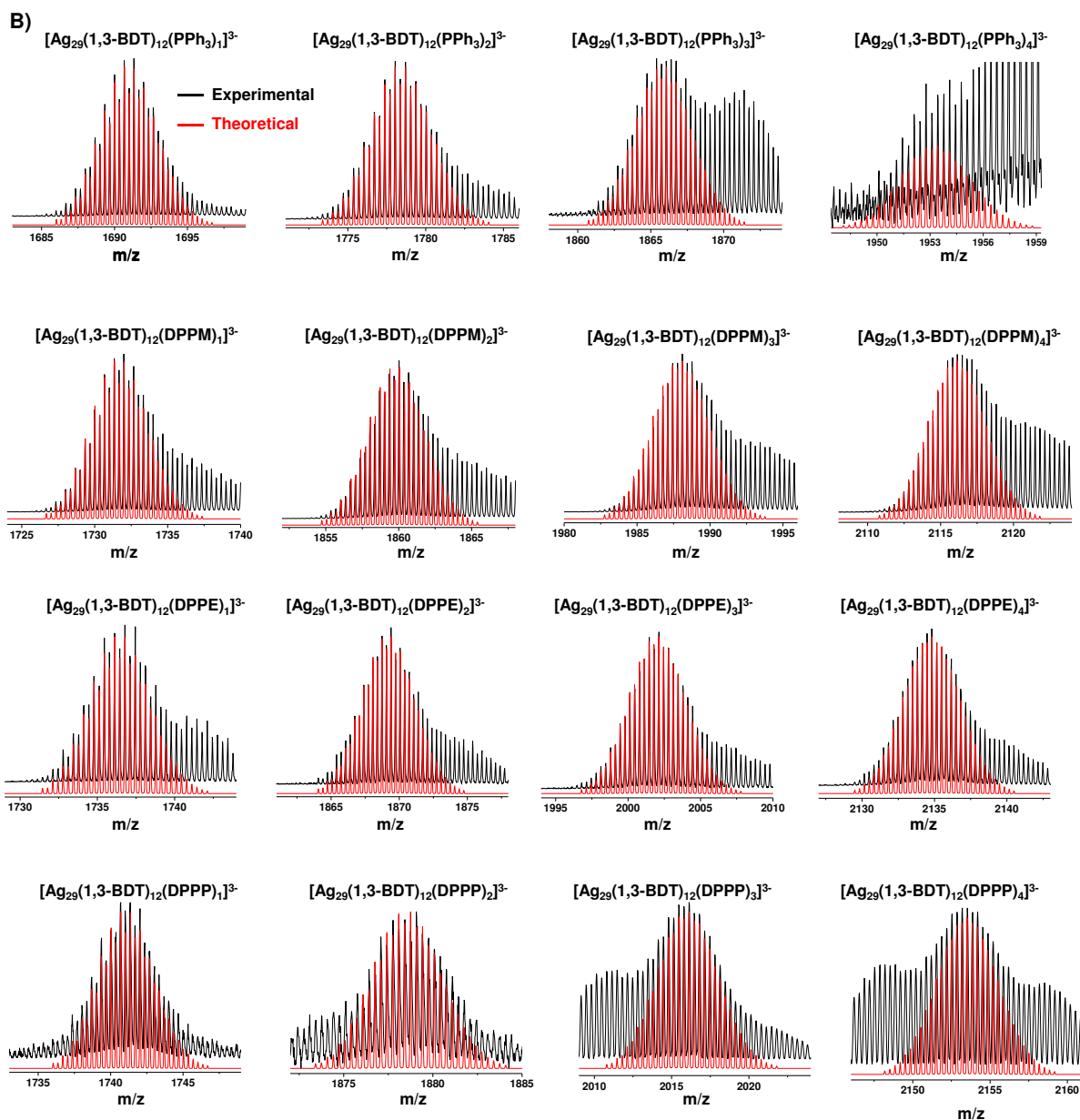
### Computational details

The structural, electronic and optical properties such as optical absorption and emission of **Ib**, **II**, **III** and **IV** were calculated using density functional theory (DFT), as implemented in Grid-Based Projector Augmented Wave method (GPAW).<sup>3, 4</sup> To include only the interactions of the valence electrons, the PAW setup was considered as Ag(4d<sup>10</sup>5s<sup>1</sup>5p<sup>6</sup>), S(3s<sup>2</sup>3p<sup>4</sup>), P(3s<sup>2</sup>3p<sup>3</sup>), C(2s<sup>2</sup>2p<sup>2</sup>) and H(1s<sup>1</sup>) with scalar-relativistic effects included for Ag. The geometry optimizations of all clusters were performed using PBE exchange functional<sup>5</sup> in real-space finite difference (FD) mode in GPAW.<sup>51</sup> having a grid spacing of 0.2 Å and the convergence criterion for the forces on each atoms was set to 0.05 eV/Å. The initial

structures of **1b** was from the reported crystal structure and the other structures were build up by addition of different diphosphines. Also, the above optimized structures were re-optimized after simplification by replacing each benzene ring of the phosphine ligands by a reduced methyl (CH<sub>3</sub>) model ligand, in order to greatly reduce the computational cost and time in time-dependent DFT (TDDFT) calculations. Further, these structures were taken for the investigation of electronic, optical absorption and emission properties. The optical absorption spectra were calculated by time-dependent DFT (TDDFT) using GPAW.<sup>6</sup> The calculated emission spectra were plotted with a Gaussian width of 0.05 eV. All visualizations were created with Visual Molecular Dynamics (VMD) software.<sup>7</sup>

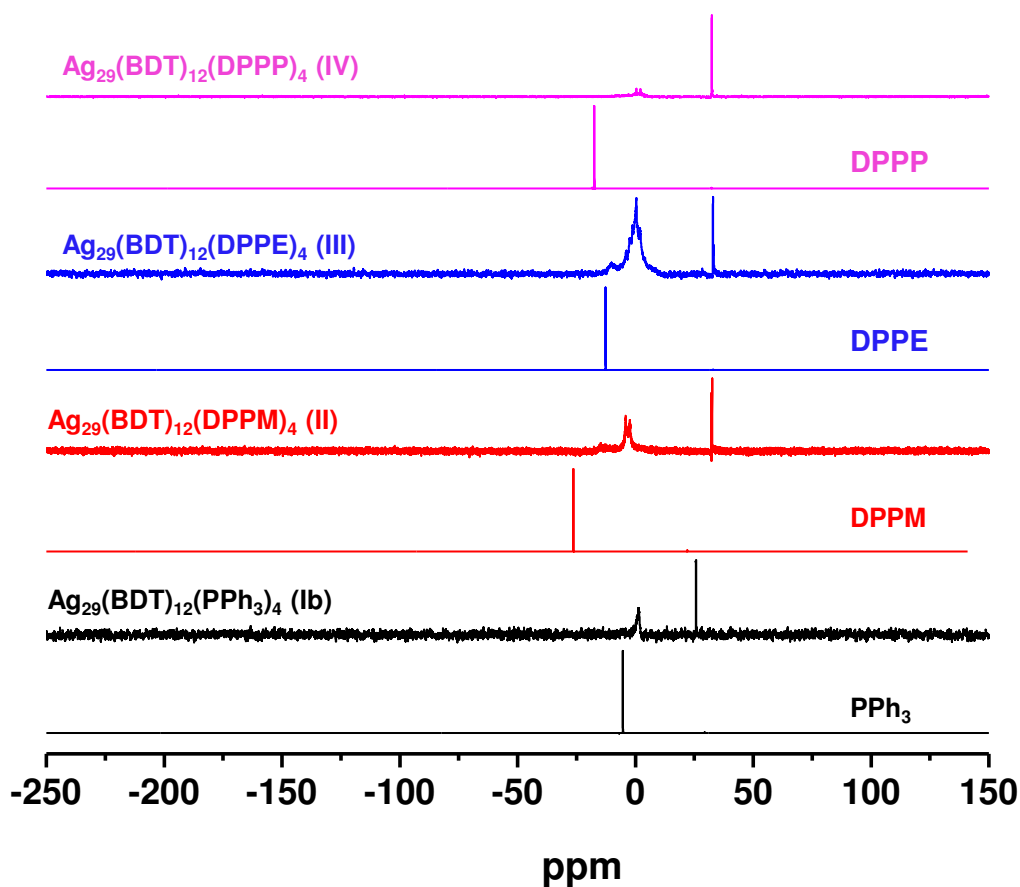
### Supplementary information 1





**Fig. S1** (A) The expanded ESI MS of **Ia** ( $m/z$  1603). The isotopic distribution shows that the separation between two peaks is 0.33 which denotes  $3^-$  charge state of the cluster. (B) The theoretical (red) and experimental (black) spectra of **Ib**, **II**, **III** and **IV**. The experimental spectra in some regions overlap with other features due to other species or their fragments.

## Supplementary information 2

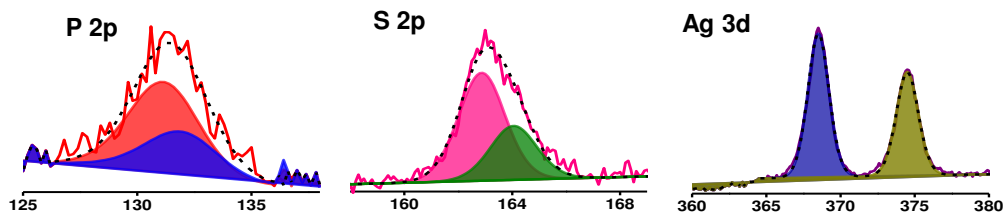


**Fig. S2** The NMR spectra of **Ib** (black), **II** (red), **III** (blue) and **IV** (pink). Corresponding phosphine ligands,  $\text{PPh}_3$ , DPPM, DPPE and DPPP show  $^{31}\text{P}$  peaks at -5.3, -26.2, -12.7 and -17.2 ppm, respectively and the corresponding clusters, **Ib**, **II**, **III** and **IV** display peaks at ~ 1.4, -3.3, -0.1, 0.4 ppm, respectively which confirm the formation of Ag-P bonds.

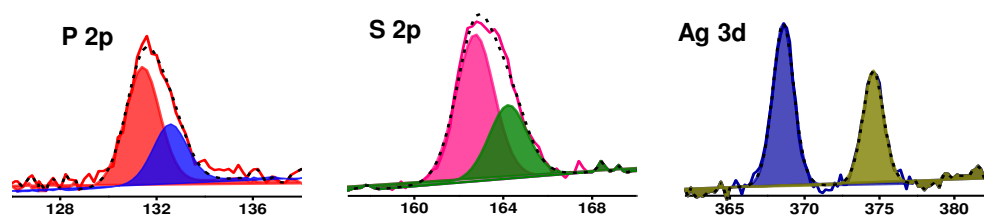


# Supplementary information 3

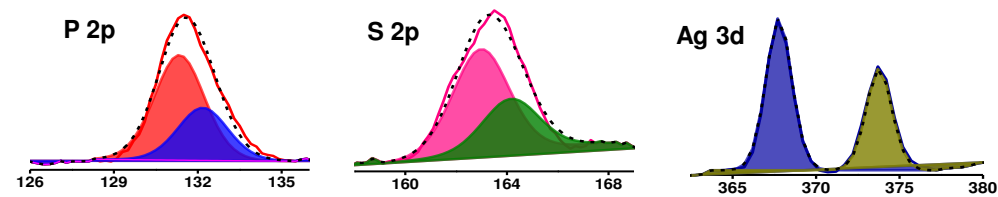
## A) $\text{Ag}_{29}@\text{PPh}_3$ (Ib)



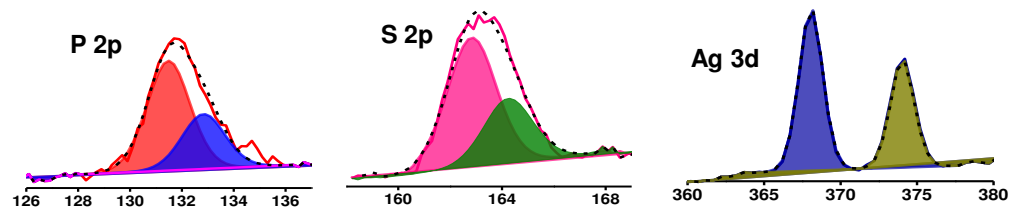
## $\text{Ag}_{29}@\text{DPPM}$ (II)



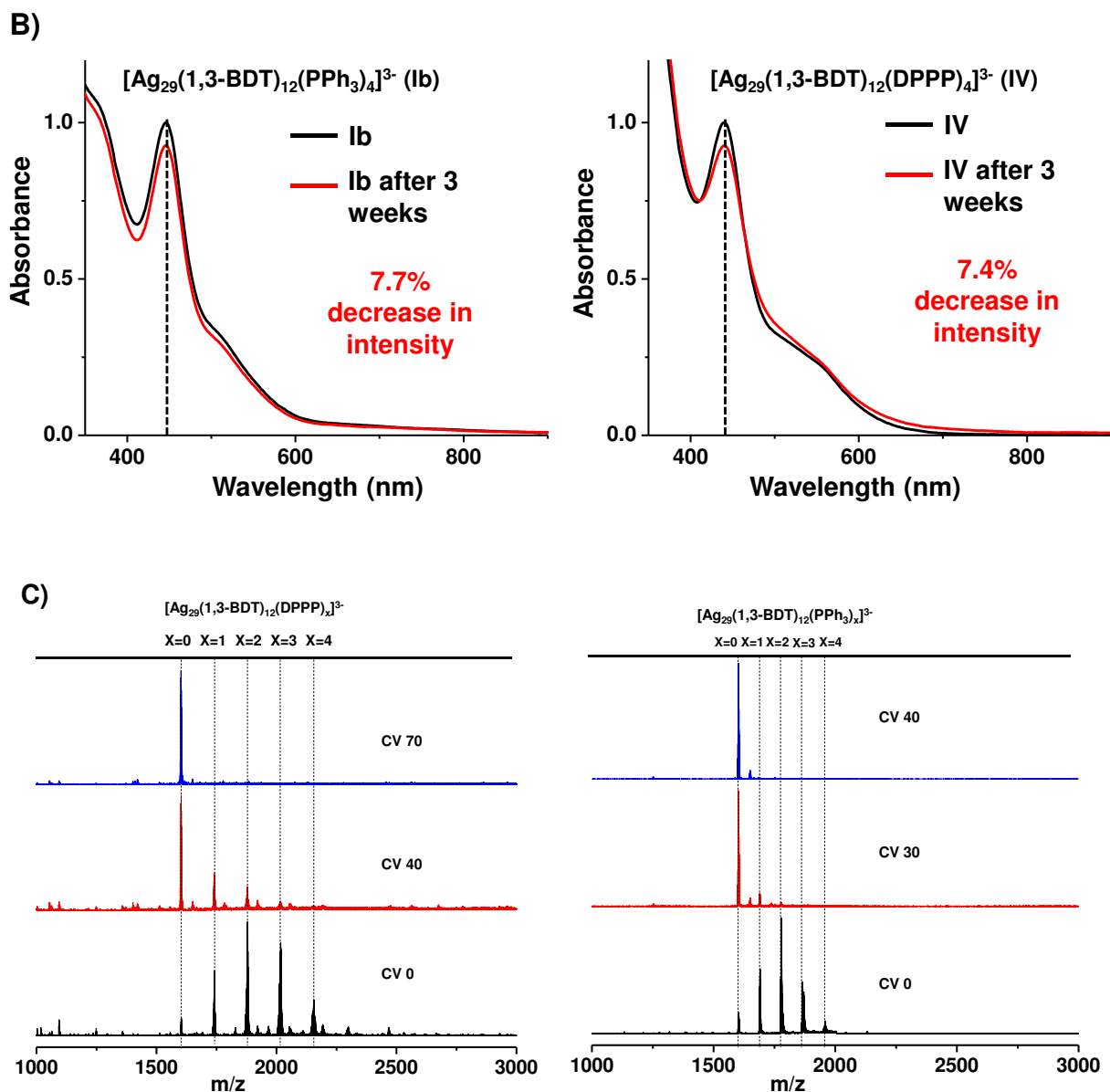
## $\text{Ag}_{29}@\text{DPPE}$ (III)



## $\text{Ag}_{29}@\text{DPPP}$ (IV)

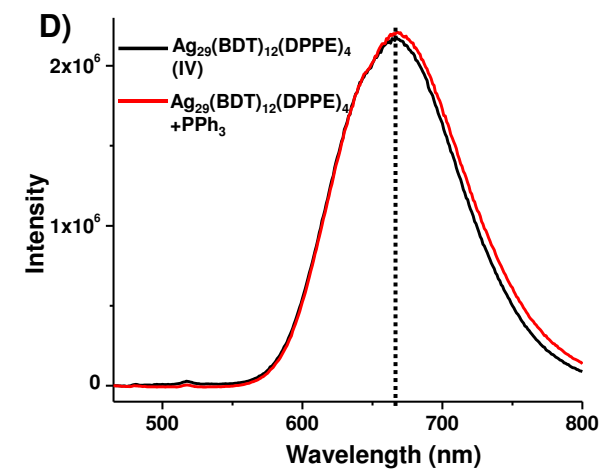
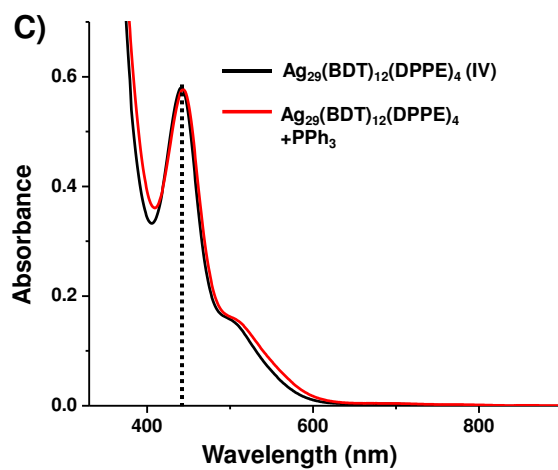
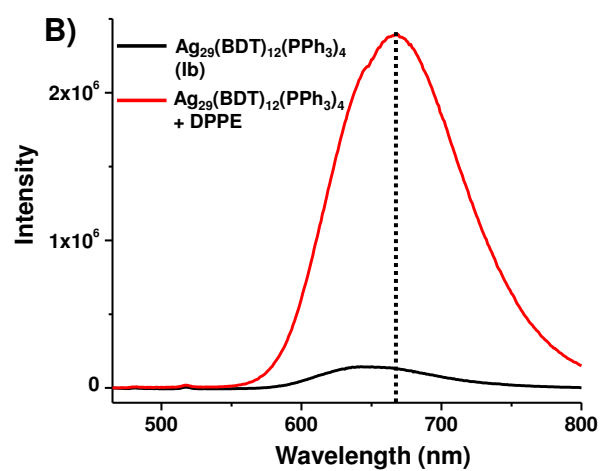
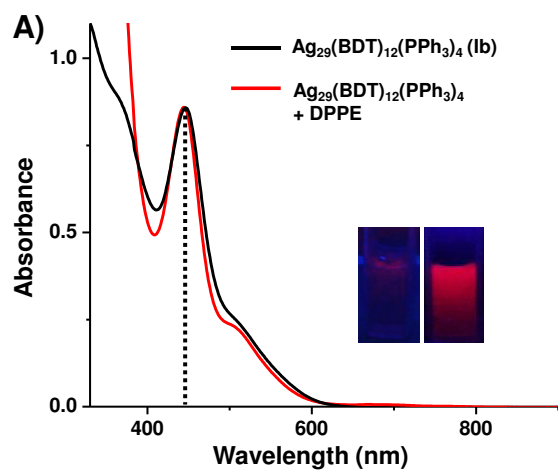


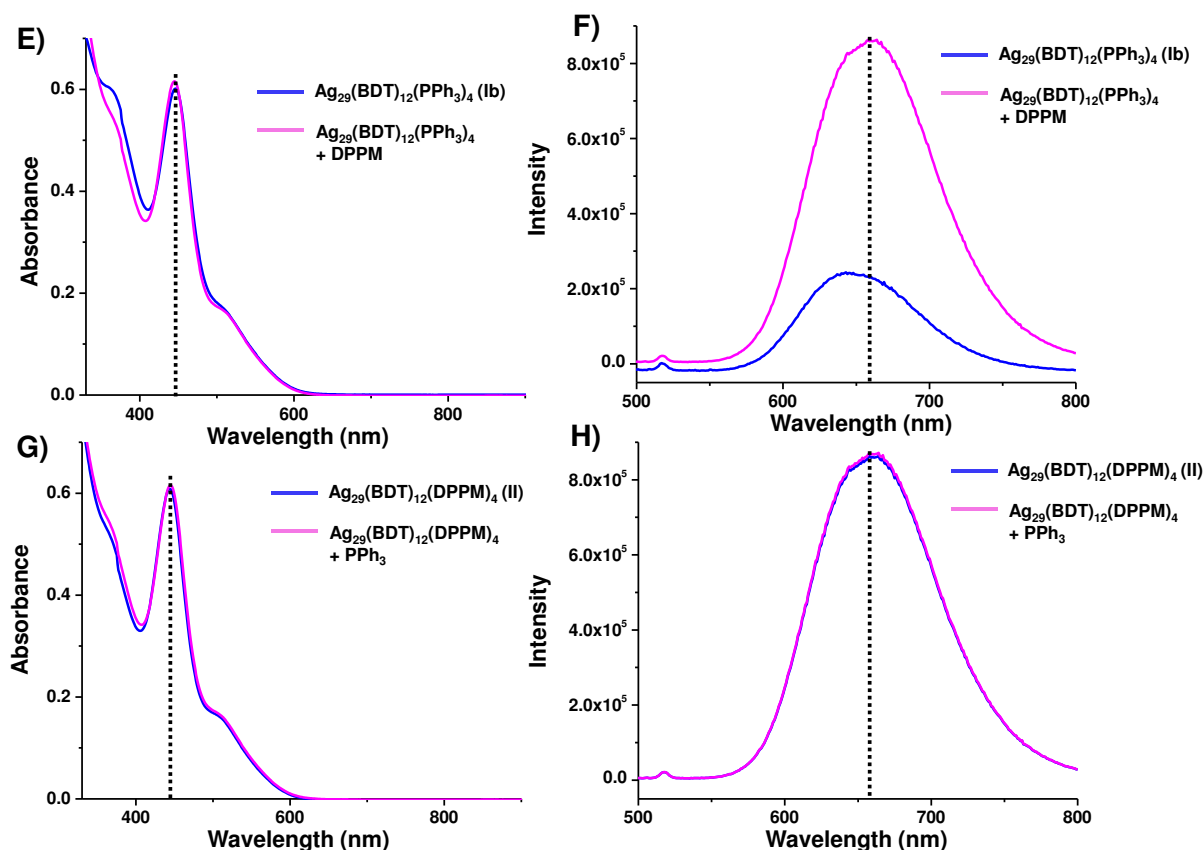
————— BE (eV) —————→



**Fig. S3** (A) XPS spectra of **Ib**, **II**, **III** and **IV**. All clusters exhibit peaks corresponding to Ag 3d, S 2p and P 2p. (B) The time-dependent absorption spectra of **Ib** and **IV** after 3 weeks. The decrease in intensity is almost the same in both the clusters (7.7% and 7.4% for **Ib** and **IV**, respectively). (C) The cone voltage (CV) dependent fragmentation study from ESI MS of **Ib** and **IV** which shows that the loss of all PPh<sub>3</sub> from **Ib** occurs at CV 40 while at CV 70 all DPPP ligands get detached from **IV**.

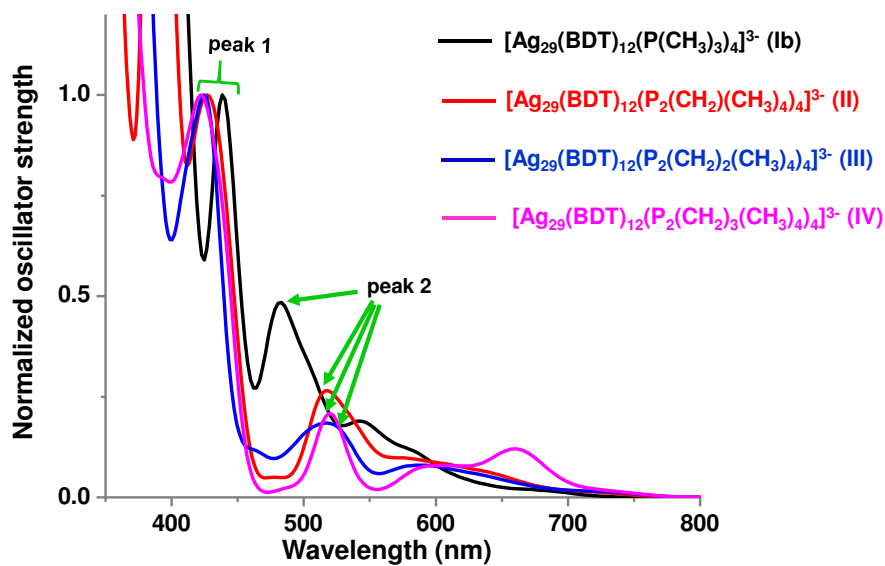
## Supplementary information 4





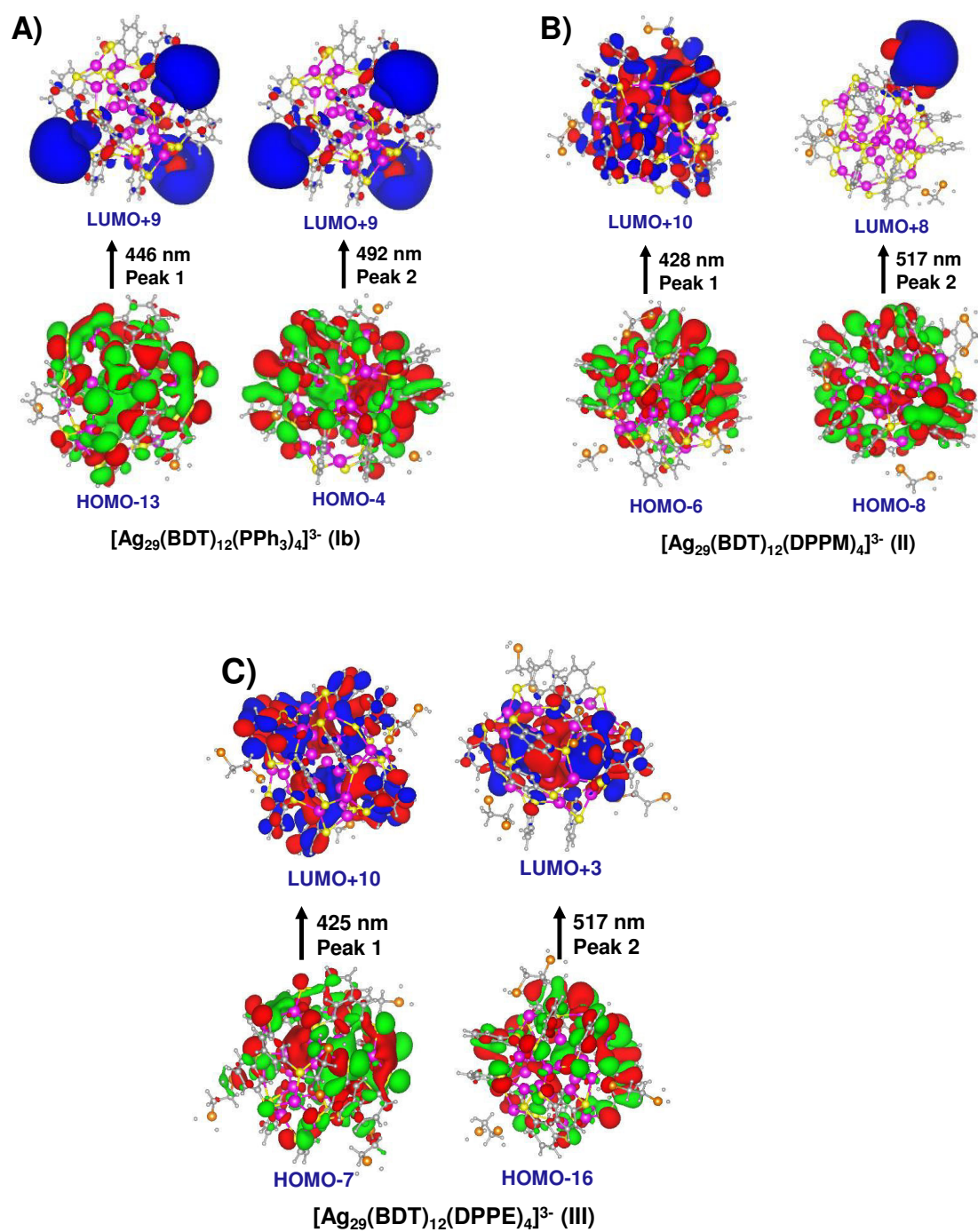
**Fig. S4** UV-vis absorption spectra (A and C) and emission spectra (B and D) of **Ib** and **III** before (black) and after (red) DPPE and  $\text{PPh}_3$  addition, respectively. The changes in both the absorption and emission spectra reveal the ability of DPPE ligand to replace  $\text{PPh}_3$  which result in the formation of **III** ligand exchanged from **Ib**. But the vice versa is not occurred. UV-vis absorption spectra (E and G) and emission spectra (F and H) of **Ib** and **II** before (blue) and after (pink) DPPM and  $\text{PPh}_3$  addition, respectively.

## Supplementary information 5



**Fig. S5** The theoretical absorption spectra of **Ib**, **II**, **III** and **IV** using the reduced model (benzene ring of phosphines are replaced by  $-\text{CH}_3$  ligand) to minimize the computational cost. The peak 1 (absorption maxima) of **II**, **III** and **IV** are blue-shifted than that of **Ib** and peak 2 are gradually red-shifted which are quite similar to the experimental observations.

## Supplementary information 6



**Fig. S6** The shape of the K-S MOs of **Ib** (A), **II** (B) and **III** (C) which denote the strongest electronic transitions related to peak 1 and 2.

**Supplementary Table S1**

**A)**

<b>System</b>	<b>Transition energy/eV</b>	<b>Transition energy/nm</b>	<b>MO transitions (eigen value)</b>	<b>Orbitals contributions</b>
<b>Ib</b>	2.782	445.7	HOMO-14 -> LUMO+8 HOMO-14 -> LUMO+9 HOMO-13 -> LUMO+7 HOMO-13 -> LUMO+9 HOMO-2 -> LUMO+11	0.116 0.192 0.116 0.45 0.0709
<b>II</b>	2.896	428.12	HOMO-8 -> LUMO+10 HOMO-6 -> LUMO+10 HOMO-4 -> LUMO+11 HOMO-4 -> LUMO+13 HOMO-1 -> LUMO+14	0.0604 0.246 0.0726 0.0748 0.0741
<b>III</b>	2.919	424.75	HOMO-16 -> LUMO+6 HOMO-7 -> LUMO+10 HOMO-5 -> LUMO+12 HOMO-4 -> LUMO+12 HOMO-2 -> LUMO+13 HOMO-1 -> LUMO+17	0.0913 0.13 0.0613 0.0826 0.0638 0.0946
<b>IV</b>	2.932	422.87	HOMO-10 -> LUMO+10 HOMO-8 -> LUMO+10 HOMO-7 -> LUMO+10 HOMO-4 -> LUMO+12 HOMO-2 -> LUMO+13	0.0544 0.0727 0.247 0.179 0.0863

**B)**

<b>System</b>	<b>Transition energy/eV</b>	<b>Transition energy/nm</b>	<b>MO transitions (eigen value)</b>	<b>Orbitals contributions</b>
<b>Ib</b>	2.520	492.0	HOMO-4 -> LUMO+9 HOMO-3 -> LUMO+8 HOMO-3 -> LUMO+9	0.374 0.371 0.101
<b>II</b>	2.399	516.8	HOMO-19 -> LUMO+1 HOMO-15 -> LUMO+3 HOMO-9 -> LUMO+7 HOMO-8 -> LUMO+8	0.112 0.0753 0.212 0.396
<b>III</b>	2.399	516.8	HOMO-19 -> LUMO HOMO-19 -> LUMO+2 HOMO-18 -> LUMO HOMO-17 -> LUMO+2 HOMO-16 -> LUMO+3	0.182 0.074 0.173 0.0626 0.199



<b>IV</b>	2.381	520.7	HOMO-19 -> LUMO+2 HOMO-18 -> LUMO+3 HOMO-17 -> LUMO+4 HOMO-16 -> LUMO+3 HOMO-16 -> LUMO+4	0.0589 0.182 0.0905 0.0743 0.317
-----------	-------	-------	---	--

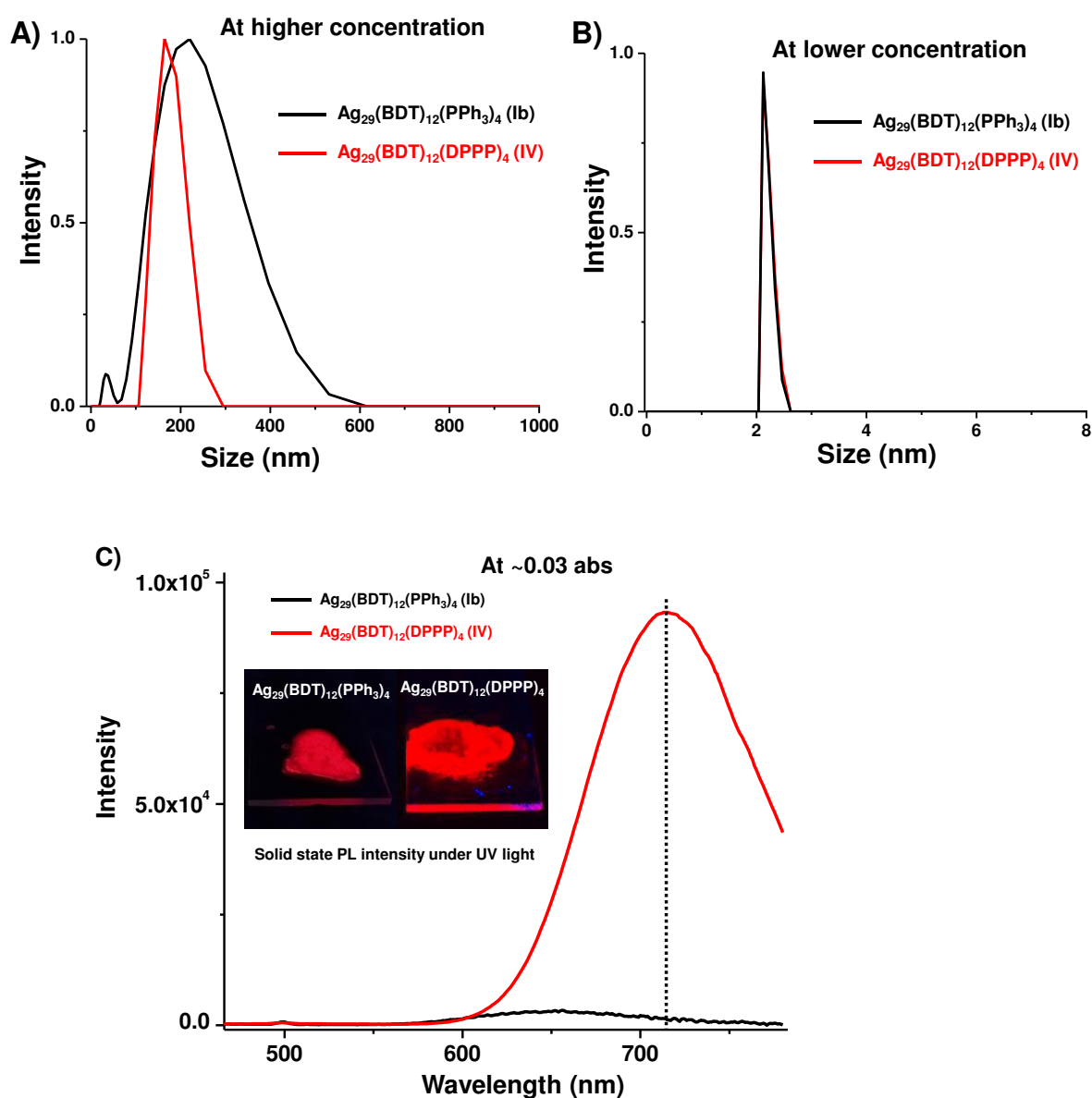
C)

<b>System</b>	<b>Transition energy/eV</b>	<b>Transition energy/nm</b>	<b>MO transitions</b>	<b>Orbitals contributions</b>
<b>Ib</b>	2.276	492.0	HOMO-14 -> LUMO+4 HOMO-13 -> LUMO+3 HOMO-8 -> LUMO+5 HOMO-7 -> LUMO+5	0.156 0.156 0.319 0.127
	2.148	577.2	HOMO-11 -> LUMO+4 HOMO-10 -> LUMO+4 HOMO-9 -> LUMO+3 HOMO-3 -> LUMO+5	0.205 0.244 0.244 0.079
	2.100	590.4	HOMO-12 -> LUMO+2 HOMO-10 -> LUMO+1 HOMO-9 -> LUMO+2 HOMO-8 -> LUMO+3 HOMO-7 -> LUMO+3 HOMO-5 -> LUMO+4	0.0556 0.0772 0.0766 0.0852 0.0633 0.0628
	2.244	552	HOMO-14 -> LUMO+4 HOMO-13 -> LUMO+3 HOMO-7 -> LUMO+5	0.0691 0.0691 0.677
<b>IV</b>	2.099	520.7	HOMO-13 -> LUMO+1 HOMO-13 -> LUMO+3 HOMO-12 -> LUMO+2 HOMO-9 -> LUMO+5 HOMO-7 -> LUMO+5 HOMO-6 -> LUMO+5	0.119 0.0636 0.0486 0.0542 0.0891 0.164
	1.884	658.0	HOMO-11 -> LUMO HOMO-10 -> LUMO HOMO-10 -> LUMO+2 HOMO-9 -> LUMO HOMO-9 -> LUMO+2 HOMO-6 -> LUMO+1 HOMO-2 -> LUMO+4	0.131 0.105 0.0593 0.178 0.0521 0.0616 0.0646
	2.099	590	HOMO-13 -> LUMO+1 HOMO-13 -> LUMO+3 HOMO-9 -> LUMO+5 HOMO-7 -> LUMO+5	0.119 0.0636 0.0542 0.0891

			HOMO-6 -> LUMO+5	0.164
--	--	--	------------------	-------

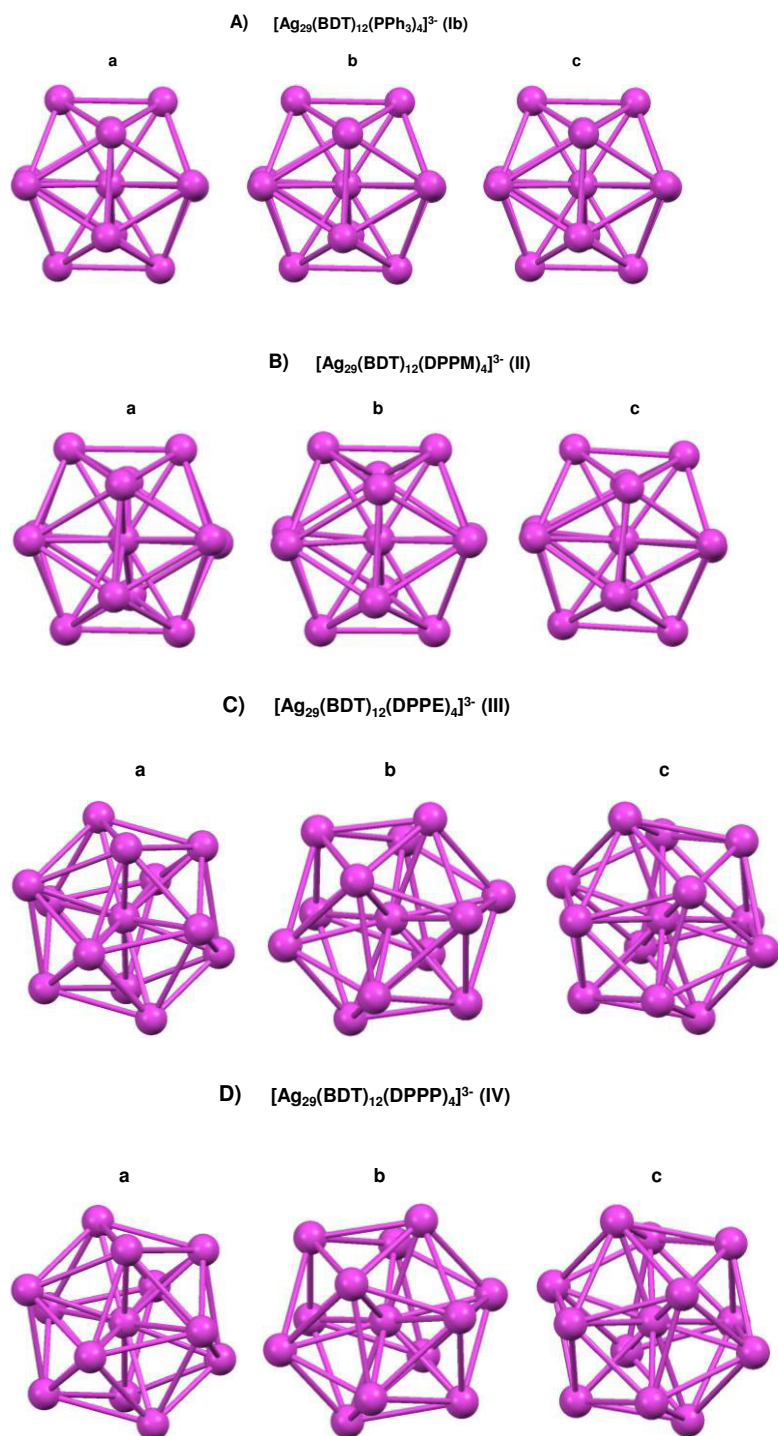
**Table S1** (A) The list of MO transitions contribute to the absorption maxima (peak 1) and (B) absorption onset (peak 2) of **Ib**, **II**, **III** and **IV**. (C) The MO transitions correspond to the peaks arise at lower energy range of **Ib** and **IV**. The transitions above 0.05 orbital contribution are considered and the strongest electronic transitions are highlighted here.

### Supplementary information 7



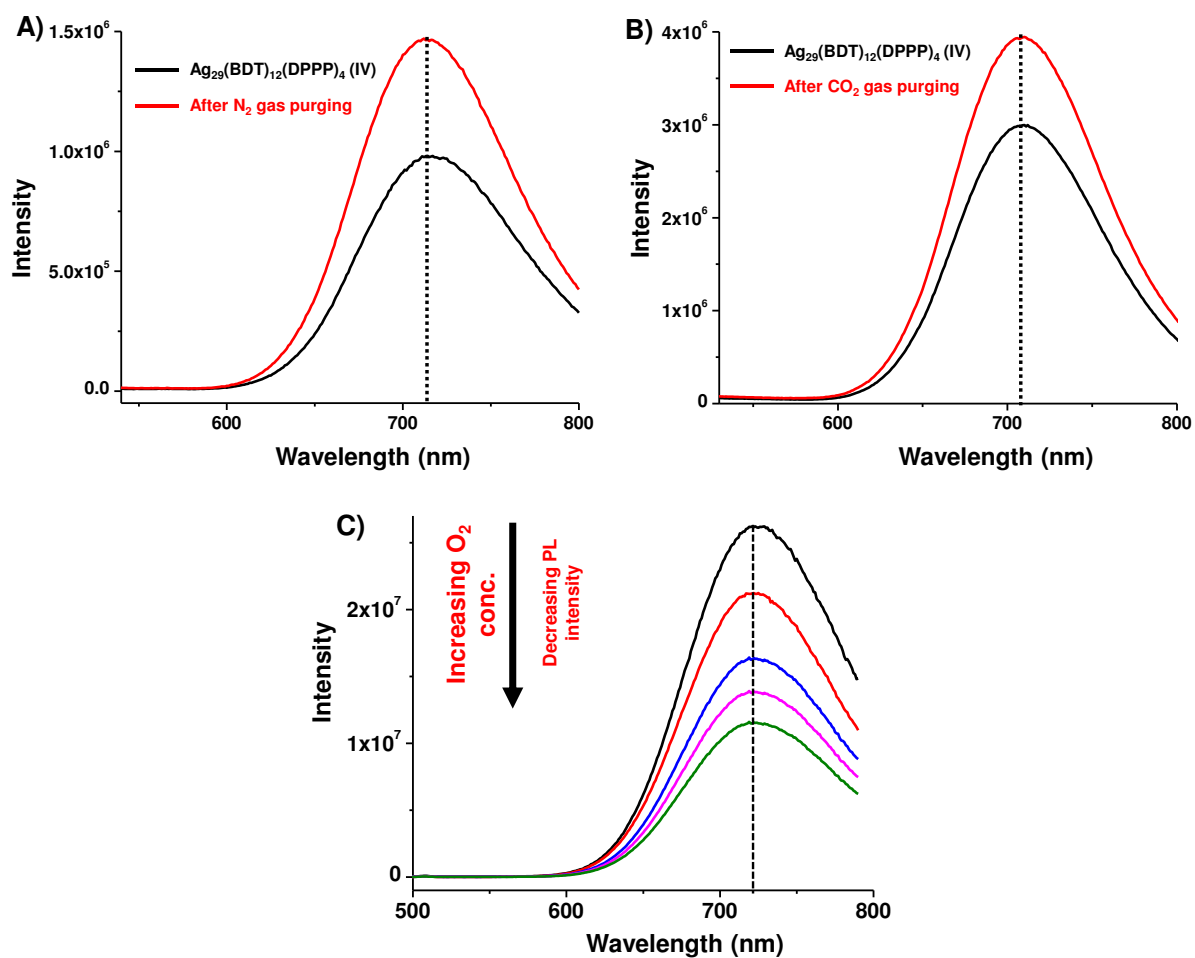
**Fig. S7** DLS particle size distribution of **Ib** and **IV** at higher (A) and lower (B) concentrations. (C) Emission spectra of **Ib** and **IV** at lower concentration having no aggregation (~0.05 absorbance). In the very low concentration **IV** display significant emission while **Ib** has no emission.

### Supplementary information 8



**Fig. S8** The Ag<sub>13</sub> icosahedral metal core of **Ib** (A), **II** (B), **III** (C) and **IV** (D). The view along Cartesian coordinates X, Y and Z axes are shown in a, b and c, respectively.

### Supplementary information 9



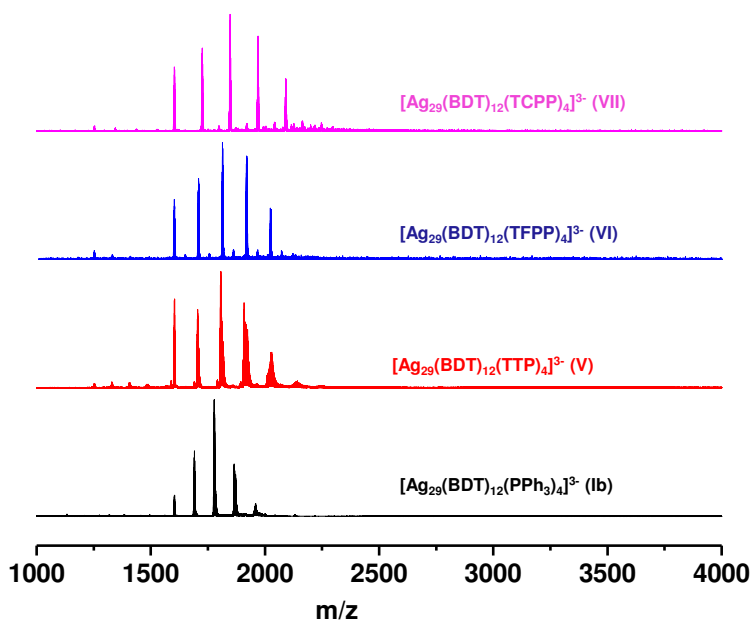
**Fig. S9** The emission spectra of **IV** after purging N<sub>2</sub> (A) and CO<sub>2</sub> (B) which show increased luminescence. (C) The emission spectra of **IV** at different concentrations of O<sub>2</sub>. With increasing O<sub>2</sub> concentration, PL intensity decreased gradually.

**Supplementary Table S2**

Cluster	$\tau_1$ ns [%]	$\tau_2$ ns [%]	$\tau_{\text{avg}}$ (ns)
<b>Ib</b>	99.65(51)	336.48(49)	214.90
<b>II</b>	108.44(17)	589.94(83)	510.49
<b>III</b>	120 (4)	1133.46(96)	1096.76
<b>IV</b>		6196.04 (100)	6196.04

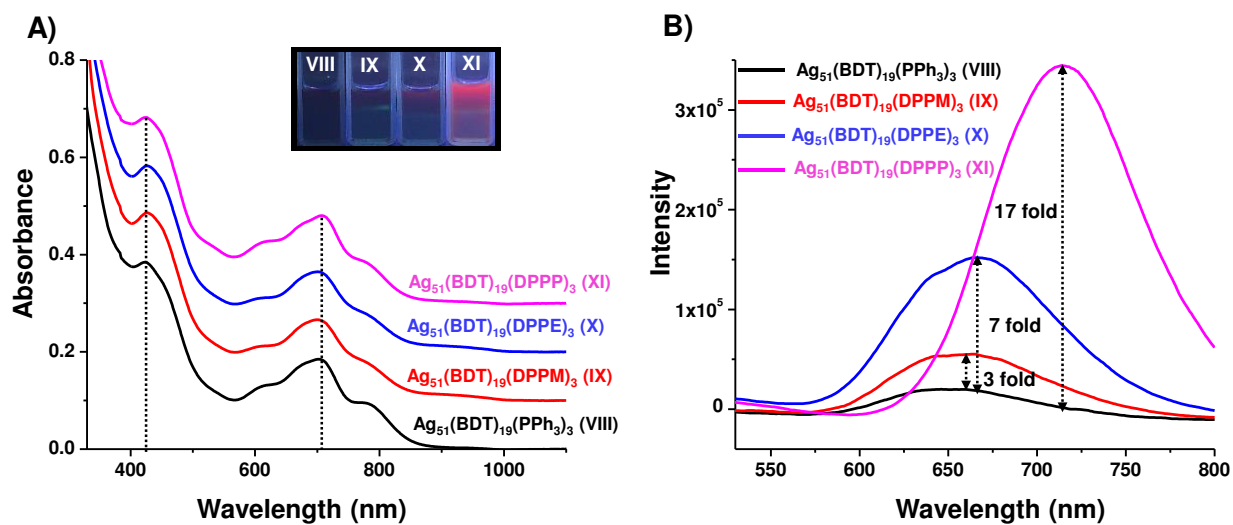
**Table S2** The lifetime values of **Ib**, **II**, **III** and **IV**. Each composed of two lifetime components and average lifetime increases with the longer phosphine ligands.

**Supplementary information 10**



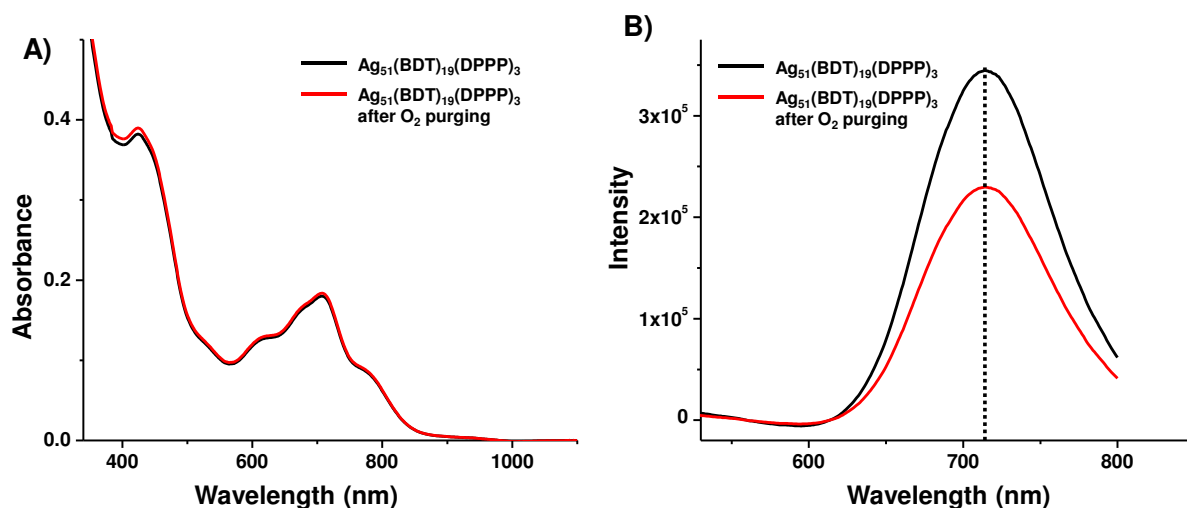
**Fig. S10** ESI MS of **V** (red), **VI** (blue) and **VII** (pink) which is compared with that of **Ib** (black). Similar to **Ib**, other clusters are showing systematic phosphine loss.

## Supplementary information 11



**Fig. S11** UV-vis absorption (A) and emission (B) spectra of **VIII** (black), **IX** (red), **X** (blue) and **XI** (pink). Inset: Photographs under visible light and UV light which show gradual increase in the PL intensity. Spectra for **IX**, **X** and **XI** are vertically shifted for clarity.

## Supplementary information 12



**Fig. S12** UV-vis absorption (A) and emission (B) spectra of **XI** before (black) and after (red) O<sub>2</sub> purging.

## References

1. L. G. AbdulHalim, M. S. Bootharaju, Q. Tang, S. Del Gobbo, R. G. AbdulHalim, M. Eddaoudi, D.-e. Jiang and O. M. Bakr, *J. Am. Chem. Soc.*, 2015, **137**, 11970-11975.
2. A. Ghosh, D. Ghosh, E. Khatun, P. Chakraborty and T. Pradeep, *Nanoscale*, 2017, **9**, 1068-1077.
3. J. J. Mortensen, L. B. Hansen and K. W. Jacobsen, *Phys. Rev. B: Condens. Matter Mater. Phys.*, 2005, **71**, 035109/035101-035109/035111.
4. J. Enkovaara, C. Rostgaard, J. J. Mortensen, J. Chen, M. Dulak, L. Ferrighi, J. Gavnholt, C. Glinsvad, V. Haikola, H. A. Hansen, H. H. Kristoffersen, M. Kuisma, A. H. Larsen, L. Lehtovaara, M. Ljungberg, O. Lopez-Acevedo, P. G. Moses, J. Ojanen, T. Olsen, V. Petzold, N. A. Romero, J. Stausholm-Moller, M. Strange, G. A. Tritsarlis, M. Vanin, M. Walter, B. Hammer, H. Hakkinen, G. K. H. Madsen, R. M. Nieminen, J. K. Nørskov, M. Puska, T. T. Rantala, J. Schiøtz, K. S. Thygesen and K. W. Jacobsen, *J. Phys.: Condens. Matter*, 2010, **22**, 253202/253201-253202/253224.
5. J. P. Perdew, K. Burke and M. Ernzerhof, *Phys. Rev. Lett.*, 1996, **77**, 3865-3868.
6. M. J. Frisch, G. W. Trucks, H. B. Schlegel, G. E. Scuseria, M. A. Robb, J. R. Cheeseman, G. Scalmani, V. Barone, B. Mennucci, G. A. Petersson, H. Nakatsuji, M. Caricato, X. Li, H. P. Hratchian, A. F. Izmaylov, J. Bloino, G. Zheng, J. L. Sonnenberg, M. Hada, M. Ehara, K. Toyota, R. Fukuda, J. Hasegawa, M. Ishida, T. Nakajima, Y. Honda, O. Kitao, H. Nakai, T. Vreven, J. A. Montgomery, J. E. Peralta, F. Ogliaro, M. Bearpark, J. J. Heyd, E. Brothers, K. N. Kudin, V. N. Staroverov, R. Kobayashi, J. Normand, K. Raghavachari, A. Rendell, J. C. Burant, S. S. Iyengar, J. Tomasi, M. Cossi, N. Rega, J. M. Millam, M. Klene, J. E. Knox, J. B. Cross, V. Bakken, C. Adamo, J. Jaramillo, R. Gomperts, R. E. Stratmann, O. Yazyev, A. J. Austin, R. Cammi, C. Pomelli, J. W. Ochterski, R. L. Martin, K. Morokuma, V. G. Zakrzewski, G. A. Voth, P. Salvador, J. J. Dannenberg, S. Dapprich, A. D. Daniels, Farkas, J. B. Foresman, J. V. Ortiz, J. Cioslowski and D. J. Fox, *Journal*, 2009, DOI: citeulike-article-id:9096580.
7. W. Humphrey, A. Dalke and K. Schulten, *J Mol Graph*, 1996, **14**, 33-38, 27-38.





# Atomically precise cluster-based white light emitters<sup>§</sup>

ESMA KHATUN, SANDEEP BOSE, MADHURI JASH and THALAPPIL PRADEEP\* 

DST Unit of Nanoscience (DST UNS) and Thematic Unit of Excellence, Department of Chemistry,  
Indian Institute of Technology Madras, Chennai, Tamil Nadu 600 036, India  
E-mail: pradeep@iitm.ac.in

MS received 31 August 2018; revised 12 September 2018; accepted 14 September 2018;  
published online 29 September 2018

**Abstract.** Materials emitting white luminescence are receiving increasing attention due to their potential applications in electroluminescent devices, information displays and fluorescent sensors. To produce white light, one must have either three primary colors, blue, green and red or two colors, blue and orange. In this paper, we have used thiol/phosphine protected red luminescent silver nanoclusters ( $\text{Ag NCs}$ ),  $[\text{Ag}_{29}(\text{BDT})_{12}(\text{PPh}_3)_4]^{3-}$  ( $\text{BDT} = 1,3\text{-benzenedithiol}$ ),  $[\text{Au}_x\text{Ag}_{29-x}(\text{BDT})_{12}(\text{PPh}_3)_4]^{3-}$  and  $\text{Ag}_{29}(\text{LA})_{12}$  ( $\text{LA} = \text{lipoic acid}$ ) as one of the fluorophores for white light emission. These clusters are mixed with blue luminescent silicon nanoparticles ( $\text{Si NPs}$ ) and green luminescent fluorescein isothiocyanate ( $\text{FITC}$ ). The mixtures show white luminescence with CIE coordinates of (0.31, 0.34), (0.33, 0.35) and (0.29, 0.31) which are in good agreement with pure white light (0.33, 0.33). The other clusters with yellow, blue, orange, etc., luminescence can also be used to make white light. This work provides a prospective pathway for white light emission based on atomically precise noble metal NCs.

**Keywords.** Nanocluster (NC); silicon nanoparticles ( $\text{Si NPs}$ ); photoluminescence (PL); fluorescein isothiocyanate (FITC); electrospray ionization mass spectrometry (ESI MS); white light emission.

## 1. Introduction

White light emission is of importance from many perspectives.<sup>1,2</sup> A number of emerging materials such as gels,<sup>3</sup> quantum dots,<sup>4</sup> supramolecular assemblies<sup>5,6</sup> and many molecular systems<sup>7</sup> have been used for white light emission. Noble metal nanoclusters (NCs) with their inherent photoluminescence (PL) make them suitable for white light emission.<sup>8</sup> Over a hundred cluster systems of this kind are known and the area is expanding tremendously. Among these NCs, protein protected NCs such as  $\text{Au}_{25}@\text{BSA}$ ,  $\text{Ag}@\text{Cys}$ ,  $\text{Ag}@\text{Lys}$ , etc., are water-soluble and highly luminescent.<sup>9–14</sup> Apart from protein protected clusters, glutathione (SG) protected clusters such as,  $\text{Au}_{25}(\text{SG})_{18}$ ,<sup>15,16</sup>  $\text{Au}_{23}(\text{SG})_{18}$ ,<sup>17</sup>  $\text{Au}_{22}(\text{SG})_{18}$ ,<sup>18</sup>  $\text{Au}_{18}(\text{SG})_{14}$ ,<sup>19</sup>  $\text{Ag}_{11}(\text{SG})_7$ ,<sup>20</sup>  $\text{Ag}_{15}(\text{SG})_{11}$ ,<sup>21</sup>  $\text{Ag}_{31}(\text{SG})_{19}$ ,<sup>22</sup>  $\text{Ag}_{32}(\text{SG})_{19}$ ,<sup>23</sup> etc., and some other clusters<sup>24–30</sup> of water-soluble thiols such as, mercaptosuccinic acid (MSA), mercaptopropionic acid (MPA),

lipoic acid (LA), dihydrolipoic acid (DHLA), etc., exhibit intense luminescence in aqueous medium. But, there are very few reports on the luminescent thiol/phosphine protected NCs in organic solvents and most of them are less emissive. However, their luminescence can be increased either by rigidifying their surface or by doping with another metal ions.<sup>31–35</sup> For a long time, Au NCs attracted attention due to their stability and excellent luminescence but, recently Ag NCs are also beginning to gain the attention of the researchers due to their new properties and various applications.  $[\text{Ag}_{29}(\text{BDT})_{12}(\text{PPh}_3)_4]^{3-}$ ,<sup>36</sup>  $[\text{Ag}_{62}\text{S}_{13}(\text{StBu})_{32}](\text{BF}_4)_4$ ,<sup>37</sup>  $[\text{Ag}_{33}\text{S}_3(\text{StBu})_{16}(\text{CF}_3\text{COO})_9(\text{NO}_3)(\text{CH}_3\text{CN})_2](\text{NO}_3)_3$ ,<sup>38</sup> etc. NCs are known to be red luminescent while  $\text{Ag}_{14}(3,4\text{-DFBT})_{12}(\text{PPh}_3)_8$  displays luminescence in the yellow region (emission maximum is at 535 nm).<sup>39</sup> The alloys of  $[\text{Ag}_{29}(\text{BDT})_{12}(\text{PPh}_3)_4]^{3-}$  using Au and Pt exhibit enhanced luminescence, near about 26 times and

\*For correspondence

<sup>§</sup>Dedicated to Professor M V George on the occasion of his 90<sup>th</sup> Birth Anniversary.

2.3 times, respectively.<sup>31,40</sup> Similarly, the luminescence increment for other Ag NCs is yet to be examined.

While most such clusters emit in the red or NIR region,<sup>2,41</sup> there are other nanosystems such as silicon (Si) nanoparticles (NPs) which emit in the blue and green regions.<sup>43–48</sup> Small-sized luminescent Si NPs are used in several applications such as solid state lighting, full-colour displays, optical sensors, and biological imaging.<sup>49,50</sup> Combining these two different categories of systems (noble metal NCs and Si NPs) with other molecular emitters, it may be possible to create stable white light emission. These molecular materials could be incorporated in appropriate matrices to produce new materials with novel properties for further advanced applications.

In this paper, we have combined well-characterized red luminescent atomically precise cluster systems  $[Ag_{29}(BDT)_{12}(PPh_3)_4]^{3-}$ ,  $[Au_xAg_{29-x}(BDT)_{12}(PPh_3)_4]^{3-}$  and  $Ag_{29}(LA)_{12}$  with Si NPs and complemented their emission with that of fluorescein isothiocyanate (FITC), a well-known molecular emitter. As these clusters were stable in water and other systems too, it was possible to make a homogeneous solution with varying concentrations of all components to accomplish white light emission with CIE coordinates of (0.31, 0.34), (0.33, 0.35) and (0.29, 0.31). Although not demonstrated here, FITC could be replaced with a yellow emitting cluster to achieve white light emission and also, it was possible to replace Si NPs with clusters so that all-cluster based white light emitters could be realized.

## 2. Experiment

### 2.1 Materials and physical measurements

Sodium borohydride ( $NaBH_4$ , 95%), 1,3-BDT ( $\geq 99\%$ ), FITC and aminopropyl trimethoxysilane (APTMS) were purchased from Sigma-Aldrich. LA and silver nitrate ( $AgNO_3$ ) were purchased from Rankem chemicals. Triphenylphosphine ( $PPh_3$ , 98%) was purchased from Spectrochem. Dichloromethane (DCM), dimethylformamide (DMF) and methanol (MeOH) were purchased from Rankem and were of HPLC grade. Sodium citrate was purchased from Sarabhai M. Chemicals. Gold (III) chloride trihydrate ( $HAuCl_4 \cdot 3H_2O$ ) was synthesized in our laboratory. All solvents and chemicals were used without further purification.

The absorption spectra were measured using a PerkinElmer Lambda 25 spectrometer. Electrospray ionization mass spectrometric (ESI MS) measurements were performed using a Waters Synapt G2-Si high-resolution mass spectrometer. PL spectra were measured in a HORIBA JOBIN YVON Nano Log instrument. The bandpass for excitation and emission was set at 3 nm. High-resolution transmission

electron microscopic (HRTEM) studies of Si NPs were performed with a JEOL 3010 instrument. The samples were prepared by drop casting Si NPs solution ( $H_2O$ ) on carbon-coated copper grids and allowing it to dry under ambient conditions.

### 2.2 Synthesis of $[Ag_{29}(1,3-BDT)_{12}(PPh_3)_4]^{3-}$

The  $[Ag_{29}(BDT)_{12}(PPh_3)_4]^{3-}$  cluster was synthesized following a reported protocol after small modifications.<sup>36</sup> About 20 mg of  $AgNO_3$  was dissolved in a mixture of 5 mL of methanol and 9 mL of DCM. Then, the solution was allowed to stir and after 5 min, 13.5  $\mu$ L of 1,3-BDT was added to the reaction mixture. Immediately, the colorless solution turned yellow which indicated the formation of silver thiolate. Then, 200 mg of  $PPh_3$  was dissolved in 0.5 mL of DCM and added to the solution. This turned the solution colorless again, indicating the formation of Ag–S–P complexes. After 10–15 min,  $\sim 11$  mg of  $NaBH_4$  (in 0.5 mL of ice cold  $H_2O$ ) was added dropwise which changed the color of the solution to dark-brown. Finally, the reaction mixture was kept at room temperature under dark conditions for 3 h. After completion of the reaction, the reddish brown precipitate was collected by centrifuging the mixture and the supernatant was discarded. Then, the precipitate was washed twice or thrice with methanol to remove the unreacted by-products. Finally, the orange colored cluster was extracted in DMF.

### 2.3 Synthesis of $[Au_xAg_{29-x}(1,3-BDT)_{12}(PPh_3)_4]^{3-}$

The above-mentioned procedure after the slight modification was used for the synthesis of Au doped  $[Ag_{29}(BDT)_{12}(PPh_3)_4]^{3-}$ , namely  $[Au_xAg_{29-x}(BDT)_{12}(PPh_3)_4]^{3-}$ . About  $\sim 6$  mg of  $HAuCl_4$  was dissolved in 5 mL of MeOH and to that solution,  $\sim 14$  mg of  $AgNO_3$  was added. Then, 9 mL of DCM was added to this mixture and kept for stirring. After 5 min,  $\sim 13.5$   $\mu$ L of 1,3-BDT was added to this mixture followed by the addition of  $\sim 200$  mg of  $PPh_3$ . Then,  $\sim 11$  mg of  $NaBH_4$  dissolved in 0.5 mL of ice cold  $H_2O$  was added dropwise in the mixture. After 3 h of reaction under dark conditions, the solution was transferred to a round-bottomed flask and dried completely by rotary evaporation. The dried material was washed with MeOH repeatedly. Then the precipitate was collected by centrifugation. Finally, DMF was used to extract the orange colored product.

### 2.4 Synthesis of $[Ag_{29}(LA)_{12}]$

The cluster was prepared by an already reported method with slight modifications.<sup>29</sup> About 20 mg of LA was dissolved in 14 mL of water and then to this solution, 7 mg of  $NaBH_4$  was added. The mixture was kept for stirring so that all LA had dissolved. Then, 4 mg of  $AgNO_3$  was dissolved in 1 mL of water followed by the addition of 10 mg of  $NaBH_4$  in 2 mL water. Next, the reaction was allowed to stir for 3 h under

dark condition at room temperature. The product cluster was stored at 4 °C temperature.

### 2.5 Synthesis of blue luminescent Si NPs

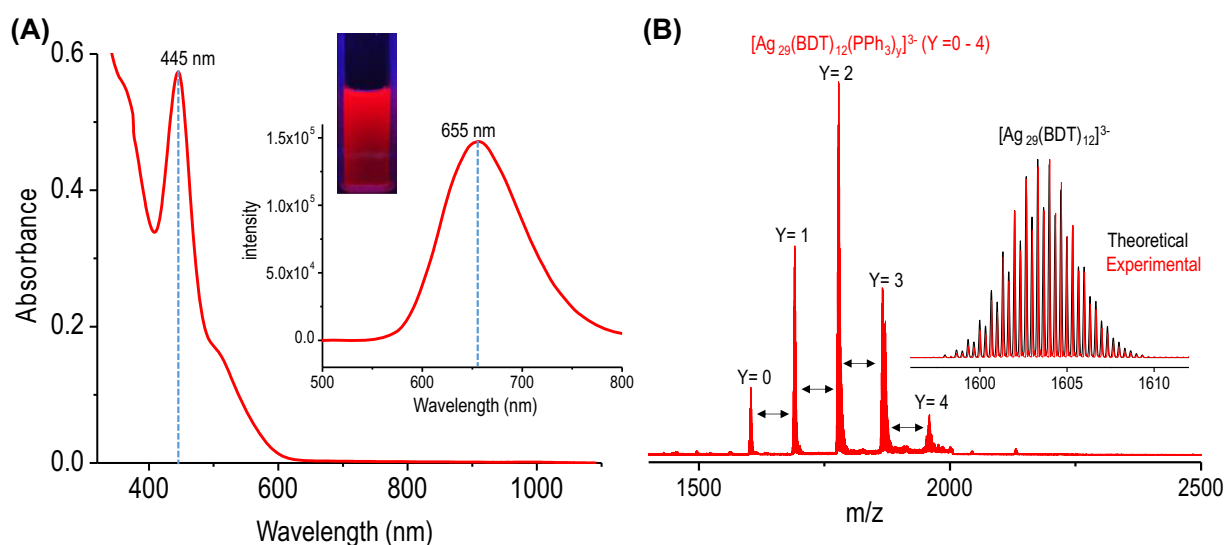
A reported procedure was followed for this synthesis with small changes.<sup>43</sup> A 20 mL aqueous solution of ~1 g sodium citrate was prepared and 1 mL of aminopropyl trimethoxysilane (APTMS) was added to this solution. This mixture was agitated homogeneously for 5 min. Then, the solution was kept at 170 °C in a hydrothermal bomb for 24 h. After the end of the reaction, it was cooled down to the room temperature and then, the transparent solution was dialyzed using a membrane of molecular weight cut off 12 kDa.

### 2.6 White light emission

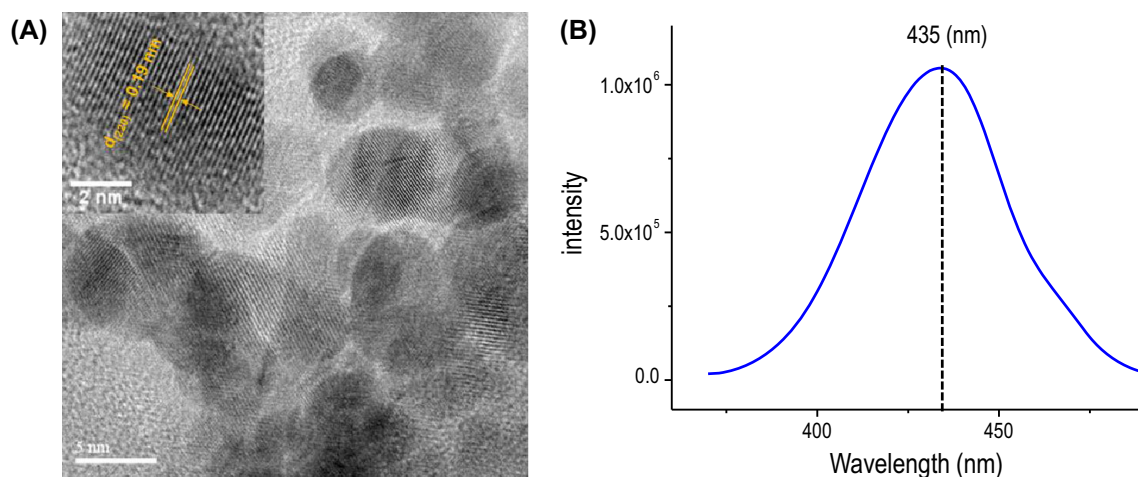
The blue luminescent Si NPs, green luminescent FITC and red luminescent  $[\text{Ag}_{29}(\text{BDT})_{12}(\text{PPh}_3)_4]^{3-}$  /  $[\text{Au}_x\text{Ag}_{29-x}(\text{BDT})_{12}(\text{PPh}_3)_4]^{3-}$  /  $\text{Ag}_{29}(\text{LA})_{12}$  cluster were mixed to get white light emission. The  $[\text{Ag}_{29}(\text{BDT})_{12}(\text{PPh}_3)_4]^{3-}$  and  $[\text{Au}_x\text{Ag}_{29-x}(\text{BDT})_{12}(\text{PPh}_3)_4]^{3-}$  clusters were soluble in organic solvents such as DMF but not in  $\text{H}_2\text{O}$ . As DMF and  $\text{H}_2\text{O}$  are miscible to each other, the DMF solutions of these clusters were added in  $\text{H}_2\text{O}$  and were stable in the DMF/ $\text{H}_2\text{O}$  mixture. The absorption and emission spectra of these clusters in DMF/ $\text{H}_2\text{O}$  were checked and the results are presented in the discussion section.  $\text{Ag}_{29}(\text{LA})_{12}$  was soluble in water, so also FITC and Si NPs. All the solvents were miscible and the mixture was stable. The excitation wavelength chosen for white light emission was 360 nm.

## 3. Results and Discussion

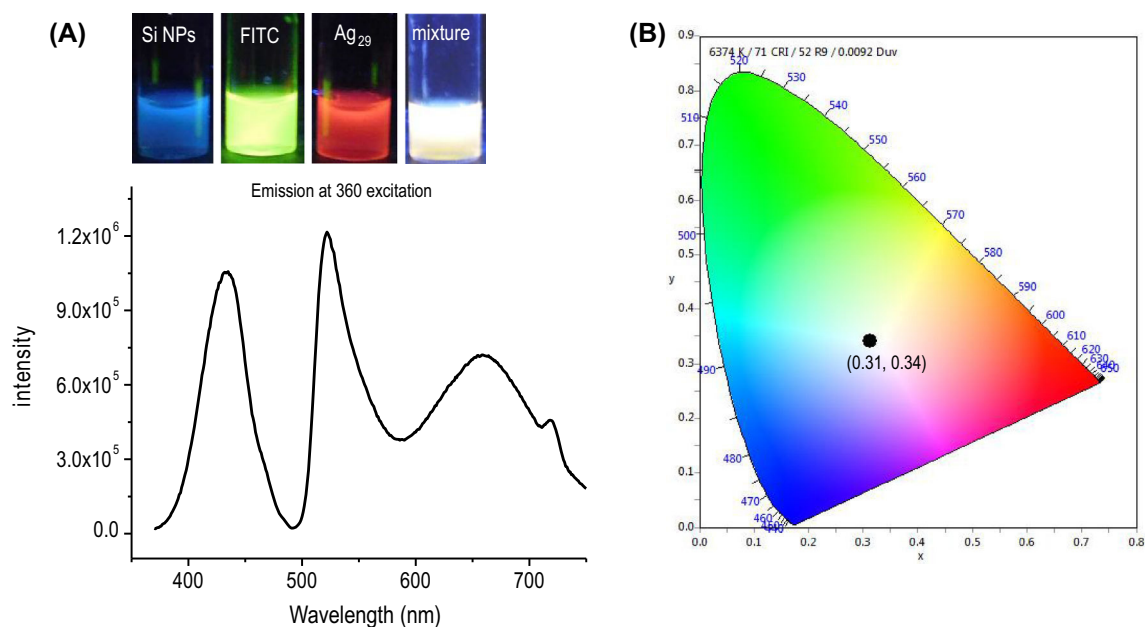
White light emission is composed of three primary colors, blue, green and red. Here, we have used Si NPs as the blue emission source, FITC as the green emission source and NCs as the red emission source. The red luminescent  $[\text{Ag}_{29}(\text{BDT})_{12}(\text{PPh}_3)_4]^{3-}$  cluster was prepared by following a reported protocol.<sup>36</sup> The cluster is highly soluble in DMF, although it is sparingly soluble in DCM, acetonitrile, etc. The as-synthesized cluster was thoroughly characterized by optical spectroscopy and ESI MS (Figure 1). The absorption spectrum of the cluster presented in Figure 1A shows a maximum at 445 nm along with a shoulder at ~512 nm. It possesses bright red luminescence under UV light as shown in the inset of Figure 1A. At 450 nm excitation, the emission maximum is at 655 nm (see inset of Figure 1A). ESI MS was performed to confirm the cluster composition which is presented in Figure 1B. It was measured in the -ve ion mode and the mass spectrum is presented in Figure 1B in a mass range of  $m/z$  1400–2500. The spectrum exhibits 5 peaks and the separation between two neighboring peaks is  $m/z$  87.33. An expanded view of ESI MS is given in Figure S1 (Supplementary Information) which shows the separation between two peaks in isotopic distribution is 0.33 suggesting 3<sup>-</sup> charge state. Thus, the separation of  $m/z$  87.33 corresponds to one  $\text{PPh}_3$  ligand (262). Theoretical isotopic distribution of  $[\text{Ag}_{29}(\text{BDT})_{12}]^{3-}$  species is shown in the inset of Figure 1B which matches exactly with the experimental isotopic distribution.



**Figure 1.** (A) The UV–Vis absorption spectrum of  $[\text{Ag}_{29}(\text{BDT})_{12}(\text{PPh}_3)_4]^{3-}$  having an absorption maximum at 445 nm. Inset: The emission spectrum of  $[\text{Ag}_{29}(\text{BDT})_{12}(\text{PPh}_3)_4]^{3-}$  at 450 nm excitation. (B) The ESI MS of  $[\text{Ag}_{29}(\text{BDT})_{12}(\text{PPh}_3)_4]^{3-}$  which shows a systematic  $\text{PPh}_3$  loss. Inset: the theoretical and the experimental isotopic distributions of  $[\text{Ag}_{29}(\text{BDT})_{12}]^{3-}$  showing perfect fitting.



**Figure 2.** (A) The HRTEM images of blue emitting Si NPs. The inset shows the lattice spacing of 0.19 nm which is arising from the (220) lattice plane of silicon. (B) The emission spectrum of Si NPs shows a maximum at 435 nm at 360 nm excitation.



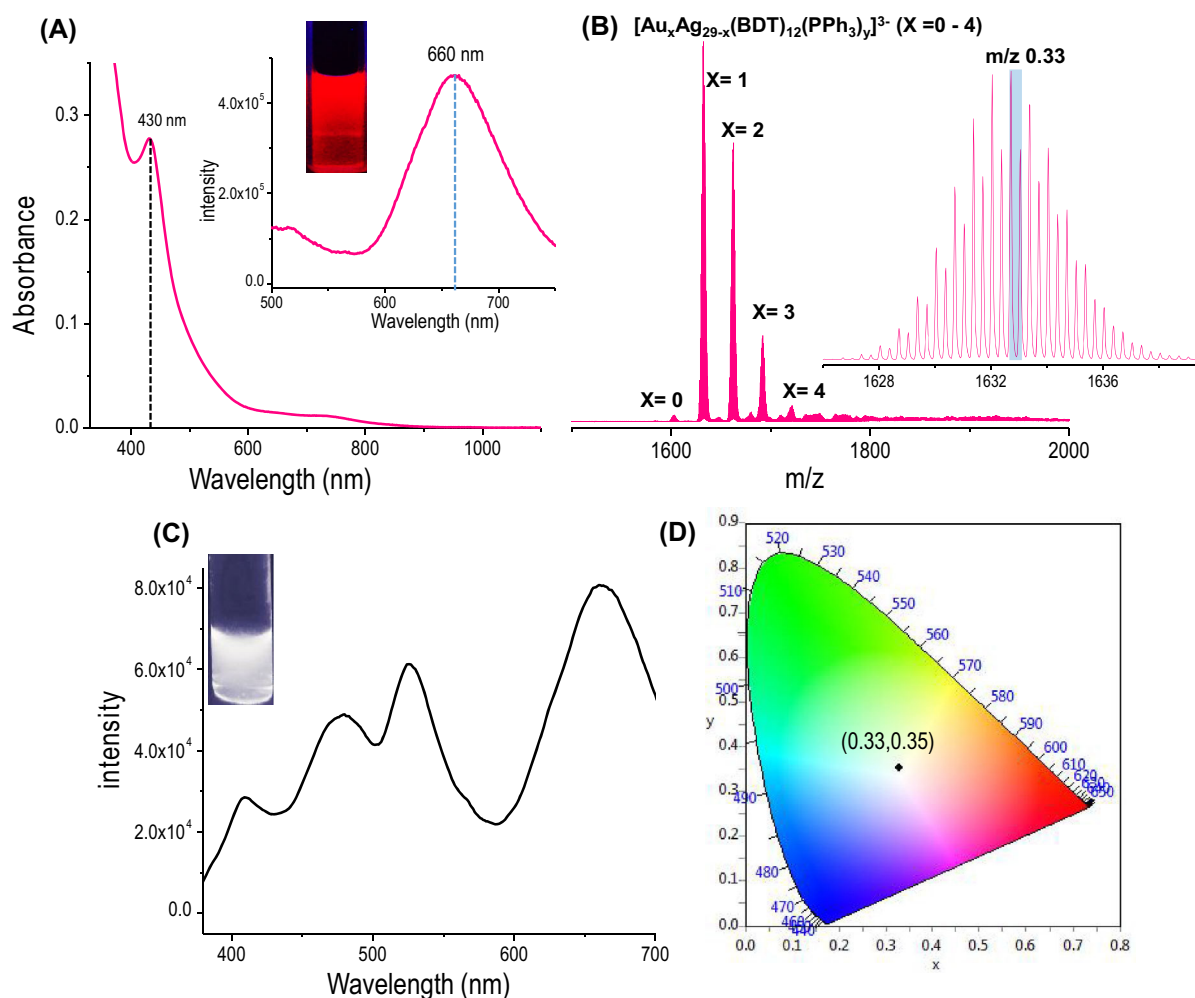
**Figure 3.** (A) White light emission from a mixture of blue luminescent Si NPs, green luminescent FITC dye and red luminescent  $[\text{Ag}_{29}(\text{BDT})_{12}(\text{PPh}_3)_4]^{3-}$  cluster. Inset: photographs under UV light. (B) Chromaticity diagram which shows the coordinates of the white light emitted (0.31, 0.34) from a mixture of blue, green and red fluorophores.

The Si NPs were prepared by a reported method using APTMS and sodium citrate as mentioned in the experimental section. The as-synthesized Si NPs were characterized using HRTEM and PL spectroscopy and the data are presented in Figure 2. The HRTEM image in Figure 2A suggests the formation of NPs which are ~5 nm in size. The NPs are showing a lattice spacing of 0.19 nm, matching with the (220) plane of silicon. It is known that the smaller sized Si NPs undergo a transition from indirect to direct bandgap semiconductor.<sup>51</sup> In this case, as the synthesized Si NPs are smaller in size, they

show luminescence. The emission spectrum is shown in Figure 2B which manifests a peak at 435 nm at 360 nm excitation.

White light is an optimal composition of three primary colors, red, green and blue. Thus, we have mixed the blue emitting Si NPs, red emitting  $[\text{Ag}_{29}(\text{BDT})_{12}(\text{PPh}_3)_4]^{3-}$  and a green emitting FITC dye. Si NPs and FITC were solubilized in H<sub>2</sub>O and  $[\text{Ag}_{29}(\text{BDT})_{12}(\text{PPh}_3)_4]^{3-}$  cluster was taken in DMF. The DMF solution of the cluster was mixed with H<sub>2</sub>O. The absorption and emission spectra were checked which suggest that





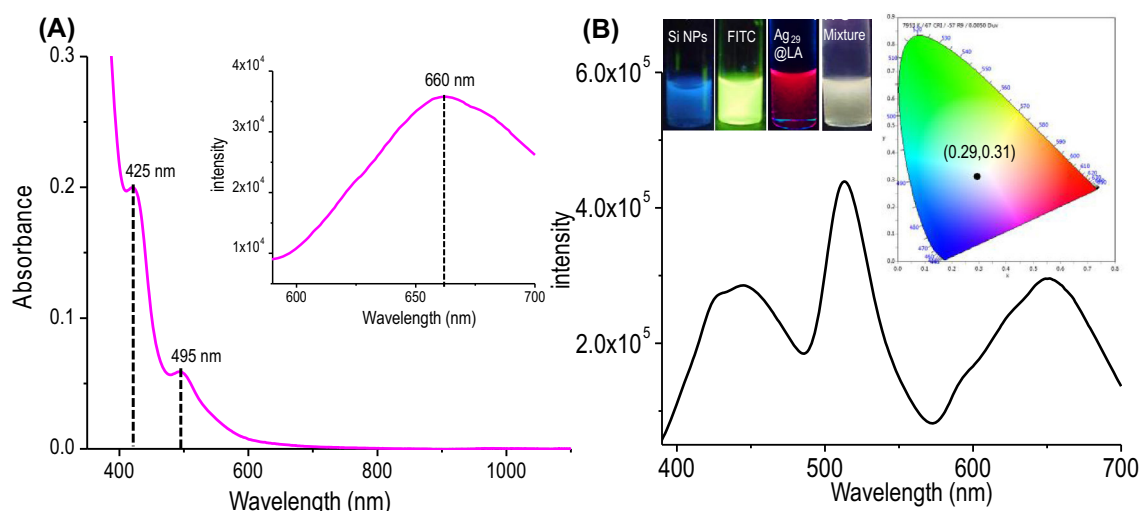
**Figure 4.** (A) The UV-Vis absorption spectrum of  $[\text{Au}_x\text{Ag}_{29-x}(\text{BDT})_{12}(\text{PPh}_3)_4]^{3-}$  having an absorption maximum at 430 nm. Inset: The emission spectrum of  $[\text{Au}_x\text{Ag}_{29-x}(\text{BDT})_{12}(\text{PPh}_3)_4]^{3-}$  at 450 nm excitation which shows an emission maximum at 690 nm. (B) The ESI MS of  $[\text{Au}_x\text{Ag}_{29-x}(\text{BDT})_{12}(\text{PPh}_3)_4]^{3-}$ ,  $X = 0 - 4$ . The inset shows expanded ESI MS which shows a separation of 0.33 confirming the  $3^-$  charge state. (C) The emission spectrum of white luminescence generated from a mixture of Si NPs, FITC and  $[\text{Au}_x\text{Ag}_{29-x}(\text{BDT})_{12}(\text{PPh}_3)_4]^{3-}$  at 360 nm excitation. Photograph of white light emission under UV light is presented in the inset. (D) The CIE chromaticity diagram of white luminescence having coordinates of (0.33, 0.35).

the cluster is stable in the DMF/ $\text{H}_2\text{O}$  mixture (Figure S2, Supplementary Information).

The individual colors of Si NP, FITC,  $[\text{Ag}_{29}(\text{BDT})_{12}(\text{PPh}_3)_4]^{3-}$  and the color of their mixture (Si NPs: FITC:  $[\text{Ag}_{29}(\text{BDT})_{12}(\text{PPh}_3)_4]^{3-}$  is 3:1:2 v/v/v) are shown in the inset of Figure 3A. The luminescence spectrum of the mixture which emits white light emission at 360 nm excitation is shown in Figure 3A. The CIE 1931 color system is the most widely used colorimetric standard and the CIE plot can be obtained from the visible spectrum. This is represented by two color coordinates, X and Y. The CIE chromaticity diagram of the mixture is presented in Figure 3B which analyzes the color characteristics of luminescent materials. The observed white light emission exhibits CIE coordinates of (0.31,

0.34) which is in good agreement to that of pure white light (0.33, 0.33). The color of individual components and the mixture under UV light are shown in the inset of Figure 3A.

The similar kind of experiment to produce white light emission was performed using the Au doped  $[\text{Ag}_{29}(\text{BDT})_{12}(\text{PPh}_3)_4]^{3-}$  cluster with enhanced luminescence. The synthetic procedure is given in the experimental section. Characterization data of the cluster by optical spectroscopy and mass spectrometry are presented in Figure 4. The absorption spectrum of  $[\text{Au}_x\text{Ag}_{29-x}(\text{BDT})_{12}(\text{PPh}_3)_4]^{3-}$  looks similar to that of  $[\text{Ag}_{29}(\text{BDT})_{12}(\text{PPh}_3)_4]^{3-}$  (Figure 4A). It exhibits an absorption maximum at 430 nm along with a small peak at 730 nm. The cluster shows luminescence at  $\sim 660$  nm



**Figure 5.** (A) The UV-Vis absorption spectrum of  $\text{Ag}_{29}(\text{L})_{12}$  having an absorption maximum at 425 nm and a shoulder at  $\sim 495$  nm. Inset: The emission spectrum of  $\text{Ag}_{29}(\text{LA})_{12}$  at 425 nm excitation shows a maximum at 660 nm. (B) The emission spectrum of white light produced by the mixture of Si NPs, FITC and  $\text{Ag}_{29}(\text{LA})_{12}$ . Inset: The CIE chromaticity diagram for white light emission which shows the color coordinates, (0.29, 0.31).

when excited at  $\sim 450$  nm as shown in the inset of Figure 4A (photograph of the cluster under UV light is presented in the inset). ESI MS was measured and it shows a bunch of peaks as shown in Figure 4B. The first peak is at  $m/z$  1603 and the charge state is  $3^-$  (see inset of Figure 4B) and the spectrum can be assigned to  $[\text{Ag}_{29}(\text{BDT})_{12}]^{3-}$ . Other peaks appear at  $\sim m/z$  1632, 1662, 1692 and 1722. The separation between the two neighboring peaks is  $\sim m/z$  30 and the charge state of all peaks is  $3^-$ , that means the mass difference is  $\sim 90$  which is equal to the mass of one Au atom minus that of one Ag atom ( $197-108$ ). The number of Au doped in this cluster is 4 which is corroborated by Figure 4B.

This cluster was also used for white light emission after mixing the DMF solution of the cluster and aqueous solutions of Si NPs as well as FITC. The cluster stability in DMF/ $\text{H}_2\text{O}$  mixture was checked and the data are shown in Figure S3 (Supplementary Information). The mixture (Si NPs: FITC:  $[\text{Au}_x\text{Ag}_{29-x}(\text{BDT})_{12}(\text{PPh}_3)_4]^{3-}$  is 2:1:4 v/v/v) shows white luminescence (emission spectrum is shown in Figure 4C) with (0.33, 0.35) CIE coordinates (Figure 4D). The value is very near to that of the pure white light (0.33, 0.33).

A water-soluble cluster  $\text{Ag}_{29}(\text{LA})_{12}$  was taken, which is similar to  $[\text{Ag}_{29}(\text{BDT})_{12}(\text{PPh}_3)_4]^{3-}$ . The detailed synthetic method is presented in the experimental section. The absorption spectrum shows a maximum at 425 nm along with a shoulder at 495 nm (Figure 5A) which is matching with the previous report.<sup>29</sup> It shows emission

maximum at 660 nm when excited at 425 nm (see inset of Figure 5A). The cluster was used for white light emission after mixing with Si NPs and FITC. The mixture (Si NPs: FITC:  $\text{Ag}_{29}(\text{LA})_{12}$  is 2:1:5 v/v/v) emits white light at 360 nm excitation and the PL spectrum of it is presented in Figure 5B. The CIE chromaticity diagram is given in the inset of Figure 5B showing color coordinates of (0.29, 0.31).

In the three cases above, white light generation was demonstrated using blue luminescent Si NPs, green luminescent FITC dye and three different red luminescent clusters. Mostly, in multicomponent systems, the white light emission is controlled through fluorescence resonance energy transfer (FRET) process between the different components. The excitation wavelength of white light emission was kept at 360 nm which is the excitation wavelength for Si NPs. Mixing of FITC and NCs in Si NPs solution resulted in quenching the emission intensity of Si NPs (from  $1.65 \times 10^6$  to  $1.05 \times 10^6$ ) while enhancing the emission intensity of  $[\text{Ag}_{29}(\text{BDT})_{12}(\text{PPh}_3)_4]^{3-}$  (from  $4.43 \times 10^5$  to  $7.2 \times 10^5$ ). The emission spectra of Si NPs, FITC and  $[\text{Ag}_{29}(\text{BDT})_{12}(\text{PPh}_3)_4]^{3-}$  at 360 nm excitation are presented in Figure S4 (Supplementary Information) and the spectrum of their mixture at the same excitation is presented in Figure 3. Note that the individual species presented have the same concentrations as in the mixture. This confirms partial energy transfer from the blue-emitting donor to the embedded energy acceptors upon excitation of Si NPs (360 nm).

#### 4. Conclusions

In conclusion, we have presented the application of Ag NCs as an emerging fluorophore for white light emission along with blue luminescent Si NPs and the green luminescent FITC dye. The highly stable  $[\text{Ag}_{29}(\text{BDT})_{12}(\text{PPh}_3)_4]^{3-}$ , its gold doped analog  $[\text{Au}_x\text{Ag}_{29-x}(\text{BDT})_{12}(\text{PPh}_3)_4]^{3-}$  ( $x = 0-4$ ) and  $[\text{Ag}_{29}(\text{LA})_{12}]$  clusters have been synthesized and characterized. The first two clusters are soluble in DMF while the last one is soluble in water. The red, blue and green emitting materials were mixed together in appropriate composition to produce white luminescence. The mixture produced white light with emission coordinates near to that of pure white light emission (0.33, 0.33). Here, for the first time, organic soluble Ag NCs are used to produce white luminescence. An aqueous suspension of Si NPs, FITC and  $\text{Ag}_{29}(\text{LA})_{12}$  has produced white light with coordinates of (0.29, 0.31).

#### Supplementary Information (SI)

Figures S1–S4 are available at [www.ias.ac.in/chemsci](http://www.ias.ac.in/chemsci).

#### Acknowledgements

We thank the Department of Science and Technology and Government of India for giving continuous support to pursue our research program on nanomaterials. E. K. and S. B. thank IIT Madras for institute doctoral fellowships. M. J. thanks the University Grants Commission (UGC) for a fellowship.

#### References

1. Feng H T, Zheng X, Gu X, Chen M, Lam J W Y, Huang X and Tang B Z 2018 White-Light Emission of a Binary Light-Harvesting Platform Based on an Amphiphilic Organic Cage *Chem. Mater.* **30** 1285
2. Kamtekar K T, Monkman A P and Bryce M R 2010 Recent Advances in White Organic Light-Emitting Materials and Devices (WOLEDs) *Adv. Mater.* **22** 572
3. Praveen V K, Ranjith C and Armaroli N 2014 White-Light-Emitting Supramolecular Gels *Angew. Chem. Int. Ed.* **53** 365
4. Shen C C and Tseng W L 2009 One-Step Synthesis of White-Light-Emitting Quantum Dots at Low Temperature *Inorg. Chem.* **48** 8689
5. Zhang M, Yin S, Zhang J, Zhou Z, Saha M L, Lu C and Stang P J 2017 Metallacycle-Cored Supramolecular Assemblies with Tunable Fluorescence Including White-Light Emission *Proc. Natl. Acad. Sci. U. S. A.* **114** 3044
6. Pan M, Liao W M, Yin S Y, Sun S S and Su C Y 2018 Single-Phase White-Light-Emitting and Photoluminescent Color-Tuning Coordination Assemblies *Chem. Rev.* **118** 8889
7. Coppo P, Duati M, Kozhevnikov V N, Hofstraat J W and De C L 2005 White-Light Emission from an Assembly Comprising Luminescent Iridium and Europium Complexes *Angew. Chem. Int. Ed. Engl.* **44** 1806
8. Bhandari S, Pramanik S, Khandelwal R and Chattopadhyay A 2016 Gold Nanocluster and Quantum Dot Complex in Protein for Biofriendly White-Light-Emitting Material *ACS Appl. Mater. Interfaces* **8** 1600
9. Xavier P L, Chaudhari K, Baksi A and Pradeep T 2012 Protein-Protected Luminescent Noble Metal Quantum Clusters: An Emerging Trend in Atomic Cluster Nanoscience *Nano Rev.* **3** 14767
10. Baksi A, Xavier P L, Chaudhari K, Goswami N, Pal S K and Pradeep T 2013 Protein-Encapsulated Gold Cluster Aggregates: The Case of Lysozyme *Nanoscale* **5** 2009
11. Xie J, Zheng Y and Ying J Y 2009 Protein-Directed Synthesis of Highly Fluorescent Gold Nanoclusters *J. Am. Chem. Soc.* **131** 888
12. Wen X, Yu P, Toh Y R, Hsu A C, Lee Y C and Tang J 2012 Fluorescence Dynamics in BSA-Protected  $\text{Au}_{25}$  Nanoclusters *J. Phys. Chem. C* **116** 19032
13. Mohanty J S, Xavier P L, Chaudhari K, Bootharaju M S, Goswami N, Pal S K and Pradeep T 2012 Luminescent, Bimetallic AuAg Alloy Quantum Clusters in Protein Templates, Bimetallic AuAg Alloy Quantum Clusters in Protein Templates *Nanoscale* **4** 4255
14. Xavier P L, Chaudhari K, Verma P K, Pal S K and Pradeep T 2010 Luminescent Quantum Clusters of Gold in Transferrin Family Protein, Lactoferrin Exhibiting FRET *Nanoscale* **2** 2769
15. Shibu E S, Muhammed M A H, Tsukuda T and Pradeep T 2008 Ligand Exchange of  $\text{Au}_{25}\text{Sg}_{18}$  Leading to Functionalized Gold Clusters: Spectroscopy, Kinetics, and Luminescence *J. Phys. Chem. C* **112** 12168
16. Muhammed M A H, Shaw A K, Pal S K and Pradeep T 2008 Quantum Clusters of Gold Exhibiting FRET *J. Phys. Chem. C* **112** 14324
17. Muhammed M A H, Verma P K, Pal S K, Kumar R C A, Paul S, Omkumar R V and Pradeep T 2009 Bright, NIR-Emitting  $\text{Au}_{23}$  from  $\text{Au}_{25}$ : Characterization and Applications Including Biolabeling *Chem. Eur. J.* **15** 10110
18. Yu Y, Luo Z, Chevrier D M, Leong D T, Zhang P and Jiang D E, Xie J 2014 Identification of a Highly Luminescent  $\text{Au}_{22}(\text{Sg})_{18}$  Nanocluster *J. Am. Chem. Soc.* **136** 1246
19. Ghosh A, Udayabhaskararao T and Pradeep T 2012 One-Step Route to Luminescent  $\text{Au}_{18}\text{Sg}_{14}$  in the Condensed Phase and Its Closed Shell Molecular Ions in the Gas Phase *J. Phys. Chem. Lett.* **3** 1997
20. Baksi A, Natarajan G, Pradeep T, Harvey S R and Wysocki V H 2016 Possible Isomers in Ligand Protected  $\text{Ag}_{11}$  Cluster Ions Identified by Ion Mobility Mass Spectrometry and Fragmented by Surface Induced Dissociation *Chem. Commun.* **52** 3805



21. Yau S H, Ashenfelter B A, Desireddy A, Ashwell A P, Varnavski O, Schatz G C, Bigioni T P and Goodson T 2017 Optical Properties and Structural Relationships of the Silver Nanoclusters  $\text{Ag}_{32}(\text{Sg})_{19}$  and  $\text{Ag}_{15}(\text{Sg})_{11}$  *J. Phys. Chem. C* **121** 1349
22. Bertorelle F, Hamouda R, Rayane D, Broyer M, Antoine R, Dugourd P, Gell L, Kulesza A, Mitric R and Bonacic-Koutecky V 2013 Synthesis, Characterization and Optical Properties of Low Nuclearity Liganded Silver Clusters  $\text{Ag}_{31}(\text{Sg})_{19}$  and  $\text{Ag}_{15}(\text{Sg})_{11}$  *Nanoscale* **5** 5637
23. Guo J, Kumar S, Bolan M, Desireddy A, Bigioni T P and Griffith W P 2012 Mass Spectrometric Identification of Silver Nanoparticles: The Case of  $\text{Ag}_{32}(\text{Sg})_{19}$  *Anal. Chem.* **84** 5304
24. Wang Z, Wu L, Cai W and Jiang Z 2012 Luminescent  $\text{Au}_{11}$  Nanocluster Superlattices with High Thermal Stability *J. Mater. Chem.* **22** 3632
25. Wang Z, Cai W and Sui J 2009 Blue Luminescence Emitted from Monodisperse Thiolate-Capped  $\text{Au}_{11}$  Clusters *ChemPhysChem* **10** 2012
26. Wu Z, Lanni E, Chen W, Bier M E, Ly D and Jin R 2009 High Yield, Large Scale Synthesis of Thiolate-Protected  $\text{Ag}_7$  Clusters *J. Am. Chem. Soc.* **131** 16672
27. Rao T U B, Nataraju B and Pradeep T 2010  $\text{Ag}_9$  Quantum Cluster through a Solid-State Route *J. Am. Chem. Soc.* **132** 16304
28. Black D M, Robles G, Lopez P, Bach S B H, Alvarez M and Whetten R L 2018 Liquid Chromatography Separation and Mass Spectrometry Detection of Silver-Lipoate  $\text{Ag}_{29}(\text{La})_{12}$  Nanoclusters: Evidence of Isomerism in the Solution Phase *Anal. Chem.* **90** 2010
29. van der Linden M, Barendregt A, van Bunningen A J, Chin P T K, Thies-Weesie D, de Groot F M F and Meijerink A 2016 Characterisation, Degradation and Regeneration of Luminescent  $\text{Ag}_{29}$  Clusters in Solution *Nanoscale* **8** 19901
30. Russier-Antoine I, Bertorelle F, Hamouda R, Rayane D, Dugourd P, Sanader Z, Bonacic-Koutecky V, Brevet P F and Antoine R 2016 Tuning  $\text{Ag}_{29}$  Nanocluster Light Emission from Red to Blue with One and Two-Photon Excitation *Nanoscale* **8** 2892
31. Soldan G, Aljuhani M A, Bootharaju M S, AbdulHalim L G, Parida M R, Emwas A H, Mohammed O F and Bakr O M 2016 Gold Doping of Silver Nanoclusters: A 26-Fold Enhancement in the Luminescence Quantum Yield *Angew. Chem. Int. Ed.* **55** 5749
32. Wang S, Meng X, Das A, Li T, Song Y, Cao T, Zhu X, Zhu M and Jin R 2014 A 200-Fold Quantum Yield Boost in the Photoluminescence of Silver-Doped  $\text{Ag}_x\text{Au}_{25-x}$  Nanoclusters: The 13<sup>th</sup> Silver Atom Matters *Angew. Chem. Int. Ed.* **53** 2376
33. Chen T, Yang S, Chai J, Song Y, Fan J, Rao B, Sheng H, Yu H and Zhu M 2017 Crystallization-Induced Emission Enhancement: A Novel Fluorescent Au-Ag Bimetallic Nanocluster with Precise Atomic Structure *Sci. Adv.* **3** e1700956
34. Pyo K, Thanthirige V D, Kwak K, Pandurangan P, Ramakrishna G and Lee D 2015 Ultrabright Luminescence from Gold Nanoclusters: Rigidifying the  $\text{Au}(\text{I})$ -Thiolate Shell *J. Am. Chem. Soc.* **137** 8244
35. Pyo K, Thanthirige V D, Yoon S Y, Ramakrishna G and Lee D 2016 Enhanced Luminescence of  $\text{Au}_{22}(\text{Sg})_{18}$  Nanoclusters Via Rational Surface Engineering *Nanoscale* **8** 20008
36. AbdulHalim L G, Bootharaju M S, Tang Q, Del Gobbo S, AbdulHalim R G, Eddaoudi M, Jiang D E and Bakr O M 2015  $\text{Ag}_{29}(\text{Bdt})_{12}(\text{Tpp})_4$ : A Tetravalent Nanocluster *J. Am. Chem. Soc.* **137** 11970
37. Li G, Lei Z and Wang Q M 2010 Luminescent Molecular Ag-S Nanocluster  $[\text{Ag}_{62}\text{S}_{13}(\text{Sbut})_{32}](\text{Bf}_4)_4$  *J. Am. Chem. Soc.* **132** 17678
38. Li B, Huang R W, Qin J H, Zang S Q, Gao G G, Hou H W and Mak T C W 2014 Thermochromic Luminescent Nest-Like Silver Thiolate Cluster *Chem. Eur. J.* **20** 12416
39. Yang H, Lei J, Wu B, Wang Y, Zhou M, Xia A, Zheng L and Zheng N 2013 Crystal Structure of a Luminescent Thiolated Ag Nanocluster with an Octahedral  $\text{Ag}_6^{4+}$  Core *Chem. Commun.* **49** 300
40. Bootharaju M S, Kozlov S M, Cao Z, Harb M, Parida M R, Hedhili M N, Mohammed O F, Bakr O M, Cavallo L and Basset J M 2017 Direct Versus Ligand-Exchange Synthesis of  $[\text{PtAg}_{28}(\text{Bdt})_{12}(\text{Tpp})_4]^{4+}$  Nanoclusters: Effect of a Single-Atom Dopant on the Optoelectronic and Chemical Properties *Nanoscale* **9** 9529
41. Wang G, Huang T, Murray R W, Menard L and Nuzzo R G 2005 Near-Ir Luminescence of Monolayer-Protected Metal Clusters *J. Am. Chem. Soc.* **127** 812
42. Liu X, Yuan J, Yao C, Chen J, Li L, Bao X, Yang J and Wu Z 2017 Crystal and Solution Photoluminescence of  $\text{MAg}_{24}(\text{Sr})_{18}$  ( $\text{M} = \text{Ag}/\text{Pd}/\text{Pt}/\text{Au}$ ) Nanoclusters and Some Implications for the Photoluminescence Mechanisms *J. Phys. Chem. C* **121** 13848
43. Bose S, Ganayee M A, Mondal B, Baidya A, Chennu S, Mohanty J S and Pradeep T 2018 Synthesis of Silicon Nanoparticles from Rice Husk and Their Use as Sustainable Fluorophores for White Light Emission *ACS Sustainable Chem. Eng.* **6** 6203
44. So W Y, Li Q, Legaspi C M, Redler B, Koe K M, Jin R and Peteanu L A 2018 Mechanism of Ligand-Controlled Emission in Silicon Nanoparticles *ACS Nano* **12** 7232
45. Heintz A S, Fink M J and Mitchell B S 2007 Mechanochemical Synthesis of Blue Luminescent Alkyl/Alkenyl-Passivated Silicon Nanoparticles *Adv. Mater.* **19** 3984
46. Kang Z T, Arnold B, Summers C J and Wagner B K 2006 Synthesis of Silicon Quantum Dot Buried  $\text{SiO}_2$  Films with Controlled Luminescent Properties for Solid-State Lighting *Nanotechnology* **17** 4477
47. Morisaki H, Ping F W, Ono H and Yazawa K 1991 Above-Band-Gap Photoluminescence from Silicon Fine Particles with Oxide Shell *J. Appl. Phys.* **70** 1869
48. Gonzalez C M and Veinot J G C 2016 Silicon Nanocrystals for the Development of Sensing Platforms *J. Mater. Chem. C* **4** 4836
49. Robidillo C J T, Islam M A, Aghajamali M, Faramus A, Sinelnikov R, Zhang X, Boekhoven J and Veinot J G C 2018 Functional Bioinorganic Hybrids from Enzymes and Luminescent Silicon-Based Nanoparticles *Langmuir* **34** 6556

50. Shen X B, Song B, Fang B, Jiang A R, Ji S J and He Y 2018 Excitation-Wavelength-Dependent Photoluminescence of Silicon Nanoparticles Enabled by Adjustment of Surface Ligands *Chem. Commun.* **54** 4947
51. Ulusoy Ghobadi T G, Ghobadi A, Okyay T, Topalli K and Okyay A K 2016 Controlling Luminescent Silicon Nanoparticle Emission Produced by Nanosecond Pulsed Laser Ablation: Role of Interface Defect States and Crystallinity Phase *RSC Adv.* **6** 112520

## SUPPLEMENTARY INFORMATION (SI)

*Special Issue on Photochemistry, Photophysics and Photobiology*

### **Atomically precise cluster-based white light emitters §**

ESMA KHATUN, SANDEEP BOSE, MADHURI JASH and THALAPPIL PRADEEP\*

DST Unit of Nanoscience (DST UNS) and Thematic Unit of Excellence, Department of Chemistry, Indian Institute of Technology Madras, Chennai 600 036, Tamilnadu, India.

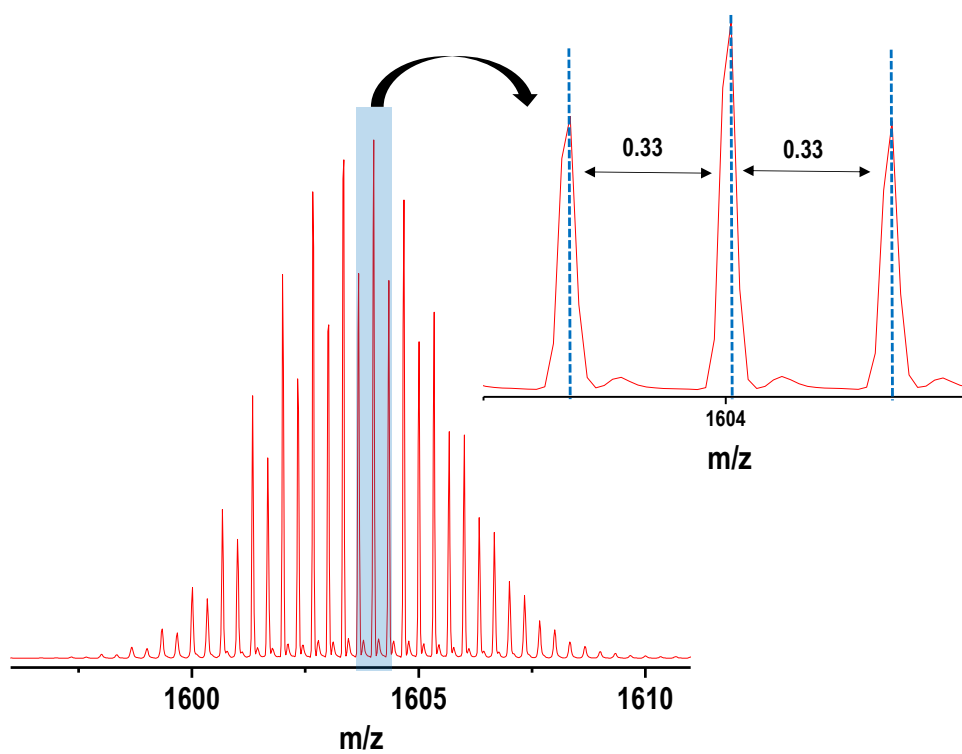
E-mail: [pradeep@iitm.ac.in](mailto:pradeep@iitm.ac.in)

§Dedicated to Professor M V George on the occasion of his 90<sup>th</sup> Birth Anniversary

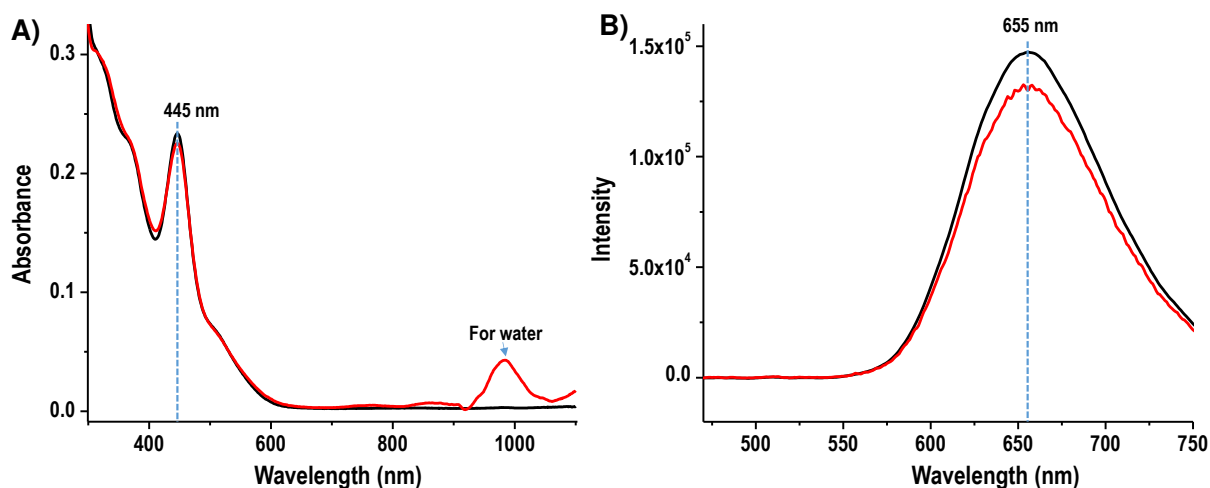
\*For correspondence

Figure S1-S4

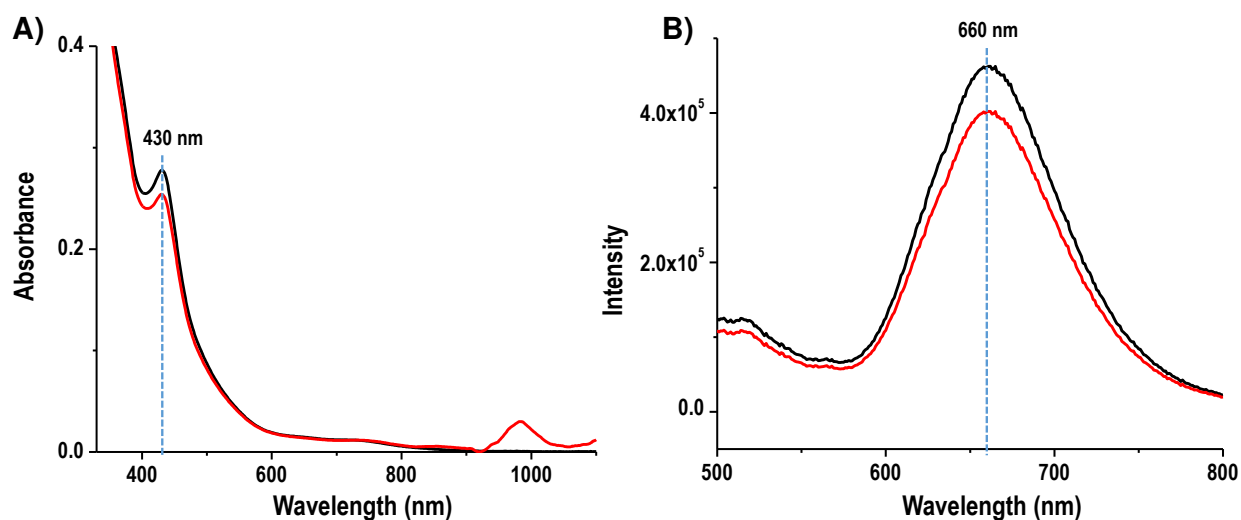
Pages 2-5



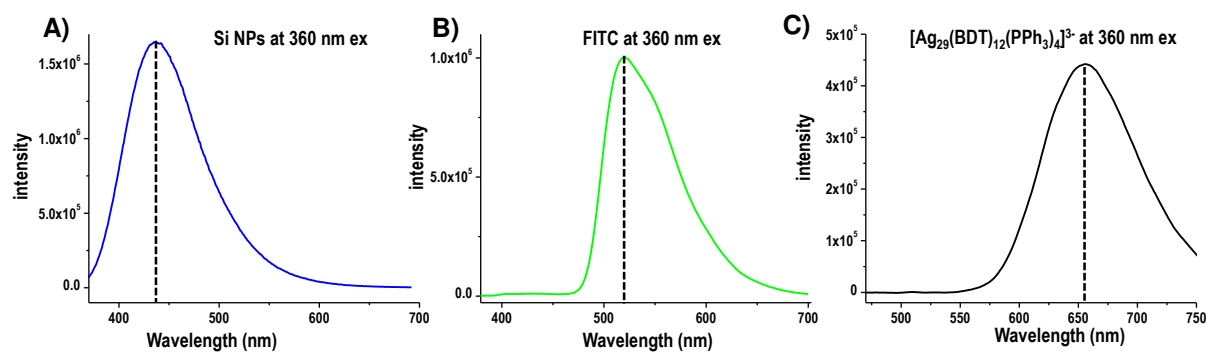
**Figure S1.** The expanded ESI MS of  $[\text{Ag}_{29}(\text{BDT})_{12}]^{3-}$  ( $m/z$  1603). The separation between two peaks is 0.33 which confirms  $3^-$  charge state of the cluster.



**Figure S2.** (A) The absorption and (B) the emission spectra of  $[Ag_{29}(BDT)_{12}(PPh_3)_4]^{3-}$  cluster in DMF (black line) and DMF/ H<sub>2</sub>O mixture (red line). The red colored absorption spectrum is having one extra peak at ~980 nm due to the presence of H<sub>2</sub>O. The other spectral features (peaks at 445 and 512 nm) of red spectrum are similar to that of black one which suggest the cluster stability in DMF/ H<sub>2</sub>O mixture. The emission spectrum of the cluster in DMF/H<sub>2</sub>O is similar to that DMF solution.



**Figure S3:** (A) The absorption and (B) the emission spectra of  $[\text{Au}_x\text{Ag}_{29-x}(\text{BDT})_{12}(\text{PPh}_3)_4]^{3-}$  cluster in DMF (black line) and DMF/  $\text{H}_2\text{O}$  mixture (red line). The red colored absorption spectrum exhibits one extra peak at  $\sim 980$  nm which is due to the presence of  $\text{H}_2\text{O}$ . The other spectral features (peaks at 430 and 730 nm) of red spectrum are similar to that of black one which suggest the cluster is stable in DMF/  $\text{H}_2\text{O}$  mixture. The cluster possesses similar emission spectrum in DMF/ $\text{H}_2\text{O}$  mixture to that of DMF solution.



**Figure S4.** The emission spectra of (A) Si NPs, (B) FITC dye and (C)  $[\text{Ag}_{29}(\text{BDT})_{12}(\text{PPh}_3)_4]^{3-}$  at 360 nm excitation. The concentrations of individual components used are the same in Figure 3.

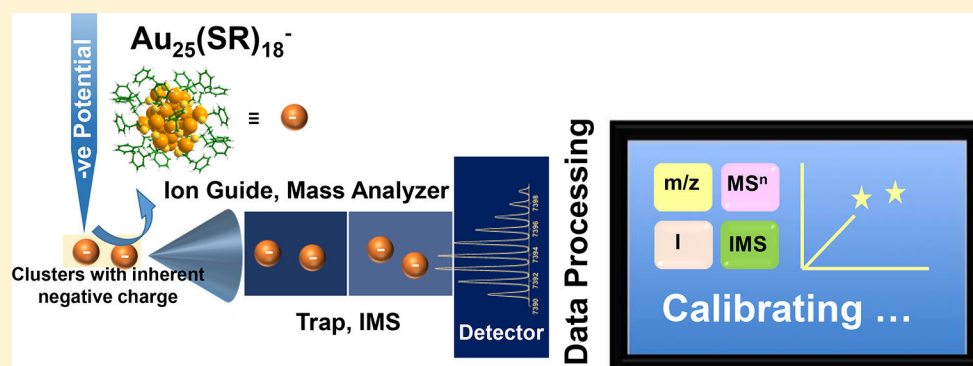


# Monolayer-Protected Noble-Metal Clusters as Potential Standards for Negative-Ion Mass Spectrometry

Ananya Bakshi,<sup>†,‡</sup> Papri Chakraborty,<sup>‡</sup> Abhijit Nag, Debasmita Ghosh, Shridevi Bhat, and Thalappil Pradeep\*<sup>§</sup>

DST Unit of Nanoscience and Thematic Unit of Excellence, Department of Chemistry, Indian Institute of Technology Madras, Chennai 600036, India

## Supporting Information



**ABSTRACT:** A detailed mass-spectrometric study of atomically precise monolayer-protected clusters revealed the potential application of such materials as mass-spectrometric standards, mostly in negative-ion mode and in the high-mass range. To date, very few molecules are known that can be efficiently ionized and detected at lower concentrations as negative ions with high signal intensities beyond  $m/z$  3000. Noble-metal clusters are molecules with definite masses, sizes, and shapes, which makes them excellent candidates to choose as standards over conventional low-molecular-weight polymers or clusters of ionic salts. They may be used as calibrants in all possible modes, including tandem mass spectrometry and ion mobility. With the advancement in materials science, more and more molecules are being added to the list that are inherently negatively charged in solution and can be examined by mass spectrometry. In this report, we demonstrate the use of three such model cluster systems for their potential to calibrate mass spectrometers in negative-ion mode. This idea can be extended to many other clusters known so far to achieve calibration in extended mass ranges.

Mass spectrometry (MS) has become an indispensable tool for the identification and characterization of organic molecules, proteins, and other biologically active species.<sup>1–4</sup> Pharmaceutical industries greatly depend on MS to determine the purity of drugs. In recent years, mass spectrometers have been used in hospitals and even during surgery.<sup>5–7</sup> It has proved to be a potential tool for biomarker identification for specific types of cancer.<sup>5</sup> The massive progress of MS in biology has prompted scientists to search for numerous proteins and peptides that can be used as standard molecules for understanding an unknown sample or calibrating instruments.<sup>4,8</sup> Most often, bigger proteins and peptides ionize reasonably well in positive-ion mode, and there are plenty of such molecules known to serve as mass-spectrometric standards.<sup>1,3,9</sup> Most of the protocols are commercialized and are being used throughout the world.

Although MS has deepened its roots in biology, it has also made a significant impact in materials science.<sup>2,10–13</sup> Recent developments in soft-ionization techniques, enhanced resolution, and high-mass ranges have enabled materials scientists

to characterize molecules of high mass-to-charge ratios ( $m/z$  few 100 kDa) by MS. Most often the molecules are ionized in negative-ion mode, and there are a limited number of molecules available that have the potential to act as negative-ion standards beyond  $m/z$  3000, although in some cases, calibrations have been performed by suitable salt sprays (mostly Cs-based salts) that form salt aggregates and can be ionized in both positive- and negative-ion modes.<sup>14</sup> The main problem with such a salt spray is the amount of salt required to get a series of well-defined peaks in the desired mass range (up to  $m/z$  7–8 kDa in negative-ion mode). Most often, very high concentrations of such salts (15–20 mg/mL or 15 000–20 000 ppm) are required, which are beyond the acceptable limit for any sensitive mass spectrometer.

Recently, a large number of materials have been solely characterized, and their compositions, including their inherent

Received: May 22, 2018

Accepted: August 31, 2018

Published: August 31, 2018



charges, have been determined by MS. Because of the lack of proper standards in the higher-mass range in negative-ion mode, it is often a difficult task to get the desired signal-to-noise ratio, the proper peak shape, and enough ion intensity with lower concentrations. Mass shifts in the higher-mass range can also be an issue in certain cases.

Atomically precise clusters are a new class of materials often characterized by MS.<sup>10,15–20</sup> They have molecule-like compositions and well-defined isotopic distributions, which enable their compositional identification via MS. Most of the clusters show a single peak corresponding to the molecular ion, although multiple charge states are also observed in a few cases. Many of these clusters are studied by single-crystal X-ray crystallography, and their compositions are further confirmed by MS. Several clusters of high molecular masses have also been detected in positive-ion mode with CsOAc as the ionization enhancer.<sup>15</sup> A large number of such clusters exist that show well-defined signals in negative-ion mode, such as  $\text{Au}_{25}(\text{SR})_{18}$ ,<sup>21</sup>  $\text{Ag}_{25}(\text{SR})_{18}$ ,<sup>22,23</sup>  $\text{Ag}_{29}(\text{S}_2\text{R})_{12}$ ,<sup>24,25</sup>  $\text{Ag}_{44}(\text{SR})_{30}$ ,<sup>26–28</sup> and others. Gold clusters as big as  $\text{Au}_{940\pm20}(\text{SCH}_2\text{CH}_2\text{Ph})_{160\pm4}$ , with a molecular ion of 207 kDa, could also be detected by electrospray-ionization mass spectrometry (ESI MS), which covers  $m/z$  ranges up to 60 kDa with four charged states of the species.<sup>29</sup> All these findings suggest that these clusters can potentially be used as standards in negative-ion MS. Several clusters are known to be ionized in positive-ion mode as well, which will allow them to be used as general mass-spectrometric standards for both ESI MS as well as matrix-assisted-laser-desorption-ionization (MALDI) MS.<sup>15,30,31</sup>

Besides having well-defined mass-spectral features, a molecule should possess the following essential characteristics to be a standard: (a) The molecule of interest should be stable in the condensed state as well as in the gas phase. It should be stable in normal temperature conditions, at which typical mass spectrometers work. As discussed above, clusters are known to show stability in these conditions. (b) Purity is essential for any molecule to be a standard. As the clusters can be crystallized, purity will not be an issue. (c) Cost effectiveness is another parameter that can be achieved by using clusters as standards. For a standard-cluster synthesis, about a few tens of dollars can produce a few milligrams of such clusters. (d) The molecule should be ionizable and detectable by different mass-spectrometric techniques, such as ESI MS, MALDI MS, and others. Clusters meet this criterion also. Although there are several other criteria to satisfy for a molecule to be a standard, we have just listed a few of them. Some others are discussed in the subsequent sections.

As monolayer-protected clusters meet the essential criteria, we have taken a few such clusters and performed ESI MS qualitatively and quantitatively. In this paper, we present detailed mass-spectrometric characterization of three clusters, namely,  $[\text{Ag}_{29}(\text{BDT})_{12}]^{3-}$  (BDT: 1,3-benzene dithiol),<sup>24</sup>  $[\text{Ag}_{25}(\text{DMBT})_{18}]^{-}$  (DMBT: 2,4-dimethylbenzene thiol),<sup>22</sup> and  $[\text{Au}_{25}(\text{PET})_{18}]^{-}$  (PET: phenylethanethiol),<sup>21</sup> which can be used as standards. The required modes of calibration, such as  $m/z$  calibration, intensity calibration, voltage calibration, MS/MS calibration, and ion-mobility calibration, are presented. This study will help to overcome the unavailability of negative-ion standards for high-mass ranges. This will also introduce a new application for such clusters. With the advancement of instrumentation and commercialization of state-of-the-art equipment, the mass-spectrometric research

endeavor in materials science is inevitable, and hence the use of such clusters as standard molecules will benefit both MS as well as materials science.

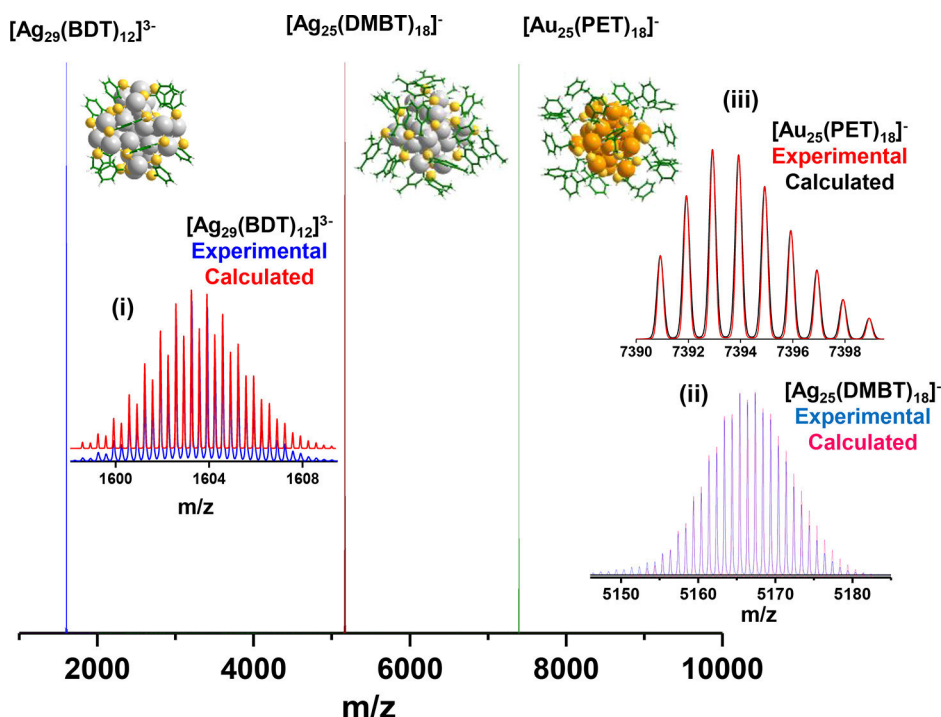
## MATERIALS AND METHODS

**Materials.** Silver nitrate ( $\text{AgNO}_3$ ), dichloromethane (DCM), phenylethanethiol (PET), 2,4-dimethylbenzene thiol (DMBT), 1,3-benzene dithiol (BDT), and sodium borohydride ( $\text{NaBH}_4$ ) were purchased from Sigma-Aldrich. Chloroauric acid ( $\text{HAuCl}_4 \cdot 3\text{H}_2\text{O}$ ) was prepared in the lab from pure gold.

At present, these clusters are not commercially available. They can be synthesized easily in a chemical laboratory following the well-established modified-Brust-synthesis method.<sup>34,35</sup> Synthesis of the three clusters described in this manuscript are presented below.

**Synthesis of  $[\text{Au}_{25}(\text{PET})_{18}]^{-}$ .** This cluster was synthesized following a previously reported method with slight modification.<sup>34,35</sup> Briefly, 40 mg of  $\text{HAuCl}_4 \cdot 3\text{H}_2\text{O}$  was dissolved in 7.5 mL of THF, and 65 mg of TOABr was mixed with the solution. The resulting mixture was stirred for around 15 min until the color of the solution changed to orange red. To this solution, 68  $\mu\text{L}$  of PET was added, and it was stirred for 1 h. The as-formed Au-PET thiolate was then reduced by adding about 39 mg of  $\text{NaBH}_4$  dissolved in ice-cold water. The color of the reaction mixture changed from yellow to brown, indicating reduction of thiolates. The solution was stirred for another 5 h for complete conversion and size focusing to achieve a high yield of  $[\text{Au}_{25}(\text{PET})_{18}]^{-}$ . After 5 h, the as-synthesized cluster was dried by a rotavapor, and excess MeOH was added to it to get rid of free thiol and excess thiolates. This process was repeated a few times to get a clean cluster sample. Then, the cluster was extracted in acetone and centrifuged. The supernatant solution was collected, leaving behind a smaller quantity of precipitate consisting of larger clusters. The acetone solution was then vacuum-dried. Finally the cluster was dissolved in DCM and centrifuged at 10 000 rpm, and the supernatant solution, which consisted of the pure cluster, was collected. The purified cluster was characterized by UV–vis-absorption spectroscopy, where characteristic peaks at 675 and 450 nm confirmed the formation of  $\text{Au}_{25}$  clusters (Figure S1). The sample was crystallized from a mixture of toluene/ethanol and kept at room temperature. This sample was used for detailed characterization by ESI MS.

**Synthesis of  $[\text{Ag}_{29}(\text{BDT})_{12}(\text{TPP})_4]^{3-}$ .** This cluster was synthesized according to the reported method.<sup>24,25</sup> About 20 mg of  $\text{AgNO}_3$  was dissolved in a 15 mL mixture of 1:2 (v/v) MeOH/DCM. To this solution, 13.5  $\mu\text{L}$  of 1,3-BDT was added, which immediately resulted in a turbid yellow solution indicating the formation of insoluble Ag–S complexes. This was followed by the addition of 200 mg of  $\text{PPh}_3$  in 1 mL of DCM, and the solution became colorless. The reaction mixture was stirred for about 15 min, and a freshly prepared solution of 10.5 mg of  $\text{NaBH}_4$  in 500  $\mu\text{L}$  of water was added to the mixture. The reaction mixture was kept in the dark and stirred for another 3 h while the dark-brown solution changed to orange. After 3 h, the reaction mixture was centrifuged, and the supernatant, consisting of unreacted thiolates and  $\text{PPh}_3$ , was discarded. The precipitate, consisting of the  $\text{Ag}_{29}$  cluster, was washed repeatedly with methanol to remove all the impurities. The purified sample was vacuum-dried and stored in a refrigerator. Dark-orange crystals of the cluster were obtained by dropcasting a concentrated solution of the cluster in DMF



**Figure 1.** ESI MS of  $[\text{Ag}_{29}(\text{BDT})_{12}]^{3-}$ ,  $[\text{Ag}_{25}(\text{DMBT})_{18}]^{-}$ , and  $[\text{Au}_{25}(\text{PET})_{18}]^{-}$  in negative-ion mode. The clusters were analyzed separately, and their respective mass spectra are overlaid in the figure, showing that a wide range of  $m/z$  calibration is possible by using these clusters as standards. Each ion shows an exact match with its calculated isotope pattern. The structures of the clusters are represented near their molecular-ion peaks. Gray: Ag, orange: Au, yellow: S, green: C, white: H.

on a glass slide. The purified cluster was characterized by UV–vis absorption (Figure S2) and used for ESI MS studies.

**Synthesis of  $[\text{Ag}_{25}(\text{DMBT})_{18}]^{-}$ .** This synthesis followed a reported protocol with slight modification.<sup>23,34</sup> About 38 mg of  $\text{AgNO}_3$  was dissolved in a mixture of 2 mL of methanol and 17 mL of DCM, and 90  $\mu\text{L}$  of 2,4-DMBT was added to it to form yellow, insoluble Ag–S complexes; the mixture was stirred at 0  $^{\circ}\text{C}$ . After about 15–17 min, 6 mg of  $\text{PPh}_4\text{Br}$  in 0.5 mL of methanol was added. This was followed by the dropwise addition of a solution of 15 mg of  $\text{NaBH}_4$  in 0.5 mL of ice-cold water. The reaction mixture was stirred for about 7–8 h. After that, stirring was discontinued, and the solution was kept at 4  $^{\circ}\text{C}$  for about 2 days. For purification of the cluster, the sample was centrifuged to remove any insoluble impurities, and DCM was removed by rotary evaporation. The precipitate was washed twice with methanol. After that, the cluster was redissolved in DCM and again centrifuged to remove any further insoluble contaminants. DCM was again removed by rotary evaporation, and the purified cluster was obtained in the powder form. Dark-black crystals of the cluster were obtained from a DCM/hexane mixture kept at 4  $^{\circ}\text{C}$  over a period of 2–7 days. The cluster was redissolved in DCM, characterized by UV–vis (Figure S3), and then used for ESI MS.

**Instrumental Details.** All the experiments described in this work were carried out in a Waters' Synapt G2Si HDMS instrument. The Synapt instrument consists of an electrospray source, quadrupole ion guide and trap, ion-mobility cell, and TOF detector. Different gases were used in different parts of the instrument. Nitrogen gas was used as the nebulizer gas. High-purity  $\text{N}_2$  was used in the ion-mobility cell, and the ions were directed through a drift tube. To reduce collision-induced fragmentation, He was used as the curtain gas before the ions entered the mobility cell. High-purity Ar gas was used for

collision-induced dissociation (CID). All the experiments were done in negative-ion mode. About 1  $\mu\text{g}/\text{mL}$  cluster ( $[\text{Ag}_{25}(\text{DMBT})_{18}]^{-}$  and  $[\text{Au}_{25}(\text{PET})_{18}]^{-}$ ) solution was prepared in DCM and directly infused with a flow rate of 10  $\mu\text{L}/\text{min}$ . Either DMF or ACN was used for  $[\text{Ag}_{29}(\text{BDT})_{12}]^{3-}$ . Minimum capillary voltage was applied to get a well-resolved mass spectrum. Other parameters used for analysis will be described in the course of the discussion. The instrument is highly sensitive to low concentrations of sample and can detect clusters down to 1  $\mu\text{M}$  concentrations.

Ions were analyzed by a time-of-flight mass analyzer. It has stacked ion optics to guide the ions to travel a specific path length depending on the acquisition-mode selected. Normally, ions move in a “V” path and the resolution obtained is in the range of 20 000–35 000. If required, ions can be deflected by an ion mirror to follow a “W” path where a resolution up to 50 000 can be achieved. Depending on the requirement, four different resolution modes can be selected, namely, sensitivity mode, resolution mode, high-resolution mode, and enhanced-resolution mode. In sensitivity mode, ions move in a shorter “V” path, the average resolution obtained for clusters is on the order of 15 000–20 000, low-concentration samples (1–10  $\mu\text{M}$ ) are sufficient to get the desired signal, and isotopic peaks might not be resolved to the baseline. In resolution mode, ions move in a longer “V” path, the average resolution obtained for clusters is on the order of 20 000–35 000, moderate concentrations (10–100  $\mu\text{M}$ ) are required to get good S/N, and isotopic peaks are well-resolved for all clusters with all types of charge states. In high-resolution and enhanced-resolution modes, ions move in shorter and longer “W” paths, respectively; the average resolution obtained for clusters is on the order of 35 000–50 000; and higher concentrations (1–10 mM) are required to get good S/N.



As we have obtained good resolution and S/N in resolution mode, we have performed all the experiments in this mode.

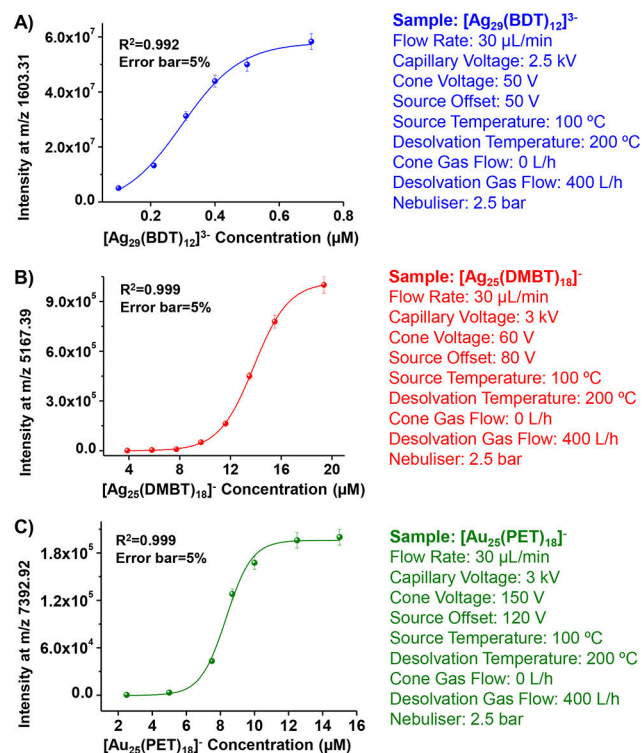
## RESULTS AND DISCUSSION

Calibration was performed using three of the above-mentioned clusters. For easier understanding, we have divided the calibration in the following parts: **Mass Calibration**, **Intensity Calibration**, **MS/MS Calibration**, and **Ion-Mobility (IM) Calibration**.

**Mass Calibration.** ESI MS of the samples was performed in the mass range of  $m/z$  100–10 000. Figure 1 shows the expanded mass spectra in the range of  $m/z$  1000–10 000. For the  $\text{Ag}_{29}(\text{BDT})_{12}(\text{TPP})_4$  cluster, a sharp peak appears at  $m/z$  1603.31, which corresponds to  $[\text{Ag}_{29}(\text{BDT})_{12}]^{3-}$ .<sup>24</sup> The TPP ligands were labile, and hence they were lost during ionization. The isotope pattern obtained matches exactly with the calculated one as shown in Figure 1 (inset i). On the other hand,  $[\text{Ag}_{25}(\text{DMBT})_{18}]^-$  shows a single peak at  $m/z$  5167.39<sup>22</sup>, and  $[\text{Au}_{25}(\text{PET})_{18}]^-$  shows a single peak at  $m/z$  7392.92. All the experimental and calculated spectra matched exactly, as shown in Figure 1 (insets ii and iii). The peak positions refer to the maximum-intensity peaks of the isotopologues.

All of these clusters can be used to calibrate the mass spectrometer. Details of the peak envelope with relative abundances and  $m/z$  positions are listed in Table S1.

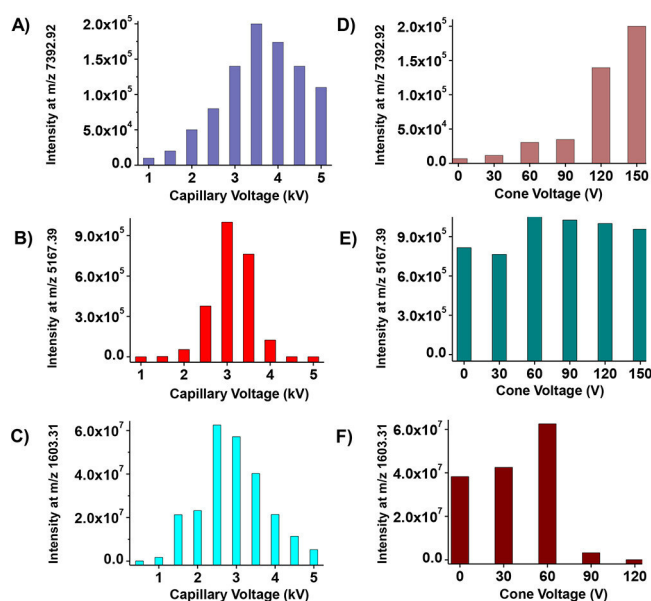
**Intensity Calibration.** *Concentration versus Intensity.* Each of the three clusters followed almost a sigmoidal increase of the ion intensity with concentration, and the mass spectra were collected at the same instrumental conditions. Figure 2 shows the plots of normalized intensity versus concentration ( $\mu\text{M}$ ) of the clusters. The parameters were kept similar to create a simplified tune file that can be used for any general



**Figure 2.** Concentration vs intensity of (A)  $[\text{Ag}_{29}(\text{BDT})_{12}]^{3-}$ , (B)  $[\text{Ag}_{25}(\text{DMBT})_{18}]^-$ , and (C)  $[\text{Au}_{25}(\text{PET})_{18}]^-$ . Optimized experimental conditions are listed along with each plot.

sample that is ionizable in negative-ion mode. Essential parameters are listed alongside the plots for the respective clusters. The same numbers of scans were averaged to avoid any error in intensity calculation.

**Voltage versus Intensity.** The maximum intensity of the desired ion was measured for the entire range of voltages. All of these clusters show increases in signal intensity with increasing capillary voltage (or ion-spray voltage) up to a certain voltage (around 3–3.5 kV). Beyond this, clusters start fragmenting because of high voltage and in-source fragmentation, resulting in decreases in ion intensity, as shown in Figure 3A–C. All the

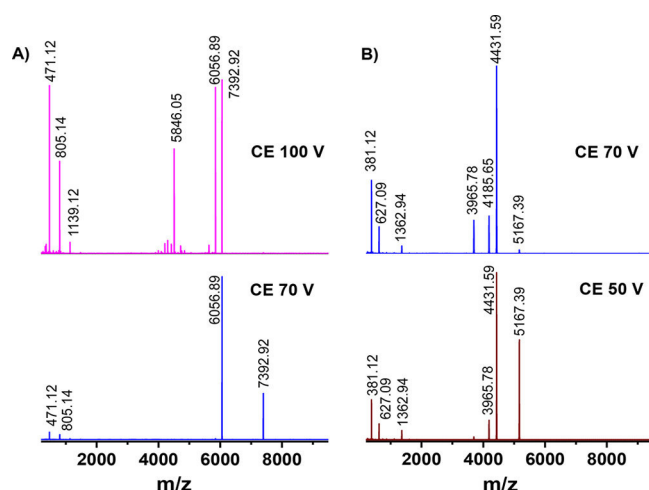


**Figure 3.** Capillary voltage vs intensity of (A)  $[\text{Au}_{25}(\text{PET})_{18}]^-$ , (B)  $[\text{Ag}_{25}(\text{DMBT})_{18}]^-$ , and (C)  $[\text{Ag}_{29}(\text{BDT})_{12}]^{3-}$ . (D–F) Dependence of cone voltage.

experiments were performed thrice and average intensity was plotted. Extraction voltage also plays a certain role in ion intensity.<sup>36,37</sup> Higher extraction voltage can also lead to fragmentation for certain molecules. However, some ions are stable throughout the extraction-voltage window. Extraction voltage also can be used to extract a preferred ion with a selective charge state. Some ions form weak dimers or polymers or gas-phase adducts, which might break if higher extraction voltages are used. For a certain molecule, choosing a certain extraction voltage is important to avoid any voltage-induced deformation as well as fragmentation.<sup>38</sup> Similarly, bias voltage may also be efficiently used for selecting a specific charge state of a selected ion. For example, for selecting a certain ion with a higher charge state, lesser bias voltage may be useful or vice versa. In the present study, capillary voltage corresponding to maximum intensity for each ion (Figure 3A–C) was selected to study the correlation with the cone (or extraction) voltage (Figure 3D–F). Although  $[\text{Au}_{25}(\text{PET})_{18}]^-$  shows a steady increase in intensity with increases in cone voltage,  $[\text{Ag}_{25}(\text{DMBT})_{18}]^-$  did not show such a dependence. On the other hand,  $[\text{Ag}_{29}(\text{BDT})_{12}]^{3-}$  showed increased intensity until 60 V, and then in-source fragmentation occurred and the intensity decreased drastically.

**MS/MS Calibration.** Each molecule has its well-defined fragmentation pattern, which is often used as a fingerprint for the molecule.<sup>39,40</sup> For unknown biomolecules, it is often

practiced that MS/MS spectra at different collision energies are collected and then matched with the reported database. For such types of molecules, exact mass is one of the most required criteria. This applies to the fragments also. Although there are several databases existing for small and large molecules and also a number of standards are available for calibration of MS/MS in positive-ion mode, very few molecules are used in negative-ion mode. The number is even smaller in the high-mass range. High concentrations of salt/salt mixtures (CsI/NaI) are mostly used for high-mass calibration.<sup>41,42</sup> These salts form (CSI)<sub>n</sub>I<sup>−</sup>-type clusters, which can cover a wide range, although this is highly dependent on the concentration used. Although *m/z* or intensity calibration is possible with these molecules, MS/MS calibration is tricky. Monolayer-protected clusters can be used to overcome this issue. Most of the clusters have well-defined fragmentation patterns that cover a low- to high-mass range. For example, [Au<sub>25</sub>(PET)<sub>18</sub>]<sup>−</sup> loses one Au<sub>4</sub>(PET)<sub>4</sub> unit, which is a neutral loss. The corresponding daughter ion, [Au<sub>21</sub>(PET)<sub>14</sub>]<sup>−</sup>, is detected at *m/z* 6056.89. Further fragmentation leads to the loss of two R groups (−SR=PET), and the fragment ion is observed at *m/z* 5846.05. These three peaks appear at higher intensities along with several other low-intensity fragments. Detailed assignment of all the peaks can be seen elsewhere<sup>43</sup> and is not in the scope of this study. Smaller thiolate fragments are seen at *m/z* 471.12 (Au(PET)<sub>2</sub><sup>−</sup>), 805.14 (Au<sub>2</sub>(PET)<sub>3</sub><sup>−</sup>), 1139.12 (Au<sub>3</sub>(PET)<sub>4</sub><sup>−</sup>), and others. Relative intensities of the peaks vary with collision energy. Fragmentation patterns at two different collision energies are shown in Figure 4A. A similar study was



**Figure 4.** (A) CID of [Au<sub>25</sub>(PET)<sub>18</sub>]<sup>−</sup> at CE 70 and 100 V (laboratory CE), showing fragments. Exact masses of the fragments are given. (B) Similar study on [Ag<sub>25</sub>(DMBT)<sub>18</sub>]<sup>−</sup>, showing its fragments.

performed on [Ag<sub>25</sub>(DMBT)<sub>18</sub>]<sup>−</sup>, and the mass spectra are shown in Figure 4B. The MS/MS pattern of [Ag<sub>29</sub>(BDT)<sub>12</sub>]<sup>3−</sup> can also be used similarly for calibration (Figure S4). Experimental conditions and relative intensities of the ions are tabulated in Table 1. The assignment of the peaks<sup>25,43</sup> is presented in the Supporting Information (Table S2).

**Ion-Mobility (IM) Calibration.** Lack of standards for IM MS for negative ions is also an important concern.<sup>44</sup> Most of the mass spectrometers use proteins as their internal standards. Proteins have a number of gas-phase conformers and have reproducible experimental collision-cross-section (CCS) val-

**Table 1.** Intensities and *m/z* Values of Fragments of [Au<sub>25</sub>(PET)<sub>18</sub>]<sup>−</sup>, [Ag<sub>25</sub>(DMBT)<sub>18</sub>]<sup>−</sup>, and [Ag<sub>29</sub>(BDT)<sub>12</sub>]<sup>3−</sup> during CID<sup>a</sup>

CID at <i>m/z</i> 7392.93 (Au <sub>25</sub> (PET) <sub>18</sub> <sup>−</sup> )			
CE 70 V		CE 100 V	
<i>m/z</i>	relative intensity (%)	<i>m/z</i>	relative intensity (%)
805.14	3.1	471.12	96.5
1139.12	5.2	805.14	53.2
5846.05	49.6	1139.12	65.1
6056.89	100.0	5846.05	95.5
7392.92	28.3	6056.89	100.0
		7392.92	1.4
CID at <i>m/z</i> 5167.39 (Ag <sub>25</sub> (DMBT) <sub>18</sub> <sup>−</sup> )			
CE 50 V		CE 70 V	
<i>m/z</i>	relative intensity (%)	<i>m/z</i>	relative intensity (%)
381.12	23.9	381.12	1.8
627.09	9.5	627.09	100.0
1362.94	5.5	1362.94	19.7
3965.78	1.6	3965.78	17.5
4185.65	11.6	4185.65	3.9
4431.59	100.0	4431.59	14.1
567.39	60.1	567.39	38.4
CID at <i>m/z</i> 1603.31 (Ag <sub>29</sub> (BDT) <sub>12</sub> <sup>3−</sup> )			
CE 70 V		CE 100 V	
<i>m/z</i>	relative intensity (%)	<i>m/z</i>	relative intensity (%)
959.99	53.3	959.99	100.0
1603.31	100.0	1603.31	29.0
1925.39	7.5	1925.39	6.7

<sup>a</sup>Collision energy (CE) is in instrumental units, although it is mentioned as being in volts.

ues. This makes them excellent choices as standards for ion mobility.<sup>45–48</sup> Small peptides<sup>49</sup> and clusters such as C<sub>60</sub><sup>50</sup> are also known to be used as standards for low-mass calibration. Polymeric amino acids such as polyalanine<sup>44,51</sup> can be used for calibration of ion mobility but only up to *m/z* 3000. Beyond this range, no standards are available for ion-mobility calibration in negative-ion mode, especially for ESI MS. Recent reports on the use of Au<sub>n</sub><sup>±</sup> clusters for MALDI TOF used citrate-capped monodispersed Au nanoparticles as internal standards and generated in situ clusters by laser ablation which could cover a mass range until *m/z* 15 000.<sup>52</sup> However, this in situ cluster formation from such Au nanoparticles is not possible in ESI MS.

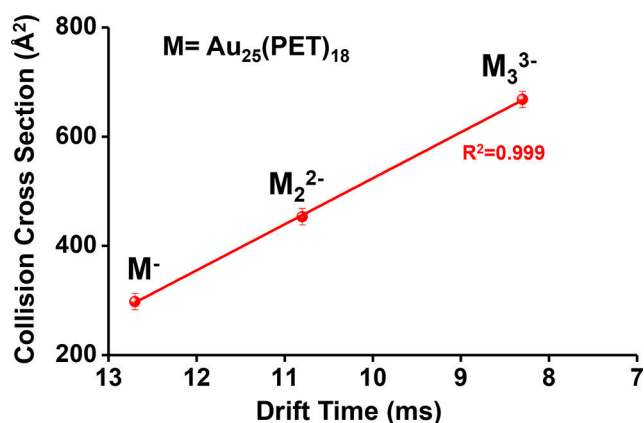
The advantages of inherent negative charge, high ionization tendency, well-defined isotope distribution, and the choice of molecules for a specific mass range make these clusters excellent standards for ion-mobility calibration. Ion-mobility drift times depend on the IMS velocity and follow a linear relation. Although the peak width changes when the IMS velocity changes, ratios of drift time (DT) and peak width (ΔDT), DT/ΔDT, should remain constant for a calibrant. We have studied the ion mobilities of all three clusters, and the data are listed in Table 2.

Drift time plots at different IMS velocities for three different clusters are shown in Figure S5. From the data, it is evident that these clusters are excellent ion-mobility standards. The [Au<sub>25</sub>(PET)<sub>18</sub>]<sup>−</sup> cluster can form polymers that are easily separable by ion mobility, and hence extended-mass-range calibration is also possible. This can be used to calibrate the

**Table 2.** Ion-Mobility-Calibration Table of  $[\text{Au}_{25}(\text{PET})_{18}]^-$ ,  $[\text{Ag}_{25}(\text{DMBT})_{18}]^-$ , and  $[\text{Ag}_{29}(\text{BDT})_{12}]^{3-}$ 

IMS calibration with $[\text{Au}_{25}(\text{PET})_{18}]^-$				
IMS velocity (m/s)	DT (ms)	$\Delta\text{DT}$	DT/ $\Delta\text{DT}$	intensity
400	8.99	0.535	16.80	269 000
500	12.17	0.720	16.87	144 000
600	15.90	0.950	16.73	65 000
IMS calibration with $[\text{Ag}_{25}(\text{DMBT})_{18}]^-$				
IMS velocity (m/s)	DT (ms)	$\Delta\text{DT}$	DT/ $\Delta\text{DT}$	intensity
400	8.02	0.829	9.67	237 000
500	10.51	1.082	9.71	195 000
600	13.41	1.385	9.68	130 000
IMS calibration with $[\text{Ag}_{29}(\text{BDT})_{12}]^{3-}$				
IMS velocity (m/s)	DT (ms)	$\Delta\text{DT}$	DT/ $\Delta\text{DT}$	intensity
400	2.01	0.244	8.23	269,000,00
500	2.56	0.273	9.37	245,000,00
600	3.05	0.336	9.07	219,000,00

CCS for the system. Dimers and trimers of  $[\text{Au}_{25}(\text{PET})_{18}]^-$  form at specific instrumental conditions, and all these polymers appear at the same  $m/z$ .<sup>34</sup> Drift time versus CCS follows a linear correlation for these species. As they are at the same  $m/z$  with different charges, it is easy to calibrate the CCS using these polymers (see Figure 5).

**Figure 5.** Drift time vs collision cross section (CCS) of  $\text{Au}_{25}(\text{PET})_{18}^-$  monomer, dimer, and trimer showing a linear relationship.

## CONCLUSION

In this paper, we tried to emphasize the use of monolayer-protected clusters as MS standards, taking three well-established clusters as examples. These clusters are shown to be used as calibrants for  $m/z$ , intensity, MS/MS, IMS, and CCS measurements. These cover most of the aspects of samples measured in ESI MS. Although only three clusters are shown as potential standards for negative-ion MS, this should not be seen as a limitation. Several clusters are reported and many of them are known to form crystals. At present, clusters with 900 metal atoms and masses exceeding 100 kDa are available, and they are detectable by MS as well. These clusters can also be used for calibrating higher-mass ranges. Another advantage of using these materials as standards is the use of them for MALDI MS; this aspect has not been studied in the present manuscript. These clusters are stable in the laser-desorption process. There has been a tremendous increase in

the number of publications in which MS is used to characterize materials. As cluster science is expanding and new molecules are being added each day, standardization of mass spectrometers for the study of clusters is indeed a necessity for the future of materials science.

## ASSOCIATED CONTENT

### Supporting Information

The Supporting Information is available free of charge on the ACS Publications website at DOI: 10.1021/acs.analchem.8b02280.

UV-vis characterization of the clusters, additional ESI MS, details of the peak envelope of the isotope pattern, and assignment of the fragments obtained in the MS/MS spectra of the clusters (PDF)

## AUTHOR INFORMATION

### Corresponding Author

\*E-mail: pradeep@iitm.ac.in. Fax: 91-44-2257-0545/0509.

### ORCID

Thalappil Pradeep: 0000-0003-3174-534X

### Present Address

<sup>†</sup>A.B.: Karlsruhe Institute of Technology (KIT), Institute of Nanotechnology, Hermann-von-Helmholtz-Platz 1, 76344 Eggenstein-Leopoldshafen, Germany.

### Author Contributions

<sup>‡</sup>A.B. and P.C. contributed equally. The manuscript was written through the contributions of all authors.

### Notes

The authors declare no competing financial interest.

## ACKNOWLEDGMENTS

A.B. thanks Indian Institute of Technology Madras (IITM) for an institute postdoctoral fellowship. P.C. thanks the Council of Scientific and Industrial Research (CSIR) for a research fellowship. A.N., D.G., and S.B. thank IITM for institute doctoral fellowships.

## REFERENCES

- (1) Mann, M. *Nat. Rev. Mol. Cell Biol.* **2016**, *17*, 678.
- (2) Rauschenbach, S.; Ternes, M.; Harnau, L.; Kern, K. *Annu. Rev. Anal. Chem.* **2016**, *9*, 473–498.
- (3) Sauer, S.; Kliem, M. *Nat. Rev. Microbiol.* **2010**, *8*, 74–82.
- (4) Zheng, Q.; Chen, H. *Annu. Rev. Anal. Chem.* **2016**, *9*, 411–448.
- (5) Eberlin, L. S.; Tibshirani, R. J.; Zhang, J.; Longacre, T. A.; Berry, G. J.; Bingham, D. B.; Norton, J. A.; Zare, R. N.; Poultsides, G. A. *Proc. Natl. Acad. Sci. U. S. A.* **2014**, *111*, 2436–2441.
- (6) Eberlin, L. S.; Norton, I.; Orringer, D.; Dunn, I. F.; Liu, X.; Ide, J. L.; Jarmusch, A. K.; Ligon, K. L.; Jolesz, F. A.; Golby, A. J.; Santagata, S.; Agar, N. Y. R.; Cooks, R. G. *Proc. Natl. Acad. Sci. U. S. A.* **2013**, *110*, 1611–1616.
- (7) Ifa, D. R.; Eberlin, L. S. *Clin. Chem.* **2016**, *62*, 111–123.
- (8) Sztaray, J.; Memboeuf, A.; Drahos, L.; Vekey, K. *Mass Spectrom. Rev.* **2011**, *30*, 298–320.
- (9) Chace, D. H. *Chem. Rev.* **2001**, *101*, 445–477.
- (10) Chakraborty, I.; Pradeep, T. *Chem. Rev.* **2017**, *117*, 8208–8271.
- (11) Krishnadas, K. R.; Bakshi, A.; Ghosh, A.; Natarajan, G.; Som, A.; Pradeep, T. *Acc. Chem. Res.* **2017**, *50*, 1988–1996.
- (12) Pradeep, T.; Bakshi, A.; Xavier, P. L. *RSC Smart Mater.* **2014**, *7*, 169–225.
- (13) Xavier, P. L.; Chaudhari, K.; Bakshi, A.; Pradeep, T. *Nano Rev.* **2012**, *3*, 14767.



- (14) Galhena, A. S.; Jones, C. M.; Wysocki, V. H. *Int. J. Mass Spectrom.* **2009**, *287*, 105–113.
- (15) Jin, R.; Zeng, C.; Zhou, M.; Chen, Y. *Chem. Rev.* **2016**, *116*, 10346–10413.
- (16) Maity, P.; Xie, S.; Yamauchi, M.; Tsukuda, T. *Nanoscale* **2012**, *4*, 4027–4037.
- (17) Kurashige, W.; Niihori, Y.; Sharma, S.; Negishi, Y. *Coord. Chem. Rev.* **2016**, *320–321*, 238–250.
- (18) Gerwien, A.; Schildhauer, M.; Thumser, S.; Mayer, P.; Dube, H. *Nat. Commun.* **2018**, *9*, 1–9.
- (19) Yao, Q.; Feng, Y.; Fung, V.; Yu, Y.; Jiang, D.-e.; Yang, J.; Xie, J. *Nat. Commun.* **2017**, *8*, 1–11.
- (20) Yao, Q.; Yuan, X.; Fung, V.; Yu, Y.; Leong, D. T.; Jiang, D.-e.; Xie, J. *Nat. Commun.* **2017**, *8*, 1–11.
- (21) Zhu, M.; Aikens, C. M.; Hollander, F. J.; Schatz, G. C.; Jin, R. *J. Am. Chem. Soc.* **2008**, *130*, 5883–5885.
- (22) Joshi, C. P.; Bootharaju, M. S.; Alhilaly, M. J.; Bakr, O. M. *J. Am. Chem. Soc.* **2015**, *137*, 11578–11581.
- (23) Krishnadas, K. R.; Baksi, A.; Ghosh, A.; Natarajan, G.; Pradeep, T. *Nat. Commun.* **2016**, *7*, 13447.
- (24) AbdulHalim, L. G.; Bootharaju, M. S.; Tang, Q.; Del Gobbo, S.; AbdulHalim, R. G.; Eddaoudi, M.; Jiang, D.-e.; Bakr, O. M. *J. Am. Chem. Soc.* **2015**, *137*, 11970–11975.
- (25) Chakraborty, P.; Baksi, A.; Khatun, E.; Nag, A.; Ghosh, A.; Pradeep, T. *J. Phys. Chem. C* **2017**, *121*, 10971–10981.
- (26) Desiredy, A.; Conn, B. E.; Guo, J.; Yoon, B.; Barnett, R. N.; Monahan, B. M.; Kirschbaum, K.; Griffith, W. P.; Whetten, R. L.; Landman, U.; Bigioni, T. P. *Nature* **2013**, *501*, 399–402.
- (27) Yang, H.; Wang, Y.; Huang, H.; Gell, L.; Lehtovaara, L.; Malola, S.; Hakkinen, H.; Zheng, N. *Nat. Commun.* **2013**, *4*, 2422.
- (28) Baksi, A.; Ghosh, A.; Mudedla, S. K.; Chakraborty, P.; Bhat, S.; Mondal, B.; Krishnadas, K. R.; Subramanian, V.; Pradeep, T. *J. Phys. Chem. C* **2017**, *121*, 13421–13427.
- (29) Kumara, C.; Zuo, X.; Cullen, D. A.; Dass, A. *ACS Nano* **2014**, *8*, 6431–6439.
- (30) Sakthivel, N. A.; Theivendran, S.; Ganeshraj, V.; Oliver, A. G.; Dass, A. *J. Am. Chem. Soc.* **2017**, *139*, 15450–15459.
- (31) Kumara, C.; Zuo, X.; Ilavsky, J.; Chapman, K. W.; Cullen, D. A.; Dass, A. *J. Am. Chem. Soc.* **2014**, *136*, 7410–7417.
- (32) Brust, M.; Walker, M.; Bethell, D.; Schiffrin, D. J.; Whyman, R. *J. Chem. Soc., Chem. Commun.* **1994**, *0*, 801–802.
- (33) Chakraborty, I.; Pradeep, T. *Chem. Rev.* **2017**, *117*, 8208–8271.
- (34) Baksi, A.; Chakraborty, P.; Bhat, S.; Natarajan, G.; Pradeep, T. *Chem. Commun.* **2016**, *52*, 8397–8400.
- (35) Bhat, S.; Baksi, A.; Mudedla, S. K.; Natarajan, G.; Subramanian, V.; Pradeep, T. *J. Phys. Chem. Lett.* **2017**, *8*, 2787–2793.
- (36) Pashynska, V. A.; Kosevich, M. V.; Heuvel, H. V. d.; Claeys, M. *Rapid Commun. Mass Spectrom.* **2006**, *20*, 755–763.
- (37) Hunt, S. M.; Sheil, M. M.; Belov, M.; Derrick, P. *Anal. Chem.* **1998**, *70*, 1812–1822.
- (38) Yan, Z.; Caldwell, G. W.; Jones, W. J.; Masucci, J. A. *Rapid Commun. Mass Spectrom.* **2003**, *17*, 1433–1442.
- (39) Dührkop, K.; Shen, H.; Meusel, M.; Rousu, J.; Böcker, S. *Proc. Natl. Acad. Sci. U. S. A.* **2015**, *112*, 12580.
- (40) Cottrell, J. S. *J. Proteomics* **2011**, *74*, 1842–1851.
- (41) Lou, X.; van Dongen, J. L. J.; Meijer, E. W. *J. Am. Soc. Mass Spectrom.* **2010**, *21*, 1223–1226.
- (42) König, S.; Fales, H. M. *J. Am. Soc. Mass Spectrom.* **1999**, *10*, 273–276.
- (43) Angel, L. A.; Majors, L. T.; Dharmaratne, A. C.; Dass, A. *ACS Nano* **2010**, *4*, 4691–4700.
- (44) Forsythe, J. G.; Petrov, A. S.; Walker, C. A.; Allen, S. J.; Pellissier, J. S.; Bush, M. F.; Hud, N. V.; Fernandez, F. M. *Analyst* **2015**, *140*, 6853–6861.
- (45) Kune, C.; Far, J.; De Pauw, E. *Anal. Chem.* **2016**, *88*, 11639–11646.
- (46) Chawner, R.; McCullough, B.; Giles, K.; Barran, P. E.; Gaskell, S. J.; Evers, C. E. *J. Proteome Res.* **2012**, *11*, 5564–5572.
- (47) Jurneczko, E.; Kalapothakis, J.; Campuzano, I. D. G.; Morris, M.; Barran, P. E. *Anal. Chem.* **2012**, *84*, 8524–8531.
- (48) Haler, J. R. N.; Kune, C.; Massonnet, P.; Comby-Zerbino, C.; Jordens, J.; Honing, M.; Mengerink, Y.; Far, J.; De Pauw, E. *Anal. Chem.* **2017**, *89*, 12076–12086.
- (49) Bush, M. F.; Campuzano, I. D. G.; Robinson, C. V. *Anal. Chem.* **2012**, *84*, 7124–7130.
- (50) Mesleh, M. F.; Hunter, J. M.; Shvartsburg, A. A.; Schatz, G. C.; Jarrold, M. F. *J. Phys. Chem.* **1996**, *100*, 16082–16086.
- (51) Lietz, C. B.; Yu, Q.; Li, L. *J. Am. Soc. Mass Spectrom.* **2014**, *25*, 2009–2019.
- (52) Kolářová, L.; Prokeš, L.; Kučera, L.; Hampl, A.; Peňa-Méndez, E.; Vaňhara, P.; Havel, J. *J. Am. Soc. Mass Spectrom.* **2017**, *28*, 419–427.



## Supporting Information

### Monolayer Protected Noble Metal Clusters as Potential Standards for Negative Ion Mass Spectrometry

Ananya Baksi,<sup>†</sup> Papri Chakraborty,<sup>†</sup> Abhijit Nag, Debasmita Ghosh, Shridevi Bhat and Thalappil Pradeep\*

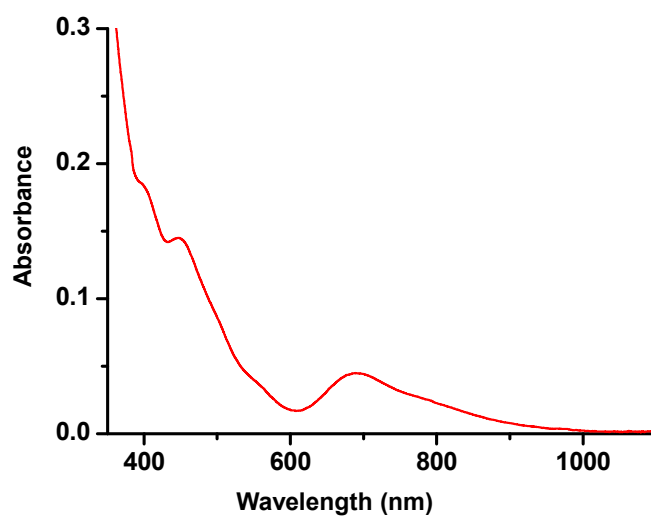
DST Unit of Nanoscience and Thematic Unit of Excellence, Indian Institute of Technology Madras, Chennai, 600036

\*Email: [pradeep@iitm.ac.in](mailto:pradeep@iitm.ac.in)

#### Table of Contents

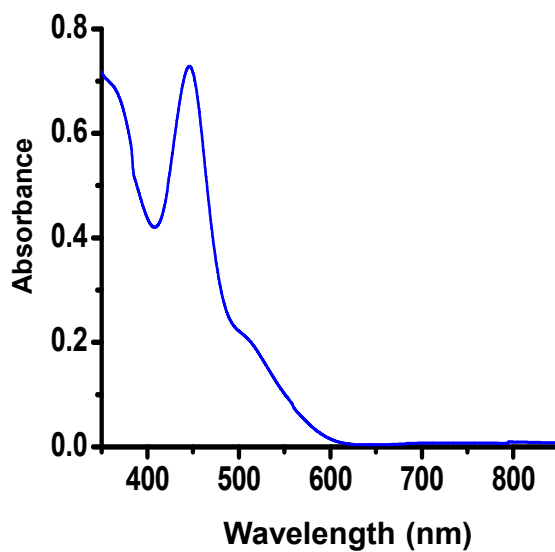
List of Figures	Description	Page Number
Figure S1	UV-vis spectrum of $[\text{Au}_{25}(\text{PET})_{18}]^-$	2
Figure S2	UV-vis spectrum of $[\text{Ag}_{29}(\text{BDT})_{12}(\text{TPP})_4]^{3-}$	2
Figure S3	UV-vis spectrum of $[\text{Ag}_{25}(\text{DMBT})_{18}]^-$	3
Figure S4	CID mass spectra of $[\text{Ag}_{29}(\text{BDT})_{12}(\text{TPP})_4]^{3-}$	3
Figure S5	Drift time plots at different IMS velocity for $[\text{Au}_{25}(\text{PET})_{18}]^-$ , $[\text{Ag}_{25}(\text{DMBT})_{18}]^-$ and $[\text{Ag}_{29}(\text{BDT})_{12}]^{3-}$ clusters.	4
Table S1	Detail of the peak envelope of the isotope pattern with relative abundances and m/z positions for $[\text{Ag}_{29}(\text{BDT})_{12}]^{3-}$ , $[\text{Ag}_{25}(\text{DMBT})_{18}]^-$ and $[\text{Au}_{25}(\text{PET})_{18}]^-$ clusters	5
Table S2	Assignment of the fragments obtained in the MS/MS spectra of $[\text{Ag}_{25}(\text{DMBT})_{18}]^-$ and $[\text{Ag}_{29}(\text{BDT})_{12}]^{3-}$ clusters.	6

## Supporting Information 1



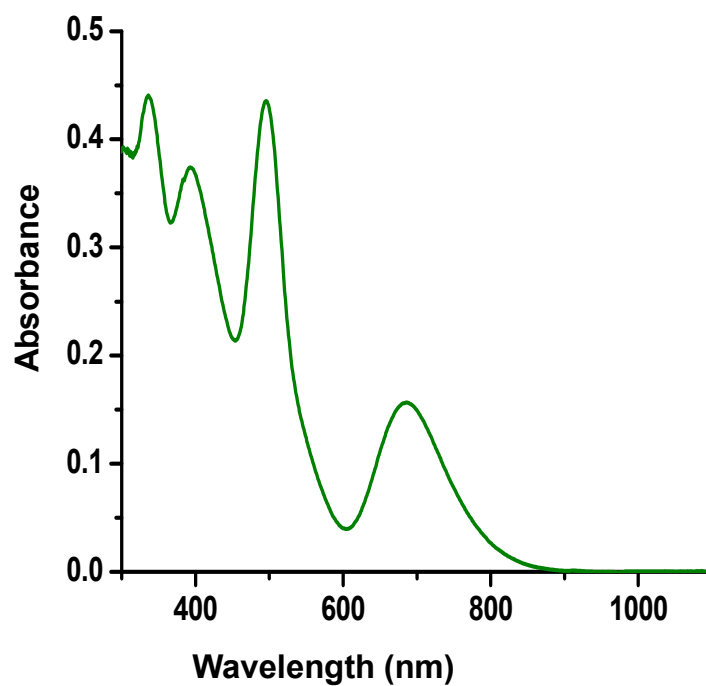
**Figure S1.** UV-vis spectrum of  $[\text{Au}_{25}(\text{PET})_{18}]^-$  showing all the characteristic bands confirming the purity of the cluster.

## Supporting Information 2



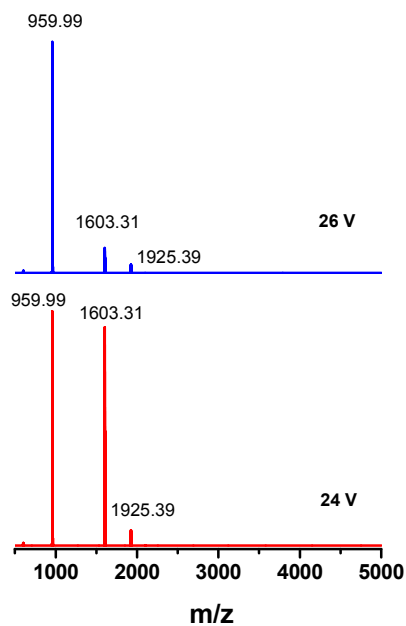
**Figure S2.** UV-vis spectrum of  $[\text{Ag}_{29}(\text{BDT})_{12}(\text{TPP})_4]^{3-}$  showing all the characteristic bands confirming the purity of the cluster.

### Supporting Information 3



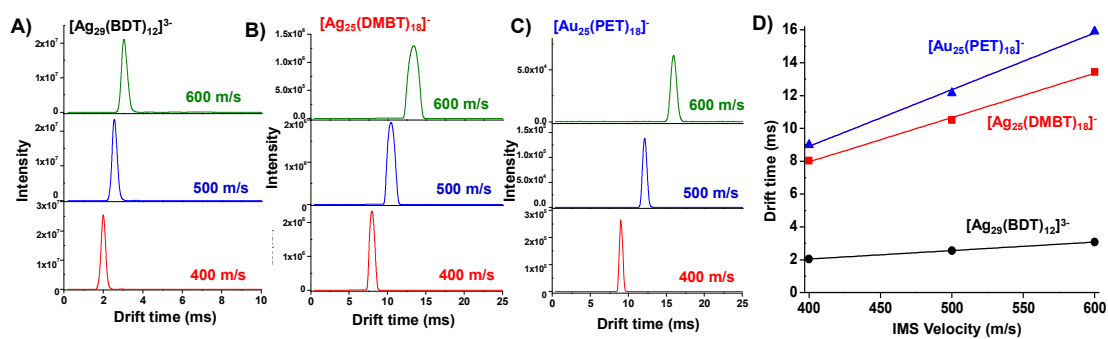
**Figure S3.** UV-vis spectrum of  $[\text{Ag}_{25}(\text{DMBT})_{18}]^+$  showing all the characteristic bands confirming the purity of the cluster.

### Supporting Information 4



**Figure S4.** CID mass spectra of  $[\text{Ag}_{29}(\text{BDT})_{12}(\text{TPP})_4]^{3-}$  at CE 24 V and 26 V laboratory CE showing fragments. Exact masses of the fragments are given.

## Supporting Information 5



**Figure S5.** Drift time plots at different IMS velocity for A)  $[\text{Au}_{25}(\text{PET})_{18}]^{-}$ , B)  $[\text{Ag}_{25}(\text{DMBT})_{18}]^{-}$  and C)  $[\text{Ag}_{29}(\text{BDT})_{12}]^{3-}$  clusters. IMS velocity and drift time shows linear relation for the clusters as shown in D).

## Supporting Tables

**Table S1.** Detail of the peak envelope of the isotope pattern with relative abundances and m/z positions for  $[\text{Ag}_{29}(\text{BDT})_{12}]^{3-}$ ,  $[\text{Ag}_{25}(\text{DMBT})_{18}]^{-}$  and  $[\text{Au}_{25}(\text{PET})_{18}]^{-}$  clusters, respectively.

$\text{Ag}_{29}(\text{BDT})_{12}^{3-}$		$\text{Ag}_{25}(\text{DMBT})_{18}^{-}$		$\text{Au}_{25}(\text{PET})_{18}^{-}$	
m/z	Relative abundance	m/z	Relative abundance	m/z	Relative abundance
1597.98	1.36	5151.39	1.74	7390.93	42.79
1598.32	1.23	5152.39	2.37	7391.93	75.31
1598.65	3.81	5153.39	5.02	7392.93	100
1598.98	3.38	5154.39	6.53	7393.93	97.96
1599.32	9.10	5155.39	12.11	7394.93	81.56
1599.65	7.94	5156.39	15.02	7395.93	58.39
1599.98	18.79	5157.39	24.75	7396.93	37.35
1600.32	16.09	5158.39	29.28	7397.93	21.58
1600.65	33.78	5159.39	43.37	7398.93	11.44
1600.98	28.36	5160.39	48.88	7399.93	5.615
1601.32	53.29	5161.39	65.66	7400.93	2.56
1601.65	43.80	5162.39	70.42	7401.93	1.10
1601.98	74.13	5163.39	86.42		
1602.32	59.60	5164.39	88.10		
1602.65	91.34	5165.39	99.31		
1602.98	71.73	5166.39	96.12		
1603.32	100	5167.39	100		
1603.65	76.59	5168.39	91.77		
1603.98	97.51	5169.39	88.42		
1604.32	72.73	5170.39	76.83		
1604.65	84.85	5171.39	68.76		
1604.98	61.53	5172.39	56.50		
1605.32	65.96	5173.39	47.07		
1605.65	46.42	5174.39	36.51		
1605.98	45.84	5175.39	28.36		
1606.32	31.26	5176.39	20.73		
1606.65	28.50	5177.39	15.03		
1606.98	18.78	5178.39	10.34		
1607.32	15.84	5179.39	7.00		
1607.65	10.07	5180.39	4.53		
1607.98	7.87	5181.39	2.86		
1608.32	4.81	5182.39	1.73		
1608.65	3.49	5183.39	1.02		
1608.98	2.05				
1609.31	1.38				

**Table S2.** Assignment of the fragments obtained in the MS/MS spectra of A)  $[\text{Ag}_{25}(\text{DMBT})_{18}]^-$  and B)  $[\text{Ag}_{29}(\text{BDT})_{12}]^{3-}$  clusters.

A) Assignment of the fragments of  $[\text{Ag}_{25}(\text{DMBT})_{18}]^-$

m/z	Assignment of the peaks
5167.39	$[\text{Ag}_{25}(\text{DMBT})_{18}]^-$
4431.59	$[\text{Ag}_{22}(\text{DMBT})_{15}]^-$
4185.65	$[\text{Ag}_{21}(\text{DMBT})_{14}]^-$
1362.94	$[\text{Ag}_5(\text{DMBT})_6]^-$
627.09	$[\text{Ag}_2(\text{DMBT})_3]^-$
381.12	$[\text{Ag}(\text{DMBT})_2]^-$

B) Assignment of the fragments of  $[\text{Ag}_{29}(\text{BDT})_{12}]^{3-}$

m/z	Assignment of the peaks
1603.31	$[\text{Ag}_{29}(\text{BDT})_{12}]^{3-}$
1925.39	$[\text{Ag}_{24}(\text{BDT})_9]^{2-}$
959.99	$[\text{Ag}_5(\text{BDT})_3]^-$

# Holey MoS<sub>2</sub> Nanosheets with Photocatalytic Metal Rich Edges by Ambient Electrospray Deposition for Solar Water Disinfection

Depanjan Sarkar, Biswajit Mondal, Anirban Som, Swathy Jakka Ravindran, Sourav Kanti Jana, C. K. Manju, and Thalappil Pradeep\*

**A new method for creating nanopores in single-layer molybdenum disulfide (MoS<sub>2</sub>) nanosheets (NSs) by the electrospray deposition of silver ions on a water suspension of the former is introduced. Electrospray-deposited silver ions react with the MoS<sub>2</sub> NSs at the liquid–air interface, resulting in Ag<sub>2</sub>S nanoparticles which enter the solution, leaving the NSs with holes of 3–5 nm diameter. Specific reaction with the S of MoS<sub>2</sub> NSs leads to Mo-rich edges. Such Mo-rich defects are highly efficient for the generation of active oxygen species such as H<sub>2</sub>O<sub>2</sub> under visible light which causes efficient disinfection of water. 10<sup>5</sup> times higher efficiency in disinfection for the holey MoS<sub>2</sub> NSs in comparison to normal MoS<sub>2</sub> NSs is shown. Experiments are performed with multiple bacterial strains and a virus strain, demonstrating the utility of the method for practical applications. A conceptual prototype is also presented.**

2D sheets derived from MX<sub>2</sub>, where M is a metal and X represents a chalcogen (S, Se, Te), exhibit interesting properties.<sup>[1]</sup> Examples include optoelectronics,<sup>[2]</sup> catalysis,<sup>[3,4]</sup> hydrogen evolution,<sup>[3,5]</sup> biomolecules detection,<sup>[6]</sup> and lithium-ion storage.<sup>[7]</sup> Both theoretical<sup>[8]</sup> and experimental<sup>[9]</sup> studies have shown that the edges are more active catalytically than the basal plane. Hence, defect-rich MoS<sub>2</sub> NSs are of more interest to researchers due to their increased effective surface area.<sup>[10]</sup> Creating such defects in a single-layer MoS<sub>2</sub> sheet is a challenge. Defects can be created by atom and electron bombardment, which requires sophisticated instrumentation. In the recent past, we have developed a methodology for creating functional nanomaterials under ambient conditions which requires no sophisticated

instrumentation.<sup>[11]</sup> In this paper, we have demonstrated a method to create defect-rich 2D nanosheets for applications like solar disinfection of water.


Drinking water scarcity is one of the most alarming problems of the modern world. Rapid, energy-efficient desalination and disinfection processes are required to address the problem.<sup>[12]</sup> 2D nanomaterials like graphene are shown to be efficient materials for water purification. There are several reports where graphene-based materials were used for the removal of arsenic,<sup>[13]</sup> salts,<sup>[14]</sup> dyes,<sup>[15]</sup> antibiotics,<sup>[16]</sup> pesticides,<sup>[17]</sup> etc. A few recent reports show that MoS<sub>2</sub> NSs have potential utility in water purification. A recent computa-

tional study shows that MoS<sub>2</sub> NSs with nanopores can effectively desalinate water.<sup>[18]</sup> They have also shown that water flux is higher (70% higher than the graphene nanopores) for a hole with Mo-rich edges.<sup>[18]</sup> In another very recent report, vertically aligned MoS<sub>2</sub> NSs were shown to be effective for disinfection of water under visible light.<sup>[19]</sup> The reactive edges of the NSs are responsible for the generation of active oxygen species like H<sub>2</sub>O<sub>2</sub> which, in turn, is the cause of disinfection.<sup>[19]</sup> Hence, vertical alignment of the MoS<sub>2</sub> NSs was made for the enhancement of reactive areas. These reports prove the tremendous potential of defect-rich MoS<sub>2</sub> NSs.

Here we report an easy, cost-effective, ambient, solution-based method to create nanopores in single-layer MoS<sub>2</sub> NSs. In this process, Ag<sup>+</sup> ions are electrosprayed on a water suspension of chemically synthesized MoS<sub>2</sub> NSs. In the course of the deposition, Ag<sup>+</sup> ions react with the NSs and form Ag<sub>2</sub>S, leaving the former with Mo-rich defects. The size of the holes can be controlled by varying the deposition time. We show that these nanoporous MoS<sub>2</sub> NSs are highly effective in water disinfection under visible light. A prototype device based on such holey MoS<sub>2</sub> has been demonstrated illustrating the applicability of such methods in field conditions.

When a high potential in the range 2–2.5 kV was applied to the nano electrospray ionization (nESI) source of 15–20 μm diameter (at the tip), through a platinum (Pt) wire electrode (0.1 mm), filled with aqueous solution of silver acetate (AgOAc), a spray plume of solvated Ag<sup>+</sup> ions was observed at the source. This plume was directed toward the surface of the grounded aqueous suspension of MoS<sub>2</sub> NSs. **Figure 1** shows the chemical

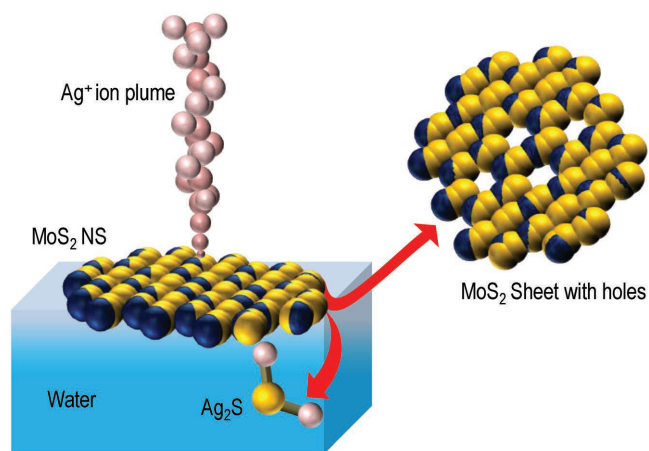
Dr. D. Sarkar, B. Mondal, Dr. A. Som, S. J. Ravindran, Dr. S. K. Jana, C. K. Manju, Prof. T. Pradeep  
DST Unit of Nanoscience (DST UNS) and Thematic Unit of Excellence (TUE)  
Department of Chemistry  
Indian Institute of Technology Madras  
Chennai 600036, India  
E-mail: pradeep@iitm.ac.in

 The ORCID identification number(s) for the author(s) of this article can be found under <https://doi.org/10.1002/gch2.201800052>.

© 2018 The Authors. Published by WILEY-VCH Verlag GmbH & Co. KGaA, Weinheim. This is an open access article under the terms of the Creative Commons Attribution License, which permits use, distribution and reproduction in any medium, provided the original work is properly cited.

DOI: 10.1002/gch2.201800052

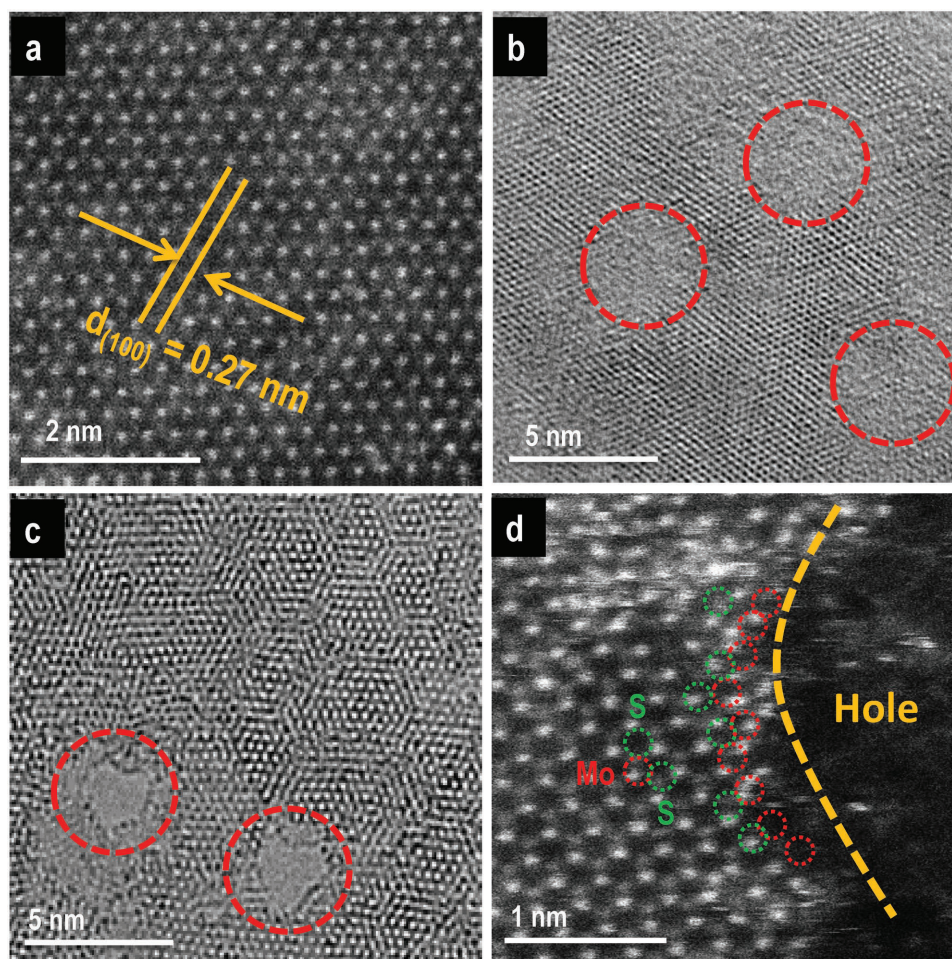




**Figure 1.** Drilling of MoS<sub>2</sub> NSs by ambient ions. Schematic representation of chemical drilling of MoS<sub>2</sub> NSs using electro-spray-deposited Ag<sup>+</sup> ions. Not to scale.

drilling process of MoS<sub>2</sub> NSs schematically where the spherical pink balls represent the solvated Ag<sup>+</sup> ions. The mass spectrum collected from the spray plume (Figure S1, Supporting Information) confirms the presence of Ag<sup>+</sup> and [Ag(H<sub>2</sub>O)]<sup>+</sup> ions. Ag<sup>+</sup> ions react with the NSs and form Ag<sub>2</sub>S NPs. With time, Ag<sub>2</sub>S NPs go into water resulting in nanoporous MoS<sub>2</sub> NSs. The whole process is demonstrated schematically in Figure 1 where 2D MoS<sub>2</sub> NS is shown using blue (represents Mo) and yellow (represents S) balls. The experimental procedure discussed in the Supporting Information. After the process of drilling, the resultant holey MoS<sub>2</sub> NS formed is also shown in Figure 1 which shows Mo-rich edges at the defect positions. This has been proved by high-angle annular dark-field transmission electron microscopy (HAADF TEM) imaging (explained in detail at a later part of the paper). X-ray photoelectron spectroscopic (XPS) measurements were also performed to support this result. The Mo 3d region after electro-spray deposition (ESD) of silver showed a blueshift of 0.3 eV in binding energy corresponding to a decrease in number of sulfide ions compared to the parent material (Figure S2, Supporting Information). A detailed description has been provided in the Supporting Information. The reaction of Ag<sup>+</sup> ions with MoS<sub>2</sub> NSs in the solution phase was also supported by a recent report from our group.<sup>[20]</sup> To prove that the deposition of ions followed by the reaction is the only reason for the defects in MoS<sub>2</sub> NSs and discard any possibility of pre-existing defects in the as-synthesized NSs, detailed characterization of the as-synthesized MoS<sub>2</sub> NSs was performed using various spectroscopic and microscopic techniques. Figure S3a (Supporting Information) shows TEM image of the as-synthesized MoS<sub>2</sub> NSs. From the TEM images, it is seen that with our synthesis, we have obtained thin single-layer sheets of MoS<sub>2</sub> with nanometer dimension. From the scanning transmission electron microscopic (STEM) image (Figure S3b, Supporting Information) it is clear that the sheets are single crystalline in nature and do not have defects. Raman spectroscopic measurement of the as-synthesized NSs was also done to further confirm the quality of the NSs. Figure S3c (Supporting Information) shows the Raman spectra collected from MoS<sub>2</sub> NSs (red trace) and MoS<sub>2</sub> bulk (black trace), respectively. Peaks

at 386 cm<sup>-1</sup> (E<sub>2g</sub>) and 404 cm<sup>-1</sup> (A<sub>1g</sub>) prove the 2D nature of the NSs. Increase in the full width at half maximum (FWHM) for A<sub>1g</sub> mode and a decrease in the peak difference of A<sub>1g</sub> and E<sub>2g</sub> modes indicate the successful exfoliation of bulk MoS<sub>2</sub> to the 2D nanoscale form.<sup>[21]</sup> UV-vis spectrum collected from the aqueous suspension of MoS<sub>2</sub> NSs also shows the characteristic peaks at 410, 620, and 672 nm (Figure S3d, Supporting Information). Electro-spray deposition experiments were performed with these sheets. The deposition time and rate were optimized. In a typical experiment, Ag<sup>+</sup> ions were electro-sprayed on a suspension of MoS<sub>2</sub> NSs (3.7 × 10<sup>-3</sup> M with respect to Mo) for 30 min at a deposition current of 60 nA. After the deposition, a portion of the NSs was seen floating on the water surface and the rest of it was in the bulk. Both of these categories of NSs were taken on a carbon-coated TEM grid for imaging. Figure 2a shows a STEM image of the as-synthesized MoS<sub>2</sub> NS. The high-resolution TEM (HRTEM) image (collected from the floating layer of NSs) in Figure 2b shows the presence of holes (indicated with red circles) in a MoS<sub>2</sub> NS. The HRTEM image was taken from a single-layer MoS<sub>2</sub> NS to prove the clear discontinuity of the lattice planes. Figure 2c shows a STEM image of MoS<sub>2</sub> NSs after the creation of holes. The image clearly shows part of a hole in a single-crystalline NS present in bulk water. The dimensions of the holes were in the range of 3–5 nm. We speculate dynamics of the suspended NSs on the liquid surface during deposition leading to the creation of holes in all the NSs. This motion can be due to the transfer of charged droplets on the water surface in presence of a tangential electric field. From the independent experiments, we know that hydroxyl ions (due to their high mobility), generated due to hydrolysis of water, are the charge carriers from the center of the spray to the ground electrode kept at the rim of the liquid reservoir, causing a hydrodynamic flow in the liquid.<sup>[22]</sup> This flow may be the reason for the presence of nanoporous sheets both on the surface of the water and in the bulk. To see the fate of the NSs with longer deposition time, an experiment was performed where the deposition time was kept at 2 h. Figure S4a (Supporting Information) shows a TEM image taken from the suspension after the experiment. In this case, we see that the whole NS was reacted and got converted to Ag<sub>2</sub>S NPs. Figure S4b (Supporting Information) shows an HRTEM image of a single Ag<sub>2</sub>S NP. This experiment also proves that Ag<sup>+</sup> ions react with MoS<sub>2</sub> NS and go to the solution as Ag<sub>2</sub>S NPs along with a portion of Mo from the reacted region, which subsequently becomes MoO<sub>4</sub><sup>2-</sup>.<sup>[20]</sup> The process of the selective reaction of incoming Ag<sup>+</sup> ions makes the holey MoS<sub>2</sub> NSs porous with Mo-rich edges. HAADF STEM image shown in Figure 2d clearly shows the Mo enriched edges of the holes in a single-layer MoS<sub>2</sub> NS. From Figure 2d, the distance between the two Mo atoms is 0.26 nm. Considering the holes as a circle of 3 nm diameter, the number of Mo atoms per hole is ≈35. Thus, due to hole formation, a 1 μm × 1 μm NS exposes ≈2.7 × 10<sup>5</sup> additional Mo atoms. Note that the STEM image of Figure 2c suggests >7800 holes μm<sup>-2</sup>. This process of creating nanoscale holes on 2D sheets by ambient ion reactions is referred to as chemical drilling. We have maintained low deposition time in order to control the size of the holes. For this reason, in all our experiments of creating nm sized holes in the MoS<sub>2</sub> NSs (except the control experiment showing longer deposition leading to complete reaction of the NSs to form Ag<sub>2</sub>S



**Figure 2.** Characterization of holey MoS<sub>2</sub> NSs. a) STEM image of the as-synthesized MoS<sub>2</sub> NSs showing no defects in it. b) HRTEM image of a MoS<sub>2</sub> NS, floating on water after the deposition process, with holes. c) STEM image of the same showing clear holes on a single NS. d) HAADF STEM image of a holey MoS<sub>2</sub> NS taken from the subphase showing a Mo enriched edge. Red circles in image (d) denote Mo and the green circles represent S.

NPs), the concentration of the Ag<sub>2</sub>S NPs formed was negligible in comparison to the amount of MoS<sub>2</sub> in solution.

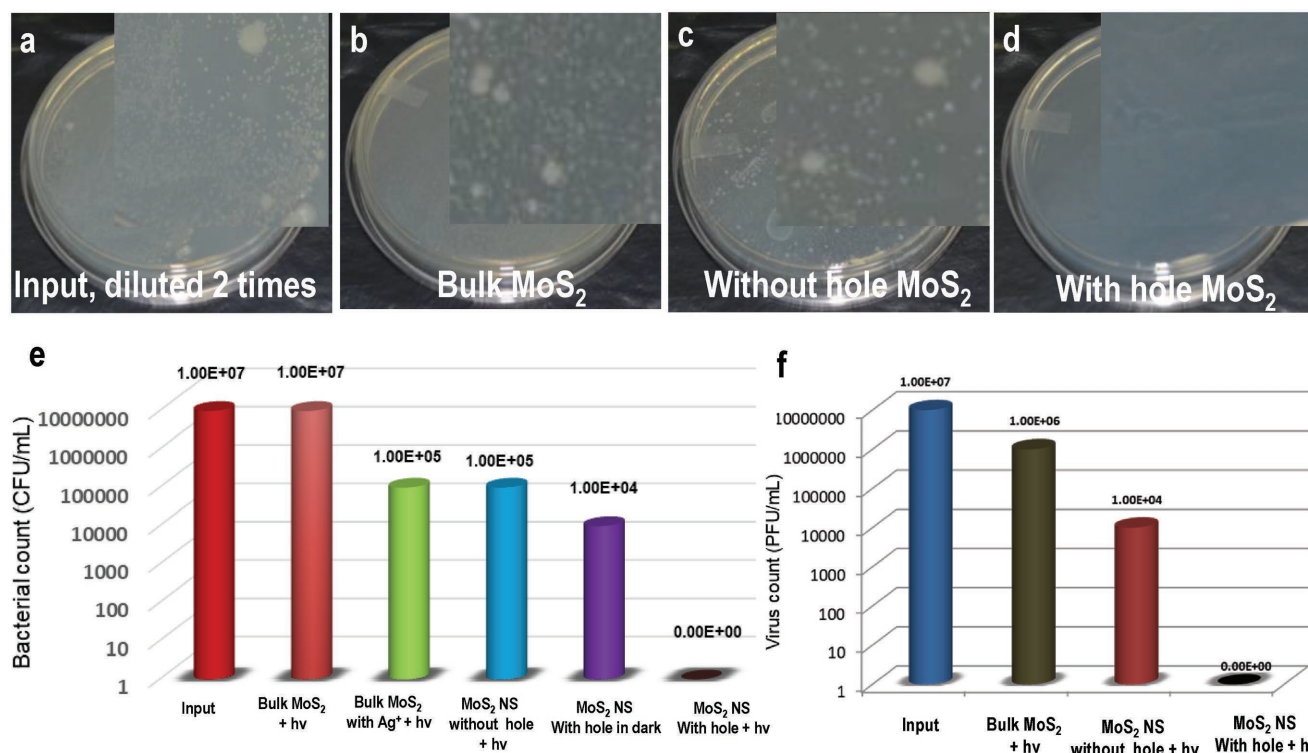
To check the efficiency of disinfection of holey MoS<sub>2</sub> NSs, we have performed a series of experiments along with several control experiments. We have tested the disinfection efficiency of the MoS<sub>2</sub> NSs using bacteria and virus-contaminated water. **Figure 3a–d** shows optical photographs of the live bacteria observed after disinfection by pour plate technique. The inset shows magnified images in each case where **Figure 3a–d** represents input concentration (diluted two times), disinfection experiment with bulk MoS<sub>2</sub>, disinfection with the as-synthesized MoS<sub>2</sub> NSs, and disinfection with holey MoS<sub>2</sub> NSs, respectively. The contaminated water when exposed to porous MoS<sub>2</sub> NSs and visible light (Supporting Information) showed 10 000 000 times reduction in bacteria, from 10<sup>7</sup> to 10<sup>0</sup> CFU mL<sup>−1</sup> for *Escherichia coli* (or 7 log reduction), in 2 h whereas the as-synthesized MoS<sub>2</sub> NSs and bulk MoS<sub>2</sub> with equivalent concentration of Ag, used for the drilling process, showed only 1% of disinfection efficiency (or 2 log reduction) (**Figure 3e**). But holey MoS<sub>2</sub> NSs in dark showed only 3 log reduction (**Figure 3e**) in the bacteria count. We note that Ag<sup>+</sup> at a concentration above 50 ppb can be an excellent disinfectant.<sup>[23]</sup> Under the same experimental

conditions, bulk MoS<sub>2</sub> showed negligible disinfection efficiency for the mentioned bacterial input. This suggests that chemical drilling makes the MoS<sub>2</sub> nanosheets photocatalytically more active. We speculate that the Mo-rich defects in the NSs provide enhanced active surface area for the generation of reactive oxygen species (ROS). The disinfection efficiency of the material was also tested with gram-positive bacteria (*Bacillus subtilis*). It was noticed that *B. subtilis* are more resistive toward H<sub>2</sub>O<sub>2</sub> than *E. coli* under the same experimental conditions (**Figure S5**, Supporting Information).

In the following part of the paper, we have shown that holey MoS<sub>2</sub> NSs are more efficient in generating at least one ROS species, namely, H<sub>2</sub>O<sub>2</sub> (see later). The disinfection efficiency of Ag<sup>+</sup> alone was also examined under the same experimental conditions taking the same amount of Ag<sup>+</sup> ions used for chemical drilling. Ag<sup>+</sup> ions showed a negligible effect on *E. coli* inactivation because the concentration of Ag<sup>+</sup> was 0.2 × 10<sup>−6</sup> M, much lower than the concentration needed for disinfection at a bacterial load of 10<sup>7</sup> CFU mL<sup>−1</sup>.

Considering the fact that the major water purification techniques used for virus removal are the addition of chlorine which produces harmful disinfection byproducts, we propose



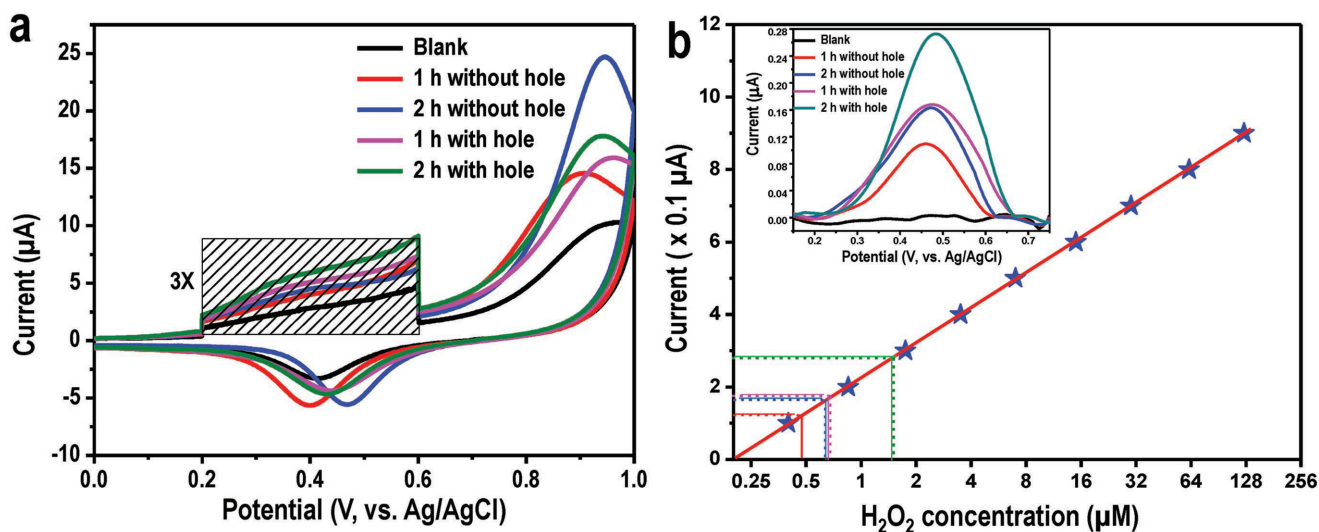


**Figure 3.** Disinfection performance of holey MoS<sub>2</sub> NSs. a–d) Optical photographs of the live bacteria observed after disinfection by pour plate technique. Inset shows magnified images in each case. a) Input concentration, diluted two times, b) disinfection experiment with bulk MoS<sub>2</sub>, c) disinfection with the as-synthesized MoS<sub>2</sub> NSs, and d) disinfection with holey MoS<sub>2</sub> NSs. Comparison of the e) antibacterial and f) antiviral activity of the porous MoS<sub>2</sub> NSs, with Mo-rich edges. The activity is compared with bulk MoS<sub>2</sub>, bulk MoS<sub>2</sub> with the same amount of Ag used for drilling, MoS<sub>2</sub> NSs without holes, and holey MoS<sub>2</sub> NSs in dark. The test organisms used was F-specific bacteriophage MS2 grown on *E. coli* (ATCC 15597-B1). In all the experiments, parameters such as light intensity, irradiation time (2 h), sample concentrations, etc., were maintained constant. The entire visible spectrum was exposed to the sample although one frequency ( $\nu$ ) is mentioned.

that the holey MoS<sub>2</sub> NSs could serve as an efficient method to reduce pathogenic viruses by a safer method. We observed that while bulk MoS<sub>2</sub> with and without Ag<sup>+</sup> and MoS<sub>2</sub> NSs without holes were unable to affect the phage significantly (Figure S6, Supporting Information), the porous MoS<sub>2</sub> NSs were found to achieve a 7 log reduction by photocatalytic disinfection (Figure 3f). Moreover, by this study, we proved that this method can disinfect virus at comparatively higher concentrations.

From earlier reports, we know that MoS<sub>2</sub> in presence of visible light can generate active oxygen species like H<sub>2</sub>O<sub>2</sub>.<sup>[19]</sup> Liu et al. have shown that the edges of MoS<sub>2</sub> NSs are more active in this reaction. We believe that generation of H<sub>2</sub>O<sub>2</sub>, in presence of visible light is one of the reasons for the disinfection of water. To prove that the holey MoS<sub>2</sub> is more efficient for the production of H<sub>2</sub>O<sub>2</sub>, a set of cyclic voltammetry (CV) experiments were performed. For all our CV experiments, we have used a pre-cleaned gold electrode as the working electrode, Ag/AgCl was used as the reference electrode, and Pt was used as the counter electrode. Prior to CV measurements of each sample, 5 mL of as-synthesized MoS<sub>2</sub> suspension was dried at 55 °C in a glass bottle. Subsequently, CV experiments were performed by adding 5 mL of 1 M phosphate buffered saline (PBS, pH ≈ 7.3) to the bottle having previously dried MoS<sub>2</sub> and electrochemical experiment was performed after exposing the dispersion to visible light (for 1 or 2 h, depending on the experiment). CV of

each sample was performed from 0 to +1 V with a fixed scan rate of 100 mV s<sup>-1</sup>. CV profiles of Au, performed in blank solution (only PBS), as well as in PBS along with as-synthesized MoS<sub>2</sub> NSs and holey MoS<sub>2</sub> NSs irradiated with visible light for 1 and 2 h, respectively, are shown in Figure 4. Each CV profile has two major peaks, one observed around +0.95 V corresponds to the formation of AuCl<sub>4</sub><sup>-</sup> during the forward potential scan (0 to +1 V) and another around +0.43 V due to the reduction of gold chloride in the reverse potential scan (+1 V to 0). Along with these, a small hump was observed in the CV scan, around +0.45 V (marked portion in the spectrum was multiplied three times for better visualization) which corresponds to the oxidation of H<sub>2</sub>O<sub>2</sub>. In order to gain a deeper insight into the sensing mechanism, we have performed CV measurements in different electrolytes like aqueous PBS, NaCl, and Na<sub>2</sub>SO<sub>4</sub> and these traces are shown in Figure S7 (Supporting Information). From such experiments, we concluded that the peak at +0.45 V is due to electrooxidation of H<sub>2</sub>O<sub>2</sub>.<sup>[24]</sup> In the course of the reaction, M–OH or M=O might be formed as intermediates which ultimately get converted to ROS. Although the reaction mixture with as-synthesized MoS<sub>2</sub> NSs shows some amount of H<sub>2</sub>O<sub>2</sub>, the holey MoS<sub>2</sub> NSs are more efficient in the generation of H<sub>2</sub>O<sub>2</sub> because of the presence of enhanced reactive surface area. Oxidation of H<sub>2</sub>O<sub>2</sub> by Au electrode was further confirmed by a control experiment (CV trace shown in Figure S8, Supporting



**Figure 4.** Quantitative detection of  $\text{H}_2\text{O}_2$  using CV. a) Cyclic voltammetry (CV) traces of 5 mL of  $\text{MoS}_2$  solution, in phosphate buffered saline (PBS), using a gold electrode. b) Quantification of  $\text{H}_2\text{O}_2$  concentration generated by holey  $\text{MoS}_2$  NSs and a calibration curve which is extracted from Figure S7a (Supporting Information) ( $\text{H}_2\text{O}_2$  oxidation current as a function of externally added  $\text{H}_2\text{O}_2$  concentration, measured with Au electrode in PBS solution). The intercepts marked with red, blue, violet, and green lines are due to  $\text{MoS}_2$  nanosheets without hole after 1 h,  $\text{MoS}_2$  nanosheets without hole after 2 h, holey  $\text{MoS}_2$  after 1 h, and holey  $\text{MoS}_2$  after 2 h, respectively. Inset shows background corrected CV traces of holey  $\text{MoS}_2$  and  $\text{MoS}_2$  NSs without hole (derived from data in a)).

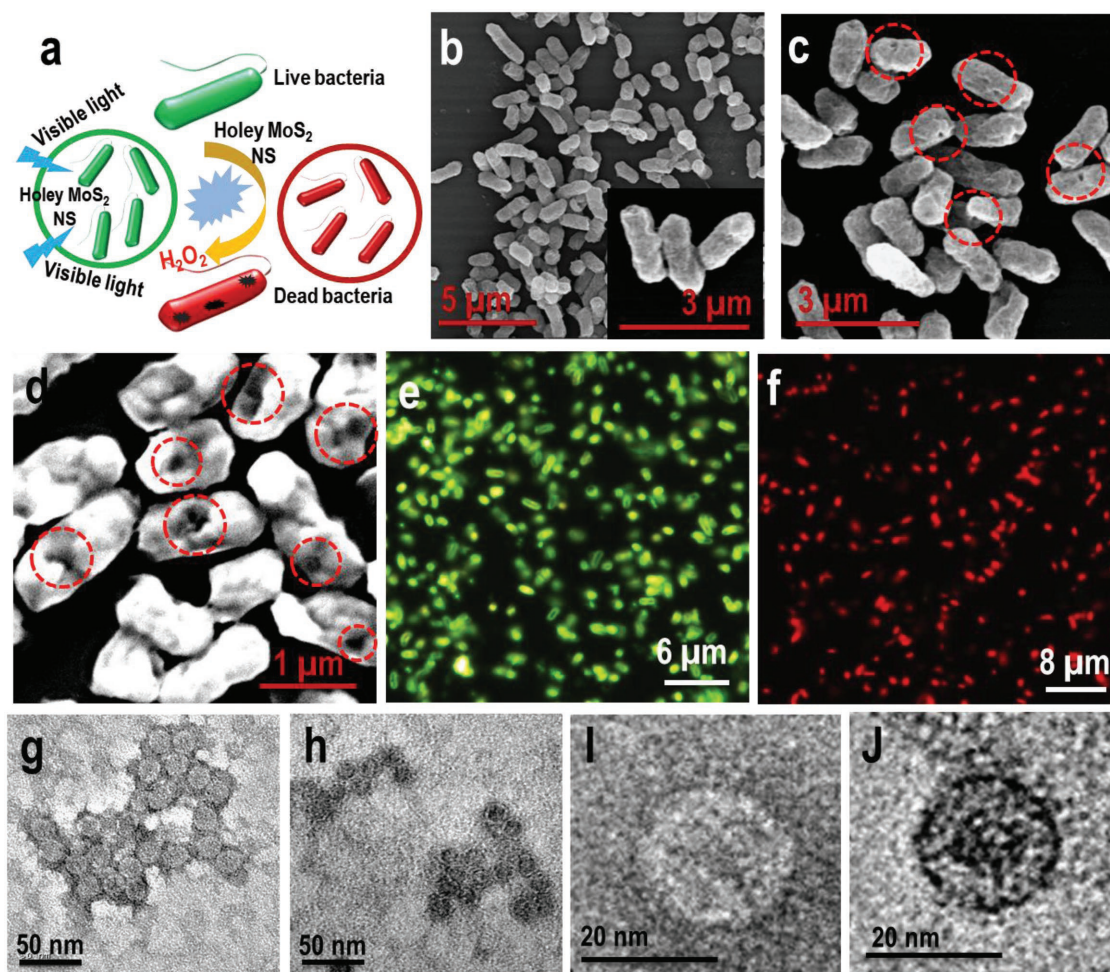
Information) performed in PBS in presence of externally added  $\text{H}_2\text{O}_2$  at different concentrations. To prove the fact that defects in the  $\text{MoS}_2$  sheets have a significant role in  $\text{H}_2\text{O}_2$  generation, a control experiment was carried out. In this experiment, two sets of holey  $\text{MoS}_2$  samples were synthesized by varying the deposition time of  $\text{Ag}^+$  (10 and 20 min at a deposition rate of 100 nA). More deposition time will enable the creation of more holes in NSs. All the other parameters were kept constant and the CV was measured successively. Figure S9 (Supporting Information) shows the feature corresponding to  $\text{H}_2\text{O}_2$  in the voltammogram. The  $\text{H}_2\text{O}_2$  concentration was higher in the second sample, that is, the  $\text{MoS}_2$  NSs with more holes (Ag deposition for 20 min). To quantify the  $\text{H}_2\text{O}_2$  generated from holey  $\text{MoS}_2$ , we have performed CV measurements (traces shown in Figure S8, Supporting Information) in PBS with successive addition of commercial  $\text{H}_2\text{O}_2$  at different concentrations ( $0.4 \times 10^{-6}$  to  $1 \times 10^{-3}$  M). The oxidation current as a function of  $\text{H}_2\text{O}_2$  concentration (Figure 4b) shows a linear behavior. Oxidation current of  $\text{H}_2\text{O}_2$  (data from Figure 4a have been shown in the inset of Figure 4b after background subtraction) produced by holey  $\text{MoS}_2$  was compared with the calibration curve (Figure 4b), giving a quantitative measurement of  $\text{H}_2\text{O}_2$  produced by various materials (Table S1, Supporting Information). We note that in the disinfection process other ROS species may also be involved, although we have detected only  $\text{H}_2\text{O}_2$ .

**Figure 5a** shows the disinfection process schematically. Scanning electron microscopy (SEM) imaging establishes the damage of bacterial cells. **Figure 5b** shows the SEM image of the bacterial cells before disinfection. Here, we see healthy cells of *E. coli*. On the other hand, **Figure 5c,d** shows the SEM images of dead *E. coli* cells at different magnifications. It is seen clearly from these images that the bacterial cells are damaged (red circles) due to reaction with  $\text{H}_2\text{O}_2$ . Similar cell damage was observed when the bacteria were treated with commercially

available  $\text{H}_2\text{O}_2$  (Figure S10, Supporting Information). Dark field fluorescence imaging of bacteria was also performed to prove 100% disinfection. Fluorescence staining experiments using dark field microscopy can distinguish between intact and membrane-permeable cells using LIVE/DEAD BacLight bacterial viability kit. The two stains used were the membrane impermeant propidium iodide (PI), causing red fluorescence of membrane permeabilized cells and SYTO 9, a nucleic acid binding green fluorescent dye that could enter into all the cells regardless of whether they were intact or permeabilized. PI fluorescing defective bacteria were observed as red (Figure 5f) when they were treated with holey  $\text{MoS}_2$  nanosheets (and irradiated) whereas untreated (and irradiated) bacteria show SYTO 9 emission (green) (Figure 5e). Membrane permeabilization is seen in all the bacteria upon treatment with holey  $\text{MoS}_2$  nanosheets proving 100% disinfection. TEM images of the virus before (Figure 5g–i) and after (Figure 5h–j) irradiation show a clear contrast difference. This is because the uranyl acetate stain enters defective viral capsids and causes a distinct difference in contrast between untreated and treated viruses. Dense dark centered capsids (defective capsids) which had taken up the uranyl acetate stain were seen as dark whereas untreated viruses were rigid and did not show the stain within.<sup>[23]</sup> All the above disinfection processes were performed under a Xenon arc lamp.

We also have designed a prototype for the disinfection of water using a commercially available low power light-emitting diode (LED) strip. **Figure 6a** shows the schematic of a prototype where holey  $\text{MoS}_2$  NSs supported on alumina were packed in a borosilicate glass tube (column size and radius were 10 in. and 3 mm inner diameter, respectively) and a LED ( $4.8 \text{ W m}^{-1}$ ) strip was wrapped around it. Contaminated water was pushed from below using a syringe pump and pure water was collected from the top. Antigravity flow of the contaminated water was chosen for longer contact of it with the holey  $\text{MoS}_2$  NSs. We have used





**Figure 5.** Imaging of bacteria and virus before and after the treatment with the samples. a) Schematic representation of the disinfection process; green and red colors represent live and dead cells, respectively. b) SEM image of *E. coli* cells before disinfection. Inset shows an SEM image of *E. coli* cells at higher magnification. c,d) SEM image of *E. coli* cells after disinfection. Red circles show the damage in the cells due to reaction with  $\text{H}_2\text{O}_2$ . e,f) Dark field fluorescence microscopic analysis of live and dead bacteria cells showing 100% disinfection after treating with holey  $\text{MoS}_2$  NSs under visible light. g,h) TEM images of virus before (live virus) and after (dead virus) the treatment with the sample (holey  $\text{MoS}_2$ ), respectively. i,j) Magnified TEM images of live and dead viruses show the clear contrast difference between the two.

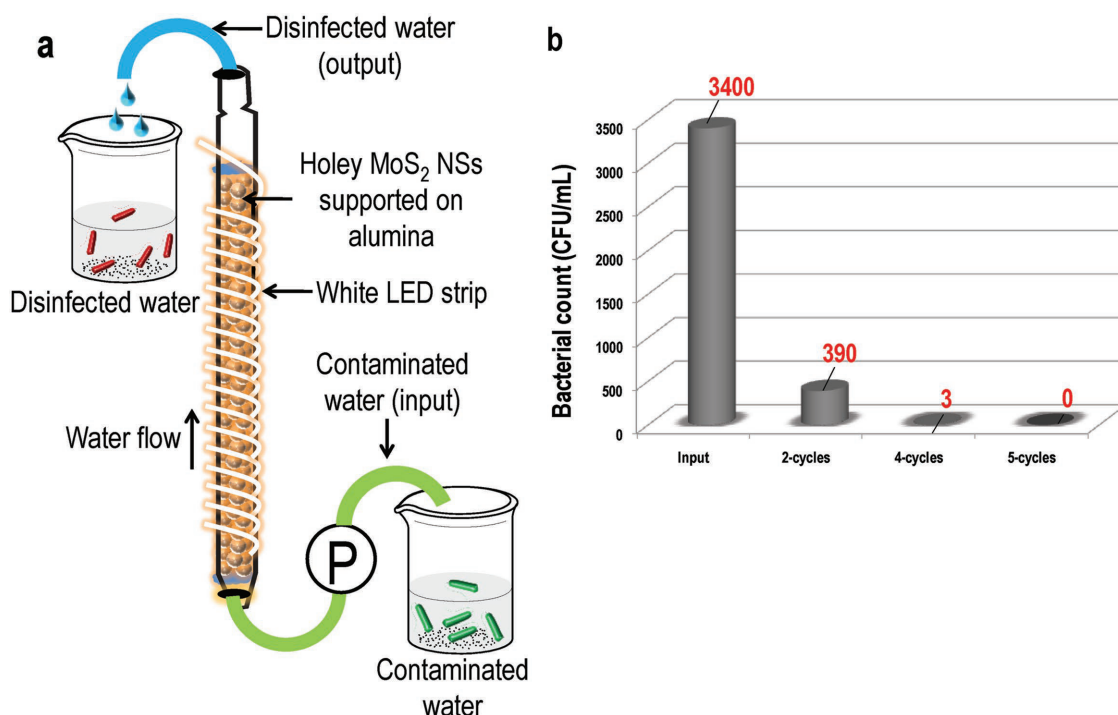
a bacterial load of  $10^3$  CFU  $\text{mL}^{-1}$  in this case. Contaminated water was passed through the column multiple times and after each cycle, the sample was taken for plating (Figure S11, Supporting Information). We see 100% disinfection after five cycles (Figure 6b). Leaching of the  $\text{MoS}_2$  NSs from the alumina support was checked using UV-vis spectroscopy and inductively coupled plasma mass spectrometry (ICP-MS) measurements (Figure S12, Supporting Information). No significant leaching was observed in ICP-MS studies. A control experiment was also performed where the column was packed with alumina and contaminated water was passed through it under the same experimental conditions mentioned above. No difference in the bacterial count was noticed between the input and output of contaminated water (Figure S13, Supporting Information).

An inexpensive ambient method was demonstrated for making nanometer-sized holes in  $\text{MoS}_2$  NSs composed of molybdenum-rich edges. Immobilized porous  $\text{MoS}_2$  NSs in water make  $\text{H}_2\text{O}_2$  upon exposure of visible light and disinfect microbially contaminated water samples. The composition

provides antibacterial and antiviral activity at concentrations of  $10^7$  CFU  $\text{mL}^{-1}$  bacteria and  $10^7$  PFU  $\text{mL}^{-1}$  virus. Mo-rich edges of  $\text{MoS}_2$  NSs are more catalytically active toward the generation of  $\text{H}_2\text{O}_2$  which in turn reacts with the bacterial and viral cells and damage them. We also show a working prototype using immobilized nanosheets on oxide supports for water disinfection using low-power LEDs. The simplicity of the process and use of very low amount of metal make this material a potential candidate for practical applications.

## Experimental Section

For testing disinfection, 5 mL of synthetic water (typically containing *E. coli* ATCC 25922 at a concentration of  $1 \times 10^7$  CFU  $\text{mL}^{-1}$ , unless otherwise mentioned) was treated with  $3.7 \times 10^{-3}$  M of  $\text{MoS}_2$  suspension (in terms of Mo) of porous  $\text{MoS}_2$  nanosheets and the photocatalytic disinfection performance was checked under visible light. Xenon lamp equipped with UV filter was used as the light source. The disinfection efficiency was compared with the controls, namely, (a) equal mass of



**Figure 6.** Disinfection performance holey MoS<sub>2</sub> using a prototype. a) Prototype for water disinfection using low power LED strips and b) plot of bacterial count after 2–5 cycles of operation.

bulk MoS<sub>2</sub>, (b) same concentration of Ag<sup>+</sup> used for chemical drilling along with bulk MoS<sub>2</sub>, and (c) as-synthesized MoS<sub>2</sub> nanosheets, all under visible light, at the same experimental conditions. A high concentration of the bacterial input was maintained considering the activity of the proposed material in the treatment of water from challenging environments. About 1 mL of the diluted samples was plated along with nutrient agar on a sterile Petri dish using the pour plate method after 2 h of reaction time. After 48 h of incubation at 37 °C, the colonies were counted and recorded.

In the case of antiviral testing,  $\approx 1 \times 10^5$  bacteriophage MS2 was used. The prepared synthetic water was shaken gently with the  $3.7 \times 10^{-3}$  M of MoS<sub>2</sub> suspension (in terms of Mo) of porous MoS<sub>2</sub> nanosheets and left for a contact time of 2 h for the photocatalytic disinfection and subsequently the viable virus count was measured by double-layer plaque assay (using *E. coli* host). The plates were incubated for a period of 20–24 h at 37 °C.

All other experimental details including synthesis of MoS<sub>2</sub> NS, electrospray deposition on MoS<sub>2</sub> NSs, bacteria and virus used for disinfection reaction, and dark field fluorescence microscopic analysis are available in the Supporting information.

## Supporting Information

Supporting Information is available from the Wiley Online Library or from the author.

## Acknowledgements

D.S. and B.M. contributed equally to this work. T.P. acknowledges financial support from the Department of Science and Technology, Government of India for his research program on nanomaterials. D.S. thanks the University Grants Commission and B.M. thanks IIT Madras for research fellowships. A.S. thanks Council of Scientific & Industrial Research for a research fellowship.

## Conflict of Interest

The authors declare no conflict of interest.

## Keywords

chemical drilling, holey-MoS<sub>2</sub> NSs, Mo-rich edges, nanometer size holes, water disinfection

Received: May 27, 2018

Revised: August 8, 2018

Published online:

- [1] C. Tan, X. Cao, X.-J. Wu, Q. He, J. Yang, X. Zhang, J. Chen, W. Zhao, S. Han, G.-H. Nam, M. Sindoro, H. Zhang, *Chem. Rev.* **2017**, *117*, 6225.
- [2] a) Z. Yin, H. Li, H. Li, L. Jiang, Y. Shi, Y. Sun, G. Lu, Q. Zhang, X. Chen, H. Zhang, *ACS Nano* **2012**, *6*, 74; b) H. S. Lee, S.-W. Min, Y.-G. Chang, M. K. Park, T. Nam, H. Kim, J. H. Kim, S. Ryu, S. Im, *Nano Lett.* **2012**, *12*, 3695.
- [3] J. Xie, H. Zhang, S. Li, R. Wang, X. Sun, M. Zhou, J. Zhou, X. W. Lou, Y. Xie, *Adv. Mater.* **2013**, *25*, 5807.
- [4] L. Yuwen, F. Xu, B. Xue, Z. Luo, Q. Zhang, B. Bao, S. Su, L. Weng, W. Huang, L. Wang, *Nanoscale* **2014**, *6*, 5762.
- [5] M. A. Lukowski, A. S. Daniel, F. Meng, A. Forticaux, L. Li, S. Jin, *J. Am. Chem. Soc.* **2013**, *135*, 10274.
- [6] C. Zhu, Z. Zeng, H. Li, F. Li, C. Fan, H. Zhang, *J. Am. Chem. Soc.* **2013**, *135*, 5998.
- [7] a) H. Jiang, D. Ren, H. Wang, Y. Hu, S. Guo, H. Yuan, P. Hu, L. Zhang, C. Li, *Adv. Mater.* **2015**, *27*, 3687; b) X. Xu, Z. Fan, S. Ding, D. Yu, Y. Du, *Nanoscale* **2014**, *6*, 5245.

- [8] B. Hinnemann, P. G. Moses, J. Bonde, K. P. Jorgensen, J. H. Nielsen, S. Horch, I. Chorkendorff, J. K. Nørskov, *J. Am. Chem. Soc.* **2005**, 127, 5308.
- [9] T. F. Jaramillo, K. P. Jorgensen, J. Bonde, J. H. Nielsen, S. Horch, I. Chorkendorff, *Science* **2007**, 317, 100.
- [10] Z. Wu, B. Li, Y. Xue, J. Li, Y. Zhang, F. Gao, *J. Mater. Chem. A* **2015**, 3, 19445.
- [11] a) D. Sarkar, M. K. Mahitha, A. Som, A. Li, M. Wlekinski, R. G. Cooks, T. Pradeep, *Adv. Mater.* **2016**, 28, 2223; b) D. Sarkar, A. Mahapatra, A. Som, R. Kumar, A. Nagar, A. Baidya, T. Pradeep, *Adv. Mater. Interfaces* **2018**, 0, 1800667.
- [12] a) M. A. Shannon, P. W. Bohn, M. Elimelech, J. G. Georgiadis, B. J. Marinas, A. M. Mayes, *Nature* **2008**, 452, 301; b) R. P. Schwarzenbach, B. I. Escher, K. Fenner, T. B. Hofstetter, C. A. Johnson, U. von Gunten, B. Wehrli, *Science* **2006**, 313, 1072; c) C. Liu, X. Xie, W. Zhao, N. Liu, P. A. Maraccini, L. M. Sassoubre, A. B. Boehm, Y. Cui, *Nano Lett.* **2013**, 13, 4288; d) B. E. Logan, M. Elimelech, *Nature* **2012**, 488, 313.
- [13] V. Chandra, J. Park, Y. Chun, J. W. Lee, I.-C. Hwang, K. S. Kim, *ACS Nano* **2010**, 4, 3979.
- [14] a) D. Cohen-Tanugi, J. C. Grossman, *Nano Lett.* **2012**, 12, 3602; b) Y. Han, Z. Xu, C. Gao, *Adv. Funct. Mater.* **2013**, 23, 3693; c) N. Pugazhenthiran, S. S. Gupta, A. Prabhat, M. Manikandan, J. R. Swathy, V. K. Raman, T. Pradeep, *ACS Appl. Mater. Interfaces* **2015**, 7, 20156.
- [15] a) G. K. Ramesha, A. V. Kumara, H. B. Muralidhara, S. Sampath, *J. Colloid Interface Sci.* **2011**, 361, 270; b) B. Li, H. Cao, *J. Mater. Chem.* **2011**, 21, 3346; c) L.-H. Ai, C.-Y. Zhang, Z.-L. Chen, *J. Hazard. Mater.* **2011**, 192, 1515.
- [16] Y. Gao, Y. Li, L. Zhang, H. Huang, J. Hu, S. M. Shah, X. Su, *J. Colloid Interface Sci.* **2012**, 368, 540.
- [17] S. S. Gupta, I. Chakraborty, S. M. Maliyekkal, T. A. Mark, D. K. Pandey, S. K. Das, T. Pradeep, *ACS Sustainable Chem. Eng.* **2015**, 3, 1155.
- [18] M. Heiraniyan, A. B. Farimani, N. R. Aluru, *Nat. Commun.* **2015**, 6, 8616.
- [19] C. Liu, D. Kong, P.-C. Hsu, H. Yuan, H.-W. Lee, Y. Liu, H. Wang, S. Wang, K. Yan, D. Lin, P. A. Maraccini, K. M. Parker, A. B. Boehm, Y. Cui, *Nat. Nanotechnol.* **2016**, 11, 1098.
- [20] B. Mondal, A. Som, I. Chakraborty, A. Bakshi, D. Sarkar, T. Pradeep, *Nanoscale* **2016**, 8, 10282.
- [21] a) C. Lee, H. Yan, L. E. Brus, T. F. Heinz, J. Hone, S. Ryu, *ACS Nano* **2010**, 4, 2695; b) H. Li, Q. Zhang, C. C. R. Yap, B. K. Tay, T. H. T. Edwin, A. Olivier, D. Baillargeat, *Adv. Funct. Mater.* **2012**, 22, 1385.
- [22] D. Sarkar, R. Singh, A. Som, C. K. Manju, M. A. Ganayee, R. Adhikari, T. Pradeep, *J. Phys. Chem. C* **2018**, 122, 17777.
- [23] J. R. Swathy, M. U. Sankar, A. Chaudhary, S. Aigal, Anshup, T. Pradeep, *Sci. Rep.* **2014**, 4, 7161.
- [24] M. Gerlache, Z. Senturk, G. Quarin, J. M. Kauffmann, *Electroanalysis* **1997**, 9, 1088.





## Supporting Information

for *Global Challenges*, DOI: 10.1002/gch2.201800052

Holey MoS<sub>2</sub> Nanosheets with Photocatalytic Metal Rich Edges by Ambient Electrospray Deposition for Solar Water Disinfection

*Depanjan Sarkar, Biswajit Mondal, Anirban Som, Swathy Jakka Ravindran, Sourav Kanti Jana, C. K. Manju, and Thalappil Pradeep\**

## Supporting Information

**Holey MoS<sub>2</sub> Nanosheets with Photocatalytic Metal Rich Edges by Ambient Electrospray Deposition for Solar Water Disinfection**

*Depanjan Sarkar,<sup>†</sup> Biswajit Mondal,<sup>†</sup> Anirban Som, Swathy Jakka Ravindran, Sourav Kanti Jana, C. K. Manju and Thalappil Pradeep\**

## EXPERIMENTAL SECTION

All the commercially available chemicals were used as is, without further purification. Silver acetate (AgOAc), molybdenum disulfide (MoS<sub>2</sub>), 1.6 M n-butyllithium in hexane and the solvent, hexane were purchased from Sigma Aldrich, India.

**Synthesis of MoS<sub>2</sub> NS.** Chemical exfoliation method was used to synthesize MoS<sub>2</sub> NSs from MoS<sub>2</sub> powder.<sup>[1]</sup> 300 mg of MoS<sub>2</sub> powder was taken in a round bottom flask, under an argon atmosphere, and 3 mL of 1.6 M n-butyllithium was added. The resulting solution was stirred for 2 days under the same conditions. Then the resulting lithium intercalated product was washed repeatedly with hexane, to remove excess reactants, followed by the addition of 100 mL of distilled water. The produced was sonicated in a bath sonicator for 1 h. This aqueous dispersion of MoS<sub>2</sub> NSs was centrifuged at a speed of 18000 rpm to remove un-exfoliated MoS<sub>2</sub>. The quality of the synthesized MoS<sub>2</sub> NSs was checked using electron microscopy, UV-Vis and Raman spectroscopy. The concentration of MoS<sub>2</sub> dispersion was determined using inductively coupled plasma mass spectrometry (ICP MS).

**Electrospray deposition on MoS<sub>2</sub> NSs.** For electrospray deposition, a home built nanoelectrospray ionization (nESI) source was used. The nESI source was made by pulling a borosilicate glass capillary (0.86 mm ID and 1.5 mm OD) into two, using a micropipette puller (Sutter Instruments, U.S.A.). Each tip, after pulling, was checked using an optical microscope to ensure the size and quality of the cut. Tips with an opening of 10-15  $\mu$ m were

used for all the deposition experiments. 10 mM aqueous solution of AgOAc was filled in the nESI tips using a micro injector pipette tip and Pt wire was inserted into the solution, making an electrode for high voltage connection. For electrospray deposition on MoS<sub>2</sub> NSs, an aqueous suspension of 3.7 mM (in terms of Mo) MoS<sub>2</sub> NS was taken in an Eppendorf vial and the Ag<sup>+</sup> ions generated by the nESI source was guided towards it. The distance between the tip of the nESI source and the surface of the MoS<sub>2</sub> solution was optimized to be 10 mm. No changes in the size or nature of the holes were observed with change in the distance between the tip and the deposition surface provided the amount of the ions were constant. The water MoS<sub>2</sub> suspension was grounded through a picoammeter using a copper strip. The deposition current was varied from 20-100 nA for different experiments.

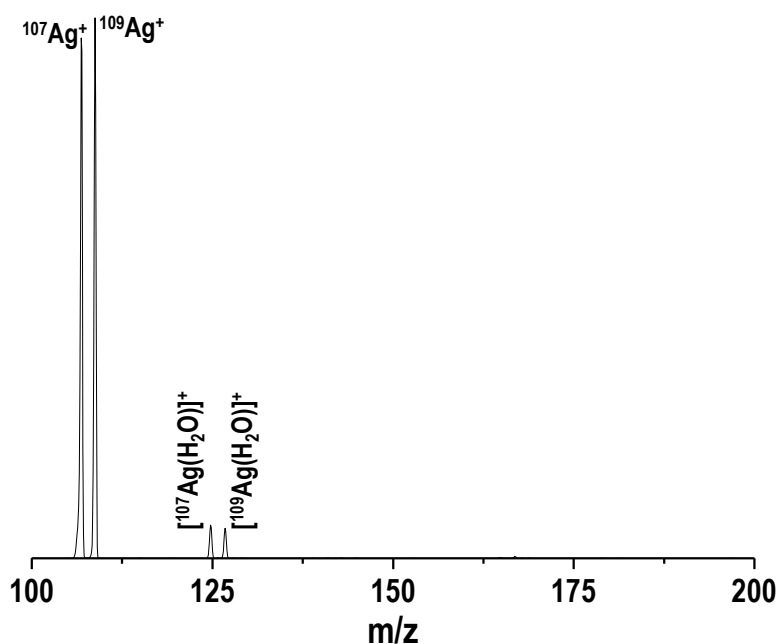
**Details of the bacteria and virus used for disinfection reaction.** *Escherichia coli* and MS2 bacteriophage, the surrogates for water borne pathogens (bacteria and viruses, respectively) were used for antimicrobial testing. Saline water condition was used for all the antibacterial and antiviral testing. A fresh single colony of the *Escherichia coli* (ATCC 10536) pre-grown on Luria–Bertani (LB) agar was used as the inoculum and cell suspensions in LB broth were allowed to grow at 37 °C to late exponential phase with a final optical density (600 nm) of 1. This was used as the input for antibacterial experiments. In the case of antiviral testing, F-specific bacteriophage MS2 (ATCC 15597-B1) was cultured using *E. coli* host C-3000 (ATCC 15597) in the logarithmic phase. Purified virus was used as input for antiviral experiments.

#### **Electrochemical measurements.**

Both cyclic voltammetry (CV) and linear sweep voltammetry (LSV) were measured by an electrochemical analyzer (CHI 600A) with conventional three-electrode configuration adopted with bulk Au (111) electrode as the working electrode, silver/silver chloride (Ag/AgCl) as the reference electrode and Pt wire as the counter electrode. Prior to any electrochemical measurement, Au electrode was cleaned manually with two different micro

polishing powders of  $\text{Al}_2\text{O}_3$  (particle size  $\sim 0.3 \mu\text{M}$  and  $0.05 \mu\text{M}$ ). All the electrochemical measurements were performed at room temperature and in phosphate buffered saline (Merck India Pvt. Ltd) solution of pH $\sim 7.3$ .

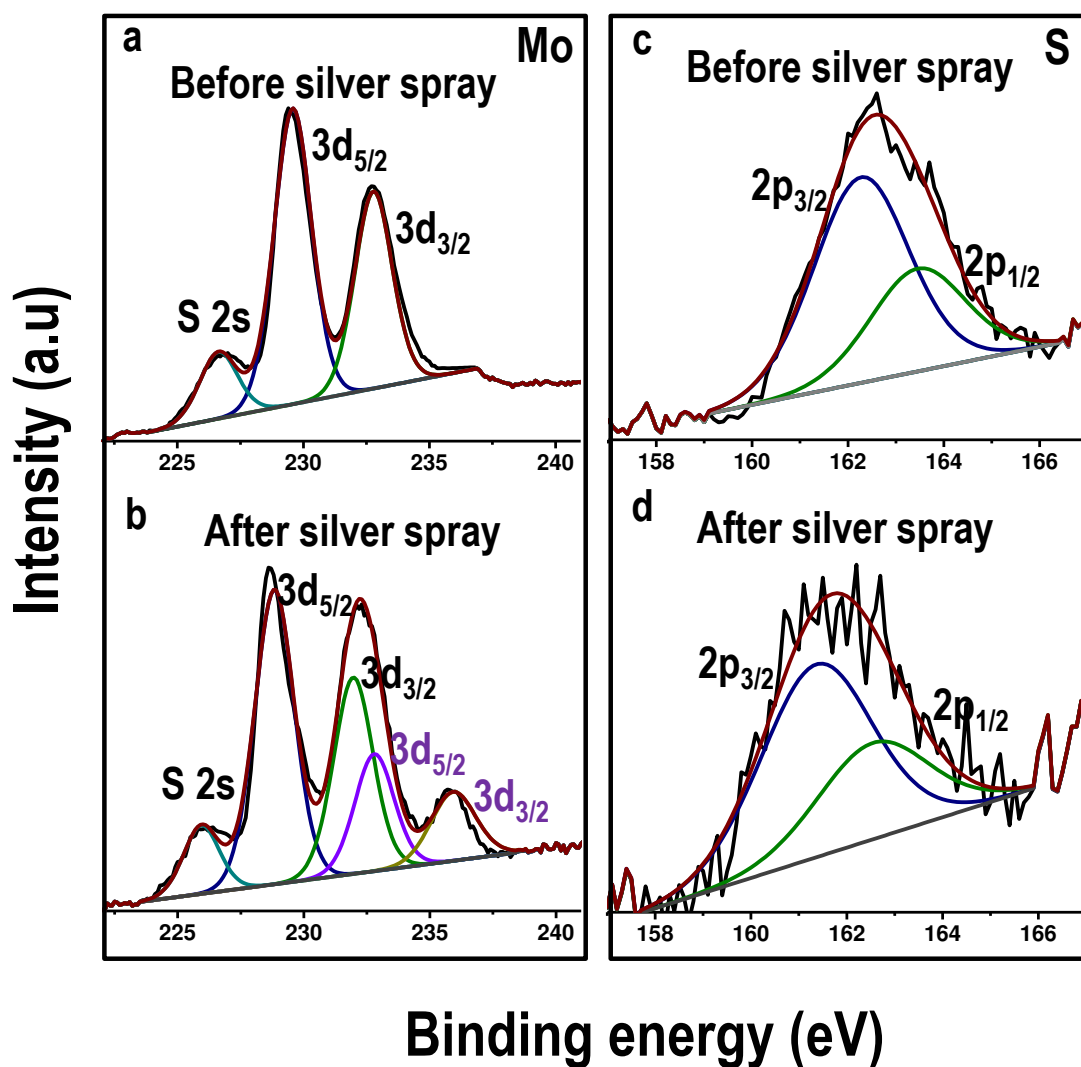
**Dark field fluorescence microscopic analysis.** Fluorescence microscopy imaging was performed using a Cytoviva microscopy system. For sample preparation, LIVE/DEAD BacLight™ bacterial viability kit (Molecular Probes, Eugene, OR) was used. At each time point, 1 mL of the sample (holey  $\text{MoS}_2$  nanosheet treated and control bacteria) was mixed with 2  $\mu\text{L}$  of PI-SYTO 9 mix (1:1) and incubated in dark for 15 min. About 0.5–1  $\mu\text{L}$  sample was spotted on a 1 mm thick ultrasonically cleaned glass slide (SCHOTT) and it was covered with a 0.145 mm thick cleaned glass cover slip (SCHOTT). Imaging was performed using 100X oil (Cargille) immersion objective.



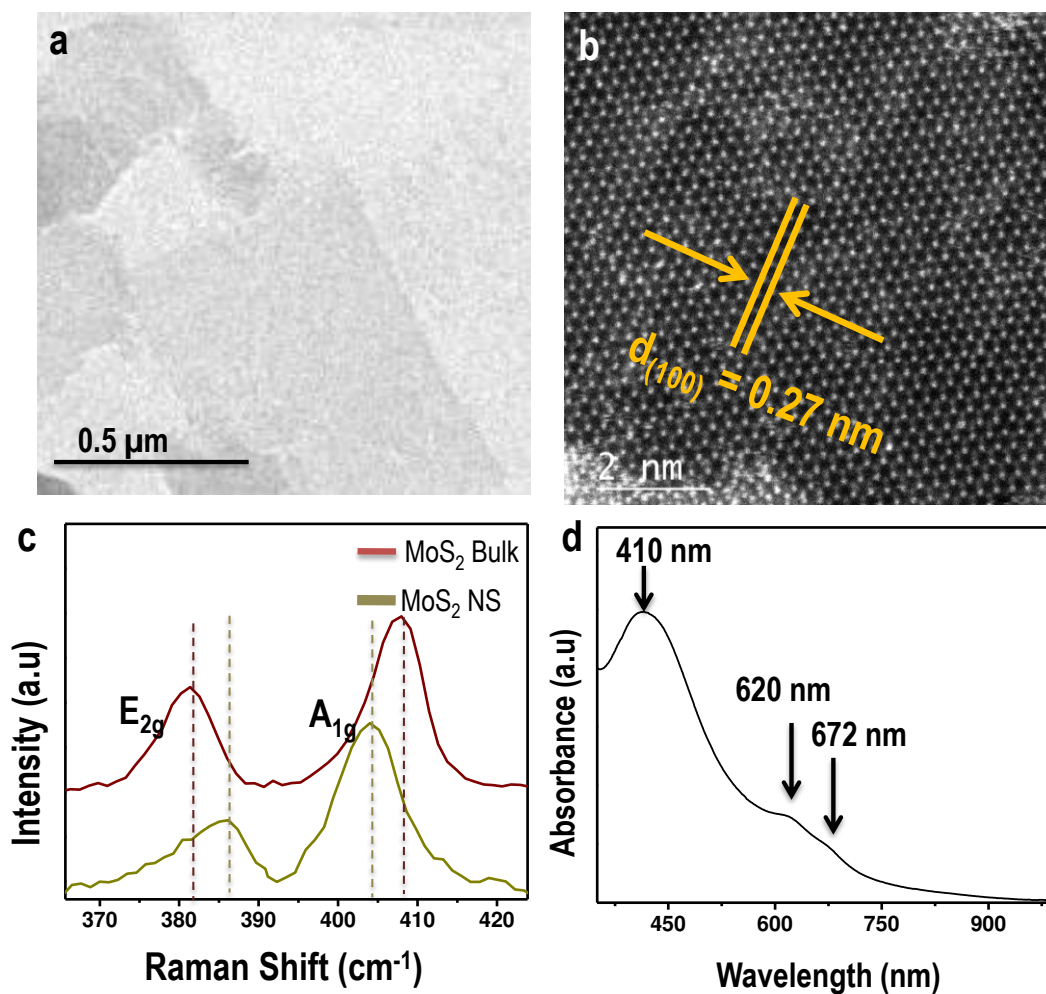
**Figure S1.** nESI of AgOAc. Mass spectrum collected from the nESI of AgOAc.

The Mo 3d region of parent materials in XPS showed two peaks at 229.5 and at 232.6 eV binding energy corresponding to  $3d_{5/2}$  and  $3d_{3/2}$  of Mo(IV). But when the XPS spectrum after the electrospray of  $\text{Ag}^+$  ions was taken, a blue shift of 0.3 eV was seen due to the decrease in

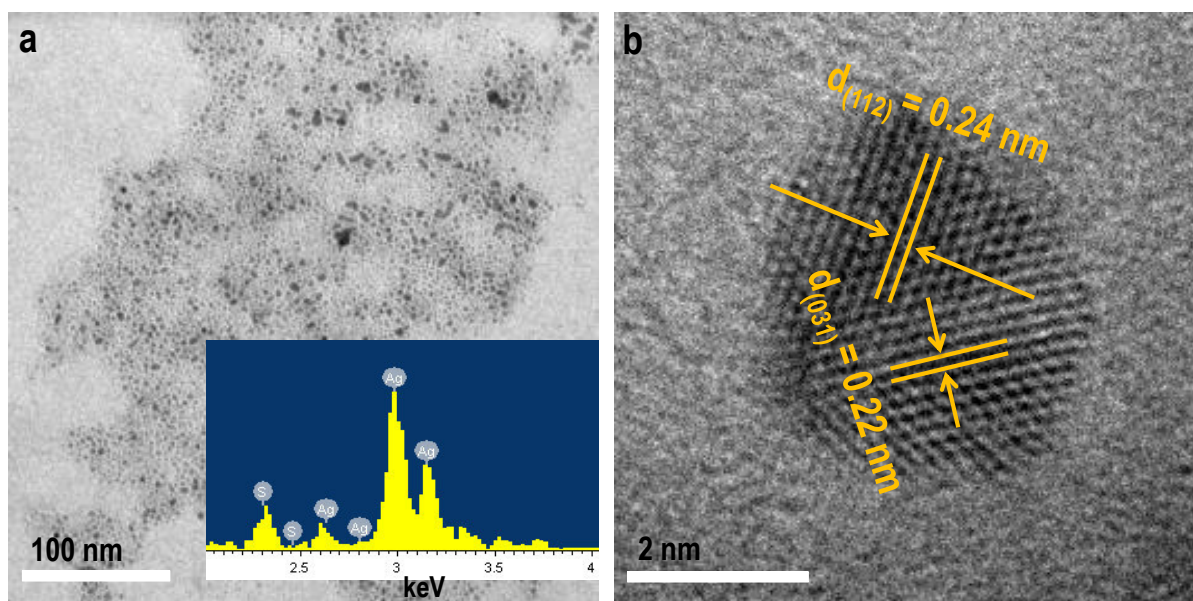
a number of sulphide ions (because of the reaction with silver). The emergence of two new peaks is attributed to the formation of  $\text{Mo(VI)O}_4^{2-}$  (as a result of the Mo sites lost due to reaction).<sup>[20]</sup>



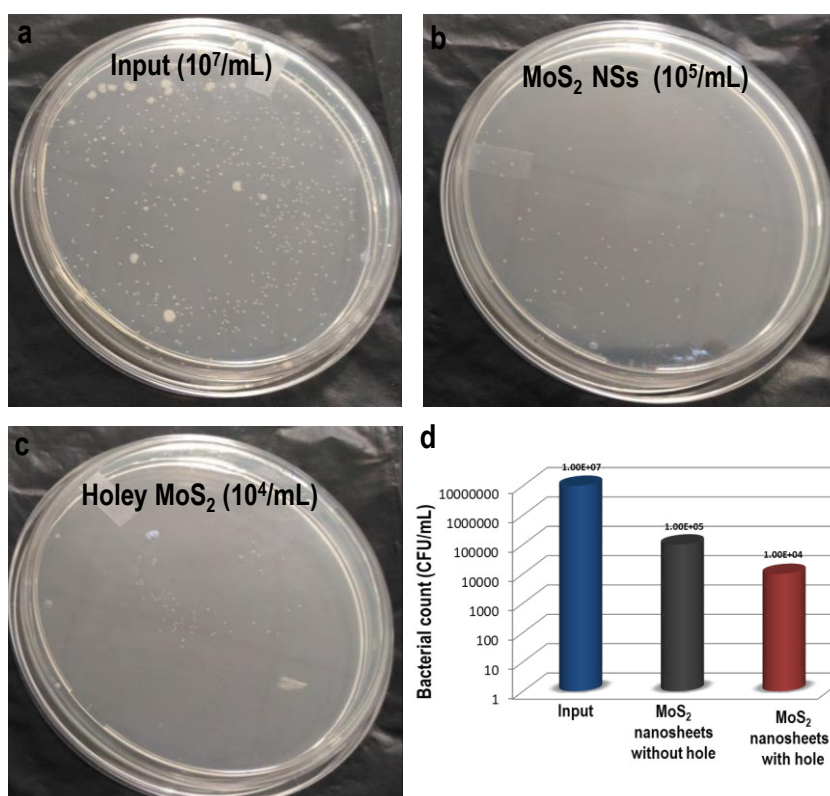
**Figure S2.** (a-b) correspond to the XPS spectra in the Mo 3d region before and after the electro spray of silver, respectively. (c-d) XPS spectra in the S 2p region before and after the electro spray of silver, respectively.



**Figure S3.** Characterization of MoS<sub>2</sub> NSs. (a) TEM image of as-synthesized MoS<sub>2</sub> nanosheet. (b) HAADF TEM image of (a) MoS<sub>2</sub> nanosheet showing that there are no defects in it. (c) Raman spectrum collected from the MoS<sub>2</sub> nanosheet and bulk MoS<sub>2</sub>. The peak difference ( $\sim 18 \text{ cm}^{-1}$ ) of E<sub>2g</sub> and A<sub>1g</sub> for MoS<sub>2</sub> NSs suggests that the sheets are one layer thick. (d) UV-Vis spectrum collected from a suspension of MoS<sub>2</sub> NSs.

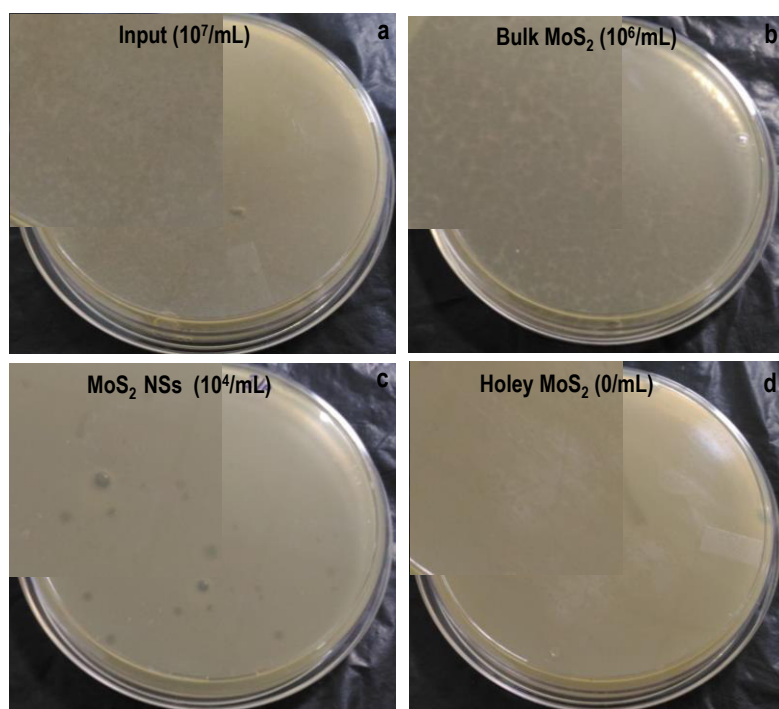


**Figure S4.** Characterization of Ag<sub>2</sub>S NPs. (a) TEM image of the MoS<sub>2</sub> nanosheet showing the complete reaction of it. Inset shows TEM energy dispersive spectrum of Ag<sub>2</sub>S particles. (b) HRTEM image of an Ag<sub>2</sub>S particle. The  $d_{(112)}$  and  $d_{(031)}$  planes of 0.24 nm and 0.22 nm suggest that the formed nanoparticles are the acanthite phase of Ag<sub>2</sub>S.

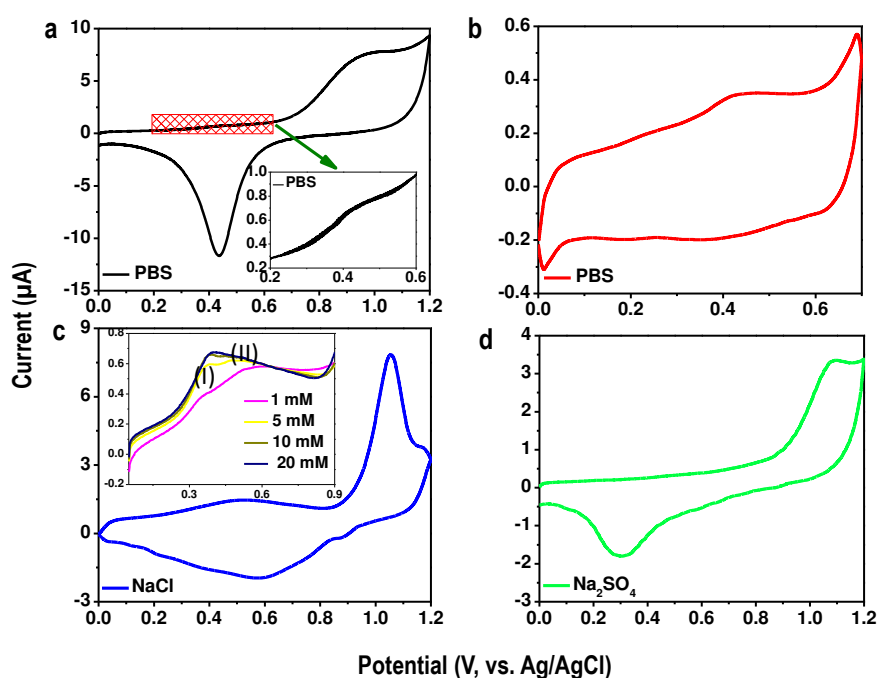


**Figure S5.** Antibacterial performance of holey MoS<sub>2</sub>. (a-c) Photograph of the antibacterial activity (with *Bacillus subtilis* bacteria) of MoS<sub>2</sub> NSs shown in (b) and with holey MoS<sub>2</sub> shown in (c). (a) Input bacterial concentration and (d) comparison of antibacterial activity of MoS<sub>2</sub> NSs and holey MoS<sub>2</sub>.





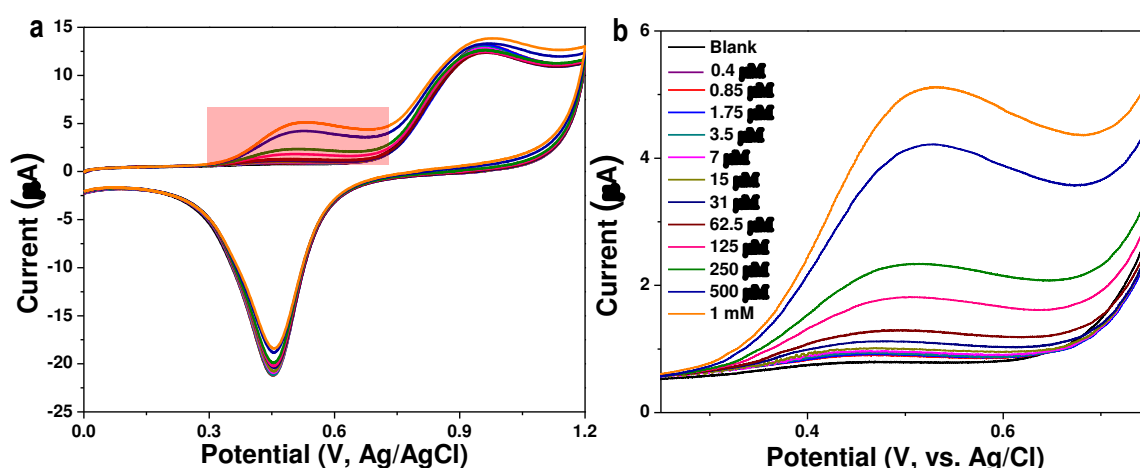
**Figure S6.** Antiviral activity of holey MoS<sub>2</sub>. (a-d) Photograph of antiviral (*bacteriophage MS2*) activity of (b) bulk MoS<sub>2</sub>, (c) MoS<sub>2</sub> NSs and (d) holey MoS<sub>2</sub>. Expanded views of the petri dishes are shown as insets.



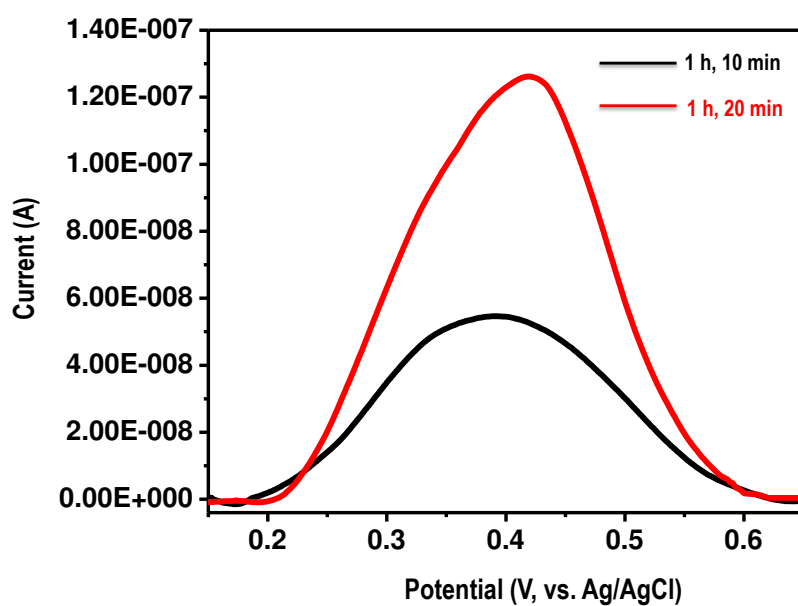
**Figure S7.** CV traces of Au electrode in different electrolytes. CV traces of gold in (a) PBS; (c) NaCl; (d) Na<sub>2</sub>SO<sub>4</sub>, respectively. (b) CV trace of gold in PBS scanned up to 0.8 V. Inset of c shows the concentration-dependent linear sweep voltammetry (LSV) traces scanned up to 0.9 V.

The CV profile of Au (Figure S7a) measured in PBS exhibits an oxidation peak at +0.95 V and a reduction peak at +0.43 V. These were not seen in the CV measured up to +0.7 V

(Figure S7b) confirming that the oxidation peak at 0.95 V was coupled with the reduction peak at +0.43 V. These were attributed to the reaction,  $\text{Au} + 4\text{Cl}^- = \text{AuCl}_4^- + 3\text{e}^-$ . Although these peaks were not seen in Figure S7b, there was a small oxidation peak at +0.45 V, which is also seen in Figure S7a. In order to understand the origin of this small peak, we performed the same CV measurement (scanned up to +1.2 V) in NaCl solution (Figure S7c) and the peak appeared again at +0.45 V along with the other peaks. However, when we performed the same experiment in  $\text{Na}_2\text{SO}_4$ , the peak around +0.45 V was not seen (Figure S7d). To assign the broad peak around +0.45 V, we performed linear sweep voltammetry (LSV) up to +0.9 V with different concentrations of NaCl (spectra shown in the inset of Figure S7c). Seemingly, the single peak observed at +0.45 V in Figure S7c was actually composed of two peaks as shown in the inset of the same figure. At lower concentrations of NaCl, the two peaks were well separated from each other and the peak separation of these two become narrower as concentration of NaCl was increased. For better clarity, we marked these peaks as I and II. First peak I was due to  $\text{Cl}^-$  adsorption on Au surface and consecutive oxidation of Au by the reaction,  $\text{Au}_{(\text{surface})}\text{Cl}^- = \text{AuCl}_{(\text{surface})} + \text{e}^-$  (peak II).<sup>[2]</sup> At lower concentration of NaCl (1 mM), coverage of  $\text{Cl}^-$  was lower and correspondingly Au oxidation was poor. However, as NaCl concentration was increased, current started increasing. Finally, maximum current was seen at 20 mM NaCl which was due to higher  $\text{Cl}^-$  coverage and therefore, maximum oxidation. Beyond 20 mM of NaCl concentration, no further change of peak current was observed. As  $\text{H}_2\text{O}_2$  comes in contact with the electrode ( $\text{H}_2\text{O}_{2(\text{bulk})} \xrightarrow{\text{Diffusion}} \text{H}_2\text{O}_{2(\text{electrode})}$ ) it gets oxidized ( $\text{H}_2\text{O}_2 = 2\text{H}^+ + \text{O}_2 + 2\text{e}^-$ ) at the same potential.



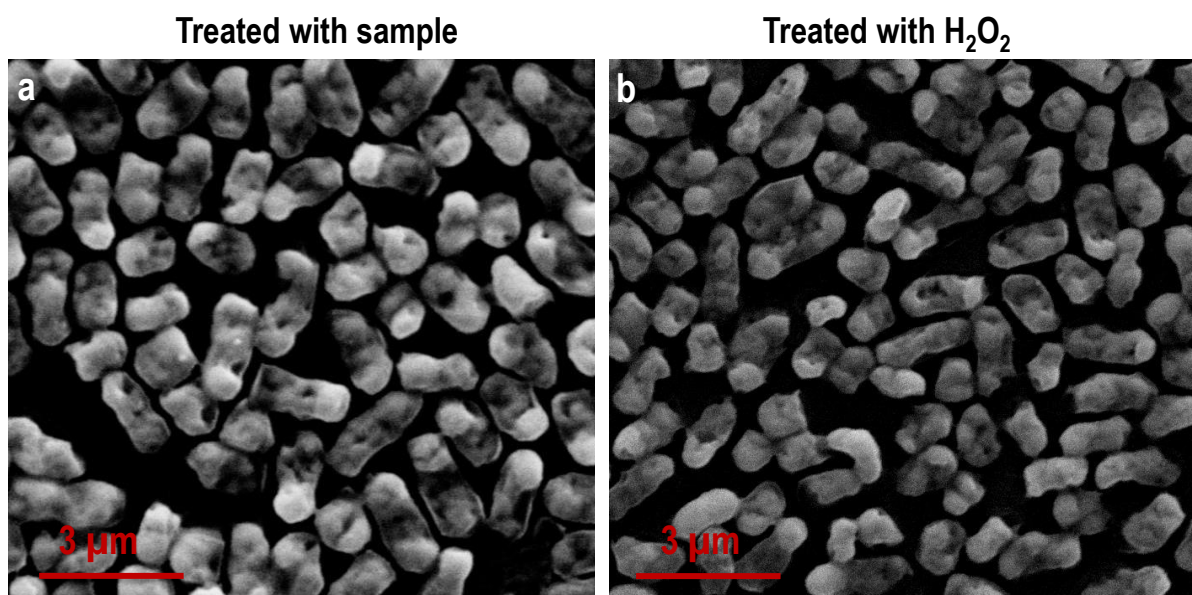
**Figure S8.** CV of externally added  $\text{H}_2\text{O}_2$ . (a) CV traces of a control experiment performed with externally added  $\text{H}_2\text{O}_2$  with different concentrations, in PBS. (b) Magnified version of the marked area of Figure S8a.



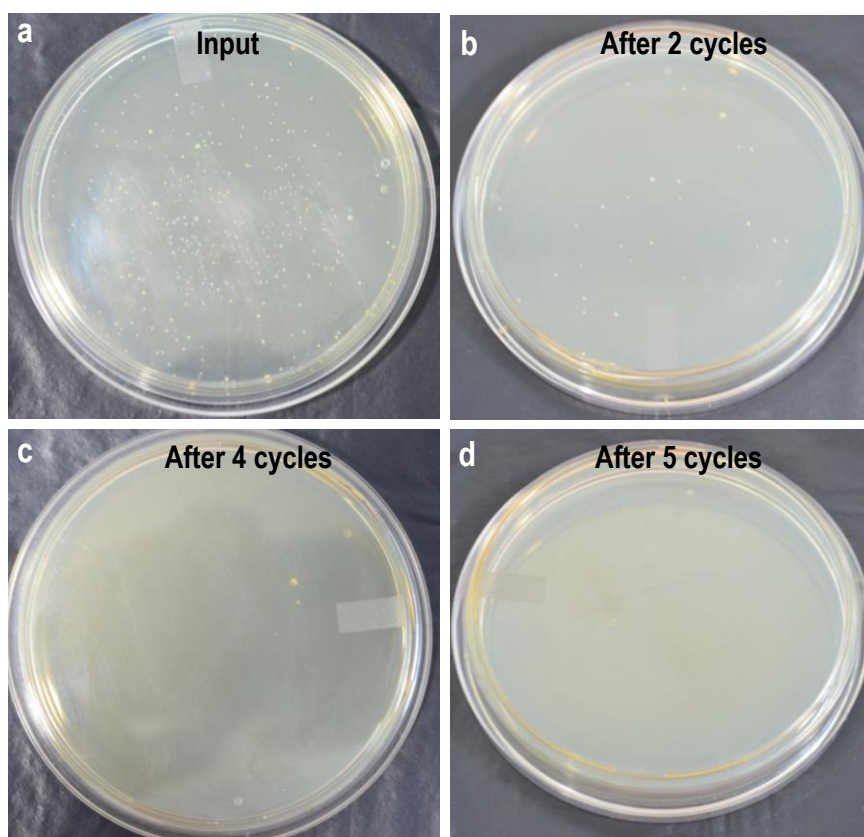
**Figure S9.** Linear sweep voltammetry (LSV) profile of MoS<sub>2</sub> NS suspensions with different time of spraying of Ag<sup>+</sup>. LSV spectrum MoS<sub>2</sub> NSs suspension after 10 and 20 min of Ag<sup>+</sup> deposition and 1h of visible light irradiation.

Samples	Concentration of H <sub>2</sub> O <sub>2</sub> (μM)
MoS <sub>2</sub> NSs without hole (1 h)	0.43
MoS <sub>2</sub> NSs without hole (2 h)	0.63
Holey MoS <sub>2</sub> NSs (1 h)	0.69
Holey MoS <sub>2</sub> NSs (1 h)	1.54

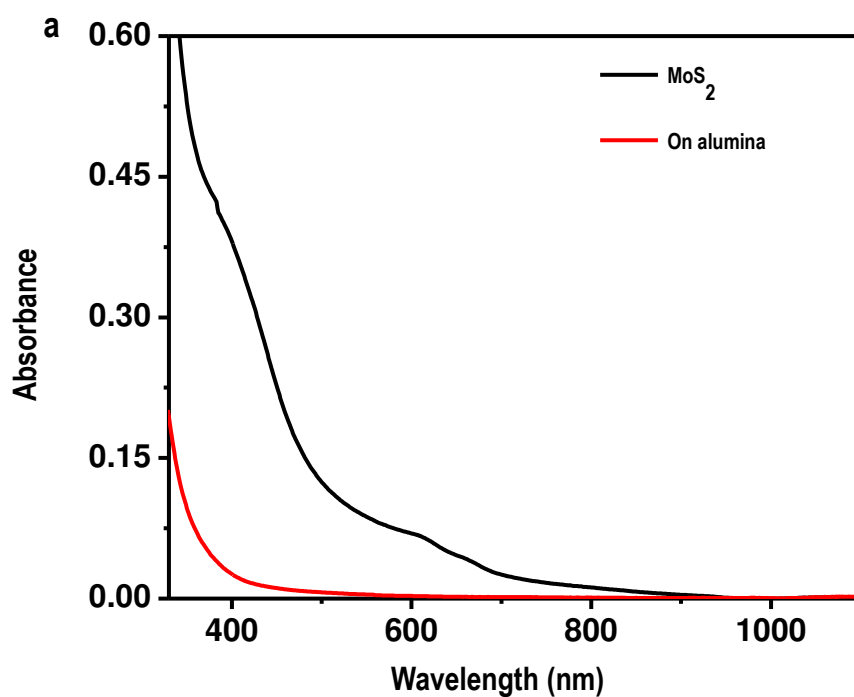
**Table S1.** Quantification of H<sub>2</sub>O<sub>2</sub> concentration generated from holey MoS<sub>2</sub> using calibration curves.



**Figure S10.** Imaging of dead bacteria. (a-b) SEM images of the bacteria (*E. coli*) after the treatment with the sample and H<sub>2</sub>O<sub>2</sub>, respectively. In both the cases, similar cell damage was observed.



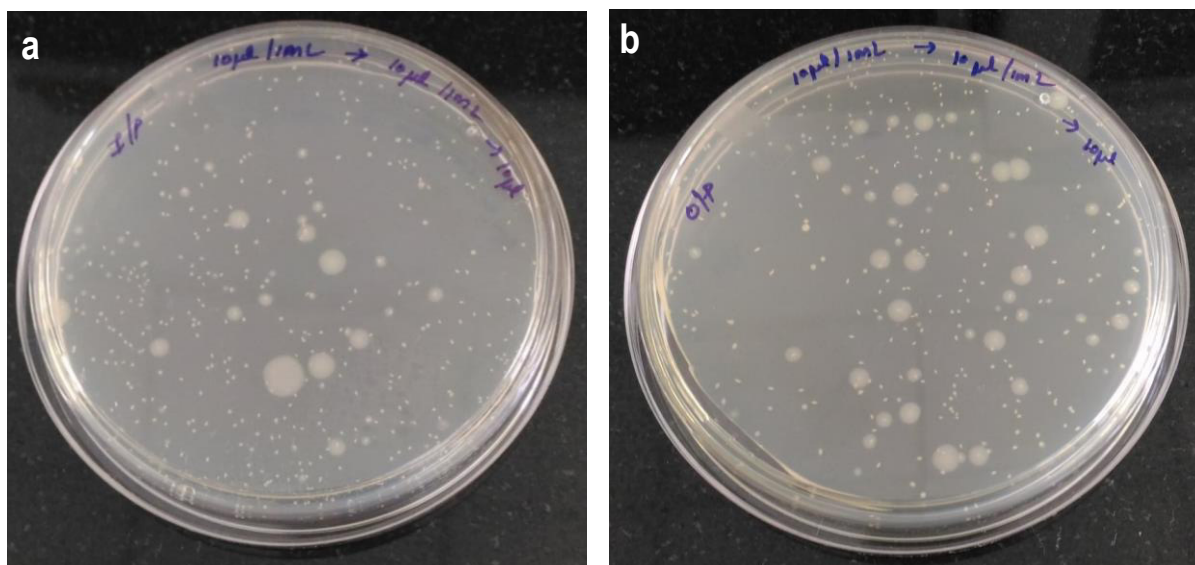
**Figure S11.** Photographs of the experiment performed with the prototype. (a) Input (contaminated water), bacteria count (b) after 2 cycles, (c) after 4 cycles and (d) after 5 cycles.



b

Sample	Mo concentration (ppb)
MoS <sub>2</sub> NSs	0.08 ppb

**Figure S12.** No leaching of MoS<sub>2</sub> from MoS<sub>2</sub>-adsorbed alumina. (a) UV-Vis spectra of MoS<sub>2</sub> NSs (black) and the supernatant (red) taken from MoS<sub>2</sub>-adsorbed alumina@water. Negligible leaching was observed. (b) ICP MS analysis of the supernatant showed negligible Mo concentration.



**Figure S13.** *E. coli* contaminated water was passed through a column packed with only alumina. Photograph of (a) Input (contaminated water) and (b) output. No disinfection was observed.

## References

- [1] a) L. Yuwen, H. Yu, X. Yang, J. Zhou, Q. Zhang, Y. Zhang, Z. Luo, S. Su, L. Wang, *Chem. Commun. (Cambridge, U. K.)* **2016**, 52, 529-532; b) L. Yuwen, F. Xu, B. Xue, Z. Luo, Q. Zhang, B. Bao, S. Su, L. Weng, W. Huang, L. Wang, *Nanoscale* **2014**, 6, 5762-5769; c) C. N. R. Rao, Ramakrishna Matte, S. S. H., U. Maitra, *Angew. Chem., Int. Ed.* **2013**, 52, 13162-13185.
- [2] a) L. Aldous, D. S. Silvester, C. Villagran, W. R. Pitner, R. G. Compton, L. M. Cristina, C. Hardacre, *New Journal of Chemistry* **2006**, 30, 1576-1583; b) Z. Shi, J. Lipkowski, *J. Electroanal. Chem.* **1996**, 403, 225-39.



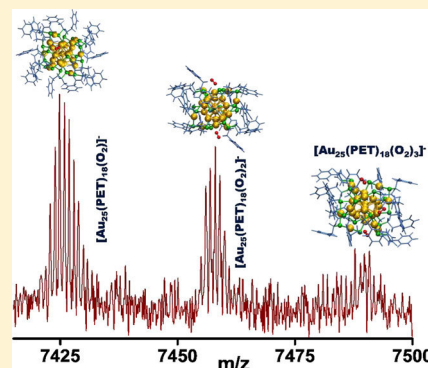
# Detection of $[\text{Au}_{25}(\text{PET})_{18}(\text{O}_2)_n]^-$ ( $n = 1, 2, 3$ ) Species by Mass Spectrometry

Shridevi Bhat, Raghu Pradeep Narayanan, Ananya Baksi, Papri Chakraborty, Ganesan Paramasivam, Rabin Rajan J. Methikkalam, Abhijit Nag, Ganapati Natarajan, and Thalappil Pradeep\*

DST Unit of Nanoscience (DST UNS) and Thematic Unit of Excellence, Department of Chemistry, Indian Institute of Technology Madras, Chennai 600036, India

## Supporting Information

**ABSTRACT:**  $[\text{Au}_{25}(\text{SR})_{18}]^-$  nanoclusters have been tested as a model catalyst in multiple oxidation reactions involving CO, alkenes, cyclohexane, and alcohols. Oxygen is used as an oxidizing agent in most of the reactions. Hence,  $\text{O}_2$  activation is of great interest in catalysis. The mechanism of these reactions, the role of intact nanoclusters as catalytically active species, and the utility of such nanoclusters as homogeneous catalysts are not completely clear. Herein, we investigate the interaction of  $[\text{Au}_{25}(\text{SR})_{18}]^-$  in solution with  $\text{O}_2$  using electrospray ionization mass spectrometry and density functional theory (DFT) calculations. Up to three  $\text{O}_2$  molecules attach to an  $[\text{Au}_{25}(\text{SR})_{18}]^-$  in dichloromethane (DCM) when  $\text{O}_2$  gas is passed through a solution of the former. Oxygen addition to the nanocluster leads to its decomposition. The nanocluster is most stable in toluene and least stable in tetrahydrofuran when kept under a continuous flow of  $\text{O}_2$ , where no  $\text{O}_2$  adduct peaks are observed. It shows intermediate stability in DCM in the presence of  $\text{O}_2$ , and the decomposition products, in this case, are of a different type compared to the former solvents. The appearance of  $\text{O}_2$  adducts and the variation in the stability of the nanocluster in different solvents is assumed to be due to the difference in oxygen solubility in these solvents. DFT calculations suggest that the first two  $\text{O}_2$  molecules interact with the surface Au atoms through the cavities formed by the ligands and staples in the nanocluster and the third  $\text{O}_2$  interacts only with 2-phenylethane thiol ligands.



## 1. INTRODUCTION

Developments in the field of heterogeneous and homogeneous catalysis by gold trace back to the early work of Haruta<sup>1–4</sup> and Hutchings.<sup>5,6</sup> They established the low-temperature catalytic oxidation of CO and selective oxidation of hydrocarbons by supported gold nanoparticles and nanoclusters. Subsequently, scientists started checking out the possibility of application of monolayer-protected nanoclusters in catalysis because of the unique structure and properties of the latter.<sup>7–9</sup> Advances in the mass spectrometry (MS) of nanoclusters have tremendously helped in gaining molecular level understanding of such systems.<sup>10,11</sup> Computational methods have backed the experiments significantly in this regard.<sup>12,13</sup> Among the thiolate-protected nanoclusters,  $[\text{Au}_{25}(\text{SR})_{18}]^-$  has emerged as a widely researched model catalyst,<sup>8,14</sup> owing to its highly reproducible synthetic protocols with a variety of ligands,<sup>15,16</sup> well-defined structure and properties,<sup>17–19</sup> and its stability in various conditions.<sup>20–22</sup>

Activation of molecular  $\text{O}_2$  is of great interest in catalysis because of its utility in a number of oxidation reactions.<sup>8,14</sup> There is an added advantage in using molecular  $\text{O}_2$  as an oxidant from the point of view of Green chemistry.<sup>23</sup> The first indirect evidence<sup>24</sup> for the interaction of  $[\text{Au}_{25}(\text{SR})_{18}]^-$  with  $\text{O}_2$  was the aerial oxidation of the nanocluster in dichloromethane (DCM) at room temperature. In this process,

inherently negatively charged  $[\text{Au}_{25}(\text{SR})_{18}]^-$  interacts with  $\text{O}_2$  present in the air and gets oxidized into neutral species when its solution is exposed to air.<sup>24</sup> On the basis of this observation,  $[\text{Au}_{25}(\text{SR})_{18}]^-$  was checked for its catalytic activity in various oxidation reactions. Lopez-Acevedo et al. suggested the possibility of  $\text{O}_2$  adsorption on  $[\text{Au}_{25}(\text{SR})_{18}]^-$  upon removing one of the  $\text{Au}_2(\text{SR})_3$  units. However, they proposed a mechanism for CO oxidation reaction by removing two  $\text{Au}_2(\text{SR})_3$  units, which rendered two nearest neighboring Au atoms free for binding with CO and  $\text{O}_2$  molecules.<sup>25</sup> Nie et al. investigated the application of oxide-supported  $[\text{Au}_{25}(\text{SR})_{18}]^-$  as a catalyst for the CO oxidation.<sup>26</sup> They conducted several experiments with various oxide supports and  $\text{O}_2$  pretreatment conditions to understand the effect of the same on this catalytic reaction. They concluded that intact nanoclusters on oxide surface catalyze the reaction. They also suggested that the interface positions between the nanocluster and the oxide support are the catalytically active sites. The experiments by Zhu et al. revealed that  $[\text{Au}_{25}(\text{SR})_{18}]^-$  can act as a homogeneous catalyst in solution phase oxidation of styrene by  $\text{O}_2$ .<sup>27</sup> Xie et al. examined the aerobic oxidation of

Received: April 5, 2018

Revised: July 28, 2018

Published: August 5, 2018



alcohols catalyzed by  $[\text{Au}_{25}(\text{SR})_{18}]^-$  calcinated on carbon nanotubes.<sup>28</sup> Liu et al. found that the  $\text{Au}_{25}$  supported on hydroxyapatite catalyzes aerobic oxidation of cyclohexane to cyclohexanol and cyclohexanone.<sup>23</sup>

The mechanism of catalysis of oxidation reactions by  $\text{Au}_{25}$  nanoclusters is still unclear even though there are a significant number of investigations of the applications of these nanoclusters as a model catalyst for these reactions. It is crucial to get a deeper understanding of the stability of the nanocluster under these reaction conditions, catalytically active centers, nature of binding between the cluster and the reactant and product species, and influence of reaction conditions. Recently, Dreier et al. carried out a reinvestigation of the homogeneous catalysis of styrene oxidation by *t*-butyl hydrogen peroxide (TBHP) using  $[\text{Au}_{25}(\text{SR})_{18}]^-$ .<sup>29</sup> They established that the nanoclusters are unstable in the presence of TBHP and undergo oxidative decomposition.  $\text{Au}(\text{I})$ -thiol precursors and decomposition products are equally effective in catalyzing styrene oxidation.<sup>29</sup> Such investigations show that there is a need to conduct fundamental research to understand the catalysis by nanoclusters, which would help in designing selective catalysts for various chemical processes.

In spite of several existing studies on the catalytic activity of the cluster in oxidation reactions, there is no clear understanding of the interaction of molecular  $\text{O}_2$  with the nanocluster. In all the investigations conducted so far, interaction with oxygen was suggested but there is no evidence for an oxygen bound cluster. Such an adduct would be the central species responsible for the oxidation of the cluster in atmospheric conditions and in other processes too. In this regard, our objective has been to answer a fundamental question, that is, whether  $[\text{Au}_{25}(\text{SR})_{18}]^-$  reacts with  $\text{O}_2$  in ambient conditions.

In this paper, the interaction between  $[\text{Au}_{25}(\text{PET})_{18}]^-$ , where PET is 2-phenylethane thiol, and molecular  $\text{O}_2$  in solution phase was examined using electrospray ionization (ESI) MS and UV/vis absorption spectroscopy. Up to three  $\text{O}_2$  attachments to  $[\text{Au}_{25}(\text{PET})_{18}]^-$  were detected in the mass spectra. This gives a direct evidence for the interaction of  $[\text{Au}_{25}(\text{PET})_{18}]^-$  with molecular  $\text{O}_2$ . Oxygen attachment to the nanocluster leads to its decomposition to smaller polymer-like products. Adduct formation between  $[\text{Au}_{25}(\text{PET})_{18}]^-$  and  $\text{O}_2$  was observed only in the case of DCM and not in toluene and tetrahydrofuran (THF). However, the nanoclusters were stable in the case of toluene for long time, in the presence of  $\text{O}_2$ . Density functional theory (DFT) calculations suggested that the interaction sites for the first and the second  $\text{O}_2$  are surface Au atoms of the nanocluster and the third  $\text{O}_2$  interacts with only PET ligands.

## 2. EXPERIMENTAL SECTION

**2.1. Materials.** Chloroauric acid trihydrate ( $\text{HAuCl}_4 \cdot 3\text{H}_2\text{O}$ ), PET, tetraoctylammonium bromide (TOAB), and sodium borohydride ( $\text{NaBH}_4$ ) were purchased from Sigma-Aldrich. Toluene, THF, DCM, and methanol were purchased from RANKEM and were of analytical grade. All the chemicals were used as such without any further purification.

**2.2. Instrumentation.** A PerkinElmer LAMBDA 25 instrument with a range of 200–1100 nm and a band pass filter of 1 nm was used for measuring UV/vis absorption spectra of the samples.

The ESI MS measurements were done by a Waters' Synapt G2Si high definition MS instrument, consisting of an

electrospray source, quadrupole ion guide/trap, ion mobility cell, and time-of-flight detector. Nitrogen gas was used as the nebulizer gas. The measurements were done in negative ion mode as  $[\text{Au}_{25}(\text{SR})_{18}]^-$  is intrinsically negatively charged. In the case of toluene samples, acetonitrile was added to facilitate the ion detection. The optimized conditions used to obtain a well-resolved MS spectrum were as follows:

sr. no.	parameters	value
1	sample concentration	10 $\mu\text{g/mL}$
2	solvents	DCM or toluene or THF
3	flow rate	30 $\mu\text{L/min}$
4	capillary voltage	3.5 kV
5	cone voltage	120–150 V
6	source offset	80–120 V
7	desolvation gas flow	400 L/h
8	trap gas flow	5 mL/min

**2.3. Synthesis of  $[\text{Au}_{25}(\text{PET})_{18}]^-$ .** A modified Brust–Schiffrin single-phase procedure was used for the synthesis of  $[\text{Au}_{25}(\text{PET})_{18}]^-$ .<sup>30</sup> Approximately 40 mg of  $\text{HAuCl}_4 \cdot 3\text{H}_2\text{O}$  was taken in 7.5 mL of THF, and ~65 mg of TOAB was added and stirred for ~15 min to get a deep-red-colored solution. Following this, 5 mol equivalents (with respect to gold) of PET was added, and the reaction mixture was stirred for approximately 2 h to get a colorless solution of Au–SR thiolate mixtures. These thiolates were reduced by ~39 mg of  $\text{NaBH}_4$  taken in 2.5 mL of ice-cold water. The reaction mixture was stirred at a constant speed of 1500 rpm at room temperature for another 6 h to get a reddish-brown-colored solution. To remove excess thiol and other impurities, THF was evaporated by vacuum drying and the nanocluster was precipitated by methanol addition. The supernatant solution containing excess thiol was discarded. This step was repeated 2–3 times followed by extraction of the nanocluster in acetone leaving behind bigger particles. The acetone was vacuum-dried, and the pure nanocluster was extracted in DCM.

**2.4. Interaction of  $[\text{Au}_{25}(\text{PET})_{18}]^-$  with  $\text{O}_2$ ,  $\text{CO}_2$ ,  $\text{N}_2$ , and Ar.** All the gases used were of high purity (99.99%). These reactions were performed in two ways. In one, the nanocluster solution in DCM was kept under  $\text{O}_2$  environment created by an  $\text{O}_2$ -filled balloon. The samples for time-dependent UV/vis spectroscopy and ESI MS were withdrawn at different time intervals using a syringe. The same procedure was followed for other gases as well. In another method,  $\text{O}_2$  gas was passed through the solution of the nanocluster in DCM with continuous stirring. The samples were withdrawn using a syringe at different time intervals and monitored using UV/vis spectroscopy and ESI MS. To check the effect of solvents on  $\text{Au}_{25}(\text{PET})_{18}-\text{O}_2$  adduct formation, the same procedure was repeated with toluene and THF.

**2.5. Molecular Docking Studies.** In order to obtain further insights into the molecular level interactions of  $\text{O}_2$  with  $[\text{Au}_{25}(\text{PET})_{18}]^-$ , molecular docking studies were performed using AutoDock 4.2.1. The DFT-optimized  $[\text{Au}_{25}(\text{PET})_{18}]^-$  structure was used for this investigation. Oxygen was used as the “ligand” and  $[\text{Au}_{25}(\text{PET})_{18}]^-$  as the “receptor” molecule. The output for ligand was saved in PDBqt format. DFT-optimized charges were used for the receptor. Receptor grids were generated using  $126 \times 126 \times 126$  grid points in xyz with grid spacing of 0.375 Å and map types were created using AutoGrid-4.2. The grid parameter file (.gpf) was saved using MGL Tools-1.4.6.50. The docking parameter files (.dpf) were generated using MGL Tools-1.4.6.50 and docking was

performed using AutoDock 4.2. The results of AutoDock generated an output file (.dlg), and the generated conformers were scored and ranked as per the interaction energy keeping the 10 lowest energy conformers. The output files generated by Lamarckian genetic algorithm were analyzed using MGL Tools-1.4.6. The conformer with lowest binding energy (BE) of the interacting molecules was used as an initial structure for DFT optimization. We sequentially docked one to three  $O_2$  molecules to  $[Au_{25}(PET)_{18}]^-$  by combining the output coordinates of the last docked  $O_2$  molecule and  $[Au_{25}(PET)_{18}]^-$  to be the new receptor and the next  $O_2$  to be docked as the ligand. The binding free energy of the  $[Au_{25}(PET)_{18}O_2]^-$  was  $-3.26$  kcal/mol.

**2.6. DFT Optimization.** The interaction of a few oxygen molecules with  $[Au_{25}(PET)_{18}]^-$  was computationally studied by considering the  $[Au_{25}(PET)_{18}(O_2)_n]^-$  ( $n = 1, 2$ , and  $3$ ) and using DFT with the projector augmented wave (PAW) method as implemented in the GPAW software package.<sup>31,32</sup> The calculations were performed in linear combination of atomic orbitals mode of GPAW which efficiently utilizes the given basis set to form the wave function for atomic species, and thus, the computational time could be greatly reduced even for larger structures. The exchange–correlation functional and basis set were the Perdew–Burke–Ernzerhof (PBE) functional<sup>33</sup> and a double- $\zeta$  plus polarization basis set,<sup>34</sup> respectively. The calculations for  $[Au_{25}(PET)_{18}(O_2)]^-$  were also done using vdW-DF2 functional, and the results obtained were compared with those obtained using PBE functional. The valence electrons of atoms in the PAW setups were Au ( $5d^{10}6s^1$ ), S ( $3s^23p^4$ ), O ( $2s^22p^4$ ), C ( $2s^22p^2$ ), and H ( $1s^1$ ) and the other electrons were kept in a frozen core, with scalar-relativistic effects for Au atoms. The most favorable conformers obtained from molecular docking simulations were taken as the initial structures for geometry optimizations. Furthermore, the electron density was calculated using a real-space grid spacing of  $0.2$  Å and the relaxation criterion was that the forces on all atoms were  $<0.05$  eV/Å, without applying any symmetry constraints. The BE of  $(O_2)_n$  molecules was calculated as the energy difference of  $[Au_{25}(PET)_{18}(O_2)_n]^-$  and the sum of isolated  $[Au_{25}(PET)_{18}]^-$  and  $(O_2)_n$  molecules. The average BE was obtained by dividing the total BE by the number of  $O_2$  molecules. The visual molecular dynamics software<sup>35</sup> was used to create the visualization of all the optimized structures.

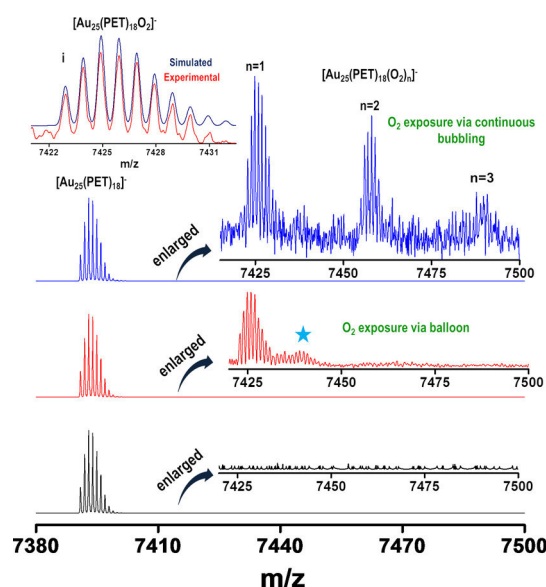
### 3. RESULTS AND DISCUSSION

We chose  $[Au_{25}(PET)_{18}]^-$  as a model system for the experiments. These nanoclusters were synthesized by the modified Brust–Schiffrin synthetic protocol<sup>30</sup> and characterized by UV/vis absorption spectroscopy and ESI MS. The UV/vis absorption spectrum of the nanocluster in DCM, given in Figure S1A, showed the characteristic features of  $[Au_{25}(PET)_{18}]^-$ . The mass spectrum of the sample, presented in Figure S1B,C, also gave the characteristic peak of  $[Au_{25}(PET)_{18}]^-$ , thus confirming the quality of our synthesis. The experiments were conducted in DCM as  $[Au_{25}(SR)_{18}]^-$  oxidizes in it upon interaction with atmospheric  $O_2$ .<sup>24</sup>

Initially, the stability of the nanocluster in the presence of  $O_2$  was checked by keeping the nanocluster solution in a continuous flow of  $O_2$  and monitoring the time-dependent UV/vis absorption spectra. These spectra are shown in Figure S2. As expected, oxidation of the nanocluster was evident in the presence of  $O_2$ , as indicated by the increase in the intensity of the  $400$  nm peak with time and the disappearance of hump

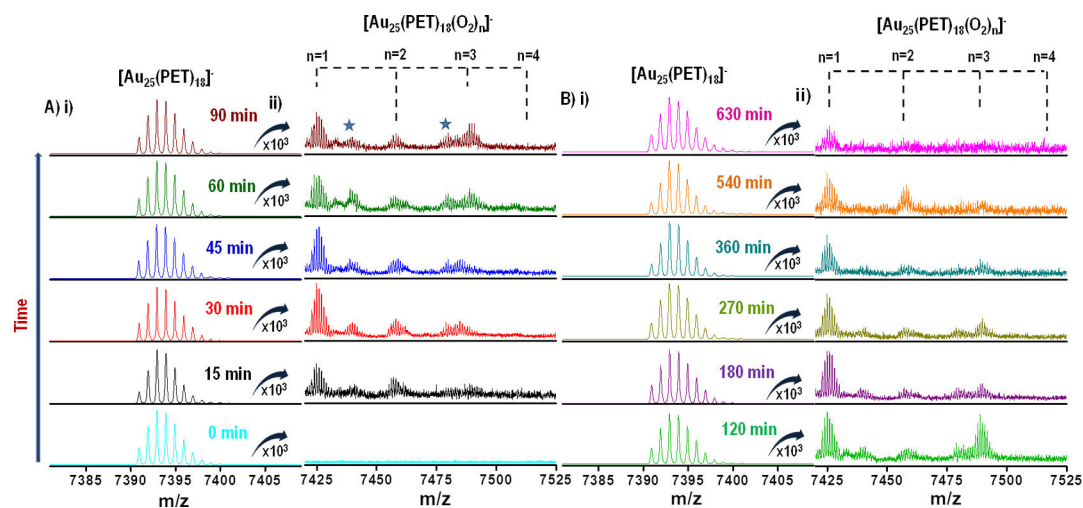
at  $800$  nm. Oxidation started occurring within  $45$  min of introduction of  $O_2$ , and it was faster than in air. In Figure S3, the UV/vis absorption spectrum of the nanocluster kept in the  $O_2$  environment for  $4$  h is compared with that of  $[Au_{25}(PET)_{18}]^-$  and air-oxidized  $[Au_{25}(PET)_{18}]^0$ . We observed the increase in intensity of  $400$  and  $450$  nm features (indicated as peaks 1 and 2 in Figure S3) as compared to both  $[Au_{25}(PET)_{18}]^-$  and  $[Au_{25}(PET)_{18}]^0$ . This spectrum corresponds to the reaction mixture consisting of parent nanocluster, its  $O_2$  adducts as well as the decomposition products (discussed later). The increase in intensity of peaks 1 and 2 could be attributed to the presence of  $O_2$  adducts and the decomposition products in the solution.

Figure 1 shows a comparison of ESI MS spectra of  $[Au_{25}(PET)_{18}]^-$  with a sample of the same kept under  $O_2$



**Figure 1.** ESI MS spectra of  $[Au_{25}(PET)_{18}]^-$  in DCM before (black trace) and after (red trace) introducing  $O_2$ . The  $O_2$  atmosphere was created using an  $O_2$ -filled balloon. Two assignments, that is,  $[Au_{25}(PET)_{18}O_3]^-$  or  $[Au_{25}(PET)_{18}(CHCl)]^-$ , are possible for the peak highlighted with an asterisk. The blue trace shows ESI MS spectrum of  $[Au_{25}(PET)_{18}]^-$  after bubbling  $O_2$  continuously for a period of  $540$  min through its solution. Inset “i” shows experimental (red trace) and simulated (dark-blue trace) mass spectra of  $[Au_{25}(PET)_{18}(O_2)]^-$ .

for  $1$  h using an  $O_2$ -filled balloon, in DCM. We observed a peak corresponding to one  $O_2$  adduct of the nanocluster, that is,  $[Au_{25}(PET)_{18}(O_2)]^-$ , at  $m/z = 7425$ . The inset “i” of the Figure 1 shows the match between experimentally observed (red trace) and simulated (dark-blue trace) mass spectra for  $[Au_{25}(PET)_{18}(O_2)]^-$  species, which are in good agreement with each other. The peak at higher mass highlighted with an asterisk could be given two assignments, that is,  $[Au_{25}(PET)_{18}O_3]^-$  or  $[Au_{25}(PET)_{18}(CHCl)]^-$ . The peak could be the result of overlap between these two species as well. However, because of the poor intensity and poorly resolved isotopic pattern of the peak, we were unable to provide an exact assignment for the same. Though there have been indirect results for the interaction of  $[Au_{25}(PET)_{18}]^-$  with  $O_2$ , for the first time we have observed the adduct species  $[Au_{25}(PET)_{18}(O_2)]^-$  in the mass spectrum. As mentioned earlier, the aerial oxidation of  $[Au_{25}(PET)_{18}]^-$  to



**Figure 2.** (A) (i) Time-dependent ESI MS spectra, up to 90 min, upon exposure of  $[\text{Au}_{25}(\text{PET})_{18}]^{-}$  to a continuous flow of  $\text{O}_2$  in DCM. In (ii), mass spectra are enlarged to show the region corresponding to the  $[\text{Au}_{25}(\text{PET})_{18}(\text{O}_2)_n]^{-}$  species. (B) (i) Time-dependent ESI MS spectra beyond 90 min in the presence of  $\text{O}_2$ . In (ii), mass spectra are expanded to show the region corresponding to the  $[\text{Au}_{25}(\text{PET})_{18}(\text{O}_2)_n]^{-}$  species. Intensity of  $[\text{Au}_{25}(\text{PET})_{18}]^{-}$  is normalized. The intensity of the parent nanocluster also decreases in this time window.

$[\text{Au}_{25}(\text{PET})_{18}]^0$  in DCM is a strong evidence for the interaction of the nanocluster with molecular  $\text{O}_2$ . This interaction takes place when the nanocluster dissolved in DCM is exposed to air for several hours.<sup>24</sup> We were not able to detect the  $\text{O}_2$  adducts of the nanocluster in mass spectra in the case of aerial oxidation process. In our experiments, pure  $\text{O}_2$  was supplied continuously and therefore the oxidation occurs within  $\sim 45$  min. Hence, we presume that the adduct formation takes place significantly only when  $\text{O}_2$  is passed directly into the solution of the nanocluster and when a large amount of  $\text{O}_2$  is present in the solution.

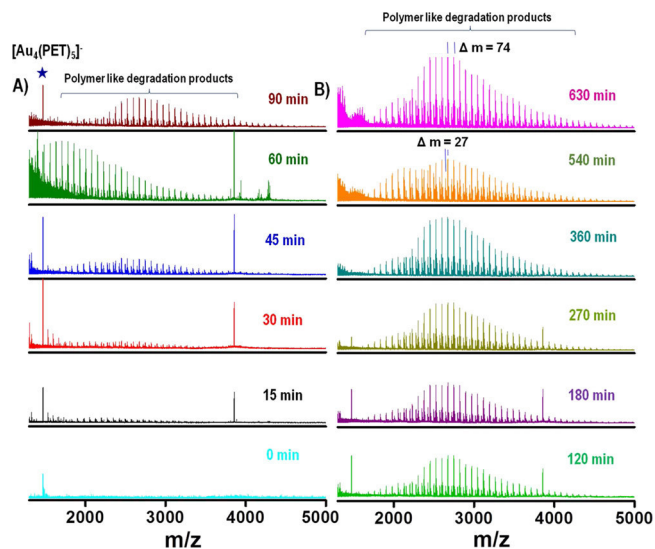
We did an experiment by taking cluster solution in DCM and bubbling  $\text{O}_2$  gas continuously through the solution, to check the effect of amount of  $\text{O}_2$  in the reaction mixture on  $\text{O}_2$  addition. The mass spectrum of the nanocluster after 540 min of continuous flow of  $\text{O}_2$  is shown in Figure 1 (blue trace). Up to three molecules of  $\text{O}_2$  were attached to the cluster in this case. This experiment proved that the amount of  $\text{O}_2$  present in solution has an effect on adduct formation. The match between the experimental and simulated mass spectra for  $[\text{Au}_{25}(\text{PET})_{18}(\text{O}_2)_2]^{-}$  and  $[\text{Au}_{25}(\text{PET})_{18}(\text{O}_2)_3]^{-}$  species is given in Figure S4. They are in good agreement with each other. The intensity of the peak corresponding to  $[\text{Au}_{25}(\text{PET})_{18}(\text{O}_2)]^{-}$  was the highest compared to other  $\text{O}_2$  adduct peaks. This could be due to the higher stability of the species compared to others. It is also possible that the different species react with each other in the reaction mixture and an equilibrium is established between them with time.

Time-dependent ESI MS measurements were done to check the variation of the relative abundance of different species in the reaction mixture with time. The spectra are presented in Figure 2. It could be noted that initially, that is, within 15 min,  $[\text{Au}_{25}(\text{PET})_{18}(\text{O}_2)]^{-}$  and  $[\text{Au}_{25}(\text{PET})_{18}(\text{O}_2)_2]^{-}$  were observed.  $[\text{Au}_{25}(\text{PET})_{18}(\text{O}_2)_3]^{-}$  started appearing in about 60 min of reaction and its intensity increased relatively with time up to 120 min, then started decreasing, and finally disappeared in the spectrum of 630 min. Thus, the reaction between the nanocluster and  $\text{O}_2$  is highly dynamic in nature.

There is a continuous formation and conversion of different species with different relative concentrations. This behavior

could be explained in two ways: either three  $\text{O}_2$  attachment to the nanocluster might be resulting in the decomposition of the nanocluster or different species in the reaction mixture might be interacting with each other to form other species. It is even possible that both these processes are occurring simultaneously.

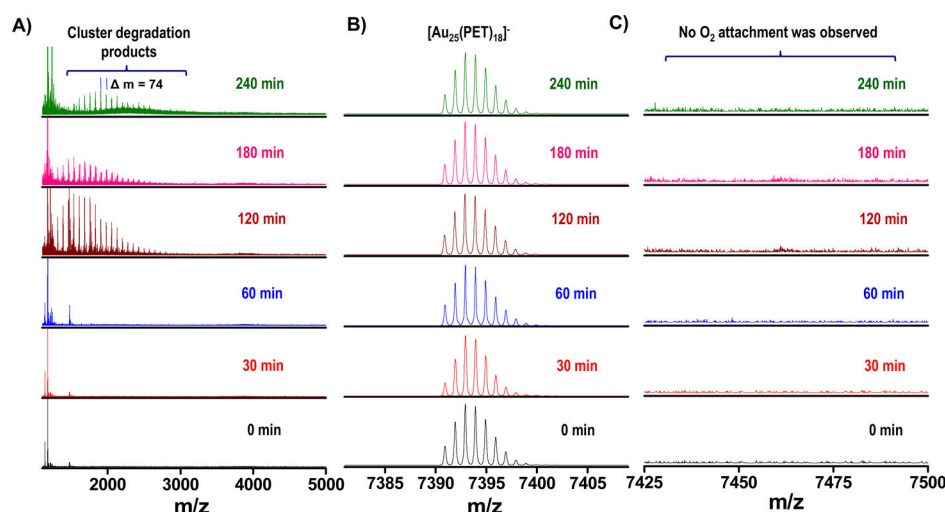
The lower mass regions of the time-dependent ESI MS data are shown in Figure 3. Decomposition of the cluster was



**Figure 3.** (A) Lower mass range ( $m/z = 1200\text{--}5000$ ) ESI MS spectra of  $[\text{Au}_{25}(\text{PET})_{18}]^{-}$  upon exposure to a continuous flow of  $\text{O}_2$ . (B) Data after 90 min. Peak highlighted with the asterisk corresponds to  $[\text{Au}_4(\text{PET})_5]^{-}$ , a commonly observed fragment in the mass spectrum of  $[\text{Au}_{25}(\text{PET})_{18}]^{-}$ .

observed because of the interaction with  $\text{O}_2$ . Initially, lower mass thiolates were formed which were shifted into higher mass with time. A common fragment of the cluster,  $[\text{Au}_4(\text{PET})_5]^{-}$ , was observed throughout. Apart from this, a series of peaks similar to polymer-like species were observed. These polymer-like thiolate peaks start at  $m/z = 1412.3$  and spacing between the consecutive peaks is 74. The isotopic





**Figure 4.** Time-dependent ESI MS spectra upon exposure of  $[\text{Au}_{25}(\text{PET})_{18}]^{-}$  to a continuous flow of  $\text{O}_2$  in toluene. Spectra in different regions are presented in (A–C). Intensity of  $[\text{Au}_{25}(\text{PET})_{18}]^{-}$  is normalized.

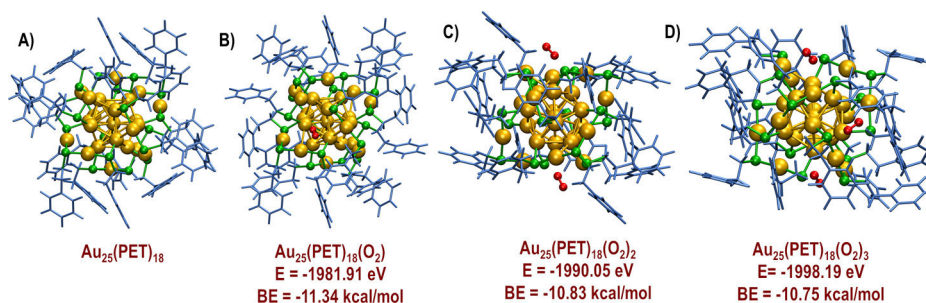
pattern indicates that these are singly charged species. All the peaks correspond to singly charged species, which implies that the leaving group is a neutral species with a mass of 74. The width of the peaks increases as we move from lower mass to higher mass. There is another set of peaks, which is at a constant spacing of 27 units from the previous set of peaks. The spacing between consequent peaks in this series too is 74 units.

To check the effect of solvent on the interaction, we carried out the same reaction in toluene keeping all other conditions the same and the interaction was monitored using time-dependent UV/vis spectroscopy and ESI MS. Time-dependent UV/vis spectra of the nanocluster in toluene kept under a continuous flow of  $\text{O}_2$  are given in Figure S5A. No  $\text{O}_2$  adducts of the nanocluster were observed in time-dependent ESI MS spectra shown in Figure 4. Degradation of the nanocluster was observed but to a lesser extent compared to that in the case of DCM. In the case of THF, the nanocluster was unstable in the presence of  $\text{O}_2$  and degraded completely within 2 h. The time-dependent UV/vis absorption spectra are shown in Figure S5B. No  $\text{O}_2$  attached species were observed in time-dependent ESI MS spectra (shown in Figure S6) of the nanocluster in THF in the presence of  $\text{O}_2$ . The degradation of the nanocluster within 2 h was observed here too. The degradation products are composed of thiolates of smaller masses. No polymer-like thiolate peaks were observed in the mass spectra in the case of THF.

The solvent variation experiments show that the cluster is more stable in toluene in the presence of  $\text{O}_2$ . In DCM, oxidation of the nanocluster happens faster than in the case of toluene and it degrades into lower mass polymeric thiolates which grow to larger polymeric species with time. The peak corresponding to the nanocluster was also present up to 6 h in the time-dependent experiments. Thus, the solution consisted of a complex mixture composed of the nanocluster, its  $\text{O}_2$  adducts, and the nanocluster degradation products. Predicting the catalytic efficiency of the nanocluster and catalytically active species involved is a difficult task in such scenarios. We note here that Dreier et al.<sup>29</sup> reported oxidative decomposition of  $[\text{Au}_{25}(\text{SR})_{18}]^{-}$  during styrene oxidation. They concluded that the Au(I) species resulting from the oxidative decomposition of the cluster are the catalytically active species in the

styrene oxidation reaction and not the nanocluster itself. The nanocluster is unstable in the case of THF in the presence of  $\text{O}_2$  and degraded within 2 h. Variation in the stability of the nanocluster in different solvents in the presence of  $\text{O}_2$  could be due to the difference in  $\text{O}_2$  solubility of the solvents. It could be noted that  $\text{O}_2$  solubility is the least in the case of toluene and the highest in the case of THF. In DCM,  $\text{O}_2$  has an intermediate solubility. Our experiments indicate that the difference in the solubility of  $\text{O}_2$  in these three solvents might affect the interaction of the nanocluster with  $\text{O}_2$ . We could detect the  $\text{O}_2$  adducts of the nanocluster only in DCM which has an intermediate value of  $\text{O}_2$  solubility. Thus, variation in the interaction of the nanocluster with  $\text{O}_2$  as well as difference in the stability of the nanocluster in different solvents could be the consequences of different  $\text{O}_2$  solubility of the solvents. Hence, in cluster catalysis, choice of the solvent or reaction medium also plays an important role.

To check the interaction of other commonly used gases such as  $\text{CO}_2$ ,  $\text{N}_2$ , and Ar with the cluster, we did similar experiments by keeping the  $[\text{Au}_{25}(\text{PET})_{18}]^{-}$  solution in DCM in the environments of these gases using respective gas-filled balloons. The time-dependent UV/vis spectra of  $[\text{Au}_{25}(\text{PET})_{18}]^{-}$  in DCM in the presence of  $\text{CO}_2$ ,  $\text{N}_2$ , and Ar are shown in Figure S7.  $\text{CO}_2$  and  $\text{N}_2$  caused gradual oxidation of the  $[\text{Au}_{25}(\text{PET})_{18}]^{-}$ , but in the Ar environment, the nanocluster was unchanged and was stable. The ESI MS spectra of the nanocluster before and after keeping in the respective gas environments are shown in Figure S8. In the case of  $\text{CO}_2$ , the intensity of the nanocluster peak was reduced drastically within 10 min and it disappeared within 15–20 min (note that the intensity of the peak corresponding to the nanocluster is normalized in Figure S8). However, the nanocluster features were intact up to 4 h in time-dependent UV/vis absorption spectra of it kept under a  $\text{CO}_2$  environment. Therefore, the disappearance of the nanocluster peak in the mass spectrum could be due to the change in ionizability of the nanocluster upon exposure to  $\text{CO}_2$  and not because of the degradation of the nanocluster. In the cases of  $\text{N}_2$  and Ar, the nanocluster was intact and no variation in the mass spectrum was observed. However, no adduct species of the nanoclusters were observed in these cases in the mass spectra.



**Figure 5.** DFT-optimized structures of (A)  $[\text{Au}_{25}(\text{PET})_{18}]^-$ , (B)  $[\text{Au}_{25}(\text{PET})_{18}(\text{O}_2)]^-$ , (C)  $[\text{Au}_{25}(\text{PET})_{18}(\text{O}_2)_2]^-$ , and (D)  $[\text{Au}_{25}(\text{PET})_{18}(\text{O}_2)_3]^-$  along with the energies of the structures and BEs. Color codes: golden yellow—Au, green—S, red—O, and blue stick models represent PET ligands.

To get an insight into the structure and nature of the bonding between the  $[\text{Au}_{25}(\text{PET})_{18}]^-$  and  $\text{O}_2$  molecules, DFT calculations were conducted. First, we determined the most favorable interaction sites for the first, second, and third  $\text{O}_2$  molecules with the cluster using molecular docking studies. The most favorable structure for each adduct given by molecular docking was then optimized using the DFT method. The DFT-optimized geometrical structures of  $[\text{Au}_{25}(\text{PET})_{18}(\text{O}_2)]^-$ ,  $[\text{Au}_{25}(\text{PET})_{18}(\text{O}_2)_2]^-$  and  $[\text{Au}_{25}(\text{PET})_{18}(\text{O}_2)_3]^-$  are shown in Figures 5 and S9. As  $[\text{Au}_{25}(\text{PET})_{18}]^-$  has a cavity-like structure on both sides formed by the ligands and the three staples around the  $C_3$  axis of the cluster,<sup>36</sup> it is possible for the  $\text{O}_2$  molecule to interact with Au atoms on the surface of the nanocluster. The interaction of  $\text{O}_2$  with Au atoms at the surface is a weak supramolecular one, involving electrostatic and van der Waals interactions with an average Au—O bond distance of 3.33 Å, and we also observed that there is a slight distortion at the base of the cavity formed by the three gold atoms on the surface of the icosahedral core because of the average contraction of Au—Au bond distance ( $\sim 0.02$  Å). Moreover, the  $\text{O}_2$  molecule was elongated slightly by the distance of 0.029 Å because of the interaction with Au atoms. The changes in the Au—S bonding interactions were found to be negligible. The calculated BE per  $\text{O}_2$  for the interaction of  $\text{O}_2$  with  $[\text{Au}_{25}(\text{PET})_{18}]^-$  is  $-11.34$  kcal/mol. The calculations for  $[\text{Au}_{25}(\text{PET})_{18}(\text{O}_2)]^-$  were also performed using vdW-DF2 functional including dispersion corrections to account for van der Waals forces. The bonding parameters obtained using PBE and vdW-DF2 functionals are compared in Table S1 (see Supporting Information). The structure of the molecule remained the same after including the dispersion corrections, and there were no significant differences in bonding parameters. We also noticed that the energy of the structure wherein the first  $\text{O}_2$  interacts with the PET ligand ( $-1981.85$  eV) is higher than the energy of structure B in Figure 5. This clearly confirms the interaction of  $\text{O}_2$  with the surface Au atoms of the nanocluster. The BE values of atomic and molecular oxygen on various surfaces of Au and bare clusters of Au obtained from the literature are listed in the Table S2, for comparison.

The most favorable interaction sites for the second  $\text{O}_2$  are at the cavities formed by the three gold atoms on the surface of the  $[\text{Au}_{25}(\text{PET})_{18}(\text{O}_2)]^-$  based on the molecular docking studies. The second  $\text{O}_2$  occupies the cavity on the opposite side of the first  $\text{O}_2$ . However, there is a distinct difference by 0.25 Å in the Au—O bond distance of the second  $\text{O}_2$  with the surface Au atoms of the nanocluster. The calculated BE per  $\text{O}_2$  for this case is  $-10.83$  kcal/mol, which is slightly lesser than

that of the one  $\text{O}_2$  attachment. Further addition of a  $\text{O}_2$  to give  $[\text{Au}_{25}(\text{PET})_{18}(\text{O}_2)_3]^-$  clearly showed that the interaction of the third  $\text{O}_2$  molecule was only with PET ligands. Introduction of three  $\text{O}_2$  significantly affected the interactions in the entire nanocluster. The bond lengths of three  $\text{O}_2$  molecules varied distinctly from 1.26 to 1.28 Å, and the largely elongated bond length of  $\text{O}_2$  was due to the interaction with the ligands. It is worth noting that the Au—O bond length for the  $\text{O}_2$  bound to the Au through the cavities (mentioned before) increases from 3.33 Å in  $[\text{Au}_{25}(\text{PET})_{18}(\text{O}_2)]^-$  to 3.48 Å in  $[\text{Au}_{25}(\text{PET})_{18}(\text{O}_2)_4]^-$  (DFT-optimized structure is given in Figure S10 in Supporting Information). This suggested that the addition of more than three  $\text{O}_2$  weakened the interactions of  $\text{O}_2$  at the cavities. The calculated BE per  $\text{O}_2$  for the case of three  $\text{O}_2$  attachments was  $-10.75$  kcal/mol. We also conducted an additional study, which showed that the addition of more number of  $\text{O}_2$  molecules in various positions to the cluster such as under the staples and above the core penetrating  $\text{O}_2$  into the cluster could cause larger changes in Au—S and Au—Au network and if these larger number of  $\text{O}_2$  molecules get under the cavity-like structure formed by Au atoms and ligands, then the cluster may distort and degrade fully.

#### 4. CONCLUSIONS

In conclusion, the interaction of  $[\text{Au}_{25}(\text{PET})_{18}]^-$  with  $\text{O}_2$  was investigated in detail using UV/vis absorption spectroscopy and ESI MS. Direct evidence for the attachment of  $\text{O}_2$  with the nanocluster was observed in the mass spectra for the first time. Up to three  $\text{O}_2$  molecules can attach to a  $[\text{Au}_{25}(\text{PET})_{18}]^-$ . It was also observed that  $\text{O}_2$  attachment causes decomposition of the nanocluster. The effect of solvents on the interaction was examined by conducting the experiments in different solvents, such as DCM, toluene, and THF. We observed the  $\text{O}_2$  adducts of the nanocluster only in the case of DCM. It was noted that the nanocluster is most stable in toluene in the presence of  $\text{O}_2$  and least stable in the case of THF. The  $\text{O}_2$  solubility of the solvent was proposed to be a deciding factor here. DFT calculations were carried out to understand the nature of bonding between the nanocluster and  $\text{O}_2$ . The first and the second  $\text{O}_2$  interact with the nanocluster by attaching to the surface Au atoms through the cavities present in the nanocluster formed by Au and ligands. The interaction of the third  $\text{O}_2$  was found to be with the PET ligands. The average BE was highest for the first  $\text{O}_2$  attachment and decreased with further  $\text{O}_2$  additions.

## ■ ASSOCIATED CONTENT

## ■ Supporting Information

The Supporting Information is available free of charge on the ACS Publications website at DOI: 10.1021/acs.jpcc.8b03220.

Characterization of  $[\text{Au}_{25}(\text{PET})_{18}]^-$ ; monitoring stability of cluster in continuous flow of  $\text{O}_2$  by time-dependent UV/vis absorption spectroscopy; comparison of UV/vis spectra of air-oxidized and  $\text{O}_2$ -treated  $[\text{Au}_{25}(\text{PET})_{18}]^-$ ; effect of solvent on the interaction of  $[\text{Au}_{25}(\text{PET})_{18}]^-$  cluster with  $\text{O}_2$ ; interaction of  $[\text{Au}_{25}(\text{PET})_{18}]^-$  with other common gases such as  $\text{CO}_2$ ,  $\text{N}_2$ , and Ar; structures of higher energy isomers; comparison of bonding parameters of  $[\text{Au}_{25}(\text{PET})_{18}(\text{O}_2)]^-$  obtained using PBE and vdW-DF2 functionals; binding energy of  $\text{O}_2$  on various surfaces of Au and bare clusters of Au from the literature; DFT-optimized structures of higher energy isomers of  $[\text{Au}_{25}(\text{PET})_{18}(\text{O}_2)]^-$ ; and Cartesian coordinates for DFT-optimized structures (PDF)

## ■ AUTHOR INFORMATION

## Corresponding Author

\*E-mail: pradeep@iitm.ac.in.

## ORCID

Thalappil Pradeep: 0000-0003-3174-534X

## Notes

The authors declare no competing financial interest.

## ■ ACKNOWLEDGMENTS

S.B. thanks IIT Madras for her senior research fellowship. The authors thank the Department of Science and Technology, Government of India for constant support for their research program.

## ■ REFERENCES

- (1) Daté, M.; Imai, H.; Tsubota, S.; Haruta, M. In situ Measurements Under Flow Condition of the CO Oxidation Over Supported Gold Nanoparticles. *Catal. Today* **2007**, *122*, 222–225.
- (2) Haruta, M. Size- and Support-Dependency in the Catalysis of Gold. *Catal. Today* **1997**, *36*, 153–166.
- (3) Haruta, M.; Kobayashi, T.; Sano, H.; Yamada, N. Novel Gold Catalysts for the Oxidation of Carbon Monoxide at a Temperature far Below 0 °C. *Chem. Lett.* **1987**, *16*, 405–408.
- (4) Haruta, M. When Gold is not Noble: Catalysis by Nanoparticles. *Chem. Rev.* **2003**, *3*, 75–87.
- (5) Hashmi, A. S. K.; Hutchings, G. J. Gold Catalysis. *Angew. Chem., Int. Ed.* **2006**, *45*, 7896–7936.
- (6) Hutchings, G. J.; Brust, M.; Schmidbaur, H. Gold-an introductory perspective. *Chem. Soc. Rev.* **2008**, *37*, 1759–1765.
- (7) Zhu, Y.; Qian, H.; Jin, R. Catalysis Opportunities of Atomically Precise Gold Nanoclusters. *J. Mater. Chem.* **2011**, *21*, 6793–6799.
- (8) Li, G.; Jin, R. Atomically Precise Gold Nanoclusters as New Model Catalysts. *Acc. Chem. Res.* **2013**, *46*, 1749–1758.
- (9) Yamazoe, S.; Koyasu, K.; Tsukuda, T. Nonscalable Oxidation Catalysis of Gold Clusters. *Acc. Chem. Res.* **2014**, *47*, 816–824.
- (10) Luo, Z.; Nachammai, V.; Zhang, B.; Yan, N.; Leong, D. T.; Jiang, D.-e.; Xie, J. Toward Understanding the Growth Mechanism: Tracing All Stable Intermediate Species from Reduction of Au(I)-Thiolate Complexes to Evolution of  $\text{Au}_{25}$  Nanoclusters. *J. Am. Chem. Soc.* **2014**, *136*, 10577–10580.
- (11) Yao, Q.; Yuan, X.; Fung, V.; Yu, Y.; Leong, D. T.; Jiang, D.-e.; Xie, J. Understanding Seed-mediated Growth of Gold Nanoclusters at Molecular Level. *Nat. Commun.* **2017**, *8*, 927.
- (12) Fernando, A.; Weerawardene, K. L. D. M.; Karimova, N. V.; Aikens, C. M. Quantum Mechanical Studies of Large Metal, Metal Oxide, and Metal Chalcogenide Nanoparticles and Clusters. *Chem. Rev.* **2015**, *115*, 6112–6216.
- (13) Weerawardene, K. L. D. M.; Häkkinen, H.; Aikens, C. M. Connections Between Theory and Experiment for Gold and Silver Nanoclusters. *Annu. Rev. Phys. Chem.* **2018**, *69*, 205–229.
- (14) Zhang, G.; Wang, R.; Li, G. Non-metallic Gold Nanoclusters for Oxygen Activation and Aerobic Oxidation. *Chin. Chem. Lett.* **2018**, *29*, 687–693.
- (15) Zhu, M.; Lanni, E.; Garg, N.; Bier, M. E.; Jin, R. Kinetically Controlled, High-Yield Synthesis of  $\text{Au}_{25}$  Clusters. *J. Am. Chem. Soc.* **2008**, *130*, 1138–1139.
- (16) Dainese, T.; Antonello, S.; Gascón, J. A.; Pan, F.; Perera, N. V.; Ruzzi, M.; Venzo, A.; Zoleo, A.; Rissanen, K.; Maran, F.  $\text{Au}_{25}(\text{SET})_{18}$ , a Nearly Naked Thiolate-Protected  $\text{Au}_{25}$  Cluster: Structural Analysis by Single Crystal X-ray Crystallography and Electron Nuclear Double Resonance. *ACS Nano* **2014**, *8*, 3904–3912.
- (17) Zhu, M.; Aikens, C. M.; Hollander, F. J.; Schatz, G. C.; Jin, R. Correlating the Crystal Structure of A Thiol-Protected  $\text{Au}_{25}$  Cluster and Optical Properties. *J. Am. Chem. Soc.* **2008**, *130*, 5883–5885.
- (18) Kawasaki, H.; Kumar, S.; Li, G.; Zeng, C.; Kauffman, D. R.; Yoshimoto, J.; Iwasaki, Y.; Jin, R. Generation of Singlet Oxygen by Photoexcited  $\text{Au}_{25}(\text{SR})_{18}$  Clusters. *Chem. Mater.* **2014**, *26*, 2777–2788.
- (19) Chong, H.; Li, P.; Wang, S.; Fu, F.; Xiang, J.; Zhu, M.; Li, Y.  $\text{Au}_{25}$  Clusters as Electron-Transfer Catalysts Induced the Intramolecular Cascade Reaction of 2-nitrobenzonitrile. *Sci. Rep.* **2013**, *3*, 3214.
- (20) Kang, X.; Chong, H.; Zhu, M.  $\text{Au}_{25}(\text{SR})_{18}$ : the captain of the great nanocluster ship. *Nanoscale* **2018**, *10*, 10758–10834.
- (21) Parker, J. F.; Fields-Zinna, C. A.; Murray, R. W. The Story of a Monodisperse Gold Nanoparticle:  $\text{Au}_{25}\text{L}_{18}$ . *Acc. Chem. Res.* **2010**, *43*, 1289–1296.
- (22) Chakraborty, I.; Pradeep, T. Atomically Precise Clusters of Noble Metals: Emerging Link between Atoms and Nanoparticles. *Chem. Rev.* **2017**, *117*, 8208–8271.
- (23) Liu, Y.; Tsunoyama, H.; Akita, T.; Xie, S.; Tsukuda, T. Aerobic Oxidation of Cyclohexane Catalyzed by Size-Controlled Au Clusters on Hydroxyapatite: Size Effect in the Sub-2 nm Regime. *ACS Catal.* **2011**, *1*, 2–6.
- (24) Zhu, M.; Eckenhoff, W. T.; Pintauer, T.; Jin, R. Conversion of Anionic  $[\text{Au}_{25}(\text{SCH}_2\text{CH}_2\text{Ph})_{18}]^-$  Cluster to Charge Neutral Cluster via Air Oxidation. *J. Phys. Chem. C* **2008**, *112*, 14221–14224.
- (25) Lopez-Acevedo, O.; Kacprzak, K. A.; Akola, J.; Häkkinen, H. Quantum Size Effects in Ambient CO Oxidation Catalysed by Ligand-Protected Gold Clusters. *Nat. Chem.* **2010**, *2*, 329–334.
- (26) Nie, X.; Qian, H.; Ge, Q.; Xu, H.; Jin, R. CO Oxidation Catalyzed by Oxide-Supported  $\text{Au}_{25}(\text{SR})_{18}$  Nanoclusters and Identification of Perimeter Sites as Active Centers. *ACS Nano* **2012**, *6*, 6014–6022.
- (27) Zhu, Y.; Qian, H.; Zhu, M.; Jin, R. Thiolate-Protected  $\text{Au}_n$  Nanoclusters as Catalysts for Selective Oxidation and Hydrogenation Processes. *Adv. Mater.* **2010**, *22*, 1915–1920.
- (28) Xie, S.; Tsunoyama, H.; Kurashige, W.; Negishi, Y.; Tsukuda, T. Enhancement in Aerobic Alcohol Oxidation Catalysis of  $\text{Au}_{25}$  Clusters by Single Pd Atom Doping. *ACS Catal.* **2012**, *2*, 1519–1523.
- (29) Dreier, T. A.; Andrea Wong, O.; Ackerson, C. J. Oxidative decomposition of  $\text{Au}_{25}(\text{SR})_{18}$  clusters in a catalytic context. *Chem. Commun.* **2015**, *51*, 1240–1243.
- (30) Wu, Z.; Suhan, J.; Jin, R. One-pot synthesis of atomically monodisperse, thiol-functionalized  $\text{Au}_{25}$  nanoclusters. *J. Mater. Chem.* **2009**, *19*, 622–626.
- (31) Mortensen, J. J.; Hansen, L. B.; Jacobsen, K. W. Real-Space Grid Implementation of the Projector Augmented Wave Method. *Phys. Rev. B: Condens. Matter Mater. Phys.* **2005**, *71*, 035109.
- (32) Enkovaara, J.; Rostgaard, C.; Mortensen, J. J.; Chen, J.; Dulak, M.; Ferrighi, L.; Gavnholt, J.; Glinsvad, C.; Haikola, V.; Hansen, H. A.; et al. Electronic Structure Calculations with GPAW: A Real-Space



Implementation of the Projector Augmented-Wave Method. *J. Phys.: Condens. Matter* **2010**, *22*, 253202.

(33) Perdew, J. P.; Burke, K.; Ernzerhof, M. Generalized Gradient Approximation Made Simple [Phys. Rev. Lett. *77*, 3865 (1996)]. *Phys. Rev. Lett.* **1997**, *78*, 1396.

(34) Larsen, A. H.; Vanin, M.; Mortensen, J. J.; Thygesen, K. S.; Jacobsen, K. W. Localized Atomic Basis Set in the Projector Augmented Wave Method. **2013**, arXiv:1303.0348v1 [cond-mat.mtrl-sci]. arXiv.org e-Print Arch., Condens. Matter, 1-11.

(35) Humphrey, W.; Dalke, A.; Schulten, K. VMD: Visual Molecular Dynamics. *J. Mol. Graphics* **1996**, *14*, 33–38.

(36) Natarajan, G.; Mathew, A.; Negishi, Y.; Whetten, R. L.; Pradeep, T. A Unified Framework for Understanding the Structure and Modifications of Atomically Precise Monolayer Protected Gold Clusters. *J. Phys. Chem. C* **2015**, *119*, 27768–27785.

## Supporting information for the paper:

### Detection of $[\text{Au}_{25}(\text{PET})_{18}(\text{O}_2)_n]^-$ ( $n=1,2,3$ ) Species by Mass Spectrometry

Shridevi Bhat,<sup>a</sup> Raghu Pradeep Narayanan,<sup>a</sup> Ananya Bakshi,<sup>a</sup> Papri Chakraborty,<sup>a</sup>  
Ganesan Paramasivam,<sup>a</sup> Rabin Rajan J. Methikkalam,<sup>a</sup> Abhijit Nag,<sup>a</sup> Ganapati  
Natarajan, and Thalappil Pradeep<sup>\*a</sup>

<sup>a</sup>*DST Unit of Nanoscience (DST UNS) and Thematic Unit of Excellence,  
Department of Chemistry, Indian Institute of Technology Madras,  
Chennai 600036, India.*

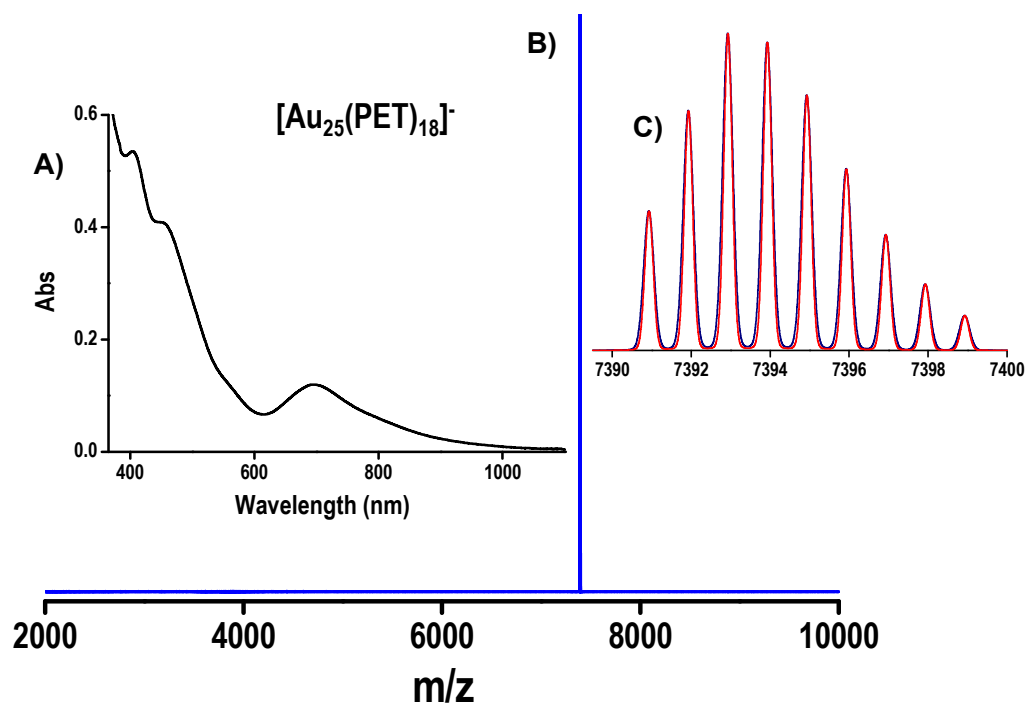
### Table of Contents

Name	Description	Page No.
Figure S1	Characterization of $[\text{Au}_{25}(\text{PET})_{18}]^-$	S3
Figure S2	Stability of $[\text{Au}_{25}(\text{PET})_{18}]^-$ kept in continuous flow of $\text{O}_2$ in DCM	S4
Figure S3	Comparison of UV/Vis spectra of air oxidized and $\text{O}_2$ treated $\text{Au}_{25}(\text{PET})_{18}$	S5
Figure S4	Experimental and simulated mass spectra for $[\text{Au}_{25}(\text{PET})_{18}(\text{O}_2)_2]^-$ and $[\text{Au}_{25}(\text{PET})_{18}(\text{O}_2)_3]^-$	S6
Figure S5	Stability of $[\text{Au}_{25}(\text{PET})_{18}]^-$ in continuous flow of $\text{O}_2$ in toluene and THF	S7
Figure S6	Time-dependent ESI MS of $[\text{Au}_{25}(\text{PET})_{18}]^-$ kept in continuous flow of $\text{O}_2$ in THF	S8
Figure S7	Stability of $[\text{Au}_{25}(\text{PET})_{18}]^-$ in presence of various gases	S9
Figure S8	ESI MS of $[\text{Au}_{25}(\text{PET})_{18}]^-$ in presence of various gases	S10
Figure S9	Structures of higher energy isomers of $[\text{Au}_{25}(\text{PET})_{18}(\text{O}_2)]^-$	S11
Table S1	Comparison of bonding parameters of $[\text{Au}_{25}(\text{PET})_{18}(\text{O}_2)]^-$ obtained using PBE functional and vdW-DF2 functional	S12
Table S2	Binding energy of $\text{O}_2$ on various surfaces of Au and bare clusters of	S13

	Au from literature	
Figure S10	DFT optimized structure of $[\text{Au}_{25}(\text{PET})_{18}(\text{O}_2)_4]^-$	S14
SI 13	Cartesian coordinates for DFT optimized structures	S15

## Supporting information 1

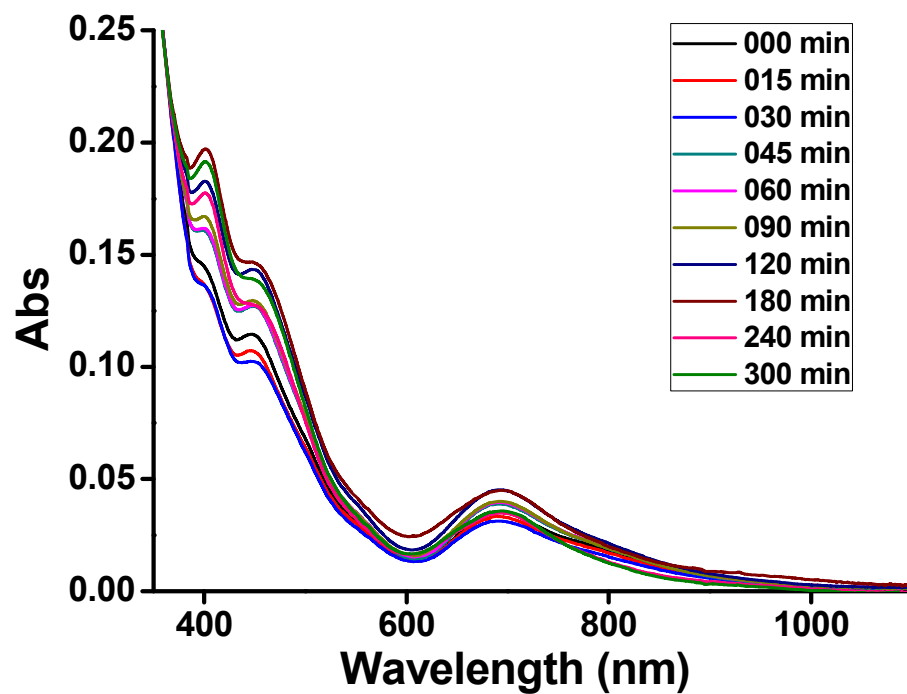
### Characterization of $[\text{Au}_{25}(\text{PET})_{18}]^-$ :



**Figure S1.** A) UV/Vis absorption spectrum and B) ESI MS of  $[\text{Au}_{25}(\text{PET})_{18}]^-$ . C) Experimental (blue trace) and simulated (red trace) mass spectra of  $[\text{Au}_{25}(\text{PET})_{18}]^-$ .

## Supporting information 2

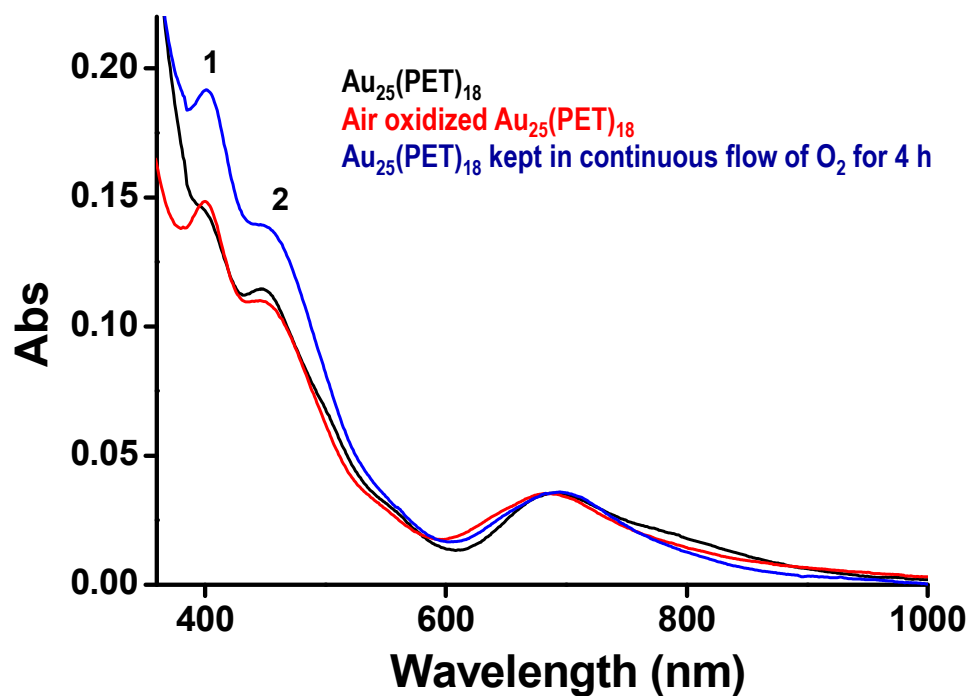
Stability of  $[\text{Au}_{25}(\text{PET})_{18}]^-$  kept in continuous flow of  $\text{O}_2$  in DCM:



**Figure S2.** Time – dependent UV/Vis absorption spectra of  $[\text{Au}_{25}(\text{PET})_{18}]^-$  kept under continuous flow of  $\text{O}_2$  in DCM.

### Supporting Information 3

#### Comparison of UV/Vis spectra of air oxidized and O<sub>2</sub> treated Au<sub>25</sub>(PET)<sub>18</sub>:

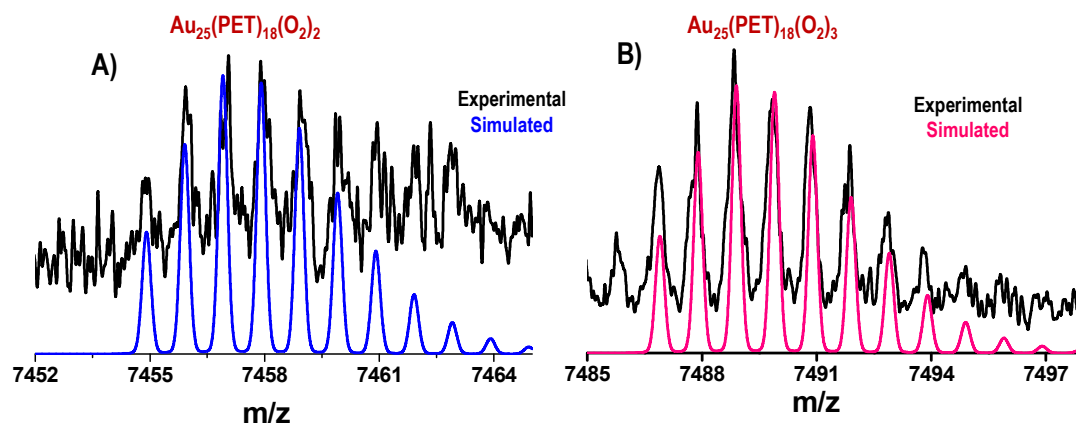


**Figure S3.** Comparison of UV/Vis absorption spectra for [Au<sub>25</sub>(PET)<sub>18</sub>]<sup>-</sup> (black trace), air oxidized nanocluster, i.e. [Au<sub>25</sub>(PET)<sub>18</sub>]<sup>0</sup> (red trace) and the same under continuous flow of O<sub>2</sub> for 4 h. The spectra are normalized at 680 nm. Peaks 1 and 2 are 400 and 450 nm absorption features of the cluster.



## Supporting Information 4

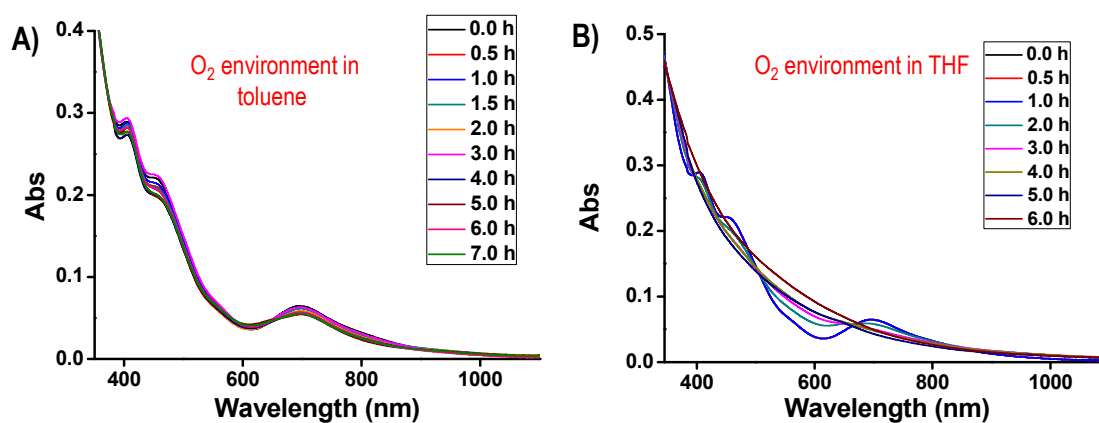
Experimental and simulated mass spectra for  $[\text{Au}_{25}(\text{PET})_{18}(\text{O}_2)_2]^-$  and  $[\text{Au}_{25}(\text{PET})_{18}(\text{O}_2)_3]^-$ :



**Figure S4.** A) Experimental and simulated mass spectra of  $[\text{Au}_{25}(\text{PET})_{18}(\text{O}_2)_2]^-$  and B)  $[\text{Au}_{25}(\text{PET})_{18}(\text{O}_2)_3]^-$ .

## Supporting Information 5

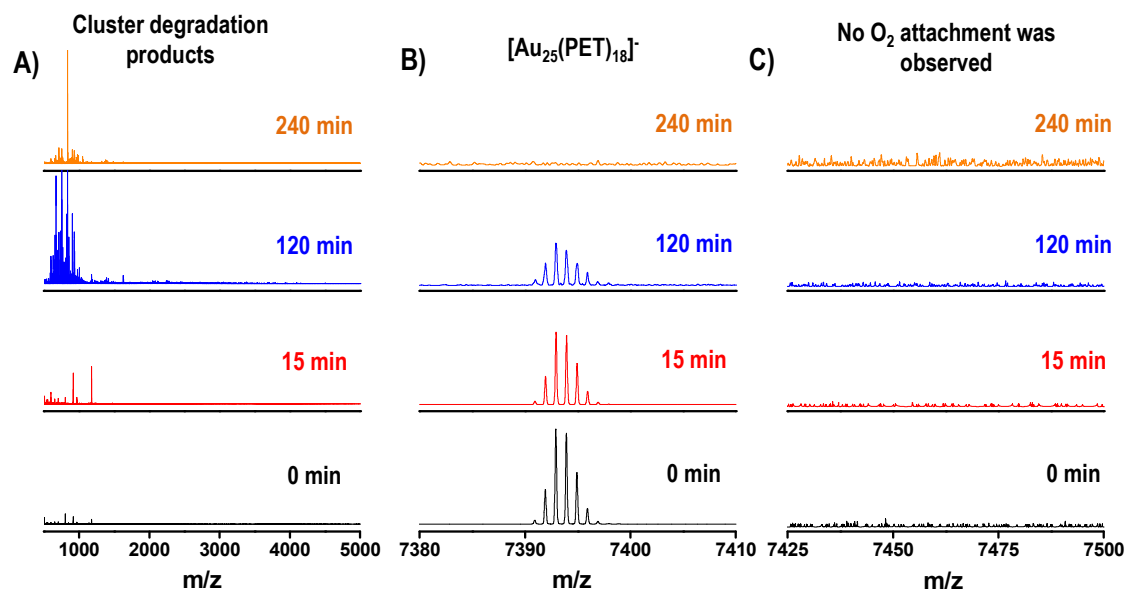
### Stability of $[\text{Au}_{25}(\text{PET})_{18}]^-$ in continuous flow of $\text{O}_2$ in toluene and THF:



**Figure S5.** A) Time – dependent UV/Vis absorption spectra of  $[\text{Au}_{25}(\text{PET})_{18}]^-$  kept under continuous flow of  $\text{O}_2$  in toluene and B) in THF.

## Supporting Information 6

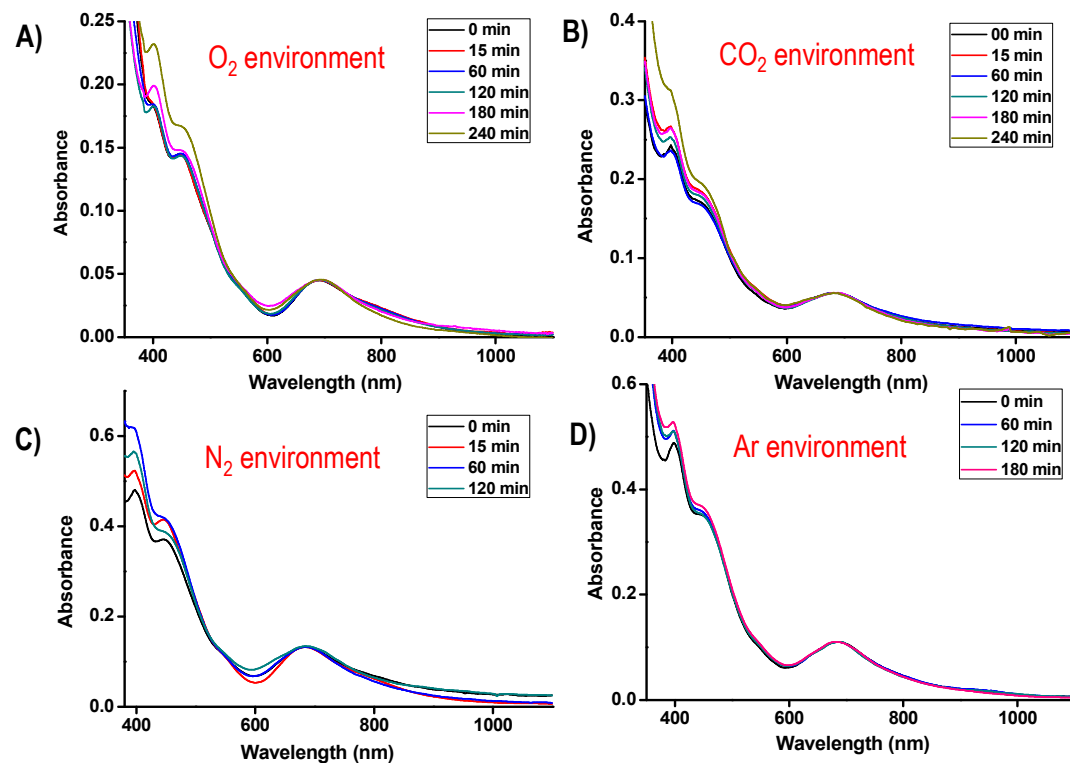
**Time-dependent ESI MS of  $[\text{Au}_{25}(\text{PET})_{18}]^-$  kept in continuous flow of  $\text{O}_2$  in THF:**



**Figure S6.** Time-dependent ESI MS upon exposure of  $[\text{Au}_{25}(\text{PET})_{18}]^-$  to a continuous flow of  $\text{O}_2$  in THF. Spectra in different mass range are presented in A), B) and C).

## Supporting Information 7

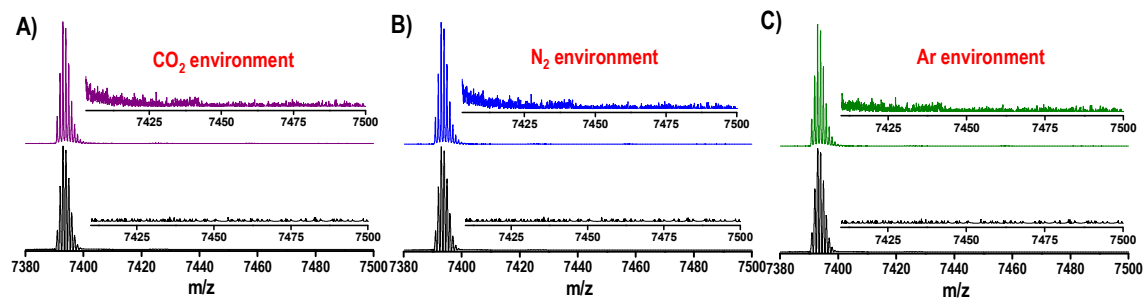
### Stability of $[\text{Au}_{25}(\text{PET})_{18}]^-$ in presence of various gases:



**Figure S7.** A) Time-dependent UV/Vis absorption spectra of  $[\text{Au}_{25}(\text{PET})_{18}]^-$  kept in  $\text{O}_2$  environment, B) in  $\text{CO}_2$  environment, C) in  $\text{N}_2$  environment, and D) in Ar environment.

## Supporting Information 8

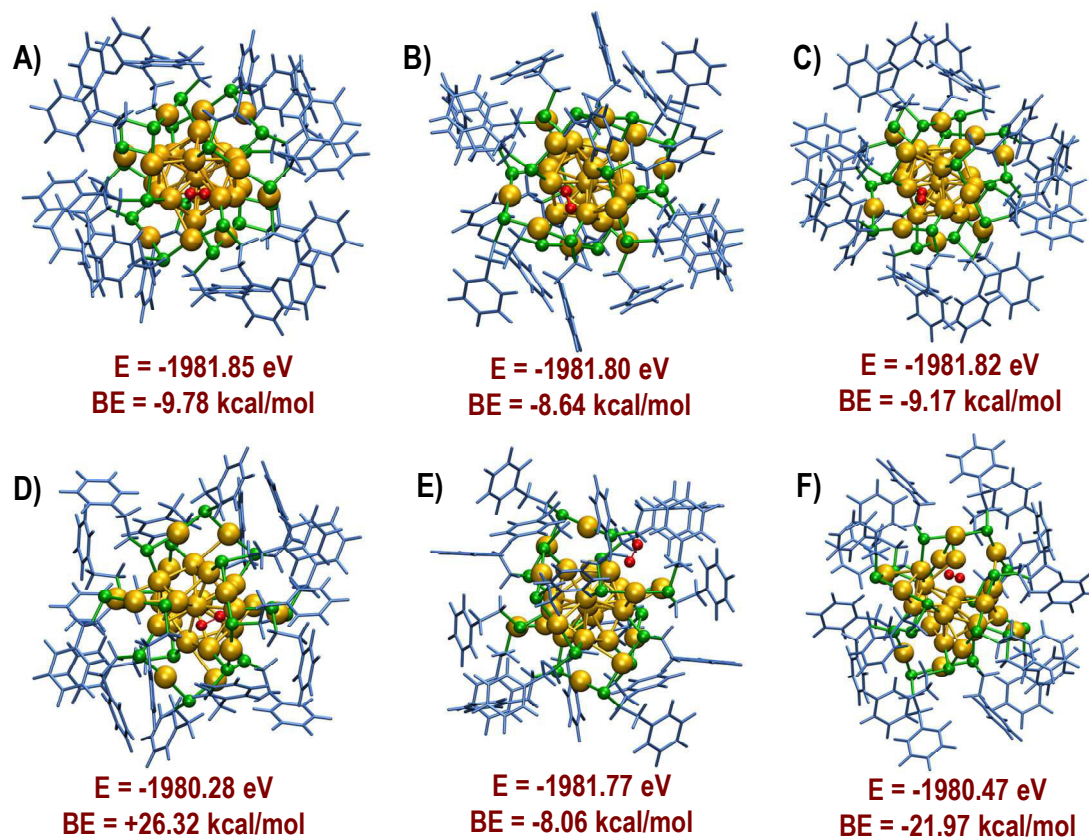
### ESI MS of $[\text{Au}_{25}(\text{PET})_{18}]^-$ in presence of various gases:



**Figure S8.** A) ESI MS of  $[\text{Au}_{25}(\text{PET})_{18}]^-$  before and after keeping in  $\text{CO}_2$  environment. B) ESI MS of  $[\text{Au}_{25}(\text{PET})_{18}]^-$  before and after keeping in  $\text{N}_2$  environment. C) ESI MS of  $[\text{Au}_{25}(\text{PET})_{18}]^-$  before and after keeping in Ar environment. The intensities of the parent clusters are normalised. We did not observe the adduct species in these cases.

## Supporting Information 9

### Structures of higher energy isomers of $[\text{Au}_{25}(\text{PET})_{18}(\text{O}_2)]^-$ :



**Figure S9.** DFT optimized structures of certain higher energy isomers of  $[\text{Au}_{25}(\text{PET})_{18}(\text{O}_2)]^-$  species along with their energies and binding energies. Color codes: Golden yellow – Au, Green – S, Red – O and Blue stick models represent PET ligands.



## Supporting Information 10

### Comparison of bonding parameters of $[\text{Au}_{25}(\text{PET})_{18}(\text{O}_2)]^-$ obtained using PBE functional and vdW-DF2 functional:

**Table S1.** Bonding parameters of  $[\text{Au}_{25}(\text{PET})_{18}(\text{O}_2)]^-$  obtained using PBE functional (without dispersion corrections) and vdW-DF2 functional (with dispersion corrections).

Bond	Bond distance (Å) using PBE functional	Bond distance (Å) vdW-DF2 functional
O – O	1.27	1.30
Au – O (core)	3.57	3.37
Au – O (staple)	3.33	3.38
Au – Au	2.87	2.97
Au – S (core)	2.44	2.54
Au – S (staple)	2.37	2.43

## Supporting Information 11

### Binding energy of O<sub>2</sub> on various surfaces of Au and bare clusters of Au from literature:

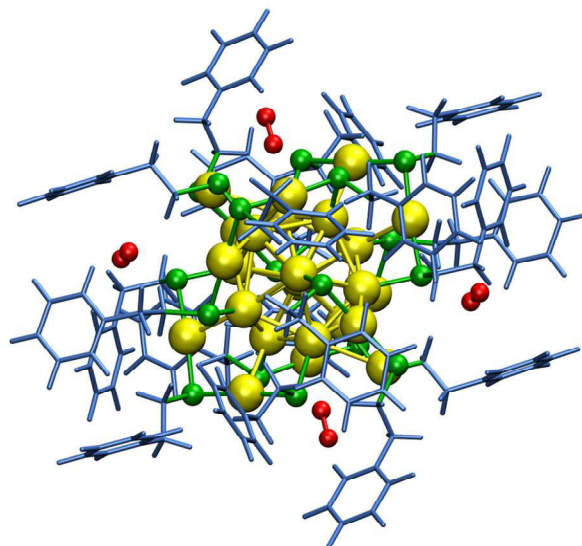
**Table S2.** Binding energy of O<sub>2</sub> on various surfaces of Au and bare clusters of Au, obtained from literature.

SI. No.	Experimental/theoretical	Au surface/cluster	Binding energy (kcal/mol)	Reference*
1	Experimental (TPD)/atomic oxygen <sup>±</sup>	Au (1 1 1)	-30 to -32 depending on coverage	1
2	Experimental (TPD)/atomic oxygen <sup>±</sup>	Au (2 1 1) step site/terrace site	-34/-33	2
3	Theoretical	10% stretched Au (1 1 1)	-1.9	3
4	Theoretical	Unstretched/10% stretched Au (2 1 1)	-3.5/-6	3
5	Theoretical	Au <sub>55</sub> cluster	-6.9/-13.1 depending on sites	4 <sup>†</sup>
6	Theoretical	Au <sub>25</sub> <sup>+</sup> , Au <sub>25</sub> <sup>0</sup> , Au <sub>25</sub> <sup>-</sup>	-13.4, -11.8, -31.6	5

\*References are given at the end. <sup>±</sup>TPD gives the dissociation energy which is equal in quantity and opposite in sign to binding energy. To avoid confusion, the TPD-derived binding energies are presented with a negative sign. <sup>†</sup> Authors use opposite sign convention in ref. 4. We have changed the sign to keep consistency with our convention. This makes it clear that all values correspond to bound oxygen.

## Supporting Information 12

DFT optimized structure of  $[\text{Au}_{25}(\text{PET})_{18}(\text{O}_2)_4]^-$ :



$[\text{Au}_{25}(\text{PET})_{18}(\text{O}_2)_4]$   
 $E = -2006.37 \text{ eV}$   
 $\text{BE} = -10.90 \text{ kcal/mol}$

**Figure S10.** DFT optimized structures of  $[\text{Au}_{25}(\text{PET})_{18}(\text{O}_2)_4]^-$ .

## Supporting information 13

### Cartesian coordinates for DFT optimized structures:

#### [Au<sub>25</sub>(PET)<sub>18</sub>O<sub>2</sub>]<sup>-</sup> cluster:

Au 15.54538 18.81844 15.48189

Au 12.71730 19.70230 17.01116

Au 11.95114 16.70619 18.92236

Au 14.20123 14.51823 17.63883

Au 14.99400 16.68663 13.39163

Au 16.43253 19.68019 12.54700

Au 18.16423 20.61777 15.61596

Au 17.69625 17.83797 17.37439

Au 13.23671 16.78695 15.89420

Au 12.02516 15.84900 12.84438

Au 14.93072 14.17526 11.42720

Au 17.17697 14.57884 13.87690

Au 16.46700 13.26345 16.53739

Au 19.28962 12.35596 14.96917

Au 20.01383 15.30853 12.99681

Au 17.78139 17.54752 14.35358

Au 16.98176 15.39446 18.61580

Au 15.59946 12.44579 19.45909

Au 13.83915 11.49743 16.35521

Au 14.27931 14.24623 14.61216

Au 18.74186 15.28503 16.09649

Au 19.96997 16.24198 19.08994

Au 17.05082 17.88679 20.54336

Au 14.79639 17.46569 18.13878

Au 15.98996 16.03501 16.00164

S 13.88870 20.58609 15.15860

S 11.44888 19.01684 18.87802

S 12.20826 14.35638 19.02059

S 17.59781 21.49437 13.50091

S 18.88429 19.93769 17.76266

S 15.09863 18.09357 11.40850

S 11.05146 16.68367 14.81878

S 12.77997 14.93888 10.80320

S 17.09443 13.30632 11.79204

S 18.12479 11.48776 16.83295

S 20.55126 13.01407 13.08814

S 19.70925 17.64824 12.85800

S 14.42250 10.65019 18.48127

S 13.13251 12.13650 14.18268

S 16.94977 14.01284 20.61363

S 20.94411 15.38648 17.12008

S 19.22485 17.16028 21.12981

S 14.87689 18.74536 20.21995

C 14.59117 22.19169 15.75064

H 15.00443 22.05795 16.77432

H 15.44403 22.41486 15.06740

C 13.57415 23.34966 15.70662

H 13.17851 23.45174 14.66800

H 14.14061 24.28690 15.93572

C 12.41589 23.21825 16.67766

C 12.60546 23.44888 18.06130

H 13.60454 23.74596 18.43883

C 11.53754 23.31026 18.96642



H 11.70921 23.49129 20.04598

C 10.25425 22.95802 18.50112

H 9.41215 22.86185 19.21511

C 10.04990 22.73625 17.12498

H 9.04744 22.46815 16.73609

C 11.12715 22.85585 16.22487

H 10.95897 22.66589 15.14562

C 9.73388 19.02882 18.18387

H 9.56739 20.04451 17.75647

H 9.67570 18.28807 17.35558

C 8.68467 18.70543 19.26218

H 8.95964 17.74033 19.75217

H 8.70893 19.49271 20.05159

C 7.30686 18.60990 18.63553

C 6.45837 19.73746 18.54757

H 6.78223 20.69521 19.00287

C 5.21626 19.65869 17.88843

H 4.56043 20.55060 17.84378

C 4.80715 18.44990 17.29093

H 3.83735 18.38850 16.76071

C 5.64026 17.31600 17.37706

H 5.33079 16.35374 16.92328

C 6.87382 17.39780 18.04814

H 7.51597 16.49739 18.12150

C 10.86658 13.83682 17.87237

H 11.00793 14.35102 16.89529

H 10.97933 12.73722 17.71328

C 9.49211 14.16870 18.48052

H 9.43979 13.76071 19.51759

H 9.43463 15.28290 18.57102

C 8.33206 13.63294 17.66459

C 7.47983 12.63492 18.19312

H 7.66436 12.25463 19.21907

C 6.41255 12.11672 17.43396

H 5.75645 11.33716 17.86729

C 6.18258 12.58661 16.12658

H 5.34941 12.17350 15.52599

C 7.02297 13.58269 15.58867

H 6.84817 13.96180 14.56254

C 8.08537 14.10504 16.35102

H 8.74120 14.89007 15.91810

C 19.22935 21.43253 12.64038

H 19.87292 22.20076 13.12662

H 19.67402 20.43015 12.82162

C 19.09636 21.67526 11.12790

H 18.63538 22.67355 10.94037

H 18.39884 20.90716 10.71121

C 20.45469 21.58936 10.45586

C 21.15772 22.75720 10.08259

H 20.68668 23.74667 10.25227

C 22.43667 22.68016 9.49770

H 22.96725 23.60863 9.20776

C 23.03748 21.42546 9.27898

H 24.04108 21.35947 8.81488

C 22.34901 20.25192 9.65034

H 22.80983 19.26009 9.47309

C 21.07099 20.33308 10.23550

H 20.53847 19.40595 10.53549

C 20.68911 19.58693 17.53686

H 20.92639 18.76399 18.25468

H 20.85664 19.18425 16.51604

C 21.57843 20.81632 17.81734

H 21.32577 21.23291 18.82176

H 22.63142 20.44500 17.87381

C 21.50279 21.90801 16.76521

C 20.64134 23.01933 16.91885

H 20.02497 23.10298 17.83668

C 20.57557 24.02135 15.93055

H 19.90258 24.89000 16.06995

C 21.37214 23.93066 14.77243

H 21.33069 24.72380 14.00073

C 22.23527 22.82839 14.60837

H 22.87231 22.74726 13.70518

C 22.29842 21.82914 15.59739

H 22.99200 20.97504 15.46464

C 13.52316 19.05894 11.36014

H 12.72036 18.34831 11.05052

H 13.29154 19.43289 12.38372

C 13.67382 20.22781 10.36615

H 14.61963 20.76449 10.62584

H 13.81003 19.81900 9.33717

C 12.52274 21.21372 10.39310

C 11.39980 21.06653 9.54623

H 11.34788 20.19713 8.86012

C 10.36359 22.02006 9.54577

H 9.49880 21.89394 8.86486

C 10.43342 23.13957 10.39767

H 9.62976 23.90092 10.38238

C 11.53469 23.28564 11.26499

H 11.59727 24.15972 11.94291

C 12.56515 22.32765 11.26495

H 13.43675 22.44816 11.94029

C 10.55484 18.41920 14.43452

H 10.45372 18.92149 15.42439

H 11.38111 18.93513 13.89746

C 9.23088 18.48315 13.64694

H 9.43083 18.24493 12.57415

H 8.54115 17.69452 14.03016

C 8.56550 19.84044 13.79788

C 7.45034 19.99050 14.65451

H 7.04069 19.10459 15.18113

C 6.84926 21.24922 14.84860

H 5.97295 21.33422 15.51993

C 7.36157 22.38550 14.19417

H 6.89091 23.37669 14.34539

C 8.47490 22.24932 13.34080

H 8.88784 23.13291 12.81754

C 9.07074 20.98917 13.14309

H 9.94119 20.89975 12.46227

C 11.82825 13.34925 10.78417

H 12.07316 12.79312 11.71628

H 10.74725 13.62112 10.81405

C 12.14012 12.46578 9.56124

H 11.76430 12.95598 8.63189

H 13.24716 12.36485 9.46139

C 11.50938 11.09814 9.76204

C 12.28894 10.00574 10.20827

H 13.38340 10.12959 10.32170

C 11.69378 8.76907 10.52254

H 12.32905 7.93347 10.87634

C 10.30076 8.60378 10.39509

H 9.82599 7.63944 10.65882

C 9.51432 9.67573 9.92796

H 8.41973 9.55157 9.81260

C 10.11489 10.90828 9.61213

H 9.48703 11.74632 9.24737

C 16.77871 11.62569 12.48764

H 17.79016 11.18296 12.65080

H 16.28988 11.73643 13.48296

C 15.93392 10.75074 11.54678

H 14.90444 11.18539 11.52325

H 16.34471 10.81888 10.51162

C 15.89148 9.30007 11.99086



C 16.58153 8.30059 11.26583

H 17.14056 8.58648 10.35181

C 16.56718 6.95535 11.68478

H 17.11049 6.19039 11.09671

C 15.86239 6.58473 12.84640

H 15.84559 5.52743 13.17543

C 15.17308 7.57130 13.58107

H 14.61319 7.29476 14.49644

C 15.18518 8.91459 13.15792

H 14.62913 9.67803 13.74131

C 17.42859 9.87914 16.24816

H 17.00228 10.01485 15.23017

H 16.58675 9.64806 16.94289

C 18.45926 8.73324 16.28185

H 18.87315 8.64725 17.31541

H 17.89797 7.78806 16.07730

C 19.59776 8.86110 15.28611

C 19.38374 8.59900 13.91170

H 18.38139 8.27995 13.56114

C 20.43021 8.73556 12.98112

H 20.23781 8.53085 11.90970

C 21.71767 9.11467 13.41174

H 22.54419 9.20871 12.67978

C 21.94802 9.36079 14.77910

H 22.95657 9.64330 15.14072

C 20.89210 9.24501 15.70484

H 21.08040 9.45691 16.77631

C 22.26825 13.04143 13.77431

H 22.45658 12.02943 14.20052

H 22.31401 13.78109 14.60454

C 23.30935 13.38827 12.69622

H 23.02853 14.36177 12.22700

H 23.28420 12.61773 11.88996

C 24.69039 13.47295 13.31852

C 25.55256 12.35330 13.34820

H 25.24311 11.41466 12.84595

C 26.79870 12.41755 14.00090

H 27.46289 11.53150 14.00172

C 27.20056 13.60176 14.64966

H 28.17615 13.65047 15.17054

C 26.35208 14.72643 14.62612

H 26.65203 15.66715 15.12833

C 25.11360 14.66010 13.96203

H 24.45908 15.55404 13.94596

C 21.07248 18.19534 13.97454

H 20.93472 17.69237 14.95823

H 20.94861 19.29503 14.12283

C 22.45167 17.87053 13.37560

H 22.52400 18.30007 12.34856

H 22.51508 16.75818 13.26269

C 23.59621 18.39181 14.22525

C 24.46611 19.38959 13.72644

H 24.30055 19.78613 12.70347

C 25.52212 19.89025 14.51324

H 26.18919 20.67288 14.10190

C 25.72400 19.40219 15.81923

H 26.54980 19.79702 16.44241

C 24.86171 18.40961 16.32931

H 25.01040 18.01654 17.35435

C 23.80873 17.90775 15.54043

H 23.13623 17.12853 15.95632

C 12.80107 10.67374 19.36387

H 12.17657 9.87506 18.90096

H 12.31972 11.65741 19.17241

C 12.95698 10.46688 20.88030

H 13.44462 9.48475 21.08626

H 13.63351 11.26539 21.27294

C 11.60030 10.54440 21.55735

C 10.87759 9.37722 21.89514

H 11.33524 8.38370 21.71032

C 9.59470 9.46036 22.47034

H 9.04826 8.53430 22.73781

C 9.00924 10.71840 22.71098

H 8.00135 10.78600 23.16569

C 9.72030 11.89016 22.37915

H 9.27291 12.88502 22.57362

C 11.00441 11.80485 21.80887

H 11.56070 12.73079 21.55236

C 11.32277 12.47634 14.37399

H 11.10037 13.31419 13.66891

H 11.12730 12.85247 15.39939

C 10.44884 11.24868 14.04796

H 10.74406 10.83921 13.05341

H 9.39823 11.61790 13.94948

C 10.49215 10.15230 15.09616

C 11.34895 9.03533 14.95975

H 11.98201 8.94598 14.05390

C 11.39501 8.03765 15.95313

H 12.06641 7.16529 15.82817

C 10.58574 8.14096 17.10142

H 10.62183 7.35560 17.88128

C 9.72099 9.24475 17.24429

H 9.07174 9.33599 18.13780

C 9.67413 10.23644 16.24716

H 8.97504 11.08880 16.36082

C 18.52204 13.04130 20.64602

H 19.33721 13.74841 20.93192

H 18.73857 12.64660 19.62717

C 18.37707 11.89372 21.66550

H 17.42084 11.36140 21.43769

H 18.26683 12.32555 22.68834

C 19.51744 10.89609 21.63252

C 20.65684 11.04632 22.45590

H 20.72512 11.92165 23.13385

C 21.68918 10.08858 22.44501

H 22.56811 10.22057 23.10577

C 21.59883 8.95943 21.60726

H 22.40128 8.19589 21.61402

C 20.47902 8.80820 20.76479

H 20.39777 7.92645 20.09835

C 19.45259 9.77137 20.77527

H 18.56686 9.64739 20.11971

C 21.42622 13.65040 17.51709

H 21.52009 13.13539 16.53282

H 20.59845 13.14669 18.06338

C 22.75378 13.58881 18.29792

H 22.55700 13.83207 19.36935

H 23.44027 14.37785 17.91040

C 23.42451 12.23447 18.14964

C 24.54485 12.09041 17.29810

H 24.95302 12.97782 16.77287

C 25.15534 10.83572 17.10865

H 26.03697 10.75513 16.44335

C 24.64512 9.69680 17.76066

H 25.11641 8.70646 17.60752

C 23.52755 9.82742 18.60861

H 23.11567 8.94265 19.13021

C 22.92410 11.08373 18.80461

H 22.05007 11.16574 19.48160

C 20.15913 18.75792 21.12559

H 19.88843 19.31149 20.19907

H 21.24151 18.49699 21.07460

C 19.86192 19.63575 22.35539



H 20.24404 19.14160 23.27983

H 18.75567 19.73595 22.46622

C 20.49383 21.00293 22.15722

C 19.71520 22.09348 21.70541

H 18.62286 21.96291 21.57877

C 20.30584 23.33649 21.40931

H 19.66950 24.17000 21.05213

C 21.69518 23.51053 21.56273

H 22.16520 24.48397 21.32474

C 22.48300 22.43662 22.02279

H 23.57539 22.56531 22.15121

C 21.88622 21.19641 22.31769

H 22.51625 20.35535 22.67178

C 15.18936 20.42288 19.51245

H 14.17773 20.87193 19.36353

H 15.66178 20.31148 18.50868

C 16.05481 21.29247 20.44086

H 17.07793 20.84272 20.45770

H 15.65478 21.23540 21.48086

C 16.10800 22.74012 19.98925

C 15.40691 23.74386 20.69780

H 14.84452 23.46360 21.61184

C 15.41393 25.08351 20.26134

H 14.85432 25.85035 20.83244

C 16.12609 25.44317 19.10017

H 16.13011 26.49388 18.75030

C 16.83174 24.45351 18.38535

H 17.39627 24.72260 17.47052

C 16.82516 23.11586 18.82600

H 17.39330 22.34857 18.25977

O 13.61022 14.60526 21.78745

O 14.20835 15.38035 20.97491

**[Au<sub>25</sub>(PET)<sub>18</sub>(O<sub>2</sub>)<sub>2</sub>]<sup>-</sup> cluster:**

O 10.01050 18.44753 16.74426

O 10.82431 17.68346 17.36026

O 21.92322 13.62408 15.35648

O 20.98204 14.41746 15.02667

Au 16.04034 18.80207 15.60997

Au 19.01409 19.94051 16.60694

Au 20.83595 16.87646 17.24625

Au 18.28827 14.60891 17.05865

Au 14.55592 17.53936 17.93042

Au 13.19268 20.10589 16.22405

Au 14.70275 19.72922 12.89164

Au 16.21716 16.83376 13.30956

Au 17.61914 17.41146 17.89019

Au 15.85074 17.66818 20.76058

Au 12.84998 15.76039 19.94477

Au 13.49540 14.90437 16.78868

Au 15.96862 13.14334 16.42211

Au 12.99447 11.99398 15.42569

Au 11.18405 15.08445 14.81238

Au 13.72182 17.34979 14.96314

Au 17.45039 14.42917 14.09981

Au 18.78327 11.84877 15.81759

Au 17.29715 12.24228 19.16145

Au 15.79316 15.11195 18.71963

Au 14.39171 14.53290 14.15027

Au 16.16332 14.29784 11.26599

Au 19.16378 16.19662 12.09440

Au 18.50947 17.05621 15.24542

Au 15.99909 15.97745 16.01925

S 16.88921 20.95136 16.38300

S 21.23009 19.16159 16.82085

S 20.58045 14.61062 17.85209

S 13.39890 21.23133 14.16637

S 15.97186 18.36744 11.42542

S 13.01426 19.32244 18.45011

S 18.06868 18.18185 20.15065

S 13.70411 17.19362 21.61479

S 11.79351 14.29498 18.43433

S 15.11870 10.98907 15.64638

S 10.79085 12.79744 15.20650

S 11.41039 17.35160 14.21710

S 18.58256 10.73730 17.88291

S 16.03231 13.60753 20.62778

S 18.99890 12.63764 13.59297

S 13.94904 13.76453 11.88025

S 18.29924 14.79729 10.39854

S 20.23474 17.63915 13.61968

C 17.06024 22.08783 14.93553

H 17.65601 21.58408 14.14387

H 16.02837 22.23663 14.54400

C 17.67968 23.44360 15.32388

H 17.08342 23.89268 16.15281

H 17.57219 24.12025 14.43987

C 19.13976 23.37720 15.73112

C 20.14763 23.16748 14.76035

H 19.86877 23.06864 13.69125

C 21.50055 23.07955 15.13656

H 22.27323 22.90898 14.36116

C 21.87087 23.21914 16.48960

H 22.93709 23.15811 16.78379

C 20.87800 23.44049 17.46381

H 21.15289 23.56103 18.53050

C 19.52252 23.51078 17.08467

H 18.74357 23.66982 17.85754

C 21.68673 19.79646 18.49764

H 21.48540 20.89174 18.48355

H 21.01551 19.32369 19.24775

C 23.15782 19.50739 18.83827

H 23.35029 18.41371 18.71917

H 23.81876 20.03719 18.11246

C 23.46337 19.95145 20.25693

C 23.97813 21.24032 20.52747

H 24.20964 21.92186 19.68332

C 24.20471 21.66578 21.85106

H 24.62104 22.67447 22.04170

C 23.91055 20.80994 22.93054

H 24.08335 21.14660 23.97031

C 23.39468 19.52389 22.67549

H 23.16168 18.83542 23.51126

C 23.17858 19.10026 21.35106

H 22.78189 18.08242 21.16270

C 20.43574 14.78241 19.67577

H 19.61317 15.49412 19.90925

H 20.15458 13.77783 20.07309

C 21.77540 15.25432 20.26584

H 22.58993 14.57977 19.91002

H 21.99024 16.26516 19.83580

C 21.77588 15.30178 21.77987

C 22.62066 14.44570 22.52394

H 23.29091 13.74681 21.98249

C 22.60632 14.45817 23.93226

H 23.26340 13.76978 24.49892

C 21.74834 15.33689 24.62132

H 21.73289 15.35007 25.72836

C 20.90585 16.20083 23.89194

H 20.22266 16.89083 24.42495

C 20.91752 16.18377 22.48333

H 20.24001 16.85873 21.91792

C 11.73860 21.03292 13.38080

H 11.81690 21.48949 12.36737



H 11.53587 19.94531 13.26626

C 10.61840 21.67582 14.21786

H 10.80690 22.76855 14.34192

H 10.63806 21.21390 15.23587

C 9.27751 21.43424 13.54877

C 8.67055 22.42249 12.73998

H 9.15403 23.41625 12.64032

C 7.45657 22.16577 12.07376

H 6.98842 22.95527 11.45522

C 6.83154 20.91159 12.20472

H 5.87223 20.71261 11.68902

C 7.42636 19.91956 13.01107

H 6.93295 18.93592 13.13370

C 8.63796 20.17682 13.68002

H 9.10070 19.39732 14.32274

C 14.70643 17.63435 10.28980

H 15.10245 16.62756 10.01388

H 13.76510 17.47282 10.85459

C 14.47410 18.48410 9.02347

H 15.45269 18.67642 8.52347

H 13.87179 17.85882 8.32010

C 13.74093 19.79483 9.25077

C 14.44187 21.01386 9.41038

H 15.54962 21.01388 9.36067

C 13.74712 22.22151 9.62217

H 14.31208 23.16637 9.74448

C 12.33961 22.23322 9.67203

H 11.79101 23.18299 9.82907

C 11.63036 21.02596 9.51312

H 10.52333 21.02426 9.55427

C 12.32699 19.82104 9.30086

H 11.75771 18.88099 9.15954

C 13.98882 20.67293 19.25449

H 14.21818 20.33578 20.29283

H 14.94720 20.80730 18.70397

C 13.16397 21.97506 19.24212

H 12.81897 22.14129 18.19187

H 12.24563 21.83196 19.85815

C 13.93015 23.19495 19.71756

C 13.90974 23.59774 21.07327

H 13.33379 22.99682 21.80655

C 14.58891 24.75719 21.49487

H 14.55309 25.05943 22.55913

C 15.29794 25.53958 20.56251

H 15.81084 26.46523 20.88792

C 15.34600 25.13757 19.21240

H 15.90043 25.74585 18.47102

C 14.67480 23.97204 18.79743

H 14.70912 23.65664 17.73440

C 18.15368 20.02471 20.08058

H 19.04161 20.25884 19.44958

H 17.26584 20.41954 19.54051

C 18.30219 20.64736 21.48242

H 17.30583 20.67035 21.98412

H 18.95822 19.99434 22.10495

C 18.90887 22.03741 21.40734

C 20.26141 22.24125 21.76827

H 20.86273 21.38660 22.13980

C 20.85576 23.51369 21.65824

H 21.91505 23.64804 21.95133

C 20.10554 24.60450 21.17938

H 20.57017 25.60602 21.08839

C 18.75829 24.41235 20.81409

H 18.15554 25.26092 20.43838

C 18.16314 23.14168 20.92875

H 17.10056 23.01225 20.63808

C 14.14727 15.96886 22.92935

H 14.69547 15.13148 22.44294

H 14.84491 16.48520 23.62815

C 12.92517 15.41473 23.68638

H 12.44458 16.22777 24.28107

H 12.17214 15.05631 22.94501

C 13.37065 14.26326 24.57227

C 13.16641 12.92365 24.16746

H 12.58488 12.71834 23.24764

C 13.69754 11.85016 24.90897

H 13.53771 10.81066 24.55987

C 14.43945 12.10144 26.07898

H 14.86946 11.26171 26.65842

C 14.62774 13.43012 26.51031

H 15.20324 13.63751 27.43400

C 14.09811 14.49917 25.76302

H 14.25851 15.54160 26.10679

C 12.44349 12.63141 18.90831

H 11.95082 11.91854 18.20561

H 13.53810 12.60323 18.70430

C 12.13240 12.27433 20.37101

H 12.73978 12.95318 21.01922

H 11.05853 12.49178 20.58257

C 12.43135 10.82177 20.70021

C 11.38198 9.91050 20.96570

H 10.33380 10.27318 20.95098

C 11.64720 8.55525 21.24723

H 10.80818 7.86144 21.44675

C 12.97250 8.08149 21.26091

H 13.18167 7.01655 21.47848

C 14.03019 8.97804 21.00414

H 15.07925 8.62015 21.01430

C 13.76326 10.33442 20.73132

H 14.60678 11.03152 20.54192

C 14.96201 9.82890 17.07469

H 14.38339 10.31844 17.88813

H 16.00326 9.66749 17.43845

C 14.32577 8.48362 16.67332

H 14.90680 8.03966 15.83040

H 14.43788 7.79150 17.54471

C 12.86078 8.57001 16.29042

C 11.87194 8.77787 17.28099

H 12.17014 8.85991 18.34558

C 10.51424 8.88161 16.92869

H 9.75733 9.05291 17.71869

C 10.11968 8.75704 15.58147

H 9.04846 8.82063 15.30859

C 11.09399 8.54009 14.58792

H 10.79883 8.43058 13.52589

C 12.45530 8.45844 14.94170

H 13.22007 8.30943 14.15303

C 10.31230 12.18295 13.53008

H 10.47247 11.08090 13.54315

H 11.00304 12.62696 12.78021

C 8.85387 12.52296 13.18323

H 8.70785 13.62602 13.27530

H 8.17099 12.03967 13.92087

C 8.54458 12.05846 11.77302

C 7.98349 10.78524 11.52449

H 7.70433 10.13805 12.38100

C 7.77217 10.33392 10.20686

H 7.32359 9.33715 10.03084

C 8.12564 11.14772 9.11288

H 7.96253 10.79029 8.07741

C 8.68384 12.41986 9.34753

H 8.96714 13.07500 8.50114

C 8.88809 12.86902 10.66504



H 9.32230 13.87421 10.83765

C 11.54398 17.18112 12.38674

H 12.38081 16.48372 12.16469

H 11.81191 18.18692 11.98297

C 10.22419 16.67631 11.78125

H 9.38667 17.32525 12.12864

H 10.03014 15.65775 12.20220

C 10.24513 16.63848 10.26562

C 9.38088 17.47020 9.51607

H 8.68294 18.14535 10.05311

C 9.40644 17.46140 8.10778

H 8.72692 18.12705 7.54119

C 10.29853 16.61415 7.42294

H 10.32274 16.60631 6.31620

C 11.16547 15.77924 8.15731

H 11.87166 15.10970 7.62846

C 11.14062 15.79003 9.56587

H 11.83291 15.13288 10.13496

C 20.25628 10.93871 18.63729

H 20.19482 10.48613 19.65370

H 20.46087 12.02683 18.74102

C 21.35870 10.28825 17.78334

H 21.15976 9.19683 17.66719

H 21.32981 10.74879 16.76524

C 22.71300 10.52339 18.42587

C 23.32594 9.54036 19.23476

H 22.83396 8.55369 19.35678

C 24.55033 9.79620 19.88313

H 25.02436 9.00864 20.50150

C 25.17639 11.04894 19.73820

H 26.13650 11.25452 20.25083

C 24.57363 12.03852 18.93483

H 25.06285 13.02508 18.81163

C 23.35689 11.77610 18.27693

H 22.88912 12.55139 17.63501

C 17.27992 14.35727 21.77209

H 16.90593 15.38498 21.99753

H 18.24312 14.47022 21.23410

C 17.45033 13.53948 23.06764

H 16.45154 13.36033 23.53109

H 18.03209 14.17502 23.77957

C 18.18163 12.22361 22.87709

C 17.48234 11.00429 22.72022

H 16.37442 11.00504 22.76135

C 18.18171 9.79796 22.51978

H 17.61986 8.85179 22.39611

C 19.58956 9.78916 22.48018

H 20.13980 8.84035 22.32805

C 20.29706 10.99757 22.63837

H 21.40456 11.00369 22.60597

C 19.59551 12.20124 22.83831

H 20.15944 13.14577 22.97271

C 18.02960 11.30325 12.76239

H 17.79209 11.66354 11.73394

H 17.07295 11.14124 13.30930

C 18.87738 10.01716 12.73414

H 19.24864 9.83237 13.77133

H 19.77895 10.18772 12.10144

C 18.11811 8.80001 12.24741

C 18.11955 8.42567 10.88357

H 18.67519 9.04647 10.15198

C 17.44014 7.27260 10.44658

H 17.46056 6.99035 9.37525

C 16.75180 6.46696 11.37444

H 16.24234 5.54304 11.03889

C 16.71973 6.84110 12.73301

H 16.17007 6.21739 13.46604

C 17.39309 7.99942 13.16255

H 17.37223 8.28878 14.23310

C 13.86482 11.91904 11.94281

H 12.98841 11.67891 12.58893

H 14.76410 11.52182 12.46231

C 13.69200 11.29742 10.54159

H 14.67946 11.27797 10.02143

H 13.02197 11.94945 9.93347

C 13.08960 9.90414 10.61637

C 11.73706 9.69612 10.25607

H 11.13149 10.54800 9.88539

C 11.14394 8.42317 10.36547

H 10.08340 8.28851 10.07404

C 11.89745 7.33303 10.84161

H 11.43549 6.33035 10.93327

C 13.24572 7.52715 11.20265

H 13.84954 6.67775 11.57592

C 13.83837 8.79940 11.08941

H 14.90076 8.93135 11.37920

C 17.84759 16.03383 9.10000

H 17.30088 16.86974 9.59098

H 17.14743 15.51869 8.40285

C 19.06425 16.59259 8.33831

H 19.54176 15.78304 7.73612

H 19.82231 16.94943 9.07567

C 18.60744 17.74322 7.45793

C 18.79407 19.08179 7.87403

H 19.35306 19.28700 8.80835

C 18.26754 20.15376 7.12837

H 18.42295 21.19227 7.48078

C 17.54591 19.90256 5.94564

H 17.12532 20.74057 5.35718

C 17.36624 18.57451 5.51071

H 16.80344 18.36802 4.58009

C 17.89268 17.50564 6.25989

H 17.74270 16.46310 5.91129

C 19.61939 19.31107 13.13158

H 20.13929 20.02614 13.81340

H 18.52790 19.36547 13.34942

C 19.91330 19.63518 11.65740

H 19.28537 18.95011 11.03716

H 20.97924 19.39868 11.42896

C 19.62634 21.08554 11.31574

C 20.68340 21.98967 11.05513

H 21.72838 21.61776 11.07106

C 20.42723 23.34664 10.77497

H 21.26849 24.03677 10.56694

C 19.10294 23.82558 10.75843

H 18.89881 24.89268 10.54643

C 18.03962 22.93702 11.01848

H 16.99393 23.30453 11.01490

C 18.29729 21.57874 11.28874

H 17.45093 20.88642 11.48199

**[Au<sub>25</sub>(PET)<sub>18</sub>(O<sub>2</sub>)<sub>3</sub>]<sup>-</sup> cluster:**

Au 16.03014 18.75615 15.58336

Au 19.04435 19.88525 16.60384

Au 20.85762 16.83549 17.23533

Au 18.30587 14.56014 17.03359

Au 14.54747 17.51485 17.90286

Au 13.17330 20.09952 16.22693

Au 14.67291 19.71564 12.91242

Au 16.22656 16.76724 13.27913

Au 17.63329 17.35290 17.87008

Au 15.85561 17.66367 20.76059

Au 12.83975 15.80827 19.92095

Au 13.45544 14.89602 16.74030



Au 15.95672 13.15084 16.43910

Au 12.86199 12.03988 15.42323

Au 11.10191 15.08613 14.78320

Au 13.71757 17.31454 14.94603

Au 17.44667 14.34369 14.05994

Au 18.79106 11.78917 15.78609

Au 17.31058 12.20710 19.12366

Au 15.79915 15.14022 18.71907

Au 14.37894 14.49830 14.10412

Au 16.13318 14.26483 11.22649

Au 19.16270 16.13940 12.06858

Au 18.55747 16.92899 15.22944

Au 16.00255 15.93896 15.98854

S 16.92055 20.87138 16.36118

S 21.26004 19.12377 16.82466

S 20.61733 14.56131 17.82579

S 13.35552 21.22120 14.16900

S 15.97140 18.37322 11.45515

S 13.02472 19.32501 18.45247

S 18.07425 18.15057 20.12581

S 13.70651 17.20054 21.61957

S 11.77284 14.34144 18.42336

S 14.97542 11.05137 15.72383

S 10.64458 12.81104 15.19136

S 11.41560 17.34392 14.17709

S 18.58204 10.67797 17.85411

S 16.04046 13.57812 20.57718

S 19.09557 12.61425 13.59964

S 13.89744 13.81728 11.81334

S 18.27848 14.75501 10.37056

S 20.24819 17.57126 13.59915

O 15.37963 9.16727 14.00541

O 15.66651 9.72300 12.88510

O 10.04440 18.21165 16.84279

O 10.98274 17.41224 17.16783

O 22.00007 13.61563 15.20557

O 21.06389 14.36198 14.78314

C 17.07709 22.02271 14.92437

H 17.68050 21.53312 14.12966

H 16.04203 22.16104 14.53370

C 17.67884 23.38486 15.32383

H 17.07201 23.82963 16.14821

H 17.56757 24.05822 14.43804

C 19.13824 23.33425 15.73369

C 20.14605 23.12275 14.76295

H 19.86598 23.01882 13.69530

C 21.49975 23.04452 15.13620

H 22.27106 22.86674 14.36112

C 21.87175 23.20072 16.48712

H 22.93884 23.15068 16.78004

C 20.87983 23.42787 17.46103

H 21.15534 23.56517 18.52595

C 19.52282 23.48307 17.08518

H 18.74702 23.64617 17.86032

C 21.72036 19.76579 18.49754

H 21.55822 20.86791 18.46758

H 21.02824 19.33063 19.25196

C 23.17857 19.43353 18.85748

H 23.33417 18.33130 18.76549

H 23.86167 19.92213 18.12343

C 23.49247 19.89964 20.26752

C 24.03715 21.18149 20.51017

H 24.28426 21.83860 19.65199

C 24.27617 21.62987 21.82362

H 24.71780 22.63192 21.99192

C 23.96092 20.80577 22.92164

H 24.14566 21.16076 23.95349

C 23.41155 19.52810 22.69533

H 23.15793 18.86498 23.54590

C 23.18491 19.08092 21.38012

H 22.76399 18.06880 21.21698

C 20.44988 14.75103 19.65092

H 19.61052 15.45163 19.86251

H 20.17975 13.74781 20.06005

C 21.76692 15.26234 20.26411

H 22.61028 14.62307 19.91037

H 21.94958 16.28571 19.84892

C 21.75659 15.29356 21.78013

C 22.59946 14.43101 22.51891

H 23.26763 13.73495 21.97189

C 22.59789 14.44561 23.92734

H 23.26464 13.76061 24.48618

C 21.74801 15.32659 24.62348

H 21.74363 15.33941 25.73076

C 20.89927 16.18904 23.89939

H 20.22550 16.88287 24.43888

C 20.90129 16.17294 22.49046

H 20.22585 16.85339 21.92989

C 11.69399 20.99965 13.39521

H 11.75753 21.47230 12.38825

H 11.51531 19.90981 13.26464

C 10.56399 21.61005 14.24293

H 10.74215 22.70199 14.38871

H 10.57939 21.12790 15.25026

C 9.22963 21.36939 13.56174

C 8.67605 22.32020 12.67423

H 9.20003 23.28448 12.51655

C 7.47311 22.05821 11.99091

H 7.05062 22.81925 11.30541

C 6.80596 20.83291 12.18245

H 5.86074 20.62377 11.64522

C 7.34689 19.87817 13.06787

H 6.82478 18.91634 13.23556

C 8.54643 20.14523 13.75454

H 8.96822 19.39412 14.45536

C 14.72755 17.61483 10.31005

H 15.12901 16.60264 10.06243

H 13.77792 17.46125 10.86378

C 14.50722 18.43719 9.02412

H 15.49104 18.63832 8.53700

H 13.92224 17.78894 8.32596

C 13.75888 19.74015 9.23507

C 14.45238 20.96151 9.40329

H 15.55968 20.96376 9.35081

C 13.75260 22.16413 9.62332

H 14.31330 23.11159 9.74863

C 12.34506 22.16618 9.67739

H 11.79252 23.11111 9.84761

C 11.64198 20.95660 9.50643

H 10.53447 20.94545 9.54620

C 12.34474 19.75686 9.28477

H 11.77908 18.81560 9.13632

C 14.02308 20.66567 19.24635

H 14.28402 20.31551 20.27323

H 14.96592 20.81601 18.67282

C 13.18269 21.95791 19.28213

H 12.78995 22.13359 18.25041

H 12.29597 21.79639 19.93932

C 13.95398 23.18129 19.73600

C 13.92835 23.60950 21.08337

H 13.34435 23.02839 21.82528

C 14.61055 24.77229 21.48845

H 14.56772 25.09740 22.54594



C 15.33256 25.53034 20.54689

H 15.85395 26.45580 20.85913

C 15.38528 25.10418 19.20421

H 15.95002 25.69658 18.45791

C 14.70554 23.93880 18.80509

H 14.73705 23.61192 17.74544

C 18.17700 19.99150 20.06315

H 19.04977 20.21987 19.40814

H 17.27773 20.40078 19.55211

C 18.37120 20.59695 21.46692

H 17.39374 20.59119 22.00694

H 19.06418 19.94477 22.04884

C 18.95285 21.99799 21.40099

C 20.30921 22.21734 21.73635

H 20.93308 21.36603 22.07709

C 20.88012 23.50171 21.64737

H 21.94177 23.64774 21.92743

C 20.10194 24.59037 21.20935

H 20.54716 25.60162 21.13688

C 18.75060 24.38326 20.86837

H 18.12612 25.23051 20.52635

C 18.17921 23.10055 20.96574

H 17.11267 22.95933 20.69766

C 14.14723 15.95389 22.91654

H 14.67957 15.11403 22.41759

H 14.85945 16.45465 23.61237

C 12.92752 15.40915 23.68186

H 12.45595 16.22684 24.27717

H 12.16685 15.05408 22.94620

C 13.37210 14.26045 24.57261

C 13.19633 12.91976 24.15843

H 12.65048 12.70840 23.21895

C 13.70720 11.84912 24.91677

H 13.55925 10.81042 24.56047

C 14.40611 12.10306 26.11232

H 14.81886 11.26658 26.70845

C 14.57478 13.43257 26.54767

H 15.11771 13.64178 27.49018

C 14.06363 14.49919 25.78413

H 14.21093 15.54101 26.13418

C 12.42008 12.69047 18.94454

H 11.92484 11.95534 18.26522

H 13.51565 12.65909 18.74120

C 12.12422 12.37366 20.42130

H 12.73019 13.07996 21.04108

H 11.05101 12.58463 20.64117

C 12.44955 10.93332 20.77841

C 11.41986 10.00834 21.06845

H 10.36739 10.35729 21.06571

C 11.71021 8.65896 21.35213

H 10.88545 7.95258 21.57018

C 13.04383 8.20646 21.34495

H 13.27334 7.14374 21.55557

C 14.08203 9.11850 21.06384

H 15.13598 8.77571 21.04904

C 13.78887 10.46854 20.78975

H 14.61767 11.17651 20.58089

C 14.77886 9.95683 17.19870

H 14.19673 10.49942 17.97450

H 15.80995 9.79731 17.59192

C 14.13261 8.59750 16.85676

H 14.73484 8.09551 16.06627

H 14.21575 7.97061 17.77950

C 12.67588 8.65969 16.43331

C 11.65863 8.90196 17.38721

H 11.92877 9.04290 18.45342

C 10.30732 8.95955 16.99803

H 9.52564 9.15661 17.75775

C 9.94762 8.75204 15.65071

H 8.88186 8.77988 15.34707

C 10.95063 8.50406 14.69352

H 10.68285 8.33587 13.63098

C 12.30474 8.46822 15.08222

H 13.09789 8.30084 14.32661

C 10.17268 12.18174 13.51663

H 10.31811 11.07713 13.54375

H 10.87148 12.60720 12.76345

C 8.72047 12.54298 13.15800

H 8.58994 13.64838 13.25480

H 8.02658 12.06499 13.88901

C 8.40379 12.09220 11.74371

C 7.80442 10.83766 11.48737

H 7.51092 10.18889 12.33745

C 7.57806 10.40097 10.16747

H 7.09910 9.41856 9.98674

C 7.95527 11.21057 9.07850

H 7.78044 10.86231 8.04249

C 8.55253 12.46411 9.31878

H 8.84988 13.11762 8.47493

C 8.77115 12.89782 10.63959

H 9.23717 13.88735 10.81633

C 11.57578 17.14541 12.35471

H 12.40429 16.43231 12.14360

H 11.85509 18.14491 11.94331

C 10.25038 16.65189 11.74817

H 9.41871 17.31030 12.09451

H 10.04890 15.63653 12.17392

C 10.26229 16.60776 10.23241

C 9.37990 17.42314 9.48662

H 8.67510 18.08782 10.02753

C 9.39186 17.40631 8.07828

H 8.69359 18.05549 7.51495

C 10.29208 16.57041 7.38893

H 10.30761 16.55873 6.28181

C 11.17615 15.75099 8.12066

H 11.88609 15.08685 7.58841

C 11.16234 15.76837 9.52904

H 11.86596 15.12221 10.09523

C 20.25881 10.89019 18.60315

H 20.21364 10.40266 19.60424

H 20.44533 11.97710 18.74604

C 21.37549 10.29581 17.72746

H 21.19849 9.20661 17.56177

H 21.34179 10.79970 16.73124

C 22.72061 10.52953 18.38972

C 23.28750 9.56964 19.25901

H 22.76524 8.60400 19.41669

C 24.50127 9.82361 19.92563

H 24.93173 9.05796 20.60048

C 25.17136 11.04657 19.72958

H 26.12775 11.24745 20.25093

C 24.61842 12.00942 18.86111

H 25.14630 12.96794 18.68967

C 23.40409 11.75428 18.19535

H 22.97120 12.51434 17.51158

C 17.27068 14.33146 21.73693

H 16.87783 15.35223 21.96129

H 18.23673 14.45973 21.20514

C 17.44055 13.51733 23.03499

H 16.44205 13.35286 23.50547

H 18.03494 14.15048 23.73860

C 18.14837 12.18954 22.84363

C 17.42105 10.98621 22.69492



H 16.31431 11.01139 22.75302

C 18.08739 9.76424 22.47958

H 17.50033 8.83170 22.36487

C 19.49406 9.72432 22.41210

H 20.01836 8.76352 22.24126

C 20.23078 10.91482 22.57254

H 21.33811 10.89406 22.52935

C 19.56069 12.13410 22.78856

H 20.15070 13.06188 22.92904

C 18.34133 11.23491 12.62956

H 18.19761 11.61280 11.58876

H 17.33837 10.97791 13.04416

C 19.27118 10.00120 12.66701

H 19.59202 9.84470 13.72588

H 20.19565 10.21222 12.07771

C 18.58667 8.74145 12.16957

C 18.38416 8.50015 10.79087

H 18.77038 9.22743 10.04824

C 17.69755 7.35254 10.35214

H 17.54808 7.17782 9.26867

C 17.20161 6.42240 11.28759

H 16.65783 5.52193 10.94178

C 17.40306 6.64741 12.66325

H 17.00933 5.92830 13.40796

C 18.09264 7.79402 13.09538

H 18.22739 7.98332 14.17911

C 13.67869 11.98460 11.78656

H 12.77871 11.78724 12.41354

H 14.53689 11.49026 12.29150

C 13.48017 11.44132 10.35741

H 14.45901 11.46567 9.82120

H 12.78223 12.11048 9.79943

C 12.91144 10.03203 10.38778

C 11.51845 9.82434 10.25716

H 10.84969 10.68762 10.06400

C 10.96643 8.53289 10.36533

H 9.87279 8.39844 10.25367

C 11.80150 7.42528 10.60992

H 11.36681 6.41061 10.70134

C 13.19203 7.61872 10.73168

H 13.86324 6.75920 10.92879

C 13.74252 8.90891 10.61508

H 14.83457 9.04626 10.73732

C 17.83039 16.00659 9.08142

H 17.29000 16.83961 9.58331

H 17.12441 15.50492 8.37976

C 19.04730 16.56781 8.32282

H 19.52659 15.76081 7.71928

H 19.80335 16.92090 9.06418

C 18.59722 17.72278 7.44387

C 18.75755 19.05872 7.87903

H 19.28863 19.26140 8.82949

C 18.24969 20.13471 7.12680

H 18.38704 21.16956 7.49698

C 17.56637 19.89227 5.91987

H 17.15634 20.73536 5.33140

C 17.40612 18.56715 5.46862

H 16.87164 18.36478 4.52015

C 17.91771 17.49479 6.22366

H 17.77942 16.45634 5.85971

C 19.63093 19.24489 13.12223

H 20.14917 19.95522 13.81062

H 18.53802 19.30340 13.33327

C 19.93268 19.57176 11.64955

H 19.32028 18.87610 11.02449

H 21.00382 19.34803 11.43111

C 19.62758 21.01679 11.30107

C 20.67193 21.93559 11.04504

H 21.72218 21.57969 11.07013

C 20.39624 23.28681 10.75631

H 21.22970 23.98823 10.55636

C 19.06484 23.74520 10.72254

H 18.84522 24.80625 10.49515

C 18.01375 22.83930 10.97300

H 16.96089 23.18466 10.94804

C 18.29152 21.48825 11.25642

H 17.45552 20.78152 11.43985

**[Au<sub>25</sub>(PET)<sub>18</sub>(O<sub>2</sub>)<sub>4</sub>]<sup>-</sup> cluster:**

Au 16.05592 18.77076 15.54684

Au 19.12815 19.87014 16.59837

Au 20.89080 16.84486 17.24376

Au 18.28901 14.60152 17.05722

Au 14.58300 17.59626 17.93455

Au 13.18103 20.11817 16.20806

Au 14.67995 19.70603 12.88724

Au 16.20274 16.75973 13.26955

Au 17.64229 17.43458 17.88568

Au 15.91244 17.68559 20.78048

Au 12.87278 15.83982 19.95328

Au 13.45313 14.95172 16.77100

Au 15.94053 13.18951 16.47788

Au 12.86668 12.06499 15.42453

Au 11.11152 15.09130 14.77903

Au 13.71493 17.34397 14.96791

Au 17.42169 14.37649 14.08445

Au 18.75729 11.79805 15.80595

Au 17.28832 12.22846 19.13128

Au 15.81775 15.21468 18.74760

Au 14.37136 14.52839 14.14576

Au 16.13923 14.26843 11.21415

Au 19.15611 16.10391 12.04414

Au 18.55599 16.98597 15.25150

Au 16.00460 15.98202 16.01315

S 17.01868 20.85634 16.28498

S 21.35092 19.11673 16.81589

S 20.58836 14.58281 17.84345

S 13.38304 21.22790 14.14421

S 15.94816 18.33633 11.42776

S 12.90144 19.28955 18.39560

S 18.14658 18.12157 20.17244

S 13.76256 17.23254 21.64111

S 11.77752 14.39822 18.44813

S 14.98056 11.08818 15.75201

S 10.64520 12.81950 15.18669

S 11.41657 17.34991 14.17797

S 18.55030 10.68195 17.87289

S 16.04498 13.62575 20.57891

S 19.07489 12.65597 13.63242

S 13.91703 13.83475 11.85913

S 18.27428 14.74565 10.32443

S 20.23533 17.53063 13.57558

C 17.24957 21.92855 14.79646

H 17.85614 21.37973 14.04367

H 16.22797 22.07249 14.37391

C 17.87344 23.29744 15.13888

H 17.25432 23.79338 15.92106

H 17.79208 23.91800 14.21148

C 19.32621 23.25959 15.58087

C 20.35719 23.00287 14.64542

H 20.10368 22.83231 13.57947

C 21.70453 22.96812 15.04947

H 22.49463 22.75689 14.30221

C 22.04921 23.21180 16.39456



H 23.11181 23.19825 16.70884

C 21.03353 23.48173 17.33257

H 21.28765 23.68365 18.39254

C 19.68347 23.49805 16.92827

H 18.88437 23.68752 17.67226

C 21.85000 19.75762 18.47827

H 21.71920 20.86362 18.44276

H 21.15519 19.34792 19.24390

C 23.30316 19.38751 18.82745

H 23.43082 18.28195 18.73072

H 23.99629 19.86272 18.09399

C 23.62409 19.83820 20.24089

C 24.22980 21.08920 20.49662

H 24.54175 21.72628 19.64464

C 24.44786 21.53174 21.81609

H 24.93607 22.50995 21.99479

C 24.05346 20.73098 22.90587

H 24.22167 21.08007 23.94270

C 23.45438 19.47845 22.66575

H 23.14608 18.83123 23.50989

C 23.24694 19.03848 21.34578

H 22.78342 18.04716 21.16977

C 20.43620 14.76711 19.66916

H 19.60854 15.47748 19.89309

H 20.15872 13.76347 20.07236

C 21.76602 15.25463 20.27075

H 22.59370 14.59695 19.91422

H 21.96444 16.27309 19.85063

C 21.76060 15.29114 21.78603

C 22.60228 14.42821 22.52475

H 23.26815 13.73042 21.97733

C 22.60104 14.44441 23.93308

H 23.26684 13.75886 24.49265

C 21.75218 15.32724 24.62815

H 21.74787 15.34219 25.73533

C 20.90544 16.19108 23.90326

H 20.23389 16.88837 24.44108

C 20.90759 16.17373 22.49471

H 20.23113 16.85277 21.93352

C 11.71768 20.99240 13.38065

H 11.77046 21.46233 12.37194

H 11.54458 19.90142 13.25573

C 10.58596 21.59305 14.23195

H 10.75978 22.68414 14.38705

H 10.60279 21.10270 15.23481

C 9.25329 21.35275 13.54713

C 8.72300 22.29474 12.63557

H 9.26509 23.24653 12.46106

C 7.51939 22.04120 11.95146

H 7.11506 22.79690 11.24987

C 6.82790 20.83298 12.16525

H 5.87671 20.63443 11.63425

C 7.34901 19.88423 13.06815

H 6.80647 18.93592 13.25105

C 8.55048 20.14254 13.75566

H 8.95853 19.39451 14.46732

C 14.69669 17.59684 10.28104

H 15.09018 16.58259 10.02783

H 13.74519 17.45107 10.83314

C 14.48757 18.43163 9.00083

H 15.47519 18.63033 8.52048

H 13.90203 17.79300 8.29418

C 13.74667 19.73794 9.21865

C 14.44715 20.95424 9.39066

H 15.55422 20.95188 9.33614

C 13.75470 22.15962 9.61783

H 14.32120 23.10287 9.74911

C 12.34744 22.16984 9.67512

H 11.80174 23.11774 9.85111

C 11.63711 20.96509 9.49963

H 10.52976 20.95957 9.54330

C 12.33268 19.76274 9.27014

H 11.76225 18.82511 9.11857

C 13.64518 20.68202 19.35075

H 13.79303 20.31558 20.39404

H 14.64583 20.93372 18.92799

C 12.71003 21.91066 19.30506

H 12.35473 22.03661 18.25371

H 11.80637 21.71375 19.92911

C 13.40284 23.18419 19.75205

C 13.62513 23.45976 21.12104

H 13.25115 22.74844 21.88421

C 14.31786 24.61675 21.52304

H 14.48447 24.81505 22.60034

C 14.79928 25.52356 20.55695

H 15.34314 26.43553 20.87075

C 14.57871 25.26370 19.19042

H 14.95630 25.96698 18.42305

C 13.88543 24.10600 18.79533

H 13.73294 23.89246 17.71821

C 18.33956 19.95563 20.21809

H 19.21963 20.18039 19.57204

H 17.45811 20.44336 19.74558

C 18.56634 20.47814 21.65110

H 17.60458 20.42314 22.21580

H 19.29077 19.81077 22.17682

C 19.11067 21.89804 21.63749

C 20.50570 22.12008 21.71782

H 21.19087 21.25806 21.84494

C 21.03924 23.42118 21.64219

H 22.13542 23.56418 21.71536

C 20.18104 24.52564 21.47525

H 20.59844 25.54924 21.40598

C 18.78919 24.31746 21.39964

H 18.10195 25.17634 21.26479

C 18.25771 23.01686 21.48803

H 17.16239 22.87064 21.40884

C 14.19247 15.98886 22.94143

H 14.74079 15.15521 22.44935

H 14.88724 16.49654 23.64954

C 12.96478 15.43096 23.68434

H 12.47557 16.24059 24.27646

H 12.22071 15.07415 22.93320

C 13.40061 14.27945 24.57466

C 13.21785 12.94121 24.15652

H 12.67624 12.73604 23.21313

C 13.71241 11.86637 24.91925

H 13.55589 10.82986 24.56224

C 14.40419 12.11419 26.12053

H 14.80196 11.27312 26.72024

C 14.58361 13.44191 26.55647

H 15.12164 13.64575 27.50261

C 14.08569 14.51236 25.79066

H 14.23616 15.55250 26.14347

C 12.37987 12.72570 18.95134

H 11.86458 12.01021 18.26652

H 13.47413 12.66293 18.74949

C 12.07058 12.40645 20.42353

H 12.66190 13.12127 21.04802

H 10.99329 12.60906 20.63070

C 12.40723 10.97135 20.79080

C 11.38601 10.04158 21.09513

H 10.32938 10.37694 21.08317



C 11.69147 8.70213 21.40808

H 10.87587 7.99234 21.64817

C 13.02974 8.26434 21.40970

H 13.27047 7.21113 21.65071

C 14.05895 9.17951 21.10707

H 15.11660 8.84804 21.10042

C 13.75112 10.52053 20.80798

H 14.57183 11.23430 20.58772

C 14.75676 10.00708 17.23388

H 14.15231 10.55319 17.98983

H 15.77942 9.85745 17.65279

C 14.12692 8.64243 16.88584

H 14.74230 8.14445 16.10276

H 14.20452 8.01684 17.81005

C 12.67453 8.69444 16.44734

C 11.64741 8.90760 17.39749

H 11.90944 9.03715 18.46718

C 10.29777 8.94912 17.00193

H 9.50876 9.12211 17.76030

C 9.94950 8.75361 15.64994

H 8.88549 8.76855 15.34006

C 10.96293 8.53614 14.69575

H 10.70559 8.37151 13.63012

C 12.31576 8.51735 15.09082

H 13.11495 8.36599 14.33712

C 10.15604 12.19942 13.51305

H 10.27467 11.09185 13.54162

H 10.86291 12.60805 12.75797

C 8.71198 12.59319 13.15230

H 8.60532 13.70093 13.24658

H 8.00421 12.13451 13.88202

C 8.38673 12.14561 11.73836

C 7.76523 10.90054 11.48914

H 7.45758 10.26633 12.34493

C 7.53028 10.45759 10.17285

H 7.03185 9.48345 10.00012

C 7.92301 11.25294 9.07821

H 7.74147 10.90317 8.04396

C 8.54057 12.49786 9.31115

H 8.85016 13.14007 8.46315

C 8.76680 12.93786 10.62892

H 9.24837 13.92161 10.79708

C 11.58771 17.15381 12.35483

H 12.41792 16.44140 12.14809

H 11.87058 18.15378 11.94815

C 10.26542 16.66443 11.74051

H 9.43571 17.32581 12.08512

H 10.05915 15.65019 12.16687

C 10.27935 16.61727 10.22497

C 9.38104 17.41609 9.48012

H 8.66798 18.07083 10.02234

C 9.38742 17.39538 8.07189

H 8.67740 18.03266 7.50938

C 10.29980 16.57296 7.38219

H 10.31412 16.55974 6.27515

C 11.19839 15.76826 8.11265

H 11.91812 15.11597 7.57926

C 11.18808 15.78726 9.52123

H 11.90074 15.14971 10.08599

C 20.22680 10.91113 18.61465

H 20.19497 10.41790 19.61366

H 20.39951 11.99954 18.76358

C 21.34313 10.33568 17.72715

H 21.16662 9.24875 17.54785

H 21.30622 10.85320 16.73791

C 22.68497 10.56731 18.39353

C 23.21948 9.62472 19.30149

H 22.67438 8.67539 19.48102

C 24.42908 9.87702 19.97544

H 24.83960 9.12421 20.67635

C 25.12353 11.08129 19.74979

H 26.07752 11.28017 20.27472

C 24.60068 12.02796 18.84596

H 25.14790 12.97147 18.65316

C 23.39088 11.77413 18.17144

H 22.97746 12.52029 17.46103

C 17.29411 14.35143 21.73818

H 16.92557 15.38091 21.96617

H 18.26097 14.45959 21.20456

C 17.45087 13.52725 23.03163

H 16.44921 13.36321 23.49485

H 18.04263 14.15348 23.74400

C 18.15781 12.19967 22.83557

C 17.43065 10.99642 22.68626

H 16.32400 11.02253 22.74699

C 18.09767 9.77398 22.47505

H 17.51133 8.84066 22.36539

C 19.50441 9.73337 22.41093

H 20.02989 8.77177 22.24909

C 20.24067 10.92524 22.56625

H 21.34786 10.90566 22.52433

C 19.57046 12.14489 22.77839

H 20.16090 13.07265 22.91789

C 18.35372 11.28672 12.62802

H 18.18020 11.68968 11.60168

H 17.36391 10.99272 13.05529

C 19.31186 10.07473 12.61257

H 19.67742 9.91057 13.65533

H 20.20725 10.31531 11.99104

C 18.63687 8.80597 12.12174

C 18.40019 8.57051 10.74721

H 18.74908 9.31047 9.99901

C 17.72544 7.41152 10.31872

H 17.54787 7.24423 9.23866

C 17.27719 6.46331 11.26019

H 16.75060 5.54853 10.92446

C 17.51291 6.68341 12.63109

H 17.16071 5.94712 13.37959

C 18.18687 7.84277 13.05352

H 18.34843 8.02795 14.13460

C 13.68336 12.00394 11.83891

H 12.78670 11.81619 12.47419

H 14.54336 11.50332 12.33574

C 13.46570 11.46612 10.41096

H 14.43562 11.50366 9.85923

H 12.75529 12.13629 9.86957

C 12.90708 10.05185 10.43233

C 11.51371 9.83778 10.31137

H 10.83731 10.70207 10.15317

C 10.97147 8.53983 10.37996

H 9.87768 8.40037 10.27408

C 11.81764 7.43127 10.57806

H 11.39281 6.40960 10.63308

C 13.20709 7.63238 10.69972

H 13.88416 6.77002 10.85828

C 13.74835 8.92950 10.62380

H 14.84091 9.06988 10.74192

C 17.83471 16.02174 9.05658

H 17.30045 16.85027 9.57281

H 17.12654 15.53608 8.34640

C 19.05943 16.58150 8.30925

H 19.54124 15.77259 7.71021

H 19.80997 16.93183 9.05752

C 18.61848 17.73624 7.42554

C 18.75122 19.07246 7.86960

H 19.25817 19.27812 8.83222

C 18.24669 20.14475 7.10954

H 18.36333 21.18071 7.48378

C 17.59484 19.89659 5.88633

H 17.18880 20.73553 5.28903

C 17.46487 18.57143 5.42546

H 16.95791 18.36649 4.46211

C 17.97313 17.50313 6.18817

H 17.86312 16.46413 5.81653

C 19.62785 19.20123 13.06841

H 20.12952 19.91847 13.76105

H 18.53022 19.25549 13.25456

C 19.95721 19.52187 11.60038

H 19.35848 18.82094 10.96755

H 21.03283 19.30050 11.40367

C 19.65051 20.96413 11.23610

C 20.69316 21.88744 10.98941



H 21.74467 21.53946 11.03860

C 20.41524 23.23477 10.68602

H 21.24764 23.94007 10.49728

C 19.08255 23.68591 10.62966

H 18.86117 24.74551 10.39821

C 18.03236 22.77658 10.87193

H 16.97930 23.11968 10.83343

C 18.31273 21.42900 11.16875

H 17.47600 20.72204 11.34702

O 16.35645 22.20128 19.21558

O 16.78990 22.80619 18.17650

O 15.39328 9.18677 14.00712

O 15.73286 9.76651 12.91563

O 9.98608 18.20954 16.79035

O 11.00238 17.57540 17.21112

O 22.01159 13.59404 15.21714

O 21.01200 14.24215 14.78249

**[Au<sub>25</sub>(PET)<sub>18</sub>(O<sub>2</sub>)]<sup>-</sup> cluster using vdw-DF2 functional**

Au 15.54188 18.90001 15.59014

Au 12.55064 19.78081 17.10935

Au 11.76473 16.70148 19.15091

Au 14.11785 14.38176 17.71113

Au 14.90713 16.69198 13.37662

Au 16.44488 19.87292 12.55371

Au 18.30990 20.79570 15.75627

Au 17.72647 17.87928 17.52419

Au 13.08598 16.73175 15.98516

Au 11.80585 15.85490 12.68717

Au 14.83302 14.14114 11.23348

Au 17.27207 14.61523 13.82787

Au 16.45289 13.18149 16.53351

Au 19.43437 12.23285 14.91693

Au 20.18178 15.27667 12.84503

Au 17.83060 17.67158 14.36301

Au 17.05203 15.35280 18.73080

Au 15.60375 12.22461 19.55660

Au 13.66702 11.30482 16.34915

Au 14.22119 14.19126 14.56582

Au 18.90694 15.34715 16.05008

Au 20.08899 16.20505 19.39822

Au 17.02643 17.90836 20.85120

Au 14.69988 17.41582 18.27314

Au 15.98762 16.02835 16.05092

S 13.77235 20.64880 15.19187

S 11.24328 19.07155 19.01919

S 12.09335 14.30050 19.20831

S 17.64838 21.70560 13.60176

S 19.02705 20.00026 17.94441

S 15.08478 18.21551 11.40500

S 10.87122 16.61866 14.77952

S 12.60651 14.89972 10.59953

S 17.04969 13.27759 11.67811

S 18.21909 11.41448 16.85082

S 20.75608 12.92396 13.00754

S 19.76583 17.67028 12.71892

S 14.32503 10.43844 18.52178

S 12.96239 12.05365 14.13399

S 17.06002 13.80632 20.69785

S 21.07274 15.44250 17.32177

S 19.26821 17.17440 21.47139

S 14.81310 18.78949 20.39922

C 14.53434 22.24562 15.81801

H 14.94429 22.07005 16.83612

H 15.38235 22.46932 15.13204

C 13.52667 23.43117 15.81822

H 13.16963 23.61345 14.77619

H 14.09047 24.33992 16.14569

C 12.33557 23.20238 16.74425

C 12.49614 23.31754 18.15089

H 13.46904 23.64300 18.56540

C 11.42660 23.01718 19.02437

H 11.57168 23.09535 20.11804

C 10.17247 22.62239 18.50024

H 9.32996 22.39424 19.18100

C 9.99722 22.52041 17.10085

H 9.02396 22.21280 16.67973

C 11.07752 22.79724 16.22919

H 10.94245 22.67766 15.13675

C 9.55028 18.96368 18.21859

H 9.34428 19.94757 17.74273

H 9.57887 18.18706 17.42198

C 8.44955 18.61316 19.25379

H 8.72740 17.66198 19.76615

H 8.39929 19.40999 20.03213

C 7.11390 18.47463 18.52832

C 6.19968 19.55640 18.45646

H 6.41990 20.48845 19.01173

C 5.02042 19.45484 17.68193

H 4.31116 20.30293 17.64420

C 4.74961 18.27375 16.95364

H 3.83966 18.20329 16.33091

C 5.64911 17.18175 17.02605

H 5.44576 16.24698 16.47049

C 6.81601 17.28241 17.81512

H 7.50976 16.42414 17.87926

C 10.75077 13.78786 18.01686

H 10.93534 14.27551 17.03312

H 10.83762 12.68373 17.88254

C 9.34694 14.16665 18.56378

H 9.23059 13.75647 19.59458

H 9.30628 15.28056 18.64025

C 8.23433 13.64153 17.65903

C 7.40322 12.57002 18.07556

H 7.55566 12.12977 19.08031

C 6.41447 12.04075 17.21288

H 5.78711 11.19547 17.55060

C 6.24002 12.58248 15.91791

H 5.46976 12.16775 15.24208

C 7.06390 13.65334 15.49116

H 6.93905 14.08577 14.48031

C 8.05032 14.18303 16.35574

H 8.69161 15.01867 16.00809

C 19.30584 21.64332 12.72996

H 19.89030 22.49633 13.13492

H 19.81810 20.70218 13.01783

C 19.19516 21.72593 11.18793

H 18.69984 22.67922 10.88878

H 18.55424 20.88530 10.83111

C 20.59701 21.62644 10.58646

C 21.34551 22.78745 10.26144

H 20.88194 23.78445 10.38910

C 22.66432 22.68302 9.76228

H 23.23200 23.59676 9.50677

C 23.25696 21.41154 9.58256

H 24.27788 21.32860 9.16764

C 22.52294 20.24632 9.91198

H 22.97095 19.24690 9.75806

C 21.20665 20.35337 10.41556

H 20.63818 19.43918 10.67589

C 20.82566 19.51429 17.69784

H 21.02549 18.69646 18.42977

H 20.95385 19.09468 16.67661

C 21.79514 20.70744 17.94689

H 21.61086 21.12937 18.96282

H 22.83337 20.29276 17.93722

C 21.67572 21.80216 16.88693

C 20.84763 22.93813 17.08634

H 20.31199 23.05973 18.04650

C 20.70375 23.91003 16.06761

H 20.05848 24.79183 16.24008

C 21.38836 23.76173 14.83863

H 21.27595 24.52202 14.04307

C 22.21982 22.63466 14.63113

H 22.75471 22.50423 13.67001

C 22.36197 21.66658 15.65075

H 23.02447 20.79885 15.48996

C 13.45487 19.15228 11.44366

H 12.64980 18.41934 11.19977

H 13.28386 19.54460 12.47138

C 13.49962 20.30634 10.40449

H 14.45241 20.86851 10.55592

H 13.53563 19.87199 9.37862



C 12.32672 21.27540 10.52958

C 11.23602 21.23806 9.62327

H 11.21059 20.45979 8.83731

C 10.20120 22.19956 9.69268

H 9.36944 22.16705 8.96490

C 10.24605 23.21626 10.67290

H 9.45423 23.98611 10.71066

C 11.30918 23.24024 11.60858

H 11.34606 24.02890 12.38294

C 12.33543 22.27229 11.54382

H 13.17076 22.29695 12.27211

C 10.46193 18.42008 14.48905

H 10.35292 18.87067 15.50048

H 11.31700 18.93062 13.98946

C 9.14968 18.58365 13.67236

H 9.37537 18.44869 12.58769

H 8.43655 17.77851 13.96923

C 8.51901 19.94737 13.94657

C 7.50202 20.07307 14.93029

H 7.14079 19.17244 15.46279

C 6.93642 21.33484 15.22474

H 6.13668 21.41215 15.98233

C 7.39311 22.49111 14.55031

H 6.95257 23.47792 14.78116

C 8.41786 22.37754 13.58310

H 8.77682 23.27663 13.05259

C 8.97943 21.11469 13.28267

H 9.77638 21.03458 12.51984

C 11.70228 13.25234 10.69831

H 11.94174 12.79733 11.68080

H 10.61253 13.47939 10.66255

C 12.09749 12.25644 9.57106

H 11.72959 12.62973 8.58655

H 13.20964 12.19418 9.52005

C 11.50080 10.88851 9.91106

C 12.26602 9.93915 10.63880

H 13.32206 10.15675 10.86793

C 11.69200 8.72892 11.08790

H 12.31741 8.01282 11.65513

C 10.33390 8.44599 10.81357

H 9.87265 7.51116 11.17976

C 9.56513 9.37417 10.07071

H 8.50858 9.15094 9.83766

C 10.14486 10.58435 9.62289

H 9.53692 11.30914 9.04572

C 16.71634 11.62190 12.49989

H 17.71798 11.14891 12.63665

H 16.27397 11.79481 13.50841

C 15.78310 10.72188 11.64916

H 14.77183 11.19058 11.66724

H 16.13480 10.71363 10.59067

C 15.74090 9.29768 12.20220

C 16.51273 8.26571 11.60667

H 17.11655 8.49170 10.70625

C 16.52866 6.96273 12.15657

H 17.13847 6.17289 11.68010

C 15.77565 6.67072 13.31829

H 15.79293 5.65382 13.74981

C 15.00014 7.69009 13.92190

H 14.40834 7.47967 14.83425

C 14.97958 8.99010 13.36411

H 14.36879 9.77458 13.84740

C 17.41783 9.81772 16.27737

H 16.98398 9.97067 15.26490

H 16.58271 9.62387 16.98880

C 18.40927 8.61958 16.28544

H 18.79850 8.47158 17.32083

H 17.82402 7.70719 16.01043

C 19.57570 8.80268 15.31655

C 19.36899 8.66358 13.91798

H 18.37643 8.35795 13.53837

C 20.41540 8.92509 13.00458

H 20.23247 8.83020 11.91778

C 21.69164 9.31139 13.47878

H 22.51190 9.51424 12.76374

C 21.91348 9.43655 14.86972

H 22.90562 9.73455 15.25302

C 20.85782 9.19286 15.78179

H 21.03115 9.32738 16.86690

C 22.44466 13.04553 13.81790

H 22.65427 12.05545 14.27949

H 22.39633 13.80603 14.62880

C 23.55546 13.41860 12.79960

H 23.27990 14.37233 12.29169

H 23.62353 12.62898 12.01626

C 24.88524 13.56031 13.53648

C 25.79269 12.47392 13.62816

H 25.56978 11.53227 13.08865

C 26.96645 12.57746 14.41023

H 27.66481 11.72279 14.47077

C 27.24505 13.76549 15.12550

H 28.15187 13.83856 15.75368

C 26.35457 14.86206 15.02816

H 26.56001 15.80260 15.57321

C 25.19076 14.75929 14.23476

H 24.51216 15.62922 14.15776

C 21.12533 18.24056 13.87415

H 20.93046 17.80314 14.87897

H 21.04871 19.34979 13.95422

C 22.53108 17.82421 13.36999

H 22.68279 18.18734 12.32733

H 22.56457 16.70795 13.34428

C 23.62521 18.36944 14.28138

C 24.47542 19.42081 13.85174

H 24.34326 19.84461 12.83673

C 25.46733 19.94372 14.71447

H 26.12119 20.76321 14.36547

C 25.62391 19.41806 16.01807

H 26.39888 19.82555 16.69248

C 24.77342 18.37434 16.45869

H 24.88217 17.95705 17.47704

C 23.78203 17.85184 15.59718

H 23.11911 17.03798 15.95507

C 12.68621 10.54580 19.42781

H 12.07729 9.69453 19.05335

H 12.18627 11.49359 19.13963

C 12.83866 10.48587 20.96733

H 13.32953 9.52872 21.26481

H 13.49457 11.32516 21.29855

C 11.45187 10.61287 21.59668

C 10.65456 9.46690 21.85541

H 11.06879 8.45929 21.65524

C 9.34756 9.59931 22.37812

H 8.74560 8.69741 22.59342

C 8.81137 10.88381 22.62969

H 7.79615 10.98788 23.05283

C 9.59353 12.03336 22.36154

H 9.18307 13.04044 22.56193

C 10.90381 11.90029 21.84806

H 11.51387 12.80029 21.63853

C 11.14928 12.50915 14.34541

H 10.94353 13.31218 13.59827

H 10.99808 12.93893 15.35828

C 10.21282 11.28871 14.09596

H 10.42184 10.86554 13.08500

H 9.16270 11.67429 14.09500

C 10.35511 10.20237 15.16213

C 11.20657 9.08226 14.97097

H 11.73781 8.95827 14.00847

C 11.37887 8.12558 15.99959

H 12.04820 7.26040 15.83540

C 10.69832 8.27181 17.23072

H 10.83493 7.52393 18.03407

C 9.84257 9.38197 17.42908

H 9.31266 9.51080 18.39281

C 9.67478 10.33765 16.40077

H 8.99970 11.19776 16.55701

C 18.65709 12.83769 20.57951

H 19.49842 13.54152 20.79160

H 18.78106 12.43229 19.54959

C 18.60963 11.69577 21.63356

H 17.64675 11.14604 21.49963



H 18.58863 12.14896 22.65205

C 19.76706 10.70889 21.51608

C 20.87448 10.75725 22.40144

H 20.91929 11.55138 23.17038

C 21.90233 9.78756 22.33173

H 22.74926 9.82792 23.04130

C 21.83456 8.75656 21.36838

H 22.62356 7.98337 21.32790

C 20.75491 8.72127 20.45259

H 20.70618 7.92992 19.68211

C 19.73419 9.69409 20.52130

H 18.88622 9.65974 19.80849

C 21.48213 13.63269 17.59474

H 21.56318 13.18671 16.57827

H 20.63358 13.12865 18.11007

C 22.81361 13.45254 18.37644

H 22.61865 13.58213 19.46778

H 23.52763 14.25094 18.06471

C 23.42634 12.08513 18.07887

C 24.43757 11.96245 17.08811

H 24.80357 12.86520 16.56212

C 24.98897 10.69860 16.77521

H 25.78212 10.62407 16.01089

C 24.52525 9.53833 17.43656

H 24.95448 8.54919 17.19124

C 23.50557 9.64941 18.40977

H 23.13892 8.74844 18.93014

C 22.96153 10.91444 18.73397

H 22.17104 10.99268 19.50433

C 20.18389 18.81445 21.32996

H 19.93508 19.25198 20.34157

H 21.27185 18.57561 21.35048

C 19.82823 19.83985 22.44274

H 20.21571 19.48388 23.42579

H 18.72001 19.92245 22.52600

C 20.43413 21.19466 22.06311

C 19.66522 22.14325 21.33825

H 18.60646 21.92961 21.12126

C 20.23866 23.34978 20.87857

H 19.60762 24.06898 20.32271

C 21.60134 23.62909 21.13560

H 22.05891 24.56406 20.76351

C 22.37810 22.69684 21.86381

H 23.44012 22.91468 22.07933

C 21.79748 21.49192 22.32425

H 22.41455 20.76772 22.89057

C 15.19382 20.42813 19.57118

H 14.20432 20.92010 19.41829

H 15.64646 20.24271 18.56889

C 16.12944 21.32016 20.42804

H 17.13416 20.83846 20.42515

H 15.76563 21.33947 21.48224

C 16.19649 22.73866 19.86864

C 15.44141 23.78596 20.45827

H 14.83994 23.57645 21.36391

C 15.43660 25.08320 19.89511

H 14.84313 25.88642 20.36851

C 16.19115 25.35368 18.72904

H 16.18517 26.36636 18.28636

C 16.95201 24.31782 18.13339

H 17.54077 24.50689 17.21509

C 16.95517 23.02333 18.70114

H 17.54869 22.22343 18.22294

O 14.09004 14.53155 21.52918

O 14.55362 15.51058 20.79662



## References

1. Gong, J.; Mullins, C. B. Surface Science Investigations of Oxidative Chemistry on Gold. *Acc. Chem. Res.* **2009**, *42*, 1063-1073.
2. Kim, J.; Samano, E.; Koel, B. E. Oxygen Adsorption and Oxidation Reactions on Au(2 1 1) Surfaces: Exposures Using O<sub>2</sub> at High Pressures and Ozone (O<sub>3</sub>) in UHV. *Surf. Sci.* **2006**, *600*, 4622-4632.
3. Xu, Y.; Mavrikakis, M. Adsorption and Dissociation of O<sub>2</sub> on Gold Surfaces: Effect of Steps and Strain. *J. Phys. Chem. B* **2003**, *107*, 9298-9307.
4. Okamoto, Y. Density-functional Calculations of Atomic and Molecular Adsorptions on 55-atom Metal Clusters: Comparison with (1 1 1) Surfaces. *Chem. Phys. Lett.* **2005**, *405*, 79-83.
5. Roldan, A.; Ricart, J. M.; Illas, F.; Pacchioni, G. O<sub>2</sub> Adsorption and Dissociation on Neutral, Positively and Negatively Charged Au<sub>n</sub> (n = 5-79) clusters. *Phys. Chem. Chem. Phys.* **2010**, *12*, 10723-10729.



Cite this: *Nanoscale*, 2018, **10**, 15714

# Preparation of gas phase naked silver cluster cations outside a mass spectrometer from ligand protected clusters in solution†

Madhuri Jash,<sup>a</sup> Arthur C. Reber,<sup>b</sup> Atanu Ghosh,<sup>a</sup> Depanjan Sarkar,<sup>a</sup> Mohammad Bodiuzzaman,<sup>a</sup> Pallab Basuri,<sup>a</sup> Ananya Bakshi,<sup>a</sup> Shiv N. Khanna <sup>\*b</sup> and Thalappil Pradeep <sup>\*a</sup>

Gas phase clusters of noble metals prepared by laser desorption from the bulk have been investigated extensively in a vacuum using mass spectrometry. However, such clusters have not been known to exist under ambient conditions to date. In our previous work, we have shown that in-source fragmentation of ligands can be achieved starting from hydride and phosphine co-protected silver clusters leading to naked silver clusters inside a mass spectrometer. In a recent series of experiments, we have found that systematic desorption of ligands of the monolayer protected atomically precise silver cluster can also occur in the atmospheric gas phase. Here, we present the results, wherein the  $[\text{Ag}_{18}\text{H}_{16}(\text{TPP})_{10}]^{2+}$  (TPP = triphenylphosphine) cluster results in the formation of the naked cluster,  $\text{Ag}_{17}^{+}$  along with  $\text{Ag}_{18}\text{H}^{+}$  without mass selection, outside the mass spectrometer, in air. These cationic naked metal clusters are prepared by passing electrosprayed ligand protected clusters through a heated tube, in the gas phase. Reactions with oxygen suggest  $\text{Ag}_{17}^{+}$  to be more reactive than  $\text{Ag}_{18}\text{H}^{+}$ , in agreement with their electronic structures. The more common thiolate protected clusters produce fragments of metal thiolates under identical processing conditions and no naked clusters were observed.

Received 22nd May 2018,

Accepted 16th July 2018

DOI: 10.1039/c8nr04146f

rsc.li/nanoscale

## Introduction

Atomically precise clusters of noble metals composed of a metal core and a ligand shell, with precise composition, structure and properties also referred to as aspicules, have been one of the most expanding areas of nanomaterials science in the recent past.<sup>1–7</sup> For monolayer protected clusters, to observe substantial catalytic activity, complete removal of the protecting ligands is essential which has been difficult for solution phase synthesized clusters. In 1986, Schmid and Klein first reported the formation of ligand free  $\text{M}_{13}$  ( $\text{M} = \text{Au}, \text{Rh}, \text{Ru}$ ) clusters from ligand stabilized  $\text{M}_{55}$  clusters by electrophoresis.<sup>8</sup> The catalytic properties of such clusters due to electronic confinement as well as unique geometry have been explored in the supported form.<sup>9–13</sup> Getting ligand free metal cores on solid supports by using high temperature often results in broad particle size distributions with the loss of atomicity.<sup>14</sup> On the other hand, these solution phase ligand protected clusters have shown their systematic fragmentation in a vacuum, often leading to metal ligand fragments in mass spectrometric studies.<sup>15–17</sup> While sequential loss of ligands producing small metal clusters is likely, no intact cluster core has been observed so far in ambient air.

<sup>a</sup>DST Unit of Nanoscience (DST UNS) and Thematic Unit of Excellence (TUE), Department of Chemistry, Indian Institute of Technology Madras, Chennai 600 036, India. E-mail: pradeep@iitm.ac.in

<sup>b</sup>Department of Physics, Virginia Commonwealth University, Richmond, Virginia 23284, USA. E-mail: snkhanna@vcu.edu

†Electronic supplementary information (ESI) available: Photograph of the instrumental set-up; characterization of  $[\text{Ag}_{18}\text{H}_{16}(\text{TPP})_{10}]^{2+}$  and  $[\text{Ag}_{18}\text{D}_{16}(\text{TPP})_{10}]^{2+}$  clusters; comparison between the experimental and the calculated spectra; formation of  $\text{Ag}_{17}^{+}$  from both  $\text{Ag}_{17}\text{H}_{14}^{+}$  and  $\text{Ag}_{17}\text{D}_{14}^{+}$ ; a full range ESI mass spectra of the  $[\text{Ag}_{18}\text{H}_{16}(\text{TPP})_{10}]^{2+}$  cluster during heating and comparison at different capillary and tube lens voltages; a full range ESI mass spectra of the  $[\text{Ag}_{18}\text{H}_{16}(\text{TPP})_{10}]^{2+}$  cluster during heating at a higher capillary and tube lens voltages; ion chronograms of selected ions;  $\text{MS}^2$  for  $\text{Ag}_{17}^{+}$ ,  $\text{Ag}_{17}\text{H}_{14}^{+}$  and  $\text{Ag}_{18}\text{H}^{+}$  ions; thermal dissociation of the thiolate protected cluster under the same experimental conditions; the effect of distance between the heating tube and the ESI source; a photograph of the instrumental set-up and a diagram used for ion/molecule reactions; comparison of the oxygen addition reaction of naked clusters with  $\text{CD}_3\text{OD}$  as the solvent and with the deuterated analogue of  $[\text{Ag}_{18}\text{H}_{16}(\text{TPP})_{10}]^{2+}$ ; comparison of the reactivity between  $\text{Ag}_{17}^{+}$  and  $\text{Ag}_{18}\text{H}^{+}$  ions with oxygen;  $\text{MS}^2$  of  $\text{Ag}_{17}\text{H}_4\text{O}^{+}$ ,  $\text{Ag}_{17}\text{H}_4\text{O}_2^{+}$ ,  $\text{Ag}_{17}\text{H}_4\text{O}_3^{+}$  and  $\text{Ag}_{17}\text{H}_4\text{O}_4^{+}$  ions; comparison of the  $\text{MS}^2$  results of  $\text{Ag}_{17}(\text{H}_2\text{O})_2\text{O}_2^{+}$  and  $\text{Ag}_{17}\text{H}_4\text{O}_4^{+}$  ions; TEM images of the  $[\text{Ag}_{18}\text{H}_{16}(\text{TPP})_{10}]^{2+}$  cluster and the electrosprayed products collected; calculated structures of  $\text{Ag}_{15}^{+}$ ,  $\text{Ag}_{17}^{+}$ ,  $\text{Ag}_{18}^{+}$  and  $\text{Ag}_{18}\text{H}^{+}$  ions; isomers of  $\text{Ag}_{18}\text{H}^{+}$  and their energies; experimental and calculated masses measured by using the LTQ and G2-Si (PDF). See DOI: 10.1039/c8nr04146f

From the early 1970s, the production and reaction of free gas phase clusters have been demonstrated by using various cluster sources, using laser vaporization, ion traps, flow-tube reactors and improved mass spectrometers. Detailed information on the structural and electronic properties of gas phase naked clusters (NCs) validates their distinct character, much different from ligand protected metal clusters in the free and supported forms.<sup>18,19</sup> The reactivity of NCs not only depends on their charge, size and intrinsic activity but also on the chemisorption, bond cleavage energy and polarity of the reacted molecules.<sup>18,20</sup> But to obtain the specific catalytic activity of a gas phase cluster, with particular atomicity, mass selection is needed to obtain satisfactory precision.

Although smaller naked metal clusters have been prepared by various processes such as thermal desorption, sputtering, laser desorption and electrospray ionization, starting from bulk metals or salts, no monolayer protected cluster was used for such investigations before. Recently, Whetten and Brodbelt have shown that by using deep UV irradiation at 193 nm (6.4 eV), NCs like  $\text{Au}_4^+$  to  $\text{Au}_{20}^+$  can be formed along with their ligand-containing product ions within the mass spectrometer in a vacuum starting from ligand protected gold clusters,  $\text{Au}_{25}(\text{SR})_{18}$  and  $\text{Au}_{36}(\text{SR})_{24}$ .<sup>21</sup> The inherent instability of the intact cluster core and the stability of the metal thiolate complexes make the observation of the intact cluster core difficult.<sup>22–24</sup> Extensive mass spectrometric studies have been conducted on ligated (mainly diphosphine) silver hydride nanoclusters by the O'Hair group, which show that all hydrides can be removed as  $\text{H}_2$  but complete removal of other ligands is not possible even using a laser.<sup>25,26</sup> Also, there have been extensive studies on the synthesis and reactivity of copper, silver and gold hydride complexes.<sup>27</sup> The recent identification of hydride and phosphine co-protected clusters of silver<sup>28</sup> and the weak ligand–metal interaction in such systems made us explore the formation of silver NCs within a mass spectrometer by in-source fragmentation and the results of these studies have been reported recently.<sup>29</sup> In our current experiment, we have observed that thermal activation of the electrosprayed cluster  $[\text{Ag}_{18}\text{H}_{16}(\text{TPP})_{10}]^{2+}$  produced highly monodispersed NC ions,  $\text{Ag}_{17}^+$  and  $\text{Ag}_{18}\text{H}^+$  in the atmospheric gas phase. The ability to create such atomically precise pieces of metals outside a mass spectrometer will allow the exploration of their unknown chemistry, glimpses of such studies are also presented here. We note that the method of atmospheric pressure thermal dissociation was first introduced to make peptide and protein ions.<sup>30,31</sup> Then the method was extended to silver salts where extremely small clusters such as  $\text{Ag}_3^+$  and  $\text{Ag}_7^-$  were produced during mass spectrometric analysis, by varying the source parameters.<sup>32</sup> Such methods have never been applied to monolayer protected atomically precise metal clusters.

Compared to the bulk and monolayer protected silver clusters, NCs can have a very different chemical reactivity due to their unique electronic and geometric structures.<sup>33,34</sup> Density functional theory (DFT) calculations have shown that the dissociation of molecular oxygen was favored in larger sized silver

NCs.<sup>35</sup> Electronic states in metallic clusters including silver clusters can be rationalized using the model of confined nearly free electron gas. For compact clusters, such a description leads to the grouping of states into shells that can be labelled as 1S, 1P, 1D, 2S, *etc.*, much in the same way as in atoms.<sup>36</sup> The numbers and upper case letters indicate the principal and angular momentum quantum numbers of the delocalized orbitals. The ground state of oxygen is a spin triplet and any activation of the oxygen molecule requires a virtual spin excitation of the cluster to accommodate the spin.<sup>37,38</sup> For clusters with singlet ground states such a spin accommodation requires a spin excitation from the singlet to the triplet configuration whose energy is determined by the gap between the highest occupied molecular orbital (HOMO) and the lowest unoccupied molecular orbital (LUMO). Consequently, clusters with a high HOMO–LUMO gap are resistant to reactions with oxygen. Here we show that the dissociation of molecular oxygen and its attachment with  $\text{Ag}_{17}^+$  happen due to the preferred HOMO–LUMO gap in the metal core. In contrast,  $\text{Ag}_{18}\text{H}^+$  shows resistance to the reaction with oxygen due to the cluster's comparatively high HOMO–LUMO gap.

## Experimental section

### Reagents and materials

Silver nitrate ( $\text{AgNO}_3$ , 99.9%) was purchased from Rankem India, triphenylphosphine (TPP, 99%), sodium borohydride ( $\text{NaBH}_4$ , 98%), sodium borodeuteride ( $\text{NaBD}_4$ , 98 atom% D) and methanol- $\text{d}_4$  ( $\text{CD}_3\text{OD}$ , 99.8 atom% D) were purchased from Sigma-Aldrich and used without further purification. HPLC grade methanol (MeOH) was from Finar chemicals and analytical grade chloroform ( $\text{CHCl}_3$ ) was from Rankem India. All the chemicals were used without further purification unless otherwise mentioned. Millipore water, obtained from Milli-Q (Millipore apparatus) with a resistivity of 18.2 M $\Omega$  cm, was used for all the experiments.

### Synthesis

The cluster  $[\text{Ag}_{18}\text{H}_{16}(\text{TPP})_{10}]^{2+}$  was synthesized by using a small modification of the reported method by Bootharaju *et al.*<sup>28</sup> In the first step, the silver precursor (20 mg of  $\text{AgNO}_3$ ) was taken in 5 mL of MeOH in a 100 mL round bottom flask and 70 mg of triphenylphosphine solution in 10 mL of chloroform was added under stirring at room temperature. After 20 minutes of reaction, 6 mg of  $\text{NaBH}_4$  in 0.5 mL of ice cold Millipore water was added. After the addition of  $\text{NaBH}_4$ , the color changed immediately from colorless to light yellow. To avoid any further oxidation of silver, the entire synthesis procedure was carried out under dark conditions. Over three hours of continuous stirring under dark conditions, the light yellow reaction mixture became dark green which indicated the formation of the  $[\text{Ag}_{18}\text{H}_{16}(\text{TPP})_{10}]^{2+}$  cluster. The solution was vacuum evaporated at room temperature and then to remove the excess silver precursor and  $\text{NaBH}_4$ , 20–22 mL cold Millipore water was added to the residue and the mixture was

sonicated for 2 minutes. After sonication, the solution was centrifuged at 3000 rpm for 5 minutes and a residue was separated. The supernatant containing soluble impurities was discarded and the precipitate consisting of the  $[\text{Ag}_{18}\text{H}_{16}(\text{TPP})_{10}]^{2+}$  cluster was dissolved in 10 mL methanol and the solution was rotavaporated at room temperature to make a dry sample. The solid green sample was collected and dissolved in 2 mL methanol and centrifuged for 5 minutes at 5000 rpm to remove excess TPP ligands. The deep green  $[\text{Ag}_{18}\text{H}_{16}(\text{TPP})_{10}]^{2+}$  cluster solution was used for further characterization. For mass spectrometry experiments, 100  $\mu\text{L}$  of the green solution was diluted to 1 mL with methanol. For synthesizing the deuterated  $\text{Ag}_{18}$  analogue, a similar method was followed by replacing  $\text{NaBH}_4$  with  $\text{NaBD}_4$ .

### Instrumentation

UV-vis spectra of nanoclusters were recorded using a PerkinElmer Lambda 25 UV-Vis spectrometer. Absorption spectra were typically obtained in the range of 200–1100 nm with a band pass filter of 1 nm. The high resolution mass spectra of  $[\text{Ag}_{18}\text{H}_{16}(\text{TPP})_{10}]^{2+}$  and  $[\text{Ag}_{18}\text{D}_{16}(\text{TPP})_{10}]^{2+}$  were recorded using a Waters Synapt G2-Si High Definition Mass Spectrometer (abbreviated as G2-Si subsequently) equipped with an electrospray ionization (ESI) source. This mass spectrometer is a combination of an electrospray source, quadrupole ion guide/trap, ion mobility cell and TOF analyzer. These cluster samples were prepared in methanol and were infused into the instrument at a flow rate of 30  $\mu\text{L min}^{-1}$ . The capillary voltage was kept at 2 kV and to avoid any in-source fragmentation, both the cone voltage and source offset were kept at 0 V. All other experiments, including the characterization of NCs described in this paper were carried out by using Thermo Scientific LTQ XL Linear Ion Trap Mass Spectrometer (abbreviated as LTQ subsequently) with a home-built nano-ESI source. A photograph of the instrumental set-up is shown in ESI S1.† The LTQ mass spectrometer is a combination of electrospray source, ion sweep cone, ion transfer capillary, quadrupole, octapole and two-dimensional linear ion trap. The following instrumental parameters were used throughout the experiments to get a good ion signal without fragmentation. Solvent: methanol; flow rate: 3  $\mu\text{L min}^{-1}$ ; ionization spray voltage: 3 kV; capillary voltage (abbreviated as CV): 45 V and tube lens voltage (abbreviated as TV): 100 V. All the mass spectrometric measurements were recorded in the positive ion mode. Tandem mass spectrometric (MS/MS or  $\text{MS}^2$ ) measurements were performed by using ultra high-pure helium gas (99.995%) in the LTQ mass spectrometer. In the MS/MS studies, mass selected ions were fragmented in the ion trap by colliding with helium. During the CID or  $\text{MS}^2$  experiments, the injection time was 300 ms and 5 microscans were averaged with an activation time (time for which the resonance excitation RF voltage was applied) of 30 ms. An activation Q value of 0.25 was applied and the isolation width and collision energy were optimized according to the particular precursor ion. Transmission electron microscopy (TEM) and high-resolution transmission electron microscopy (HRTEM) were performed

using a JEOL 3010, 300 kV instrument at an accelerating voltage of 200 kV. A lower accelerating voltage was used to reduce beam-induced damage. Energy dispersive spectra (EDS) were collected using an Oxford Semistem system equipped with the TEM. Samples were dropcast onto carbon-coated copper grids, 300-mesh, (spi Supplies, 3530C-MB) and dried under ambient conditions before examining under TEM.

### Theoretical methods

Theoretical studies on the electronic and geometric structures of the silver clusters were performed using first principles methods with the Amsterdam density functional (ADF) code.<sup>39</sup> A generalized gradient approximation (GGA) functional proposed by Perdew, Burke, and Ernzerhof (PBE) was used to incorporate the exchange and correlation effects.<sup>40</sup> Slater-type orbitals (STO) located at the atomic sites were used to express the atomic wave function, and the cluster wave functions were formed *via* a linear combination of these atomic orbitals. The studies used a TZ2P basis set and a large frozen electron core.<sup>41</sup> The total energies and the forces at the atomic sites were computed and a quasi-Newton method was used to optimize the structures without any symmetry restriction. The energy of the clusters with different spin multiplicities was also calculated to identify the lowest energy structure. Scalar-relativistic effects were included *via* zero-order regular approximation (ZORA).<sup>42</sup> Time-dependent density functional theory, TDDFT, was used to confirm the accuracy of the HOMO–LUMO gaps.

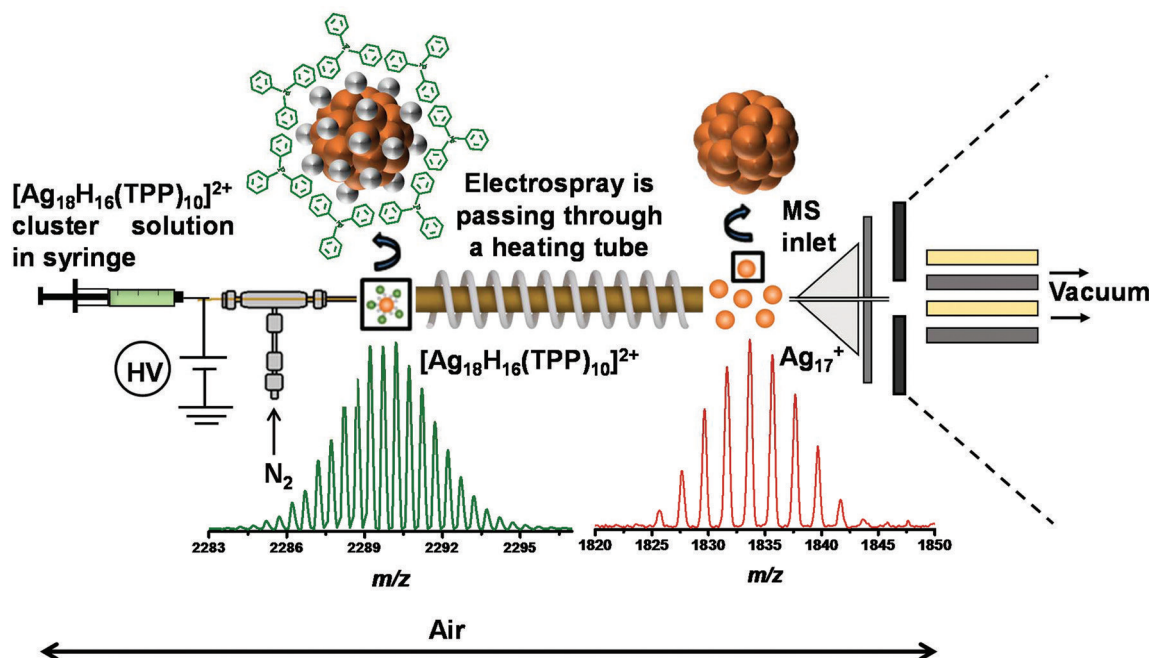
## Results and discussion

In a typical experiment, the monolayer protected cluster  $[\text{Ag}_{18}\text{H}_{16}(\text{TPP})_{10}]^{2+}$  was prepared as reported previously with some modifications in the synthetic procedure (details are presented in the Experimental section).<sup>28</sup> All the characteristic features in the UV-vis spectrum along with the isotopically resolved peak of the molecular ion,  $[\text{Ag}_{18}\text{H}_{16}(\text{TPP})_{10}]^{2+}$  in the electrospray ionization high resolution mass spectrum (ESI HRMS) confirm the identity and purity of the cluster (details are in the ESI†). The cluster solution is green in color and it shows two peaks in absorption spectroscopy at 545 and 614 nm with a shoulder at 444 nm (Fig. S2(A)†). The mass spectrum shows a sharp peak at  $m/z$  2290 in the  $m/z$  1100–5000 window. Expansion of the high resolution mass spectrum shows the isotopic separation of  $m/z$  0.5 due to the 2+ charge state of the parent cluster  $[\text{Ag}_{18}\text{H}_{16}(\text{TPP})_{10}]^{2+}$ , matching exactly with the calculated one shown in the corresponding inset (Fig. S2(B) and (C)†). The composition of the cluster was further established using G2-Si by changing the  $\text{NaBH}_4$  used for the synthesis to  $\text{NaBD}_4$ , where the hydride ions are replaced by deuteride ions forming  $[\text{Ag}_{18}\text{D}_{16}(\text{TPP})_{10}]^{2+}$  (Fig. S3†). Due to this replacement, there was a shift in the peak position ( $\Delta m/z = 8$ , where  $\Delta m$  is 16 and  $z$  is +2). Electrosprayed cluster ions were passed through a heating tube to create NCs, which were analyzed using the nano-ESI mode of the LTQ mass spectrometer.

As the G2-Si mass spectrometer could not be modified to fit the new ion source, prepared outside the mass spectrometer by electrospraying the monolayer protected cluster, needed to conduct these experiments, we have used our LTQ mass spectrometer to detect NCs. A schematic of the set-up is shown in Fig. 1. The heating tube was made of copper (outer diameter 1/8" and inner diameter 0.066") with a total length of 50 cm. This copper tube was wrapped with a heating coil connected to a variable resistance transformer. The exit of the ESI source was inside the heating tube so that the maximum ion signal could be obtained. The distance between the heating tube and the inlet of the LTQ mass spectrometer was approximately 5 mm and could be varied. Electrospray of the cluster solution was performed at a voltage of +3 kV with N<sub>2</sub> as the nebulizing gas (25 psi pressure). This voltage is important to get a stable ion signal in the mass spectrometer. The temperature of the heating tube was controlled to get the desired species. The ions exiting the heating tube were analyzed using the LTQ mass spectrometer in positive mode under the following conditions to obtain the optimized peak intensities: capillary temperature, 250 °C; CV, +45 V; TV, +100 V and flow rate, 3  $\mu\text{L min}^{-1}$ . At lower values of the instrumental parameters, the peak intensity was less due to inefficient ionization. On increasing the values of spray voltage (+3 kV) and flow rate (3  $\mu\text{L min}^{-1}$ ), there was no change in peak intensity keeping all other factors the same. The typical injection time was 100 ms and 5 micro scans were averaged to get a good spectrum in all the experiments. To perform the ion/molecule reaction exclusively with O<sub>2</sub> gas, the ions were passed through a

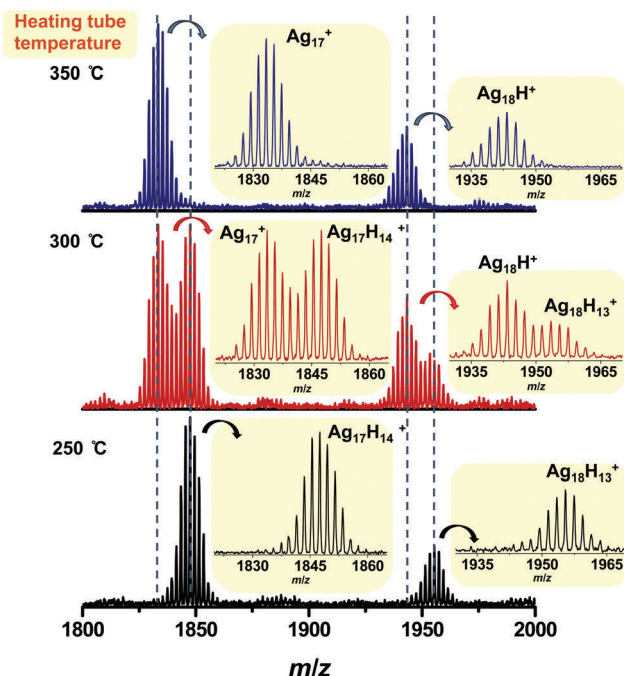
Swagelok coupling with different flow rates of O<sub>2</sub> gas. Here, electrospray plays a very important role in the success of the experiment. Without electrospray, we were not able to prepare these NCs in the gas phase and also study their gas phase reactions.

Continuous monitoring of the mass spectra at various temperatures of the heating tube shows a systematic loss of ligands and the formation of Ag NCs as shown in Fig. 2. Each ion exhibited an isotopically resolved mass spectrum which matched perfectly with its corresponding calculated pattern (Fig. S4†). Here the isotopic distribution is mainly due to silver and not due to hydrogen. This is because <sup>107</sup>Ag and <sup>109</sup>Ag isotopes of silver are present in almost similar natural abundances (<sup>107</sup>Ag, 51.839% and <sup>109</sup>Ag, 48.161%) but in the case of hydrogen, <sup>1</sup>H has a very high natural abundance (99.98%) in comparison with <sup>2</sup>H and <sup>3</sup>H. The parent cluster [Ag<sub>18</sub>H<sub>16</sub>(TPP)<sub>10</sub>]<sup>2+</sup> lost the phosphine instantaneously and formed the clusters, Ag<sub>17</sub>H<sub>14</sub><sup>+</sup> and Ag<sub>18</sub>H<sub>13</sub><sup>+</sup>, with peaks centered at *m/z* 1847 and 1955, respectively. During this conversion process, the charge state of the cluster ion changes from 2+ to 1+ which is confirmed by the isotopic separation of *m/z* 2 in the resulting cluster ion. Then gradual loss of hydrogen was observed in the mass spectra keeping the charge state constant at 1+ and finally the species Ag<sub>17</sub><sup>+</sup> and Ag<sub>18</sub><sup>+</sup> were the end products seen, centered at *m/z* 1833 and 1943, respectively. The ion observed and their charge states can be largely understood from their closed electronic shells. Ag<sub>18</sub>H<sup>+</sup> (45%) and Ag<sub>17</sub><sup>+</sup> (100%) were the only ions in the mass spectrum in the 1100–2000 *m/z* window. Compared to our previous work where



**Fig. 1** Schematic representation of the experimental set-up where the naked cluster, Ag<sub>17</sub><sup>+</sup> was prepared in air by electrospraying the monolayer protected cluster [Ag<sub>18</sub>H<sub>16</sub>(TPP)<sub>10</sub>]<sup>2+</sup> through a heated tube and the products were detected by a mass spectrometer. Schematic structures and experimental mass spectra of the corresponding cluster ions are shown in the inset showing that the parent ion is a dication (by using G2-Si) and the product is a monocation (by using LTQ). Isotopic separations are therefore *m/z* 0.5 and 2, respectively.





**Fig. 2** ESI mass spectra of the  $[\text{Ag}_{18}\text{H}_{16}(\text{TPP})_{10}]^{2+}$  cluster (using LTQ) with varying temperature of the heating tube. At 250 °C,  $\text{Ag}_{17}\text{H}_{14}^{+}$  and  $\text{Ag}_{18}\text{H}_{13}^{+}$  were detected. At 300 °C,  $\text{Ag}_{17}^{+}$  and  $\text{Ag}_{18}\text{H}^{+}$  were seen along with their hydride clusters and at 350 °C, only  $\text{Ag}_{17}^{+}$  and  $\text{Ag}_{18}\text{H}^{+}$  were seen. Isotopic distributions of these ions are shown in the inset.

only  $\text{Ag}_{17}^{+}$  was formed by in-source fragmentation of the parent cluster, here both  $\text{Ag}_{17}^{+}$  and  $\text{Ag}_{18}\text{H}^{+}$  appeared as a result of the thermal ligand desorption from the parent cluster, outside the mass spectrometer. The full range (150–2000  $m/z$ ) ESI mass spectra of this conversion process is shown in Fig. S5† where during heating, oxidation peaks of  $[\text{Ag}(\text{TPP})]^{+}$ ,  $[\text{Ag}(\text{TPP})_2]^{+}$  and  $\text{TPP}^{+}$  appear in the lower mass region. By this method, we could get both of these products ( $\text{Ag}_{17}^{+}$  and  $\text{Ag}_{18}\text{H}^{+}$ ) prepared outside the mass spectrometer, whereas to get selectively any one of these products in 100% relative abundance, we had to do mass selection. However, the ratio of  $\text{Ag}_{18}\text{H}^{+}$  to  $\text{Ag}_{17}^{+}$  could be changed depending on the transfer medium and the distance between the heating tube and the mass spectrometer inlet. Systematic loss of hydrogen occurs in the form of  $\text{H}_2$ , as revealed by tandem mass spectrometric studies. The formation of  $\text{Ag}_{18}\text{H}^{+}$  and  $\text{Ag}_{17}^{+}$  from the precursors,  $\text{Ag}_{18}\text{H}_{13}^{+}$  and  $\text{Ag}_{17}\text{H}_{14}^{+}$  proceed through the loss of 6 and 7 dihydrogen species, respectively, as shown by independent studies.<sup>29</sup> The conversion process was also studied starting with  $[\text{Ag}_{18}\text{D}_{16}(\text{TPP})_{10}]^{2+}$  instead of  $[\text{Ag}_{18}\text{H}_{16}(\text{TPP})_{10}]^{2+}$ . The ESI mass spectrum shows the formation of  $\text{Ag}_{17}\text{D}_{14}^{+}$  centered at  $m/z$  1861, shifted by 14 mass units from  $\text{Ag}_{17}\text{H}_{14}^{+}$  ( $\Delta m/z = 14$ , where  $\Delta m$  is 14 and  $z$  is +1). The formation of  $\text{Ag}_{17}^{+}$  via  $\text{Ag}_{17}\text{D}_{14}^{+}$  confirms the reaction path (Fig. S6†). In the mass spectrum of  $\text{Ag}_{17}\text{D}_{14}^{+}$ , 100% exchange of hydrogen with deuterium was not there due to the presence of non-deuterated solvents in the synthesis procedure, which results in additional peaks of lower intensity.

**Table 1** Experiments under different instrumental conditions

Expt	Heating tube temp. (°C)	CV (V)	TV (V)	Results in between 1100–2000 $m/z$ window
1.a	Room temp.	45	100	No silver clusters were detected
1.b	Room temp.	140	240	$\text{Ag}_{17}\text{H}_{14}^{+}$ alone
2.a	250	45	100	$\text{Ag}_{17}\text{H}_{14}^{+}$ and $\text{Ag}_{18}\text{H}_{13}^{+}$
2.b	250	140	240	$\text{Ag}_{17}^{+}$ along with $\text{Ag}_{16}^{+}$ and $\text{Ag}_{15}^{+}$
3.a	350	45	100	$\text{Ag}_{17}^{+}$ and $\text{Ag}_{18}\text{H}^{+}$
3.b	350	140	240	$\text{Ag}_{17}^{+}$ and $\text{Ag}_{18}\text{H}^{+}$ were fragmented partially and appeared along with smaller core size naked silver clusters

These observations make us conclude that when ions were transferred from the atmosphere to vacuum, in-source fragmentation occurred at higher CV and TV (expt b), but not at our typical mass spectrometer parameters where CV and TV were set to 45 V and 100 V, respectively, (expt a). Full range mass spectra as a function of temperature at a CV and TV of up to 140 V and 240 V, respectively, are shown in Fig. S8.

To better understand the formation mechanism of clusters and the fragility of ions, experiments were performed at two sets of CV and TV (a and b) by keeping all other instrumental parameters the same. These conditions are labeled as 1, 2 and 3 in Table 1 and the data are shown in Fig. S7.† In one set, the CV and TV were typical instrument parameters, used for all other experiments and were set as 45 V and 100 V, respectively (a). In another set, the CV and TV were set as 140 V and 240 V, respectively (b).

Ion chromatograms and  $\text{MS}^2$  spectra of selected ions are shown in Fig. S9 and S10,† respectively. The  $\text{MS}^2$  spectra of  $\text{Ag}_{17}\text{H}_{14}^{+}$  and  $\text{Ag}_{18}\text{H}^{+}$  gave back the nearest stable NC,  $\text{Ag}_{17}^{+}$  as a result of the hydride and  $\text{AgH}$  loss, respectively. A similar kind of  $\text{AgH}$  loss from  $\text{Ag}_n\text{H}^{+}$  (where  $n = 2, 4$  and  $6$ ) was reported before.<sup>43</sup> Whereas the NC  $\text{Ag}_{17}^{+}$  itself gave smaller size NCs,  $\text{Ag}_{16}^{+}$  and  $\text{Ag}_{15}^{+}$ . It is noteworthy that  $\text{MS}^3$  of  $\text{Ag}_{17}\text{H}_{14}^{+}$  and  $\text{Ag}_{18}\text{H}^{+}$  also gave the smaller NCs of silver. The occurrence of  $\text{Ag}_{18}\text{H}^{+}$  instead of  $\text{Ag}_{18}^{+}$  in the product ions is due to the greater stability of the even-numbered electrons in the silver clusters as both Ag and H are one electron systems.<sup>44</sup> The same experiment with thiolate protected clusters (Fig. S11†) did not create any NCs due to the strong Ag–S bond compared to the weak Ag–P and Ag–H bonds.

NCs are expected to be highly reactive; however, we find that they can be transported through air, in the presence of the nebulizing  $\text{N}_2$  gas, without much loss in intensity at a separation of 5 mm between the NC source and the mass spectrometer. This is significant as the distance is  $8.4 \times 10^4$  times the mean free path of  $\text{N}_2$  at standard temperature and pressure (STP). The distance was kept at 5 mm due to the divergence of the ions exiting the heating tube limiting the number of ions collected by the mass spectrometer. The transfer length can be increased further by using a transfer tube, which confines the ions. Increasing the pressure of the nebulizing gas reduces the transmission loss which also helps in increasing the transfer length and we could increase the length this way to 10 cm.

Experiments were done by varying the distance between the heating tube and the MS inlet to study the reactions of  $\text{Ag}_{17}^{+}$

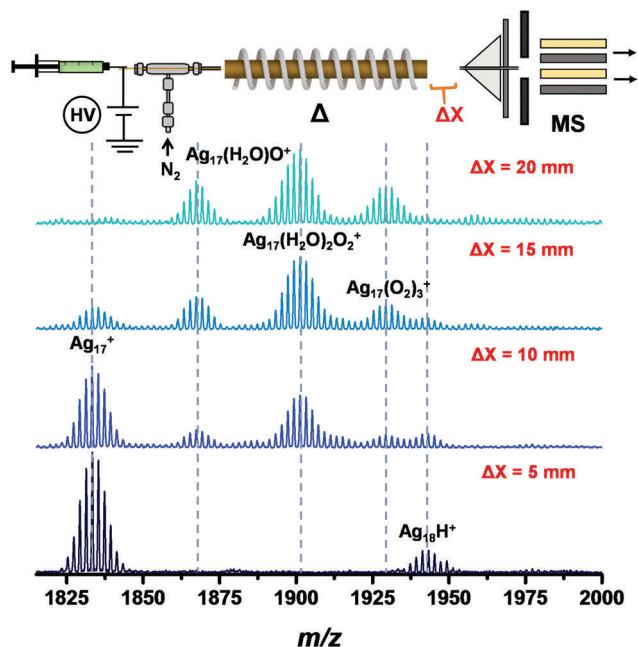


Fig. 3 ESI mass spectra of  $\text{Ag}_{17}^+$  upon varying the distance ( $\Delta X$ ) between the heating tube and the MS inlet (by a moving stage in the  $xy$  plane). The peaks observed are a combination of the  $(\text{H}_2\text{O})_m$  and  $(\text{O})_n$  additions on the naked cluster, which arise due to air.

with atmospheric constituents, at a nebulizer gas pressure of 25 psi (Fig. 3). The intensity of  $\text{Ag}_{17}^+$  decreased with the distance due to the additional products of oxygen and water present in the ambient environment. There were mixed oxygen and water addition peaks of  $\text{Ag}_{17}^+$  along with oxygen alone species. It was observed that the attachment of water happened only when there was prior oxygen attachment. It is known that water reacts only with pre-oxidized silver clusters of  $\text{Ag}_3^+$ ,  $\text{Ag}_5^+$ ,  $\text{Ag}_7^+$ , and  $\text{Ag}_9^+$ , formed by thermal decomposition of silver salts.<sup>32</sup> For  $\text{Ag}_{18}\text{H}^+$ , however, no ligation was observed which can be due to its high HOMO–LUMO gap. We also noticed that upon increasing the distance between the ESI source and the heating tube, as ambient air flowed through the heating tube,  $\text{Ag}_{17}\text{H}_{14}^+$  appeared back again. This result is attributed to the lower temperature within the heating tube, favorable for the formation of  $\text{Ag}_{17}\text{H}_{14}^+$  from the parent cluster,  $[\text{Ag}_{18}\text{H}_{16}(\text{TPP})_{10}]^{2+}$  (Fig. S12†).

Oxygen was crossed with the flowing mixture of  $\text{Ag}_{17}^+$  and  $\text{Ag}_{18}\text{H}^+$  and products as well as unreacted cluster ions were detected with the LTQ at different flow rates of oxygen, as shown in Fig. 4. A photograph and schematic diagram of this set-up used for ion/molecule reaction with oxygen are shown in S13.†  $\text{Ag}_{17}^+$  shows four oxygen adduct peaks (labeled 1 to 4) and  $\text{Ag}_{18}\text{H}^+$  shows three low intensity oxygen adduct peaks (labeled 1 to 3). For each adduct peak, the isotopic separation is  $m/z$  2, which confirms their 1+ charge state. At low temperature, nearly about 50 K,  $\text{O}_2$  adsorbs (molecular adsorption) on cationic silver clusters as demonstrated for  $\text{Ag}_2^+$ .<sup>45</sup> But for hot silver clusters, the absorbed molecular oxygen dissociates to atomic oxygen, resulting in  $\text{Ag}_n\text{O}^+$  from  $\text{Ag}_n\text{O}_2^+$ . Our results

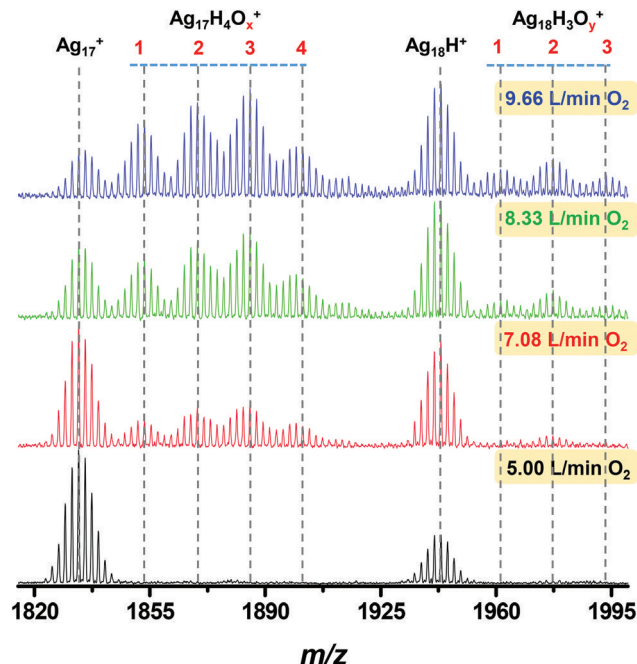


Fig. 4 ESI mass spectra of  $\text{Ag}_{17}^+$  and  $\text{Ag}_{18}\text{H}^+$  ion clusters after reaction with oxygen ( $\text{O}_2$ ) gas at different flow rates.

suggest the dissociative adsorption of oxygen which may be due to the higher temperature used for the preparation of NCs. Several reports studied the mechanism of oxygen adsorption on silver clusters along with their structures, depending on the number of silver atoms and temperature.<sup>46–49</sup> Schmidt *et al.* reported that due to the positive charge on silver clusters, the chemisorption of more than one oxygen molecule, an electron acceptor, is difficult on  $\text{Ag}_n^+$  clusters ( $n < 22$ ) at 77 K.<sup>50</sup> But in our experiments,  $\text{Ag}_{17}^+$  shows a maximum adsorption of two oxygen molecules outside the mass spectrometer, though there is an early report of the adsorption of a maximum of three oxygen molecules for  $\text{Ag}_2^+$  at 120 K.<sup>51</sup> During the oxidation of NCs, in the case of  $\text{Ag}_{17}^+$ , each oxygen atom addition is followed by four hydrogen atom additions and for the adducts of  $\text{Ag}_{18}\text{H}^+$ , there were two hydrogen atom additions. For a better understanding of the source of the hydrogens, we have performed experiments in two different ways. In the first case, we have prepared the  $[\text{Ag}_{18}\text{H}_{16}(\text{TPP})_{10}]^{2+}$  cluster and dissolved it in  $\text{CD}_3\text{OD}$  instead of  $\text{CH}_3\text{OH}$  to understand if there is any role of solvent in the hydrogen attachment. But here we did not observe any different result, as shown in Fig. S14,† which made us conclude that hydrogens are not coming from the solvent. In the second case, we have prepared  $[\text{Ag}_{18}\text{D}_{16}(\text{TPP})_{10}]^{2+}$  by using  $\text{NaBD}_4$  instead of  $\text{NaBH}_4$  and dissolved the product in  $\text{CH}_3\text{OH}$ . At a heating tube temperature of 350 °C, we observed  $\text{Ag}_{17}^+$  and  $\text{Ag}_{18}\text{D}^+$  as the NCs and then we performed the oxygen addition reaction. For  $\text{Ag}_{17}\text{H}_4\text{O}_x^+$  and  $\text{Ag}_{18}\text{H}_3\text{O}_y^+$ , no shifted peaks were seen (Fig. S15A†). However, for the  $\text{Ag}_{18}\text{H}_3\text{O}_y^+$  peaks, there was some minor contribution from the deuterated species too which appeared as low intense middle peaks, mainly visible for the  $\text{Ag}_{18}\text{H}_3\text{O}_2^+$  ion

(Fig. S15B†). These results made us conclude that water in the ambient environment or within the ion trap is the only source of hydrogen during oxygen addition reactions. Comparing the intensities of  $\text{Ag}_{17}^+$  and  $\text{Ag}_{18}\text{H}^+$  at different oxygen gas flow rates, we can conclude that  $\text{Ag}_{18}\text{H}^+$  is most abundant at the highest flow rate of oxygen and the relative intensity of  $\text{Ag}_{17}^+$  is decreasing faster than  $\text{Ag}_{18}\text{H}^+$  *i.e.*,  $\text{Ag}_{18}\text{H}^+$  is more resistant to oxygen. The plot of the relative intensity of  $\text{Ag}_{17}^+$  with the flow rate of oxygen confirms this (Fig. S16†).

We have also performed CID experiments on each of the four oxygen addition peaks of  $\text{Ag}_{17}^+$  for a better understanding of their structures (Fig. S17†). During collisions with He gas in the trap, collision energy was increased gradually up to the threshold of fragmentation of the precursor cluster ion. With increasing collision energy, the intensities of the parent cluster ions ( $\text{Ag}_{17}\text{H}_4\text{O}^+$ ,  $\text{Ag}_{17}\text{H}_4\text{O}_2^+$ ,  $\text{Ag}_{17}\text{H}_4\text{O}_3^+$  and  $\text{Ag}_{17}\text{H}_4\text{O}_4^+$ ) decayed along with increasing intensity of the fragment ions. For  $\text{Ag}_{17}\text{H}_4\text{O}^+$ , collisional activation results in the detachment of oxygen and hydrogen atoms and the appearance of  $\text{Ag}_{17}^+$  as the fragmented ion.  $\text{Ag}_{17}\text{H}_4\text{O}_2^+$  fragmented directly to  $\text{Ag}_{17}^+$  without giving the  $\text{Ag}_{17}\text{O}^+$  ion, which indicates that it can be molecular adsorption. But in the case of  $\text{Ag}_{17}\text{H}_4\text{O}_3^+$  and  $\text{Ag}_{17}\text{H}_4\text{O}_4^+$ , they go through an intermediate,  $\text{Ag}_{17}\text{O}_2^+$  to  $\text{Ag}_{17}^+$ . From these results, we see that  $\text{Ag}_{17}\text{O}^+$  and  $\text{Ag}_{17}\text{O}_3^+$  are not formed as intermediates during the fragmentation of  $\text{Ag}_{17}\text{H}_4\text{O}_4^+$ , which confirms that  $\text{Ag}_{17}\text{H}_4\text{O}_4^+$  is formed due to the adsorption of two molecular oxygens. As reported for  $\text{Ag}_2^+$ , the molecular adsorption peaks were transformed to atomic adsorption peaks by increasing the temperature from 50 K to 130 K.<sup>45</sup> But for  $\text{Ag}_{17}^+$ , molecular oxygen attachments are seen even at higher temperature. The temperature at which molecular oxygen will dissociate to give atomic oxygen can be varied by the adsorption site or the nano-facet and the presence of defects.<sup>52</sup> Though it is very difficult to interpret, we can assume that our experimental temperature may be lower than the transition temperature needed for adsorbed molecular oxygen on  $\text{Ag}_{17}^+$  to dissociate.

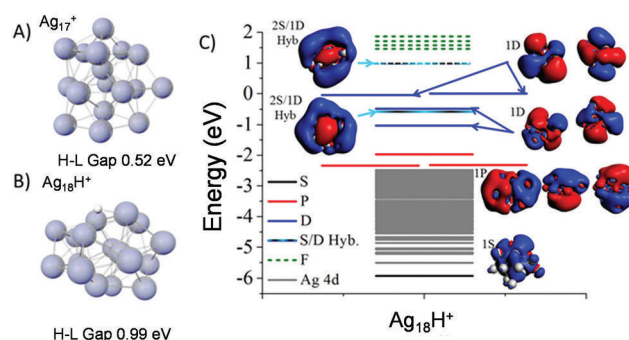
During the ion/molecule reactions, from Figs. 3 and 4, it was noted that the ions labelled  $\text{Ag}_{17}(\text{H}_2\text{O})_2\text{O}_2^+$  and  $\text{Ag}_{17}\text{H}_4\text{O}_4^+$  have the same elemental composition although their formation methods were different. The first one was prepared by increasing the distance between the heating tube and the mass spectrometer inlet and the second one was prepared by the reaction with oxygen gas exclusively. The intensities of  $\text{Ag}_{17}(\text{H}_2\text{O})_2\text{O}_2^+$  and  $\text{Ag}_{17}\text{H}_4\text{O}_4^+$  were of the order of  $10^1$  and  $10^0$ , respectively. To get a clearer idea of their structures, we have done CID experiments at the same collision energy, which showed different results for each of them (Fig. S18†). From these results, we conclude that though their composition is the same, their structures are different. In two tables (Tables S22 and S23†) we have summarized the experimental and calculated masses of the assigned clusters observed.

In order to explore the possibility of using the products of electrospray, we have collected the products at heating tube temperatures of 250 °C and 350 °C, on surfaces held under ambient conditions. The collected products were dispersed in

MeOH and  $\text{CDCl}_3$  to perform ESI mass spectrometry and NMR spectroscopy, respectively. Note that MS and NMR studies were conducted after centrifugation to avoid experimental artefacts. No features of hydride protected or NCs were observed in both ESI mass spectra and NMR spectra indicating that the clusters have undergone aggregation. TEM analysis of the products (without centrifugation) confirmed this and the data were compared with that of the  $[\text{Ag}_{18}\text{H}_{16}(\text{TPP})_{10}]^{2+}$  cluster. The parent cluster shows an average particle size  $1.68 \pm 0.19$  nm, whereas the collected electrosprayed products (both at 250 °C and 350 °C of the heating tube) showed only nanoparticles of variable sizes (Fig. S19†). The images suggest that the bare clusters aggregate on the collected surfaces. This leads to poor extraction in solution, unlike organic reaction products.<sup>53</sup> Soft landing on suitable substrates may help their collection without aggregation.<sup>54</sup>

To understand the  $\text{O}_2$  resistant reactivity of  $\text{Ag}_{18}\text{H}^+$ , we used first-principles theoretical methods and investigated the geometric and electronic structures of  $\text{Ag}_{17}^+$  and  $\text{Ag}_{18}\text{H}^+$ . As mentioned previously, metal clusters with large HOMO–LUMO gaps tend to be resistant to reactions with  $\text{O}_2$ , while clusters with unpaired electrons or small HOMO–LUMO gaps are highly reactive with  $\text{O}_2$ . In the present case, both  $\text{Ag}_{17}^+$  and  $\text{Ag}_{18}\text{H}^+$  have an even number of electrons corresponding to 16 and 18 valence electrons.  $\text{Ag}_{17}^+$  is found to have an icosahedral core with a 4 atom cap structure decorating the icosahedral core (Fig. 5(A)). The HOMO–LUMO gap of  $\text{Ag}_{17}^+$  is found to be 0.52 eV, which is a relatively low value, consistent with the cluster being reactive with  $\text{O}_2$ . Only one isomer within 0.2 eV of the lowest energy structure was found, and it also had a low HOMO–LUMO gap of 0.46 eV. Time-dependent density functional theory, TD-DFT, was used to confirm the accuracy of the HOMO–LUMO gaps, and we find that the singlet excitation energy for  $\text{Ag}_{17}^+$  is 0.47 eV, and the triplet excitation energy is 0.49 eV. Our previous studies on a variety of clusters indicate that metal clusters are resistant to the  $\text{O}_2$  reaction when the HOMO–LUMO gaps are typically around or greater than 1 eV (Fig. S20†).

$\text{Ag}_{18}\text{H}^+$  is found to have an oblate structure with a HOMO–LUMO gap of 0.99 eV (Fig. 5(B)), large enough to expect the



**Fig. 5** Structure and the HOMO–LUMO gap of (A)  $\text{Ag}_{17}^+$  and (B)  $\text{Ag}_{18}\text{H}^+$  clusters. (C) The electronic structure of  $\text{Ag}_{18}\text{H}^+$ . The electronic shell structure is  $[1S^2][1P^6][1D^8] 2S/1D^2 || 2S/1D^2 [1F^{14}]$ , with the  $1D_z^2$  and  $2S$  orbitals hybridizing.



cluster to be resistant to O<sub>2</sub> etching. Alternative structures and their energetics are given in Fig. S21.† TD-DFT finds that the excitation energy and triplet energy for the cluster are 0.94 eV, and the triplet excitation energy is 0.96 eV. The H binding energy is 2.26 eV which is approximately equal to the binding energy per atom of H<sub>2</sub>, and the ionization potential of Ag<sub>18</sub>H<sup>+</sup> is a relatively low value of 5.25 eV. Each Ag atom provides one valence electron, as does the H atom, so the cluster may be thought of as having 18 valence electrons. The nearest closed electronic shell for silver is expected to be at 20 valence electrons. The relatively large HOMO–LUMO gap may be explained by the oblate structure of the cluster resulting in a splitting of the 1D orbitals giving an electronic structure of  $|1S^2|1P^6|1D^8|1D/2S^2||1D/2S^2|1F^{14}|$ , as shown in Fig. 5(C). The Ag 4d states (90 states) are shown by the grey region and the double line separates the occupied and unoccupied states. The 1D<sub>z</sub><sup>2</sup> and the 2S orbitals have the same symmetry, so they hybridize and split due to the oblate structure pushing up in energy the orbitals with more nodes along the compressed axis.<sup>55</sup> The oblate distortion is seen in many of the low energy isomers, with the isomers having HOMO–LUMO gaps between 0.70 and 1.10 eV. The similar structure of the silver cores results in similar electronic structures in the different isomers, so they may also show enhanced resistance to O<sub>2</sub> reactivity.

## Conclusions

We conclude that naked metal cluster ions can be formed outside a mass spectrometer starting from ligand protected, atomically precise clusters prepared in solution. The reactivity of these NCs to oxygen shows selectivity, which depends on their HOMO–LUMO gaps. It is likely that atmospheric gas phase NCs can be used as reagents and catalysts. They may be deposited on a suitable support to create useful materials. Again the oxidized silver clusters can also be used as an oxidizing agent to oxidize CO or NO<sub>2</sub>. We have studied various phosphine protected silver clusters ([Ag<sub>18</sub>H<sub>16</sub>(TPP)<sub>10</sub>]<sup>2+</sup> and [Ag<sub>25</sub>H<sub>22</sub>(DPPE)<sub>8</sub>]<sup>2+</sup> (DPPE = 1,2-bis(diphenylphosphino) ethane)) and thiolate protected silver clusters ([Ag<sub>25</sub>(DMBT)<sub>18</sub>]<sup>3−</sup> (DMBT = 2,4-dimethylbenzenethiol), [Ag<sub>44</sub>(FTP)<sub>30</sub>]<sup>4−</sup> (FTP = 4-fluorothiophenol) and [Ag<sub>59</sub>(DCBT)<sub>32</sub>]<sup>3−</sup> (DCBT = 2,5-dichlorobenzenethiol)), and gold clusters ([Au<sub>25</sub>(PET)<sub>18</sub>]<sup>−</sup> (PET = 2-phenylethanethiol)) available in our laboratory.<sup>6,7,28</sup> From all of these experiments, we conclude that [Ag<sub>18</sub>H<sub>16</sub>(TPP)<sub>10</sub>]<sup>2+</sup> alone forms silver NCs outside the mass spectrometer.

## Conflicts of interest

The authors declare no competing financial interests.

## Acknowledgements

MJ and AG thank UGC for their senior research fellowships. MD thanks UGC for his junior research fellowship. DS and AB

thank the IIT Madras for the Institute Post-Doctoral fellowships and PB thanks IIT Madras for his junior research fellowship. We thank the Department of Science and Technology for the constant support to our research program. This theoretical work (ACR and SNK) was supported by the US Department of Energy (DOE) under the award Number DE-SC0006420.

## References

- 1 R. L. Whetten, J. T. Khoury, M. M. Alvarez, S. Murthy, I. Vezmar, Z. L. Wang, P. W. Stephens, C. L. Cleveland, W. D. Luedtke and U. Landman, *Adv. Mater.*, 1996, **8**, 428–433.
- 2 R. Jin, *Nanoscale*, 2015, **7**, 1549–1565.
- 3 P. Maity, S. Xie, M. Yamauchi and T. Tsukuda, *Nanoscale*, 2012, **4**, 4027–4037.
- 4 W. Kurashige, Y. Niihori, S. Sharma and Y. Negishi, *J. Phys. Chem. Lett.*, 2014, **5**, 4134–4142.
- 5 S. Knoppe and T. Bürgi, *Acc. Chem. Res.*, 2014, **47**, 1318–1326.
- 6 I. Chakraborty and T. Pradeep, *Chem. Rev.*, 2017, **117**, 8208–8271.
- 7 R. Jin, C. Zeng, M. Zhou and Y. Chen, *Chem. Rev.*, 2016, **116**, 10346–10413.
- 8 G. Schmid and N. Klein, *Angew. Chem., Int. Ed. Engl.*, 1986, **25**, 922–923.
- 9 P.-T. Chen, E. C. Tyo, M. Hayashi, M. J. Pellin, O. Safonova, M. Nachtegaal, J. A. van Bokhoven, S. Vajda and P. Zapol, *J. Phys. Chem. C*, 2017, **121**, 6614–6625.
- 10 S. Lee, C. Fan, T. Wu and S. L. Anderson, *J. Am. Chem. Soc.*, 2004, **126**, 5682–5683.
- 11 H. Tsunoyama, N. Ichikuni, H. Sakurai and T. Tsukuda, *J. Am. Chem. Soc.*, 2009, **131**, 7086–7093.
- 12 Z. Wu, G. Hu, D.-E. Jiang, D. R. Mullins, Q.-F. Zhang, L. F. Allard, L.-S. Wang and S. H. Overbury, *Nano Lett.*, 2016, **16**, 6560–6567.
- 13 I. Diez and R. H. A. Ras, *Nanoscale*, 2011, **3**, 1963–1970.
- 14 M. Turner, V. B. Golovko, O. P. H. Vaughan, P. Abdulkin, A. Berenguer-Murcia, M. S. Tikhov, B. F. G. Johnson and R. M. Lambert, *Nature*, 2008, **454**, 981.
- 15 K. P. Kerns, B. C. Guo, H. T. Deng and A. W. Castleman, *J. Chem. Phys.*, 1994, **101**, 8529–8534.
- 16 L. A. Angel, L. T. Majors, A. C. Dharmaratne and A. Dass, *ACS Nano*, 2010, **4**, 4691–4700.
- 17 A. Baksi, S. R. Harvey, G. Natarajan, V. H. Wysocki and T. Pradeep, *Chem. Commun.*, 2016, **52**, 3805–3808.
- 18 Z. Luo, A. W. Castleman and S. N. Khanna, *Chem. Rev.*, 2016, **116**, 14456–14492.
- 19 T. E. Dermota, Q. Zhong and A. W. Castleman, *Chem. Rev.*, 2004, **104**, 1861–1886.
- 20 S. J. Riley, *Ber. Bunsenges. Phys. Chem.*, 1992, **96**, 1104–1109.
- 21 D. M. Black, C. M. Crittenden, J. S. Brodbelt and R. L. Whetten, *J. Phys. Chem. Lett.*, 2017, **8**, 1283–1289.
- 22 M. G. Taylor and G. Mpourmpakis, *Nat. Commun.*, 2017, **8**, 15988.

- 23 P. Chakraborty, A. Baksi, E. Khatun, A. Nag, A. Ghosh and T. Pradeep, *J. Phys. Chem. C*, 2017, **121**, 10971–10981.
- 24 R. Jin, S. Zhao, Y. Xing and R. Jin, *CrystEngComm*, 2016, **18**, 3996–4005.
- 25 M. Krstić, A. Zavras, G. N. Khairallah, P. Dugourd, V. Bonačić-Koutecký and R. A. J. O'Hair, *Int. J. Mass Spectrom.*, 2017, **413**, 97–105.
- 26 M. Girod, M. Krstić, R. Antoine, L. MacAleese, J. Lemoine, A. Zavras, G. N. Khairallah, V. Bonačić-Koutecký, P. Dugourd and R. A. J. O'Hair, *Chem. – Eur. J.*, 2014, **20**, 16626–16633.
- 27 A. J. Jordan, G. Lalic and J. P. Sadighi, *Chem. Rev.*, 2016, **116**, 8318–8372.
- 28 M. S. Bootharaju, R. Dey, L. E. Gevers, M. N. Hedhili, J.-M. Basset and O. M. Bakr, *J. Am. Chem. Soc.*, 2016, **138**, 13770–13773.
- 29 A. Ghosh, M. Bodiuzzaman, A. Nag, M. Jash, A. Baksi and T. Pradeep, *ACS Nano*, 2017, **11**, 11145–11151.
- 30 H. Chen, L. S. Eberlin and R. G. Cooks, *J. Am. Chem. Soc.*, 2007, **129**, 5880–5886.
- 31 L. S. Eberlin, Y. Xia, H. Chen and R. G. Cooks, *J. Am. Soc. Mass Spectrom.*, 2008, **19**, 1897–1905.
- 32 M. Wlekinski, D. Sarkar, A. Hollerbach, T. Pradeep and R. G. Cooks, *Phys. Chem. Chem. Phys.*, 2015, **17**, 18364–18373.
- 33 B. D. Leskiw, A. W. Castleman Jr., C. Ashman and S. N. Khanna, *J. Chem. Phys.*, 2001, **114**, 1165–1169.
- 34 H. Häkkinen, *Adv. Phys.: X*, 2016, **1**, 467–491.
- 35 S. Klacar, A. Hellman, I. Panas and H. Grönbeck, *J. Phys. Chem. C*, 2010, **114**, 12610–12617.
- 36 A. W. Castleman and S. N. Khanna, *J. Phys. Chem. C*, 2009, **113**, 2664–2675.
- 37 A. C. Reber, S. N. Khanna, P. J. Roach, W. H. Woodward and A. W. Castleman, *J. Am. Chem. Soc.*, 2007, **129**, 16098–16101.
- 38 Z. Luo, G. U. Gamboa, J. C. Smith, A. C. Reber, J. U. Reveles, S. N. Khanna and A. W. Castleman, *J. Am. Chem. Soc.*, 2012, **134**, 18973–18978.
- 39 G. te Velde, F. M. Bickelhaupt, E. J. Baerends, C. Fonseca Guerra, S. J. A. van Gisbergen, J. G. Snijders and T. Ziegler, *J. Comput. Chem.*, 2001, **22**, 931–967.
- 40 J. P. Perdew, K. Burke and M. Ernzerhof, *Phys. Rev. Lett.*, 1996, **77**, 3865–3868.
- 41 E. Van Lenthe and E. J. Baerends, *J. Comput. Chem.*, 2003, **24**, 1142–1156.
- 42 E. van Lenthe, E. J. Baerends and J. G. Snijders, *J. Chem. Phys.*, 1994, **101**, 9783–9792.
- 43 G. N. Khairallah and R. A. J. O'Hair, *Dalton Trans.*, 2005, 2702–2712, DOI: 10.1039/B505645B.
- 44 R. Fournier, *J. Chem. Phys.*, 2001, **115**, 2165–2177.
- 45 L. D. Socaciu, J. Hagen, U. Heiz, T. M. Bernhardt, T. Leisner and L. Wöste, *Chem. Phys. Lett.*, 2001, **340**, 282–288.
- 46 M. Schmidt, A. Masson and C. Bréchnignac, *Phys. Rev. Lett.*, 2003, **91**, 243401.
- 47 M. Schmidt, P. Cahuzac, C. Bréchnignac and H.-P. Cheng, *J. Chem. Phys.*, 2003, **118**, 10956–10962.
- 48 Y.-N. Wu, M. Schmidt, J. Leygnier, H.-P. Cheng, A. Masson and C. Bréchnignac, *J. Chem. Phys.*, 2012, **136**, 024314.
- 49 T. M. Bernhardt, *Int. J. Mass Spectrom.*, 2005, **243**, 1–29.
- 50 M. Schmidt, A. Masson, H.-P. Cheng and C. Bréchnignac, *ChemPhysChem*, 2015, **16**, 855–865.
- 51 M. J. Manard, P. R. Kemper and M. T. Bowers, *Int. J. Mass Spectrom.*, 2003, **228**, 865–877.
- 52 L. Vattuone, L. Savio and M. Rocca, *Phys. Rev. Lett.*, 2003, **90**, 228302.
- 53 P. Liu, R. G. Cooks and H. Chen, *Angew. Chem., Int. Ed.*, 2015, **54**, 1547–1550.
- 54 J. Laskin, G. E. Johnson, J. Warneke and V. Prabhakaran, *Angew. Chem., Int. Ed. Engl.*, 2018, DOI: 10.1002/anie.201712296.
- 55 A. C. Reber and S. N. Khanna, *Acc. Chem. Res.*, 2017, **50**, 255–263.

## Supporting Information

### Preparation of gas phase naked silver cluster cations outside a mass spectrometer from ligand protected clusters in solution

Madhuri Jash,<sup>a</sup> Arthur C. Reber,<sup>b</sup> Atanu Ghosh,<sup>a</sup> Depanjan Sarkar,<sup>a</sup> Mohammad Bodiuzzaman,<sup>a</sup> Pallab Basuri,<sup>a</sup> Ananya Baksi,<sup>a</sup> Shiv N. Khanna,<sup>\*b</sup> and Thalappil Pradeep<sup>\*a</sup>

<sup>a</sup>DST Unit of Nanoscience (DST UNS) and Thematic Unit of Excellence (TUE), Department of Chemistry, Indian Institute of Technology Madras, Chennai 600 036, India

<sup>b</sup>Department of Physics, Virginia Commonwealth University, Richmond, Virginia 23284, United States

\*To whom correspondence should be addressed. E-mail: [pradeep@iitm.ac.in](mailto:pradeep@iitm.ac.in); [snkhanna@vcu.edu](mailto:snkhanna@vcu.edu)

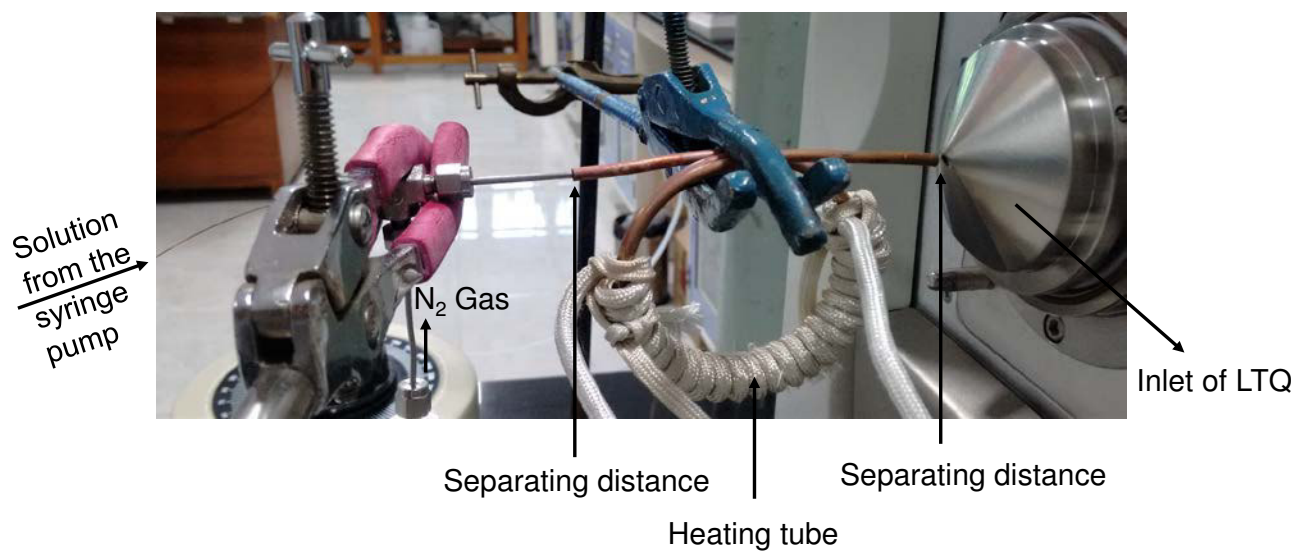
## Table of Contents

Name	Description	Page No.
S1	Photograph of the instrumental set-up	3
S2	Characterization of $[\text{Ag}_{18}\text{H}_{16}(\text{TPP})_{10}]^{2+}$ cluster	4
S3	Characterization of $[\text{Ag}_{18}\text{D}_{16}(\text{TPP})_{10}]^{2+}$ cluster	5
S4	Comparison between the experimental and the calculated spectra	6
S5	Full range ESI mass spectra of $[\text{Ag}_{18}\text{H}_{16}(\text{TPP})_{10}]^{2+}$ cluster during heating	7
S6	Formation of $\text{Ag}_{17}^{+}$ from both $\text{Ag}_{17}\text{H}_{14}^{+}$ and $\text{Ag}_{17}\text{D}_{14}^{+}$	8
S7	Comparison of ESI mass spectra of $[\text{Ag}_{18}\text{H}_{16}(\text{TPP})_{10}]^{2+}$ cluster during heating at different capillary and tube lens voltage	9
S8	Full range ESI mass spectra of $[\text{Ag}_{18}\text{H}_{16}(\text{TPP})_{10}]^{2+}$ cluster during heating at higher capillary and tube lens voltage	10
S9	Ion chronograms of selected ions	11
S10	$\text{MS}^2$ for $\text{Ag}_{17}^{+}$ , $\text{Ag}_{17}\text{H}_{14}^{+}$ and $\text{Ag}_{18}\text{H}^{+}$ ions	12
S11	Thermal dissociation of thiolate protected cluster with same experimental conditions	13
S12	Effect of distance between the heating tube and the ESI source	14
S13	Photograph of the instrumental set-up and diagram used for ion/molecule reactions	15
S14	Comparison of oxygen addition reaction of naked clusters with $\text{CD}_3\text{OD}$ as solvent	16
S15	Comparison of oxygen addition reaction of naked clusters created from $[\text{Ag}_{18}\text{H}_{16}(\text{TPP})_{10}]^{2+}$ and $[\text{Ag}_{18}\text{D}_{16}(\text{TPP})_{10}]^{2+}$	17
S16	Comparison of reactivity between $\text{Ag}_{17}^{+}$ and $\text{Ag}_{18}\text{H}^{+}$ ions with oxygen	18
S17	$\text{MS}^2$ of $\text{Ag}_{17}\text{O}^{+}$ , $\text{Ag}_{17}\text{O}_2^{+}$ , $\text{Ag}_{17}\text{O}_3^{+}$ and $\text{Ag}_{17}\text{O}_4^{+}$ ions	19
S18	Comparison of $\text{MS}^2$ results of $\text{Ag}_{17}(\text{H}_2\text{O})_2\text{O}_2^{+}$ and $\text{Ag}_{17}\text{H}_4\text{O}_4^{+}$ ions	20

S19	TEM images of $[\text{Ag}_{18}\text{H}_{16}(\text{TPP})_{10}]^{2+}$ cluster and the electrosprayed products collected	21
S20	The calculated structures of $\text{Ag}_{15}^+$ , $\text{Ag}_{17}^+$ , $\text{Ag}_{18}^+$ , and $\text{Ag}_{18}\text{H}^+$ ions	22
S21	Isomers of $\text{Ag}_{18}\text{H}^+$ and their energies	23
S22	Experimental and calculated masses measured with the LTQ	24
S23	Experimental and calculated masses measured using the G2-Si	25

## Supporting information 1

### Photograph of the instrumental set-up:

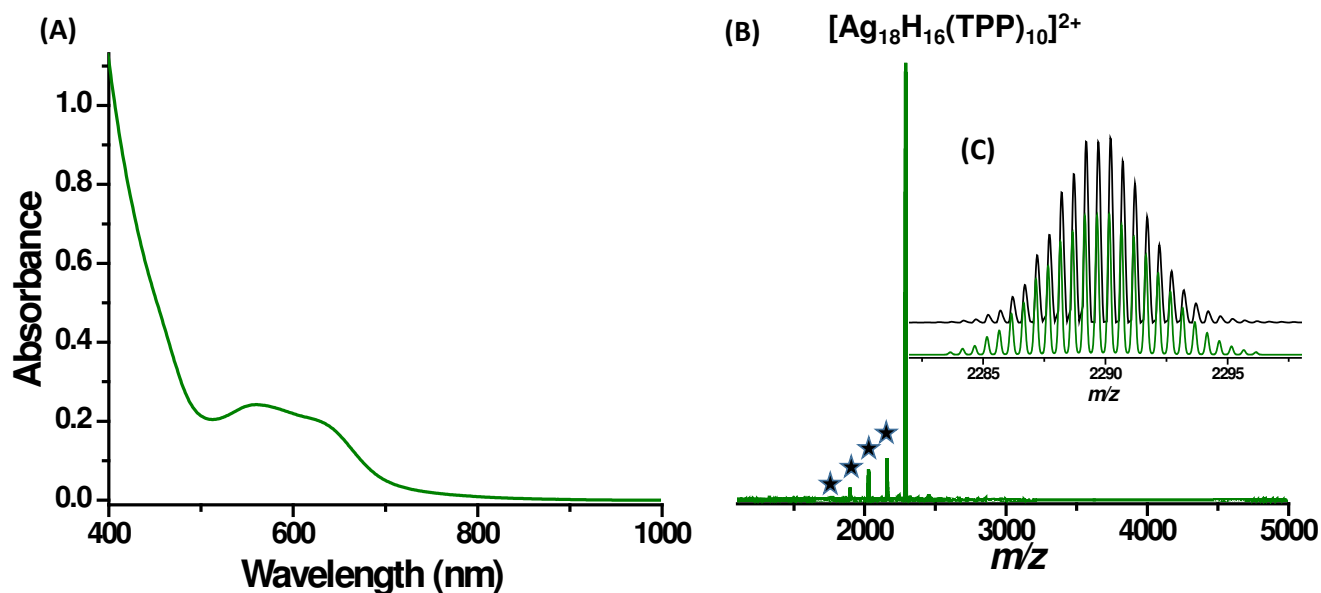


**S1:** Photograph of the instrumental set-up used for the creation of naked cluster ions.



## Supporting information 2

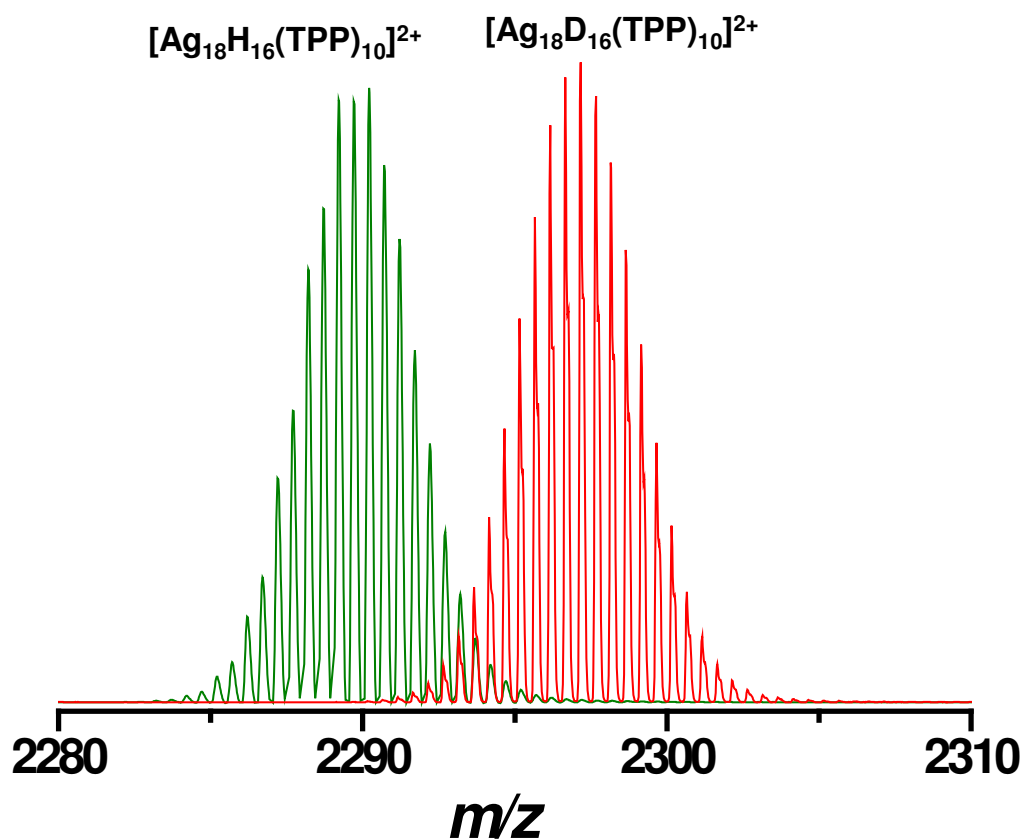
### Characterization of $[\text{Ag}_{18}\text{H}_{16}(\text{TPP})_{10}]^{2+}$ cluster:



**Fig. S2** (A) UV-vis absorption spectrum of  $[\text{Ag}_{18}\text{H}_{16}(\text{TPP})_{10}]^{2+}$  cluster in MeOH showing characteristic absorption features. (B) ESI mass spectrum of the cluster in positive mode (using the G2-Si) is showing a sharp peak at  $m/z$  2290 which is assigned as  $[\text{Ag}_{18}\text{H}_{16}(\text{TPP})_{10}]^{2+}$ . Other small peaks separated by  $m/z$  131 are due to  $\text{PPh}_3$  loss which are shown by asterisks. (C) Peak at  $m/z$  2290 is expanded, which is matching well with the calculated isotope pattern of  $[\text{Ag}_{18}\text{H}_{16}(\text{TPP})_{10}]^{2+}$ .

### Supporting information 3

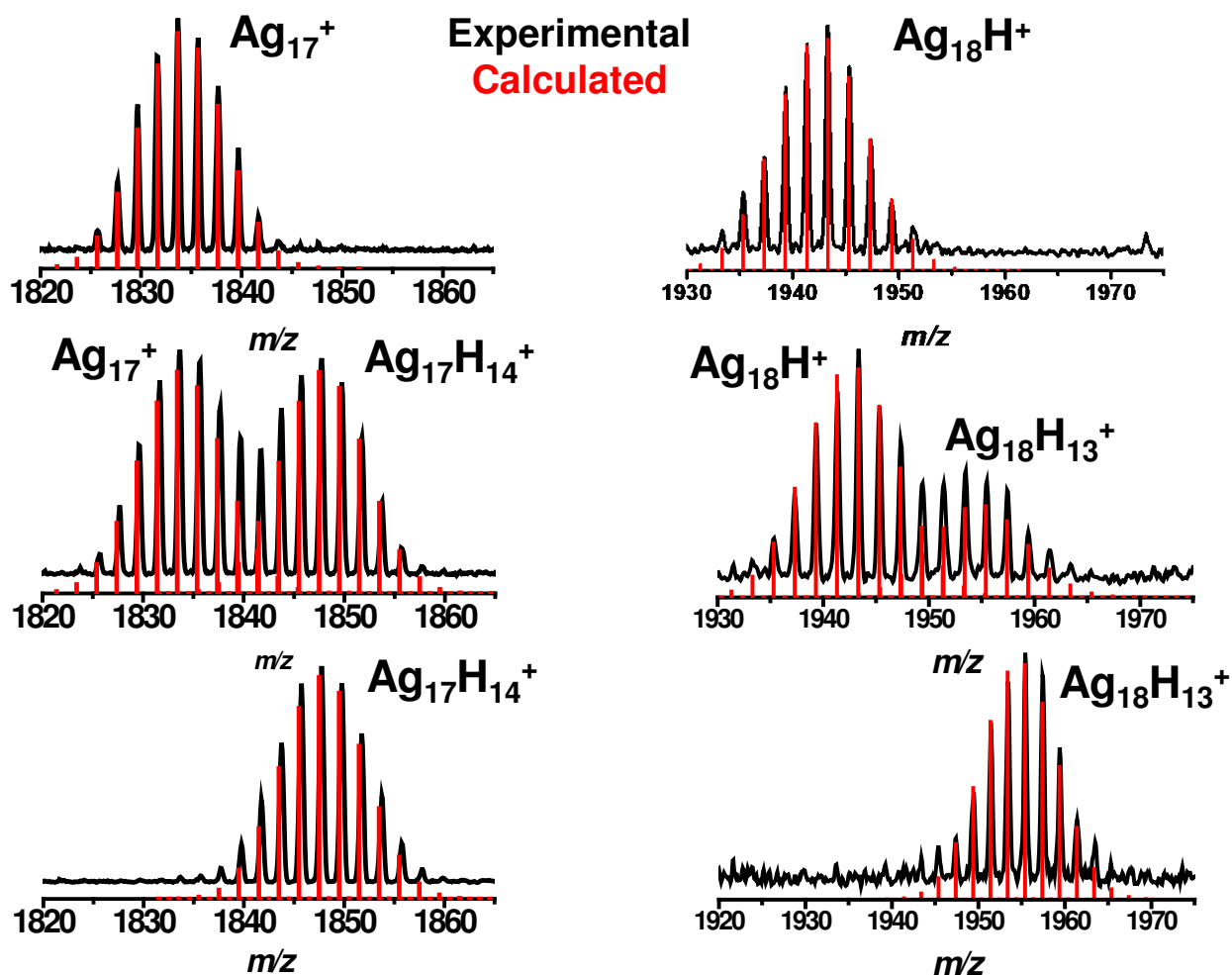
#### Characterization of $[\text{Ag}_{18}\text{D}_{16}(\text{TPP})_{10}]^{2+}$ cluster:



**Fig. S3** ESI mass spectra of  $[\text{Ag}_{18}\text{H}_{16}(\text{TPP})_{10}]^{2+}$  and  $[\text{Ag}_{18}\text{D}_{16}(\text{TPP})_{10}]^{2+}$  cluster ions (using the G2-Si). The mass shift is due to the exchange of hydride ions with deuteride ions. In  $[\text{Ag}_{18}\text{D}_{16}(\text{TPP})_{10}]^{2+}$ , 100% exchange of hydrogen with deuterium was not there due to the presence of non-deuterated solvents in the synthesis.

## Supporting information 4

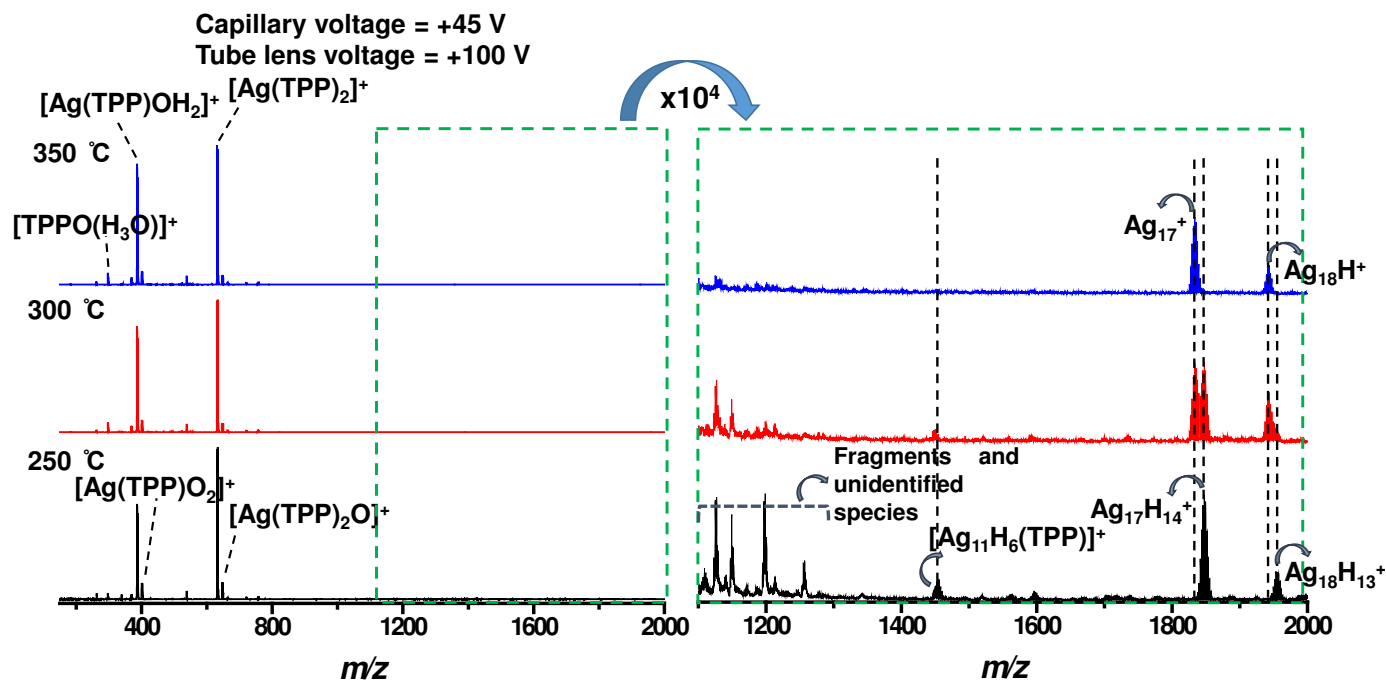
Comparison between the experimental and the calculated spectra:



**Fig. S4** Experimental mass spectra of  $\text{Ag}_{17}\text{H}_{14}^+$ ,  $\text{Ag}_{17}^+$ ,  $\text{Ag}_{18}\text{H}_{13}^+$  and  $\text{Ag}_{18}\text{H}^+$  ions match well with the calculated isotopic patterns.

## Supporting information 5

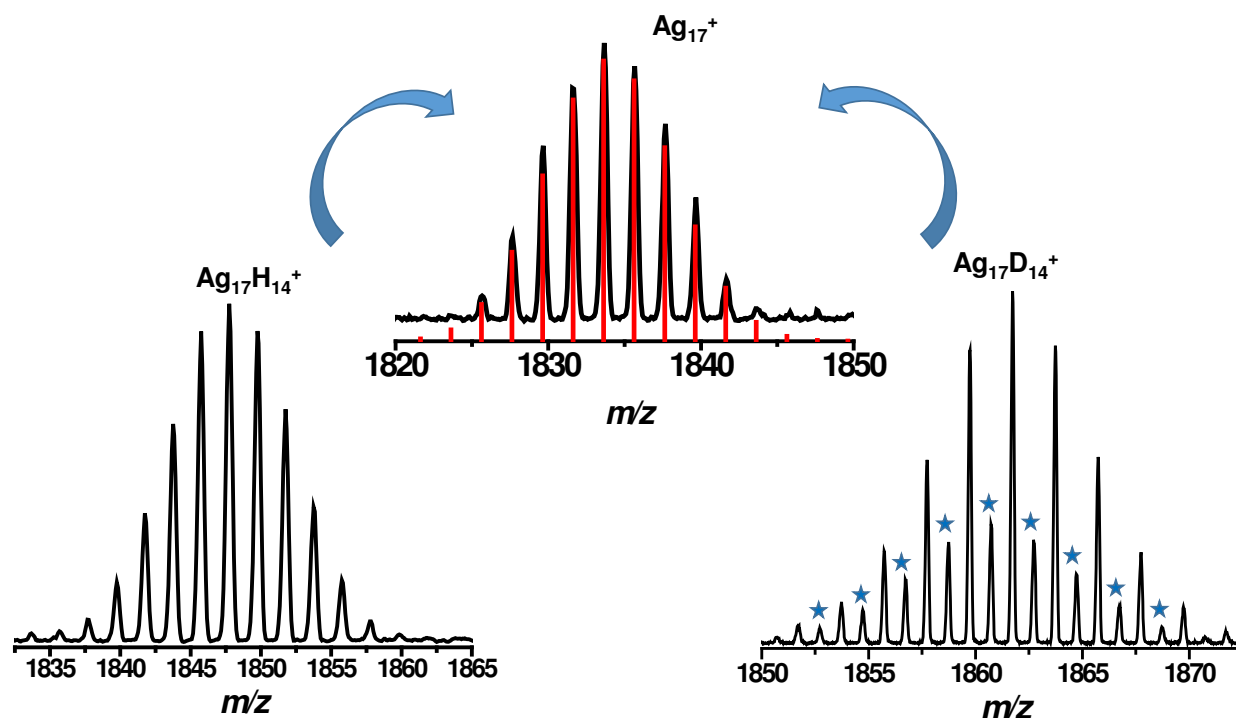
### Full range ESI mass spectra of $[\text{Ag}_{18}\text{H}_{16}(\text{TPP})_{10}]^{2+}$ cluster during heating:



**Fig. S5** Full range ESI mass spectra of  $[\text{Ag}_{18}\text{H}_{16}(\text{TPP})_{10}]^{2+}$  cluster with varying the heating tube temperature from 250 °C to 350 °C at CV and TV of 45 V and 100 V, respectively. At 250 °C,  $\text{Ag}_{17}\text{H}_{14}^+$  and  $\text{Ag}_{18}\text{H}_{13}^+$  were detected and at 300 °C,  $\text{Ag}_{17}^+$  and  $\text{Ag}_{18}\text{H}^+$  were seen along with their hydride clusters. Finally, at 350 °C only  $\text{Ag}_{17}^+$  and  $\text{Ag}_{18}\text{H}^+$  were seen without mass selection. At lower mass region, there were oxidation peaks of  $[\text{Ag}(\text{TPP})]^+$ ,  $[\text{Ag}(\text{TPP})_2]^+$  and  $\text{TPP}^+$ .

## Supporting information 6

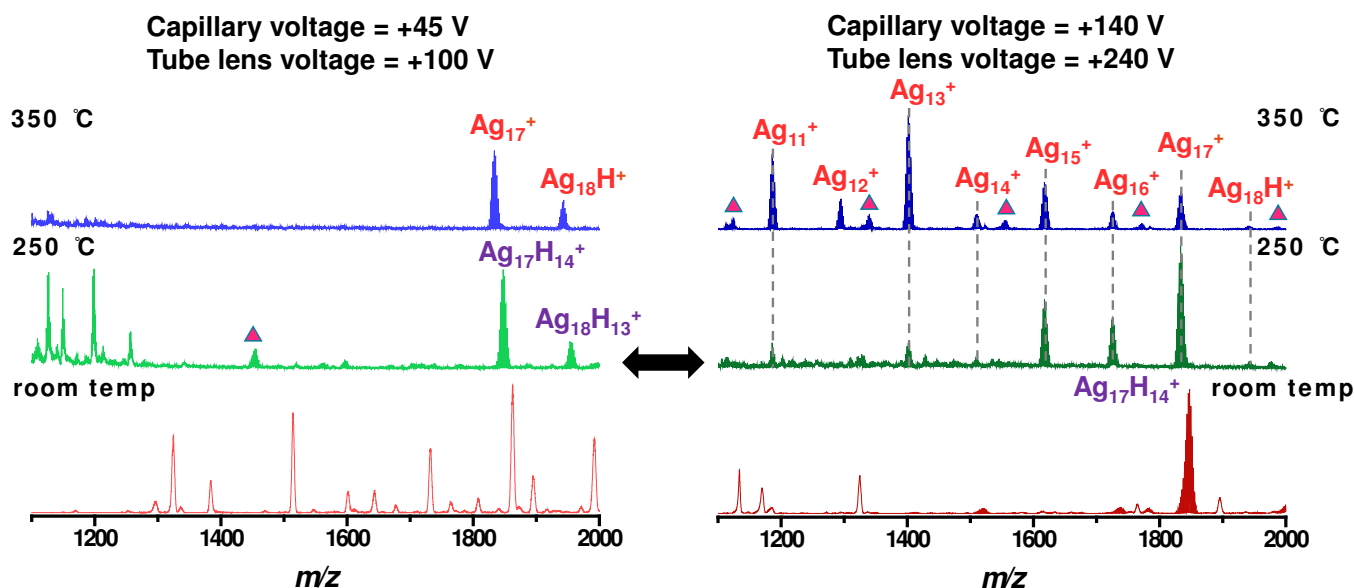
### Formation of $\text{Ag}_{17}^+$ from both $\text{Ag}_{17}\text{H}_{14}^+$ and $\text{Ag}_{17}\text{D}_{14}^+$ :



**Fig. S6** ESI mass spectra of  $\text{Ag}_{17}\text{H}_{14}^+$  and  $\text{Ag}_{17}\text{D}_{14}^+$  starting from  $[\text{Ag}_{18}\text{H}_{16}(\text{TPP})_{10}]^{2+}$  and  $[\text{Ag}_{18}\text{D}_{16}(\text{TPP})_{10}]^{2+}$ , respectively. In the spectrum of  $\text{Ag}_{17}\text{D}_{14}^+$ , the peaks shown by asterisks (35%) are arising due to the presence of hydrogen, which are coming due to the partial isotope exchange (principally due to  $\text{Ag}_{17}\text{D}_{13}\text{H}^+$ ), due to the presence of non-deuterated solvents.  $\text{Ag}_{17}\text{H}_{14}^+$  and  $\text{Ag}_{17}\text{D}_{14}^+$  are both converted to  $\text{Ag}_{17}^+$  at 350 °C.

## Supporting information 7

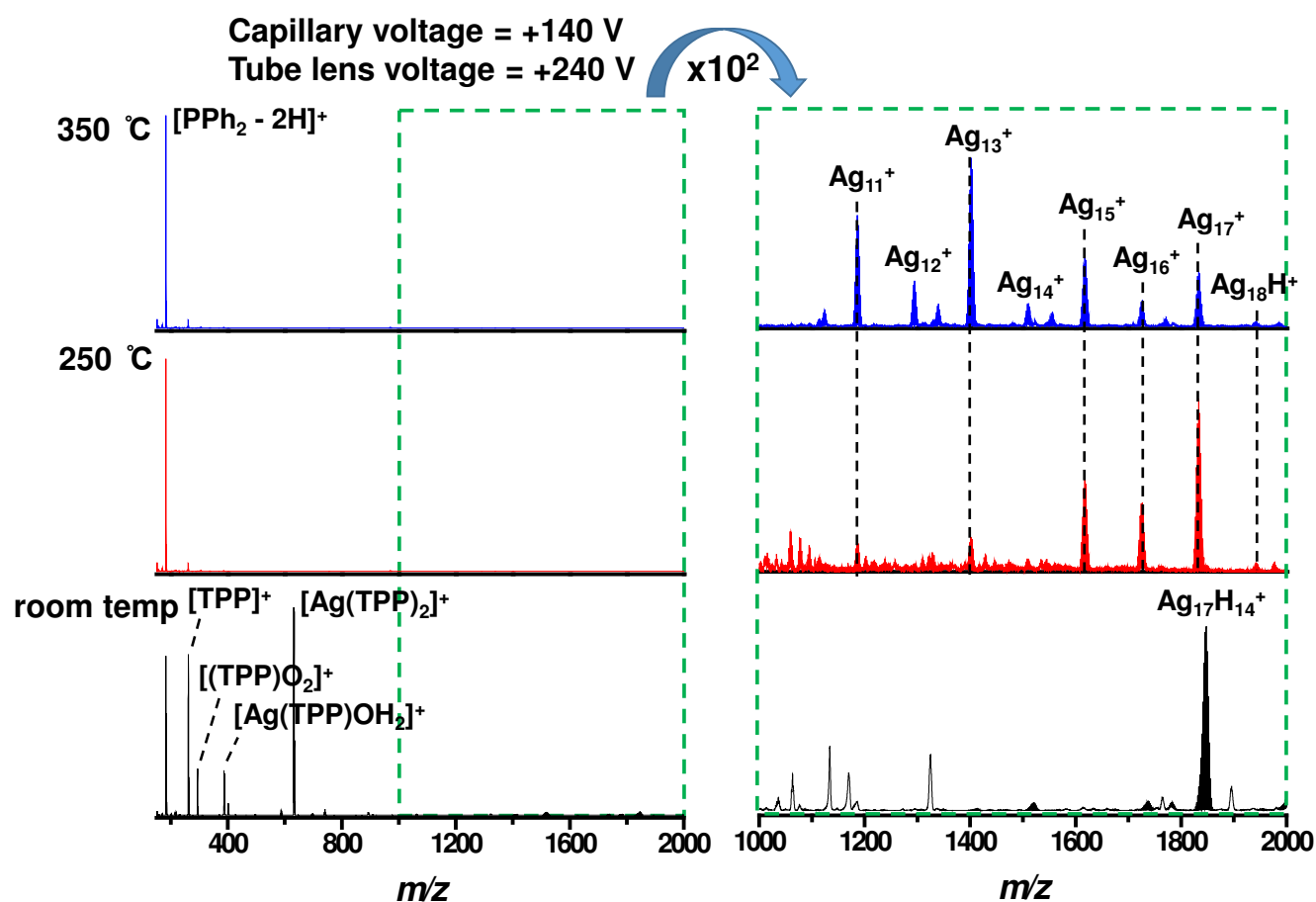
### Comparison of ESI mass spectra of $[\text{Ag}_{18}\text{H}_{16}(\text{TPP})_{10}]^{2+}$ cluster during heating at different capillary and tube lens voltage:



**Fig. S7** ESI mass spectra of  $[\text{Ag}_{18}\text{H}_{16}(\text{TPP})_{10}]^{2+}$  cluster with varying the heating tube temperature at CV and TV of 45 V and 100 V (left) and 140 V and 240 V (right). These two sets of CV and TV give different results at different temperatures of heating tube which is mainly due to the in-source fragmentation at higher CV and TV. Finally at 350 °C, at CV and TV of 45 V and 100 V, only  $\text{Ag}_{17}^+$  and  $\text{Ag}_{18}\text{H}^+$  were seen without mass selection, whereas at CV and TV of 140 V and 240 V, naked clusters along with smaller core sizes appear due to fragmentation. The weak features shown by pink triangles are due to  $[\text{Ag}_x(\text{TPP})_y]^+$  clusters. Note the difference in intensities of odd and even numbered clusters.

## Supporting information 8

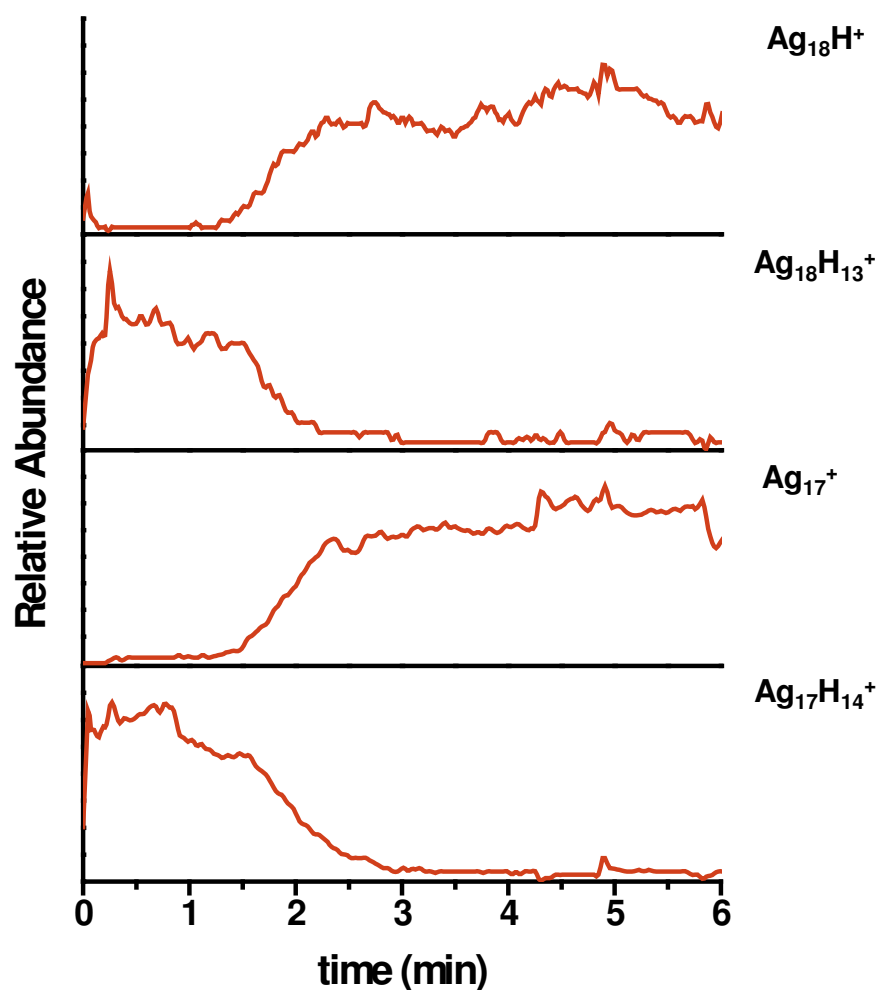
Full range ESI mass spectra of  $[\text{Ag}_{18}\text{H}_{16}(\text{TPP})_{10}]^{2+}$  cluster during heating at higher capillary and tube lens voltage:



**Fig. S8** Full range ESI mass spectra of  $[\text{Ag}_{18}\text{H}_{16}(\text{TPP})_{10}]^{2+}$  cluster with varying heating tube temperature from room temperature to 350 °C at CV and TV of 140 V and 240V. At room temperature,  $\text{Ag}_{17}\text{H}_{14}^+$  was detected along with some low mass region peaks. At 250 °C,  $\text{Ag}_{11}^+$ ,  $\text{Ag}_{13}^+$ ,  $\text{Ag}_{15}^+$ ,  $\text{Ag}_{16}^+$ ,  $\text{Ag}_{17}^+$  and  $\text{Ag}_{18}\text{H}^+$  were seen. Finally at 350 °C, all the naked clusters of silver along with  $\text{Ag}_{17}^+$  and  $\text{Ag}_{18}\text{H}^+$  were detected.

## Supporting information 9

### Ion chronograms of selected ions:

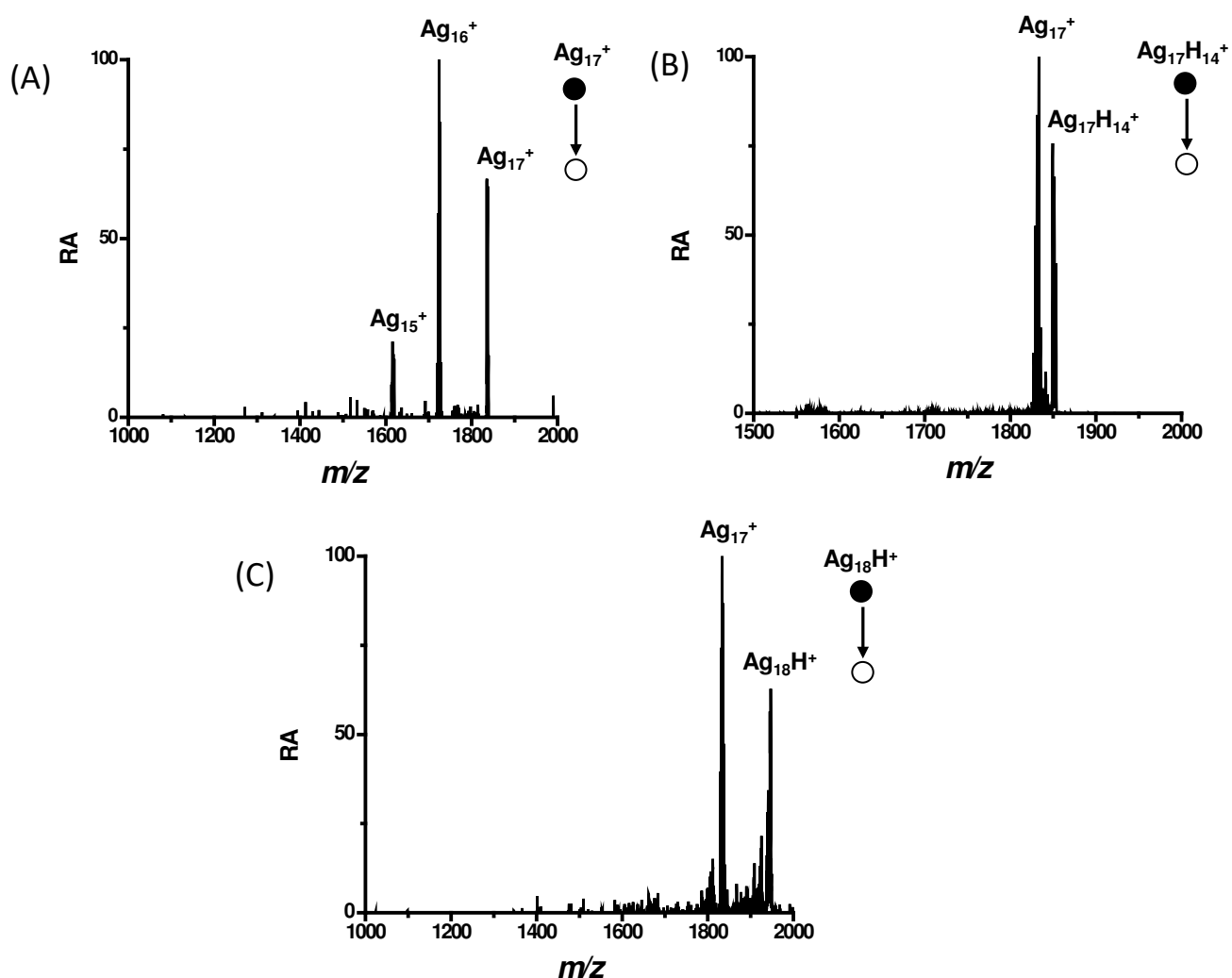


**Fig. S9** Ion chronograms of selected ions during the formation of naked clusters. At time zero the temperature was 250 °C and there were only existence of  $\text{Ag}_{17}\text{H}_{14}^+$  and  $\text{Ag}_{18}\text{H}_{13}^+$ . Then slowly temperature was raised to 350 °C over a few minutes, which results the appearance of  $\text{Ag}_{17}^+$  and  $\text{Ag}_{18}\text{H}^+$ .



## Supporting information 10

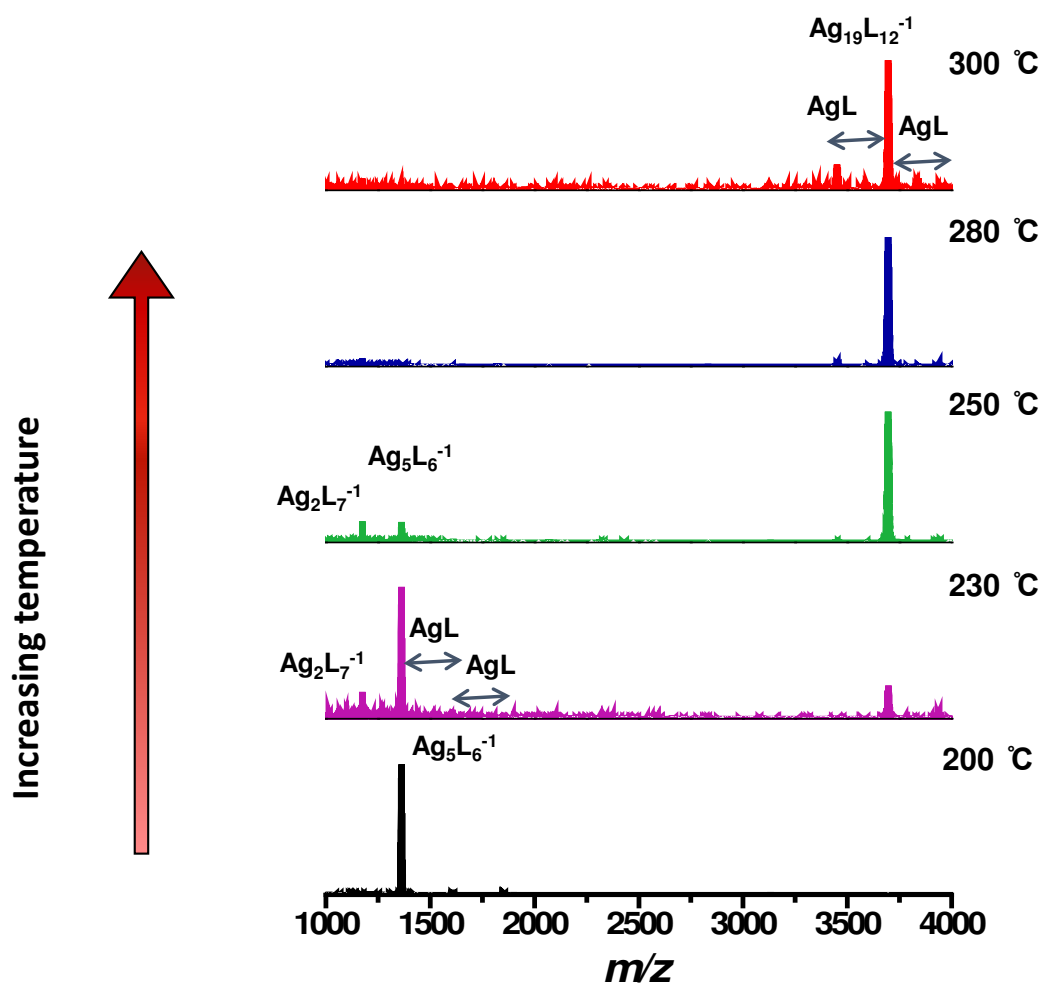
### MS<sup>2</sup> for Ag<sub>17</sub><sup>+</sup>, Ag<sub>17</sub>H<sub>14</sub><sup>+</sup> and Ag<sub>18</sub>H<sup>+</sup> ions:



**Fig. S10** MS<sup>2</sup> for (A) Ag<sub>17</sub><sup>+</sup>, (B) Ag<sub>17</sub>H<sub>14</sub><sup>+</sup>, (C) Ag<sub>18</sub>H<sup>+</sup> ions and the isolation widths are *m/z* 10, 10 and 8, respectively centered at the middle of the isotopic clusters. The collision energies used for the Ag<sub>17</sub><sup>+</sup>, Ag<sub>17</sub>H<sub>14</sub><sup>+</sup> and Ag<sub>18</sub>H<sup>+</sup> ions are 37, 17 and 24 in instrumental units, respectively. Due to higher collision energy, Ag<sub>17</sub><sup>+</sup> breaks into smaller sized naked clusters whereas the hydrides of silver ions give back the metallic core, Ag<sub>17</sub><sup>+</sup>. RA refers to relative abundance.

## Supporting information 11

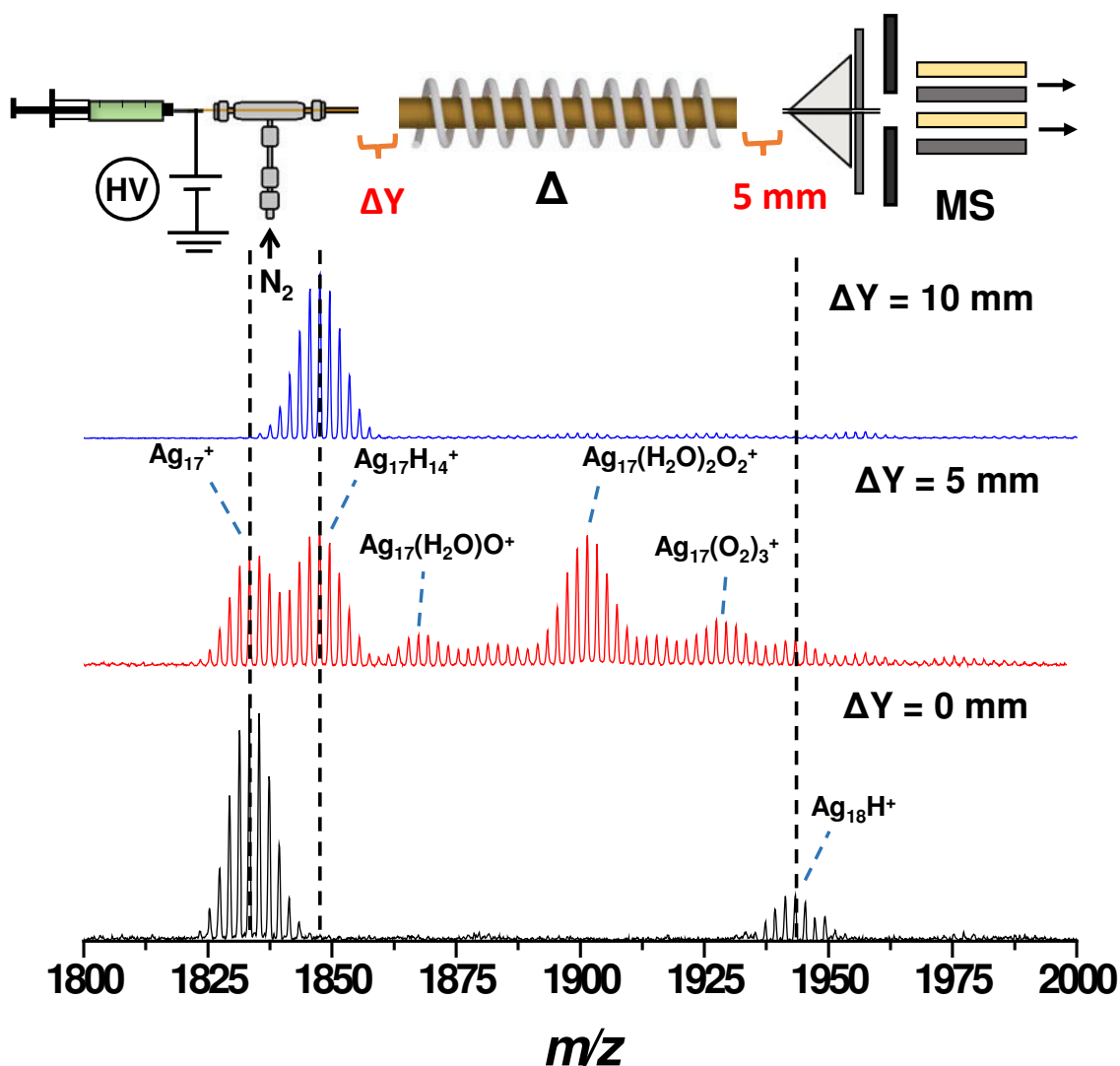
Thermal dissociation of thiolate protected cluster with the same experimental conditions:



**Fig. S11** ESI mass spectra of  $[\text{Ag}_{25}(\text{DMBT})_{18}]^{3-}$  cluster at different temperatures (same conditions like before) after electrospraying the cluster solution. The thermal dissociation results in  $[\text{Ag}_m\text{L}_n]^{-1}$  but not the naked cluster. Note that these clusters are thiolate protected, for them the mass spectra show intense features till the mass limit of the instrument ( $m/z$  4000).

## Supporting information 12

### Effect of distance between the heating tube and the ESI source:

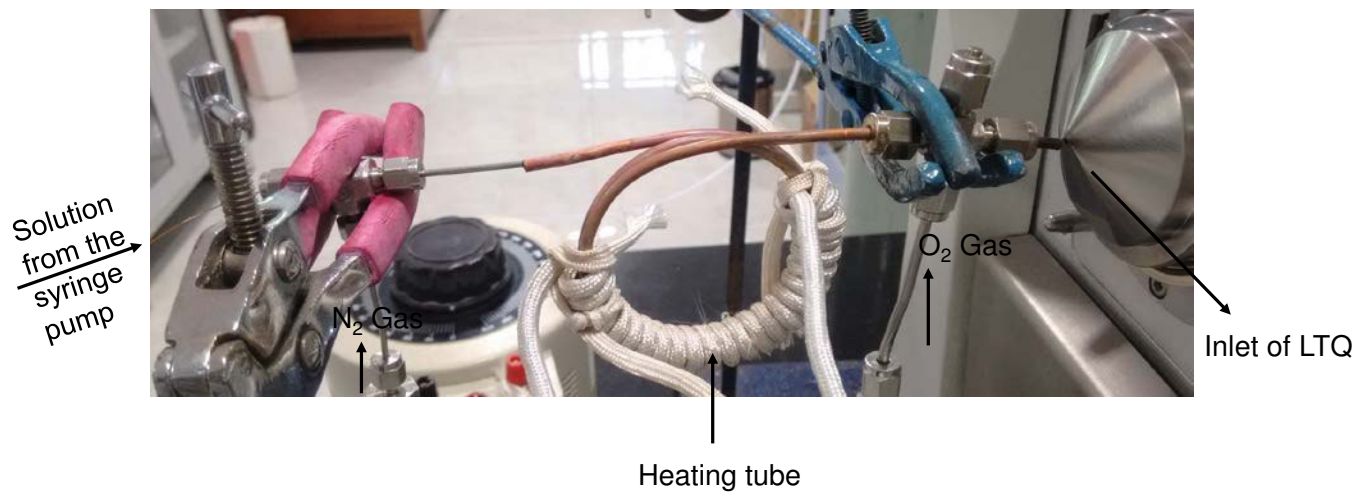


**Fig. S12** ESI mass spectra of  $\text{Ag}_{17}^+$  with varying distances ( $\Delta Y$ ) between the heating tube and ESI source keeping the constant 5 mm distance between the heating tube and inlet. Here, with increasing  $\Delta Y$ ,  $\text{H}_2\text{O}$  and  $\text{O}_2$  addition peaks of  $\text{Ag}_{17}^+$  appear along with the  $\text{Ag}_{17}\text{H}_{14}^+$  peak. At last, only  $\text{Ag}_{17}\text{H}_{14}^+$  peak appears due to the decreasing temperature, as more air flows through the heating tube.

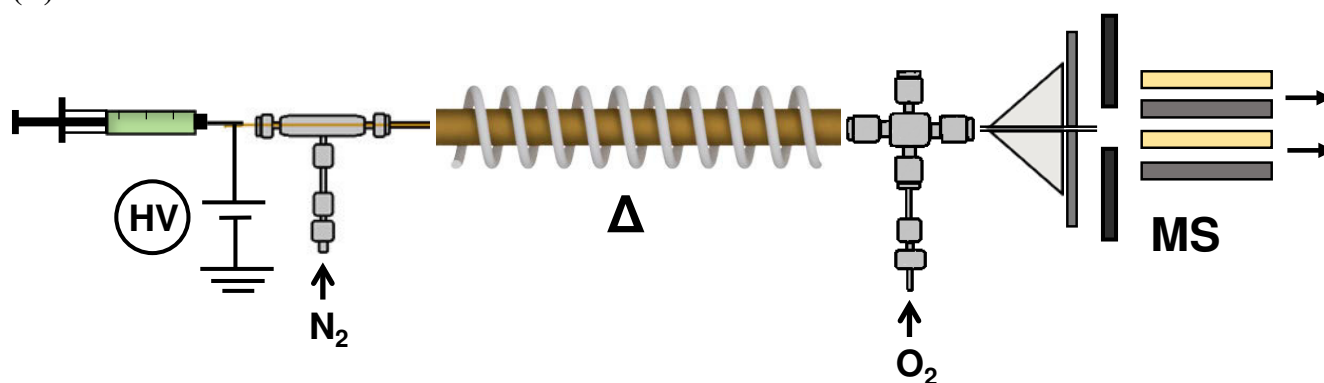
## Supporting information 13

### Photograph of the instrumental set-up and diagram used for ion/molecule reactions:

(A)



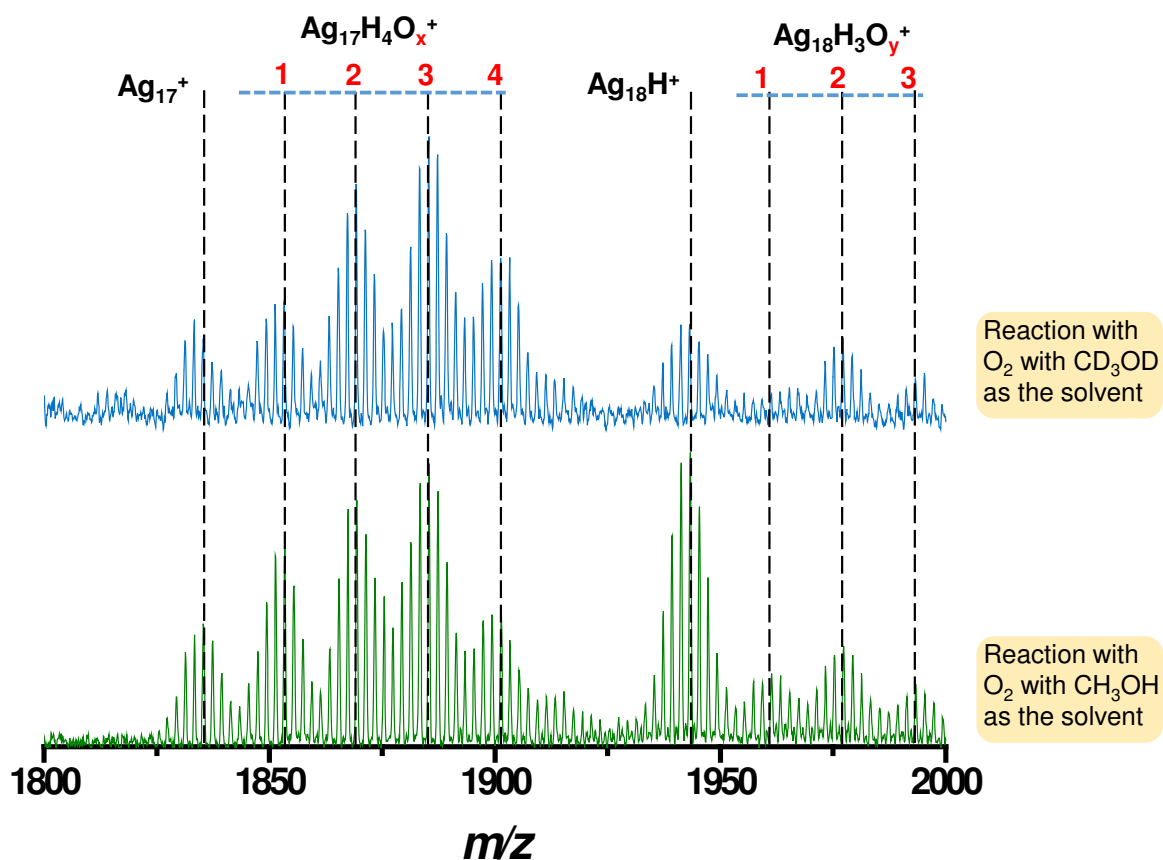
(B)



**S13:** (A) Photograph and (B) schematic diagram of the instrumental set-up used for ion/molecule reactions of naked cluster ions with oxygen.

## Supporting information 14

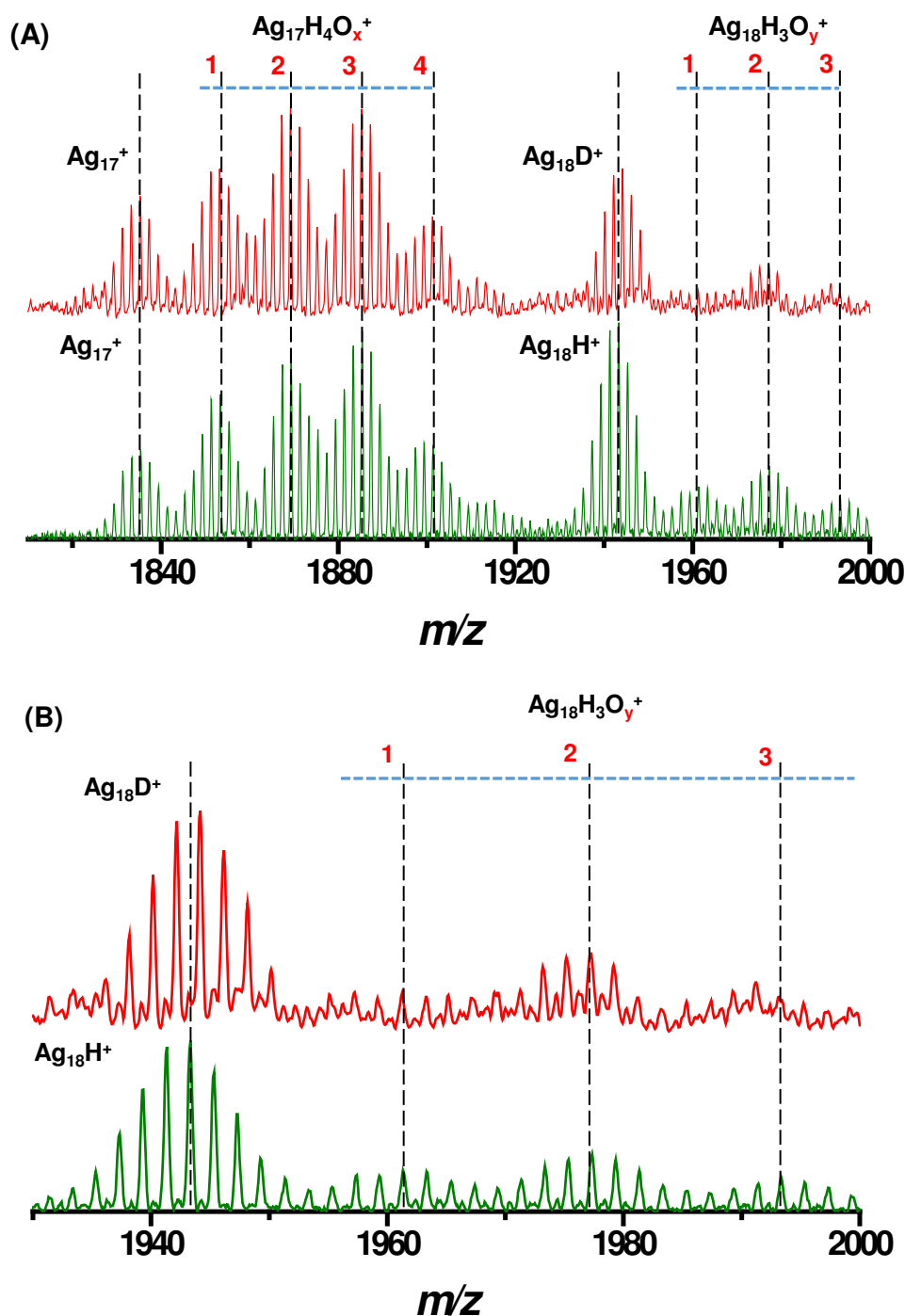
### Comparison of oxygen addition reaction of naked clusters with CD<sub>3</sub>OD as solvent:



**Fig. S14** ESI mass spectra of  $Ag_{17}^+$  and  $Ag_{18}H^+$  ion clusters after reaction with oxygen ( $O_2$ ) gas in presence of  $CD_3OD$  and  $CH_3OH$  as the two different solvents. There were no shifts for the  $Ag_{17}H_4O_x^+$  and  $Ag_{18}H_3O_y^+$  peaks in the case of deuterated and non-deuterated methanol as the solvents.

## Supporting information 15

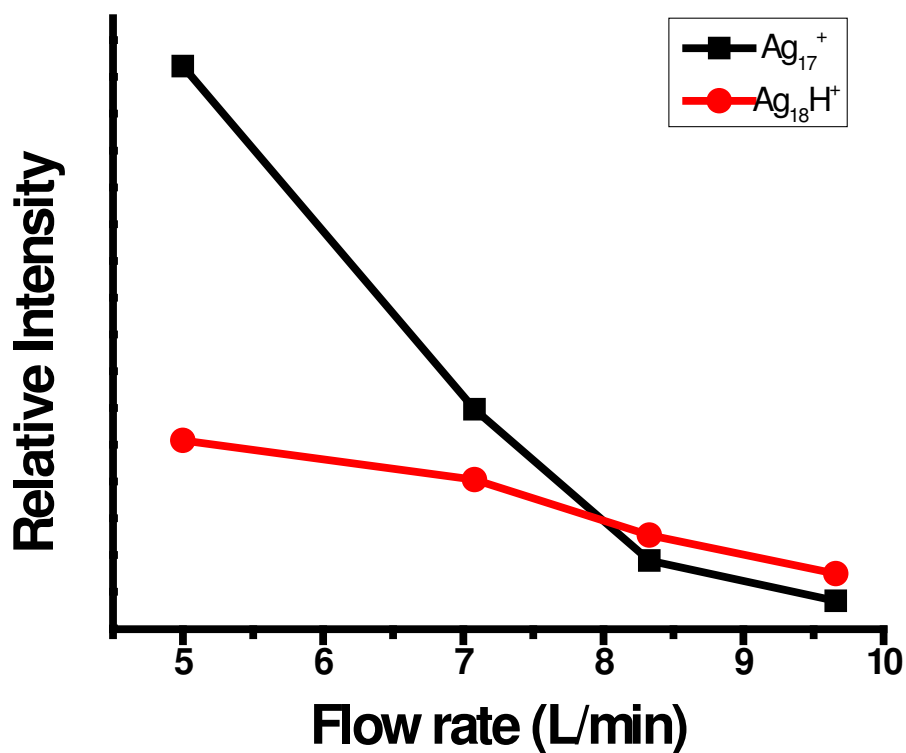
Comparison of oxygen addition reaction of naked clusters created from  $[\text{Ag}_{18}\text{H}_{16}(\text{TPP})_{10}]^{2+}$  and  $[\text{Ag}_{18}\text{D}_{16}(\text{TPP})_{10}]^{2+}$ :



**Fig. S15** (A) ESI mass spectra of  $\text{Ag}_{17}^+$ ,  $\text{Ag}_{18}\text{H}^+$  (green) and  $\text{Ag}_{17}^+$  and  $\text{Ag}_{18}\text{D}^+$  (red) after reaction with oxygen ( $\text{O}_2$ ) gas. (B) Magnified view of the isotopic separation of  $\text{Ag}_{18}\text{H}_3\text{O}_y^+$ , generated from both  $\text{Ag}_{18}\text{H}^+$  (green) and  $\text{Ag}_{18}\text{D}^+$  (red). Top and bottom spectra in each case were generated from  $[\text{Ag}_{18}\text{D}_{16}(\text{TPP})_{10}]^{2+}$  and  $[\text{Ag}_{18}\text{H}_{16}(\text{TPP})_{10}]^{2+}$ , respectively. MS/MS of oxygen added peaks of  $\text{Ag}_{18}\text{H}/\text{D}^+$  could not be performed due to poor intensity.

## Supporting information 16

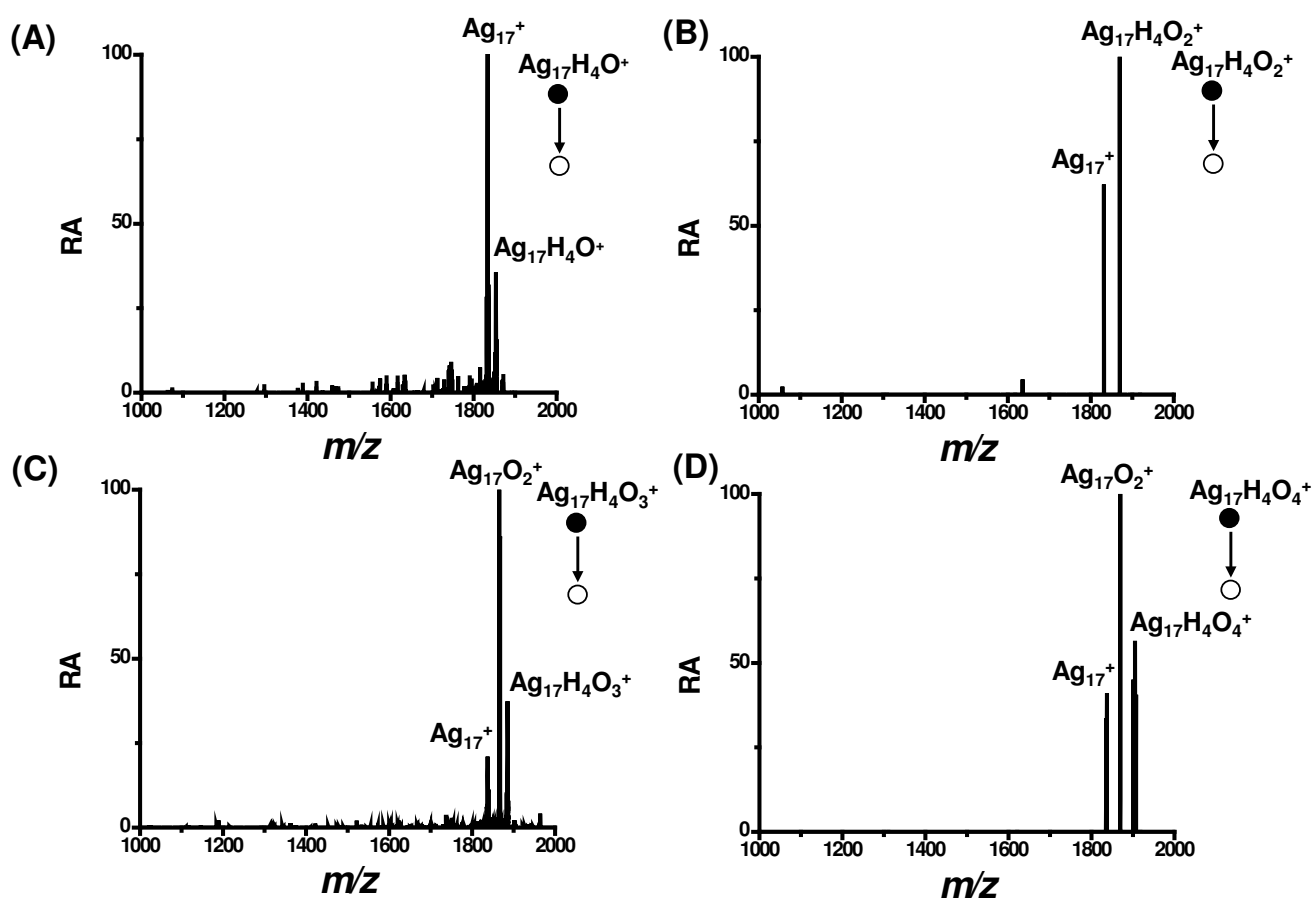
Comparison of reactivity between  $\text{Ag}_{17}^+$  and  $\text{Ag}_{18}\text{H}^+$  ions with oxygen:



**Fig. S16** Relative intensities of  $\text{Ag}_{17}^+$  and  $\text{Ag}_{18}\text{H}^+$  as function of oxygen flow rate which shows the faster reactivity of  $\text{Ag}_{17}^+$  with oxygen compared to the  $\text{Ag}_{18}\text{H}^+$ .

## Supporting information 17

### MS<sup>2</sup> of Ag<sub>17</sub>H<sub>4</sub>O<sup>+</sup>, Ag<sub>17</sub>H<sub>4</sub>O<sub>2</sub><sup>+</sup>, Ag<sub>17</sub>H<sub>4</sub>O<sub>3</sub><sup>+</sup> and Ag<sub>17</sub>H<sub>4</sub>O<sub>4</sub><sup>+</sup> ions:

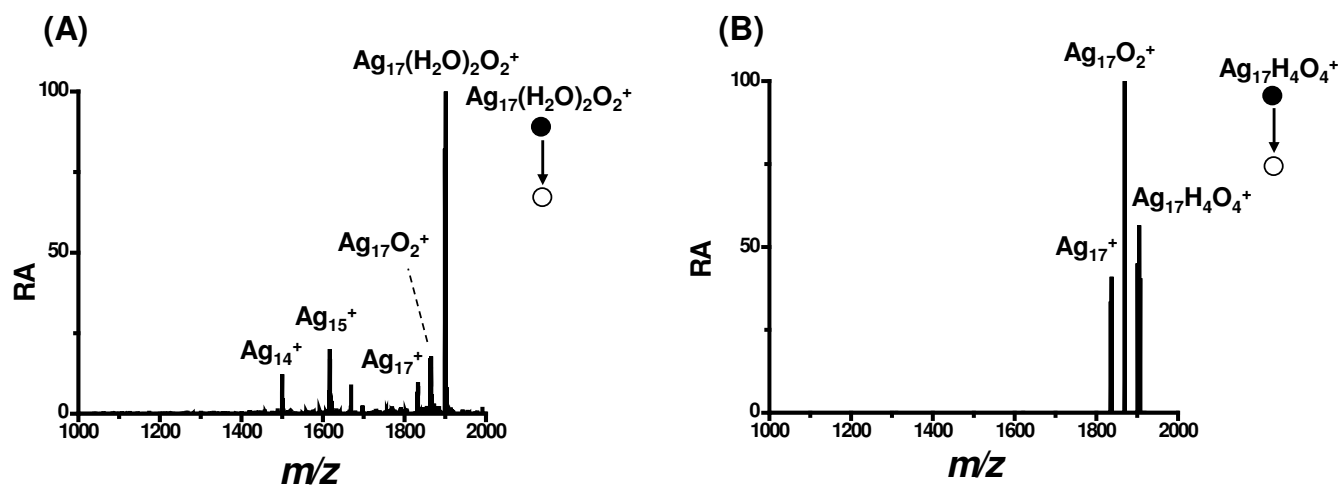


**Fig. S17** MS<sup>2</sup> of (A) Ag<sub>17</sub>H<sub>4</sub>O<sup>+</sup>, (B) Ag<sub>17</sub>H<sub>4</sub>O<sub>2</sub><sup>+</sup>, (C) Ag<sub>17</sub>H<sub>4</sub>O<sub>3</sub><sup>+</sup> and (D) Ag<sub>17</sub>H<sub>4</sub>O<sub>4</sub><sup>+</sup> and the isolation widths are  $m/z$  5, 4.5, 4 and 3, respectively centered at the middle of the isotopic clusters. The collision energies used for Ag<sub>17</sub>H<sub>4</sub>O<sup>+</sup>, Ag<sub>17</sub>H<sub>4</sub>O<sub>2</sub><sup>+</sup>, Ag<sub>17</sub>H<sub>4</sub>O<sub>3</sub><sup>+</sup> and Ag<sub>17</sub>H<sub>4</sub>O<sub>4</sub><sup>+</sup> are 28, 50, 28 and 50 in instrumental units, respectively. For all these cases, due to collisional activation, there is oxygen detachment which results in the parent Ag<sub>17</sub><sup>+</sup> cluster. RA refers to relative abundance.



## Supporting information 18

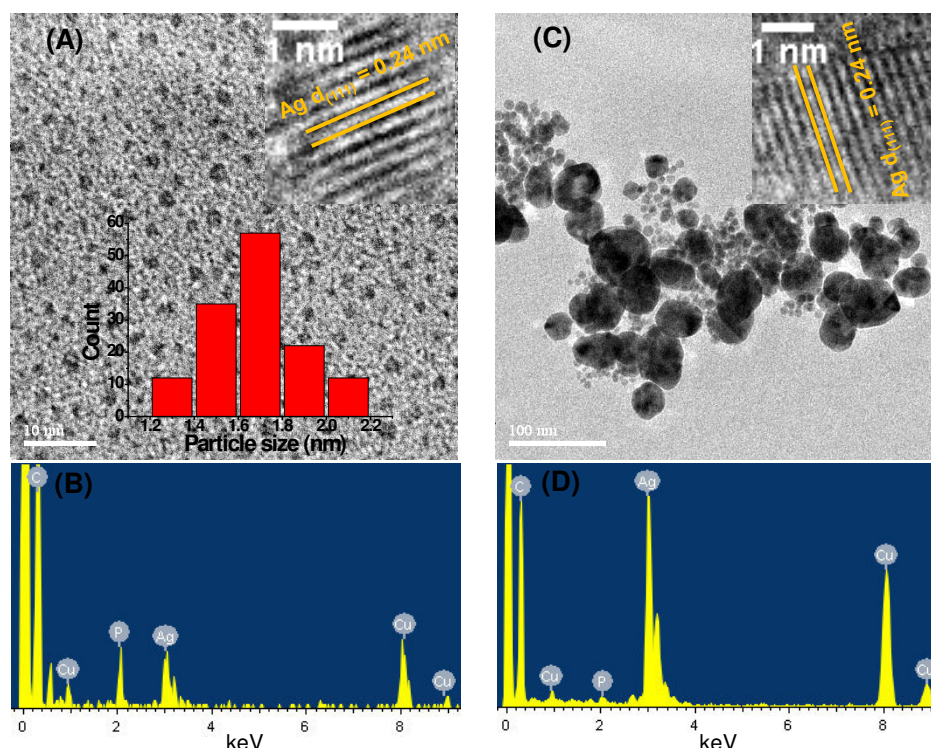
### Comparison of MS<sup>2</sup> results of Ag<sub>17</sub>(H<sub>2</sub>O)<sub>2</sub>O<sub>2</sub><sup>+</sup> and Ag<sub>17</sub>H<sub>4</sub>O<sub>4</sub><sup>+</sup> ions:



**Fig. S18** MS<sup>2</sup> spectra of (A) Ag<sub>17</sub>(H<sub>2</sub>O)<sub>2</sub>O<sub>2</sub><sup>+</sup> and (B) Ag<sub>17</sub>H<sub>4</sub>O<sub>4</sub><sup>+</sup> at the collision energy of 50 in instrumental units. The isolation widths were  $m/z$  5 and 3, respectively centered at the middle of the isotopic clusters. RA refers to relative abundance.

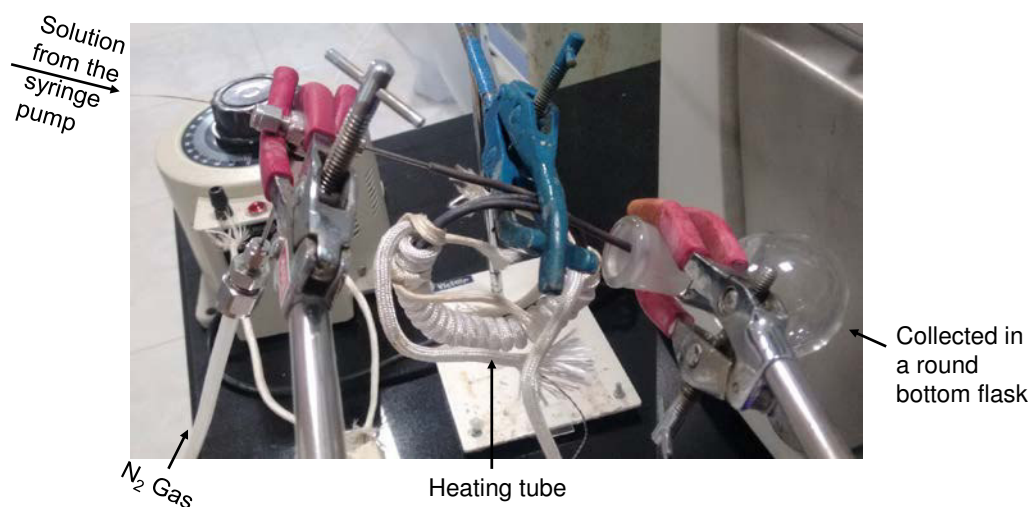
## Supporting information 19

### TEM images of $[\text{Ag}_{18}\text{H}_{16}(\text{TPP})_{10}]^{2+}$ cluster and the electrosprayed products collected:



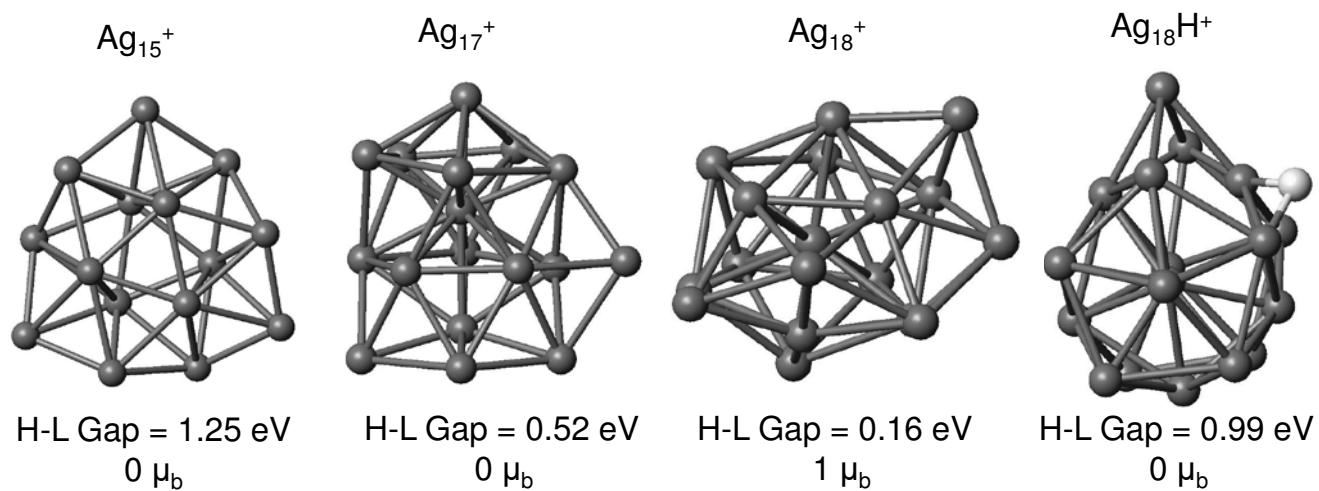
**Fig. 19** (A) TEM image of  $[\text{Ag}_{18}\text{H}_{16}(\text{TPP})_{10}]^{2+}$  cluster before electrospray. Particle distribution shows an average size of  $1.68 \pm 0.19 \text{ nm}$  for the nanoclusters. Lattice spacing of  $0.24 \text{ nm}$  of  $d_{(111)}$  of plane of silver is marked in the inset. (B) EDS spectrum of cluster confirms the composition. (C) TEM image of the collected electrosprayed product of  $[\text{Ag}_{18}\text{H}_{16}(\text{TPP})_{10}]^{2+}$  cluster at the heating tube temperature of  $350^\circ\text{C}$ . In inset, lattice spacing of  $0.24 \text{ nm}$  is marked which confirmed the  $d_{(111)}$  plane of silver. (D) EDS spectrum of the collected product at heating tube temperature of  $350^\circ\text{C}$ .

The products of electrospray were collected using a set-up as shown below.



## Supporting information 20

The calculated structures of  $\text{Ag}_{15}^+$ ,  $\text{Ag}_{17}^+$ ,  $\text{Ag}_{18}^+$ , and  $\text{Ag}_{18}\text{H}^+$  ions:

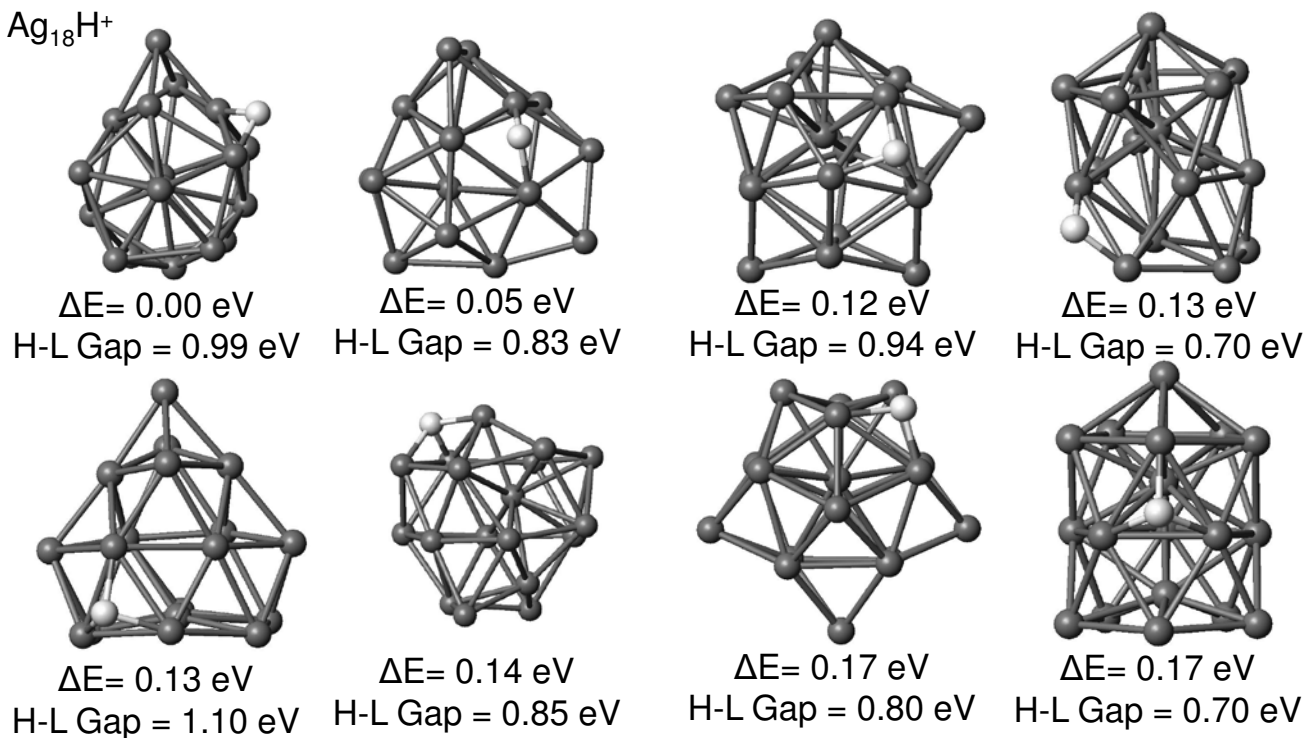


**Fig. S20** The structure and HOMO- LUMO gaps of  $\text{Ag}_{15}^+$ ,  $\text{Ag}_{17}^+$ ,  $\text{Ag}_{18}^+$  and  $\text{Ag}_{18}\text{H}^+$ .  $\text{Ag}_{15}^+$  was found to be resistant to  $\text{O}_2$  etching due to very high HOMO-LUMO gap.

## Supporting information 21

### Isomers of $\text{Ag}_{18}\text{H}^+$ and their energies:

$\text{Ag}_{18}\text{H}^+$



**Fig. S21** The structures, relative energies and HOMO-LUMO gaps of the lowest energy isomers for  $\text{Ag}_{18}\text{H}^+$ .

**Table S22****Experimental and calculated masses measured with the LTQ:**

The most abundant peak of the isotopic cluster is used to define the m/z value.

Experimental m/z	Calculated m/z	Assignment $[\text{Ag}_m(\text{PPh}_3)_n(\text{PPh}_2)_o\text{H}_p\text{O}_q(\text{H}_2\text{O})_r]^{z+}$						
		Ag (m)	PPh <sub>3</sub> (n)	PPh <sub>2</sub> (o)	H (p)	O (q)	H <sub>2</sub> O (r)	Charge (z)
183.00	182.95			1*				1
262.17	262.09		1					1
294.08	294.08		1			2		1
297.17	297.10		1		1	1	1	1
386.83	387.01	1	1		2	1		1
400.83	400.99	1	1			2		1
631.17	631.09	1	2					1
647.17	647.08	1	2			1		1
1185.92	1185.95	11						1
1294.75	1294.86	12						1
1401.67	1401.76	13						1
1454.08	1454.09	11	1		6			1
1510.50	1510.67	14						1
1521.67	1521.75	14			10			1
1617.42	1617.57	15						1
1726.33	1726.48	16						1
1737.58	1737.56	16			11			1
1833.42	1833.38	17						1
1847.50	1847.49	17			14			1
1853.42	1853.41	17			4	1		1
1867.33	1867.39	17				1	1	1
1869.42	1869.40	17			4	2		1
1885.33	1885.40	17			4	3		1
1901.33	1901.39	17				2	2	1
1901.42	1901.39	17			4	4		1
1929.33	1929.35	17				6		1
1943.42	1943.30	18			1			1
1955.50	1955.39	18			13			1
1961.25	1961.31	18			3	1		1
1977.33	1977.30	18			3	2		1
1993.33	1993.30	18			3	3		1

\*Peak is seen with two hydrogens losses.

**Table S23****Experimental and calculated masses measured using the G2-Si:**

The most abundant peak of the isotopic cluster is used to define the m/z value.

Experimental m/z	Calculated m/z	Assignment $[\text{Ag}_m(\text{PPh}_3)_n\text{H}_o]^{z+}$			
		Ag (m)	PPh <sub>3</sub> (n)	H (o)	Charge (z)
2290.1587	2290.2152	18	10	16	2
2159.3291	2159.6199	18	9	16	2
2028.3219	2028.5740	18	8	16	2
1897.3425	1897.5281	18	7	16	2
1765.8406	1765.9827	18	6	16	2

# Electrohydrodynamic Assembly of Ambient Ion-Derived Nanoparticles to Nanosheets at Liquid Surfaces

Depanjan Sarkar,<sup>†</sup> Rajesh Singh,<sup>‡</sup> Anirban Som,<sup>†</sup> C. K. Manju,<sup>†</sup> Mohd Azhardin Ganayee,<sup>†</sup> Ronojoy Adhikari,<sup>\*,‡,§</sup> and Thalappil Pradeep<sup>\*,†</sup>

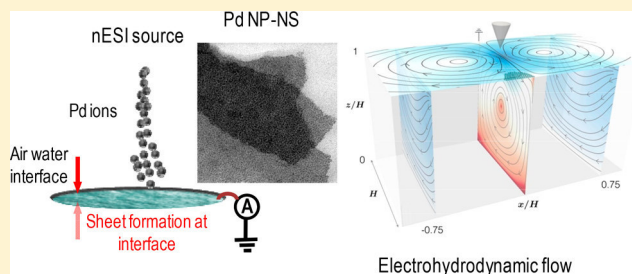
<sup>†</sup>DST Unit of Nanoscience (DST UNS) and Thematic Unit of Excellence (TUE), Department of Chemistry, Indian Institute of Technology Madras, Chennai 60036, India

<sup>‡</sup>The Institute of Mathematical Sciences, HBNI, CIT Campus, Chennai 600113, India

<sup>§</sup>Department of Applied Mathematics and Theoretical Physics (DAMTP), Centre for Mathematical Sciences, University of Cambridge, Wilberforce Road, Cambridge CB3 0WA, United Kingdom

## S Supporting Information

**ABSTRACT:** We describe an ambient ion-based method to create free-standing metal nanosheets, which in turn are composed of nanoparticles of the corresponding metal. These nanoparticle-nanosheets (NP-NSs) were formed by the electrospray deposition (ESD) of metal ions on a liquid–air interface leading to nanoparticles that self-organize under the influence of electrohydrodynamic flows, driven by the electric field induced by the applied potential. Such a two-dimensional organization of noble metals is similar to the assembly of molecules at liquid–air interface and has the possibility of creating a category of new materials useful for diverse applications. Enhanced catalytic activity of the formed NP-NSs for Suzuki–Miyaura coupling reaction was demonstrated, which was attributed to their large surface-to-volume ratios.



## 1. INTRODUCTION

Molecular interactions at liquid–air interfaces have been investigated from the times of Agnes Pockels.<sup>1–3</sup> Structures assembled at liquid–air interfaces and subsequently transferred to solid surfaces have contributed to the understanding of two-dimensional (2D) films of diverse materials.<sup>4–16</sup> While stable molecules and particles arrange at the interface due to surfactancy, it is possible to create nanostructures at the interface directly, starting from atomic precursors. A new methodology introduced recently to synthesize metal NPs on solid surfaces by ambient electrolytic spray<sup>17,18</sup> as well as electrospray<sup>19</sup> can be adapted to liquid surfaces leading to synthesis and assembly simultaneously without the use of reducing agents. Electrospray has been used earlier to assemble polymer beads at liquid surfaces.<sup>20</sup> Superiority of electrolytic spray (direct ionization of noble metals from the corresponding electrodes by electrochemical corrosion) and electrospray (ionization of metal ions from its precursor salts) to make metal NPs over previous methods<sup>21–24</sup> lies in the fact that they do not involve any components other than the metal precursors. This ambient and direct method of synthesis is less expensive in comparison to processes like physical vapor deposition (PVD) (used for synthesis of metal NPs)<sup>22,25</sup> as no sophisticated instrumentation is used. Most important advantage of this method is that it can be performed at room temperature in air. On the other hand, a technique like PVD, a well-studied technique for creating diverse variety of

thin films, can be performed in vacuum at elevated temperatures but has more precision (in terms of thickness control) over this ambient technique. Ambient electrospray deposition (ESD), being a very new technique for materials synthesis, offers new possibilities in terms of easy manipulation of concentrations, variation of mixtures to create alloys, incorporation of soluble precursors, etc. Parameters like deposition rate, deposition time, distance from the nESI tip to the collector surface, etc. have similarities with PVD operations. Atmospheric processing offers various advantages in the utilization of the film as in the case of catalysis. Along with several advantages, the method comes with a disadvantage of lack of precise control over the thickness of the 2D sheets. Controlling ionization efficiency, nature of ions formed, purity of the ions, etc., can cause limitations in the film deposited. The presence of an electrical double layer at the liquid–air interface and its mobility in response to moderate electric fields can drive directed motion at both the surface and the bulk of the liquid which, in turn, can guide suspended NPs into ordered assemblies.

With this objective, we performed a series of experiments by which NPs of Pd were synthesized, without any reducing agent, on the surface of a water reservoir which then self-

Received: May 2, 2018

Revised: July 16, 2018

Published: July 16, 2018



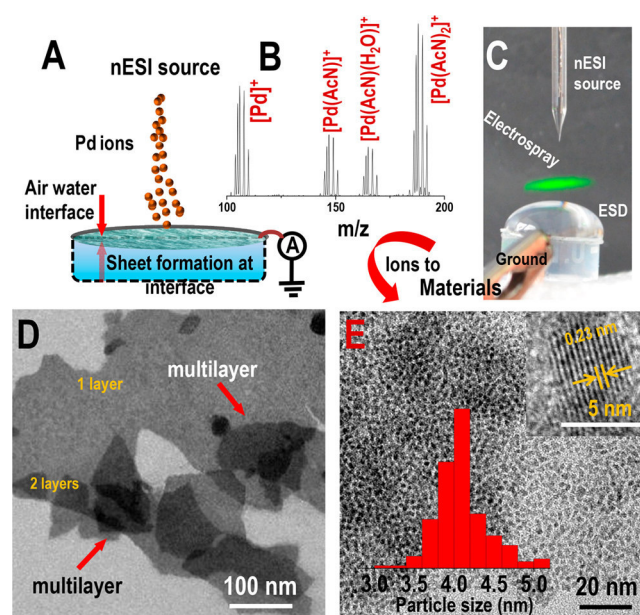
assembled to form nanoparticle-nanosheets (NP-NSs). Visualization of the surface and bulk motion of the liquid, using colored dyes, suggested that fluid flow is the principal mechanism underlying this spontaneous assembly, which has been modeled below. The resulting free-standing NP-NS was used for applications such as heterogeneous catalysis for C–C bond formation. Pd is well-known as a catalyst for C–C bond formation. Here we show enhanced activity of the 2D NP-NSs due to their high active surface area. The simplicity and versatility of this methodology, which allows for diverse precursors and varying liquids, opens up the possibility of creating a rich variety of nanoscale materials for studying novel physicochemical phenomena.

## 2. EXPERIMENTAL DETAILS

In all our deposition experiments, electrospray deposition was used. Electrospray deposition experiments were performed using a homemade nanoelectrospray (nESI) setup. A borosilicate glass capillary of 1.5 mm outer diameter and 0.86 mm inner diameter was pulled into two parts leaving an opening of 15–20  $\mu\text{m}$ , at the tip. These microtips, filled with the precursor solution, were used as the ion source. A positive DC potential of 1.5–2.5 kV was applied through a platinum (Pt) wire electrode to generate the electrospray. The Pt wire was immersed into the precursor solution. The electrospray plume, ejected from the tip of the glass capillary, was collected over a grounded liquid surface (deionized water (DI) water taken in a 1 mL plastic vial) to synthesize NP-NSs. A copper strip stuck on the inside wall of the vial was connected to the ground through a picoammeter; hence the copper strip works as the ground electrode. 5 mM solutions of  $\text{PdCl}_2$ ,  $\text{Au}(\text{OAc})_3$  in acetonitrile and  $\text{AgOAc}$  in water were used as precursors for the respective metals. In the cases of Pd and Au, DI water was used as the deposition surface, and in the case of Ag, it was changed to ethylene glycol (EG). We have deposited Pd and Au on water as the precursor salts are insoluble in water. In the cases of Ag and Ni, the liquid was changed from water to ethylene glycol (EG) to ensure reduced solubility of  $\text{AgOAc}$  and  $\text{Ni}(\text{II})$  acetate tetrahydrate, used as the precursors for Ag and Ni, respectively. In contrast, when water was used as a deposition substrate, Ag NPs did not form the nanosheet. The liquid surface was grounded through a picoammeter to measure the deposition current. All deposition experiments were performed at a typical deposition current of 60–70 nA. After a certain time of deposition, a thin layer was seen floating on the liquid surface, which was found to be a metal sheet made of NPs. As we used nESI for deposition for all our experiments, spreading of solvent may not have much role in the observed process. In the case of nESI, the size of droplets is very small. Hence, when they travel a distance of around 10 mm from the source to deposit on the liquid surface, most of the solvent evaporates.

## 3. RESULTS AND DISCUSSION

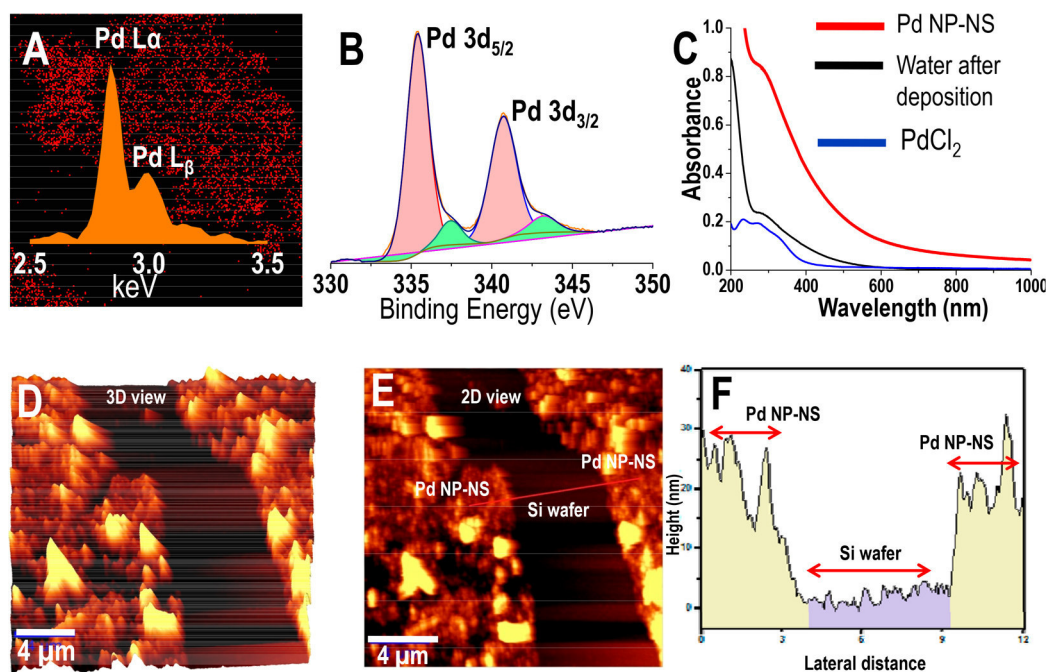
Experiments were conducted as shown in Figure 1A, wherein a nanoelectrospray ion (nESI) source gently deposits ions (at 60–70 nA) on a grounded liquid surface. Experimental details of the methodology are described in the section [Experimental Details](#) and [Supporting Information](#). A schematic representation of the experimental setup with complete dimensional details is shown in Figure S1, [Supporting Information](#). At first, we collected the mass spectrum (Figure 1B) from an



**Figure 1.** (A) Schematic of the electrospray deposition of  $\text{PdCl}_2$  on water surface, (B) mass spectrum of  $\text{PdCl}_2$  solution in acetonitrile, collected using nESI source, and (C) optical photograph of electrospray deposition at air–water interface. The electrospray was visualized using a green laser pointer showing scattering from the droplets. Liquid was grounded by a metal clip. (D, E) TEM images of the formed Pd NP-NS collected from the liquid surface after washing with water, at different magnifications. Inset of (E) shows HRTEM image of Pd sheet showing that it is made of nearly uniform crystalline Pd NPs and a size distribution histogram for the Pd NPs.

electrosprayed solution of  $\text{PdCl}_2$  in acetonitrile (AcN). Peaks corresponding to  $\text{Pd}^+$  and solvated  $\text{Pd}^+$  ions such as  $[\text{Pd}(\text{AcN})]^+$ ,  $[\text{Pd}(\text{AcN})(\text{H}_2\text{O})]^+$ , and  $[\text{Pd}(\text{AcN})_2]^+$  with their characteristic isotopic patterns confirm that the droplets generated in electrospray contain Pd in its +1 state. Electrospray, being reducing in nature, converts Pd(II) to Pd(I) within the charged droplets (Figure 1B). These  $\text{Pd}^+$  ions along with the counteranions ( $\text{Cl}^-$  in this case) were deposited on a grounded water surface. The spray plume also contains salt clusters (Figure S2), but the major species are metal ions and their solvated ions. The counteranions go into the water and the metal ions get reduced to form the NPs (discussed in detail below). A copper strip was attached to the wall of the container and it was grounded through a picoammeter. In the course of deposition,  $\text{Pd}^+$  ions got reduced to Pd(0) by taking electrons from the grounded electrode. Figure 1C shows an optical photograph of the deposition process. A green laser pointer was shone on the spray plume for its better visualization. After 1 h of deposition at a deposition current 40 nA, an orange colored film was seen floating on water. This film was collected on different substrates by scooping it from water and was characterized using various techniques. Figure 1D shows a TEM image of clean Pd NP-NSs. Detailed TEM imaging was performed to prove that the sheet was made of Pd NPs. Figure 1E shows a TEM image of the as-synthesized Pd NP-NSs, and inset shows a high-resolution transmission electron microscopic (HRTEM) image of the NPs present in the sheet, respectively. Figure 1E clearly shows the presence of monodisperse Pd NPs in the sheet. The average size of Pd NPs was around 4 nm. Inset of Figure 1E shows a size distribution histogram for the NPs. The lattice distance of these NPs





**Figure 2.** (A) EDS mapping and spectrum of the Pd NP-NSs, showing the presence of only Pd, (B) X-ray photoelectron spectrum showing that Pd is in its zero valence state with slight contribution from a surface oxide layer, (C) UV-vis spectra of Pd NP-NS, water after Pd deposition and PdCl<sub>2</sub> in ACN. For the Pd sheet, as there is scattering, the Y axis may be taken as extinction. (D, E) AFM images of the Pd NP-NSs and (F) height profile taken across the red line in (E). 3D views are shown to illustrate the roughness. The image was taken deliberately by including a crack in the film to measure the film thickness. The film was taken on a silicon wafer.

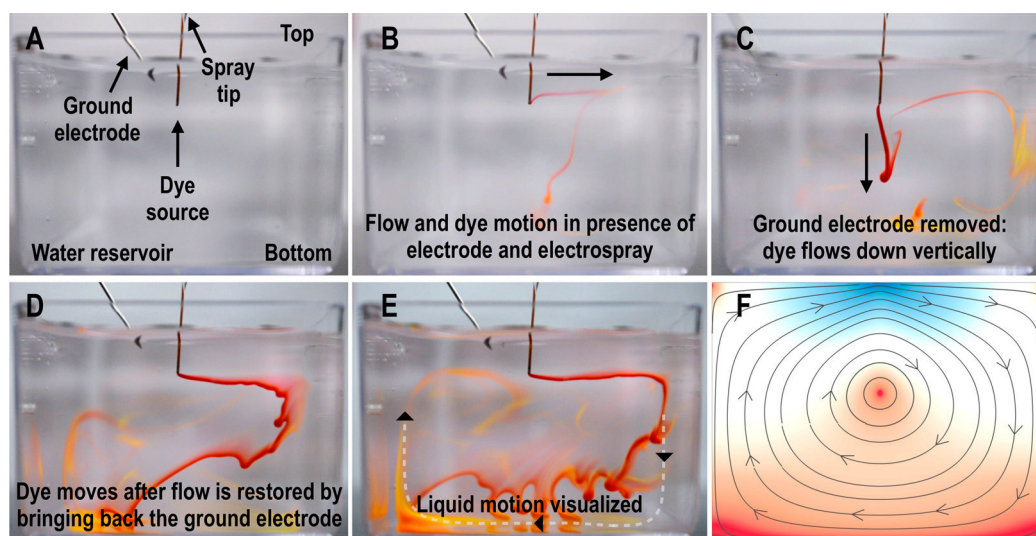
matches with the (111) plane of Pd, proving the metallic nature of the Pd NPs. The deposited Pd ions were neutralized at the interface and aggregated to form Pd NPs.

Monodispersity of the NPs suggests that the uniformity of the droplets has a significant role in controlling the particle size because the uniform droplets may contain identical number of metal ions, which in turn make the NPs after reduction. The NPs were assumed to be born as soon as the charged droplets, containing similar number of ions, impacted the water surface. We can calculate the number of atoms present in a 4 nm Pd NP and correlate that to the droplet size. From the literature of size distribution of electrosprayed droplets, we know that in the case of acetonitrile, the charged droplets are approximately 700 nm in diameter. These droplets shrink (within 3.5 ms) to 100 nm size while traveling in air.<sup>26</sup> In our case, we assume the droplets that reach the surface of the water after 10 mm travel in air are 250 nm in size. Hence the volume of the droplet is  $8.1 \times 10^{-15}$  mL. The number of Pd ions present in the droplet considering the concentration of the Pd solution (5 mM) is 24 486. The number of atoms present in a 4 nm Pd NP is around 26 000 (considering 137 pm as the metallic radius of Pd). These two numbers are close enough to conclude that the droplet size is a very important factor for the monodispersity of the NPs, although further efforts are needed to verify this aspect, and we are continuing to investigate this. We performed other measurements to understand the material better.

Energy dispersive spectroscopic (EDS) analysis of the same shows the presence of only Pd in the sheet (Figure 2A). A detailed EDS spectrum is presented in Figure S3, where no impurities are detected. Hence we speculate that the chloride ions (counterpart of the precursor) go into the water reservoir. This was proved by measuring the conductivity of the water with respect to deposition time (Figure S4); the plot shows a

linear enhancement. Figure 2B shows the X-ray photoelectron spectrum (XPS) of Pd NP-NSs with peaks due to Pd 3d<sub>5/2</sub> (335.4 eV) and Pd 3d<sub>3/2</sub> (340.7 eV), which support the presence of Pd(0). The XPS spectrum does not show the presence of any other species like chlorine, proving that these particles are unprotected. For the XPS study, more material was collected on the sample plate by collecting the NP-NS multiple times. EDS spectrum collected from the Pd NP-NSs (Figure S3) shows that the NSs are made of 100% Pd. There are no organic substances present as protecting species. Hence, we believe that the NPs are bare metal particles. We see the presence of small amounts of oxygen in EDS and a weak feature due to Pd<sup>2+</sup> in XPS. This surface oxide may be the bridge for the NPs to form NSs, along with van der Waals forces. Figure 2C shows the UV-vis spectra of the Pd NP-NSs (red trace, solid state UV-vis spectrum of Pd NP-NS, coated on a quartz coverslip), the water on which the deposition happened (black trace), and the precursor PdCl<sub>2</sub> solution (blue trace).

The difference between the blue and red traces clearly proves that the salt solution has transformed to metal NPs upon ESD, at room temperature. The hump near 300 nm is a characteristic feature of Pd NPs due to the plasmonic excitation, which occurs around 340 nm for naked Pd NPs in a pure dispersion in toluene (0.2 mg/mL).<sup>27</sup> The UV-vis spectrum of the water after deposition (black trace) also shows the same feature corresponding to Pd NPs. This implies that some portion of Pd NPs goes into the water due to the generated flow field in water, whereas most of them stay at the interface and arrange to form Pd NP-NSs. Quantitative analysis shows that approximately 85% of the Pd comes at the surface. This metallic sheet can be made over a large area; Figure S5A shows a TEM image of such a NP-NS over an area of 80 μm<sup>2</sup>. The image shows the presence of excess Pd on the sheet, due



**Figure 3.** (A) Electro spray deposition setup. (B) Advection of the dye by the flow when the spray is present. (C) Cessation of flow, with the dye falling vertically, when the spray is absent. (D) Resumption of the advection as the spray is again turned on and (E) circulation of the dye as it is carried along by the fluid streamlines. (F) Streamlines of a theoretically computed flow which compares well with circulation seen in (E).

to longer deposition time, which can be removed by washing with deionized (DI) water. The sheets can be scooped out of the liquid surface with a spatula or coverslip or similar supports. After the ESD synthesis, the as-synthesized Pd NP-NSs were collected and washed with DI water by taking them in an Eppendorf vial and shaking the vial manually. Figure S5B shows the TEM image of the same sheet after washing. In this case, we see very clean sheets of Pd made of Pd NPs. The sheet was broken into small parts after washing, retaining their morphology, proving the stability of these NP-NSs. When the film thickness is large, the film could resist mechanical damage. Control experiments were performed for better understanding the phenomena as will be discussed below. Here, we speculate that the electron transfer from the grounded electrode to the metal ions was assisted by the hydroxyl ions ( $\text{OH}^-$ ). High mobility of the  $\text{OH}^-$  ions resulted in fast transfer of electrons, leading to the formation of uniform Pd NPs at the water surface.  $\text{OH}^-$  ions are also responsible for the formation of a mobile electrical double layer which drives an electrohydrodynamic flow at both the surface and the bulk of water.

The Pd NPs move in the flow field (see below) and arrange themselves to form a thin nanosheet at the air–water interface. A quantitative theory of this phenomenon is provided below. Atomic force microscopy (AFM) was performed on the Pd NP-NSs to understand the thickness. Figure 2D and Figure 2E show the AFM images of the Pd NP-NSs, in 3D and 2D views, respectively. Figure 2F shows a height profile of a Pd NP-NS showing an average thickness of 26 nm and a roughness of  $\pm 12$  nm. The thickness presented above is calculated from the AFM image. In a typical thickness of 26 nm, the NP-NSs contain approximately four monolayers. However, the thickness of the layers formed on the liquid surface may be different as the film may get modified during the process of sample preparation.

Although the assembly of the NPs is not highly ordered so that it can be named as hexagonal assembly, deposition at a very low deposition current, i.e., a slow deposition rate, leads to a relatively better-ordered structure, whereas a fast deposition leads to an increased disorder. Figure S6A and Figure S6B show TEM images of Pd NP-NSs synthesized by slow (30 nA) and fast (80 nA) ESD conditions, respectively. Such a current

can be carried by the residual  $\text{OH}^-$  ions present ( $6.023 \times 10^{16}$  ions/L) in neutral water. A control experiment was performed to show the role of  $\text{OH}^-$ . ESD of acetonitrile solution of  $\text{PdCl}_2$  was performed under the same conditions. In this case the deposition was over acidic pH (pH 4) and no NP-NSs were observed (Figure S7). At low pH due to the lack of  $\text{OH}^-$  ions, the precursor salt did not reduce completely to form Pd NPs. Hence the metal ions did not neutralized completely and as a result they combined with their counterions and remained as salt after deposition, on top of the liquid which can be seen in the TEM image and EDS spectrum in Figure S7A, although part of it was reduced to form crystalline NPs as shown in Figure S7B. Due to the salt deposition, free movement of the bare NPs was hindered leading to aggregation instead of 2D assembly of NSs. Free-standing metal NP-NSs were made using other metals also. Parts A, B, and C of Figure S8 show the TEM images of NP-NSs made of silver, gold, and nickel, respectively. In the case of gold, an acetonitrile solution of  $\text{Au(III)}$  acetate was electro sprayed on water. Just like the case of Pd, formation of a thin film was seen at the air–water interface. The thin film was collected on a TEM grid for characterization. The more common  $\text{HAuCl}_4$  salt was not suitable as it exists as  $\text{H}^+$  and  $\text{AuCl}_4^-$  in solution and does not form NPs by this process. From experiments discussed in the Supporting Information, we know that the solubility of the precursor salt, dispersibility of the formed NPs, and surface tension of the liquid substrate play crucial roles in the NP-NS formation. Ag NP-NSs were synthesized using other silver precursors like silver nitrate and silver perchlorate (Figure S9).

ESD was also performed with a mixture of precursors to make bimetallic NP-NSs. In this experiment, mixed precursor solutions of two different metals (Ag–Pd and Au–Pd) were electro spray deposited on top of the water surface. 10 mM solutions of silver acetate (in water), palladium chloride (in ACN), and 5 mM solution of gold acetate (in ACN) were used as precursors. All other experimental parameters were identical to the previous experiments. Figure S10A and Figure S10B show the TEM images taken after ESD of Au–Pd and Ag–Pd mixtures, respectively. It is evident from the TEM images that the metal NPs were assembled and phase separated. The

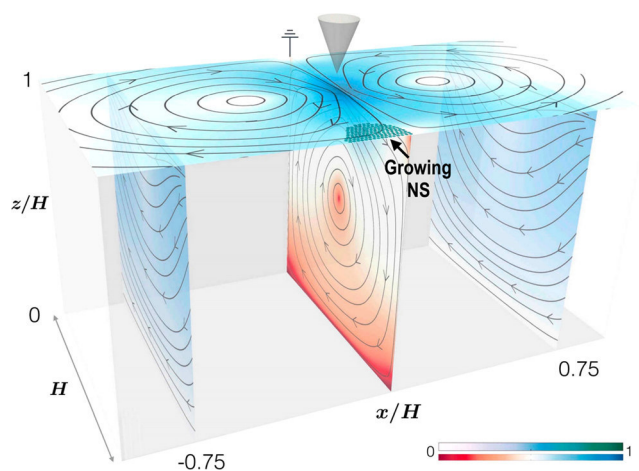


mobilities of different ions may play crucial roles in separating them. EDS mapping (Figure S10C–F) images clearly show that the NPs aggregated separately, when deposited from a mixed precursor solution. It appears that the kinetics of reduction of different metals by this method is different which results in phase separation than alloying.

The above experimental results demonstrate that NP-NS formation is robust against alterations of metal in the electrospray and the liquid on whose surface the spray falls. Thus, generic physical mechanisms rather than specific chemical mechanisms must be at play, which leads us to the following conjecture. Spray deposition creates additional ionic species in the liquid, a fraction of which are adsorbed at the liquid–air interface, producing a strongly charged electrical double layer.<sup>28</sup> It is known, for instance, that such a double layer forms at room temperature at the air–water interface with a negative  $\zeta$ -potential of a few tens of millivolts. The tangential electric field at the liquid–air interface provides an electromotive force on the double layer, setting it in motion along the electric field if the  $\zeta$ -potential is positive and opposite to it if the  $\zeta$ -potential is negative. Viscous stresses in the liquid set adjacent fluid layers into motion which then develops into a steady-state fluid flow with a circulatory character, the latter property being a consequence of finite compressibility and container volume. The flow can continuously advect NPs dispersed in the bulk of the liquid to the liquid–air interface, and its surface component can guide NPs to assemble into packed structures.

To test the validity of this conjecture, we visualize the surface and bulk flow in the liquid both in the presence and in the absence of electrospray, as shown in Figure 3. The flow experiment was shown in a square shaped container for the following two reasons: (i) calculations were performed assuming a square shape container as the collector for ESD and (ii) to prove that the shape of the container does not have any effect in the formation of the NSs. We maintained an identical distance between the center of the spray and the ground electrode in both the cases. The experimental setup is shown in panel A. In the presence of electrospray, the dye does not fall vertically, as would be expected, but is advected tangential to the liquid–air interface; see panel B. In contrast, when the spray is absent by removing the ground electrode, the dye falls vertically under gravity, with no detectable tangential convection; see panel C. The tangential convection resumes when the spray is restored and the process can be repeated at will with completely predictable results; see panels E and F. The general circulatory pattern of the bulk fluid flow reveals itself once the dye is transported along the fluid streamlines, given a sufficient duration of spraying (see video S1 provided in Supporting Information). We have also shown the flow of the liquid at the surface using both experimental and theoretical surface flow. As shown in the Figure S11 (and in video S2), the combined effect of electrospray and tangential electric field from the electrode leads to a convective flow field in which the particles are driven to the edge of the container (opposite the electrode). The electrohydrodynamic flow brings the particles within the range of the short-range attraction and packs the particles into a 2D sheet.<sup>29</sup> Once the particles are packed to form the 2D sheet, the film formed is stabilized by a tiny oxide layer present between the particles. This is the reason for the particles not to fall apart once the flow is off.

Figure 4 shows the results of a theoretical computation of these streamlines, which is in excellent qualitative agreement



**Figure 4.** Theoretically computed streamlines of electrohydrodynamic flow in long channel whose cross section is a square of sides  $H$ . The spray from the cone above deposits charges at the air–liquid interface which are then set into motion by the tangential electric field. For a negative interfacial  $\zeta$ -potential, the resulting flow puts NS away from the ground electrode. The bulk fluid, though electrically neutral, is set into motion due to viscous stresses. The combined action of the surface and bulk flow guides the nanoparticles into ordered aggregates at the edge of the channel opposite the electrode.

with the experiment. We now outline the quantitative aspects of the electrohydrodynamic computation that yields the streamlines. The basis of our computations is the electrohydrodynamic system of equations first proposed by Taylor and Melcher,<sup>30</sup> where conservation of fluid momentum and electric charge are combined with constitutive equations for the mechanical and electrical stress, assuming that the fluid is mechanically Newtonian (viscosity  $\eta$ ) and electrically a linear dielectric (permittivity  $\epsilon$ ) and an ohmic conductor (conductivity  $\sigma$ ).

In the regime of slow viscous flow relevant to the present experiment, this implies

$$\nabla \cdot (\mathbf{T}^m + \mathbf{T}^e) = 0 \quad (1)$$

where  $T_{ij}^m = -p\delta_{ij} + \eta_{ijkl}\nabla_k v_l$  and  $T_{ij}^e = \epsilon E_i E_j - 1/2 \epsilon E^2 \delta_{ij}$  are, respectively, Cartesian components of the mechanical and electrical stress tensors,  $v_i$  and  $E_i$  are the Cartesian components of the fluid flow. The fluid flow is assumed to be incompressible,  $\nabla \cdot \mathbf{v} = 0$ , and the electric field is assumed to be irrotational,  $\nabla \times \mathbf{E} = 0$ . With the constitutive equations,  $\mathbf{D} = \epsilon \mathbf{E}$ , for the displacement  $\mathbf{D}$  and  $\mathbf{J} = \sigma \mathbf{E}$  for the current density  $\mathbf{J}$ , the electric charge distribution  $\rho$  obeys the Maxwell and continuity equations

$$\nabla \cdot \mathbf{D} = \rho \quad (2)$$

$$\partial \rho + \nabla \cdot (\mathbf{J} + \rho \mathbf{v}) = 0 \quad (3)$$

and the above three coupled systems of equations, when supplemented by interfacial boundary conditions, determine the fluid flow, electric field, and charge distribution.

We solve the above equations in a rectangular channel of square cross section whose length is much greater its width  $H$ . We assume the limit in which the charge relaxation time  $\tau = \epsilon/\sigma$  ( $\sim 10^{-5}$  s for water) and the flow time scale  $\tau' = \eta H/\gamma$  ( $\sim 10^{-4}$  s for water, where  $\gamma$  is the surface tension) are both rapid compared to the remaining time scales so that the bulk is electroneutral and all free charges are confined to the interface.

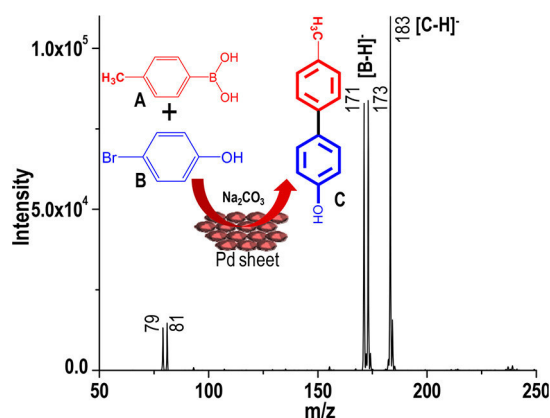
We assume a constant tangential electric field and a Gaussian free charge density profile  $\rho(\mathbf{r}) \sim \exp[-r^2/(2a^2)]$  where  $a$  is the characteristic width. We ensure that the ratio  $a/H$  matches experiment. Then, the fluid flow can be expressed as an integral over all boundaries as

$$\mathbf{v}(\mathbf{r}) = \int \mathbf{G}(\mathbf{r}, \mathbf{r}') \cdot \mathbf{f}^s(\mathbf{r}') dS + \int \mathbf{K}(\mathbf{r}, \mathbf{r}') \cdot \mathbf{nv}^s(\mathbf{r}') dS \quad (4)$$

where  $\mathbf{f}^s = \rho\mathbf{E}$  is the interfacial force density,  $\mathbf{v}^s$  is the interfacial velocity,  $\mathbf{G}$  is a Green's function of Stokes flow, and  $\mathbf{K}$  is its associated stress tensor. The integral can be completed following procedures outlined in the [Supporting Information](#), and the streamlines of the flow can be numerically computed. The result of the above computation is shown in [Figure 4](#). The circulatory streamlines are clearly visible in both the bulk and surface flows which are, as explained above, central to the mechanism of self-assembly of NPs.

Pd in its zero oxidation state is very well-known for catalyzing C–C bond formation reactions. Hence, the catalytic activity of the synthesized Pd NP-NS was tested for the Suzuki–Miyaura coupling reaction. For this, the as-synthesized Pd NP-NSs were taken on quartz coverslips and dipped into a reaction mixture of a boronic acid and an organohalide. An aqueous solution of  $\text{Na}_2\text{CO}_3$  was added to the reaction mixture to make it basic in nature. After the addition of the catalyst, the reaction mixture was stirred in a round-bottom flask at room temperature and the product was analyzed using mass spectrometry.

[Figure 5](#) shows a mass spectrum of the reaction mixture containing 4-bromophenol (reactant I) and 4-tolylboronic acid



**Figure 5.** Mass spectrum collected after Pd NP-NS catalyzed coupling reaction between 4-tolylboronic acid and 4-bromophenol. Inset shows the structures of the reactants and the product.

(reactant II) in the presence of Pd NP-NS (0.02 mg) catalyst after 30 min of stirring. Intense peak at  $m/z$  183 in the mass spectrum corresponds to the reaction product, i.e., 4'-methyl[1,1'-biphenyl]-4-ol (III). The inset shows the molecular structures of the reactants and the product. The mass spectrum also shows two peaks for II at  $m/z$  171 and 173, due to the equal abundance of the isotopes of Br. Sodium bromide ( $\text{NaBr}$ ) is a byproduct in this reaction leading to the presence of peaks corresponding to bromide ion ( $\text{Br}^-$ ) in the mass spectrum (peaks at  $m/z$  79  $\text{Br}^-$  and 81  $\text{Br}^-$ ).

Control experiments were performed to prove that the Pd NP-NS catalyst is essential for the coupling reaction. The mass spectrum ([Figure S12A](#)) collected from a mixture of the same

reactants, without a catalyst, after 30 min did not show any peak other than the reactants. A comparative study was also carried out to estimate the efficiency of our catalyst. In this experiment, commercially available tetrakis(triphenylphosphine)palladium(0) was used as the catalyst (1 mg) for one set of reaction (reaction mixture X). In the other set (reaction mixture Y), Pd NP-NS was used as the catalyst. All the other parameters such as the concentration of the reactants, solvent, temperature and reaction time were kept constant in both the cases. [Figure S12B](#) and [S12C](#) show the mass spectrum collected from the reaction mixtures X and Y, respectively, after 30 min of stirring. The efficiency (calculated considering only the metal percentage in both the cases) of Pd NP-NS catalyst was approximately 23 times higher than the commercial catalyst. The 2D nature and surface roughness exposing more catalytically active sites may be attributed as the main reason for higher efficiency. From the AFM data ([Figure 2D](#) and [Figure 2E](#)) it is also evident that the surface of the NP-NSs is highly rough. It was tested for C–C coupling reactions for various boronic acids and organic halides (see [Table S1](#), [Figure S13](#), and [S14](#)). UV–vis spectroscopy also supports the C–C bond formation showing a broad hump around 450 nm (the red trace in [Figure S15](#)), a characteristic feature of biphenyl compounds. All the data presented here prove that the Pd NP-NSs are more efficient catalysts for Suzuki–Miyaura coupling reaction. Stability and reusability of the catalyst were also checked using UV–vis spectroscopy and TEM imaging. A detailed description of this is given in the [Supporting Information](#) ([Figure S16](#)).

## 4. CONCLUSIONS

In summary, we report an ambient ion based method of making free-standing 2D metal sheets made of bare NPs, at the liquid–air interface. An electrohydrodynamic flow field was generated by ESD on the liquid surface, which in turn assisted the assembly of the NPs. This is the first report of generating such a flow field in fluids using ESD. The NP-NSs were made under ambient conditions at room temperature from metal salt precursors. We showed that such sheets can be made of different elements such as Pd, Au, Ag, and Ni. Synthesized 2D NP-NSs were used as efficient and reusable heterogeneous catalysts for C–C bond formation reactions. The methodology suggested can be used for organized nanoscale films of metals under ambient conditions. The structure and composition of the assemblies can be varied easily to obtain new properties.

## ■ ASSOCIATED CONTENT

### Supporting Information

The Supporting Information is available free of charge on the ACS Publications website at DOI: [10.1021/acs.jpcc.8b04169](https://doi.org/10.1021/acs.jpcc.8b04169).

Experimental details, schematic representation of the experimental setup; detailed TEM EDS spectrum of Pd NP-NSs; plot of conductivity of bulk water, on whose surface deposition happened, vs deposition time; TEM image of Pd NP-NS before and after washing with DI water; TEM images of Pd NP-NS synthesized by slow and fast electrospray deposition; TEM images of Pd NPs formed after ESD of  $\text{PdCl}_2$  on formic acid solution; TEM images of NP-NSs made of silver, gold, and nickel; TEM image of silver NP-NS made from silver perchlorate and silver nitrate; mass spectrum of control experiments, experimental and theoretical surface flows;

mass spectrum collected from the reaction mixtures (serial no. 2–5) mentioned in Table S1; mass spectrum collected from the reaction mixtures (serial no. 6–10) mentioned in Table S1; UV–vis spectrum; proof of stability and reusability of the catalyst; structures of reactants and products; theoretical details of electrohydrodynamic flow (PDF)

Video S1 of fluid flow visualization (AVI)

Video S2 of surface flow visualization (AVI)

## AUTHOR INFORMATION

### Corresponding Authors

\*R.A.: e-mail, [rjoy@imsc.res.in](mailto:rjoy@imsc.res.in).

\*T.P.: e-mail, [pradeep@iitm.ac.in](mailto:pradeep@iitm.ac.in).

### ORCID

Anirban Som: 0000-0002-6646-679X

Thalappil Pradeep: 0000-0003-3174-534X

### Notes

The authors declare no competing financial interest.

## ACKNOWLEDGMENTS

We thank the Nano Mission, Department of Science and Technology, Government of India, for continued support of our research program. D.S. and M.A.G. thank the University Grants Commission, A.S. and C.K.M. thank the Council of Scientific and Industrial Research for research fellowships.

## REFERENCES

- (1) Pockels, A. The angle of contact and the spreading of liquids on solid substances. *Phys. Z.* **1914**, *15*, 39–46.
- (2) Reich, K. Out of the Shadows. Contributions of Twentieth-Century Women to Physics edited by Nina Byers and Gary Williams. *Acta Crystallogr., Sect. A: Found. Crystallogr.* **2008**, *64* (3), 432.
- (3) Rayleigh. Surface Tension. *Nature* **1891**, *43*, 437.
- (4) Natansohn, A.; Rochon, P. Photoinduced Motions in Azo-Containing Polymers. *Chem. Rev. (Washington, DC, U. S.)* **2002**, *102* (11), 4139–4175.
- (5) Li, X.; Zhang, G.; Bai, X.; Sun, X.; Wang, X.; Wang, E.; Dai, H. Highly conducting graphene sheets and Langmuir-Blodgett films. *Nat. Nanotechnol.* **2008**, *3* (9), 538–542.
- (6) Cote, L. J.; Kim, F.; Huang, J. Langmuir-Blodgett assembly of graphite oxide single layers. *J. Am. Chem. Soc.* **2009**, *131* (3), 1043–1049.
- (7) Kim, J.; Cote, L. J.; Kim, F.; Yuan, W.; Shull, K. R.; Huang, J. Graphene Oxide Sheets at Interfaces. *J. Am. Chem. Soc.* **2010**, *132* (23), 8180–8186.
- (8) Whang, D.; Jin, S.; Wu, Y.; Lieber, C. M. Large-Scale Hierarchical Organization of Nanowire Arrays for Integrated Nanosystems. *Nano Lett.* **2003**, *3* (9), 1255–1259.
- (9) Fendler, J. H. Self-Assembled Nanostructured Materials. *Chem. Mater.* **1996**, *8* (8), 1616–1624.
- (10) Kim, F.; Kwan, S.; Akana, J.; Yang, P. Langmuir-Blodgett nanorod assembly. *J. Am. Chem. Soc.* **2001**, *123* (18), 4360–4361.
- (11) Lu, Y.; Liu, G. L.; Lee, L. P. High-Density Silver Nanoparticle Film with Temperature-Controllable Interparticle Spacing for a Tunable Surface Enhanced Raman Scattering Substrate. *Nano Lett.* **2005**, *5* (1), 5–9.
- (12) Zasadzinski, J. A.; Viswanathan, R.; Madsen, L.; Garnæs, J.; Schwartz, D. K. Langmuir-Blodgett films. *Science (Washington, DC, U. S.)* **1994**, *263* (5154), 1726–33.
- (13) Hammond, P. T. Form and function in multilayer assembly: New applications at the nanoscale. *Adv. Mater. (Weinheim, Ger.)* **2004**, *16* (15), 1271–1293.
- (14) Langmuir, I.; Blodgett, K. B. A new method of investigating unimolecular films. *Kolloid-Z.* **1935**, *73*, 258–263.
- (15) Blodgett, K. B. Monomolecular films of fatty acids on glass. *J. Am. Chem. Soc.* **1934**, *56*, 495.
- (16) Lee, S.-L.; Lin, C.-H.; Cheng, K.-Y.; Chen, Y.-C.; Chen, C.-h. Stability of Guest-Incorporated 2D Molecular Networks. *J. Phys. Chem. C* **2016**, *120* (44), 25505–25510.
- (17) Li, A.; Luo, Q.; Park, S.-J.; Cooks, R. G. Synthesis and Catalytic Reactions of Nanoparticles formed by Electrospray Ionization of Coinage Metals. *Angew. Chem., Int. Ed.* **2014**, *53* (12), 3147–3150.
- (18) Li, A.; Baird, Z.; Bag, S.; Sarkar, D.; Prabhath, A.; Pradeep, T.; Cooks, R. G. Using Ambient Ion Beams to Write Nanostructured Patterns for Surface Enhanced Raman Spectroscopy. *Angew. Chem., Int. Ed.* **2014**, *53* (46), 12528–12531.
- (19) Sarkar, D.; Mahitha, M. K.; Som, A.; Li, A.; Wlekinski, M.; Cooks, R. G.; Pradeep, T. Metallic Nanobrushes Made using Ambient Droplet Sprays. *Adv. Mater. (Weinheim, Ger.)* **2016**, *28* (11), 2223–2228.
- (20) Nie, H.-L.; Dou, X.; Tang, Z.; Jang, H. D.; Huang, J. High-Yield Spreading of Water-Miscible Solvents on Water for Langmuir-Blodgett Assembly. *J. Am. Chem. Soc.* **2015**, *137* (33), 10683–10688.
- (21) Quintanilla, A.; Valvo, M.; Lafont, U.; Kelder, E. M.; Kreutzer, M. T.; Kapteijn, F. Synthesis of Anisotropic Gold Nanoparticles by Electrospraying into a Reductive-Surfactant Solution. *Chem. Mater.* **2010**, *22* (5), 1656–1663.
- (22) Sugioka, D.; Kameyama, T.; Kuwabata, S.; Torimoto, T. Single-step preparation of two-dimensionally organized gold particles via ionic liquid/metal sputter deposition. *Phys. Chem. Chem. Phys.* **2015**, *17* (19), 13150–13159.
- (23) Sugioka, D.; Kameyama, T.; Kuwabata, S.; Yamamoto, T.; Torimoto, T. Formation of a Pt-Decorated Au Nanoparticle Monolayer Floating on an Ionic Liquid by the Ionic Liquid/Metal Sputtering Method and Tunable Electrocatalytic Activities of the Resulting Monolayer. *ACS Appl. Mater. Interfaces* **2016**, *8* (17), 10874–10883.
- (24) Hamada, T.; Sugioka, D.; Kameyama, T.; Kuwabata, S.; Torimoto, T. Electrocatalytic activity of bimetallic Pd-Au particle films prepared by sequential sputter deposition of Pd and Au onto hydroxyl-functionalized ionic liquid. *Chem. Lett.* **2017**, *46* (7), 956–959.
- (25) Anantha, P.; Cheng, T.; Tay, Y. Y.; Wong, C. C.; Ramanujan, R. V. Facile production of monodisperse nanoparticles on a liquid surface. *Nanoscale* **2015**, *7* (40), 16812–16822.
- (26) Wortmann, A.; Kistler-Momotova, A.; Zenobi, R.; Heine, M. C.; Wilhelm, O.; Pratsinis, S. E. Shrinking Droplets in Electrospray Ionization and Their Influence on Chemical Equilibria. *J. Am. Soc. Mass Spectrom.* **2007**, *18* (3), 385–393.
- (27) Quiros, I.; Yamada, M.; Kubo, K.; Mizutani, J.; Kurihara, M.; Nishihara, H. Preparation of alkanethiolate-protected palladium nanoparticles and their size dependence on synthetic conditions. *Langmuir* **2002**, *18* (4), 1413–1418.
- (28) Björneholm, O.; Hansen, M. H.; Hodgson, A.; Liu, L.-M.; Limmer, D. T.; Michaelides, A.; Pedevilla, P.; Rossmeisl, J.; Shen, H.; Tocci, G.; Tyrode, E.; Walz, M.-M.; Werner, J.; Bluhm, H. Water at Interfaces. *Chem. Rev.* **2016**, *116* (13), 7698–7726.
- (29) Shoji, T.; Shibata, M.; Kitamura, N.; Nagasawa, F.; Takase, M.; Murakoshi, K.; Nobuhiro, A.; Mizumoto, Y.; Ishihara, H.; Tsuboi, Y. Reversible photoinduced formation and manipulation of a two-dimensional closely packed assembly of polystyrene nanospheres on a metallic nanostructure. *J. Phys. Chem. C* **2013**, *117* (6), 2500–2506.
- (30) Melcher, J. R.; Taylor, G. I. Electrohydrodynamics: A Review of the Role of Interfacial Shear Stresses. *Annu. Rev. Fluid Mech.* **1969**, *1* (1), 111–146.

## Supporting Information

# Electrohydrodynamic Assembly of Ambient Ion-Derived Nanoparticles to Nanosheets at Liquid Surfaces

Depanjan Sarkar,<sup>[a]</sup> Rajesh Singh,<sup>[b]</sup> Anirban Som,<sup>[a]</sup> C. K. Manju,<sup>[a]</sup> Mohd Azhardin Ganayee,<sup>[a]</sup>

Ronojoy Adhikari,\*<sup>[b,c]</sup> Thalappil Pradeep\*<sup>[a]</sup>

[a] Department DST Unit of Nanoscience (DST UNS) and Thematic Unit of Excellence (TUE), Department of Chemistry, Indian Institute of Technology Madras Chennai – 60036, India.

[b] The Institute of Mathematical Sciences-HBNI CIT Campus, Chennai 600113, India.

[c] Department of Applied Mathematics and Theoretical Physics (DAMTP), Centre for Mathematical Sciences University of Cambridge Wilberforce Road, Cambridge CB3 0WA, United Kingdom.

### Table of Contents

Item	Description	Page No.
<b>Materials and methods</b>	Experimental details	S3
<b>Figure S1</b>	Schematic representation of the experimental set-up	S4
<b>Figure S2</b>	Wide range mass spectrum	S4
<b>Figure S3</b>	Detailed TEM EDS spectrum of Pd NP-NSs	S5
<b>Figure S4</b>	Plot of conductivity of the water, on which deposition happened,	S5

	vs deposition time	
<b>Figure S5</b>	TEM images of Pd NP-NS before and after washing with DI water	S6
<b>Figure S6</b>	TEM image of Pd NP-NS synthesized by slow and fast electrospray deposition, respectively	S6
<b>Figure S7</b>	TEM images of Pd NPs formed after ESD of PdCl <sub>2</sub> on formic acid solution	S7
<b>Figure S8</b>	TEM images of NP-NSs made of silver, gold and nickel	S7
<b>Figure S9</b>	TEM image of silver NP-NS made from silver perchlorate and silver nitrate	S7
<b>Figure S10</b>	TEM images of bimetallic NP-NSs	S8
<b>Figure S11</b>	Experimental and theoretical surface flows	S8
<b>Figure S12</b>	Mass spectrum of control experiments	S9
<b>Figure S13</b>	Mass spectrum collected from the reaction mixtures (serial no. 2-5) mentioned in Table S1	S10
<b>Figure S14</b>	Mass spectrum collected from the reaction mixtures (serial no. 6-10) mentioned in Table S1	S11
<b>Figure S15</b>	UV-Vis spectrum	S11
<b>Figure S16</b>	Stability and reusability of the catalyst	S12
<b>Table S1</b>	Structures of reactants and products	S10
<b>Theoretical details</b>	Theoretical details of electrohydrodynamic flow	S13
<b>Video S1</b>	Video of fluid flow visualization	S15
<b>Video S2</b>	Video of fluid flow visualization at the surface	



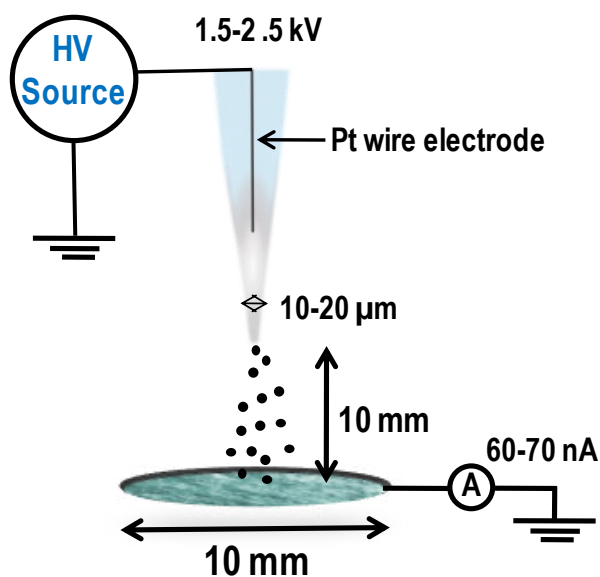
## Experimental Details

**Materials:** All the chemicals used for the experiments were commercially available and were used without any purification. Palladium(II) chloride ( $\text{PdCl}_2$ ), Silver acetate ( $\text{AgOAc}$ ), gold(III) acetate ( $\text{Au(OAc)}_3$ ) and tetrakis(triphenylphosphene) palladium(0) were purchased from Sigma Aldrich, India. 4-Methylphenylboronic acid, benzboronic acid, 4-bromophenol, 4-bromobenzoic acid, 4-bromoaniline, 4-iodophenol and 4-iodobenzoic acid were purchased from Avra Synthesis Pvt. Ltd. Hyderabad, India. HPLC grade acetonitrile (Sigma Aldrich, India) was used as solvent for all spray synthesis. A mixture of ethanol and locally available deionized water was used as the solvent for all the coupling reactions. Ethanol was purchased from Jiangsu Huaxi International Trade Co., Ltd., China.

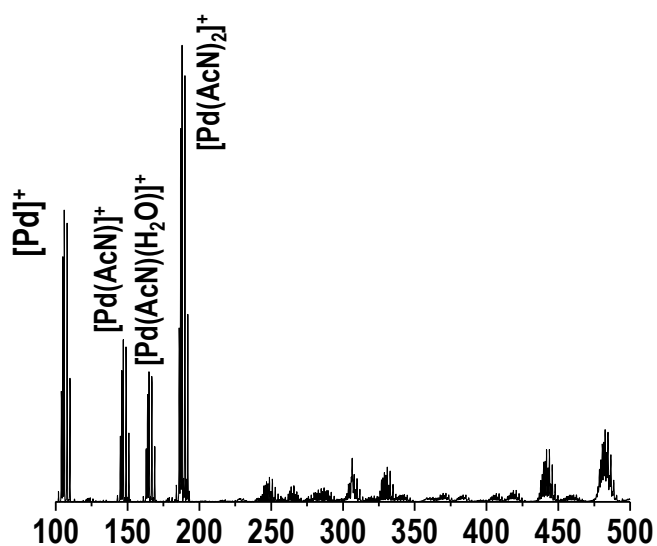
**Instruments:** For all experiments, nanospray emitters were made using a micropipette puller (P-97) purchased from Sutter instrument, USA. Mass spectra were collected using an ion trap LTQ XL (Thermo Scientific, San Jose, California) mass spectrometer. For all mass spectrometry experiments, the spectrum was acquired both in positive and negative ion modes depending upon the functional groups of the compounds, in the mass range of  $m/z$  50 to 500 under the following conditions: source voltage 3-5 kV, positive and negative (depending upon the analyte), capillary temperature  $150^\circ\text{C}$ , capillary voltage  $\pm 45$  V and tube lens voltage  $\pm 100$  V,  $\pm$  V are needed for positive and negative modes, respectively. Transmission electron microscopy (TEM) and high-resolution transmission electron microscopy (HRTEM) were performed using an accelerating voltage of 200 kV on a JEOL 3010, 300 kV instrument equipped with a UHR polepiece. A Gatan 794 multiscan CCD camera was used for image acquisition. EDS spectra were collected on Oxford Semi STEM system housed on the TEM. Samples were taken onto 300-mesh, carbon coated copper grids (spi Supplies, 3530C- MB) by scooping it from the liquid surface and drying under ambient conditions before examining in TEM. X-ray photoelectron spectroscopic (XPS) measurements were conducted using an Omicron ESCA probe



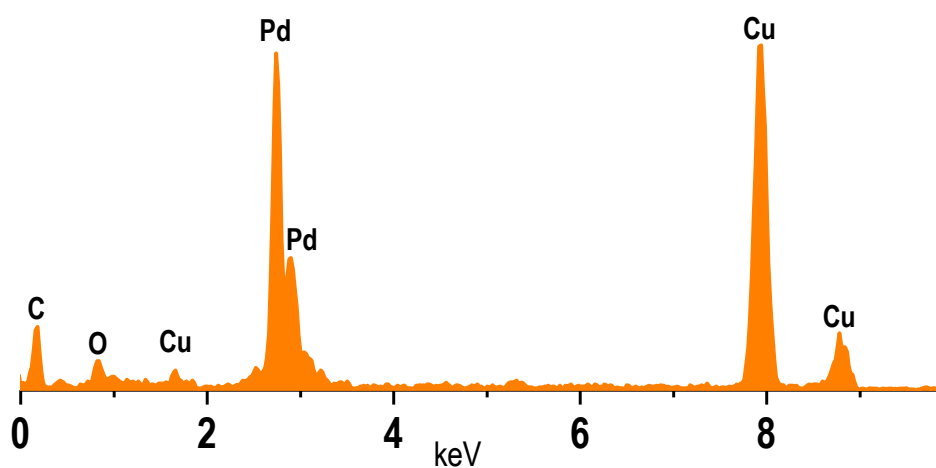
spectrometer with polychromatic  $\text{MgK}\alpha$  X-rays ( $h\nu=1253.6$  eV). Ultraviolet-visible (UV-Vis) spectra were measured with a PerkinElmer Lambda 25 instrument in the wavelength range of 200–1100 nm.



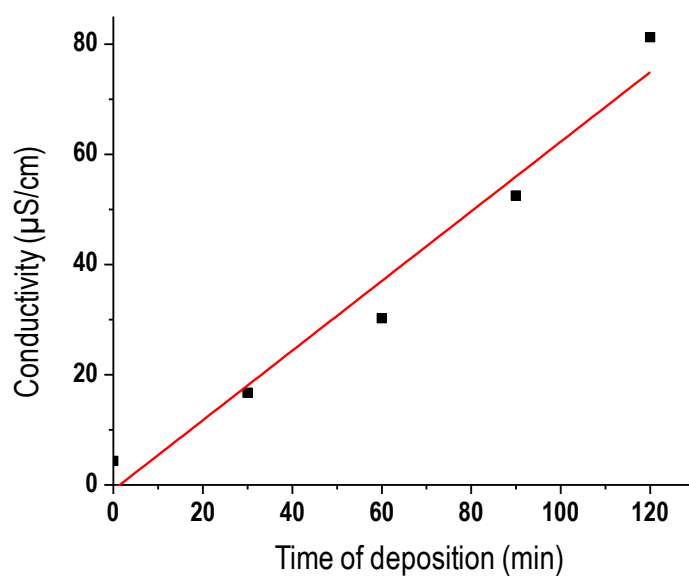
**Figure S1.** Schematic representation of the experimental set-up with dimensional details.



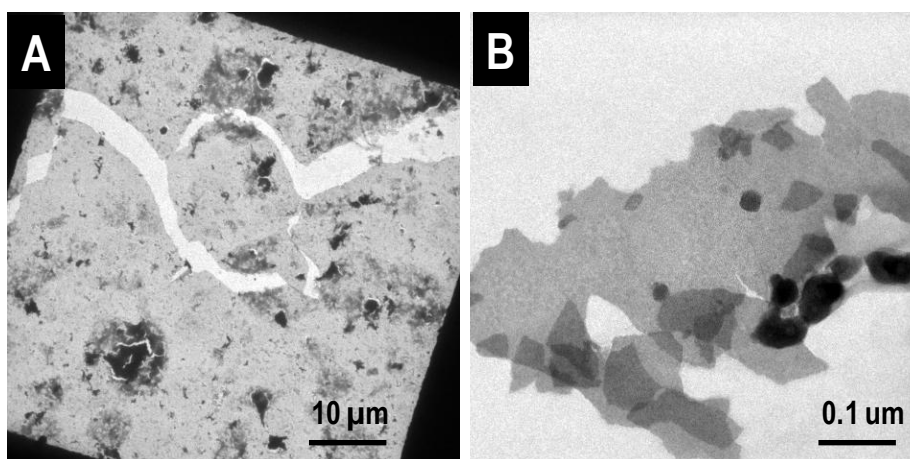
**Figure S2.** Mass spectrum collected from nESI of  $\text{PdCl}_2$  showing the presence of salt clusters.



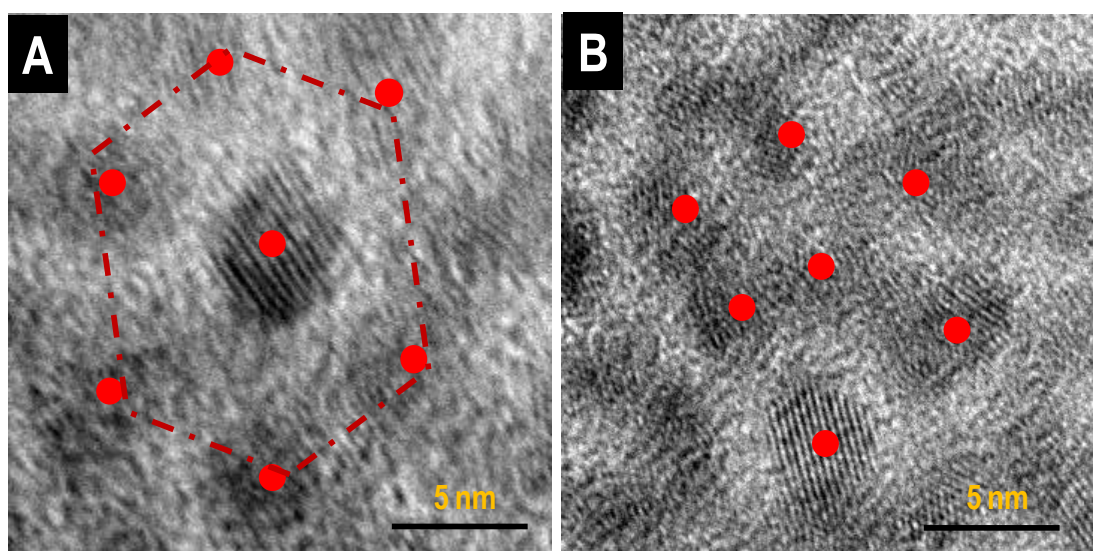
**Figure S3.** Detailed TEM EDS spectrum of Pd NP-NSs. Peaks due to C and Cu are from the TEM grid.



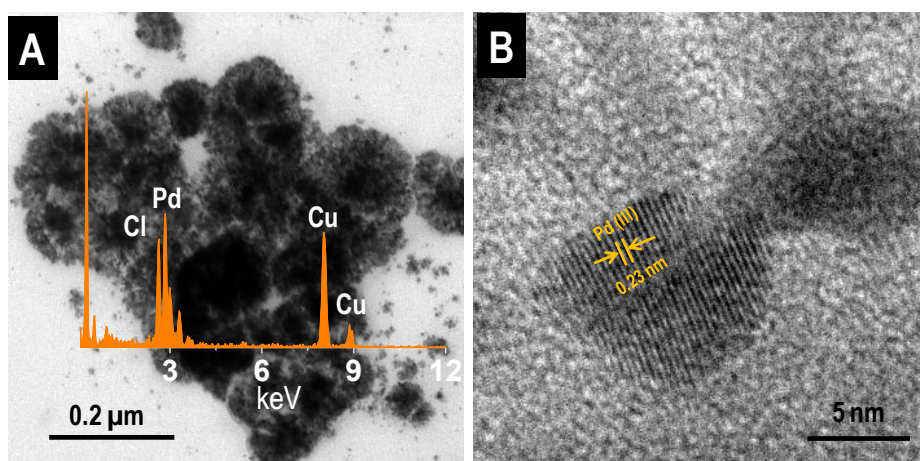
**Figure S4.** Plot of conductivity of the water, on which deposition happened, vs deposition time, showing linear enhancement in conductivity.



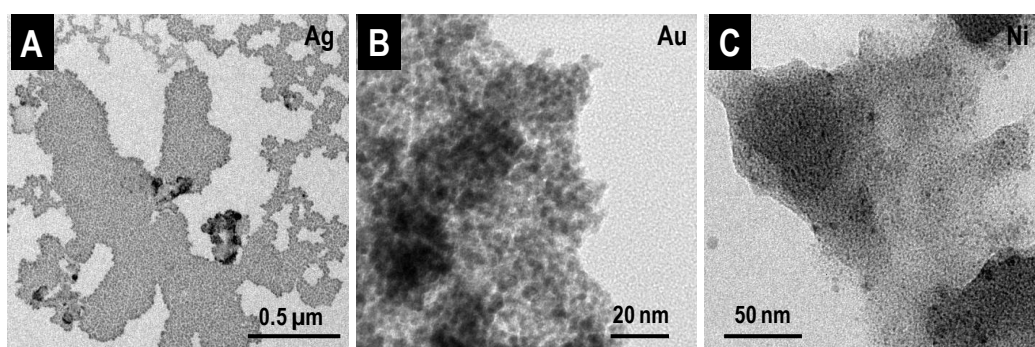
**Figure S5.** A) TEM image of as-synthesized Pd NP-NS over 80  $\mu\text{m}^2$  area, B) Pd NP-NS after washing with DI water.



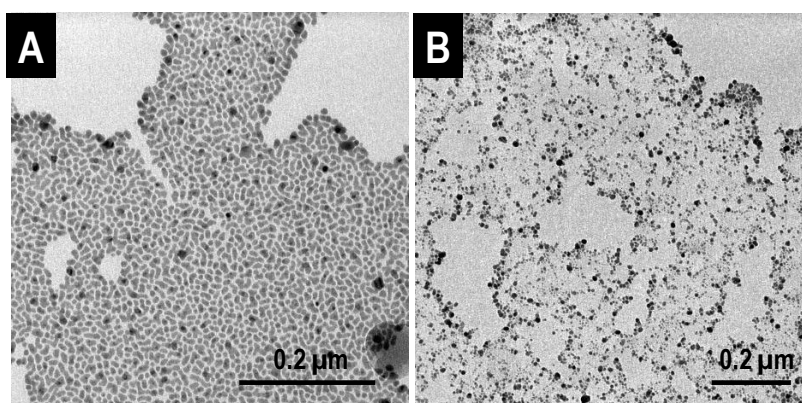
**Figure S6.** A and B show TEM image of Pd NP-NS synthesized by slow (30 nA) and fast (80 nA) electrospray deposition, respectively. Some particles are marked to show the regularity.



**Figure S7.** A) TEM images of Pd NPs formed after electrospray deposition of  $\text{PdCl}_2$  on formic acid solution. In this case, sheet formation was not observed. EDS spectrum shows salt deposition. B) Part of the NPs are composed of metallic Pd as shown by the lattice planes (Pd).

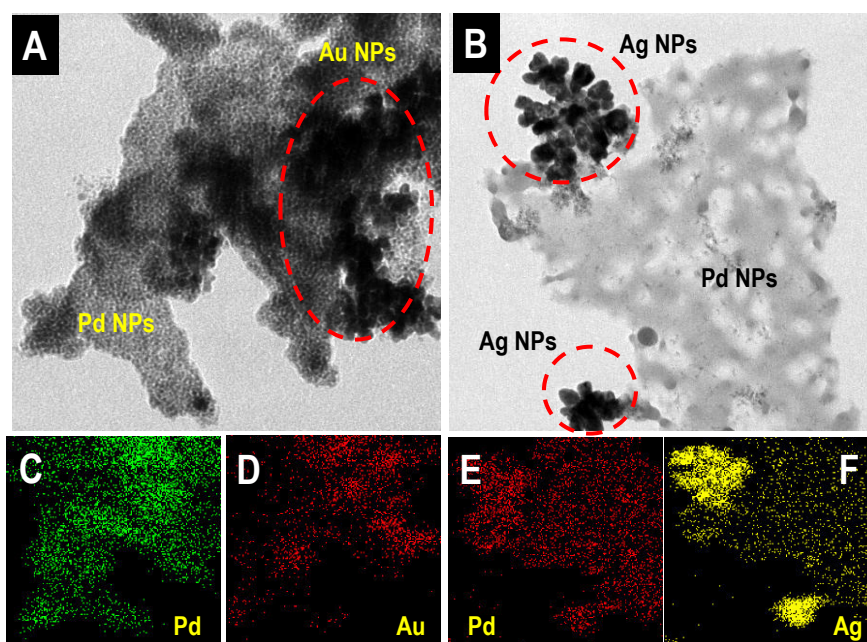


**Figure S8.** A, B and C) TEM images of NP-NSs made of silver, gold and nickel, respectively.

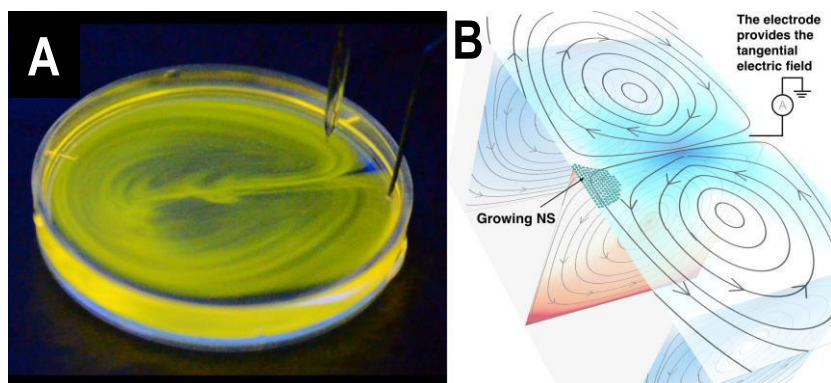


**Figure S9.** TEM image of silver NP-NS made from A) silver perchlorate and B) silver nitrate.

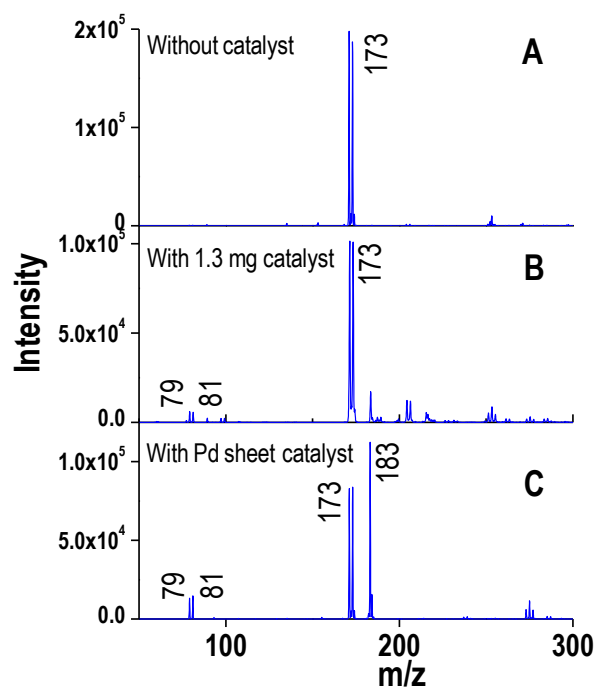




**Figure S10.** A) TEM image of Au-Pd NP-NS, B) TEM image of Ag-Pd NP-NS showing phase separated metal NPs. C-F) TEM EDS mapping of elements showing that the metal NPs aggregated themselves separately rather than making an alloy.



**Figure S11.** A) Dye visualization of the surface flow, B) theoretical streamlines showing the liquid flow at the surface. This surface flow drives nanoparticles away from the cathode and towards the opposite wall, while bulk flow recirculates the particles to the surface. The result is the growth of NS at the surface of the container.



**Figure S12.** A) Mass spectrum collected from the reaction mixture of p-tolylboronic acid and p-bromophenol without catalyst, B) with 1.3 mg commercial catalyst, and C) with Pd NP-NS catalyst.

Mass spectrum collected from the reaction mixture of commercial catalyst showed a few orders of magnitude less intense peak at  $m/z$  183 (the reaction product) as compared to the reaction mixture where Pd NP-NSs were used as catalyst (Figure S11). Hence, it is clear that Pd NP-NS showed higher catalytic efficiency than the commercially available Pd(0) catalyst.

**Table S1.** Structures of reactants and products.

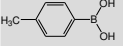

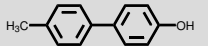


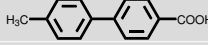
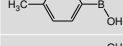

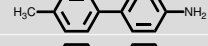




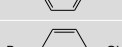





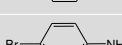

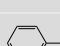


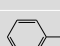

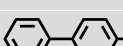
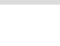
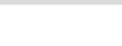
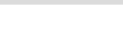
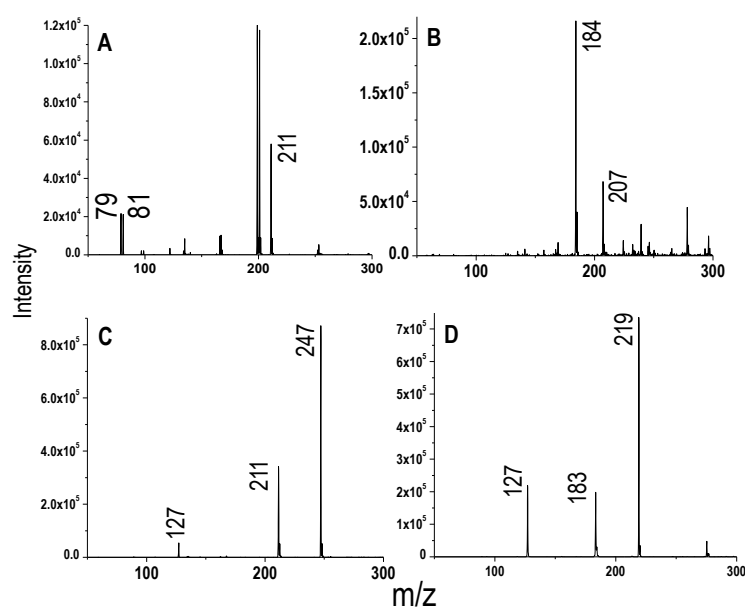
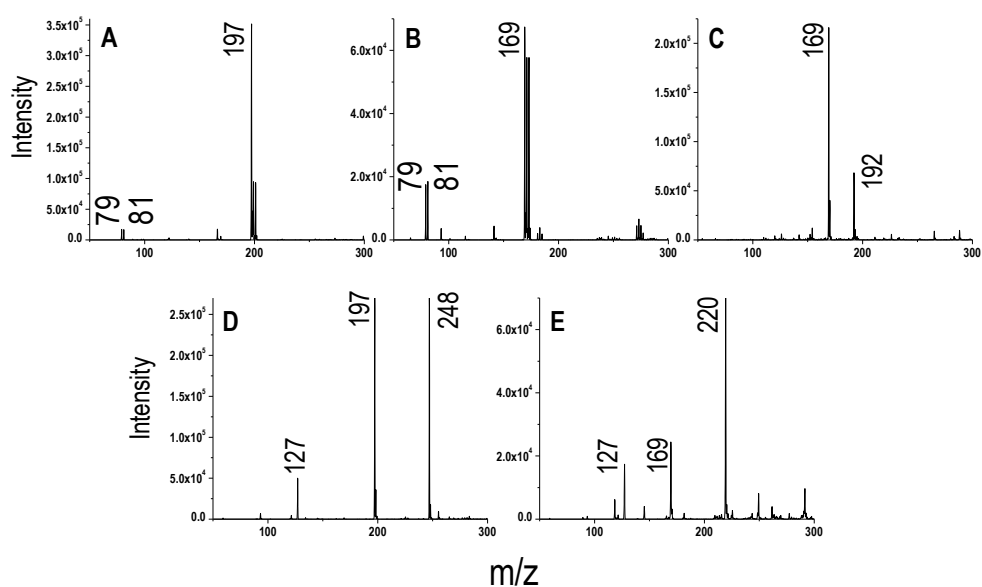
Sl. No.	Reactant A	Reactant B	Product	<i>m/z</i>
1				183
2				211
3				184
4				183
5				211
6				169
7				197
8				169
9				169
10				197

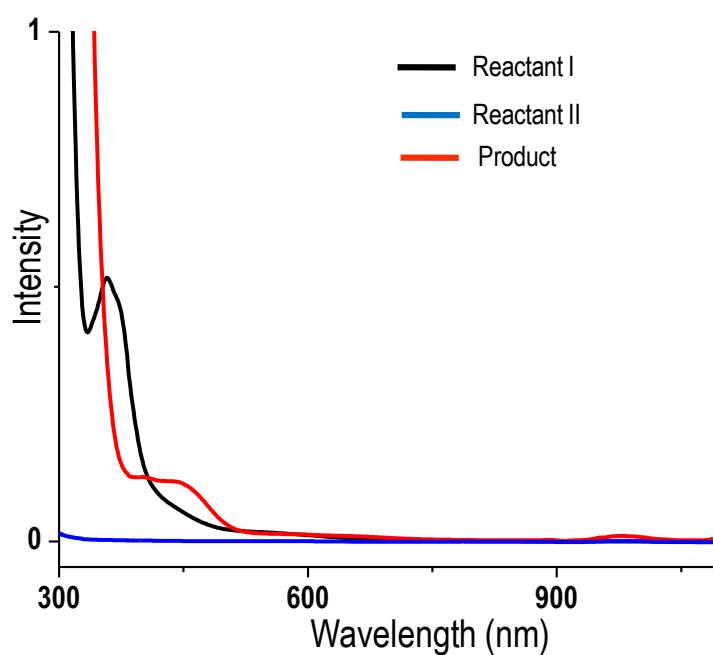
Table S1 shows the chemical structures of reactants, products and *m/z* values of the product for all the entries. Figures S11 (serial number 2-5 above) and S12 (serial number 6-10 above) show mass spectra collected from the different reaction mixtures.



**Figure S13.** Mass spectrum collected from the reaction mixtures (serial no. 2-5) mentioned in Table S1.

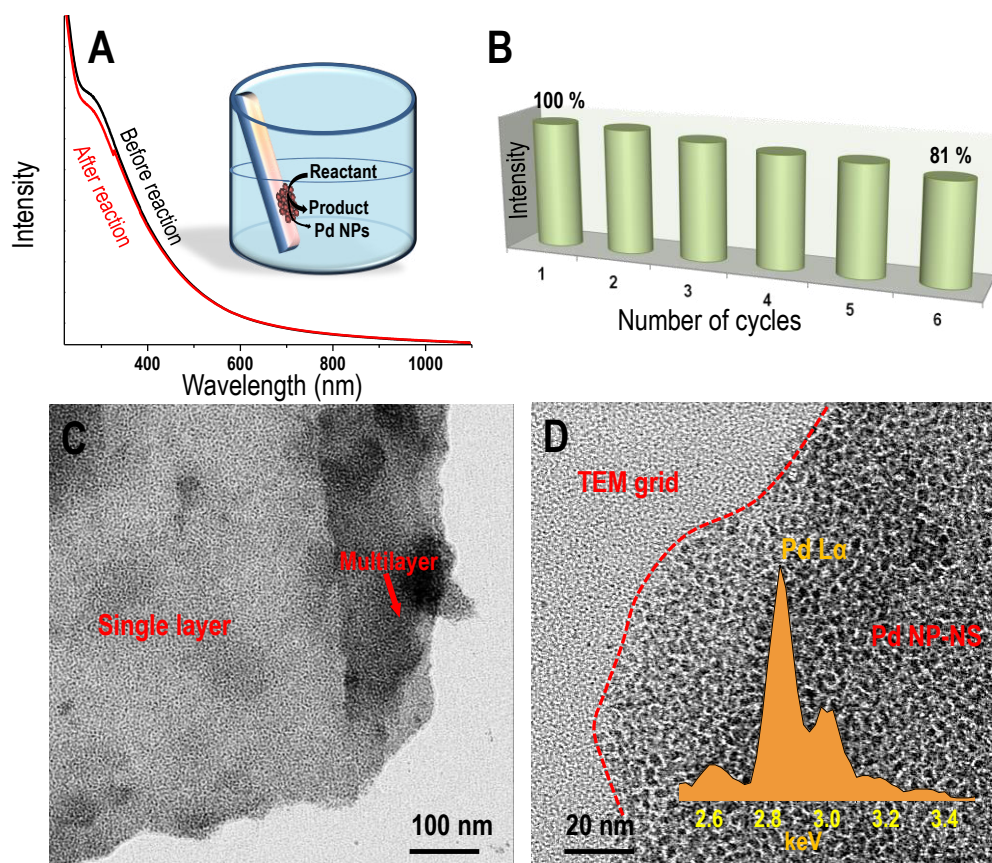


**Figure S14.** Mass spectrum collected from the reaction mixtures (serial no. 6-10) mentioned in Table S1.



**Figure S15.** UV-Vis spectrum collected for the reactants and product. The black and blue traces are UV-Vis spectra of 4-iodophenol and 4-tolylphenylboronic acid, respectively.





**Figure S16.** A) UV-Vis spectra of Pd NP-NS before and after the catalysis reaction, showing that catalysis does not change the nature of the sheet; inset shows a schematic representation of the catalysis experiment with minimal leaching of the Pd NPs into the reaction mixture. B) Intensity (absolute intensity of the product in mass spectrum) vs number of cycles for the same catalyst, showing that after 6 cycles also 81% of the catalytic activity was restored, C and D) TEM images of the Pd NP-NS after reaction showing that the nature of the sheet remains almost unchanged, inset in D shows the EDS spectrum taken from the same.

**Reusability of the catalyst:** Figure S14A shows the solid state UV-Vis spectrum of Pd NP-NS before and after catalysis. The spectrum was identical in both the cases. A small decrease in the intensity can be due to the loss of a small portion of Pd NP-NS while washing. Reusability of the catalyst was also checked. Figure S14B shows a plot of the absolute intensity of the product formed when the same catalyst was used again for a particular coupling reaction. Efficiency of the catalyst can be calculated taking the absolute intensity of the peak, in the mass spectrum, corresponding to the product. It proves

that after 6 cycles of catalysis reaction, about 81% of the catalytic activity was retained. Figure 5C and D show TEM images of the Pd NP-NSs after the reaction, proving that the NPs are intact and are similar in size. EDS spectrum of the Pd NP-NS after the reaction exhibits only Pd. These data prove that the Pd NP-NS act as a catalyst for the coupling reactions and the same catalyst can be reused for many reactions.

**Theoretical details:** In this section, we detail the theoretical method for obtaining the electrohydrodynamic flow described in the main text. In the experiment, free charged ions are sprayed using electrospray at the air-water interface of a container with an electrode on its surface. The electrospray of charges leads to a free charge density  $\rho$  on the interface between the two surfaces. The net current density at the air-water interface, in presence of flow  $v$ , is given as

$$J = \sigma E + \rho v \quad (1)$$

where  $\sigma$  is the conductivity of the liquid and  $E$  is the electric field intensity. In a homogeneous and incompressible fluid  $\sigma$  and  $\epsilon$  are constant and  $\nabla \cdot v = 0$ . Using the continuity equation, given in the main text, we have

$$(\partial_t + v \cdot \nabla) \rho + \frac{\sigma}{\epsilon} \rho = 0 \quad (2)$$

This sets a relaxation time scale  $\tau = \epsilon / \sigma$ . The relaxation time in a fluid when surface charges is then obtained using the ratio of the dielectric constant and the conductivity<sup>1</sup>. This has been used to estimate time scales in the main text. The estimated time scale is much faster than the remaining time scales and thus we conclude that there is electrohydrodynamic coupling only at the interface and not in the bulk.

The interfacial force density  $f^s$  can be obtained from the electrical stress tensor  $T_{ij}^e = \epsilon E_i E_j - 1/2 \epsilon E^2 \delta_{ij}$  as

$$f^s = \nabla \cdot T^e = \rho E - 0.5 E^2 \nabla \epsilon \quad (3)$$

Here we have used the Maxwell equation  $\nabla \cdot D = \rho$ , where  $D = \epsilon E$  is the electric displacement vector, to obtain the above expression of interfacial force density. For a homogeneous system,  $\epsilon$  is constant, and the second term in the above equation goes to zero. The expression of the interfacial force density  $f^s$  on the interface is then given as

$$f^s = \rho E \quad (4)$$

We now use the above expression for the interfacial force density to obtain the fluid flow. The fluid flow  $v$  is obtained from the solution of the Stokes equation

$$\nabla \cdot v = 0, \quad \nabla \cdot T^m = 0 \quad (5)$$

where  $T^m = -pI + \eta(\nabla v + (\nabla v)^T)$  is the fluid stress,  $p$  is the fluid pressure and  $\eta$  is the viscosity of the fluid. The above is then solved in a rectangular geometry of fluid flow, where the flow satisfies the no-slip condition on the two side walls and the bottom wall of a long rectangular container.

The boundary integral representation of the Stokes equation has been used to determine the flow<sup>2</sup>. The explicit expression of the boundary integral representation of Stokes flow has been given in Eq.(4) of the main text. This is given in terms of a Green's function  $G$  which vanishes at the container walls. Then, the integral has contributions only from the interface. We assume a constant tangential electric field  $E$  and a Gaussian free charge density profile  $\rho$  at the interface. Finally, we neglect the second term of the integral, in Eq.(4) of the main text, as it is sub-dominant compared to the first term. With these assumptions, the integral can be completed and the streamlines of the flow can be numerically computed. The approximate solution of the flow at any point  $r$  in the bulk is then given as

$$v(r) = \int G(r, r') \cdot f^s(r') dS \approx \sum_j G(r, R_j) \cdot (Q \exp(-r^2/2a^2) E) \quad (6)$$

Here  $f^s(r) = \rho E$  is the interfacial force density obtained in Equation 4. The integration is completed by considering the fact that the density of the charges can be written as  $\rho(r) = \sum_j Q \delta(r - R_j) \exp(-r^2/2a^2)$ , where  $a$  is the characteristic width and  $Q$  is the strength of charge. We ensure that the ratio  $a/H$  is consistent with the experiment. The Green's function  $G$  is obtained from the series sum of the Lorentz-Blake tensor<sup>3</sup> about the side walls. The Lorentz-Blake tensor ensures no-slip condition at the bottom wall by construction, while the boundary condition at side walls is implemented by the series sum of the Lorentz-Blake tensor. The resulting flow expression is then computed numerically from Equation 6 to obtain the streamlines in Figure 3 of the main text.

#### **Video of electrohydrodynamic fluid flow visualization:**

**Video S1.** Electrohydrodynamic fluid flow, visualized using a dye (Rhodamine 6g) in a rectangular container. The file presents theoretical aspects in the beginning followed by a video of the experiment.

**Video S2.** Electrohydrodynamic fluid flow at the surface of the liquid, visualized using a dye (Rhodamine 6g) under UV light in a circular container.

#### **References**

1. Melcher, J. R.; Taylor, G. I., Electrohydrodynamics: A Review of the Role of Interfacial Shear Stresses. *Annual Review of Fluid Mechanics* **1969**, *1* (1), 111-146.
2. C. Pozrikidis, Boundary Integral and Singularity Methods for Linearized Viscous Flow, *Cambridge University Press, Cambridge*, **1992**.
3. Blake, J. R., A note on the image system for a Stokeslet in a no-slip boundary, *Proc. Camb. Phil. Soc.* **1971**, *70*, 303–310.

# Bent Keto Form of Curcumin, Preferential Stabilization of Enol by Piperine, and Isomers of Curcumin $\beta$ -Cyclodextrin Complexes: Insights from Ion Mobility Mass Spectrometry

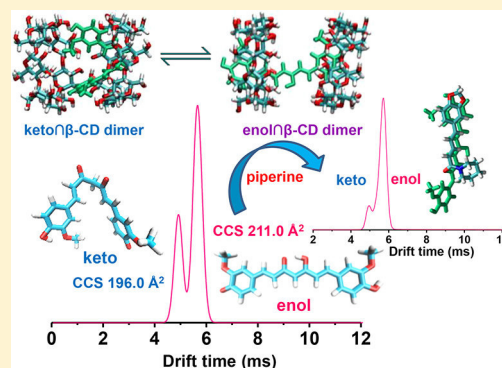
Abhijit Nag,<sup>†</sup> Papri Chakraborty,<sup>†</sup> Ganapati Natarajan,<sup>†</sup> Ananya Bakshi,<sup>†</sup> Sathish Kumar Mudedla,<sup>‡</sup> Venkatesan Subramanian,<sup>‡</sup> and Thalappil Pradeep<sup>\*,†</sup>

<sup>†</sup>DST Unit of Nanoscience and Thematic Unit of Excellence, Department of Chemistry, Indian Institute of Technology Madras, Chennai-600036, India

<sup>‡</sup>Chemical Laboratory, CSIR-Central Leather Research Institute, Adyar, Chennai 600020, India

## Supporting Information

**ABSTRACT:** A detailed examination of collision cross sections (CCSs) coupled with computational methods has revealed new insights into some of the key questions centered around curcumin, one of the most intensively studied natural therapeutic agents. In this study, we have distinguished the structures and conformers of the well-known enol and the far more elusive keto form of curcumin by using ion mobility mass spectrometry (IM MS). The values of the theoretically predicted isomers were compared with the experimental CCS values to confirm their structures. We have identified a bent structure for the keto form and the degree of bending was estimated. Using IM MS, we have also shown that ESI MS reflects the solution phase structures and their relative populations, in this case. Piperine, a naturally occurring heterocyclic compound, is known to increase the bioavailability of curcumin. However, it is still not clearly understood which tautomeric form of curcumin is better stabilized by it. We have identified preferential stabilization of the enol form in the presence of piperine using IM MS. Cyclodextrins (CDs) are used as well-known carriers in the pharmaceutical industry for increasing the stability, solubility, bioavailability, and tolerability of curcumin. However, the crystal structures of supramolecular complexes of curcumin $\beta$ -CD are unknown. We have determined the structures of different isomers of curcumin $\beta$ -CD ( $\alpha$ - and  $\beta$ -CD) complexes by comparing the CCSs of theoretically predicted structures with the experimentally obtained CCSs, which will further help in understanding the specific role of the structures involved in different biological activities.



Many of the chemical and pharmacological details of curcumin, one of the most intensively investigated biomolecules with long history, are still unknown. The molecule even now is the subject of over 1400 publications annually.<sup>1</sup> It is known that two tautomeric forms of curcumin, namely, keto and enol, exist in solution,<sup>2</sup> and they have been detected by various tools such as nuclear magnetic resonance spectroscopy (NMR).<sup>2</sup> The crystal structure of the enol form and its planar conformation can be deduced from X-ray diffraction,<sup>3</sup> while the conformation of the keto form is known with much less certainty due to the lack of single crystal data, excepting that of a cocrystal with 4,4'-bipyridine-*N,N'*-dioxide, which shows a planar keto structure.<sup>4</sup> This might be due to inherent structural asymmetries in the keto isomer arising from conformational freedom around the keto  $-\text{C}(\text{CO})-\text{C}(\text{CO})-\text{C}-$  bonds, which inhibits crystallization. The solution phase structure of curcumin is also of great importance due to its biological<sup>5–8</sup> and pharmacological activities including antitumor,<sup>9</sup> antioxidant,<sup>10,11</sup> anti-inflammatory,<sup>12,13</sup> anti-HIV<sup>14</sup> (human immunodeficiency virus), anti-Alzheimer's,<sup>15–17</sup> anticancer,<sup>18,19</sup> antihepatotoxic,<sup>20</sup> and cardio-

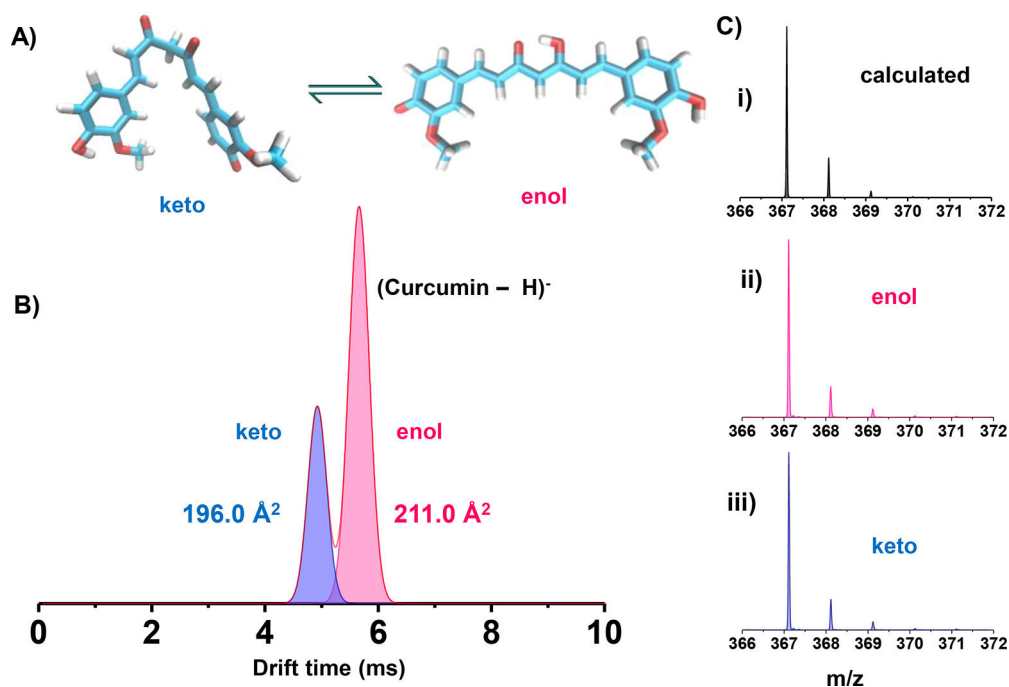
vascular protection activities.<sup>21</sup> The keto form is important in certain biochemical reactions and biological activities. The “NADPH-dependent curcumin/dihydrocurcumin reductase” enzyme acts on the keto form of curcumin to form tetrahydrocurcumin,<sup>22</sup> whereas the enol is the active form for the control of Alzheimer's disease.<sup>23</sup> Furthermore, it is also very difficult to detect the conformation of the keto form from NMR data in the solution phase. Simple isolation of these species and their quantitation will be useful from many perspectives as both these forms are different in biological activity.

The possible conformational keto isomers have so far been predicted only theoretically,<sup>24,25</sup> by comparative energy analysis of different conformers obtained using various approaches such as force-field conformer searches, molecular dynamics and density functional theory (DFT). However, these predicted keto structures<sup>24</sup> have not been verified

Received: December 15, 2017

Accepted: July 11, 2018

Published: July 11, 2018



**Figure 1.** (A) Schematic representation of deprotonated keto–enol tautomers of curcumin. (B) Drift time profile of curcumin ( $m/z = 367$ ) showing the two isomeric species with drift times of 4.92 and 5.72 ms, with CCS values, 196.0 and 211.0 Å<sup>2</sup>, respectively. (C) Relative peak intensities of isotopologues of keto and enol tautomers of curcumin, which are matching with the calculated relative peak intensities of isotopologues.

experimentally and this represents a gap which we will address in this Article.

The bioavailability of curcumin is known to be enhanced by the presence of molecules such as piperine.<sup>26,27</sup> An understanding of the preferential stabilization of the two forms by different molecules will help in formulating curcumin. There have been reports that curcumin gets transported across the blood–brain barrier (BBB).<sup>16,28–30</sup> Its enhanced delivery into the brain is of importance to neurological diseases such as Alzheimer's.<sup>7,16,17,23,31–33</sup>

A major problem in curcumin-based drugs is the low solubility of the molecule in an aqueous medium. An obvious choice to enhance solubility is cyclodextrins (CDs) and  $\beta$ -CD has been used extensively in medical formulations. However, the preferential stabilization of the keto–enol forms of curcumin is unclear from spectroscopy. Crystal structures of these supramolecular complexes are unknown.<sup>34–37</sup>

A combination of ion mobility mass spectrometry, theoretical calculations including molecular docking and CCS calculations can reveal the structures of these complexes. In this Article, we propose the structures and conformations of the well-known enol and the far more elusive keto form of curcumin by using ion mobility mass spectrometry (IM MS). The CCS values measured from IM MS are compared with the calculated CCS values of the theoretically predicted isomers, confirming the structures. We identify the degree of bending of the keto tautomer using this method. We show that IM MS manifests the tautomers of curcumin and represents their solution phase populations, in this case. We show that the enol form of curcumin is selectively enhanced in the presence of piperine. The structures of keto $\cap$ CD and enol $\cap$ CD (the  $\cap$  symbol refers to partial encapsulation, A encapsulated in B is denoted as A $\cap$ B).<sup>38</sup> are elucidated by using IM MS. The

experimental observations are fully supported by DFT, CCS, and molecular docking studies.

## EXPERIMENTAL SECTION

**Instrumentation. Mass Spectral Measurements.** All mass spectrometric measurements were conducted using a Waters Synapt G2Si High Definition Mass Spectrometer equipped with electrospray ionization (ESI) and ion mobility (IM) separation techniques. All the samples were analyzed in negative ESI mode. More details about the measurements are given in [Supporting Information \(SI\)](#).

## RESULTS AND DISCUSSION

**Separation of Keto–Enol Forms of Curcumin by IM MS.** Curcumin is a  $\beta$ -diketone system, which shows tautomerism between keto and enol forms. However, because of rapid interconvertibility of the tautomers, separation and complete characterization of the individual keto and enol forms remain challenging. Ion mobility mass spectrometry (IM MS) has power to separate ions not only by  $m/z$  ratio but also by their shape.<sup>39–45</sup> It has the capability to separate isomers depending on the difference in their collision cross sections while passing through a buffer gas (as for example N<sub>2</sub> and He) in the mobility cell under the influence of a weak electric field. Curcumin solution (0.05 mM in methanol) was directly electrosprayed for the IM MS measurement. In the negative ion mode, the peak corresponding to  $[M-H]^-$  (deprotonated form) was detected at  $m/z$  367 along with its isotopologues 368 and 369. The molecule was ionized by losing a proton from the phenolic –OH. IM MS experiments were performed on the deprotonated form  $[M-H]^-$ . Two well-separated peaks were observed at 5.72 and 4.92 ms, as shown in [Figure 1B](#). The highest intense peak came at 5.72 ms, whereas the weaker one arrived at 4.92 ms in the drift scale bar ([Figure 1B](#)). Two peaks

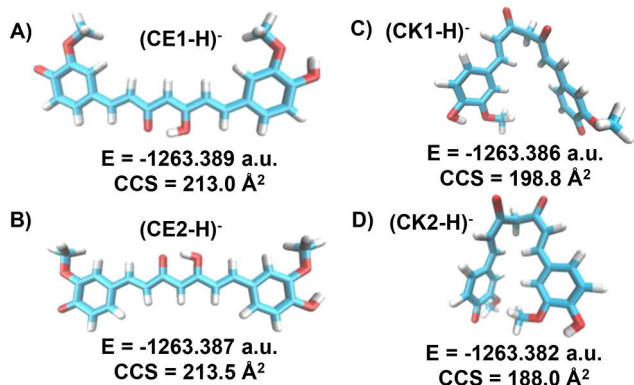


in the mobilogram represent the tautomeric nature of ionized curcumin. The corresponding species have the same chemical formula because the relative intensities of all the isotopologues are the same (see Figure 1C). The corresponding collision cross sections (CCSs) were 196.0 and 211.0 Å<sup>2</sup>, respectively (Figure 1B).

**CID of Keto–Enol Forms of Curcumin in the Transfer Cell.** To get more insight into the structure of the isomers, collision-induced dissociation (CID) was performed. The spectrometer has two collision cells; trap CID (situated before IMS) and transfer CID (located after IMS). Transfer CID was used to carry out fragmentation after ion mobility separation.<sup>46</sup> This enables us to fragment both the tautomers individually. The *m/z* values, 149, 175, 191, and 217 were the fragmented species from the 4.92 ms tautomer (Figure S1A). The peaks at *m/z* 175 and 191 were specific to the keto form of curcumin.<sup>47,48</sup> The 5.72 ms tautomer fragmented and gave peaks at *m/z* 134, 149, 173, and 217 (Figure S1B).<sup>47,48</sup> The characteristic fragment of enol appeared at *m/z* 173.

Intensity ratio of the peaks gave an equilibrium constant of 4.5 for the enol–keto equilibrium (Figure S6), which is comparable with the solution phase.<sup>49</sup> Deprotonation from both the forms did not affect the equilibrium constant. More details are discussed later.

**DFT and CCS Calculations of Different Structures of Curcumin.** We generated four curcumin conformers (two for enol and two for keto) from our conformer searches and subsequent DFT optimization. The two enol conformers abbreviated as (CE1–H)<sup>–</sup> and (CE2–H)<sup>–</sup> and are shown in Figure 2A and B. We also generated two keto conformers



**Figure 2.** DFT optimized structures of deprotonated keto and enol tautomers of curcumin with their total energies and theoretically calculated CCS values. Here, CE and CK represent *cis*-enol and -keto, respectively. Panels A and B show different types of enol tautomers like (CE1–H)<sup>–</sup> and (CE2–H)<sup>–</sup>, respectively, with optimized energies and CCS values. Panels C and D indicate the different types of keto tautomers like (CK1–H)<sup>–</sup> and (CK2–H)<sup>–</sup>, respectively, with optimized energies and CCS values.

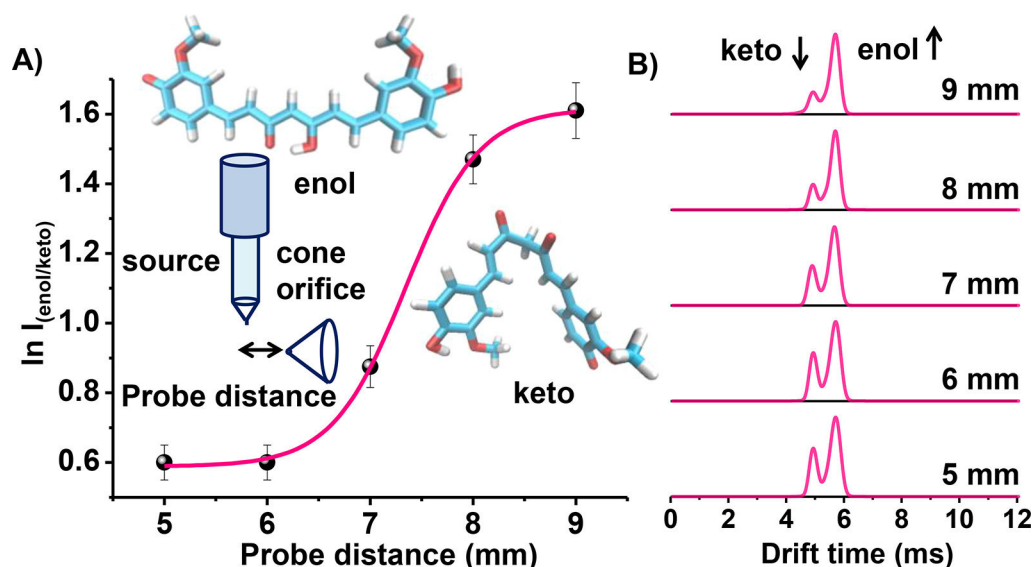
labeled (CK1–H)<sup>–</sup> and (CK2–H)<sup>–</sup>, which are shown in Figures 2C and D. The letters C in the conformer names indicates the *cis* configurations about the –C–(C=O)–C–(C=O)–C– bonds, followed by E or K to indicate enol or keto. The more details on the naming of keto–enol tautomers are given in Figure S2. The numbers 1 or 2 indicate the energy rank for the same type of *cis* configurations so that (CE1–H)<sup>–</sup> was the lowest energy *cis*-enol tautomer and (CK1–H)<sup>–</sup> was the lowest energy *cis*-keto tautomer. Among the enol conformers, the energetic ordering was (CE1–H)<sup>–</sup> < (CE2–

H)<sup>–</sup> (+0.002 a.u), where the energy relative to the (CE1–H)<sup>–</sup> is given in brackets. (CE1–H)<sup>–</sup> was the most stable tautomer and the energy difference between (CE1–H)<sup>–</sup> and (CE2–H)<sup>–</sup> is very small (0.002 a.u) as they were quite similar in structure apart from the spatial position of the –OMe group, which was *cis* with respect to the keto–enolic group in the case of (CE1–H)<sup>–</sup> and *trans* in the case of (CE2–H)<sup>–</sup>.

All of the enol tautomers were planar while the two keto structures were bent about the diketone group in varying degrees. It is convenient to introduce a bending angle to characterize the degree of this bending, rather than specify all the relevant dihedral angles in the seven-carbon chain bridging the two phenyl groups. The degree of bending of the seven carbon chain about its central carbon atom in the diketone group may be defined as the angle ACB, where C central carbon atom and A and B are the two carbon atoms located in the benzene rings which bond to the end atoms of the seven carbon chain, as shown in Figure S4. The bending angles of the (CK1–H)<sup>–</sup> and (CK2–H)<sup>–</sup> conformers were 75° and 65°, respectively. The relative stability of the keto conformers was indicated by their energetic ordering, (CK1–H)<sup>–</sup> < (CK2–H)<sup>–</sup> (+0.004 a.u), where the difference between the conformer energy and (CK1–H)<sup>–</sup> energy is given in brackets. The L- and U-shaped conformations for the keto, (CK1–H)<sup>–</sup> and (CK2–H)<sup>–</sup>, respectively (Figures 2C and D) were stabilized by weak intramolecular interactions, such as  $\pi$ – $\pi$  interactions and van der Waals interactions between atoms in the seven-carbon chain and between the two benzene rings and their –O and –OMe functional groups, all of which contribute to lowering of the total energy. Because of these interactions, (CK2–H)<sup>–</sup> was more bent compared to both (CK1–H)<sup>–</sup>.

The experimental difference in drift time reflected the planar enol and the L-shaped bent keto structures. The latter is more compact and it has a shorter drift time. The calculated CCSs of 213.0 Å<sup>2</sup> for (CE1–H)<sup>–</sup> and 198.8 Å<sup>2</sup> for (CK1–H)<sup>–</sup> matched well with our experimental result of 211.0 and 196.0 Å<sup>2</sup>, for enol and keto, respectively (Table S1), which confirms that the enol form had a planar structure, and keto form has a bent structure with a bending angle of 75°. Hence, using this combined structural and energetic study along with a comparison of the CCS values with the experiment, we have confirmed the well-known structure of enol, and the likely candidate of the keto tautomer, including its degree of bending. We note that (CE1–H)<sup>–</sup> and (CE2–H)<sup>–</sup> were close in energy and have similar CCS values. Therefore, it is likely that they both are coexisting. However, for the keto form, though all the structures are similar in energy (shown in Table S1), their CCS values are widely different and therefore it is likely that only (CK1–H)<sup>–</sup> exists. The energy differences are in fact insignificant when the computational errors and the effective temperature of the ion mobility cell are considered.

**Correlation between Solution- and Gas-Phase Structures of Curcumin.** In solution, the enol form is stabilized by intramolecular H-bonding, while the keto form is stabilized by intermolecular H-bonding with the solvent.<sup>49</sup> In nonpolar solvents, populations of the enol form will be more compared to keto form. Reverse is the true for polar solvents.<sup>49</sup> In our IM MS study also same thing has happened. With change of solvent, from nonpolar to polar, the intensity of both the peaks changed drastically (Figure S5). With the increase of polarity of the solvent (from hexane to 1:1 methanol–water mixture), the intensity of the keto form was enhanced compared to the enol form. In a protic solvent, the keto form is enhanced



**Figure 3.** (A) Plot of the natural logarithm of keto/enol peak intensity ratios against different probe distances from 5 to 9 mm. (B) With the increase in probe distance, enol form enhances in intensity. The two structures are shown in panel A. A schematic representation of the probe distance parameter is illustrated in panel A.

because intermolecular hydrogen bonding with the solvent will be preferred compared to the intramolecular H-bonding. From the data presented in Figure S5, it is clear that the solution phase population is reflected in the gas phase, in this case. Condition of the ESI source of the instrument has great influence on the abundance of tautomers.<sup>50,51</sup> To establish the solution and gas phase correlation and to support the structural information, three source parameters were varied while a few others were kept constant.<sup>50,52</sup> Results are presented as follows: (1) The Synapt G2Si has a probe adjuster, through which the distance of the spraying position of the capillary to the cone orifice can be varied from 5 to 9 mm (Figure 3A). The ratio of the two tautomeric forms displays dramatic change in intensity with the variation of probe distance. In a very recent report, Xia et al. has shown that changing the probe position, desolvation temperature, capillary voltage, sample infusion flow rate and cone voltage, the relative populations of the tautomers can be changed in the case of *p*-hydroxybenzoic acid.<sup>50</sup> When the probe tip is close to the cone aperture, that is, under high field conditions, ions can preserve their solution based ionic structures. But when the distance between the spray needle and the entrance orifice is more, that is, under low field condition, gas phase ion population is enhanced. This phenomenon can be justified by charge ion evaporation and charge residue models. In our IM MS study, when the sprayer capillary was kept away from the cone orifice, the enol form was enhanced and the keto form was drastically reduced (Figure 3B). Therefore, with the increase in probe distance, the enol form got enhanced, which is more stable in the gas phase. As the probe distance is increased, the ions are going more into the gas phase as solvent evaporation is facilitated. But the drift time of both the tautomers, that is, their CCS values remains constant with the change of probe distance, which suggests that the structures of the two forms remain the same as in the solution state in this case.

(2) Temperature of the atmospheric pressure ion source also impacts the relative ratio of the tautomer populations. In our mass spectrometer, the temperature of the enclosed spray chamber is influenced mainly by the desolvation-gas temper-

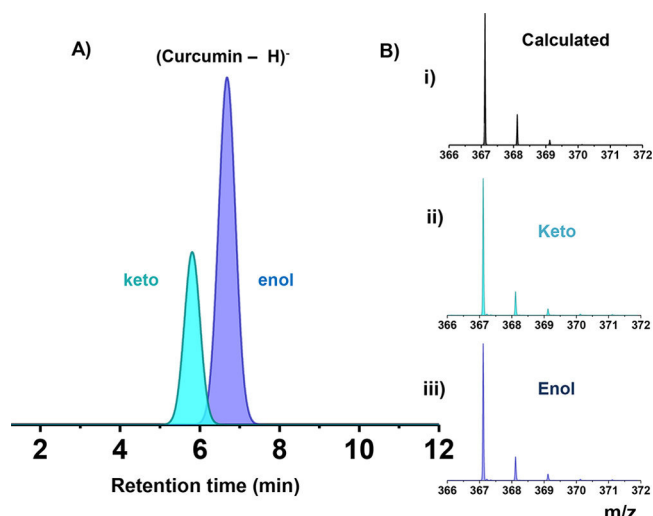
ature (DT). To measure the effect of temperature on both the tautomeric forms, DT was varied from 40 to 600 °C (Figure S6A). With the increase of DT, the intensity of the keto form was enhanced (Figure S6B). Disruption of the enolic hydrogen bond with increase of temperature favored the shifting of the equilibrium toward the keto form. The same phenomenon has happened in solution phase.<sup>49</sup> The drift time values of the keto and enol forms did not change with the increase of temperature, which suggests that the same structures are retained in the gas phase, which are also the solution phase structures. The ratio of enol/keto forms was 4.5 (equilibrium constant) at a desolvation temperature of 40 °C and probe distance of 6 mm, which is comparable with the solution phase data from previous literature.<sup>49</sup>

(3) We observed that the cone voltage had a great influence on the tautomeric ratio (Figure S7). As the cone voltage was raised, gaseous ions experienced acceleration in this region, collided with the background gases and underwent fragmentation.<sup>53–55</sup> When the cone voltage was high, the keto form was favored and the reverse was true when the cone voltage was low. This can be because of the breakage of enolic hydrogen bond, and hence the conversions into the keto form. We have also performed the cone voltage study to see the different rates of insource fragmentation for the two tautomers. But, no additional change in fragmentation was seen with the increase of cone voltage. This is shown in Figure S8. This study supports the breakage of hydrogen bond with the increase of cone voltage, which results in conversion of enol to keto form.

In summary, variation of source parameters supported the correlation between gas phase and solution phase structures in this case. However, we are aware of the issues involved in the generalization of such studies. Therefore, we have limited the discussions of ESI MS data being reflective of solution phase structures to the present studies.

**Comparison with the Solution Phase.** Further, to confirm the solution phase tautomerism, we separated the keto–enol forms by ultraperformance liquid chromatography (UPLC) (Figure 4A). After the two tautomers were separated using UPLC, fragmentation (CID) of both the tautomeric



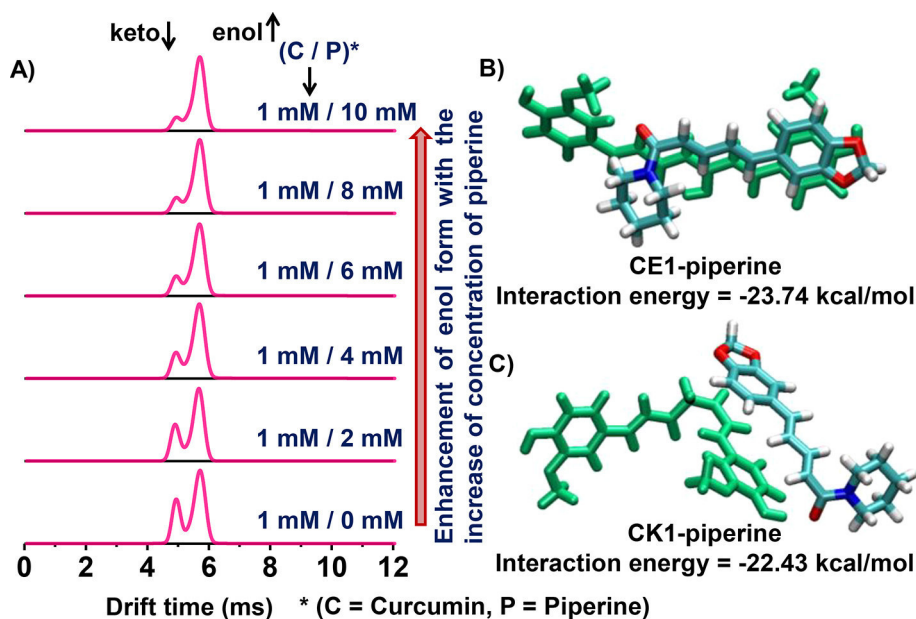


**Figure 4.** (A) UPLC separated keto enol tautomers of curcumin. (B) Relative peak intensities of isotopologues of keto and enol tautomers of curcumin, which are matching with the calculated peak intensities of isotopologues.

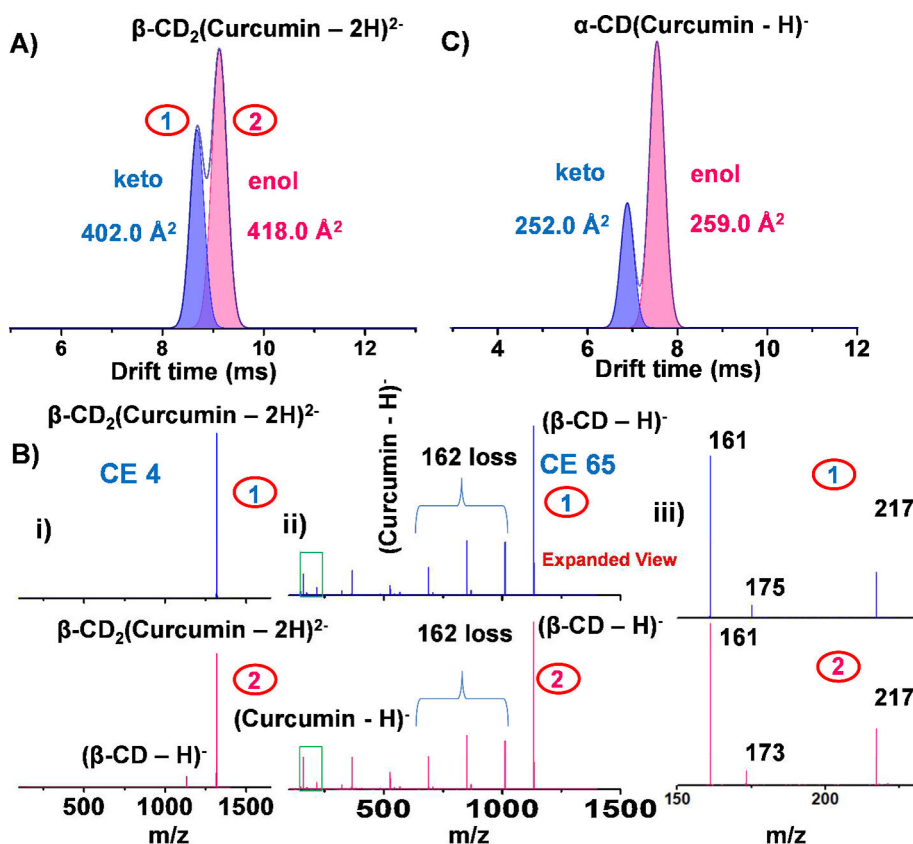
species was performed (Figure S9B). Here, the fragmentation pattern of each tautomer was matched with the CID data of ESI IM MS. This study further reinforced that the solution phase tautomeric structure of curcumin is retained in the gas phase in this case.

**Interaction of Curcumin with Piperine.** Piperine is a naturally occurring heterocyclic compound found in all forms of pepper (black, white, and green), and this molecule is responsible for its pungency and heat. Dietary polyphenols like piperine and curcumin have been studied for their effect on prevention of breast cancer.<sup>56,57</sup> Mammosphere formation<sup>58</sup> is a marker of breast cancer cell lines. Curcumin and black pepper compounds both inhibited mammosphere formation. They did not also cause any toxicity, therefore showing that

curcumin, piperine, or piperine–curcumin adduct could be possible cancer preventive agents. On the other hand, piperine enhances the bioavailability of curcumin. However, it is still not clearly understood that which tautomeric form of curcumin is better stabilized by it. Ion mobility mass spectrometry showed that with the increase of the concentration of piperine, the intensity of the enol form was enhanced and the population of keto form was decreased (Figure 5A). This shows that with the use of piperine, one can selectively enhance the enol form. The supramolecular adduct of curcumin–piperine was detected in ESI MS (Figure S10). The preferential stabilization of the enol form in the adduct and its enhanced population in solution in the presence of piperine was reflected in the IM MS measurement. To understand the mechanism of the enhancement of the enol form, a DFT study was performed. We took four lowest energy tautomers: 2 enols [(CE1–H)<sup>−</sup> and (CE2–H)<sup>−</sup>] and 2 ketos [(CK1–H)<sup>−</sup> and (CK2–H)<sup>−</sup>]. Each tautomer was interacted with piperine considering the different possibilities of hydrogen bonds and  $\pi$ – $\pi$  interactions. The optimized geometries are shown in Figures S11–S15 and the calculated relative energies are listed in Table S2. Among the lowest energy structures of the complexes of each tautomer of curcumin with piperine (Table S4), the difference in the energies of the complexes with (CE1–H)<sup>−</sup> (−23.51 kcal/mol) and (CE2–H)<sup>−</sup> (−20.60 kcal/mol) is marginal as the complexes are stabilized through similar  $\pi$ – $\pi$  stacking interaction. The complex of (CK1–H)<sup>−</sup> with piperine is stabilized by both hydrogen bonding and  $\pi$ – $\pi$  stacking interactions between six-membered rings of piperine and aliphatic double bond of curcumin. These interactions are absent in the case of (CK2–H)<sup>−</sup>. Because of this, the interaction energy is more negative for (CK1–H)<sup>−</sup> (−23.08 kcal/mol) than for (CK2–H)<sup>−</sup> (−22.18 kcal/mol) (Table S4). However, the complexes of piperine with enol form of curcumin are more stable than that of the keto form, with respect to the total energy.



**Figure 5.** (A) Shift of the keto–enol equilibrium toward the enol form with increase in piperine concentration in the solution. (B and C) DFT optimized lowest energy structures of CE1–piperine and CK1–piperine complexes, respectively. Green color is used for keto and enol tautomers of curcumin.



**Figure 6.** (A) Drift time profile of curcumin- $\beta$ -cyclodextrin (1:2) inclusion complex; two peaks are indicating the isomeric structures. (B) (i and ii) MSMS fragmentation at transfer CID cell of both the isomeric peaks 1 and 2 shown in panel A, with different collision energies, 4 and 65 V, respectively. (iii) Expanded view of the  $m/z$  region 150–230, shown in panel ii as a box. (C) Two isomeric species of the  $\alpha$ -cyclodextrin-curcumin (1:1) complex.

The large difference in the energies of the enol ( $E_{(\text{CE1-H})^-} = -1263.389$  au) and keto ( $E_{(\text{CK1-H})^-} = -1263.386$  au) forms of curcumin is also preserved during their complexation with piperine. Further, similar trend was observed for the proton added forms of the respective species (see Table S3). The interaction energy of CE1 is marginally higher than CK1 (Figure 5B and C).

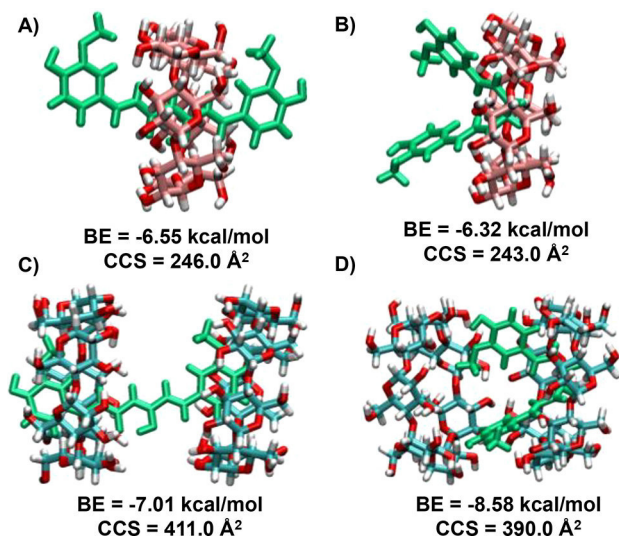
**Determination of Structures of Curcumin $\cap$ Cyclodextrin Complexes.** Cyclodextrins (CDs) are cyclic oligosaccharides with a lipophilic central cavity and hydrophilic outer surface. Hydrophilic drug/CD complexes are synthesized by the inclusion of lipophilic drug moieties in the central CD cavity. While the guest molecule is safeguarded by the lipophilic cavity from the aqueous environment, the polar outer surface of the CD molecule furnishes the solubilizing effect. CDs have been used frequently as solubilizing, stabilizing, and drug delivery agents in pharmaceutical preparations for enhancing the bioavailability of the drug.<sup>59</sup> We predicted the structures of the isomers of curcumin $\cap$ CD complexes using molecular docking and then applied the projection approximation (PA) method<sup>60</sup> to compute their CCS values and compared them with the experimental values obtained from IMS MS to confirm the structures.

A mixture of curcumin and  $\beta$ -CD was infused through a standard electrospray ion source into the spectrometer at a concentration of  $\sim 0.05$  mM (water/methanol, 1:1). The negative ion peak at  $m/z$  1317 (2:1  $\beta$ -CD:curcumin inclusion complex) was selected and passed through the ion mobility cell. Two distinct isomeric peaks were detected with the drift

time values of 8.69 and 9.13 ms, respectively (Figure 6A). The CCS values of the two peaks were 402.0 and 418.0  $\text{\AA}^2$ , respectively. To get more information about the structure, CID fragmentation was performed in the transfer cell. We selectively fragmented both the isomers. At a collision energy 4 V,  $\beta$ -CD loss was observed from the 9.13 ms drift time isomer, while the other isomer with drift time of 8.69 ms did not fragment at that energy. This suggested that the latter isomer is slightly more stable compared to the former. Further increase of collision energy gave rise to the curcumin molecular ion peak and the sequential loss of 162 from CD (Figure 6B(ii)). This loss is due to the glucopyranose unit, typical signature of the CD.<sup>61</sup> Upon expanding the mass range of  $m/z$  150–230 for both the isomers, we find that the peaks at  $m/z$  173 and 175 are, respectively the fragmented species from the isomers at drift times of 9.13 and 8.69 ms (Figure 6B(iii)). This confirmed that the isomers were derived from the enol and keto tautomers of curcumin, respectively. We expanded our study to the  $\alpha$ -CD-curcumin complex. In this case, the 1:1 inclusion complex ( $\alpha$ -CD:curcumin) was chosen and transferred through the ion mobility cell. Here also, two isomeric peaks were detected. The corresponding CCS and drift time values were 252.0 and 259.0  $\text{\AA}^2$  and 6.89 and 7.55 ms, respectively (Figure 6C). The CCS values of the curcumin $\cap$ CD complexes provide additional verification of the bent structure of keto as a planar keto form will show identical CCS value as that of the enol.

**Molecular Docking Study of Curcumin $\cap$ Cyclodextrin Complexes.** Molecular docking simulations of curcumin

tautomers, CE1 and CK1 with  $\alpha$ - and  $\beta$ -CD monomers and  $\beta$ -CD dimers were used to determine the structures of their inclusion complexes, using the Autodock 4.2 and AutoDock Tools programs. The interactions are basically vdW, hydrogen bonding, electrostatic, and hydrophobic in nature, and therefore, a force field with these terms as implemented in the Autodock program was appropriate. As our primary objective was to determine the structures of the complexes by comparing their calculated CCS values with the experiment, we did not perform any DFT calculations.<sup>62–65</sup> This is reasonable since the majority of the interactions are non-covalent. The docking search was designed to perform global optimization (GO) for the two-molecule problem with a single curcumin (lowest energy enol CE1 and keto CK1) as the “ligand” and  $\alpha$ -CD as the “receptor”. We obtained ten lowest energy isomers for CE1 $\cap$  $\alpha$ -CD complex with the CE1 stabilized inside the cavity of CD. The structures were identical with slight changes in the orientation of CE1 and showed similar binding energies (BEs) in the range of  $-6.55$  to  $-6.46$  kcal/mol. Docking studies on CK1 $\cap$  $\alpha$ -CD complex also gave ten lowest energy structures with the BEs in the range of  $-6.32$  to  $-6.30$  kcal/mol. The CCS values of the structures with lowest BE for CE1 $\cap$  $\alpha$ -CD ( $246.0 \text{ \AA}^2$ ) and for CK1 $\cap$  $\alpha$ -CD ( $243.0 \text{ \AA}^2$ ) matched closely with the experimental data (Figure 6C) as shown in the Figures 7A and B. The Autodock 4.2



**Figure 7.** (A and B) CE1 and CK1 docked  $\alpha$ -cyclodextrin, respectively. (C and D) Same for  $\beta$ -cyclodextrin dimer. The binding energies and CCS values are listed below the structure. The structures shown are the energy minimum forms.

program cannot simultaneously carry out the GO problem for three molecules. Hence for the case of 2:1  $\beta$ -CD:curcumin complexes, we followed different procedures to obtain an approximate solution to the three molecules GO problem:

(1) We first docked the curcumin tautomer (CE1 and CK1 separately as the “ligand”) with one  $\beta$ -CD as the “receptor” (Figure S18). Then, taking its newly docked lowest energy structure (Figure S18) as the “receptor”, we subsequently docked the second  $\beta$ -CD as the “ligand” (Figure S19).

(2) In another approach, various initial configurations of the two  $\beta$ -CD molecules were considered by arranging them in HH configuration (H stands for head, see molecular docking in SI), with different separations [4 (Figure S20B), 5 (Figure

7C), and 6  $\text{\AA}$  (Figure S20A) for CE1 $\cap$ dimer  $\beta$ -CD] and angles [ $\theta = 30^\circ$  (Figure S21A),  $40^\circ$  (Figure 7D), and  $65^\circ$  (Figure S21B) for CK1 $\cap$ dimer  $\beta$ -CD] between their central axis of rotation. Now, this double CD system was treated as the “receptor” molecule and the curcumin molecule (CE1 and CK1 separately) as the “ligand”. Additional details are included in SI. The lowest energy structures of the complexes were obtained from the second approach for the three molecule GO problem. The structures of CE1 $\cap$ dimer  $\beta$ -CD resembled a dumbbell with a separation of 5  $\text{\AA}$  between the two CDs, with a BE of  $-7.03$  kcal/mol and with the calculated CCS value of  $411.0 \text{ \AA}^2$  (Figure 7C). In the lowest energy structure of CK1 $\cap$ dimer  $\beta$ -CD, one end of the L-shaped keto form (CK1) was encapsulated between the two CDs lying at an angle of  $40^\circ$  and the other end of the keto was protruding outward from the gap. This structure showed a BE of  $-8.58$  kcal/mol and calculated CCS value of  $390.0 \text{ \AA}^2$  (Figure 7D). The calculated CCS values of the lowest energy structures were in close agreement with the experimental CCS values (Tables S5 and S6), which supported the proposed structures of the inclusion complexes.

## CONCLUSION

Our study shows that the two structural forms of curcumin, namely, keto and enol forms can be isolated in the gas phase. The gas phase populations represent the solution phase populations in this case. We found a new bent keto structure by ion mobility studies and verified its structure including its degree of bending, by simulations. The enol form can be selectively stabilized by the presence of piperine. Both the forms can be complexed with cyclodextrin, although there is a slight preference for the keto form for the  $\beta$ -CD dimer. The IM MS experiments and theoretical calculations that were performed by docking studies have enabled us to obtain exhaustive structural information about the curcumin and curcumin $\cap$ CD complexes which could not be unambiguously characterized through standard methods such as X-ray crystallography and NMR. We could predict the actual structure of curcumin $\cap$ CD inclusion complexes with the help of IM MS measurements and theoretical CCS calculations. This study shows the application of IM MS to identify the structural details of commonly used natural products. Insights from the studies such as the stabilization of enol by piperine will be of immediate value to the medical community as the enol form is active toward the Alzheimer's disease.

## ASSOCIATED CONTENT

### Supporting Information

The Supporting Information is available free of charge on the ACS Publications website at DOI: 10.1021/acs.analchem.7b05231.

Experimental details, computational details, DFT optimized structures of curcumin, curcumin–piperine complexes, solvent dependent study, and cone voltage dependent study (PDF)

Molecular docking study and CCS calculations (PDF)

## AUTHOR INFORMATION

### Corresponding Author

\*Fax: +91-44 2257-0545. E-mail: pradeep@iitm.ac.in.

### ORCID

Venkatesan Subramanian: 0000-0003-2463-545X



Thalappil Pradeep: 0000-0003-3174-534X

## Notes

The authors declare no competing financial interest.

## ACKNOWLEDGMENTS

We thank the Department of Science and Technology, Government of India, for constantly supporting our research program on nanomaterials. A.N. thanks IIT Madras for a doctoral fellowship. P.C. thanks the Council of Scientific and Industrial Research (CSIR) for her research fellowship. A.B. thanks IIT Madras for a Postdoctoral fellowship. S.K.M. thanks DST-INSPIRE for his senior research fellowship.

## REFERENCES

- (1) Nelson, K. M.; Dahlin, J. L.; Bisson, J.; Graham, J.; Pauli, G. F.; Walters, M. A. *J. Med. Chem.* **2017**, *60*, 1620–1637.
- (2) Payton, F.; Sandusky, P.; Alworth, W. L. *J. Nat. Prod.* **2007**, *70*, 143–146.
- (3) Sanphui, P.; Goud, N. R.; Khandavilli, U. B. R.; Bhanoth, S.; Nangia, A. *Chem. Commun.* **2011**, *47*, 5013–5015.
- (4) Su, H.; He, H.; Tian, Y.; Zhao, N.; Sun, F.; Zhang, X.; Jiang, Q.; Zhu, G. *Inorg. Chem. Commun.* **2015**, *55*, 92–95.
- (5) Argyropoulou, A.; Aligiannis, N.; Trougakos, I. P.; Skaltsounis, A.-L. *Nat. Prod. Rep.* **2013**, *30*, 1412–1437.
- (6) Barry, J.; Fritz, M.; Brender, J. R.; Smith, P. E. S.; Lee, D.-K.; Ramamoorthy, A. *J. Am. Chem. Soc.* **2009**, *131*, 4490–4498.
- (7) Wanninger, S.; Lorenz, V.; Subhan, A.; Edelmann, F. T. *Chem. Soc. Rev.* **2015**, *44*, 4986–5002.
- (8) Mitra, K.; Gautam, S.; Kondaiah, P.; Chakravarty, A. R. *Angew. Chem., Int. Ed.* **2015**, *54*, 13989–13993.
- (9) Renfrew, A. K.; Bryce, N. S.; Hambley, T. W. *Chem. Sci.* **2013**, *4*, 3731–3739.
- (10) Jovanovic, S. V.; Boone, C. W.; Steenken, S.; Trinoga, M.; Kaskey, R. B. *J. Am. Chem. Soc.* **2001**, *123*, 3064–3068.
- (11) Jovanovic, S. V.; Steenken, S.; Boone, C. W.; Simic, M. G. *J. Am. Chem. Soc.* **1999**, *121*, 9677–9681.
- (12) Vemula, P. K.; Li, J.; John, G. *J. Am. Chem. Soc.* **2006**, *128*, 8932–8938.
- (13) Pu, H.-L.; Chiang, W.-L.; Maiti, B.; Liao, Z.-X.; Ho, Y.-C.; Shim, M. S.; Chuang, E.-Y.; Xia, Y.; Sung, H.-W. *ACS Nano* **2014**, *8*, 1213–1221.
- (14) Jordan, W. C.; Drew, C. R. *J. Natl. Med. Assoc.* **1996**, *88*, 333–333.
- (15) Ran, C.; Xu, X.; Raymond, S. B.; Ferrara, B. J.; Neal, K.; Bacskai, B. J.; Medarova, Z.; Moore, A. J. *Am. Chem. Soc.* **2009**, *131*, 15257–15261.
- (16) Tiwari, S. K.; Agarwal, S.; Seth, B.; Yadav, A.; Nair, S.; Bhatnagar, P.; Karmakar, M.; Kumari, M.; Chauhan, L. K. S.; Patel, D. K.; Srivastava, V.; Singh, D.; Gupta, S. K.; Tripathi, A.; Chaturvedi, R. K.; Gupta, K. C. *ACS Nano* **2014**, *8*, 76–103.
- (17) Zhang, X.; Tian, Y.; Li, Z.; Tian, X.; Sun, H.; Liu, H.; Moore, A.; Ran, C. *J. Am. Chem. Soc.* **2013**, *135*, 16397–16409.
- (18) Zhang, J.; Liang, Y.-C.; Lin, X.; Zhu, X.; Yan, L.; Li, S.; Yang, X.; Zhu, G.; Rogach, A. L.; Yu, P. K. N.; Shi, P.; Tu, L.-C.; Chang, C.-C.; Zhang, X.; Chen, X.; Zhang, W.; Lee, C.-S. *ACS Nano* **2015**, *9*, 9741–9756.
- (19) Banerjee, S.; Chakravarty, A. R. *Acc. Chem. Res.* **2015**, *48*, 2075–2083.
- (20) Girish, C.; Pradhan, S. C. *J. Pharmacol. Pharmacother.* **2012**, *3* (2), 149–155.
- (21) Aggarwal, B. B.; Harikumar, K. B. *Int. J. Biochem. Cell Biol.* **2009**, *41*, 40–59.
- (22) Hassaninasab, A.; Hashimoto, Y.; Tomita-Yokotani, K.; Kobayashi, M. *Proc. Natl. Acad. Sci. U. S. A.* **2011**, *108*, 6615–6620.
- (23) Yanagisawa, D.; Shirai, N.; Amatsubo, T.; Taguchi, H.; Hirao, K.; Urushitani, M.; Morikawa, S.; Inubushi, T.; Kato, M.; Kato, F.; Morino, K.; Kimura, H.; Nakano, I.; Yoshida, C.; Okada, T.; Sano, M.; Wada, Y.; Wada, K.-n.; Yamamoto, A.; Tooyama, I. *Biomaterials* **2010**, *31*, 4179–4185.
- (24) Kolev, T. M.; Velcheva, E. A.; Stamboliyska, B. A.; Spitteller, M. *Int. J. Quantum Chem.* **2005**, *102*, 1069–1079.
- (25) Galasso, V.; Kovač, B.; Modelli, A.; Ottaviani, M. F.; Pichierri, F. *J. Phys. Chem. A* **2008**, *112*, 2331–2338.
- (26) Prasad, S.; Tyagi, A. K.; Aggarwal, B. B. *Cancer Res. Treat* **2014**, *46*, 2–18.
- (27) Shoba, G.; Joy, D.; Joseph, T.; Majeed, M.; Rajendran, R.; Srinivas, P. S. S. R. *Planta Med.* **1998**, *64*, 353–356.
- (28) Pahuja, R.; Seth, K.; Shukla, A.; Shukla, R. K.; Bhatnagar, P.; Chauhan, L. K. S.; Saxena, P. N.; Arun, J.; Chaudhari, B. P.; Patel, D. K.; Singh, S. P.; Shukla, R.; Khanna, V. K.; Kumar, P.; Chaturvedi, R. K.; Gupta, K. C. *ACS Nano* **2015**, *9*, 4850–4871.
- (29) Krol, S.; Macrez, R.; Docagne, F.; Defer, G.; Laurent, S.; Rahman, M.; Hajipour, M. J.; Kehoe, P. G.; Mahmoudi, M. *Chem. Rev.* **2013**, *113*, 1877–1903.
- (30) Cui, Y.; Zhang, M.; Zeng, F.; Jin, H.; Xu, Q.; Huang, Y. *ACS Appl. Mater. Interfaces* **2016**, *8*, 32159–32169.
- (31) Randino, R.; Grimaldi, M.; Persico, M.; De Santis, A.; Cini, E.; Cabri, W.; Riva, A.; D'Errico, G.; Fattorusso, C.; D'Ursi, A. M.; Rodriguez, M. *Sci. Rep.* **2016**, *6*, 38846.
- (32) Lim, G. P.; Chu, T.; Yang, F.; Beech, W.; Frautschy, S. A.; Cole, G. M. *J. Neurosci.* **2001**, *21*, 8370–8377.
- (33) Chojnacki, J. E.; Liu, K.; Yan, X.; Toldo, S.; Selden, T.; Estrada, M.; Rodriguez-Franco, M. I.; Halquist, M. S.; Ye, D.; Zhang, S. *ACS Chem. Neurosci.* **2014**, *5*, 690–699.
- (34) Heo, D. N.; Ko, W.-K.; Moon, H.-J.; Kim, H.-J.; Lee, S. J.; Lee, J. B.; Bae, M. S.; Yi, J.-K.; Hwang, Y.-S.; Bang, J. B.; Kim, E.-C.; Do, S. H.; Kwon, I. K. *ACS Nano* **2014**, *8*, 12049–12062.
- (35) Yadav, V. R.; Suresh, S.; Devi, K.; Yadav, S. *AAPS PharmSciTech* **2009**, *10*, 752.
- (36) Mangolim, C. S.; Moriwaki, C.; Nogueira, A. C.; Sato, F.; Baesso, M. L.; Neto, A. M.; Matioli, G. *Food Chem.* **2014**, *153*, 361–370.
- (37) Yallapu, M. M.; Jaggi, M.; Chauhan, S. C. *Macromol. Biosci.* **2010**, *10*, 1141–1151.
- (38) Lehn, J.-M. In *Supramolecular Chemistry*; Wiley-VCH Verlag GmbH & Co. KGaA: Weinheim, Germany, 2006; pp 1–9.
- (39) Zhou, M.; Dagan, S.; Wysocki, V. H. *Angew. Chem., Int. Ed.* **2012**, *51*, 4336–4339.
- (40) Weston, D. J.; Bateman, R.; Wilson, I. D.; Wood, T. R.; Creaser, C. S. *Anal. Chem.* **2005**, *77*, 7572–7580.
- (41) Hofmann, J.; Hahm, H. S.; Seeberger, P. H.; Pagel, K. *Nature* **2015**, *526*, 241.
- (42) Domalain, V.; Hubert-Roux, M.; Tognetti, V.; Joubert, L.; Lange, C. M.; Rouden, J.; Afonso, C. *Chem. Sci.* **2014**, *5*, 3234–3239.
- (43) Hofmann, J.; Stuckmann, A.; Crispin, M.; Harvey, D. J.; Pagel, K.; Struwe, W. B. *Anal. Chem.* **2017**, *89*, 2318–2325.
- (44) Gray, C. J.; Schindler, B.; Migas, L. G.; Pičmanová, M.; Allouche, A. R.; Green, A. P.; Mandal, S.; Motawia, M. S.; Sánchez-Pérez, R.; Bjarnholt, N.; Möller, B. L.; Rijs, A. M.; Barran, P. E.; Compagnon, I.; Eysers, C. E.; Flitsch, S. L. *Anal. Chem.* **2017**, *89*, 4540–4549.
- (45) Chakraborty, P.; Bakshi, A.; Mudedla, S. K.; Nag, A.; Paramasivam, G.; Subramanian, V.; Pradeep, T. *Phys. Chem. Chem. Phys.* **2018**, *20*, 7593.
- (46) Schröder, D.; Buděšínský, M.; Roithová, J. *J. Am. Chem. Soc.* **2012**, *134*, 15897–15905.
- (47) Jiang, H.; Somogyi, Á.; Jacobsen, N. E.; Timmermann, B. N.; Gang, D. R. *Rapid Commun. Mass Spectrom.* **2006**, *20*, 1001–1012.
- (48) Kawano, S.-i.; Inohana, Y.; Hashi, Y.; Lin, J.-M. *Chin. Chem. Lett.* **2013**, *24*, 685–687.
- (49) Bhatia, N. K.; Kishor, S.; Katyal, N.; Gogoi, P.; Narang, P.; Deep, S. *RSC Adv.* **2016**, *6*, 103275–103288.
- (50) Xia, H.; Attygalle, A. B. *Anal. Chem.* **2016**, *88*, 6035–6043.
- (51) Anwar, A.; Psutka, J.; Walker, S. W. C.; Dieckmann, T.; Janizewski, J. S.; Larry Campbell, J.; Scott Hopkins, W. *Int. J. Mass Spectrom.* **2018**, *429*, 174.

- (52) Ghosh, D.; Baksi, A.; Mudedla, S. K.; Nag, A.; Ganayee, M. A.; Subramanian, V.; Pradeep, T. *J. Phys. Chem. C* **2017**, *121*, 13335–13344.
- (53) Pertel, R. *Int. J. Mass Spectrom. Ion Phys.* **1975**, *16*, 39–52.
- (54) Katta, V.; Chowdhury, S. K.; Chait, B. T. *Anal. Chem.* **1991**, *63*, 174–178.
- (55) Hunt, S. M.; Sheil, M. M.; Belov, M.; Derrick, P. J. *Anal. Chem.* **1998**, *70*, 1812–1822.
- (56) Zheng, J.; Zhou, Y.; Li, Y.; Xu, D.-P.; Li, S.; Li, H.-B. *Nutrients* **2016**, *8*, 495.
- (57) Park, W.; Amin, A. R. M. R.; Chen, Z. G.; Shin, D. M. *Cancer Prev. Res.* **2013**, *6*, 387–400.
- (58) Manuel Iglesias, J.; Belouqui, I.; Garcia-Garcia, F.; Leis, O.; Vazquez-Martin, A.; Eguiara, A.; Cufi, S.; Pavon, A.; Menendez, J. A.; Dopazo, J.; Martin, A. G. *PLoS One* **2013**, *8*, e77281.
- (59) Jana, B.; Mohapatra, S.; Mondal, P.; Barman, S.; Pradhan, K.; Saha, A.; Ghosh, S. *ACS Appl. Mater. Interfaces* **2016**, *8*, 13793–13803.
- (60) Siu, C.-K.; Guo, Y.; Saminathan, I. S.; Hopkinson, A. C.; Siu, K. W. M. *J. Phys. Chem. B* **2010**, *114*, 1204–1212.
- (61) Nag, A.; Baksi, A.; Krishnapriya, K. C.; Gupta, S. S.; Mondal, B.; Chakraborty, P.; Pradeep, T. *Eur. J. Inorg. Chem.* **2017**, *2017*, 3072–3079.
- (62) Muhammad, E. F.; Adnan, R.; Latif, M. A. M.; Abdul Rahman, M. B. *J. Inclusion Phenom. Macrocyclic Chem.* **2016**, *84*, 1–10.
- (63) Shityakov, S.; Salmas, R. E.; Durdagi, S.; Roewer, N.; Förster, C.; Broscheit, J. *J. Mol. Struct.* **2017**, *1134*, 91–98.
- (64) Zhao, Q.; Zhang, W.; Wang, R.; Wang, Y.; Ouyang, D. *Curr. Pharm. Des.* **2017**, *23* (3), 522–531.
- (65) Wang, R.; Zhou, H.; Siu, S. W. I.; Gan, Y.; Wang, Y.; Ouyang, D. *J. Nanomater.* **2015**, *2015*, 193049.

## Supporting Information for the Paper

### **Bent Keto Form of Curcumin, Preferential Stabilization of Enol by Piperine, and Isomers of Curcumin $\cap$ Cyclodextrin Complexes: Insights from Ion Mobility Mass Spectrometry**

Abhijit Nag<sup>†</sup>, Papri Chakraborty<sup>†</sup>, Ganapati Natarajan<sup>†</sup>, Ananya Baksi<sup>†</sup>, Sathish Kumar Mudedla<sup>‡</sup>, Venkatesan Subramanian<sup>‡</sup> and Thalappil Pradeep<sup>\*†</sup>

<sup>†</sup>DST Unit of Nanoscience and Thematic Unit of Excellence, Department of Chemistry, Indian Institute of Technology Madras, Chennai-600036, India

\*Email: [pradeep@iitm.ac.in](mailto:pradeep@iitm.ac.in)

<sup>‡</sup>Chemical Laboratory, CSIR-Central Leather Research Institute, Adyar, Chennai 600020, India

#### **Table of contents**

Name	Description	Page no.
	Experimental and computational details	S4-S7
Figure S1	Fragmentation of keto-enol forms of curcumin	S8
Figure S2	Schematic representation of cis keto-enol forms of curcumin	S9
Figure S3	DFT optimized EDP (CE1-H) <sup>-</sup> structure	S9
Figure S4	Bending angles of keto forms	S10

Table S1	Experimental and theoretical CCS values	S10
Figure S5	Solvent dependent study of keto-enol isomers	S11
Figure S6	Plot of the natural logarithm of enol/keto peak intensity ratios against the desolvation gas temperature	S12
Figure S7	Plot of the natural logarithm of enol/keto peak intensity ratios against the different cone voltages	S13
Figure S8	Cone voltage dependent fragmentation study	S14
Figure S9	UPLC separation of keto-enol forms of curcumin	S15
Figure S10	ESI MS of the supramolecular complex of curcumin-piperine	S16
Figure S11	DFT optimized structures of (CE1-H) <sup>-</sup> -piperine interactions	S17
Figure S12	DFT optimized structures of (CE2-H) <sup>-</sup> -piperine interactions	S18
Figure S13	DFT optimized structures of (CK1-H) <sup>-</sup> -piperine interactions	S19
Figure S14	DFT optimized structures of (CK2-H) <sup>-</sup> -piperine interactions	S20
Table S2	Relative energies of the (curcumin-H) <sup>-</sup> -piperine complexes	S21
Table S3	Most stable curcumin-piperine complexes with their interaction energies	S21
Table S4	Most stable (curcumin-H) <sup>-</sup> -piperine complexes with their interaction energies	S22

Figure S15	DFT optimized lowest energy structures of CE1-piperine, CE2-piperine, CK1-piperine and CK2-piperine, respectively	S22
Figure S16	Drift time profile of curcumin- $\beta$ -cyclodextrin (1:2) inclusion complex	S23
Figure S17	Drift time profile of curcumin- $\alpha$ -cyclodextrin (1:1) inclusion complex	S24
Figure S18	CE1 and CK1 docked $\beta$ -cyclodextrin structures, respectively with binding energies	S25
Figure S19	Docking of $\beta$ -cyclodextrin-CE1 and $\beta$ -cyclodextrin-CK1, respectively with second $\beta$ -cyclodextrin	S25
Figure S20	CE1 docked $\beta$ -cyclodextrin dimer structures at different distances of cyclodextrin dimers	S26
Figure S21	CK1 docked $\beta$ -cyclodextrin dimer structure with different angles of cyclodextrin dimers	S26
Table S5	CE1-docked $\beta$ -cyclodextrin dimers with binding energies and CCS values	S27
Table S6	CK1-docked $\beta$ -cyclodextrin dimers with binding energies and CCS values	S27



## Experimental methods

### Chemicals

Curcumin ( $C_{21}H_{20}O_6$ , 94% pure), piperine ( $C_{17}H_{19}NO_3$ , 97% pure),  $\alpha$ -cyclodextrin ( $C_{36}H_{60}O_{30}$ , 98% pure), and  $\beta$ -cyclodextrin ( $C_{42}H_{70}O_{35}$ , 97%) were obtained from Sigma-Aldrich. Methanol (99.9 % pure), Hexane (97% pure), DMSO (99.9% pure) and milli Q water were used throughout the experiment.

### Instrumentation

All mass spectrometric measurements were conducted using a Waters Synapt G2Si High Definition Mass Spectrometer equipped with electrospray ionization (ESI) and ion mobility (IM) separation. All the samples were analyzed in negative ESI mode. The instrument was calibrated using sodium formate ( $m/z$  20–1500) as a calibrant for the low mass range. For IMS measurements, the ions of interest were selected by a quadrupole mass filter and passed through the IMS cell for isomer separation where nitrogen was used as a buffer gas. Typical experimental parameters were: desolvation gas temperature, for temperature dependent, study it was varied from 40 to 600 °C ; capillary voltage, 3 kV; sample cone, 0 V; source offset, 0 V; trap collision energy, 2 V; trap gas flow, 2 mL/min; helium cell gas flow, 180 mL/min; IMS gas flow, 80 mL/min; trap DC bias, 40 V; IMS wave height, 40 V and IMS wave velocity, 750 m/s. The collision voltage in the transfer cell was raised until fragmentations were seen properly (4-60 V). The concentration of the sample was 0.05 mM and it was infused at a flow rate of 10  $\mu$ L/min.

Parameters for cyclodextrin-curcumin inclusion complexes: Capillary voltage, 3 kV; sample cone, 20 V; source offset, 20 V; trap collision energy, 2 V; trap gas flow, 2 mL/min; helium cell gas flow, 180 mL/min; IMS gas flow, 80 mL/min; trap DC bias, 40 V; IMS wave height, 40 V; IMS wave velocity, 400 m/s.

We used the recent literature on negative ion mode traveling wave ion mobility mass spectrometry calibrations.<sup>1</sup> Polyalanine was used as a calibrant. We compared the CCS values of Leucine enkephalin with a reported paper.<sup>1</sup> Then we carried out the experiments.

### UPLC Separation Method

Standard curcumin solutions (0.05 mM in methanol) were prepared. The UPLC instrument is ACQUITY from Waters. An ACQUITY UPLC BEH C18 1.7  $\mu$  column was kept at 40 °C. The

mobile phase was water/acetonitrile (50/50). The flow rate of the mobile phase was set at 0.5 mL/min. Mass spectrometry data were collected using a Waters Synapt G2Si High Definition Mass Spectrometer equipped with electrospray ionization (ESI) in the negative ion mode. The capillary voltage was 3.0 kV for negative ion detection. MS/MS fragmentation spectra of curcumin were acquired with the precursor ion,  $m/z$  367.

### **ESI MS for curcumin-piperine interactions**

The ESI MS for curcumin piperine interactions has been performed in ethanol.

### **Computational methods**

Initial geometries of the curcumin was taken from the PDB files (enol), cif files (enol)<sup>2-5</sup> in the literature, and also built from their structural formulae using Avogadro software.<sup>6</sup> Since only the enol form has been crystallized, we built the keto structure by modifying the enol group by moving the H atom and the initial keto geometry was supported by a co-crystal structure.<sup>6</sup> First, we carried out a conformational isomer search on the enol and keto forms of curcumin using a genetic algorithm and weighted rotor searches using Avogadro. The parameters of the genetic algorithm were, Children=10, Mutability=10, and Convergence=50 Scoring method=Energy. We used an MMFF94 force field. All the structures were modeled by utilizing Avogadro software packages<sup>6</sup> and the visualizations presented were created using Visual Molecular Dynamics (VMD) software.<sup>7</sup> The crystal structures of alpha-CD<sup>8</sup> and beta-CD<sup>9</sup> were taken from PDB files. The enol form was unchanged in this search due to the closed hydrogen bond. The input geometries for the keto conformer search were two different enol isomers which are known from their crystal structures and are distinguished by opposite positions of the -OH with respect to the -OMe group on both ends of the molecule.

We found that the keto form bends into many conformations, and we classified those by the degree and angle of bending. We generated several isomers using different random seeds. A conformer search was carried out using a genetic algorithm in Avogadro to obtain a few different keto isomers which were distinguished by the degree of bending.

DFT geometry optimization for all these isomer structures was carried out using the B3LYP functional and the 6-311++G(d,p) basis set, as implemented in the NWChem program.<sup>10</sup> We used the deprotonation site at one of the phenolic -OH form (Figure S3) groups for both the keto-enolic and diketone forms. For the enol form, the deprotonation at the phenolic -OH is

energetically preferred to that at the enolic -OH, as it does not involve the breakage of the intramolecular keto-enolic hydrogen bond.

Electrostatic charges (ESP charges), which are known to yield more accurate CCS values than Mulliken partial charges, for the optimized structures were calculated by fitting to the electrostatic potential calculated using DFT as above with the Merz-Singh-Kollman scheme as implemented in NWChem.<sup>10</sup> These ESP charges were applied for the estimation of theoretical CCSs using the trajectory method (TM) as implemented in the MOBCAL program<sup>11-13</sup> in its modified version for N<sub>2</sub> gas.<sup>13</sup>

The trajectory method (TM) in Mobcal is quite CPU intensive as it runs in serial mode and we restricted its use to only the isomers of curcumin alone, and for the larger curcumin-cyclodextrin complexes we employed the Projection Approximation (PA) method in Mobcal which is known to give accurate values in the size range of molecules of our interest.

A molecular docking<sup>14</sup> study using Autodock 4.2 was applied to build the curcumin $\cap$ CD inclusion complexes.

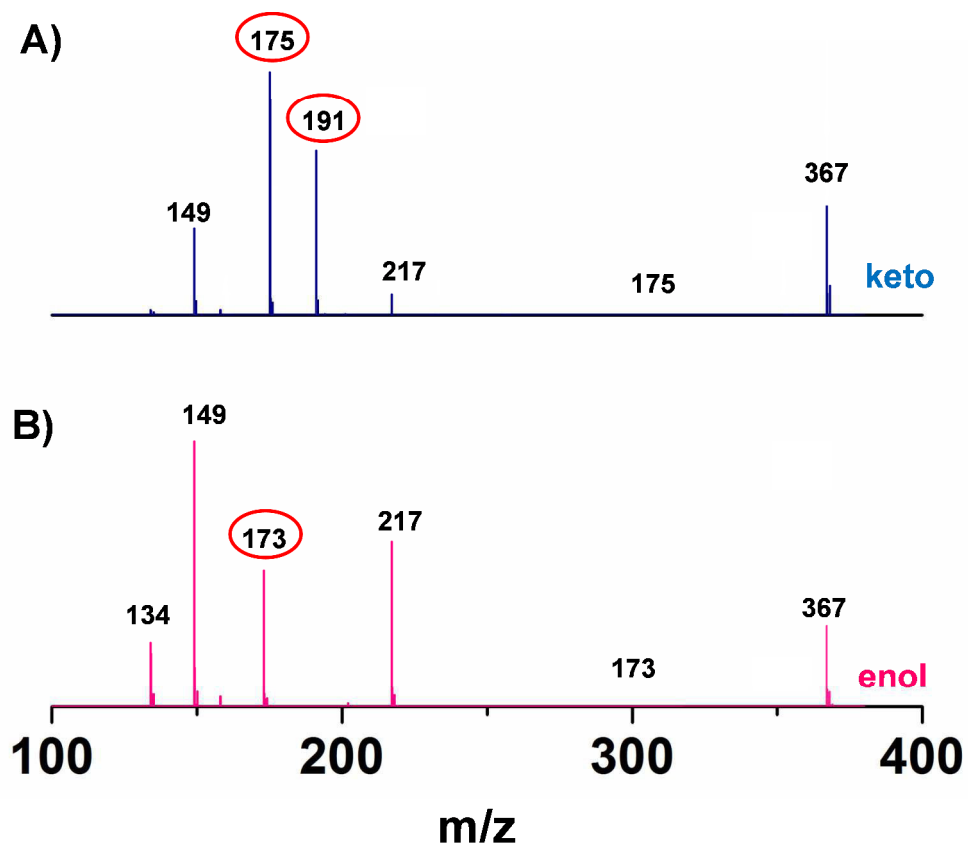
### **Computational methods for curcumin-piperine interactions:**

Piperine and curcumin have aromatic six-membered rings and hydrogen bond donors and acceptors. Thus they can interact through hydrogen bond and  $\pi$ - $\pi$  stacking interactions. We have interacted piperine with the each isomer of curcumin through hydrogen bond and  $\pi$ - $\pi$  stacking interactions. The different possible geometries were optimized using density functional theory calculations. Previous literature showed that Minnesota functionals are suitable for the description of non-covalent interactions.<sup>15,16</sup> All the geometries were optimized using the M06-2X/6-31G\* level of theory. The vibrational analysis revealed that the optimized geometries were corresponding to true minima on the potential energy surface. All the calculations were performed with the help of GAUSSIAN 09 software.

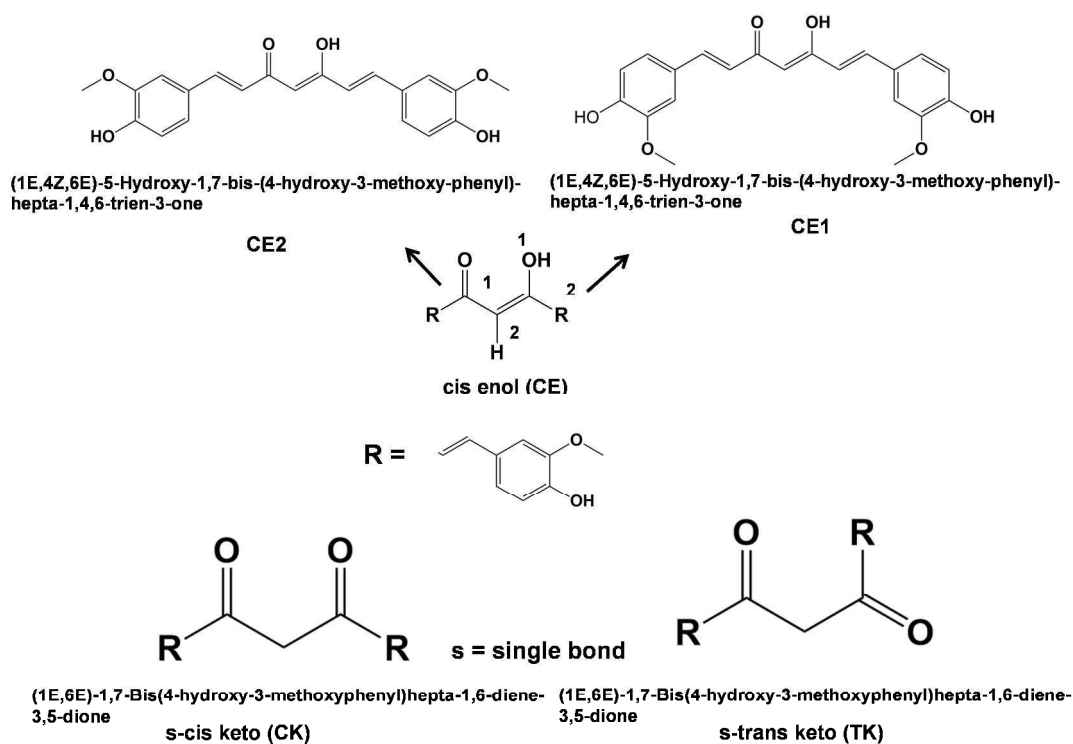
### **Molecular docking study**

We assigned Gasteiger charges to all atoms by following the procedure as implemented in Autodock. For simplicity, we neglected torsional freedom on all molecules which would also result in the glucopyranose units being rotated with respect to each other. The free energies of binding were calculated by summing the intermolecular and internal and torsional terms and

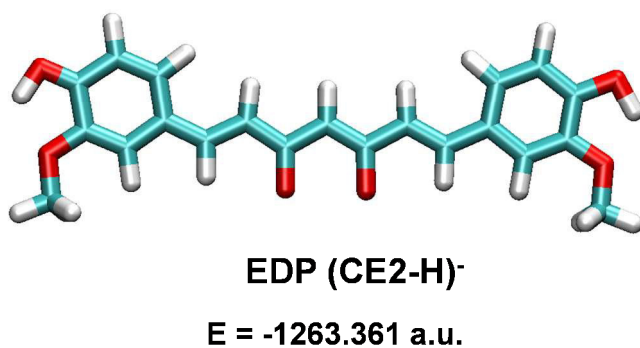
subtracting the unbound energy which is a calculation that is performed within the Autodock program. The size of the search space in which the curcumin isomer (keto/enol) was to be moved was a cube with a side of length of 126 points with point spacing of 0.375 Å.  $\alpha$ -CD is the smallest CD consisting of six glucopyranose units and  $\beta$ -CD consists of seven glucopyranose units. The CD molecule consisting of the ring of glucopyranose units has a wide rim known as the head (H) to which the secondary OH groups are bonded and the tail which is a narrower rim to which primary OH groups are added. Head-head orientation in CD dimer was found as the most stable in MD compared to head-tail and tail-tail, as a result of the larger number of intermolecular hydrogen bonds.<sup>17</sup> During the docking simulations, in the monomer complexes, the curcumin isomers (CE1 and CK1) were taken as the “ligand” i.e. the movable molecule whose degrees of freedom would be varied and CDs ( $\alpha$ - and  $\beta$ -) as the “receptor” which was the fixed and completely rigid central molecule.



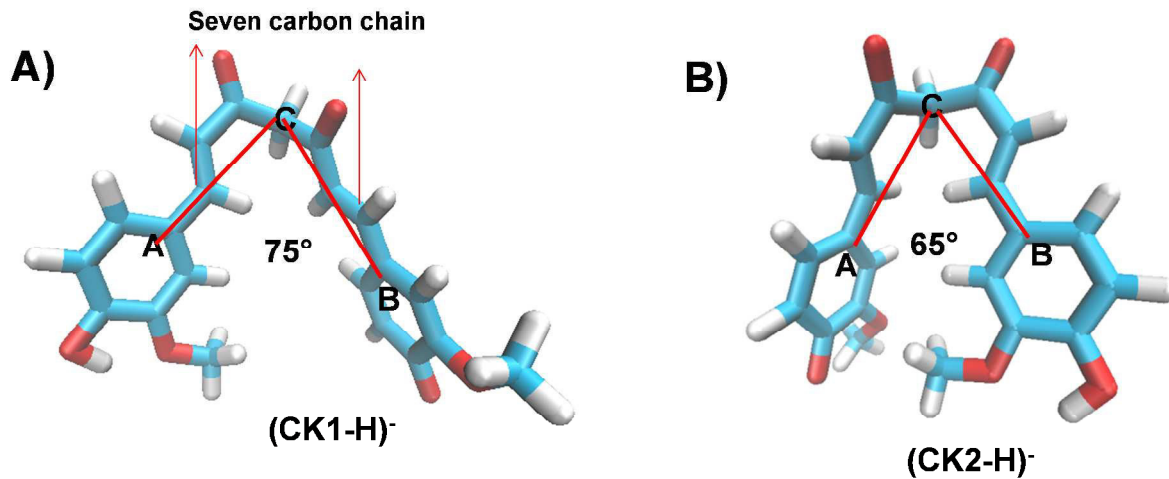
**Figure S1.** CID mass spectra and fragmentation patterns of isomeric forms of curcumin in transfer CID; **A)** keto form and **B)** enol form. Note the encircled peaks in **A** and in **B**, which are the characteristic fragmentation patterns of keto and enol forms, respectively.



**Figure S2.** Schematic representation of cis keto-enol forms of curcumin.



**Figure S3.** DFT optimized EDP (CE2-H)<sup>-</sup> structure, where EDP stands for enol deprotonation.

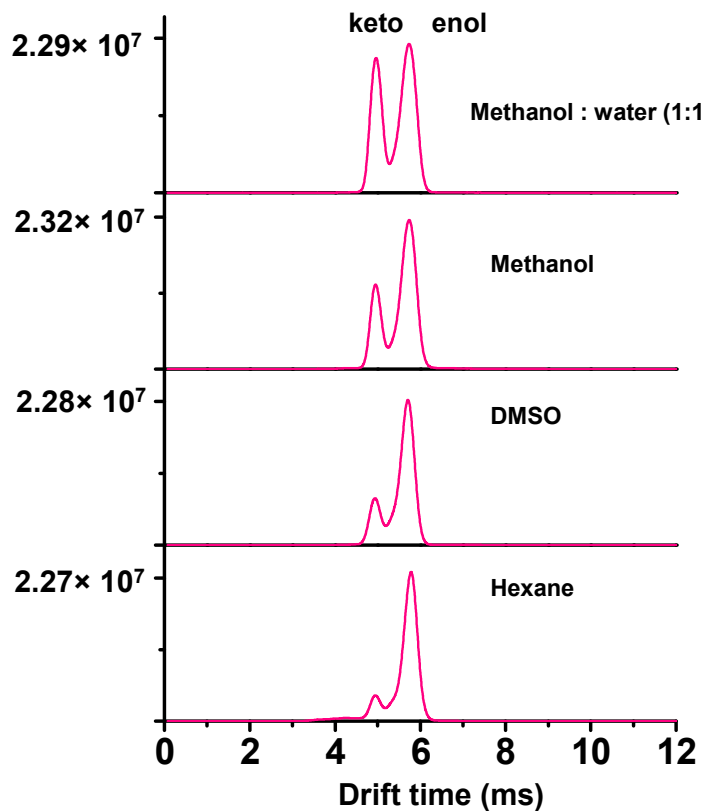


**Figure S4. A) & B)** Bending angles of (CK1-H)<sup>-</sup> & (CK2-H)<sup>-</sup> 75° & 65°, respectively.

**Table S1.** Experimental and theoretical CCS values

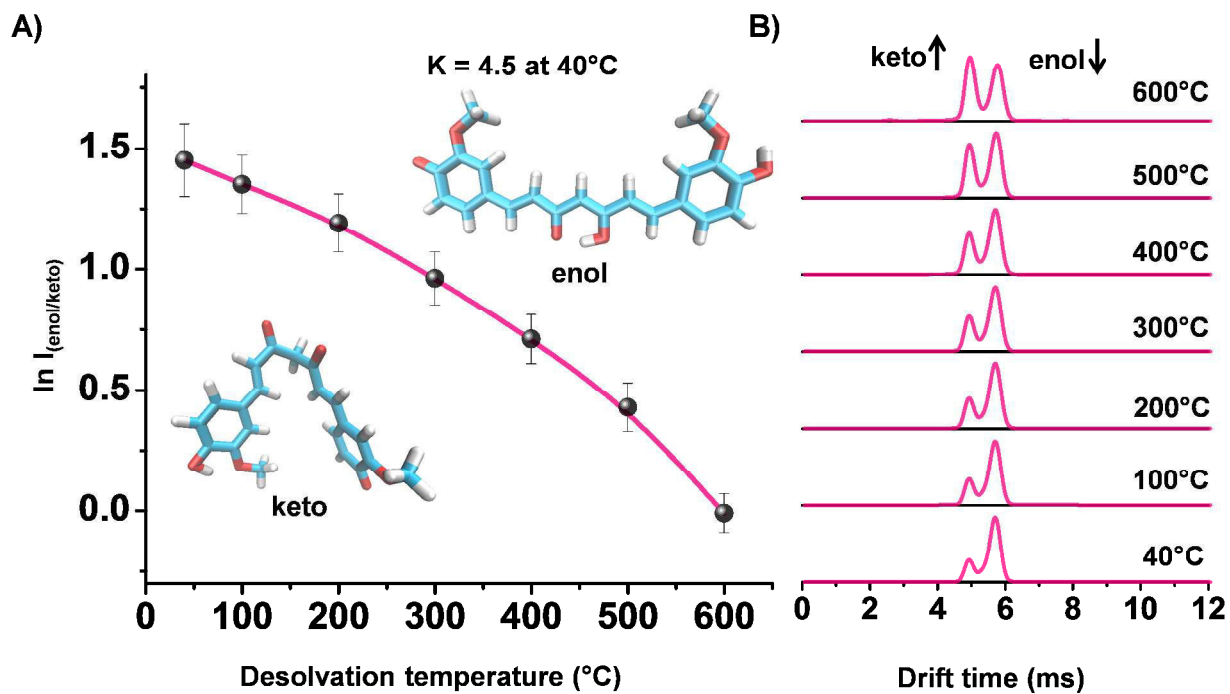
Possible isomers	Energy (in a.u.)	Calculated CCS by TM ( Å <sup>2</sup> )	Exp. CCS ( Å <sup>2</sup> )
(CE1-H) <sup>-</sup>	-1263.389	213.0	211.0
(CE2-H) <sup>-</sup>	-1263.387	213.5	
(CK1-H) <sup>-</sup>	-1263.386	198.8	196.0
(CK2-H) <sup>-</sup>	-1263.382	188.0	

\* The isomer labels imply the follows: C, *cis*; E and K, enol and keto.

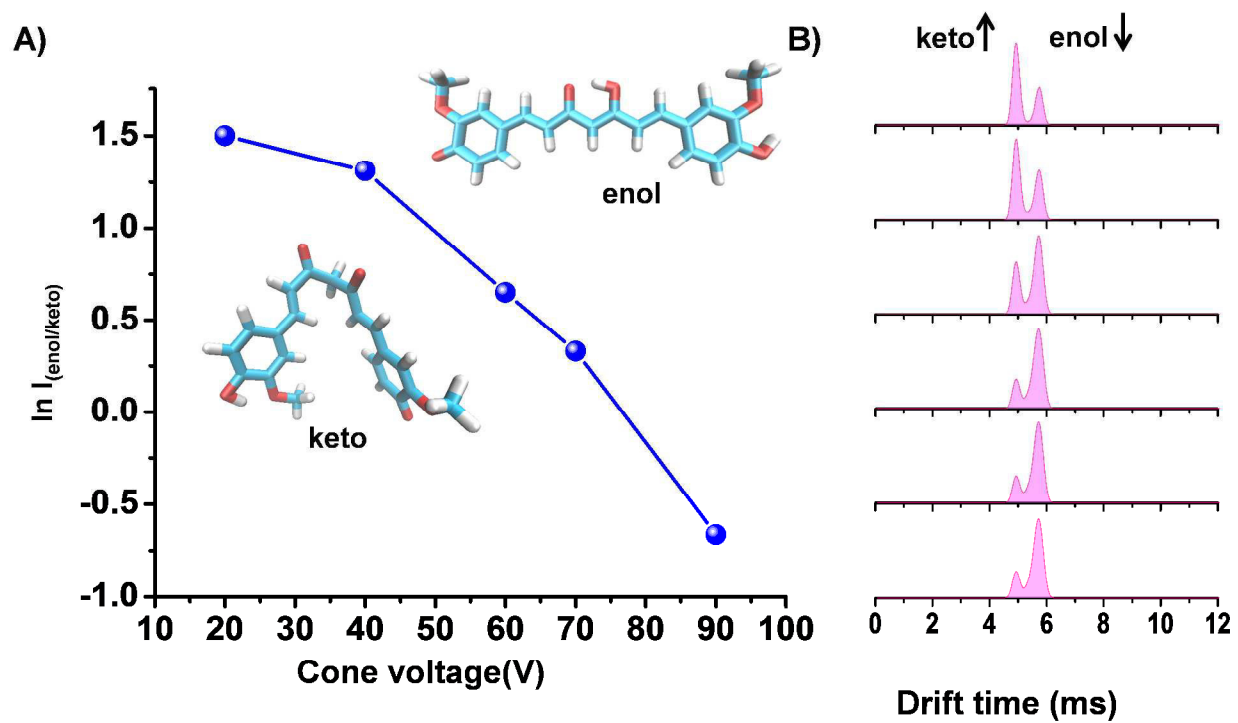


**Figure S5.** Solvent dependent study of keto-enol isomers. Keeping the concentration of curcumin constant, solvents were changed from non-polar to polar (hexane to methanol/water). With the increase of polarity, the keto form is enhanced.

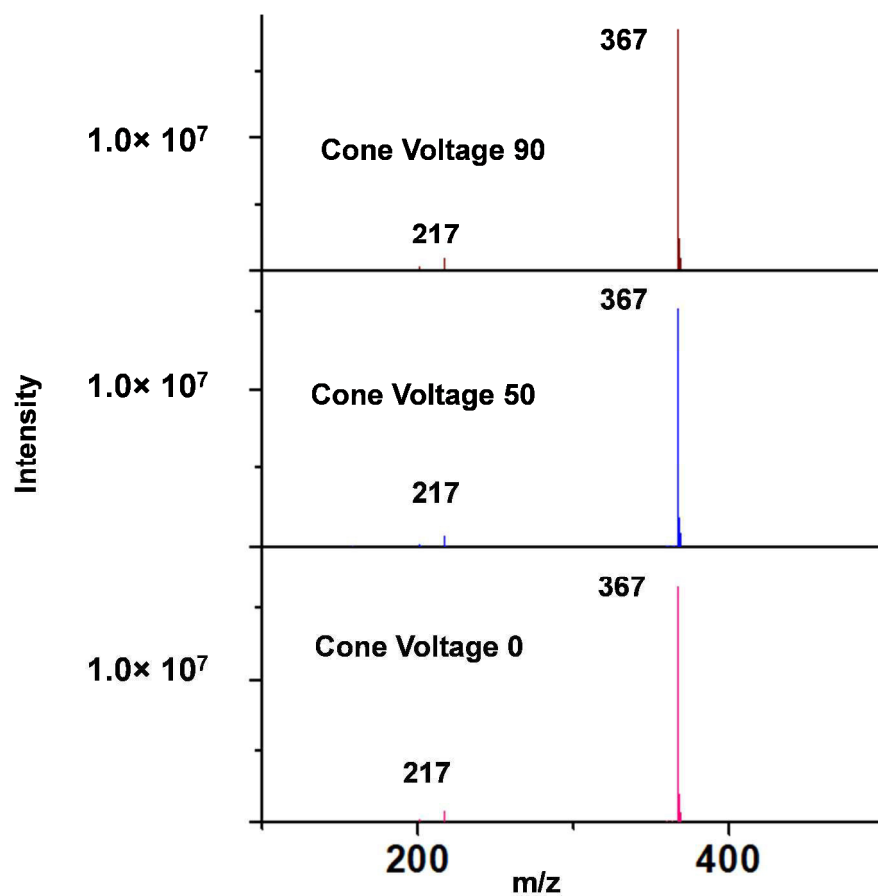




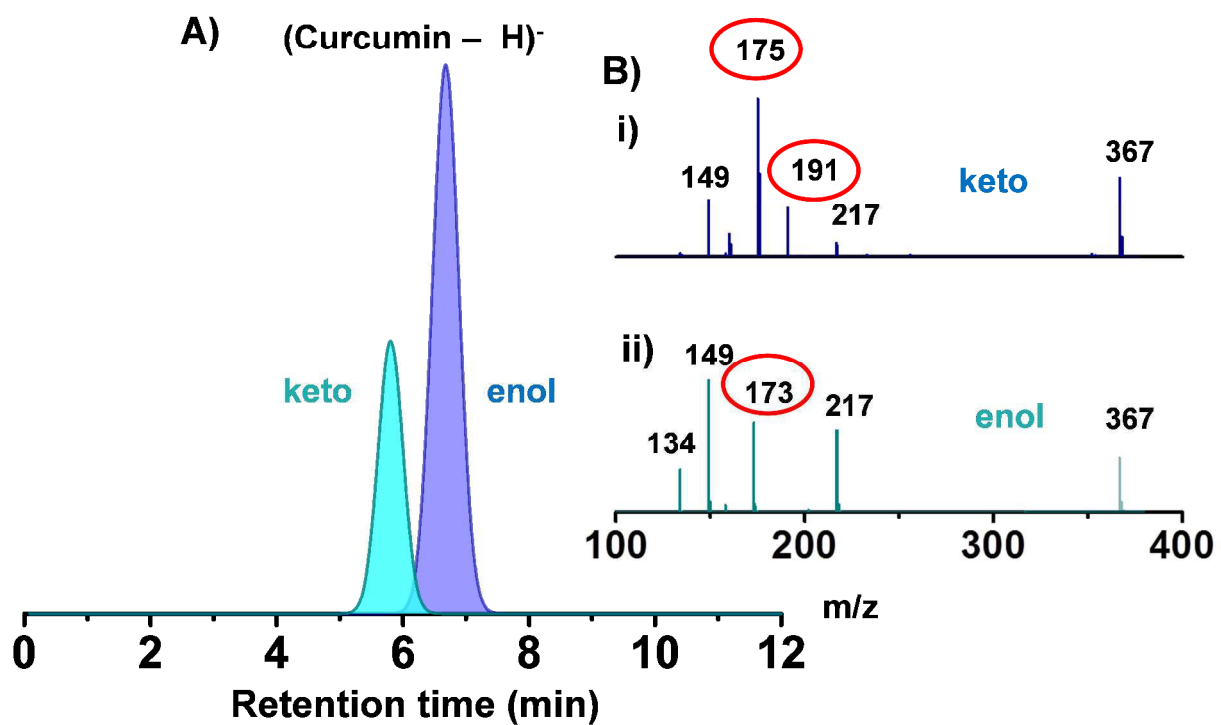
**Figure S6.** A) Plot of the natural logarithm of keto/enol peak intensity ratios against different desolvation temperatures from 40 to 600 °C. B) With the increase of desolvation temperature, the keto form is enhanced. The lowest energy enol and keto structures are also shown in A).



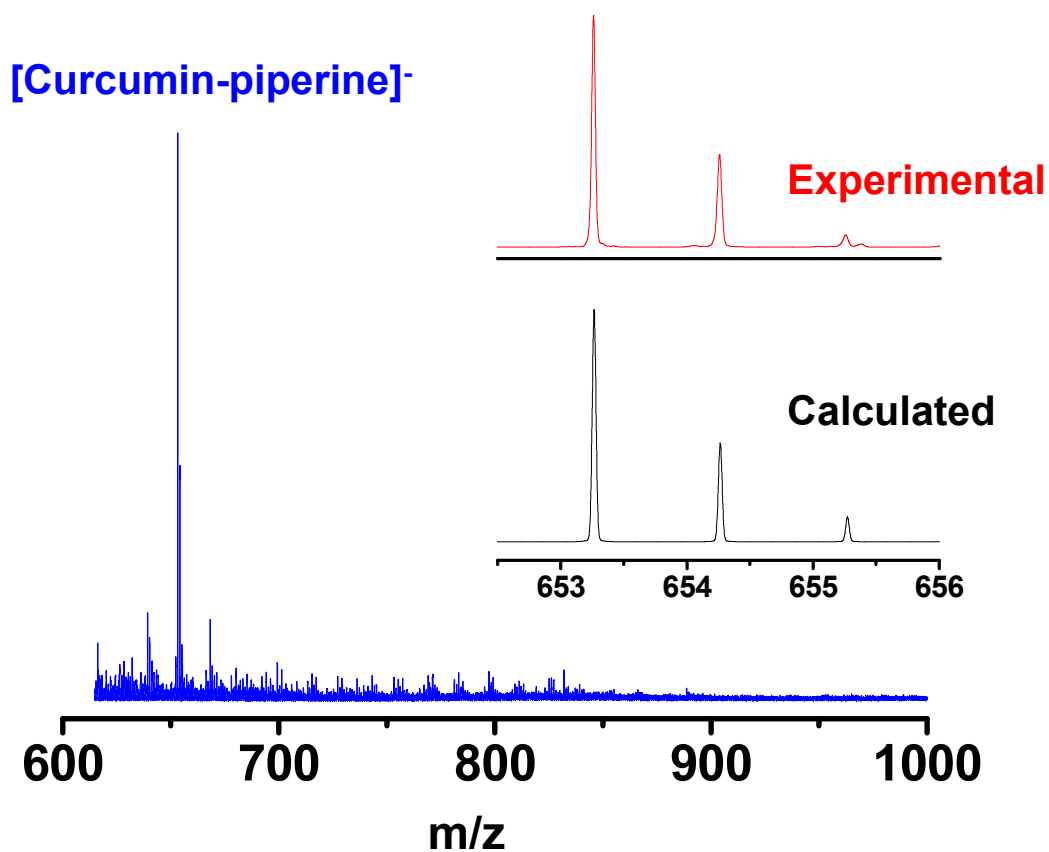
**Figure S7.** A) Plot of the natural logarithm of keto/enol peak intensity ratios against the different cone voltages, from 15 V to 90 V. B) With the increase in cone voltage, the enol form decreases.



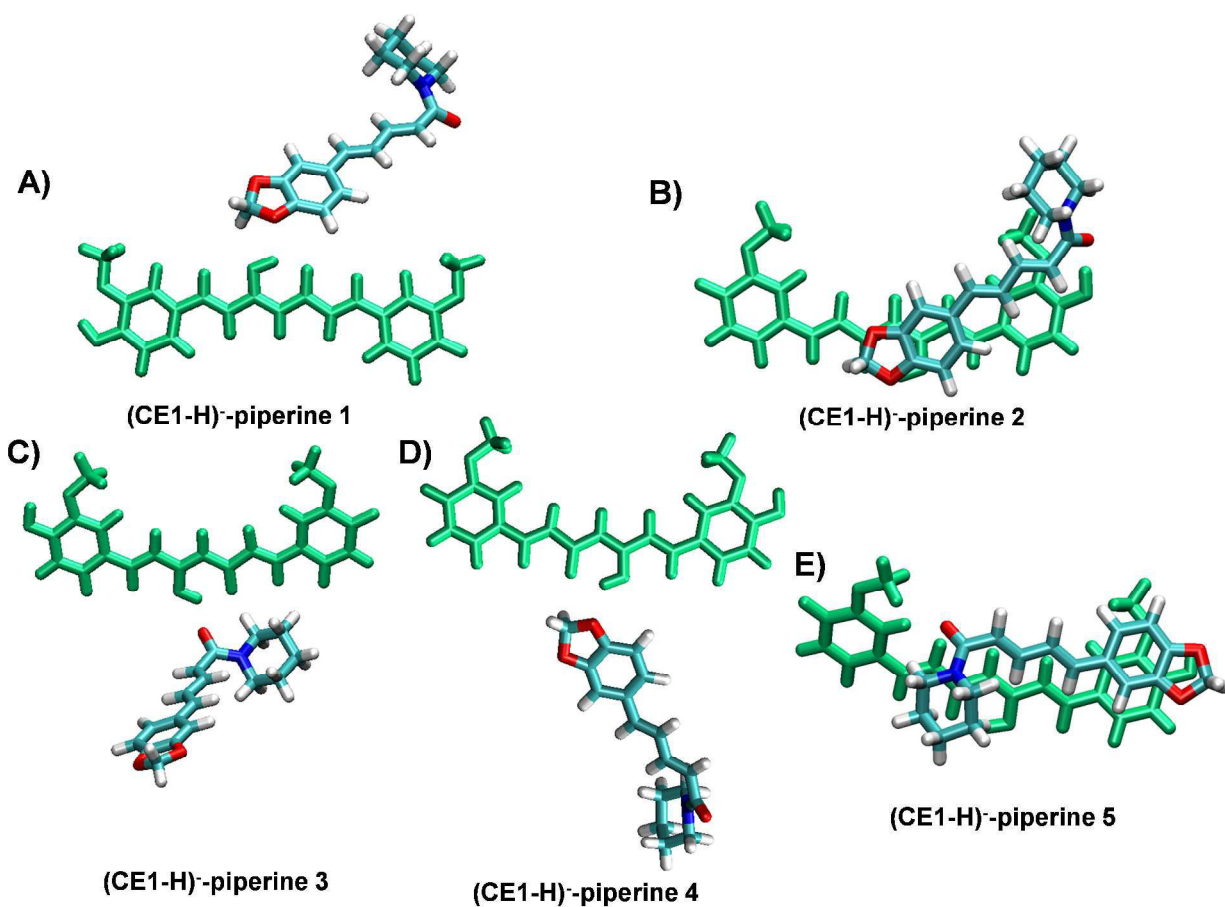
**Figure S8.** Cone voltage-dependent fragmentation study. No additional change in fragmentation was seen with the increase of cone voltage.



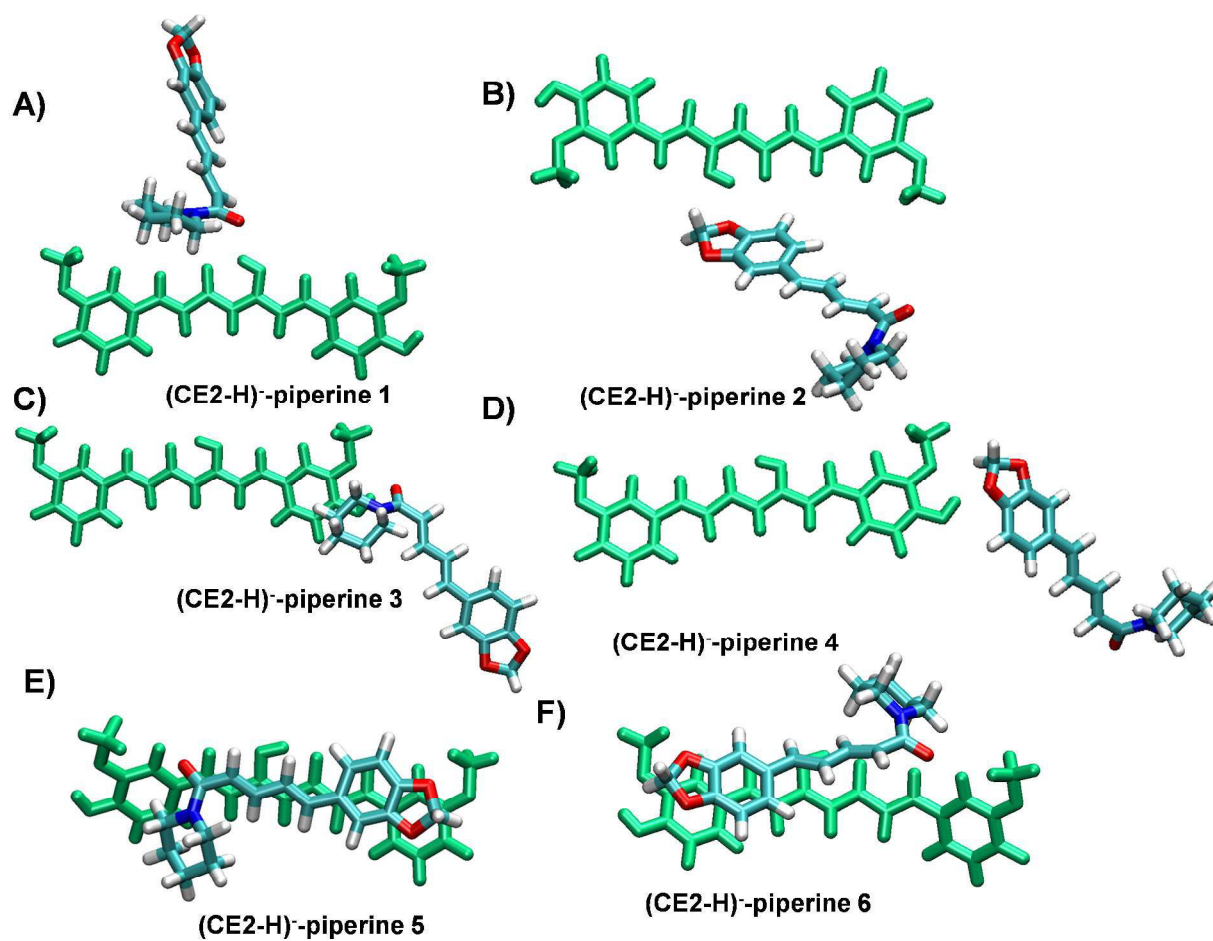
**Figure S9.** A) UPLC separated keto enol tautomers of curcumin. B) The MSMS fragmentation of the keto (i) and enol (ii) forms of curcumin. Tautomer specific peaks are encircled.



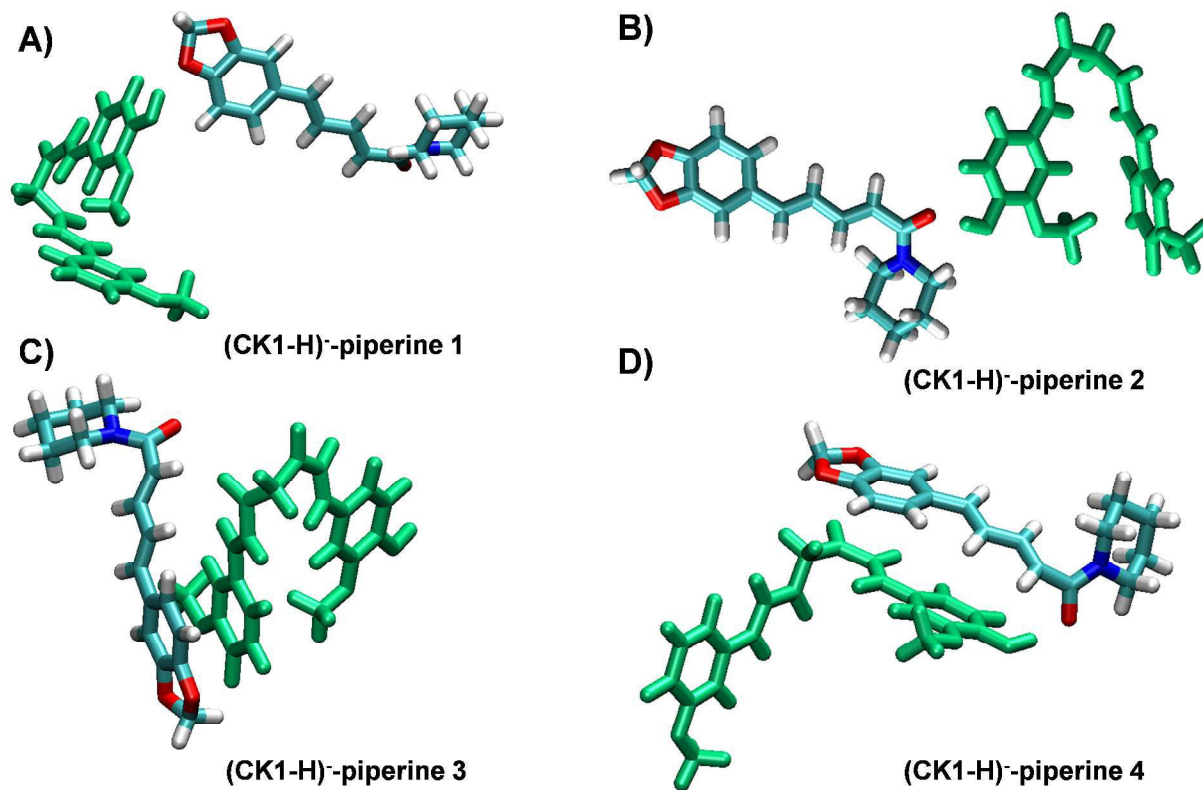
**Figure S10.** ESI MS of supramolecular adducts of curcumin-piperine complex in ethanol. Inset of the mass spectrum showing that the peak intensities of the isotopologues of the calculated and experimental are matching.



**Figure S11.** DFT optimized structures of deprotonated (CE1-H)<sup>-</sup>-piperine interactions. Different possibilities of structural combination between deprotonated (CE1-H)<sup>-</sup> and piperine are shown in A)-E). Among all E) is the lowest energy structure.

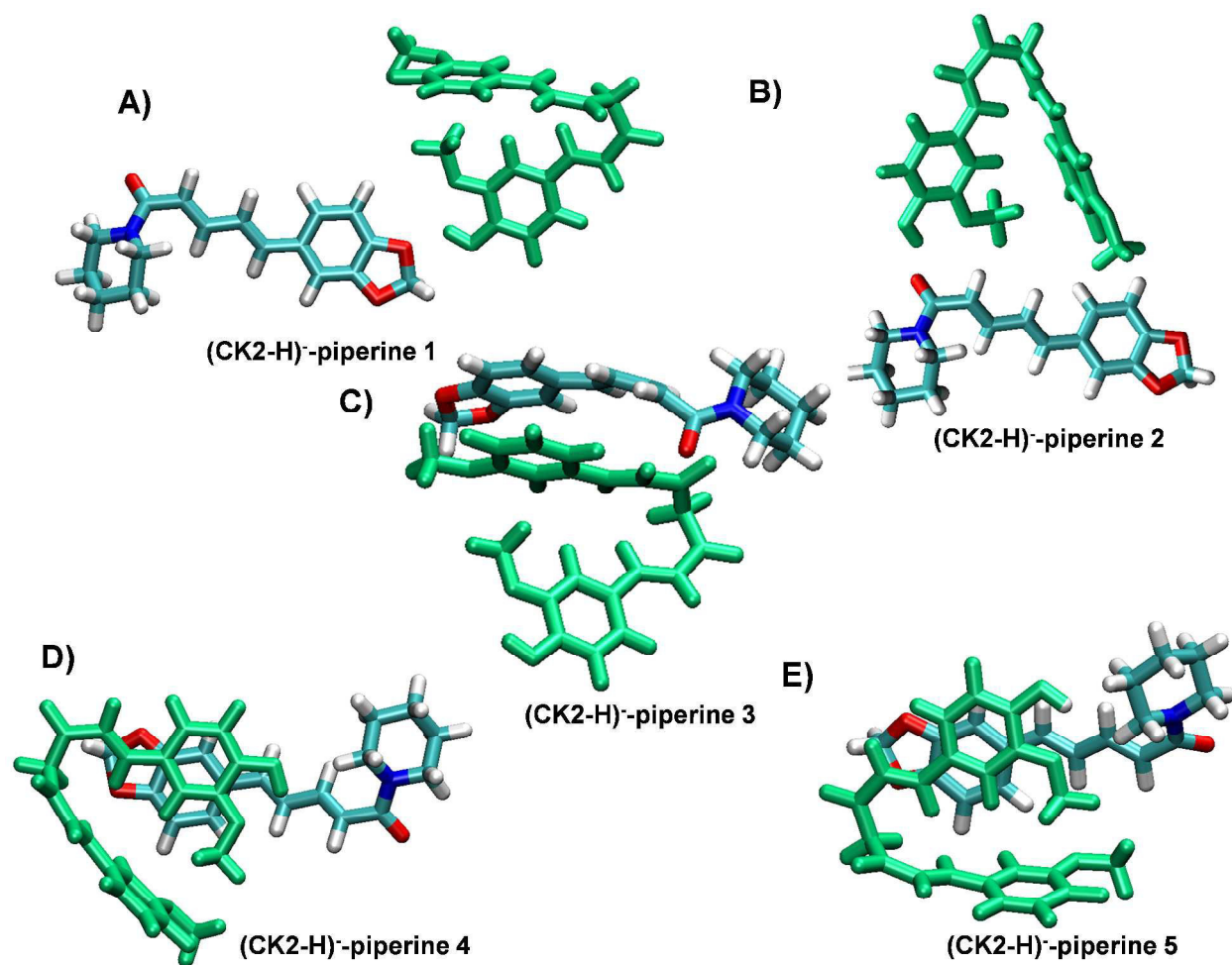


**Figure S12.** DFT optimized structures of deprotonated (CE2-H)<sup>-</sup>-piperine interactions. Different possibilities of structural combination between deprotonated (CE2-H)<sup>-</sup> and piperine are shown in A)-F). Among all E) is the lowest energy structure.



**Figure S13.** DFT optimized structures of deprotonated (CK1-H)<sup>-</sup>-piperine interactions. Different possibilities of structural combination between deprotonated (CK1-H)<sup>-</sup> and piperine are shown in A)-D). Among all D) is the lowest energy structure.





**Figure S14.** DFT optimized structures of deprotonated (CK2-H)<sup>-</sup>-piperine interactions. Different possibilities of structural combination between deprotonated (CK2-H)<sup>-</sup> and piperine are shown in A)-E). Among all E) is the lowest energy structure.

**Table S2.** Relative energies of the (curcumin H)<sup>-</sup>-piperine complexes.

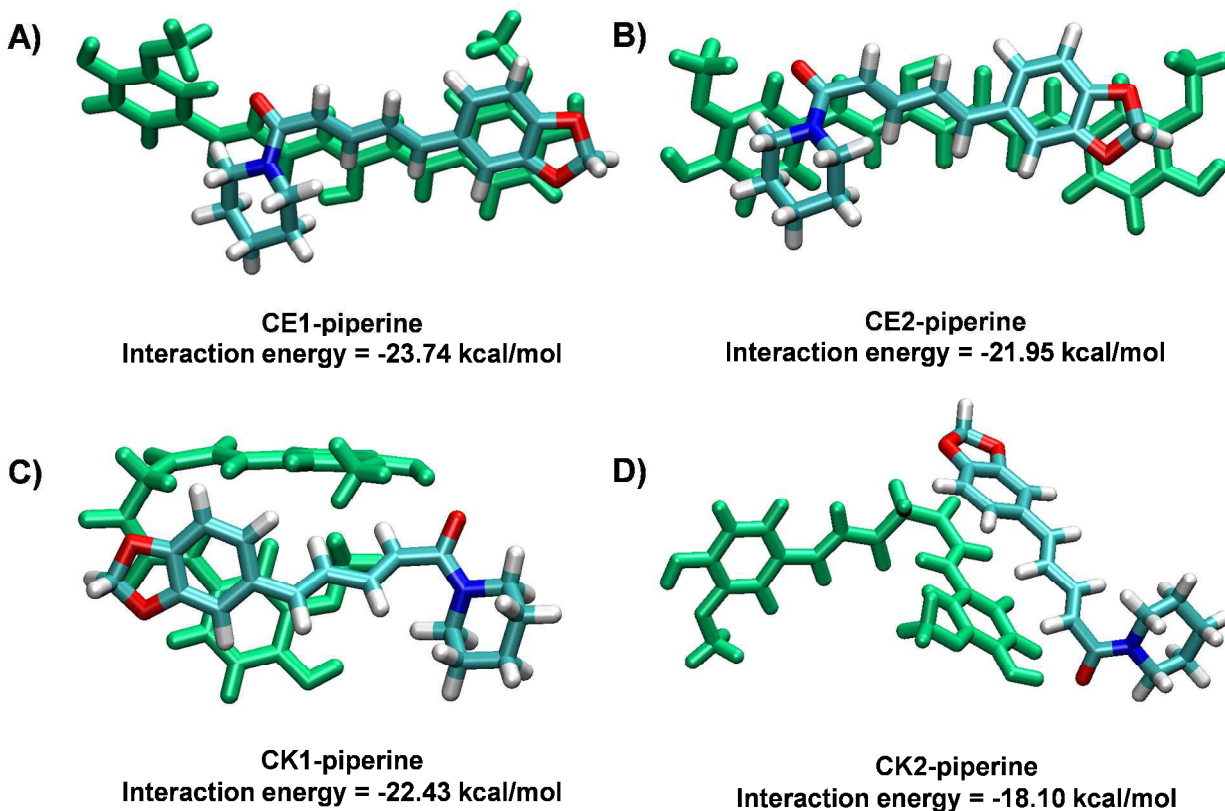
Deprotonated forms of curcumin	Different conformers of curcumin-piperine complexes	Relative energy (kcal/mol)
(CE1-H) <sup>-</sup>	(CE1-H) <sup>-</sup> -piperine 1	20.99
(CE1-H) <sup>-</sup>	(CE1-H) <sup>-</sup> -piperine 2	2.77
(CE1-H) <sup>-</sup>	(CE1-H) <sup>-</sup> -piperine 3	0.69
(CE1-H) <sup>-</sup>	(CE1-H) <sup>-</sup> -piperine 4	20.99
(CE1-H) <sup>-</sup>	(CE1-H) <sup>-</sup> -piperine 5	0.00
(CE2-H) <sup>-</sup>	(CE2-H) <sup>-</sup> -piperine 1	17.76
(CE2-H) <sup>-</sup>	(CE2-H) <sup>-</sup> -piperine 2	18.91
(CE2-H) <sup>-</sup>	(CE2-H) <sup>-</sup> -piperine 3	12.68
(CE2-H) <sup>-</sup>	(CE2-H) <sup>-</sup> -piperine 4	17.30
(CE2-H) <sup>-</sup>	(CE2-H) <sup>-</sup> -piperine 5	0.00
(CE2-H) <sup>-</sup>	(CE2-H) <sup>-</sup> -piperine 6	3.23
(CK1-H) <sup>-</sup>	(CK1-H) <sup>-</sup> -piperine 1	15.22
(CK1-H) <sup>-</sup>	(CK1-H) <sup>-</sup> -piperine 2	8.76
(CK1-H) <sup>-</sup>	(CK1-H) <sup>-</sup> -piperine 3	10.83
(CK1-H) <sup>-</sup>	(CK1-H) <sup>-</sup> -piperine 4	0.00
(CK2-H) <sup>-</sup>	(CK2-H) <sup>-</sup> -piperine 1	14.76
(CK2-H) <sup>-</sup>	(CK2-H) <sup>-</sup> -piperine 2	8.07
(CK2-H) <sup>-</sup>	(CK2-H) <sup>-</sup> -piperine 3	3.46
(CK2-H) <sup>-</sup>	(CK2-H) <sup>-</sup> -piperine 4	3.23
(CK2-H) <sup>-</sup>	(CK2-H) <sup>-</sup> -piperine 5	0.00

**Table S3.** Most stable curcumin (without proton loss)-piperine complexes with their interaction energies.

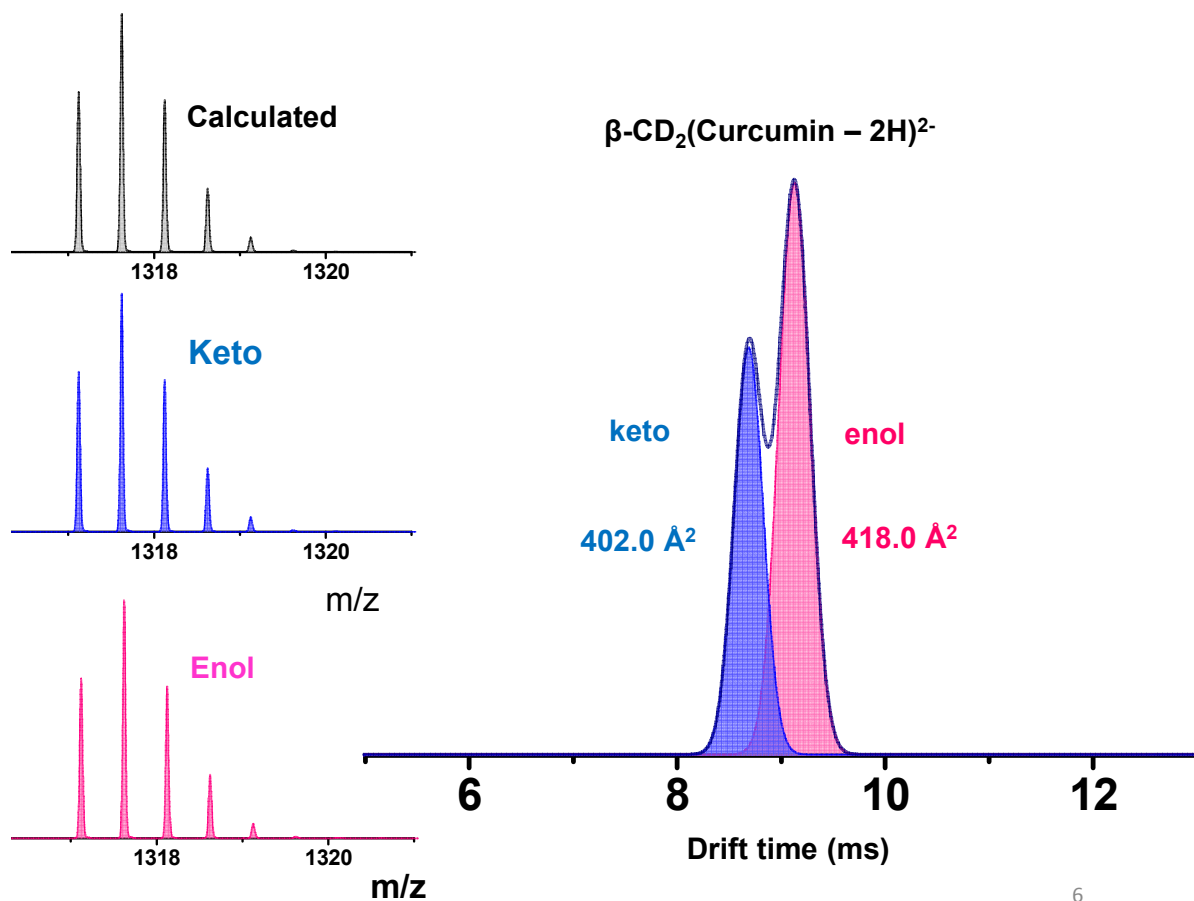
Curcumin-piperine complexes	Interaction energy (kcal/mol)
CE1-piperine 5	-23.74
CE2-piperine 5	-21.95
CK1-piperine 4	-22.43
CK2-piperine 5	-18.10

**Table S4.** Most stable curcumin deprotonated-piperine complexes with their interaction energies.

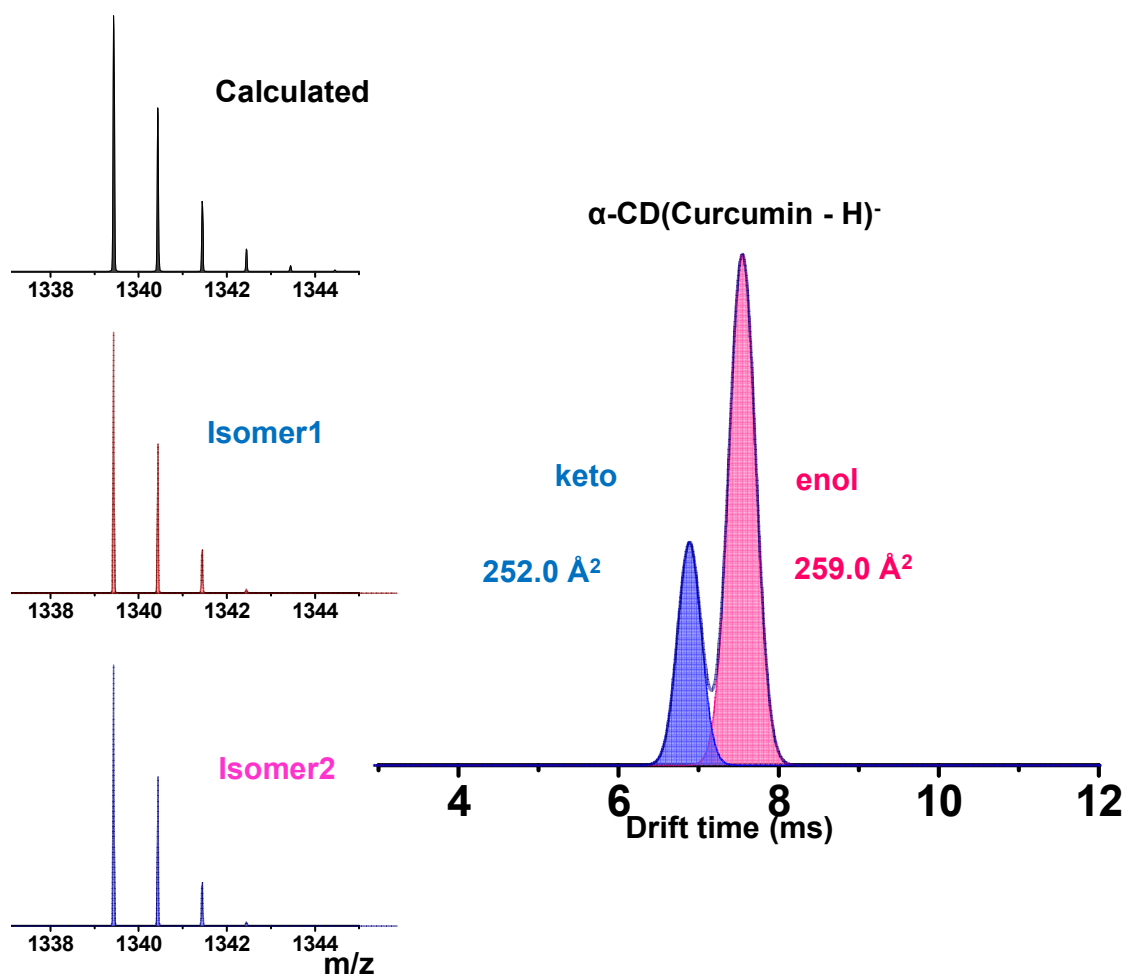
(Curcumin-H) <sup>-</sup> -piperine complexes	Interaction energy (kcal/mol)
(CE1-H) <sup>-</sup> -piperine 5	-23.51
(CE2-H) <sup>-</sup> -piperine 5	-20.60
(CK1-H) <sup>-</sup> -piperine 4	-23.08
(CK2-H) <sup>-</sup> -piperine 5	-22.18



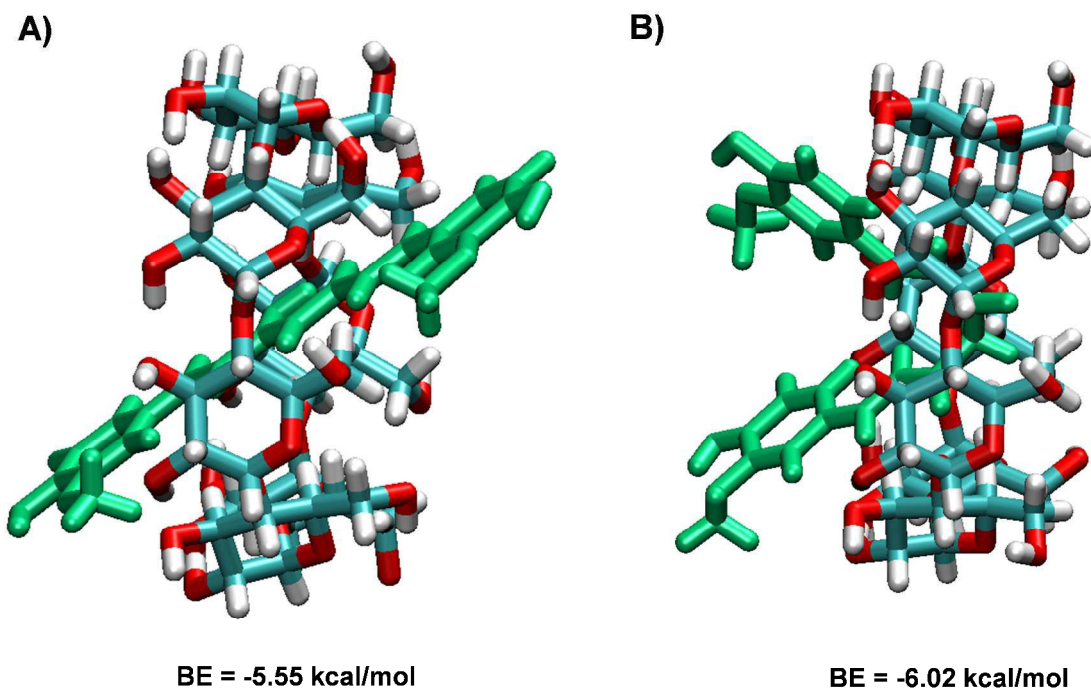
**Figure S15.** DFT optimized lowest energy structures of A) CE1-piperine, B) CE2-piperine, C) CK1-piperine and D) CK2-piperine, respectively.



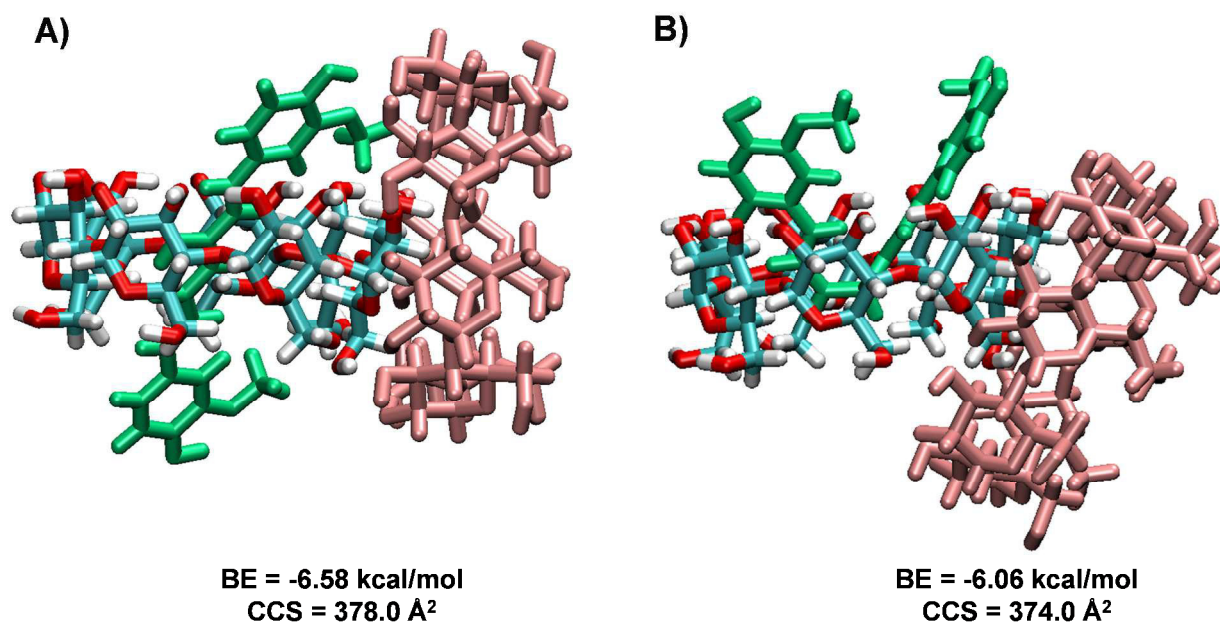
**Figure S16.** Drift time profile of curcumin- $\beta$ -cyclodextrin (1:2) inclusion complex; two peaks are indicating the isomeric structures. Inset of drift time profile represents the relative peak intensities of isotopologues of keto and enol inclusion complexes of curcumin which are matching with the calculated peak intensities of the isotopologues.



**Figure S17.** Drift time profile of curcumin- $\alpha$ -cyclodextrin (1:1) inclusion complex; two peaks are indicating the isomeric structures. Inset of drift time profile represents the relative peak intensities of isotopologues of keto and enol inclusion complexes of curcumin which are matching with the calculated peak intensities of the isotopologues.

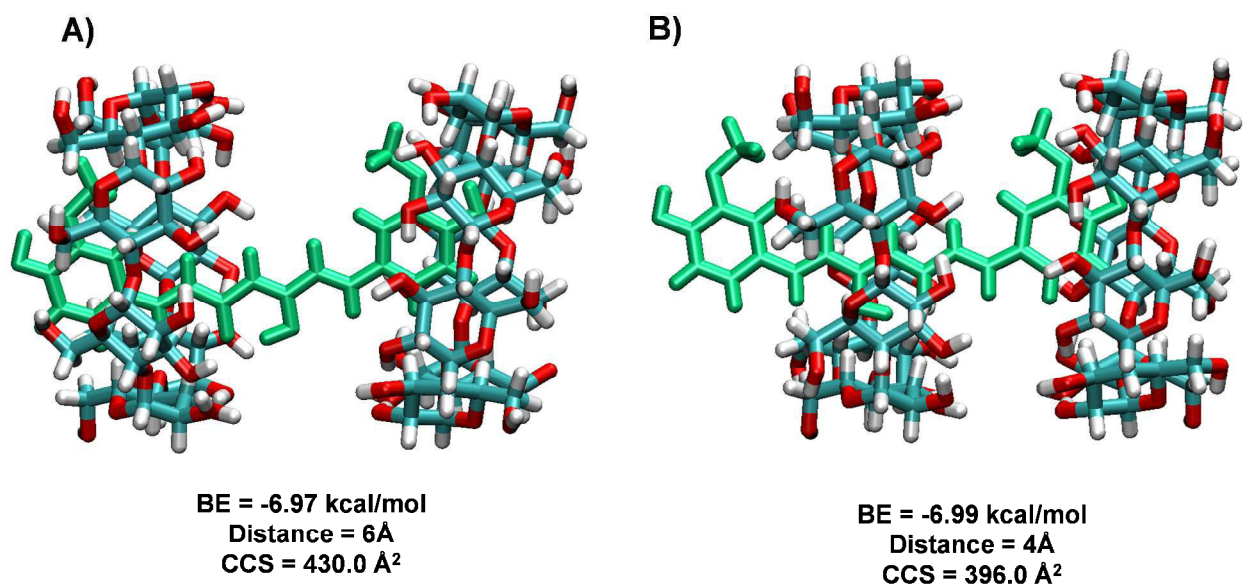


**Figure S18.** A) & B) CE1 and CK1 docked  $\beta$ -cyclodextrin structures, respectively with binding energies.

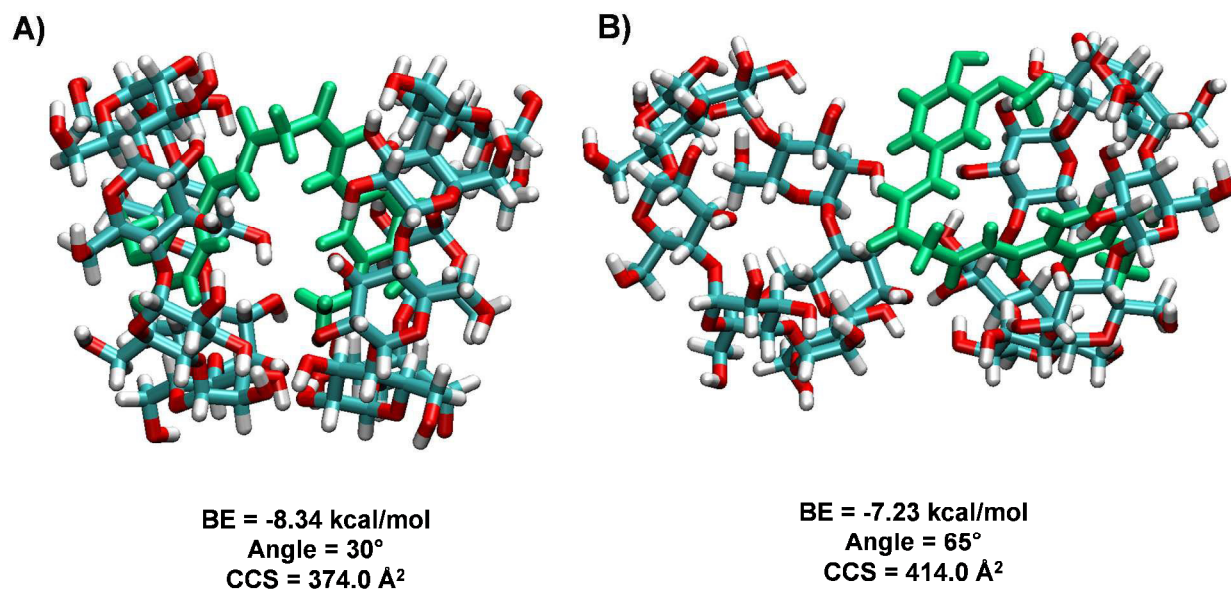


**Figure S19.** A) & B) Docking of  $\beta$ -cyclodextrin-CE1 and  $\beta$ -cyclodextrin-CK1, respectively with second  $\beta$ -cyclodextrin. Binding energies and CCS values are given below the structures.





**Figure S20.** CE1 docked  $\beta$ -cyclodextrin dimer structures. **A)** & **B)** The two  $\beta$ -cyclodextrin dimers were kept apart at 6 Å and 4 Å, respectively. The binding energies, distances and CCS values are provided below each structure.



**Figure S21.** CK1 docked  $\beta$ -cyclodextrin dimer structure. **A)** and **B)** The two  $\beta$ -cyclodextrin dimers were kept apart at different angles 30° and 65°, respectively. The binding energies, angles between the two cyclodextrin and CCS values are given below each structure.

**Table S5.** CE1-docked  $\beta$ -cyclodextrin dimers with binding energies and CCS values, which are shown for different separation distances of the CD dimers.

Distance between two $\beta$ -cyclodextrins ( $\text{\AA}^2$ )	Binding energy of lowest energy conformer (kcal/mol)	Calculated CCS value of lowest energy conformer ( $\text{\AA}^2$ )	Exp. CCS values ( $\text{\AA}^2$ )
4	-6.99	396.0	418.0
5	-7.01	411.0	
6	-6.97	430.0	

**Table S6.** CK1 docked  $\beta$ -cyclodextrin dimer with binding energy and CCS values.

Angle between two $\beta$ -cyclodextrins	Binding energy of lowest energy conformer (kcal/mol)	Calculated CCS value of lowest energy conformer ( $\text{\AA}^2$ )	Exp. CCS values ( $\text{\AA}^2$ )
30°	-8.34	374.0	402.0
40°	-8.58	390.0	
65°	-7.23	414.0	

## References

- (1) Forsythe, J. G.; Petrov, A. S.; Walker, C. A.; Allen, S. J.; Pellissier, J. S.; Bush, M. F.; Hud, N. V.; Fernandez, F. M. *Analyst* **2015**, *140*, 6853-6861.
- (2) Slabber, C. A.; Grimmer, C. D.; Robinson, R. S. *J. Nat. Prod.* **2016**, *79*, 2726-2730.
- (3) Renuga Parameswari, A.; Devipriya, B.; Jenniefer, S. J.; Thomas Muthiah, P.; Kumaradhas, P. *J. Chem. Crystallogr.* **2012**, *42*, 227-231.
- (4) Sanphui, P.; Goud, N. R.; Khandavilli, U. B. R.; Nangia, A. *Cryst. Growth Des.* **2011**, *11*, 4135-4145.
- (5) Sanphui, P.; Goud, N. R.; Khandavilli, U. B. R.; Bhanoth, S.; Nangia, A. *Chem. Commun.* **2011**, *47*, 5013-5015.
- (6) Hanwell, M. D.; Curtis, D. E.; Lonie, D. C.; Vandermeersch, T.; Zurek, E.; Hutchison, G. R. *J. Cheminform.* **2012**, *4*, 17.
- (7) Humphrey, W.; Dalke, A.; Schulten, K. *J. Mol. Graphics* **1996**, *14*, 33-38.



- (8) Puliti, R.; Mattia, C. A.; Paduano, L. *Carbohydr. Res.* **1998**, *310*, 1-8.
- (9) Aree, T.; Chaichit, N. *Carbohydr. Res.* **2002**, *337*, 2487-2494.
- (10) Valiev, M.; Bylaska, E. J.; Govind, N.; Kowalski, K.; Straatsma, T. P.; Van Dam, H. J. J.; Wang, D.; Nieplocha, J.; Apra, E.; Windus, T. L.; de Jong, W. A. *Comput. Phys. Commun.* **2010**, *181*, 1477-1489.
- (11) Shvartsburg, A. A.; Mashkevich, S. V.; Baker, E. S.; Smith, R. D. *J. Phys. Chem. A* **2007**, *111*, 2002-2010.
- (12) Mesleh, M. F.; Hunter, J. M.; Shvartsburg, A. A.; Schatz, G. C.; Jarrold, M. F. *J. Phys. Chem.* **1996**, *100*, 16082-16086.
- (13) Siu, C.-K.; Guo, Y.; Saminathan, I. S.; Hopkinson, A. C.; Siu, K. W. M. *J. Phys. Chem. B* **2010**, *114*, 1204-1212.
- (14) Xuan-Yu, M.; Hong-Xing, Z.; Mihaly, M.; Meng, C. *Curr. Comput. Aided Drug Des.* **2011**, *7*, 146-157.
- (15) Mudedla, S. K.; Balamurugan, K.; Subramanian, V. *J. Phys. Chem. C* **2014**, *118*, 16165-16174.
- (16) Mudedla, S. K.; Balamurugan, K.; Kamaraj, M.; Subramanian, V. *Phys. Chem. Chem. Phys.* **2016**, *18*, 295-309.
- (17) Bonnet, P.; Jaime, C.; Morin-Allory, L. *J. Org. Chem.* **2001**, *66*, 689-692.

# Patterned Nanobrush Nature Mimics with Unprecedented Water-Harvesting Efficiency

Depanjan Sarkar, Anindita Mahapatra, Anirban Som, Ramesh Kumar, Ankit Nagar, Avijit Baidya, and Thalappil Pradeep\*

Water scarcity is one of the most alarming problems of the planet. An ambient ion based method is developed to make hydrophilic-hydrophobic patterned silver nanowires (NWs) as humidity harvesters of unprecedented efficiency. Such water harvesters are developed by two-step surface modification of the as-synthesized NWs (known from a report earlier) using electrospray. These patterned NWs of  $\approx 20 \mu\text{m}$  length and  $\approx 200 \text{ nm}$  width grown over a relatively large area ( $2 \times 2 \text{ cm}^2$ ) exhibit atmospheric water capture (AWC) efficiency of  $56.6 \text{ L m}^{-2} \text{ d}^{-1}$ , the highest reported so far. The whole fabrication process of the surface is performed under ambient conditions with a home-built nanoelectrospray ion source, without the help of any sophisticated instrumentation. The synthesized material combines and mimics two exciting examples of AWC in nature, which are cactae and Namib Desert beetles, which utilize AWC for their living. It is believed that the combination of the special features of the above two natural species helps to achieve the highest water capture efficiency reported till date. A working prototype using this surface for AWC is also fabricated.

Availability of clean fresh water is one of the measures of development of a society. However, water resources have become severely depleted or highly polluted due to the demands of rapid economic growth as well as poor management in most parts of the planet. This has resulted in water scarcity to be one of the gravest social risks of the modern world while it was considered to be an environmental risk a few years ago.<sup>[1]</sup> Around 1.2 billion people, or almost one-fifth of the world's population already live in areas with water shortage, and another 500 million more people are being pushed to this situation. By the year 2025, 1.8 billion people will be living in regions with sheer water paucity, and two-thirds of the world's population could be living in water-stressed circumstances. Atmospheric water capture is being considered as a possible solution for providing clean water to people living in those areas, for sometime now.

Dr. D. Sarkar, A. Mahapatra, Dr. A. Som, R. Kumar, A. Nagar, A. Baidya, Prof. T. Pradeep  
 DST Unit of Nanoscience (DST UNS) and Thematic Unit of Excellence (TUE)  
 Department of Chemistry  
 Indian Institute of Technology Madras  
 Chennai 60036, India  
 E-mail: pradeep@iitm.ac.in

The ORCID identification number(s) for the author(s) of this article can be found under <https://doi.org/10.1002/admi.201800667>.

DOI: 10.1002/admi.201800667

This is due to the fact that at any given moment, the earth's atmosphere contains an astounding 37.5 million billion gallons of water as vapor,<sup>[2]</sup> and an efficient device to capture a fraction of this water vapor, in a cost-effective way would help solve the water crisis.

Over the period of human existence, it has become apparent that biomimicking is the most efficient way to tackle such problems. When we look into nature, there are organisms, which in the course of evolution have acquired physical traits that enabled them to capture atmospheric water, even in the most arid corners of our planet. One such example is the *Stenocara* beetle of Namib Desert which capture water on its hardened forewings.<sup>[3]</sup> Electron microscopic images of these have revealed unique array of hydrophilic regions distributed on a superhydrophobic background,<sup>[4]</sup> creating a surface

energy gradient, which facilitates efficient condensation and transportation of atmospheric water. Another such example is spider silk, which shows unique periodic spindle-knot structure when wetted and efficiently collects water from atmosphere through the combination of surface energy gradient and Laplace pressure difference. Other inspirations from nature are some cactaceae species which live in arid environments and are extremely drought-tolerant.<sup>[5]</sup> These species are shown to have structures with spines and trichomes which enable them to condense humidity efficiently from the atmosphere. Grasslands are also examples of natural atmospheric water harvesters. Hence, micro/nanostructuring of the water-collecting surface plays a critical role in determining the efficiency of water capture. With the advancement of nanotechnology, significant efforts have been directed toward fabricating surfaces with similar morphological features and chemical patterning to enable efficient water capture.<sup>[6,7]</sup> However, these natural and nature-mimicked surfaces collect atmospheric water in the form of dew/fog and require the temperature to drop below the dew point to cause condensation. For building a practical and round-the-clock operating atmospheric water generator, it is important to cool the condensing surfaces and the surrounding air efficiently, with minimum energy input. Heat transfer efficiency of the condensing surface material is as important as the water transfer efficiency for creating a viable radiative condenser. Although many biomimetic, patterned surfaces have been made for fog collection, inspired by active condensing

surfaces found in nature,<sup>[7,8]</sup> most of these make use of polymers or polymer-hybrids, which might not be best suited for radiative condensers due to their poor heat-transfer efficiencies.

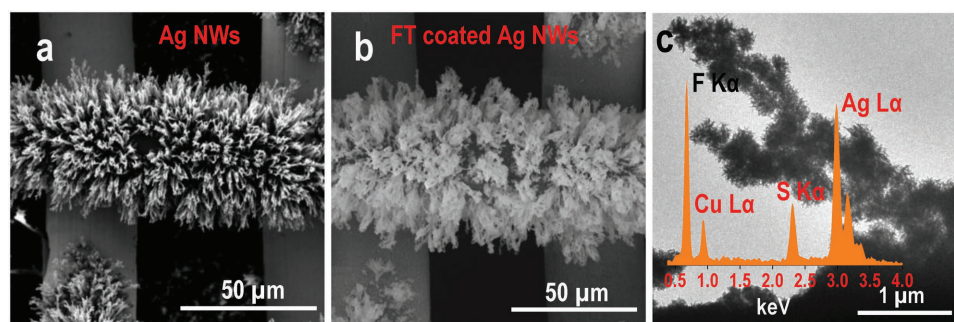
Metallic nanostructures are of great interest in recent research due to their excellent electrical and thermal conductivity.<sup>[9–11]</sup> The enhanced electric field around these structures makes them potential substrates for surface-enhanced Raman spectroscopy (SERS)<sup>[10,12]</sup> enabling sensing of various biological and nonbiological compounds present in water.<sup>[13]</sup> Apart from these, metallic nanostructures exhibit interesting mechanical properties,<sup>[14]</sup> while maintaining high degree of porosity,<sup>[15]</sup> ordered arrays,<sup>[16]</sup> and many more. Even though such nanostructures have potential applications in different areas, it has been difficult to synthesize them over large areas for commercial applications. Several methods have been developed to create patterned nanostructures which include chemical<sup>[17]</sup> and physical<sup>[18]</sup> vapor deposition, plasma chemical method,<sup>[19]</sup> spray pyrolysis,<sup>[20]</sup> etc. They can also be synthesized using photolithography<sup>[21]</sup> or electron beam lithography<sup>[9,22]</sup> as top-down approaches. Template mediation<sup>[23]</sup> and self-assembly are also used for making desired nanostructures. However, all these methods need special conditions like vacuum, high temperature, templates, etc. Ambient, solution state techniques to create well-defined metallic nanostructures over large areas are still limited. In an earlier report from our group, long (80  $\mu\text{m}$ ) nanowire (NW) arrays were made through electrospray ionization-induced creation and deposition of Ag nanoparticles (NPs), under ambient conditions.<sup>[24]</sup> These wires could be grown over several  $\text{cm}^2$  areas to make a metallic grassland like morphology. In this report, we have shown growth of these structures over 4  $\text{cm}^2$  area; however, they can also be grown over several tens of  $\text{cm}^2$  area using a programmable moving stage.

Here, we report the creation of a hydrophilic-hydrophobic patterned humidity-collecting surface as an efficient radiative atmospheric water capture device, by chemical modification of the metallic grasslands through electrospray deposition (ESD). While the use of NW arrays maximize the available surface area for water condensation, chemical modification of the NW surface helps with the quick transfer of the condensed water and regeneration of active sites for further condensation to happen. The surface modification strategy also improved the mechanical strength and stability of the NWs in water. In the design of the surface, we have successfully fabricated surfaces which mimic the hairy structures of cactae which in turn

have hydrophilic-hydrophobic patterns resembling the wings of *Stenocara* beetles along with superior heat transfer capabilities of metallic nanostructures. A combination of all these effects led to high water capture efficiency ( $56.6 \text{ L d}^{-1} \text{ m}^{-2}$ ) at a prototype-scale. Although we have used Ag NWs reported previously<sup>[24]</sup> as the initial building block of our patterned NWs, the present work focuses on a method of creating hydrophilic-hydrophobic patterned NWs using two simple steps, which mimic the above mentioned examples from nature and combine their special features to achieve highest water capture efficiency reported till date.

Hydrophilic-hydrophobic patterned Ag NWs were fabricated using ESD at room temperature in air. A schematic representation of the ESD process along with the dimensional descriptions is shown in Figure S1 (Supporting Information). As the growth of unpatterned NWs was described previously,<sup>[24]</sup> we present only the essential aspects here. A detailed description of the synthesis and characterization (electron microscopy, elemental analysis) of the Ag NWs on an empty transmission electron microscopy (TEM) grid, which form the core of the patterned NWs, is given in the Supporting Information (Figures S2–S8, Supporting Information). For all our AWC experiments, we have selected stainless steel (SS) wire mesh as the substrate to create a cost-effective substrate for the application. Figure S9a,b (Supporting Information) shows scanning electron microscopy (SEM) images of the Ag NWs grown on an empty TEM grid and SS wire mesh, respectively, proving identical morphology of the NWs on both the surfaces. Hence, for all our water capture experiments, we used the hydrophilic-hydrophobic patterned Ag NWs grown on SS wire meshes (50  $\mu\text{m}$ ). Use of a larger mesh size would reduce the active area for water condensation because of the reduction of number of wires (on which the Ag NWs are grown) in a specified area. On the other hand, use of a lower mesh size would increase the number of wires (on which the Ag NWs are grown) but it would also reduce the active surface area by affecting the size of the Ag NWs. The Ag NWs grown on a reduced mesh size SS wire mesh were smaller in size because of the coulombic repulsion between the growing NWs. We have also compared the growth of these NWs on top of meshes of different shapes.

Figure 1a shows a SEM image of the as-synthesized Ag NWs on a SS wire mesh using ESD. It shows an arrangement of 1D NWs, which upon extension will resemble a grassland-like structure. This can be created over a larger area of the order of



**Figure 1.** Electron microscopic characterization of the hydrophilic-hydrophobic patterned Ag NWs. a) SEM image of the as-synthesized Ag NWs on a 50  $\mu\text{m}$  SS wire mesh, b) SEM image of similar NWs after fluorothiol coating. Difference in contrast is due to the organic content. c) TEM image of the FT-coated Ag NWs, showing the intact morphology of the material, EDS spectrum (inset) showing presence of F, S, and Ag. Cu is due to the grid.

4 cm<sup>2</sup>. Figure S10 (Supporting Information) shows a large-area SEM image (300 μm<sup>2</sup>) of the Ag NWs on a TEM grid. These metallic NWs were the core of the patterned NWs with specific hydrophilic regions on a hydrophobic background. Fabrication of the patterned NWs was designed by successive ESD processes, as explained below.

At first, as-synthesized Ag NWs were subjected to an electrospray coating of a fluorothiol (FT), namely, 3,3,4,4,5,5,6,6,7,7,8,8,9,9,10,10,10-heptadecafluoro-1-decanethiol. A solution in dichloromethane (DCM) and acetonitrile (AcN) mixture was used for ESD of FT. This made the Ag NWs superhydrophobic in nature by the formation of a chemical bond between Ag and the thiol group, of the FT. Metal-sulfur bond is strong and is the basis of one class of self-assembled monolayers.<sup>[25]</sup> Figure 1b shows a SEM image of FT-coated Ag NWs. The change in contrast (with the image in Figure 1a) is due to the coating of a nonconducting layer of FT on the metal. To prove the superhydrophobic nature of the surface, the contact angle of a water droplet on it was measured. Surface energy of the FT-coated surface was so low that a water droplet did not stand static on the surface. Figure S11 (Supporting Information) shows images of a water droplet rolling on the FT-coated Ag NWs. No pinning of the droplet was observed, proving the superhydrophobicity of the surface. Figure S12a–c (Supporting Information) shows optical images of a water droplet bouncing off from the FT-coated Ag brush substrate while another water droplet is stranded on the bare stainless steel wire mesh. This proves that the FT coating on the Ag brushes made them superhydrophobic in nature. Figure S12d (Supporting Information) shows contact angle measurement of a water droplet on stainless steel wire mesh before (normal wire mesh) and after modification (FT-coated Ag NWs). Contact angle of the water droplet was measured to be ≥125° in the case of normal mesh indicating that the normal stainless steel surface is hydrophobic (90° < θ<sub>c</sub> < 150°). Measurement of resting contact angle was not possible for the superhydrophobic surface as it was too slippery for the droplet to sit on it. Hence, the contact angle was measured when the water droplet was touching the surface. A measurement of advancing and receding contact angles (173° and 166°, respectively) was also performed (Figure S13, Supporting Information). The contact angle hysteresis (173°–166° = 7°), is within the desired 10° for good superhydrophobicity. These measurements prove the superhydrophobic nature of the Ag NWs after FT coating. Roughness due to the presence of NWs also plays a significant role in acquiring superhydrophobicity. Control experiments were performed with normal stainless steel wire mesh and using the same sprayed with FT. It was seen that water droplets did not bounce off from the normal stainless steel mesh but wetted it instead, shown in Figure S14a (Supporting Information), clearly indicating that it was not superhydrophobic. Then FT was sprayed on the stainless steel mesh and the same experiment was repeated, images of which are shown in Figure S14b (Supporting Information). Here also the droplets did not bounce off and got stuck to the surface. However, when sprayed over by FT, the stainless steel mesh surface becomes hydrophobic to some extent. Hence, the presence of Ag NWs, providing surface roughness in nm scale, was essential to make it superhydrophobic. ESD is a gentle process; hence, it does not harm the morphology of the as-synthesized

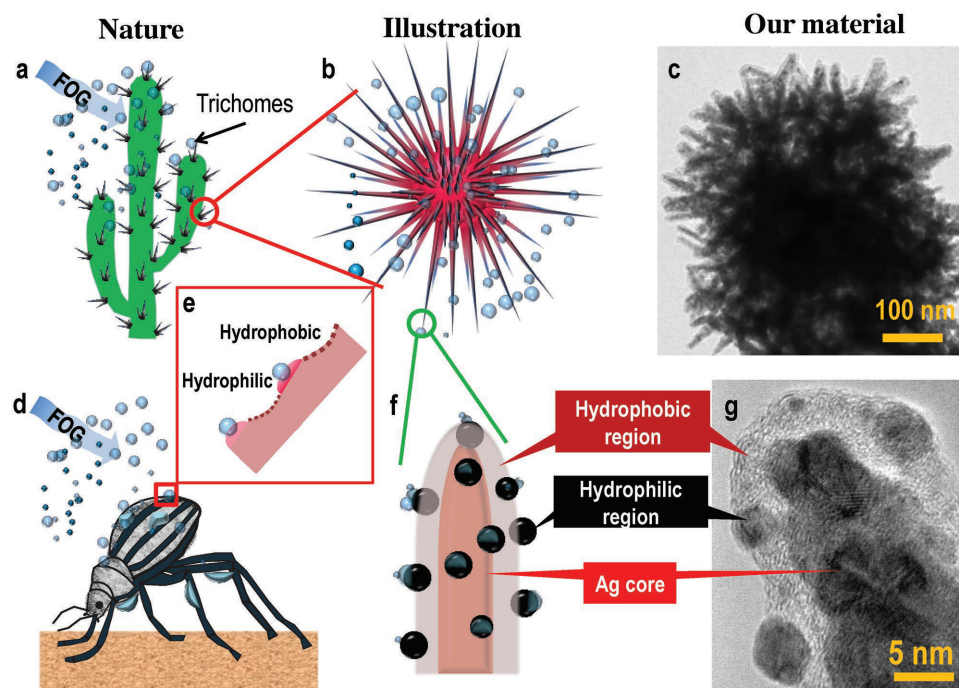
nanobrushes. This was the prime reason for us to choose ESD of FT over Ag NWs. Other procedures of FT coating, such as spray coating with a mechanical sprayer were not useful. Although the spray-coated surface became superhydrophobic, it destroyed the morphology of the NWs (Figure S15, Supporting Information). To optimize the ESD time for FT coating, a time-dependent ESD experiment was performed (spray time of 2, 4, 6, 8, and 10 min) on five different spots containing identical Ag NWs. It was observed that each spot became superhydrophobic proving that ESD of FT for 2 min was enough to make the surface superhydrophobic. However, these FT-coated NWs lost their morphology when subjected to water wash. In view of that we have enhanced the ESD time of FT to 20 min at a rate of 20 nA deposition current. In this case, the FT-coated NWs retained their morphology after water wash. This indicates that ESD of FT also has a role in imparting stability to the Ag nanobrushes by Ag–S bond formation (there is another aspect how ESD of FT provides stability to the Ag NWs which will be discussed at the end of this paragraph). Hence, for all other experiments, the above mentioned time and rate of ESD was taken as optimum. Figure 1c shows a TEM image of the FT-coated Ag NWs. Inset in Figure 1c shows an energy-dispersive spectrum (EDS) taken from these NWs showing the presence of all the expected elements (Ag, S, and F).

From our data we know that our Ag NWs are made by an organization of NPs. During the ESD of FT on Ag NWs, the NPs constituting the NWs coalesce with each other, making a solid metallic core inside. Figure S16 (Supporting Information) shows the TEM images of the Ag NWs before and after FT coating. From these images, we can easily compare and come to a conclusion that the NPs in the FT-coated Ag NWs are fused, providing a solid core on which the superhydrophobic coating of FT is formed. This solid metallic core gives strength to the NWs, making them more resistant toward mechanical strain.

In the second step, we have performed ESD of AgOAc (aqueous solution, 10 × 10<sup>−3</sup> M) over the superhydrophobic NWs to create Ag NP decorated NWs. These bare Ag NPs act as hydrophilic protrusions on the superhydrophobic NWs. In the following paragraph, we describe the structure of our material using electron microscopic images. The contact angle of a water droplet was measured after creating the hydrophilic zones. Figure S17 (Supporting Information) shows that the contact angle of a water droplet was 152°. Reduction of the contact angle, with respect to the superhydrophobic NWs, proves the presence of hydrophilic protrusions.

In Figure 2, we represent our material and compare it with the examples available in nature. Figure 2a shows a cartoon of a cactus with water droplets on the trichomes. Figure 2b shows a schematic of the cactus showing that its sharp spines and trichomes are responsible for water capture. Figure 2c shows a TEM image of our material which resembles the hairy structure of a cactus although the scales shown are different. Figure 2d shows a cartoon of a *Stenocara* beetle and the hydrophobic-hydrophilic patterning of the wings (Figure 2e). Figures 2f,g show a schematic of the synthesized hydrophilic-hydrophobic patterned Ag NW and a TEM image of the same with three distinct regions: (i) the Ag-core, (ii) hydrophobic coating on the Ag-core, and (iii) tiny hydrophilic regions (Ag NPs, see below for its synthesis) on the hydrophobic background. Ag core gives





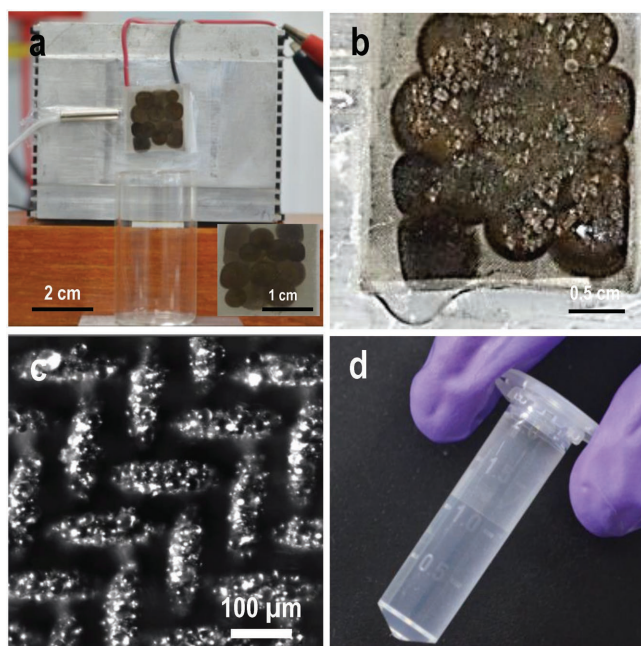
**Figure 2.** Graphical demonstration of the natural species with atmospheric water-harvesting capabilities, illustration of their special properties and comparison with our material. a) Graphical representation of a cactus, b) illustration of hairy structure of cactus, c) TEM image of a single Ag NW showing similar hairy structures resembling the cactus, d) graphical representation of a *Stenocara* beetle collecting water from atmosphere, e) schematic representation of hydrophobic-hydrophilic patterning of their wings, f) illustration of our superhydrophobic-hydrophilic patterned Ag NW showing a solid Ag core, a superhydrophobic coating on the core, and hydrophilic regions (Ag NPs) on the superhydrophobic background, and g) TEM image of a single Ag NW showing all three regions.

the strength to the brushes, while the FT coating creates the hydrophobic background. Subsequent ESD of Ag on this FT-coated surface resulted in Ag NPs decoration all over the NWs. These Ag NPs, embedded in the FT layer, act as hydrophilic zones, known to be responsible for the condensation of atmospheric water. A schematic illustration of atmospheric water capture by these hydrophilic-hydrophobic patterned NWs is shown in Figure 2f.

A 2 cm × 2 cm SS wire mesh covered by these patterned NWs was created and used for water capture experiments described in the following sections. Evaluation of humidity condensation was performed using this surface mounted on a Peltier cooler, which was then videographed (Video S1, Supporting Information) using a microscope. Two experiments, one control (with normal stainless steel mesh) and another with the prepared surface, were performed to test the efficiency of the nanostructured material for atmospheric water capture. In both the experiments, the surface being examined was carefully mounted on a Peltier cooler, using silver paste as glue, so that it remained in adequate contact with the cooling stage. The entire arrangement was placed atop the viewing stage of an inverted fluorescence microscope (Leica), in a controlled room with 40% relative humidity and 28 °C temperature (the dew point at this condition ≈ 13 °C). An arrangement was made for illumination of the surface being examined, for the purpose of microscopy. Time-lapse optical microscopy of the stainless steel mesh as well as the prepared surface upon exposure to cool humid air was performed to monitor droplet

nucleation and condensation. The temperature of the surface under examination was maintained at 12 °C, measured with a thermocouple. Figure S18a,b (Supporting Information) shows the optical images of a normal stainless steel wire mesh after 60 and 120 s of collection, respectively. Condensation of water droplets was seen on the wire mesh. Figure S18c,d (Supporting Information) shows the optical images of condensation of water on the stainless steel wire mesh containing superhydrophobic Ag NWs with hydrophilic protrusions. It is seen that the amount of water captured in this case is much larger in comparison to a normal wire mesh. In a time span of 2 min, a volume of  $2.6 \times 10^{-6}$  L water was captured (approximately calculated from the number of droplets considering them to be spheres,  $\approx 1.3 \times 10^{-8}$  L of water was captured over the normal SS wire mesh) on the brushes, even though the humidity was less and no water vapor was forcefully passed over the surface during the experiment. The video clearly shows nucleation of tiny water droplets on the patterned NWs followed by fusion of them to bigger droplets. Once the droplet is larger in size, it rolls off the surface because of its superhydrophobic nature.

Transport of the condensed water is a crucial criterion of any atmospheric water capture material. Hence, we calculated the water collection rate of the surface on a 2 × 2 cm<sup>2</sup> area considering all the parameters like, condensation rate, transport of the collected water, etc. Figure 3a shows an optical photograph of the total setup where the hydrophilic-hydrophobic patterned NWs containing SS wire mesh was firmly mounted (the black



**Figure 3.** Optical and microscopic photographs of the condensed water droplets on a  $2 \times 2 \text{ cm}^2$  area. a) Optical photograph of the water collection setup. Inset shows a photograph of the hydrophilic-hydrophobic patterned surface over a  $2 \times 2 \text{ cm}^2$  area. Each ESD results in a 5 mm dia dark colored disk indicating the growth of NWs. This process was repeated multiple times to cover the  $2 \times 2 \text{ cm}^2$  area. b) Zoomed optical photograph of the surface after switching on the Peltier cooler showing condensed water droplets on it and dripping of water at the bottom of the surface. c) Optical photograph (at a  $100\times$  magnification) of the Ag NWs with condensed water droplets. d) Optical photograph of the collected water in a 2 mL vial.

square surface) on a Peltier cooler, using a carbon tape. Carbon tape was used in this case, instead of silver paste, for better transport of the collected water. Inset of Figure 3a shows a photograph of the surface. A 12 V DC fan was used for cooling the hot side of the Peltier cooler. Temperature of the surface was measured and kept constant ( $7.5^\circ\text{C}$ ) during the experiment. The above experiment was performed inside an air-conditioned room where the relative humidity was 48% and the ambient temperature was  $26^\circ\text{C}$ . There was no forced airflow. Figure 3b shows the formation of water droplets on the hydrophilic-hydrophobic patterned nanobrushes, just after switching on the Peltier cooler. Figure 3c shows an optical microscopic image of the surface at  $100\times$  magnification, clearly showing the accumulated droplets on it. In the above experiment, 3.75 mL of water was collected in 13 h. If we convert the water collection to  $\text{L d}^{-1} \text{ m}^{-2}$  area, it comes to  $7.9 \text{ L d}^{-1} \text{ m}^{-2}$ . Figure 3d shows an optical photograph of the collected water in a 2 mL vial. Control experiments were performed to compare the water capture efficiency of the hydrophilic-hydrophobic patterned NWs with as-synthesized Ag NWs and hydrophilic Ag NWs. Although the parent surfaces without chemical functionalization were unstable during water capture experiments, we made the structures stable by exposing them to 4-mercaptobenzoic acid. In addition to enhanced stability during water capture, this functionalization made the surface hydrophilic. Such surfaces showed a

water capture efficiency of  $4.3 \text{ L d}^{-1}$  under the same conditions as before.

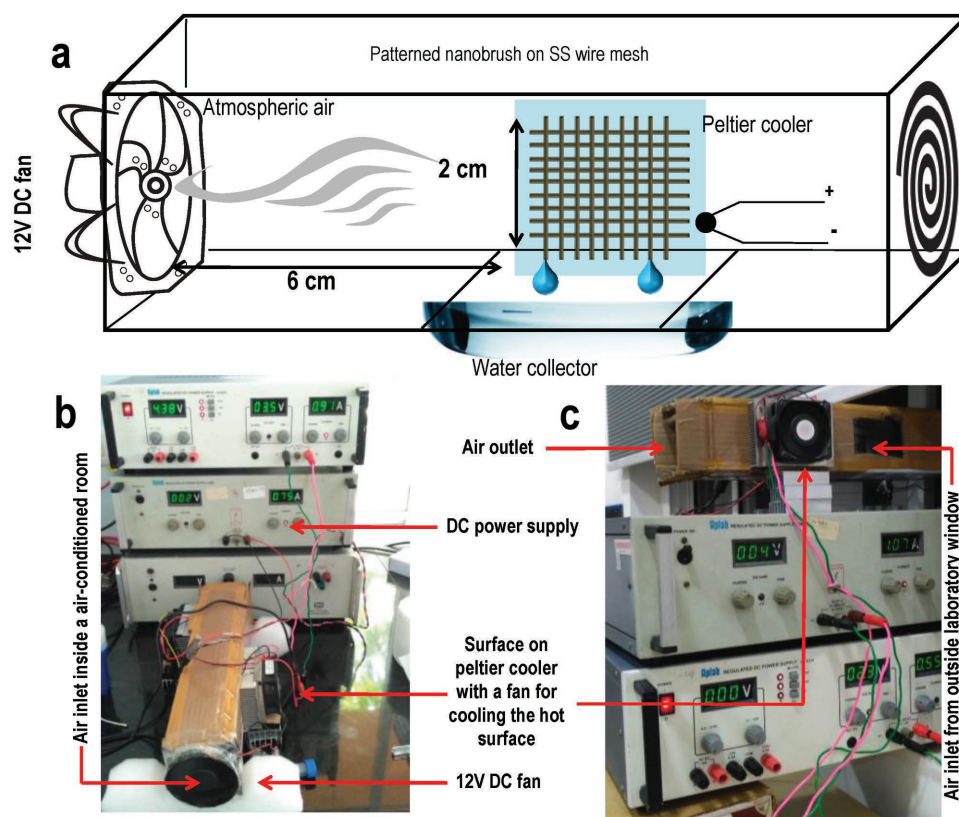
For the next set of experiments, we designed a prototype to evaluate the water capture efficiency of the surface in presence of air flow. **Figure 4a** shows a schematic of the prototype. In these experiments, a 12V DC (air flow speed of  $2.55 \text{ m s}^{-1}$  volume 103–105 cfm) fan was used to blow atmospheric air toward the cold hydrophilic-hydrophobic patterned surface. Two sets of experiments were performed with this prototype: (i) inside an air-conditioned room (at lower humidity) (Figure 4b shows an optical photograph of the setup), and (ii) outside the lab, under ambient conditions (Figure 4c shows a photograph). Conditions and data collected from these experiments are described here. In the first set of experiments, surface temperature and average relative humidity were  $8^\circ\text{C}$  and 58%, respectively. The water collection efficiency was  $26.8 \text{ L d}^{-1} \text{ m}^{-2}$ . In the second set of experiments, the temperature of the surface was kept the same and average relative humidity was  $\approx 87\%$ . In this case, the water collection efficiency was  $56.5 \text{ L d}^{-1} \text{ m}^{-2}$ . This is the highest water collection reported till date by any surface. The high efficiency of water collection can be attributed to the combination of cactus effect as well as hydrophilic-hydrophobic patterning. Water droplets start nucleating on the hydrophilic regions and as they grow larger in size, they start to roll off from the surface, generating fresh surface for collection.

For long-term use of the substrate, stability of the brushes is an important aspect. Reusability and the morphology of the surface were checked after the water capture experiment. Figures S19a,b (Supporting Information) show SEM images of the hydrophilic-hydrophobic patterned Ag nanobrushes after five cycles of water capture. The images show that the morphology of the brushes is almost intact after the experiment. Figures S19c,d (Supporting Information), respectively, show contact angle measurements of a water droplet on the substrate before and after the water capture experiment. The contact angle was found to be the same in both the cases, proving that the nature of the surface is the same after dew collection.

An ambient solution-state method of creating hydrophilic-hydrophobic patterned 1D Ag NWs, using electrospray deposition in three simple steps, is presented. The whole synthesis including the Ag NWs (the core of the patterned NWs) was performed at room temperature without the help of any sophisticated instrumentation. This method of synthesis enabled us to create a material that could mimic two efficient natural atmospheric water harvesters. Combination of hydrophilic patterns on a superhydrophobic background along with hairy structures of the Ag NWs led to highest water capture efficiency, reported till date. We also built a prototype and tested its water capture efficiency under various conditions. At  $\approx 87\%$  relative humidity, our material showed a water capture efficiency of  $56.5 \text{ L d}^{-1} \text{ m}^{-2}$ .

## Experimental Section

For all experiments, nanospray emitters were made using a micropipette puller (P-97) purchased from Sutter Instrument, USA. To confirm the



**Figure 4.** Prototype of the atmospheric water capture experiment. a) Schematic and b,c) photographs of water capture experiments inside and outside the laboratory. The photograph in (c) shows that the air inlet of the prototype is kept outside the laboratory window.

presence of solvated  $\text{Ag}^+$  ions, mass spectra were collected using an ion trap LTQ XL (Thermo Scientific, San Jose, CA) mass spectrometer. Indium tin oxide-coated glass slides (Toshniwal brothers (SR) Pvt. Ltd., India) was the usual deposition substrate. Locally available stainless steel wire mesh was used as a surface to grow the Ag NWs. All TEM measurements were performed using a JEOL 3010 (JEOL Japan) transmission electron microscope. Copper TEM grids were purchased from SPI Supplies. A FEI Quanta 100 instrument with tungsten filament source was used for SEM imaging. EDS analyses were performed with an attachment on the SEM instrument. Contact angle and contact angle hysteresis (CAH) of water droplet on the different coated substrates were measured using a Holmarc contact angle meter. Optical photographs of water droplets condensed over the hydrophilic-hydrophobic patterned Ag NWs and normal SS mesh was performed using a 100 $\times$  objective fitted to a Leica DFC365 FX microscope. Optical photographs of the surface, prototype, and water droplets bouncing off the surface were captured using a Nikon D5100 camera using an 18–55 mm lens. Videos were also captured using the same camera.

research fellowship. A.S. thanks Council of Scientific and Industrial Research for a research fellowship.

## Conflict of Interest

The authors declare no conflict of interest.

## Keywords

nature mimics, prototype, superhydrophobic-hydrophilic patterned NWs, water harvesting

Received: May 2, 2018

Revised: June 17, 2018

Published online:

## Supporting Information

Supporting Information is available from the Wiley Online Library or from the author.

## Acknowledgements

T.P. acknowledges financial support from the Department of Science and Technology, Government of India for his research program on nanomaterials. D.S. thanks the University Grants Commission for a

- [1] Global Risks Report by World Economic Forum, **2017**.
- [2] <https://whyfiles.org/2010/how-much-water-is-in-the-atmosphere/index.html> (accessed: 2010).
- [3] a) A. R. Parker, C. R. Lawrence, *Nature* **2001**, 414, 33; b) S. M. Kang, I. You, W. K. Cho, H. K. Shon, T. G. Lee, I. S. Choi, J. M. Karp, H. Lee, *Angew. Chem., Int. Ed.* **2010**, 49, 9401; c) X. Zeng, L. Qian, X. Yuan, C. Zhou, Z. Li, J. Cheng, S. Xu, S. Wang, P. Pi, X. Wen, *ACS Nano* **2017**, 11, 760; d) J. Hou, H. Zhang, Q. Yang, M. Li, Y. Song, L. Jiang, *Angew. Chem., Int. Ed.* **2014**, 53, 5791; e) B. White, A. Sarkar, A.-M. Kietzig, *Appl. Surf. Sci.* **2013**, 284, 826; f) S. G. Naidu, *J. Insect Physiol.* **2001**, 47, 1429.



- [4] J. Hou, H. Zhang, Q. Yang, M. Li, Y. Song, L. Jiang, *Angew. Chem., Int. Ed. Engl.* **2014**, 53, 5791.
- [5] J. Ju, H. Bai, Y. Zheng, T. Zhao, R. Fang, L. Jiang, *Nat. Commun.* **2012**, 3, 2253/1.
- [6] a) H. Bai, L. Wang, J. Ju, R. Sun, Y. Zheng, L. Jiang, *Adv. Mater.* **2014**, 26, 5025; b) G.-T. Kim, S.-J. Gim, S.-M. Cho, N. Koratkar, I.-K. Oh, *Adv. Mater.* **2014**, 26, 5166; c) M. Cao, J. Ju, K. Li, S. Dou, K. Liu, L. Jiang, *Adv. Funct. Mater.* **2014**, 24, 3235; d) H. Zhu, Z. Guo, W. Liu, *Chem. Commun.* **2016**, 52, 3863; e) K.-C. Park, P. Kim, A. Grinthal, N. He, D. Fox, J. C. Weaver, J. Aizenberg, *Nature* **2016**, 531, 78; f) S. K. Nune, D. B. Lao, D. J. Heldebrandt, J. Liu, M. J. Olszta, R. K. Kukkadapu, L. M. Gordon, M. I. Nandasiri, G. Whyatt, C. Clayton, D. W. Gotthold, M. H. Engelhard, H. T. Schaefer, *Nat. Nanotechnol.* **2016**, 11, 791.
- [7] S. C. Thickett, C. Neto, A. T. Harris, *Adv. Mater.* **2011**, 23, 3718.
- [8] D. T. Edmonds, F. Vollrath, *Proc. R. Soc. London, Ser. B* **1992**, 248, 145.
- [9] S. A. Maier, P. G. Kik, H. A. Atwater, S. Meltzer, E. Harel, B. E. Koel, A. A. G. Requicha, *Nat. Mater.* **2003**, 2, 229.
- [10] M. Moskovits, *J. Raman Spectrosc.* **2005**, 36, 485.
- [11] H. Wang, D. W. Brandl, P. Nordlander, N. J. Halas, *Acc. Chem. Res.* **2007**, 40, 53.
- [12] a) K. A. Willets, R. P. Van Duyne, *Annu. Rev. Phys. Chem.* **2007**, 58, 267; b) P. L. Stiles, J. A. Dieringer, N. C. Shah, R. P. Van Duyne, *Annu. Rev. Anal. Chem.* **2008**, 1, 601.
- [13] a) L. Zhang, F. X. Gu, J. M. Chan, A. Z. Wang, R. S. Langer, O. C. Farokhzad, *Clin. Pharmacol. Ther.* **2008**, 83, 761; b) J. N. Anker, W. P. Hall, O. Lyandres, N. C. Shah, J. Zhao, R. P. Van Duyne, *Nat. Mater.* **2008**, 7, 442; c) A. Kolmakov, M. Moskovits, *Annu. Rev. Mater. Res.* **2004**, 34, 151.
- [14] a) Z. W. Pan, Z. R. Dai, Z. L. Wang, *Science* **2001**, 291, 1947; b) Z. L. Wang, J. Song, *Science* **2006**, 312, 242.
- [15] a) K. Hristovski, P. Westerhoff, J. Crittenden, *J. Hazard. Mater.* **2008**, 156, 604; b) Y. Han, X. Wu, Y. Ma, L. Gong, F. Qu, H. Fan, *CrystEngComm* **2011**, 13, 3506; c) X. Wang, W. Cai, Y. Lin, G. Wang, C. Liang, *J. Mater. Chem.* **2010**, 20, 8582.
- [16] X. Wang, C. J. Summers, Z. L. Wang, *Nano Lett.* **2004**, 4, 423.
- [17] a) A. Y. Khodakov, W. Chu, P. Fongarland, *Chem. Rev.* **2007**, 107, 1692; b) K. L. Choy, *Prog. Mater. Sci.* **2003**, 48, 57; c) L. Hu, D. S. Hecht, G. Gruener, *Chem. Rev.* **2010**, 110, 5790; d) M. Kumar, Y. Ando, *J. Nanosci. Nanotechnol.* **2010**, 10, 3739.
- [18] a) Y. C. Kong, D. P. Yu, B. Zhang, W. Fang, S. Q. Feng, *Appl. Phys. Lett.* **2001**, 78, 407; b) M. M. Hawkeye, M. J. Brett, *J. Vac. Sci. Technol., A* **2007**, 25, 1317; c) U. Helmersson, M. Lattemann, J. Bohlmark, A. P. Ehiassarian, J. T. Gudmundsson, *Thin Solid Films* **2006**, 513, 1.
- [19] R. P. Garrod, L. G. Harris, W. C. E. Schofield, J. McGettrick, L. J. Ward, D. O. H. Teare, J. P. S. Badyal, *Langmuir* **2007**, 23, 689.
- [20] a) T. Xia, M. Kovochich, M. Liong, L. Madler, B. Gilbert, H. Shi, J. I. Yeh, J. I. Zink, A. E. Nel, *ACS Nano* **2008**, 2, 2121; b) G. L. Messing, S. C. Zhang, G. V. Jayanthi, *J. Am. Ceram. Soc.* **1993**, 76, 2707; c) S. A. Studenikin, N. Golego, M. Cocivera, *J. Appl. Phys.* **1998**, 84, 2287; d) I. Cesar, A. Kay, J. A. G. Martinez, M. Graetzel, *J. Am. Chem. Soc.* **2006**, 128, 4582.
- [21] a) Y. Xia, G. M. Whitesides, *Angew. Chem., Int. Ed.* **1998**, 37, 550; b) Y. Xia, J. A. Rogers, K. E. Paul, G. M. Whitesides, *Chem. Rev.* **1999**, 99, 1823; c) G. M. Whitesides, E. Ostuni, S. Takayama, X. Jiang, D. E. Ingber, *Annu. Rev. Biomed. Eng.* **2001**, 3, 335; d) E. W. H. Jager, E. Smela, O. Inganäs, *Science* **2000**, 290, 1540.
- [22] a) L. Jiao, L. Zhang, X. Wang, G. Diankov, H. Dai, *Nature* **2009**, 458, 877; b) S. A. Maier, M. L. Brongersma, P. G. Kik, S. Meltzer, A. A. G. Requicha, H. A. Atwater, *Adv. Mater.* **2001**, 13, 1501.
- [23] a) B. Freund, S. Suresh, *Thin Film Materials Stress, Defect Formation and Surface Evolution*, Cambridge University Press, Cambridge **2003**; b) S. I. Stupp, V. LeBonheur, K. Walker, L. S. Li, K. E. Huggins, M. Keser, A. Amstutz, *Science* **1997**, 276, 384; c) J. V. Barth, G. Costantini, K. Kern, *Nature* **2005**, 437, 671; d) Y. Zhang, L. Zhang, C. Zhou, *Acc. Chem. Res.* **2013**, 46, 2329; e) H.-W. Liang, S. Liu, J.-Y. Gong, S.-B. Wang, L. Wang, S.-H. Yu, *Adv. Mater.* **2009**, 21, 1850.
- [24] D. Sarkar, M. K. Mahitha, A. Som, A. Li, M. Wlekinski, R. G. Cooks, T. Pradeep, *Adv. Mater.* **2016**, 28, 2223.
- [25] C. Vericat, M. E. Vela, G. Corthey, E. Pensa, E. Cortes, M. H. Fonticelli, F. Ibanez, G. E. Benitez, P. Carro, R. C. Salvarezza, *RSC Adv.* **2014**, 4, 27730.





## Supporting Information

for *Adv. Mater. Interfaces*, DOI: 10.1002/admi.201800667

**Patterned Nanobrush Nature Mimics with Unprecedented  
Water-Harvesting Efficiency**

*Depanjan Sarkar, Anindita Mahapatra, Anirban Som, Ramesh  
Kumar, Ankit Nagar, Avijit Baidya, and Thalappil Pradeep\**

## Supporting Information

**Patterned Nanobrush Nature Mimics with Unprecedented Water Harvesting Efficiency**

*Depanjan Sarkar, Anindita Mahapatra, Anirban Som, Ramesh Kumar, Ankit Nagar, Avijit Baidya and Thalappil Pradeep\**

**Synthesis and characterization of Ag NWs**

For electrospray deposition, a homemade nanoelectrospray (nESI) source was made by pulling a borosilicate glass capillary (0.86 mm inner diameter, 1.5 mm outer diameter, and 10 cm length) into two. The pulling was performed in a controlled fashion in order to achieve an inner diameter of approximately 15  $\mu\text{m}$  at the tip. These tips were used as nESI sources in all our deposition experiments. For the elrctrospray process, a nESI tip was filled with a 10 mM aqueous solution of silver acetate ( $\text{AgOAc}$ ) using a micro injector and a potential in the range of 2-2.5 kV was applied to it through a platinum wire (0.1 mm diameter, Sigma Aldrich) electrode. In all the experiments, the home-built nanoelectrospray (nESI) source was used to deliver charged droplets of aqueous  $\text{AgOAc}$  solution onto a conductive stainless steel wire mesh placed on top of an indium tin oxide (ITO) coated glass collector. In case of transmission electron microscopy (TEM) measurement, the droplets were collected on an empty (without carbon coating) TEM grid. The wire mesh or the empty TEM grid acts as a static mask between the ITO slide and the spray plume. The ITO slide was grounded through a picoammeter to measure the deposition current. Pt wire was used as an electrode due to its inert nature towards other reagents. A plume of charged droplets containing solvated silver ions like  $\text{Ag}(\text{H}_2\text{O})^+$  and  $\text{Ag}(\text{H}_2\text{O})_2^+$  was ejected from the nESI tip, as confirmed by mass spectrometry. Figure S1 shows a schematic representation of the experimental set up with dimensional details. Figure S2 show a mass spectrum collected from electrospray of  $\text{AgOAc}$  solution.

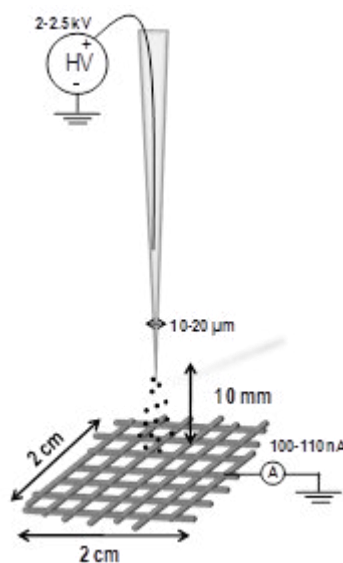


Figure S1. Schematic representation of the ESD set up. Representation of the dimensional details.

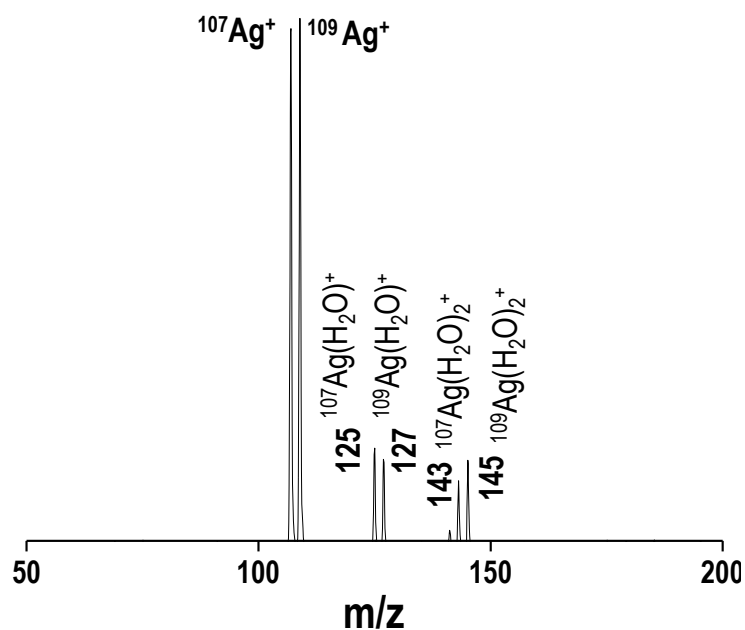


Figure S2. Mass spectrum collected from an aqueous solution of Ag(OAc).

In the course of electrospray deposition, a black circular spot (typical diameter 2-5 mm depending on the distance between the nESI tip and the collector) due to the incoming spray plume appeared on the mask (SS wire mesh/empty TEM grid) itself. These were taken for further characterization. Deposition time can be varied to control the sizes of the NWs. For our experiments we have used NWs made by 6h deposition at a rate of 100-110 nA deposition current.

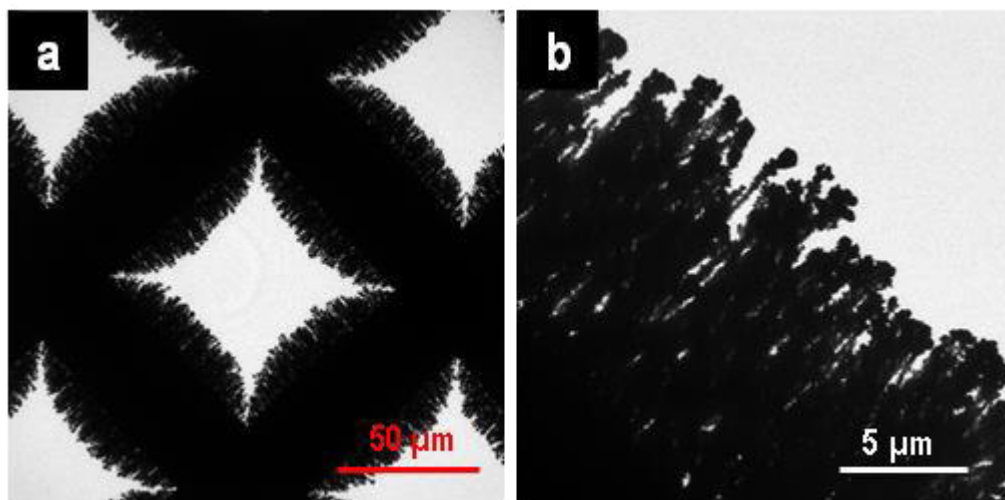


Figure S3. TEM images of as-synthesized Ag NWs. TEM images of it at different magnifications.

Electron microscopy imaging was performed to understand the black spot on the mask. TEM imaging of the grid revealed an unusual brush-like growth of nanowires, with a head on stacking of bare Ag NPs comprising each nanowire. Figure S3a and b show TEM images of such nanowires at different magnifications. The higher magnification image in Figure S3b clearly shows that the Ag nanobrushes have a linear morphology, some of them somewhat

bent. The growth in each Ag NW is shown to be one-dimensional and not dendritic although the electron beam induced adhesion of the wires is possible; they are clearly not branched. These brush-like growth was only seen on the mask. On the other hand, the ITO collector below the mask collected Ag NPs. Figure S4a and b show TEM images of the Ag NPs formed on the collector while deposition. In this case, a carbon coated TEM grid was used as the collector instead of an ITO slide.

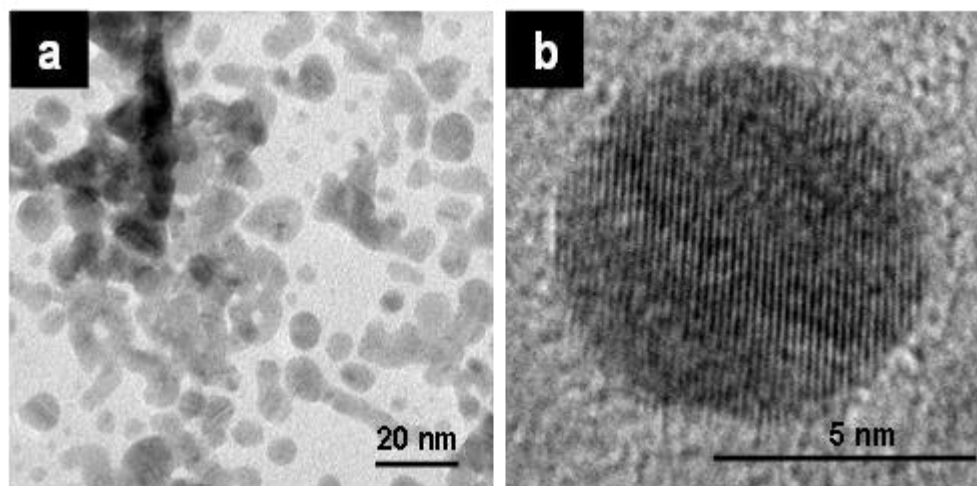


Figure S4. TEM images of Ag NPs. a) and b) TEM images of Ag NPs formed on the collector during electrospray deposition.

Detailed investigation revealed that the Ag NWs are typically assembled in small groups (nanobristles) and these in turn are arranged on the surface to create a nanobrush. A single nanobristle is actually a braid of several NWs which in turn possesses pearl-necklace type morphology. Figure S5a shows a TEM image of a nanobristle of the synthesized nanobrushes. From the image it is clearly seen that each bristle is a braid of several thinner nanowires. Figure S5b shows higher magnification TEM image taken from a single NW. Head on arrangement of the Ag NPs leading to pearl-necklace morphology is clearly seen.

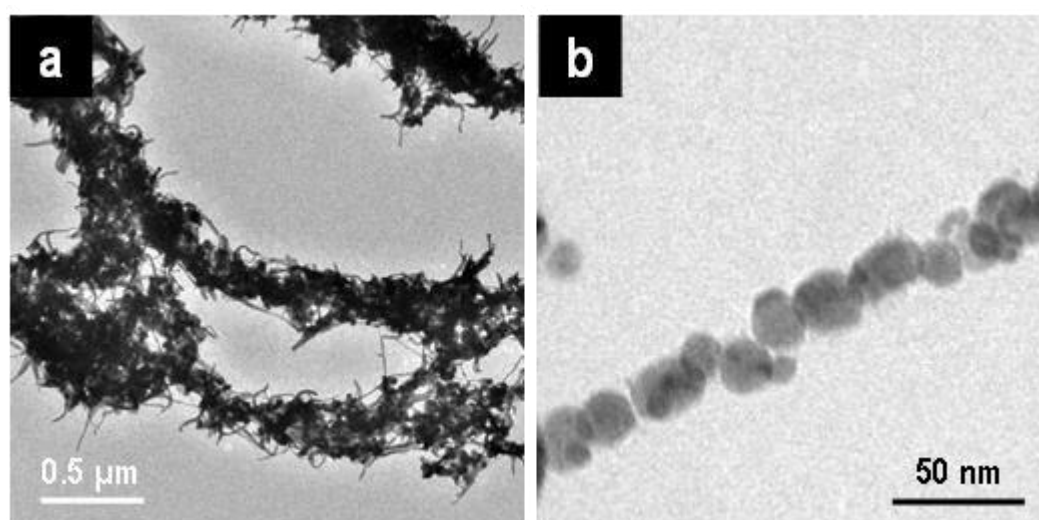


Figure S5. TEM images of a single NW. a) single bristle of the Ag nanobrush, b) single building block of a bristle showing pearl-necklace type morphology.

The above data prove that the deposition of solvated metal ions results in neutralization, aggregation and orientation to form 1D nanostructures.

Careful investigation of the TEM data tell us further interesting facts. A TEM image of a single square of the empty TEM grid (Figure S6a) shows uniform assembly of bristles protruding out from the edges. The bristles appear apparently continuous in low magnification (Figure S6a), but upon closer inspection, they have a rough surface because of the braiding of individual NWs (Figure S6b). Figure S7 shows a high resolution transmission electron microscopy (HRTEM) image from the tip of a NW showing crystalline NPs in the NWs. The measured Ag (111) lattice spacing and energy dispersive spectroscopy (EDS) (Figure S8) confirm the presence of crystalline AgNPs.

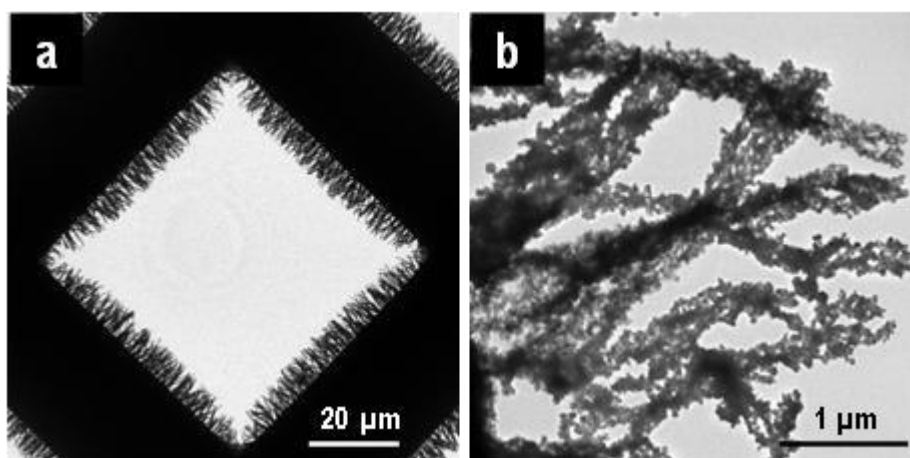


Figure S6. One dimensional nature of the Ag NWs. a) TEM image of a single square of an empty TEM grid, b) higher magnification image of the nanobristles showing the surface roughness.

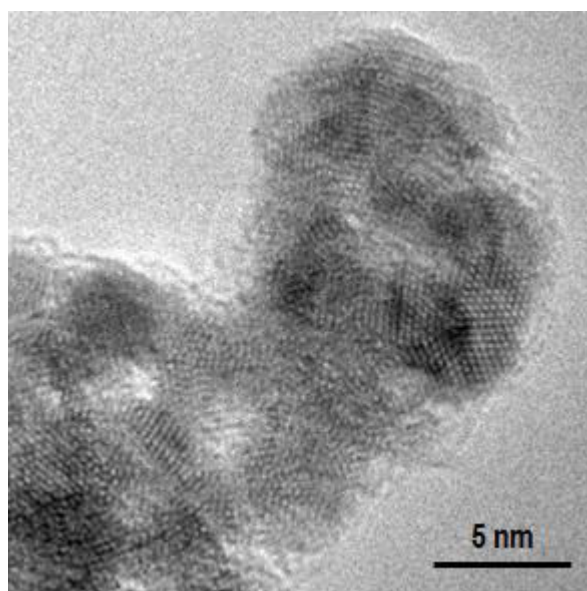


Figure S7. Crystallinity of the Ag NPs. High resolution transmission electron microscopy (HRTEM) image of a tip of a nanobristle showing the presence of crystalline Ag NPs.

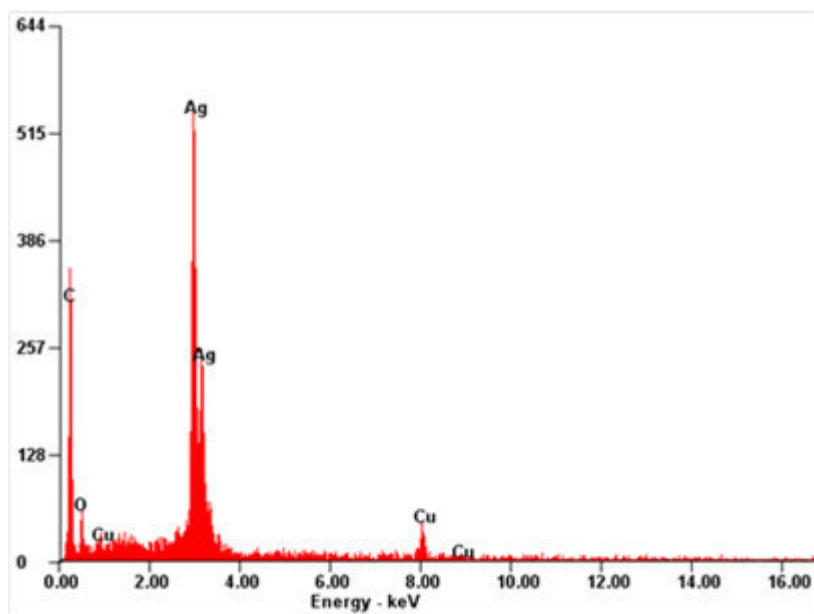


Figure S8. Elemental analysis. SEM EDS spectrum collected from the Ag nanobrushes.

TEM images may imply that the NW structures are formed only at the edges of the square apertures of the mesh. But that is not the case. For better understanding of the nanobrush growth, SEM analysis was performed on the circular spot ( $\sim 1.5$ - $2.5$  mm in diameter, depending upon the distance of the collector surface from the spray emitter) on the mask. Figure S9a and b show SEM images taken for Ag nanobrushes grown on an empty TEM grid and a SS wire mesh, respectively.

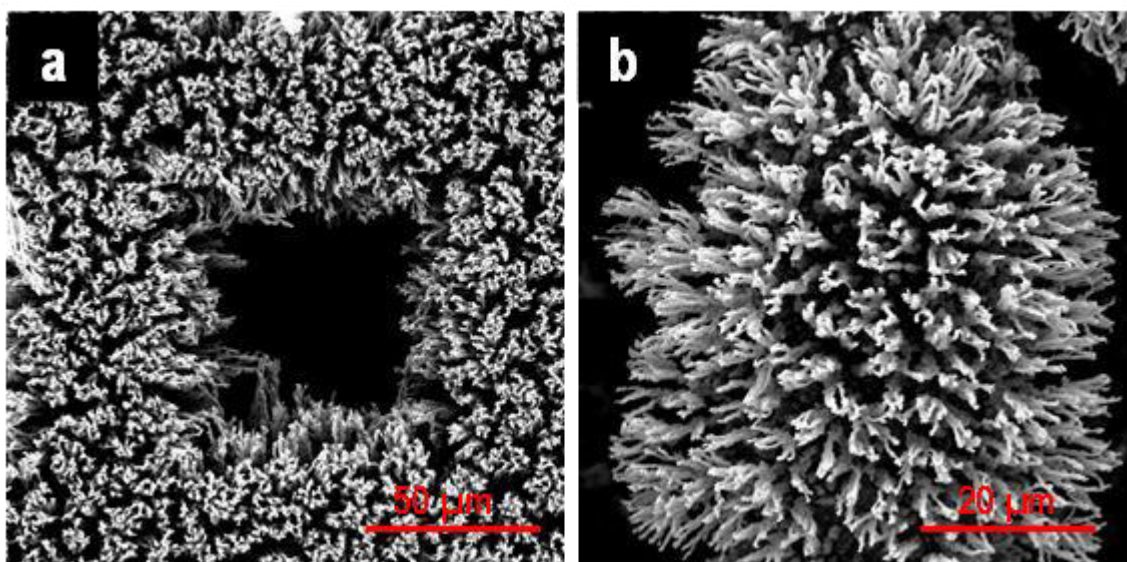


Figure S9. SEM images of the as-synthesized Ag NWs. SEM image of it grown on a) empty TEM grid, b) SS wire mesh.

SEM images show that the growth of the Ag nanobrushes are extended all over the grid/SS wire mesh providing a grassland like morphology. Conducting mesh is essential for the



growth. Control experiments were performed to prove that the size and shape of the mesh do not effect the growth. On the other hand, a conducting mesh as mask is the essential criteria for the NWs growth.

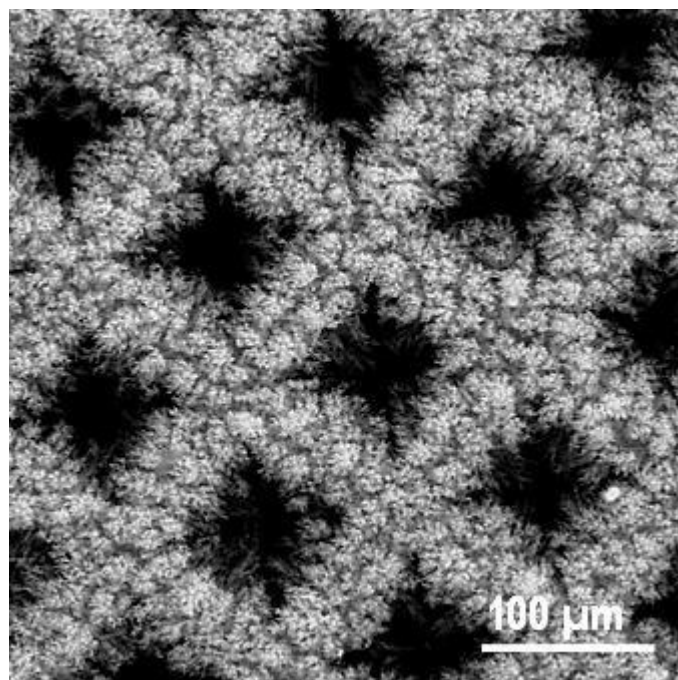


Figure S10. Large area image. SEM image of the AgNWs grown over a large area.

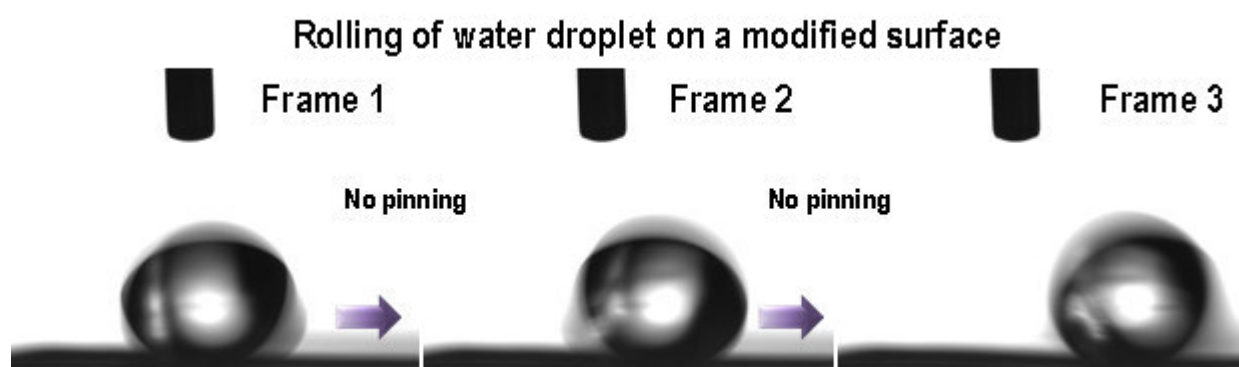


Figure S11. Droplet pinning experiment. Images of a water droplet rolling on the FT-coated Ag brushes. No pinning of the droplet was observed, proving the superhydrophobicity of the surface.

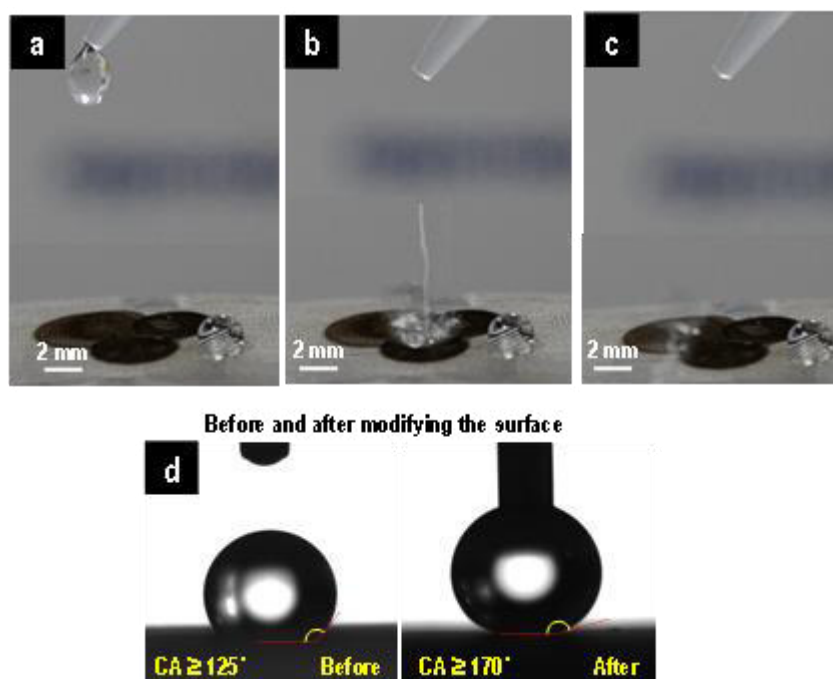


Figure S12. Proof of superhydrophobicity. a-c) Optical images of a water droplet bouncing off from the FT coated Ag brush substrate while another water droplet is stranded on the bare stainless steel wire mesh. d) Contact angle measurement on the superhydrophobic Ag nanobrushes.

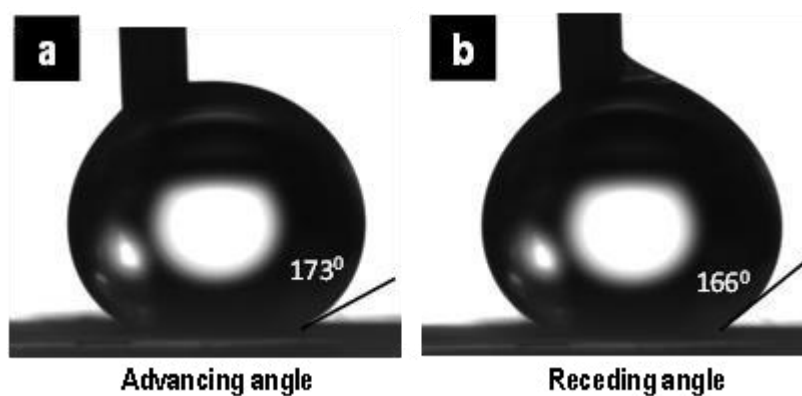


Figure S13. Advancing and receding angle. Measurement of a) advancement and b) receding contact angle of a water droplet on the superhydrophobic nanobrushes. The drop had to be held by touching it with a pipette tip.



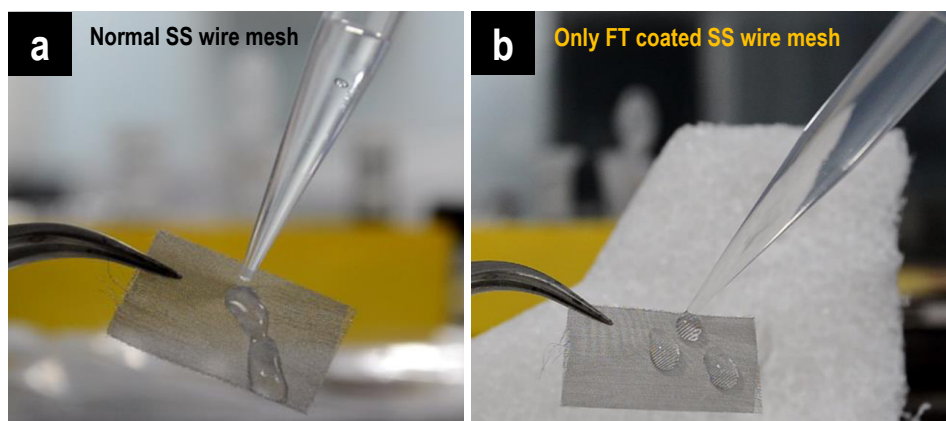


Figure S14. Control experiments. a) Optical image of water droplets on normal SS wire mesh, b) optical image of water droplet sticking on a FT-coated SS wire mesh. Here also the droplets did not bounce off and got stuck to the surface. However, when it was sprayed with FT, the stainless steel mesh surface became hydrophobic to some extent.

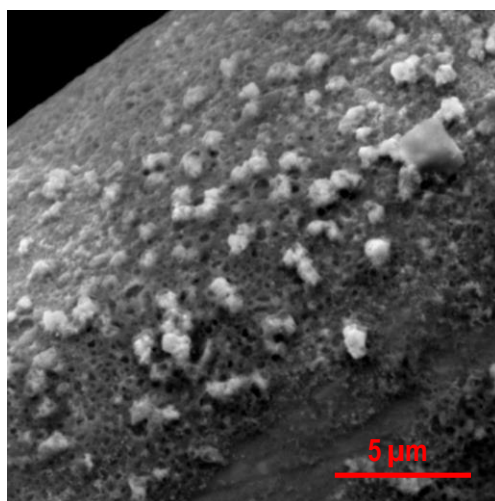


Figure S15. Control experiment. SEM image showing that the morphology of the Ag NWs was destroyed after spray coating of FT with a commercial sprayer.

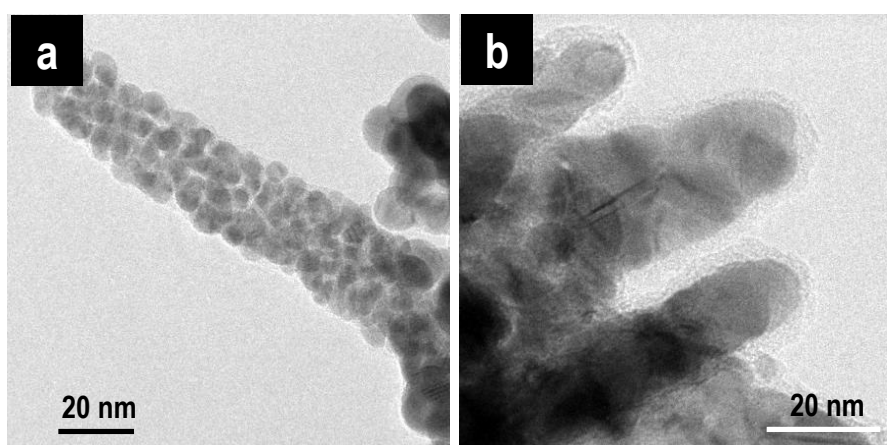


Figure S16. TEM images of the surface modified Ag NWs. TEM images of the Ag NWs a) before and b) after FT coating on the Ag NWs.

**Proof of superhydrophobicity:** To confirm the surface energy of the modified surface, the wettability was studied with static and dynamic contact angle measurements. The surface energy of the FT modified Ag nanobrushes is so low that water droplet did not stick on to it. The water droplets rolls off (no pinning) easily (Figure S11). To understand the wetting property in detail, contact angle hysteresis (CAH) was measured through dynamic CA experiment and shown in Figure S13. Static contact angle (CA) of water drop was measured before and after the experiment to check the change in wettability of the surface. For both the cases, CA was observed to be greater than  $170^\circ$  (Figure S19 c and d). This can relate with the stability and durability of the modified brushes.

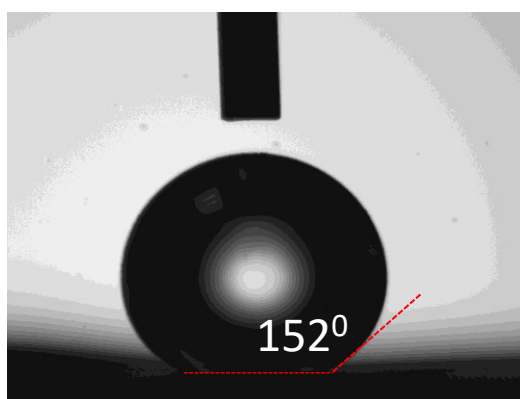


Figure S17. Contact angle measurement after the creation of hydrophilic zones over the super hydrophobic NWs.

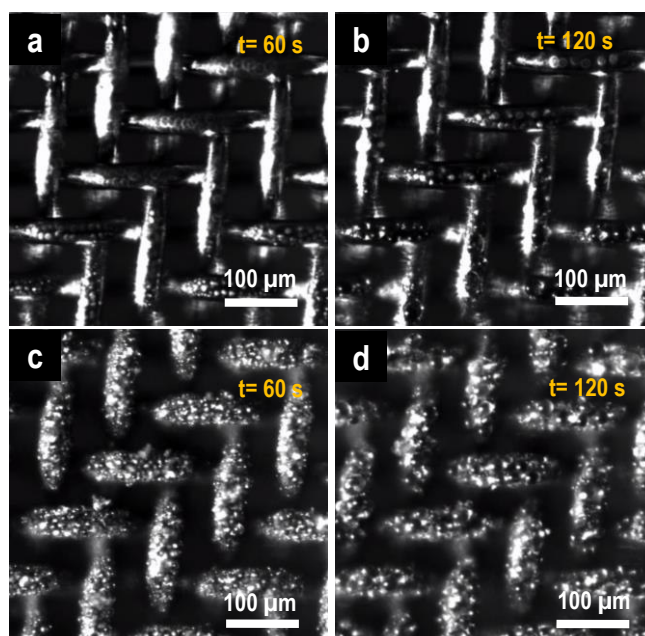


Figure S18. Optical microscopic images of water droplet condensed on the surface. a) and b) Optical images of a normal stainless steel wire mesh after 60 and 120 seconds of cooling, respectively. Condensation of water droplets was seen on the wire mesh. c) and d) Optical images of condensation of water on the stainless steel wire mesh containing superhydrophobic Ag nanobrush with hydrophilic protrusions. It is seen that the amount of water captured in this case is much larger in comparison to the normal wire mesh.

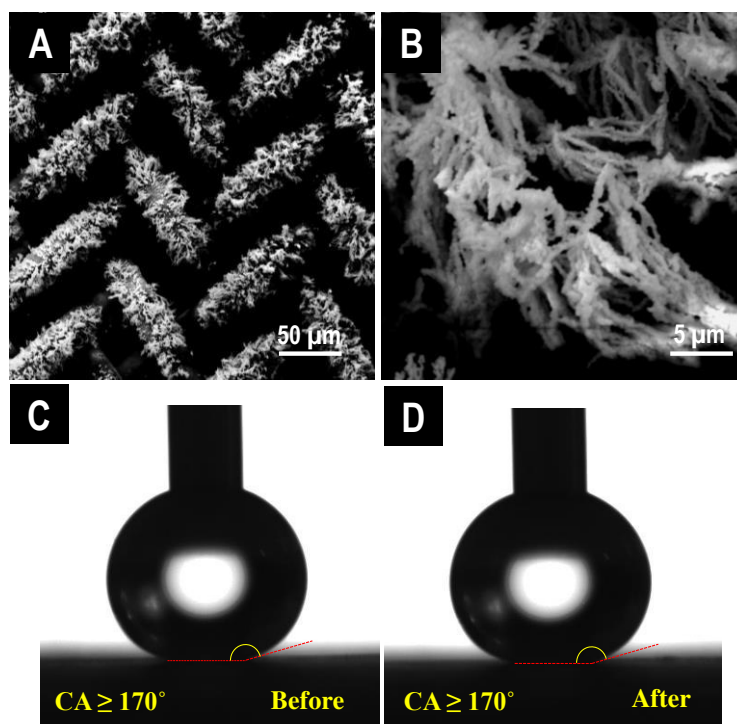


Figure S19. Test of stability of the surface. a) and b) SEM images of the superhydrophobic brushes after 5 cycles of water capture experiment, showing the morphology is intact, c) and d) contact angle of a water droplet on the same showing that the superhydrophobic nature of the surface is largely unchanged during the water capture experiments.

Video S1. Atmospheric water capture by the hydrophilic-hydrophobic patterned NWs under an optical microscope.

Video S2. Atmospheric water capture on a hydrophilic-hydrophobic patterned area ( $4 \text{ cm}^2$ ) using our prototype. The white spots seen in the video are due to the residue of the silver paste used for contact between the surface and the Peltier cooler. In subsequent experiments, we changed this to carbon take for better water transport.

# Species-Specific Uptake of Arsenic on Confined Metastable 2-Line Ferrihydrite: A Combined Raman-X-Ray Photoelectron Spectroscopy Investigation of the Adsorption Mechanism

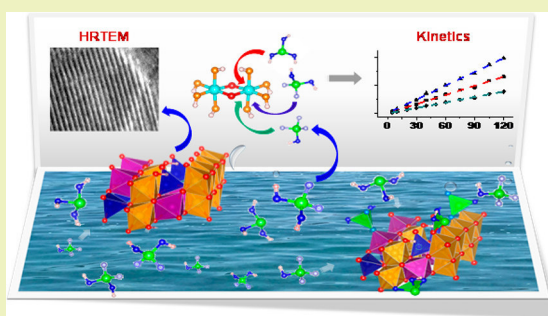
Chennu Sudhakar, Avula Anil Kumar,<sup>1</sup> Radha Gobinda Bhuin, Soujit Sen Gupta, Ganapati Natarajan, and Thalappil Pradeep\*<sup>2</sup>

DST Unit of Nanoscience (DST UNS) and Thematic Unit of Excellence (TUE), Department of Chemistry, Indian Institute of Technology Madras, Chennai 600036, India

## Supporting Information

**ABSTRACT:** The present study is targeted toward understanding the interaction between important and technologically relevant polymorphs of iron oxides/oxyhydroxides with arsenic species at neutral pH. The existence of various arsenic (As) species in solution was verified by Raman measurements. Their species-dependent adsorption on the affordable arsenic removal media, confined metastable 2-line ferrihydrite (CM2LF) was investigated. The results were compared with common adsorption media, hematite ( $\alpha\text{-Fe}_2\text{O}_3$ ) and magnetite ( $\text{Fe}_3\text{O}_4$ ). X-ray photoelectron spectroscopy was used to investigate the changes in the core levels of Fe 2p and As 3d resulting from the uptake of arsenic species. Binding of various As species with CM2LF was confirmed by FTIR studies. Raman adsorption data were found to fit a pseudo-second-order model. Results of this study show the synthesized nanocomposite of CM2LF to be very effective for the removal of As(III) and As(V) species in comparison to various materials at neutral pH. A model for the adsorption of As(III) and As(V) species in water on a ferrihydrite particle was developed. This accounted for the large uptake capacity.

**KEYWORDS:** Arsenic species, Uptake capacity, CM2LF, Hematite, Magnetite, Adsorption mechanism



## INTRODUCTION

Arsenic is one of the major contaminants in drinking water in many parts of the world. Various parts of India, Bangladesh, Cambodia, South Africa, Argentina, United States, and other countries have arsenic in the groundwater to an extent more than the permissible limit, namely  $10\text{ }\mu\text{g L}^{-1}$  (10 ppb) prescribed by the World Health Organization (WHO).<sup>1,2</sup> Arsenic and its associated problems are still a great threat to human health, although arsenic in water was first reported by Benjamin Martin way back in 1759.<sup>3</sup> Arsenic occurs in natural waters as either arsenite (As(III)) or arsenate (As(V)).<sup>4</sup> Both forms of arsenic have strong affinity for iron oxide/oxyhydroxide surfaces near neutral pH.<sup>5,6</sup> The speciation of arsenic is an important aspect for understanding its mobility, bioavailability, and toxicity in groundwater.<sup>7</sup> A comprehensive solution for arsenic contamination was not evident as efforts made previously have faced various challenges. Arsenic in the environment has been addressed in various ways in terms of technology, and all of them have certain limitations.<sup>8</sup>

In this context, there is a need to explore the use of nanomaterials for arsenic mitigation due to their large surface area and enhanced surface reactivity. In the past decade, various nanostructured composites have been used to remove arsenic from water, namely, graphene oxide– $\text{MnFe}_2\text{O}_4$  nano-hybrids,<sup>9</sup> Fe–Cu binary oxides,<sup>10</sup> nanocrystalline  $\text{TiO}_2$ ,<sup>3,11,12</sup>

superparamagnetic  $\text{Mg}_{0.27}\text{Fe}_{2.5}\text{O}_4$ ,<sup>13</sup> GO– $\text{ZrO}(\text{OH})_2$  nanocomposites,<sup>14</sup> GNP/Fe–Mg oxide,<sup>15</sup> etc. Recently, researchers have looked at several bioadsorbents like *Eichhornia crassipes* which are locally available. Powders of the roots of *Eichhornia crassipes*, possessing multiple functional groups ( $-\text{OH}$ ,  $-\text{NH}_2$ , and  $-\text{COOH}$ ) on the surface, were used for the potential removal of arsenic species from wastewater.<sup>16</sup>

However, to know the exact binding mechanism of different arsenic species on the surfaces, various spectroscopic studies are required such as Raman spectroscopy, Fourier-transform infrared spectroscopy (FTIR), and X-ray photoelectron spectroscopy (XPS). These studies too have limitations due to the difficulty in understanding adsorbed species in water and the mode of complexation onto the surfaces. To understand the complexation of arsenic onto oxides, some efforts have been made by Gustafsson et al.<sup>17</sup> using computational methods. Authors have used the Diffuse Layer Model (DLM)<sup>18</sup> and Three-Plane CD-MUSIC Model (TPCD)<sup>19</sup> to account for the data. It has been seen that at different pH conditions, both As(III) and As(V) exist as different species.<sup>20,21</sup> These species bind on different adsorbents

Received: March 17, 2018

Revised: June 4, 2018

Published: June 11, 2018



differently,<sup>22–25</sup> which also depend on the concentration of the species.<sup>23,26</sup>

Adsorption of As(III) and As(V) on amorphous aluminum and iron oxides using vibrational spectroscopy was investigated by Goldberg et al.<sup>20</sup> According to the report, Al–O–As stretching frequency appeared between 844 to 865  $\text{cm}^{-1}$  for pH 5–9, while Fe–O–As frequency was observed between 817 to 824  $\text{cm}^{-1}$  for pH 5–10.5. Arsenate forms inner sphere complexes on both amorphous Al and Fe oxides, while As(III) forms inner and outer sphere complexes on amorphous Fe oxide and only outer sphere complexes on amorphous Al oxide. Arsenic speciation in the aqueous phase was studied in detail using Raman spectroscopy by Müller et al.<sup>21</sup> They studied the binding mechanism of As(III) and As(V) on 2-line ferrihydrite, goethite, hematite, and ferrihydrite using Raman and diffuse reflectance infrared Fourier-transform (DRIFT) spectroscopy. In solution phase, As(III) and As(V) showed various Raman features. However, the As(III/V) adsorbed samples of ferrihydrite and ferrihydrite showed Raman feature of Fe–O–As as a broad band, centered around 840  $\text{cm}^{-1}$  at pH 5.5 and 9. In the case of As(V), this band was more intense and better resolved than As(III). To know the oxidation state of As, extended X-ray absorption fine structure (EXAFS) spectroscopy was performed which confirmed that no change occurred in the oxidation state of As(III) and As(V) after adsorption. EXAFS and X-ray absorption near edge structure (XANES) spectroscopy studies were widely used to know the mode of complexation of arsenic species on iron oxide/oxyhydroxide.

Wang et al.<sup>22</sup> investigated the surface speciation of As(III) and As(V) on green rust by EXAFS and XANES spectroscopies. They found polymeric species of As(III) on the surface of green rust. Bhandari et al.<sup>27</sup> studied the effect of light on ferrihydrite with As(III) at pH 5 using XANES and attenuated total reflection-FTIR (ATR-FTIR) spectroscopy. They observed the oxidation of As(III) which was bound to the surface of ferrihydrite. During the adsorption process, the release of Fe(II) ions into solution from ferrihydrite was noticed. Nguema et al.<sup>28</sup> performed As(III) sorption with 2-line ferrihydrite, hematite, goethite and lepidocrocite using EXAFS and XANES spectroscopies. They found bidentate binuclear corner sharing ( $^2\text{C}$ ) complexes in all cases but bidentate mononuclear edge sharing ( $^2\text{E}$ ) complexes additionally for ferrihydrite and hematite. In the environment, the known polymorphs of iron oxides/hydroxides/oxyhydroxides are about sixteen.<sup>29</sup> Hematite ( $\alpha\text{-Fe}_2\text{O}_3$ ), magnetite ( $\text{Fe}_3\text{O}_4$ ), goethite ( $\alpha\text{-FeOOH}$ ), and ferrihydrite ( $\text{Fe}_2\text{O}_3 \cdot 0.5\text{H}_2\text{O}$ ) are the commonly available polymorphs and are used for various industrial and scientific applications. Hematite (HEM), magnetite (MAG), and ferrihydrite (Fh)-based materials were used extensively in water purification for the removal of heavy metal ions (Pb and As).<sup>30–32</sup> Higher surface area of iron oxides favors larger adsorption capacity for arsenate.<sup>33</sup> Iron oxide nanoparticles are also effective for the removal of other metals such as V, Cr, Co, Mn, Se, Mo, Cd, Sb, Tl, Th, and U.<sup>34</sup> Use of nano-adsorbents for the removal of heavy metal ions from water is particularly attractive as they can be altered suitably to achieve greater surface area and stronger binding capacity. Magnetite nanoparticles have certain advantages due to their superparamagnetic properties, ease of preparation, and biocompatibility. However, agglomeration and the loss of magnetic strength over time resulting from auto-oxidation limits the commercial application of bare iron oxide nano-

particles.<sup>35,36</sup> We had introduced a low cost engineered nanomaterial, named as confined metastable 2-line ferrihydrite (CM2LF), having a high adsorption capacity of 100  $\text{mg/g}$ <sup>37</sup> as a solution for arsenic contamination in drinking water. Detailed characterization, comparison with other materials, batch and cartridge studies, mechanical properties, regeneration, reuse, and post adsorption characterization have been reported earlier by Kumar et al.<sup>37</sup> The material has been implemented in various parts of West Bengal, Uttar Pradesh, Karnataka, and Punjab states of India for arsenic removal with continuous monitoring, and the technology has reached over 600 000 people now.

Present work mainly focuses on the adsorption kinetics of common As species ( $\text{H}_3\text{AsO}_3$ ,  $\text{H}_2\text{AsO}_4^{1-}$ , and  $\text{HAsO}_4^{2-}$ ) which exist at pH 7. The oxidation state of iron in CM2LF, MAG, and HEM upon complexation with As species was studied using XPS. The mode of adsorption of various species on these adsorbents was studied using FTIR spectroscopy. Based on these, a mechanistic model of complexation on nanoscale materials was developed.

## ■ EXPERIMENTAL SECTION

Stock solutions of 100 mM As(III) and As(V) were prepared using  $\text{NaAsO}_2$  and  $\text{Na}_2\text{HAsO}_4 \cdot 7\text{H}_2\text{O}$ , respectively. A combination of As(III) and As(V) is referred to as As(mix). A stock solution of 100 mM As(mix) solution was prepared by mixing equimolar amounts of  $\text{NaAsO}_2$  and  $\text{Na}_2\text{HAsO}_4 \cdot 7\text{H}_2\text{O}$ . The pH of the stock solutions was adjusted to 7 by adding diluted HCl and diluted NaOH, whenever necessary.

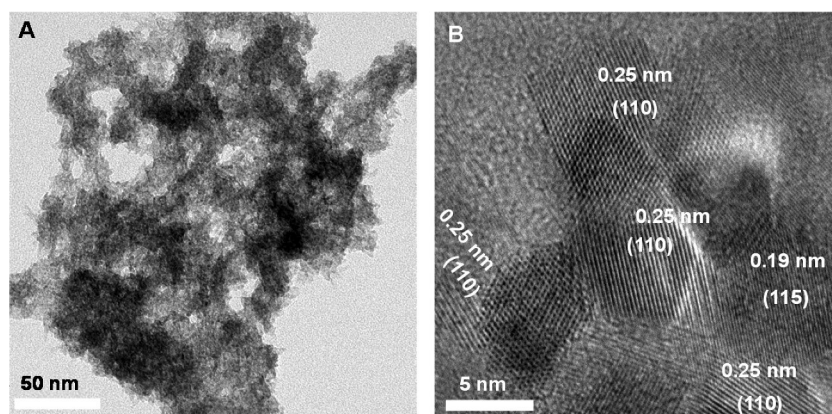
Further, 200 mg of the material (CM2LF/MAG/HEM) was added to 150 mL of arsenic stock solution (As(III)/As(V)/As(mix)) in a 250 mL polypropylene conical flask. The flask was kept in an orbital shaker for 24 h, until an adsorption equilibrium was reached. The solution was centrifuged and the residue (i.e., the arsenic adsorbed material) was washed several times with deionized water to remove unreacted arsenic species from the surface of the material. Subsequently, the cleaned residue was dried at room temperature and a pellet was made using an IR pelletizer. The pellet was kept in a vacuum desiccator for 48 h for complete drying and also to protect it from the surrounding environment, before performing XPS and IR measurements.

To understand the adsorption kinetics of arsenic, Raman measurements were performed. For this, 3–7 g of the material (CM2LF/MAG/HEM) was added to 40–50 mL of 150 mL of arsenic (As(III)/As(V)/As(mix)) solutions in a 250 mL polypropylene conical flask. The solution was kept in an orbital shaker, and 1 mL of the solution was collected at various time intervals at 5, 10, 15, 20, 40, 60, 90, and 120 min, respectively. The solutions were subjected to centrifugation, immediately after collecting them. The material if any, separated as residue, was discarded and Raman measurements were performed using the supernatant.

In this work, each material, viz., CM2LF/MAG/HEM has been investigated thoroughly for interaction with As(III), As(V), and As(mix), respectively.

**Materials.** Sodium arsenite ( $\text{NaAsO}_2$ ) and disodium hydrogen arsenate ( $\text{Na}_2\text{HAsO}_4 \cdot 7\text{H}_2\text{O}$ ) were purchased from SD Fine Chemicals Limited. Hematite ( $\alpha\text{-Fe}_2\text{O}_3$ ) was purchased from Merck Chemicals Pvt. Ltd., India. Magnetite ( $\text{Fe}_3\text{O}_4$ ) was purchased from Alfa Aesar (A Johnson Matthey Company, USA). Sodium hydroxide (NaOH) was purchased from Rankem Glasswares and Chemicals Pvt. Ltd., India. Hydrochloric acid (HCl) was purchased from Merck Life Science Pvt. Ltd., India. All chemicals were of analytical grade and were used without further purification. Deionized (DI) water was used throughout the experiments.

**Instrumentation.** HRTEM images of the sample were obtained with JEM 3010 (JEOL, Japan) operating at 200 kV (to reduce beam induced damage) with an ultrahigh-resolution polepiece. Samples for



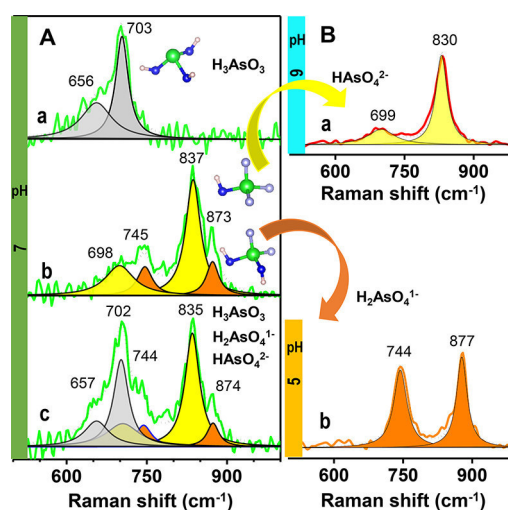
**Figure 1.** (A) HRTEM image of the 2-line ferrihydrite composite (CM2LF). (B) Lattice resolved image of part A.

HRTEM studies were prepared by dropping the dispersion on amorphous carbon films supported on a copper grid and subsequent drying. XPS measurements were done using an ESCA Probe TPD spectrometer of Omicron Nanotechnology. Polychromatic Al K $\alpha$  was used as the X-ray source ( $h\nu = 1486.6$  eV). Samples were mounted as pellets on a carbon tape, supported on the sample stub. Constant analyzer energy of 20 eV was used for the measurements. Binding energy was calibrated with respect to C 1s at 284.8 eV. All the XPS spectra were deconvoluted using CasaXPS software. Raman spectroscopy was performed using CRM Alpha 300 S microRaman spectrometer of WiTec GmbH (Germany). A glass slide with a cavity (which can hold 100  $\mu$ L of the sample solution) was mounted on the piezoelectric scan stage of the setup. The spectra were collected at 633 nm laser excitation where a long band-pass filter, placed in the path of signal effectively cuts off the Rayleigh scattering. The signal was then dispersed using a 600 grooves per mm grating, and the dispersed light was collected by a Peltier-cooled charge coupled device. The other parameters of the instrument were kept as integration time, 70 s and accumulation, once. The background subtraction of spectrum was done using a second-order polynomial. All the Raman spectra were deconvoluted using OriginPro 9.0 software. A PerkinElmer FTIR spectrometer was used to measure the infrared spectra. The spectrometer resolution was kept at 4  $\text{cm}^{-1}$ . Identification of the phase(s) of CM2LF sample was carried out by XRD (Bruker AXS, D8 Discover, USA) using the Cu K $\alpha$  radiation at  $\lambda = 1.5418$  Å. Various model building softwares were used to build the structures. The rectangular slab, nanosphere, and cube were built by using VESTA and Avogadro 1.2.0 software.

## RESULTS AND DISCUSSION

Figure 1A shows a TEM image of CM2LF. It appears largely amorphous and continues to remain the same at ambient conditions even after extensive interaction with As(III) and As(V) spiked water. Upon continuous electron beam irradiation, lattice planes are seen under HRTEM due to beam induced crystallization (Figure 1B). Figure S9 shows the XRD data of CM2LF. It shows the 2-line ferrihydrite phase with characteristic features at  $35.5^\circ$  and  $62.3^\circ$  corresponding to the (110) and (115) planes. The observed lattice planes are in agreement with the Cambridge Crystallographic Database (CCD) (JCPDS, 46-1315).<sup>37–39</sup>

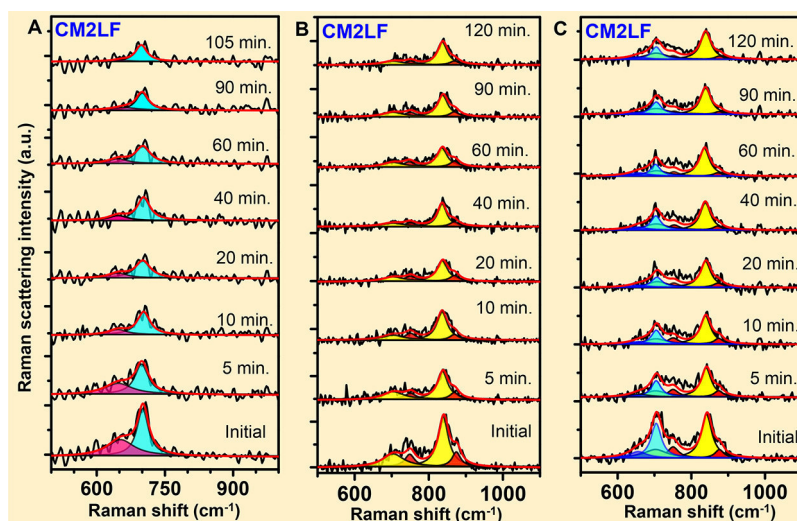
To understand the degree of protonation, polymerization, and speciation of As(III) and As(V) oxides<sup>40</sup> at room temperature, Raman spectra were measured at pH 7 (Figure 2Aa,Ab). As(III) in solution has two vibrational features at 703 and 656  $\text{cm}^{-1}$  (Figure 2Aa) which correspond to the  $A_1$  and E modes of  $\text{H}_3\text{AsO}_3$  ( $C_{3v}$  symmetry when all OH groups are equivalent). The peak at 703  $\text{cm}^{-1}$  corresponds to symmetric stretching ( $A_1$ ) while the other peak at 656  $\text{cm}^{-1}$  represents



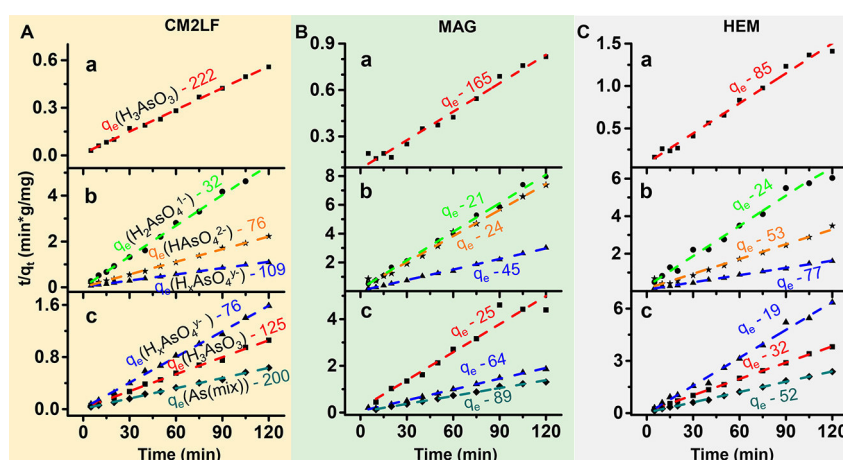
**Figure 2.** Raman spectra of aqueous arsenite and arsenate species. (A) Data at pH 7 for (a) As(III), (b) As(V), and (c) As(mix). Expanded view of As(V) showing different species at other pH values. (B) Most of the As(V) is in the form of (a)  $\text{HAsO}_4^{2-}$  at pH 9 and as (b)  $\text{H}_2\text{AsO}_4^{1-}$  at pH 5. Data have been fitted with their components.

the asymmetric stretching (E) of  $\text{As}-\text{OH}$ ,<sup>21</sup> respectively. As(V) in solution shows four vibrational features (after deconvolution) at 873, 837, 745, and 698  $\text{cm}^{-1}$  (Figure 2Ab). To understand the kind of speciation of As(III) and As(V) in the aqueous phase, we have performed the studies by varying pH, according to the  $\text{pK}_a$  value of their corresponding acids, and the data are shown in the Supporting Information, Figure S1. As(V) in solution exists as  $\text{H}_2\text{AsO}_4^{1-}$  and  $\text{HAsO}_4^{2-}$  species in the pH window of 5–9, as reported.<sup>37,20,21</sup> Species  $\text{H}_2\text{AsO}_4^{1-}$  and  $\text{HAsO}_4^{2-}$  belong to  $C_{2v}$  (when the OH groups are equivalent) and  $C_{3v}$  (when the OH group is considered as a moiety) point groups, respectively.  $C_{2v}$  has four vibrational modes, viz.,  $A_1$ ,  $A_2$ ,  $B_1$ , and  $B_2$  while  $C_{3v}$  has two vibrational modes, viz.,  $A_1$  and E which are Raman active. The vibrational modes of the species  $\text{H}_2\text{AsO}_4^{1-}$  and  $\text{HAsO}_4^{2-}$  were discussed by Müller et al.<sup>21</sup> As(V) solution was made at pH 5 and pH 9, separately. At pH 9, it shows two features at 830 and 699  $\text{cm}^{-1}$  (Figure 2Ba) whereas at pH 5, they were observed at 877 and 744  $\text{cm}^{-1}$  (Figure 2Bb). The higher frequency peaks of the spectra (at 830 and 877  $\text{cm}^{-1}$ ) correspond to the symmetric stretching of  $\text{As}=\text{O}$ , while the lower frequency peaks (699 and 744  $\text{cm}^{-1}$ ) represent the symmetric stretching of  $\text{As}-\text{OH}$ , respectively. With this explanation, we can assign the Figure





**Figure 3.** Time dependent Raman spectra of the interaction of CM2LF with (A) As(III), (B) As(V), and (C) As(mix).



**Figure 4.** Pseudo-second-order kinetics graph for (A) CM2LF, (B) MAG, and (C) HEM, where plots a, b, and c represent As(III), As(V), and As(mix) removal, respectively. The unit of  $q_e$  and  $q_t$  is mg/g. The  $q_t$  of each data point was evaluated using eq 3 of Supporting Information 4.

2Ab vibrational frequencies 837, 698 and 873, 745  $\text{cm}^{-1}$  to  $\text{HAsO}_4^{2-}$  and  $\text{H}_2\text{AsO}_4^{1-}$ , respectively. In the case of As(mix) in solution, at pH 7, the observed six vibrational features (after deconvolution) are almost close to the vibrational frequencies of the individual As(III) and As(V) species ( $\text{H}_3\text{AsO}_3$ ,  $\text{HAsO}_4^{2-}$ , and  $\text{H}_2\text{AsO}_4^{1-}$ ) as discussed earlier. We did not see any additional features which also confirm that there are no adducts between As(III) and As(V) in solution as a result of mixing. Further details about As–O or As–OH stretching frequencies of arsenic oxides are discussed in Goldberg et al.<sup>20</sup>

The adsorption kinetics of various arsenic species in solution at pH 7 was studied for different materials, CM2LF, MAG, and HEM. The intensities of As(III), As(V), and As(mix) species decreased upon interaction with CM2LF with time, as shown in Figure 3. Similar decay in intensities of the arsenic species is seen in the case of MAG and HEM as shown in the Supporting Information, Figures S2 and S3, respectively. The data suggest that upon interaction with CM2LF, MAG, and HEM, the arsenic species in solution remained the same. Area under the peaks correspond to concentration in solution, and the data suggest that equilibrium is reached in 20 min as shown in Figure S4. The kinetic graphs in Figure S4A,B follow a pseudo-second-order expression. The similar data for MAG and HEM

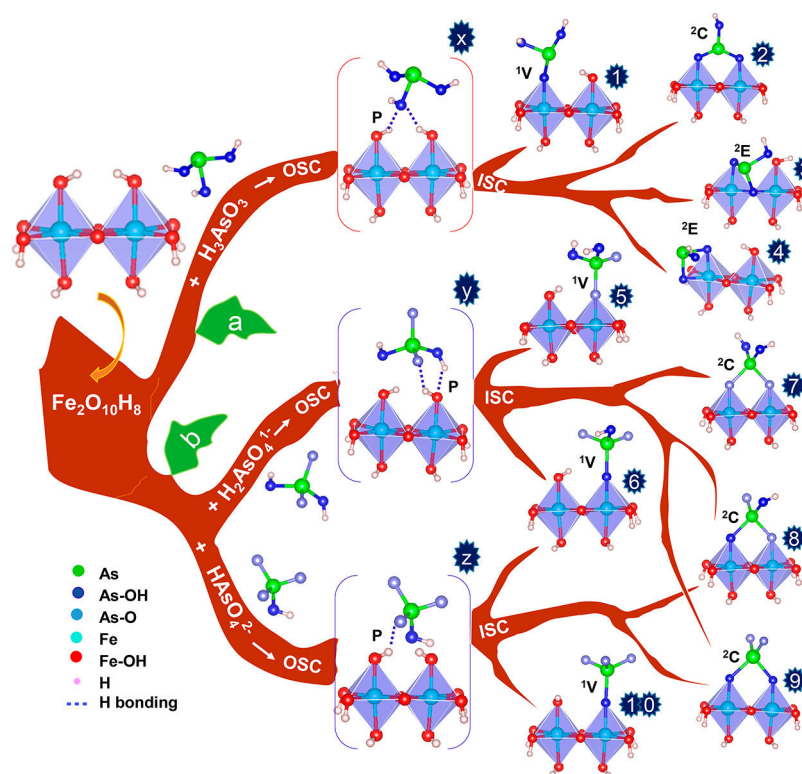
are shown in Figures S5 and S6, respectively. We observed that the concentration of As(III) and As(V) in solution reduced faster for CM2LF but not for MAG and HEM. Appropriate analyses of the data are presented in the Supporting Information.

Raman measurements of various concentrations of As(III) and As(V) are shown in the Supporting Information, Figure S7A,B, respectively. The correlation between the area under the peak and the concentration of As(III) and As(V) solutions are shown in Figure S7C,D, respectively. To understand the adsorption kinetics and uptake capacity, we plotted  $t/q_t$  versus  $t$  (Figure 4); the rate constants ( $k$ ) and adsorption capacity ( $q_e$ ) of all the materials were calculated using the slopes and intercepts of the plots. The results are tabulated in Table 1. Similar adsorption models for the uptake of arsenic have been reported earlier.<sup>9,30,41</sup>

The obtained rate constants for CM2LF and HEM are equal for As(III) adsorption but less for MAG (Table 1). We assume that this may be due to the difference in availability of surface –O<sup>−</sup>/–OH groups on all three materials. While in the case of As(V), MAG shows faster kinetics in comparison to CM2LF and HEM, even though it shows less uptake of As(V). As we know that As(V) in solution exists as  $\text{H}_2\text{AsO}_4^{1-}$  and  $\text{HAsO}_4^{2-}$

Table 1. Adsorption Data in Terms of Initial Rates, Rate Constants, and Uptake of As at Equilibrium

adsorbate 150 mL	adsorbent (g)	species pH 7	$q_e$ (mg/g) $\pm$ 5%	$k$ (min(mg/g)) <sup>-1</sup> $\pm$ 5%	initial rate $h = kq_e^2 \pm 10\%$	$R^2$
50 mM As(III)	CM2LF : 3 g	H <sub>3</sub> AsO <sub>3</sub>	222	$1.5 \times 10^{-3}$	74	0.99
	MAG : 3 g	H <sub>3</sub> AsO <sub>3</sub>	165	$0.4 \times 10^{-3}$	11	0.99
	HEM : 3 g	H <sub>3</sub> AsO <sub>3</sub>	85	$1.5 \times 10^{-3}$	11	0.99
40 mM As(V)	CM2LF : 7 g	H <sub>2</sub> AsO <sub>4</sub> <sup>3-</sup>	109	$5.0 \times 10^{-3}$	59	0.99
		H <sub>2</sub> AsO <sub>4</sub> <sup>1-</sup>	32	$60.0 \times 10^{-3}$	61	0.99
		HAsO <sub>4</sub> <sup>2-</sup>	76	$20.0 \times 10^{-3}$	115	0.99
	MAG : 7 g	H <sub>2</sub> AsO <sub>4</sub> <sup>3-</sup>	45	$19.0 \times 10^{-3}$	38	0.98
		H <sub>2</sub> AsO <sub>4</sub> <sup>1-</sup>	21	$25.0 \times 10^{-3}$	11	0.98
		HAsO <sub>4</sub> <sup>2-</sup>	24	$17.0 \times 10^{-3}$	10	0.98
	HEM : 7 g	H <sub>2</sub> AsO <sub>4</sub> <sup>3-</sup>	77	$2.0 \times 10^{-3}$	12	0.98
		H <sub>2</sub> AsO <sub>4</sub> <sup>1-</sup>	24	$12.0 \times 10^{-3}$	7	0.98
		HAsO <sub>4</sub> <sup>2-</sup>	53	$4.5 \times 10^{-3}$	13	0.98
50 mM As(mix)	CM2LF : 5 g	As(mix)	200	$3.0 \times 10^{-3}$	120	0.99
		H <sub>3</sub> AsO <sub>3</sub>	125	$7.0 \times 10^{-3}$	109	0.99
		H <sub>2</sub> AsO <sub>4</sub> <sup>3-</sup>	76	$8.5 \times 10^{-3}$	49	0.99
	MAG : 5 g	As(mix)	89	$4.0 \times 10^{-3}$	32	0.99
		H <sub>3</sub> AsO <sub>3</sub>	25	$5.0 \times 10^{-3}$	31	0.95
		H <sub>2</sub> AsO <sub>4</sub> <sup>3-</sup>	64	$12.0 \times 10^{-3}$	49	0.99
	HEM : 5 g	As(mix)	52	$13.0 \times 10^{-3}$	35	0.99
		H <sub>3</sub> AsO <sub>3</sub>	32	$13.0 \times 10^{-3}$	13	0.99
		H <sub>2</sub> AsO <sub>4</sub> <sup>3-</sup>	20	$40.0 \times 10^{-3}$	16	0.97

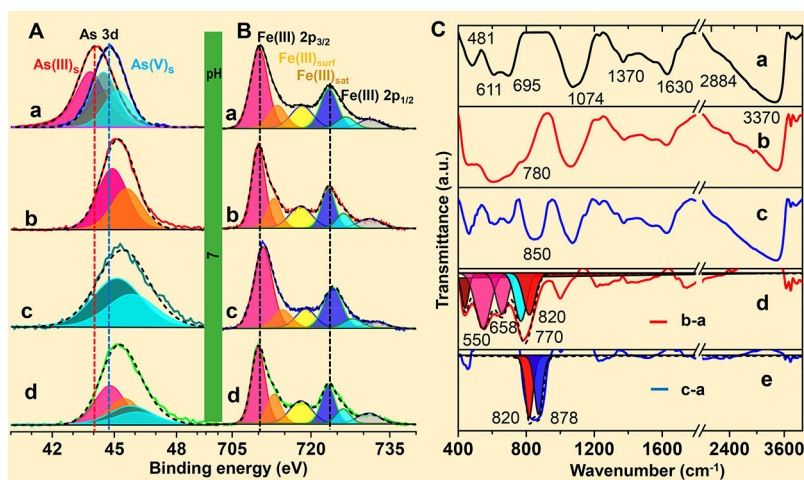


**Figure 5.** A model of As complexes with Fe<sub>2</sub>O<sub>10</sub>H<sub>8</sub> cluster. Path a, As(III) complexes and path b, As(V) complexes. OSC, outer sphere complexes (x, y, and z). ISC, inner sphere complexes (1 to 10). Transformation of OSC to ISC by ligand exchange is shown.

at pH 7, we were interested to know which species will have faster kinetics toward iron oxides/oxyhydroxides. Data of Table 1 reveal that H<sub>2</sub>AsO<sub>4</sub><sup>1-</sup> shows higher rate constant than HAsO<sub>4</sub><sup>2-</sup> for CM2LF, MAG, and HEM at pH 7 irrespective of their different surface structures. Further studies were conducted using As(mix) and As(V), which showed higher

rate constant than As(III). Thus, As(V) interaction with all the materials is faster in comparison to As(III) due to the difference in the species in the solution phase. As(V) shows faster adsorption kinetics as compared to As(III). It is due to As(V) (H<sub>2</sub>AsO<sub>4</sub><sup>1-</sup>/HAsO<sub>4</sub><sup>2-</sup>) possessing more polarizable hydration sphere than As(III) (H<sub>3</sub>AsO<sub>3</sub>). Nucleophilicity





**Figure 6.** XPS spectrum of (A) As 3d and (B) Fe 2p. As 3d region of (A) (a) NaAsO<sub>2</sub> (red trace) and Na<sub>2</sub>HAsO<sub>4</sub>·7H<sub>2</sub>O (blue trace). Comparison of the positions may be noted. (b) As(III), (c) As(V), and (d) As(mix) adsorbed on CM2LF. Spectra are fitted for the 3d<sub>5/2</sub> and 3d<sub>3/2</sub> features. (B) (a) CM2LF before adsorption, (b–d) Fe 2p after adsorption, as before. (C) FTIR spectra (a) CM2LF before adsorption. Spectra of (b) As(III) and (c) As(V) adsorbed materials. (d) Spectra after subtraction (curve b–a). (e) Spectra after subtraction (curve c–a).

plays an important role in the inner sphere complexation process (ligand exchange mechanism). More nucleophilic ligands ( $-\text{O}^- > -\text{OH}$ ) can easily replace the labile groups ( $-\text{OH}/\text{H}_2\text{O}^+$ ). In acidic pH, most of the singly coordinated oxygens are present on the surface of adsorbent in the form of  $\text{H}_2\text{O}^+/-\text{OH}$  groups. As the pH becomes basic, the singly coordinated oxygens change to  $-\text{OH}/-\text{O}^-$ . Thus, at pH 7, the surface of adsorbent can be composed of  $\text{H}_2\text{O}^+/-\text{O}^-/-\text{OH}$  groups. Repulsions existing between  $\text{Fe}-\text{Q}^-$  (adsorbent) and  $\text{As}-\text{Q}^-$  (adsorbate) groups are the cause of reduced adsorption of As(V) than As(III). As(V) has more nucleophilic ligands ( $-\text{As}-\text{O}^-$ ) as compared to As(III) ( $-\text{As}-\text{OH}$ ). Thus, we can conclude that nucleophilicity is one of the key factors leading to faster adsorption kinetics for As(V) than As(III) at pH 7. The effect of nucleophilicity of ligands and the difference in molecular basis of the adsorption process for As(III) and As(V) are shown in Figure S10.

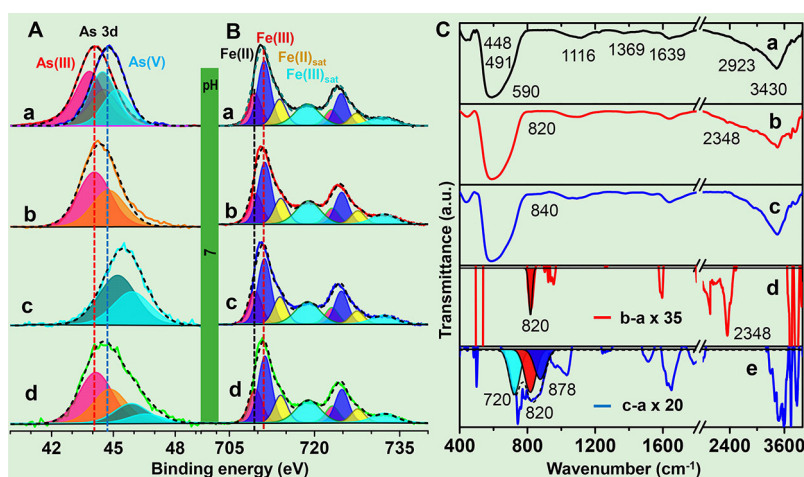
Adsorption at equilibrium has shown that As(III) uptake is higher than As(V) for CM2LF and HEM (Table 1) and not for MAG. We believe that decrease in availability of adsorption sites for As(III) due to the initial occupation of them by As(V) and also pH of the solution are the major reasons for reduced uptake by MAG. Among the adsorbents studied, the rate constant is highest for MAG for As(V) uptake. It also shows the lowest rate constant for As(III) uptake (Table 1).

**Effect of Competing Ions.** We further studied the influence of competing ions on arsenic adsorption for CM2LF, MAG, and HEM to improve the application of materials for point-of-use water purification. We have considered the ions which are generally present in natural water:  $\text{NO}_3^-$ ,  $\text{CO}_3^{2-}$ ,  $\text{PO}_4^{3-}$ ,  $\text{SO}_4^{2-}$ ,  $\text{Cl}^-$ , and  $\text{HCO}_3^-$  and performed experiments for As(III) and As(V), separately. As(III) adsorption was more than that of As(V) for all the materials. The corresponding data are shown in Figure S11. CM2LF removes As(III) and As(V) effectively as compared to MAG and HEM even in the presence of competing ions. The data show that the influence of  $\text{PO}_4^{3-}$  ion was considerably higher than that of other ions for all the materials.

In the following, we present a model for the adsorption of arsenic species on CM2LF based on the data available. For this model, a unit of the substrate is considered. For FeOOH based

materials, the  $\text{Fe}_2\text{O}_3\cdot\text{H}_2\text{O}$  unit, an edge share hydroxyl terminated bioctahedron is taken as the model system. Possible complexes that can be formed via ligand exchange mechanism upon the adsorption of As(III) and As(V) on this model cluster at pH 7 are shown in Figure 5. We may recall that the  $\text{Fe}_2\text{O}_3$  cluster is the common unit (two octahedra present in edge sharing fashion) of 2-line ferrihydrite, MAG and HEM. The oxide upon exposure to water will have hydroxylated surfaces making this model realistic. There are two kinds of adsorption geometries (physical and chemical) possible in the case of As species. Physical adsorption leads to outer sphere (physically bonded species (P) through hydrogen bonding) complexes while chemical adsorption result in inner sphere (chemically bonded) complexes. Most of the outer sphere complexes can transform to inner sphere complexes through ligand exchange mechanism as indicated by the pathways (“path a” and “path b”). In Figure 5, x, y and z represent the outer sphere complexes formed through hydrogen bonding between As species and iron oxides/oxyhydroxides as reported.<sup>26,42</sup> The inner sphere complexes are (1) monodentate mononuclear (<sup>1</sup>V), (2) bidentate binuclear corner sharing (<sup>2</sup>C), and (3) bidentate mononuclear/binuclear edge sharing (<sup>2</sup>E). The ratio of outer to inner sphere complexes depend on the pH of the solution.<sup>23,26</sup> Complex 2 from Figure 5 (“path a”) and complexes 7, 8, and 9 from Figure 5 (“path b”) represent the <sup>2</sup>C complexes. The complexes 7, 8, and 9 are structurally similar and differ in the degree of protonation of As(V) species. As(III) and As(V) have more tendency to form <sup>2</sup>C complexes (thermodynamically favorable) than other possible structures<sup>28,43,44</sup> for all the adsorbents used in this work. Bidentate mononuclear edge sharing (<sup>2</sup>E) complexes were found in the case of As(III) with ferrihydrite and HEM.<sup>28</sup> Complex 1 from Figure 5 (“path a”) and complexes 5, 6, and 10 from Figure 5 (“path b”) show monodentate mononuclear (<sup>1</sup>V) complexes. These are found to increase in intensity noticeably at pH 7–10<sup>23,22</sup> in the case of As(III) and at pH 5–10<sup>26,42</sup> in the case of As(V) with iron oxides/oxyhydroxides.

The XPS analysis of arsenic standards in the solid form (As(III)<sub>s</sub> and As(V)<sub>s</sub>, subscript “s” refers to solid state) are shown in Figure 6Aa, 7Aa, and Figure S8Aa. The measurements were done using standard arsenic compounds viz.,



**Figure 7.** XPS spectrum of (A) As 3d and (B) Fe 2p. As 3d region of (A) (a)  $\text{NaAsO}_2$  (red trace) and  $\text{Na}_2\text{HAsO}_4 \cdot 7\text{H}_2\text{O}$  (blue trace). Comparison of the positions may be noted. (b) As(III), (c) As(V), and (d) As(mix) adsorbed on MAG. Spectra are fitted for the  $3d_{5/2}$  and  $3d_{3/2}$  features. (B) (a) MAG before adsorption, (b, c, and d) Fe 2p after adsorption, as before. (C) FTIR spectra (a) MAG before adsorption. Spectra of (b) As(III) and (c) As(V) adsorbed materials. (d) Spectra after subtraction (curve b-a). (e) Spectra after subtraction (curve c-a).

$\text{NaAsO}_2$  for As(III) and  $\text{Na}_2\text{HAsO}_4$  for As(V). The As 3d peak appears at 44.2 and 44.8 eV for As(III)<sub>s</sub> and As(V)<sub>s</sub>, respectively.<sup>45</sup> The As 3d peak was deconvoluted into  $3d_{5/2}$  and  $3d_{3/2}$ , while Fe 2p was fitted with three pairs of peaks for CM2LF and HEM as reported.<sup>46,47</sup> The lower binding energy peak corresponds to  $-\text{Fe}-\text{O}-\text{Fe}-$  groups, the next higher one refers to surface  $>\text{Fe}-\text{OH}$  groups ( $\text{Fe(III)}_{\text{surf}}$ ) followed by a satellite peak ( $\text{Fe(III)}_{\text{sat}}$ ).<sup>46</sup> XPS data of each peak before and after arsenic (As(III), As(V), and As(mix)) interaction with all three materials used in this work are shown in Table S1. The standard As 3d peak was redshifted from 44.2 to 45.1 and 44.7 eV upon As(III) interaction with CM2LF (Figure 6Ab) and HEM (Supporting Information, Figure S8Ab), respectively. The observed results suggest that most of the  $\text{H}_3\text{AsO}_3$  species on the surface of CM2LF and HEM are chemically bonded or may have got converted to As(V). In the case of As(V) adsorption on CM2LF and HEM, the As 3d peak redshifts from a value of 44.8 to 45.3 and 46.5 eV for CM2LF (Figure 6Ac) and HEM (Supporting Information, Figure S8Ac), respectively. The redshift of As 3d peak was higher in the case of HEM and lower for CM2LF (broaden to higher binding energy side). Lower redshift can refer to physically adsorbed and higher redshift can suggest chemically adsorbed species. The FTIR characteristic features of CM2LF before arsenic adsorption (Figure 6Ca) shows Fe–O stretching frequencies of 2-line ferrihydrite at 481, 611, and 695  $\text{cm}^{-1}$ , respectively. Peaks at 1074, 1370, and 3370  $\text{cm}^{-1}$  are due to asymmetric C–O–C stretching, N–H deformation, and N–H stretching of chitosan (the polymer used to make CM2LF), respectively. The C=O stretching of amide and C–H stretching of the polymer were noticed at 1630 and 2884  $\text{cm}^{-1}$ , respectively, as reported by Kumar et al.<sup>37</sup> The peak at 3370  $\text{cm}^{-1}$  suggest the stretching vibrations of adsorbed water and hydroxyl groups of CM2LF. The free  $\text{H}_3\text{AsO}_3$  molecules in water show stretching vibrations of As–OH at 703 and 656  $\text{cm}^{-1}$  (Figure 2Aa), which gives a new peak at 780  $\text{cm}^{-1}$  upon interaction with CM2LF<sup>26,28</sup> due to which enhancement of Fe–O peaks of CM2LF was observed in the 600–700  $\text{cm}^{-1}$  region. The enhancement may be due to the overlap of  $\text{H}_3\text{AsO}_3$  (As–OH) stretching vibrations and Fe–O vibrations of CM2LF. This effect can be noticed from the subtracted

spectrum, curve b-a of Figure 6Cd. The fitted curve b-a shows the adsorbed  $\text{H}_3\text{AsO}_3$  features at 550, 658, and 770  $\text{cm}^{-1}$ . The 770  $\text{cm}^{-1}$  is due to chemically adsorbed species and the other two, 550 and 658  $\text{cm}^{-1}$  suggest physically adsorbed (hydrogen bonded)  $\text{H}_3\text{AsO}_3$  (As–OH stretching) on CM2LF. The results were supported by the work of Sverjensky et al.<sup>23</sup> and Fukushima et al.<sup>26</sup> These authors studied arsenic speciation on ferrihydrite surface using IR and extended X-ray adsorption fine structure (EXAFS) spectroscopies and applied the extended triple layer model (ETLM). The <sup>2</sup>C complexes dominate than the <sup>1</sup>V and P complexes for As(III) and As(V). In the present study, the ratio of physical to chemical adsorption is more for As(V) than for As(III) due to difference in the extent of deprotonation of arsenic species and increase of  $-\text{O}^-$  groups on the surface of the adsorbent. The results suggest that the effect of pH is more on As(V) than As(III).

In the case of MAG, the Fe  $2p_{3/2}$  was deconvoluted into four peaks which correspond to Fe(II), Fe(III) and two separate shakeup peaks for Fe(II) ( $\text{Fe(II)}_{\text{sat}}$ ) and Fe(III) ( $\text{Fe(III)}_{\text{sat}}$ ), respectively.<sup>46,48</sup> Similarly, the deconvolution was done for Fe  $2p_{1/2}$ . Upon As(III) interaction with MAG, no considerable change was observed in As 3d. The peak shifted from 44.2 to 44.3 eV (Figure 7Ab) while in the case of As(V), it redshifted from 44.8 to 45.5 eV (Figure 7Ac). Thus, we can conclude that most of the  $\text{H}_3\text{AsO}_3$  species are physically adsorbed and  $\text{H}_x\text{AsO}_4^{y-}$  species are chemically adsorbed on MAG. In both the cases, there was no considerable change in peak positions, intensity ratio, and fwhm of Fe(II) and Fe(III). These suggest that there was no conversion of Fe(II) to Fe(III) and vice versa. The characteristic features of MAG in FTIR before arsenic exposure (Figure 7Ca) shows the Fe–O stretching frequencies at 448, 491, and 590  $\text{cm}^{-1}$ , respectively. Peaks at 1639 and 3430  $\text{cm}^{-1}$  are due to bending and stretching vibrations of adsorbed water on MAG. Peak at 2348  $\text{cm}^{-1}$  is due to free  $\text{CO}_2$  in the spectrometer.

A peak at 820  $\text{cm}^{-1}$  was found upon interaction of As(III) and As(V) with CM2LF and MAG. This feature due to Fe–O–As stretching vibrations of the bidentate binuclear (<sup>2</sup>C) complex<sup>49</sup> occurs in the range of pH 7 to 9, which confirms that the arsenic species ( $\text{H}_3\text{AsO}_3$  and  $\text{H}_2\text{AsO}_4^{1-}$  and  $\text{HAsO}_4^{2-}$ ) are forming the inner sphere complexes on the surface of these

Table 2. Correlation of Adsorption Models and Spectroscopic Data

adsorbate pH 7	adsorbent	As 3d shift (eV)	Fe 2p <sub>3/2</sub> shift (eV)	IR features (cm <sup>-1</sup> )	suggested complexes <sup>a</sup>
As(III) (H <sub>3</sub> AsO <sub>3</sub> )	CM2LF	+ 0.9	0.1	820	complex 2
				550, 658	complex x
	MAG	+ 0.1	0		complex x
	HEM	+ 0.5	− 0.2	820	complex 2/1 may be complex 2
As(V) (HAsO <sub>4</sub> <sup>2−</sup> / H <sub>2</sub> AsO <sub>4</sub> <sup>1−</sup> )	CM2LF	+ 0.5	+ 0.1	820	complex (7/8/9)
	MAG	+ 0.7	+ 0.3	820	complex (7/8/9)
				720	complex (y and z)
	HEM	+ 1.5	− 0.2		complex (7/8/9)

<sup>a</sup>Complexes refer to those in Figure 5, assigned on the basis of FTIR features and As 3d peak shift values.

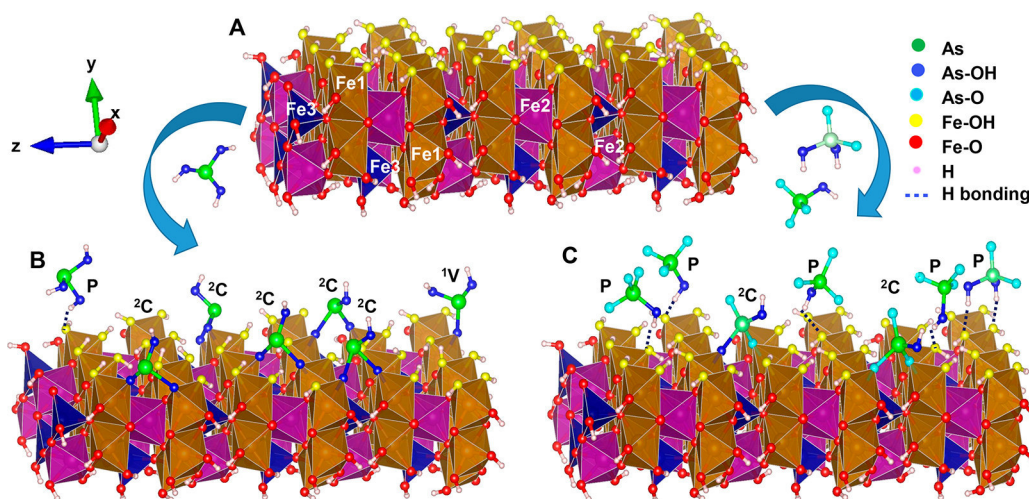


Figure 8. Schematic of a 110 plane of ferrihydrite at pH 7 (A) before adsorption, (B) after As(III) adsorption, and (C) after As(V) adsorption.

materials. CM2LF and MAG show a special feature at 878 cm<sup>-1</sup> after As(V) adsorption which represents the As=O stretching vibrations<sup>49</sup> of H<sub>x</sub>AsO<sub>4</sub><sup>y−</sup>. Figures 6Ad, 7Ad, and Figure S8Ad show that As(III) is more interactive than As(V) at pH 7, in the case of As(mix). The results were supported by Raman data (Table 1). The correlation of adsorption models (Figure 5) and spectroscopic data (XPS and IR) based on the present work is summarized in Table 2.

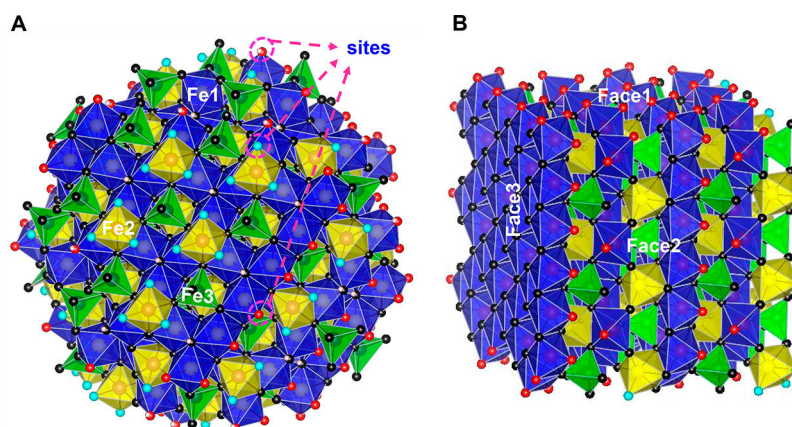
The XPS data (Table 2) suggest that there is no considerable change in Fe 2p upon interaction with arsenic (As(III)/As(V)), which implies that the Fe atoms involved in the complexation did not undergo any chemical change for all the materials reported in this work. We assume that formation of the complexes follows the ligand exchange mechanism. The stability of the complexation of arsenic species with ferric hydroxides was reported by Farrell et al.<sup>42</sup> The stability of the complexes is in the order: bidentate binuclear (>(FeO)<sub>2</sub>AsOH ≈ <sup>2</sup>C) > monodentate mononuclear (>(FeO)–As(OH)<sub>2</sub> ≈ <sup>1</sup>V) > physical adsorption (P).

In the following, we discuss an understanding of the adsorption of arsenic species on CM2LF. In Figure 8, we used the unit cell parameters of 2-line ferrihydrite as reported in Michel et al.<sup>39,50</sup> to construct a rectangular slab having top and bottom surfaces parallel to the (110) plane of FeOOH (Figure 8A). The top surface contains oxygen atoms (in yellow). In general, the ferrihydrite structure has three symmetry-distinct Fe atoms. Here, we represented them as octahedra Fe1 center (dark yellow), octahedra Fe2 center (indigo), and tetrahedra

Fe3 center (blue) as reported by Pinney et al.<sup>50</sup> The CM2LF –O<sup>−</sup>/–OH groups were shown in yellow/red, while arsenic attached –O<sup>−</sup> and –OH groups are marked in sky blue and blue, respectively. XPS and FTIR results suggest that arsenic species bind the surface Fe atoms through a ligand exchange mechanism, at pH 7. The results are supported by the literature.<sup>23,21,24,25,20,26</sup> In the ligand exchange mechanism, As–O<sup>−</sup>/–OH groups replace the Fe–O<sup>−</sup>/–OH groups. The formation of possible stable complexes of As(III) and As(V) with 2-line ferrihydrite are shown in Figure 8B,C, respectively. As(III) forms <sup>2</sup>C (major) and <sup>1</sup>V (minor) complexes while As(V) forms <sup>2</sup>C, <sup>1</sup>V (minor) and P (major) complexes.

We generated a 2-line ferrihydrite nanosphere of 2.6 nm in diameter (Figure 9A) and constructed a cube (Figure 9B) such that the surface area of the cube equals the surface area of the nanosphere ( $6a^2 = 4\pi r^2$ ). The diameter chosen was to simulate the experiment. Possible sites for adsorption were counted as the number of singly coordinated oxy/hydroxy (Fe–O<sup>−</sup>/–OH) groups from Fe1 (octahedral, blue color) and Fe2 (octahedral, yellow color) centers available on the surface of the nanosphere and cube. Only one site was counted if more than one site was present on the same center due to possible steric hindrance of the complexed species. Ideally, 86 sites were counted for the nanosphere and 54 sites were possible for the cube. We applied two constraints to get maximum arsenic uptake capacity of 2-line ferrihydrite. (1) All the particles (nanosphere or cube) were assumed to be well separated to make all the sites available for adsorption and (2) all the





**Figure 9.** A generated nanosphere model of 2.6 nm diameter by using the unit cell parameters of 2-line ferrihydrite. Singly coordinated oxygens attached to the Fe1 and Fe2 centers are represented with red and sky blue colors, respectively. (B) A cube of the same sample using the information presented. We developed a model of a cubic particle of FeOOH with arsenic adsorption, such that its surface area is equal to the surface area of a 2.6 nm sphere.

arsenic species were attached to the surface Fe atoms as monodentate mononuclear (<sup>1</sup>V) or bidentate mononuclear in an edge sharing (<sup>2</sup>E) fashion assuming that one arsenic species should occupy one site and the other possible complexes (bidentate binuclear (<sup>2</sup>C) and physical adsorption (P)) were excluded. The density of 2.6 nm particle is 3.5 g/cm<sup>3</sup> as reported.<sup>51</sup> Correspondingly,  $32.21 \times 10^{-21}$  g and  $23.25 \times 10^{-21}$  g are the masses of a single nanosphere and a cube, respectively, which are calculated using density and volume of the specific geometry (here the density of nanosphere and cube were assumed as equal). Further,  $3.1 \times 10^{19}$  nanospheres or  $4.3 \times 10^{19}$  cubes are needed to make 1 g of 2-line ferrihydrite. The total number of sites available on nanospheres ( $3.1 \times 10^{19} \times 86 = 2.666 \times 10^{21} = 4.426 \times 10^{-3}$  moles of sites) or cubes ( $4.3 \times 10^{19} \times 54 = 2.322 \times 10^{21} = 3.856 \times 10^{-3}$  moles of sites) for 1 g of 2-line ferrihydrite were calculated. In the case of nanospheres, ideally, the maximum adsorption capacities for As(III) and As(V) were about 557 and 620 mg/g (where all the sites fully occupied by H<sub>3</sub>AsO<sub>3</sub> or H<sub>x</sub>AsO<sub>4</sub><sup>y-</sup> species), respectively, while in the case of cubes, they were about 485 and 543 mg/g for As(III) and As(V), respectively. The theoretical calculations suggest that the shape and geometry of nanoparticle present in 2-line ferrihydrite can profoundly affect its uptake capacity. The experimental uptake capacity could reach almost half of the theoretical value.

## CONCLUSIONS

Species-dependent arsenic adsorption on iron oxides/oxyhydroxides was investigated by Raman spectroscopy. Time dependent Raman measurements allowed us to understand an effective material for better arsenic uptake for various species, H<sub>2</sub>AsO<sub>4</sub><sup>1-</sup> and HAsO<sub>4</sub><sup>2-</sup>, at neutral pH. The studies suggested that their complexation with iron oxides/oxyhydroxides was driven by the ligand exchange mechanism which could lead to the formation of Fe–O–As bonds at neutral pH. Complementary data were obtained from vibrational spectroscopy. CM2LF showed the highest arsenic adsorption capacity than the commonly available polymorphs of iron oxides (MAG and HEM) at neutral pH. CM2LF showed effective removal of As(III) and As(V) in natural waters which supported its use in point-of-use water purification applications. Using the adsorption kinetics, understanding of the species present on the surfaces and speciation of arsenite and arsenate ions known

previously, a model of an arsenic adsorbed nanoparticle of FeOOH was arrived at. This model explains observed results accurately.

## ASSOCIATED CONTENT

### Supporting Information

The Supporting Information is available free of charge on the ACS Publications website at DOI: [10.1021/acssuschemeng.8b01217](https://doi.org/10.1021/acssuschemeng.8b01217).

Aqueous Raman spectra of arsenic speciation under various pH conditions; time dependent Raman spectra for the interaction of MAG and HEM with As species; representation of data in terms of area under the peak and concentration of species with time; XPS spectra of As 3d and Fe 2p before and after arsenic adsorption; XRD pattern of CM2LF; molecular basis model of the adsorption process; effect of competing ions on arsenic adsorption (PDF)

## AUTHOR INFORMATION

### Corresponding Author

\*E-mail: [pradeep@iitm.ac.in](mailto:pradeep@iitm.ac.in). Phone: +91-44 2257 4208. Fax: +91-44 2257 0545/0509.

### ORCID

Avula Anil Kumar: [0000-0001-6878-8736](https://orcid.org/0000-0001-6878-8736)

Thalappil Pradeep: [0000-0003-3174-534X](https://orcid.org/0000-0003-3174-534X)

### Notes

The authors declare no competing financial interest.

## ACKNOWLEDGMENTS

The authors thank Mohd. Azhardin Ganayee and Tripti Ahuja for their technical support in conducting the Raman measurements. The authors also thank Ganesan Paramasivam for his help in constructing a 2.6 nm sphere of 2-line ferrihydrite. Radha Gobinda Bhuin who is currently working at University Erlangen-Nürnberg, Egerlandstrasse, Germany, Sophisticated Analytical Instrument Facility at IIT Madras is thanked for the FTIR measurements. The authors thank the Department of Science and Technology (Government of India) for constantly supporting our research program on nanomaterials.

## REFERENCES

- (1) *Guidelines for Drinking-Water Quality*; WHO Press, World Health Organization: Switzerland, 2011.
- (2) Amini, M.; Abbaspour, K. C.; Berg, M.; Winkel, L.; Hug, S. J.; Hoehn, E.; Yang, H.; Johnson, C. A. Statistical modeling of global geogenic arsenic contamination in groundwater. *Environ. Sci. Technol.* **2008**, *42* (10), 3669.
- (3) Bhattacharya, P.; Polya, D.; Jovanovic, D., Eds. *Best Practice Guide on the Control of Arsenic in Drinking Water*; IWA Publishing: London, 2017; DOI: 10.2166/9781780404929.
- (4) Mahler, J.; Persson, I.; Herbert, R. B. Hydration of arsenic oxyacid species. *Dalton Transactions* **2013**, 42 (5), 1364.
- (5) Yan, W.; Vasic, R.; Frenkel, A. I.; Koel, B. E. Intraparticle reduction of arsenite (As(III)) by nanoscale zerovalent iron (nZVI) investigated with in situ X-ray absorption spectroscopy. *Environ. Sci. Technol.* **2012**, *46* (13), 7018.
- (6) Raven, K. P.; Jain, A.; Loeppert, R. H. Arsenite and arsenate adsorption on ferrihydrite: Kinetics, equilibrium, and adsorption envelopes. *Environ. Sci. Technol.* **1998**, *32* (3), 344.
- (7) Mota, A. M.; Pinheiro, J. P.; Simões Gonçalves, M. L. Electrochemical methods for speciation of trace elements in marine waters. *Dynamic Aspects. J. Phys. Chem. A* **2012**, *116* (25), 6433.
- (8) Ahmad, A.; et al. Arsenic Remediation of Drinking Water: An Overview. In *Best Practice Guide on the Control of Arsenic in Drinking Water*; Bhattacharya, P., Polya, D., Jovanovic, D., Eds.; IWA Publishing: London, 2017; DOI: 10.2166/9781780404929\_079.
- (9) Kumar, S.; Nair, R. R.; Pillai, P. B.; Gupta, S. N.; Iyengar, M. A. R.; Sood, A. K. Graphene oxide–MnFe<sub>2</sub>O<sub>4</sub> magnetic nanohybrids for efficient removal of lead and arsenic from water. *ACS Appl. Mater. Interfaces* **2014**, *6* (20), 17426.
- (10) Habuda-Stanić, M.; Nujić, M. Arsenic removal by nanoparticles: a review. *Environ. Sci. Pollut. Res.* **2015**, *22* (11), 8094.
- (11) Pena, M.; Meng, X.; Korfiatis, G. P.; Jing, C. Adsorption mechanism of arsenic on nanocrystalline titanium dioxide. *Environ. Sci. Technol.* **2006**, *40* (4), 1257.
- (12) Litter, M. I. Last advances on TiO<sub>2</sub>-photocatalytic removal of chromium, uranium and arsenic. *Current Opinion in Green and Sustainable Chemistry* **2017**, *6*, 150.
- (13) Tang, W.; Su, Y.; Li, Q.; Gao, S.; Shang, J. K. Superparamagnetic magnesium ferrite nanoadsorbent for effective arsenic (III, V) removal and easy magnetic separation. *Water Res.* **2013**, *47* (11), 3624.
- (14) Luo, X.; Wang, C.; Wang, L.; Deng, F.; Luo, S.; Tu, X.; Au, C. Nanocomposites of graphene oxide-hydrated zirconium oxide for simultaneous removal of As(III) and As(V) from water. *Chem. Eng. J.* **2013**, *220* (Supplement C), 98.
- (15) La, D. D.; Patwari, J. M.; Jones, L. A.; Antolasic, F.; Bhosale, S. V. Fabrication of a GNP/Fe–Mg binary oxide composite for effective removal of arsenic from aqueous solution. *ACS Omega* **2017**, *2* (1), 218.
- (16) Lin, S.; Yang, H.; Na, Z.; Lin, K. A novel biodegradable arsenic adsorbent by immobilization of iron oxyhydroxide (FeOOH) on the root powder of long-root Eichhornia crassipes. *Chemosphere* **2018**, *192*, 258.
- (17) Gustafsson, J. P.; Bhattacharya, P. Geochemical modelling of arsenic adsorption to oxide surfaces. *Trace Metals and other Contaminants in the Environment* **2007**, *9*, 159.
- (18) Dzombak, D. A.; Morel, F. M. M. *Surface Complexation Modeling: Hydrous Ferric Oxide*; John Wiley and Sons: New York, 1990.
- (19) Hiemstra, T.; Van Riemsdijk, W. H. A surface structural approach to ion adsorption: The charge distribution (CD) model. *J. Colloid Interface Sci.* **1996**, *179* (2), 488.
- (20) Goldberg, S.; Johnston, C. T. Mechanisms of arsenic adsorption on amorphous oxides evaluated using macroscopic measurements, vibrational spectroscopy, and surface complexation modeling. *J. Colloid Interface Sci.* **2001**, *234* (1), 204.
- (21) Müller, K.; Ciminelli, V. S. T.; Dantas, M. S. S.; Willscher, S. A comparative study of As(III) and As(V) in aqueous solutions and adsorbed on iron oxy-hydroxides by Raman spectroscopy. *Water Res.* **2010**, *44* (19), 5660.
- (22) Wang, Y.; Morin, G.; Ona-Nguema, G.; Juillot, F.; Guyot, F.; Calas, G.; Brown, G. E. Evidence for different surface speciation of arsenite and arsenate on green rust: An EXAFS and XANES study. *Environ. Sci. Technol.* **2010**, *44* (1), 109.
- (23) Sverjensky, D. A.; Fukushima, K. A predictive model (ETLM) for As(III) adsorption and surface speciation on oxides consistent with spectroscopic data. *Geochim. Cosmochim. Acta* **2006**, *70* (15), 3778.
- (24) Arts, D.; Abdus Sabur, M.; Al-Abadleh, H. A. Surface interactions of aromatic organoarsenical compounds with hematite nanoparticles using ATR-FTIR: Kinetic studies. *J. Phys. Chem. A* **2013**, *117* (10), 2195.
- (25) ThomasArrigo, L. K.; Mikutta, C.; Byrne, J.; Barmettler, K.; Kappler, A.; Kretzschmar, R. Iron and arsenic speciation and distribution in organic flocs from streambeds of an arsenic-enriched peatland. *Environ. Sci. Technol.* **2014**, *48* (22), 13218.
- (26) Fukushima, K.; Sverjensky, D. A. A predictive model (ETLM) for arsenate adsorption and surface speciation on oxides consistent with spectroscopic and theoretical molecular evidence. *Geochim. Cosmochim. Acta* **2007**, *71* (15), 3717.
- (27) Bhandari, N.; Reeder, R. J.; Strongin, D. R. Photoinduced oxidation of arsenite to arsenate on ferrihydrite. *Environ. Sci. Technol.* **2011**, *45* (7), 2783.
- (28) Ona-Nguema, G.; Morin, G.; Juillot, F.; Calas, G.; Brown, G. E. EXAFS analysis of arsenite adsorption onto two-line ferrihydrite, hematite, goethite, and lepidocrocite. *Environ. Sci. Technol.* **2005**, *39* (23), 9147.
- (29) Jubb, A. M.; Allen, H. C. Vibrational spectroscopic characterization of hematite, maghemite, and magnetite thin films produced by vapor deposition. *ACS Appl. Mater. Interfaces* **2010**, *2* (10), 2804.
- (30) Chandra, V.; Park, J.; Chun, Y.; Lee, J. W.; Hwang, I.-C.; Kim, K. S. Water-dispersible magnetite-reduced graphene oxide composites for arsenic removal. *ACS Nano* **2010**, *4* (7), 3979.
- (31) Rout, K.; Mohapatra, M.; Anand, S. 2-Line ferrihydrite: synthesis, characterization and its adsorption behaviour for removal of Pb(II), Cd(II), Cu(II) and Zn(II) from aqueous solutions. *Dalton Trans.* **2012**, 41 (11), 3302.
- (32) Sengupta, A.; Mallick, S.; Bahadur, D. Tetragonal nanostructured zirconia modified hematite mesoporous composite for efficient adsorption of toxic cations from wastewater. *J. Environ. Chem. Eng.* **2017**, *5* (5), 5285.
- (33) Carabante, I.; Mouzon, J.; Kumpiene, J.; Gran, M.; Fredriksson, A.; Hedlund, J. Reutilization of porous sintered hematite bodies as effective adsorbents for arsenic(V) removal from water. *Ind. Eng. Chem. Res.* **2014**, *53* (32), 12689.
- (34) Shipley, H. J.; Engates, K. E.; Guettner, A. M. Study of iron oxide nanoparticles in soil for remediation of arsenic. *J. Nanopart. Res.* **2011**, *13* (6), 2387.
- (35) Alijani, H.; Shariatnia, Z. Effective aqueous arsenic removal using zero valent iron doped MWCNT synthesized by in situ CVD method using natural  $\alpha$ -Fe<sub>2</sub>O<sub>3</sub> as a precursor. *Chemosphere* **2017**, *171* (Supplement C), 502.
- (36) Rashid, M.; Sterbinsky, G. E.; Pinilla, M. Á. G.; Cai, Y.; O'Shea, K. E. Kinetic and mechanistic evaluation of inorganic arsenic species adsorption onto humic acid grafted magnetite nanoparticles. *J. Phys. Chem. C* **2018**, ASAP, DOI: 10.1021/acs.jpcc.7b12438.
- (37) Kumar, A. A.; Som, A.; Longo, P.; Sudhakar, C.; Bhuin, R. G.; Gupta, S. S.; Anshup; Sankar, M. U.; Chaudhary, A.; Kumar, R.; Pradeep, T. Confined metastable 2-line ferrihydrite for affordable point-of-use arsenic-free drinking water. *Adv. Mater.* **2017**, *29* (7), 1604260.
- (38) Towe, K. M.; Bradley, W. F. Mineralogical constitution of colloidal "hydrous ferric oxides. *J. Colloid Interface Sci.* **1967**, *24* (3), 384.
- (39) Michel, F. M.; Ehm, L.; Antao, S. M.; Lee, P. L.; Chupas, P. J.; Liu, G.; Strongin, D. R.; Schoonen, M. A. A.; Phillips, B. L.; Parise, J. B. The structure of ferrihydrite, a nanocrystalline material. *Science* **2007**, *316* (5832), 1726.

- (40) Gout, R.; Pokrovski, G.; Schott, J.; Zwick, A. Raman spectroscopic study of arsenic speciation in aqueous solutions up to 275°C. *J. Raman Spectrosc.* **1997**, *28* (9), 725.
- (41) Yang, J.-C.; Yin, X.-B. CoFe<sub>2</sub>O<sub>4</sub>@MIL-100(Fe) hybrid magnetic nanoparticles exhibit fast and selective adsorption of arsenic with high adsorption capacity. *Sci. Rep.* **2017**, *7*, 40955.
- (42) Farrell, J.; Chaudhary, B. K. Understanding arsenate reaction kinetics with ferric hydroxides. *Environ. Sci. Technol.* **2013**, *47* (15), 8342.
- (43) Liu, C.-H.; Chuang, Y.-H.; Chen, T.-Y.; Tian, Y.; Li, H.; Wang, M.-K.; Zhang, W. Mechanism of arsenic adsorption on magnetite nanoparticles from water: Thermodynamic and spectroscopic studies. *Environ. Sci. Technol.* **2015**, *49* (13), 7726.
- (44) Catalano, J. G.; Zhang, Z.; Park, C.; Fenter, P.; Bedzyk, M. J. Bridging arsenate surface complexes on the hematite (012) surface. *Geochim. Cosmochim. Acta* **2007**, *71* (8), 1883.
- (45) Wagner, C. D.; Riggs, W. M.; Davis, L. E.; Moulder, J. F.; Mullenberg, G. E. *Handbook of X-ray Photoelectron Spectroscopy*; Physical Electronics Division, Perkin-Elmer Corporation: Minnesota, 1979.
- (46) Grosvenor, A. P.; Kobe, B. A.; Biesinger, M. C.; McIntyre, N. S. Investigation of multiplet splitting of Fe 2p XPS spectra and bonding in iron compounds. *Surf. Interface Anal.* **2004**, *36* (12), 1564.
- (47) Gupta, R. P.; Sen, S. K. Calculation of multiplet structure of core  $3p$  -vacancy levels. II. *Phys. Rev. B* **1975**, *12* (1), 15.
- (48) Beji, Z.; Sun, M.; Smiri, L. S.; Herbst, F.; Mangeney, C.; Ammar, S. Polyol synthesis of non-stoichiometric Mn-Zn ferrite nanocrystals: structural /microstructural characterization and catalytic application. *RSC Adv.* **2015**, *5* (80), 65010.
- (49) Jia, Y.; Xu, L.; Wang, X.; Demopoulos, G. P. Infrared spectroscopic and X-ray diffraction characterization of the nature of adsorbed arsenate on ferrihydrite. *Geochim. Cosmochim. Acta* **2007**, *71* (7), 1643.
- (50) Pinney, N.; Kubicki, J. D.; Middlemiss, D. S.; Grey, C. P.; Morgan, D. Density functional theory study of ferrihydrite and related Fe-oxyhydroxides. *Chem. Mater.* **2009**, *21* (24), 5727.
- (51) Hiemstra, T.; Van Riemsdijk, W. H. A surface structural model for ferrihydrite I: Sites related to primary charge, molar mass, and mass density. *Geochim. Cosmochim. Acta* **2009**, *73* (15), 4423.

## Supporting Information

### Species-specific uptake of arsenic on confined metastable 2-line ferrihydrite:

#### A combined Raman-XPS investigation of the adsorption mechanism

*Chennu Sudhakar,<sup>†</sup> Avula Anil Kumar,<sup>†</sup> Radha Gobinda Bhui,<sup>†</sup> Soujit Sen Gupta,<sup>†</sup> Ganapati*

*Natarajan<sup>†</sup> and Thalappil Pradeep<sup>\*,†</sup>*

<sup>†</sup> DST Unit of Nanoscience (DST UNS) and Thematic Unit of Excellence (TUE), Department of Chemistry, Indian Institute of Technology Madras, Chennai 600036, India.

\* Corresponding author

Thalappil Pradeep: [pradeep@iitm.ac.in](mailto:pradeep@iitm.ac.in)

Thalappil Pradeep, DST Unit of Nanoscience (DST UNS) and Thematic Unit of Excellence (TUE), Department of Chemistry, Indian Institute of Technology Madras, Chennai 600036, India.

Tel.: +91-44 2257 4208; Fax: +91-44 2257 0545/0509

## SUPPORTING INFORMATION CONTENT

Total number of pages: 17

Total number of figures: 11

Total number of tables: 1

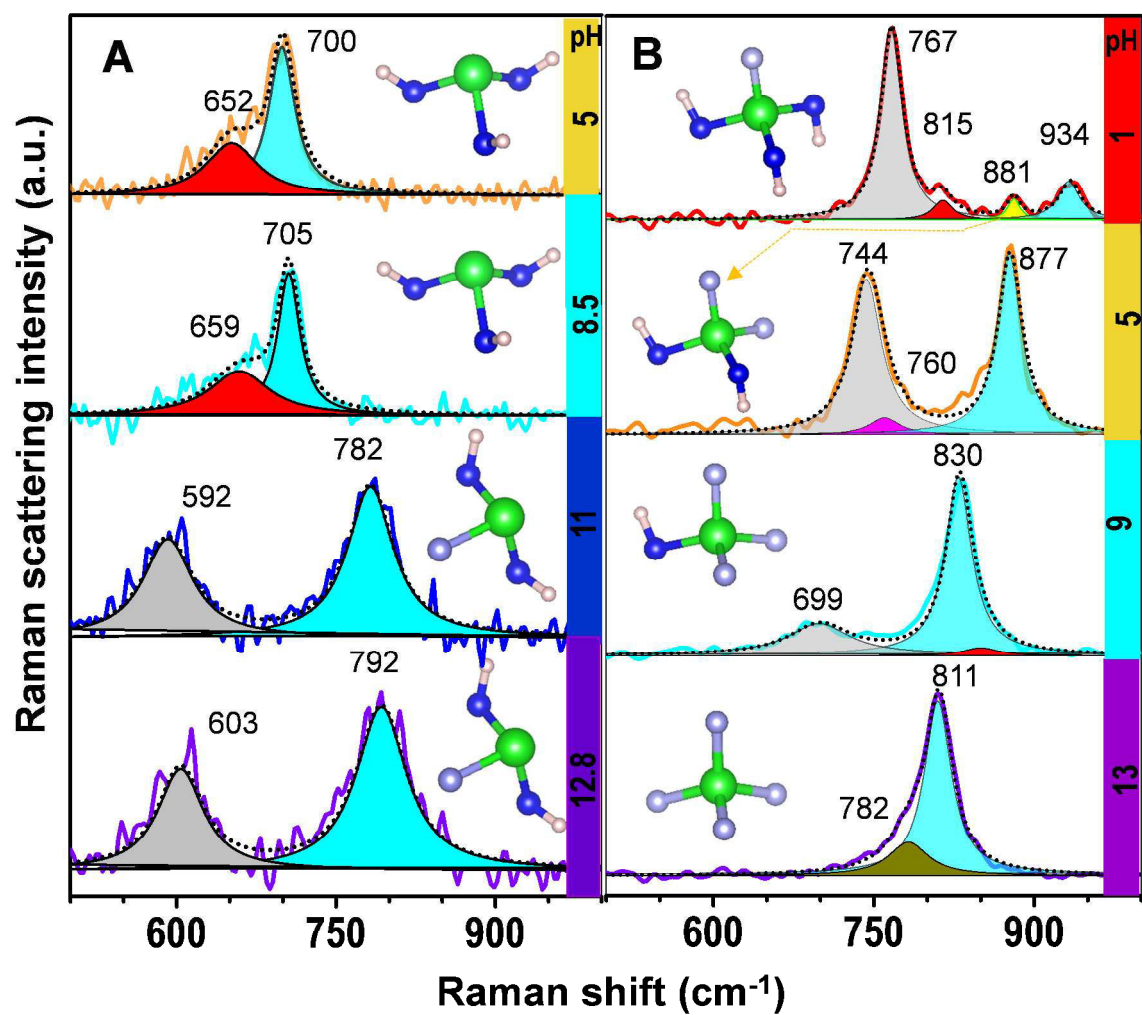


## TABLE OF CONTENTS

<b>Sl. No.</b>	<b>Items</b>	<b>Description</b>	<b>Page No.</b>
<b>1</b>	Supporting Information 1	Aqueous Raman spectra of arsenic species at various pH	3
<b>2</b>	Supporting Information 2	Time dependent Raman spectra for the interaction of MAG with As	4
<b>3</b>	Supporting Information 3	Time dependent Raman spectra for the interaction of HEM with As	5
<b>4</b>	Supporting Information 4	Reflection of Figure 3 data expressed in terms of area under the peak and concentration of species with time	6
<b>5</b>	Supporting Information 5	Reflection of Figure S2 data expressed in terms of area under the peak and concentration of species with time	8
<b>6</b>	Supporting Information 6	Reflection of Figure S3 data expressed in terms of area under the peak and concentration of species with time	9
<b>7</b>	Supporting Information 7	The correlation between area under the peak and concentration of species present in solution	10
<b>8</b>	Supporting Information 8	XPS spectra of As 3d and Fe 2p of HEM before and after arsenic adsorption	12
<b>9</b>	Supporting Information 9	The XRD pattern of CM2LF	13
<b>10</b>	Supporting Information 10	The molecular basis model of the adsorption process	14
<b>11</b>	Supporting Information 11	The effect of competing ions on arsenic adsorption	16

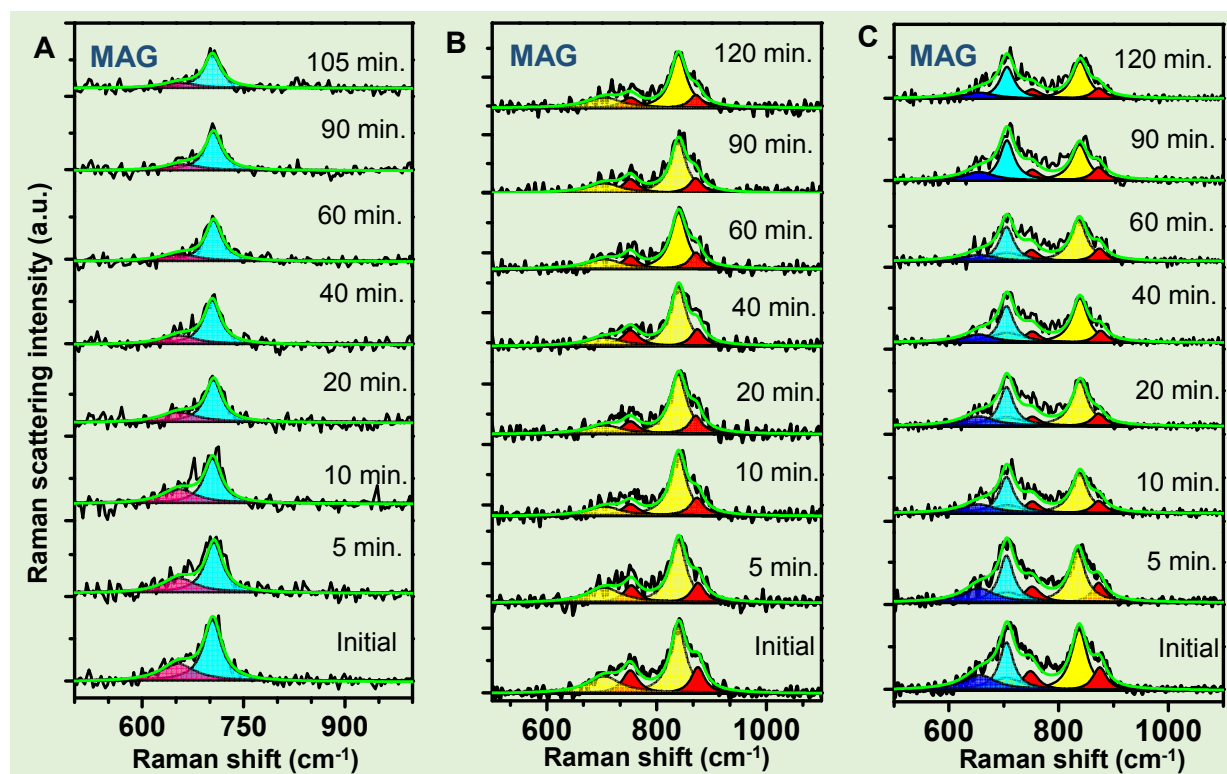
12	Supporting Table 1	XPS data of before and after arsenic adsorption	17
----	--------------------	---	----

### Supporting Information 1



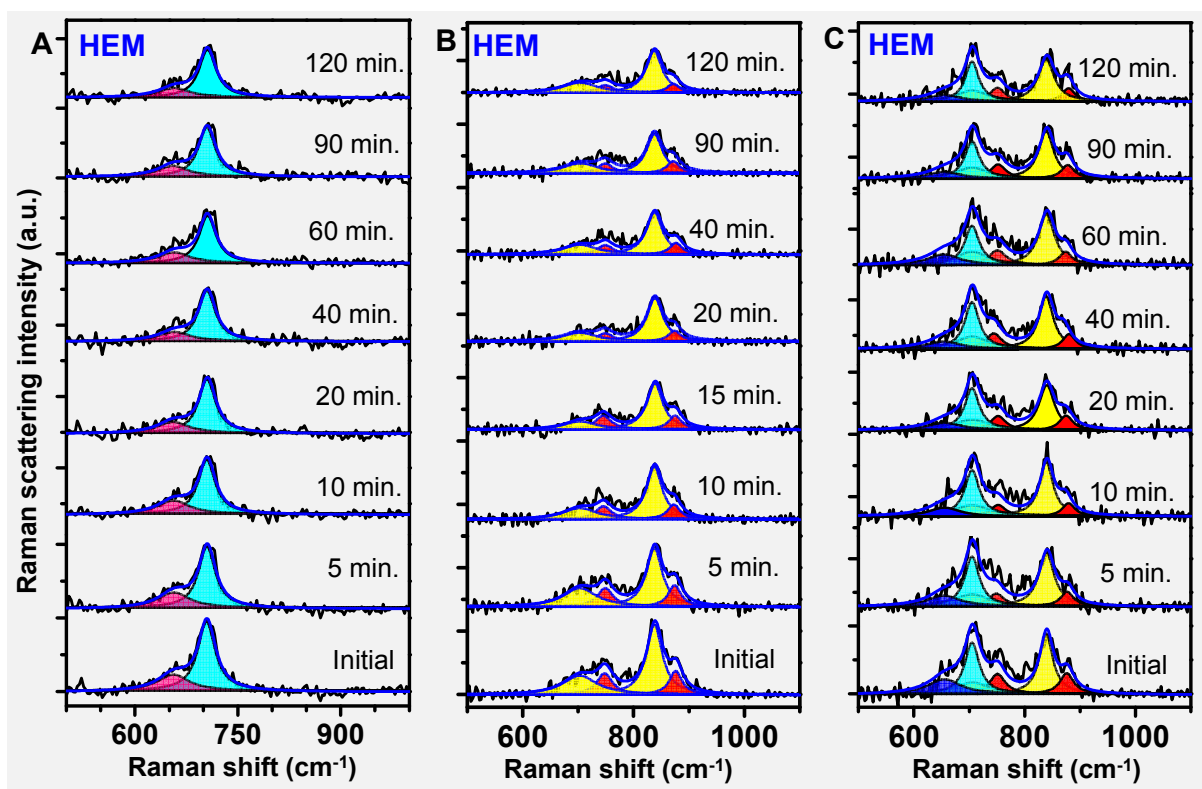
**Figure S1.** Aqueous Raman spectra. A) As(III), B) As(V) speciation under various pH conditions. pH values are indicated on the right.

## Supporting Information 2



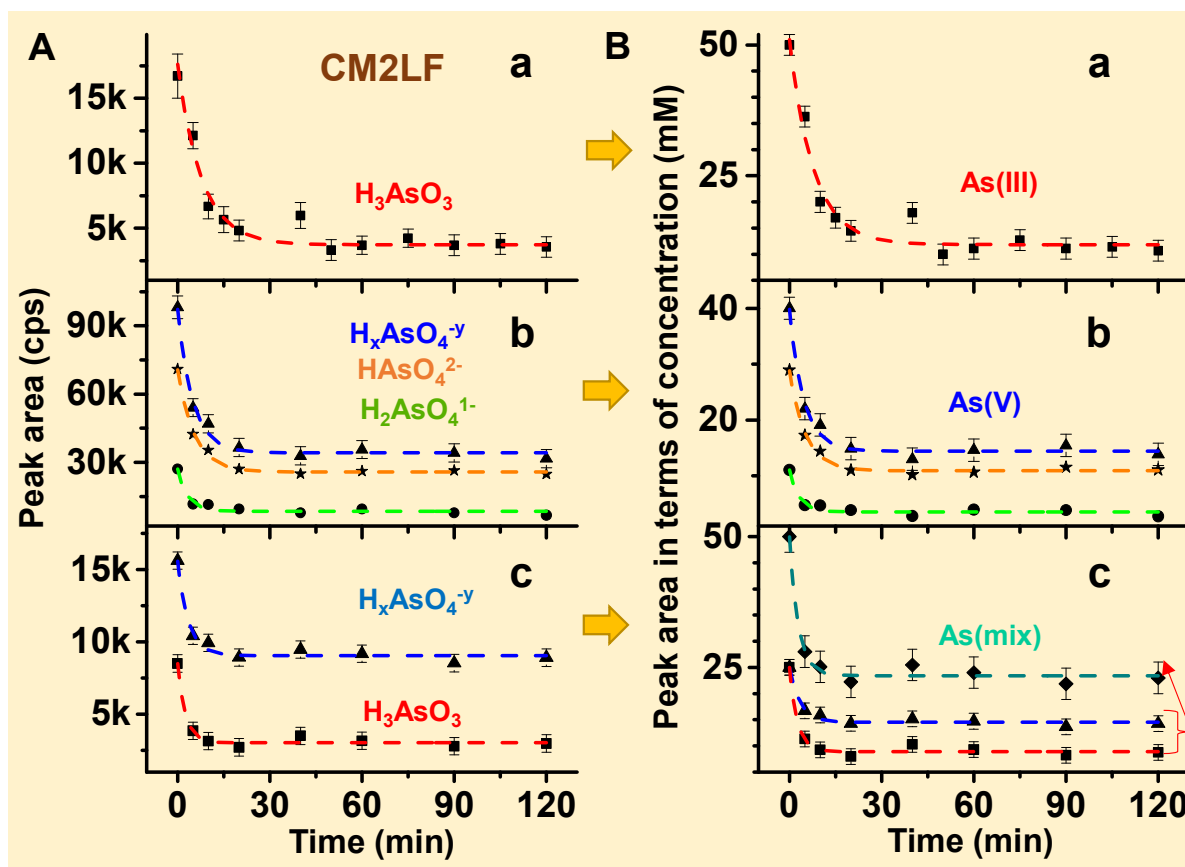
**Figure S2.** Time dependent Raman spectra for the interaction of MAG with A) As(III), B) As(V) and C) As(mix). Peaks have been fitted with their components.

### Supporting Information 3



**Figure S3.** Time dependent Raman spectra for the interaction of HEM with A) As(III), B) As(V) and C) As(mix). Peaks have been fitted with their components.

## Supporting Information 4



**Figure S4.** Representation of data presented in Figure 3 in terms of area under the peak (A) and concentration of species (B).

Adsorption kinetics can be expressed by using pseudo-second-order equation:

$$\frac{dq_t}{dt} = k(q_e - q_t)^2 \quad \text{Equation (1)}$$

Where,  $q_t$  is the adsorption capacity of given material at time  $t$ ,  $q_e$  is the adsorption capacity of the material at equilibrium and  $k$  is the pseudo-second-order rate constant, where initial rate is  $h = kq_e^2$ . Integration of equation (1) with limits  $t = 0$  to  $t$  and applying boundary conditions  $q_t = 0$  at  $t = 0$  gives,

$$\frac{t}{q_t} = \left(\frac{1}{q_e}\right)t + \frac{1}{kq_e^2} \quad \text{Equation (2)}$$

The values of  $k$  and  $q_e$  can be calculated by plotting  $t/q_t$  versus  $t$ .

#### **Conversion of concentration of solution (mM) into $q_t$ :**

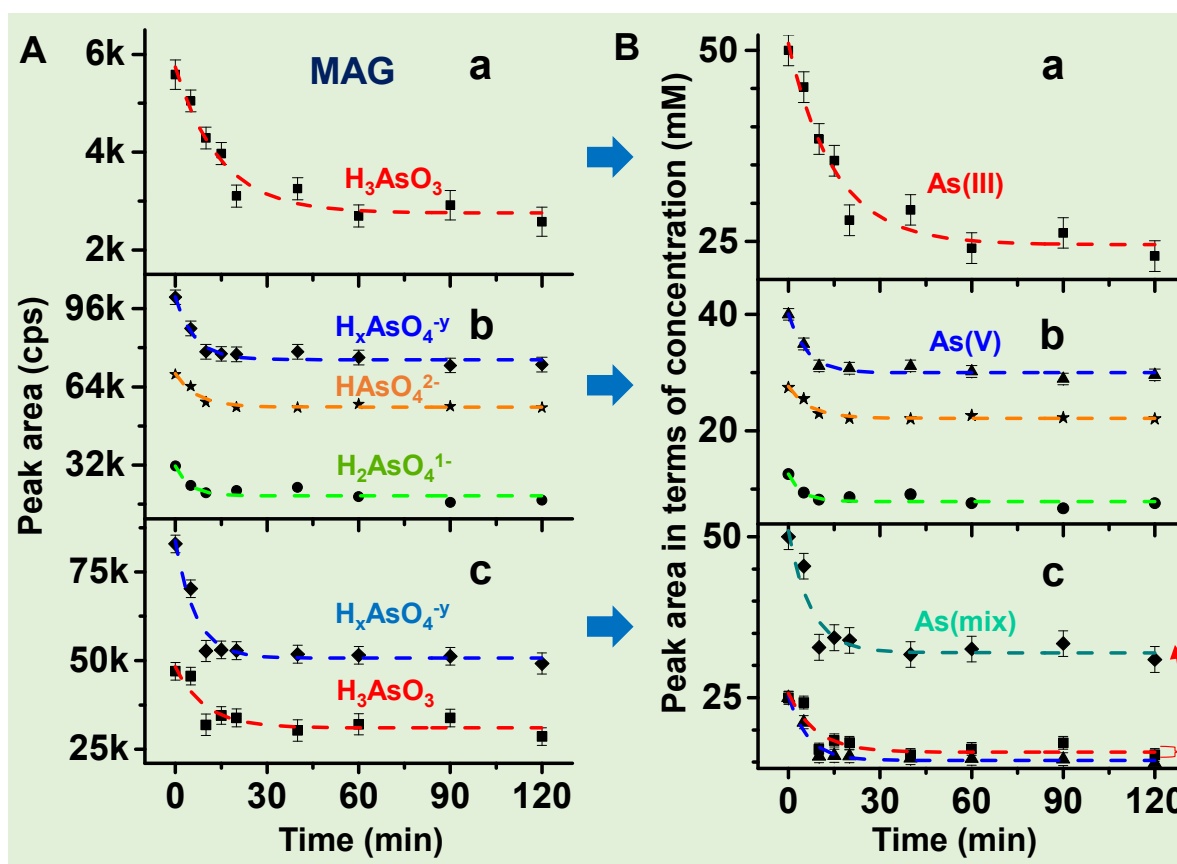
Concentration of solution ( $x$ )  $\rightarrow xM_{wt} \approx C_t$

$M_{wt}$  is the molecular weight of arsenic species present in solution.

$$q_t = \left(\frac{C_0 - C_t}{m}\right)V \quad \text{Equation (3)}$$

Where,  $C_0$  (mg/g) is the concentration of solution at time  $t = 0$ ,  $C_t$  (mg/g) is the concentration of solution at time  $t$ ,  $V$  is the volume of solution in liters (L) and  $m$  is the mass of material used in grams (g).

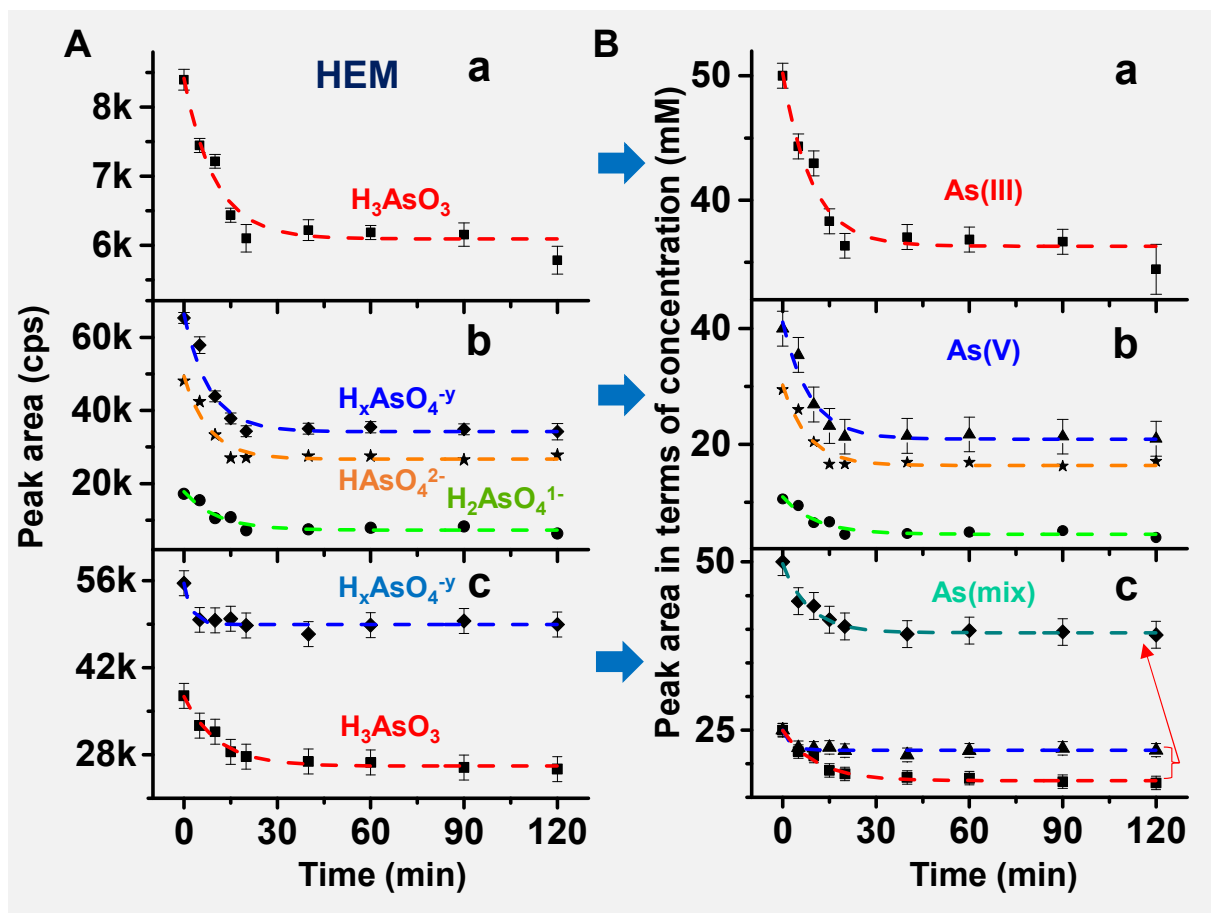
## Supporting Information 5



**Figure S5.** Representation of data presented in Figure S2 in terms of area under the peak (A) and concentration of species (B).

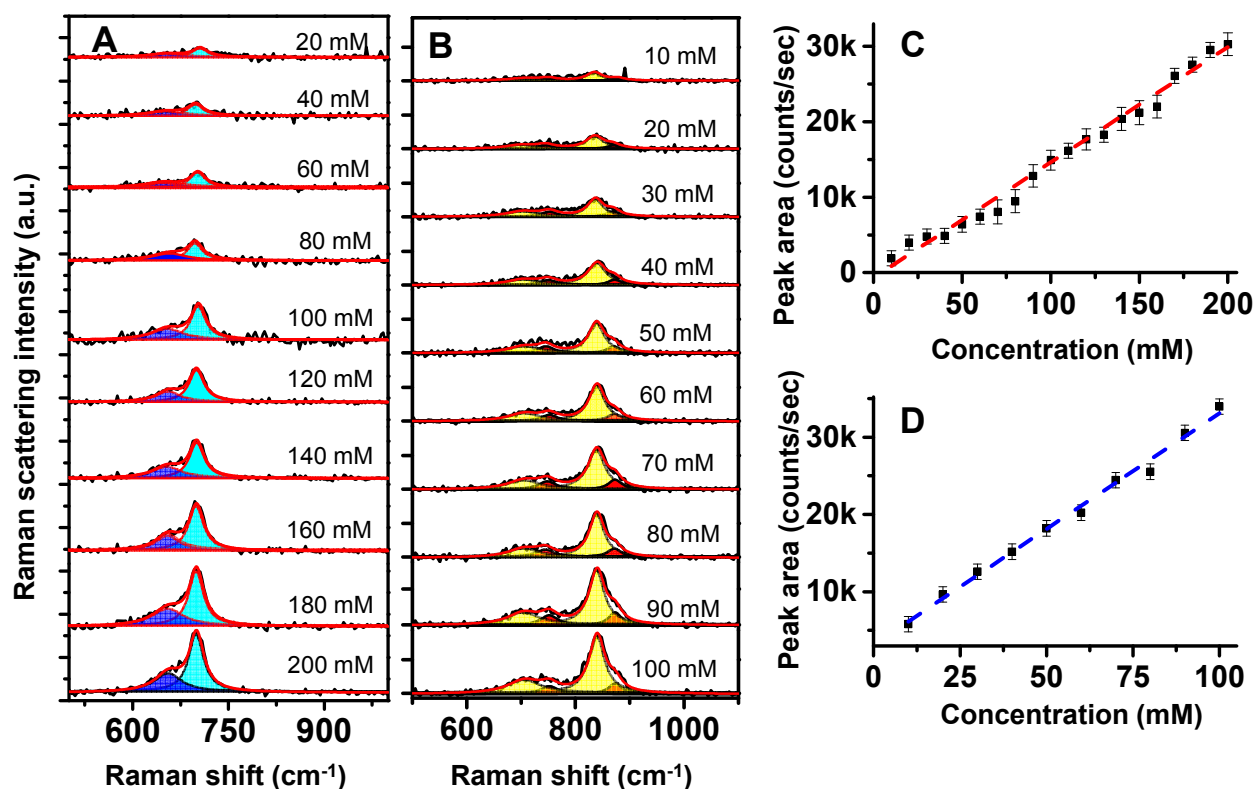


## Supporting Information 6



**Figure S6.** Representation of data presented in Figure S3 in terms of area under the peak (A) and concentration of species (B).

## Supporting Information 7



**Figure S7.** A) and B) Raman spectra for the various concentrations of pure As(III) and As(V) solutions at pH 7. C) Representation of data presented in A and D) Representation of data presented in B in terms of area under the peak Vs concentration of the species. Peaks have been fitted with their components.

**The correlation between area under the peak and concentration of solution:**

$$y = mx + c \quad \text{Equation (4)}$$

Equation 4 can be applied for both As(III) and As(V) solutions.

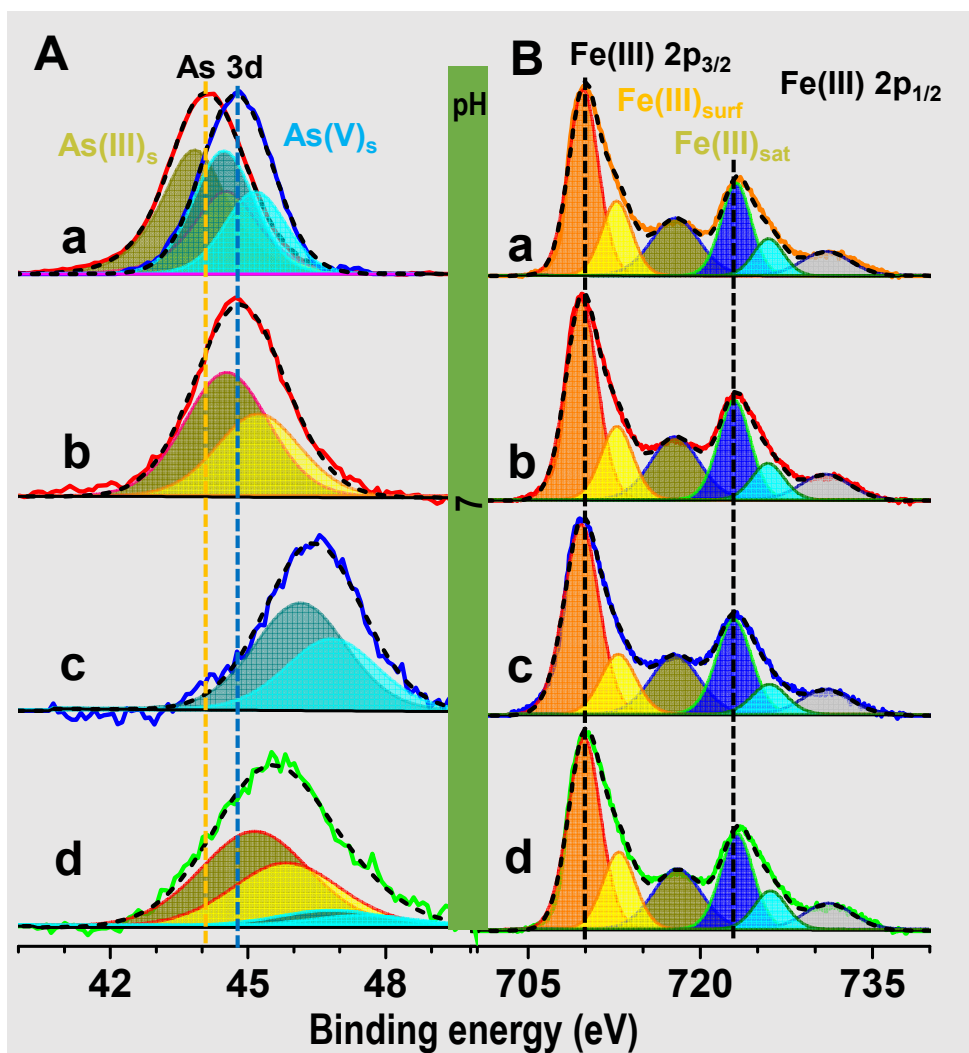
Where,  $y$  is area under the peak,  $x$  is concentration of the solution (mM),  $c$  is the  $y$  intercept and  $m$  is slope of line of the plot of  $y$  versus  $x$ . For calculating the unknown concentrations of solution, the  $(x, y)$  data points of line in Figure S7C and FigureS7D were taken as reference for As(III) and As(V), respectively.

**To find unknown concentration of solution ( $x_u$ ):**

$$x_u = \left( \frac{y_m - c}{m} \right) \quad \text{Equation (5)}$$

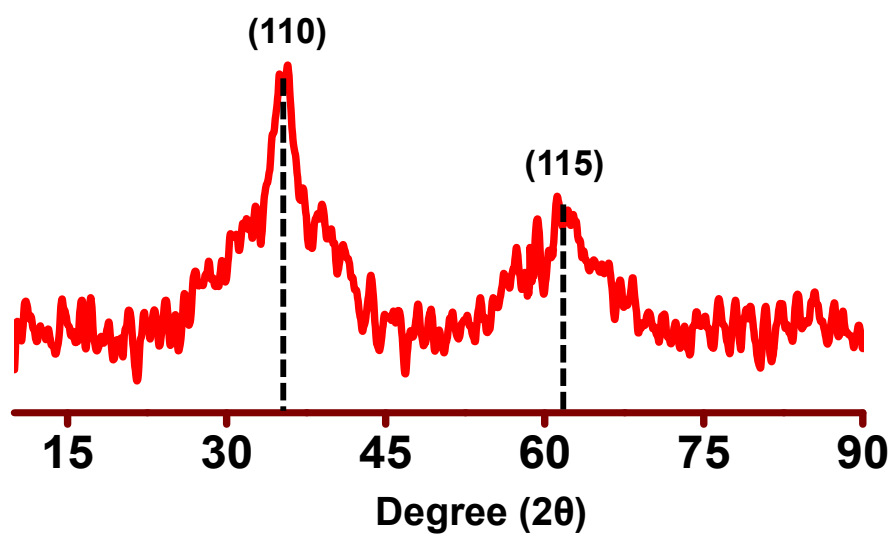
$y_m$  is area under the peak of unknown solution multiplied with laser intensity correction factor (K). K values vary with Raman measurement parameters during experiment. The each set of experimental data have different K value. K defined based on reference  $(x, y)$  data and the initial concentration of solution data  $(x_0, y_0)$ .

## Supporting Information 8



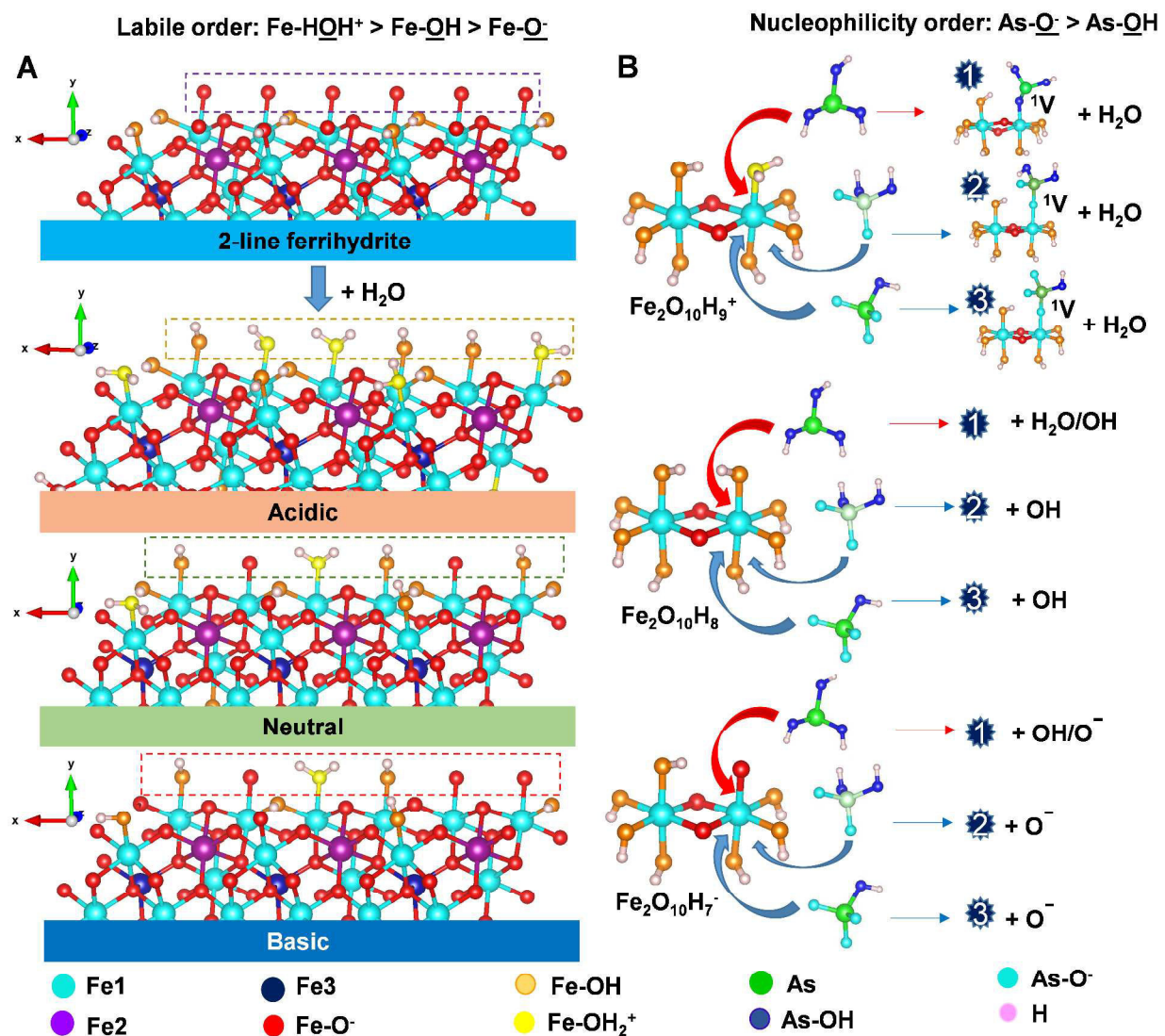
**Figure S8.** XPS spectrum of A) As 3d and B) Fe 2p. As 3d region of Aa) NaAsO<sub>2</sub> (red trace) and Na<sub>2</sub>HAsO<sub>4</sub>·7H<sub>2</sub>O (blue trace). Comparison of the positions may be noted. b) As(III), c) As(V) and d) As(mix) adsorbed on HEM. Spectra are fitted for the 3d<sub>5/2</sub> and 3d<sub>3/2</sub> features. Ba) HEM before adsorption, b), c) and d) are Fe 2p after adsorption, as before. Peaks have been fitted with their components.

### Supporting information 9



**Figure S9.** XRD pattern of CM2LF. Specific lines are labeled.

## Supporting information 10

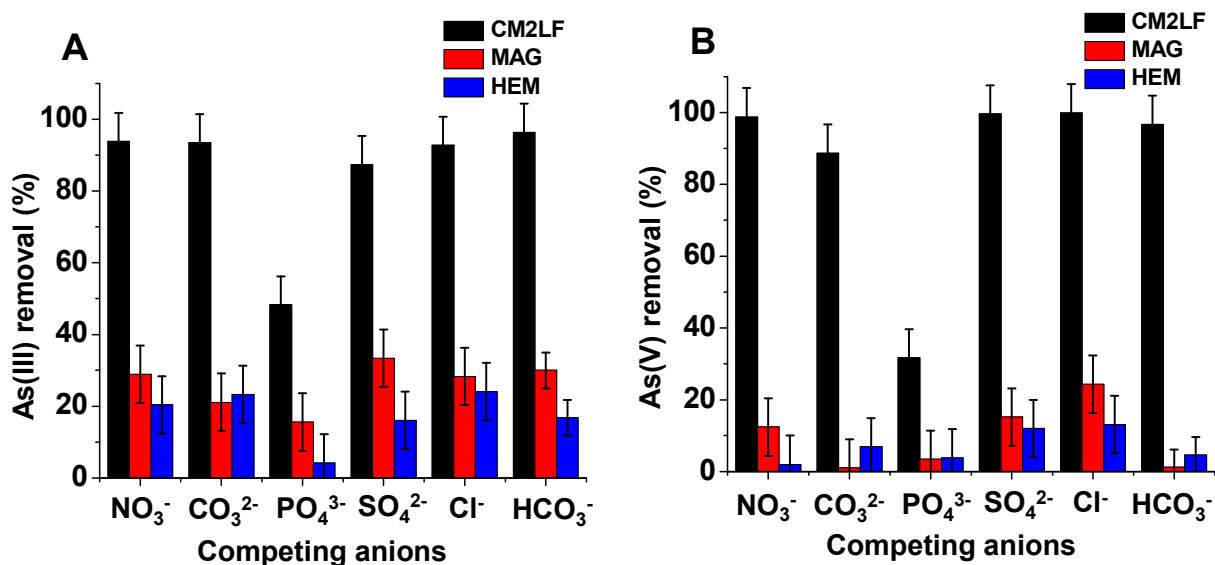


**Figure S10.** Schematic representation of the (010) plane of 2-line ferrihydrite surface under different conditions. A) Singly/doubly coordinated oxygens involving in protonation or deprotonation according to the solution pH. The singly coordinated surface oxygens ( $\text{H}_2\text{O}^+/-\text{O}^-/\text{OH}$ ) are shown in dotted rectangular boxes. B) The labile nature of singly coordinated oxygens of the cluster,  $\text{Fe}_2\text{O}_{10}\text{H}_y$  ( $y = 9/8/7$ ) involved in the ligand exchange mechanism with As(III) and As(V) under different conditions. In each case, the preference of complexation is in the order, 3

> 2 > 1. As(III) gives complex 1 ( $^1V$ ), while As(V) results in complex 2 ( $^1V$ ) and complex 3 ( $^1V$ ), respectively ( $^1V$ : Monodentate mononuclear complex). The 2-line ferrihydrite is composed of Fe1 and Fe2 centers which differ in the octahedral environment ( $FeO_6$ ) but, Fe3 center is in tetrahedral environment ( $FeO_4$ ) as shown in Figure 8A.



## Supporting information 11



**Figure S11.** The influence of competing ions on arsenic adsorption for CM2LF, MAG and HEM with an input concentration of  $1.0 \text{ mg L}^{-1}$  for both A) As(III) and B) As(V), separately. 100 mL arsenic contaminated deionized water was taken with 25 mg of CM2LF/MAG/HEM and the incubation time was kept as 150 min. The individual ion concentration taken was 1 mM, before spiking arsenic in water.

**Supporting Table 1**

**Table S1.** XPS data of before and after arsenic adsorption.

Energy levels (eV)	CM2LF	MAG	HEM
<b>Before As treatment</b>			
<b>As 3d</b>	NaAsO <sub>2</sub> : 44.2      Na <sub>2</sub> HAsO <sub>4</sub> .7H <sub>2</sub> O : 44.8		
	----	---	----
<b>Fe 2p<sub>3/2</sub></b>	710.1	Main peak : 710.4 Fe(II) : 709.5 Fe(III) : 711.2	710
<b>Fe 2p<sub>1/2</sub></b>	723.2	Main peak : 724.0 Fe(II) : 723.1 Fe(III) : 724.8	723.1
<b>After As(III) treatment</b>			
<b>As 3d</b>	45.1	44.3	44.7
<b>Fe 2p<sub>3/2</sub></b>	710.0	Main peak : 710.4 Fe(II) : 709.6 Fe(III) : 711.3	709.8
<b>Fe 2p<sub>1/2</sub></b>	723.1	Main peak : 724.0 Fe(II) : 723.2 Fe(III) : 724.9	722.9
<b>After As(V) treatment</b>			
<b>As 3d</b>	45.3	45.5	46.5
<b>Fe 2p<sub>3/2</sub></b>	712.2	Main peak : 710.7 Fe(II) : 709.5 Fe(III) : 711.2	709.8
<b>Fe 2p<sub>1/2</sub></b>	725.3	Main peak : 724.3 Fe(II) : 723.1 Fe(III) : 724.8	722.9



Cite this: *J. Mater. Chem. C*, 2018, **6**, 5754

Received 21st December 2017,  
Accepted 11th May 2018

DOI: 10.1039/c7tc05858f

rsc.li/materials-c

## Towards atomically precise luminescent Ag<sub>2</sub>S clusters separable by thin layer chromatography†

C. K. Manju,  Jyoti Sarita Mohanty, Depanjan Sarkar,  Sudhakar Chennu and Thalappil Pradeep \*

Here, we report the synthesis of monolayer protected, luminescent and atomically precise silver sulfide (Ag<sub>2</sub>S) clusters. Cluster formation was studied by varying the conditions of the reaction. Matrix assisted laser desorption ionization mass spectrometry (MALDI MS) was used to monitor the growth of clusters to nanoparticles (NPs). Clusters of different nuclearity were obtained at a lower temperature, and were efficiently separated by thin layer chromatography (TLC). One of the clusters was assigned as Ag<sub>158</sub>S<sub>79</sub>(SBB)<sub>32</sub>, where SBB is 4-*tert*-butylbenzyl mercaptan.

## Introduction

Colloidal semiconductor nanoparticles (NPs), also called quantum dots (QDs), have been considered as one of the major advances in materials science.<sup>1–3</sup> QDs attracted intense research interest since their discovery in the 1980s due to their unique physical and chemical properties which include broad absorption, narrow emission, and negligible photobleaching.<sup>4–6</sup> Cadmium chalcogenides (CdS and CdSe) have been the most studied nanocrystals.<sup>5</sup> But toxicity of cadmium based materials is a great concern in many of their potential applications. In recent years, researchers started focusing on the less toxic silver chalcogenide systems (Ag<sub>2</sub>E, where E = S, Se).<sup>7</sup> Silver chalcogenides have a low band gap (~1.0, 0.15 and 0.67 eV for bulk Ag<sub>2</sub>S, Ag<sub>2</sub>Se and Ag<sub>2</sub>Te, respectively) and are active in the near-infrared (NIR) region. NIR emitting QDs have great impact in biomedical diagnostics and therapy.<sup>8</sup> Ag<sub>2</sub>S NPs with tunable emission from 690 to 1200 nm were successfully synthesized by Jiang *et al.*<sup>9</sup> 2-Mercaptopropionic acid (2-MPA) coated NIR emitting Ag<sub>2</sub>S were prepared by Hocaoglu *et al.*<sup>10</sup> The same group reported the synthesis of emission tunable cyto/hemocompatible NIR emitting Ag<sub>2</sub>S QDs by *meso*-2,3-dimercapto succinic acid (DMSA) decomposition.<sup>11</sup> Here DMSA acts as both the sulfur source and the protecting agent. Hong *et al.* showed *in vivo* fluorescence imaging with Ag<sub>2</sub>S quantum dots in the range of 900–1300 nm.<sup>12</sup> Tunable visible to NIR emitting Ag<sub>2</sub>S QDs were synthesized and used for integrin targeted cancer imaging by Tang *et al.*<sup>13</sup>

NPs having only a few atoms have structure and properties different from NPs and bulk materials.<sup>14,15</sup> NPs of this kind are known as nanoclusters, which have to be treated differently. Synthesis of atomically precise clusters of noble metals gained great interest after the pioneering work of Brust and co-workers in 1994.<sup>16</sup> Clusters of gold and silver are the most studied systems of which there are many examples today.<sup>14,15</sup> Many of these structures have been solved by single crystal X-ray diffraction (XRD).<sup>17–21</sup> Clusters of silver and copper chalcogenides have been studied in detail by Fuhr *et al.* and they have summarized this work recently.<sup>22</sup> These coinage metal chalcogenide clusters were understood mainly from their crystal structures. The inherent insolubility of these clusters in organic solvents limited their nuclear magnetic resonance (NMR) and mass spectral characterization, which are the extensively used techniques in the case of noble metal clusters.<sup>23</sup> There are a few mass spectral studies on cadmium and zinc chalcogenide clusters as well.<sup>24–26</sup>

Nanoclusters of different materials find applications in various fields like sensing, catalysis, bioimaging, *etc.* owing to their unique chemical and physical properties. In order to understand the unique optical and luminescence properties, pure materials are essential. Some of the synthetic methods result in differently sized clusters, which need further separation. Different methods like high-pressure liquid chromatography (HPLC), polyacrylamide gel electrophoresis (PAGE), solvent extraction, and thin layer chromatography (TLC) have been used for cluster separation.<sup>27–31</sup> Recently gel permeation chromatography was used for the separation of indium phosphide (InP) clusters from InP QDs.<sup>32</sup>

In this report, we describe the synthesis of highly soluble monolayer protected silver sulfide clusters. The influence of temperature of synthesis on the optical properties of the prepared clusters was studied. Cluster formation was investigated using mass spectrometry. Monodisperse clusters were obtained by tuning

DST Unit of Nanoscience (DST UNS) and Thematic Unit of Excellence, Department of Chemistry, Indian Institute of Technology Madras, Chennai 600036, India.

E-mail: pradeep@iitm.ac.in

† Electronic supplementary information (ESI) available: MALDI MS of solvent dependent cluster synthesis, MALDI MS of Ag<sub>2</sub>S-70 and TLC separated Ag<sub>2</sub>S-70, ESI MS of Ag<sub>2</sub>S-60 and TLC separated clusters, TEM images of TLC separated Ag<sub>2</sub>S-60 and EDS spectrum of Ag<sub>2</sub>S-80 cluster. See DOI: 10.1039/c7tc05858f

the temperature of the reaction. Here, for the first time, we show that mixed semiconductor clusters can be separated by simple TLC.

## Experimental section

### Materials and methods

All the chemicals used were commercially available and were used without further purification. Silver acetate ( $\text{CH}_3\text{COOAg}$ , 99.99%), sulfur powder (100 mesh 99.5%), octadecene (ODE, technical grade, 90%), oleyl amine (OA, technical grade, 70%) and 4-*tert*-butylbenzyl mercaptan (BBSH) were obtained from Sigma Aldrich, India. Toluene (99.5%) and tetrahydrofuran (THF, 99.5%) were purchased from Merck, India, and methanol (99.5%) was from Finar, India.

### Synthesis of cluster

Silver sulfide clusters were synthesized by a reported method used for the synthesis of mixed silver chalcogenide clusters.<sup>33</sup> About 0.1 mmol silver acetate and 4 mmol BBSH were taken in a three necked round bottom flask containing 5 ml ODE. This mixture was stirred for 1 h at 60 °C under continuous Ar purging followed by the addition of 0.05 mmol of sulfur powder to the mixture and it was stirred for 2 h. Then the reaction mixture was cooled to room temperature and the cluster was purified by methanol precipitation and centrifugation. The purified cluster was soluble in toluene, THF, DCM, DMF, *etc.* Clusters in toluene were used for further studies. Different clusters were synthesized by changing the temperature at which sulfur was added such as 70, 80 and 90 °C.

### TLC experiment

3  $\mu\text{l}$  of cluster samples were pipetted to the TLC plate and dried in air. After drying, the plate was eluted with THF/MeOH mixture. After the separation, the bands were cut from the TLC plate and extracted in THF.

### Instrumentation

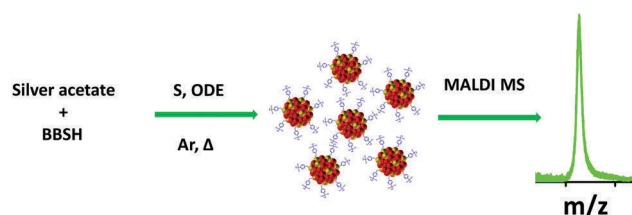
Absorbance spectra were measured using a PerkinElmer Lambda 25 instrument in the range of 200–1100 nm. Matrix assisted desorption ionization mass spectrometry (MALDI MS) studies were conducted using a Voyager-DE PRO Biospectrometry Workstation from Applied Biosystems. A pulsed nitrogen laser of 337 nm was used for MALDI MS studies. Mass spectrum was collected in both positive and negative ion modes. The matrix used was DCTB (*trans*-2-[3-(4-*tert*-butylphenyl)-2-methyl-2-propenylidene]malononitrile). High-resolution transmission electron microscopy (HRTEM) was performed using a JEOL 3010 (JEOL Ltd) instrument. The sample dissolved in toluene was drop casted on a carbon coated copper grid, dried at room temperature and was used for TEM measurements. Jobin Yvon NanoLog instrument was used for photoluminescence measurements. Thermogravimetric (TG) analyses were carried out on a PerkinElmer TGA7 instrument. FEI quanta 200 scanning electron microscope fitted with a tungsten filament was used for energy dispersive spectroscopy (EDS) measurements. All electrospray

ionization mass spectrometric (ESI MS) measurements were performed in an ion trap LTQ XL mass spectrometer of Thermo Scientific, San Jose, CA, USA. X-ray photoelectron spectroscopy (XPS) measurements were conducted using an Omicron ESCA probe spectrometer with polychromatic Mg K $\alpha$  X-rays ( $h\nu = 1253.6 \text{ eV}$ ).

## Results and discussion

A single step procedure was followed for the synthesis of  $\text{Ag}_2\text{S}$  clusters (Scheme 1). In a typical reaction, silver formed yellow silver thiolate with BBSH. After the addition of sulfur powder, the solution turned brownish, which was the result of the formation of  $\text{Ag}_2\text{S}$ . Properties and particle size of silver sulfide clusters can be tuned by different parameters such as temperature, silver:ligand and silver:sulfur ratios. Here cluster growth was studied by changing the temperature of the reaction as this is the most important parameter affecting crystal growth and properties of the resultant material.<sup>10,11</sup> Sulfur was added to the reaction mixture at 60, 70, 80 and 90 °C. The clusters synthesized at different temperatures are denoted as  $\text{Ag}_2\text{S}$ -60,  $\text{Ag}_2\text{S}$ -70,  $\text{Ag}_2\text{S}$ -80, and  $\text{Ag}_2\text{S}$ -90 hereafter.

Monolayer protected clusters are understood largely by mass spectrometry, which gives the atomic composition of the cluster. Molecular understanding of noble metal clusters is well known in the literature, whereas similar studies on semiconductor QDs are very few. Earlier reported MALDI MS of silver chalcogenide clusters showed a series of peaks in the higher mass region, along with the molecular ion peaks. This observation was explained in terms of the aggregation of clusters, after desorption of the SR group.<sup>34,35</sup> MALDI MS spectra of the clusters observed here are shown in Fig. 1 (full range MALDI MS spectra is shown in Fig. S1, ESI<sup>†</sup>). In this case, we did not observe similar kinds of cluster aggregation in MALDI MS. Only specific peaks were seen. Reactions at 60 and 70 °C gave a mixture of clusters in the range of 20 and 25.5 kDa (Fig. 1 orange and violet). When the temperature of the reaction was 60 °C, intensity of the 20 kDa cluster was higher. The peak at 25.5 kDa started increasing when the temperature of the reaction was raised to 70 °C. The appearance of two peaks in the MALDI MS was not due to cluster aggregation and will be explained later in the paper. A single mass species was obtained when the temperature of the reaction was increased to 80 °C (Fig. 1 pink trace). Further increase in temperature gave bigger NPs, which were not ionizable in MALDI (cyan trace). It was observed that the medium of synthesis also plays a significant role in cluster formation (Fig. S2, ESI<sup>†</sup>). Cluster synthesis was performed in different solvents like ODE,



**Scheme 1** Scheme used for the synthesis of BBSH protected luminescent silver sulfide clusters.

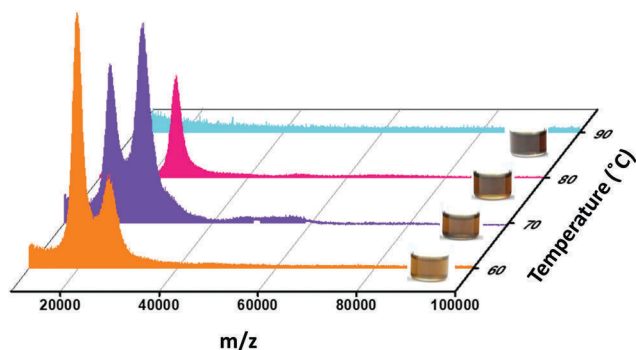


Fig. 1 MALDI MS spectrum of  $\text{Ag}_2\text{S}$  clusters synthesized at different temperatures (temperatures shown on the right). Inset shows the visible light photograph of the same.

toluene, and OA at 80 °C (at this temperature only a single product forms). While ODE gave a single product, toluene gave clusters with different nuclearity. In the case of OA, no cluster formation was observed, rather it resulted in NPs.

Absorption and emission properties of these clusters were studied to understand the effect of temperature on the particle size (Fig. 2).  $\text{Ag}_2\text{S}$ -60 showed a broad absorption around 660 nm. In the case of  $\text{Ag}_2\text{S}$ -70, the absorption was red shifted to 740 nm. As we increased the reaction temperature further, prominent absorption features were not observed. The photoluminescence spectrum of  $\text{Ag}_2\text{S}$ -60 and  $\text{Ag}_2\text{S}$ -70 showed two emission features one in the visible ( $\lambda_{\text{ex}} = 600$  nm) and another in the NIR ( $\lambda_{\text{ex}} = 700$  nm) region, which are due to mixed clusters. The 25.5 kDa cluster synthesized at 80 °C showed a NIR emission around 1020 nm ( $\lambda_{\text{ex}} = 700$  nm).  $\text{Ag}_2\text{S}$ -90 NPs emitted around 1080 nm ( $\lambda_{\text{ex}} = 700$  nm). Seemingly the higher

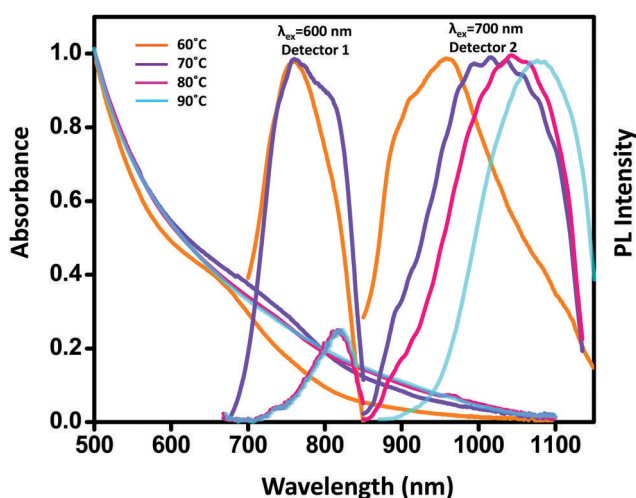


Fig. 2 Temperature dependent UV-vis and photoluminescence spectra of  $\text{Ag}_2\text{S}$  clusters. UV-vis and photoluminescence spectra of  $\text{Ag}_2\text{S}$ -60,  $\text{Ag}_2\text{S}$ -70,  $\text{Ag}_2\text{S}$ -80 and  $\text{Ag}_2\text{S}$ -90 clusters are given in orange, violet, pink and cyan traces respectively. Two detectors were used for measuring the PL data of the sample. In the first detector (Detector 1), the intensity falls down drastically above 800 nm due to the poor efficiency of this detector above this wavelength. The second detector (Detector 2) is sensitive only in the 850–1450 nm window.

temperature synthesis shows only one major emission due to one cluster and the low temperature synthesis shows two emission due to two clusters, which agreement with the mass spectra.

TLC has been shown as an efficient and simple technique for the separation of atomically precise gold clusters.<sup>30,31</sup> Here, we show the separation of mixed  $\text{Ag}_2\text{S}$  clusters using TLC. Good separation was achieved using THF/methanol mixture (80 : 20) as the solvent (Fig. 3). Choice of solvent was important in the case of separation. When eluted with 100% THF, whole sample moved with the solvent front. The addition of proper ratio of methanol separated the cluster. An optical photograph of the TLC plate used for separation is shown in Fig. 3. The two bands were cut from the TLC plate and the bands were extracted by THF and used for characterization. MALDI MS was measured using the extracted sample which showed a single peak for individual bands (Fig. 3). Band one was the larger 25.5 kDa cluster and band two was the smaller 20 kDa cluster. As expected, the heavier cluster moved only a shorter length on the TLC plate. The TLC purified clusters were showing a peak representing the dimers of the cluster in MALDI MS. Similarly  $\text{Ag}_2\text{S}$ -70 cluster was also separated by TLC (Fig. S3, ESI†).

ESI MS of the cluster was measured for understanding the exact composition of the synthesized clusters. The clusters synthesized in this process were neutral leading to difficulty in ionization in ESI.† Ionization enhancers like cesium acetate were also used for enhancing the possibility of ionization. After the addition of ionization enhancers, we could observe some cluster fragments

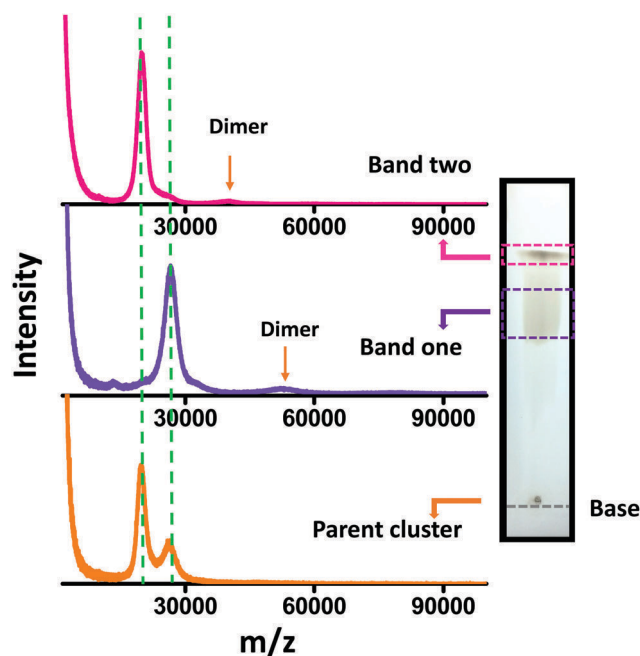
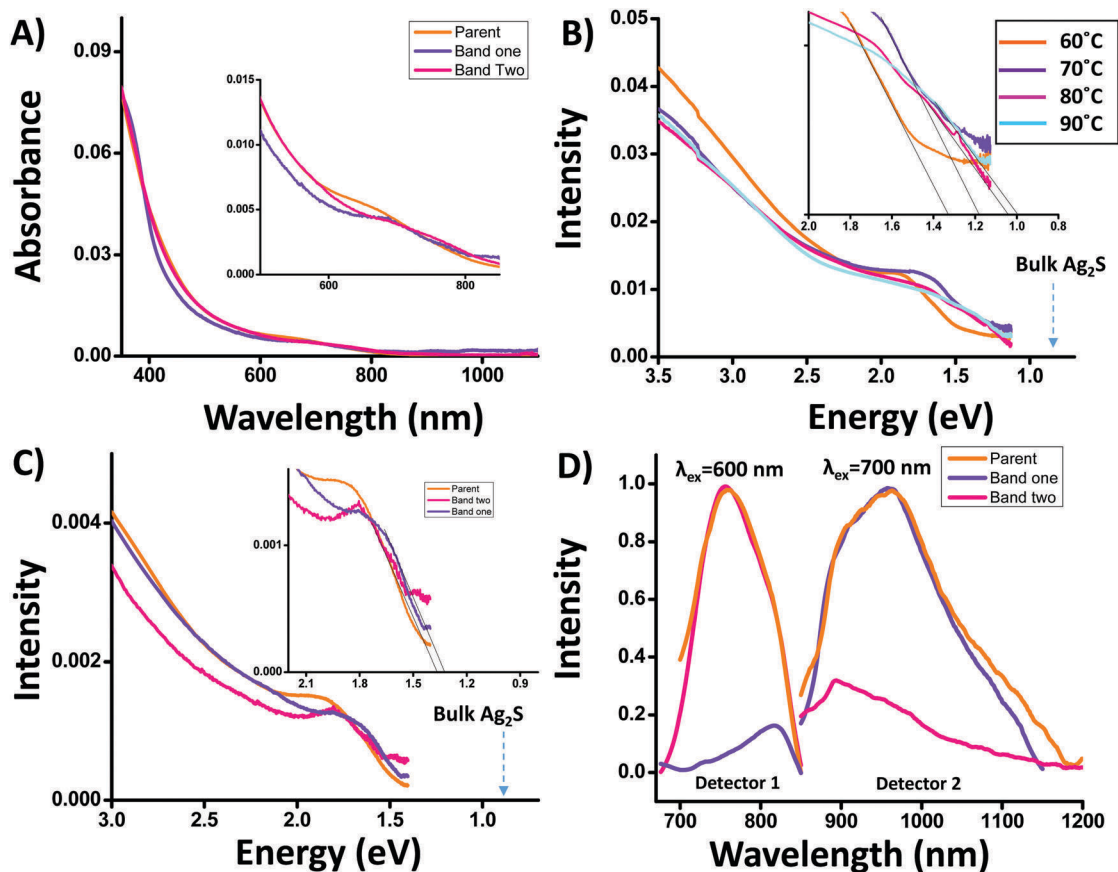


Fig. 3 TLC separation of  $\text{Ag}_2\text{S}$ -60 clusters. MALDI MS data of the parent sample (orange trace) and TLC separated clusters (violet trace shows a peak at 25.5 kDa is due to band one and pink trace shows a peak at 20 kDa is due to band two) confirming the separation by TLC. Optical photograph of the TLC plate used for the separation. Slight overlap of TLC bands resulted in a weak 25.5 kDa peak in the spectrum of band two. Some of the parent cluster get adsorbed strongly at the TLC plate and are not extractable are shown as a spot at the base.





**Fig. 4** (A) Comparative UV-vis spectra of parent (orange trace) and TLC separated (violet trace for band one and pink trace for band two)  $\text{Ag}_2\text{S}$ -60 clusters. (B) Jacobian corrected absorption spectra of different clusters synthesized. Inset shows the expanded spectra for band gap determination. (C) Jacobian corrected absorption spectra of the parent and TLC separated  $\text{Ag}_2\text{S}$ -60 clusters are compared. Spectra is expanded in the set for band gap calculation. (D) Photoluminescence spectra of parent and TLC separated clusters are compared. TLC band one was of a bigger cluster emitting in the NIR region. Band two was of smaller 20 kDa cluster which showed emission in the visible region. The sudden decrease in intensity above 800 nm for band one in the visible region is due to the poor detector efficiency in this window.

in the positive ion mode (Fig. S4, ESI†). Same fragment peaks were seen in the TLC separated clusters indicating that these are fragments of the cluster.

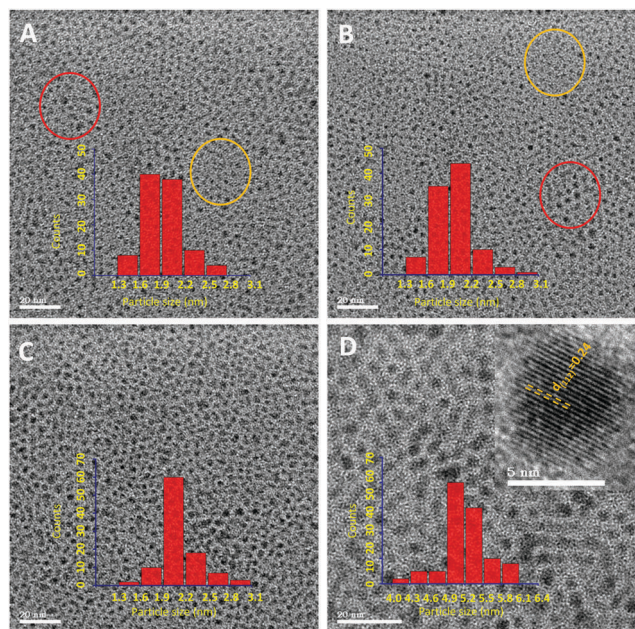
$\text{Ag}_2\text{S}$  is a narrow band gap semiconductor having a band gap of 0.9 eV. UV-vis spectra of parent clusters and those of separated bands are shown in Fig. 4A. The synthesized clusters showed a larger band gap compared to the bulk. Fig. 4B shows a comparative absorption spectra of these clusters plotted in terms of energy. This plot is obtained by doing the Jacobian correction (see ESI†).<sup>14</sup> Fig. 4C shows the Jacobian corrected plot for parent and TLC separated clusters. Extrapolation of the linear region of the energy plot to the horizontal axis gives the band gap of the synthesized clusters.  $\text{Ag}_2\text{S}$ -60, -70, -80 and -90 showed band gap values 1.33, 1.18, 1.08 and 1.00 eV respectively. TLC separated  $\text{Ag}_2\text{S}$ -60 clusters showed small change in band gap (Fig. 4C). Band one was 1.32 and band two was 1.36 eV. It was shown that the parent cluster has two emission peaks (Fig. 2). The bands collected after TLC gave single emission bands (Fig. 4D).

TEM images of these clusters showed mixed particle distribution for  $\text{Ag}_2\text{S}$ -60 (Fig. 5A) and  $\text{Ag}_2\text{S}$ -70 (Fig. 5B). In Fig. 5A and B different cluster populations are marked red circles for

larger and yellow circles for smaller clusters. Monodisperse particles were seen in the case of  $\text{Ag}_2\text{S}$ -80, which is in good agreement with the presence of single peak in MALDI MS (Fig. 5C).  $\text{Ag}_2\text{S}$  particles of 5 nm size were formed at 90 °C (Fig. 5D). HRTEM image of one particle is shown in the inset of Fig. 5D. TEM images of TLC separated clusters are shown in Fig. S5 (ESI†).

XPS analysis was performed to confirm the elemental composition of the cluster. Survey spectra showed the presence of silver and sulfur. Silver binding energy was matching with the reported values of monovalent silver.  $\text{Ag}_2\text{S}$ -60 parent cluster, TLC separated band 1 and band 2 showed Ag  $3d_{5/2}$  binding energies at 368.2, 368.4, and 368.3 eV and Ag  $3d_{3/2}$  binding energies at 374.3, 374.4, and 374.2 eV, respectively (Fig. 6A). Binding energy values were 162.1, 162.1, and 161.8 eV respectively for S  $2p_{3/2}$  and 163.4, 163.3, and 162.9 eV, respectively for S  $2p_{1/2}$ , for the above mentioned samples (Fig. 6B). These values are comparable to those of sulfide ( $\text{S}^{2-}$ ) species.

Thermogravimetric analysis of the  $\text{Ag}_2\text{S}$ -80 cluster was performed under nitrogen atmosphere. TG curve shows 23% weight loss, which is expected to be due to the organic ligand



**Fig. 5** TEM images of  $\text{Ag}_2\text{S}$ -60 (A),  $\text{Ag}_2\text{S}$ -70 (B),  $\text{Ag}_2\text{S}$ -80 (C), and  $\text{Ag}_2\text{S}$ -90 (D). In image (A) and (B), mixed clusters are marked by red (big) and yellow (small) circles. Image (C) is more uniform in size.  $\text{Ag}_2\text{S}$ -90 (image D) is of bigger nanoparticles, which are not observable in MALDI MS. HRTEM image of one particle is given in the inset of D. Lattice spacing of 0.24 nm is marked, which is the  $d_{(112)}$  plane of  $\text{Ag}_2\text{S}$ . Particle distribution for each sample is shown in each TEM image. Particle distribution was obtained by expanding the image and counting manually.

desorption (Fig. S6, ESI†). This means that 23% of the 25.45 kDa mass is due to the SBB ligand. The remaining mass is attributed to the  $\text{Ag}_2\text{S}$  core. It is also likely that the ligand can desorb as R-S-R, R-S-S-R or R-R. However, most of the desorption in thiolate protected clusters is seen as R-S-S-R.<sup>36,37</sup> Absence of molecular ion peaks in the ESI MS made the assignment of a molecular formula difficult. The mass loss of 23% in a 25.45 kDa cluster is 5854 Da. Therefore, the number of ligands can be

calculated by dividing this mass by thiol mass, which is 179.41. This suggests that there can be  $\sim 32$  ligands in the clusters. The remaining mass of 19 569 Da (after subtracting mass due to thiol) is due to the Ag-S core and this can contain  $\sim 79$   $\text{Ag}_2\text{S}$  units. The molecular composition can be inferred based on the factors such as the mass of the molecular ion, core size, etc. With the ligand loss determined from the TG, the total molecular formula may be given as  $\text{Ag}_{158}\text{S}_{79}(\text{SBB})_{32}$ . This is in agreement with the observed Ag:S ratio of 1:0.65 (Fig. S7, ESI†). A cluster of this kind having a nuclearity of  $\text{Ag}_{158}\text{S}_{79}(\text{SBB})_{32}$  accounts for all the experimental data.

## Summary

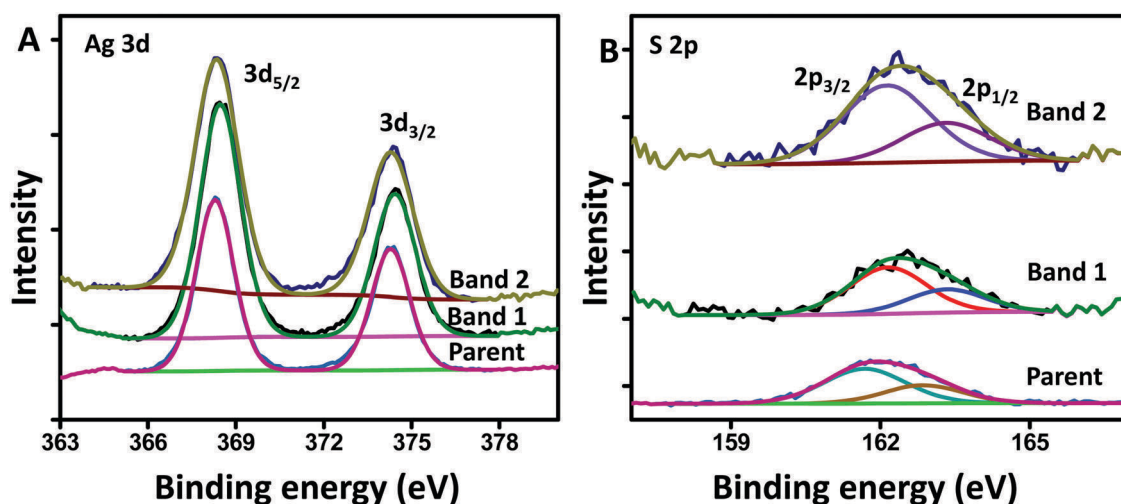
In conclusion, we synthesized a series of monolayer protected  $\text{Ag}_2\text{S}$  clusters. These clusters were highly soluble in organic solvents, which made the evaluation of solution phase properties possible. Clusters showed quantum confinement. Reactions at 60 °C and 70 °C gave a mixture of 20 kDa and 25.5 kDa clusters. Monodisperse 25.5 kDa clusters were obtained at 80 °C. These clusters were separated by simple thin layer chromatography. The separated clusters were soluble in common organic solvents. A tentative composition was proposed for one such cluster based on various analytical data.

## Conflicts of interest

There are no conflicts to declare.

## Acknowledgements

We thank the Department of Science and Technology, Government of India for constantly supporting our research program on nanomaterials. CKM and JSM thank the CSIR for a research fellowship. DS and SC thank IIT Madras for their fellowships.



**Fig. 6** XPS spectra  $\text{Ag}_2\text{S}$ -60 parent cluster and TLC separated clusters. (A) Specific regions of Ag (A) and S (B). Appropriate background subtraction and peak fitting have been performed.



## References

- 1 R. Gui, H. Jin, Z. Wang and L. Tan, *Coord. Chem. Rev.*, 2015, **296**, 91–124.
- 2 R. Freeman and I. Willner, *Chem. Soc. Rev.*, 2012, **41**, 4067–4085.
- 3 P. Wu, T. Zhao, S. Wang and X. Hou, *Nanoscale*, 2014, **6**, 43–64.
- 4 J. Chang and E. R. Waclawik, *RSC Adv.*, 2014, **4**, 23505–23527.
- 5 L. Jing, X. Huang, Y. Li, M. Gao, S. V. Kershaw, A. L. Rogach, Y. Li, X. Huang, Y. Li and M. Gao, *Chem. Rev.*, 2016, **116**, 10623–10730.
- 6 M. F. Frasco and N. Chaniotakis, *Sensors*, 2009, **9**, 7266–7286.
- 7 S. I. Sadovnikov and A. I. Gusev, *J. Mater. Chem. A*, 2017, **5**, 17676–17704.
- 8 Y. Zhang, G. Hong, Y. Zhang, G. Chen, F. Li, H. Dai and Q. Wang, *ACS Nano*, 2012, **6**, 3695–3702.
- 9 P. Jiang, Z.-Q. Tian, C.-N. Zhu, Z.-L. Zhang and D.-W. Pang, *Chem. Mater.*, 2012, **24**, 3–5.
- 10 I. Hocaoglu, M. N. Cizmeciyan, R. Erdem, C. Ozen, A. Kurt, A. Sennaroglu and H. Y. Acar, *J. Mater. Chem.*, 2012, **22**, 14674–14681.
- 11 I. Hocaoglu, F. Demir, O. Birer, A. Kiraz, C. Sevrin, C. Grandfils and H. Yagci Acar, *Nanoscale*, 2014, **6**, 11921–11931.
- 12 G. Hong, J. T. Robinson, Y. Zhang, S. Diao, A. L. Antaris, Q. Wang and H. Dai, *Angew. Chem., Int. Ed.*, 2012, **51**, 9818–9821.
- 13 R. Tang, J. Xue, B. Xu, D. Shen, G. P. Sudlow and S. Achilefu, *ACS Nano*, 2015, **9**, 220–230.
- 14 I. Chakraborty and T. Pradeep, *Chem. Rev.*, 2017, **117**, 8208–8271.
- 15 R. Jin, C. Zeng, M. Zhou and Y. Chen, *Chem. Rev.*, 2016, **116**, 10346–10413.
- 16 M. Brust, M. Walker, D. Bethell, D. J. Schiffrin and R. Whyman, *J. Chem. Soc., Chem. Commun.*, 1994, 801–802, DOI: 10.1039/C39940000801.
- 17 A. Das, T. Li, K. Nobusada, C. Zeng, N. L. Rosi and R. Jin, *J. Am. Chem. Soc.*, 2013, **135**, 18264–18267.
- 18 M. W. Heaven, A. Dass, P. S. White, K. M. Holt and R. W. Murray, *J. Am. Chem. Soc.*, 2008, **130**, 3754–3755.
- 19 P. D. Jadzinsky, G. Calero, C. J. Ackerson, D. A. Bushnell and R. D. Kornberg, *Science*, 2007, **318**, 430–433.
- 20 A. Desireddy, B. E. Conn, J. Guo, B. Yoon, R. N. Barnett, B. M. Monahan, K. Kirschbaum, W. P. Griffith, R. L. Whetten, U. Landman and T. P. Bigioni, *Nature*, 2013, **501**, 399–402.
- 21 C. P. Joshi, M. S. Bootharaju, M. J. Alhilaly and O. M. Bakr, *J. Am. Chem. Soc.*, 2015, **137**, 11578–11581.
- 22 O. Fuhr, S. Dehnen and D. Fenske, *Chem. Soc. Rev.*, 2013, **42**, 1871–1906.
- 23 S. Bestgen, O. Fuhr, B. Breitung, V. S. Kiran Chakravadhanula, G. Guthausen, F. Hennrich, W. Yu, M. M. Kappes, P. W. Roesky and D. Fenske, *Chem. Sci.*, 2017, **8**, 2235–2240.
- 24 Y. Wang, Y.-H. Liu, Y. Zhang, F. Wang, P. J. Kowalski, H. W. Rohrs, R. A. Loomis, M. L. Gross and W. E. Buhro, *Angew. Chem., Int. Ed.*, 2012, **51**, 6154–6157.
- 25 Y. Wang, Y. Zhang, F. Wang, D. E. Giblin, J. Hoy, H. W. Rohrs, R. A. Loomis and W. E. Buhro, *Chem. Mater.*, 2014, **26**, 2233–2243.
- 26 Y. Wang, Y. Zhou, Y. Zhang and W. E. Buhro, *Inorg. Chem.*, 2015, **54**, 1165–1177.
- 27 Y. Niihori, C. Uchida, W. Kurashige and Y. Negishi, *Phys. Chem. Chem. Phys.*, 2016, **18**, 4251–4265.
- 28 T. U. B. Rao and T. Pradeep, *Angew. Chem., Int. Ed.*, 2010, **49**, 3925–3929.
- 29 A. Ghosh, J. Hassinen, P. Pulkkinen, H. Tenhu, R. H. A. Ras and T. Pradeep, *Anal. Chem.*, 2014, **86**, 12185–12190.
- 30 C. Yao, S. Tian, L. Liao, X. Liu, N. Xia, N. Yan, Z. Gan and Z. Wu, *Nanoscale*, 2015, **7**, 16200–16203.
- 31 S. Tian, Y.-Z. Li, M.-B. Li, J. Yuan, J. Yang, Z. Wu and R. Jin, *Nat. Commun.*, 2015, **6**, 8667.
- 32 L. Xie, Y. Shen, D. Franke, V. Sebastian, M. G. Bawendi and K. F. Jensen, *J. Am. Chem. Soc.*, 2016, **138**, 13469–13472.
- 33 C. K. Manju, I. Chakraborty and T. Pradeep, *J. Mater. Chem. C*, 2016, **4**, 5572–5577.
- 34 C. Anson, A. Eichhoefer, I. Issac, D. Fenske, O. Fuhr, P. Sevilano, C. Persau, D. Stalke and J. Zhang, *Angew. Chem., Int. Ed.*, 2008, **47**, 1326–1331.
- 35 D. Fenske, C. E. Anson, A. Eichhoefer, O. Fuhr, A. Ingendoh, C. Persau and C. Richert, *Angew. Chem., Int. Ed.*, 2005, **44**, 5242–5246.
- 36 N. Nishida, M. Hara, H. Sasabe and W. Knoll, *Jpn. J. Appl. Phys., Part 1*, 1996, **35**, 5866–5872.
- 37 G. Kataby, T. Prozorov, Y. Koltypin, H. Cohen, C. N. Sukenik, A. Ulman and A. Gedanken, *Langmuir*, 1997, **13**, 6151–6158.

## Electronic supplementary information (ESI):

### **Towards atomically precise luminescent Ag<sub>2</sub>S clusters separable by thin layer chromatography**

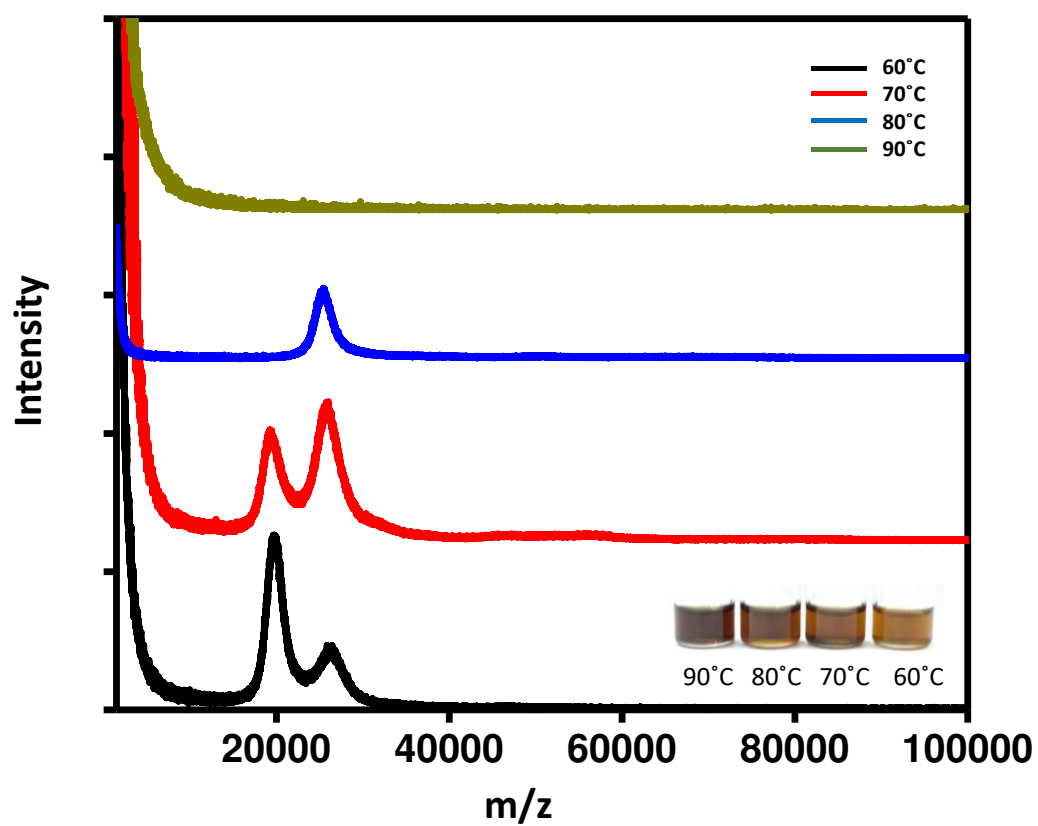
C. K. Manju, Jyoti Sarita Mohanty, Depanjan Sarkar, Sudhakar Chennu and Thalappil Pradeep<sup>a\*</sup>

*DST Unit of Nanoscience (DST UNS) and Thematic Unit of Excellence,  
Department of Chemistry, Indian Institute of Technology Madras,  
Chennai 600036, India.*

## Table of contents

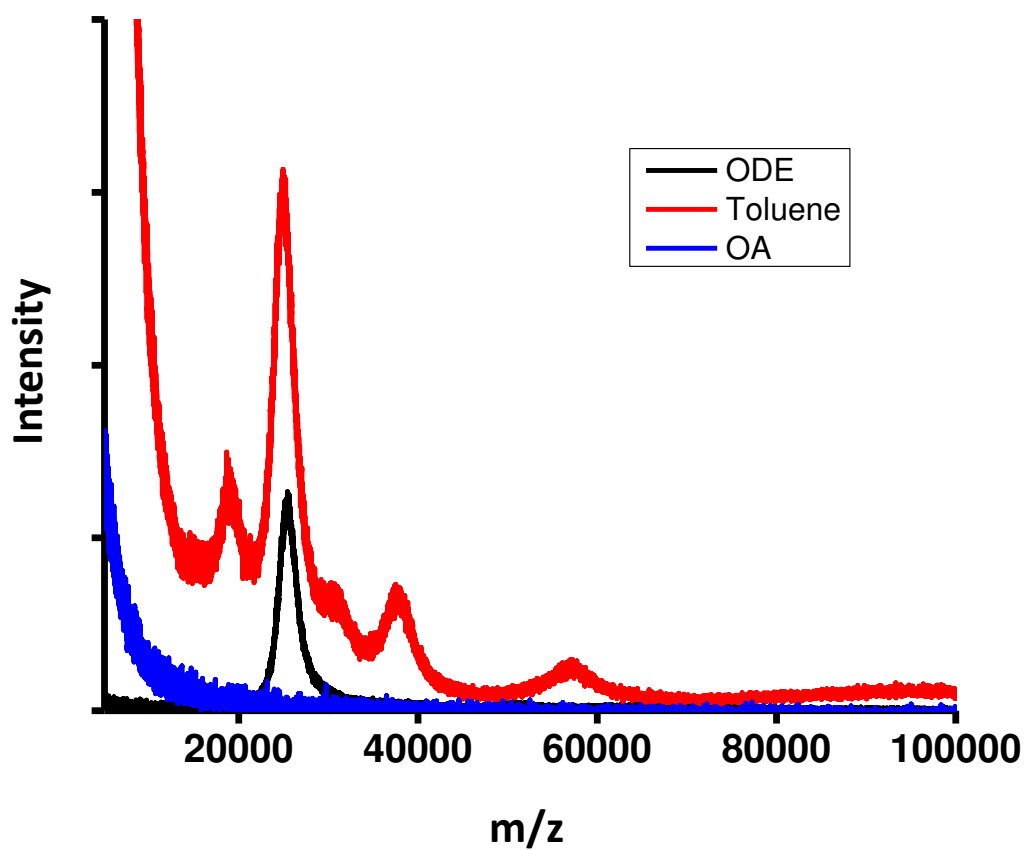
No	Description	Page No
<b>S1</b>	Full range MALDI MS of clusters synthesized at different temperature	2
<b>S2</b>	MALDI MS of solvent dependent cluster synthesis	3
<b>S3</b>	MALDI MS of Ag <sub>2</sub> S-70 and TLC separated Ag <sub>2</sub> S-70	4
<b>S4</b>	ESI MS of Ag <sub>2</sub> S-60 and TLC separated clusters	5
<b>S5</b>	TEM images of TLC separated Ag <sub>2</sub> S-60	6
<b>S6</b>	TG data of Ag <sub>2</sub> S-80	7
<b>S7</b>	EDS spectrum of Ag <sub>2</sub> S-80 cluster	8
<b>S8</b>	Jacobian Correction	8
<b>S9</b>	Cluster assignment	9

## Supporting information 1



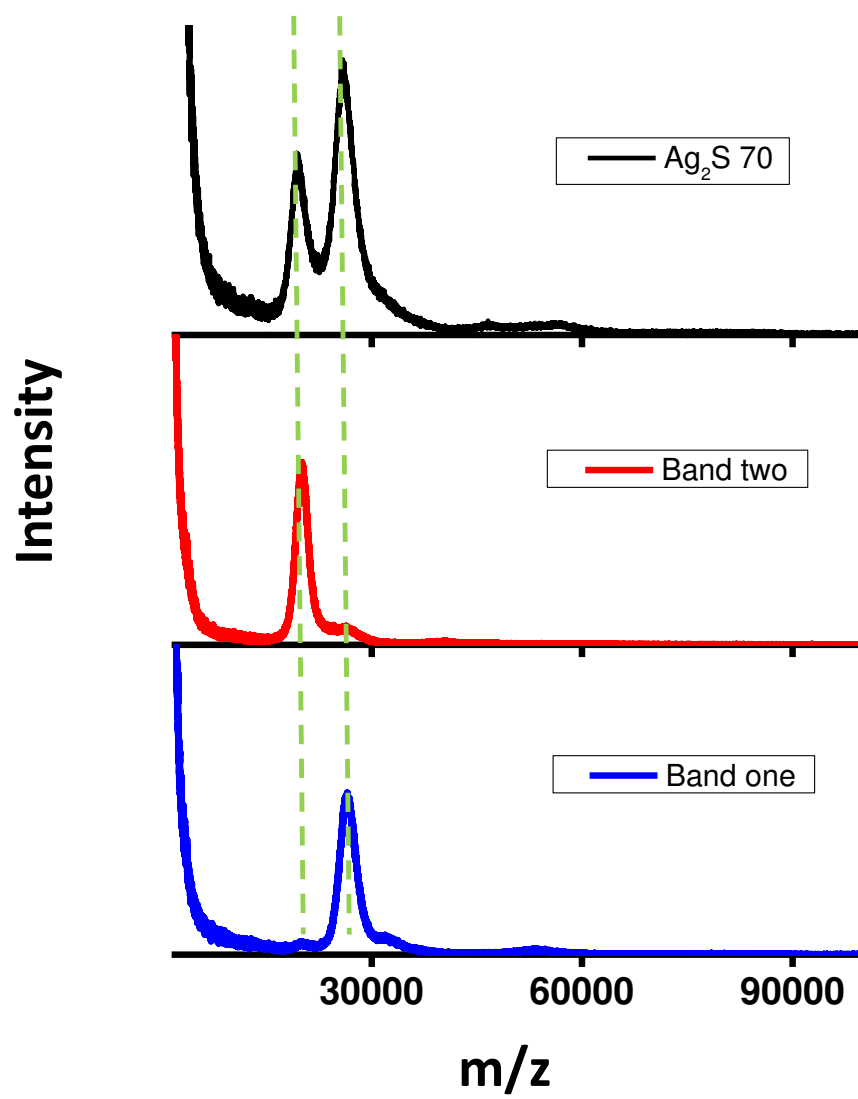
**Fig. S1.** Full range MALDI MS spectra of  $\text{Ag}_2\text{S}$  clusters synthesized at different temperature.

## Supporting information 2



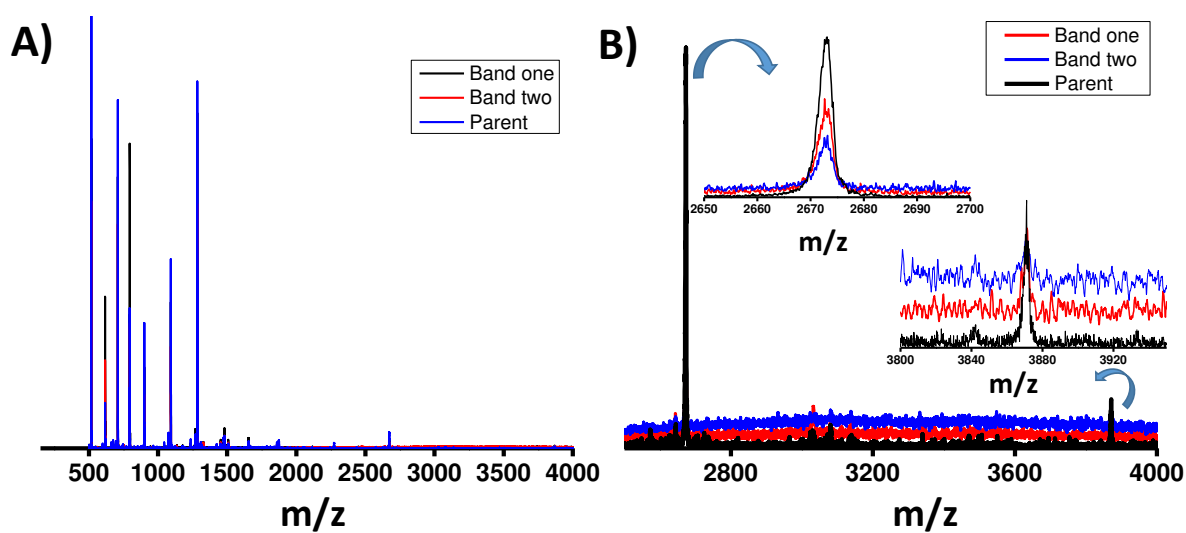
**Fig. S2** MALDI MS of solvent dependent  $\text{Ag}_2\text{S}$  cluster formation. Octadecene (ODE) is only one species. Use of toluene gives multiple population and oleylamine (OA) resulted in bigger quantum dots.

### Supporting information 3



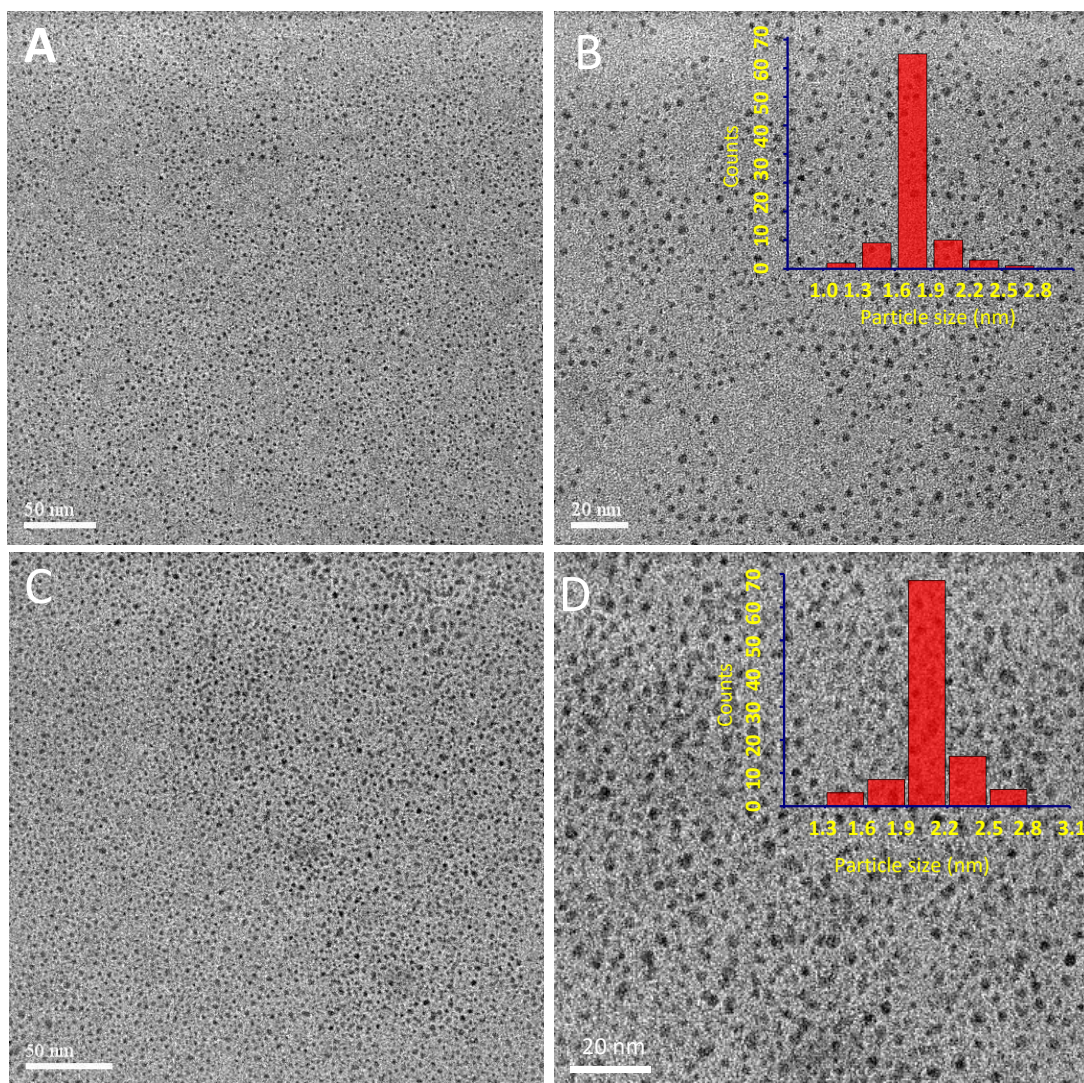
**Fig. S3** MALDI MS of parent Ag<sub>2</sub>S-70 and TLC separated bands.

## Supporting information 4



**Fig. S4** ESI MS of Ag<sub>2</sub>S-60 and TLC separated clusters. Cesium acetate was used as an ionization enhancer as the cluster was not having any charge. (A) Shows full range mass spectra were cesium clusters are seen in the lower range (below 2000 m/z). (B) MS shows cluster fragments in the positive mode. Specific regions are expanded in the inset.

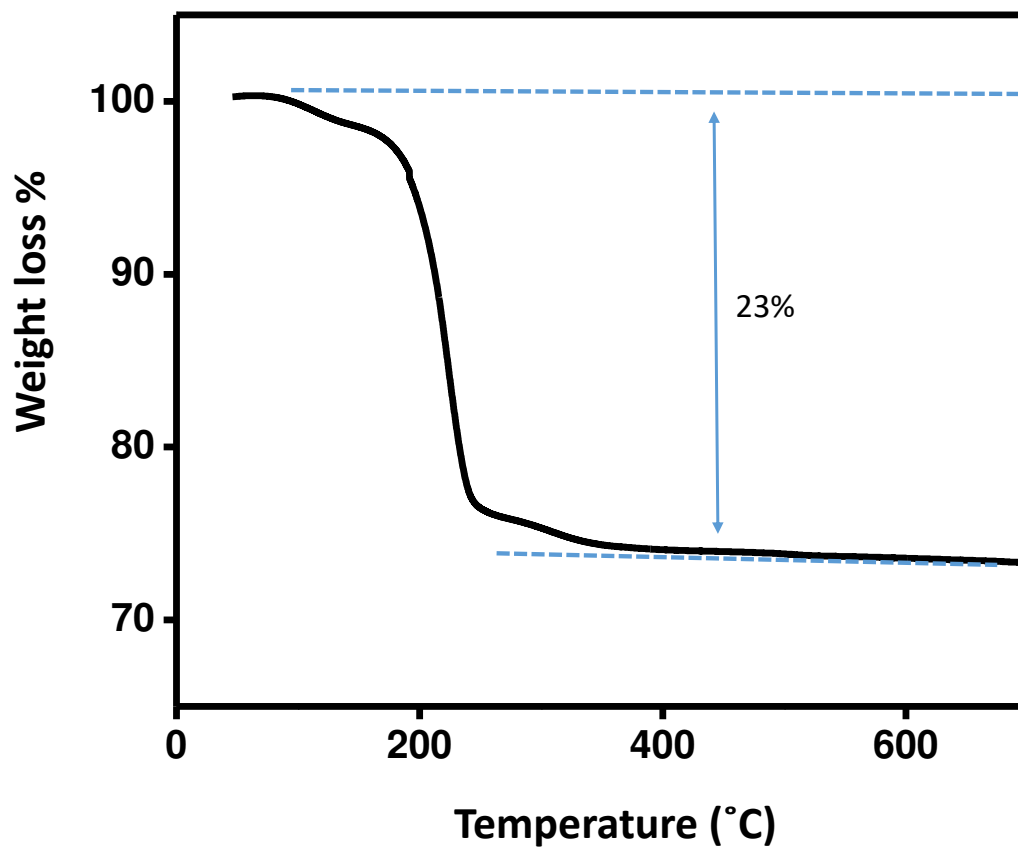
## Supporting information 5



**Fig. S5** TEM images of TLC separated  $\text{Ag}_2\text{S}$ -60 clusters. (A) and (B) Band two and (C) and (D) band one, at different magnifications.

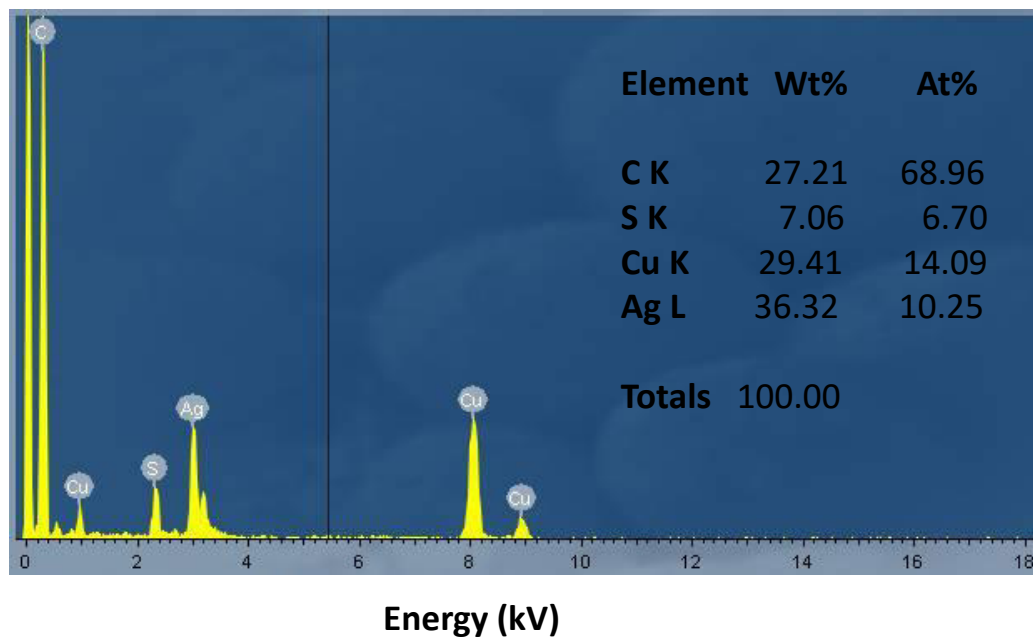


## Supporting information 6



**Fig. S6** TG data of Ag<sub>2</sub>S-80 showing 23% weight loss due to the protecting BBSH group.

## Supporting information 7



**Fig S7.** EDS spectrum of purified Ag<sub>2</sub>S-80 cluster. Ag:S ratio of 1:0.65.

## Supporting information 8

### Jacobian correction:

This uses the equations

$$E = hc/\lambda$$

$$f(E) dE = f(\lambda) d(\lambda)$$

$$f(E) = f(\lambda) (dE/d\lambda) = f(\lambda) (d/dE)(hc/E)$$

$$= f(\lambda) (hc/E^2)$$

The factor ( $hc/E^2$ ), known as the Jacobian factor, is used to scale the signal values along with wavelength conversion [wavelength (in nm) =  $1239.8/(\text{energy (eV)})$ ]. Normally, it is plotted by multiplying the absorbance value with the factor  $1/W^2$ , where W is the value in electronvolts corresponding to the wavelength in nanometers

## Supporting information 9

### Cluster assignment:

MALDI MS peak for  $\text{Ag}_2\text{S}$ -80 = 25450 Da

TG showed 23% weight loss.

This weight loss is due to organic ligand.

$$\begin{aligned} 23\% \text{ of } 25450 &= (23 \times 25450)/100 \\ &= 5854 = \text{Total ligand mass} \end{aligned}$$

$$\text{Mass of one SBB ligand} = 179.41$$

$$\text{No of ligands} = 5854/179.41$$

$$\sim 32$$

Cluster core mass is calculated by subtracting the total ligand mass from cluster mass

$$\text{This is} = 25450 - 5854 = 19596 \text{ Da}$$

This cluster core mass can contain 79  $\text{Ag}_2\text{S}$  units

$$\text{Mass of } \text{Ag}_2\text{S} = 248$$

$$19596/248 \approx 79$$

From this, the cluster core can be assigned as  $\text{Ag}_{158}\text{S}_{79}$ . Hence the total molecular formula may be given as  $(\text{Ag}_{158}\text{S}_{79})\text{SBB}_{32}$ . This is in agreement with the Ag:S ratio of 1:0.65 obtained from EDS measurement.

Cite this: *Nanoscale*, 2018, 10, 9851

Received 1st April 2018,

Accepted 7th May 2018

DOI: 10.1039/c8nr02629g

rsc.li/nanoscale

## Polymorphism of $\text{Ag}_{29}(\text{BDT})_{12}(\text{TPP})_4^{3-}$ cluster: interactions of secondary ligands and their effect on solid state luminescence†

 Abhijit Nag,<sup>a</sup> Papri Chakraborty,<sup>a</sup> Mohammad Bodiuzzaman,<sup>a</sup> Tripti Ahuja,<sup>a</sup>  
 Sudhadevi Antharjanam<sup>b</sup> and Thalappil Pradeep \*<sup>a</sup>

**We present the first example of polymorphism (cubic & trigonal) in single crystals of an atomically precise monolayer protected cluster,  $\text{Ag}_{29}(\text{BDT})_{12}(\text{TPP})_4^{3-}$ . We demonstrate that C–H... $\pi$  interactions of the secondary ligands (TPP) are dominant in a cubic lattice compared to a trigonal lattice, resulting in a greater rigidity of the structure, which in turn, results in a higher luminescence efficiency in it.**

Molecular species of noble metals often referred to as nanoclusters<sup>1–7</sup> (NC) or aspicules<sup>8,9</sup> have become an important research direction of advanced materials science. Some unprecedented structures and novel properties have been discovered, which enable new applications in catalysis, sensing, and optoelectronics.<sup>10–12</sup> Ligand structures on metal surfaces and their non-covalent interactions drive self-organization of such systems leading to single crystals which may also be regarded as nanoparticle superlattices.<sup>13–16</sup> While the primary ligands of a given cluster often protect the metal core, secondary ligands also contribute to the cluster stabilization for several of the emerging clusters.<sup>17–21</sup> Therefore, intercluster interactions mediated through primary ligands or secondary ligands or a combination become possible, making different cluster assemblies. In the following, we describe the crystallization of two polymorphs of a well-known cluster,<sup>18</sup>  $\text{Ag}_{29}(\text{BDT})_{12}(\text{TPP})_4^{3-}$ , by the dominant primary and secondary ligand interactions.

In the case of a well-known silver cluster,<sup>15</sup>  $\text{Ag}_{44}(\text{p-MBA})_{30}\text{Na}_4$ , abbreviated as  $\text{Ag}_{44}$ , crystallization of the cluster occurs through hydrogen bonding (HB), a characteristic of carboxylic acid-bearing entities. The hexagonal network of HB resembles that of acid crystals such as terephthalic acid,<sup>22</sup> tri-

mesic acid<sup>23</sup> and hexakis(4-carboxyphenyl)benzene.<sup>24</sup> As expected, protonation of the carboxylate groups on the cluster surface becomes a prerequisite of cluster formation. Similar non-covalent interactions can be observed in clusters such as  $\text{Au}_{102}$ ,<sup>14</sup>  $\text{Au}_{246}$ ,<sup>13</sup>  $\text{Au}_{103}$ ,<sup>16</sup> etc. (the formulae are abbreviated), where primary interactions are HB, C–H... $\pi$  and van der Waals (vdW) in nature, depending upon the ligands. These interactions, although weak, may have important electronic consequences such as luminescence. In this work, we explore the C–H... $\pi$  and vdW interactions within the two polymorphs (cubic and trigonal) of the  $[\text{Ag}_{29}(\text{BDT})_{12}(\text{TPP})_4]^{3-}$  cluster and their consequences in luminescence.

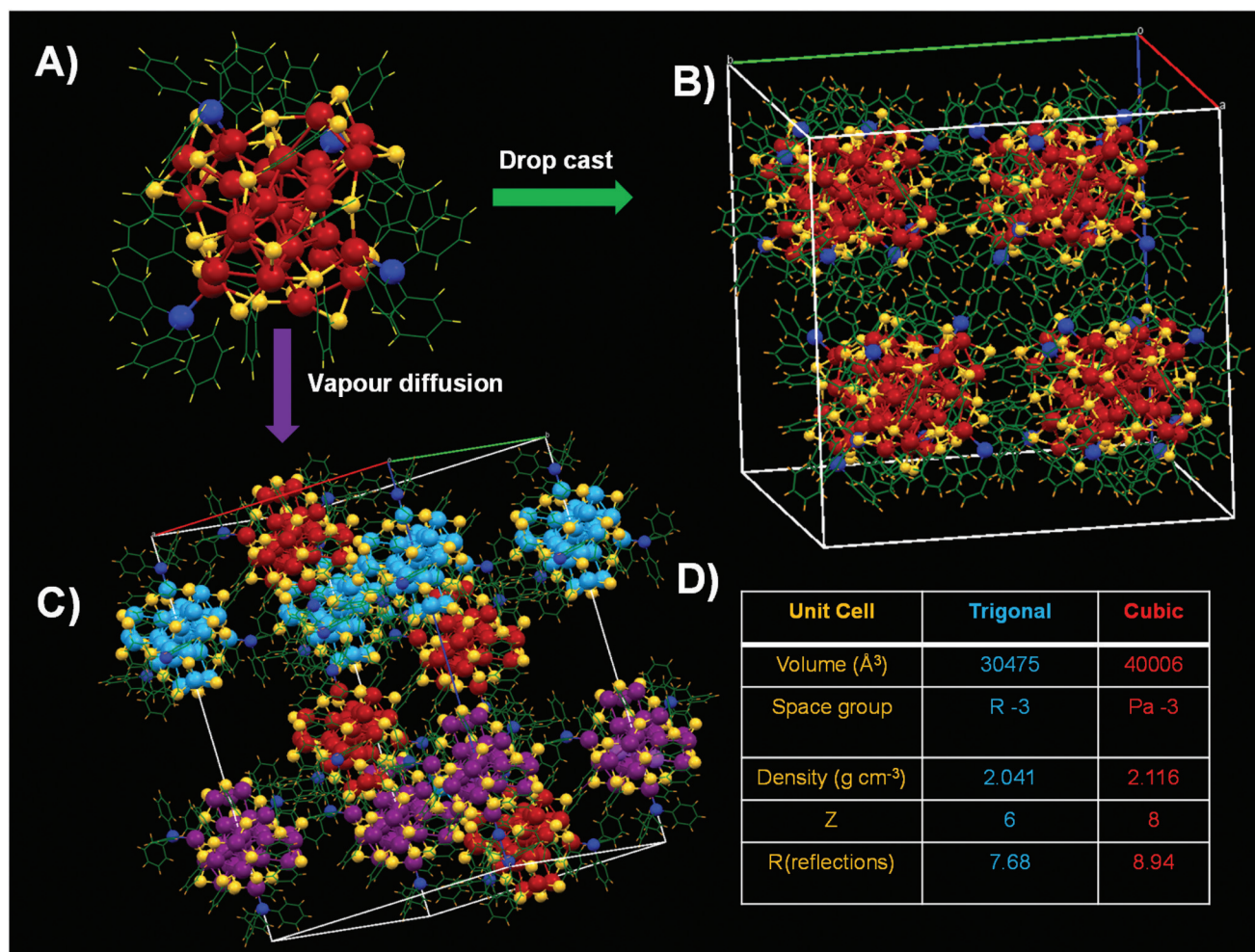
Bakr *et al.* reported the crystallization of  $\text{Ag}_{29}(\text{BDT})_{12}(\text{TPP})_4^{3-}$  by slow evaporation of a dimethylformamide (DMF) solution of the cluster, drop cast on a microscope slide.<sup>18</sup> More details of the crystallization processes are given in the ESI.† This method produced crystals which were packed in a cubic (C) lattice with a space group of  $\text{Pa}\bar{3}$  (Fig. 1B). We changed the crystallization method of the NC to the vapor diffusion of methanol into a DMF solution of the clusters ( $\sim 10 \text{ mg mL}^{-1}$ ). X-ray crystallographic analysis was performed at 296 K on the crystals obtained by this modified method. The crystal system was trigonal (T) (Fig. 1C) with the space group  $\text{R}\bar{3}$  (Fig. 1D). So,  $\text{Ag}_{29}(\text{BDT})_{12}(\text{TPP})_4^{3-}$  forms two polymorphs, T and C. Note that the color of the NCs of two polymorphs (orange for C and dark red for T) are visibly different under an optical microscope (Fig. S1†). The  $R_1$  value for the C system is 8.94 but that of the T case is 7.68. The volume, density, and Z (number of molecules per unit cell) for this new T polymorph of the cluster are less compared to the previously reported C system (Fig. 1D). The reduced density of the T makes it possible to incorporate solvent molecules (DMF and methanol) in the unit cell.

The molecular structure of the NC is the same as that of the previously reported NC. The NC is composed of an  $\text{Ag}_{13}$  icosahedral core. Twelve silver atoms (green) cap all the 12 Ag atoms of the icosahedron, giving rise to four tetrahedrally oriented trigonal prisms (Fig. S2†). The remaining four Ag atoms (blue) face-cap the core at four tetrahedral positions.

<sup>a</sup>DST Unit of Nanoscience (DST UNS) and Thematic Unit of Excellence, Department of Chemistry, Indian Institute of Technology Madras, Chennai 600036, India.  
E-mail: pradeep@iitm.ac.in; Fax: +91-44 2257-0545

<sup>b</sup>Sophisticated Analytical Instruments Facility (SAIF), Indian Institute of Technology Madras, Chennai 600036, India

†Electronic supplementary information (ESI) available. See DOI: 10.1039/c8nr02629g



**Fig. 1** (A) Crystal structure of Ag<sub>29</sub>(BDT)<sub>12</sub>(TPP)<sub>4</sub><sup>3-</sup>. (B) Trigonal unit cell of the NC obtained by the vapour diffusion method. (C) Cubic unit cell of the NC obtained by the drop casting method. (D) Comparison of the unit cell parameters for both the polymorphs.

The four TPP (phosphorus as pink) ligands are connected with the tetrahedrally oriented four silver atoms (Fig. S2†).

One S moiety of the BDT ligand is attached to each of the 12 Ag atoms of the icosahedron and the remaining S moieties bridge Ag atoms of each Ag<sub>3</sub>S<sub>6</sub> crown. The total number of S atoms is 24 {(24 = 12 S atoms attach to the 12 Ag icosahedron core + 4) × (Ag<sub>3</sub>S<sub>6</sub> crown motif)}.

For the T system, in the (001) plane (view from the Z-axis) of the crystal lattice, the NCs get organized into a hexagonal lattice with a 3-fold axis passing through the center of the molecule (Fig. 2A), while for the (100) (view from the X-axis) (Fig. 2B) and (010) (view from the Y-axis) (Fig. 2C) planes, the NCs get decorated into a rectangular lattice. Viewing from the Z axis, the NCs form two different parallel (001) and (00-1) planes. Each NC from the two (001) and (00-1) planes has a center of inversion (Fig. 2D). The interparticle distance of 1.79 nm (less than the 2.74 nm overall size of the NCs) arises from ligand interlocking. For the C system, the NCs assemble into a simple square lattice in the (001) plane (view from the Z axis). The interparticle distance is 1.75 nm, less than the

overall size 2.74 nm of the nanocrystal. In the case of Au<sub>246</sub>, the interparticle distance was of 3.1 nm, less than the 3.3 nm overall size of the NC.<sup>13</sup>

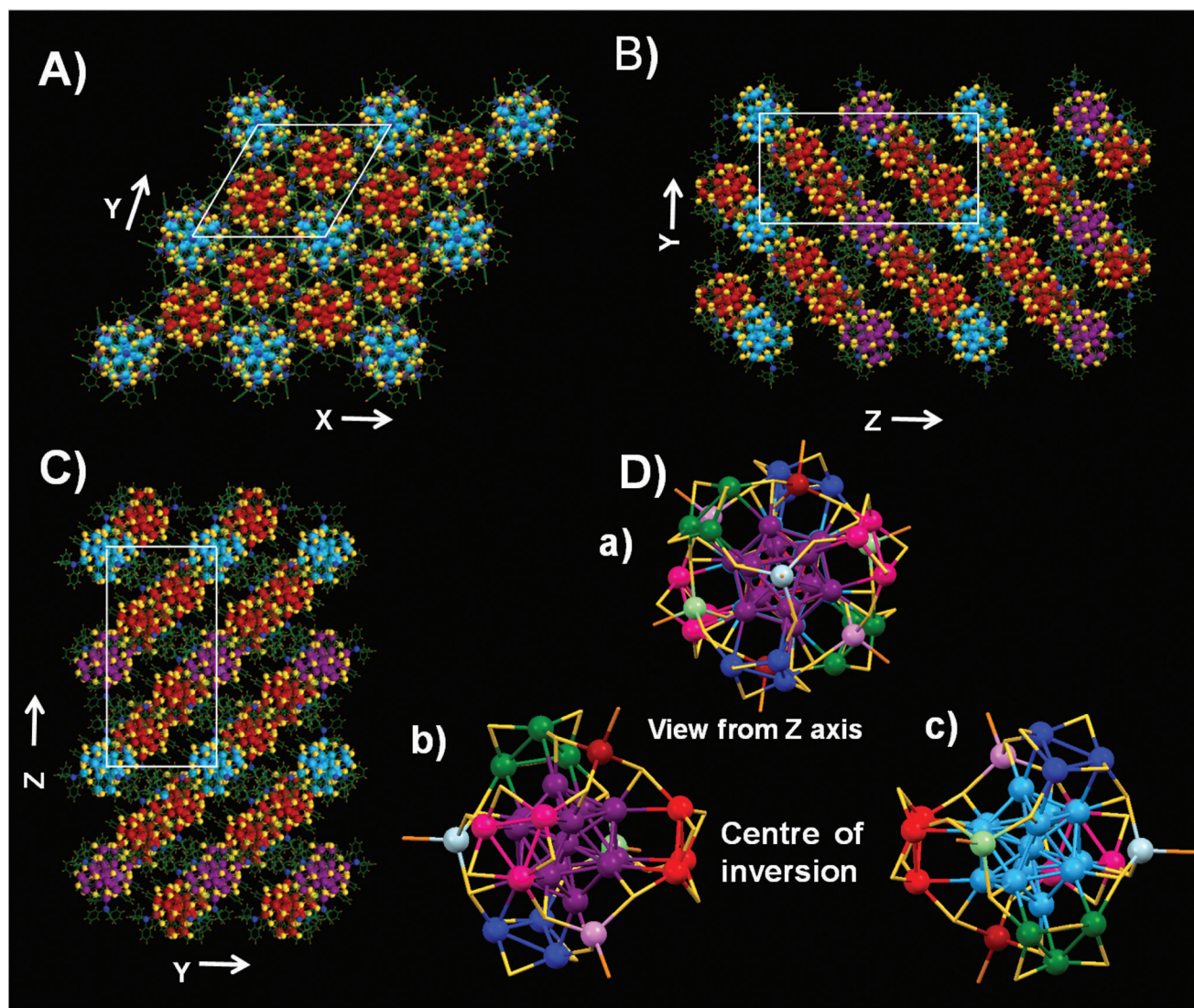
When zooming into the surfaces of the NCs, the T and C packing are related to the alignment of their surface ligands. The BDT (primary) and TPP (secondary) ligands are highly ordered and are self-assembled on the silver surface (Fig. S3–5 & S7, 8†).

For the T system, the BDT ligands of the two NCs formed cyclohexane chair patterns in the unit cell. C–H...π and H...H vdW are the interactions present to form such types of cyclohexane chair structures (Fig. 3A). For a NC, there will be a maximum of four such types of interactions in a T unit cell. The C–H...π and H...H distances were ~2.82 and ~2.36 Å, respectively. In the C system, every NC has the same six types of interactions with slight changes in the distances.

For BDT and TPP ligands, there are two types of interactions: (i) intra-cluster interactions and (ii) inter-cluster interactions.

(i) The C–H groups of the TPP ligands (red) interact with the benzene ring of the BDT ligands in intra-cluster inter-





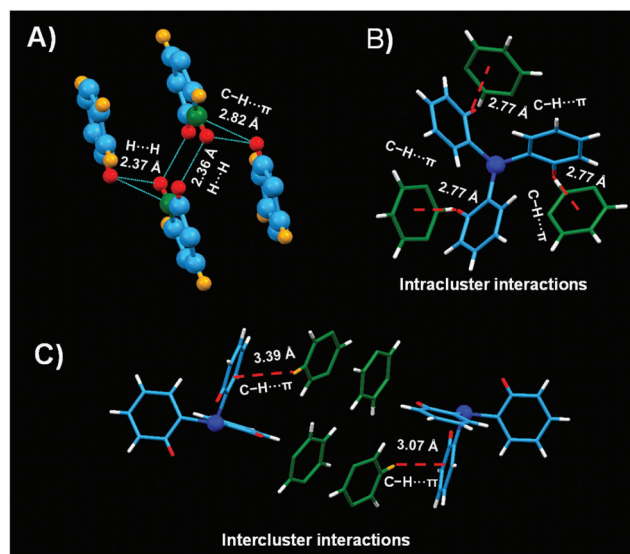
**Fig. 2** Packing of the crystal view from the (A) Z-axis, (B) Y-axis and (C) X-axis. (D) (a) View of the cluster packing from the Z-axis. Two NCs formed two different (001) and (00-1) layered planes; (b) and (c) are the two different clusters of (a). They have a center of inversion.

actions (Fig. 3B & S5A†). For C and T systems, the interactions are similar with small changes in interaction distances. Here, C-H... $\pi$  interaction distances are  $\sim 2.77$  and  $2.92$  Å for the C and the T systems, respectively. The orientations of the benzene rings of the TPP are controlled by these C-H... $\pi$  interactions. The TPP ligands fit into the cavity formed by the BDT ligands by these types of interactions (Fig. 3B).

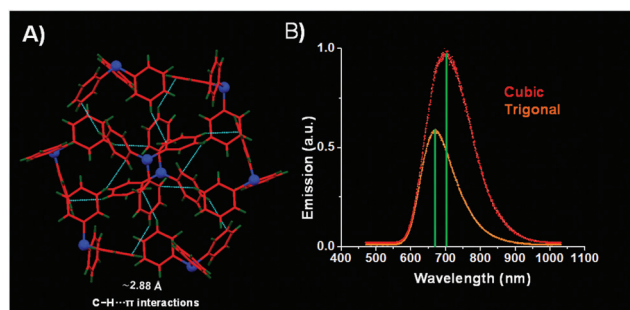
(ii) The C-H groups of the BDT (orange) interact with the benzene ring of the TPP leading to inter-cluster interactions (Fig. 3C & S5B†). Here also, the interactions are similar with slight changes in interaction distances for both types of unit cells. The C-H... $\pi$  interaction distances are  $\sim 3.07$ – $3.39$  Å and  $2.92$  Å for the C and the T systems, respectively.

T-shaped C-H... $\pi$  interactions are present between the TPP ligands in the C unit cell (Fig. 4A). In a unit cell, eight TPP ligands, by interlocking each other, form a hexagonal shape

through C-H... $\pi$  interactions from the eight NCs (Fig. 4A). The average C-H... $\pi$  distance was  $\sim 2.88$  Å. Strong C-H... $\pi$  interactions of the TPP ligands form a polymeric chain to hold each NC (Fig. S7A†). Every NC is directly or indirectly connected with the other NCs by C-H... $\pi$  interactions of the TPP ligands. This distance is consistent with the reported value for typical C-H... $\pi$  interactions in the Au<sub>246</sub> NCs<sup>13</sup> with -SPh-*p*-CH<sub>3</sub> ligands ( $2.88 \pm 0.42$  Å) but somewhat larger than the C-H... $\pi$  distance in the Au<sub>103</sub> NCs<sup>16</sup> composed of -S-Nap ligands ( $2.76 \pm 0.05$  Å). In the T system, the C-H... $\pi$  interaction distances for TPP ligands were in the range of  $\sim 3.12$ – $3.37$  Å (Fig. S8D†). Here, the interaction energy is less compared to C as the distance is larger. There are breakages in C-H... $\pi$  interactions for TPP ligands (Fig. S8B & C†). Such orientations and self-organized surface patterns of ligands are reminiscent of the  $\alpha$ -helix<sup>25</sup> and  $\beta$ -sheet in proteins, and also in the recently



**Fig. 3** (A) Interactions among the BDT ligands from two different NCs in the trigonal structure. The BDT ligands of the two NCs formed cyclohexane chair patterns in the unit cell. (B) Intra-cluster interactions between C–H of the TPP with the benzene ring of BDT in the cubic system. (C) Inter-cluster interactions between C–H of the BDT with the benzene ring of the TPP in the cubic system.



**Fig. 4** (A) C–H... $\pi$  interactions of the TPP ligands in the cubic system. (B) Emission spectra of the single crystals for both the cubic and the trigonal systems.

reported  $\text{Au}_{246}^{13}$  and  $\text{Au}_{103}^{16}$  NCs. So, NCs could exhibit a level of structural complexity comparable to that of biomolecules.

The secondary structures of proteins are mainly stabilized by hydrogen bonds.<sup>26</sup> Here, the surface patterns on the NCs are stabilized by intermolecular C–H... $\pi$  and vdW interactions.

We note that the surface patterns and orientations are induced by specific crystallization because the C–H... $\pi$  interactions are different for different crystal systems of the same NC.

The emission spectra of both NCs, collected at room temperature, are shown in Fig. 4B. Both the NCs can be efficiently excited at  $\lambda_{\text{max}} = 532$  nm. Upon comparing both the NCs, two main features were observed:

(i) The cubic NCs are more luminescent than the trigonal NCs: Inter C–H... $\pi$  interactions for secondary ligands (TPP) are more facilitated in C than in T (Fig. S7 & 8†). As a result, the C lattice becomes more rigid compared to the T lattice. Greater rigidity, in turn, results in a higher luminescence efficiency for the C system.<sup>27</sup> The C–H... $\pi$  interactions significantly restrict the intramolecular rotations and vibrations and thus enhance the radiative transitions considerably in the crystalline state.<sup>28</sup> Secondary ligands play a crucial role to increase the luminescence efficiency of the NCs.

(ii) A red shift of the emission band occurs for the cubic NCs by more than 30 nm: The red shift can be explained in terms of electronic coupling between the NCs *via* interactions between the transition dipole moments of the individual  $\text{Ag}_{29}(\text{BDT})_{12}(\text{TPP})_4$  NCs and the induced dipole moments in the neighboring  $\text{Ag}_{29}(\text{BDT})_{12}(\text{TPP})_4$  NCs in the single crystal. This interaction is expected to lower the transition energy.<sup>29,30</sup> The red shift of the emission band is expected to be caused by a combined effect of the electronic coupling and the non-radiative decay pathways occurring through electron–phonon interactions that lower the emission energy.<sup>18</sup>

## Conclusions

In summary, we demonstrate that polymorphism exists in atomically precise cluster systems. The packing of  $[\text{Ag}_{29}(\text{BDT})_{12}(\text{TPP})_4]^{3-}$  clusters into two different polymorphic forms, cubic and trigonal, was favored by different patterns of intercluster and intracluster interactions. The greater extent of C–H... $\pi$  interactions in the cubic NCs makes them more rigid and hence more luminescent than the trigonal NCs. This also highlights the role of secondary ligands in enhancing the luminescence properties of the clusters. The discovery of polymorphism in atomically precise clusters opens up a new dimension in nanoparticle engineering, presenting the possibility of engineering NC unit cells with enhanced optical, mechanical and electrical properties.

## Conflicts of interest

There are no conflicts to declare.

## Acknowledgements

We acknowledge the Department of Science and Technology, Government of India for constantly supporting our research program on nanomaterials. A. N. and T. A. thank IIT Madras for doctoral fellowships. P. C. thanks the Council of Scientific and Industrial Research (CSIR) for her research fellowship. M. B. thanks the University Grants Commission (UGC) for his research fellowship.



## References

- 1 I. Chakraborty and T. Pradeep, *Chem. Rev.*, 2017, **117**, 8208–8271.
- 2 R. Jin, C. Zeng, M. Zhou and Y. Chen, *Chem. Rev.*, 2016, **116**, 10346–10413.
- 3 M. Zhu, C. M. Aikens, F. J. Hollander, G. C. Schatz and R. Jin, *J. Am. Chem. Soc.*, 2008, **130**, 5883–5885.
- 4 M. W. Heaven, A. Dass, P. S. White, K. M. Holt and R. W. Murray, *J. Am. Chem. Soc.*, 2008, **130**, 3754–3755.
- 5 C. P. Joshi, M. S. Bootharaju, M. J. Alhilaly and O. M. Bakr, *J. Am. Chem. Soc.*, 2015, **137**, 11578–11581.
- 6 H. Qian, W. T. Eckenhoff, Y. Zhu, T. Pintauer and R. Jin, *J. Am. Chem. Soc.*, 2010, **132**, 8280–8281.
- 7 N. A. Sakthivel, S. Theivendran, V. Ganeshraj, A. G. Oliver and A. Dass, *J. Am. Chem. Soc.*, 2017, **139**, 15450–15459.
- 8 G. Natarajan, A. Mathew, Y. Negishi, R. L. Whetten and T. Pradeep, *J. Phys. Chem. C*, 2015, **119**, 27768–27785.
- 9 K. R. Krishnadas, A. Bakshi, A. Ghosh, G. Natarajan, A. Som and T. Pradeep, *Acc. Chem. Res.*, 2017, **50**, 1988–1996.
- 10 G. Li and R. Jin, *Acc. Chem. Res.*, 2013, **46**, 1749–1758.
- 11 S. Yamazoe, T. Yoskamtorn, S. Takano, S. Yadnum, J. Limtrakul and T. Tsukuda, *Chem. Rec.*, 2016, **16**, 2338–2348.
- 12 W. W. Xu, B. Zhu, X. C. Zeng and Y. Gao, *Nat. Commun.*, 2016, **7**, 13574.
- 13 C. Zeng, Y. Chen, K. Kirschbaum, K. J. Lambright and R. Jin, *Science*, 2016, **354**, 1580–1584.
- 14 P. D. Jadzinsky, G. Calero, C. J. Ackerson, D. A. Bushnell and R. D. Kornberg, *Science*, 2007, **318**, 430–433.
- 15 B. Yoon, W. D. Luedtke, R. N. Barnett, J. Gao, A. Desireddy, B. E. Conn, T. Bigioni and U. Landman, *Nat. Mater.*, 2014, **13**, 807.
- 16 T. Higaki, C. Liu, M. Zhou, T.-Y. Luo, N. L. Rosi and R. Jin, *J. Am. Chem. Soc.*, 2017, **139**, 9994–10001.
- 17 M. J. Alhilaly, M. S. Bootharaju, C. P. Joshi, T. M. Besong, A.-H. Emwas, R. Juarez-Mosqueda, S. Kaappa, S. Malola, K. Adil, A. Shkurenko, H. Häkkinen, M. Eddaoudi and O. M. Bakr, *J. Am. Chem. Soc.*, 2016, **138**, 14727–14732.
- 18 L. G. AbdulHalim, M. S. Bootharaju, Q. Tang, S. Del Gobbo, R. G. AbdulHalim, M. Eddaoudi, D.-e. Jiang and O. M. Bakr, *J. Am. Chem. Soc.*, 2015, **137**, 11970–11975.
- 19 M. S. Bootharaju, R. Dey, L. E. Gevers, M. N. Hedhili, J.-M. Basset and O. M. Bakr, *J. Am. Chem. Soc.*, 2016, **138**, 13770–13773.
- 20 P. Chakraborty, A. Nag, G. Paramasivam, G. Natarajan and T. Pradeep, *ACS Nano*, 2018, **12**, 2415–2425.
- 21 A. Ghosh, M. Bodiuzzaman, A. Nag, M. Jash, A. Bakshi and T. Pradeep, *ACS Nano*, 2017, **11**, 11145–11151.
- 22 M. C. Etter, *Acc. Chem. Res.*, 1990, **23**, 120–126.
- 23 S. V. Kolotuchin, E. E. Fenlon, S. R. Wilson, C. J. Loweth and S. C. Zimmerman, *Angew. Chem., Int. Ed. Engl.*, 1996, **34**, 2654–2657.
- 24 K. Kobayashi, T. Shirasaka, E. Horn and N. Furukawa, *Tetrahedron Lett.*, 2000, **41**, 89–93.
- 25 J. D. Dunitz, *Angew. Chem., Int. Ed.*, 2001, **40**, 4167–4173.
- 26 L. Pauling, R. B. Corey and H. R. Branson, *Proc. Natl. Acad. Sci. U. S. A.*, 1951, **37**, 205–211.
- 27 K. A. Denault, J. Brgoch, M. W. Gaultois, A. Mikhailovsky, R. Petry, H. Winkler, S. P. DenBaars and R. Seshadri, *Chem. Mater.*, 2014, **26**, 2275–2282.
- 28 T. Chen, S. Yang, J. Chai, Y. Song, J. Fan, B. Rao, H. Sheng, H. Yu and M. Zhu, *Sci. Adv.*, 2017, **3**, e1700956.
- 29 H. Döllefeld, H. Weller and A. Eychmüller, *J. Phys. Chem. B*, 2002, **106**, 5604–5608.
- 30 J. Zhang, C. Rowland, Y. Liu, H. Xiong, S. Kwon, E. Shevchenko, R. D. Schaller, V. B. Prakapenka, S. Tkachev and T. Rajh, *J. Am. Chem. Soc.*, 2015, **137**, 742–749.

## Electronic Supplementary Information

### Polymorphism of $\text{Ag}_{29}(\text{BDT})_{12}(\text{TPP})_4^{3-}$ Cluster: Interactions of Secondary Ligands and Their Effect on Solid State Luminescence

Abhijit Nag<sup>a</sup>, Papri Chakraborty<sup>a</sup>, Mohammad Bodiuzzaman<sup>a</sup>, Tripti Ahuja<sup>a</sup>, Sudhadevi Antharjanam<sup>b</sup> and Thalappil Pradeep<sup>\*a</sup>

<sup>a</sup> DST Unit of Nanoscience and Thematic Unit of Excellence, Department of Chemistry, Indian Institute of Technology Madras, Chennai-600036, India, \*Email: pradeep@iitm.ac.in

<sup>b</sup> Sophisticated Analytical Instruments Facility (SAIF), Indian Institute of Technology Madras

Name	Description	Page No.
	Experimental details	2-3
Fig. S1	Optical images of the crystals	4
Fig. S2	UV-vis and ESI MS of $[\text{Ag}_{29}(\text{BDT})_{12}(\text{TPP})_4]^{3-}$	5
Fig. S3	Packing of the BDT ligands in a trigonal unit cell	6
Fig. S4	Packing of the cluster and BDT ligands	7
Fig. S5	Packing of the BDT and TPP ligands in trigonal and cubic systems	8
Fig. S6	Intracluster and intercluster C-H... $\pi$ interactions between the BDT and TPP ligands for both the systems	9

Fig. S7	Packing of the TPP ligands and interactions in cubic unit cell	10
Fig. S8	Packing of TPP ligands and interactions in trigonal unit cell	11
Table S1	Crystal data and structure refinement	12

## Materials and methods

### Chemicals

All chemicals including silver nitrate ( $\text{AgNO}_3$ , 99%), benzene-1,3-dithiol (BDT, 99%), sodium borohydride ( $\text{NaBH}_4$ , 99.99% metals basis), and triphenylphosphine (TPP, 97%) were purchased from Sigma-Aldrich and used without further purification. Solvents including methanol, dichloromethane and DMF were used from Sigma Aldrich as received.

**Synthesis of  $[\text{Ag}_{29}(\text{BDT})_{12}(\text{TPP})_4]^{3-}$  cluster:**  $[\text{Ag}_{29}(\text{BDT})_{12}(\text{TPP})_4]^{3-}$  clusters were synthesized following a reported protocol<sup>[1]</sup> with slight modifications. About 20 mg of  $\text{AgNO}_3$  was dissolved in a mixture of 2 mL methanol and 10 mL DCM. To this reaction mixture, about 13.5  $\mu\text{L}$  of the 1,3-BDT ligand was added. The mixture was stirred for about 15 mins and then about 10.5 mg of  $\text{NaBH}_4$  dissolved in 500  $\mu\text{L}$  of ice-cold water was added. The stirring was continued under dark conditions for about 5 h. Then, the reaction mixture was centrifuged, the precipitate was discarded, and the clusters were obtained as the orange supernatant. The solution was evaporated by rotary evaporation; the orange residue was washed with methanol and finally dissolved in DMF. The solution was characterized by UV-vis and ESI MS, which confirmed the formation of  $[\text{Ag}_{29}(\text{BDT})_{12}(\text{TPP})_4]^{3-}$  clusters (Figure S1).

**Crystallization of  $[\text{Ag}_{29}(\text{BDT})_{12}(\text{TPP})_4]^{3-}$  by drop cast method:** This was performed following the reported method<sup>[1]</sup>. The thoroughly dried powder was dispersed in 400  $\mu\text{L}$  of DMF, vortexed for at least 1 min, and then filtered using a syringe filter with a pore size 220 nm. The filtered sample was then spotted on microscope glass plates and left to evaporate slowly at room temperature under air in a dark box placed in a ventilated fume hood. After approximately 2

days, several square dark orange crystals were harvested. We used the reported cubic unit cell throughout the paper.

**Crystallization of  $[\text{Ag}_{29}(\text{BDT})_{12}(\text{TPP})_4]^{3-}$  by vapour diffusion method:**  $[\text{Ag}_{29}(\text{BDT})_{12}(\text{TPP})_4]^{3-}$  (10 mg) was dissolved in DMF (1 mL). The solution was filtered and MeOH (ca. 3 mL) was allowed to vapour diffuse into the solution. After 3 months, red orange crystals suitable for X-ray crystallographic analysis were obtained.

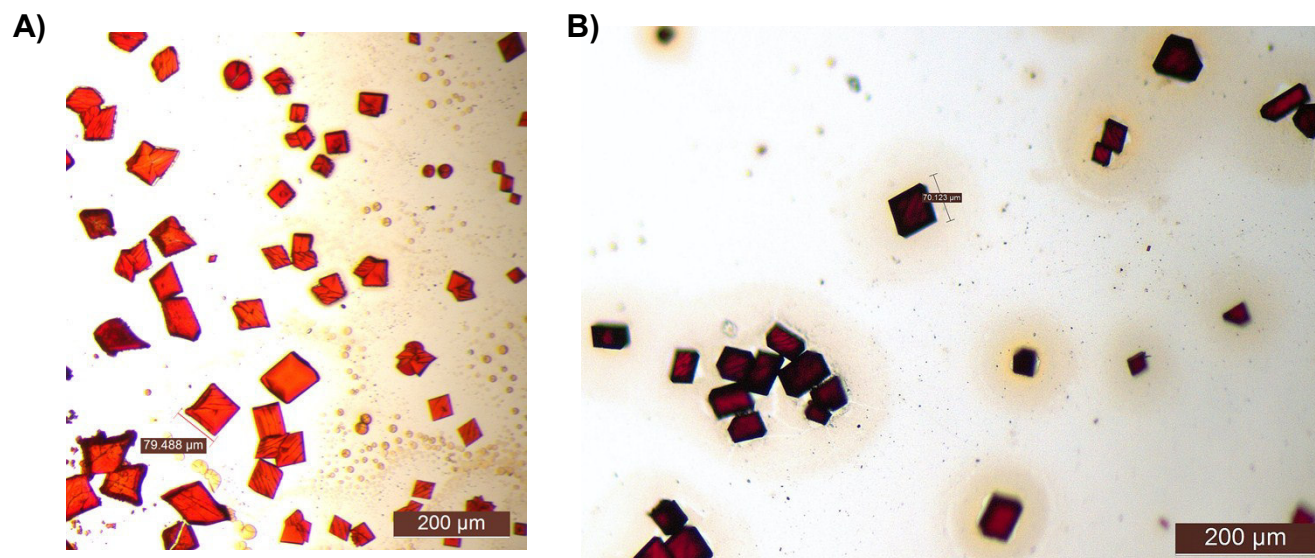
## Instrumentation

The UV-vis spectra were measured using a PerkinElmer Lambda 25 UV-vis spectrophotometer. Mass spectrometric measurements were done in a Waters Synapt G2-Si high-resolution mass spectrometer.

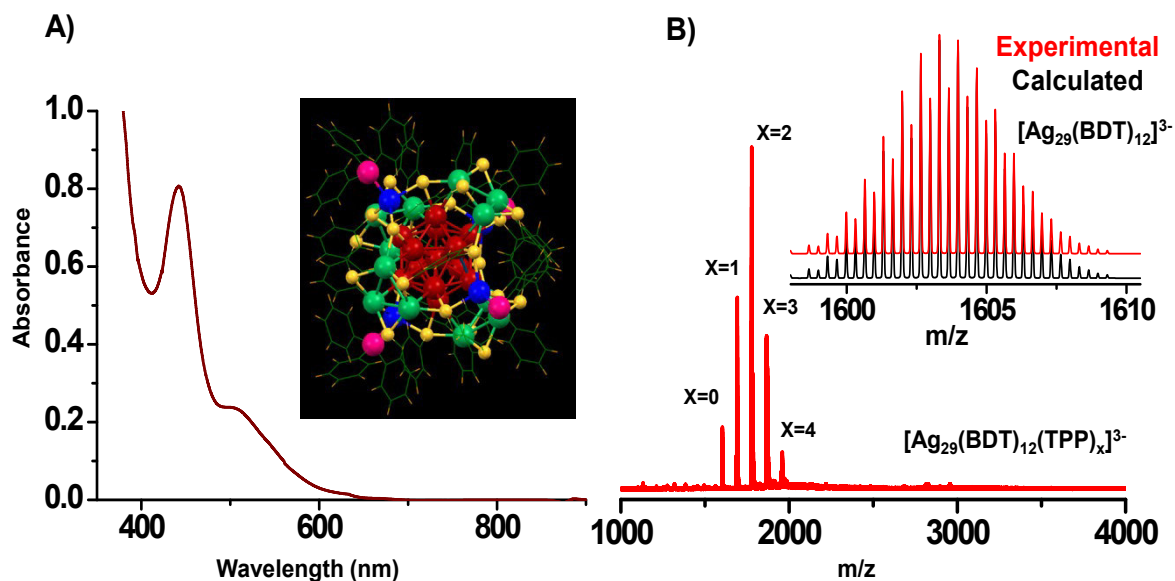
Emission spectra were collected in a Witec GmbH, Alpha-SNOM alpha300 S confocal Raman instrument equipped with 532 nm laser as the excitation source.

## X-ray Crystallography

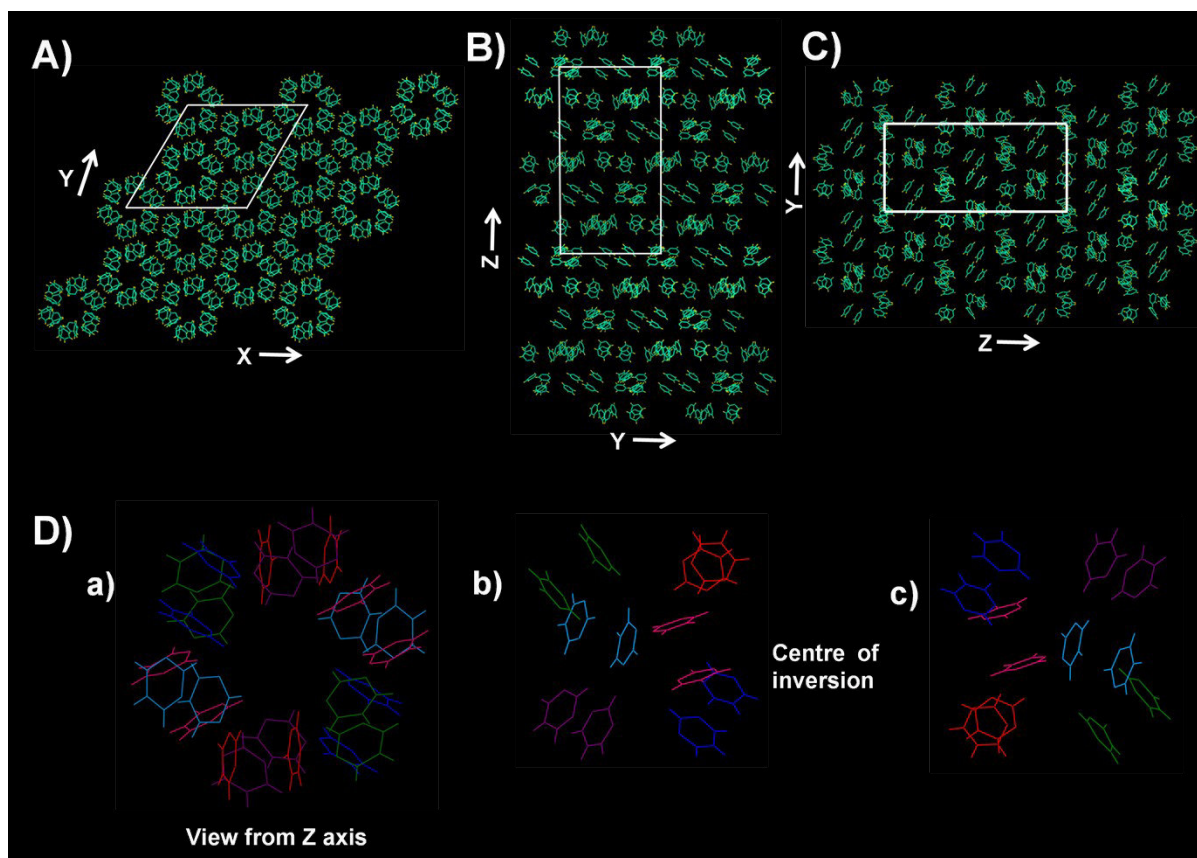
Single crystal data were measured using a Bruker D8 VENTURE APEX3 CMOS diffractometer using  $\text{CuK}\alpha$  ( $\lambda = 1.54178 \text{ \AA}$ ). Indexing was performed using APEX3. Data integration and reduction were performed using SaintV8.37A. Absorption correction was performed by multi-scan method implemented in SADABS. Space group was determined using XPREP implemented in APEX3. Structure was solved using Direct Methods (SHELXT-2014) and refined using SHELXL-2014 (full-matrix least-squares on  $F^2$ ) contained in WinGX v1.80.05. Crystal data and refinement conditions are shown in Table S1. The crystal data has been deposited to the Cambridge Structural Database and the CCDC number: 1812439.



**Fig. S1.** Optical images of the crystals **A)** Cubic and **B)** Trigonal unit cells. Note that from optical images, crystal systems could be distinguished.

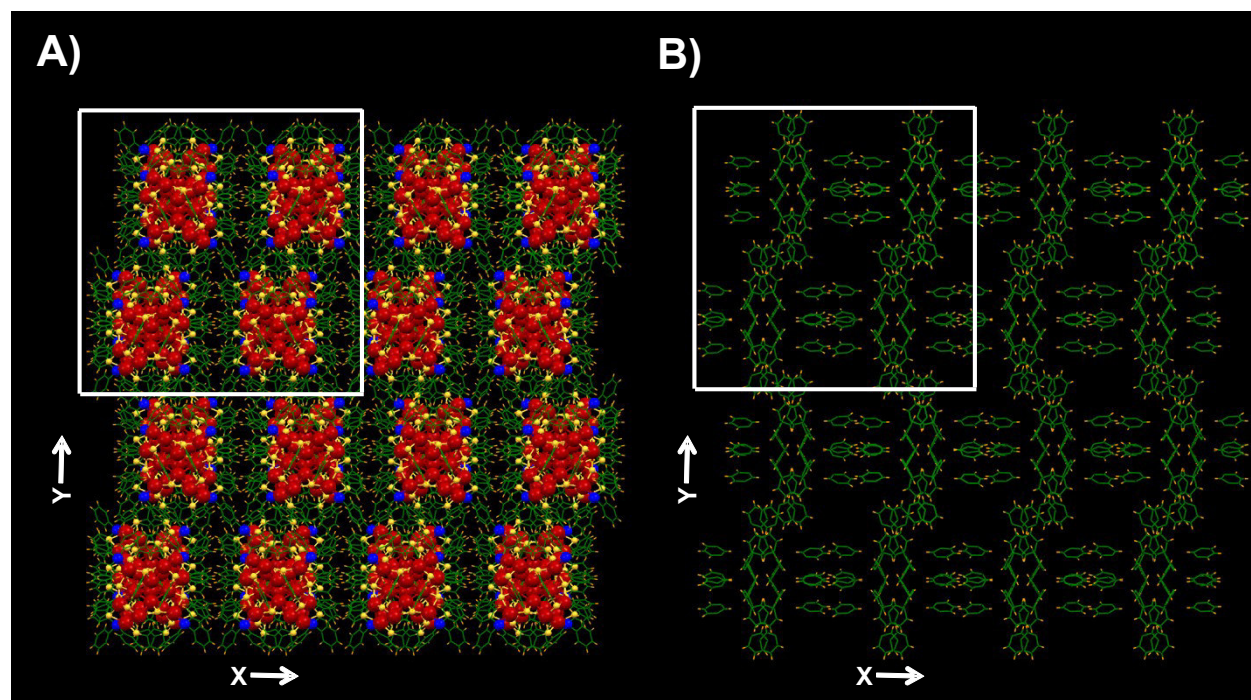


**Fig. S2.** **A)** UV-vis and **B)** ESI MS of  $\text{Ag}_{29}(\text{BDT})_{12}(\text{TPP})_4^{3-}$ . Inset of **A)** shows the DFT optimized structure of cluster and inset of **B)** shows the experimental and calculated isotope patterns of  $\text{Ag}_{29}(\text{BDT})_{12}(\text{TPP})_4^{3-}$ . MS measurement results in the sequential loss of TPP during ionization, marked as X = 0 to 4.

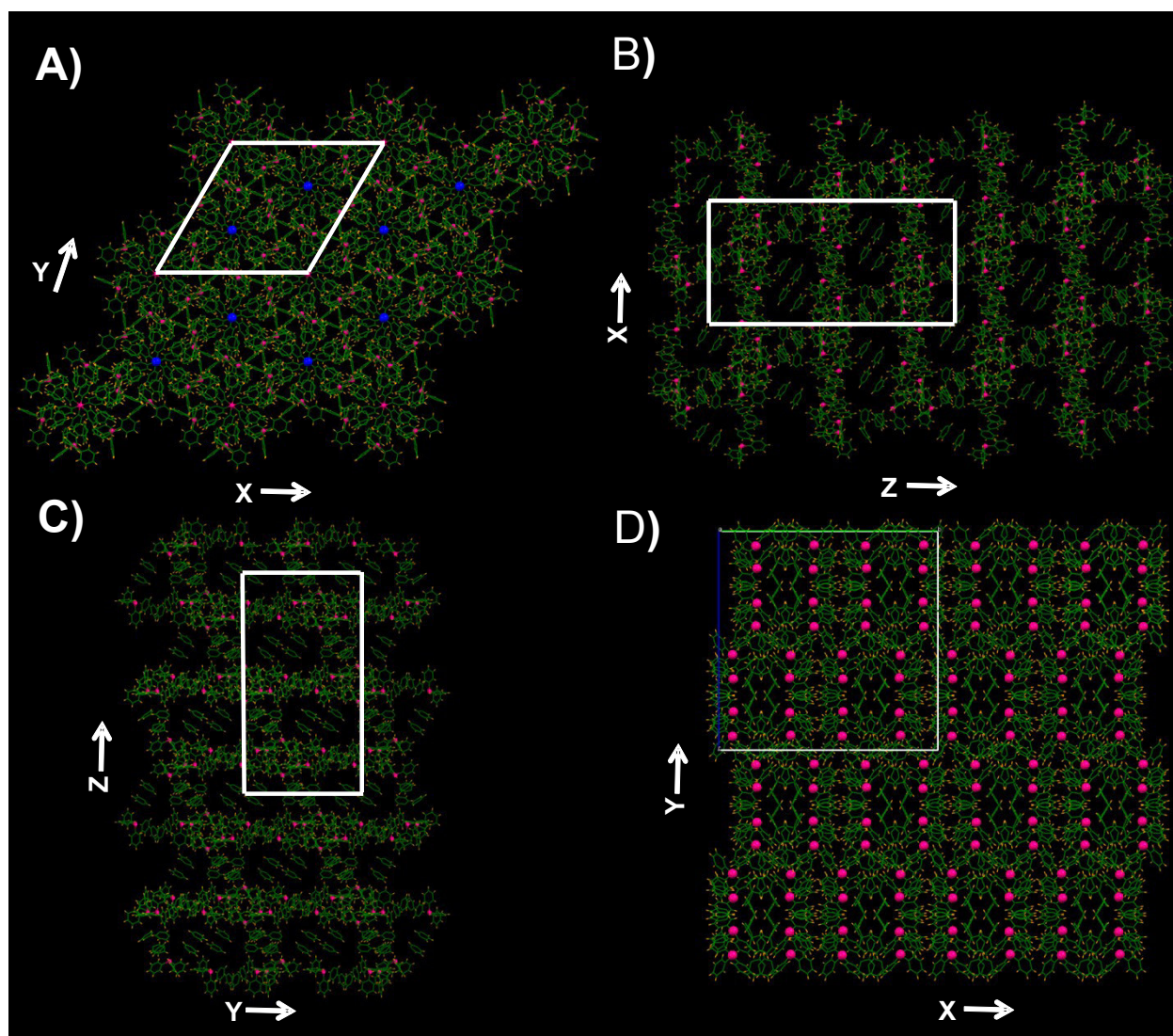


**Fig. S3.** Packing of the BDT ligands, viewed from, **A)** Z-axis, **B)** Y-axis and **C)** X-axis. **D)** **a)** View of the cluster packing from Z-axis. Two NCs formed two different (001) and (00-1) layered planes. **b)** and **c)** are the BDT ligands of the two different clusters of **a)**. They have a center of inversion.

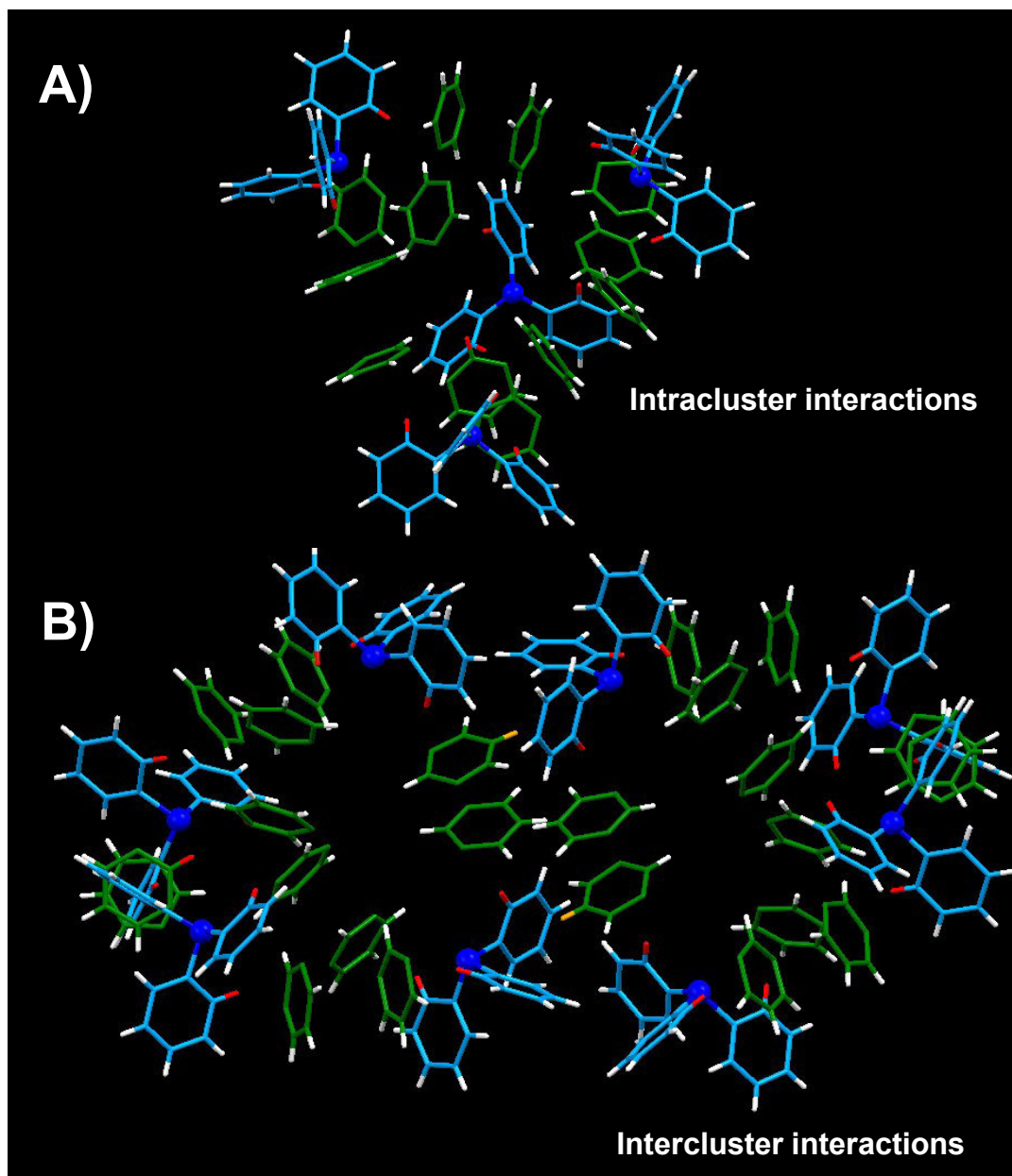




**Fig. S4.** Packing of the A) cluster and B) BDT ligands, viewed from Z-axis of the cubic unit cell.

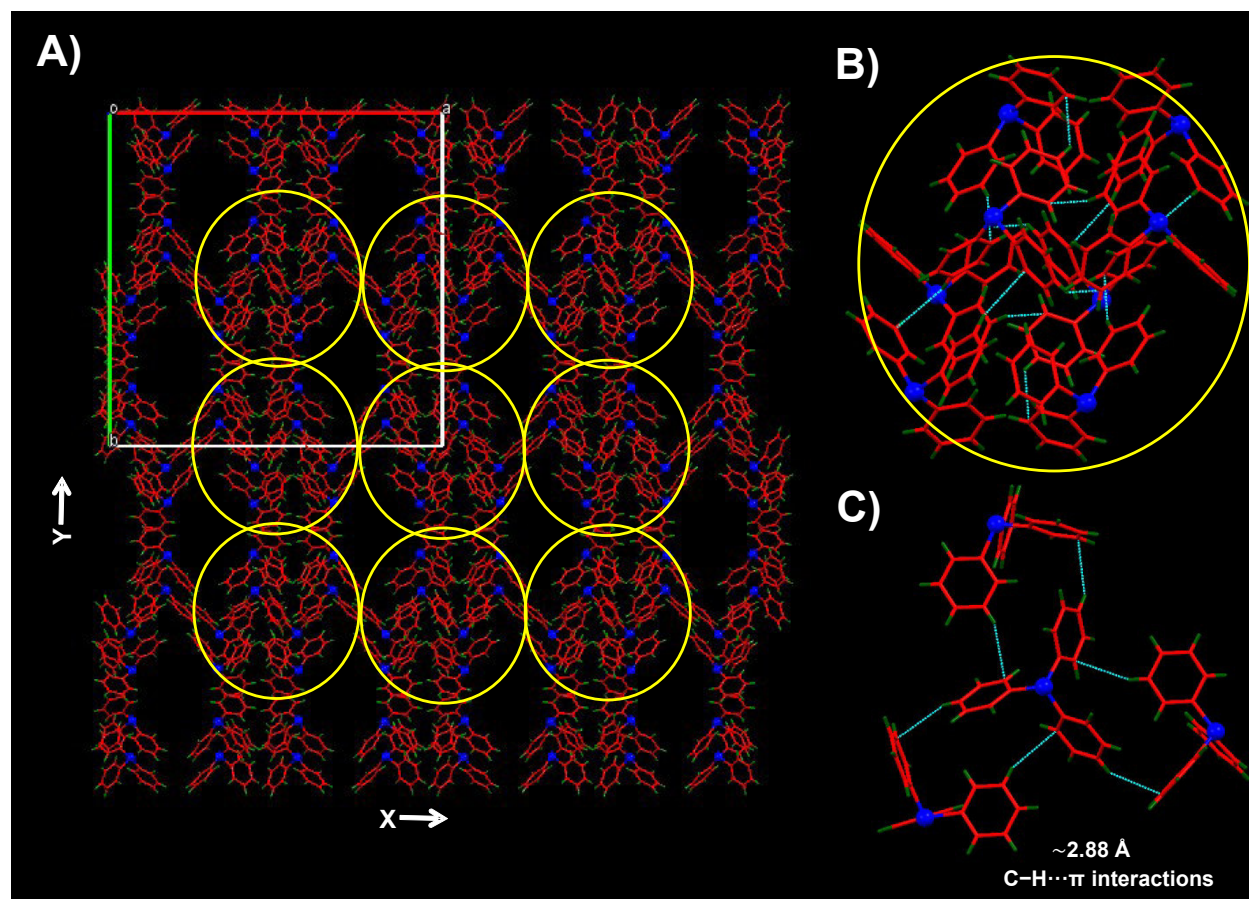


**Fig. S5.** Packing of the BDT and TPP ligands viewed from, **A)** Z-axis, **B)** Y-axis and **C)** X-axis of the trigonal unit cell. **D)** Packing of the BDT and TPP ligands viewed from the Z-axis of the cubic system.

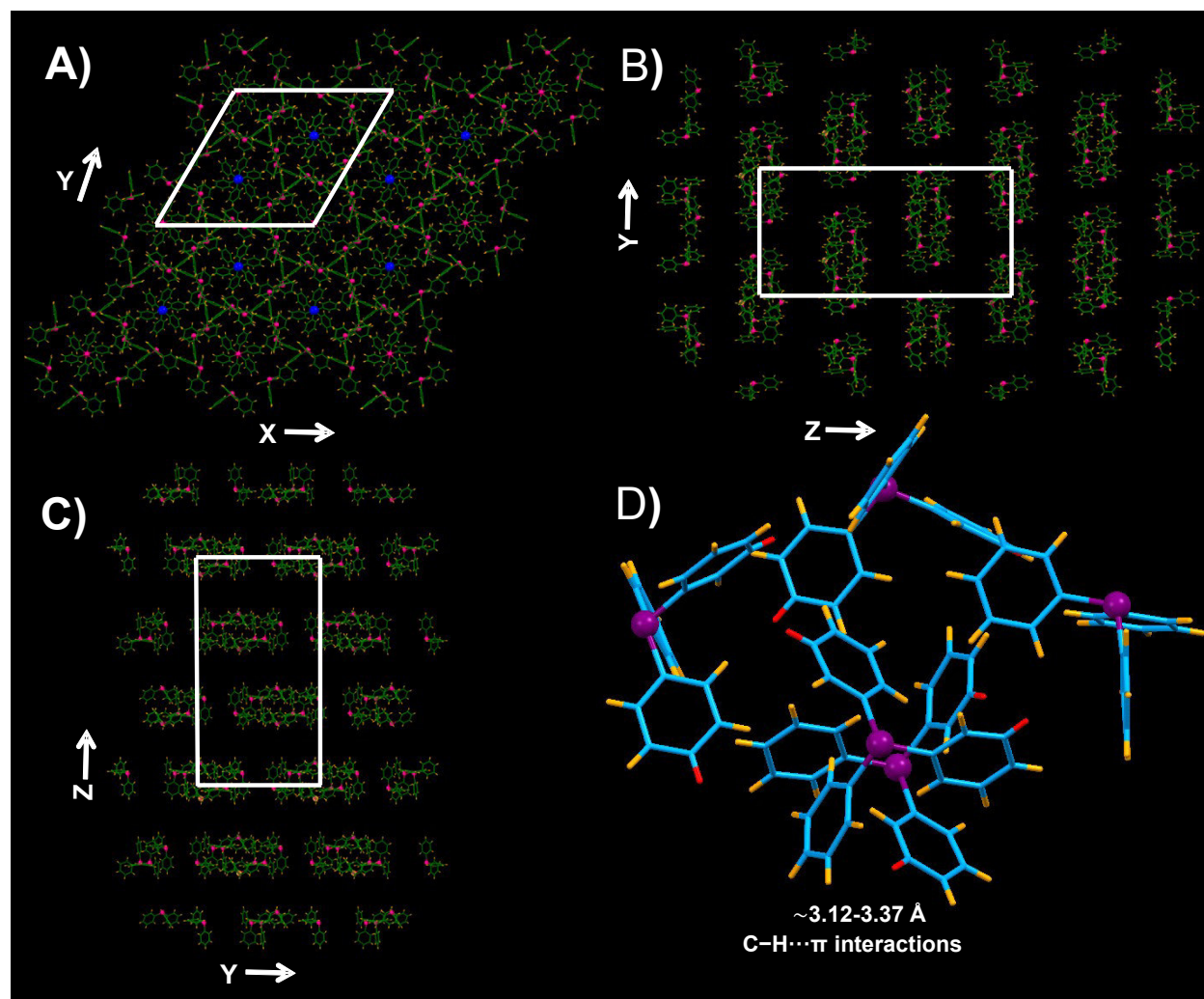


**Fig. S6.** A) Intracluster and B) Intercluster C-H... $\pi$  interactions between the BDT and TPP ligands for both the systems. The red and orange colored hydrogens represent the intracluster and intercluster interactions, respectively with the nearest benzene ring.





**Fig. S7.** A) Packing of the TPP ligands viewed from, Z-axis. B) An expanded view of the yellow circle. C) C-H... $\pi$  interactions between the TPP ligands.



**Fig. S8.** Packing of the TPP ligands viewed from, **A)** Z-axis, **B)** Y-axis and **C)** X-axis of the trigonal unit cell. **D)** C-H... $\pi$  interactions between the TPP ligands. The red color hydrogens represent the interactions with the nearest benzene ring.

**Table S1.** Crystal data and structure refinement

Identification code	AG29R3
Empirical formula	C159 H108 Ag29 N3 O10 P4 S24
Formula weight	6242.03
Temperature	296(2) K
Wavelength	1.54178 Å
Crystal system	Trigonal
Space group	R-3
Unit cell dimensions	a = 27.4634(6) Å $\alpha = 90^\circ$ . b = 27.4634(6) Å $\beta = 90^\circ$ . c = 46.6552(16) Å $\gamma = 120^\circ$ .
Volume	30474.7(17) Å <sup>3</sup>
Z	6
Density (calculated)	2.041 Mg/m <sup>3</sup>
Absorption coefficient	24.818 mm <sup>-1</sup>
F(000)	17820
Crystal size	0.150 x 0.100 x 0.100 mm <sup>3</sup>
Theta range for data collection	3.218 to 46.668°.
Index ranges	-25 ≤ h ≤ 25, -25 ≤ k ≤ 25, -43 ≤ l ≤ 43
Reflections collected	173079
Independent reflections	5939 [R(int) = 0.3629]
Completeness to theta = 46.668°	99.7 %
Absorption correction	Semi-empirical from equivalents
Max. and min. transmission	0.7451 and 0.3859
Refinement method	Full-matrix least-squares on F <sup>2</sup>
Data / restraints / parameters	5939 / 210 / 662
Goodness-of-fit on F <sup>2</sup>	1.059
Final R indices [I > 2sigma(I)]	R1 = 0.0768, wR2 = 0.1520
R indices (all data)	R1 = 0.1609, wR2 = 0.1907
Extinction coefficient	n/a
Largest diff. peak and hole	0.910 and -0.686 e.Å <sup>-3</sup>

## References

- [1] L. G. AbdulHalim, M. S. Bootharaju, Q. Tang, S. Del Gobbo, R. G. AbdulHalim, M. Eddaoudi, D.-e. Jiang, O. M. Bakr, *J. Am. Chem. Soc.* **2015**, *137*, 11970-11975.

## ORIGINAL ARTICLE

# Metals in urine in relation to the prevalence of pre-diabetes, diabetes and atherosclerosis in rural India

Ganesan Velmurugan,<sup>1</sup> Krishnan Swaminathan,<sup>1,2</sup> Ganesh Veerasekar,<sup>2</sup> Jonathan Q Purnell,<sup>3</sup> Sundaresan Mohanraj,<sup>2</sup> Mani Dhivakar,<sup>1</sup> Anil Kumar Avula,<sup>1</sup> Mathew Cherian,<sup>2</sup> Nalla G Palaniswami,<sup>2</sup> Thomas Alexander,<sup>3</sup> Thalappil Pradeep<sup>1</sup>

► Additional material is published online only. To view please visit the journal online (<http://dx.doi.org/10.1136/oemed-2018-104996>).

<sup>1</sup>Department of Chemistry, DST Unit of Nanoscience and Thematic Unit of Excellence in Water Research, Indian Institute of Technology Madras, Chennai, Tamil Nadu, India

<sup>2</sup>KMCH Research Foundation, Kovai Medical Centre and Hospital, Coimbatore, Tamil Nadu, India

<sup>3</sup>Department of Medicine, Oregon Health & Science University, Portland, Oregon, USA

## Correspondence to

Dr Krishnan Swaminathan, KMCH Research Foundation, Kovai Medical Centre and Hospital, Coimbatore, TN 641 014, India; [snehasswaminathan@gmail.com](mailto:snehasswaminathan@gmail.com) and Thalappil Pradeep, Indian Institute of Technology Madras; [pradeep@iitm.ac.in](mailto:pradeep@iitm.ac.in)

GV and KS contributed equally.

Received 4 January 2018

Revised 21 March 2018

Accepted 30 March 2018

## ABSTRACT

**Objective** Diabetes and cardiovascular diseases are growing burdens in rural communities worldwide. We have observed a high prevalence of diabetes among rural farming communities in India and sought to evaluate the association of non-traditional risk factors, such as metals, with diabetes and other cardiometabolic risk factors in this community.

**Methods** Anthropometric measurements, chemistries and carotid intima-media thickness were determined in 865 participants of the Kovai Medical Center and Hospital-Nallampatti Non-Communicable Disease Study-I (KMCH-NNCD-I, 2015), a cross-sectional study conducted in a farming village in South India. Urinary metal levels were determined by inductively coupled plasma-mass spectrometry analysis and corrected to urinary creatinine level. Statistical analyses were performed to study the association between urinary metal levels and clinical parameters.

**Results** 82.5% of the study population were involved in farming and high levels of toxic metals were detected in the synthetic fertilisers used in the study village. The prevalence of pre-diabetes, diabetes and atherosclerosis was 43.4%, 16.2% and 10.3%, respectively. On logistic regression analysis, no association of traditional risk factors such as body mass index, blood pressure and total cholesterol with disease conditions was observed, but urinary levels of metals such as arsenic, chromium, aluminium and zinc showed an association with diabetes, while arsenic and zinc showed an association with pre-diabetes and atherosclerosis.

**Conclusions** Our data suggest a probable role of metals in the aetiology of diabetes and cardiovascular diseases in rural communities. Identifying and eliminating the causes of increased levels of these environmental chemicals could have a beneficial impact on the burden of non-communicable diseases in rural population.

## INTRODUCTION

With successes in the treatment and eradication of many communicable diseases worldwide, non-communicable diseases (NCDs) such as obesity, type 2 diabetes mellitus (T2D) and cardiovascular diseases (CVDs) have become major threats to population health, particularly in South Asia.<sup>1</sup> The WHO projects diabetes prevalence to expand from 422 million (8.5%) in 2014 to 592 million (12%) in 2035.<sup>2</sup> Recently, either pre-diabetes or T2D has been found in six out of ten adults in large South Asian cities such as Chennai, Delhi and Karachi.<sup>3</sup>

## Key messages

### What is already known about this subject?

- There has been a worrying increase in the prevalence of diabetes and cardiovascular diseases in rural India.
- Previous studies indicate the probable role of environmental chemicals such as toxic metals in the epidemic of metabolic diseases.
- But the association of metals and metabolic diseases in the rural world has been largely overlooked.

### What are the new findings?

- Our cross-sectional study of 865 subjects from a village in South India indicated a high prevalence of pre-diabetes, diabetes and atherosclerosis with no association with traditional risk factors.
- Urine metals showed an association with pre-diabetes, diabetes and atherosclerosis in this rural population.

### How might this impact on policy or clinical practice in the foreseeable future?

- This study adds to the growing body of evidence that the use of metals in anthropogenic activities contributes to increasing burden of metabolic diseases in the rural world.
- This study implicates the necessity for inclusion of metals in clinical diagnostics and therapies could be developed on targeting metal chelation.

Globally, a high prevalence of T2D, dyslipidaemia and hypertension has been observed in educated and more affluent groups in urban areas.<sup>4</sup> Such studies reinforce the idea that urbanisation, westernisation and affluence have significant roles in the explosion of NCDs. Intuitively, one would expect a low prevalence of NCDs in a rural population, where adherence to traditional lifestyles includes more physical activity and access to a more nutrient-rich (less processed foods) diet. However, our recent studies have demonstrated increased burden of T2D and CVDs in rural India.<sup>5–9</sup> Anecdotally, in recent years we have also observed increasing numbers of farmers in rural India seeking medical management for diabetes and hypertension who do not have the traditional risk factors for these



**To cite:** Velmurugan G, Swaminathan K, Veerasekar G, et al. *Occup Environ Med* Epub ahead of print: [please include Day/Month/Year]. doi:10.1136/oemed-2018-104996



conditions, such as older age, physical inactivity, high-fat diet and obesity. This provided us with the rationale to investigate the role of other, non-traditional risk factors for NCDs in rural Indian communities.

As an example of a non-traditional risk factor, evidence is accumulating that environmental chemicals may be linked with increased risk for T2D and CVDs. Much of this evidence is summarised in two position statements released by the Endocrine Society on the role of environmental endocrine-disrupting chemicals in population health and disease.<sup>10,11</sup> Epidemiological studies from urban areas have shown an association of metals such as cadmium, arsenic, lead, mercury and uranium with T2D<sup>12,13</sup> and CVDs.<sup>14</sup> These toxic metals are ubiquitous environmental contaminants and have been implicated in abnormal glucose metabolism, beta cell dysfunction and atherosclerosis.<sup>12–15</sup> Synthetic fertilisers and pesticides are rich sources of toxic metals in rural farming regions. However, the role of metals in the aetiology of NCDs in rural farming populations, where metal-rich agrochemicals are used,<sup>16</sup> is poorly understood. Therefore, the aim of this study is to examine the associations of urinary metals with the prevalence of T2D, other cardiovascular risk factors and atherosclerosis in Nallampatti, a typical Indian farming village dominated by modern synthetic chemical-based agricultural practices.

## MATERIALS AND METHODS

### Kovai Medical Center and Hospital-Nallampatti Non-Communicable Disease Study-I

Nallampatti is a typical farming village in Tamil Nadu, South India (latitude: 11°21'2.39" N; longitude: 77°32'4.79" E) (online supplementary figure 1) with a population of around 3000. All participants older than 20 years of age and native of that village were invited to participate in this study through pamphlets and word of mouth. This study, named the 'Nallampatti non-communicable disease study-I – 2015 (NNCD-I, 2015)',<sup>7</sup> was conducted every Sunday during a period of 4 weeks (15 March–5 April 2015). Informed written consent was obtained from all participants prior to participation and followed the principles of the Declaration of Helsinki.

### Data collection

Demographics, anthropometric data, non-fasting blood and spot urine samples were collected from all consented participants as previously described.<sup>7</sup> Body weight was measured using an electronic weighing scale (SECA 813), height was measured by a stadiometer (SECA 208), and waist circumference was measured in centimetres using a non-stretchable measuring tape between the costal margins and the iliac crest at the end of expiration. Blood pressure was recorded using the electronic Omron machine in sitting position in the right arm (Model HEM-7130, Omron Healthcare, Singapore) on two occasions 15 min apart. The average value was used to determine the hypertension status.

Serum and plasma samples were prepared from whole blood collected appropriately by standard protocols. Glycated haemoglobin (HbA<sub>1c</sub>) was measured using an automated high-performance liquid chromatography method (D-10-Bio-Rad), cystatin-c was determined by nephelometric method (BN ProSpec-Siemens), glucose was measured using a glucose oxidase – peroxidase method and lipid levels were measured using an automated analyser (Abbott Architect ci8200), and uric acid and creatinine levels were measured using the endpoint method (Abbott Architect ci8200). Urine protein was determined using commercially available kits as per manufacturers' instructions

and haemoglobin was determined by sodium lauryl sulfate method (Sysmex XN).

Carotid intima-media thickness (CIMT) was measured using two high-resolution B-mode ultrasound machines (GE Healthcare, Venue 40, USA), in supine position on a scan bed with the head of the patient resting comfortably, neck slightly hyperextended and the head tilted towards the opposite of the examined side. Both left and right common carotid arteries were depicted. The imaging was performed on field by two trained, final-year radiology residents under the supervision of a senior radiologist.

### Definition of outcomes

Diabetes was defined as either having a history of diabetes on medications or diagnosed with HbA<sub>1c</sub> of  $\geq 6.5\%$ . People with self-reported diabetes were confirmed by reviewing their medical records and their medications. For those reported as non-diabetic, HbA<sub>1c</sub>  $\geq 6.5\%$  was considered diabetic, and HbA<sub>1c</sub> ranging between 5.7% and 6.4% was defined as pre-diabetic, as per the American Diabetes Association guidelines (2017). Obesity and central obesity were defined using the criteria specific for Indian populations as body mass index (BMI)  $\geq 25 \text{ kg/m}^2$  and waist circumference  $\geq 90 \text{ cm}$  for men and  $\geq 80 \text{ cm}$  for women, respectively.<sup>17</sup> Hypertension was defined as either having a history of hypertension on medications or a systolic blood pressure  $\geq 140 \text{ mm Hg}$  and/or diastolic blood pressure  $\geq 90 \text{ mm Hg}$ . Abnormal non-fasting lipid levels were defined as total cholesterol  $\geq 200 \text{ mg/dL}$ , low-density lipoprotein-cholesterol (LDL-C)  $\geq 130 \text{ mg/dL}$ , high-density lipoprotein-cholesterol (HDL-C)  $< 40 \text{ mg/dL}$  in men and  $< 50 \text{ mg/dL}$  in women, and non-HDL-C  $\geq 160 \text{ mg/dL}$ .<sup>18</sup> Participants with self-reported diseases were confirmed by review of their medical records and medications. Carotid atherosclerosis was defined as a CIMT  $\geq 1 \text{ mm}$  in either left or right or in both measurements.<sup>19</sup>

### Metal analysis in fertilisers

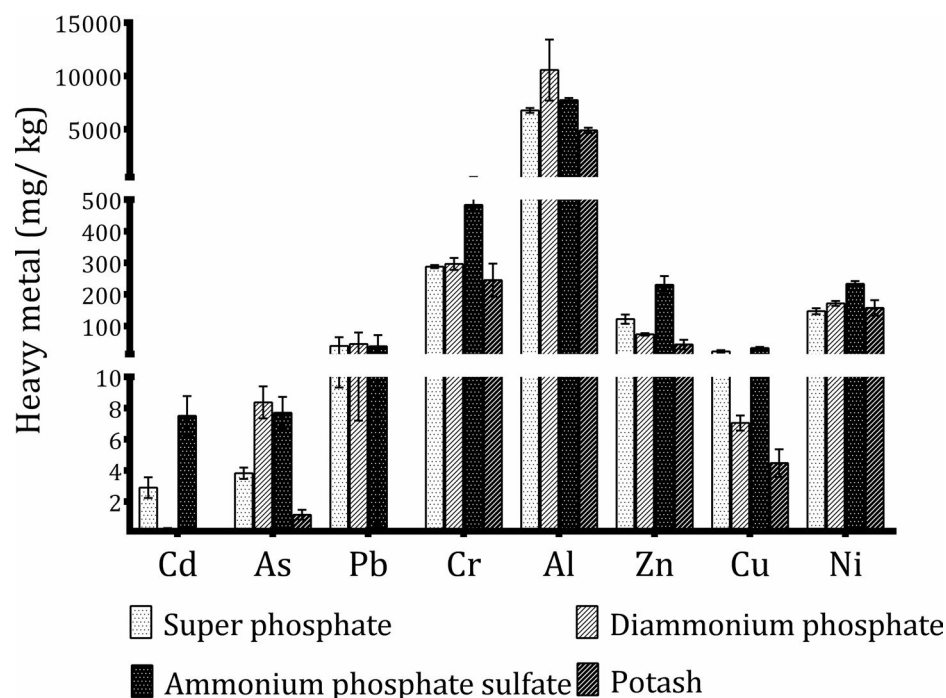
Fertiliser samples frequently used in the study village were purchased from agrochemical shops in the village and the surrounding area of 10 km. All the fertiliser products were government-subsidised products. Briefly, 1 g of the fertiliser sample was digested in a microwave oven in nitric acid:perchloric acid (2:1) mixture as per standard protocols. Finally, the level of metals was studied by inductively coupled plasma-mass spectrometry (ICP-MS (NexION 300X; PerkinElmer, USA)) and expressed as mg/kg of fertiliser.

### Assessment of exposure to metals

Among the 865 participants, 18 cases missing urine samples or other information were excluded from the study. Urine samples were immediately frozen and shipped for storage in a  $-80^\circ \text{C}$  deep freezer. The level of metals such as cadmium, arsenic, lead, chromium, aluminium, zinc, copper and nickel in urine was determined using ICP-MS (NexION 300X; PerkinElmer) as per the standard protocol.<sup>20</sup> Briefly, 200  $\mu\text{L}$  of urine sample was diluted with 1.8 mL diluent (5% nitric acid + 1.5% ethanol) and filtered through a 20  $\mu\text{m}$  filter. The filtrate was subjected to ICP-MS analysis. The concentrations of metals were normalised to urinary creatinine and expressed as  $\mu\text{g/mg}$  creatinine.

### Statistical methods

All statistical analyses were performed using the statistical software SPSS V.20.0. Urine metal concentrations were categorised in quartiles based on the weighted sample distribution. The association between risk factors and disease outcomes was studied



**Figure 1** Concentration of toxic metals in the synthetic fertilisers being used in the study village.

by multiple logistic regression analysis, with age, sex, familial diabetic history, BMI, systolic and diastolic blood pressure, LDL-C, smoking, and alcohol and tobacco usage as confounders for adjustment in diabetes and pre-diabetes. In the case of atherosclerosis, along with above-mentioned confounders, diabetes and familial ischaemic heart disease history were used for adjustment. For each metal, we used logistic regression to estimate ORs and CI levels for diabetes, pre-diabetes and carotid atherosclerosis by comparing each quartile with the lowest quartile. Our logistic regression models were fitted with appropriate degrees of adjustment. In each analysis, we also evaluated the significance of the differences of the average proportion of disorder across the four quartiles of the model by a generalised maximum likelihood Wald  $\chi^2$  test. Subsequently, we tested for linear trends across quartiles of urine metals by including the median of each quartile as a continuous variable in logistic regression models. Spearman's correlation coefficient was calculated between metals and cardiometabolic risk factors. Statistical significance was determined on the basis of two-sided p values of  $<0.05$ .

## RESULTS

Out of 865 participants in our study, 82.7% ( $n=715$ ) were involved in chemical-based farming practices. Rice is the staple food of the people, and largely grown from their own land is used for day-to-day consumption. All the characteristics of the study population are shown in online supplementary table 1. The prevalence of pre-diabetes and diabetes in this population based on HbA<sub>1c</sub> levels was 43.4% and 16.2%, respectively. Out of the total diabetes population ( $n=141$ ), 79 (56%) were self-reported and the rest (44%) were newly diagnosed based on HbA<sub>1c</sub> analysis. Pre-diabetes and diabetes were almost equally prevalent among both sexes, while atherosclerosis prevalence was relatively higher among men. Among people with pre-diabetes and diabetes, more than 50% were middle-aged (41–60 years). A very low prevalence of diabetes and atherosclerosis was noted among young-aged

people (20–40 years). On multivariate regression analysis after adjustment for confounders, among the traditional risk factors, only age and BMI showed an association with diabetes and pre-diabetes, while in the case of atherosclerosis only age showed a significant association (online supplementary table 2).

On our survey of agricultural practices in the study village, we found that superphosphate, diammonium phosphate, ammonium phosphate sulfate and potash were the major synthetic fertilisers being used. The level of toxic metals was extremely high in all types of phosphate fertilisers but not in potash fertiliser (figure 1). No significant difference in the level of aluminium, zinc, copper and nickel was found between the types of fertilisers. An increased level of these urinary metals was noted among the people with pre-diabetes, diabetes and atherosclerosis in comparison with non-diabetic and non-atherosclerotic people, respectively (online supplementary table 3). On correlation and regression analyses of the urinary metals with cardiometabolic risk factors (HbA<sub>1c</sub>, systolic and diastolic blood pressure, BMI, total cholesterol, CMT-left, CMT-right and cystatin-c), only HbA<sub>1c</sub> and CMT showed significant correlation with the metals (table 1). Hence subsequent analyses focused only on diabetes, pre-diabetes and atherosclerosis.

Based on metal accumulation, the population was divided into quartiles (online supplementary table 4). Significant trends for pre-diabetes associated with the highest quartile of metal compared with the lowest quartile of metal (table 2) were found for arsenic and zinc. Significant trends for T2D associated with the highest quartile of metal compared with the lowest quartile of metal (table 3) were found for arsenic, chromium, aluminium and zinc. Similar to pre-diabetes, significant trends for carotid atherosclerosis associated with the highest quartile of metal compared with the lowest quartile of metal (table 4) were found for arsenic and zinc. Among the metals studied, arsenic and zinc showed association with pre-diabetes, diabetes and atherosclerosis.

**Table 1** Correlation analysis between the cardiometabolic risk factors and urinary metals

	Correlation coefficient								
	HbA <sub>1c</sub>	Systolic BP	Diastolic BP	BMI	Total cholesterol	LDL-cholesterol	CIMT-left	CIMT-right	Cystatin-c
Cadmium	0.08*	0.01	−0.03	−0.11	−0.00	−0.03	0.02	−0.01	0.01
Arsenic	0.16***	0.37	0.02	0.01	0.10**	0.07*	0.18†	0.16†	0.09*
Lead	0.13***	−0.01	−0.03	−0.12	−0.03	−0.04	0.14†	0.13***	0.06
Chromium	0.12**	−0.01	−0.02	−0.14	−0.08	−0.07	0.07*	0.07*	0.03
Aluminium	0.09**	0.01	−0.02	−0.14	−0.04	−0.05	0.08*	0.08*	0.02
Zinc	0.17***	0.02	0.01	−0.05	0.02	−0.01	0.13***	0.12***	0.12***
Copper	0.11**	0.03	0.01	−0.08	0.01	−0.01	0.02	0.02	0.03
Nickel	0.92**	0.01	−0.03	−0.12	−0.07	−0.06	−0.02	0.01	0.03

Spearman's correlation, two-tailed: \*p&lt;0.05, \*\*p&lt;0.01, \*\*\*p&lt;0.001, †p&lt;0.0001.

BMI, body mass index; BP, blood pressure; CIMT, carotid intima-media thickness; HbA<sub>1c</sub>, glycated haemoglobin; LDL, low-density lipoprotein.

## DISCUSSION

Although the prevalence of NCDs is commonly reported in urban populations, the WHO (2014) has estimated that 47% of the global and 67% of the Indian population live in rural villages, where NCDs are often underestimated or overlooked. Our study highlights the burden of diabetes and pre-diabetes in a rural population of India, which exceeds that estimated in the urban population centres, and raises vital questions on the association between traditional cardiometabolic risk factors and prevalent hyperglycaemic continuum in rural India. In terms of pre-diabetes, it is possible that the criteria for pre-diabetes (HbA<sub>1c</sub> 5.7–6.4) determined by the American Diabetes Association may over-represent pre-diabetes in an Indian population. We are particularly concerned that a high proportion of rural population in our study has either diabetes or pre-diabetes, far higher than a similar, larger study done in rural India.<sup>6</sup> This led us to question whether traditional risk factors alone are enough to explain the huge prevalence of NCD in this population.

Because other studies have linked toxic metals in fertilisers and other agricultural products with islet cell impairment and diabetes risk, we studied the relationships between excretion rates of several metals and prevalence of pre-diabetes, T2D

and carotid atherosclerosis. The association and possible role of two metals, arsenic and zinc, with diabetes, pre-diabetes and atherosclerosis in our study are especially intriguing. Possible links between exposure to arsenic and incident of diabetes have been reported in urban studies from various parts of the world.<sup>13 14</sup> This element has been proposed to increase the risk of diabetes by multiple mechanisms, including altered gene expression, increased oxidative stress, upregulation of inflammatory markers such as interleukin-6 and tumour necrosis factor alpha, disruption of glucose uptake and transport, increased gluconeogenesis, pancreatic beta cell dysfunction due to amyloid deposition, adipocyte differentiation and altered gut microbiota.<sup>21 22</sup> Oxidised LDL-C and several inflammatory molecules have also been implicated in arsenic-associated atherosclerosis risk.<sup>23</sup>

Synthetic phosphate fertilisers are important sources of metals, particularly arsenic, which can accumulate in soil with repeated application.<sup>16</sup> Arsenic accumulated in the soil easily enters into the groundwater or is readily adsorbed by plants, entering the animal kingdom, including humans, through the food chain. This is especially a concerning issue in the Indian context, where often poor monitoring, lack of

**Table 2** ORs (95% CI) of pre-diabetes associated with quartiles of urinary metals (n=847)

	Model	OR (95% CI)				P <sub>trend</sub>
		Quartile 1	Quartile 2	Quartile 3	Quartile 4	
Cadmium	Unadjusted	1.00	1.23 (0.81 to 1.86)	1.19 (0.78 to 1.80)	<b>1.80 (1.18 to 2.75)</b>	0.110
	Adjusted*	1.00	1.09 (0.69 to 1.71)	1.02 (0.65 to 1.60)	<b>1.67 (1.06 to 2.64)</b>	0.352
Arsenic	Unadjusted	1.00	1.46 (0.96 to 2.22)	<b>1.82 (1.20 to 2.77)</b>	<b>2.14 (1.40 to 3.26)</b>	<0.001
	Adjusted*	1.00	<b>1.41 (1.01 to 2.21)</b>	<b>1.75 (1.12 to 2.73)</b>	<b>1.93 (1.23 to 3.04)</b>	<0.001
Lead	Unadjusted	1.00	1.02 (0.68 to 1.54)	1.24 (0.82 to 1.89)	1.48 (0.97 to 2.24)	<b>0.044</b>
	Adjusted*	1.00	0.91 (0.59 to 1.43)	1.29 (0.82 to 2.03)	1.36 (0.86 to 2.15)	0.065
Chromium	Unadjusted	1.00	1.10 (0.73 to 1.66)	1.17 (0.77 to 1.77)	<b>1.54 (1.01 to 2.35)</b>	<b>0.048</b>
	Adjusted*	1.00	1.08 (0.69 to 1.69)	1.16 (0.74 to 1.83)	1.48 (0.93 to 2.36)	0.069
Aluminium	Unadjusted	1.00	0.98 (0.65 to 1.48)	1.16 (0.76 to 1.77)	1.40 (0.92 to 2.13)	0.082
	Adjusted*	1.00	1.03 (0.66 to 1.59)	1.14 (0.72 to 1.80)	1.53 (0.97 to 2.41)	0.102
Zinc	Unadjusted	1.00	1.12 (0.75 to 1.69)	<b>2.16 (1.42 to 3.28)</b>	<b>1.49 (1.02 to 2.27)</b>	<b>0.005</b>
	Adjusted*	1.00	1.10 (0.71 to 1.72)	<b>2.18 (1.39 to 3.42)</b>	<b>1.24 (1.09 to 1.96)</b>	<b>0.006</b>
Copper	Unadjusted	1.00	1.12 (0.75 to 1.70)	1.48 (0.98 to 2.25)	1.47 (0.97 to 2.24)	<b>0.032</b>
	Adjusted*	1.00	1.26 (0.81 to 1.95)	1.45 (0.93 to 2.28)	<b>1.57 (1.00 to 2.46)</b>	0.085
Nickel	Unadjusted	1.00	1.07 (0.71 to 1.62)	1.39 (0.92 to 2.12)	1.46 (0.96 to 2.23)	<b>0.038</b>
	Adjusted*	1.00	1.03 (0.66 to 1.61)	1.23 (0.78 to 1.94)	1.36 (0.86 to 2.16)	0.077

\*Adjusted: multivariate adjustment included age, sex, education, occupation, waist circumference, body mass index, diastolic and systolic blood pressure, low-density lipoprotein-cholesterol, familial diabetic history, smoking, and alcohol and tobacco usage. The OR or p trend value shown in bold indicates statistical significance.

**Table 3** ORs (95% CI) of diabetes associated with quartiles of urinary metals (n=847)

		OR (95% CI)				P <sub>trend</sub>
	Model	Quartile 1	Quartile 2	Quartile 3	Quartile 4	
Cadmium	Unadjusted	1.00	1.25 (0.72 to 2.17)	1.07 (0.61 to 1.87)	1.60 (0.91 to 2.79)	0.142
	Adjusted*	1.00	0.99 (0.54 to 1.84)	0.92 (0.49 to 1.72)	1.46 (0.79 to 2.75)	0.352
Arsenic	Unadjusted	1.00	<b>2.05 (1.14 to 3.71)</b>	<b>2.44 (1.35 to 4.42)</b>	<b>2.94 (1.63 to 5.30)</b>	<b>0.001</b>
	Adjusted*	1.00	1.87 (0.98 to 3.57)	<b>2.44 (1.27 to 4.69)</b>	<b>2.68 (1.40 to 3.80)</b>	<b>0.005</b>
Lead	Unadjusted	1.00	<b>1.34 (0.75 to 2.38)</b>	<b>2.09 (1.22 to 3.60)</b>	<b>1.90 (1.10 to 3.31)</b>	0.091
	Adjusted*	1.00	<b>1.35 (0.56 to 3.25)</b>	<b>2.46 (1.10 to 5.50)</b>	<b>2.70 (1.16 to 6.32)</b>	0.134
Chromium	Unadjusted	1.00	1.04 (0.58 to 1.89)	1.69 (0.96 to 2.97)	<b>2.15 (1.22 to 3.77)</b>	<b>0.034</b>
	Adjusted*	1.00	1.05 (0.58 to 2.02)	1.87 (0.99 to 3.51)	<b>2.40 (1.26 to 4.56)</b>	<b>0.012</b>
Aluminium	Unadjusted	1.00	0.79 (0.43 to 1.46)	<b>1.93 (1.11 to 3.35)</b>	<b>1.80 (1.02 to 3.16)</b>	<b>0.019</b>
	Adjusted*	1.00	0.86 (0.44 to 1.67)	<b>2.03 (1.10 to 3.74)</b>	<b>2.19 (1.16 to 4.12)</b>	<b>0.025</b>
Zinc	Unadjusted	1.00	<b>2.15 (1.14 to 4.04)</b>	<b>3.54 (1.87 to 6.71)</b>	<b>4.12 (2.23 to 7.60)</b>	<b>&lt;0.001</b>
	Adjusted*	1.00	<b>2.10 (1.10 to 4.38)</b>	<b>3.93 (1.96 to 7.87)</b>	<b>3.32 (1.70 to 6.49)</b>	<b>&lt;0.001</b>
Copper	Unadjusted	1.00	<b>1.51 (0.85 to 2.67)</b>	<b>1.98 (1.13 to 3.46)</b>	<b>2.16 (1.25 to 3.74)</b>	<b>0.048</b>
	Adjusted*	1.00	<b>1.32 (0.57 to 3.09)</b>	<b>1.66 (0.76 to 3.67)</b>	<b>2.27 (1.02 to 5.02)</b>	0.272
Nickel	Unadjusted	1.00	0.85 (0.48 to 1.51)	1.34 (0.76 to 2.33)	1.47 (0.85 to 2.54)	0.187
	Adjusted*	1.00	0.75 (0.40 to 1.41)	1.12 (0.61 to 2.08)	1.36 (0.74 to 2.57)	0.256

\*Adjusted: multivariate adjustment included age, sex, education, occupation, waist circumference, body mass index, diastolic and systolic blood pressure, low-density lipoprotein-cholesterol, familial diabetic history, smoking, and alcohol and tobacco usage. The OR or p trend value shown in bold indicates statistical significance.

quality control mechanisms, ignorance of the danger and poor training are prevalent with farmers opting for more toxic chemicals to expedite and enhance crop yields. A World Bank report (2010) revealed that South Asia is the leader in synthetic fertiliser consumption, which is primarily applied for cultivation of rice, the staple food of this subcontinent.

Our recent study showcased the accumulation of different metals including arsenic in different varieties of rice.<sup>24</sup> The rice grown in the fields in the study village applied with the metal-rich fertilisers is largely used for their consumption. South Indian people will consume 200–400 g of rice per day, and hence it is logical to link the metals in agrochemicals with rice consumption and urinary metals. There have been studies linking higher white rice intake to elevated risk of

T2D, especially in Asian populations. This has led to coining of a new terminology called ‘Riceabetes’.<sup>25</sup> Over the last few years, there has been a heightened concern on the levels of arsenic in rice and vegetables.<sup>24–26</sup> It is therefore reasonable to speculate that arsenic may be one ‘cog in the wheel’ contributing to an increase in diabetes and CVDs in rural India. Apart from arsenic, zinc was the only other metal associated with pre-diabetes, diabetes and carotid atherosclerosis in our study. Phosphate fertilisers were shown to be rich in both arsenic and zinc.<sup>27</sup> An unexpected finding in our study was the association of urinary zinc with diabetes, pre-diabetes and atherosclerosis. Numerous studies, both in vivo and in vitro, had demonstrated the beneficial effects of zinc in both type 1 and type 2 diabetes.<sup>28–29</sup> Zinc has antioxidant

**Table 4** ORs (95% CI) of atherosclerosis associated with quartiles of urinary metals (n=847)

		ORs (95% CI)				P <sub>trend</sub>
	Model	Quartile 1	Quartile 2	Quartile 3	Quartile 4	
Cadmium	Unadjusted	1.00	0.99 (0.52 to 1.90)	1.15 (0.61 to 2.16)	1.33 (0.72 to 2.46)	0.309
	Adjusted*	1.00	0.76 (0.38 to 1.52)	0.96 (0.48 to 1.90)	1.12 (0.57 to 2.18)	0.486
Arsenic	Unadjusted	1.00	<b>2.94 (1.28 to 6.76)</b>	<b>2.63 (1.13 to 6.11)</b>	<b>5.69 (2.59 to 12.5)</b>	<b>&lt;0.001</b>
	Adjusted*	1.00	<b>2.65 (1.11 to 6.31)</b>	<b>2.45 (1.02 to 5.90)</b>	<b>5.56 (2.42 to 12.7)</b>	<b>&lt;0.001</b>
Lead	Unadjusted	1.00	1.39 (0.68 to 2.86)	<b>2.05 (1.05 to 4.04)</b>	<b>2.23 (1.14 to 4.35)</b>	<b>0.008</b>
	Adjusted*	1.00	1.29 (0.61 to 2.75)	1.95 (0.94 to 4.04)	<b>2.29 (1.14 to 4.75)</b>	<b>0.012</b>
Chromium	Unadjusted	1.00	1.13 (0.56 to 2.28)	1.86 (0.97 to 3.54)	1.78 (0.93 to 3.41)	<b>0.032</b>
	Adjusted*	1.00	1.08 (0.52 to 2.27)	1.84 (0.92 to 3.72)	1.77 (0.87 to 3.61)	0.065
Aluminium	Unadjusted	1.00	1.06 (0.52 to 2.16)	1.56 (0.80 to 3.02)	<b>2.17 (1.15 to 4.08)</b>	<b>0.036</b>
	Adjusted*	1.00	1.20 (0.57 to 2.55)	1.50 (0.74–3.05)	<b>2.54 (1.28 to 5.06)</b>	0.056
Zinc	Unadjusted	1.00	1.89 (0.88 to 4.04)	<b>2.90 (1.41 to 5.97)</b>	<b>2.88 (1.40 to 5.93)</b>	<b>0.002</b>
	Adjusted*	1.00	1.92 (0.86 to 4.29)	<b>2.86 (1.33 to 6.14)</b>	<b>2.13 (1.06 to 4.59)</b>	<b>0.001</b>
Copper	Unadjusted	1.00	0.88 (0.45 to 1.71)	1.51 (0.82 to 2.76)	1.10 (0.58 to 2.08)	0.409
	Adjusted*	1.00	0.87 (0.43 to 1.76)	1.30 (0.68 to 2.52)	0.99 (0.50 to 2.00)	0.658
Nickel	Unadjusted	1.00	0.90 (0.47 to 1.70)	1.10 (0.59 to 2.02)	1.05 (0.56 to 1.94)	0.738
	Adjusted*	1.00	0.82 (0.41 to 1.63)	0.85 (0.44 to 1.66)	0.75 (0.45 to 1.77)	1.056

\*Adjusted: multivariate adjustment included age, sex, education, occupation, waist circumference, body mass index, glycated haemoglobin, diastolic and systolic blood pressure, low-density lipoprotein-cholesterol, familial ischaemic heart disease history, smoking, and alcohol and tobacco usage. The OR or p trend value shown in bold indicates statistical significance.



properties, stimulates glycolysis, inhibits gluconeogenesis, reversibly inhibits alpha glucosidase activity in intestines, enhances glucose transport in adipocytes, increases the expression of peroxisome proliferator-activated receptor gamma and thereby promoting adipogenesis, increases free insulin concentrations and inhibits amyloid fibrillogenesis that is implicated in beta cell destruction.<sup>28</sup> Therefore, it was surprising to see a positive association between increasing urinary zinc concentrations and diabetes in our study. The answer may lie in the observations from as early as 1970s of 'hyperzincuria' in subjects with diabetes compared with the control population.<sup>30</sup> Studies have shown that subjects with type 1 diabetes excrete four times more zinc in the urine compared with non-diabetic controls.<sup>31</sup> The exact molecular mechanisms to explain a link between hyperzincuria and diabetes are not clear at this point but may relate to reduced renal tubular absorption of zinc due to hyperglycaemia and insulin deficiency. While it is a speculation to link hyperzincuria to CVDs at this point, there are studies linking hyperzincuria to incipient nephropathy and 'Near Sudden Unexplained Death Syndrome'.<sup>32</sup> Further research is needed to evaluate the mechanisms of hyperzincuria and its association with diabetes and CVDs in a rural population.

The role of chromium and aluminium, the other two metals showing an association with T2D in our study, is less clear. Besides synthetic fertiliser use, the other possible sources of these elements might be leaching from cooking utensils since chromium, which is associated with stainless steel and aluminium utensils, is commonly used for cooking purposes in rural India. This metal is linked to hyperinsulinaemia and insulin resistance.<sup>33</sup> However, the biological roles or plausible mechanisms of these two metals in relation to diabetes or CVDs need to be investigated.

Our study has several limitations. The sampling was convenient as it was difficult to do randomised cluster sampling as it may be perceived as an offence by the local population. Anyone >20 years of age was invited for study through door to door and speaker announcements. A total of 865 participants turned up for the study. As a cross-sectional study it cannot establish causality of any of the significant relationships we find. We cannot rule out the possibility that changes in metabolism, lifestyle or medication use after the development of diabetes affected exposure, absorption or excretion of some metals. Another limitation is the use of a single urine metal measurement, which may not reflect cumulative exposure and does not address the route of exposure or different forms of the metals. A 24-hour urine sample may have been preferable to a spot urine sample, but we adjusted for creatinine to control for concentration dilution of urine. Also, the use of only HbA<sub>1c</sub> to determine undiagnosed diabetes may have missed some people who would have been considered to have diabetes based on fasting glucose or 2-hour glucose after a glucose challenge. Due to logistics and manpower issues, we were not able to have an independent review of carotid intima thickness nor could we do quality assurance on measurement readings. Finally, exposure to these metals may involve coexposure to other potentially harmful substances, and we cannot rule out confounding by substances not measured.

In conclusion, our study provides new evidence that suggests a probable role of metals in the prevalence of diabetes and CVDs in rural India. If verified, these data should simultaneously lead to implementation of large-scale epidemiological and mechanistic studies on the role of metals in the aetiopathogenesis of the hyperglycaemic spectrum and CVDs in rural populations

and prompt governmental action to closely monitor fertilisation practices or promote safer alternative farming practices.

**Acknowledgements** The authors acknowledge the KMCH nursing and radiology team and M/s Microlabs for their assistance in sample and data collection. GVel acknowledges Indian Institute of Technology Madras for providing Institute Post-doctoral fellowship. The authors acknowledge all the volunteers and village heads for their cooperation in the execution of this study.

**Contributors** Conceived and designed the experiments: GVel, KS, GVee, MC, NGP, TA and TP. Involved in sample collection: GVel, KS, GVee and NGP. Performed the experiments: GVel, KS, SM, MD and AKA. Analysed the data: GVel, KS, GVee, JQP and TP. Contributed reagents/materials/analysis tools: KS, JQP, MC, NGP, TA and TP. Wrote the manuscript: GVel and KS. Revised the manuscript: JQP, SM, MD, AKA, GVee, MC, NGP, TA and TP.

**Funding** The work is funded by DST-Nano Mission, Government of India and KMCH Research Foundation, India.

**Competing interests** None declared.

**Patient consent** Obtained.

**Ethics approval** The study design and protocol were approved by KMCH Ethics Committee, Kovai Medical Center and Hospital Limited, Coimbatore (approval no EC/AP/02/2015 dated 16 February 2015).

**Provenance and peer review** Not commissioned; externally peer reviewed.

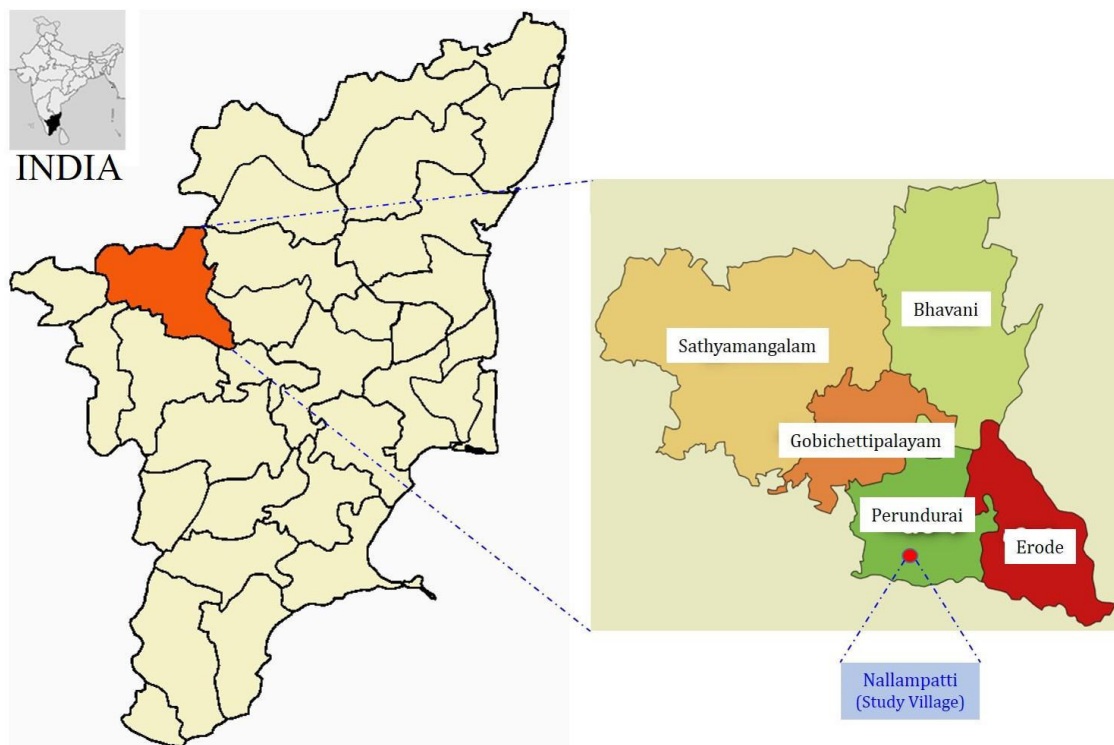
© Article author(s) (or their employer(s) unless otherwise stated in the text of the article) 2018. All rights reserved. No commercial use is permitted unless otherwise expressly granted.

## REFERENCES

- 1 Siegel KR, Patel SA, Ali MK. Non-communicable diseases in South Asia: contemporary perspectives. *Br Med Bull* 2014;111:31–44.
- 2 World Health Organization. *Global Report on Diabetes*: WHO, 2016.
- 3 Deepa M, Grace M, Binukumar B, et al. High burden of prediabetes and diabetes in three large cities in South Asia: The Center for Cardio-metabolic Risk Reduction in South Asia (CARRS) Study. *Diabetes Res Clin Pract* 2015;110:172–82.
- 4 Ali MK, Bhaskarapillai B, Shivashankar R, et al. Socioeconomic status and cardiovascular risk in urban South Asia: The CARRS Study. *Eur J Prev Cardiol* 2016;23:408–19.
- 5 Misra P, Upadhyay RP, Misra A, et al. A review of the epidemiology of diabetes in rural India. *Diabetes Res Clin Pract* 2011;92:303–11.
- 6 Anjana RM, Pradeepa R, Deepa M, et al. Prevalence of diabetes and pre-diabetes (impaired fasting glucose and/or impaired glucose tolerance) in urban and rural India: phase I results of the Indian Council of Medical Research-India Diabetes (ICMR-INDIAB) study. *Diabetologia* 2011;52:3022–7.
- 7 Swaminathan K, Veerasekar G, Kuppusamy S, Ganesh V, Sujatha K, et al. Noncommunicable disease in rural India: Are we seriously underestimating the risk? The Nallampatti noncommunicable disease study. *Indian J Endocrinol Metab* 2017;21:90–5.
- 8 Velmurugan G, Ramprasath T, Swaminathan K, et al. Gut microbial degradation of organophosphate insecticides induces glucose intolerance via gluconeogenesis. *Genome Biol* 2017;18:8.
- 9 Velmurugan G, Ramprasath T, Gilles M, et al. Gut Microbiota, Endocrine-Disrupting Chemicals, and the Diabetes Epidemic. *Trends Endocrinol Metab* 2017;28:612–25.
- 10 Diamanti-Kandarakis E, Bourguignon JP, Giudice LC, et al. Endocrine-disrupting chemicals: an Endocrine Society scientific statement. *Endocr Rev* 2009;30:293–342.
- 11 Gore AC, Chappell VA, Fenton SE, et al. EDC-2: The Endocrine Society's Second Scientific Statement on Endocrine-Disrupting Chemicals. *Endocr Rev* 2015;36:E1–E150.
- 12 Navas-Acien A, Silbergeld EK, Pastor-Barriuso R, et al. Arsenic exposure and prevalence of type 2 diabetes in US adults. *JAMA* 2008;300:814–22.
- 13 Menke A, Gualler E, Cowie CC. Metals in urine and Diabetes in US Adults. *Diabetes* 2016;65:164–71.
- 14 Lind PM, Olsén L, Lind L. Circulating levels of metals are related to carotid atherosclerosis in elderly. *Sci Total Environ* 2012;416:80–8.
- 15 Alissa EM, Ferns GA. Heavy metal poisoning and cardiovascular disease. *J Toxicol* 2011;2011:1–21.
- 16 Gimeno-García E, Andreu V, Boluda R. Heavy metals incidence in the application of inorganic fertilizers and pesticides to rice farming soils. *Environ Pollut* 1996;92:19–25.
- 17 Pradeepa R, Anjana RM, Joshi SR, et al. Prevalence of generalized & abdominal obesity in urban & rural India—the ICMR-INDIAB Study (Phase-I) [ICMR- NDIAB-3]. *Indian J Med Res* 2015;142:139–50.
- 18 Jacobson TA, Ito MK, Maki KC, et al. National lipid association recommendations for patient-centered management of dyslipidemia: part 1—full report. *J Clin Lipidol* 2015;9:129–69.

- 19 Jacoby DS, Mohler III ER, Rader DJ. Noninvasive atherosclerosis imaging for predicting cardiovascular events and assessing therapeutic interventions. *Curr Atheroscler Rep* 2004;6:20–6.
- 20 *Urine multi-element analysis ICP-DRC-MS (2012) Laboratory procedure manual*. USA: Centre for disease control and prevention.
- 21 Tseng CH. The potential biological mechanisms of arsenic-induced diabetes mellitus. *Toxicol Appl Pharmacol* 2004;197:67–83.
- 22 Díaz-Villaseñor A, Burns AL, Hiriart M, *et al*. Arsenic-induced alteration in the expression of genes related to type 2 diabetes mellitus. *Toxicol Appl Pharmacol* 2007;225:123–33.
- 23 Karim MR, Rahman M, Islam K, *et al*. Increases in oxidized low-density lipoprotein and other inflammatory and adhesion molecules with a concomitant decrease in high-density lipoprotein in the individuals exposed to arsenic in Bangladesh. *Toxicol Sci* 2013;135:17–25.
- 24 Deb D, Sengupta S, Pradeep T. A profile of metals in rice (*Oryza sativa* ssp. *Indica*) landraces. *Curr Sci* 2015;09:407–9.
- 25 Bell DS. Riceabetes: is the association of type 2 diabetes with rice intake due to a high carbohydrate intake or due to exposure to excess inorganic arsenic? *Postgrad Med* 2015;127:781–2.
- 26 Davis MA, Mackenzie TA, Cottingham KL, *et al*. Rice consumption and urinary arsenic concentrations in U.S. children. *Environ Health Perspect* 2012;120:1418–24.
- 27 Jayasumana C, Fonseka S, Fernando A, *et al*. Phosphate fertilizer is a main source of arsenic in areas affected with chronic kidney disease of unknown etiology in Sri Lanka. *Springerplus* 2015;4:90.
- 28 Ranasinghe P, Pigera S, Galappatthy P, *et al*. Zinc and diabetes mellitus: understanding molecular mechanisms and clinical implications. *Daru* 2015;23:44.
- 29 Simon SF, Taylor CG. Dietary zinc supplementation attenuates hyperglycemia in db/db mice. *Exp Biol Med* 2001;226:43–51.
- 30 Pidduck HG, Wren PJ, Evans DA. Hyperzincuria of diabetes mellitus and possible genetical implications of this observation. *Diabetes* 1970;19:240–7.
- 31 Heise CC, King JC, Costa FM, *et al*. Hyperzincuria in IDDM women. Relationship to measures of glycemic control, renal function, and tissue catabolism. *Diabetes Care* 1988;11:780–6.
- 32 Pansin P, Wathanavaha A, Tosukhowong P, *et al*. Magnesium and zinc status in survivors of sudden unexplained death syndrome in northeast Thailand. *Southeast Asian J Trop Med Public Health* 2002;33:172–9.
- 33 Longnecker MP, Daniels JL. Environmental contaminants as etiologic factors for diabetes. *Environ Health Perspect* 2001;109:871.

## Nallampatti – Noncommunicable Disease Study



**Supplementary figure 1:** Geographic location of the study village - Nallampatti. The red dot indicates the study village. (Latitude: 11°21'2.39" N; Longitude: 77°32'4.79" E).



**Supplementary Table 1:** Characteristics of the participants of Nallampatti non-communicable disease-I study – 2015 (NNCD-I, 2015).

KMCH-NNCD, 2015		Whole Population (n=865)	Pre-diabetes (n=371)	Diabetes (n=142)	Carotid Atherosclerosis (n=90)
		Percent	Percent	Percent	Percent
Sex	Male	48.0	43.1	59.6	67.5
	Female	52.0	56.9	40.4	32.5
Age (years)	20 - 40	32.9	25.3	5.7	2.3
	41 - 60	46.6	53.7	57.4	46.1
	Above 60	20.5	21.0	36.9	51.7
Alcohol intake (only Males)	Daily	2.7	2.0	3.8	1.8
	Occasionally	50.4	47.3	58.2	64.9
	Never	47.0	50.7	38.0	33.3
Smoking (only Males)	Daily	31.2	20.5	32.8	35.7
	Occasionally	25.0	14.0	30.3	34.0
	Never	43.8	55.5	36.8	30.3
Tobacco Use	Daily	14.2	17.5	16.2	12.2
	Occasionally	11.5	11.0	8.5	20.8
	Never	74.3	71.5	75.4	67.1
BMI (kg/m <sup>2</sup> )	Obese ( $\geq 25$ )	31.6	34.2	36.2	32.6
	Underweight ( $\leq 18.5$ )	13.2	11.2	6.4	18
HbA1c (%)	Diabetes ( $\geq 6.5$ )	16.2	--	--	32.6
	Prediabetes (5.7-6.4)	43.4	--	--	48.4
Blood Pressure (mm Hg)	Hypertension ( $\geq 140/90$ )	37.8	33.0	49.6	54.0
Total Cholesterol (mg/dL)	Hypercholesterolemia ( $\geq 200$ )	33.4	40.4	34.6	39.4
CIMT (mm)	Atherosclerosis ( $\geq 1$ )	10.3	11.6	20.5	--

**Supplementary Table 2:** Multiple regression analysis between traditional risk factors and disease outcomes

	Univariate analysis			Multivariate analysis*		
	Risk ratio	95% C.I	P value	Risk ratio	95% C.I	P value
<b>Pre diabetes</b>						
<b>Age</b>	1.05	1.03 - 1.06	<b>&lt;0.001</b>	1.05	1.03 - 1.06	<b>&lt;0.001</b>
<b>Sex</b>	1.19	0.88 - 1.60	0.254	1.29	0.92 - 1.81	0.146
<b>BMI</b>	1.07	1.04 - 1.16	<b>&lt;0.001</b>	1.08	1.02 - 1.17	<b>0.009</b>
<b>Waist Circumference</b>	1.03	1.01 - 1.05	<b>&lt;0.001</b>	0.99	0.97 - 1.03	0.960
<b>Education</b>	1.82	1.29 - 2.58	<b>0.001</b>	1.15	0.77 - 1.74	0.493
<b>Diabetes</b>						
<b>Age</b>	1.10	1.08 - 1.12	<b>&lt;0.001</b>	1.10	1.07 - 1.12	<b>&lt;0.001</b>
<b>Sex</b>	0.64	0.43 - 0.95	<b>0.026</b>	0.80	0.49 - 1.29	0.368
<b>BMI</b>	1.10	1.05 - 1.16	<b>&lt;0.001</b>	1.16	1.06 - 1.27	<b>0.002</b>
<b>Waist Circumference</b>	1.05	1.03 - 1.07	<b>&lt;0.001</b>	0.99	0.96 - 1.04	0.850
<b>Education</b>	2.04	1.32 - 3.16	<b>0.001</b>	1.05	0.61 - 1.80	0.863
<b>Carotid Atherosclerosis</b>						
<b>Age</b>	1.09	1.07 -1.12	<b>&lt;0.001</b>	1.08	1.06 -1.11	<b>&lt;0.001</b>
<b>Sex (Male)</b>	0.41	0.26 -0.66	<b>&lt;0.001</b>	0.49	0.23 -1.05	0.067
<b>BMI</b>	1.01	0.96 -1.06	0.706	1.02	0.91 -1.13	0.782
<b>Waist Circumference</b>	1.03	1.00 -1.05	<b>0.020</b>	1.01	0.96-1.06	0.657
<b>Education</b>	2.07	1.32 -3.25	<b>0.002</b>	1.47	0.82 -2.63	0.198
<b>Pre-diabetes</b>	1.86	1.05 -3.28	<b>0.033</b>	1.10	0.58 -2.08	0.764
<b>Diabetes</b>	3.29	1.96 -5.54	<b>&lt;0.001</b>	1.37	0.76 -2.48	0.297
<b>Hypertension</b>	2.67	1.71 -4.16	<b>&lt;0.001</b>	1.39	0.83 -2.29	0.205
<b>Smoking</b>	2.71	1.72 -4.30	<b>&lt;0.001</b>	1.43	0.73 -2.79	0.297
<b>Total Cholesterol</b>	1.00	0.99 -1.01	0.202	1.39	0.94 -1.01	0.223
<b>Triglyceride</b>	1.00	0.99 -1.00	0.352	1.00	0.99 -1.01	0.134
<b>LDL Cholesterol</b>	1.01	0.99 -1.01	0.119	1.03	0.99 -1.07	0.112
<b>HDL Cholesterol</b>	0.98	0.96 -1.00	0.116	1.01	0.97 -1.06	0.501
<b>Non-HDL cholesterol</b>	1.03	0.94 - 1.00	0.183	1.22	0.88- 1.01	0.232

Multivariate adjustment included age, sex, education, occupation, waist circumference, BMI, diastolic and systolic blood pressure, LDL-cholesterol, familial diabetic history, smoking, alcohol and tobacco usage. p-value showed in boldness indicates the statistical significance.

**Supplementary table 3:** Average value of different urinary metals among the whole population, diabetic, pre-diabetic, non-diabetic, atherosclerosis and non-atherosclerosis population.

	Range of Metals in Urine (µg/mg creatinine)			
	Quartile I	Quartile II	Quartile III	Quartile IV
<b>Cadmium</b>	0.03 - 0.04	0.04 - 1.68	1.69 - 4.53	>13.89
<b>Arsenic</b>	1.44 - 18.91	18.92 - 39.78	39.79 - 82.2	≥ 82.3
<b>Lead</b>	0.12 - 39.43	39.44 - 86.27	86.28 - 200.97	≥ 200.98
<b>Chromium</b>	2.65 - 14.35	14.36 - 28.19	28.20 - 52.07	≥ 52.08
<b>Aluminium</b>	0.04 - 118.23	118.24 - 319.13	319.14 - 868.25	≥ 868.26
<b>Zinc</b>	107.72 - 890.00	891.10 - 1477.56	1477.57 - 2538.39	≥ 2538.40
<b>Copper</b>	0.60 - 25.41	25.42 - 52.07	52.08 - 118.47	≥ 118.48
<b>Nickel</b>	2.72 - 19.40	19.41 - 39.28	39.29 - 78.92	≥ 78.93

**Supplementary Table 4:** The range of heavy metals used for categorization of quartiles.

Metal	Mean $\pm$ SE of Metals ( $\mu\text{g}/\text{mg}$ creatinine)					
	Whole Population	Non-diabetes	Pre-diabetes	Diabetes	Non-atherosclerosis	Atherosclerosis
	Mean $\pm$ SE	Mean $\pm$ SE	Mean $\pm$ SE	Mean $\pm$ SE	Mean $\pm$ SE	Mean $\pm$ SE
<b>Cadmium</b>	22.8 $\pm$ 2.4	22.2 $\pm$ 4.0	19.0 $\pm$ 2.3	33.5 $\pm$ 9.2	20.1 $\pm$ 2.1	46.0 $\pm$ 13.9
<b>Arsenic</b>	97.5 $\pm$ 7.9	74.7 $\pm$ 7.2	109.9 $\pm$ 12.9	99.8 $\pm$ 16.1	88.9 $\pm$ 7.9	170.7 $\pm$ 31.0
<b>Lead</b>	220.4 $\pm$ 36.1	175.0 $\pm$ 18.9	262.2 $\pm$ 81.7	214.3 $\pm$ 30.4	214.9 $\pm$ 40.0	267.1 $\pm$ 49.1
<b>Chromium</b>	43.6 $\pm$ 1.9	42.2 $\pm$ 3.9	41.5 $\pm$ 2.0	52.6 $\pm$ 4.8	42.7 $\pm$ 2.0	50.9 $\pm$ 5.9
<b>Aluminium</b>	846.8 $\pm$ 57.4	790.6 $\pm$ 98.3	883.0 $\pm$ 87.5	903.8 $\pm$ 118.5	794.4 $\pm$ 57.0	1294 $\pm$ 248.5
<b>Zinc</b>	2249 $\pm$ 96.7	1955 $\pm$ 124.6	2257 $\pm$ 158.5	2930 $\pm$ 282.6	2188 $\pm$ 99.2	2761 $\pm$ 362.9
<b>Copper</b>	121.6 $\pm$ 9.5	122.9 $\pm$ 19.2	115.1 $\pm$ 10.2	137.9 $\pm$ 21.6	121.2 $\pm$ 10.3	124.7 $\pm$ 22.3
<b>Nickel</b>	79.7 $\pm$ 7.6	76.7 $\pm$ 13.4	82.8 $\pm$ 12.4	79.5 $\pm$ 21.6	81.0 $\pm$ 8.4	68.8 $\pm$ 10.4

# Atomically Precise Nanocluster Assemblies Encapsulating Plasmonic Gold Nanorods

Amrita Chakraborty, Ann Candice Fernandez, Anirban Som, Biswajit Mondal, Ganapati Natarajan, Ganesan Paramasivam, Tanja Lahtinen, Hannu Häkkinen, Nonappa,\* and Thalappil Pradeep\*

**Abstract:** The self-assembled structures of atomically precise, ligand-protected noble metal nanoclusters leading to encapsulation of plasmonic gold nanorods (GNRs) is presented. Unlike highly sophisticated DNA nanotechnology, this strategically simple hydrogen bonding-directed self-assembly of nanoclusters leads to octahedral nanocrystals encapsulating GNRs. Specifically, the *p*-mercaptobenzoic acid (*p*MBA)-protected atomically precise silver nanocluster,  $\text{Na}_4[\text{Ag}_{44}(\text{pMBA})_{30}]$ , and *p*MBA-functionalized GNRs were used. High-resolution transmission and scanning transmission electron tomographic reconstructions suggest that the geometry of the GNR surface is responsible for directing the assembly of silver nanoclusters via H-bonding, leading to octahedral symmetry. The use of water-dispersible gold nanoclusters,  $\text{Au}_{\sim 250}(\text{pMBA})_n$  and  $\text{Au}_{102}(\text{pMBA})_{44}$ , also formed layered shells encapsulating GNRs. Such cluster assemblies on colloidal particles are a new category of precision hybrids with diverse possibilities.

Atomically precise monolayer-protected nanoclusters of noble metals<sup>[1–3]</sup> such as  $\text{Au}_{25}(\text{SR})_{18}$ ,  $\text{Ag}_{25}(\text{SR})_{18}$ ,  $\text{Ag}_{44}(\text{SR})_{30}$ , and  $\text{Au}_{102}(\text{SR})_{44}$  owing to their small size and quantum confinement of electrons lead to discrete energy levels, making their optical absorption spectra reminiscent of dye molecules. Near-infrared emission and unusual catalysis are some of the fascinating properties of such clusters. Over the past one decade, there has been tremendous progress in the

synthesis, characterization, and studies of their diverse properties. Recent reports of inter-nanocluster reactions<sup>[4]</sup> and isomorphous transformations<sup>[5]</sup> have expanded the scope of their science. Moreover, it has been recently shown that by tuning the inter-nanocluster H-bonding, free-standing 2D nanosheets and capsids with monolayer thick shells can be achieved using *p*MBA-protected gold nanoclusters.<sup>[6,7]</sup> On the other hand, noble metal nanoparticles, especially gold nanorods (GNRs),<sup>[8,9]</sup> owing to their anisotropic surface plasmonic excitations and extreme sensitivity to chemical environments have been one of the most intensely researched nanosystems. The unique plasmonic properties of gold nanoparticles have been exploited recently to achieve plasmon-molecular resonance coupling using small organic dye molecules<sup>[10]</sup> as well as quantum dots.<sup>[11]</sup> Such a plasmon-exciton coupling shows remarkably altered fluorescence (enhanced or quenched), possibly allowing the amplification of plasmonic signals in devices. Therefore, it is relevant to investigate whether colloidal-scale molecules such as atomically precise quantum clusters affect the plasmon of nanoparticles when placed at sufficient proximity. In this context, the *p*MBA-protected silver nanocluster  $(\text{Na}_4[\text{Ag}_{44}(\text{pMBA})_{30}])$ ,<sup>[12,13]</sup> which is of great interest owing to its intense and broad multiband optical absorption property,<sup>[14]</sup> is a suitable candidate because of its facile synthesis and the presence of H-bonding ligands. Furthermore, earlier study from our group has shown that  $\text{Ag}_{44}$  can show fundamentally different assemblies to direct hierarchical structures when interacted with 1D (anisotropic) tellurium nanowires.<sup>[15]</sup> With these motivations, we undertook an investigation into the precision assemblies of noble metal nanoclusters on GNR surfaces in solution. In our experiments we observed a quantitative transformation of clusters to composite cages where one nanorod was incorporated per cage. This fascinating observation warranted a detailed structural investigation, as such assemblies have been achieved previously using highly sophisticated DNA nanotechnology.<sup>[16]</sup>


The GNRs ( $d \approx 10$  nm,  $l \approx 30$  nm) were synthesized according to an established method<sup>[17]</sup> in presence of cetyltrimethylammonium bromide (CTAB) and are denoted as GNR@CTAB (Supporting Information, Figure S1). To incorporate the hydrogen bonding functionalities on GNR surfaces, ligand exchange was performed using *p*MBA and the resulting *p*MBA protected nanorods are denoted as GNR@*p*MBA (Figure 1b; Supporting Information, Figure S2). The ligand exchange was monitored by measuring the zeta ( $\zeta$ ) potential (Supporting Information, Figure S2) which changed from +51 mV (GNR@CTAB) to −2.6 mV

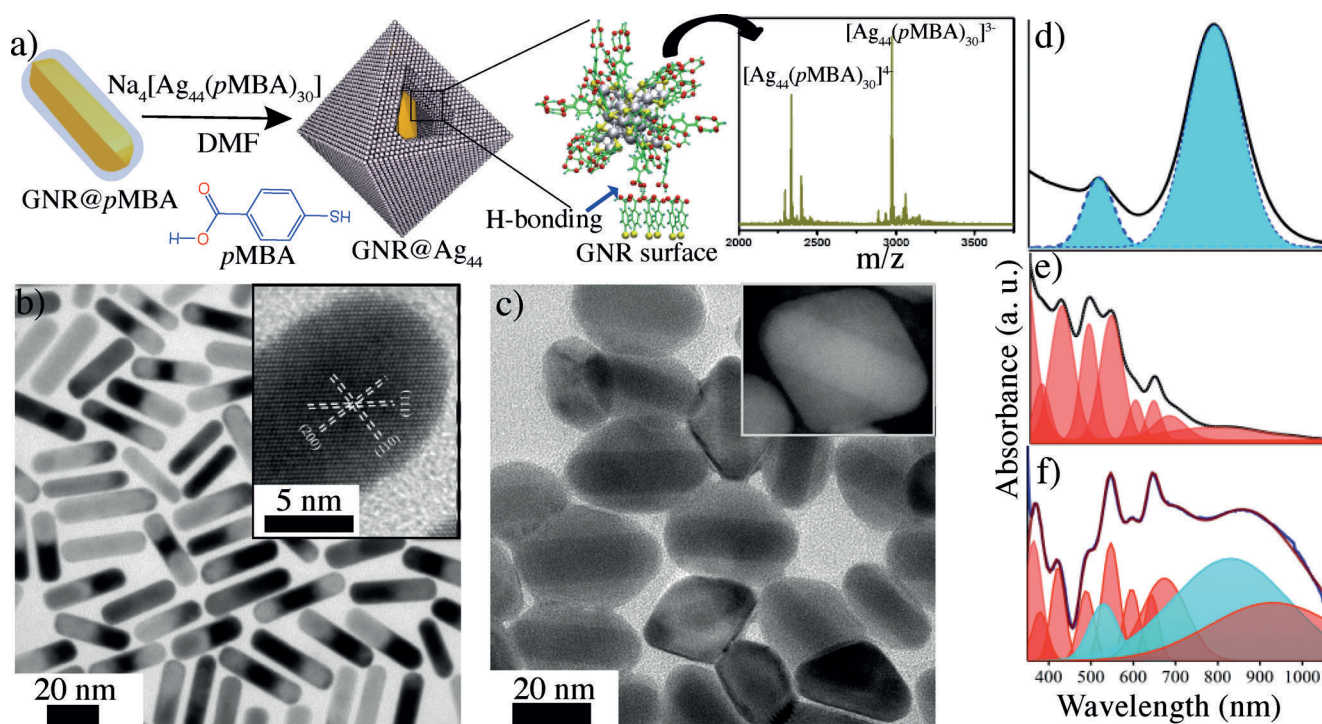
[\*] A. Chakraborty, A. C. Fernandez, Dr. A. Som, B. Mondal, Dr. G. Natarajan, Dr. G. Paramasivam, Prof. T. Pradeep  
DST Unit of Nanoscience and Thematic Unit of Excellence, Department of Chemistry, Indian Institute of Technology Madras  
Chennai 600036 (India)  
E-mail: pradeep@iitm.ac.in

Dr. Nonappa  
Departments of Applied Physics and Bioproducts & Biosystems,  
Aalto University  
Puumiehenkuja 2, P.O. Box 15100, 00076 Aalto (Finland)  
E-mail: nonappa@aalto.fi

Dr. T. Lahtinen, Prof. H. Häkkinen  
Departments of Chemistry and Physics, Nanoscience Centre,  
University of Jyväskylä  
Survontie 9, 40014 Jyväskylä (Finland)

A. C. Fernandez  
Current address: Department of Chemistry, University of Massachusetts  
710 N. Pleasant Street, Amherst, MA 01003 (USA)

 Supporting information and the ORCID identification number(s) for the author(s) of this article can be found under:  
<https://doi.org/10.1002/anie.201802420>.



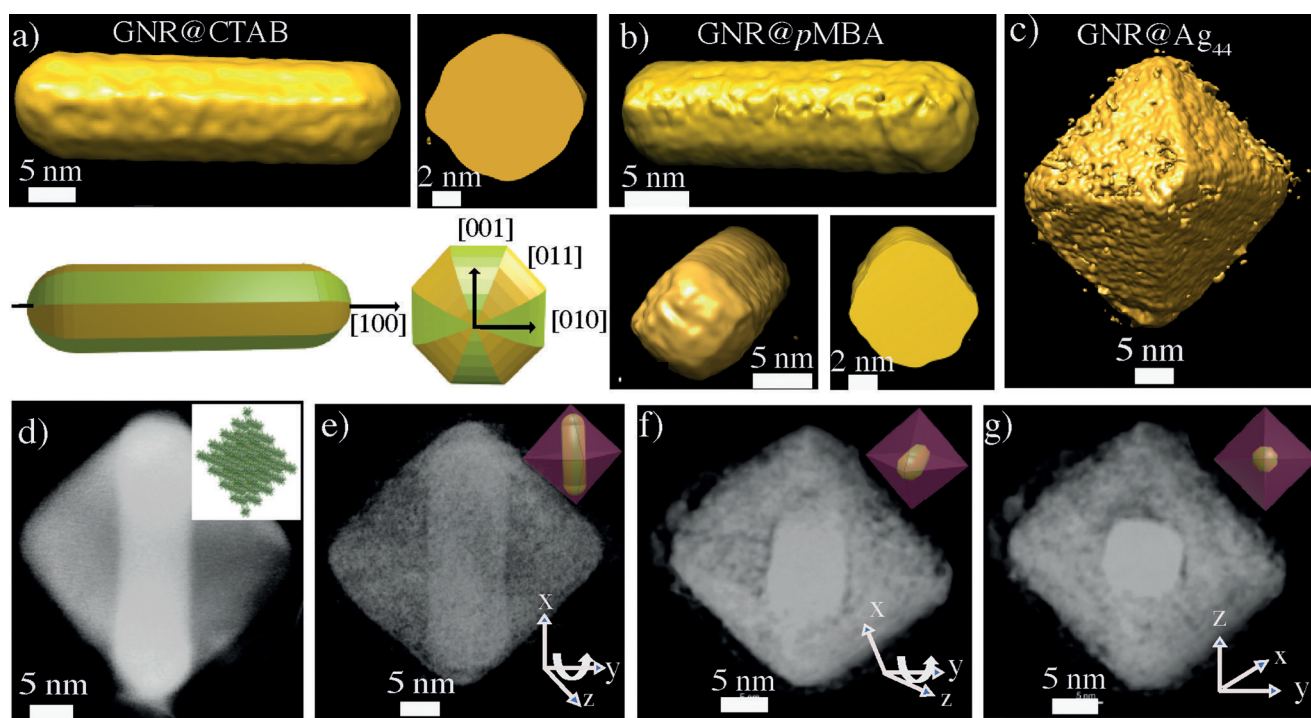
**Figure 1.** a) Representation of the self-assembly of  $\text{Ag}_{44}$  (curved arrow directs to the ESI MS of the cluster) on the  $\text{GNR@pMBA}$  surface, b) TEM image of  $\text{GNR@pMBA}$  (inset shows an HRTEM image of a single nanorod), c) TEM image of  $\text{GNR@Ag}_{44}$  (inset shows dark field STEM image of a composite particle), and d)–f) UV/Vis spectra of  $\text{GNR@pMBA}$ ,  $\text{Ag}_{44}$ , and  $\text{GNR@Ag}_{44}$ , respectively.

( $\text{GNR@pMBA}$ ). The presence of sulfur and the existence of Au–S bond in  $\text{GNR@pMBA}$  were confirmed using Raman spectroscopy, scanning transmission electron microscopy, energy-dispersive X-ray (EDX STEM) spectroscopy, and X-ray photoelectron spectroscopy (Supporting Information, Figures S2, S3). The modified GNRs were purified and redispersed either in *N,N*-dimethylformamide (DMF) or water for further experiments. The silver nanocluster  $\text{Na}_4[\text{Ag}_{44}(\text{pMBA})_{30}]^{13-}$  and water dispersible gold nanoclusters,  $\text{Au}_{102}(\text{pMBA})_{44}^{18-}$  and  $\text{Au}_{250}(\text{pMBA})_n^{19-}$  (from here on abbreviated as  $\text{Ag}_{44}$ ,  $\text{Au}_{102}$ , and  $\text{Au}_{250}$ , respectively), were prepared according to previous reports (see the Supporting Information for detailed synthesis and characterization). Figure 1a pictorially describes the self-assembly of  $\text{Ag}_{44}$  on  $\text{GNR@pMBA}$ . In our experiment, a dispersion of  $\text{GNR@pMBA}$  in DMF was allowed to interact with  $\text{Ag}_{44}$  dissolved in DMF (characterized by absorption spectroscopy and electrospray ionization (ESI) mass spectrometry; Supporting Information, Figure S4), at room temperature. This allowed  $\text{Ag}_{44}$  clusters to assemble on GNR surfaces through systematic H-bonding via carboxylic acid dimerization of the bound ligands (Supporting Information, Figure S3a), giving rise to a well-defined geometry of the end product (Figure 1c). After 20 h of incubation time, the product was extracted by centrifugation and was characterized (Supporting Information, Figure S5). The  $\text{GNR@pMBA}$  has two characteristic plasmonic peaks at 520 nm and 780 nm in its absorption spectrum (Figure 1d), whereas  $\text{Ag}_{44}$  shows molecule-like electronic spectrum (Figure 1e). When the resulting composite dispersed in DMF was studied, it displayed the absorption spectrum containing the peaks arising from both

$\text{GNR@pMBA}$  as well as  $\text{Ag}_{44}$  as evident from peak fitting (Figure 1f). The supramolecularly self-assembled composite superstructure is denoted as  $\text{GNR@Ag}_{44}$ , where the individual components preserve their identities. However, significant broadening along with a shift in peak position at the NIR region was observed for the composite material, owing to the electronic interactions between them. Transmission electron microscopy (TEM) and scanning transmission electron microscopy (STEM) revealed the formation of self-assembled superstructures encapsulating a single GNR in each nanocrystal (Figure 1c). Remarkably, a systematic optimization leads to a system where neither free GNR nor excess cluster exists in the medium and the final material has a definite morphology. Moreover, stability of this nanohybrid material is comparable with that of the  $\text{Ag}_{44}$  crystal. It can be redispersed in DMF by mild sonication without breaking the cluster assemblies, even after months of its preparation. The clusters can be regained from the composite only by probe sonication in an acidic medium (Supporting Information, Figure S6).

To gain insights into the morphology of  $\text{GNR@Ag}_{44}$ , and thus to have a better understanding of the assembly of clusters on the GNR surface, TEM and STEM tomography reconstructions were performed on  $\text{GNR@CTAB}$ ,  $\text{GNR@pMBA}$ , and  $\text{GNR@Ag}_{44}$ .  $\text{GNR@CTAB}$  showed the reported geometry where the sides consist of four  $\langle 110 \rangle$  and four  $\langle 100 \rangle$  facets arranged alternately (Figure 2a; Supporting Information, Video S1).<sup>[20]</sup> However, owing to larger interatomic distances, the bonding between the surface gold atoms is relatively weaker on the  $\langle 110 \rangle$  facet compared to the  $\langle 100 \rangle$  facet leading to the formation of stronger bonds with





**Figure 2.** TEM and STEM tomography: a) TEM 3D reconstructed structure of GNR@CTAB (top left) and its cross-sectional view (top right) along with graphical representations of the side (bottom left) and top (bottom right) views showing octagonal geometry; b) side (top) and top (bottom left) views of GNR@pMBA, cross sectional view (bottom right) showing slightly distorted octagonal geometry; c) GNR@Ag<sub>44</sub> showing octahedral geometry. d) Dark-field STEM tomography of GNR@Ag<sub>44</sub> showing the octahedral nanocage and encapsulation and orientation of GNR within (inset: theoretically obtained Ag<sub>44</sub> assembly giving octahedral shape). e)–g) Rotational views of the nanocomposite along y axis (insets show corresponding representations).

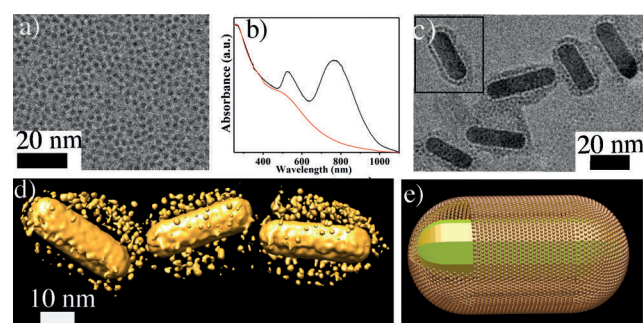
adsorbed or bonded atoms (here *pMBA* molecules) on the former surface. In this process, the Au <100> surface undergoes bond breaking in the inner layers whereas Au <110> shows a missing row reconstruction.<sup>[21,22]</sup> This leads to a distortion of the inherent octagonal shape of the GNR surface, when functionalized by *pMBA* (Figure 2b; Supporting Information, Video S2). The GNR@Ag<sub>44</sub>, as shown in Figure 2c and 2d is octahedral. There are reports of similar geometry when gold,<sup>[23]</sup> silver,<sup>[24]</sup> or palladium<sup>[25]</sup> shells have been grown on GNRs. It is evident that there is a competing growth on the two sets of side facets of GNRs. Upon preferential growth of the metals on the <110> surface facets compared to the <100>, there is a gradual enlargement of the latter and finally all <110> facets disappear.<sup>[25]</sup> Although it was technically impossible to detect the surface facets of the cluster cages owing to the beam intolerance of the clusters in that high resolution, we suggest that in this case also the Ag<sub>44</sub> clusters assemble faster on the <110> surface facets than <100> causing the similar geometry. Herein, the nanorods are oriented diagonally, which denotes the size of the cages, by the length of nanorods. Figure 2e–g shows the views of the stepwise rotation of a single GNR@Ag<sub>44</sub> particle by an overall angle of 90° along the y axis. From these results, it can be further confirmed that Ag<sub>44</sub> self-assemble on GNR surfaces leading to an octahedral shape (Supporting Information, Video S3) where the GNR is oriented along the corners. Ag<sub>44</sub> is known to crystallize into a triclinic lattice<sup>[26]</sup> in which each cluster has a specific orientation, which satisfies

translational periodicity. In presence of some specific counterion, it is also known to form an isotropic FCC arrangement.<sup>[27]</sup> Directional hydrogen bonding between the ligands is mainly responsible for the intercluster (both intralayer and interlayer) interactions leading to the crystals. Based on the crystal morphology, only a cubic crystal lattice system can give rise to a bulk crystal form which is octahedral. We suggest that the underlying lattice structure of our octahedral assemblies is FCC in which the orientations of the hydrogen bonds between two connected cluster units may have disorder, but isotropic van der Waals interactions hold the FCC lattice together. The *pMBA* molecules attached to the GNR interact with the *pMBA* molecules on Ag<sub>44</sub> clusters, weakening the hydrogen bonding between the ligands of individual clusters. The GNR@*pMBA* surface imposes orientational constraints to the assembly and an ordered orientation of the clusters may not be possible. A careful observation of different stages of growth suggests that in the beginning, the Ag<sub>44</sub> was attached almost evenly to the entire surface of the GNRs (Supporting Information, Figure S7b). Gradually, as the sides (body) of the GNRs exhibited more van der Waals interaction compared to the pyramidal tips owing to their larger surface area, Ag<sub>44</sub> started to assemble on the side (body) surfaces preferentially. This interaction was highest at the center of the sides (body) of the GNRs, since it has the greatest number of significant contributions from both halves of the rods which gradually gets lower towards the tips of the GNRs. This, coupled with the preferential attachment of cluster units to



the  $\text{Au} \langle 110 \rangle$  than  $\text{Au} \langle 100 \rangle$  surface facets of  $\text{GNR@pMBA}$ , results in the anisotropic growth. As a result, the overall morphology of the nanocages encapsulating a single GNR happens to be an octahedron. An inset in Figure 2d shows a model of the octahedral crystal of  $\text{Ag}_{44}$  derived from its FCC lattice. TEM tomographic images of some other shapes obtained owing to the incomplete growth of clusters are shown in the Supporting Information, Figure S8. In a medium with  $\text{pH} > 7$ , where  $\text{pMBA}$  exists in its anionic form, the assembly did not take place. Also, when the cluster was added to  $\text{GNR@CTAB}$  without functionalizing with  $\text{pMBA}$ , the assembly was not observed (Supporting Information, Figure S9), suggesting that the hydrogen bonding is the basis of the structure.

To validate the generality of our approach, we used the water-dispersible gold nanocluster  $\text{Au}_{250}$  (Figure 3a) to perform the assembly. Unlike  $\text{Ag}_{44}$ , the gold nanoclusters assembly on GNRs was carried out in water ( $\text{pH} \approx 7$ ) keeping



**Figure 3.**  $\text{GNR@pMBA}$  with  $\text{Au}_{250}$  nanoclusters in water: a) TEM image of  $\text{Au}_{250}$ , b) UV/Vis absorption spectra of  $\text{Au}_{250}$  (red) and  $\text{GNR@Au}_{250}$  (black), c) TEM images showing layered shell around  $\text{GNR@pMBA}$  when treated with aqueous  $\text{Au}_{250}$ , d) 3D reconstructed structures from the TEMs and e) 3D graphical representation of  $\text{GNR@Au}_{250}$ .

all the other conditions the same. On reacting with  $\text{GNR@pMBA}$ , the gold nanoclusters formed a similar nano-assembly named as  $\text{GNR@Au}_{250}$ , whose optical spectrum is also a composite of the components (Figure 3b). However, unlike  $\text{GNR@Ag}_{44}$ , the composite shows no specific morphology, rather it gave either one or multilayer shell structures (Figure 3c). Figure 3d (Supporting Information, Video S4) show the TEM tomography reconstruction of  $\text{GNR@Au}_{250}$  (Figure 3e shows the graphical representation of the same). Absence of any specific morphology in this case, even on completion of the reaction, can be due to the fact that  $\text{Au}_{250}$  has to be partially deprotonated to facilitate water dispersibility.<sup>[6,7]</sup> As a result, not all of the ligands are involved in H-bonding, which decreases the packing density. Similar structures have been obtained on treating GNRs with  $\text{Au}_{102}$  (Supporting Information, Figure S10). Thus, irrespective of the solvent this approach can be useful to condense any noble metal nanocluster, protected by hydrogen-bond-forming ligand on GNRs, which act as the nucleating sites.

In conclusion, we have shown that composite nanostructures composed of two well-defined regimes of nano-systems, namely gold nanorods and the  $\text{Na}_4[\text{Ag}_{44}(\text{pMBA})_{30}]$

cluster, can be created by non-covalent assembly. Systematic hydrogen-bond-induced self-assembly of  $\text{Ag}_{44}$  clusters on the  $\text{pMBA}$  functionalized gold nanorods encapsulates the GNRs completely, leading to octahedral composite nanocages. Interestingly, this hybrid nanomaterial shows unusually high stability at room temperature. The identities of GNR and the cluster are manifested in the spectroscopic properties of the composite. This simple method of controlled self-assembly of colloidal objects may be useful for creating larger hierarchical structures. Using  $\text{Au}_{250}$  we have shown that this approach is rather general in terms of nanoclusters and the solvent involved. However, luminescent quantum clusters might show metal-enhanced luminescence when they reside close to the plasmonic nanoparticles which should improve the detection limits of nanocluster-based sensors. Thus, creation of such precision assemblies with low polydispersity addresses the most crucial issues of controlled nanoparticle encapsulation and suggests a direction forward for the synthesis of more complex materials.

## Acknowledgements

We thank the Department of Science and Technology, Government of India for supporting our research. A.C. and B.M. thank the Council of Scientific and Industrial Research and IIT Madras, respectively for their research fellowships. Academy of Finland Center of Excellence (HYBER), Nano-microscopy Center, Aalto University is thanked for the instrumentation facilities. We also thank Dr. P. Engelhardt for his technical support and T.-R. Tero for the characterization of the  $\text{Au}_{250}$  cluster.

## Conflict of interest

The authors declare no conflict of interest.

**Keywords:** atomically precise nanoclusters · hydrogen bonding · plasmonic gold nanorods · self-assembly · supramolecular chemistry

**How to cite:** *Angew. Chem. Int. Ed.* **2018**, *57*, 6522–6526  
*Angew. Chem.* **2018**, *130*, 6632–6636

- [1] I. Chakraborty, T. Pradeep, *Chem. Rev.* **2017**, *117*, 8208–8271.
- [2] R. Jin, *Nanoscale* **2015**, *7*, 1549–1565.
- [3] P. Maity, S. Xie, M. Yamauchi, T. Tsukuda, *Nanoscale* **2012**, *4*, 4027.
- [4] K. R. Krishnadas, A. Ghosh, A. Baksi, I. Chakraborty, G. Natarajan, T. Pradeep, *J. Am. Chem. Soc.* **2016**, *138*, 140–148.
- [5] K. R. Krishnadas, A. Baksi, A. Ghosh, G. Natarajan, T. Pradeep, *Nat. Commun.* **2016**, *7*, 13447.
- [6] Nonappa, T. Lahtinen, J. S. Haataja, T. R. Tero, H. Häkkinen, O. Ikkala, *Angew. Chem. Int. Ed.* **2016**, *55*, 16035–16038; *Angew. Chem.* **2016**, *128*, 16269–16272.
- [7] Nonappa, O. Ikkala, *Adv. Funct. Mater.* **2017**, <https://doi.org/10.1002/adfm.201704328>.
- [8] S. E. Lohse, C. J. Murphy, *Chem. Mater.* **2013**, *25*, 1250–1261.
- [9] X. Huang, S. Neretina, M. A. El-Sayed, *Adv. Mater.* **2009**, *21*, 4880–4910.

- [10] L. Zhao, T. Ming, H. Chen, Y. Liang, J. Wang, *Nanoscale* **2011**, *3*, 3849.
- [11] D. Nepal, L. F. Drummy, S. Biswas, K. Park, R. A. Vaia, *ACS Nano* **2013**, *7*, 9064–9074.
- [12] H. Yang, Y. Wang, H. Huang, L. Gell, L. Lehtovaara, S. Malola, H. Häkkinen, N. Zheng, *Nat. Commun.* **2013**, *4*, 3422.
- [13] A. Desireddy, B. E. Conn, J. Guo, B. Yoon, R. N. Barnett, B. M. Monahan, K. Kirschbaum, W. P. Griffith, R. L. Whetten, U. Landman, T. Bigioni, *Nature* **2013**, *501*, 399–402.
- [14] O. M. Bakr, V. Amendola, C. M. Aikens, W. Wenseleers, R. Li, L. D. Negro, G. C. Schatz, F. Stellacci, *Angew. Chem. Int. Ed.* **2009**, *48*, 5921–5926; *Angew. Chem.* **2009**, *121*, 6035–6040.
- [15] A. Som, I. Chakraborty, T. A. Maark, S. Bhat, T. Pradeep, *Adv. Mater.* **2016**, *28*, 2827–2833.
- [16] C. Zhang, X. Li, C. Tian, G. Yu, Y. Li, W. Jiang, C. Mao, *ACS Nano* **2014**, *8*, 1130–1135.
- [17] A. K. Samal, T. S. Sreeprasad, T. Pradeep, *J. Nanopart. Res.* **2010**, *12*, 1777–1786.
- [18] Y. Levi-Kalisman, P. D. Jadzinsky, N. Kalisman, H. Tsunoyama, T. Tsukuda, D. A. Bushnell, R. D. Kornberg, *J. Am. Chem. Soc.* **2011**, *133*, 2976–2982.
- [19] T. Lahtinen, E. Hulkko, K. Sokołowska, T.-R. Tero, V. Saarnio, J. Lindgren, M. Pettersson, H. Häkkinen, L. Lehtovaara, *Nanoscale* **2016**, *8*, 18665–18674.
- [20] B. Goris, S. Bals, W. Van den Broek, E. Carbo-Argibay, S. Gomez-Grana, L. M. Liz-Marzan, G. Van Tendeloo, *Nat. Mater.* **2012**, *11*, 930–935.
- [21] Z. L. Wang, R. P. Gao, B. Nikoobakht, M. A. El-Sayed, *J. Phys. Chem. B* **2000**, *104*, 5417–5420.
- [22] H. Hu, L. Reven, A. Rey, *J. Phys. Chem. B* **2013**, *117*, 12625–12631.
- [23] Y. Xiang, X. Wu, D. Liu, L. Feng, K. Zhang, W. Chu, W. Zhou, S. Xie, *J. Phys. Chem. C* **2008**, *112*, 3203–3208.
- [24] E. C. Cho, P. H. C. Camargo, Y. Xia, *Adv. Mater.* **2010**, *22*, 744–748.
- [25] X. Yanjuan, W. Xiaochun, L. Dongfang, J. Xingyu, C. Weiguo, L. Zhiyuan, M. Yuan, Z. Weiya, X. Sishen, *Nano Lett.* **2006**, *6*, 2290–2294.
- [26] B. Yoon, W. D. Luedtke, R. N. Barnett, J. Gao, A. Desireddy, B. E. Conn, T. Bigioni, U. Landman, *Nat. Mater.* **2014**, *13*, 807–811.
- [27] Q. Yao, Y. Yu, X. Yuan, Y. Yu, D. Zhao, J. Xie, J. Y. Lee, *Angew. Chem. Int. Ed.* **2015**, *54*, 184–189; *Angew. Chem.* **2015**, *127*, 186–191.

Manuscript received: February 24, 2018

Accepted manuscript online: April 1, 2018

Version of record online: April 30, 2018

## Supporting Information

### **Atomically Precise Nanocluster Assemblies Encapsulating Plasmonic Gold Nanorods**

*Amrita Chakraborty, Ann Candice Fernandez, Anirban Som, Biswajit Mondal, Ganapati Natarajan, Ganesan Paramasivam, Tanja Lahtinen, Hannu Häkkinen, Nonappa,\* and Thalappil Pradeep\**

anie\_201802420\_sm\_miscellaneous\_information.pdf  
anie\_201802420\_sm\_Video\_S1.avi  
anie\_201802420\_sm\_Video\_S2.avi  
anie\_201802420\_sm\_Video\_S3.avi  
anie\_201802420\_sm\_Video\_S4.avi

**Author Contributions**

Ann Candice Fernandez initiated this work as a summer student at IITM.

## Supporting Information

## Table of Contents

No.	Title	Page No.
1	Chemicals used	3
2	Experimental details	3
3	Instrumentation	4
Figure S1	Characterization of GNR@CTAB	5
Figure S2	Characterization of GNR@pMBA	6
Figure S3	Proof of Au-S bond in GNR@pMBA	6
Figure S4	Characterization of Ag <sub>44</sub> (pMBA) <sub>30</sub>	7
Figure S5	Characterization of GNR@Ag <sub>44</sub>	8
Figure S6	Cluster recovery from the composite	9
Figure S7	Time dependent TEM images of GNR@Ag <sub>44</sub>	10

Figure S8	Different morphologies from tomography	10
Figure S9	Control experiment with GNR@CTAb and Ag <sub>44</sub>	11
Figure S10	Characterization of Au <sub>102</sub> and GNR@Au <sub>102</sub>	11
Video S1	Tomographic reconstruction of GNR@CTAB	Attached
Video S2	Tomographic reconstruction of GNR@pMBA	Attached
Video S3	Tomographic reconstruction of GNR@Ag <sub>44</sub>	Attached
Video S4	Tomographic reconstruction of GNR@Au <sub>250</sub>	Attached
4	References	12

**Chemicals used:**

Tetrachloroauric acid trihydrate ( $\text{HAuCl}_4 \cdot 3\text{H}_2\text{O}$ ), Cetyltrimethyl ammonium bromide (CTAB) and ascorbic acid were purchased from Sigma Aldrich. Silver nitrate ( $\text{AgNO}_3$ , 99%), 4-mercaptobenzoic acid (*p*MBA, 97%), trisodium citrate dihydrate (99%), and sodium borohydride ( $\text{NaBH}_4$ , 99.99%) were purchased from Aldrich. Dimethylformamide (DMF, AR grade), dimethyl sulfoxide (DMSO, AR grade), toluene (AR grade), methanol (AR grade), ammonium acetate, citric acid, sodium chloride ( $\text{NaCl}$ ) and sodium hydroxide ( $\text{NaOH}$ ) pellets were procured from RANKEM, India. All the chemicals were used without further purification. De-ionized water was used in all the experiments.

**Experimental Details****Synthesis of Gold nanorods:**

Gold nanorod (GNR) synthesis was performed following a seedless synthetic protocol as reported from our group<sup>1</sup> with a slight modification. Briefly, to a 50 mL solution of 100 mM CTAB, 2.5 mL of 10 mM  $\text{HAuCl}_4 \cdot 3\text{H}_2\text{O}$ , 325  $\mu\text{L}$  of 10 mM  $\text{AgNO}_3$ , and 350  $\mu\text{L}$  of 100 mM ascorbic acid were added sequentially. All the solutions were mixed under mild stirring in a synthesizer keeping the temperature fixed at 28 °C. The solution was incubated for 5 min and 500  $\mu\text{L}$  of freshly prepared  $\text{NaBH}_4$  solution (1.67 mM in ice cold DI water) was added in one shot. Prior to  $\text{NaBH}_4$  addition, the stirring was stopped and the mixture was kept unperturbed overnight. After this, the GNRs were washed with water to remove the excess CTAB from the solution. For getting better uniformity, fractional centrifugation was carried out; i.e., the GNR solution was centrifuged at 7000 rpm for 20 min, the precipitate containing the larger particles were discarded. The supernatant was then separated and centrifuged stepwise at 12000 and 14000 rpm in a similar way. TEM study has shown that the precipitate after centrifuging at 12000 rpm furnished the best uniformity. This precipitate was redispersed in deionized (DI) water and again centrifuged twice at 12500 rpm each time for 15 min. At every step, the precipitate was shaken under vortex to prevent aggregation.

**Synthesis of  $\text{Ag}_{44}(\text{pMBA})_{30}$  and purification:**

We followed the procedure by Desireddy et al.<sup>2</sup> In brief, 128 mg of  $\text{AgNO}_3$  and 173 mg of *p*MBA were added in a beaker containing DMSO and water mixed in 4:7 volume ratio under constant stirring. 50%  $\text{CsOH}$  (in water) was added dropwise until the cloudy thiolates became clear. Once a greenish-yellow color appeared, 283 mg of  $\text{NaBH}_4$  in 9 mL of water was added dropwise to obtain a brown solution. The color of this solution changed to deep red after 1 h revealing the confirmation of the cluster formation. DMF was used to purify this crude cluster, which precipitated the cluster, and the solution was centrifuged. Then the residue was removed and the cluster was extracted in citric acid containing DMF solution. Thus all the protons of carboxylic acid were protonated making the cluster soluble in DMF. The extracted cluster was again precipitated using toluene, and the solution was centrifuged. Then the acidification step was repeated one more time. After this, the precipitate was redissolved in 25 mL of DMF to get the purified cluster. Notably, when all carboxylates are protonated, there is no need of citric acid, and DMF can extract the cluster directly. Protonation is the key step for this purification.

**Synthesis of  $\text{Au}_{102}(\text{pMBA})_{44}$ :**

The synthesis was performed according to a previously published method.<sup>3</sup> In a typical synthesis 0.209 g (0.50 mmol)  $\text{HAuCl}_4 \cdot 3\text{H}_2\text{O}$  was dissolved in 19 mL of Millipore water (denoted as solution A). In a separation container 0.292 g (1.89 mmol) *para*-mercaptobenzoic acid (*p*MBA) was dissolved in 18.43 mL of water containing 0.57 mL of 10 M  $\text{NaOH}$  (denoted as solution B). Then, in the following order, 75 mL of methanol, 17.8 mL of previously prepared solution A and 15.5 mL of previously prepared solution B were quickly added to a 1 L reaction vessel containing 51.5 mL of water equipped with a stirring bar and a screw cap. The reaction mixture was stirred at room temperature. After 20 h, when a white precipitate was formed, 20.8 mg (0.55 mmol) solid  $\text{NaBH}_4$  was added to it. The reaction mixture turned black immediately upon the addition of solid  $\text{NaBH}_4$  and after stirring for 5 h, methanol was added to the reaction vessel until the total volume was approximately 800 mL followed by the addition of 40 mL 5 M  $\text{NH}_4\text{OAc}$ . The reaction mixture was centrifuged at 3500 rpm for 5 min. The supernatants were discarded and the black precipitate was air dried for 1 and dissolved in 400  $\mu\text{L}$  of water. To the solution, 1 mL 2 M  $\text{NH}_4\text{OAc}$  was added, followed by methanol until the total volume was 90 mL and centrifuged at 3500 rpm for 10 min. The resulting supernatant was discarded and the black precipitate was allowed to air dry for 15 min. The air-dried sample was further subjected for fractional precipitation to obtain atomically precise nanoclusters.

**Purification of  $\text{Au}_{102}(\text{pMBA})_{44}$  by fractional precipitation:**

All particles in each conical were dissolved in about 9.24 mL millipore water and then combined into one 50 mL conical flask. To it, 2 M 0.76 mL  $\text{NH}_4\text{OAc}$  and 2.5 mL methanol were added and the suspension in the conical was mixed and centrifuged at 3500 rpm for 12 min. The resulting supernatant was then decanted into a new 50 mL conical flask, to which 12.5 mL methanol were added, the suspension in the conical was once again mixed and centrifuged at 3500 rpm for 12 min. Supernatant was then decanted into a new 50 mL conical and methanol was added until the total volume was 45 mL. The suspension in the conical was mixed and divided into two 50 mL centrifuge tubes which were then centrifuged at 3500 rpm for 15 min. The resulting supernatant was decanted and the precipitate ( $\text{Au}_{102}(\text{pMBA})_{44}$ ) was air-dried.

**Synthesis of  $\text{Au}_{\sim 250}(\text{pMBA})_n$ .**

This also was synthesized using a reported procedure.<sup>4</sup> About 0.246 g (1.60 mmol) of *p*MBA was dissolved in 19 mL of methanol and 0.107 g (0.27 mmol) of  $\text{HAuCl}_4 \cdot 3\text{H}_2\text{O}$  was dissolved in 9.7 mL of methanol. Then 9.07 mL of 33 mM  $\text{HAuCl}_4$  solution was mixed with



18.14 mL of 84 mM *p*MBA solution. Next, 68 mL of water was added to this mixture followed by dropwise addition of 2.69 mL 2 M NaOH with stirring, while maintaining the pH ~11). The solution was transferred into a 1 L capped plastic reaction vessel and after 20 h of vigorous stirring at room temperature, a mixture of 23.21 mL of methanol and 68.28 mL of water were added. Then 2.37 mL of freshly prepared 0.19 M aqueous NaBH<sub>4</sub> solution was added and the reaction was stirred for another 4.5 h. The reaction was quenched by adding 16 mL of 0.1M NaCl solution and 32 mL of methanol. The mixture was centrifuged at 3500 rpm for 15 min. The supernatant was decanted and the black precipitates were allowed to air dry. The solid was dissolved in 1:3 methanol/water mixture and centrifuged at 3500 rpm for 15 min. Supernatant was removed and solid product Au<sub>250</sub>(*p*MBA)<sub>n</sub> was allowed to dry under ambient conditions.

**Surface functionalization of GNRs by *p*MBA:** In order to make the GNRs react with Ag<sub>44</sub>(*p*MBA)<sub>30</sub>, their surfaces were functionalized by *p*MBA which essentially replaced the CTAB molecules. For that, the clean GNRs were incubated in 0.1 mM aqueous *p*MBA solution (1:1 v/v) for 3 h. Then it was centrifuged again and the supernatant containing excess *p*MBA was discarded. To ensure uniform functionalization, this process was repeated thrice. At the final step, the precipitate was redispersed in the appropriate medium (DMF for silver cluster and water for gold clusters) to carry out further studies.

**Reaction between GNR@*p*MBA and Ag<sub>44</sub>:** To the GNR@*p*MBA dispersed in 1 mL of DMF, 300  $\mu$ L, as-synthesized Ag<sub>44</sub> cluster was added. The mixture was shaken well initially for proper mixing and then kept undisturbed at room temperature for 20 h.

**Reaction between GNR@*p*MBA and Au nanoclusters:** In order to study the self-assembly, the nanoclusters (1.0 mg) was dissolved in 100  $\mu$ L of 1.0 M sodium hydroxide solution and diluted the total volume to 1.0 mL using milliQ water. This partially deprotonates the carboxylic acid groups (~22 –COOH groups) and stabilizes the nanocluster dispersion. Due to strong electrostatic repulsion aggregation of nanoclusters were prevented and the nanoclusters exist as individual clusters (Cryo-TEM). However, considerable number of COOH groups are still in their protonated form and are available for H-bonding. This property has been utilized to bind the gold nanoclusters to GNR surface. In this case, to the 1 mL of aqueous dispersion of GNR@*p*MBA, 100  $\mu$ L and 50  $\mu$ L of as synthesized Au<sub>250</sub> and Au<sub>102</sub> clusters were added respectively.

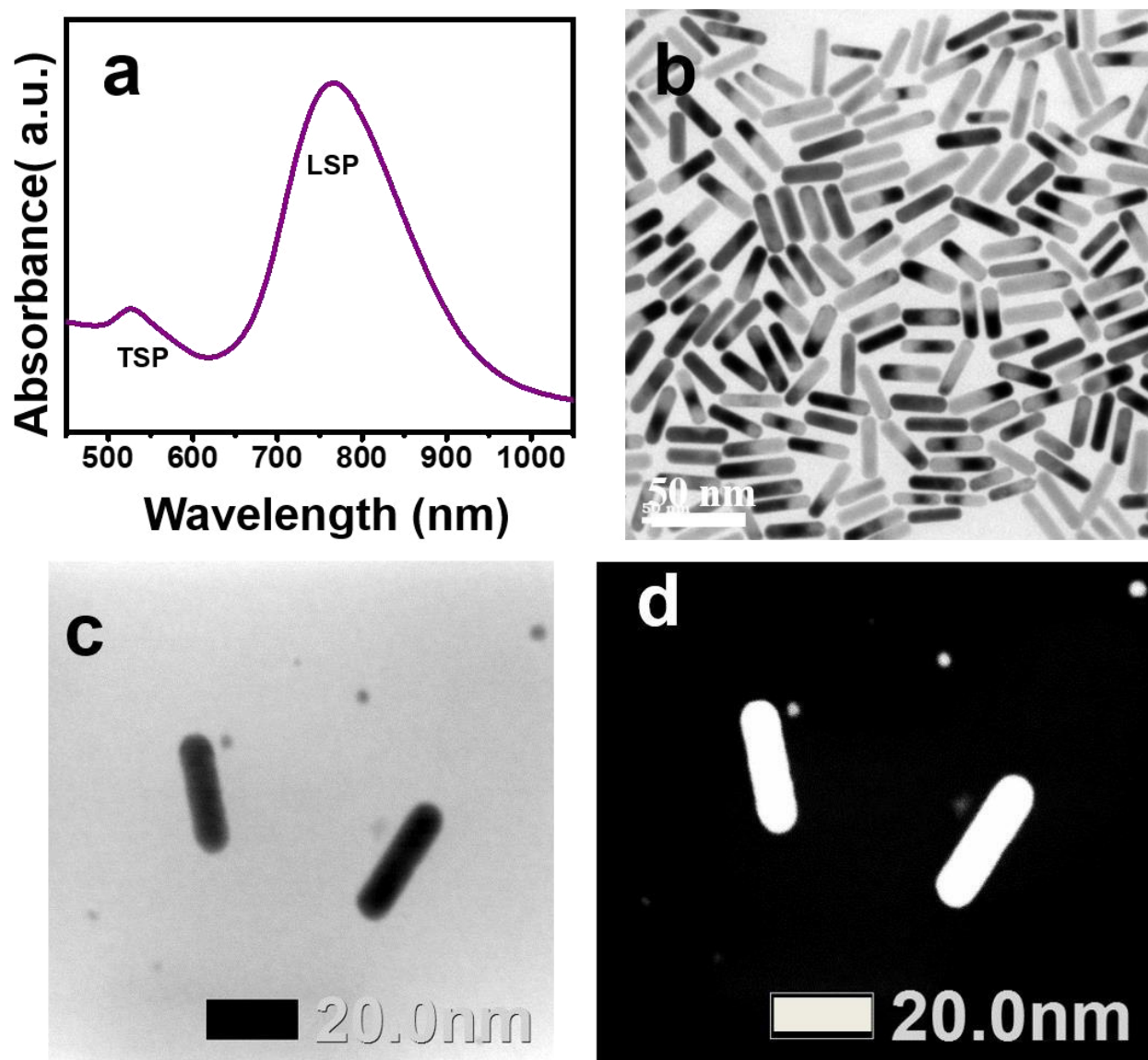
#### Instrumentation

The UV-vis absorption spectra were recorded using a PerkinElmer Lambda 25 UV-vis spectrometer. A Waters Synapt G2-Si high definition mass spectrometer equipped with electrospray ionization was used in the negative mode. All TEM measurements were made using a JEOL 3010 (JEOL Japan) transmission electron microscope. Raman measurements were made using a Confocal Raman micro spectrometer (Witec GmbH, Germany) with 532 nm and 633 nm laser excitation.

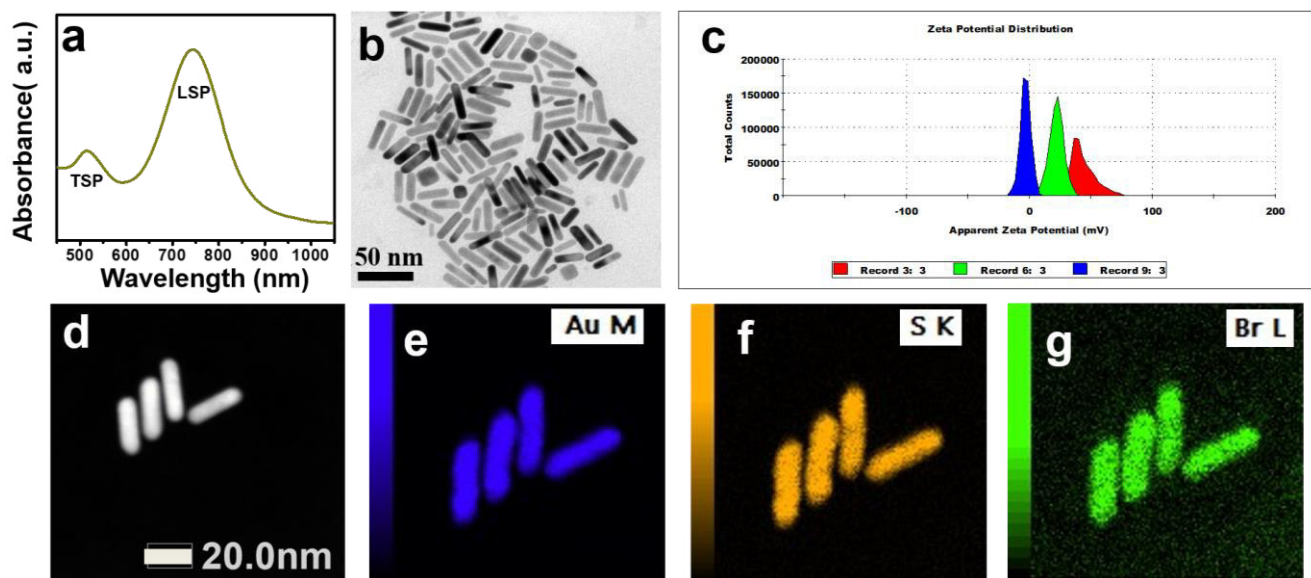
SerialEM and 3D reconstruction: Electron tomographic tilt series were acquired with the SerialEM software package. Samples were tilted between  $\pm 69^\circ$  angles with  $2^\circ$  increment steps. Prealignment of tilt image series was done and the fine alignment and cropping were executed with IMOD. The images were binned 2-4 times to reduce noise and computation time. Maximum entropy method (MEM) reconstruction scheme was carried out with a custom-made program on Mac or Linux cluster with regularization parameter value of  $\lambda = 1.0e-3$ . The STEM imaging was performed using JEOL JEM-2800 high throughput electron microscope operated at 200 kV with simultaneous bright field (BF) and dark field (DF) STEM imaging.

#### Making of the Hexagonal crystal structure of Ag<sub>44</sub>(*p*MBA)<sub>30</sub> cluster:

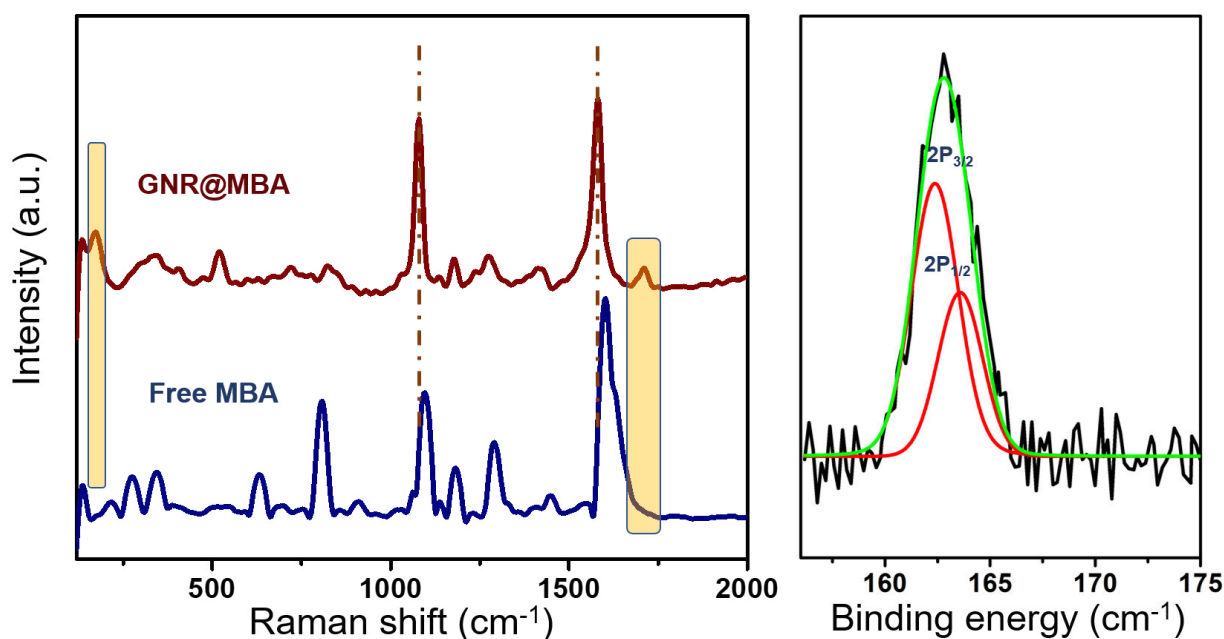
It was built by replacing the octahedral lattice points by Ag<sub>44</sub>(*p*MBA)<sub>30</sub> clusters and the octahedral Ag<sub>44</sub>(*p*MBA)<sub>30</sub> crystal structure was visualized using visual molecular dynamics (VMD) software).



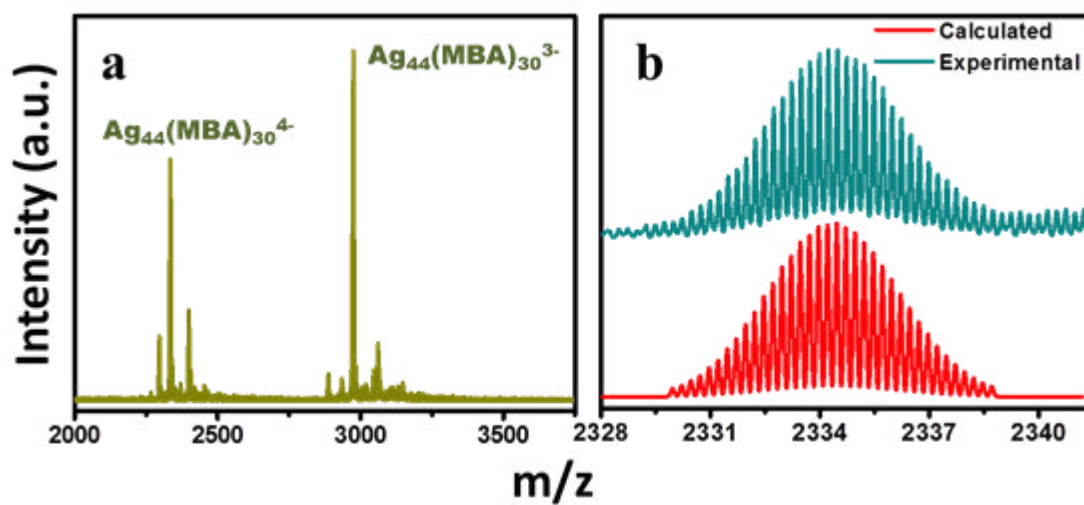
**Figure S1.** Characterization of GNR@CTAB : (a) Absorption spectrum showing transverse (TSP) and longitudinal surface plasmon (LSP) resonances (b) TEM image, (c) bright field and (d) dark field STEM images.



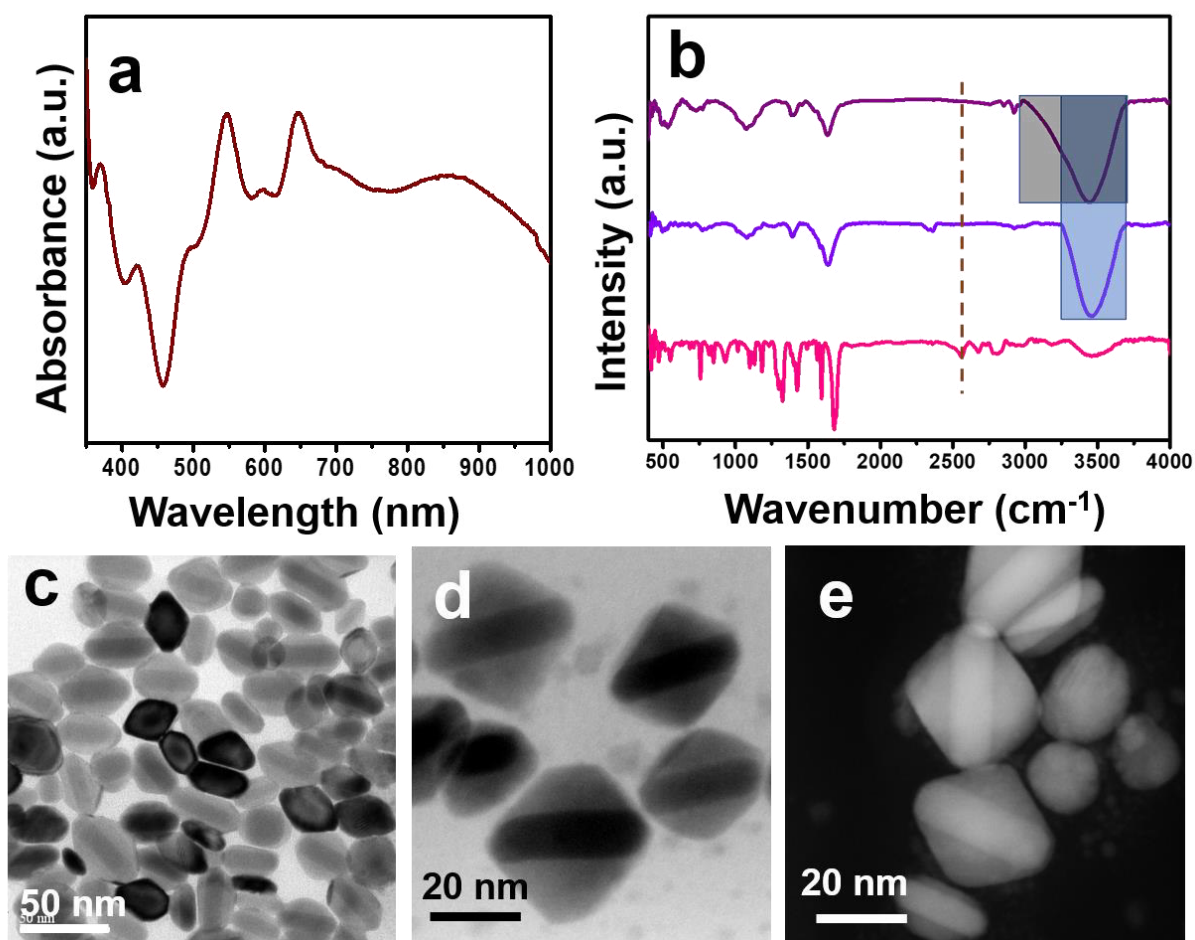
**Figure S2.** Characterization of GNR@pMBA : (a) Absorption spectrum showing transverse (TSP) and longitudinal surface plasmon (LSP) resonances (b) TEM image, (c) change in zeta potential with MBA functionalization on GNR surfaces: GNR@CTAB, 1 step MBA functionalized GNR and 3 step MBA functionalized GNR are denoted by red, green and blue curves, respectively; (d) dark field STEM image, STEM elemental mapping of Au (e), (f) S and (g) Br. Images d-g has the same scale bar.



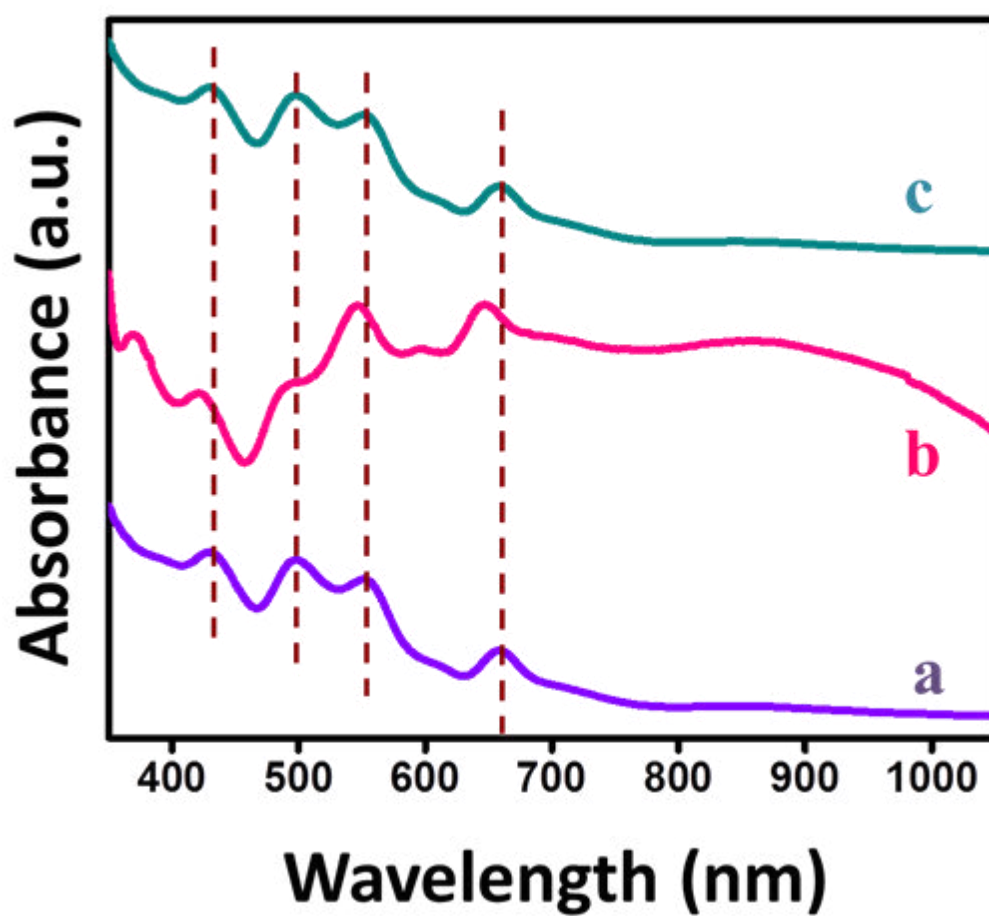
**Figure S3.** Proof of Au-S bond in GNR@pMBA: (a) comparative Raman spectra of free MBA and GNR@pMBA shows an intense Au-S-C stretching (ref 5) at  $175\text{ cm}^{-1}$  in the case of GNR@pMBA. The new peak at  $1710\text{ cm}^{-1}$  corresponds to C=O stretching corresponding to the neutral -COOH group. The presence of peaks at  $1590$  and  $1080\text{ cm}^{-1}$  in GNR@pMBA assigned to the aromatic ring vibrations show little shift as a result of the binding to the metal surface. The peaks at  $1370$ - $1380\text{ cm}^{-1}$  are ascribed to the presence of a small number of COO- groups (ref 6). The specific peaks are marked. (b) The peak at  $162.5\text{ eV}$  in XPS is the characteristic feature of Au-S bond.



**Figure S4.** Characterization of  $\text{Ag}_{44}(\text{pMBA})_{30}$ : (a) ESI mass spectrum and (b) Expanded view of molecular ion peak  $[\text{Ag}_{44}(\text{pMBA})_{30}]^{4-}$  along with the theoretical spectrum of the same ion.

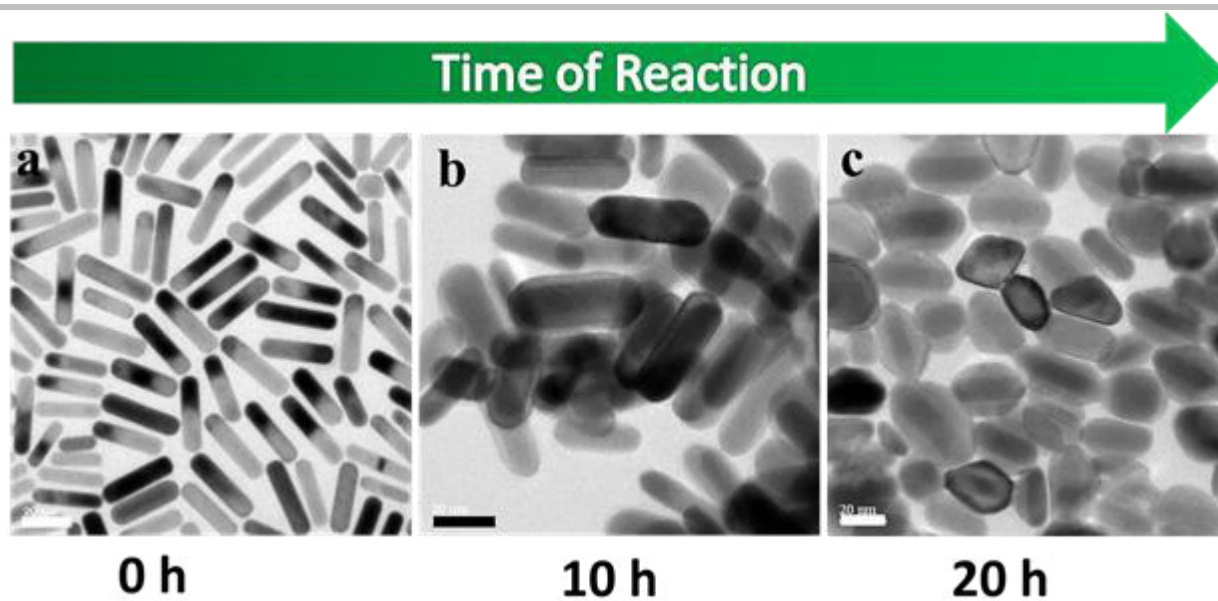


**Figure S5.** Characterization of GNR@Ag<sub>44</sub>: (a) Absorption Spectrum, (b) Comparative infrared spectra of free pMBA, Ag<sub>44</sub> and GNR@Ag<sub>44</sub> – all in the solid state. Significant broadening of the signal near 3500 cm<sup>-1</sup> is an indication of H- bonding between pMBA moieties in the final composite material. The characteristic S-H peak at 2550 cm<sup>-1</sup> in solid pMBA disappears in case of GNR@Ag<sub>44</sub>, which supports the formation of Au-S bond. (c) TEM, (d) Bright Field STEM and (e) Dark Field STEM images of GNR@Ag<sub>44</sub>.

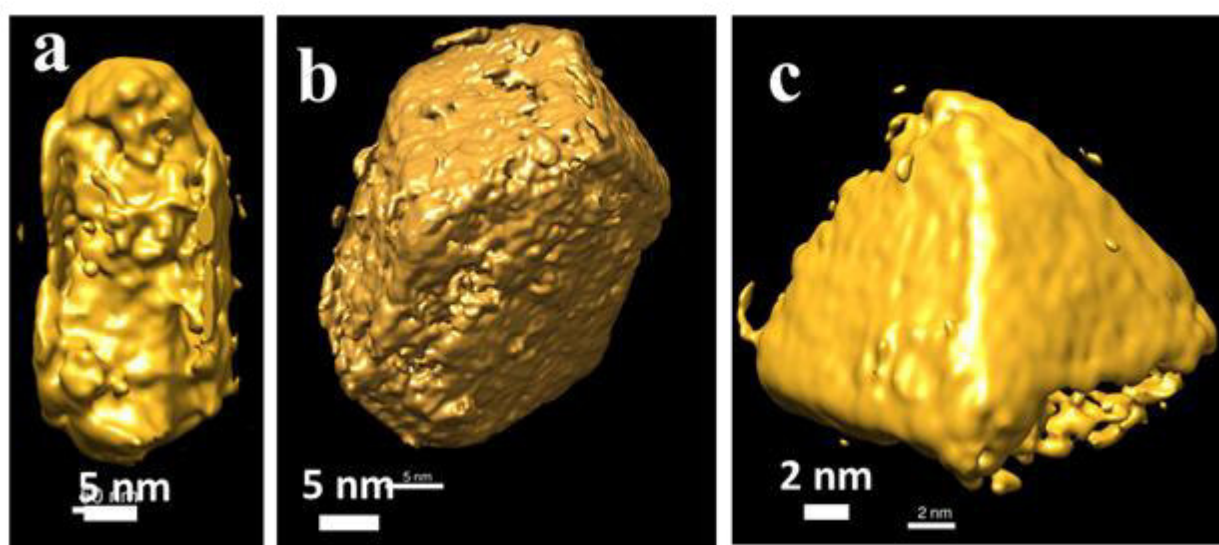


**Figure S6.** Absorption spectra of (a)  $\text{Ag}_{44}$  cluster before reaction, (b)  $\text{GNR@Ag}_{44}$  composite and (c)  $\text{Ag}_{44}$  cluster separated from the composite using probe sonication in DMF. The peaks at 681, 574, 506, and 440 nm occur at the same positions in a and c, showing that the clusters can be separated from the composite keeping their intrinsic properties intact.



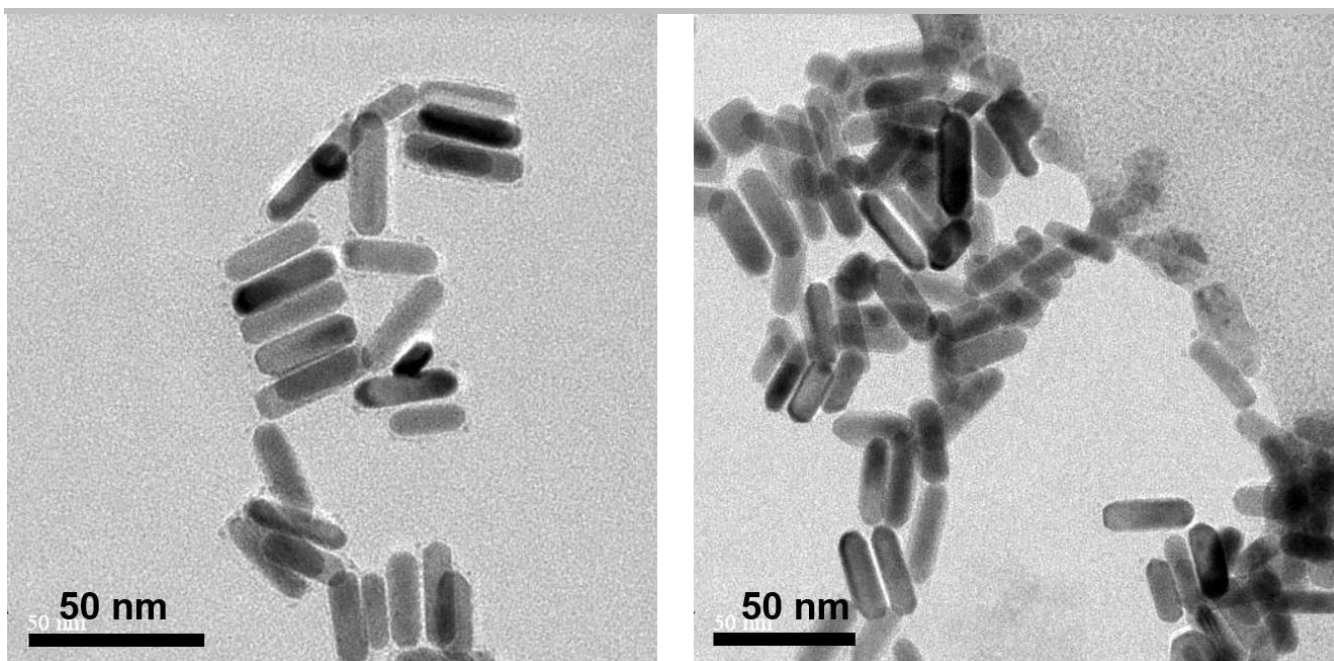


**Figure S7.** TEM images of the cluster assembly on the GNR@pMBA surface after (a) 0 h, (b) 10 h and (c) 20 h. (scale bar shows 20 nm in each case).

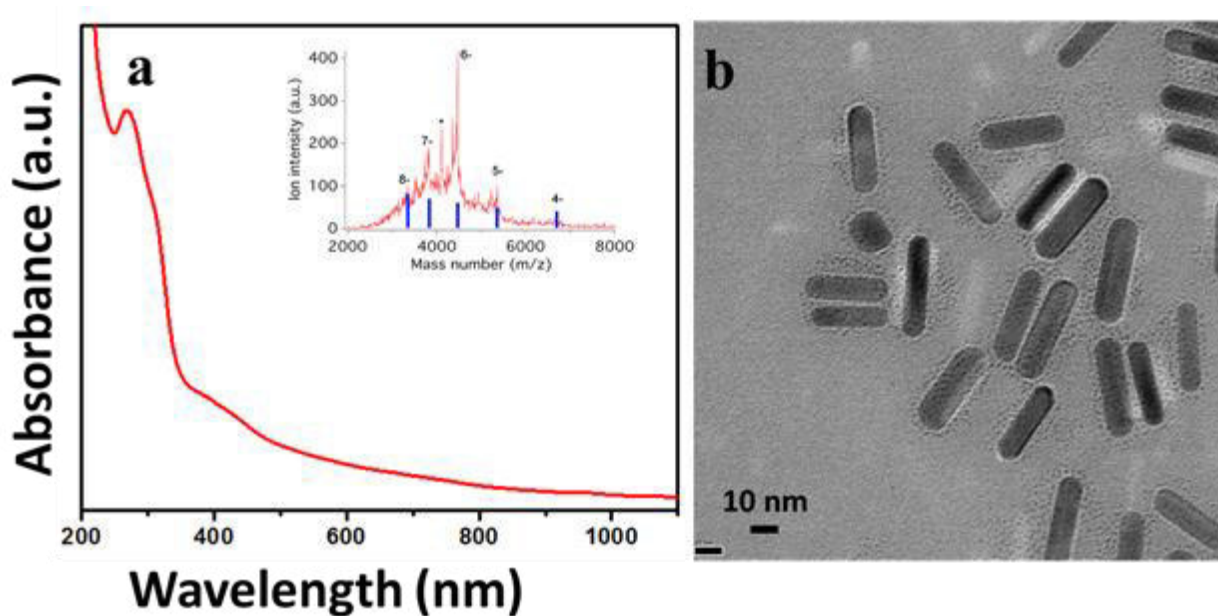


**Figure S8.** TEM tomography of different other morphologies: (a) limited cluster growth at an initial stage, (b) truncated octahedral structure obtained at a later stage, and (c) square pyramidal structure obtained when clusters assembled at only one side of the GNR@pMBA.





**Figure S9.** Control experiment when  $\text{Ag}_{44}$  was added to  $\text{GNR@CTAB}$  : a) very few clusters are there surrounding the GNRs, b) clusters are there assembling within themselves, but not interacting with the GNRs. This proves that H-bonding functionality has to be there on the GNR surface.



**Figure S10.** (a) UV-Vis absorption spectrum of  $\text{Au}_{102}(\text{pMBA})_{44}$  (inset shows the ESI mass spectrum<sup>4</sup> where the calculated mass numbers of  $\text{Au}_{102}(\text{pMBA})_{44}$  are marked with blue bars and the corresponding charge state is given above each calculated mass number, peak of a minor impurity is marked with an asterisk), and (b) TEM image of  $\text{GNR@Au}_{102}$ .

**Supporting videos are given separately.**

Video S1: TEM Tomographic reconstruction of GNR@CTAB.

Video S2: TEM Tomographic reconstruction of GNR@pMBA.

Video S3: TEM Tomographic reconstruction of GNR@Ag<sub>44</sub>.

Video S4: TEM Tomographic reconstruction of GNR@Au<sub>250</sub>.

**References**

- [1] A. K. Samal, T. S. Sreeprasad, T. Pradeep, *J. Nanoparticle Res.* **2010**, *12*, 1777–1786.
- [2] A. Desireddy, B. E. Conn, J. Guo, B. Yoon, R. N. Barnett, B. M. Monahan, K. Kirschbaum, W. P. Griffith, R. L. Whetten, U. Landman, *Nature* **2013**, *501*, 399–402.
- [3] K. Salorinne, T. Lahtinen, S. Malola, J. Koivisto, H. Häkkinen, *Nanoscale* **2014**, *6*, 7823–7826.
- [4] T. Lahtinen, E. Hulkko, K. Sokołowska, T.-R. Tero, V. Saarnio, J. Lindgren, M. Pettersson, H. Häkkinen, L. Lehtovaara, *Nanoscale* **2016**, *8* (44), 18665–18674.
- [5] T. Bürgi, *Nanoscale*, **2015**, *7*, 15553–155567.
- [6] A. Michota, J. Bukowska, *J. Raman Spectrosc.* **2003**, *34*, 21–25.

# Synthesis of Silicon Nanoparticles from Rice Husk and their Use as Sustainable Fluorophores for White Light Emission

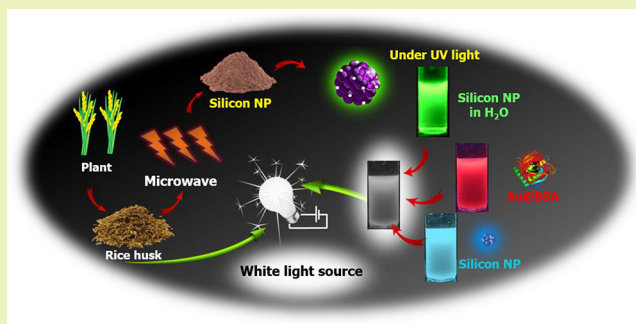
Sandeep Bose, Mohd. Azhardin Ganayee, Biswajit Mondal, Avijit Baidya,<sup>†</sup> Sudhakar Chennu, Jyoti Sarita Mohanty, and Thalappil Pradeep<sup>\*†</sup>

DST Unit of Nanoscience (DST UNS) and Thematic Unit of Excellence (TUE), Department of Chemistry, Indian Institute of Technology Madras, Chennai–600 036, India

## Supporting Information

**ABSTRACT:** Silicon nanoparticles (Si NPs) exhibiting observable luminescence have many electronic, optical, and biological applications. Owing to reduced toxicity, they can be used as cheap and environmentally friendly alternatives for cadmium containing quantum dots, organic dyes, and rare earth-based expensive phosphors. Here, we report an inexpensive silicon precursor, namely rice husk, which has been employed for the synthesis of Si NPs by rapid microwave heating. The Si NPs of ~4.9 nm diameter exhibit observable green luminescence with a quantum yield of ~60%. They show robust storage stability and photostability and have constant luminescence during long-term UV irradiation extending over 48 h, in contrast to other luminescent materials such as quantum dots and organic dyes which quenched their emission over this time window. Green luminescent Si NPs upon mixing with synthesized red and blue luminescent Si NP species are shown to be useful for energy-efficient white light production. The resulting white light has a color coordinate of (0.31, 0.27) which is close to that of pure white light (0.33, 0.33). The performance of our white light emitting material is comparable to that of a commercial white light emitting diode (WLED) bulb and is shown to be better than that of a commercial compact fluorescent lamp (CFL).

**KEYWORDS:** Rice husk, Silicon nanoparticles, Luminescence, Microwave, White light emission



## INTRODUCTION

Silicon as a source of light has been the dream of scientists for several years. Silicon in the thin film form is one of the major foundations of modern society. Until now it has been used as the base material for the development of photovoltaics<sup>1–5</sup> and microelectronics,<sup>6</sup> but silicon emitting light can bring a revolution in photonics,<sup>7</sup> optoelectronics,<sup>8</sup> and biotechnology.<sup>9</sup> In the early 1990s, Canham discovered the emission of visible light from silicon which he attributed to the porous nature of silicon and that finding paved the way for research on luminescent silicon nanoparticles (Si NPs).<sup>10,11</sup> Since then it has been more than two decades of ongoing research which has moved the focus from porous silicon to colloidal Si NPs or silicon quantum dots.<sup>12–21</sup> Printing such thin films require inks based on silicon. Applications of inks composed of Si NPs vary from printable electronics, flexible solar cells, solar roofing, etc. As these particles are biodegradable with an expected environmental lifetime of the order of 6 months with reduced toxicity, they hold great promise in biotechnological applications such as bioimaging<sup>9,22–27</sup> and can be used as a replacement for quantum dots. Production of Si NPs requires high energy processing as silicon exists in nature as SiO<sub>2</sub> which requires energy ( $\Delta H = 169.7$  kcal/mol at ~3000 K for the reaction,  $\text{SiO}_2 + \text{C} = \text{Si} + \text{CO}_2$ ) for its reduction.<sup>28</sup> Nanoparticles of silicon are particularly useful to create stable

and solvent compatible suspensions. They are also useful due to their inherent changes in the electronic, optical, and mechanical properties. Sustainable manufacturing of Si NPs is important for cheaper, energy efficient, and consequently affordable technologies.

Si NPs have been made chemically by various methods involving chemical reductants. They have also been made by using microwave synthesis,<sup>29</sup> hydrothermal synthesis,<sup>30</sup> chemical vapor deposition,<sup>31</sup> laser ablation,<sup>32</sup> mechanochemical method,<sup>33</sup> plasma assisted aerosol precipitation,<sup>34</sup> sonochemical synthesis,<sup>35</sup> and even room temperature solution phase reduction where the ligand is used for multiple purposes such as capping as well as reduction.<sup>36</sup> All these reactions invariably require costly chemicals, uncommon instrumentation and procedures, harsh experimental conditions, and long time. Most of the time, chemical methods used a few commonly available starting materials such as aminopropyltrimethoxysilane and its variants which are expensive. Si NPs possess weak aqueous solubility due to the presence of hydrophobic groups on the surface (e.g., Si–H bond), and this is a major limitation for their use in biomedical applications. Several methods have

**Received:** December 28, 2017

**Revised:** March 5, 2018

**Published:** March 9, 2018



been reported for Si NPs functionalization with hydrophilic groups but functionalization often leads to decrease in quantum yield.<sup>37</sup> Again, synthesis involves the top-down method where precursors, such as silicon powder, SiO<sub>2</sub>, nanowires, etc., were used. Below we present a bottom-up approach for the synthesis of hydrophilic Si NPs preserving high quantum yield.

Rice husk as a resource is estimated to be available to the extent of 770 million tons annually, which is generally used as a heat source in rice mills and hence readily available. Our method uses a simple, one-pot, rapid microwave reduction of silicon precursors in the husk presumably by carbon precursors under conditions of ambient pressure and high temperature, available in a microwave. The particles are stable at room temperature and at different experimental conditions for an extended period of time allowing them to be useful for applications.

## ■ EXPERIMENTAL SECTION

**Materials.** Rice grains were purchased from a local market in Chennai (Tamil Nadu, India). Sodium hydroxide was purchased from Merck Life Science Private Ltd. CdTe (Red luminescent) quantum dot sample was a gift from Prof. E. Prasad's lab (Dept. of Chemistry, IIT Madras). For preparing solutions, Milli-Q (Millipore) water was used as the solvent. Perylene dye was purchased from Sigma-Aldrich for quantum yield calculations. Aminopropyl trimethoxysilane (APTMS) was purchased from Sigma-Aldrich and was used for the synthesis of blue Si NPs. For the synthesis of Au@BSA, both HAuCl<sub>4</sub> and the protein, bovine serum albumin (BSA), were purchased from Sigma-Aldrich.

**Synthesis of Green Luminescent Si NPs.** About 2 g of rice husk were ground to make a fine powder. To that powder, about 10 mL of aqueous NaOH (1M) was added. No additional reducing and protecting agents were added to it. This mixture was heated in a microwave oven (2.45 GHz, 600 W). During the reaction, as the solution was dried, 5 mL of solvent was added and heated and the process was continued for 1 h at an interval of 10 min. Finally, the microwaved solution was taken out and centrifuged to remove any unreacted materials present. The supernatant was collected and analyzed, and it was found to contain Si NPs.

**Removal of Anthocyanin Dye from Si NPs.** Rice grains contain pigments like anthocyanin which in basic medium shows green luminescence. Removal of anthocyanin from the Si NPs was necessary to make sure that the observed luminescence was due to Si NPs and not due to anthocyanin. The separation was done using Amicon Ultra-15 Centrifugal Filter Units, with a molecular weight cutoff of 10 kDa. As the molecular weight of Si NPs was different from anthocyanin, they were easily separated. To remove any adsorbed anthocyanin, the particles were washed repeatedly.

**Quantum Yield Calculation of Si NPs.** For the green luminescent Si NPs, the PL quantum yield was calculated using perylene dye as a reference, taken in cyclohexane. Freshly prepared solution was used to avoid errors. Perylene has excitation and emission maxima in the range of 360–420 and 430–530 nm, respectively. For comparison with Si NPs, the excitation wavelength chosen was 420 nm. At this excitation wavelength, the optical densities of both the dye and Si NPs were adjusted to the same values. Photoluminescence (PL) spectra of the solutions of the same optical density solutions were recorded and areas of the PL curves were calculated. Integrated PL intensities vs corresponding optical densities were plotted and fitted with a straight line to yield two slopes which could be employed in determining the quantitative output using the established equation:

$$\Phi_{\text{Si}} = \Phi_{\text{Dye}} (K_{\text{Si}}/K_{\text{Dye}}) (\text{RI})_{\text{Si}}^2 / (\text{RI})_{\text{Dye}}^2$$

where  $K_{\text{Si}}$  and  $K_{\text{Dye}}$  stand for straight line slopes and  $(\text{RI})_{\text{Si}}$ ,  $(\text{RI})_{\text{Dye}}$ ,  $\Phi_{\text{Si}}$ , and  $\Phi_{\text{Dye}}$  represent the refractive indices of the solvents and quantum yields of the Si NPs and the dye, respectively.<sup>38</sup>

**Comparison of Photostability of Fluorescein Isothiocyanate Dye, CdTe Quantum Dots, and Si NPs.** For the photostability comparison, the PL intensities of all the luminescent materials were adjusted to the same value. Equal volumes of all the samples were taken for better comparison. The measurements were performed under a 365 nm UV lamp with a power of 6 W.

**pH Stability and Time-Dependent Stability of Si NPs.** pH values of the silicon nanoparticle solutions were adjusted by adding aq NaOH and HCl dropwise. A digital pH meter (MP-1 PLUS, Susima technologies) was used for the measurement of pH of the solution. Fluorescence intensities of the samples were measured using Horiba Yvon Nanolog (FL-1000) fluorimeter. Time-dependent luminescence intensity measurements were performed over a period of 1 month to check the stability of the nanoparticles. The measurements were performed at an interval of 3 days.

**White Light Emission.** A mixture of green Si NPs (rice husk synthesized), blue luminescent Si NPs (APTMS synthesized), and red luminescent Au@BSA clusters were prepared to demonstrate white light emission. The materials were selected such that they all show emission at the given excitation range as well as they are soluble in the same solvent, i.e. water. The excitation wavelength chosen was 360 nm.

**Synthesis of Blue Emitting Si NPs.** About 0.8 g of sodium citrate was dissolved in 20 mL of water. To this solution, 1 mL of aminopropyl trimethoxysilane (APTMS) was added and agitated homogeneously for 2 min. Then the solution was transferred into a hydrothermal bomb and was kept at 170 °C for 24 h and cooled to room temperature. The transparent solution was dialyzed using a membrane with molecular weight cut off 12 kDa and stored at 4 °C for use.

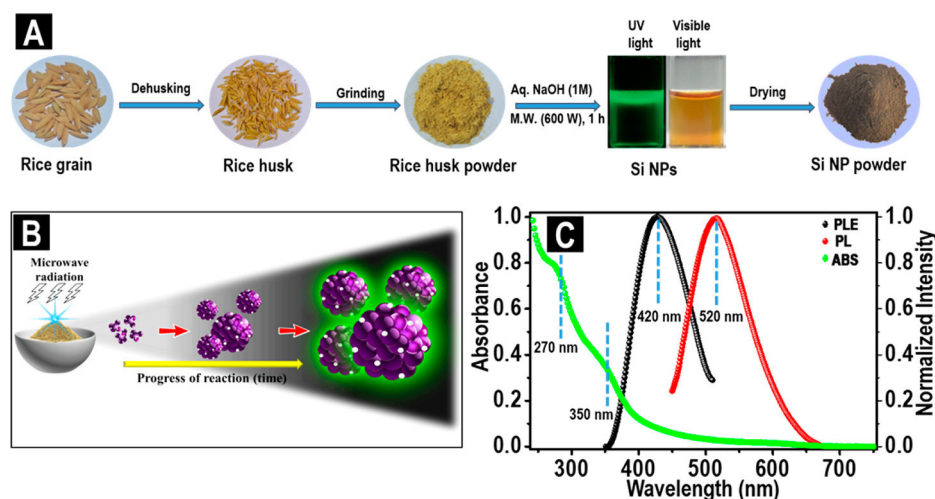
**Synthesis of Au@BSA Cluster.** A 10 mL portion of the aqueous solution of HAuCl<sub>4</sub> (6 mM) was added to 10 mL of BSA (25 mg/mL). The solution was stirred for 5 min, and 1 mL of NaOH (1M) was subsequently added. The pH of the solution was kept at 12. The reaction was continued with mild stirring for 24 h. The color of the solution changed from golden yellow to dark orange. The solution exhibits intense luminescence under UV light. The sample was dialyzed using a membrane with molecular weight cut off 12 kDa, and the purified sample was kept at 4 °C for further use.

**Luminous Efficacy Measurements of CFL, WLED, and Our Material.** A compact fluorescent lamp (CFL) and white light emitting diode (WLED) of power 14 and 5 W, respectively were bought for the luminous flux comparison. The luminous flux of the emitting material was given as, luminous flux ( $\phi_v$ ) = illuminance ( $E_v$ ) × surface area (A).

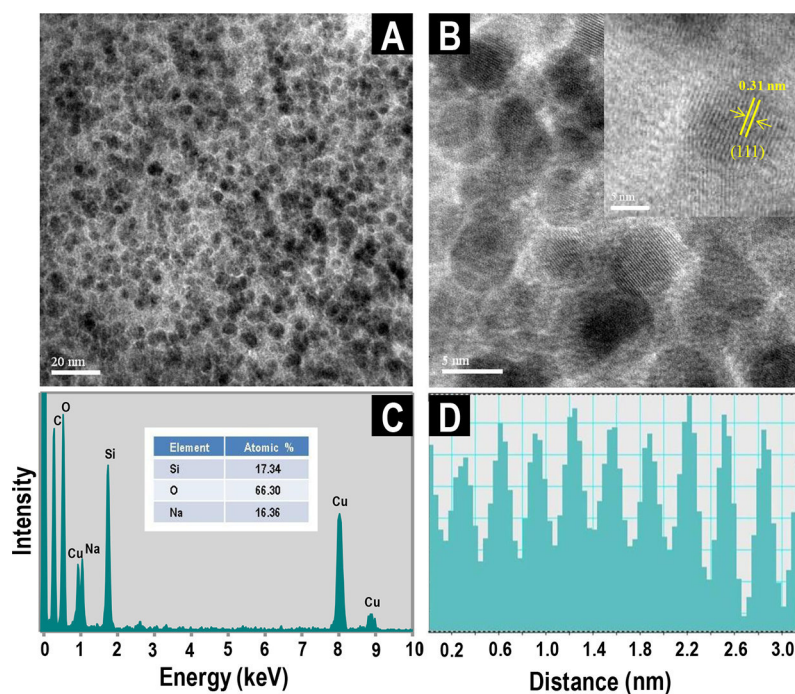
For easier calculation of the surface area, a spherical CFL and a WLED were purchased. Surface area of CFL and WLED are  $4\pi r^2$  where  $r$  is the radius of the spherical bulbs. Surface areas of cylindrical Petri dish on which our material was coated is  $2\pi rh + \pi r^2$ . The illuminance was measured using a Lux meter. Luminous efficacy was calculated as luminous flux per unit power. For the illuminance measurement, the distance from the source to the Lux meter sensor was kept constant. A (3 W, 3 V) UV LED was used as the source for white light emission.

## ■ RESULTS AND DISCUSSION

**Synthesis, Mechanism, and Optical Properties of Si NPs.** Synthesis of silica nanoparticles from rice husk biomass is an established area both in research and in industry. Such materials are considered as a sustainable source of high quality silica for diverse applications.<sup>39–41</sup> There are previous reports on the synthesis of porous silica particles by microwave irradiation of chemically process rice husk.<sup>42</sup> Reports are also available on the magnesiothermic reduction of silica to silicon which was utilized as an electrode material.<sup>43</sup> Both these methods do not report synthesis of luminescent Si NPs. Our synthetic methodology does not utilize prior chemical processing and avoid the use of external reducing agent.



**Figure 1.** (A) Procedures involved in the synthesis of green luminescent Si NPs. (B) Schematic illustration of nanoparticle nucleation, growth, and coalescence leading to smaller Si NPs. (C) Absorption (ABS), excitation (PLE), and emission spectra (PL) of the Si NPs.

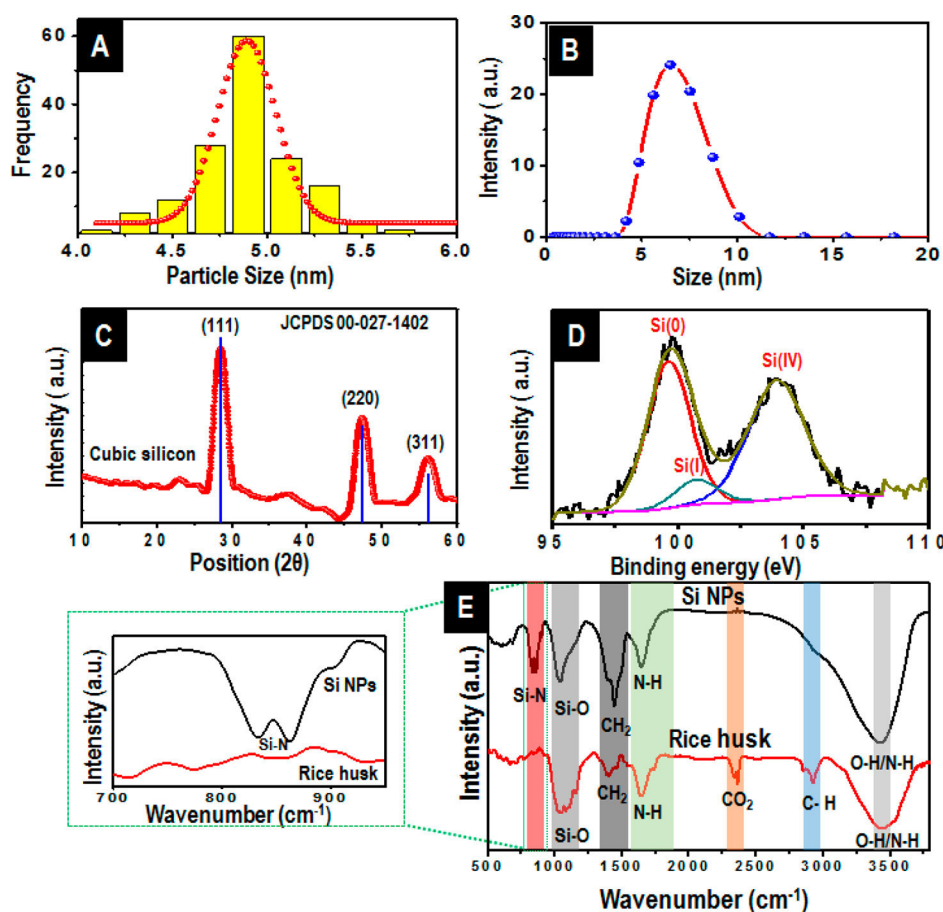


**Figure 2.** (A) Large area TEM image of the rice husk synthesized Si NPs. (B) HRTEM image of the Si NPs and the inset shows a lattice spacing of 0.31 nm arising from the (111) plane of silicon. (C) EDAX spectrum of Si NPs along with the atomic percentages of the elements present. Carbon and copper are from the grid although some carbon is present in the sample too. (D) Lattice distance profile of Si NPs for the (111) crystal plane. It is the profile of 10 consecutive lattice planes, an average of which was considered as the lattice distance between the planes.

The synthetic procedure used is shown in Figure 1A. Fine powder of husk was taken and 1 M NaOH was added dropwise with stirring. The solution was heated in a microwave oven for an hour in a porcelain crucible. Finally it was taken out and cooled to room temperature and separated from anthocyanin by centrifugal ultrafiltration. The Si NPs were stored at 4 °C for further use. One of the advantages of this method of synthesis of Si NPs is that no additional reducing agent was used for reducing silica to silicon. The reduction was presumably due to the carbon backbone materials (cellulose, hemicellulose, lignin, *etc.*) present in it and the exact mechanism of reduction is not clearly understood. Reduction of silica to silicon by carbon takes place at extremely high temperatures, i.e., at ~3000 °C which follows the reaction,  $\text{SiO}_2 + \text{C} = \text{Si} + \text{CO}_2$ . Although the

temperature employed here is only 170 °C, it is presumably the local temperature around the particles that is attributed to the reduction which can be as high as the reduction temperature of silica.

The growth of Si NPs upon microwave heating may occur via the formation of smaller nuclei followed by Ostwald ripening (Figure 1B). Once a sufficient number of nuclei form, Ostwald ripening occurs by the coalescence of smaller particles onto the larger ones in order to reduce the surface free energy. In our case, microwave heating was performed for 1 h to get the required nanoparticles. Figure 1C displays the normalized UV–vis absorption, excitation as well as photoluminescence of the nanoparticles. The  $\lambda_{\text{ex}}$  of these nanoparticles was 420 nm and the emission at the corresponding excitation was 520 nm.



**Figure 3.** (A) Size distribution of Si NPs from the TEM image with an average size of 4.9 nm. (B) DLS size measurement of green emitting Si NPs shows an average size of 6.5 nm. (C) XRD characterization of the as Si NPs along with the standard JCPDS data for cubic silicon. (D) XPS spectrum of Si NPs showing features of Si(0) due to silicon core and Si(I) due to oxidized silicon surface. The strong main feature at 103.7 eV is due to silica. (E) FTIR spectra of the Si NPs and rice husk with the regions marked showing possible functionalities. Specific region is expanded on the left.

Distinct absorption features of the nanoparticles were observed at 270 and 350 nm. The energy at 350 nm corresponds to the intrinsic direct  $\Gamma$ – $\Gamma$  band gap of silicon and is a commonly observed peak in Si NPs.<sup>38</sup> Peak at 270 nm corresponds to the L–L transition of silicon.<sup>44</sup> The existence of two peaks gave an indication of the presence of silicon particles in solution. The solution appears brown under white light illumination and exhibits green luminescence under ultraviolet light. The solution upon freeze-drying gave a dark brown powder (Figure 1A). The system has yielded unreacted silica particles also. The silica particles were removed carefully by changing the pH. The estimated yield of Si NPs was 5%.

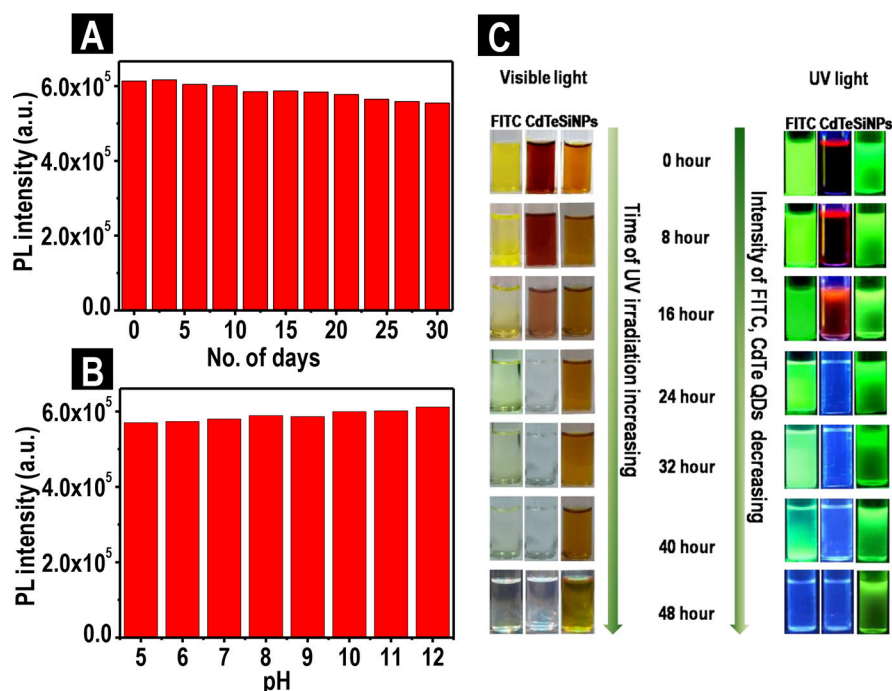
**TEM and EDS Characterization of Si NPs.** Figure 2A shows a large area TEM image of Si NPs displaying the high population of nanoparticles formed during the synthesis. Nanoparticles are largely spherical in nature as shown in the HRTEM image (Figure 2B) having a lattice distance of 0.31 nm matching with the (111) plane of cubic silicon. There were no additional reducing agents or protecting ligands added to the solution. The spherical nature of the nanoparticle is an indication of surface protection presumably by the oxygen and nitrogen containing decomposition products of rice husk. EDAX spectrum and lattice distance (Figure 2C and D) profiles further confirm the existence of Si NPs in solution.

**Structure and Surface Characterization of Si NPs.** The nanoparticles feature excellent hydrophilic nature owing to the nature of surface functionalities. In order to check the

dispersibility of Si NPs, organic solvents, i.e. DCM and hexane, were added to the aqueous dispersion (Figure S13A and B) and the mixture was shaken. As organic solvents are nonpolar and hydrophobic in nature, the Si NPs were not dispersible and a separate layer was formed whereas the Si NPs were dispersed in water. Figure 3A showed the size distribution of the nanoparticles and average size of these nanoparticles observed was  $4.9 \pm 0.2$  nm demonstrating their highly monodisperse nature. Additional information on size of the nanoparticles in solution was collected by DLS measurements. The size of the nanoparticle observed was 6.5 nm (Figure 3B), slightly higher than that observed in TEM owing to distinct surface states of Si NPs under different measurement environments (DLS measurements are based on hydrodynamic radius which includes the surface ligands).<sup>16,36,45–47</sup> Zeta potential of the Si NPs were measured to be  $-27.1$  mV. This gives an idea about the groups at the surface of Si NPs which are likely to be composed of O and N containing species.

Figure 3C displays the XRD features of the as synthesized nanoparticles. Standard diffraction peaks at  $28.4^\circ$ ,  $47.3^\circ$ , and  $56.1^\circ$  corresponding to (111), (220), and (311) crystallographic planes, respectively, matching with the XRD pattern of cubic silicon. For comparison, JCPDS data of cubic silicon (file no. 00-027-1402) are also presented for reference. Figure 3D shows the XPS spectrum of the synthesized nanoparticles. The deconvoluted spectrum shows the presence of different oxidation states of silicon present in the sample. Peaks at





**Figure 4.** (A) Variation of PL intensity of Si NPs as a function of time. (B) Variation of PL intensity as a function of pH. (C) Photostability comparison and photograph of FITC, CdTe QDs, and Si NPs under continuous UV irradiation up to 48 h.

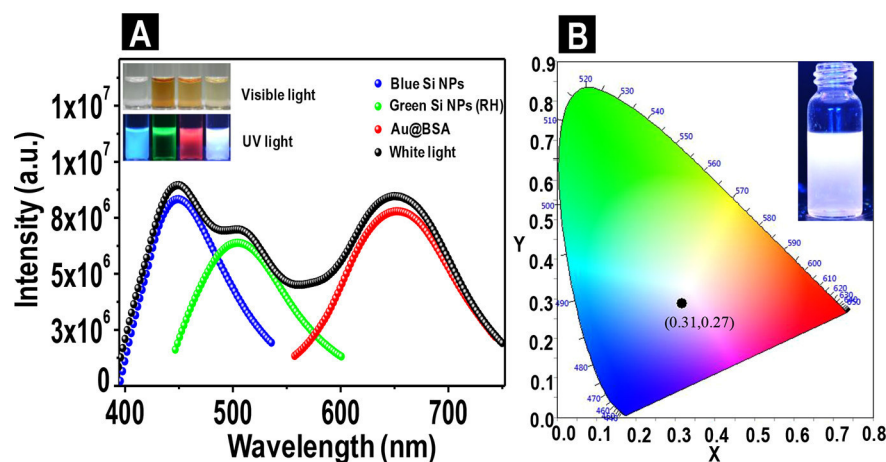
~99.6, 100.7, and 103.7 eV confirm the presence of Si(0), Si(I), and Si(IV) oxidation states, respectively. The Si(0) state indicates the formation of reduced silicon. The Si(I) state is probably due to surface oxidation by the attachment of oxygen and nitrogen containing species as protecting agents. The oxidation state of (IV) indicates the unreacted silica present in the form of silicates of sodium (NaOH was added). In contrast, the XPS spectrum of rice husk (Figure S7) exhibits two peaks in the energy range of 101 and 103.5 eV, attributed to the suboxides and oxides of silicon (silica), respectively. The XPS data clearly suggest the reduction of Si(IV) to Si(0) in the prepared Si NPs by microwave reduction. In order to acquire molecular information, FTIR spectra (Figure 3F) of the Si NPs were measured along with the precursor rice husk. Rice husk shows a peak at  $\sim 3435\text{ cm}^{-1}$  due to the vibrational stretching of N–H/O–H bonds present. Similarly, peaks at 2923, 1645, 1455, and  $1405\text{ cm}^{-1}$  correspond to  $\text{sp}^3$  C–H stretching, N–H bending,  $\text{CH}_2$  bending, and C–N stretching, respectively. Peaks at 2923 and  $1455\text{ cm}^{-1}$  indicate the presence of carbon backbone materials like cellulose, hemicelluloses, etc. Peaks at 1645 and  $1405\text{ cm}^{-1}$  indicate the presence of amino/amide groups, probably due to the presence of proteins/amino acids present in it. Peaks at 2342 and  $2361\text{ cm}^{-1}$  arise due to background  $\text{CO}_2$ . Peaks at  $1040\text{ cm}^{-1}$  correspond to Si–O stretching. In striking contrast, one can clearly see the additional peaks at 833 and  $857\text{ cm}^{-1}$  ascribed to the Si–N stretching vibrations in Si NPs confirming the existence of Si–N bonds which are missing in the IR spectrum of rice husk.<sup>47</sup> Similarly, peaks at 1045, 1645, 1445, and  $1405\text{ cm}^{-1}$  are due to Si–O, N–H,  $\text{CH}_2$ , and C–N stretching and bending vibrations, respectively. FTIR characterization gives an idea about the nature of the surface ligands protecting the Si NP core.

**pH and Photostability Comparison.** Photoluminescence spectrum of Si NPs at an interval of 3 days, for a period of 1 month was studied (Figure S15A). The figure shows that there is no shift in the emission maximum during this period

indicating that the Si NPs are quite stable and do not degrade or change with time (Figure 4A). The decrease in intensity from the first day of the measurement and after 30 days is only 12%. Preservation the PL properties for longer period can be effective for bioimaging as well as biosensing. In order to function effectively in biological media, the nanoparticles should be stable over a wide range of pH as different biological systems work under different pH conditions. The fluorescence spectrum as a function of pH was measured (Figure S15B). The pH was varied from 5 to 12 covering the pH range of most microorganisms. Variation in fluorescence intensity (Figure 4B) was within 9% when the pH was changed from basic (pH 12) to acidic environment (pH 5). Si NPs possess excellent photostability under UV-irradiation, preserving its stability as well as brightness. Photostability comparisons were performed among the green luminescent nanoparticles, CdTe quantum dots, and fluorescein isothiocyanate (FITC) dye under UV lamp. Under UV light, CdTe degraded faster; after 24 h, it was completely degraded, whereas the dye quenched owing to photobleaching. The PL intensity of CdTe quantum dots decreased by more than 80% in the first 16 h (Figure S10) and was completely quenched by 24 h. A similar trend was observed in the case of the dye. However, the fluorescence of nanoparticles was intact. There were several methods reported such as biomimetic synthesis of Si NPs where the synthesis was cheap, facile, and green, but the quantum yield obtained was low in the range of 15–20%.<sup>29</sup> Reports of ultra bright luminescent Si NPs having quantum yield up to 90% has been reported, but such methods used are expensive as well as toxic precursors.<sup>43</sup> In contrast, our material is competitive enough with a quantum yield of  $\sim 60\%$  (Figure S8) which used an inexpensive precursor.

**Si NPs Utilized in White Light Production.** Nowadays white light emitting materials have gained significant attention as major components in light emitting devices (LEDs).<sup>48</sup> Taking into consideration the huge energy demand, especially



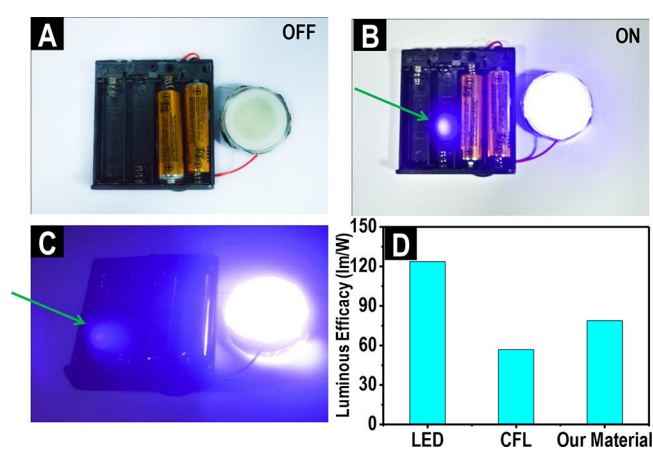


**Figure 5.** (A) Emission of white light from a mixture of blue (Si NPs), green (RH-Si NPs), and red (Au@BSA) luminescent materials. (inset) Photographs of different luminescent materials under UV and visible light. (B) Chromaticity diagram showing the coordinates of the white light emitted (0.31, 0.27) after mixing the materials.

in developing economies, WLEDs are important for energy saving. Low cost and environment friendly WLEDs utilizing organic and inorganic molecules have attracted huge interest in recent years and can be substitutes for expensive rare-earth based sources or Cd based inorganic quantum dots.<sup>49–51</sup> Herein, the synthesized green luminescent Si NPs were mixed with blue emitting Si NPs and red emitting Au@BSA<sup>52</sup> clusters to produce white light and the performance of the composite material was checked. The inset in Figure 5A shows the individual colors under UV and visible light as well as the white light obtained after mixing the solutions (in a 2:1:1 volume ratio of blue, green, and red luminescent materials). The wavelength selected for excitation was 365 nm. Figure 5A shows the individual PL spectra of the luminescent nanoparticles along with the spectrum of white light emitted from the mixed sample.

The color characteristics from the luminescent materials were analyzed using a CIE 1931 chromaticity diagram. The CIE coordinates observed (Figure 5B) for the white light was (0.31, 0.27) which is in excellent agreement with the pure white light coordinates of (0.33, 0.33).

**Application of the White Emitting Material as a Light Source.** Luminescence from the material is generally observed in the colloidal phase. Often aggregation induced quenching lowers the luminescence properties when the sample was dried to films or powders.<sup>53,54</sup> However, in order to use the material directly as a phosphor in WLEDs, high quality luminescence from the material in the solid state is needed. In order to check the solid state emission, the material was mixed with cellulose as a supporting material and kept at 60 °C for drying on a Petri dish and its luminescence was checked. A UV LED was purchased, and a Petri dish coated with the material was placed above it. Figure 6A–C are demonstrations of the usability of the materials as a white light source. It displays excellent white light emission in the solid state ensuring its potential application in the field of WLEDs. The performance of our material was compared with the commercial WLEDs and CFLs. Figure 6D shows such a comparison. The luminous efficacy of our material was superior to the commercial CFLs. Temperature-dependent luminescence measurements were performed to check the thermal stability of white light emitting material. It showed negligible change over the measured range of temperatures. The material was not only unaltered to the



**Figure 6.** (A) Photographic image of the material coated Petri dish connected to a 3 V, 3 W UV LED when the battery was turned off, under visible light. (B) Photographic image of the same material emitting white light when the battery was turned on under visible light. (C) Photographic image of the material emitting white light when the battery was turned on under dark. A white spot marked with an arrow appeared in B and C due to camera reflection. (D) Luminous efficacy comparison of our material with a commercial WLED and CFL.

applied temperature but also was endowed with stability over a longer period of time (Figure S11 and S12) making it suitable as a phosphor material in LEDs.

## CONCLUSION

In summary, we have demonstrated a one-pot solution-processed low temperature synthesis of Si NPs showing bright green emission from a cheap, readily available precursor, namely rice husk without using expensive equipment, harsh conditions, and complicated procedures. The synthetic method is rapid and cost-effective and can be applied for mass production (0.1 g of Si NPs from 2 g of rice husk). The nanoparticles exhibit excellent monodispersity and water dispersibility, high photo- and pH-stability and high quantum yield, and hold promise for a wide range of optoelectronic and bioimaging applications. Owing to their reduced toxicity, they can be employed as alternatives to inorganic quantum dots and organic dyes. The material offers stable solution as well as solid state luminescence, reflecting their capabilities as a sensor and

can be utilized as a phosphor material for the production of white LEDs and lasers, thereby extending its applicability for domestic, industrial, and research purposes. Rice husk synthesized Si NPs may facilitate their use for solar cells, biosensors, printable electronics, etc., and may be used in the advancement of nanoparticle-based bioimaging.

## ■ ASSOCIATED CONTENT

### ■ Supporting Information

The Supporting Information is available free of charge on the ACS Publications website at DOI: 10.1021/acssuschemeng.7b04911.

TEM images of the rice husk synthesized Si NPs in the presence of microwave and their absence without microwave; absorption features of Si NPs, anthocyanin, Si NPs + anthocyanin; TEM images of the residue and supernatant after separation using 10 kDa molecular mass cutoff tubes; EDS and elemental mapping of rice husk to show the silica structure; Excitation wavelength-dependent emission spectra of Si NPs; full range XPS spectrum along with O 1s, C 1s, Na 1s spectra of Si NPs; XPS spectra of rice husk sample; data corresponding to quantum yield determinations; TEM images showing the unaltered Si NPs on changing pH; PL data to show photostability of Si NPs; time-dependent white light emission data; temperature-dependent intensity of white light; hydrophilic nature of Si NPs; solid state white light emission of the material and time- and pH-dependent PL of the Si NPs (PDF)

## ■ AUTHOR INFORMATION

### Corresponding Author

\*E-mail: [pradeep@iitm.ac.in](mailto:pradeep@iitm.ac.in).

### ORCID

Avijit Baidya: 0000-0001-5215-2856

Thalappil Pradeep: 0000-0003-3174-534X

### Notes

The authors declare no competing financial interest.

## ■ ACKNOWLEDGMENTS

We thank the department of science and technology, Government of India, for constantly supporting our research program of nanomaterials. S.B., B.M., and J.S.M. thank IIT Madras for their research fellowships. A.B. thanks the DST for a fellowship. M.A.G. thanks the UGC for a fellowship. S.C. thanks the CSIR for a fellowship. We thank Dr. Soumya Sivalingam for providing the CdTe quantum dots.

## ■ REFERENCES

- (1) Savin, H.; Repo, P.; von Gastrow, G.; Ortega, P.; Calle, E.; Garin, M.; Alcubilla, R. Black silicon solar cells with interdigitated back-contacts achieve 22.1% efficiency. *Nat. Nanotechnol.* **2015**, *10*, 624–628.
- (2) Oh, J.; Yuan, H.-C.; Branz, H. M. An 18.2%-efficient black-silicon solar cell achieved through control of carrier recombination in nanostructures. *Nat. Nanotechnol.* **2012**, *7*, 743–748.
- (3) Jeong, S.; McGehee, M. D.; Cui, Y. All-back-contact ultra-thin silicon nanowire solar cells with 13.7% power conversion efficiency. *Nat. Commun.* **2013**, *4*, 3950.
- (4) Toor, F.; Branz, H. M.; Page, M. R.; Jones, K. M.; Yuan, H.-C. Multi-scale surface texture to improve blue response of nanoporous black silicon solar cells. *Appl. Phys. Lett.* **2011**, *99*, 103501.
- (5) Tian, B.; Zheng, X.; Kempa, T. J.; Fang, Y.; Yu, N.; Yu, G.; Huang, J.; Lieber, C. M. Coaxial silicon nanowires as solar cells and nanoelectronic power sources. *Nature* **2007**, *449*, 885–889.
- (6) Hirschman, K. D.; Tsybeskov, L.; Duttagupta, S. P.; Fauchet, P. M. Silicon-based visible light-emitting devices integrated into micro-electronic circuits. *Nature* **1996**, *384*, 338–341.
- (7) Priolo, F.; Gregorkiewicz, T.; Galli, M.; Krauss, T. F. Silicon nanostructures for photonics and photovoltaics. *Nat. Nanotechnol.* **2014**, *9*, 19–32.
- (8) Ng, W. L.; Lourenco, M. A.; Gwilliam, R. M.; Ledain, S.; Shao, G.; Homewood, K. P. An efficient room-temperature silicon-based light-emitting diode. *Nature* **2001**, *410*, 192–194.
- (9) Park, J.-H.; Gu, L.; von Maltzahn, G.; Ruoslahti, E.; Bhatia, S. N.; Sailor, M. J. Biodegradable luminescent porous silicon nanoparticles for in vivo applications. *Nat. Mater.* **2009**, *8*, 331–336.
- (10) Cullis, A. G.; Canham, L. T. Visible light emission due to quantum size effects in highly porous crystalline silicon. *Nature* **1991**, *353*, 335–338.
- (11) Canham, L. T. Silicon quantum wire array fabrication by electrochemical and chemical dissolution of wafers. *Appl. Phys. Lett.* **1990**, *57*, 1046–1048.
- (12) Pavesi, L.; Dal Negro, L.; Mazzoleni, C.; Franzo, G.; Priolo, F. Optical gain in silicon nanocrystals. *Nature* **2000**, *408*, 440–444.
- (13) Ding, Z.; Quinn, B. M.; Haram, S. K.; Pell, L. E.; Korgel, B. A.; Bard, A. J. Electrochemistry and electrogenerated chemiluminescence from silicon nanocrystal quantum dots. *Science* **2002**, *296*, 1293–1297.
- (14) Tsybeskov, L.; Lockwood, D. J.; McCaffrey, J. P.; Labbe, H. J.; Fauchet, P. M.; White, B., Jr.; Diener, J.; Kovalev, D.; Koch, F.; Grom, G. F. Ordering and self-organization in nanocrystalline silicon. *Nature* **2000**, *407*, 358–361.
- (15) Gu, L.; Hall, D. J.; Qin, Z.; Anglin, E.; Joo, J.; Mooney, D. J.; Howell, S. B.; Sailor, M. J. In vivo time-gated fluorescence imaging with biodegradable luminescent porous silicon nanoparticles. *Nat. Commun.* **2013**, *4*, 3326.
- (16) Zhong, Y.; Peng, F.; Wei, X.; Zhou, Y.; Wang, J.; Jiang, X.; Su, Y.; Su, S.; Lee, S.-T.; He, Y. Microwave-Assisted Synthesis of Biofunctional and Fluorescent Silicon Nanoparticles Using Proteins as Hydrophilic Ligands. *Angew. Chem., Int. Ed.* **2012**, *51*, 8485–8489.
- (17) Mastronardi, M. L.; Hennrich, F.; Henderson, E. J.; Maier-Flaig, F.; Blum, C.; Reichenbach, J.; Lemmer, U.; Kubel, C.; Wang, D.; Kappes, M. M.; Ozin, G. A. Preparation of Monodisperse Silicon Nanocrystals Using Density Gradient Ultracentrifugation. *J. Am. Chem. Soc.* **2011**, *133*, 11928–11931.
- (18) Anthony, R. J.; Cheng, K.-Y.; Holman, Z. C.; Holmes, R. J.; Kortshagen, U. R. An All-Gas-Phase Approach for the Fabrication of Silicon Nanocrystal Light-Emitting Devices. *Nano Lett.* **2012**, *12*, 2822–2825.
- (19) Purkait, T. K.; Iqbal, M.; Wahl, M. H.; Gottschling, K.; Gonzalez, C. M.; Islam, M. A.; Veinot, J. G. C. Borane-catalyzed room-temperature hydrosilylation of alkenes/alkynes on silicon nanocrystal surfaces. *J. Am. Chem. Soc.* **2014**, *136*, 17914–17917.
- (20) Mastronardi, M. L.; Henderson, E. J.; Puzzo, D. P.; Ozin, G. A. Small Silicon, Big Opportunities: The Development and Future of Colloidally-Stable Monodisperse Silicon Nanocrystals. *Adv. Mater.* **2012**, *24*, 5890–5898.
- (21) Ganguly, S.; Kazem, N.; Carter, D.; Kauzlarich, S. M. Colloidal synthesis of an exotic phase of silicon: the BC8 structure. *J. Am. Chem. Soc.* **2014**, *136*, 1296–1299.
- (22) Cheng, X.; Lowe, S. B.; Reece, P. J.; Gooding, J. J. Colloidal silicon quantum dots: from preparation to the modification of self-assembled monolayers (SAMs) for bio-applications. *Chem. Soc. Rev.* **2014**, *43*, 2680–2700.
- (23) Peng, F.; Su, Y.; Zhong, Y.; Fan, C.; Lee, S.-T.; He, Y. Silicon Nanomaterials Platform for Bioimaging, Biosensing, and Cancer Therapy. *Acc. Chem. Res.* **2014**, *47*, 612–623.
- (24) McVey, B. F. P.; Tilley, R. D. Solution Synthesis, Optical Properties, and Bioimaging Applications of Silicon Nanocrystals. *Acc. Chem. Res.* **2014**, *47*, 3045–3051.

- (25) Montalti, M.; Cantelli, A.; Battistelli, G. Nanodiamonds and silicon quantum dots: ultrastable and biocompatible luminescent nanoprobes for long-term bioimaging. *Chem. Soc. Rev.* **2015**, *44*, 4853–4921.
- (26) Dasog, M.; Kehrle, J.; Rieger, B.; Veinot, J. G. C. Silicon Nanocrystals and Silicon-Polymer Hybrids: Synthesis, Surface Engineering, and Applications. *Angew. Chem., Int. Ed.* **2016**, *55*, 2322–2339.
- (27) He, Y.; Fan, C.; Lee, S.-T. Silicon nanostructures for bioapplications. *Nano Today* **2010**, *5*, 282–295.
- (28) Wai, C. M.; Hutchison, S. G. Free energy minimization calculation of complex chemical equilibria. Reduction of silicon dioxide with carbon at high temperature. *J. Chem. Educ.* **1989**, *66*, 546–549.
- (29) Wu, S.; Zhong, Y.; Zhou, Y.; Song, B.; Chu, B.; Ji, X.; Wu, Y.; Su, Y.; He, Y. Biomimetic Preparation and Dual-Color Bioimaging of Fluorescent Silicon Nanoparticles. *J. Am. Chem. Soc.* **2015**, *137*, 14726–14732.
- (30) Zhang, J.; Yu, S.-H. Highly photoluminescent silicon nanocrystals for rapid, label-free and recyclable detection of mercuric ions. *Nanoscale* **2014**, *6*, 4096–4101.
- (31) Zhu, J.; Yu, Z.; Burkhard, G. F.; Hsu, C. M.; Connor, S. T.; Xu, Y.; Wang, Q.; McGehee, M.; Fan, S.; Cui, Y. Optical Absorption Enhancement in Amorphous Silicon Nanowire and Nanocone Arrays. *Nano Lett.* **2009**, *9*, 279–282.
- (32) Morales, A. M.; Lieber, C. M. A laser ablation method for the synthesis of crystalline semiconductor nanowires. *Science* **1998**, *279*, 208–211.
- (33) Heintz, A. S.; Fink, M. J.; Mitchell, B. S. Mechanochemical synthesis of blue luminescent alkyl/alkenyl-passivated silicon nanoparticles. *Adv. Mater.* **2007**, *19*, 3984–3988.
- (34) Mangolini, L.; Kortshagen, U. Plasma-assisted synthesis of silicon nanocrystal inks. *Adv. Mater.* **2007**, *19*, 2513–2519.
- (35) Arul Dhas, N.; Raj, C. P.; Gedanken, A. Preparation of Luminescent Silicon Nanoparticles: A Novel Sonochemical Approach. *Chem. Mater.* **1998**, *10*, 3278–3281.
- (36) Zhong, Y.; Peng, F.; Bao, F.; Wang, S.; Ji, X.; Yang, L.; Su, Y.; Lee, S.-T.; He, Y. Large-Scale Aqueous Synthesis of Fluorescent and Biocompatible Silicon Nanoparticles and Their Use as Highly Photostable Biological Probes. *J. Am. Chem. Soc.* **2013**, *135*, 8350–8356.
- (37) Erogbogbo, F.; Yong, K. T.; Roy, I.; Xu, G.; Prasad, P. N.; Swihart, M. T. Biocompatible Luminescent Silicon Quantum Dots for Imaging of Cancer Cells. *ACS Nano* **2008**, *2*, 873–878.
- (38) Li, Q.; Luo, T.-Y.; Zhou, M.; Abroshan, H.; Huang, J.; Kim, H. J.; Rosi, N. L.; Shao, Z.; Jin, R. Silicon Nanoparticles with Surface Nitrogen: 90% Quantum Yield with Narrow Luminescence Bandwidth and the Ligand Structure Based Energy Law. *ACS Nano* **2016**, *10*, 8385–8393.
- (39) Adam, F.; Appaturi, J. N.; Iqbal, A. The utilization of rice husk silica as a catalyst: Review and recent progress. *Catal. Today* **2012**, *190*, 2–14.
- (40) Bakar, R. A.; Yahya, R.; Gan, S. N. Production of High Purity Amorphous Silica from Rice Husk. *Procedia Chem.* **2016**, *19*, 189–195.
- (41) Bansal, V.; Ahmad, A.; Sastry, M. Fungus-Mediated Biotransformation of Amorphous Silica in Rice Husk to Nanocrystalline Silica. *J. Am. Chem. Soc.* **2006**, *128*, 14059–14066.
- (42) Praneetha, S.; Murugan, A. V. Development of Sustainable development of sustainable rapid microwave assisted process for extg. nanoporous Si from earth abundant agricultural residues and their carbon-based nanohybrids for lithium energy storage. *ACS Sustainable Chem. Eng.* **2015**, *3*, 224–236.
- (43) Kim, K. H.; Lee, D. J.; Cho, K. M.; Kim, S. J.; Park, J.-K.; Jung, H.-T. Complete magnesiothermic reduction reaction of vertically aligned mesoporous silica channels to form pure silicon nanoparticles. *Sci. Rep.* **2015**, *5*, 9014.
- (44) Holmes, J. D.; Ziegler, K. J.; Doty, R. C.; Pell, L. E.; Johnston, K. P.; Korgel, B. A. Highly Luminescent Silicon Nanocrystals with Discrete Optical Transitions. *J. Am. Chem. Soc.* **2001**, *123*, 3743–3748.
- (45) He, Y.; Zhong, Y.-L.; Peng, F.; Wei, X.-P.; Su, Y.-Y.; Lu, Y.-M.; Su, S.; Gu, W.; Liao, L.-S.; Lee, S.-T. One-Pot Microwave Synthesis of Water-Dispersible, Ultraphoto- and pH-Stable, and Highly Fluorescent Silicon Quantum Dots. *J. Am. Chem. Soc.* **2011**, *133*, 14192–14195.
- (46) Li, Q.; He, Y.; Chang, J.; Wang, L.; Chen, H.; Tan, Y.-W.; Wang, H.; Shao, Z. Surface-Modified Silicon Nanoparticles with Ultrabright Photoluminescence and Single-Exponential Decay for Nanoscale Fluorescence Lifetime Imaging of Temperature. *J. Am. Chem. Soc.* **2013**, *135*, 14924–14927.
- (47) Zhong, Y.; Sun, X.; Wang, S.; Peng, F.; Bao, F.; Su, Y.; Li, Y.; Lee, S.-T.; He, Y. Facile, Large-Quantity Synthesis of Stable, Tunable-Color Silicon Nanoparticles and Their Application for Long-Term Cellular Imaging. *ACS Nano* **2015**, *9*, 5958–5967.
- (48) Gather, M. C.; Kohnen, A.; Meerholz, K. White organic light-emitting diodes. *Adv. Mater.* **2011**, *23*, 233–248.
- (49) Wang, J.; Lin, W.; Li, W. Three-channel fluorescent sensing via organic white light-emitting dyes for detection of hydrogen sulfide in living cells. *Biomaterials* **2013**, *34*, 7429–7436.
- (50) Mukherjee, S.; Thilagar, P. Organic white-light emitting materials. *Dyes Pigm.* **2014**, *110*, 2–27.
- (51) Chen, J.; Zhao, D.; Li, C.; Xu, F.; Lei, W.; Sun, L.; Nathan, A.; Sun, X. W. All Solution-processed Stable White Quantum Dot Light-emitting Diodes with Hybrid ZnO@TiO<sub>2</sub> as Blue Emitters. *Sci. Rep.* **2015**, *4*, 4085.
- (52) Baksi, A.; Mitra, A.; Mohanty, J. S.; Lee, H.; De, G.; Pradeep, T. Size Evolution of Protein-Protected Gold Clusters in Solution: A Combined SAXS-MS Investigation. *J. Phys. Chem. C* **2015**, *119*, 2148–2157.
- (53) Zhu, S.; Meng, Q.; Wang, L.; Zhang, J.; Song, Y.; Jin, H.; Zhang, K.; Sun, H.; Wang, H.; Yang, B. Highly Photoluminescent Carbon Dots for Multicolor Patterning, Sensors, and Bioimaging. *Angew. Chem., Int. Ed.* **2013**, *52*, 3953–3957.
- (54) Qu, S.; Wang, X.; Lu, Q.; Liu, X.; Wang, L. A Biocompatible Fluorescent Ink Based on Water-Soluble Luminescent Carbon Nanodots. *Angew. Chem., Int. Ed.* **2012**, *51*, 12215–12218.

## Supporting Information

### **Synthesis of Silicon Nanoparticles from Rice Husk and their Use as Sustainable Fluorophores for White Light Emission**

Sandeep Bose, Mohd. Azhardin Ganayee, Biswajit Mondal, Avijit Baidya, Sudhakar Chennu, Jyoti Sarita Mohanty, Thalappil Pradeep\*

DST Unit of Nanoscience (DST UNS), and Thematic Unit of Excellence (TUE),  
Department of Chemistry, Indian Institute of Technology Madras, Chennai - 600 036,  
India

\*Email: pradeep@iitm.ac.in

#### ***Index***

<i>Instrumental details</i>	<i>Page S2</i>
<i>Figure S1 TEM image of the rice husk synthesized SiNPs in presence and absence of microwave</i>	<i>Page S3</i>
<i>Figure S2 Absorption features of SiNPs, anthocyanin, SiNPs + anthocyanin</i>	<i>Page S4</i>
<i>Figure S3 TEM images of the anthocyanin and SiNPs after separation using molecular mass cut-off tubes</i>	<i>Page S5</i>
<i>Figure S4 EDAX and elemental mapping of rice husk to show the silica nature</i>	<i>Page S6</i>
<i>Figure S5 Excitation wavelength dependent emission spectra of SiNPs</i>	<i>Page S7</i>
<i>Figure S6 Full range XPS spectrum along with O1s, C1s, N1s spectra of SiNPs</i>	<i>Page S8</i>
<i>Figure S7 XPS spectra of rice husk sample</i>	<i>Page S9</i>
<i>Figure S8 Absorbance against normalized PL intensity plot for slope calculation and quantum yield determination</i>	<i>Page S10</i>
<i>Figure S9 TEM images showing the unaltered SiNPs on changing pH</i>	<i>Page S11</i>
<i>Figure S10 PL intensity plot as a function of time to show photostability of SiNPs</i>	<i>Page S12</i>
<i>Figure S11 Time dependent white light emission and its unchanged</i>	<i>Page S13</i>

*intensity as a function of time*

*Figure S12 Temperature dependent intensity of white light to show thermal stability* Page S14

*Figure S13 Hydrophilic nature of SiNPs* Page S14

*Figure S14 Solid state white light emission of the material.* Page S15

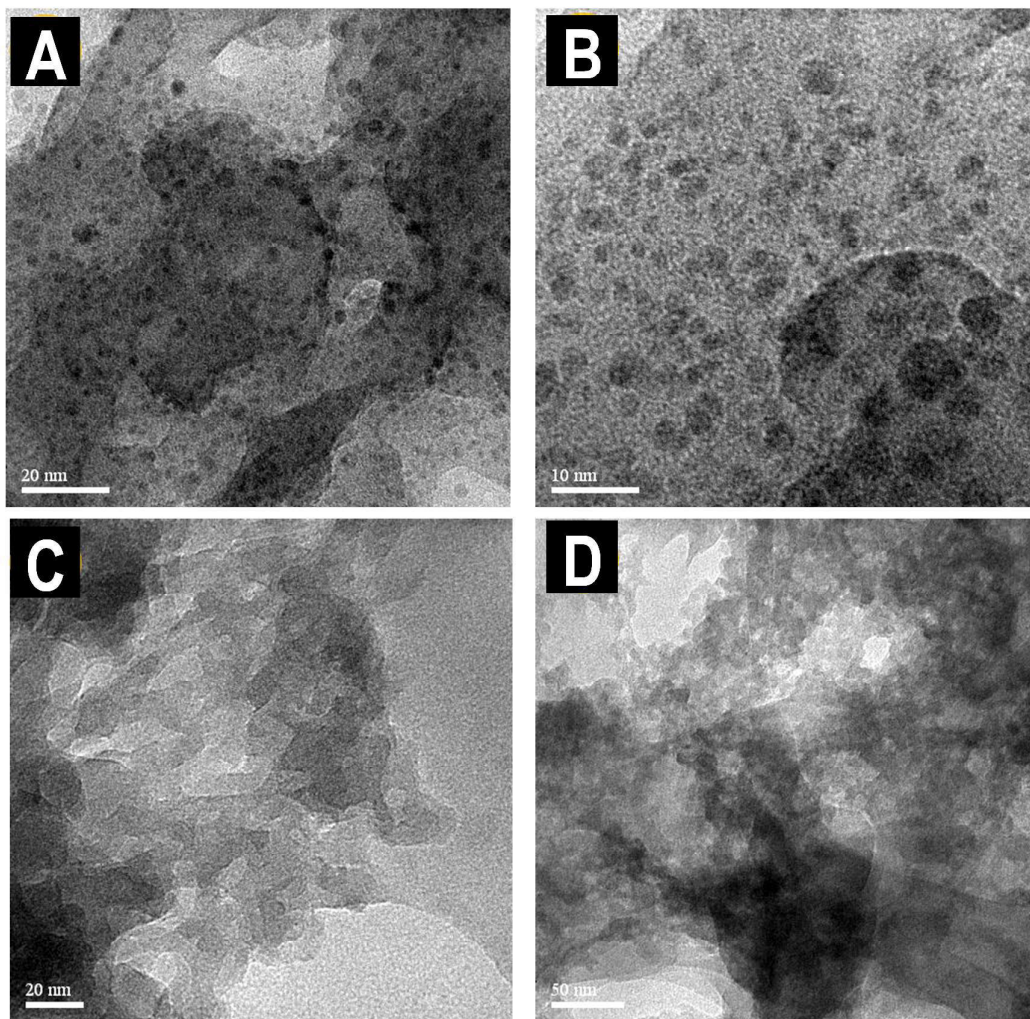
*Figure S15 Time dependent and pH dependent PL spectra of the Si NPs* Page S16

## **Instrumentation**

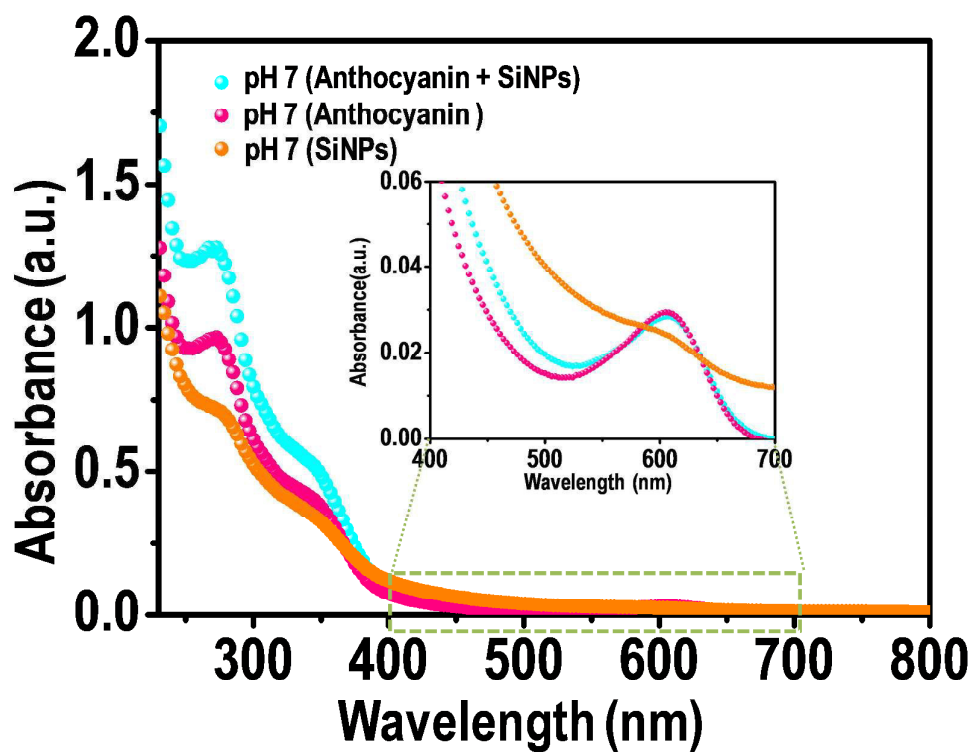
Si NPs were characterized by transmission electron microscopy (TEM), high resolution transmission electron microscopy (HRTEM), powder X-ray diffraction (PXRD), photoluminescence (PL), UV-Vis absorption and X-ray photoelectron spectroscopy (XPS). UV-Vis absorption spectra were measured using a Perkin Elmer Lambda 25 spectrophotometer in the range of 200-1100 nm. Photoluminescence measurements were performed using a Horiba JobinYvon Nanolog (FL 1000) fluorimeter. The band pass for excitation and emission was set at 3 nm. The excitation wavelength was set at 420 nm. Powder XRD was measured using Bruker D8 Advance diffractometer. The peaks at angles 28, 42 and 56 degrees correspond to (111), (220) and (311) planes of silicon nanoparticles. All the TEM/HRTEM and EDS measurements were done using JEOL 3010 (JEOL Japan) operating at 200 kV. SEM measurements were performed using FEI Quanta 200 operating at 30 kV equipped with EDS. XPS measurements were carried out using Omicron ESCA probe spectrometer with polychromatic Mg K $\alpha$  X-rays ( $h\nu = 1253.6$  eV). The photostability studies were performed with a Philips TL 6W UV lamp. DLS measurements were carried out using Malvern Zetasizer Nano (ZSP) (Temperature, 25°C; scan, 100; dispersant, water; refractive index, 1.33; viscosity, 0.08872 cP; dielectric constant, 78.5). A Jasco FT/IR-4100 type A spectrometer was utilized for recording the FTIR spectra (Scan, 64; resolution 4 cm<sup>-1</sup>). All the



photographic images were taken with Nikon D5100 DSLR camera. Luminous flux measurements were carried out using Kusam Mecro KM-Lux-99 digital Luxmeter.

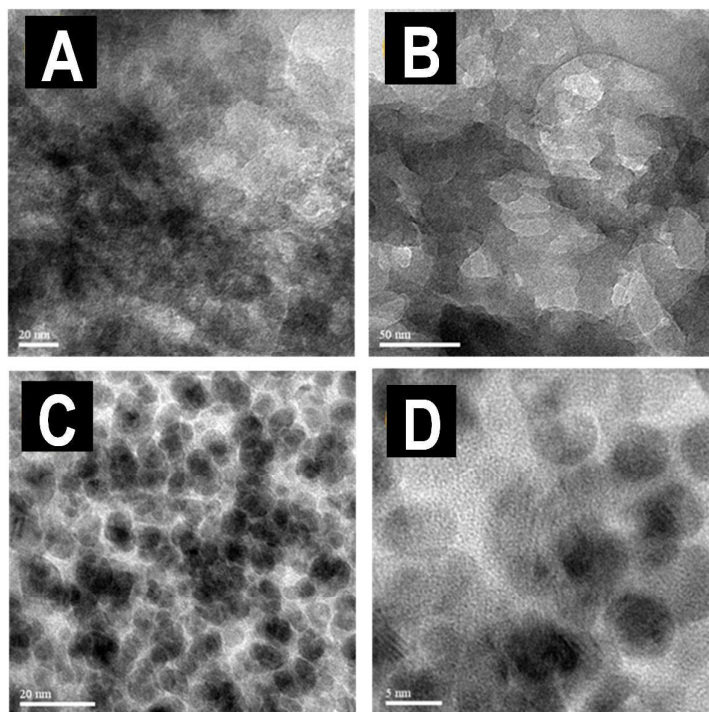


**Figure S1.** (A) & (B) TEM images of the SiNPs derived from the microwave treatment of rice husk powder & NaOH mixture. (C) & (D) TEM image of the rice husk powder and NaOH mixture showing the absence of nanoparticles without microwave treatment.

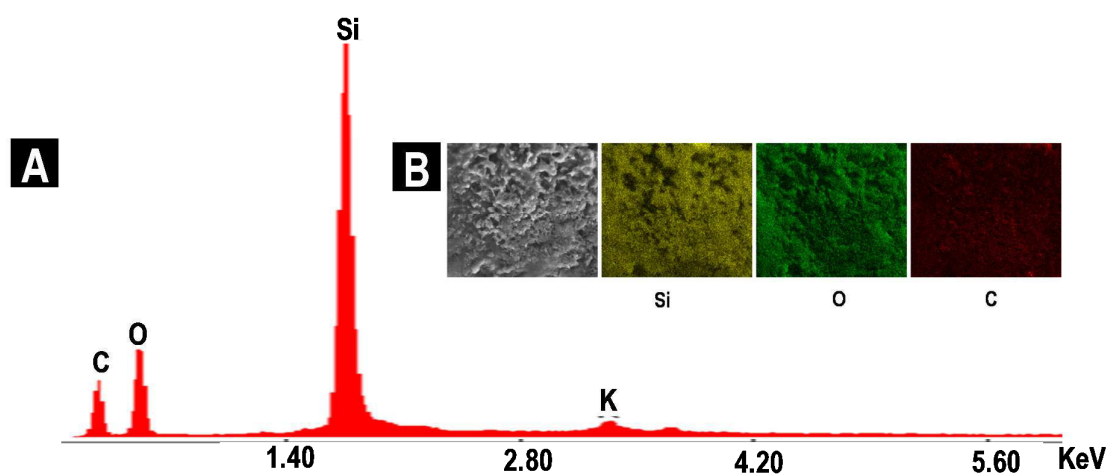


**Figure S2.** Absorption features of anthocyanin + SiNPs (cyan) at pH 7. Absorption features anthocyanin (pink) separated from Si NPs (orange) using molecular mass cut off centrifuge tubes shows absorption peak around 600 nm which is characteristic of anthocyanin and is absent in SiNPs.

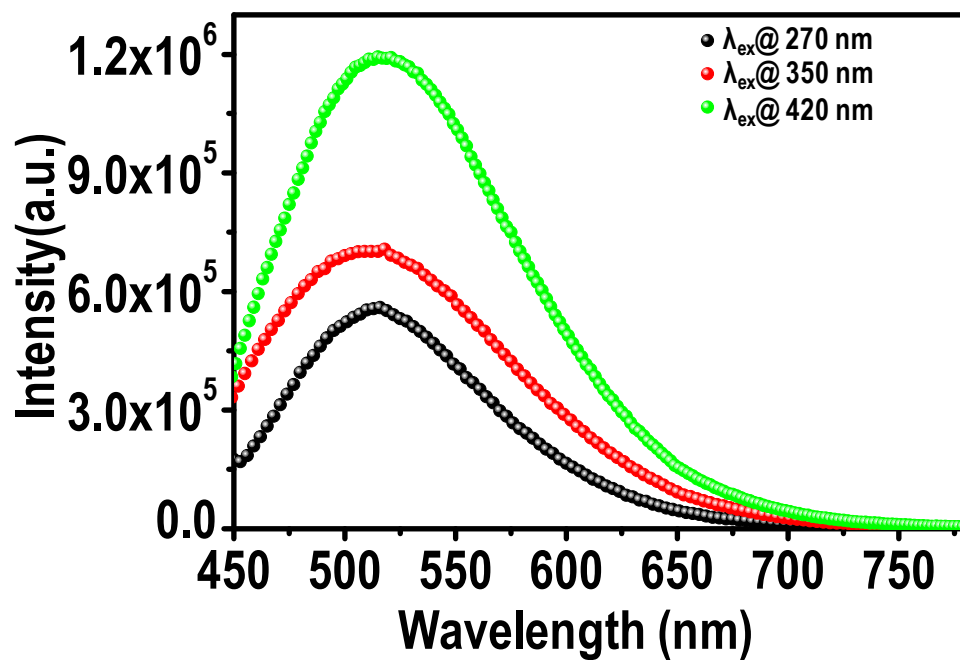




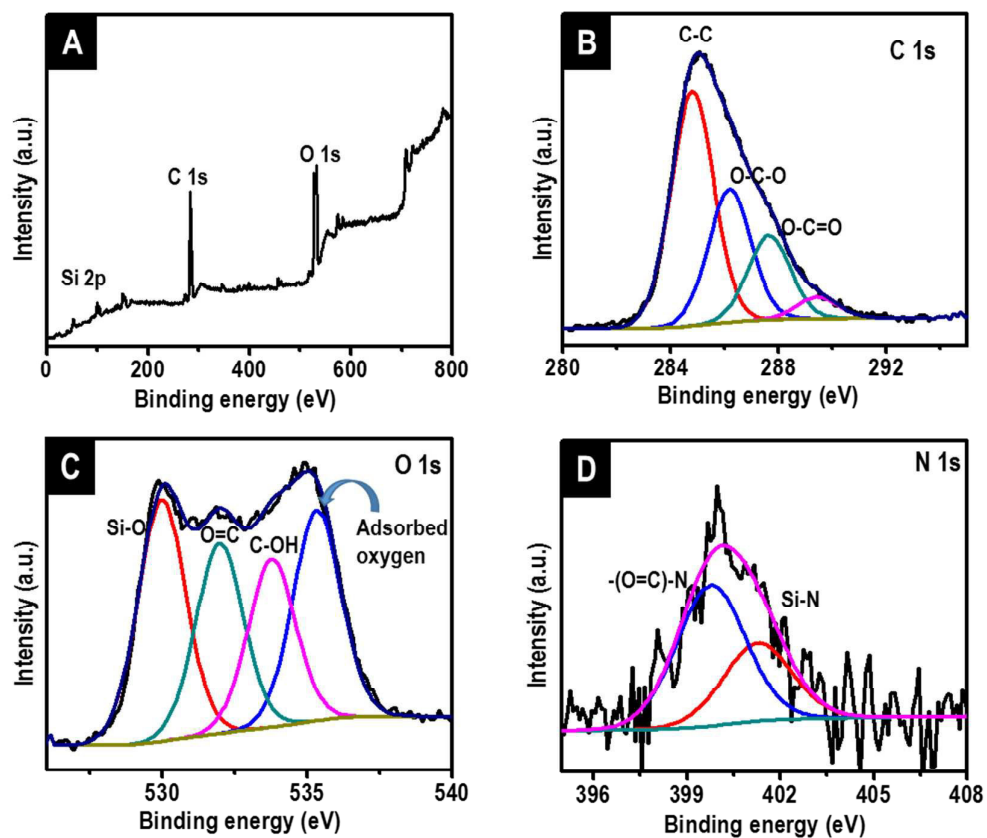
**Figure S3.** (A) & (B) shows the TEM image of the supernatant separated from the Si NPs using molecular mass cut off tubes which may contain silica and anthocyanin but no crystalline Si NPs. Similarly (C) & (D) shows the TEM images of the SiNPs separated. The Si NPs were collected as residue where as anthocyanin was collected as supernatant. This method of separation SiNPs from anthocyanin was quite efficient.



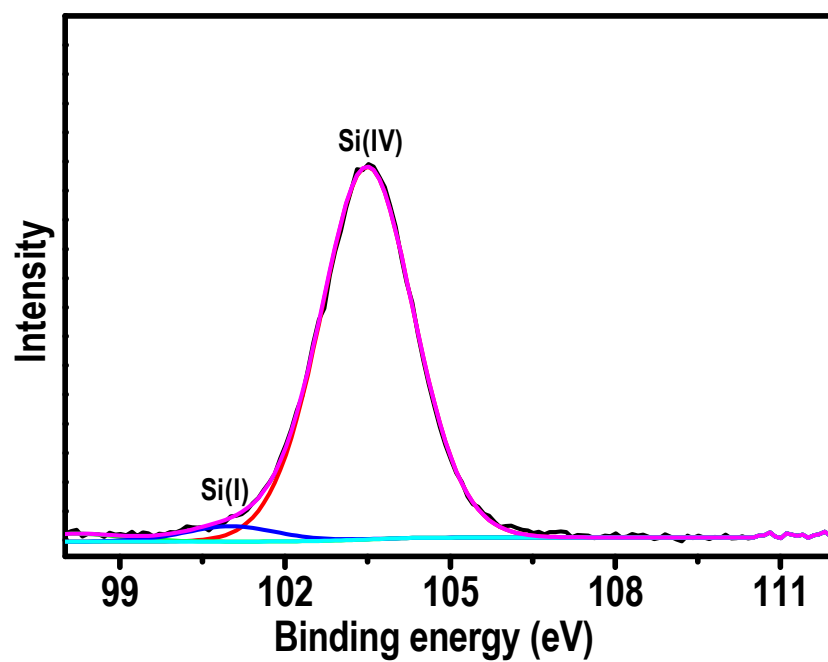
**Figure S4.** (A) SEM-EDAX spectrum of rice husk powder. (B) Elemental mapping of rice husk powder to show the elements present in it. It is clearly evident that rice husk contains high quantity of silicon in the form of silica. The carbon and oxygen are coming from the cellulose/hemicellulose and silica present in rice husk.



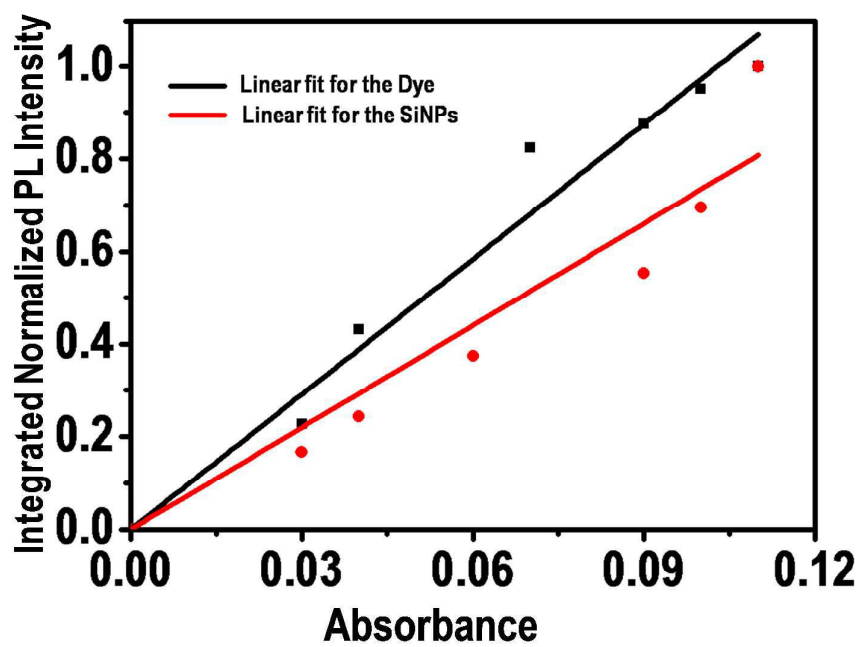
**Figure S5.** Excitation wavelength dependent emission spectra of Si NPs shows no shift in emission on changing the excitation wavelength.



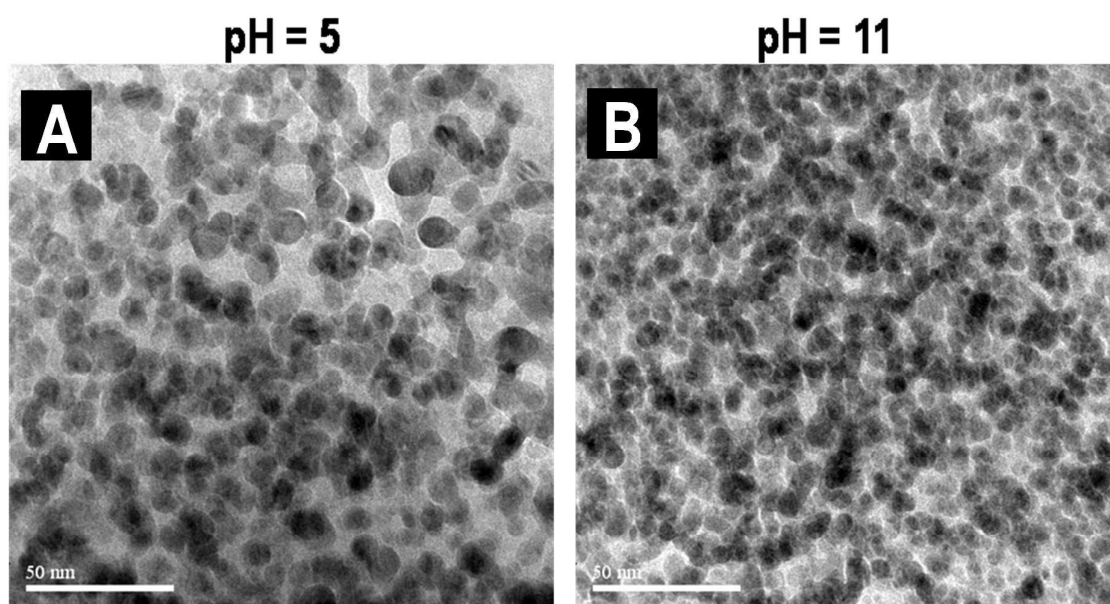
**Figure S6.** (A) Full range XPS spectrum of the Si NPs. (B), (C), (D) shows the C 1s, O 1s, N 1s spectra of microwave synthesized Si NPs respectively.



**Figure S7.** XPS spectrum of (rice husk powder + NaOH) mixture. It shows the absence of Si(0) features and only Si(IV) features are present. The Si(0) features at 99.6 eV appears only after microwave irradiation.

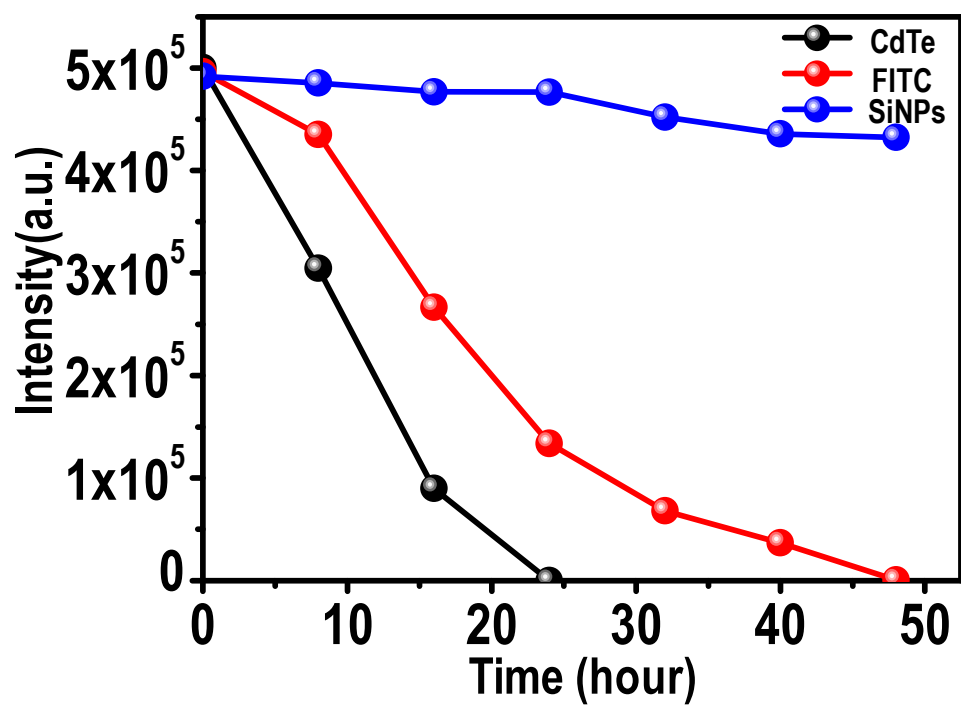


**Figure S8.** Plot of normalized PL intensity against absorbance to calculate slope (K) of the graph. The quantum yield was calculated to be 0.58.

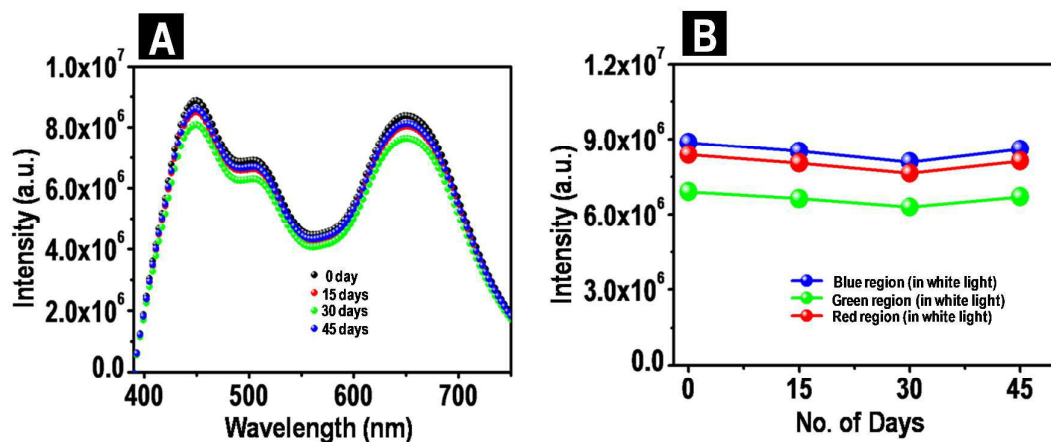


**Figure S9.** (A) & (B) are TEM images of Si NPs at pH 5 & 11 ensuring the existence of Si NPs i.e. the stability of nanoparticles do not change on changing pH.

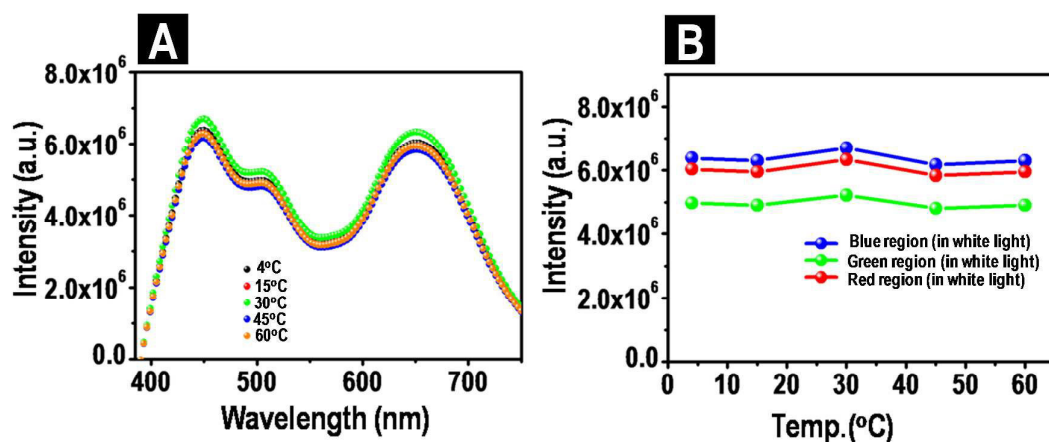




**Figure S10.** Plot of PL intensities of CdTe, FITC, Si NPs as a function of time.



**Figure S11.** (A) Plot of the resulting white light emission of the mixture as a function of wavelength at different time interval to check the stability of material. As white light is a mixture of 3 colours i.e. blue, green & red, white light PL show three different regions namely blue emitting region, green emitting region, red emitting region. Figure (B) is a plot of intensity variations of different regions of white light over a period of 45 days.



**Figure S12.** (A) Plot of resulting white emission of the material as a function of wavelength at different temperatures of the solution to check the thermal stability of the material. (B) Plot of PL intensities of different regions i.e. blue, green & red regions of white light as a function of temperature. Almost no change in intensities were observed indicating thermal stability of the material over the measured range of temperature.



**Figure S13.** (A) & (B) shows the excellent hydrophilic nature of the as-prepared Si NPs where organic solvents having different densities i.e. DCM and Hexane were used to check its miscibility with water dispersible Si NPs.

**Under UV light**

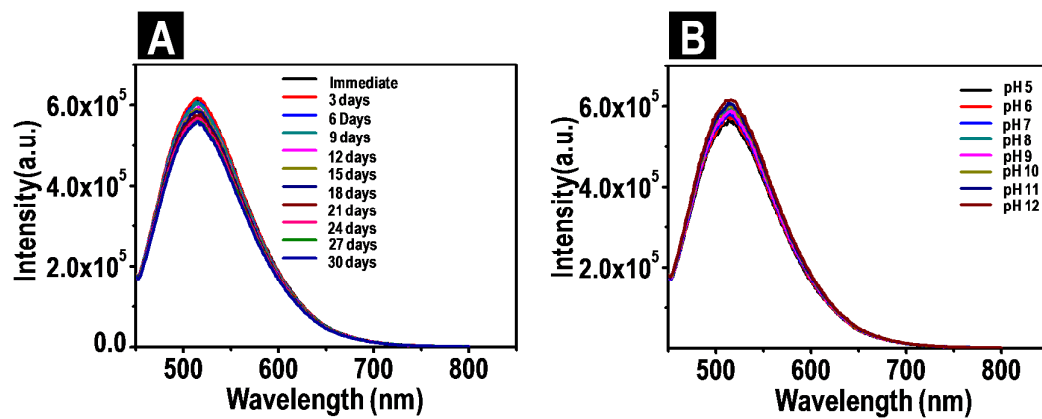


**Normal Petri Dish**



**Petri Dish Coated with Material**

**Figure S14.** Photographic image of the normal petri dish and petri dish coated with material under UV light.



**Figure S15.** (A) Time dependent photoluminescence spectra of the green luminescent Si NPs. (B) pH dependent photoluminescence spectra of the Si NPs.

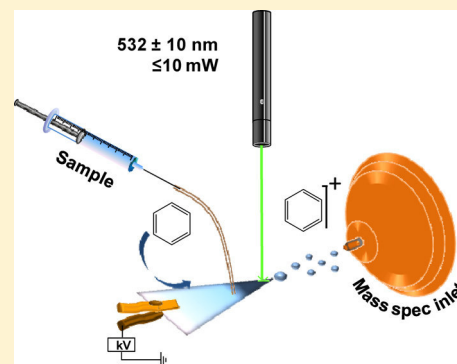
# Detection of Hydrocarbons by Laser Assisted Paper Spray Ionization Mass Spectrometry (LAPSI MS)

Pallab Basuri,<sup>†</sup> Depanjan Sarkar,<sup>†</sup> Ganesan Paramasivam, and Thalappil Pradeep\*<sup>‡</sup>

DST Unit of Nanoscience (DST UNS), Thematic Unit of Excellence (TUE), Department of Chemistry, Indian Institute of Technology Madras, Chennai 600036, India

## Supporting Information

**ABSTRACT:** Here we introduce a new ambient ionization technique named laser assisted paper spray ionization mass spectrometry (LAPSI MS). In it, a  $532 \pm 10$  nm,  $\leq 10$  mW laser pointer was shone on a triangularly cut paper along with high voltage, to effect ionization. The analyte solution was continuously pushed through a fused silica capillary, using a syringe pump, at a preferred infusion rate. LAPSI MS promises enhanced ionization with high signal intensity of polycyclic aromatic hydrocarbons (PAHs), which are normally not ionizable with similar ionization methods involving solvent sprays. LAPSI MS works both in positive and negative modes of ionization. A clear enhancement of signal intensity was visualized in the total ion chromatogram for most analytes in the presence of the laser. We speculate that the mechanism of ionization is field assisted photoionization. The field-induced distortion of the potential well can be large in paper spray as the fibers comprising the paper are separated at tens of nanometers apart, and consequently, the analyte molecules are subjected to very large electric fields of the order of  $10^7$  Vcm<sup>-1</sup>. Ionization occurs from their distorted electronic states of reduced ionization energy, using the laser. Negative ion detection is also demonstrated, occurring due to the capture of produced photoelectrons. LAPSI MS can be used for monitoring in situ photoassisted reactions like the decarboxylation of mercaptobenzoic acid in the presence of gold and silver nanoparticles and the dehydrogenation reaction of 2,3-dihydro-1H-isoindole, which were chosen as examples. As an application, we have shown that paraffin oil, which is usually nonionizable by paper spray or by electrospray ionization can be efficiently detected using this technique. Impurities like mineral oils were detected easily in commercially available coconut oil, pointing the way to applications of social relevance.



Ambient ionization methods such as electrospray ionization (ESI),<sup>1</sup> desorption electrospray ionization (DESI),<sup>2–4</sup> low temperature plasma (LTP)<sup>5</sup> ionization, etc., have emerged as some of the most important directions in modern mass spectrometry. One of the important subclasses of this discipline is paper spray ionization mass spectrometry,<sup>6,7</sup> which has importance in several analytical situations such as blood clot analysis,<sup>8,9</sup> forensic analysis,<sup>10</sup> food adulteration,<sup>11,12</sup> monitoring catalysis reactions,<sup>13,14</sup> etc. Variation of the same, such as leaf spray (LS)<sup>15,16</sup> ionization, has also been useful in a number of situations. Despite important advantages, the technique has certain limitations in analyzing specific categories of analytes such as alkanes, olefins, polycyclic aromatic hydrocarbons (PAHs), etc. This stems from the fact that the electrospray technique in general is inefficient in causing ionization for certain classes of molecules. For such molecular systems, an approach to overcome this limitation is to use other stimuli complementing the electric field available in paper spray.

We show that a simple laser pointer is adequate to assist the electric field and cause measurable ion intensity for a diverse variety of analytes. This modified paper spray referred to as laser assisted paper spray ionization mass spectrometry (LAPSI MS) is introduced in this article. The paper illustrates the application of this technique for several aromatic molecules that

are not amenable for common paper spray ionization. In order to establish the field assisted photoionization process, experiments have been conducted with analytes of different ionization potentials. The experimental methodology has been applied to an important situation involving the detection of paraffin oil<sup>17</sup> (a common example of hydrocarbons) in adulterated coconut oil. It further shows the utility of the methodology of paper spray in detecting laser-induced transformations.

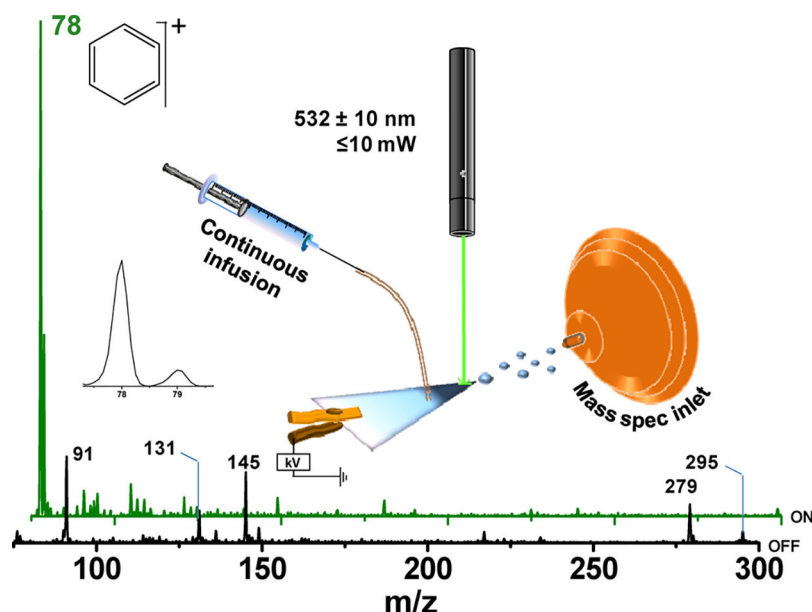
## MATERIALS AND METHODS

**Chemicals and Sample Preparation.** All the chemicals were purchased commercially and used without further purification. Benzene, naphthalene, pyrene, benzanthracene, C<sub>60</sub>, and paraffin oil were purchased from Sigma-Aldrich. Mercaptobenzoic acid (MBA), 3-dihydro-1H-isoindole, HPLC grade methanol, and toluene were purchased from Sigma or Rankem. Au and Ag nanoparticles (Au NPs and Ag NPs) were synthesized in the laboratory following the reported methodology.<sup>18,19</sup> Pure coconut oil was prepared by a standard

Received: December 14, 2017

Accepted: March 9, 2018

Published: March 9, 2018



**Figure 1.** Mass spectrum of benzene in presence (green trace) and absence of laser (black trace). Inset shows schematic of the experimental setup of laser assisted paper spray ionization mass spectrometry (LAPSI MS). A green diode laser was pointed at the tip of the paper with a continuous supply of analyte through a fused silica capillary. The figure is not to scale. Peaks in the laser-off condition are due to the background, indicating impurities on the paper.

protocol by milling. Adulterated coconut oil samples were purchased from the local market.

**LAPSI MS.** In LAPSI MS, we have introduced a green laser pointer ( $532 \pm 10$  nm,  $\leq 10$  mW), (UKTECHLAB, U.K.) along with standard paper spray mass spectrometry. The inset of the Figure 1 schematically demonstrates the experimental setup. A Thermo Scientific LTQ XL mass spectrometer was used for all of the mass spectrometric measurements. A Whatman 42 filter paper was cut into a triangular shape (Figure S1) and was connected to a high voltage power supply through a copper clip in such a way that one of the vertices was pointed toward the inlet of the mass spectrometer. The average area of the paper was  $3.2 \text{ cm}^2$  for all of the experiments. The distance between the tip of the paper and the mass spectrometer inlet was set to be 10 mm in all the cases. The laser was placed vertically at a distance of 10 cm from the paper. The laser spot was the tip of the paper, and the visible spot diameter was approximately 3 mm. Although the laser runs on a battery, it was connected to a switch mode power supply (SMPS) to give constant input power, enabling constant laser intensity throughout the experiments. The spray voltage was varied from 1 to 5 kV depending on the analyte.

The capillary and tube lens voltages were set to  $\pm 45$  and  $\pm 100$  V for positive and negative modes, respectively. The capillary temperature was  $250^\circ\text{C}$ , and the sheath gas pressure was set to zero. The solvent or the analyte solution was continuously supplied to the paper through a fused silica capillary ( $300 \mu\text{m}$  outer diameter,  $100 \mu\text{m}$  inner diameter), connected to a  $500 \mu\text{L}$  Hamilton gas-tight syringe, using a syringe pump. The solution infusion rate was optimized by trial and error to be  $8 \mu\text{L}/\text{min}$  for all our experiments. Methanol, toluene, and a mixture of these two solvents were used as solvents for experiments such as in situ dehydrogenation, ionization of  $\text{C}_{60}$ , and ionization of polycyclic aromatic hydrocarbons.

**Synthesis of Au NPs.** Citrate protected Au NPs were synthesized by the reduction of  $\text{HAuCl}_4 \cdot 3\text{H}_2\text{O}$  with trisodium

citrate using the Turkevich method.<sup>18</sup> About 10 mL of an aqueous solution of  $5 \text{ mM HAuCl}_4 \cdot 3\text{H}_2\text{O}$  was taken and diluted with 180 mL of distilled water followed by heating until it started boiling. An aqueous solution of trisodium citrate (10 mL, 0.5%) was added to it and then heated again until the solution become wine red in color. The solution was cooled and used directly as the catalyst for in situ monitoring of laser-induced transformations.

**Synthesis of Ag NPs.** The Turkevich method was used for the synthesis of citrate protected Ag NPs.<sup>19</sup> About 40 mg of trisodium citrate was added to a 1 mM aqueous solution of silver nitrate at  $100^\circ\text{C}$ , and the solution was heated until a pale yellow color was observed. The final solution was cooled and used in LAPSI MS.

**Monitoring in Situ Chemical Reactions.** Citrate protected Au NPs and Ag NPs were drop cast over the filter paper and kept for drying under laboratory conditions. It was cut into a triangular shape for LAPSI MS measurements. The spray voltage was set to 3 kV during the experiment. In the case of the decarboxylation reaction,<sup>20</sup> an ethanolic solution of MBA ( $50 \mu\text{M}$ ) was used as the reactant. For the dehydrogenation reaction,<sup>21</sup> a  $50 \text{ pM}$  solution of 2,3-dihydro-1H-isoinole in methanol was pushed directly to the paper source, and the mass spectrum was collected in presence and absence of the laser.

**Detection of Adulteration in Coconut Oil.** A mixture of methanol and toluene (1:1 (V/V) ratio) was used to make the solution of both paraffin oil and coconut oil. Pure coconut oil was used as the standard sample. Standard mixtures were made by mixing paraffin oil (1, 5, 10, 20, and 30%) in a solution of coconut oil. Experiments were conducted in two different ways. In the first case, we spotted the oil on the paper source and then eluted it with a solvent mixture to collect the mass spectrum. In the second case, the solution of oil was fed to the paper source continuously. The data were compared with those of the adulterated sample of the oil obtained from the market.

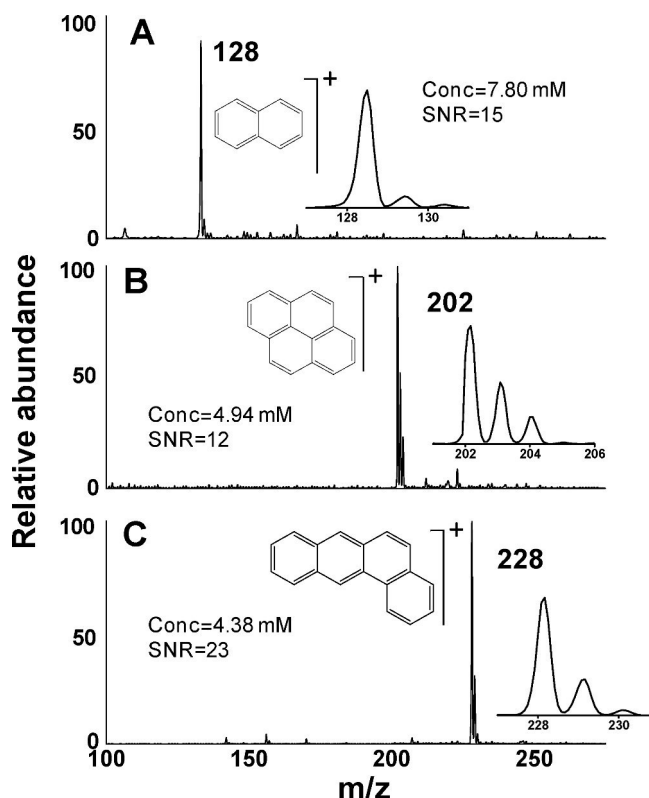
**DFT Calculations.** The structures of all the analytes were optimized at the level of theory consisting the hybrid B3LYP



DFT functional<sup>22,23</sup> and cc-pvtz basis set<sup>24</sup> as implemented in the Gaussian 09 software package.<sup>25</sup> The vibrational frequencies were also calculated to confirm that the optimized structures are on local minima along the potential energy surface. The IP of analytes is calculated with and without application of the electric field by subtracting the energy of neutral analytes from their ionic state. The IPs are calculated by varying the applied electric field from 0 to 500 MV/cm on all three axes ( $x$ ,  $y$ ,  $z$ ) and are plotted. The electric field is modeled by applying an electric dipole field by defining 0.0002 au for 1 MV/cm in all three directions.

## RESULTS AND DISCUSSION

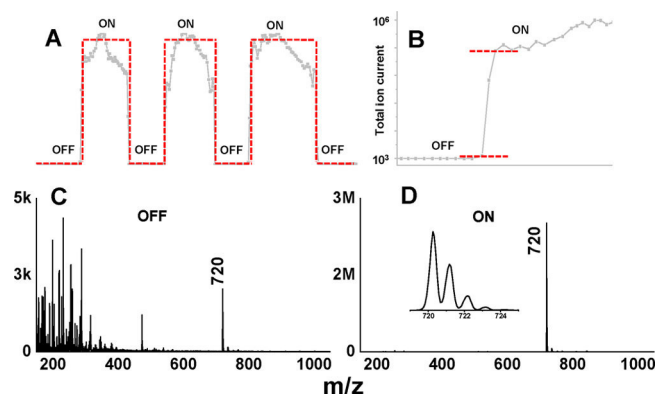
**Characterization of LAPSI MS.** In standard paper spray, molecules like benzene cannot be ionized. However, LAPSI MS



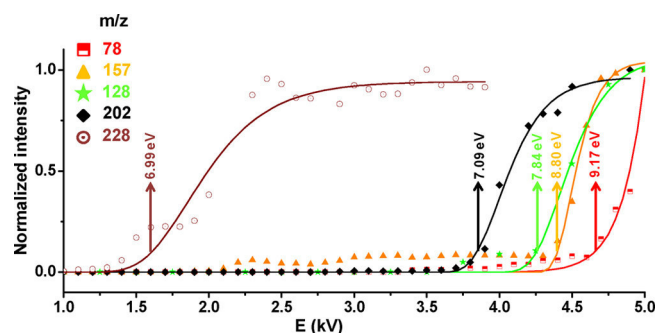
**Figure 2.** LAPSI MS spectra of PAHs: (A) naphthalene, (B) pyrene, and (C) benzantracene in positive ion mode. Isotope distributions of the species are shown.

gives a clean spectrum for benzene with an isotopic distribution (Figure 1). The peak corresponding to benzene disappeared completely in the absence of the laser. This shows that LAPSI MS can be a potent method to ionize hydrocarbons that cannot be ionized easily in standard paper spray conditions.

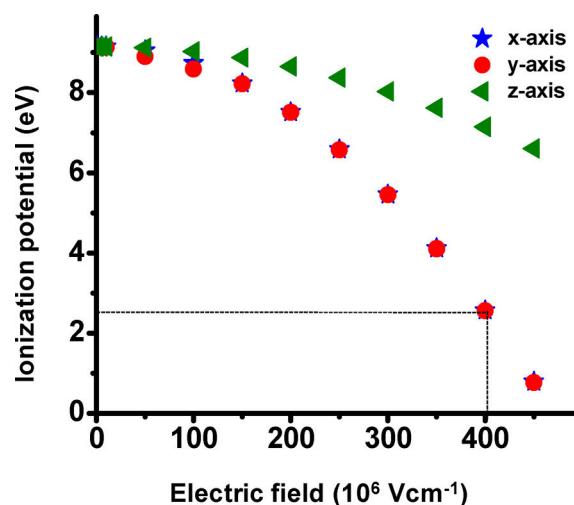
The same methodology can be applied to ionize other aromatic hydrocarbons. Figure 2A–C shows the mass spectra collected for naphthalene, pyrene, and benzantracene, respectively, in positive mode, where the peaks at  $m/z$  128, 202, and 228 represent the molecular cations of the respective analyte. The inset shows the isotopic distributions in all cases. It clearly shows that LAPSI MS has the capability to ionize certain types of molecules in their molecular ion form, and polycyclic aromatic hydrocarbons are one such category.



**Figure 3.** (A,B) Selected ion chronogram for  $m/z$  720 under laser-on/off conditions. (C,D) Mass spectrum of  $C_{60}$  in negative mode in the absence and presence of laser, respectively. Inset in D shows the isotopic distribution of  $C_{60}$ . Compare the intensities of C and D (5k vs 3M) or ( $5 \times 10^3$  vs  $3 \times 10^6$ ).



**Figure 4.** Voltage dependence in the ion intensity of benzene ( $m/z$  78), bromobenzene ( $m/z$  157), naphthalene ( $m/z$  128), pyrene ( $m/z$  202), and benzantracene ( $m/z$  228). Arrows indicate the IPs of the analytes measured.



**Figure 5.** Calculated IPs of benzene in the presence of high electric fields along  $x$ ,  $y$ , and  $z$  directions. Ionization threshold at 2.3 eV is marked.

The effect of laser-induced enhancement in ionization is dramatic in the case of  $C_{60}$ . Figure 3 illustrates  $10^3$  fold enhancement in the molecular ion intensity of  $C_{60}$  in the presence of laser. The laser was switched on and off in a periodic fashion approximately at the same time interval. The

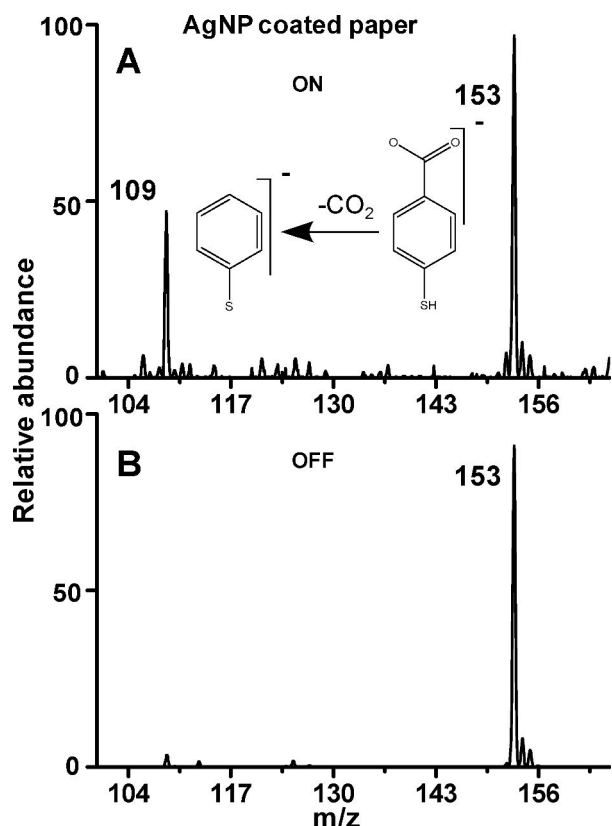


Figure 6. In situ monitoring of decarboxylation reaction on Ag-NP-coated paper in (A) presence and (B) absence of laser.

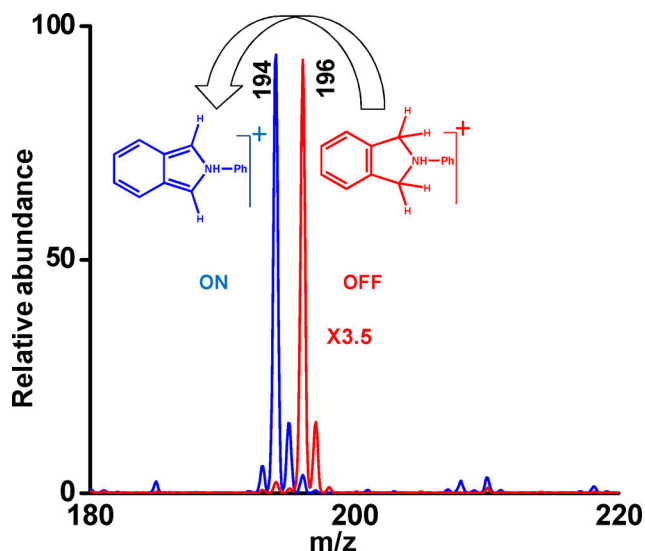


Figure 7. Mass spectrum collected for the dehydrogenation reaction of 3-dihydro-1H-isoindole.

chronogram in Figure 3A is a selected ion chronogram for the peak at  $m/z$  720 (molecular anion of  $C_{60}$ ). It clearly reflects the enhancement of the  $C_{60}$  signal intensity in the presence of laser. Figure 3C,D allows us to compare the mass spectrum taken for  $C_{60}$  (1 mg/mL or 1.39 mM) in laser-off and laser-on conditions. The intensity of the molecular ion is so high that we cannot see any background in this case. These results indicate that the LAPSI MS method works well both in positive and negative ion modes. Concerning the limit of detection of

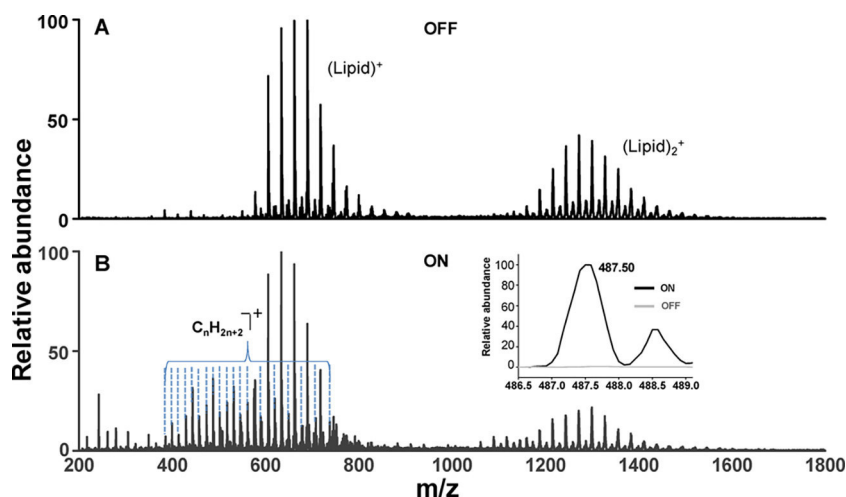
this ionization, we note that the method can detect analytes at a concentration of 1.04 nM taking  $C_{60}$  as an example. Quantification was possible as demonstrated from real samples, and this will be discussed later. We note that quantitative analysis of  $C_{60}$  was possible in the laser-off condition also (Figure S7).

LAPSI MS is an ambient ionization technique involving a low power laser along with a high voltage of the standard paper spray method. The mechanism of ionization is different from the usual laser desorption ionization techniques where a high energy laser is used directly to produce ions such as in matrix assisted laser desorption ionization (MALDI),<sup>26</sup> laser desorption/ionization (LDI),<sup>27</sup> or techniques involving a laser and electrospray, such as electrospray assisted laser desorption ionization (ELDI)<sup>28</sup> and laser ablation electrospray ionization (LAESI).<sup>29</sup> It has also been shown that a UV pulsed laser produces soft ionization during DESI imaging due to the solvent cage effect.<sup>30</sup> In order to understand the mechanism of the observed ionization event, ion yield was measured from the selected ion chronogram of various analytes with increasing electric field. Plot of normalized intensity vs applied potential shown in Figure 4 proves the direct correlation between ionization potential (IP) and applied voltage.

The field assisted photo ionization can be explained with the example of benzene. With a 532 nm laser, the available photon energy is 2.33 eV. Therefore, without the assistance of an electric field, the photon energy is inadequate to cause ionization, as the IP of benzene is 9.17 eV. For an applied potential of 4.8 kV, which can be termed as threshold potential, the benzene molecules feel an electric field of more than  $10^7$  V  $cm^{-1}$  at the sharp tip of the triangular paper.<sup>31</sup> This is due to the fact that the molecules are trapped in between the fibers of the paper. Figure S1 shows a scanning electron microscopy image (SEM) of the triangularly cut paper. Where we can see that the diameter of the fibers at the tip of the paper is in the range of 10 to 20  $\mu m$ , which produces a sufficient electric field for ionization. This electric field causes a distortion of the ground state to a large extent, which brings down the ionization potential to 2.33 eV. Depending on the  $\pi$  system of the molecule, the threshold ionization voltage varies. From Figure 4, it shows that the threshold ionization voltage decreases with increasing  $\pi$  electron density in the molecule. In the case of benzene, the threshold voltage is around 4.8 kV, and at the same time, benzantracene needs only around 2.5 kV to start ionization.

Density functional theory (DFT) was useful in understanding the change in IP of the analytes. Field dependent IP was calculated using different methods.<sup>32,33</sup> Herein, the field dependent IP has been calculated at B3LYP/cc-pVDZ level of theory. Figure S2A–E shows the energy optimized structures for benzene, bromobenzene, naphthalene, pyrene, and benzantracene and their orientations with respect to the applied electric fields. Figures 5 and S3A–D show the IPs for all the analytes in the presence of electric fields ranging from 0 to 500 MV/cm along all the three axes. Due to the high IP of benzene (9.17 eV, calculated at zero field), it required a larger electric field for ionization. In general, for all the molecules, the influence of electric field on the IP along the  $z$  axis is less in comparison to other axes. This may be because the molecules are planar, and the field is considered normal to that plane.

Although IP at low electric fields (up to 100 MV/cm) differs slightly along the  $x$  and  $y$  axes for benzene, the calculated IPs are invariant at higher electric fields as shown in Figure 5, and it



**Figure 8.** Mass spectrum of coconut oil, sold in local market recorded in (A) absence and (B) presence of the laser. A specific region is expanded in the inset to show the difference.

is attributed to the high molecular symmetry ( $D_{6h}$ ) of benzene. When the field reaches 408 MV/cm, the IP is reduced to 2.3 eV along both the axes. Hence, benzene exhibits ionization when the laser is applied at this electric field. In support to the speculated mechanism, other analytes studied also follow a similar behavior. Figure S3 shows a clear decrease in the threshold ionization voltage with increasing electron density in the system.

Control experiments were performed to check the importance of the laser in LAPSI MS. Figure S4 shows that there is no ionization in the absence of laser even up to 5 kV of spray voltage for benzantracene and bromobenzene. However, ionization occurs in the presence of laser. Figure S4 also shows comparison of LAPSI with ESI and standard PSI using benzantracene as the analyte (all the parameters were the same in all cases). ESI as well as standard PSI do not show a peak at  $m/z$  228 due to benzantracene, while LAPSI shows an intense signal. Hence, both ESI and PSI are inadequate to detect the molecule. This result clearly indicates that the ionization mechanism of LAPSI MS is distinctly different from that of ESI and also from that of field enhanced ionization of PSI.<sup>31</sup>

We speculate that the enhanced ionization of  $C_{60}$  in the negative ion mode follows a one electron capture mechanism. The ionization involves solvent ionization first followed by capture of the released electron by the un-ionized  $C_{60}$  molecule. Figure S5 shows that the enhancement in signal intensity in the case of  $C_{60}$  in the negative ion mode equals approximately the intensity enhancement for toluene in the positive ion mode, in the presence of laser. These results support the speculated mechanism of electron capture by  $C_{60}$ . For further confirmation of the mechanism, we have taken  $C_{60}$  in two different solvents, dichloromethane (DCM) and chloroform, which are unresponsive to LAPSI MS in the studied potential range. Figure S6B,C presents the results where we can see from the selected ion chronogram that the intensity of  $m/z$  720 remains constant during the laser-on and -off conditions in both DCM and chloroform but was increased in the case of toluene (Figure S6A). This confirms the mechanism. While enhancement was detected for  $C_{60}^-$ , a similar effect has not seen for analytes forming positive ions. This may require the use of a proper electron capturing agent.

### Monitoring an in Situ Photochemical Reactions by

**LAPSI MS.** LAPSI MS provides extra advantages, as it involves irradiation of a laser on the paper, which allows one to monitor photochemical reactions. Figure 6 presents decarboxylation of *p*-MBA over Ag nanoparticle-coated paper. During the laser-off condition, the detected mass peak at  $m/z$  153 corresponds to *p*-MBA [ $M - H$ ] in the negative ion mode over Ag NP-coated paper (Figure 6B). But when the laser was turned on, a peak at  $m/z$  109, which corresponds to the decarboxylated product of *p*-MBA appeared (Figure 6A). A similar result was seen in the case of Au NP-coated paper (Figure S8).

We have also performed a dehydrogenation reaction on 2,3-dihydro-1*H*-isoindole in the presence of the laser. Figure 7 shows the mass spectrum of the reaction during laser-on and -off conditions. The peak at  $m/z$  196 is the molecular ion of 2,3-dihydro-1*H*-isoindole in the positive ion mode during the laser-off condition. When the laser was turned on, the molecule loses two hydrogens to get aromatized, and the product peak at  $m/z$  194 was formed.

### Detection of Hydrocarbons as Adulterants in Coconut Oil by LAPSI MS.

In order to use this methodology in an analytical context, we chose to study the adulteration of vegetable oils by mineral oils, which is a common problem in many countries. As shown in Figure 8, LAPSI MS was able to detect the presence of paraffin oil in commonly sold coconut oil, purchased from the market. It is important to note that paraffin oil is undetectable in conventional paper spray or by electrospray ionization. By preparing a standard sample and correlating the intensity of the selected ion at  $m/z$  487.50 (which corresponds to the average mass of species,  $C_{33}H_{59}O_2^+$ ,  $C_{34}H_{63}O^+$ , and  $C_{35}H_{67}^+$  (Figure S9), which are present in the mass spectrum of paraffin oil<sup>34</sup>), we found that the extent of contamination is about 10%. Figure S10 provides the chronogram and the mass spectrum of pure paraffin oil by LAPSI MS. The envelope of mass peaks in the spectrum correspond to the hydrocarbons present in the paraffin oil. Figure S11 represents the mass spectrum taken for pure coconut oil, where the first bunch of mass peaks corresponds to the lipids present in the coconut oil. The next bunch of lipids are the dimers of the same. In this range, upon application of laser, no additional peak was observed.



## CONCLUSIONS

In conclusion, we have introduced a new form of paper spray mass spectrometry called laser assisted paper spray ionization mass spectrometry (LAPSI MS), useful for the detection of saturated and unsaturated hydrocarbons, by including a simple  $532 \pm 10$  nm,  $\leq 10$  mW green pointer laser to it. This method extends the scope of ambient ionization. We show that the photoionization is field assisted from various control experiments. Solvent-induced ionization enhancement of  $C_{60}$  has also been demonstrated. We show the capability of the system to monitor some of the photoinduced transformations in situ. We hope that this analytical methodology will be useful for the easy detection of analytes in diverse situations. As ionization is photoassisted, use of other light sources is possible by varying the threshold potential used for ionization.

## ASSOCIATED CONTENT

### Supporting Information

The Supporting Information is available free of charge on the ACS Publications website at DOI: 10.1021/acs.analchem.7b05213.

SEM of the paper, details of DFT calculations, control experiments, mass spectra of pure paraffin, coconut oil, and a standard mixture of the two (PDF)

## AUTHOR INFORMATION

### Corresponding Author

\*E-mail: [pradeep@iitm.ac.in](mailto:pradeep@iitm.ac.in); Phone: +91-44-22574208; Fax: +91-44-2257 0509/0545.

### ORCID

Thalappil Pradeep: 0000-0003-3174-534X

### Author Contributions

<sup>†</sup>P.B. and D.S. contributed equally.

### Notes

The authors declare no competing financial interest.

## ACKNOWLEDGMENTS

The authors thank the Department of Science and Technology, Government of India, for equipment support through the Nano Mission. P.B. and G.P. acknowledge IIT Madras for providing Institute Doctoral and Postdoctoral fellowships. D.S. thanks UGC for a fellowship.

## REFERENCES

- (1) Yamashita, M.; Fenn, J. B. *J. Phys. Chem.* **1984**, *88*, 4451–4459.
- (2) Takats, Z.; Wiseman, J. M.; Gologan, B.; Cooks, R. G. *Science (Washington, DC, U. S.)* **2004**, *306*, 471–473.
- (3) Chen, H.; Talaty, N. N.; Takats, Z.; Cooks, R. G. *Anal. Chem.* **2005**, *77*, 6915–6927.
- (4) Cotte-Rodriguez, I.; Takats, Z.; Talaty, N.; Chen, H.; Cooks, R. G. *Anal. Chem.* **2005**, *77*, 6755–6764.
- (5) Harper, J. D.; Charipar, N. A.; Mulligan, C. C.; Zhang, X.; Cooks, R. G.; Ouyang, Z. *Anal. Chem. (Washington, DC, U. S.)* **2008**, *80*, 9097–9104.
- (6) Wang, H.; Liu, J.; Cooks, R. G.; Ouyang, Z. *Angew. Chem., Int. Ed.* **2010**, *49*, 877–880 S877/871-S877/877.
- (7) Liu, J.; Wang, H.; Manicke, N. E.; Lin, J.-M.; Cooks, R. G.; Ouyang, Z. *Anal. Chem. (Washington, DC, U. S.)* **2010**, *82*, 2463–2471.
- (8) Espy, R. D.; Teunissen, S. F.; Manicke, N. E.; Ren, Y.; Ouyang, Z.; van Asten, A.; Cooks, R. G. *Anal. Chem. (Washington, DC, U. S.)* **2014**, *86*, 7712–7718.
- (9) Yannell, K. E.; Kesely, K. R.; Chien, H. D.; Kissinger, C. B.; Cooks, R. G. *Anal. Bioanal. Chem.* **2017**, *409*, 121–131.
- (10) Domingos, E.; de Carvalho, T. C.; Pereira, I.; Vasconcelos, G. A.; Thompson, C. J.; Augusti, R.; Rodrigues, R. R. T.; Tose, L. V.; Santos, H.; Araujo, J. R.; Vaz, B. G.; Romao, W. *Anal. Methods* **2017**, *9*, 4400–4409.
- (11) Wang, Q.; Zheng, Y.; Zhang, X.; Han, X.; Wang, T.; Zhang, Z. *Analyst (Cambridge, U. K.)* **2015**, *140*, 8048–8056.
- (12) Reeber, S. L.; Gadi, S.; Huang, S.-B.; Glish, G. L. *Anal. Methods* **2015**, *7*, 9808–9816.
- (13) Banerjee, S.; Basheer, C.; Zare, R. N. *Angew. Chem., Int. Ed.* **2016**, *55*, 12807–12811.
- (14) Sarkar, D.; Sen Gupta, S.; Narayanan, R.; Pradeep, T. *J. Am. Soc. Mass Spectrom.* **2014**, *25*, 380–387.
- (15) Zhang, N.; Li, Y.; Zhou, Y.; Hou, J.; He, Q.; Hu, X.-G.; Jia, Y.-M.; Yu, C.-Y.; Nie, Z. *Anal. Methods* **2013**, *5*, 2455–2460.
- (16) Sarkar, D.; Srimany, A.; Pradeep, T. *Analyst (Cambridge, U. K.)* **2012**, *137*, 4559–4563.
- (17) Jjunju, F. P. M.; Badu-Tawiah, A. K.; Li, A.; Soparawalla, S.; Roqan, I. S.; Cooks, R. G. *Int. J. Mass Spectrom.* **2013**, *345–347*, 80–88.
- (18) Kimling, J.; Maier, M.; Okenve, B.; Kotaidis, V.; Ballot, H.; Plech, A. J. *J. Phys. Chem. B* **2006**, *110*, 15700–15707.
- (19) Turkevich, J.; Stevenson, P. C.; Hillier, J. *Discuss. Faraday Soc.* **1951**, *11*, 55–75.
- (20) Chakraborty, I.; Som, A.; Adit Maark, T.; Mondal, B.; Sarkar, D.; Pradeep, T. *J. Phys. Chem. C* **2016**, *120*, 15471–15479.
- (21) Tsai, H.-H. G.; Chung, M.-W.; Chou, Y.-K.; Hou, D.-R. *J. Phys. Chem. A* **2008**, *112*, 5278–5285.
- (22) Becke, A. D. *J. Chem. Phys.* **1993**, *98*, 5648–5652.
- (23) Lee, C.; Yang, W.; Parr, R. G. *Phys. Rev. B: Condens. Matter Mater. Phys.* **1988**, *37*, 785–789.
- (24) Dunning, T. H., Jr. *J. Chem. Phys.* **1989**, *90*, 1007–1023.
- (25) Frisch, M. J.; Trucks, G. W.; Schlegel, H. B.; Scuseria, G. E.; Robb, M. A.; Cheeseman, J. R.; Scalmani, G.; Barone, V.; Mennucci, B.; Petersson, G. A.; Nakatsuji, H.; Caricato, M.; Li, X.; Hratchian, H. P.; Izmaylov, A. F.; Bloino, J.; Zheng, G.; Sonnenberg, J. L.; Hada, M.; Ehara, M.; Toyota, K.; Fukuda, R.; Hasegawa, J.; Ishida, M.; Nakajima, T.; Honda, Y.; Kitao, O.; Nakai, H.; Vreven, T.; Montgomery, J. A., Jr.; Peralta, J. E.; Ogliaro, F.; Bearpark, M.; Heyd, J. J.; Brothers, E.; Kudin, K. N.; Staroverov, V. N.; Kobayashi, R.; Normand, J.; Raghavachari, K.; Rendell, A.; Burant, J. C.; Iyengar, S. S.; Tomasi, J.; Cossi, M.; Rega, N.; Millam, J. M.; Klene, M.; Knox, J. E.; Cross, J. B.; Bakken, V.; Adamo, C.; Jaramillo, J.; Gomperts, R.; Stratmann, R. E.; Yazyev, O.; Austin, A. J.; Cammi, R.; Pomelli, C.; Ochterski, J. W.; Martin, R. L.; Morokuma, K.; Zakrzewski, V. G.; Voth, G. A.; Salvador, P.; Dannenberg, J. J.; Dapprich, S.; Daniels, A. D.; Farkas, O.; Foresman, J. B.; Ortiz, J. V.; Cioslowski, J.; Fox, D. J. *Gaussian 09, Revision C.01*; Gaussian, Inc.: Wallingford, CT, 2009.
- (26) Hillenkamp, F.; Karas, M.; Beavis, R. C.; Chait, B. T. *Anal. Chem.* **1991**, *63*, 1193A–1203A.
- (27) Vidova, V.; Novak, P.; Strohalm, M.; Pol, J.; Havlicek, V.; Volny, M. *Anal. Chem. (Washington, DC, U. S.)* **2010**, *82*, 4994–4997.
- (28) Huang, M.-Z.; Hsu, H.-J.; Lee, J.-Y.; Jeng, J.; Shiea, J. J. *Proteome Res.* **2006**, *5*, 1107–1116.
- (29) Nemes, P.; Vertes, A. *Anal. Chem. (Washington, DC, U. S.)* **2007**, *79*, 8098–8106.
- (30) Lee, J. K.; Jansson, E. T.; Nam, H. G.; Zare, R. N. *Anal. Chem. (Washington, DC, U. S.)* **2016**, *88*, 5453–5461.
- (31) Espy, R. D.; Muliadi, A. R.; Ouyang, Z.; Cooks, R. G. *Int. J. Mass Spectrom.* **2012**, *325–327*, 167–171.
- (32) Deleuze, M. S.; Claes, L.; Kryachko, E. S.; Francois, J. P. *J. Chem. Phys.* **2003**, *119*, 3106–3119.
- (33) Davari, N.; Åstrand, P. O.; Unge, M.; Lundgaard, L. E.; Linhjell, D. *AIP Adv.* **2014**, *4*, 037117.
- (34) Tose, L. V.; Cardoso, F. M. R.; Fleming, F. P.; Vicente, M. A.; Silva, S. R. C.; Aquije, G. M. F. V.; Vaz, B. G.; Romao, W. *Fuel* **2015**, *153*, 346–354.

# Supporting Information

## Detection of Hydrocarbons by Laser Assisted Paper Spray Ionization Mass Spectrometry (LAPSI MS)

Pallab Basuri<sup>†</sup>, Depanjan Sarkar<sup>†</sup>, Ganesan Paramasivam and Thalappil Pradeep\*

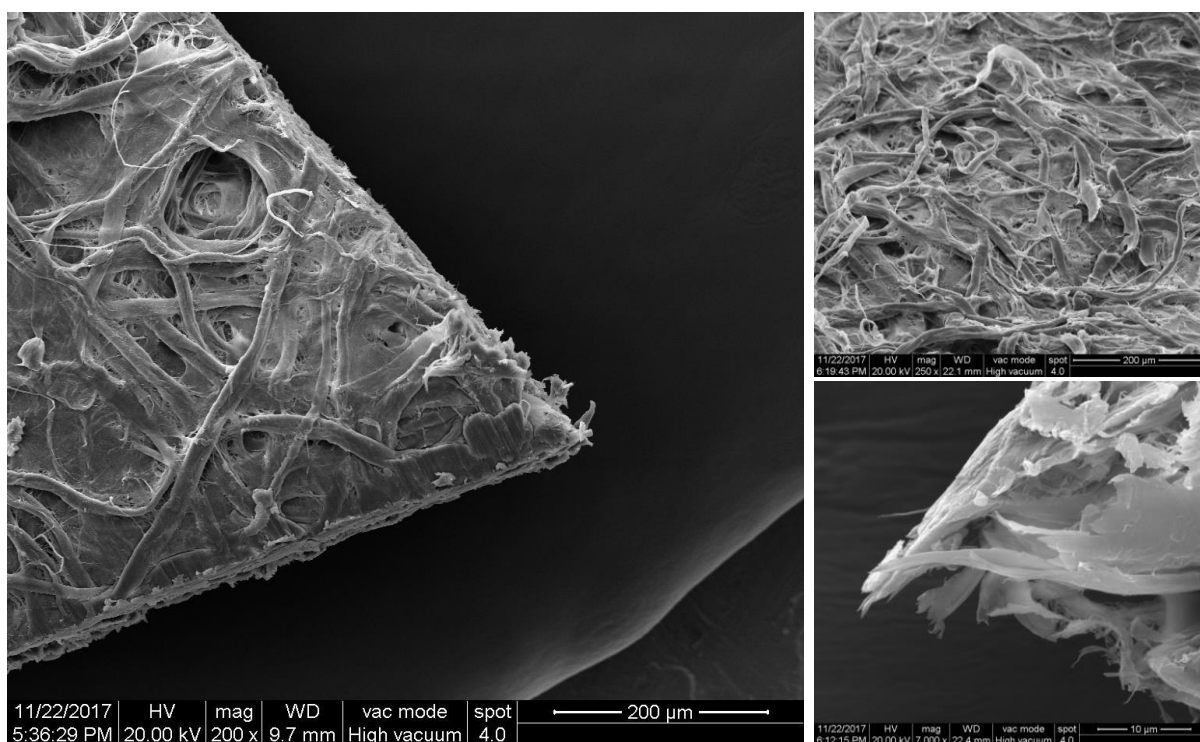
*DST Unit of Nanoscience (DST UNS) and Thematic Unit of Excellence,  
Department of Chemistry, Indian Institute of Technology Madras,  
Chennai 600036, India.*

\*E-mail: [pradeep@iitm.ac.in](mailto:pradeep@iitm.ac.in),

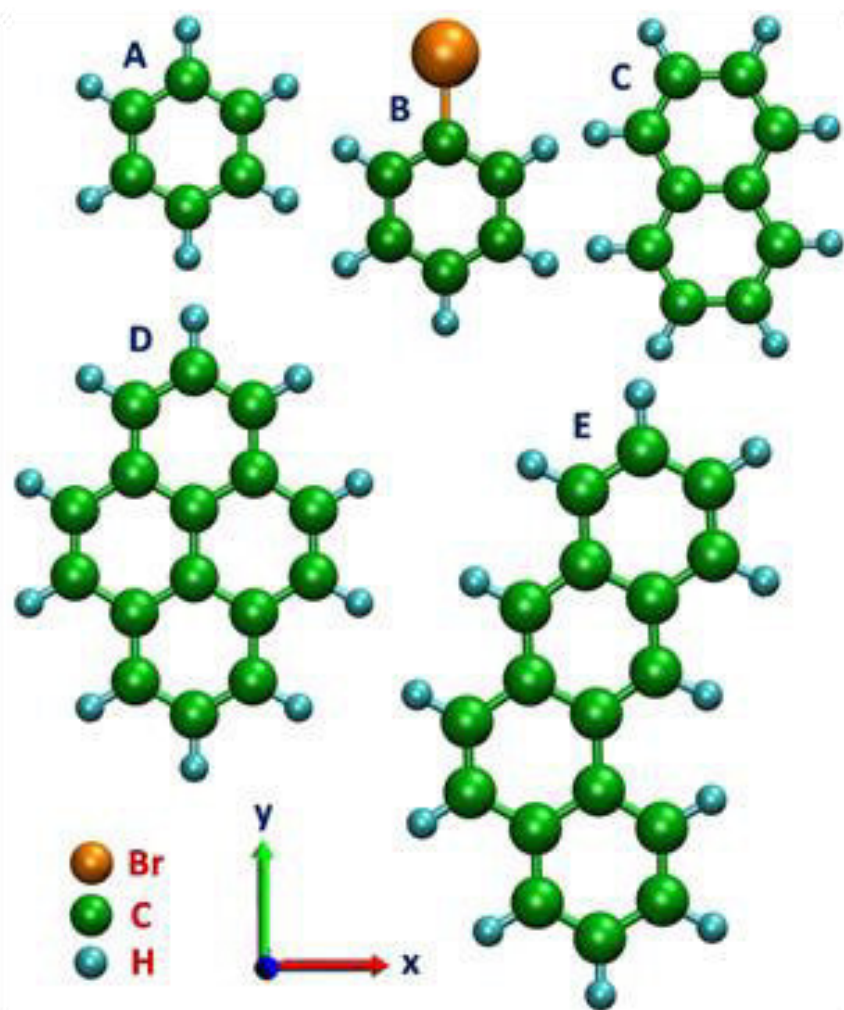
Fax: 91-44-2257 0545

### Content list

Number	Description	Page Number
Figure S1	SEM images of the triangularly cut Whatman 42 filter paper.	2
Figure S2	DFT optimized structures of PAHs and their orientation for the applied electric fields.	3
Figure S3	The IPs of all the considered molecules in the presence of high electric fields.	4
Figure S4	Comparative mass spectrum of benzanthracene (m/z 228) and bromobenzene (m/z 157). A), D) ESI MS, B), E) PS MS and C), F) LAPSI MS.	5
Figure S5	Chromatograms of C <sub>60</sub> in negative ion mode and toluene in positive ion mode are merged together in laser on/off conditions.	6
Figure S6	Selected ion chromatogram of C <sub>60</sub> using A) chloroform, B) dichloromethane (DCM) and C) toluene at laser on/off conditions.	7
Figure S7	Selected ion intensity vs concentration plot of C <sub>60</sub> in the absence of laser. Intensity of the molecular anion at m/z 720 of C <sub>60</sub> varies linearly with its concentration in the solution.	8
Figure S8	Mass spectrum para-marcaptobenzoic acid on AuNPs-coated paper in, A) presence and B) absence of laser.	9
Figure S9	Standard mixture of coconut oil and paraffin oil in different ratio with laser off (left) and on (right) conditions.	10
Figure S10	Chromatogram and mass spectrum of pure paraffin oil in LAPSI MS in positive ion mode.	11
Figure S11	Mass spectrum of pure coconut oil.	12

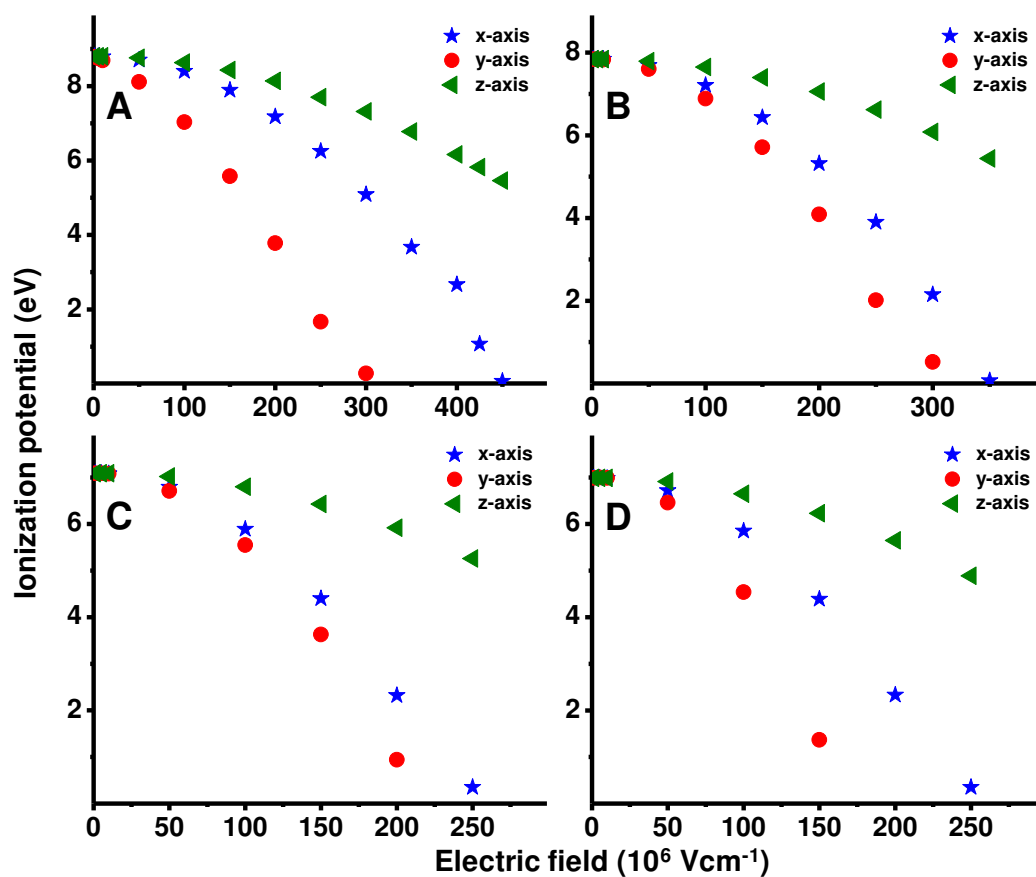


**Figure S1.** SEM images of the Whatman 42 filter paper under different magnifications.

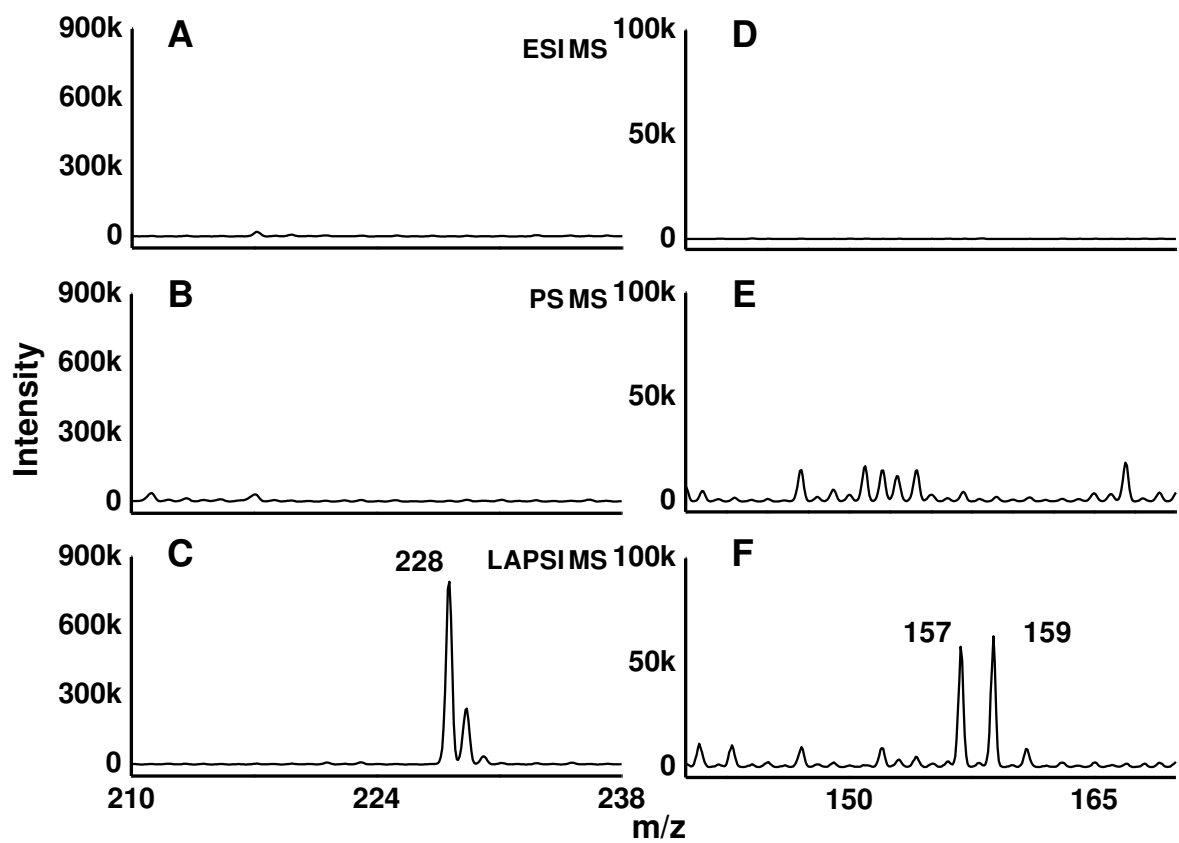


**Figure S2.** The optimized structures for a) benzene, b) bromobenzene, c) naphthalene, d) pyrene and e) benzanthracene and their orientation for the applied electric fields.

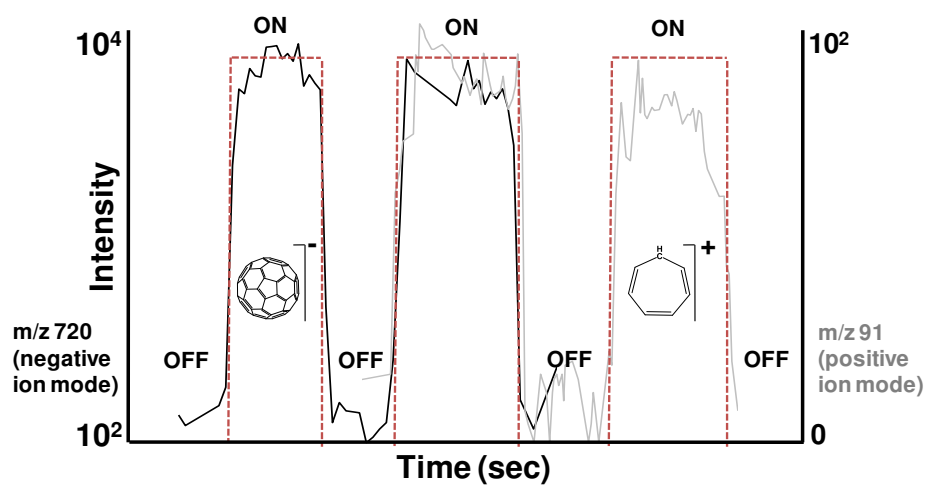




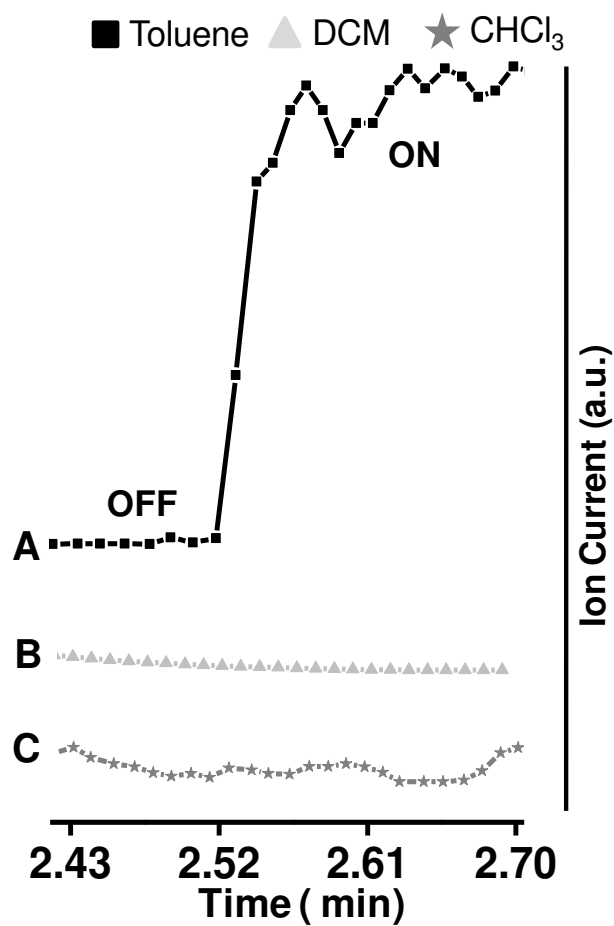
**Figure S3.** Calculated IPs of A) bromobenzene, B) naphthalene, C) pyrene and D) benzanthracene in presence of high electric fields along x, y and z directions.



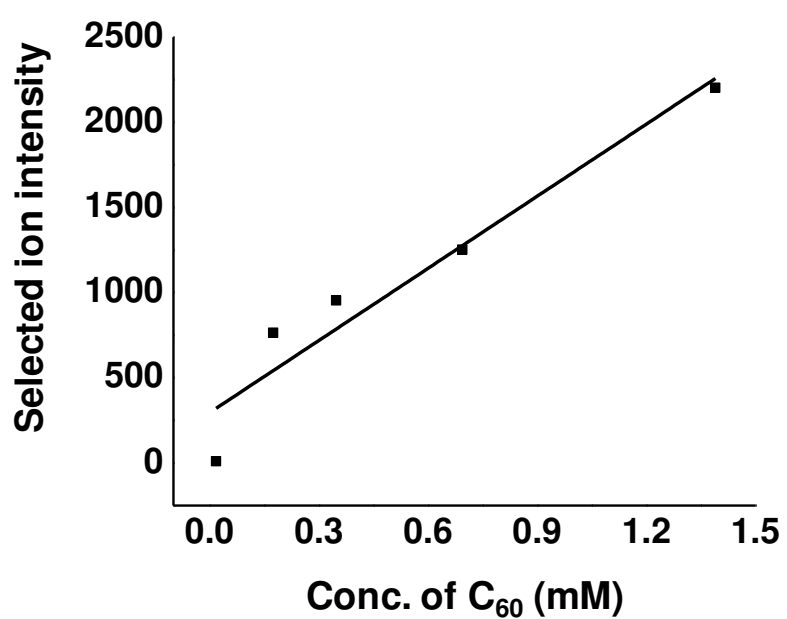
**Figure S4.** Comparative mass spectrum of benzantracene (m/z 228) and bromobenzene (m/z 157). A), D) ESI MS, B), E) PS MS and C), F) LAPSI MS.



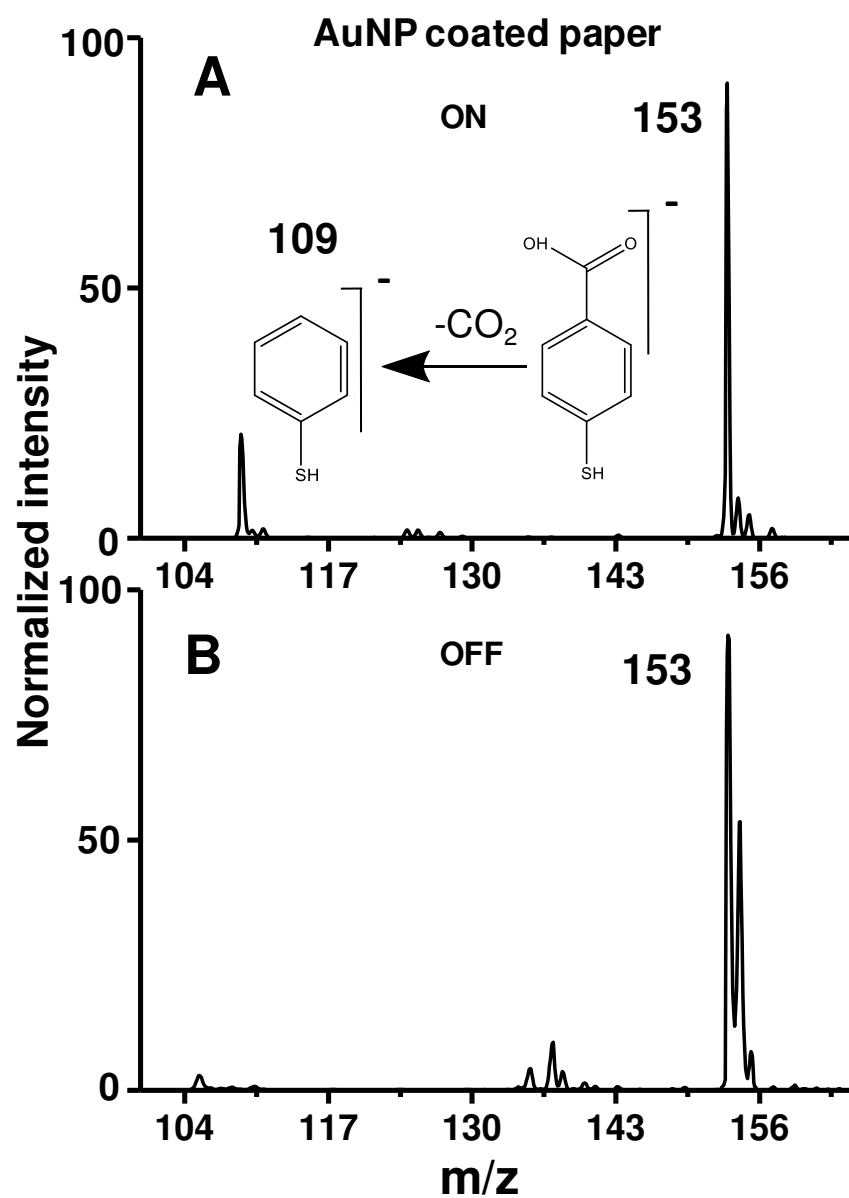
**Figure S5.** Chromatograms of C<sub>60</sub> in negative ion mode and toluene in positive ion mode are merged together in laser on/off conditions.



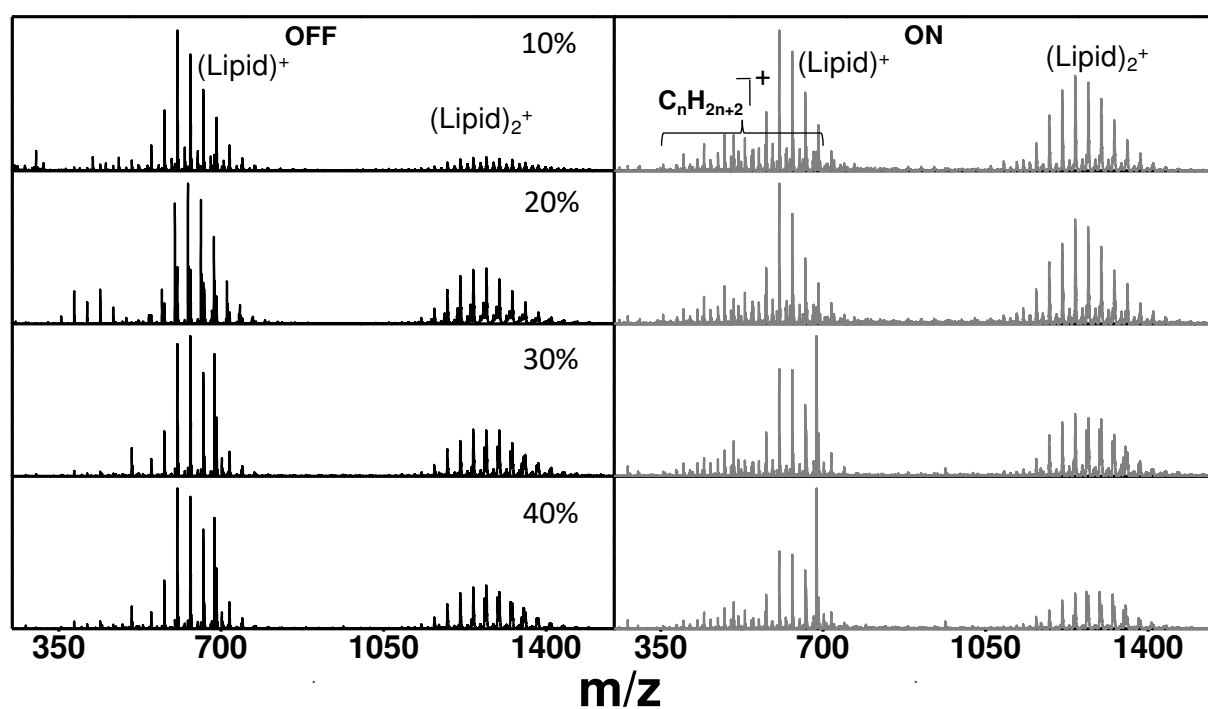
**Figure S6.** Selected ion chromatogram of  $C_{60}$  using A) toluene, B) dichloromethane (DCM) and C) chloroform in laser on/off conditions.



**Figure S7:** Selected ion intensity vs concentration plot of  $C_{60}$  in the absence of laser. Intensity of the molecular anion at  $m/z$  720 of  $C_{60}$  varies linearly with its concentration in the solution.

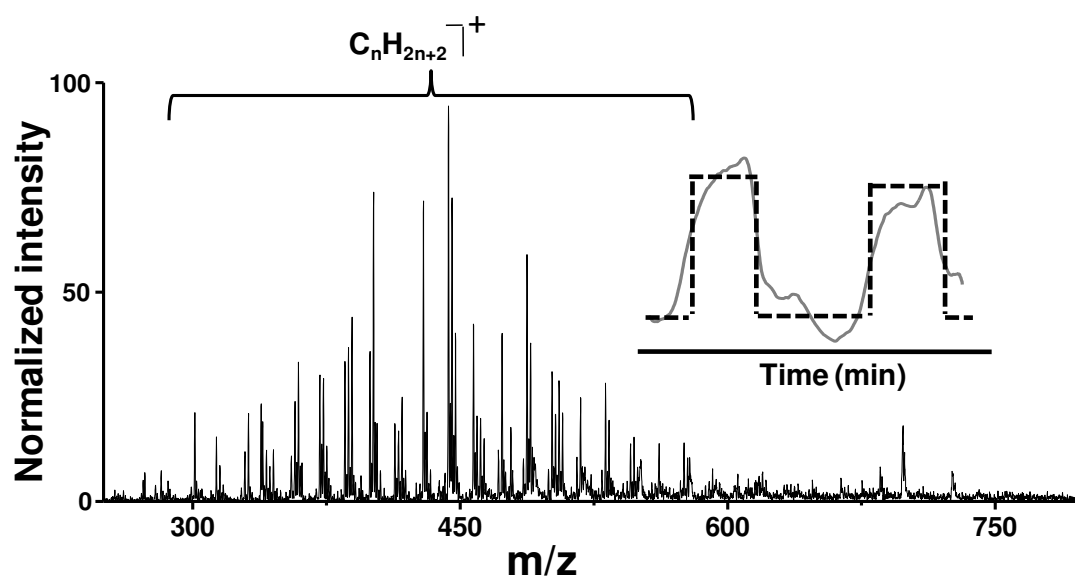


**Figure S8.** Mass spectrum para-mercaptobenzoic acid on AuNPs-coated paper in, A) presence and B) absence of laser. Less intense peaks in the laser off condition are due to background.

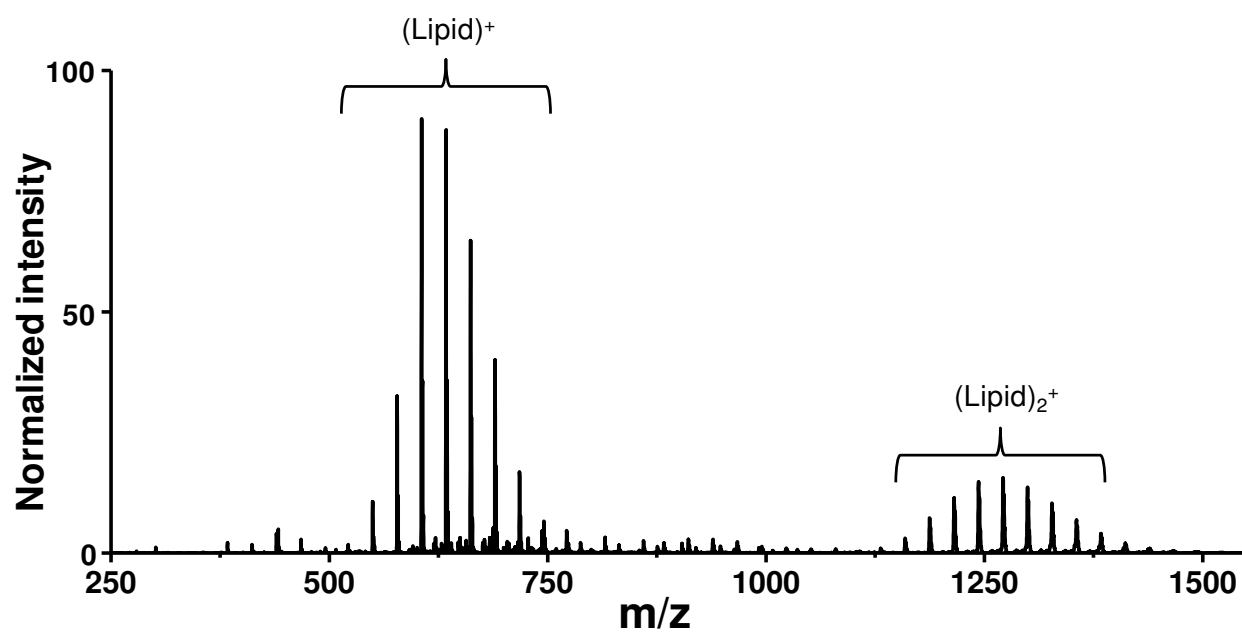


**Figure S9.** Standard mixture of coconut oil and paraffin oil in different ratios with laser off (left) and on (right) conditions.





**Figure S10.** Chromatogram and mass spectrum of pure paraffin oil in LAPSI MS in positive ion mode.



**Figure S11.** Mass spectrum of pure coconut oil.

# Fabrication of a Waterborne Durable Superhydrophobic Material Functioning in Air and under Oil

Avijit Baidya, Sarit Kumar Das, Robin H. A. Ras, and Thalappil Pradeep\*

A fundamental challenge in artificially structured/ chemically modified superhydrophobic surfaces is their poor chemical, mechanical, and structural robustness toward different mechanical abrasions. This limits their application potential in different fields of science and technology. Herein, a waterborne superhydrophobic material composed of clay particles is developed through a one-pot chemical modification in ambient conditions, forming durable micro-nano dual-structured coatings over a range of substrates, without adhesive. This chemical modification inverts the inherent hydrophilic nature of clay particles and provides an excellent superhydrophobic surface having a water contact angle  $>170^\circ$  ( $\pm 2^\circ$ ) and contact angle hysteresis  $<5^\circ$  ( $\pm 2^\circ$ ). The coating shows excellent durability against various induced damages and works efficiently both in air and within oils. The observed property is due to the controlled surface energy obtained by the incorporated chemical functionalities and enhanced surface roughness facilitated by the hydrophobic effect during slow evaporation of water from the coating material. Being a stable water dispersion, it enables large area coatings, thereby minimizing safety and environmental concerns. Use of this material to develop rugged waterproof-paper for paper-based technologies is also demonstrated. As clay is commercially available and economical, it is believed, this scalable organic-solvent-free superhydrophobic material will have a positive impact on various industries.

## 1. Introduction

Designing materials for the preparation of water repellent thin films with robust and durable characteristics has attracted considerable attention over the years because of their wide possible applications in different fields of science and engineering. In this context, superhydrophobic surfaces, having potential uses in self-cleaning,<sup>[1]</sup> drag reduction,<sup>[2]</sup> anti-corrosion,<sup>[3]</sup> anti-icing,<sup>[4]</sup> sensing,<sup>[5]</sup> atmospheric water capture,<sup>[6]</sup> microfluidic devices,<sup>[7]</sup> water-oil separation,<sup>[8]</sup> construction materials,<sup>[9]</sup> etc., are intensely researched upon. Such surfaces not only force water droplets to roll off, but they also keep themselves clean even from viruses and bacteria, thereby preventing biofouling.<sup>[10]</sup> However, designing surfaces of such kind needs both artificial micro/nano-scale structuring and chemical modifications with low surface energy molecules.<sup>[11]</sup> Although various synthetic methodologies have been introduced,<sup>[7,12]</sup> stability, cost, complicated manufacturing processes, and restrictions in large area production limit the use of such surfaces for practical

applications.<sup>[13]</sup> In contrast, coating with chemically modified materials processed by wet chemical methods is affordable and is known as an alternate way to prepare such surfaces in large areas.<sup>[14]</sup> Though use of polymers,<sup>[15]</sup> cellulosic materials,<sup>[16]</sup> clays,<sup>[17]</sup> and oxide nanoparticles<sup>[18]</sup> is well known in this context, in most of the cases, organic solvents are used as a component of the reaction medium,<sup>[18,19]</sup> which pose concerns related to safety, environmental pollution, operational cost, and solvent compatibility of the substrates. In this context, a few reports on the development of aqueous coating materials for water repellent surfaces are known.<sup>[14,17,20]</sup> Recently, a nonfluorinated silane-based coating material having tunable wetting property has been synthesised in a highly acidic condition.<sup>[21]</sup> However, storage of such materials even for a few hours is an issue due to the uncontrollable hydrolysis of silanes in the presence of tiny amounts of water. Thus, there is a need to develop a stable superhydrophobic coating material in water at neutral pH and ambient conditions with affordable materials leading to coatings that overcome the problems outlined earlier.


One of the persistent problems of such chemically functionalised superhydrophobic surfaces is the poor stability and durability of the coating that readily gets abraded, for example,

A. Baidya, Prof. T. Pradeep  
DST Unit of Nanoscience  
Thematic Unit of Excellence  
Department of Chemistry  
Indian Institute of Technology Madras  
Chennai 600036, India  
E-mail: pradeep@iitm.ac.in

A. Baidya, Prof. R. H. A. Ras  
Department of Applied Physics  
Aalto University School of Science  
Puumiehenkuja 2, 02150 Espoo, Finland

A. Baidya, Prof. S. K. Das  
Department of Mechanical Engineering  
Indian Institute of Technology Madras  
Chennai 600036, India

Prof. R. H. A. Ras  
Department of Bioproducts and Biosystems  
Aalto University School of Chemical Engineering  
Kemistintie 1, 02150 Espoo, Finland

 The ORCID identification number(s) for the author(s) of this article can be found under <https://doi.org/10.1002/admi.201701523>.

DOI: 10.1002/admi.201701523

even with the mild touch of tissue paper, leading to permanent loss of the surface property.<sup>[13b,22]</sup> Binding ability of the material with substrates having different surface morphology also affects the durability of the coating. To overcome these problems, although the use of adhesives and presurface modifications has been introduced,<sup>[22a,23]</sup> these methods have their own limitations depending on the nature of the adhesives and the surfaces to be coated. Nevertheless, the instability of such water repelling coatings toward various chemical stresses is still a major disadvantage. In this context, superamphiphobic surfaces, another class of materials, were developed that repel both water and oil.<sup>[24]</sup> The surface energies of these surfaces are so low that they can maintain a thin layer of air between the surface and liquids, which can subsequently result in rolling off of liquid. A few reports on the development of superhydrophobic surfaces (through chemically functionalized coating materials) that function equally well both in air and within oil are known.<sup>[22a,23,25]</sup> However, the use of hazardous organic/non-aqueous solvent systems and instability of the coatings without additives are the major limitations.

Fabrication of durable superhydrophobic fabrics with chemically processed materials is also a challenge despite having huge application potential of such flexible substrates in different paper-based technologies.<sup>[5a,7,26]</sup> Fibrous surface morphology may prevent efficient coating, which results in pinning/sticking of water droplets on uncoated areas. Moreover, being soft and fibrous in structure, water droplets do not acquire enough energy or backward force to bounce off and get trapped within the fibrous microstructure.

In this study, a waterborne superhydrophobic material is developed from a hydrophilic clay particle building block that provides excellently durable superhydrophobic coatings at room temperature over a series of substrates (both soft and hard) without any adhesive. This demonstrates the novelty and possible industrial viability of the methodology. The material is environment friendly, stable, and can be made in large scale for different applications. Incorporated chemical functionalities controlled the surface energy of the material such that the coated substrate functions equally well, both in air and within oil. The coating showed excellent stability and unaltered water repelling property against various mechanical, chemical, and environmental stresses. Being a water-based dispersion, it enables efficient and large area coatings by conventional coating procedures, thereby minimizing environmental impact. Applicability of the material to develop a flexible waterproof paper is also demonstrated.

## 2. Synthesis

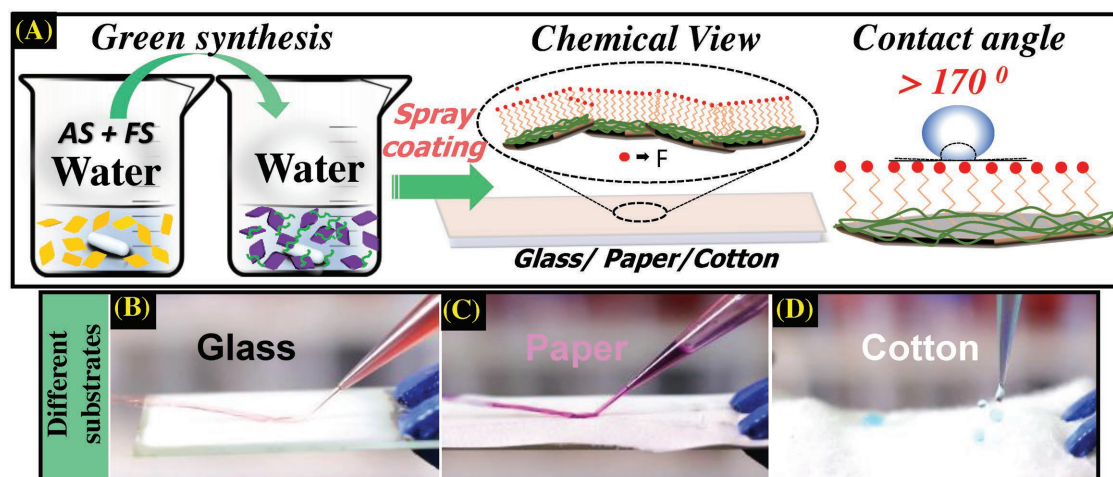
The waterborne superhydrophobic material was synthesised by an easy chemical modification of kaolinite clay at room temperature with two functional silanes. Chemically, these aluminosilicate clay sheets consist of numerous hydroxyl groups on the surface, which are reactive in the well-dispersed condition in water. In the synthetic protocol, water dispersed clay sheets (6 wt%) were mixed with two different functional silanes, 1H,1H,2H,2H-perfluorooctyltriethoxysilane (FS, 2 wt%) and 3-(2-aminoethylamino)propyltrimethoxysilane (AS, 1 wt%), and

kept under vigorous stirring conditions for 6 to 7 h. Whereas silanization reaction in general is very fast in aqueous medium, because of the low solubility of FS in water, at first it gets adsorbed on the clay surface and hydrolyzes slowly in water and gets attached covalently to the clay surface.<sup>[16a]</sup> Thus, a water dispersed functionalized clay composite was obtained and spray coated on different substrates followed by drying at room temperature. Quantitatively, 1 mL of the as-prepared composite solution was mixed with water in 1:1 ratio and sprayed over a glass slide and a paper, having an area of  $75 \times 26 \text{ mm}^2$ . Upon drying at room temperature ( $30^\circ\text{C}$ ), a superhydrophobic film of nearly  $8 \mu\text{m}$  thickness (on a glass surface) was obtained, which shows a high CA  $> 170^\circ (\pm 2^\circ)$  and low CAH  $< 5^\circ (\pm 2^\circ)$  for water. However, to facilitate faster evaporation, the coated substrates were dried in warmer condition ( $45^\circ\text{C}$ ) occasionally, without affecting the properties of the material. Later on, this water-based material was stored at room temperature in the laboratory environment for more than a year without any special precaution.

## 3. Results and Discussion

Figure 1A illustrates the methodology used for the preparation of the superhydrophobic film over various substrates. Briefly, the complete reversal of the hydrophilic property of clay particles was achieved through a chemical functionalization with two different functional silanes, FS and AS, in water at room temperature. Applicability of this waterborne material was tested both with hard and soft substrates such as glass, cotton, and fabrics having different morphologies. In addition to fluoroalkyl functionalization of the clay sheets, the surface has inherent micro and nanostructures, as will be demonstrated later. It was seen that water droplets are spherical on superhydrophobic surfaces (both hard and soft) and bounce easily (Figure 1B–D). Moreover, bouncing off of water droplets even on modified cotton surface (Figure 1D) shows the universal applicability and efficiency of the material. These effects were captured in Video S1 (Supporting Information). Being dispersed in water, functionalized clay sheets sit readily on hydrophilic fibers and get coated efficiently all over the surface of cylindrical fibers by strong capillary action and large surface tension force.<sup>[27]</sup> The extent of water repelling property of the material on fibrous soft surfaces was revealed from the unstable, frictionless movement of water drops on modified paper, demonstrated in Figure S1 and Video S2 (Supporting Information). This can be compared with the lotus leaf effect, a well-known example of the natural superhydrophobic property.

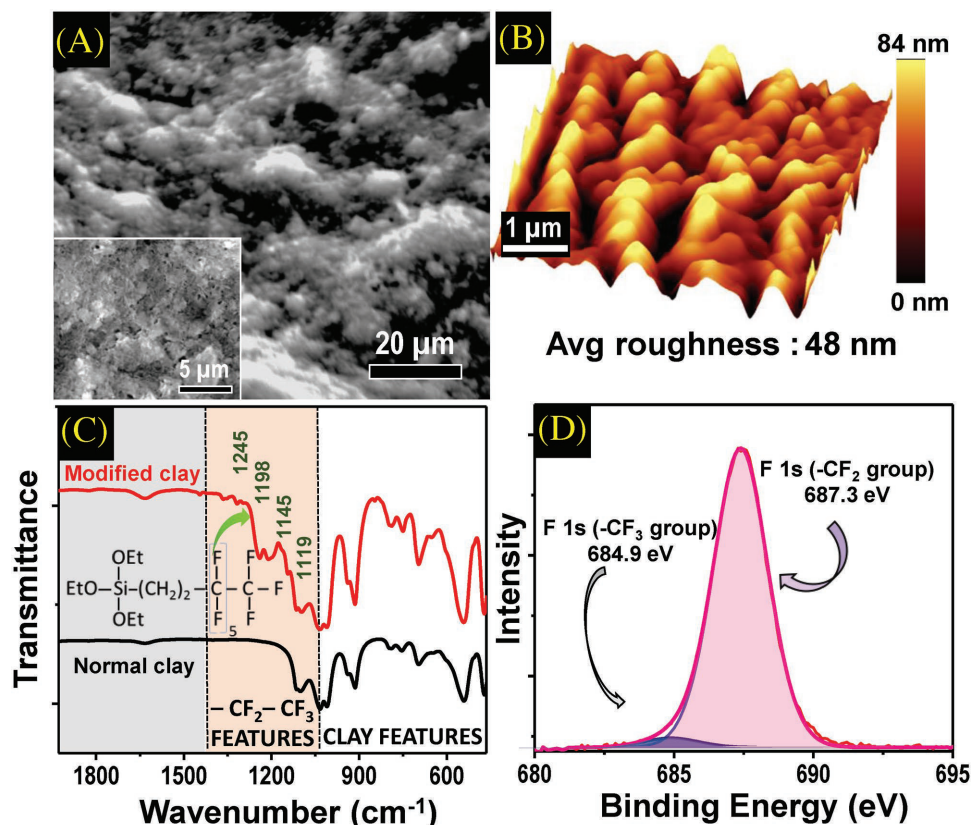
The surface morphology of the modified clay coated thin film (on glass) was imaged by scanning electron microscopy (SEM) with a tilt angle of  $45^\circ$ . The image (Figure 2A) manifests the periodic micrometer-sized features over the surface. Such features were observed throughout the surface and were formed during drying of the material at room temperature. While SEM showed micrometer scale surface structures, atomic force microscopy (AFM) revealed the enhancement of surface roughness in the nanometer regime (Figure 2B) as compared to a normal clay coated thin film (Figure S2, Supporting Information). In the case of a modified clay coated thin film, average surface



**Figure 1.** A) Schematic representation of the waterborne superhydrophobic material (synthesis of the dispersion and the prepared thin film). Continuous jet flow on coated B) glass, C) filter paper, and D) bouncing of water on modified cotton surface.  $\text{KMnO}_4$ ,  $\text{CoCl}_2$ , and  $\text{CuSO}_4$  aqueous solutions were used in (B), (C), and (D), respectively, instead of pure water to add color contrast.

roughness was 48 nm whereas it was 24 nm for the normal clay coated thin film. This enhancement in roughness is related to the hydrophobic effect,<sup>[28]</sup> namely, an interaction between water and low surface energy molecules (here, fluorinated

clay particles) that minimize the interaction energy and make the particles organize during drying of the aqueous coating. Such dual structured surfaces can be compared with nano-pillar or nanogras surfaces as well.<sup>[29]</sup> Figure S3 (Supporting



**Figure 2.** Characterization of the coating. A) SEM image of coated glass substrate showing the uniform and periodic micrometerscale features of the surface. The surface was tilted by 45°. The inset shows the morphology of the same surface at a tilt angle of 0°. B) AFM image shows the nanoscale roughness present on the surface. C) FT-IR of the dried material. Peaks at 1119, 1145, 1198, and 1245  $\text{cm}^{-1}$  (shaded area) indicate the presence of  $\text{-C-F}$  functionalities in the modified clay. D) XPS shows the presence of fluorine in the sample which is coming from FS.

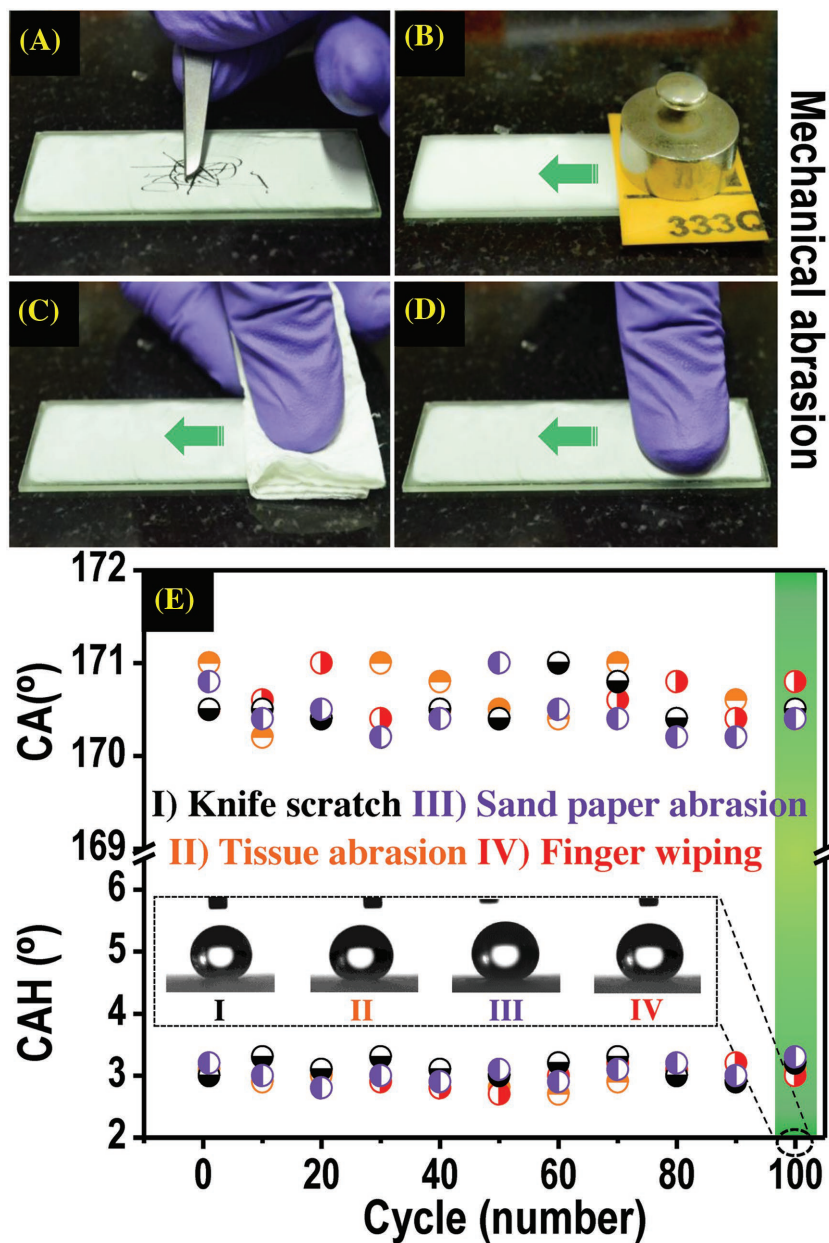


Information) shows a cross-sectional SEM image of the superhydrophobic thin film suggesting a layer-by-layer structure of the coating.

Along with the surface morphology, chemical features of the surface also play an important role in obtaining such extreme water repellent characteristics of the thin films. Infrared (IR) spectroscopy and X-ray photoelectron spectroscopy (XPS) reflect the chemical composition of the coated thin film. Figure 2C shows the IR spectra of unmodified clay and functionalized clay materials. Vibrational features are observed at 1119, 1145, 1198, and 1245  $\text{cm}^{-1}$ , respectively, assigned to the stretching and bending modes of C–F bonds in FS ( $-\text{CF}_2$  and  $-\text{CF}_3$  functionalities). Intense peaks at 687.3 and 684.9 eV in the XPS spectrum correspond to the F1s of  $-\text{CF}_2$  and  $-\text{CF}_3$  groups, respectively, of FS (Figure 2D). Both microscopic and spectroscopic measurements suggested the reasons of superhydrophobicity that are related to the surface roughness as well as the presence of low surface energy molecules.

Stability/durability of the coating is one of the most desired criteria when applications of such surfaces are concerned. In this context, use of additives to improve the strength and stability of superhydrophobic coatings has been reported, which essentially enhances the binding ability of the coating material. In contrast, our material (without any adhesive) with diamino functional groups interlinks the clay sheets and helps to anchor them efficiently over substrates during the evaporation process through spontaneous in situ polymerization. Anchoring induced stability was studied with various artificially induced mechanical stresses. For instance, the coated surface was subjected to hard mechanical stresses such as sandpaper abrasion test with a load of 50 g and knife scratch tests (Figure 3A,B). Although the coating on the surface got damaged to some extent with knife scratch, its superhydrophobic property remained intact (Video S3, Supporting Information). Interestingly, water repellent property was preserved for the sand paper abraded (with a load of 50 g) surface even after multiple abrasion cycles (Video S4, Supporting Information). These reflect the advantage of having multilayer surfaces, because even if the upper layers of the coating get affected, underlying layers can make the water to roll off.<sup>[30]</sup> Durability of the coating was also evaluated by soft mechanical stresses like tissue paper abrasion and finger wiping test (Figure 3C,D). In this case, abraded surfaces were observed to maintain their superhydrophobic property with easy

movement of water streams over them (Videos S5 and S6, Supporting Information). For all the cases, retention of the water repelling nature of the abraded surfaces was evaluated thoroughly with contact angle (CA) and contact angle hysteresis (CAH) measurements after each experiment (Figure 3E) where each experiment consisted of ten complete abrasion cycles of corresponding tests (details are given in the Experimental Section). Consistent values of CA and CAH at an average of

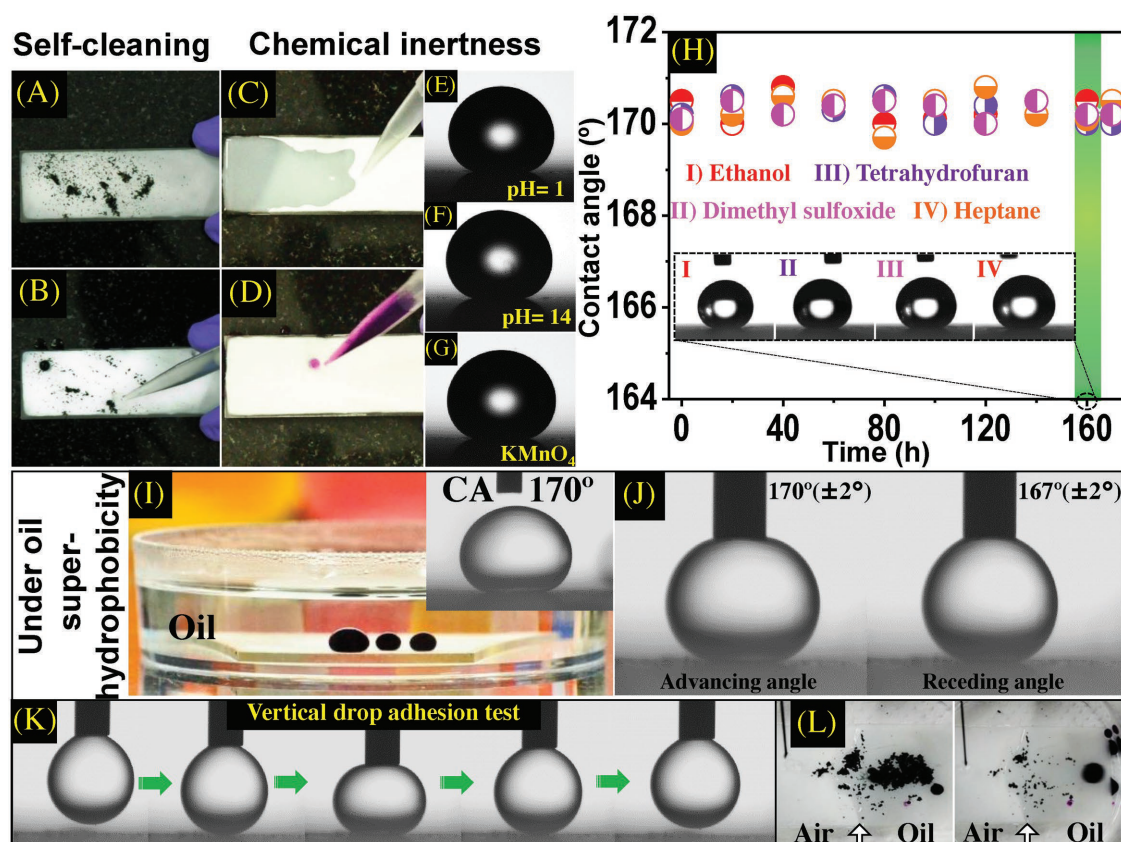


**Figure 3.** Induced hard and soft mechanical damages on spray-coated glass substrates. Hard mechanical damages: A) scratching with a knife and B) sand paper abrasion with 50 g of load. Soft mechanical damages: C) abrasion with tissue paper and D) finger wiping. E) Durability/longevity test with the above-mentioned mechanical tests. Change of CA and CAH of water droplet during the multiple abrasion cycles (of different mechanical tests). In every case, CA and CAH were measured after each experiment, consisting of ten consecutive abrasion cycles. Inset: Photograph showing static contact angle of water on the tested surfaces (after the ninth experiment or 90<sup>th</sup> abrasion cycles).

170° ( $\pm 2^\circ$ ) and 3° ( $\pm 2^\circ$ ), respectively, after each experiment showed the durability of the material against external forces. These mechanically perturbed surfaces were further studied with wettability sensitive vertical drop test (water droplet from the needle was moved vertically and contacted the surface and drawn back) and droplet drag test (water droplet from the needle was dragged over the surface back and forth for 5 cm). Videos S7 and S8 (Supporting Information) show the unchanged wettability of the surfaces after the above-mentioned tests on the mechanically abraded surfaces that can be directly related with CAH of water droplets over these surfaces.

Having low surface energy, the coated glass surface showed self-cleaning property where graphite powder was used as dirt that eventually got washed away with the rolling water droplets (Figure 4A,B and Video S9, Supporting Information). Coated surface (paper, Whatman 44) was also observed to show bacterial resistance when it was exposed to bacterial species (Figure S4, Supporting Information) under favorable growth conditions and nutrients. This was compared with normal

paper where precipitation of bile salts around the uncoated paper indicates the bacterial growth. Chemical robustness of this superhydrophobic surface was tested with various solvents with a wide range of polarities (ethanol, dimethyl sulfoxide, dimethylformamide (DMF), tetrahydrofuran (THF), toluene, hexane, heptane, and *n*-octane). For all the cases, coated surface was observed to retain its initial properties and remain unaffected after cyclic washing with multiple organic solvents, demonstrated in Figure 4C,D and Video S10 (Supporting Information) (ethanol treated surface is demonstrated here). Chemical durability of the material was further tested in detail with various hazardous aqueous solutions. For example, water with pH = 1 and 14 and highly oxidizing  $\text{KMnO}_4$  solutions were used for this. Experiments were done in two ways. First, these solutions were used directly to measure the static and dynamic contact angles of the respective droplets. In every case, the static contact angle was observed in the range of 170° ( $\pm 2^\circ$ ) (Figure 4E–G) with low contact angle hysteresis, below 5° ( $\pm 2^\circ$ ) (Figure S5, Supporting Information). This proves the stability



**Figure 4.** A,B) Self-cleaning property of superhydrophobic material coated glass surface. Iron oxide powder ( $\text{Fe}_2\text{O}_3$ ) was used as the model dirt. C,D) Coated surface retains its water repelling behavior even after artificially induced chemical damages with various organic solvents (ethanol treated surface is demonstrated here). E–G) Static contact angle of water droplets having pH = 1, 14 and oxidizing agent  $\text{KMnO}_4$ . H) Durability/longevity of the coating under extreme hazardous conditions. Surfaces were kept inside various organic solvents having different polarity and the static contact angle of water droplet was measured after taking the surface out from the solvent in a regular time interval for 170 h (details are provided in the Experimental Section). Inset: Photograph showing static contact angle of water on a 160 h oil treated surface. I) The superhydrophobic coating also remained functional inside/under oil (*n*-octane) and forced water droplets to sit as a sphere whereas wetting takes place on a normal surface. Inset: Static contact angle of water droplet on coated glass within the oil (*n*-octane). Extent of under-oil superhydrophobicity. J) CAH measurement and K) vertical drop adhesion test with a water droplet, when the coated surface was immersed in oil (*n*-octane). L) Self-cleaning property of the coated surface at the air–solid–oil interface. A portion of the surface was kept inside oil (*n*-octane, taken as a model long chain hydrocarbon); an inorganic salt (potassium permanganate) was placed over it as a model of dirt. Rolling water droplets removed all the dirt from both the interfaces and made the surface clean.



and chemical inertness of the material. In the second case, the experimental solutions were used to wet the surface (similar to the experiment with organic solvents). However, in all the cases, their droplets bounced and rolled off easily over the surface. Durability of the coating under such chemical stresses was further tested by keeping the surfaces within the solvents for a long time (170 h for each solvent). For each solvent system, the same surface was used repeatedly for the entire experiment. After long incubation time also, surfaces retained their property and kept functioning efficiently. These were seen in the CA values at regular time intervals of 20 h for a duration of 7 d (Figure 4H). To identify the change in wettability of the superhydrophobic coating in detail, the treated (7 d solvent treated) surfaces were also studied by CAH measurements (Figure S6A, Supporting Information), droplet drag and vertical drop experiments that are very sensitive toward surface wettability. Data corresponding to the THF treated surface are shown in Figure S6B (pictorially and graphically) and Video S11 of the Supporting Information.

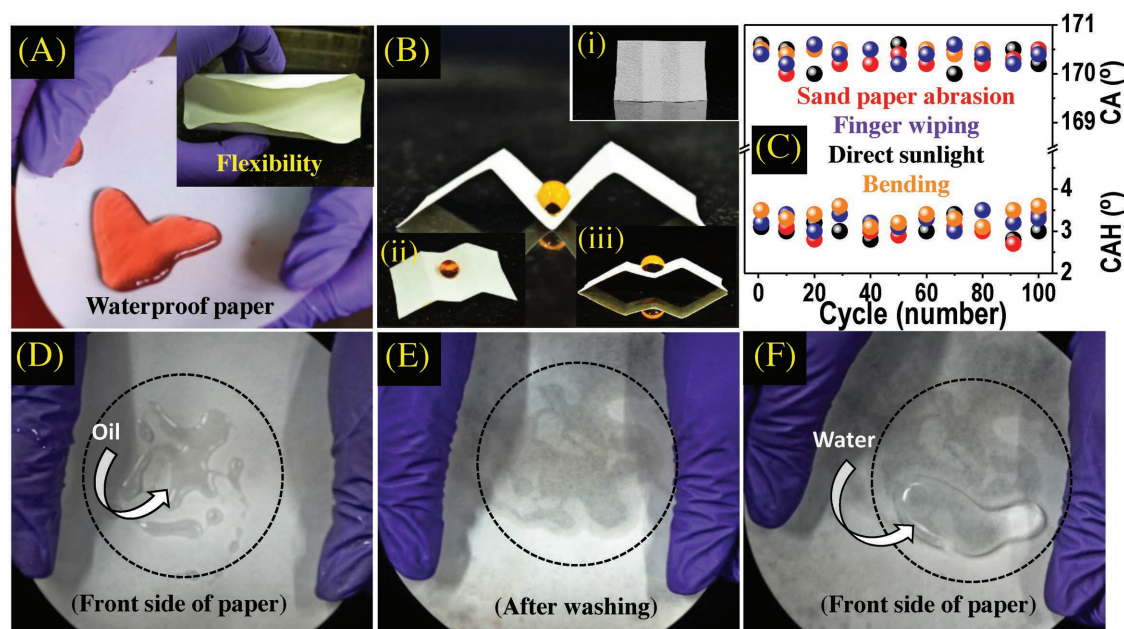
Oils, having low surface tension, easily get into the surface of microstructures and remove the air layer that is essential for superhydrophobicity. Water droplets possess lower interfacial tension inside oils compared to the air–water interface. Both of these enhance the possibility of pinning of water droplets on the surface. However, in our case, the superhydrophobic surface was observed to function also at the oil–solid interface with equal efficiency and maintains high static and dynamic contact angles for water droplets. A similar water repelling phenomenon at the oil–solid interface is well known for slippery liquid-infused porous surface, where low surface tension oils are introduced within a porous matrix.<sup>[31]</sup> In such cases, water droplets sit over these oil-wetted surfaces and remain surrounded by air. Whereas, in the present work, water droplet sits on a superhydrophobic surface and is surrounded by oil. Spherical shape of the colored water droplets on the superhydrophobic surface kept inside oil is pictorially presented in Figure 4I. The inset shows the measured static contact angle of the water drop inside *n*-octane, which was observed to be  $170^\circ (\pm 2^\circ)$ . Video S12 (Supporting Information) demonstrates the bouncing off of water droplets on the modified clay coated surface kept inside oil. For laboratory experiments, non-polar long chain hydrocarbons (such as *n*-octane) were used as models for oil. Extent of such under-oil superhydrophobicity was further studied in detail with CAH measurements (Figure 4J) and vertical drop adhesion test inside oil (Figure 4K). In this case also CAH was observed to be  $3^\circ (\pm 2^\circ)$ . Self-cleaning property of the surface when a portion of the surface was kept inside oil was also demonstrated with rolling water droplets (Figure 4L). Water droplets roll off easily through both the phases (air and oil) despite sudden change in the interfacial tension and kept the surface clean from dirt (potassium permanganate was used as dirt). This is demonstrated in Video S13 (Supporting Information). To study the response of water repellent coatings against perturbed water droplets (as the interfacial tension of water droplets within oil is lower than in air and it takes time to reach equilibrium), coated surface was tested with droplet pinning test where the surface was kept inside oils with colored water droplets over it for a long time. Even after 1 h of incubation, droplets restored their spherical shape and started

rolling upon mild shaking with hand (Figure S7, Supporting Information). This can easily relate to previously demonstrated excellent under-oil superhydrophobicity (Figure 4I–K). Video S14 (Supporting Information) shows the displacement of these water droplets on the superhydrophobic surface kept under oil (initial and final positions of droplets are marked with colored circles). As the material functions well both in air–solid and oil–solid interfaces, it provides an easy cleaning strategy both for the surfaces (kept under oil) and oil. This is demonstrated in Figure S8 and Video S15 (Supporting Information). While the dirt on the surface (under oil) can be collected with water drops and removed through capillary action (for paper) or mild shaking (induced force), small water drops in the oil can be removed easily by coalescing them on the superhydrophobic surface (kept under oil) followed by mild vibration/shaking. We believe that such a technique will be useful for oil pipelines and oil tankers.

Being dispersed in water, these chemically modified clay sheets sit on fibrous materials efficiently through surface tension forces or strong capillary action<sup>[27]</sup> and coat it efficiently without affecting the mechanical flexibility of the substrate. This was demonstrated with a coated filter paper (Whatman 44) shown in Figure 5A. Figure 5B pictorially represents the effect of bending/twisting on the water-repelling nature of the coated paper. For this, a colored water droplet was placed on a strained folded paper that forced droplet to change its shape to oval. However, water repelling nature of the paper remains intact and no stain of the colored drop was observed even after 10 min (Figure 5B (i); folded paper was kept vertically). Droplet on the relatively relaxed folded paper is shown pictorially in Figure 5B ((ii) and (iii); side and top views). Durability of this waterproof paper against various mechanical abrasions (sand paper abrasion and finger wiping test) and environmental stresses (effect of sunlight and effect of bending) was evaluated through static CA and CAH measurements in a cyclic fashion and the data are plotted in Figure 5C (details of the experiments are discussed in the Experimental Section). Retained superhydrophobicity of the coated paper under these conditions, a much desired property for various paper-based technologies, shows its applicability in day-to-day use.

The extent of binding of the material with fibrous substrates like filter paper (Whatman 44) was further demonstrated with a harsh oil washing experiment where viscous oil-absorbed coated paper was washed with organic solvents to remove the oil. Because of the superhydrophobic and oleophilic nature of the material, viscous paraffin oil absorbs over the coated paper easily as can be seen from the dark patches even on the opposite side of the paper (Figure S9, Supporting Information). These oil patches were subjected to multiple cleaning cycles with different organic solvents (ethanol and acetone). Though removing oil from the paper is difficult as it enters within the pores of the paper and gets immobilised on the fibers, interestingly, the washed filter paper showed almost equal water repelling nature (Figure 5D–F and Video S16, Supporting Information) and kept on functioning. This supported the excellent durability of the material as well as the developed waterproof paper.

Obtained excellent superhydrophobic property along with the unique characteristics of the thin film can be explained with



**Figure 5.** Demonstration of durability of waterproof paper. A) Unstable water drops on coated filter paper (lotus leaf effect). The inset shows the retained mechanical flexibility of the paper after coating. B) Induced twisting/bending on the coated paper. Colored water drop on the folded paper that changed its shape to oval due to induced strain by the folded paper. Inset: (i) vertical view of the folded paper after removal of water drop (after 10 min). Any stain of the color drop was not observed. (ii)–(iii) Water drop on relatively relaxed folded waterproof paper. C) Durability/longevity of waterproof paper under various mechanical and environmental stresses. Measured static CA and CAHs of water droplet after a regular time interval (details are provided in the Experimental Section). D–F) Oil washing test. D) Paraffin oil adhering on the coated filter paper. E) The same paper after washing thoroughly with acetone and ethanol to remove oil. F) Washed paper shows almost similar water repelling property.

the chemical functionalities incorporated on clay particle along with the surface morphology of the film. Though the clay materials having silicate structure are hydrophilic, simultaneous functionalization with FS and AS inverts its physical property and induces durable water repellency once it is coated over surfaces (Figure 1). First, anchored FS on the surface of clay sheets increases the hydrophobicity of the particles and facilitates the arrangement/orientation of chemically modified clay particles (keeping the fluorinated hydrocarbon chain outer side) during the evaporation of water. Such a process is mostly governed by the hydrophobic effect, namely, an interaction between water and hydrophobic component of the dispersion. This also promotes the enhancement in the average roughness on the film, which is much needed for superhydrophobicity. Second, the use of AS increases the dispersibility of the FS-modified clay particles. However, during the drying process, the amine groups mostly stay in the inner side (toward water) because of the same hydrophobic effect. Again, AS increases the strength and durability of the superhydrophobic coating by connecting the functionalized clay sheets as well as anchoring them over the surfaces. As this polymerization is only observed/feasible upon evaporation of water, the water dispersed material stays unaffected until water is present. This helps in storing the material in closed conditions at room temperature for a period over a year without any special precautions. Finally, the decorated functionalities control the surface free energy of the film in such a way that the coated surfaces show equally efficient activity both in air and under oil. This was reflected in a high contact angle of  $170^\circ (\pm 2^\circ)$ , with low hysteresis (below  $5^\circ \pm 2^\circ$ ) for water droplets both at air–solid and oil–solid interfaces.

## 4. Conclusion

In conclusion, we developed a versatile and simple waterborne composite material from hydrophilic clay particle building blocks, which provides a durable superhydrophobic coating on large areas over a wide variety of substrates (without using any adhesive), having diverse surface morphology and physical characteristics. The material forms superhydrophobic thin films easily at room temperature that withstood various mechanical and chemical stresses. In particular, the surface showed excellent water repelling property even after 100 cycles of various mechanical abrasions such as sand paper abrasion and finger wiping. Interestingly, the coated thin film functions equally well at both air–solid and oil–solid interfaces, which is due to the controlled surface energy obtained by the incorporated chemical functionalities and hydrophobic effect-induced enhanced surface roughness during the slow evaporation of water from the coating material. Moreover, surface tension-induced better and effective binding capability of the clay sheets with soft and fibrous substrates<sup>[27]</sup> makes it possible to design a flexible waterproof paper, a promising materials platform for paper-based technologies.<sup>[26]</sup>

## 5. Experimental Section

**Chemical:** All the chemicals were available commercially and were used without further purification. Kaolinite clay was purchased from Alpha Minerals and Chemicals. FS was purchased from Aldrich. AS was purchased from Rishichem Distributors. Ethanol, dimethyl sulfoxide, heptane, hexane, *n*-octane, toluene, DMF, THF, and paraffin oil

(AR grade) were procured from RANKEM, India. Sand paper (P320) was purchased from a local hardware shop.

**Durability Test with Cyclic Mechanical Perturbation:** The durability of the coating was tested by measuring the static CA of water droplets after imparting cyclic mechanical stresses on the surfaces. Hard mechanical stresses include scratching with knife and sand paper abrasion test. For scratching with a knife, ten different scratches were made on the same surface and subjected to CA measurements after every scratch. Sand paper abrasion test was performed by keeping a sand paper between the coated surface with a load of 50 g and the sand paper was moved ten complete cycles over the surface. CA of water droplets was measured after every ten cycles and continued similarly for ten times. Soft mechanical stresses were induced in the form of tissue paper abrasion and finger wiping abrasion. The same methodology (mentioned above) was used in this case also. For each test (both hard and soft mechanical stresses) the same surface was used repeatedly.

**Durability Test for the Waterproof Paper:** Durability of the flexible waterproof paper was tested with induced mechanical abrasions and various environmental stresses. For mechanical abrasion, sand paper abrasion (with a load of 50 g), and finger wiping tests, samples were evaluated through static CA and CAH measurements after every ten complete cycles where each cycle consisted of back and forth movements for 5 cm each. Environmental stresses like direct sunlight exposure and effect of bending/twisting of waterproof paper were also studied with CA and CAH measurements. For the effect of direct sunlight exposure, the coated paper was kept under sunlight and evaluated with CA and CAH measurements after each 5 h of exposure. This was further continued for ten times. For bending/twisting tests, the coated paper was twisted in different possible ways (90°, 180°, rolling, etc.) and CA and CAH were checked after every ten cycles of twisting. The data are plotted in Figure 5C.

**Bacterial Resistance Test:** Bacterial resistance test was done with Gram-negative *Escherichia coli* (ATCC 10536). Details of the experiments are given in a previously reported article.<sup>[20b]</sup> In short, *E. coli* was inoculated in 10 mL of Luria–Bertani broth (Himedia) and kept overnight in an air bath shaker at 37 °C and 300 rpm to reach the exponential growth phase. Later, the bacterial solution was centrifuged at 3000 rpm for 5 min to remove the used media and washed twice with sterile saline. The suspension was diluted further to make the plating concentrations as 10<sup>7</sup> colony forming units per millileter. This was measured by using the spread plate method. Resulting solution was used for the bacterial resistance experiment.

## Supporting Information

Supporting Information is available from the Wiley Online Library or from the author.

## Acknowledgements

The authors thank the Department of Science and Technology, Government of India, for constantly supporting their research program on nanomaterials. A.B. acknowledges support of INSPIRE Fellowship, Department of Science and Technology, Government of India. R.H.A.R. acknowledges support from the European Research Council (ERC-2016-CoG No. 725513 “SuperRepel”) and the Academy of Finland Centres of Excellence Programme (2014–2019). This work was supported by the Finnish National Agency for Education.

## Conflict of Interest

The authors declare no conflict of interest.

## Keywords

aqueous coatings, durable coatings, superhydrophobic materials, under oil, waterproof paper

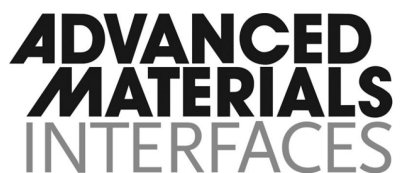
Received: November 20, 2017

Revised: February 20, 2018

Published online: April 3, 2018

- [1] a) T. Sun, L. Feng, X. Gao, L. Jiang, *Acc. Chem. Res.* **2005**, *38*, 644; b) L. Feng, S. Li, Y. Li, H. Li, L. Zhang, J. Zhai, Y. Song, B. Liu, L. Jiang, D. Zhu, *Adv. Mater.* **2002**, *14*, 1857; c) X. Zhang, Z. Li, K. Liu, L. Jiang, *Adv. Funct. Mater.* **2013**, *23*, 2881.
- [2] a) K. B. Golovin, J. W. Gose, M. Perlin, S. L. Ceccio, A. Tuteja, *Philos. Trans. R. Soc., A* **2016**, *374*, 20160189; b) Y. C. Jung, B. Bhushan, *ACS Nano* **2009**, *3*, 4155.
- [3] a) M. F. Haase, D. O. Grigoriev, H. Möhwald, D. G. Shchukin, *Adv. Mater.* **2012**, *24*, 2429; b) F. Zhang, L. Zhao, H. Chen, S. Xu, D. G. Evans, X. Duan, *Angew. Chem., Int. Ed.* **2008**, *47*, 2466; c) K. Liu, M. Zhang, J. Zhai, J. Wang, L. Jiang, *Appl. Phys. Lett.* **2008**, *92*, 183103.
- [4] a) L. Mishchenko, B. Hatton, V. Bahadur, J. A. Taylor, T. Krupenkin, J. Aizenberg, *ACS Nano* **2010**, *4*, 7699; b) P. Guo, Y. Zheng, M. Wen, C. Song, Y. Lin, L. Jiang, *Adv. Mater.* **2012**, *24*, 2642; c) K. Golovin, S. P. R. Kobaku, D. H. Lee, E. T. DiLoreto, J. M. Mabry, A. Tuteja, *Sci. Adv.* **2016**, *2*, e1501496; d) L. Cao, A. K. Jones, V. K. Sikka, J. Wu, D. Gao, *Langmuir* **2009**, *25*, 12444.
- [5] a) Y. Zhang, T. Ren, T. Li, J. He, D. Fang, *Adv. Mater. Interfaces* **2016**, *3*, 1600672; b) L.-P. Xu, Y. Chen, G. Yang, W. Shi, B. Dai, G. Li, Y. Cao, Y. Wen, X. Zhang, S. Wang, *Adv. Mater.* **2015**, *27*, 6878; c) H. K. Lee, Y. H. Lee, Q. Zhang, I. Y. Phang, J. M. R. Tan, Y. Cui, X. Y. Ling, *ACS Appl. Mater. Interfaces* **2013**, *5*, 11409; d) A. Ebrahimi, P. Dak, E. Salm, S. Dash, S. V. Garimella, R. Bashir, M. A. Alam, *Lab Chip* **2013**, *13*, 4248.
- [6] a) Y. Zheng, H. Bai, Z. Huang, X. Tian, F.-Q. Nie, Y. Zhao, J. Zhai, L. Jiang, *Nature* **2010**, *463*, 640; b) A. R. Parker, C. R. Lawrence, *Nature* **2001**, *414*, 33.
- [7] C. Li, M. Boban, S. A. Snyder, S. P. R. Kobaku, G. Kwon, G. Mehta, A. Tuteja, *Adv. Funct. Mater.* **2016**, *26*, 6121.
- [8] a) G. Kwon, E. Post, A. Tuteja, *MRS Commun.* **2015**, *5*, 475; b) J. Li, L. Yan, X. Tang, H. Feng, D. Hu, F. Zha, *Adv. Mater. Interfaces* **2016**, *3*, 1500770.
- [9] H. Husni, M. R. Nazari, H. M. Yee, R. Rohim, A. Yusuff, M. A. Mohd Ariff, N. N. R. Ahmad, C. P. Leo, M. U. M. Junaidi, *Constr. Build. Mater.* **2017**, *144*, 385.
- [10] a) F. Hizal, N. Rungraeng, J. Lee, S. Jun, H. J. Busscher, H. C. van der Mei, C.-H. Choi, *ACS Appl. Mater. Interfaces* **2017**, *9*, 12118; b) R. Blossey, *Nat. Mater.* **2003**, *2*, 301; c) D. C. Leslie, A. Waterhouse, J. B. Berthet, T. M. Valentin, A. L. Watters, A. Jain, P. Kim, B. D. Hatton, A. Nedder, K. Donovan, E. H. Super, C. Howell, C. P. Johnson, T. L. Vu, D. E. Bolgen, S. Rifai, A. R. Hansen, M. Aizenberg, M. Super, J. Aizenberg, D. E. Ingber, *Nat. Biotechnol.* **2014**, *32*, 1134; d) A. B. Tesler, P. Kim, S. Kolle, C. Howell, O. Ahanotu, J. Aizenberg, *Nat. Commun.* **2015**, *6*, 8649; e) W. Barthlott, C. Neinhuis, *Planta* **1997**, *202*, 1.
- [11] a) A. Nakajima, K. Hashimoto, T. Watanabe, *Monatsh. Chem.* **2001**, *132*, 31; b) S. G. Lee, D. S. Ham, D. Y. Lee, H. Bong, K. Cho, *Langmuir* **2013**, *29*, 15051.
- [12] a) D. J. Lee, H. M. Kim, Y. S. Song, J. R. Youn, *ACS Nano* **2012**, *6*, 7656; b) J. Song, Y. Lu, J. Luo, S. Huang, L. Wang, W. Xu, I. P. Parkin, *Adv. Mater. Interfaces* **2015**, *2*, 1500350; c) S. Liu, H. Zhou, H. Wang, Y. Zhao, H. Shao, Z. Xu, Z. Feng, D. Liu, T. Lin, *Adv. Mater. Interfaces* **2017**, *4*, 1700027; d) C. Yu, M. Cao,

- Z. Dong, J. Wang, K. Li, L. Jiang, *Adv. Funct. Mater.* **2016**, 26, 3236; e) D. Wu, J.-N. Wang, S.-Z. Wu, Q.-D. Chen, S. Zhao, H. Zhang, H.-B. Sun, L. Jiang, *Adv. Funct. Mater.* **2011**, 21, 2927; f) Y. Li, S. Chen, M. Wu, J. Sun, *Adv. Mater.* **2014**, 26, 3344; g) S. G. Lee, H. S. Lim, D. Y. Lee, D. Kwak, K. Cho, *Adv. Funct. Mater.* **2013**, 23, 547.
- [13] a) S. Wang, K. Liu, X. Yao, L. Jiang, *Chem. Rev.* **2015**, 115, 8230; b) L. Wen, Y. Tian, L. Jiang, *Angew. Chem., Int. Ed.* **2015**, 54, 3387.
- [14] a) K. Chen, S. Zhou, S. Yang, L. Wu, *Adv. Funct. Mater.* **2015**, 25, 1035; b) T. M. Schutzius, I. S. Bayer, J. Qin, D. Walldrop, C. M. Megaridis, *ACS Appl. Mater. Interfaces* **2013**, 5, 13419.
- [15] M. K. Tiwari, I. S. Bayer, G. M. Jursich, T. M. Schutzius, C. M. Megaridis, *ACS Appl. Mater. Interfaces* **2010**, 2, 1114.
- [16] a) H. Teisala, M. Tuominen, J. Kuusipalo, *Adv. Mater. Interfaces* **2014**, 1, 1300026; b) M. P. Sousa, J. F. Mano, *ACS Appl. Mater. Interfaces* **2013**, 5, 3731; c) J. Guo, W. Fang, A. Welle, W. Feng, I. Filpponen, O. J. Rojas, P. A. Levkin, *ACS Appl. Mater. Interfaces* **2016**, 8, 34115.
- [17] J. E. Mates, T. M. Schutzius, I. S. Bayer, J. Qin, D. E. Walldrop, C. M. Megaridis, *Ind. Eng. Chem. Res.* **2014**, 53, 222.
- [18] L. Li, B. Li, J. Dong, J. Zhang, *J. Mater. Chem. A* **2016**, 4, 13677.
- [19] a) S. S. Latthe, C. Terashima, K. Nakata, M. Sakai, A. Fujishima, *J. Mater. Chem. A* **2014**, 2, 5548; b) C.-F. Wang, S.-J. Lin, *ACS Appl. Mater. Interfaces* **2013**, 5, 8861.
- [20] a) H. Ye, L. Zhu, W. Li, H. Liu, H. Chen, *J. Mater. Chem. A* **2017**, 5, 9882; b) A. Baidya, M. A. Ganayee, S. Jakka Ravindran, K. C. Tam, S. K. Das, R. H. A. Ras, T. Pradeep, *ACS Nano* **2017**, 11, 11091.
- [21] Z. Tang, D. W. Hess, V. Breedveld, *J. Mater. Chem. A* **2015**, 3, 14651.
- [22] a) Y. Lu, S. Sathasivam, J. Song, C. R. Crick, C. J. Carmalt, I. P. Parkin, *Science* **2015**, 347, 1132; b) I. A. Larmour, S. E. J. Bell, G. C. Saunders, *Angew. Chem., Int. Ed.* **2007**, 46, 1710; c) X. Tian, T. Verho, R. H. A. Ras, *Science* **2016**, 352, 142; d) X. Deng, L. Mammen, H.-J. Butt, D. Vollmer, *Science* **2012**, 335, 67.
- [23] B. Chen, J. Qiu, E. Sakai, N. Kanazawa, R. Liang, H. Feng, *ACS Appl. Mater. Interfaces* **2016**, 8, 17659.
- [24] a) A. K. Kota, Y. Li, J. M. Mabry, A. Tuteja, *Adv. Mater.* **2012**, 24, 5838; b) A. Tuteja, W. Choi, M. Ma, J. M. Mabry, S. A. Mazzella, G. C. Rutledge, G. H. McKinley, R. E. Cohen, *Science* **2007**, 318, 1618; c) A. Tuteja, W. Choi, J. M. Mabry, G. H. McKinley, R. E. Cohen, *Proc. Natl. Acad. Sci. USA* **2008**, 105, 18200; d) H. Zhou, H. Wang, H. Niu, Y. Zhao, Z. Xu, T. Lin, *Adv. Funct. Mater.* **2017**, 27, 1604261; e) A. Baidya, S. K. Das, T. Pradeep, *Global Challenges* **2018**, 2, 1700097.
- [25] N. Wang, Y. Lu, D. Xiong, C. J. Carmalt, I. P. Parkin, *J. Mater. Chem. A* **2016**, 4, 4107.
- [26] X. Hou, Y. S. Zhang, G. T.-d. Santiago, M. M. Alvarez, J. Ribas, S. J. Jonas, P. S. Weiss, A. M. Andrews, J. Aizenberg, A. Khademhosseini, *Nat. Rev. Mater.* **2017**, 2, 17016.
- [27] B. Chang, Q. Zhou, Z. Wu, Z. Liu, R. Ras, K. Hjort, *Micromachines* **2016**, 7, 41.
- [28] E. E. Meyer, K. J. Rosenberg, J. Israelachvili, *Proc. Natl. Acad. Sci. USA* **2006**, 103, 15739.
- [29] J. Shieh, F. J. Hou, Y. C. Chen, H. M. Chen, S. P. Yang, C. C. Cheng, H. L. Chen, *Adv. Mater.* **2010**, 22, 597.
- [30] T. Verho, C. Bower, P. Andrew, S. Franssila, O. Ikkala, R. H. A. Ras, *Adv. Mater.* **2011**, 23, 673.
- [31] a) J. D. Smith, R. Dhiman, S. Anand, E. Reza-Garduno, R. E. Cohen, G. H. McKinley, K. K. Varanasi, *Soft Matter* **2013**, 9, 1772; b) T.-S. Wong, S. H. Kang, S. K. Y. Tang, E. J. Smythe, B. D. Hatton, A. Grinthal, J. Aizenberg, *Nature* **2011**, 477, 443.



## Supporting Information

for *Adv. Mater. Interfaces*, DOI: 10.1002/admi.201701523

**Fabrication of a Waterborne Durable Superhydrophobic  
Material Functioning in Air and under Oil**

*Avijit Baidya, Sarit Kumar Das, Robin H. A. Ras, and  
Thalappil Pradeep\**



Copyright WILEY-VCH Verlag GmbH & Co. KGaA, 69469 Weinheim, Germany, 2016.

## Supporting Information

### **Fabrication of a waterborne durable superhydrophobic material functioning in air and under oil**

*Avijit Baidya,<sup>a,b,c</sup> Sarit Kumar Das,<sup>c</sup> Robin H. A. Ras,<sup>b,d</sup> and Thalappil Pradeep<sup>\*a</sup>*

<sup>a</sup>DST Unit of Nanoscience, Thematic Unit of Excellence, Department of Chemistry, Indian Institute of Technology Madras, Chennai, India

<sup>b</sup>Department of Applied Physics, Aalto University School of Science, Puumiehenkuja 2, 02150 Espoo, Finland

<sup>c</sup>Department of Mechanical Engineering, Indian Institute of Technology Madras, Chennai 600036, India

<sup>d</sup>Department of Bioproducts and Biosystems, Aalto University School of Chemical Engineering, Kemistintie 1, 02150 Espoo, Finland

E-mail: [pradeep@iitm.ac.in](mailto:pradeep@iitm.ac.in)

### **Table of contents**

#### **Text**

Description	Page No.
Instrumentation	2
Supporting Information figures	3

#### **Figures**

Figure No.	Description	Page No.
S1	Water on superhydrophobic paper and normal paper	3
S2	AFM image of unmodified clay, spray coated on glass substrate	4
S3	Cross-sectional SEM images, thickness of coating on glass	4
S4	Bacterial resistance test	4
S5	Contact angle hysteresis (CAH) of water droplets (pH=1, 14 and KMnO <sub>4</sub> solution) over the coated glass substrates.	5
S6	CAH of water droplet before and after 170 h organic solvent treatment (THF treated sample)	5

S7	Mobility of water droplet on normal glass and coated glass after 1 h of incubation within oil ( <i>n</i> -octane)	5
S8	Cleaning of water droplet from normal glass and coated glass within oil ( <i>n</i> -octane)	6
S9	Demonstration of the superhydrophobic but oleophilic nature of flexible waterproof paper	6

Video No.	Description
Video S1	Water stream on various coated substrates
Video S2	Water on coated and normal filter paper (lotus leaf effect)
Video S3	Knife scratching test
Video S4	Sand abrasion test with a load of 50 g
Video S5	Tissue paper wiping test
Video S6	Finger wiping test
Video S7	Vertical drop test (after different mechanical abrasion)
Video S8	Water drop drag test (after different mechanical abrasion)
Video S9	Self-cleaning property (at air)
Video S10	Effect of organic solvent (ethanol)
Video S11	Effect of organic solvent (after 170 h THF treatment)
Video S12	Under-oil superhydrophobicity (bounce of water drop on the surface kept inside oil, <i>n</i> -octane)
Video S13	Self-cleaning at air and oil phase
Video S14	Mobility of water drop on the surface (under oil)
Video S15	Washing with tissue paper on the coated glass surface (under oil)
Video S16	Robustness of coating cleaning of absorbed paraffin oil

## Instrumentation

AFM imaging was done with Witec alpha300 S confocal Raman spectrometer with an AFM attachment (Zeiss 20x objective). AFM imaging was carried out in non-contact mode with a cantilever with the following parameters: thickness 4  $\mu\text{m}$ , length 125  $\mu\text{m}$ , width 30  $\mu\text{m}$ , resonance frequency 320 kHz and force constant 42 N/m.

Electron microscopy imaging was done using a FEI Quanta 200 environmental scanning electron microscope (ESEM) with EDAX EDS system, to study the surface morphology of the coated substrate in different magnifications.



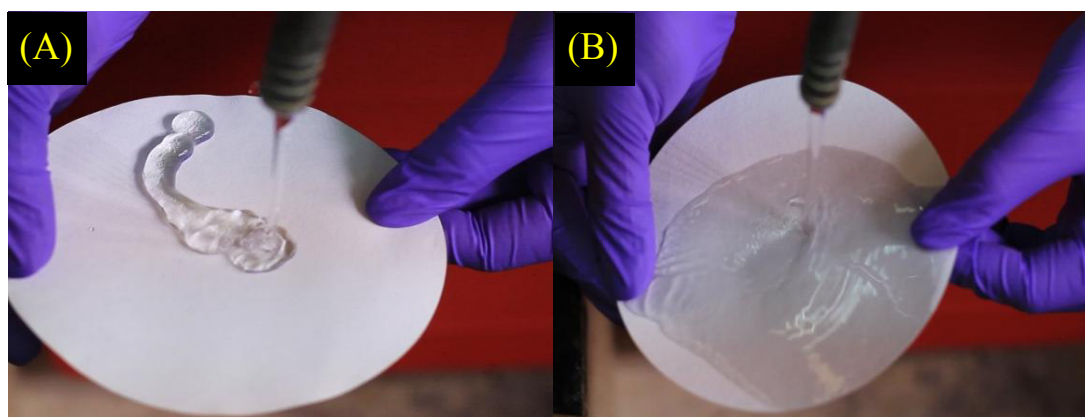
IR spectrum was collected using a PerkinElmer SpectrumOne FT-IR spectrometer.

X-Ray photoelectron spectroscopy (XPS) measurements were carried out using an Omicron ESCA Probe spectrometer with polychromatic Mg K $\alpha$  X-rays (1253.6 eV). The X-ray power applied was 300 W. The pass energy was 50 eV for survey scans and 20 eV for specific regions. Sample solution was spotted on stainless steel (SS) XPS sample plates and dried in vacuum. The base pressure of the instrument was  $5.0 \times 10^{-10}$  mbar. The binding energy was calibrated with respect to adventitious C1s feature at 285 eV.

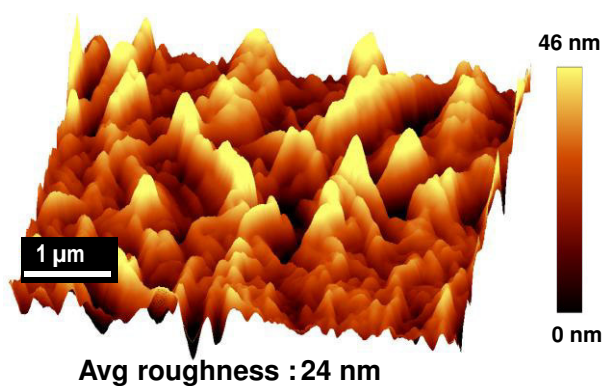
Contact angle and contact angle hysteresis (CAH) of water droplet on the different coated substrates were measured using a Holmarc contact angle meter.

Nikon D5100 camera was used to capture all the pictures and videos.

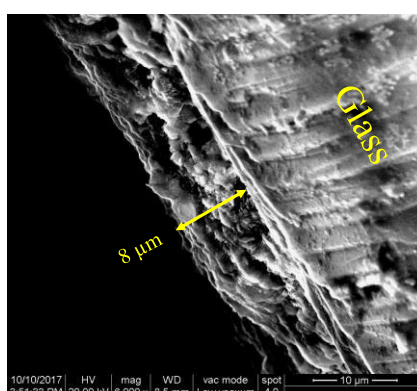
Spray of the water dispersed material was performed with Badger Air-Brush Co 360-9, Universal Airbrush.



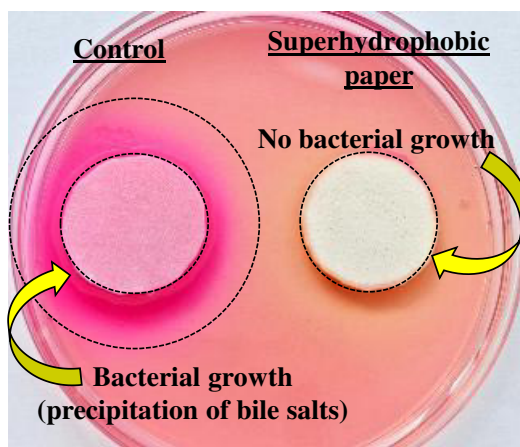
**Figure S1.** Water flows on A) superhydrophobic material coated filter paper (Lotus leaf effect) and B) normal filter paper. Water moves in a frictionless fashion on the coated surface whereas it wets the normal filter paper.



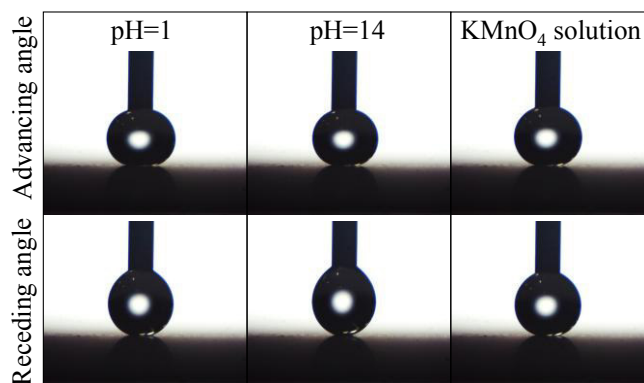
**Figure S2.** AFM image of unmodified clay, spray coated on glass substrate.



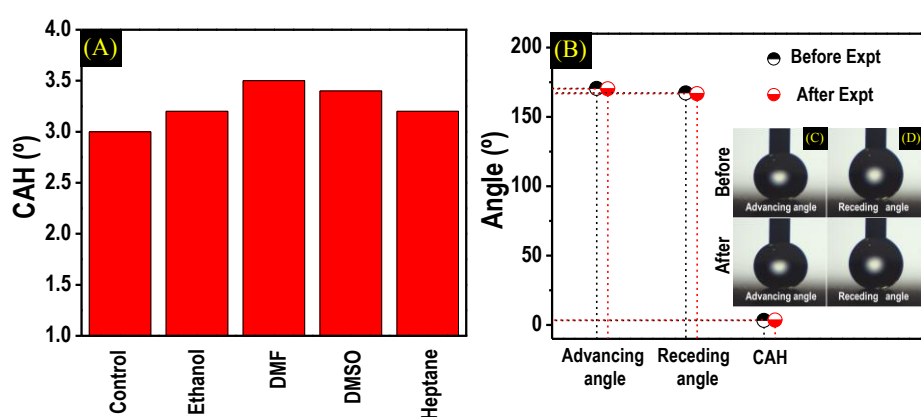
**Figure S3.** Cross-sectional SEM image. Thickness of the coating is shown.



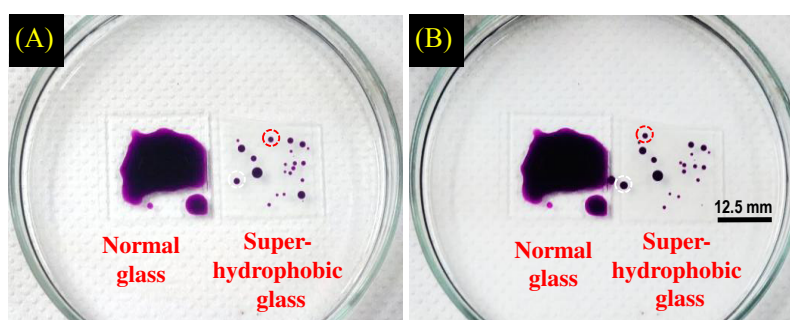
**Figure S4.** Demonstration of bacterial resistance property of superhydrophobic paper. This was compared with uncoated paper.



**Figure S5.** A) Contact angle hysteresis (CAH) of water droplets (pH=1, 14 and  $\text{KMnO}_4$  solution) over the coated glass substrates.

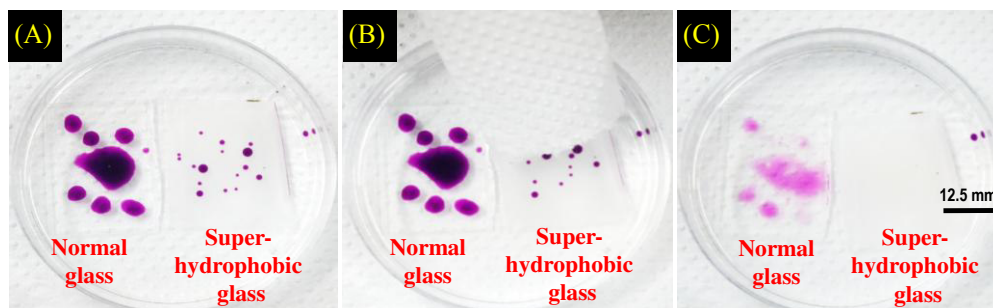


**Figure S6.** A) Contact angle hysteresis (CAH) values of water droplet over 170 h chemically (different organic solvent) treated surface. B) Graphical and pictorial representations of advancing angle, receding angle and CAH of water droplet over 170 h tetrahydrofuran (THF) treated surface (before and after). Images of C) advancing angle and D) receding angle (before and after). Experiments were done in air-water-solid interface.

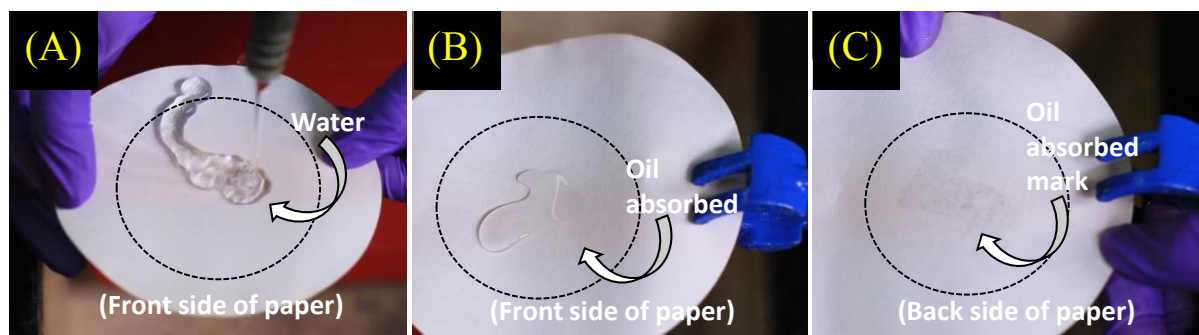


**Figure S7.** Mobility of water droplets on oil immersed coated surface upon mild shaking with hand. Droplets were kept inside oil on the surface for an hour before the experiment.  $\text{KMnO}_4$

solution was used here for the visual effect. Colored water droplet moved by vibration with hand (initial (A) and final (B) positions are marked for two individual droplets with red and white circles, respectively).



**Figure S8.** Cleaning of water droplets from oil immersed coated surface; normal glass as a reference.  $\text{KMnO}_4$  solution was used here for the visual effect. Colored water droplets were wiped off completely from the superhydrophobic surface with tissue paper. A) Before wiping, initial condition, B) during wiping and C) after wiping, final condition.



**Figure S9.** Demonstration of the superhydrophobic but oleophilic nature of flexible waterproof paper. (A) Unstable water drops on coated filter paper (lotus effect). (B-C) Paraffin oil on coated filter paper, part of which is absorbed by the paper (front side, B) and back side (C) of the same filter paper (with absorbed oil).

Videos are presented separately.

# Fullerene-Functionalized Monolayer-Protected Silver Clusters: $[\text{Ag}_{29}(\text{BDT})_{12}(\text{C}_{60})_n]^{3-}$ ( $n = 1-9$ )

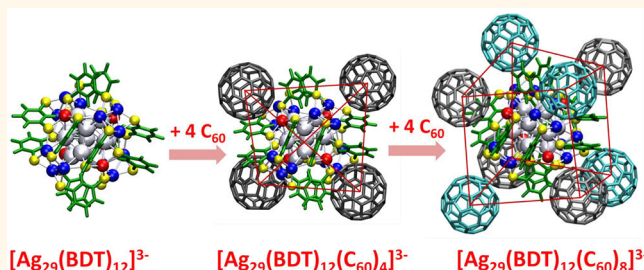
Papri Chakraborty, Abhijit Nag, Ganesan Paramasivam, Ganapati Natarajan, and Thalappil Pradeep\*<sup>✉</sup>

DST Unit of Nanoscience (DST UNS) and Thematic Unit of Excellence (TUE), Department of Chemistry, Indian Institute of Technology Madras, Chennai 600 036, India

## Supporting Information

**ABSTRACT:** We report the formation of supramolecular adducts between monolayer-protected noble metal nano-clusters and fullerenes, specifically focusing on a well-known silver cluster,  $[\text{Ag}_{29}(\text{BDT})_{12}]^{3-}$ , where BDT is 1,3-benzenedithiol. We demonstrate that  $\text{C}_{60}$  molecules link with the cluster at specific locations and protect the fragile cluster core, enhancing the stability of the cluster. A combination of studies including UV-vis, high-resolution electrospray ionization mass spectrometry, collision-induced dissociation, and nuclear magnetic resonance spectroscopy revealed structural details of the fullerene-functionalized clusters,  $[\text{Ag}_{29}(\text{BDT})_{12}(\text{C}_{60})_n]^{3-}$  ( $n = 1-9$ ). Density functional theory (DFT) calculations and molecular docking simulations affirm compatibility between the cluster and  $\text{C}_{60}$ , resulting in its attachment at specific positions on the surface of the cluster, stabilized mainly by  $\pi-\pi$  and van der Waals interactions. The structures have also been confirmed from ion mobility mass spectrometry by comparing the experimental collision cross sections (CCSs) with the theoretical CCSs of the DFT-optimized structures. The gradual evolution of the structures with an increase in the number of fullerene attachments to the cluster has been investigated. Whereas the structure for  $n = 4$  is tetrahedral, that of  $n = 8$  is a distorted cube with a cluster at the center and fullerenes at the vertices. Another fullerene,  $\text{C}_{70}$ , also exhibited similar behavior. Modified clusters are expected to show interesting properties.

**KEYWORDS:** monolayer-protected clusters, fullerenes, supramolecular functionalization, hybrid nanostructures, host-guest chemistry, mass spectrometry, ion mobility



Study of atomically precise clusters of noble metals, covering over 100 well-defined molecular systems, is an expanding discipline.<sup>1-4</sup> Among these, the clusters investigated thoroughly include  $\text{Au}_{25}(\text{SR})_{18}$ ,<sup>5,6</sup>  $\text{Au}_{38}(\text{SR})_{24}$ ,<sup>7</sup>  $\text{Au}_{102}(\text{SR})_{44}$ ,<sup>8</sup>  $\text{Ag}_{25}(\text{SR})_{18}$ ,<sup>9</sup>  $\text{Ag}_{44}(\text{SR})_{30}$ ,<sup>10,11</sup>  $\text{Ag}_{29}(\text{S}_2\text{R})_{12}$ ,<sup>12</sup> etc. While single-crystal X-ray diffraction has been used to solve their crystal structures, mass spectrometric techniques, especially electrospray ionization (ESI) and matrix-assisted laser desorption ionization (MALDI), have been the principal tools to understand their molecular composition.<sup>13,14</sup> These clusters show specific signatures in their optical absorption and luminescence spectra which depend strongly on the ligand-metal interface.<sup>15,16</sup>

Several ligand-protected noble metal clusters of the type  $\text{Au}_{25}(\text{SR})_{18}$ ,  $\text{Ag}_{25}(\text{SR})_{18}$ ,  $\text{Ag}_{29}(\text{S}_2\text{R})_{12}$ , etc. are negatively charged and exist with counterions in their crystal lattice. The inherent charge and electron density of the clusters are typically distributed at the ligand-metal interface. In addition, appropriate molecular dimensions of the system and orientation of the ligands on the cluster surface can induce specific host-guest interactions.<sup>17</sup> These suggest a possibility of exploring supramolecular chemistry of monolayer-protected clusters. An important chemical probe to utilize such properties

of the clusters is fullerenes due to their tendency to form self-assembled structures.<sup>18-20</sup>  $\text{C}_{60}$  is known to form supramolecular complexes with a wide variety of molecules like rotaxanes, catenanes,<sup>21</sup> calixarenes,<sup>22</sup> cyclodextrins,<sup>23</sup> cucurbiturils,<sup>24</sup> crown ethers,<sup>25</sup> and porphyrins.<sup>26-28</sup> Such complexes are mainly stabilized by  $\pi-\pi$ , C-H- $\pi$ , or van der Waals (vdW) interactions.<sup>29,30</sup>

Fullerenes, due to their large number of lowest unoccupied molecular orbitals, which are typically degenerate, can also accept multiple electrons, leading to polyanionic species. Compounds such as  $\text{K}_n\text{C}_{60}$  ( $n = 1-6$ )<sup>31,32</sup> are well-known for interesting properties such as metallicity and superconductivity.<sup>33-35</sup> In addition to complete electron transfer leading to  $(\text{C}_{60})_n^-$ ,  $\text{C}_{60}$  is also known to form partial charge transfer complexes with donors such as tetrathiafulvalene,<sup>36,37</sup> dithia-diazafulvalene,<sup>38</sup> tetraphenyldipyranilidene, and metallo-cenes.<sup>39</sup> The extent of charge transfer is also limited by the close approach of the molecules and steric factors affecting the overlap of molecular orbitals.<sup>40</sup>

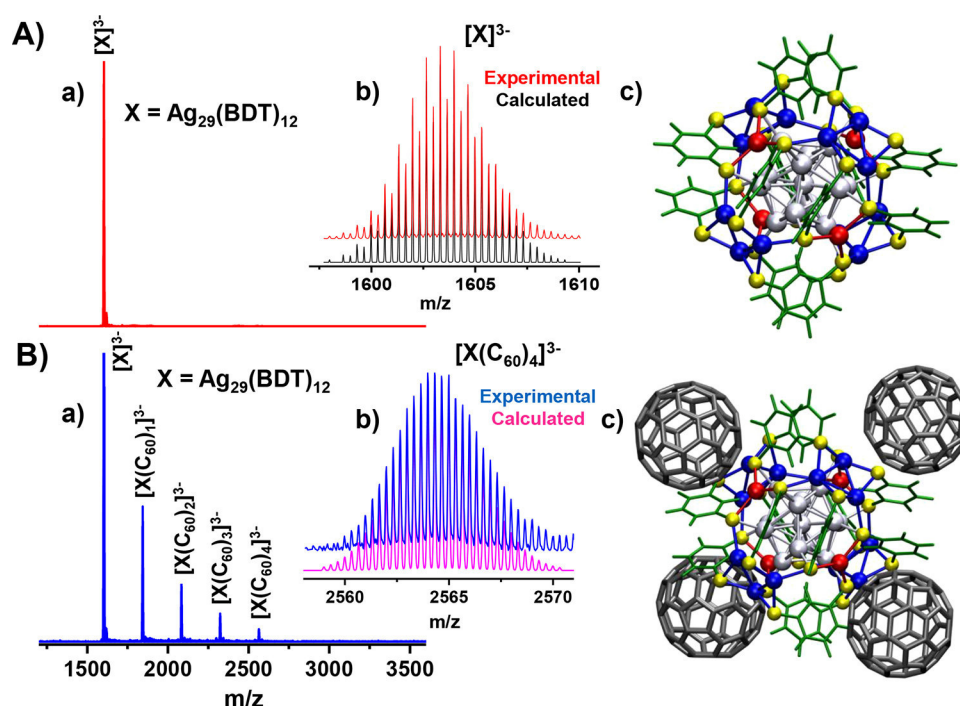
**Received:** November 1, 2017

**Accepted:** February 14, 2018

**Published:** February 14, 2018







**Figure 1.** (A) (a) Full range ESI MS, (b) experimental and calculated isotope patterns, and (c) DFT-optimized structure of the  $[Ag_{29}(BDT)_{12}]^{3-}$  cluster. (B) (a) ESI MS of  $[Ag_{29}(BDT)_{12}(C_{60})_n]^{3-}$  ( $n = 1-4$ ) complexes, (b) experimental and calculated isotope patterns of  $[Ag_{29}(BDT)_{12}(C_{60})_4]^{3-}$ , and (c) schematic of the possible structure of  $[Ag_{29}(BDT)_{12}(C_{60})_4]^{3-}$ . Color codes for the atoms in the inset pictures: yellow, S atoms; gray, Ag atoms of the icosahedral ( $Ag_{13}$ ) core and the bonds connecting them; blue, 12 Ag atoms of the trigonal planes in the exterior shell and the bonds connecting them to the S atoms of the  $Ag_3S_3$  motifs; red, four Ag atoms face-capping the core at four tetrahedral positions of  $[Ag_{29}(BDT)_{12}]^{3-}$  and the bonds connecting each of these Ag atoms to the neighboring three S atoms; green, BDT ligands; black,  $C_{60}$  molecules.

The foregoing suggests the possibility to create intercluster compounds of monolayer-protected clusters with fullerenes. In view of the specific geometry of the clusters, accessibility of  $C_{60}$  to the cluster surface may be limited, allowing specific composition of the adducts to be feasible. Considering the easiness of accessibility of the metal cluster surface, we chose  $[Ag_{29}(BDT)_{12}]^{3-12}$  as the cluster of choice for these investigations, which confirmed our conjecture. Our studies involved mass spectrometry extensively along with critical inputs from NMR spectroscopy and computational studies. The cluster–fullerene complexes,  $[Ag_{29}(BDT)_{12}(C_{60})_n]^{3-}$  ( $n = 1-4$ ), were mainly stabilized by vdW forces and  $\pi$ – $\pi$  interactions of the fullerenes with the benzene rings of the BDT ligands of the cluster, and they can be characterized completely in the gaseous and solution phases. We further show that, by controlling the conditions, the entire surface of the cluster can be functionalized by fullerenes, which forms close-packed structures. Density functional theory (DFT) calculations and molecular docking simulations were used to elucidate the structure of the fullerene-protected clusters,  $[Ag_{29}(BDT)_{12}(C_{60})_n]^{3-}$  ( $n = 1-4, 8$ , and  $9$ ). Studies suggest the occupation of tetrahedral sites of the cluster by  $C_{60}$ . When these positions were occupied as in the case of  $[Ag_{29}(BDT)_{12}(TPP)_4]^{3-}$ , where TPP is triphenylphosphine,  $C_{60}$  substitution did not occur, supporting the structural predictions. Interaction of the cluster with another fullerene,  $C_{70}$ , is also presented in this study.

## RESULTS AND DISCUSSION

$[Ag_{29}(BDT)_{12}]^{3-}$  cluster<sup>12</sup> was synthesized following a reported protocol with slight modifications, as described in the

Experimental section and characterized using optical absorption and ESI MS studies (Figure S1). The structure consists of a  $Ag_{13}$  icosahedral core, which is further capped by 12 Ag atoms of the exterior shell. These 12 Ag atoms form four tetrahedrally oriented trigonal prisms, and another four Ag atoms face-cap the 13 atom core at four tetrahedral positions. This tetrahedral orientation is shown in Figure 1A(c), where the four Ag atoms resemble the vertices (V) of a tetrahedron and four trigonal planes formed by the 12 Ag atoms lie over the faces (F) of the tetrahedron (see Figure S2 for more details). We follow this notation throughout the paper. Additional structural insight may be derived from a three-dimensional view (Video V1 in the Supporting Information).

**Characterization of  $[Ag_{29}(BDT)_{12}(C_{60})_n]^{3-}$  ( $n = 1-4$ ) Complexes.** Complexes of  $C_{60}$  with the cluster,  $[Ag_{29}(BDT)_{12}]^{3-}$ , were obtained by adding a solution of  $C_{60}$  in toluene to the solution of the cluster in DMF in various molar ratios. In Figure 1A, panel (a) shows the ESI MS of the synthesized  $[Ag_{29}(BDT)_{12}]^{3-}$  cluster, which exhibits the molecular ion peak around  $m/z$  1603. Experimental and calculated isotope patterns are shown in (b). DFT-optimized structure based on the crystal structure of the cluster<sup>12</sup> is in (c). Reactivity of  $C_{60}$  with  $[Ag_{29}(BDT)_{12}]^{3-}$  was studied by ESI MS, as shown in Figure 1B. A series of peaks appeared upon addition of  $C_{60}$ . Expansion of these peaks showed that the separation between each of the peaks present in the isotope pattern was 0.33, which corresponded to a charge state of  $3^-$  for the addition complexes, as well. The peaks were separated by  $m/z$  240, which corresponded to the addition of  $C_{60}$  (mass of  $C_{60}$  is  $240 \times 3 = 720$ ). The number of  $C_{60}$  additions increased with increase in the concentration of  $C_{60}$  added to the cluster

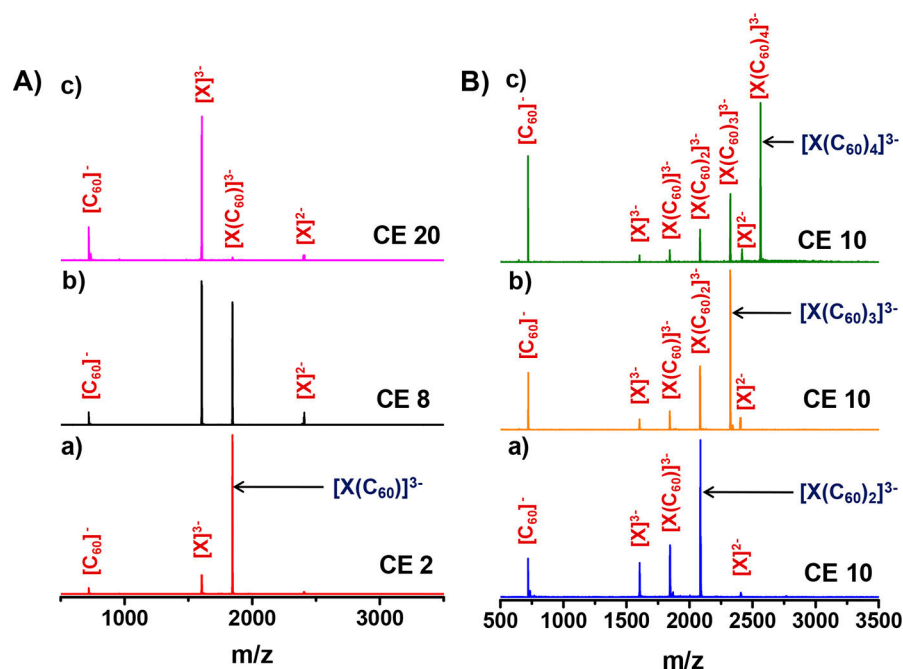
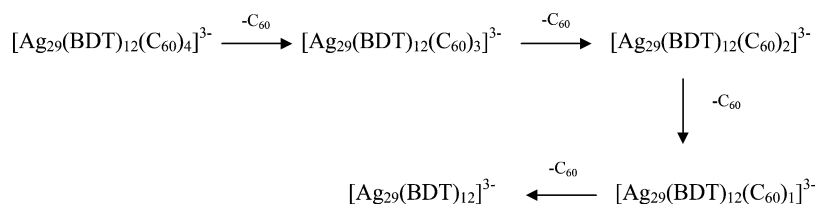


Figure 2. (A) CID study on  $[X(C_{60})]^{3-}$  at increasing collision energies (CE in instrumental units) of 2 (a), 8 (b), and 20 (c). (B) CID spectrum of  $[X(C_{60})_n]^{3-}$  ( $n = 2-4$ ) are shown in (a-c), respectively, at CE 10,  $X = Ag_{29}(BDT)_{12}$ .

#### Scheme 1. Fragmentation Pathway of $[Ag_{29}(BDT)_{12}(C_{60})_n]^{3-}$ ( $n = 1-4$ ) Complexes



(Figure S3). At an optimum concentration, where the cluster/fullerene molar ratio was 1:4, up to four  $C_{60}$  additions were observed in ESI MS, as shown in Figure 1B(a). The experimentally obtained isotope patterns were matched with the calculated patterns to further confirm their composition. The isotope patterns of one of the complexes,  $[Ag_{29}(BDT)_{12}(C_{60})_4]^{3-}$ , is shown in (b), and the rest are included in the Supporting Information (Figure S4). From a comparison of the absorption spectra of the adducts with that of the cluster and  $C_{60}$ , it appeared that the absorption features of the adducts were mainly additive with slight changes in the absorbance when compared to their added spectrum (Figure S5). There was an increase in the absorbance of the  $C_{60}$  features in their adducts. Though such changes reflected the possibility of some electronic coupling between the cluster and the fullerenes, it was very small, and the interactions were mainly supramolecular in nature.<sup>29,41</sup>

As the parent  $[Ag_{29}(BDT)_{12}]^{3-}$  clusters were synthesized without the co-protection from the TPP ligands, they were stable only for a few hours.<sup>12</sup> However, functionalization with  $C_{60}$  increased the stability of the cluster. The complexes were stable for more than a week (Figure S6).  $C_{60}$  molecules act as secondary ligands protecting the cluster core. The dithiol ligands of the cluster are bound in such a fashion that, surrounding each tetrahedral vertex position of the cluster, benzene rings of three of the BDT ligands are oriented in a way that can enhance the stabilization of a  $C_{60}$  molecule at those

positions by  $\pi$ - $\pi$  interaction and also by C-H- $\pi$  contacts at the ligand periphery. Also, appropriate geometry and increased accessibility of the cluster surface allows  $C_{60}$  molecules to come in close proximity of the cluster, which reveals the importance of the structure in the formation of such complexes. A schematic of the most plausible structure of  $[Ag_{29}(BDT)_{12}(C_{60})_4]^{3-}$  is shown in Figure 1B(c).

The binding of fullerenes to the cluster was further supported by elemental analysis. The Ag/S/C atomic ratio for the fullerene adducts of the cluster as obtained from scanning electron microscopy (SEM)/energy-dispersive X-ray spectroscopy (EDS) was 1:0.82:9.07 (expected atomic ratio in  $[Ag_{29}(BDT)_{12}(C_{60})_4]^{3-}$  is 1:0.83:10.76) (Figure S7A). In the case of only the cluster, SEM/EDS showed a Ag/S/C atomic ratio of 1:0.80:2.26 (expected atomic ratio in  $[Ag_{29}(BDT)_{12}]^{3-}$  is 1:0.83:2.48) (Figure S7B). The percentage of C in the composite material ( $[Ag_{29}(BDT)_{12}(C_{60})_n]^{3-}$  ( $n = 1-4$ )) increased in comparison to the parent cluster ( $[Ag_{29}(BDT)_{12}]^{3-}$ ), and the atomic ratios were in close agreement with the expected atomic ratios from their molecular formulas. The slightly reduced carbon content in the experiment in comparison to the theoretical value in  $[Ag_{29}(BDT)_{12}(C_{60})_4]^{3-}$  was due to the various  $C_{60}$  adducts ( $n = 1-4$ ) possible in the sample.

**Collision-Induced Dissociation (CID) Studies.** We carried out CID studies on each of these complexes,  $[Ag_{29}(BDT)_{12}(C_{60})_n]^{3-}$  ( $n = 1-4$ ) (Figure 2) to gain further



insight into the structure and nature of interactions.<sup>42,43</sup> For the simplest case of one C<sub>60</sub> addition to the cluster, [Ag<sub>29</sub>(BDT)<sub>12</sub>(C<sub>60</sub>)]<sup>3−</sup>, upon increasing the collision energy (CE, instrumental unit), C<sub>60</sub> was lost from the cluster, and [Ag<sub>29</sub>(BDT)<sub>12</sub>]<sup>3−</sup> and C<sub>60</sub><sup>−</sup> were detected (Figure 2A). Apart from that, [Ag<sub>29</sub>(BDT)<sub>12</sub>]<sup>2−</sup> was also detected in very low intensities. The dissociation pattern was similar for the other higher complexes also, which showed sequential loss of C<sub>60</sub> molecules with an increase in CE. In Figure 2B, we have presented a CID spectra for [Ag<sub>29</sub>(BDT)<sub>12</sub>(C<sub>60</sub>)<sub>n</sub>]<sup>3−</sup> (*n* = 2–4) at CE 10. A systematic energy-dependent study is included in the Supporting Information (Figure S8). CID suggests that the probable fragmentation pathway of these complexes is by the loss of neutral C<sub>60</sub> molecules, as shown in Scheme 1.

Some contribution of charge separation during fragmentation leads to the formation of [Ag<sub>29</sub>(BDT)<sub>12</sub>]<sup>2−</sup> and C<sub>60</sub><sup>−</sup>. Even without any applied collision energy, some extent of dissociation was observed in all cases. Such a behavior was also reflected in the intensity pattern of the complexes observed in ESI MS, as shown in Figure 1B(a). Fragmentation during ionization thus complicates the exact quantification of the proportion of each of these complexes in solution.

**NMR Study.** NMR experiments were performed in order to evaluate the interaction between the cluster and the C<sub>60</sub> molecules (Figure 3). The <sup>13</sup>C NMR was taken in a binary

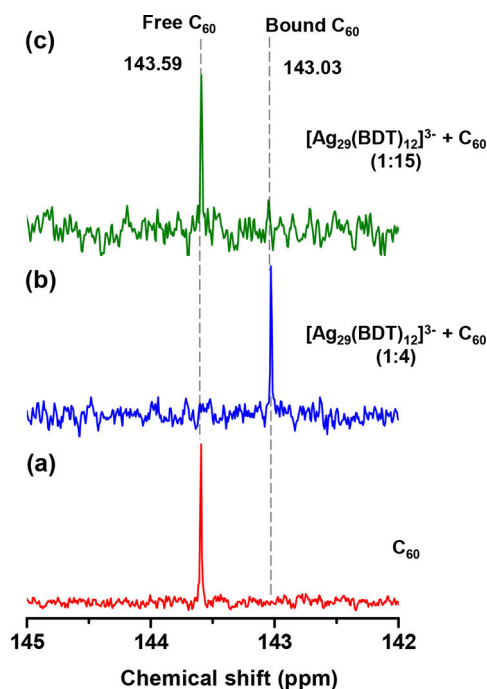


Figure 3. NMR of (a) C<sub>60</sub> showing a peak at 143.59 ppm, (b) adducts at a cluster/fullerene molar ratio of 1:4 showing a peak at 143.03 ppm for the C<sub>60</sub> molecules in the bound state, and (c) adducts at an excess concentration of C<sub>60</sub> (cluster/fullerene molar ratio of 1:15) showing a predominant peak for free C<sub>60</sub> (143.59 ppm) and a less intense peak for bound C<sub>60</sub> (143.03 ppm).

solvent mixture, DMF/toluene (2:1 v/v). The peak for C<sub>60</sub> was observed around 143.59 ppm (Figure 3a). NMR for the complexes was taken at a cluster/fullerene molar ratio of 1:4. Upon addition of the cluster, with no change in solvent composition, there was an upfield shift to 143.03 ppm (Figure 3b). Thus, when compared to the NMR of C<sub>60</sub> in the same

solvents, in the presence of the cluster, an upfield shift of about 0.56 ppm was seen, which can be attributed to the shielding effect of the  $\pi$ -conjugated system of C<sub>60</sub>.<sup>44–46</sup> This revealed that the electron density of C<sub>60</sub> was slightly increased in the presence of the clusters. Though at the 1:4 molar ratio, a single peak was observed for the C<sub>60</sub> molecules in their bound state, NMR of the adducts in the presence of excess fullerene (molar ratio of 1:15) showed a predominant peak for free C<sub>60</sub> and a low intense peak for bound C<sub>60</sub> (Figure 3c).

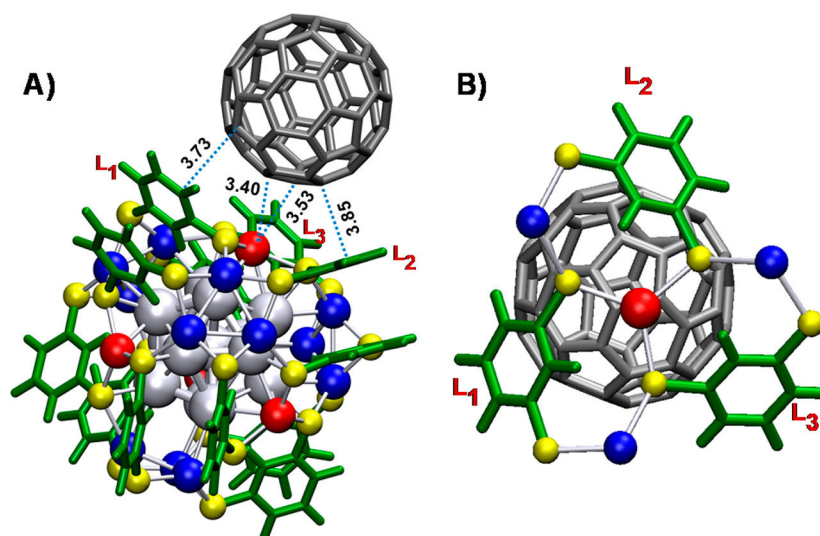
#### Formation of [Ag<sub>29</sub>(BDT)<sub>12</sub>(C<sub>60</sub>)<sub>n</sub>]<sup>3−</sup> (*n* > 4) Complexes.

Upon reaction of the cluster with an excess concentration of C<sub>60</sub> (cluster/fullerene molar ratio was 1:15), a higher number of attachments (*n* = 1–12) were observed in ESI MS, though at low intensities (Figure S9). This suggests that the cluster can become highly protected by the C<sub>60</sub> molecules so that the entire surface of the cluster is covered by fullerenes.

**Computational Modeling To Understand the Structures of [Ag<sub>29</sub>(BDT)<sub>12</sub>(C<sub>60</sub>)<sub>n</sub>]<sup>3−</sup> (*n* = 1–4, 8, and 9).** The interaction of the fullerenes, C<sub>60</sub> and C<sub>70</sub>, on the surface of [Ag<sub>29</sub>(BDT)<sub>12</sub>]<sup>3−</sup> cluster was computationally studied using DFT with the projector-augmented wave method as implemented in GPAW<sup>47,48</sup> using the Perdew–Burke–Ernzerhof (PBE) functional<sup>49</sup> and DZP (double- $\zeta$  plus polarization) LCAO basis set. We searched structures in DFT by attaching C<sub>60</sub>/C<sub>70</sub> at possible locations (tetrahedral vertex sites) on the cluster surface considering geometrical compatibility and stabilization by the supramolecular forces. The orientation of fullerenes at the cluster surface (to facilitate interaction with hexagonal (C<sub>6</sub>) face, pentagonal (C<sub>5</sub>) face, 6–6 bond, and 6–5 bond) was also varied to search the lowest energy conformers of the adducts. Complete computational details are included in the Supporting Information.

**Structure of [Ag<sub>29</sub>(BDT)<sub>12</sub>(C<sub>60</sub>)]<sup>3−</sup>. DFT Calculations.** The DFT-optimized geometry of the lowest energy isomer of [Ag<sub>29</sub>(BDT)<sub>12</sub>(C<sub>60</sub>)]<sup>3−</sup> with C<sub>60</sub> at the vertex position of the cluster, with a 6–5 bond of C<sub>60</sub> closest to the vertex Ag atom, is shown in Figure 4. The orientation of C<sub>60</sub> having a 6–5 bond closest to the metal center is known in the case of several C<sub>60</sub>/metalloporphyrin complexes.<sup>50</sup> However, the energy difference between the different calculated isomers of [Ag<sub>29</sub>(BDT)<sub>12</sub>(C<sub>60</sub>)]<sup>3−</sup> obtained by rotation of C<sub>60</sub> at the vertex site of the cluster was very narrow and was in the range of 0.044 eV (Table S1). The staples containing the three BDT ligands surrounding the vertex Ag atom of the cluster form a concave cavity suitable for embracing the convex  $\pi$ -surface of C<sub>60</sub><sup>51,52</sup> (Figure 4B), with  $\pi$ – $\pi$  interactions being the major promoting forces behind such host–guest complexation. The magnitude of the calculated binding energy (−16.77 kcal/mol) also confirms the contribution of the vdW interaction in the system. The fullerene is clasped in the bowl of the three BDT ligands but slightly off-center from the C<sub>3</sub> axis of the cluster passing through the vertex Ag atom and the center of the icosahedron. Hence, the interaction of the fullerene with the three BDT ligands surrounding the vertex position is not similar. The interaction is stronger with the closest contacts of 3.73 and 3.85 Å for two BDT ligands (marked as “L<sub>1</sub>” and “L<sub>2</sub>” in Figure 4) than the other ligand (marked as “L<sub>3</sub>”) lying at a distance of 4.19 Å.

Here, the stabilization of the cluster, [Ag<sub>29</sub>(BDT)<sub>12</sub>]<sup>3−</sup>, by the fullerene interacting at the vertex takes place in two ways. Initially, C<sub>60</sub> is captured by the benzene rings of BDT ligands through  $\pi$ – $\pi$  interactions. Later, C<sub>60</sub> stabilizes the unpassivated Ag atom by  $\eta^2$  interaction at a 6–5 bond of the fullerene.<sup>53–55</sup>



**Figure 4.** (A) DFT-optimized lowest energy structure of  $[\text{Ag}_{29}(\text{BDT})_{12}(\text{C}_{60})]^{3-}$  in which a fullerene interacts at a vertex position of the cluster. (B) Enlarged view of the staples around the vertex Ag atom showing how the three BDT ligands partially embrace the curved  $\pi$ -surface of  $\text{C}_{60}$ . The bond distances are in Å.

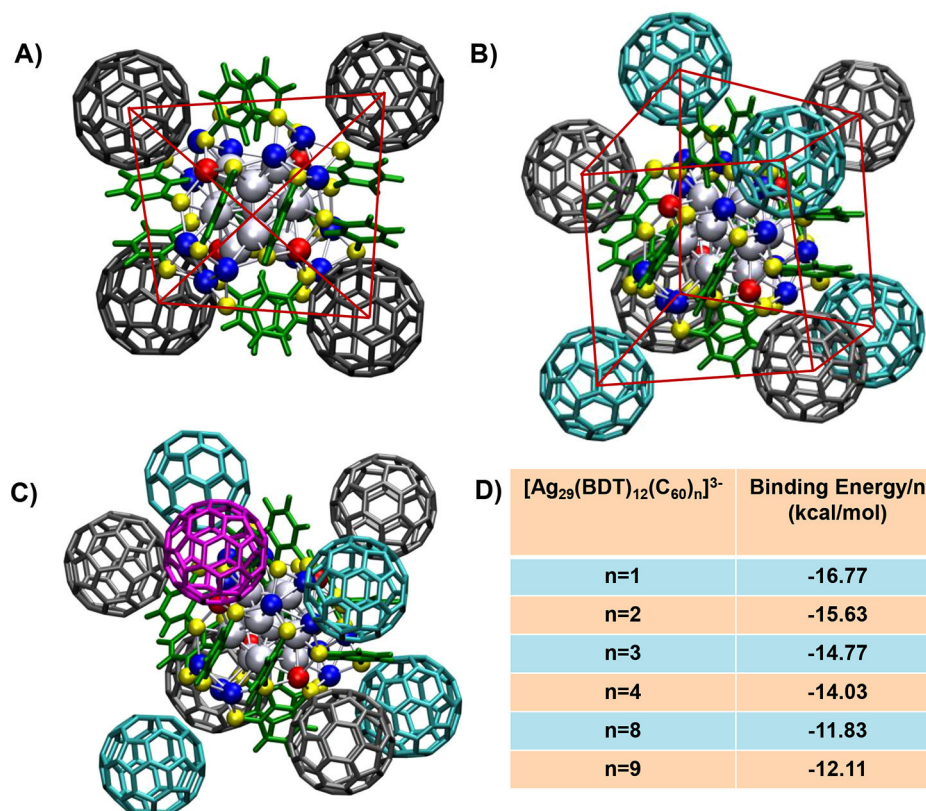
This is favored by ionic and vdW interactions formed between the positive charge accumulation on the Ag atom and the negative charge density localized on the 6–5 bonds of the fullerene, located at a distance of 3.40–3.53 Å from the Ag atom. The calculated Bader charges on the silver atom, Ag (+0.3080e) and on the carbon atoms of the 6–5 bond of fullerene (−0.0032e and −0.0170e) indicate weak ionic interactions. The total changes in Bader charges, including vacuum corrections on the individual molecules  $[\text{Ag}_{29}(\text{BDT})_{12}]^{3-}$  and  $\text{C}_{60}$  when these were in contact, were 0.35e and −0.50e, respectively, and this indicates that  $\text{C}_{60}$  acts as an electron acceptor and acquires a net charge of −0.15e from  $[\text{Ag}_{29}(\text{BDT})_{12}]^{3-}$ , and this imparts a partial ionic bonding in the adduct. This electron transfer also explains the chemical shift observed in the NMR measurements.

As the intermolecular interactions between the cluster and the fullerene were mainly dominated by the supramolecular effects, we also incorporated vdW correction in DFT. The lowest energy structure predicted by the vdW-DF2 functional (Figure S10) suggests slight changes in the orientation of fullerene as compared to the structure obtained by the PBE functional and allows closer contacts at a distance of 3.56 Å with the two BDT ligands and 3.67 Å with the third one. The relative contributions of  $\pi$ – $\pi$  interactions between the aromatic ligands and the fullerene *versus* electrostatic interactions between the fullerene and the Ag core depend on various factors such as the specific binding geometry, binding site, number of fullerenes, the size, and type of ligands. We carried out a computational study of the ligand binding energy in the case of the lowest energy isomer of  $[\text{Ag}_{29}(\text{BDT})_{12}(\text{C}_{60})]^{3-}$  (where  $\text{C}_{60}$  was attached at a tetrahedral vertex position) and found that 60% of the binding energy arises from the  $\pi$ – $\pi$  interactions. The remaining 40% arises from binding interactions of the metal core and surface  $\text{AgS}_3$  motif with  $\text{C}_{60}$  through weak ionic forces and associated van der Waals interactions. Binding at this vertex site would be most affected by the aromaticity of the ligands due to the proximity of the fullerene to the ligands. It may be assumed in this case that a smaller ligand than BDT might permit the  $\text{C}_{60}$  to come closer at the vertex site and possibly increase the ionic binding to the

$\text{AgS}_3$  motif. Complete computational details used for calculating the relative contributions of binding energy have been presented in the Supporting Information (Figure S11). The structure of  $[\text{Ag}_{29}(\text{BDT})_{12}(\text{C}_{60})]^{3-}$  was also optimized using the finite difference grid method of GPAW to obtain more accurate results and to verify the results from the more efficient LCAO basis method (Table S1).

We searched possibilities of other configurational isomers of  $[\text{Ag}_{29}(\text{BDT})_{12}(\text{C}_{60})]^{3-}$  in DFT by attaching  $\text{C}_{60}$  at the tetrahedrally oriented trigonal faces in the exterior shell of the cluster as the three partially exposed silver atoms at each of these faces may also exhibit some reactivity (Table S2). Though the calculated binding energy (−15.63 kcal/mol) indicates the possibility of some interaction, this was weaker compared to the interaction at the vertex position (−16.77 kcal/mol). We found that a  $\text{C}_{60}$  interacting at this position is at a distance of 3.54–3.81 Å from the Ag atoms, which is larger than the distance of 3.40–3.53 Å of a  $\text{C}_{60}$  at the vertex site, and the position lacks the  $\pi$ – $\pi$  interaction as the benzene rings of the BDT ligands are far away (Figure S12). DFT calculations show that binding of  $\text{C}_{60}$  at the vertex position of the cluster is the lowest energy isomer.

**Molecular Docking of  $[\text{Ag}_{29}(\text{BDT})_{12}]^{3-}$  with  $\text{C}_{60}$ .** To verify our lowest energy structure of  $[\text{Ag}_{29}(\text{BDT})_{12}(\text{C}_{60})]^{3-}$  obtained from the DFT studies based on the assumption that fullerenes would be seated in the tetrahedral symmetry positions, we further carried out a global structure search by molecular docking simulations using AutoDock4.2 and its associated software<sup>56</sup> to confirm the global minimum energy geometry of a cluster and a fullerene in close proximity. This approach was used as a complete search over all the relevant rotational, and translational degrees of freedom of the fullerene with respect to the cluster was unfeasible in DFT due to the computational cost. We used  $\text{C}_{60}$  (or  $\text{C}_{70}$ ) as the “ligand”, that is, the movable molecule. The “receptor” molecule was  $[\text{Ag}_{29}(\text{BDT})_{12}]^{3-}$ , and this was the fixed and completely rigid central molecule. For simplification, we did not use any torsion and charge parameters for the fullerene ligands. Bader charges from the optimized structures obtained in GPAW were used for all the atoms of  $[\text{Ag}_{29}(\text{BDT})_{12}]^{3-}$ .



**Figure 5.** DFT-optimized lowest energy structures of (A)  $[\text{Ag}_{29}(\text{BDT})_{12}(\text{C}_{60})_4]^{3-}$ , (B)  $[\text{Ag}_{29}(\text{BDT})_{12}(\text{C}_{60})_8]^{3-}$ , and (C)  $[\text{Ag}_{29}(\text{BDT})_{12}(\text{C}_{60})_9]^{3-}$ . Color codes:  $\text{C}_{60}$  at vertex position are black, at faces are cyan, and additional fullerene placed between the face and vertex in the case of  $[\text{Ag}_{29}(\text{BDT})_{12}(\text{C}_{60})_9]^{3-}$  is purple. (D) Table showing binding energy of the complexes.

The structure showing the lowest binding energy ( $-10.29$  kcal/mol) in the docking study is shown in Figure S13. It shows that  $\text{C}_{60}$  binds at the vertex position, and this further verifies that this position is the lowest energy site for attachment of a fullerene to the cluster.

The structure of this force-field global minimum geometry (FFGMG) of the adduct obtained from the docking studies has the  $\text{C}_{60}$  shifted further toward two of the BDT ligands and offset to a greater degree from the  $\text{C}_3$  axis passing through the center of the icosahedron and the vertex Ag atom. When the FFGMG of the adduct was used as an initial structure for DFT optimization (Figure S14), it showed a slightly higher binding energy ( $-16.37$  kcal/mol) compared to that of our lowest energy structure ( $-16.77$  kcal/mol) obtained from DFT studies by our initial symmetry-based method. Molecular docking simulation utilizes only noncovalent interactions and does not treat charge transfer. The distance of  $\text{C}_{60}$  from the Ag atom ( $4.18$  Å) is greater in the case of the FFGMG of the adduct. Also, there is stronger  $\pi$ - $\pi$  interaction with two BDT ligands ( $3.16$  and  $3.41$  Å) and no interaction with the third ligand (distance  $>5.89$  Å) in the case of the molecular docking simulation (Figure S13). These changes may be attributed to the energy differences observed in the DFT optimization of the FFGMG of the adduct compared to our initial DFT-optimized lowest energy structure. Hence, electronic charge transfer effects and weak bonding with the Ag atom also contribute substantially to the binding. Also due to the rigid ligand and the receptor, additional structural relaxations on the cluster and fullerene were forbidden in the force-field docking studies, which might contribute to lowering the total energy in DFT.

#### Structures of $[\text{Ag}_{29}(\text{BDT})_{12}(\text{C}_{60})_n]^{3-}$ ( $n = 2-4, 8$ , and $9$ ).

To reduce the computational cost, the structures of the other higher complexes,  $[\text{Ag}_{29}(\text{BDT})_{12}(\text{C}_{60})_n]^{3-}$  ( $n > 1$ ) were optimized only by using the PBE functional without vdW corrections, and some simplified results are presented (Table S3). Figure 5A shows the lowest energy optimized structure of  $[\text{Ag}_{29}(\text{BDT})_{12}(\text{C}_{60})_4]^{3-}$ , where the  $\text{C}_{60}$  molecules are attached at all four vertices. The structure is tetrahedral (see the 3D view in supplementary Video V2), and the fullerenes are well separated with no additional fullerene-fullerene interactions. Here, the preferred orientation of the 6-5 bond of  $\text{C}_{60}$  was preserved as in the case of  $n = 1$  for all the positions. In contrast, the lowest energy structures in the case of  $n = 2$  and  $3$  (Figure S15) preferred some other orientations of  $\text{C}_{60}$ . We could not find any systematic trend in the orientation of the fullerenes as a function of their number. This could be due to a change in overall symmetry of the structures that affect the overall electron delocalization. In all cases, the interaction was weak and the energy difference between the different orientations of  $\text{C}_{60}$  interacting at a particular site was very narrow, which suggests the possibility of isomerism in the complexes due to the rotation of fullerene molecules.

Experiments showed the attachment of  $n > 4$   $\text{C}_{60}$  to the cluster when reacted with an excess concentration of  $\text{C}_{60}$ . After all the tetrahedral vertex positions are occupied by the fullerenes, additional fullerenes may attach at the four tetrahedrally oriented trigonal faces formed by the 12 Ag atoms in the exterior shell. The calculated binding energy ( $-15.63$  kcal/mol) for  $\text{C}_{60}$  attaching at this position (Figure S12) supports such possibilities. Figure 5B shows the optimized structure of  $[\text{Ag}_{29}(\text{BDT})_{12}(\text{C}_{60})_8]^{3-}$ , where all the tetrahedral



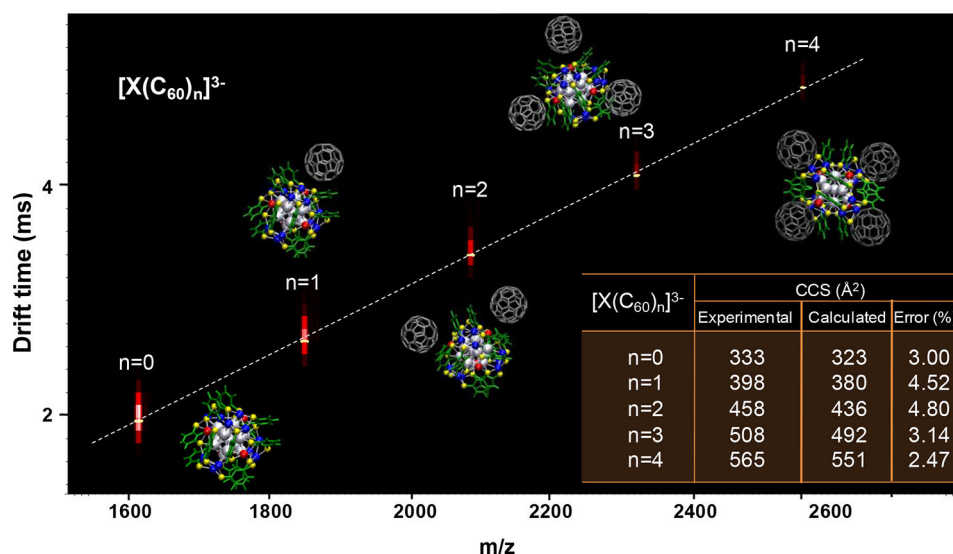


Figure 6. Plot of drift time of the complexes with their  $m/z$  values. Lowest energy structures of the species are shown beside their respective spots. Table in the inset of the figure shows the experimental and calculated CCS values.

vertex and face positions are occupied by  $C_{60}$  molecules. The overall geometry of  $[Ag_{29}(BDT)_{12}(C_{60})_8]^{3-}$  resembles a distorted cube (see the 3D view in [supporting Video V3](#)). The distortion is because of the nature of the asymmetric  $\pi$ – $\pi$  interaction of the BDT ligands. The length of the cube (indicated in [Figure S16](#)) is in the range of 12–15  $\text{\AA}$ , which is comparable to the lattice parameter (14.13  $\text{\AA}$ ) of the face-centered cubic lattice of  $C_{60}$ .<sup>57</sup>

Experiments show that an even greater number than eight attachments of  $C_{60}$  to the cluster is possible. The structure of  $[Ag_{29}(BDT)_{12}(C_{60})_9]^{3-}$  was constructed by adding another  $C_{60}$  facing the surface of  $[Ag_{29}(BDT)_{12}(C_{60})_8]^{3-}$ , between two  $C_{60}$  molecules located at a vertex and a face, as shown in [Figure 5C](#). The interaction of the ninth  $C_{60}$  was stronger in this position compared to other locations due to three different interactions. First, it introduces fullerene–fullerene  $\pi$ – $\pi$  interaction at a distance in the range of 3.18–3.42  $\text{\AA}$ . Further, it has  $\pi$ – $\pi$  interaction with one of the BDT ligands and interaction with one of the Ag atoms at the face. The calculated binding energies of the lowest energy structures of the adducts ( $[Ag_{29}(BDT)_{12}(C_{60})_n]^{3-}$  ( $n = 1$ –4, 8, and 9)) are listed in the table shown in [Figure 5D](#). The binding energy is found to decrease in magnitude with an increase in the number of  $C_{60}$  attachments due to the decrease in electrostatic interactions. As the number of fullerenes increases, more charge is transferred and the partial charges on the cluster decrease. This decreases the strength of the weak ionic interactions of the metal core and surface motif atoms with each fullerene, and thus the binding energy per fullerene decreases in magnitude. In the case of attachment of the ninth  $C_{60}$ , the binding energy increases in magnitude compared to that in the case of eight fullerenes due to its slightly different position between the face and vertex sites and additional fullerene–fullerene attractive vdW and  $\pi$ – $\pi$  interactions. Some additional possibilities of attachment of the ninth  $C_{60}$  over the two BDT ligands also exist ([Figure S17](#)). The addition of further fullerenes in a similar manner will form a sphere-like layer over the surface of the cluster.

**Structural Insights from Ion Mobility Mass Spectrometry (IM MS) Studies.** We used IM MS to further confirm the structure of the complexes,  $[Ag_{29}(BDT)_{12}(C_{60})_n]^{3-}$  ( $n = 1$ –4). [Figure 6](#) represents a 2D map showing the variation of the drift

time with the  $m/z$  of the species. While passing through a buffer gas, drift time of the molecules depends on their collision cross sections (CCSs). We calculated the CCS values of our DFT-optimized lowest energy structures using the projection approximation (PA) method with nitrogen as the buffer gas as implemented in the Mobcal program package<sup>58,59</sup> and compared them to the experimental values obtained from IM MS. The table in the inset of [Figure 6](#) shows the calculated and experimental CCS of  $[Ag_{29}(BDT)_{12}(C_{60})_n]^{3-}$  ( $n = 0$ –4).

We further constructed several other theoretical possibilities of other configurational isomers of the complexes and calculated their CCS values by the PA method to set narrow bounds to our lowest energy structures.<sup>60</sup> [Figure S18](#) shows other less favorable structures of  $[Ag_{29}(BDT)_{12}(C_{60})_4]^{3-}$  with all  $C_{60}$  molecules attached at (a) the faces of the tetrahedrally oriented trigonal planes in the exterior shell of the cluster (CCS 580  $\text{\AA}^2$ , error 2.65% greater with respect to experimental CCS), (b) crowded around one vertex site of the cluster by fullerene–fullerene interaction (CCS 516  $\text{\AA}^2$ , error 8.6% less with respect to experimental CCS), and (c) over the BDT ligands (CCS 598  $\text{\AA}^2$ , error 5.84% greater with respect to experimental CCS). In all cases, the error in the CCS with respect to the experimental values are larger compared to the structure with  $C_{60}$  molecules attached at the four vertices.

IM MS study did not show the presence of any other isomers, which clearly confirms that one stable structure for  $[Ag_{29}(BDT)_{12}(C_{60})_4]^{3-}$  is formed by attachment of  $C_{60}$  molecules at the vertex positions on the surface of the cluster.

**Confirmation of the  $C_{60}$  Binding Sites.** The vertex Ag atoms of the cluster are also known to be functionalized by TPP ligands in case of  $[Ag_{29}(BDT)_{12}(TPP)_4]^{3-}$ .<sup>12</sup> When TPP was added to the cluster–fullerene complexes,  $[Ag_{29}(BDT)_{12}(C_{60})_n]^{3-}$  ( $n = 1$ –4),  $C_{60}$  molecules were immediately replaced by TPP and  $[Ag_{29}(BDT)_{12}(TPP)_n]^{3-}$  ( $n = 1$ –4) was formed ([Figure S19](#)). This further confirmed the position of the  $C_{60}$  attachment on the cluster surface. We have also tried to exchange the TPP ligands from the  $[Ag_{29}(BDT)_{12}(TPP)_4]^{3-}$  cluster with  $C_{60}$ , but such replacement was not favorable. The formation of the Ag–P bond passivates the Ag atom to a greater extent compared to that of the fullerenes which exhibit only weak vdW and electrostatic interactions. Hence, we

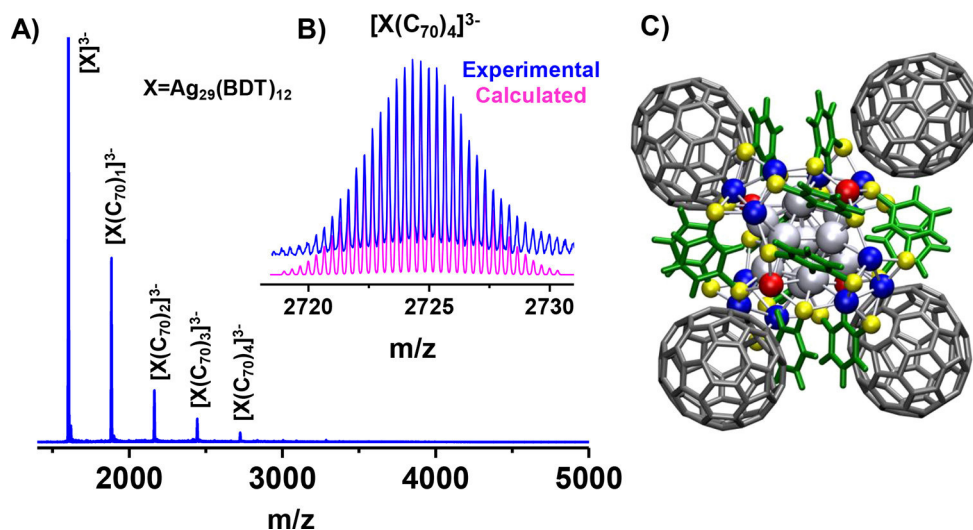


Figure 7. (A) ESI MS of  $[Ag_{29}(BDT)_{12}(C_{70})_n]^{3-}$  ( $n = 1-4$ ), (B) experimental and calculated isotope patterns of  $[Ag_{29}(BDT)_{12}(C_{70})_4]^{3-}$ , and (C) DFT-optimized lowest energy structure of  $[Ag_{29}(BDT)_{12}(C_{70})_4]^{3-}$ .

observed a competitive binding. We have also studied if there was any effect of electrostatic shielding on the binding of fullerenes. For this, salts such as NaCl, KCl, or KOAc were added to the solutions, but salts did not inhibit the binding of fullerenes (Figure S20).

**Characterization of the Complexes of C<sub>70</sub> with  $[Ag_{29}(BDT)_{12}]^{3-}$ .** The cluster exhibited similar reactivity with another fullerene, C<sub>70</sub>. At an optimum cluster/C<sub>70</sub> molar ratio of 1:4, up to four C<sub>70</sub> attachments to the cluster were observed in ESI MS (Figure 7). As discussed in the case of C<sub>60</sub>, UV–vis studies (Figure S21), CID (Figure S22), replacement of C<sub>70</sub> with TPP (Figure S23), and higher attachments at an excess concentration of C<sub>70</sub> (Figure S24) reflected similar behavior. DFT calculations and molecular docking simulations further confirmed the formation of similar structures. Complete details are included in the Supporting Information (Figures S25–S29 and Table S4).

The DFT-optimized lowest energy structure of  $[Ag_{29}(BDT)_{12}(C_{70})]^{3-}$  (Figure S25) shows that C<sub>70</sub> lies at a distance of 3.42–3.55 Å from the vertex Ag atom, similar to that of C<sub>60</sub> (3.40–3.53 Å). However, due to its larger size, C<sub>70</sub> exhibits stronger  $\pi$ – $\pi$  binding interaction with the aromatic ligands compared to C<sub>60</sub> with a closer contact of 3.32 and 3.49 Å with the two BDT ligands. For C<sub>60</sub>, distance from two nearest BDT ligands was 3.73 and 3.85 Å, as calculated using the PBE functional. C<sub>70</sub> is similarly far from the third BDT ligand at a distance of 4.36 Å. Stronger interaction is also reflected in the binding energy value of –18.68 kcal/mol for the lowest energy structure of  $[Ag_{29}(BDT)_{12}(C_{70})]^{3-}$  compared to –16.77 kcal/mol for  $[Ag_{29}(BDT)_{12}(C_{60})]^{3-}$ . The structures of  $[Ag_{29}(BDT)_{12}(C_{70})_n]^{3-}$  ( $n = 2-4$ ) (Figure S29) were also similar to that of C<sub>60</sub>. The lowest energy structure for  $n = 4$  (BE = –15.59 kcal/mol) is presented in Figure 7B. The calculated CCS values of the DFT-optimized lowest energy structures of the complexes,  $[Ag_{29}(BDT)_{12}(C_{70})_n]^{3-}$  ( $n = 1-4$ ), also matched well with the experimental CCS obtained from the IM MS study (Figure S30). The orientational changes in C<sub>70</sub> were more significant compared to C<sub>60</sub>, and this can be attributed to the larger size and ellipsoidal shape of C<sub>70</sub>, which affects the  $\pi$ – $\pi$  and vdW interactions significantly.

## CONCLUSION

In summary, we demonstrate that adducts of fullerenes are formed with monolayer-protected clusters. The complexation was assisted due to the compatible structure of the cluster and the orientation of the ligands that form tetrahedral concave cavities at the cluster surface, compatible with the convex  $\pi$ -surface of fullerenes. DFT calculations and molecular docking simulations show that vdW and  $\pi$ – $\pi$  interactions along with some weak binding with the Ag atoms facilitated the formation of the cluster–fullerene conjugates. Although our study was centered around a detailed discussion of the interaction of fullerenes C<sub>60</sub> and C<sub>70</sub> with one specific cluster,  $[Ag_{29}(BDT)_{12}]^{3-}$ , it can be extended to other monolayer-protected clusters, as well. Creating such cluster–fullerene composites in the solid state would further expand research in this field. Such composites can be interesting materials for study not only because of their structures but also due to their properties such as electrical conductivity, photoinduced charge transfer, as well as optical and mechanical properties. They can find applications in photovoltaics, sensors, and even in medical science.

## EXPERIMENTAL SECTION

**Reagents and Materials.** All the materials except the clusters were commercially available and used without further purification. Silver nitrate (AgNO<sub>3</sub>, 99.9%) was purchased from Rankem, India. 1,3-Benzenedithiol (1,3-BDT), sodium borohydride (NaBH<sub>4</sub>), and fullerenes C<sub>60</sub> (99.5%) and C<sub>70</sub> (98%) were purchased from Sigma-Aldrich. Triphenylphosphine (TPP) was purchased from Spectrochem, India. All the solvents, dichloromethane (DCM), methanol (MeOH), ethanol (EtOH), dimethylformamide (DMF), and toluene were of the HPLC grade and were used without further distillation. Deuterated solvents DMF-*d*<sub>7</sub> and toluene-*d*<sub>8</sub>, used for NMR measurements, were purchased from Sigma-Aldrich.

**Instrumentation.** The UV–vis spectra were measured using a PerkinElmer Lambda 25 UV–vis spectrophotometer. Mass spectrometric measurements were done in a Waters Synapt G2-Si high-definition mass spectrometer. The instrument was well equipped with electrospray ionization and ion mobility separation techniques. NMR measurements were done in a Bruker 500 MHz NMR spectrometer. SEM and EDS analyses were performed in a FEI QUANTA-200 SEM. Further details of instrumentation are mentioned in the Supporting Information.

**Synthesis of  $[\text{Ag}_{29}(\text{BDT})_{12}]^{3-}$  Clusters.**  $[\text{Ag}_{29}(\text{BDT})_{12}]^{3-}$  clusters were synthesized following a reported protocol<sup>12</sup> with slight modifications. About 20 mg of  $\text{AgNO}_3$  was dissolved in a mixture of 2 mL of methanol and 10 mL of DCM. To this reaction mixture, about 13.5  $\mu\text{L}$  of the 1,3-BDT ligand was added. The mixture was stirred for about 15 min, and then about 10.5 mg of  $\text{NaBH}_4$  dissolved in 500  $\mu\text{L}$  of ice-cold water was added. The stirring was continued under dark conditions for about 5 h. Then, the reaction mixture was centrifuged, the precipitate was discarded, and the clusters were obtained as the orange supernatant. The solution was evaporated by rotary evaporation, and the orange residue was washed with methanol and finally dissolved in DMF. The solution was characterized by UV–vis and ESI MS, which confirmed the formation of  $[\text{Ag}_{29}(\text{BDT})_{12}]^{3-}$  clusters (Figure S1). However, as the clusters were synthesized without the TPP ligands, they were stable only for a few hours.<sup>12</sup>

**Synthesis of  $[\text{Ag}_{29}(\text{BDT})_{12}(\text{C}_{60})_n]^{3-}$  Complexes.** Immediately after the synthesis of  $[\text{Ag}_{29}(\text{BDT})_{12}]^{3-}$  clusters, a solution of  $\text{C}_{60}$  (in toluene) was added to the cluster solution in DMF. The addition of fullerenes increased the stability of the clusters significantly. The reactivity was monitored using UV–vis and ESI MS studies. The addition of another fullerene,  $\text{C}_{70}$ , also showed a similar behavior.

**Computational Methods.** The interaction of the fullerenes,  $\text{C}_{60}$  and  $\text{C}_{70}$ , on the surface of the  $[\text{Ag}_{29}(\text{BDT})_{12}]^{3-}$  cluster was computationally studied using DFT with the projector-augmented wave method as implemented in GPAW<sup>47,48</sup> using the PBE functional<sup>49</sup> and DZP (double- $\zeta$  plus polarization) LCAO basis set. We searched structures in DFT by attaching  $\text{C}_{60}/\text{C}_{70}$  at possible locations (tetrahedral sites) on the cluster surface considering geometrical compatibility and stabilization by the supramolecular forces. After identifying the most favorable binding site, we generated the structures of  $[\text{Ag}_{29}(\text{BDT})_{12}(\text{C}_{60})_n]^{3-}$  ( $n = 1\text{--}4, 8$ , and  $9$ ) based on symmetry considerations, and the structures were optimized in DFT. The orientation of fullerenes at the cluster surface (to facilitate interaction with hexagonal ( $\text{C}_6$ ) face, pentagonal ( $\text{C}_5$ ) face, 6–6 bond, and 6–5 bond) was varied to search the lowest energy conformers of the adducts. In addition, we verified the lowest energy structure of  $[\text{Ag}_{29}(\text{BDT})_{12}(\text{C}_{60})]^{3-}$  by molecular docking simulations using AutoDock4.2 and its associated software<sup>56</sup> to confirm the global minimum energy geometry of a cluster and a fullerene in close proximity, subject to some constraints, which we then optimized in DFT and compared the energy and geometry with our initial DFT-optimized lowest energy structure. Furthermore, in some cases, we optimized the structures using the finite-difference method in GPAW and also by using a van der Waals functional. The CCS of the DFT-optimized structures was calculated with the PA with nitrogen as the buffer gas as implemented in the Mobcal program package.<sup>58,59</sup> Complete computational details are included in the Supporting Information.

## ASSOCIATED CONTENT

### Supporting Information

The Supporting Information is available free of charge on the ACS Publications website at DOI: 10.1021/acsnano.7b07759.

Instrumentation, computational methods, optical absorption studies, additional ESI MS for the characterization of the cluster-fullerene adducts, and complete computational details for all possible isomers of the complexes (PDF)

Video V1: 3D view of the structure of  $[\text{Ag}_{29}(\text{BDT})_{12}]^{3-}$  (MPG)

Video V2: 3D view of the structure of  $[\text{Ag}_{29}(\text{BDT})_{12}(\text{C}_{60})_4]^{3-}$  (MPG)

Video V3: 3D view of the structure of  $[\text{Ag}_{29}(\text{BDT})_{12}(\text{C}_{60})_8]^{3-}$  (MPG)

## AUTHOR INFORMATION

### Corresponding Author

\*E-mail: pradeep@iitm.ac.in.

### ORCID

Thalappil Pradeep: 0000-0003-3174-534X

### Author Contributions

P.C. synthesized the clusters, designed and conducted all experiments. P.C. and A.N. carried out the ESI MS measurements, G.P. carried out the DFT calculations, A.N. and G.N. carried out the molecular docking simulations. The computational part was supervised by G.N., and the whole project was supervised by T.P. The manuscript was written through contributions of all authors.

### Notes

The authors declare no competing financial interest.

## ACKNOWLEDGMENTS

P.C. thanks the Council of Scientific and Industrial Research (CSIR) for a research fellowship. A.N. thanks IIT Madras for an Institute Doctoral fellowship. G.P. thanks IIT Madras for an Institute Postdoctoral fellowship. We thank the Department of Science and Technology, Government of India, for continuous support of our research program.

## REFERENCES

- (1) Chakraborty, I.; Pradeep, T. Atomically Precise Clusters of Noble Metals: Emerging Link between Atoms and Nanoparticles. *Chem. Rev.* **2017**, *117*, 8208–8271.
- (2) Jin, R.; Zeng, C.; Zhou, M.; Chen, Y. Atomically Precise Colloidal Metal Nanoclusters and Nanoparticles: Fundamentals and Opportunities. *Chem. Rev.* **2016**, *116*, 10346–10413.
- (3) Mathew, A.; Pradeep, T. Noble Metal Clusters: Applications in Energy, Environment, and Biology. *Part. Part. Syst. Char.* **2014**, *31*, 1017–1053.
- (4) Fang, J.; Zhang, B.; Yao, Q.; Yang, Y.; Xie, J.; Yan, N. Recent Advances in the Synthesis and Catalytic Applications of Ligand-Protected, Atomically Precise Metal Nanoclusters. *Coord. Chem. Rev.* **2016**, *322*, 1–29.
- (5) Heaven, M. W.; Dass, A.; White, P. S.; Holt, K. M.; Murray, R. W. Crystal Structure of the Gold Nanoparticle  $[\text{N}(\text{C}_8\text{H}_{17})_4]^-[\text{Au}_{25}(\text{SCH}_2\text{CH}_2\text{Ph})_{18}]$ . *J. Am. Chem. Soc.* **2008**, *130*, 3754–3755.
- (6) Zhu, M.; Aikens, C. M.; Hollander, F. J.; Schatz, G. C.; Jin, R. Correlating the Crystal Structure of a Thiol-Protected  $\text{Au}_{25}$  Cluster and Optical Properties. *J. Am. Chem. Soc.* **2008**, *130*, 5883–5885.
- (7) Lopez-Acevedo, O.; Tsunoyama, H.; Tsukuda, T.; Häkkinen, H.; Aikens, C. M. Chirality and Electronic Structure of the Thiolate-Protected  $\text{Au}_{38}$  Nanocluster. *J. Am. Chem. Soc.* **2010**, *132*, 8210–8218.
- (8) Jadzinsky, P. D.; Calero, G.; Ackerson, C. J.; Bushnell, D. A.; Kornberg, R. D. Structure of a Thiol Monolayer-Protected Gold Nanoparticle at 1.1 Å Resolution. *Science* **2007**, *318*, 430–433.
- (9) Joshi, C. P.; Bootharaju, M. S.; Alhilaly, M. J.; Bakr, O. M.  $[\text{Ag}_{25}(\text{SR})_{18}]^-$ : The “Golden” Silver Nanoparticle. *J. Am. Chem. Soc.* **2015**, *137*, 11578–11581.
- (10) Yang, H.; Wang, Y.; Huang, H.; Gell, L.; Lehtovaara, L.; Malola, S.; Häkkinen, H.; Zheng, N. All-Thiol-Stabilized  $\text{Ag}_{44}$  and  $\text{Au}_{12}\text{Ag}_{32}$  Nanoparticles with Single-Crystal Structures. *Nat. Commun.* **2013**, *4*, 2422.
- (11) Desireddy, A.; Conn, B. E.; Guo, J.; Yoon, B.; Barnett, R. N.; Monahan, B. M.; Kirschbaum, K.; Griffith, W. P.; Whetten, R. L.; Landman, U.; Bigioni, T. P. Ultrastable Silver Nanoparticles. *Nature* **2013**, *501*, 399–402.
- (12) AbdulHalim, L. G.; Bootharaju, M. S.; Tang, Q.; Del Gobbo, S.; AbdulHalim, R. G.; Eddaoudi, M.; Jiang, D.-e.; Bakr, O. M.  $[\text{Ag}_{29}(\text{BDT})_{12}(\text{TPP})_4]^-$ : A Tetravalent Nanocluster. *J. Am. Chem. Soc.* **2015**, *137*, 11970–11975.



- (13) Lu, Y.; Chen, W. Application of Mass Spectrometry in the Synthesis and Characterization of Metal Nanoclusters. *Anal. Chem.* **2015**, *87*, 10659–10667.
- (14) Harkness, K. M.; Cliffl, D. E.; McLean, J. A. Characterization of Thiolate-Protected Gold Nanoparticles by Mass Spectrometry. *Analyst* **2010**, *135*, 868–874.
- (15) Weerawardene, K. L. D. M.; Aikens, C. M. Theoretical Insights into the Origin of Photoluminescence of  $\text{Au}_{25}(\text{SR})_{18}^-$  Nanoparticles. *J. Am. Chem. Soc.* **2016**, *138*, 11202–11210.
- (16) Dou, X.; Yuan, X.; Yu, Y.; Luo, Z.; Yao, Q.; Leong, D. T.; Xie, J. Lighting up Thiolated Au@Ag Nanoclusters via Aggregation-Induced Emission. *Nanoscale* **2014**, *6*, 157–161.
- (17) Mathew, A.; Natarajan, G.; Lehtovaara, L.; Häkkinen, H.; Kumar, R. M.; Subramanian, V.; Jaleel, A.; Pradeep, T. Supramolecular Functionalization and Concomitant Enhancement in Properties of  $\text{Au}_{25}$  Clusters. *ACS Nano* **2014**, *8*, 139–152.
- (18) Martin, N.; Nierengarten, J. F. *Supramolecular Chemistry of Fullerenes and Carbon Nanotubes*; Wiley-VCH, 2012; p 403.
- (19) Tashiro, K.; Aida, T. Metalloporphyrin Hosts for Supramolecular Chemistry of Fullerenes. *Chem. Soc. Rev.* **2007**, *36*, 189–197.
- (20) Diederich, F.; Gomez-Lopez, M. Supramolecular Fullerene Chemistry. *Chem. Soc. Rev.* **1999**, *28*, 263–277.
- (21) Schuster, D. I.; Li, K.; Guldi, D. M.; Ramey, J. Novel Porphyrin-Fullerene Assemblies: from Rotaxanes to Catenanes. *Org. Lett.* **2004**, *6*, 1919–1922.
- (22) Haino, T.; Yanase, M.; Fukazawa, Y. Crystalline Supramolecular Complexes of  $\text{C}_{60}$  with Calix[5]arenes. *Tetrahedron Lett.* **1997**, *38*, 3739–3742.
- (23) Murthy, C. N.; Geckeler, K. E. The Water-Soluble  $[\beta]$ -Cyclodextrin- $[\text{C}_{60}]$  Fullerene Complex. *Chem. Commun.* **2001**, 1194–1195.
- (24) Fileti, E.; Colherinhas, G.; Malaspina, T. Predicting the Properties of a New Class of Host-Guest Complexes:  $\text{C}_{60}$  Fullerene and CB[9] Cucurbituril. *Phys. Chem. Chem. Phys.* **2014**, *16*, 22823–22829.
- (25) Moreira, L.; Calbo, J.; Krick Calderon, R. M.; Santos, J.; Illescas, B. M.; Arago, J.; Nierengarten, J. F.; Guldi, D. M.; Orti, E.; Martin, N. Unveiling the Nature of Supramolecular Crown Ether- $\text{C}_{60}$  Interactions. *Chem. Sci.* **2015**, *6*, 4426–4432.
- (26) Boyd, P. D. W.; Hodgson, M. C.; Rickard, C. E. F.; Oliver, A. G.; Chaker, L.; Brothers, P. J.; Bolskar, R. D.; Tham, F. S.; Reed, C. A. Selective Supramolecular Porphyrin/Fullerene Interactions. *J. Am. Chem. Soc.* **1999**, *121*, 10487–10495.
- (27) Sun, D.; Tham, F. S.; Reed, C. A.; Chaker, L.; Boyd, P. D. W. Supramolecular Fullerene-Porphyrin Chemistry. Fullerene Complexation by Metalated “Jaws Porphyrin” Hosts. *J. Am. Chem. Soc.* **2002**, *124*, 6604–6612.
- (28) Wang, Y.-B.; Lin, Z. Supramolecular Interactions between Fullerenes and Porphyrins. *J. Am. Chem. Soc.* **2003**, *125*, 6072–6073.
- (29) Yamamura, M.; Hongo, D.; Nabeshima, T. Twofold Fused Concave Hosts Containing Two Phosphorus Atoms: Modules for the Sandwich-Type Encapsulation of Fullerenes in Variable Cavities. *Chem. Sci.* **2015**, *6*, 6373–6378.
- (30) Sun, D.; Tham, F. S.; Reed, C. A.; Chaker, L.; Burgess, M.; Boyd, P. D. W. Porphyrin–Fullerene Host–Guest Chemistry. *J. Am. Chem. Soc.* **2000**, *122*, 10704–10705.
- (31) Haddon, R. C. Electronic structure, Conductivity and Superconductivity of Alkali Metal Doped  $\text{C}_{60}$ . *Acc. Chem. Res.* **1992**, *25*, 127–33.
- (32) Stephens, P. W.; Mihaly, L.; Lee, P. L.; Whetten, R. L.; Huang, S.-M.; Kaner, R.; Diederich, F.; Holczer, K. Structure of Single-Phase Superconducting  $\text{K}_3\text{C}_{60}$ . *Nature* **1991**, *351*, 632–634.
- (33) Rosseinsky, M. J.; Ramirez, A. P.; Glarum, S. H.; Murphy, D. W.; Haddon, R. C.; Hebard, A. F.; Palstra, T. T. M.; Kortan, A. R.; Zahurak, S. M.; Makhija, A. V. Superconductivity at 28 K in  $\text{Rb}_x\text{C}_{60}$ . *Phys. Rev. Lett.* **1991**, *66*, 2830–2832.
- (34) Hebard, A. F.; Rosseinsky, M. J.; Haddon, R. C.; Murphy, D. W.; Glarum, S. H.; Palstra, T. T. M.; Ramirez, A. P.; Kortan, A. R. Superconductivity at 18 K in Potassium-Doped  $\text{C}_{60}$ . *Nature* **1991**, *350*, 600–601.
- (35) Holczer, K.; Klein, O.; Huang, S.-m.; Kaner, R. B.; Fu, K. J.; Whetten, R. L.; Diederich, F. Alkali-Fulleride Superconductors: Synthesis, Composition, and Diamagnetic Shielding. *Science* **1991**, *252*, 1154.
- (36) Plotniece, M.; Kampars, V. Review: Novel Donor-Acceptor Systems of Tetrathiafulvalenes-Fullerene  $\text{C}_{60}$  (TTF- $\text{C}_{60}$ ). *Rigas Teh. Univ. Zinat. Raksti, Ser. 1* **2005**, *10*, 23–36.
- (37) Pradeep, T.; Singh, K. K.; Sinha, A. P. B.; Morris, D. E. A Stable Fullerene Charge-Transfer Complex in the Solid State: HMTTEF- $\text{C}_{60}$ . *J. Chem. Soc., Chem. Commun.* **1992**, 1747–1748.
- (38) Konarev, D. V.; Lyubovskaya, R. N.; Semkin, V. N.; Graja, A. Donor-Acceptor Interactions in  $\text{C}_{60}$  Complexes with Initially Planar  $\pi$ -Donors. *Mol. Cryst. Liq. Cryst. Sci. Technol., Sect. C* **1998**, *11*, 35–42.
- (39) Konarev, D. V.; Lyubovskaya, R. N.; Drichko, N. y. V.; Yudanova, E. I.; Shul'ga, Y. M.; Litvinov, A. L.; Semkin, V. N.; Tarasov, B. P. Donor-Acceptor Complexes of Fullerene  $\text{C}_{60}$  with Organic and Organometallic Donors. *J. Mater. Chem.* **2000**, *10*, 803–818.
- (40) Konarev, D. V.; Semkin, V. N.; Graja, A.; Lyubovskaya, R. N. Steric Conditions for Donor–Acceptor Interactions in  $\text{C}_{60}$  Complexes with Planar Organic Donors. *J. Mol. Struct.* **1998**, *450*, 11–22.
- (41) Pursell, J. L.; Pursell, C. J. Host–Guest Inclusion Complexation of  $\alpha$ -Cyclodextrin and Triiodide Examined Using UV–Vis Spectrophotometry. *J. Phys. Chem. A* **2016**, *120*, 2144–2149.
- (42) Wood, J. M.; Kahr, B.; Hoke, S. H.; Dejarne, L.; Cooks, R. G.; Ben-Amotz, D. Oxygen and Methylene Adducts of  $\text{C}_{60}$  and  $\text{C}_{70}$ . *J. Am. Chem. Soc.* **1991**, *113*, 5907–5908.
- (43) Morand, K. L.; Hoke, S. H.; Eberlin, M. N.; Payne, G.; Cooks, R. G. Quadrupole Ion Trap Mass Spectrometry of Fullerenes. *Org. Mass Spectrom.* **1992**, *27*, 284–288.
- (44) Okada, H.; Komuro, T.; Sakai, T.; Matsuo, Y.; Ono, Y.; Omote, K.; Yokoo, K.; Kawachi, K.; Kasama, Y.; Ono, S.; Hatakeyama, R.; Kaneko, T.; Tobita, H. Preparation of Endohedral Fullerene Containing Lithium ( $\text{Li}@\text{C}_{60}$ ) and Isolation as Pure Hexafluorophosphate Salt ( $[\text{Li}^+@\text{C}_{60}][\text{PF}_6^-]$ ). *RSC Adv.* **2012**, *2*, 10624–10631.
- (45) Haino, T.; Yanase, M.; Fukunaga, C.; Fukazawa, Y. Fullerene Encapsulation with Calix[5]arenes. *Tetrahedron* **2006**, *62*, 2025–2035.
- (46) Anderson, T. K. W.; Sanders, J. K. M.; Pantos, G. D. The Sergeants-and-Soldiers Effect: Chiral Amplification in Naphthalene-diimide Nanotubes. *Org. Biomol. Chem.* **2010**, *8*, 4274–4280.
- (47) Mortensen, J. J.; Hansen, L. B.; Jacobsen, K. W. Real-Space Grid Implementation of the Projector Augmented Wave Method. *Phys. Rev. B: Condens. Matter Mater. Phys.* **2005**, *71*, 035109.
- (48) Enkovaara, J.; Rostgaard, C.; Mortensen, J. J.; Chen, J.; Dulak, M.; Ferrighi, L.; Gavnholt, J.; Glinisvad, C.; Haikola, V.; Hansen, H. A.; Kristoffersen, H. H.; Kuisma, M.; Larsen, A. H.; Lehtovaara, L.; Ljungberg, M.; Lopez-Acevedo, O.; Moses, P. G.; Ojanen, J.; Olsen, T.; Petzold, V.; et al. Electronic Structure Calculations with GPAW: a Real-Space Implementation of the Projector Augmented-Wave Method. *J. Phys.: Condens. Matter* **2010**, *22*, 253202.
- (49) Perdew, J. P.; Burke, K.; Ernzerhof, M. Generalized Gradient Approximation Made Simple. *Phys. Rev. Lett.* **1997**, *78*, 1396–1396.
- (50) Ishii, T.; Aizawa, N.; Yamashita, M.; Matsuzaka, H.; Kodama, T.; Kikuchi, K.; Ikemoto, I.; Iwasa, Y. First Syntheses of Cocrystallites Consisting of Anti-formed Metal Octaethylporphyrins with Fullerene  $\text{C}_{60}$ . *J. Chem. Soc., Dalton Trans.* **2000**, 4407–4412.
- (51) Filatov, A. S.; Ferguson, M. V.; Spisak, S. N.; Li, B.; Campana, C. F.; Petrukhina, M. A. Bowl-Shaped Polyarenes as Concave–Convex Shape Complementary Hosts for  $\text{C}_{60}^-$  and  $\text{C}_{70}^-$  Fullerenes. *Cryst. Growth Des.* **2014**, *14*, 756–762.
- (52) Perez, E. M.; Martin, N. Curves Ahead: Molecular Receptors for Fullerenes Based on Concave-Convex Complementarity. *Chem. Soc. Rev.* **2008**, *37*, 1512–1519.
- (53) Jayaratna, N. B.; Olmstead, M. M.; Kharisov, B. I.; Dias, H. V. R. Coinage Metal Pyrazolates  $[(3,5-(\text{CF}_3)_2\text{Pz})\text{M}]_3$  ( $\text{M} = \text{Au}, \text{Ag}, \text{Cu}$ ) as Buckycatchers. *Inorg. Chem.* **2016**, *55*, 8277–8280.



- (54) Halim, M.; Kennedy, R. D.; Suzuki, M.; Khan, S. I.; Diaconescu, P. L.; Rubin, Y. Complexes of Gold(I), Silver(I), and Copper(I) with Pentaaryl[60]fullerides. *J. Am. Chem. Soc.* **2011**, *133*, 6841–6851.
- (55) Olmstead, M. M.; Maitra, K.; Balch, A. L. Formation of a Curved Silver Nitrate Network that Conforms to the Shape of  $C_{60}$  and Encapsulates the Fullerene-Structural Characterization of  $C_{60}\{Ag-(NO_3)\}_5$ . *Angew. Chem., Int. Ed.* **1999**, *38*, 231–233.
- (56) Morris, G. M.; Huey, R.; Lindstrom, W.; Sanner, M. F.; Belew, R. K.; Goodsell, D. S.; Olson, A. J. AutoDock4 and AutoDockTools4: Automated Docking with Selective Receptor Flexibility. *J. Comput. Chem.* **2009**, *30*, 2785–2791.
- (57) Quo, Y.; Karasawa, N.; Goddard, W. A. Prediction of Fullerene Packing in  $C_{60}$  and  $C_{70}$  Crystals. *Nature* **1991**, *351*, 464–467.
- (58) von Helden, G.; Hsu, M. T.; Gotts, N.; Bowers, M. T. Carbon Cluster Cations with up to 84 Atoms: Structures, Formation Mechanism, and Reactivity. *J. Phys. Chem.* **1993**, *97*, 8182–8192.
- (59) Shvartsburg, A. A.; Jarrold, M. F. An Exact Hard-Spheres Scattering Model for the Mobilities of Polyatomic Ions. *Chem. Phys. Lett.* **1996**, *261*, 86–91.
- (60) Greisch, J. F.; Amsharov, K. Y.; Weippert, J.; Weis, P.; Böttcher, A.; Kappes, M. M. From Planar to Cage in 15 Easy Steps: Resolving the  $C_{60}H_{21}F_9^- \rightarrow C_{60}^-$  Transformation by Ion Mobility Mass Spectrometry. *J. Am. Chem. Soc.* **2016**, *138*, 11254–11263.

## Supporting Information

### Fullerene-Functionalized Monolayer-Protected Silver Clusters:



Papri Chakraborty, Abhijit Nag, Ganesan Paramasivam, Ganapati Natarajan and  
Thalappil Pradeep\*

DST Unit of Nanoscience (DST UNS) and Thematic Unit of Excellence (TUE), Department of  
Chemistry, Indian Institute of Technology Madras, Chennai 600 036, India

\*Corresponding author: Fax: + 91-44 2257-0545

\*E-mail: [pradeep@iitm.ac.in](mailto:pradeep@iitm.ac.in)

### Table of Contents

Name	Description	Page No.
	Experimental and computational details	S5-S6
Figure S1	UV-vis and ESI MS of $[\text{Ag}_{29}(\text{BDT})_{12}]^{3-}$	S7
Figure S2	Structure of $[\text{Ag}_{29}(\text{BDT})_{12}]^{3-}$ resembling a tetrahedron	S7
Figure S3	ESI MS showing adduct formation at various cluster: $\text{C}_{60}$ molar ratios	S8
Figure S4	Experimental and calculated isotope patterns of $[\text{Ag}_{29}(\text{BDT})_{12}(\text{C}_{60})_n]^{3-}$ (n=1-3)	S8
Figure S5	UV-vis spectra showing changes upon addition of $\text{C}_{60}$ to $[\text{Ag}_{29}(\text{BDT})_{12}]^{3-}$ cluster	S9
Figure S6	UV-vis spectra showing increase in the stability of the cluster upon addition of $\text{C}_{60}$	S9

Figure S7	SEM/EDS of the adducts	S10
Figure S8	CID on the complexes $[\text{Ag}_{29}(\text{BDT})_{12}(\text{C}_{60})_n]^{3-}$ (n=2-4)	S11
Figure S9	ESI MS showing attachment of n>4 $\text{C}_{60}$ to the cluster at excess concentration of $\text{C}_{60}$	S12
Figure S10	Structure of $[\text{Ag}_{29}(\text{BDT})_{12}(\text{C}_{60})]^{3-}$ optimized using vdW-DF2 functional in LCAO	S13
Figure S11	Geometry for computing binding energy contribution from the interaction of only the three BDT ligands with $\text{C}_{60}$	S13-S14
Figure S12	Lowest energy structure of $[\text{Ag}_{29}(\text{BDT})_{12}(\text{C}_{60})]^{3-}$ with $\text{C}_{60}$ attached at a face of the tetrahedrally oriented trigonal prisms in the exterior shell of the cluster	S14
Figure S13	Force field global minimum geometry (FFGMG) of the adduct $[\text{Ag}_{29}(\text{BDT})_{12}(\text{C}_{60})]^{3-}$ obtained from docking studies	S15
Figure S14	DFT optimized structure of FFGMG of $[\text{Ag}_{29}(\text{BDT})_{12}(\text{C}_{60})]^{3-}$	S16
Figure S15	Lowest energy structure of $[\text{Ag}_{29}(\text{BDT})_{12}(\text{C}_{60})_n]^{3-}$ (n=2-3)	S17
Figure S16	Structure of $[\text{Ag}_{29}(\text{BDT})_{12}(\text{C}_{60})_8]^{3-}$ resembling a distorted cube	S17
Figure S17	Structure of $[\text{Ag}_{29}(\text{BDT})_{12}(\text{C}_{60})_9]^{3-}$	S18
Figure S18	Possible structures of less favorable configurational isomers of $[\text{Ag}_{29}(\text{BDT})_{12}(\text{C}_{60})_4]^{3-}$ and their CCS calculation	S18
Figure S19	ESI MS showing replacement of $\text{C}_{60}$ by TPP	S19
Figure S20	ESI MS of the adducts in presence of salts	S20

Figure S21	UV-vis spectra showing changes upon addition of C <sub>70</sub> to [Ag <sub>29</sub> (BDT) <sub>12</sub> ] <sup>3-</sup>	S21
Figure S22	CID on the adducts [Ag <sub>29</sub> (BDT) <sub>12</sub> (C <sub>70</sub> ) <sub>n</sub> ] <sup>3-</sup> (n=1-2)	S22
Figure S23	ESI MS showing replacement of C <sub>70</sub> by TPP	S23
Figure S24	ESI MS showing attachment of n>4 C <sub>70</sub> to the cluster at excess concentration of C <sub>70</sub>	S24
Figure S25	Lowest energy structure of [Ag <sub>29</sub> (BDT) <sub>12</sub> (C <sub>70</sub> )] <sup>3-</sup> with C <sub>70</sub> attached at the vertex of the cluster	S24
Figure S26	Lowest energy structure of [Ag <sub>29</sub> (BDT) <sub>12</sub> (C <sub>70</sub> )] <sup>3-</sup> with C <sub>70</sub> attached at the tetrahedrally oriented trigonal face position of the cluster	S25
Figure S27	FFGMG of the adduct [Ag <sub>29</sub> (BDT) <sub>12</sub> (C <sub>70</sub> )] <sup>3-</sup> obtained from docking studies	S26
Figure S28	DFT optimized structure of FFGMG of [Ag <sub>29</sub> (BDT) <sub>12</sub> (C <sub>70</sub> )] <sup>3-</sup>	S27
Figure S29	Lowest energy structures of [Ag <sub>29</sub> (BDT) <sub>12</sub> (C <sub>70</sub> ) <sub>n</sub> ] <sup>3-</sup> (n=2-3)	S27
Figure S30	Plot of drift time vs m/z of the C <sub>70</sub> adducts, comparison of experimental and calculated CCS values of the structures	S28
Table S1	DFT energies of the isomers of [Ag <sub>29</sub> (BDT) <sub>12</sub> (C <sub>60</sub> )] <sup>3-</sup> (C <sub>60</sub> attached at a tetrahedral vertex position of the cluster)	S29
Table S2	DFT energies for isomers of [Ag <sub>29</sub> (BDT) <sub>12</sub> (C <sub>60</sub> )] <sup>3-</sup> (C <sub>60</sub> attached at a face of the tetrahedral trigonal planes in the exterior shell of the cluster)	S29

Table S3	DFT energies for lowest energy isomers of $[\text{Ag}_{29}(\text{BDT})_{12}(\text{C}_{60})_n]^{3-}$ (n=2-4) with $\text{C}_{60}$ molecules attached at the vertex positions of the cluster	S30
Table S4	DFT energies for lowest energy isomers of $[\text{Ag}_{29}(\text{BDT})_{12}(\text{C}_{70})_n]^{3-}$ (n=1-4)	S31-32
	Co-ordinates of the DFT optimized lowest energy structure of $[\text{Ag}_{29}(\text{BDT})_{12}(\text{C}_{60})_4]^{3-}$	S34-43
Video V1	3D view of the structure of $[\text{Ag}_{29}(\text{BDT})_{12}]^{3-}$	
Video V2	3D view of the structure of $[\text{Ag}_{29}(\text{BDT})_{12}(\text{C}_{60})_4]^{3-}$	
Video V3	3D view of the structure of $[\text{Ag}_{29}(\text{BDT})_{12}(\text{C}_{60})_8]^{3-}$	

Videos V1, V2 and V3 are given separately.

## Experimental Details

### Instrumentation

The UV-vis spectra were measured using a PerkinElmer Lambda 25 UV-vis spectrophotometer. Mass spectrometric measurements were done in a Waters Synapt G2-Si high-resolution mass spectrometer. NMR measurements were done in a Bruker 500 MHz NMR spectrometer.

### ESI MS and IM MS measurements

All samples were measured in the negative electrospray ionization mode. The instrument was calibrated using NaI as the calibrant. All samples were measured keeping almost the same conditions with slight modification wherever required. The optimized conditions for measuring ESI MS were as follows:

Sample concentration: 1  $\mu\text{g/mL}$

Diluents: DMF and toluene

Sample flow rate: 20-30  $\mu\text{L/min}$

Capillary voltage: 3 kV

Cone voltage: 20 V

Source offset: 20 V

Source temperature: 100°C

Desolvation temperature: 150 °C

Desolvation gas flow: 400 L/h

For collision-induced dissociation (CID) studies, the molecular ion peaks were first selected in the quadrupole and then fragmented in the trap by varying the collision energies in the range of 0-50 V. Trap pressure of 10 mL/min was used during the CID experiments.

For ion mobility measurements, the optimized conditions were as follows:

IMS wave velocity: 400 m/s

IMS wave height: 40.0 V

### Computational Details:

The PAW setup was Ag( $4d^{10}5s^15p^6$ ), S( $3s^23p^4$ ), C( $2s^22p^2$ ) and H( $1s^1$ ) with scalar-relativistic effects included for Ag. The size of the simulation box was taken such that the distance between the wall of the box and the edge of the cluster is a minimum of 3 Å. The initial

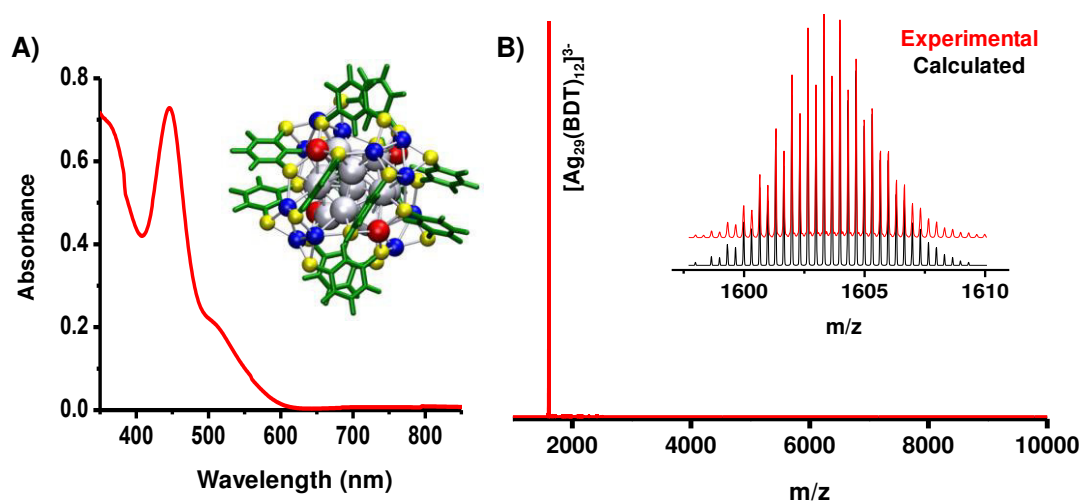
structure of  $[\text{Ag}_{29}(\text{BDT})_{12}]^{3-}$  was optimized by taking the crystal structure of  $[\text{Ag}_{29}(\text{BDT})_{12}(\text{TPP})_4]^{3-}$ , as reported by Bakr et al.<sup>1</sup> and removing its TPP ligands. The geometric optimizations of the fullerene ligated clusters were mainly carried out using the PBE exchange functional<sup>2</sup> and a double zeta polarization (DZP) basis set, with a grid spacing of 0.2 Å in LCAO<sup>3</sup> mode, with the convergence criteria as 0.05 eV/Å for the residual forces acting on atoms without any symmetry constraints. Further, the calculated ground state geometry and energy of the single C<sub>60</sub> attached adduct was compared with the vdW-DF2 functional.<sup>4</sup> The strength of the interaction between the fullerene ligands and  $[\text{Ag}_{29}(\text{BDT})_{12}]^{3-}$  cluster was studied by calculating the binding energy of C<sub>60</sub> or C<sub>70</sub>, by subtracting the sum of energies of isolated  $[\text{Ag}_{29}(\text{BDT})_{12}]^{3-}$  cluster and fullerenes from the total energy of the adducts,  $[\text{Ag}_{29}(\text{BDT})_{12}(\text{C}_{60})_n]^{3-}$  or  $[\text{Ag}_{29}(\text{BDT})_{12}(\text{C}_{70})_n]^{3-}$ . The structure of  $[\text{Ag}_{29}(\text{BDT})_{12}(\text{C}_{60})]^{3-}$  was also optimized using the finite difference (FD) grid method for better accuracy and to compare the results obtained by the LCAO basis method.

Molecular docking studies have been carried out using AutoDock 4.2 and AutoDock Tools programs.<sup>5</sup> The crystal structures of  $[\text{Ag}_{29}(\text{BDT})_{12}]^{3-}$ , C<sub>60</sub><sup>6</sup> and C<sub>70</sub><sup>7</sup> were used for this study. We used C<sub>60</sub> (or C<sub>70</sub>) as the “ligand” *i.e.* the movable molecule whose rotational and translational degrees of freedom would be varied during the docking. The ‘receptor’ molecule was  $[\text{Ag}_{29}(\text{BDT})_{12}]^{3-}$ , and this was the fixed and completely rigid central molecule. We assigned only partial charges from DFT for all atoms of  $[\text{Ag}_{29}(\text{BDT})_{12}]^{3-}$ . For simplicity, we did not consider any charge for the movable ligand, C<sub>60</sub> or C<sub>70</sub>. Receptor grids were generated using 126 × 126 × 126 grid points with a grid spacing of 0.375 Å and map types for all the ligand atoms were created using AutoGrid 4.6. The docking was performed using the Lamarckian genetic algorithm<sup>8</sup> within AutoDock 4.2. The van der Waals radius  $\sigma$  (Å) and well depth  $\epsilon$  (kcal/mol) for Ag of 2.63 Å and 4.560 kcal/mol, respectively, were taken from well-tested sources in literature<sup>9-10</sup> and these were added to the Autodock parameter file which does not contain them by default. The free energies of binding were calculated by summing the intermolecular and internal terms and subtracting the unbound energies which is a calculation that is performed within the Autodock program.

All structures were built up using the Avogadro software package<sup>11</sup> and all visualizations were created with visual molecular dynamics (VMD) software.<sup>12</sup>

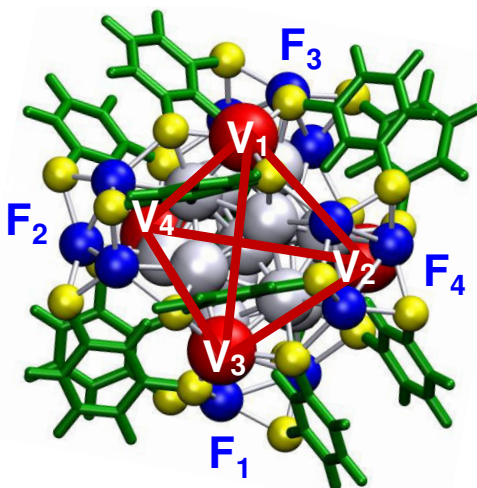


## Supporting Information 1



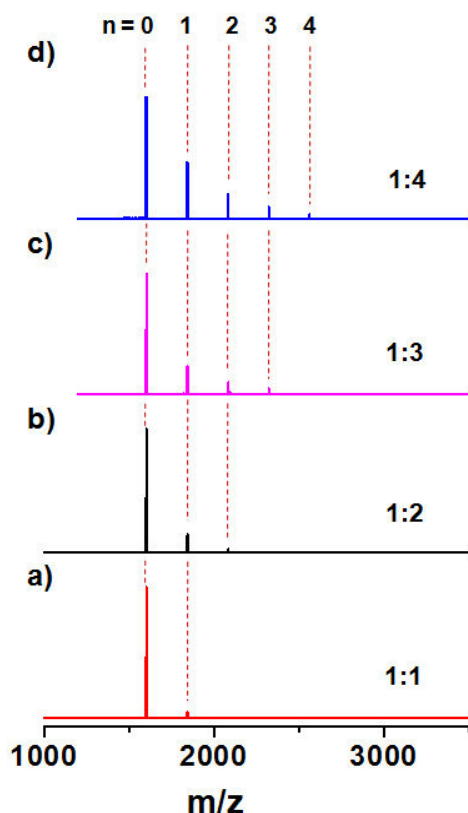
**Figure S1.** A) UV-vis and B) ESI MS of  $[\text{Ag}_{29}(\text{BDT})_{12}]^{3-}$ . Inset of A) shows the DFT optimized structure of the cluster and inset of B) shows the experimental and calculated isotope patterns of  $[\text{Ag}_{29}(\text{BDT})_{12}]^{3-}$ . Color codes for the atoms in the inset pictures: grey: silver atoms of the icosahedral ( $\text{Ag}_{13}$ ) core, blue: silver atoms of the trigonal planes in the exterior shell, red: four silver atoms face capping the core at four tetrahedral positions of  $[\text{Ag}_{29}(\text{BDT})_{12}]^{3-}$ , yellow: S atoms and green: BDT ligands.

## Supporting Information 2



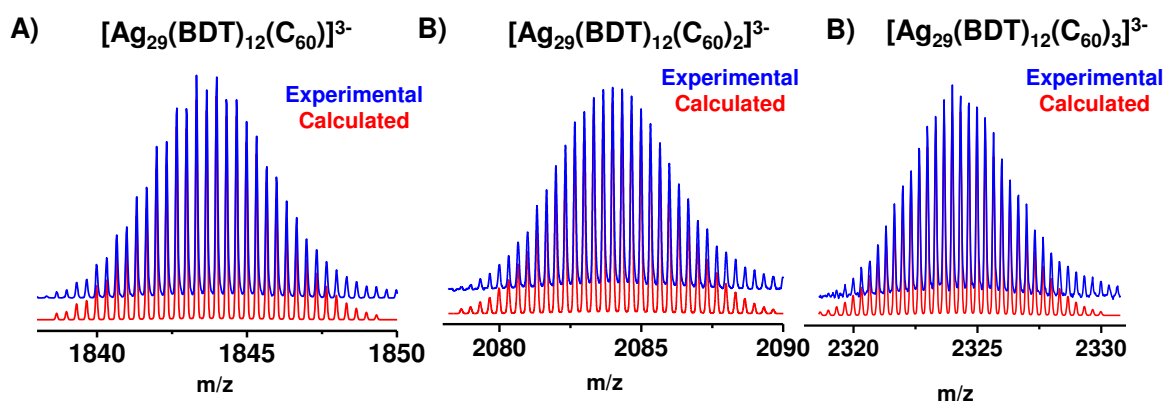
**Figure S2.** Structure of the cluster resembling tetrahedron. The four Ag atoms (red) of the outer shell represent the vertices ( $V_1, V_2, V_3, V_4$ ) of the tetrahedron. The four trigonal planes formed by the 12 Ag atoms (blue) in the exterior shell lie over the tetrahedral faces ( $F_1, F_2, F_3, F_4$ ) of the cluster.

### Supporting Information 3



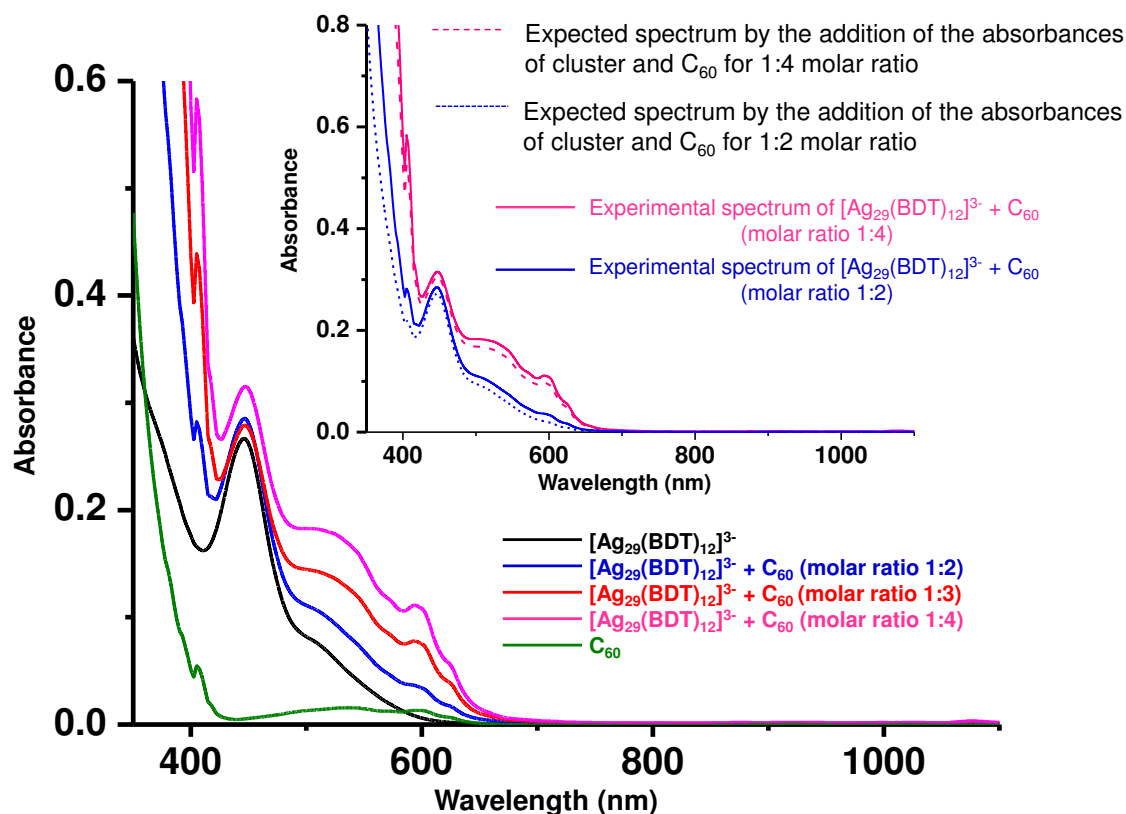
**Figure S3.** Formation of adducts,  $[\text{Ag}_{29}(\text{BDT})_{12}(\text{C}_{60})_n]^{3-}$  at cluster:fullerene molar ratios of (a) 1:1, (b) 1:2, (c) 1:3 and (d) 1:4. The label, 'n' is the no. of  $\text{C}_{60}$  molecules attached to the cluster.

### Supporting Information 4



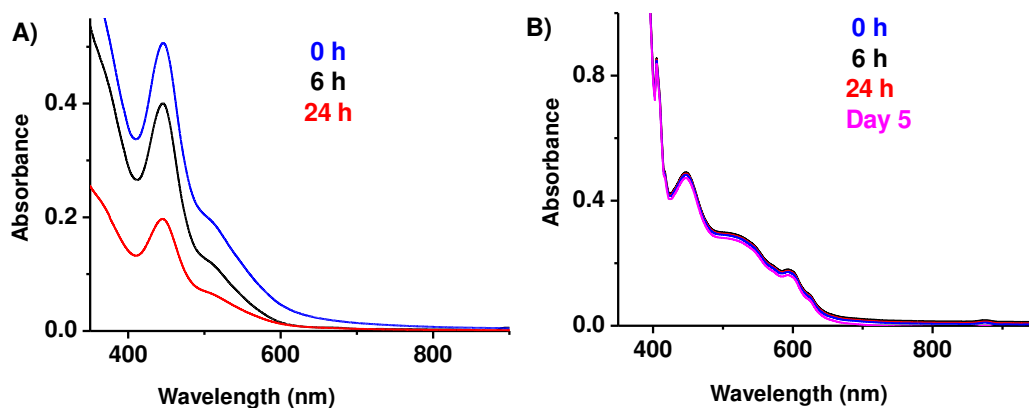
**Figure S4.** Experimental and calculated isotope patterns of  $[\text{Ag}_{29}(\text{BDT})_{12}(\text{C}_{60})_n]^{3-}$  ( $n=1-3$ ) are shown in A), B) and C), respectively.

## Supporting Information 5



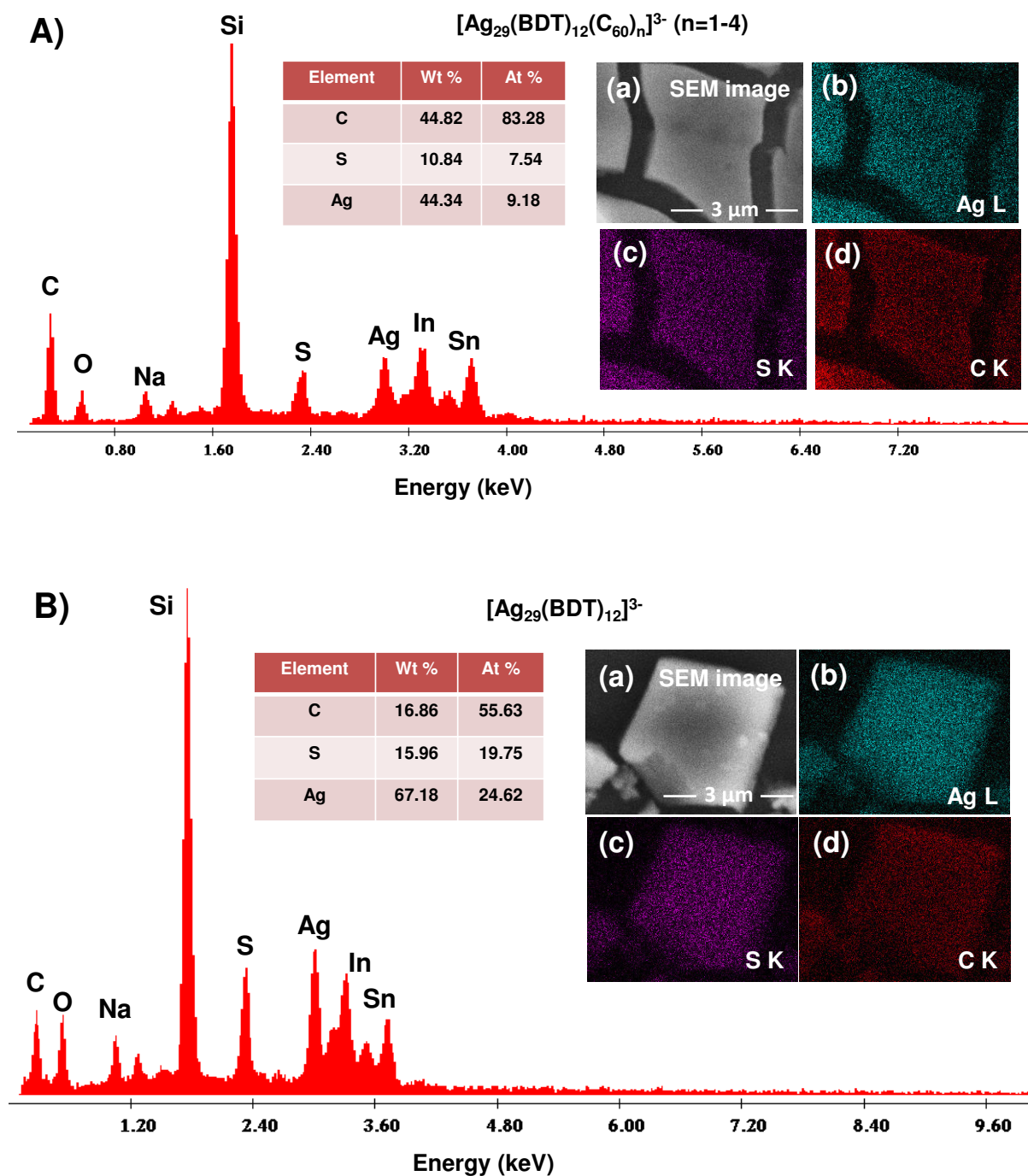
**Figure S5.** UV-vis spectra showing changes upon addition of  $C_{60}$  to  $[Ag_{29}(BDT)_{12}]^{3-}$  cluster. Inset of the figure shows a comparison of the experimental spectra with that of the spectra predicted (shown by dotted lines) by adding the absorbances of the cluster and the fullerene at a particular ratio.

## Supporting Information 6



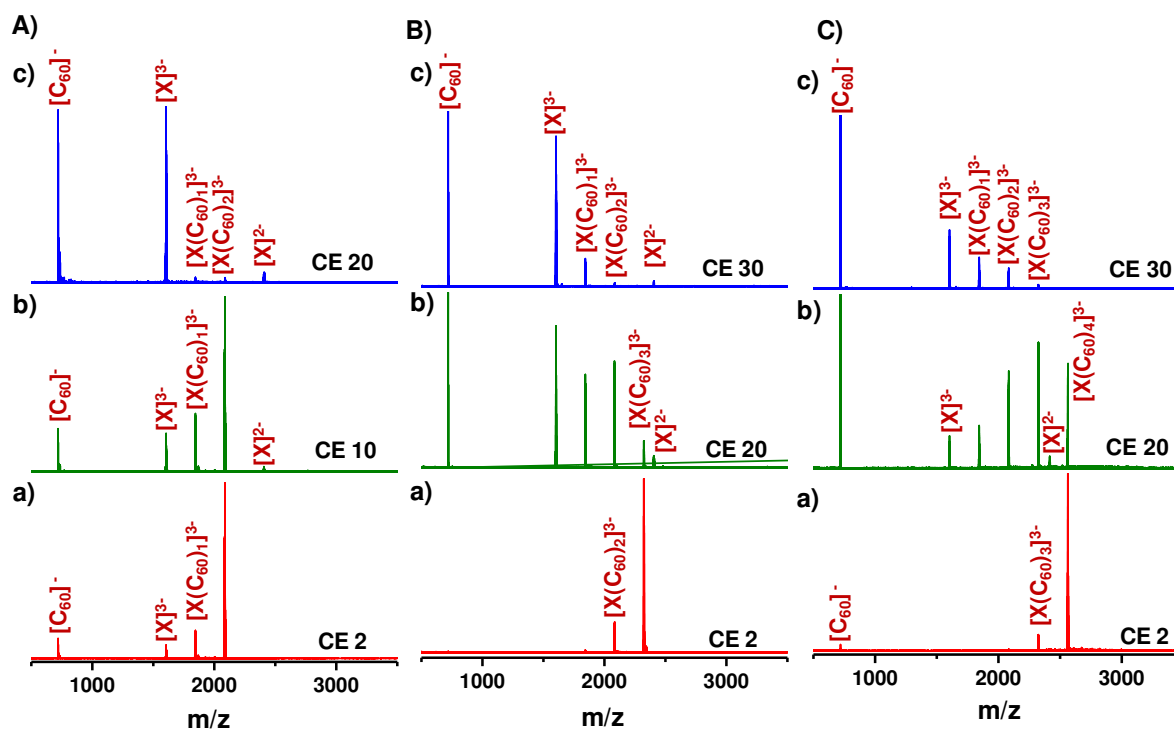
**Figure S6.** UV-vis spectra showing that the stability of **A)**  $[Ag_{29}(BDT)_{12}]^{3-}$  decreases significantly within 24 h while **B)** the fullerene-adducts of the cluster is stable even up to 5 days.

## Supporting Information 7



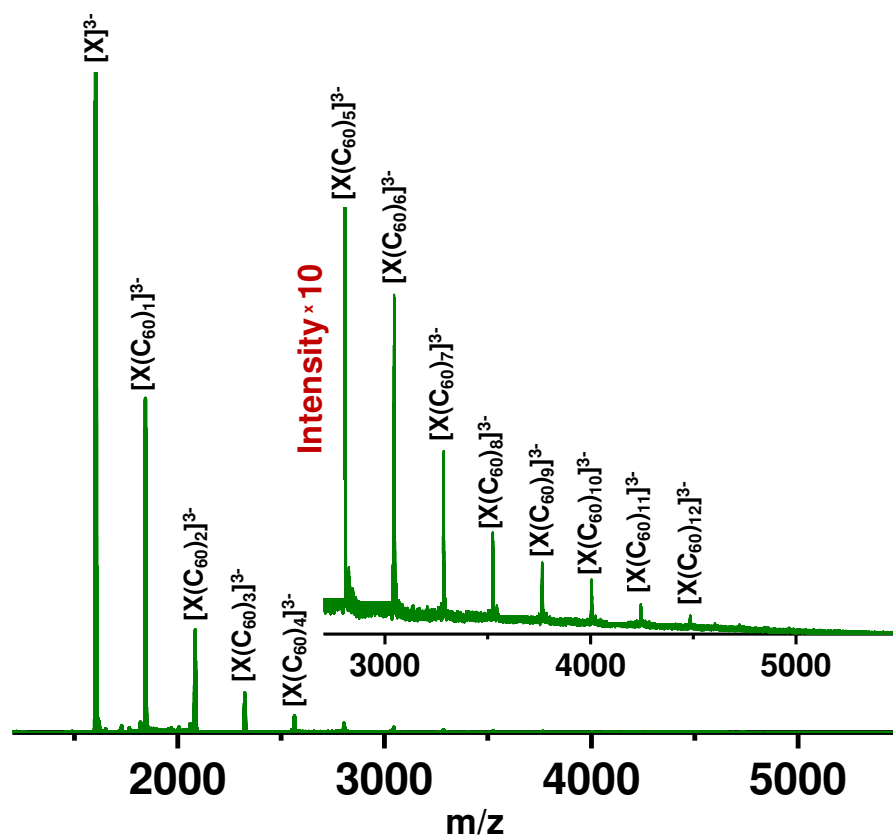
**Figure S7.** SEM/EDS of **A)** the composite  $[\text{Ag}_{29}(\text{BDT})_{12}(\text{C}_{60})_n]^{3-}$  ( $n=1-4$ ), and **B)**  $[\text{Ag}_{29}(\text{BDT})_{12}]^{3-}$ , insets show (a) SEM image of the material from which EDS was taken, elemental mapping of (b) Ag, (c) S, and (d) C, respectively in each case. The peaks for the other elements (Si, In, Sn, etc.) are from the ITO coated glass slide on which the samples were spotted for taking SEM/EDS. Atomic ratios disregarding other elements are listed in the tables.

## Supporting Information 8



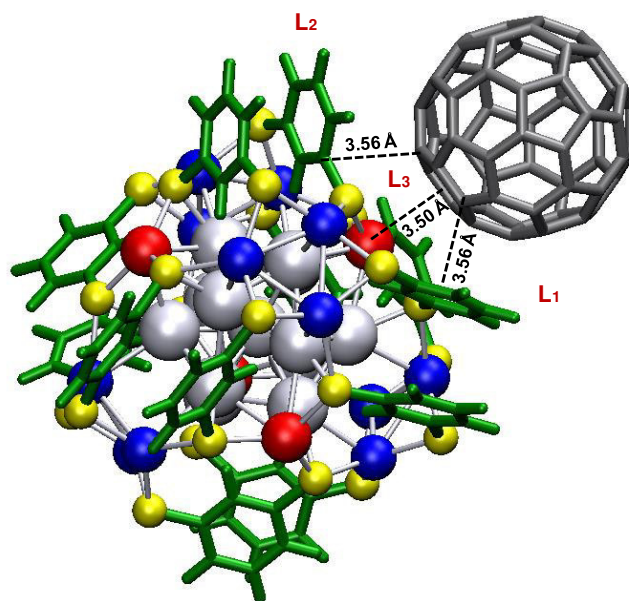
**Figure S8.** CID with increasing CE for **A)**  $[X(C_{60})_2]^{3-}$ , **B)**  $[X(C_{60})_3]^{3-}$  and **C)**  $[X(C_{60})_4]^{3-}$ ,  $X = Ag_{29}(BDT)_{12}$ .

## Supporting Information 9



**Figure S9.** ESI MS of  $[Ag_{29}(BDT)_{12}]^{3-}$  cluster in presence of excess  $C_{60}$  showing the formation of  $[Ag_{29}(BDT)_{12}(C_{60})_n]^{3-}$  (n=1-12) adducts, X= $Ag_{29}(BDT)_{12}$ .

## Supporting Information 10

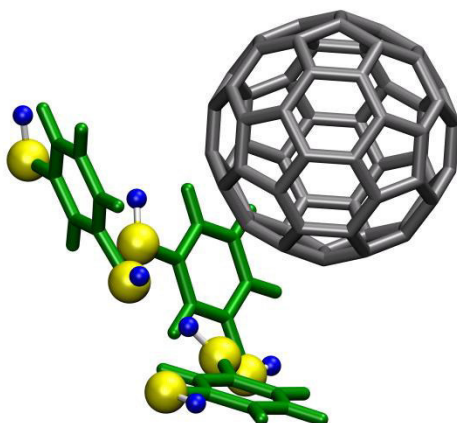


**Figure S10.** Lowest energy geometrical structure of  $[\text{Ag}_{29}(\text{BDT})_{12}(\text{C}_{60})]^{3-}$  optimized using the vdW-DF2 functional in LCAO mode. BDT ligands  $\text{L}_1$  and  $\text{L}_2$  are at a distance of 3.56 Å and  $\text{L}_3$  is at a distance of 3.67 Å at the closest contact. Binding energy = -30.39 kcal/mol.

## Supporting Information 11

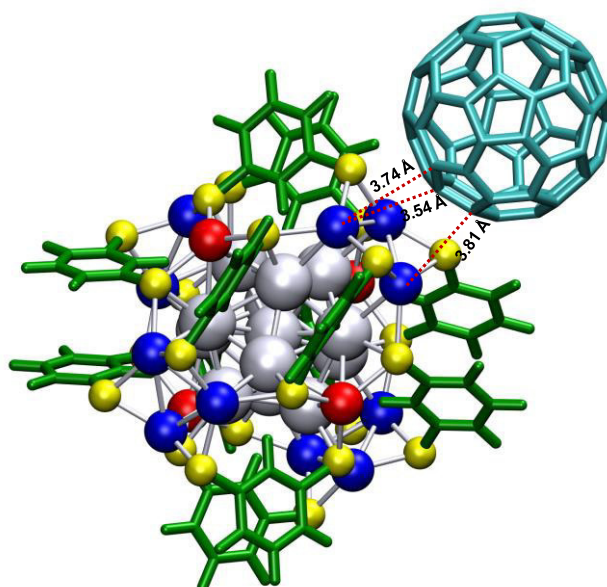
The following procedure was used to carry out the computational study of the binding energy. We considered a system consisting of only the three BDT ligands and  $\text{C}_{60}$  in the same configuration as in the original structure of  $[\text{Ag}_{29}(\text{BDT})_{12}(\text{C}_{60})]^{3-}$ . We passivated the S atoms on the BDT ligands with H atoms and used a vdW-DF2 functional. We found that the binding energy was -18.24 kcal/mol and it was a fraction of the total binding energy, -30.39 kcal/mol (calculated by vdW-DF2 functional). Subtracting the ligand binding energy from the total binding energy gives the residual binding energy of -12.15 kcal/mol due to the metal cluster and its proximal surface  $\text{AgS}_3$  motif which interacts via weak ionic and van der Waals interactions.





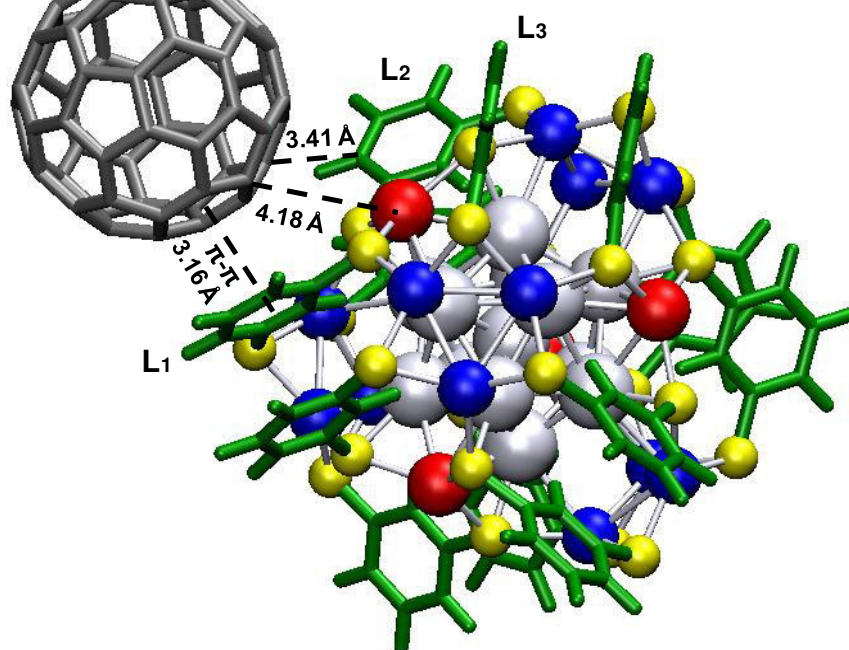
**Figure S11.** Geometry used for computing the binding energy contribution from the interaction between the fullerene and three BDT ligands. The three ligands and the fullerene are kept in the same configuration as in the full model of  $[\text{Ag}_{29}(\text{BDT})_{12}(\text{C}_{60})]^{3-}$ . The S atoms of the BDT ligands are passivated with H atoms. Color codes: black:  $\text{C}_{60}$ , green: BDT, yellow: S, blue: H.

## Supporting Information 12



**Figure S12.** DFT optimized lower energy configurational isomer of  $[\text{Ag}_{29}(\text{BDT})_{12}(\text{C}_{60})]^{3-}$  formed by attaching  $\text{C}_{60}$  at the tetrahedrally oriented trigonal face of the cluster,  $E = -1477.049$  eV,  $\text{BE} = -15.63$  kcal/mol.

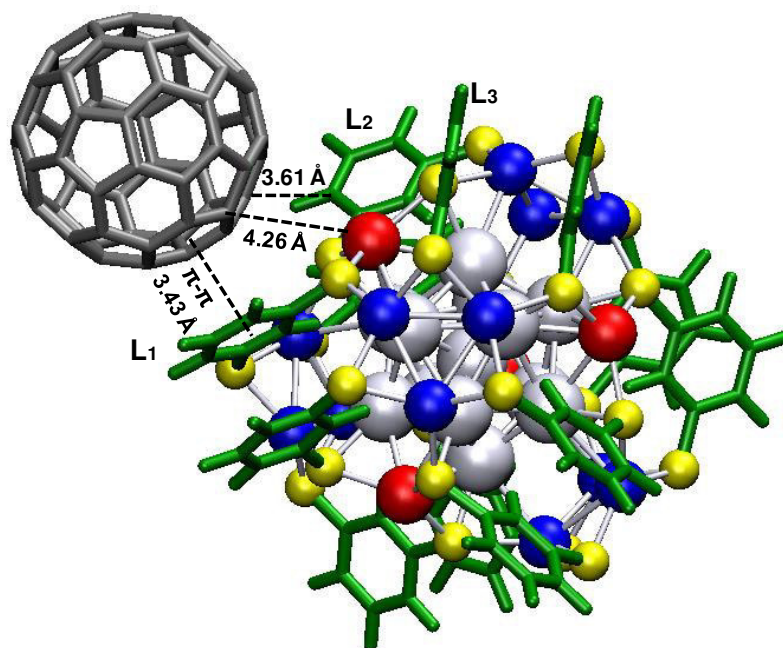
## Supporting Information 13



**Figure S13.** The orientation of the cluster and the fullerene in the force-field global minimum geometry (FFGMG) of the adduct,  $[\text{Ag}_{29}(\text{BDT})_{12}(\text{C}_{60})]^{3-}$ .

**Note.** The 10 lowest minima structures that were obtained from the molecular docking simulations showed binding energies in the range of -10.29 to -10.23 kcal/mol. All the lowest energy structures gave nearly the same geometry of the adduct with slight changes in the orientation of  $\text{C}_{60}$  and interaction around the three BDT ligands at the vertex position. The lowest energy conformer showing a binding energy of -10.29 kcal/mol is shown in the above figure (Figure S13).  $\text{C}_{60}$  remains at a distance of about 4.18 Å from the vertex Ag atom. The benzene ring of one of the BDT ligands ( $\text{L}_1$ ) lies in nearly a direct parallel overlap with a hexagonal ring of  $\text{C}_{60}$  at a distance of 3.16 Å. Another BDT ligand ( $\text{L}_2$ ) has partial interaction with  $\text{C}_{60}$  and the other ligand  $\text{L}_3$  is far away and has no interaction at all.

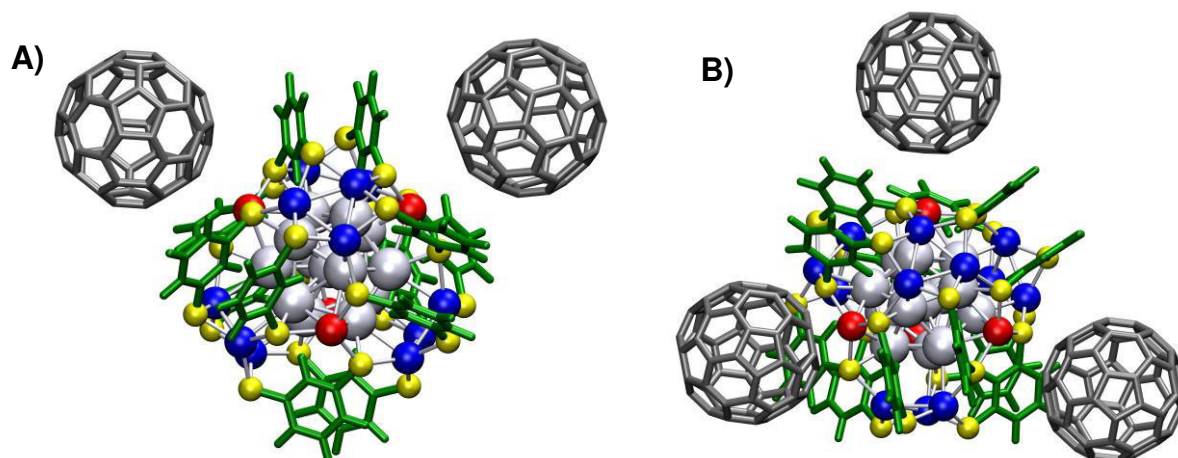
## Supporting Information 14



**Figure S14.** DFT optimized structure of the FFGMG of the adduct. Energy (E) = -1478.108750 eV, Binding energy (BE) = -16.37 kcal/mol.

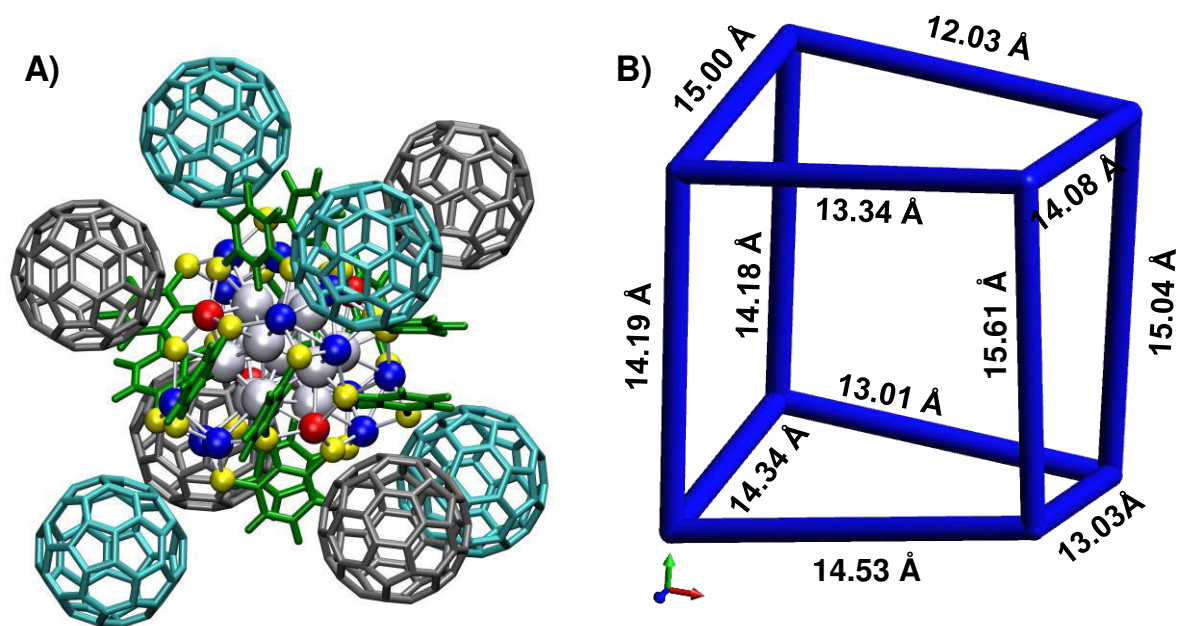
**Note.** DFT optimization causes slight variations in the structure of the FFGMG of the adduct obtained from docking studies. The distance of C<sub>60</sub> from the vertex Ag atom slightly increases to 4.26 Å (4.18 Å in case of FFGMG). Also, the distance from the BDT ligand L<sub>1</sub> increases from 3.16 Å to 3.43 Å and L<sub>2</sub> increases from 3.41 Å to 3.61 Å after DFT optimization. This is due to additional relaxations considered in DFT.

## Supporting Information 15



**Figure S15.** DFT optimized lowest energy structure of  $[\text{Ag}_{29}(\text{BDT})_{12}(\text{C}_{60})_n]^{3-}$ , **A)** n=2 and **B)** n=3.

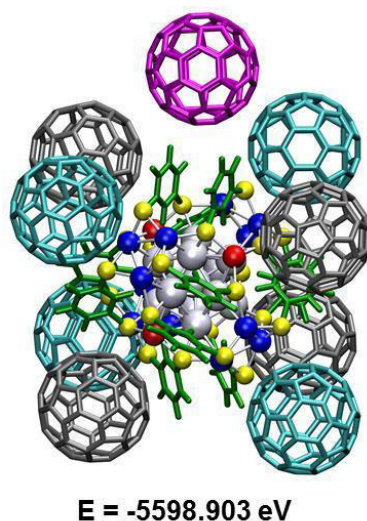
## Supporting Information 16



**Figure S16.** Structure of **A)**  $[\text{Ag}_{29}(\text{BDT})_{12}(\text{C}_{60})_8]^{3-}$  resembling a distorted cube, **(B)**. The length of the sides of the cube is marked in the figure.

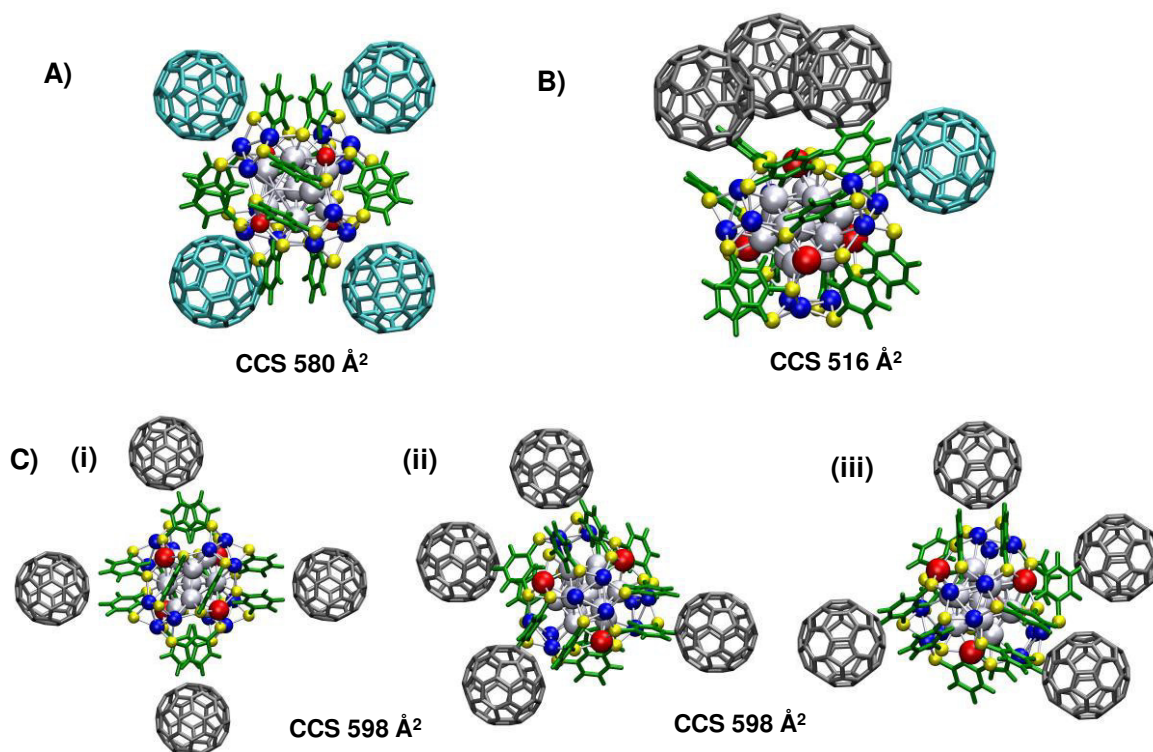


## Supporting Information 17



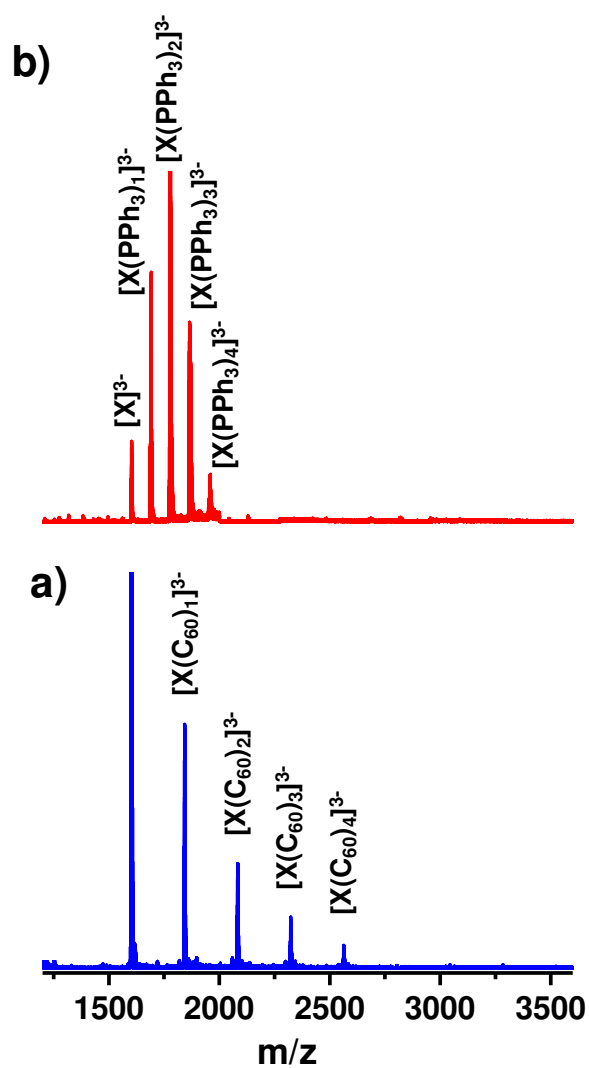
**Figure S17.** Structure of  $[\text{Ag}_{29}(\text{BDT})_{12}(\text{C}_{60})_9]^{3-}$  with 9<sup>th</sup>  $\text{C}_{60}$  placed over two BDT ligands.

## Supporting Information 18



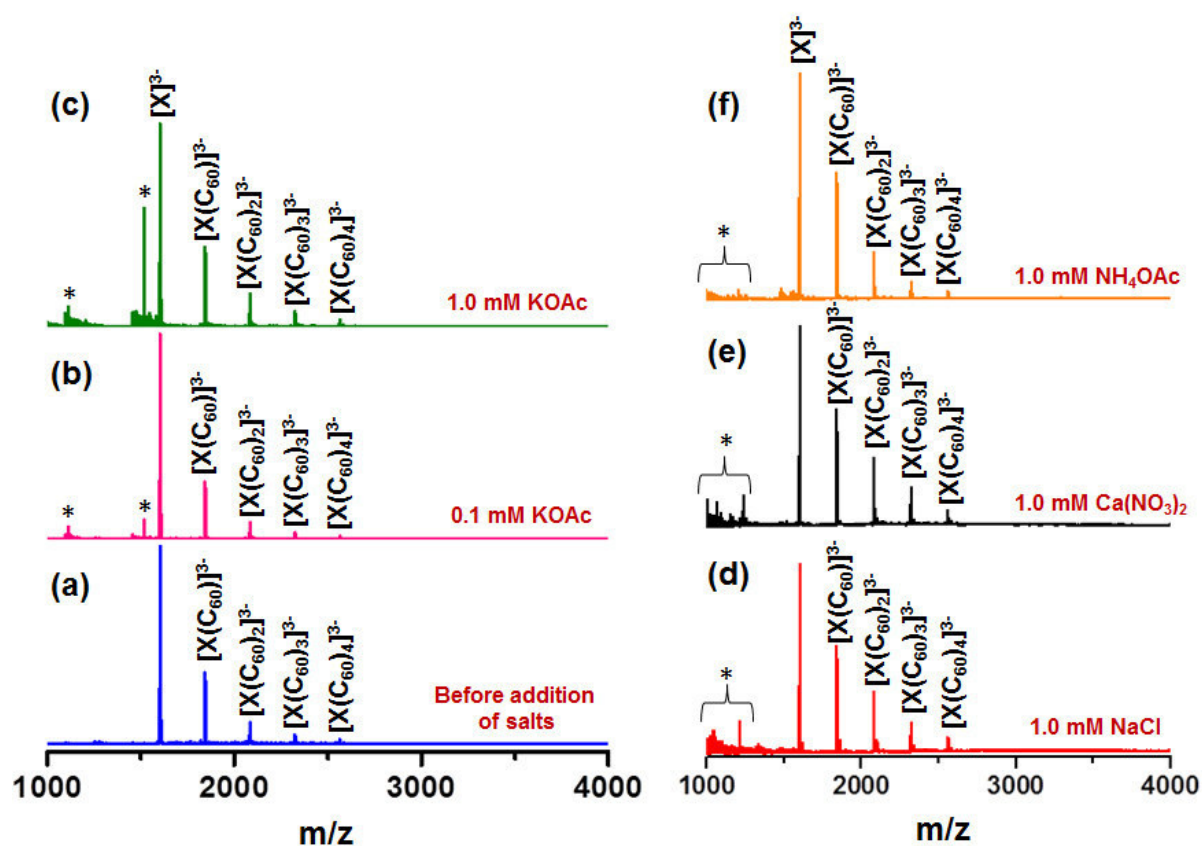
**Figure S18.** Possibilities of less favourable configurational isomers of  $[\text{Ag}_{29}(\text{BDT})_{12}(\text{C}_{60})_4]^{3-}$  with all  $\text{C}_{60}$  molecules **A)** attached at the four tetrahedrally oriented trigonal faces (CCS 580 Å<sup>2</sup>), **B)** crowded around one vertex site by fullerene-fullerene interaction (CCS 516 Å<sup>2</sup>) and **C)** attached over the BDT ligands in three different possible ways (CCS 598 Å<sup>2</sup> in each case).

## Supporting Information 19



**Figure S19.** ESI MS of (a)  $[X(C_{60})_n]^{3-}$  ( $n=1-4$ ) and (b) showing replacement of  $C_{60}$  upon addition of  $PPh_3$ ,  $X=Ag_{29}(BDT)_{12}$ .

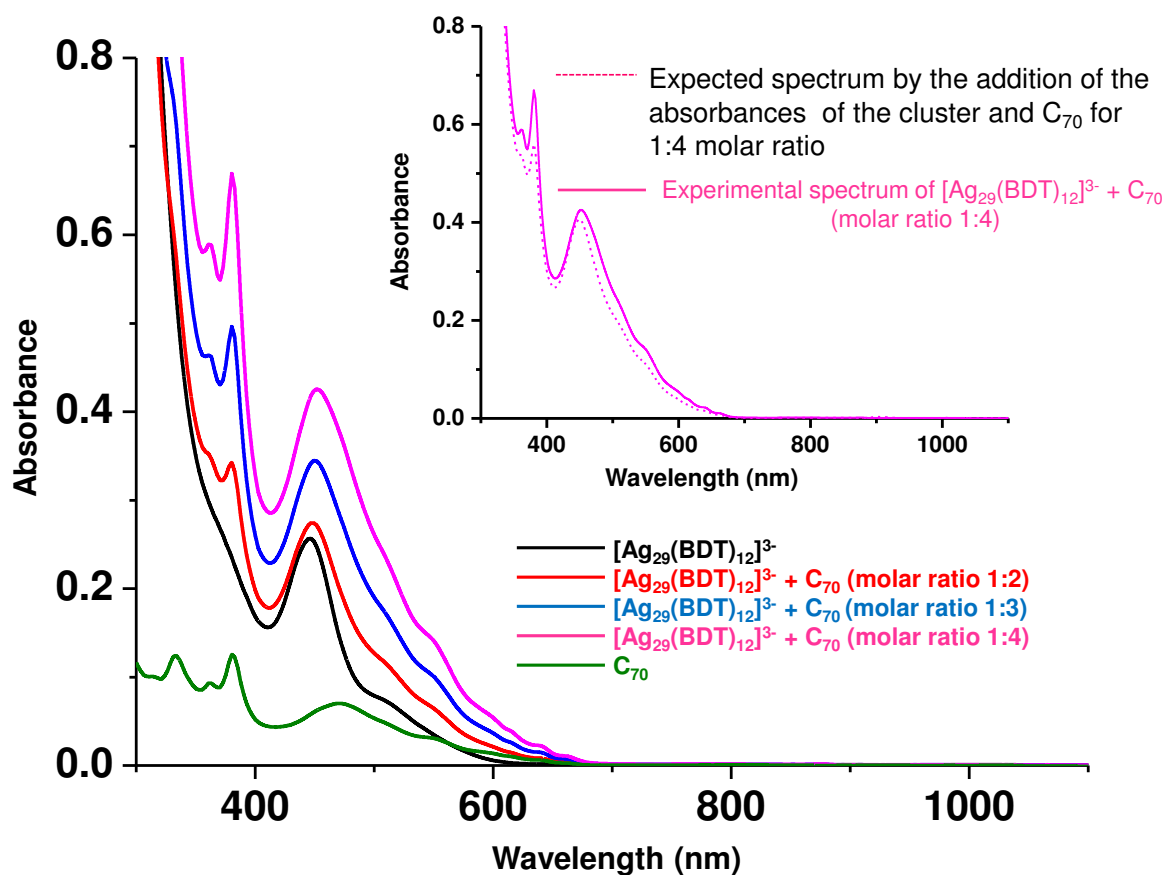
## Supporting Information 20



**Figure S20.** ESI of the adducts  $[Ag_{29}(BDT)_{12}(C_{60})_n]^{3-}$  ( $n=1-4$ ) (a) before addition of salts; in presence of (b) 0.1 mM KOAc, (c) 1.0 mM KOAc, (d) 1.0 mM NaCl, (e) 1.0 mM  $Ca(NO_3)_2$  and (f) 1.0 mM  $NH_4OAc$ . The asterisks (\*) indicate unassigned peaks.

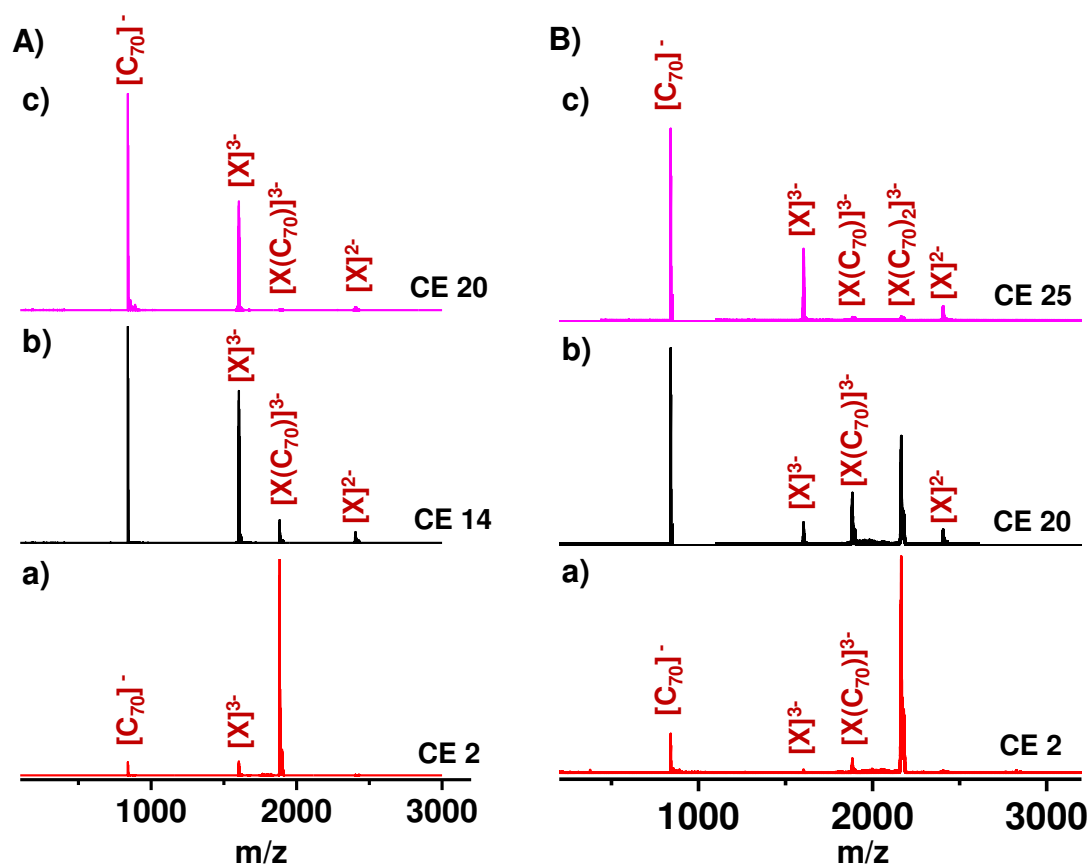


## Supporting Information 21



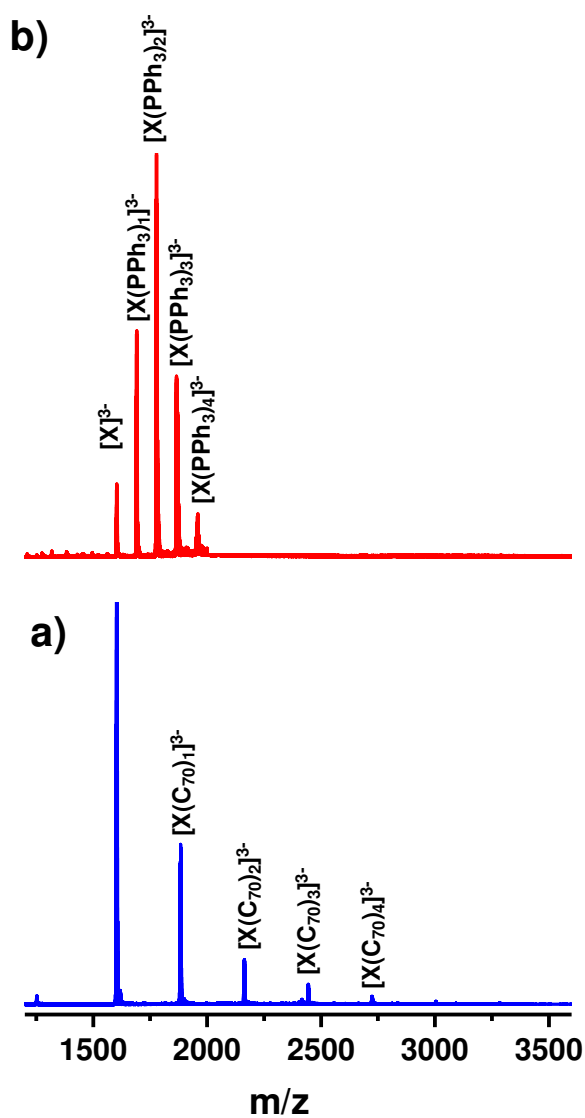
**Figure S21.** UV-vis spectra showing changes upon addition of  $\text{C}_{70}$  to  $[\text{Ag}_{29}(\text{BDT})_{12}]^{3-}$  cluster. Inset of the figure shows a comparison of the experimental spectra with that of the spectra predicted (shown by dotted lines) by adding the absorbances of the cluster and the fullerene at a particular ratio (1:4 molar ratio).

## Supporting Information 22



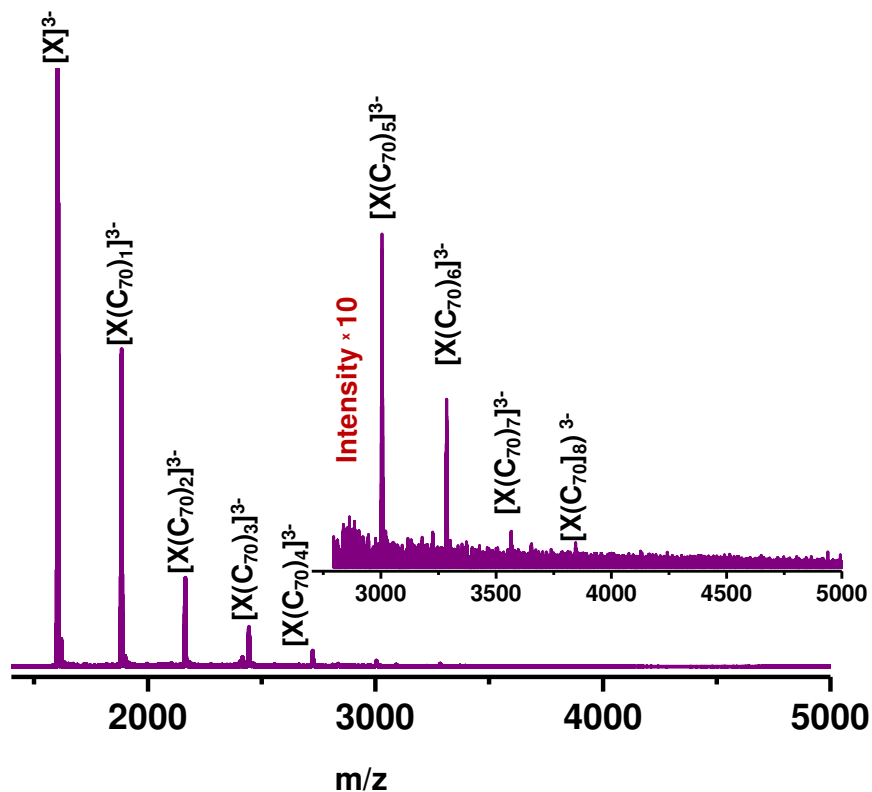
**Figure S22.** CID at increasing CE for **A)**  $[X(C_{70})]^{3-}$  and **B)**  $[X(C_{70})_2]^{3-}$ ,  $X = Ag_{29}(BDT)_{12}$ .

## Supporting Information 23



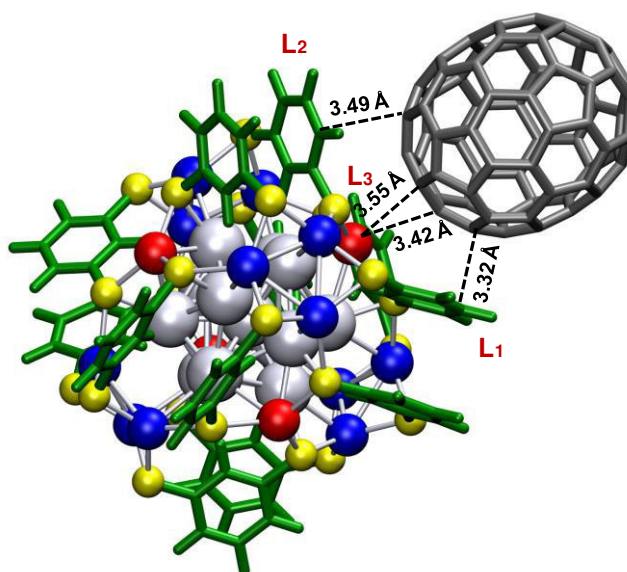
**Figure S23.** ESI MS of (a)  $[X(C_{70})_n]^{3-}$  ( $n=1-4$ ) and (b) showing replacement of  $C_{70}$  upon addition of  $PPh_3$ ,  $X=Ag_{29}(BDT)_{12}$ .

## Supporting Information 24



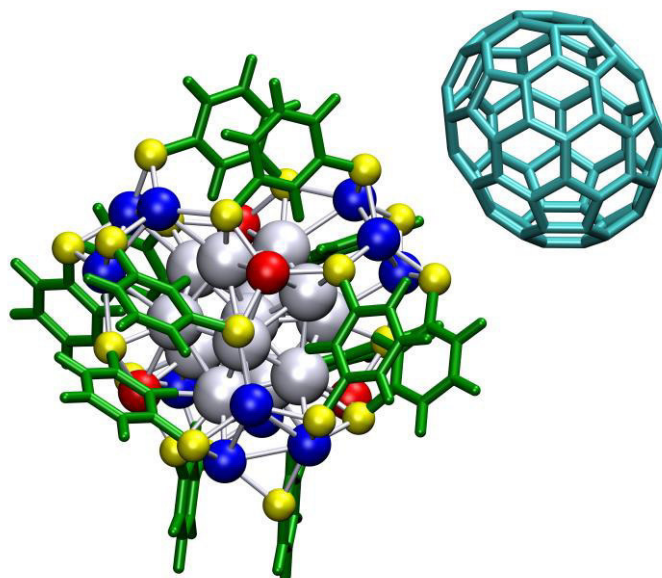
**Figure S24.** ESI MS of  $[Ag_{29}(BDT)_{12}]^{3-}$  cluster in presence of excess  $C_{70}$  showing the formation of  $[Ag_{29}(BDT)_{12}(C_{70})_n]^{3-}$  ( $n=1-8$ ) adducts,  $X=Ag_{29}(BDT)_{12}$ .

## Supporting Information 25



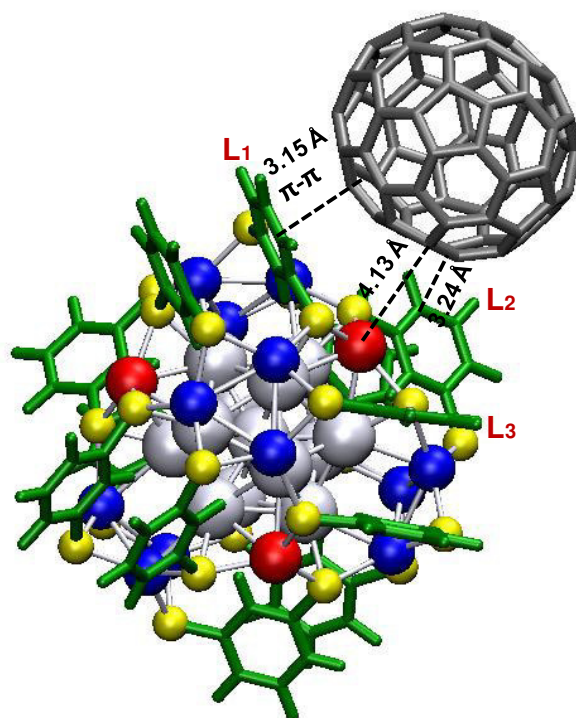
**Figure S25.** DFT optimised lowest energy structure of  $[Ag_{29}(BDT)_{12}(C_{70})]^{3-}$ .

## Supporting Information 26



**Figure S26.** DFT optimized lower energy isomeric structure of  $[\text{Ag}_{29}(\text{BDT})_{12}(\text{C}_{70})]^{3-}$  formed by attaching  $\text{C}_{70}$  at the face position of the cluster,  $E=-1566.762$  eV,  $\text{BE}= -17.99$  kcal/mol. The distance of  $\text{C}_{70}$  from the face Ag atoms is  $3.91 - 3.97$  Å.

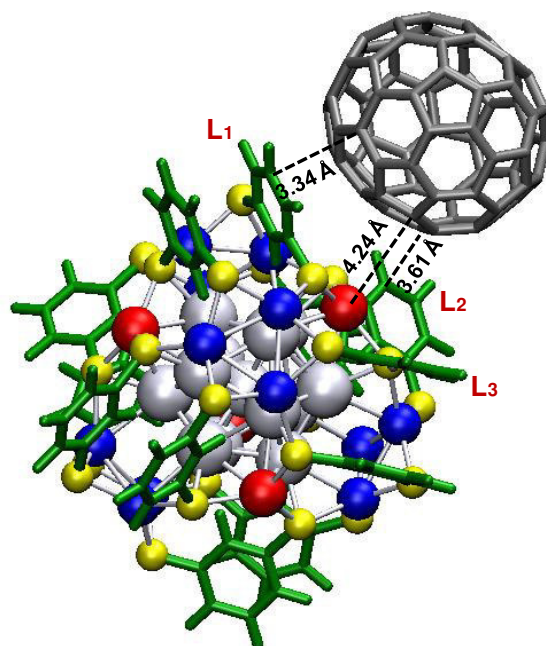
## Supporting Information 27



**Figure S27.** The orientation of the cluster and  $C_{70}$  in the force-field global minimum geometry (FFGMG) of the adduct  $[Ag_{29}(BDT)_{12}(C_{70})]^{3-}$ .

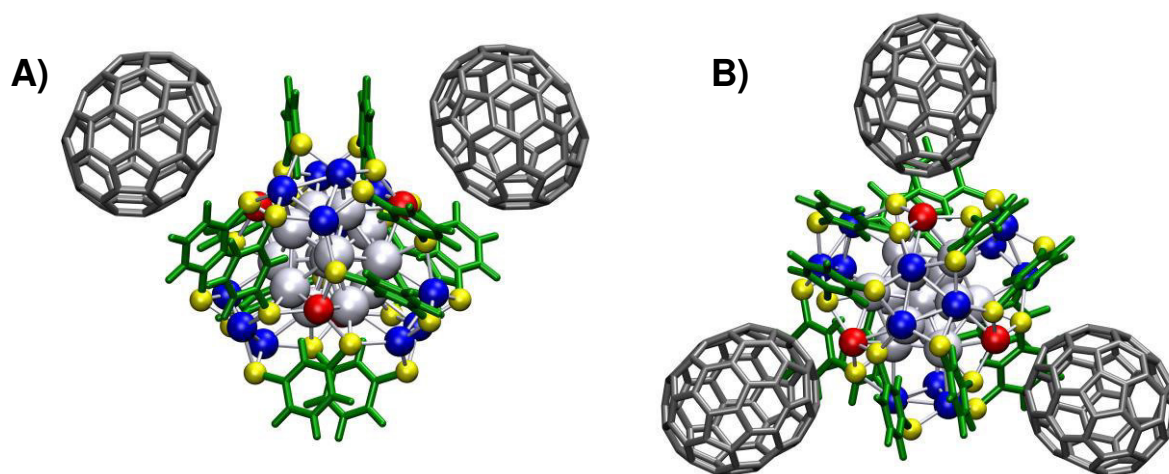
**Note.** The 10 lowest minima structures that were obtained from the molecular docking simulations showed binding energies in the range of -10.99 to -10.96 kcal/mol. All the lowest energy structures gave nearly the same geometry of the adduct, similar to the case of  $C_{60}$ . The lowest energy conformer showing a binding free energy of -10.99 kcal/mol is shown in the above figure (Figure S27).  $C_{70}$  remains at a distance of about 4.13 Å from the vertex Ag atom. The benzene ring of one of the BDT ligands ( $L_1$ ) lies in nearly parallel overlap with a hexagonal ring of  $C_{70}$  at a distance of 3.15 Å. Another BDT ligand ( $L_2$ ) has partial interaction with  $C_{70}$  and the other ligand  $L_3$  is far away and has no interaction at all.

## Supporting Information 28



**Figure S28.** DFT optimized structure of the FFGMG of the adduct, Energy (E) = -1566.719694 eV, Binding energy (BE) = -17.07 kcal/mol.

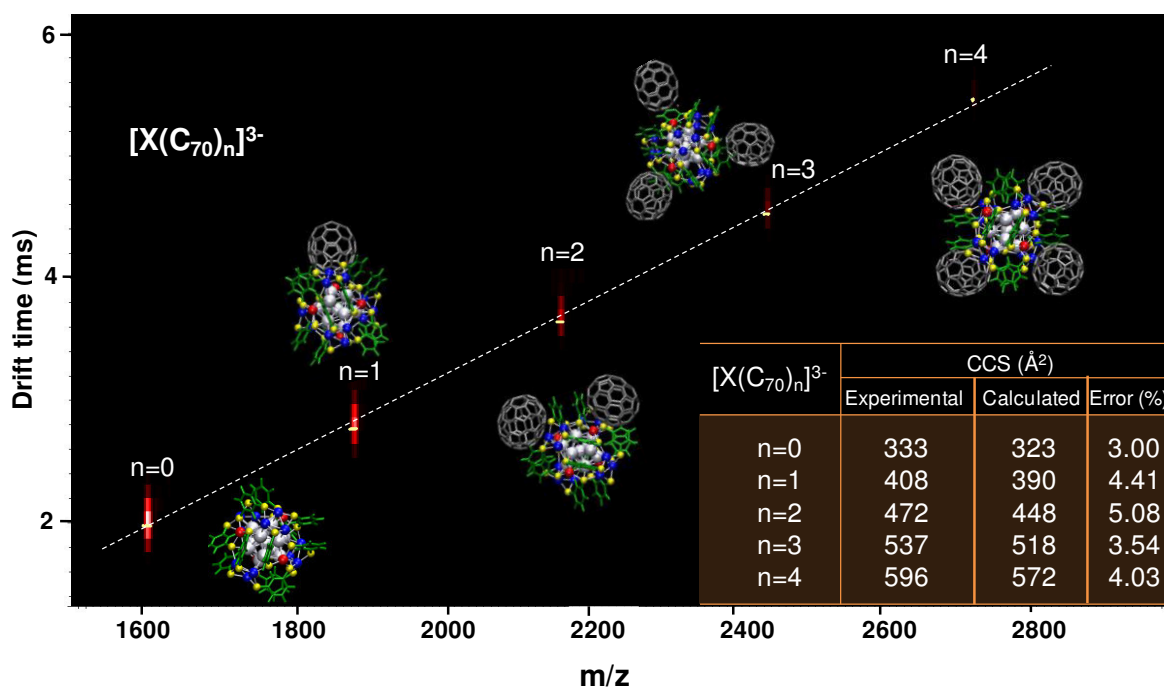
## Supporting Information 29



**Figure S29.** DFT optimized lowest energy structure of  $[\text{Ag}_{29}(\text{BDT})_{12}(\text{C}_{70})_n]^{3-}$  **A)**  $n=2$  and **B)**  $n=3$ .



## Supporting Information 30



**Figure S30.** The plot of drift time of the adducts  $[Ag_{29}(BDT)_{12}(C_{70})_n]^{3-}$  with their  $m/z$  values. Lowest energy structures of the adducts are shown beside their respective spots. The table in the inset of the figure shows the experimental and the calculated CCS values.

## Supporting Tables

### Supporting Table S1

(a) Table showing energies\* for lowest energy isomers of  $[\text{Ag}_{29}(\text{BDT})_{12}(\text{C}_{60})]^{3-}$  where  $\text{C}_{60}$  is attached at a tetrahedral vertex position of the cluster (the energies of the lowest energy structure are written in bold)

Orientation of $\text{C}_{60}$ facing the vertex Ag atom	Lowest energy state (E/eV)	Binding Energy BE (kcal/mol)
$\text{C}_6$ face	-1478.079	-15.75
$\text{C}_5$ face	-1478.087	-15.93
6-6 bond	-1478.120	-16.70
<b>6-5 bond</b>	<b>-1478.123</b>	<b>-16.77</b>

\*calculated at PBE/dzp level of theory in LCAO mode

(b) Table showing comparison of LCAO and FD energies for lowest energy structure of  $[\text{Ag}_{29}(\text{BDT})_{12}(\text{C}_{60})]^{3-}$

LCAO Energy (eV)		FD Energy (eV)	
PBE/dzp	vdW-DF2/dzp	PBE/dzp	vdW-DF2/dzp
-1478.123	-5743.130	-1534.580	-5813.108

### Supporting Table S2

Table showing energies\* for isomeric structure of  $[\text{Ag}_{29}(\text{BDT})_{12}(\text{C}_{60})]^{3-}$  obtained by attaching  $\text{C}_{60}$  at a tetrahedrally oriented trigonal face of the cluster (the energies of the lowest energy structure are written in bold)

Orientation of $\text{C}_{60}$ facing the Ag atoms	Lowest energy state (E/eV)	Binding Energy BE (kcal/mol)
$\text{C}_6$ face	-1477.025	-15.07
$\text{C}_5$ face	-1476.999	-14.48
6-6 bond	-1477.020	-14.96
<b>6-5 bond</b>	<b>-1477.049</b>	<b>-15.63</b>

\*calculated at PBE/dzp level of theory in LCAO mode.

## Supporting Table S3

(A) Table showing energies\* for lowest energy isomers of  $[\text{Ag}_{29}(\text{BDT})_{12}(\text{C}_{60})_n]^{3-}$  ( $n=2$ )

(the energies of the lowest energy structure are written in bold)

Orientation of $\text{C}_{60}$ facing the vertex Ag atom	Lowest energy state (E/eV)	Binding Energy/n BE (kcal/mol)
$\text{C}_6$ face	-1992.374	-14.68
$\text{C}_5$ face	-1992.439	-15.43
<b>6-6 bond</b>	<b>-1992.456</b>	<b>-15.63</b>
6-5 bond	-1992.408	-15.07

\*calculated at PBE/dzp level of theory in LCAO mode.

(B) Table showing energies\* for lowest energy isomers of  $[\text{Ag}_{29}(\text{BDT})_{12}(\text{C}_{60})_n]^{3-}$  ( $n=3$ )

(the energies of the lowest energy structure are written in bold)

Orientation of $\text{C}_{60}$ facing the vertex Ag atom	Lowest energy state (E/eV)	Binding Energy/n BE (kcal/mol)
$\text{C}_6$ face	-2507.650	-14.02
<b><math>\text{C}_5</math> face</b>	<b>-2507.747</b>	<b>-14.77</b>
6-6 bond	-2507.641	-13.95
6-5 bond	-2507.723	-14.58

\*calculated at PBE/dzp level of theory in LCAO mode.

(C) Table showing energies\* for lowest energy isomers of  $[\text{Ag}_{29}(\text{BDT})_{12}(\text{C}_{60})_4]^{3-}$  ( $n=4$ )

(the energies of the lowest energy structure are written in bold)

Orientation of $\text{C}_{60}$ facing the vertex Ag atom	Lowest energy state (E/eV)	Binding Energy/n BE (kcal/mol)
$\text{C}_6$ face	-3022.924	-13.68
$\text{C}_5$ face	-3022.983	-14.02
6-6 bond	-3022.848	-13.24
<b>6-5 bond</b>	<b>-3022.985</b>	<b>-14.03</b>

\*calculated at PBE/dzp level of theory in LCAO mode.

## Supporting Table S4

(A) Table showing energies for lowest energy isomers\* of  $[\text{Ag}_{29}(\text{BDT})_{12}(\text{C}_{70})_n]^{3-}$  ( $n=1$ ) for  $\text{C}_{70}$  attached at vertex position (the energies of the lowest energy structure are written in bold)

Orientation of $\text{C}_{70}$ facing the vertex Ag atom	Lowest energy state (E/eV)	Binding Energy/n BE (kcal/mol)
$\text{C}_6$ face	-1566.770	-18.22
<b><math>\text{C}_5</math> face</b>	<b>-1566.785</b>	<b>-18.68</b>
6-6 bond	-1566.728	-17.30
6-5 bond(1)	-1566.756	-17.99
6-5 bond(2)	-1566.745	-17.76

\*calculated at PBE/dzp level of theory in LCAO mode.

**Note.** 6-5 bond(1) is the bond at the edge of the major axis and 6-5 bond(2) is the bond at the edge of the minor axis of the ellipsoidal  $\text{C}_{70}$ .

(B) Table showing energies\* for the isomeric structure of  $[\text{Ag}_{29}(\text{BDT})_{12}(\text{C}_{70})_n]^{3-}$  ( $n=1$ ) formed by attaching  $\text{C}_{70}$  at face position of the cluster (The energies of the lowest energy structure are written in bold.)

Orientation of $\text{C}_{70}$ facing the Ag atoms	Lowest energy state (E/eV)	Binding Energy/n BE (kcal/mol)
<b><math>\text{C}_6</math> face</b>	<b>-1566.762</b>	<b>-17.99</b>
$\text{C}_5$ face	-1566.745	-17.76
6-6 bond	-1566.711	-16.83
6-5 bond(1)	-1566.755	-17.99
6-5 bond(2)	-1565.628	-16.83

\*calculated at PBE/dzp level of theory in LCAO mode.

(C) Table showing energies\* for lowest energy isomers of  $[\text{Ag}_{29}(\text{BDT})_{12}(\text{C}_{70})_n]^{3-}$  ( $n=2$ ) for  $\text{C}_{70}$  attached at vertex positions (the energies of the lowest energy structure are written in bold)

Orientation of $\text{C}_{70}$ facing the vertex Ag atom	Lowest energy state (E/eV)	Binding Energy/n BE (kcal/mol)
<b><math>\text{C}_6</math> face</b>	<b>-2169.597</b>	<b>-16.60</b>
$\text{C}_5$ face	-2169.560	-16.14
6-6 bond	-2169.534	-15.91
6-5 bond(1)	-2169.572	-16.37
6-5 bond(2)	-2169.571	-16.35

\*calculated at PBE/dzp level of theory in LCAO mode.

**D)** Table showing energies\* for lowest energy isomers of  $[\text{Ag}_{29}(\text{BDT})_{12}(\text{C}_{70})_n]^{3-}$  ( $n=3$ ) for  $\text{C}_{70}$  attached at vertex position (The energies of the lowest energy structure are written in bold.)

Orientation of $\text{C}_{70}$ facing the vertex Ag atom	Lowest energy state (E/eV)	Binding Energy/n BE (kcal/mol)
$\text{C}_6$ face	-2773.419	-15.52
$\text{C}_5$ face	-2773.422	-15.54
6-6 bond	-2773.390	-15.29
6-5 bond(1)	-2773.441	-15.68
<b>6-5 bond(2)</b>	<b>-2773.490</b>	<b>-16.07</b>

\*calculated at PBE/dzp level of theory in LCAO mode.

**E)** Table showing energies\* for lowest energy isomers of  $[\text{Ag}_{29}(\text{BDT})_{12}(\text{C}_{70})_n]^{3-}$  ( $n=4$ ) for  $\text{C}_{70}$  attached at vertex position (the energies of the lowest energy structure are written in bold)

Orientation of $\text{C}_{70}$ facing the vertex Ag atom	Lowest energy state (E/eV)	Binding Energy/n BE (kcal/mol)
$\text{C}_6$ face	-3375.085	-15.04
$\text{C}_5$ face	-3377.299	-15.29
6-6 bond	-3377.241	-14.97
<b>6-5 bond(1)</b>	<b>-3377.352</b>	<b>-15.59</b>
6-5 bond(2)	-3377.313	-15.38

\*calculated at PBE/dzp level of theory in LCAO mode.

**Note.** ESI MS characterization clearly reveals an inherent charge state of -3 for  $[\text{Ag}_{29}(\text{BDT})_{12}]$  cluster as during ionization no counter ions or external ionizing agent was added. The charge is expected to be balanced by counter cations, though it remains unsolved from its reported crystal structure.  $[\text{Ag}_{29}(\text{BDT})_{12}]^{3-}$  is a stable superatom system ( $29-24+3=8e$ ), BDT is a dithiol and contributes 2 electrons per ligand. The charge on the cluster is due to its inherent electron delocalization.<sup>1</sup> So, we have considered the anionic cluster itself as a reagent, instead of representing its charge-balanced form with the counter ions.

## References

1. AbdulHalim, L. G.; Bootharaju, M. S.; Tang, Q.; Del Gobbo, S.; AbdulHalim, R. G.; Eddaoudi, M.; Jiang, D.-e.; Bakr, O. M.  $\text{Ag}_{29}(\text{BDT})_{12}(\text{TPP})_4$ : A Tetravalent Nanocluster. *J. Am. Chem. Soc.* **2015**, *137*, 11970-11975.
2. Perdew, J. P.; Burke, K.; Ernzerhof, M. Generalized Gradient Approximation Made Simple. *Phys. Rev. Lett.* **1997**, *78*, 1396-1396.
3. Larsen, A. H.; Vanin, M.; Mortensen, J. J.; Thygesen, K. S.; Jacobsen, K. W. Localized Atomic Basis Set in the Projector Augmented Wave Method. *Phys. Rev. B* **2009**, *80*, 195112.
4. Lee, K.; Murray, É. D.; Kong, L.; Lundqvist, B. I.; Langreth, D. C. Higher-Accuracy van der Waals Density Functional. *Phys. Rev. B* **2010**, *82*, 081101.
5. Morris, G. M.; Huey, R.; Lindstrom, W.; Sanner, M. F.; Belew, R. K.; Goodsell, D. S.; Olson, A. J. AutoDock4 and AutoDockTools4: Automated Docking with Selective Receptor Flexibility. *J. Comput. Chem.* **2009**, *30*, 2785-2791.
6. Kroto, H. W.; Heath, J. R.; O'Brien, S. C.; Curl, R. F.; Smalley, R. E. *Nature* **1985**, *318*, 162-164.
7. Valsakumar, M. C.; Subramanian, N.; Yousuf, M.; Sahu, P. C.; Hariharan, Y.; Bharathi, A.; Sankara Sastry, V.; Janaki, J.; Rao, G. V. N.; Radhakrishnan, T. S.; Sundar, C. S. Crystal Structure of Solid  $\text{C}_{70}$ . *Pramana* **1993**, *40*, L137-L144.
8. Fuhrmann, J.; Rurainski, A.; Lenhof, H. P.; Neumann, D. A New Lamarckian Genetic Algorithm for Flexible Ligand-Receptor Docking. *J. Comput. Chem.* **2010**, *31*, 1911-8.
9. Pohjolainen, E.; Chen, X.; Malola, S.; Groenhof, G.; Häkkinen, H. A Unified AMBER-Compatible Molecular Mechanics Force Field for Thiolate-Protected Gold Nanoclusters. *J. Chem. Theory Comput.* **2016**, *12*, 1342-1350.
10. Heinz, H.; Vaia, R. A.; Farmer, B. L.; Naik, R. R. Accurate Simulation of Surfaces and Interfaces of Face-Centered Cubic Metals Using 12-6 and 9-6 Lennard-Jones Potentials. *J. Phys. Chem. C* **2008**, *112*, 17281-17290.
11. Hanwell, M. D.; Curtis, D. E.; Lonie, D. C.; Vandermeersch, T.; Zurek, E.; Hutchison, G. R. Avogadro: An Advanced Semantic Chemical Editor, Visualization, and Analysis Platform. *J. Chem. informatics* **2012**, *4*, 17.
12. Humphrey, W.; Dalke, A.; Schulten, K. VMD: Visual Molecular Dynamics. *J. Mol. Graph* **1996**, *14*, 33-8, 27-8.

## Coordinates of the DFT- optimized geometries

**Lowest energy structure of  $[\text{Ag}_{29}(\text{BDT})_{12}(\text{C}_{60})_4]^{3-}$  (optimized using PBE/dzp level of theory in LCAO)**

Energy = -3022.985 eV (-111.093 Hartrees)

Ag	16.18178	15.91615	15.88513
Ag	18.61536	16.04478	17.33675
Ag	17.64014	18.36763	16.00480
Ag	16.30933	17.37863	18.34110
Ag	16.16871	14.37995	18.28323
Ag	18.57601	15.87619	14.36041
Ag	14.66116	18.31309	15.84715
Ag	17.71198	13.52714	15.75779
Ag	16.03487	17.43913	13.49253
Ag	13.80881	15.74293	17.41410
Ag	13.73752	16.00056	14.43058
Ag	14.72944	13.45847	15.97655
Ag	16.27612	14.44181	13.44876
Ag	20.43122	17.74357	19.26794
Ag	19.55463	20.19402	17.68649
Ag	17.96862	19.29261	20.14873
Ag	18.96549	13.26202	18.49675
Ag	18.77802	18.65421	13.23098
Ag	13.54588	18.48027	18.63148
Ag	14.52508	12.42999	20.06776
Ag	20.33987	14.24186	12.40783
Ag	12.72658	20.09171	14.23124
Ag	19.55448	11.74562	14.03231
Ag	14.32064	19.30943	11.73600
Ag	12.02423	14.00638	19.29630
Ag	12.81628	11.60449	17.65001
Ag	17.94240	12.53981	11.59193
Ag	11.89812	17.68058	12.55327
Ag	13.51763	13.25358	13.23751
S	15.39198	18.60587	20.38524
S	20.66523	15.18061	18.53227
S	18.89933	20.39536	15.10244
S	17.12740	13.07695	20.26119
S	20.55740	16.83154	13.07057
S	13.36150	20.28041	16.82414
S	19.05050	11.52534	16.62453



S	16.90977	18.79151	11.50109
S	11.80616	16.59467	18.73056
S	11.74594	15.07553	13.12589
S	13.39580	11.47760	15.05077
S	15.34063	13.12938	11.47461
S	19.51865	17.95133	21.58683
S	21.87746	19.26657	17.92717
S	18.21863	21.62108	19.24241
S	13.00252	13.69608	21.59215
S	21.85411	12.71296	13.67308
S	14.00050	21.60477	12.70352
S	14.22862	10.14333	19.08146
S	19.36225	13.96396	10.11844
S	10.41766	19.12410	13.95810
S	10.51102	12.52644	17.95121
S	18.23313	10.23503	12.53186
S	12.82436	17.97498	10.24262
C	14.91534	17.34902	21.57691
C	21.85378	14.71388	17.27112
C	17.64792	21.59272	14.62911
C	15.02185	17.63764	22.95809
C	23.23837	14.85828	17.53459
C	17.92982	22.97462	14.75080
H	15.48139	18.58715	23.29211
H	23.57571	15.38569	18.44744
H	18.86915	23.31073	15.23012
C	14.51792	16.71118	23.89171
C	24.17201	14.30681	16.63181
C	17.00496	23.90838	14.24181
H	14.59034	16.93889	24.97351
H	25.25494	14.38286	16.85857
H	17.22988	24.99009	14.32501
C	13.91235	15.51099	23.47743
C	23.75393	13.63910	15.46789
C	15.81071	23.49522	13.62307
H	13.50543	14.80095	24.22264
H	24.49395	13.18724	14.78020
H	15.10248	24.24100	13.21368
C	13.81541	15.20558	22.09501
C	22.36899	13.54418	15.16469
C	15.50715	22.11197	13.52104
C	14.33210	16.13296	21.16470
C	21.44094	14.08497	16.07964
C	16.43591	21.18203	14.03504

H	14.25775	15.90406	20.08356
H	20.36048	13.99320	15.85599
H	16.20801	20.10109	13.95556
C	17.60166	14.30070	21.48741
C	21.77926	17.32946	14.28962
C	14.57974	21.51121	17.30836
C	17.46310	13.99579	22.86283
C	23.15383	17.21348	13.97236
C	14.26523	22.88544	17.17631
H	16.97810	13.05115	23.17395
H	23.46488	16.73779	13.02287
H	13.31423	23.19272	16.70093
C	17.95559	14.90610	23.81968
C	24.10966	17.71696	14.87650
C	15.17320	23.84615	17.66420
H	17.84993	14.66666	24.89673
H	25.18664	17.62868	14.63175
H	14.92961	24.92238	17.56075
C	18.57781	16.10805	23.43458
C	23.72296	18.33245	16.08148
C	16.37955	23.46709	18.28203
H	18.96938	16.80835	24.19768
H	24.48507	18.73408	16.77647
H	17.07684	24.23370	18.67147
C	18.70169	16.43261	22.05742
C	22.34712	18.44260	16.41338
C	16.70664	22.09228	18.41133
C	18.20446	15.51720	21.10525
C	21.39499	17.92829	15.50735
C	15.79783	21.13503	17.91175
H	18.30203	15.76079	20.03001
H	20.32005	18.00795	15.76075
H	16.04928	20.06128	18.01147
C	17.80627	10.29961	17.04592
C	17.33841	17.55039	10.27400
C	10.58418	17.00091	17.48219
C	16.63193	10.66312	17.73601
C	18.01636	16.36842	10.63843
C	10.93838	17.74005	16.33611
H	16.43869	11.72956	17.95968
H	18.23066	16.16844	11.70593
H	12.00180	17.98428	16.15330
C	15.69265	9.69898	18.16062
C	18.44012	15.42838	9.67473

C	9.97356	18.17819	15.40274
C	15.94868	8.33287	17.87569
C	18.15606	15.68556	8.30786
C	8.60852	17.86214	15.64588
H	15.22826	7.56142	18.20869
H	18.47310	14.95602	7.53800
H	7.83500	18.21281	14.93617
C	17.11175	7.96951	17.17307
C	17.47069	16.85902	7.94231
C	8.25460	17.09285	16.76821
H	17.29840	6.90110	16.94735
H	17.24516	17.04725	6.87357
H	7.19105	16.83383	16.93954
C	18.04488	8.93618	16.75039
C	17.05988	17.79915	8.90835
C	9.22595	16.65517	17.69318
H	18.95547	8.64095	16.19525
H	16.52649	18.72210	8.61032
H	8.93835	16.04941	18.57338
C	10.54172	14.49800	14.32762
C	14.59877	10.27236	14.48325
C	14.76587	14.33441	10.27143
C	10.94049	13.94324	15.56211
C	15.83692	10.67183	13.93672
C	14.22497	15.57486	10.67189
H	12.01022	13.96711	15.84906
H	16.12428	11.74133	13.96240
H	14.25368	15.86094	11.74187
C	10.01537	13.32768	16.43291
C	16.71123	9.74571	13.32907
C	13.61808	16.45188	9.74681
C	8.64608	13.30187	16.05580
C	16.33374	8.37666	13.30333
C	13.59341	16.07729	8.37739
H	7.90579	12.81858	16.72205
H	17.00402	7.63883	12.82263
H	13.12271	16.75152	7.63695
C	8.24052	13.88302	14.84016
C	15.11795	7.96939	13.88106
C	14.15953	14.85496	7.97189
H	7.16966	13.86086	14.55404
H	14.83378	6.89820	13.85745
H	14.13143	14.56904	6.90154
C	9.17216	14.48025	13.96813

C	14.24135	8.90157	14.47113
C	14.74244	13.97341	8.90274
H	8.84862	14.91559	13.00323
H	13.27786	8.57748	14.90843
H	15.16018	13.00107	8.57773
C	22.48965	25.17260	12.45608
C	22.60202	23.85293	13.07519
C	23.58590	25.72771	11.76171
C	23.80867	23.12755	12.97458
C	24.83402	24.97587	11.65389
C	24.94123	23.69941	12.24820
C	21.13855	25.30430	11.91559
C	21.31997	23.16887	12.91867
C	23.36971	26.42966	10.49805
C	23.77668	21.69064	12.70784
C	25.39076	25.21326	10.32364
C	25.61047	22.61548	11.53138
C	20.41601	24.06693	12.20111
C	24.48484	26.11059	9.60836
C	24.89051	21.37486	11.81587
C	20.92892	25.98611	10.69716
C	21.28938	21.78230	12.65810
C	22.06463	26.55586	9.97436
C	22.53837	21.03091	12.54886
C	26.03828	24.16676	9.63157
C	26.15093	22.84612	10.24768
C	19.51245	23.54540	11.25141
C	24.25645	25.93023	8.22691
C	24.72950	20.40772	10.80148
C	19.99097	25.44731	9.71520
C	20.34827	21.24090	11.67673
C	21.82798	26.36903	8.54398
C	22.37287	20.02765	11.49918
C	25.80153	23.97890	8.20093
C	25.98632	21.84194	9.19745
C	19.29867	24.24693	9.98834
C	19.47592	22.10856	10.98479
C	22.90537	26.06262	7.68434
C	23.45031	19.71911	10.64170
C	24.92735	24.84647	7.51026
C	25.28459	20.64739	9.47054
C	20.54693	25.68314	8.38443
C	21.01976	20.15586	10.95862
C	25.77017	22.54189	7.93246

C	19.13026	23.24350	8.93819
C	19.23993	21.92157	9.55445
C	22.73904	25.05923	6.63437
C	23.21405	19.53318	9.21130
C	23.98834	24.30707	6.52757
C	24.34780	20.10647	8.48756
C	20.38621	24.71360	7.37134
C	20.79182	19.97625	9.57740
C	24.86300	22.02107	6.98362
C	19.66426	23.47379	7.65236
C	19.88600	20.87433	8.86303
C	21.50201	24.39511	6.48304
C	21.90886	19.66116	8.68939
C	23.95690	22.91940	6.26847
C	24.14122	20.78141	7.26503
C	20.33380	22.38950	6.93731
C	20.44516	21.11553	7.53472
C	21.46925	22.95852	6.21397
C	21.69457	20.36511	7.42643
C	22.67596	22.23313	6.10777
C	22.78958	20.91287	6.72443
C	7.82249	21.43408	25.05359
C	6.43986	21.60413	24.61126
C	8.54662	20.28360	24.67423
C	5.82793	20.61706	23.80841
C	7.91214	19.26024	23.84474
C	6.57577	19.42381	23.41980
C	8.46945	22.74504	25.02927
C	6.23251	23.01925	24.31173
C	9.94349	20.39992	24.26014
C	4.98568	21.01079	22.67976
C	8.91796	18.74603	22.91783
C	6.19637	19.08078	22.05003
C	7.48596	23.72550	24.57260
C	10.17289	19.44960	23.17504
C	5.21382	20.06092	21.59268
C	9.81785	22.85745	24.62625
C	5.41902	23.39964	23.22268
C	10.56870	21.66589	24.23707
C	4.78381	22.37783	22.39200
C	8.55204	18.42005	21.59417
C	7.16872	18.59092	21.15233
C	7.88481	24.78660	23.73031
C	11.01616	19.80078	22.09939

C	5.23836	20.51257	20.25457
C	10.23030	23.95710	23.75474
C	5.83181	24.49875	22.35160
C	11.44551	22.02822	23.12555
C	4.80540	22.84549	21.00703
C	9.42735	18.78087	20.48281
C	7.19247	19.05620	19.76713
C	9.28127	24.90533	23.31557
C	7.04304	25.18078	22.60195
C	11.66297	21.11196	22.07451
C	5.03088	21.92854	19.95736
C	10.63917	19.45802	20.73082
C	6.24101	19.99909	19.32400
C	11.23601	23.44386	22.82730
C	5.45207	24.15666	20.98276
C	8.58928	19.17065	19.35166
C	9.30349	25.37265	21.93063
C	7.91997	25.54242	21.48952
C	11.68735	21.57760	20.68856
C	5.90677	22.28935	18.84268
C	11.05624	20.55505	19.85680
C	6.65369	21.09742	18.45030
C	11.25788	23.89232	21.48948
C	6.30140	24.50264	19.90928
C	8.98823	20.23121	18.50950
C	10.27228	24.87138	21.03489
C	7.55619	25.20795	20.16714
C	11.49252	22.94612	20.40062
C	6.53044	23.55678	18.82013
C	10.23944	20.93656	18.77144
C	8.00535	21.21050	18.05709
C	9.89592	24.52814	19.66511
C	8.56113	24.69605	19.23758
C	10.64970	23.33928	19.27355
C	7.92671	23.67473	18.40546
C	10.03493	22.35166	18.47383
C	8.65170	22.52281	18.03290
C	23.74664	11.77469	25.79438
C	24.28700	10.43710	26.03082
C	24.50233	12.72381	25.07259
C	25.56543	10.09301	25.53980
C	25.82540	12.36761	24.56210
C	26.34774	11.07596	24.79262
C	22.31123	11.64511	25.55032

C	23.18461	9.48094	25.93440
C	23.85014	13.57949	24.08327
C	25.78685	8.78203	24.93020
C	25.99171	13.00541	23.25788
C	27.05126	10.37214	23.72160
C	21.96413	10.22819	25.63751
C	24.77127	13.75428	22.96216
C	26.70492	8.95467	23.80675
C	21.68197	12.46734	24.59132
C	23.39931	8.21472	25.34572
C	22.46412	13.45150	23.84544
C	24.72193	7.85923	24.83525
C	26.67201	12.32515	22.22416
C	27.20830	10.98606	22.46039
C	20.99946	9.68558	24.76032
C	24.27026	13.79114	21.64310
C	26.52774	8.20029	22.62601
C	20.67986	11.90639	23.68624
C	22.39921	7.65169	24.44006
C	21.94451	13.49779	22.48060
C	24.53912	7.07603	23.61408
C	26.15607	12.36854	20.85751
C	27.02600	10.20418	21.23771
C	20.34328	10.53741	23.77191
C	21.22222	8.37527	24.15037
C	22.83488	13.66065	21.39845
C	25.42651	7.24334	22.52873
C	24.97479	13.08607	20.57288
C	26.69204	8.83426	21.32041
C	20.84051	12.54478	22.38283
C	23.10315	6.94768	23.37000
C	26.37747	11.05810	20.24694
C	20.15637	9.75382	22.55047
C	20.70041	8.41735	22.78589
C	22.65405	12.87580	20.18038
C	24.90951	7.28747	21.16235
C	23.97364	12.52250	19.66742
C	25.69218	8.27088	20.41536
C	20.66488	11.78747	21.20422
C	22.60311	6.99339	22.05094
C	25.40736	10.51483	19.37521
C	20.31968	10.36875	21.29093
C	21.38112	7.73844	21.75249
C	21.58535	11.95970	20.08099



C	23.52280	7.16625	20.92788
C	24.18857	11.25978	19.07366
C	25.05959	9.09753	19.46247
C	21.02640	9.66611	20.22052
C	21.54582	8.37292	20.44668
C	21.80848	10.64752	19.47290
C	22.86894	8.01912	19.93738
C	23.08551	10.30549	18.97765
C	23.62455	8.96887	19.21689
C	11.68876	6.29434	9.53317
C	12.23326	7.14867	8.48022
C	11.73118	6.72206	10.87791
C	12.79909	8.39929	8.81167
C	12.32348	8.01291	11.22103
C	12.84854	8.83866	10.20419
C	10.48993	5.64020	9.01197
C	11.37124	7.02442	7.30703
C	10.57744	6.50790	11.74915
C	12.52503	9.56837	7.97843
C	11.53574	8.59826	12.30446
C	12.60434	10.27990	10.23259
C	10.29242	6.09401	7.63639
C	10.45518	7.66801	12.62953
C	12.40415	10.73047	8.85672
C	9.37515	5.43268	9.85382
C	11.10613	8.15428	6.50249
C	9.42057	5.87332	11.24693
C	11.69556	9.44806	6.84247
C	11.29535	9.98873	12.33049
C	11.84200	10.84480	11.27764
C	8.98761	6.32345	7.14770
C	9.17729	8.15737	12.97617
C	11.45176	11.73151	8.57049
C	8.02455	5.67222	9.34853
C	9.75595	8.39200	5.99603
C	8.09825	6.38290	11.60309
C	10.71047	10.48535	6.54553
C	9.97155	10.49578	12.68437
C	10.85246	11.88025	10.97955
C	7.83344	6.10861	8.01881
C	8.71434	7.49180	6.31284
C	7.97951	7.50503	12.45129
C	10.59001	11.60470	7.39781
C	8.93079	9.59834	13.00793

C	10.66290	12.31901	9.65152
C	7.23493	6.25904	10.43035
C	9.51102	9.83349	6.02268
C	9.69819	11.66313	11.84917
C	6.84613	7.14554	7.72291
C	7.39128	8.00075	6.66968
C	6.99335	8.54252	12.15541
C	9.26700	12.11391	7.75400
C	7.58197	9.83564	12.49872
C	9.31271	12.55552	9.14676
C	6.28186	7.26028	10.14542
C	8.23313	10.32515	6.36818
C	8.39473	11.89539	11.36285
C	6.08441	7.71093	8.76890
C	7.15594	9.39272	6.69807
C	6.15726	8.42202	11.02411
C	8.10884	11.48589	7.24761
C	7.31758	10.96413	11.69250
C	8.19806	12.34795	9.98790
C	5.83800	9.15138	8.79733
C	6.36565	9.97713	7.77998
C	5.88304	9.59033	10.19066
C	6.95533	11.27041	8.11987
C	6.45601	10.83823	10.51945
C	7.00080	11.69259	9.46566



Cite this: *Phys. Chem. Chem. Phys.*,  
2018, 20, 7593

# Understanding proton capture and cation-induced dimerization of $[\text{Ag}_{29}(\text{BDT})_{12}]^{3-}$ clusters by ion mobility mass spectrometry†

Papri Chakraborty,<sup>‡a</sup> Ananya Baksi,<sup>‡§a</sup> Sathish Kumar Mudedla,<sup>b</sup> Abhijit Nag,<sup>a</sup>  
Ganesan Paramasivam,<sup>a</sup> Venkatesan Subramanian<sup>id b</sup> and Thalappil Pradeep<sup>id \*a</sup>

Proton transfer reactions have been a topic of fundamental interest in several areas of chemistry and biology. However, such reactivity has not been explored in detail for nanoscale materials. In this article, we present a unique reaction of an atomically precise monolayer-protected silver nanocluster,  $[\text{Ag}_{29}(\text{BDT})_{12}]^{3-}$ , with a proton ( $\text{H}^+$ ). Under controlled conditions, the strong proton affinity facilitated a complete conversion of the cluster to its protonated form,  $[\text{Ag}_{29}(\text{BDT})_{12}\text{H}]^{2-}$ . Moreover, binding of alkali metal ions ( $\text{Li}^+$ ,  $\text{Na}^+$ ,  $\text{K}^+$ ,  $\text{Rb}^+$  and  $\text{Cs}^+$ ) induced specific structural changes and also favored dimerization of the cluster. In this case, the cations acted as a bridge between the two clusters and the degree of dimerization was specific to the size of the cations. The conformational changes and separation of the alkali-metal ion bound dimers from their respective monomers have been investigated by ion mobility mass spectrometry (IM MS) and tandem mass spectrometric studies. Density functional theory (DFT) calculations have been used to determine the possible structures of the monomers and the dimers. Similar reactivity of the cluster can also be extended to other metal ions. While the present study helps to expand the ion-chemistry of atomically precise clusters, gas-phase basicity of the molecule can be explored in further detail and this can find applications in the areas of sensing and materials in general.

Received 6th December 2017,  
Accepted 12th February 2018

DOI: 10.1039/c7cp08181b

rsc.li/pccp

## 1. Introduction

Monolayer-protected clusters are emerging as an interesting family of nanomaterials. These nanoscale materials are becoming increasingly important due to their structures, diverse properties, and widespread applications.<sup>1–5</sup> Condensed phase science of these clusters is expanding in different directions due to their potential applications in sensing, catalysis, imaging, etc. Up to now, several clusters have been crystallized and their structures have been solved by X-ray crystallography. Some of the noted examples are clusters like  $\text{Au}_{25}(\text{SR})_{18}$ ,<sup>6</sup>  $\text{Au}_{38}(\text{SR})_{24}$ ,<sup>7</sup>  $\text{Au}_{102}(\text{SR})_{44}$ ,<sup>8</sup>  $\text{Ag}_{44}(\text{SR})_{30}$ ,<sup>9</sup>  $\text{Ag}_{25}(\text{SR})_{18}$ ,<sup>10</sup>  $\text{Ag}_{29}(\text{S}_2\text{R})_{12}$ ,<sup>11</sup> etc. These clusters are well characterized by distinct absorption features

and also by mass spectrometry. Isotope patterns obtained from high resolution mass spectrometric techniques have helped to identify their molecular formulae and hence the exact composition of the clusters in the gas phase. Solution-phase properties of the clusters have been studied for a long time. However, gas-phase studies provide new insights into understanding their properties, and recently such studies have become important.<sup>12–15</sup> Another emerging field is intercluster reactions.<sup>16</sup> Detection of intermediate products helps to understand the reaction mechanism.<sup>17</sup> Several interactions like H-bonding, van der Waals forces, and dipole-dipole interactions exist and they can result in the formation of different types of adducts of clusters.  $\text{Ag}_{44}(\text{p-MBA})_{30}$  (*p*-MBA is *para* mercapto benzoic acid) clusters remain hydrogen bonded to their neighboring ones in their superlattice structures.<sup>18</sup> Such interactions are important in controlling highly precise cluster-mediated self-assemblies.<sup>19</sup>  $\text{Au}_{25}(\text{SBu})_{18}$  (SBu is butane thiolate) is known to form a linear polymer in its crystal structure *via* Au–Au single bonds stabilized by appropriate orientation of the clusters.<sup>20</sup> An intercluster reaction between  $[\text{Au}_{25}(\text{SR})_{18}]^-$  and  $[\text{Ag}_{25}(\text{SR})_{18}]^-$  also involves the formation of a transient dianionic adduct,  $[\text{Au}_{25}\text{Ag}_{25}(\text{SR})_{36}]^{2-}$ .<sup>16</sup> Polymeric forms of  $[\text{Au}_{25}(\text{SR})_{18}]^-$  clusters have been detected in the gas phase.<sup>21</sup> However, aurophilic interaction is one of the essential factors favoring such a dimerization process,

<sup>a</sup> DST Unit of Nanoscience (DST UNS) and Thematic Unit of Excellence,  
Department of Chemistry, Indian Institute of Technology Madras,  
Chennai 600036, India. E-mail: pradeep@iitm.ac.in; Fax: +91-44 2257-0545

<sup>b</sup> Chemical Laboratory, CSIR-Central Leather Research Institute, Adyar, Chennai,  
600020, India

† Electronic supplementary information (ESI) available: Additional ESI MS,  
UV-vis and computational details. See DOI: 10.1039/c7cp08181b

‡ These authors contributed equally.

§ Presently a postdoctoral fellow at Karlsruhe Institute of Technology (KIT),  
Institute of Nanotechnology, Hermann-von-Helmholtz-Platz 1, 76344 Eggenstein-  
Leopoldshafen, Germany.

which was reflected in the absence of any dimerization in the structurally similar  $[\text{Ag}_{25}(\text{SR})_{18}]^-$  cluster. Similarly,  $[\text{Ag}_{29}(\text{S}_2\text{R})_{12}]^{3-}$  also does not dimerize, possibly due to the lack of suitable interactions to favor such a process.

In this article, we present a new aspect of cluster dimerization mediated through cations. This is possibly due to additional interactions that arise in the system due to the incorporation of a new metal center. We have characterized and separated the dimers by ion-mobility mass spectrometry (IM MS). IM MS studies help in understanding the structure and conformational dynamics present in a system.<sup>22</sup> Though such techniques have been used extensively to study proteins and macromolecules,<sup>23–27</sup> recently these techniques have also become useful in the case of clusters.<sup>28,29</sup> Reactivity of the cluster with a series of alkali metal ions ( $\text{Li}^+$ ,  $\text{Na}^+$ ,  $\text{K}^+$ ,  $\text{Rb}^+$  and  $\text{Cs}^+$ ) and their effect on the dimerization process have been studied. Ion-mobility and dissociation studies reflect the similarity in their structures. Such interactions can be expanded across a number of similar metals. Another aspect that is brought about in this article is the uniqueness of the interaction of the  $[\text{Ag}_{29}(\text{BDT})_{12}]^{3-}$  cluster with protons. Interaction of hydrogen with  $[\text{Au}_{25}(\text{SR})_{18}]$  clusters has been studied theoretically, which predicts that hydrogen can behave as a metal atom in the clusters and contribute its one electron to the superatomic free-electron count.<sup>30</sup> Hydride protected Ag, Cu and Fe clusters have also been characterized.<sup>31–34</sup> Herein, we explore the reactivity of a proton ( $\text{H}^+$ ) with the cluster  $[\text{Ag}_{29}(\text{BDT})_{12}]^{3-}$ .  $\text{H}^+$  interacts with the cluster to form  $[\text{Ag}_{29}(\text{BDT})_{12}\text{H}]^{2-}$ . Affinity towards protons can give an idea regarding the gas-phase basicity of a molecule.<sup>35–39</sup> Proton-transfer reactions are of immense importance in chemistry and in biomolecular processes.<sup>40–43</sup> So, it has been an important area of research for years and such studies have been performed for a wide range of molecules starting from small molecules, amino acids, peptides and proteins. Structural changes resulting from the interaction of the cluster with a proton as well as alkali metal ions have been studied by density functional theory calculations. Computational studies are also presented to understand the possible structures for the dimers.

## 2. Experimental section

### 2.1 Reagents and materials

All the materials were commercially available and used without further purification. Silver nitrate ( $\text{AgNO}_3$ , 99.9%) was purchased from Rankem, India. 1,3-Benzene dithiol (1,3-BDT), sodium borohydride ( $\text{NaBH}_4$ ), and formic acid (98%) were purchased from Sigma Aldrich. Triphenylphosphine (TPP) was purchased from Spectrochem, India. Ammonium acetate ( $\text{NH}_4\text{OAc}$ ), sodium acetate ( $\text{NaOAc}$ ), lithium bromide ( $\text{LiBr}$ ), potassium acetate ( $\text{KOAc}$ ), rubidium bromide ( $\text{RbBr}$ ) and cesium acetate ( $\text{CsOAc}$ ) were purchased from Sigma Aldrich. All the solvents, dichloromethane (DCM), methanol ( $\text{MeOH}$ ), ethanol ( $\text{EtOH}$ ), acetonitrile (ACN) and dimethylformamide (DMF), were of HPLC grade and were used without further distillation.

### 2.2 Synthesis of the $[\text{Ag}_{29}(\text{BDT})_{12}(\text{TPP})_4]$ cluster

The  $[\text{Ag}_{29}(\text{BDT})_{12}(\text{TPP})_4]$  cluster was synthesized following a reported protocol with slight modifications.<sup>11</sup> About 20 mg of  $\text{AgNO}_3$  was dissolved in a mixture of 5 mL of methanol and 10 mL of DCM. To this reaction mixture, about 13.5  $\mu\text{L}$  of 1,3-benzene dithiol (1,3-BDT) ligand was added. Then, the mixture was kept under stirring conditions. Shortly after this, 200 mg of TPP dissolved in 1 mL of DCM was added to the reaction mixture. The solution turned colorless indicating the formation of a Ag–S–P complex. After about 10 min, 10.5 mg of  $\text{NaBH}_4$  dissolved in 500  $\mu\text{L}$  of ice-cold water was added. Upon addition of  $\text{NaBH}_4$ , the solution turned dark brown in color immediately. Gradually, the color changed to orange. Continuous stirring was carried out for 3 h under dark conditions. The reaction mixture was then centrifuged and the supernatant was discarded. The precipitate was washed twice with methanol and then dissolved in DMF and centrifuged. The precipitate was discarded and the supernatant contained the purified clusters dissolved in DMF.

### 2.3 Instrumentation

The UV-vis spectra were measured using a PerkinElmer Lambda 25 UV-vis spectrometer. Mass spectrometric measurements were carried out in a Waters Synapt G2-Si high definition mass spectrometer. The instrument is well equipped with electrospray ionization and ion mobility separation techniques. A concentration of about  $1 \mu\text{g mL}^{-1}$  was used for the cluster solution. Samples were infused at a flow rate of  $20 \mu\text{L min}^{-1}$ . The source and desolvation temperatures were set at  $100^\circ\text{C}$  and  $200^\circ\text{C}$ , respectively. Soft ionization conditions involving capillary voltage: 1.5 kV, cone voltage: 0 V, source offset: 0 V, source and desolvation temperature:  $50^\circ\text{C}$ , and desolvation gas flow rate:  $100 \text{ L h}^{-1}$  were used for preventing the TPP loss during the ionization and observing the intact TPP protected clusters.

### 2.4 Computational details

We used density functional theory (DFT) with projector augmented waves (PAWs) as implemented in GPAW.<sup>44,45</sup> The PAW setup used was  $\text{Ag}(4d^{10}5s^1)$ ,  $\text{S}(3s^23p^4)$ ,  $\text{C}(2s^22p^2)$ ,  $\text{P}(3s^23p^3)$ ,  $\text{H}(1s^1)$ ,  $\text{Na}(3s^1)$  and  $\text{Cs}(5s^25p^66s^1)$ , with scalar-relativistic effects included for Ag. The PBE<sup>46</sup> functional and DZP (double zeta plus polarization) basis set were chosen in LCAO mode<sup>47</sup> to improve the efficiency of the calculations. The geometry optimizations were carried out with a grid spacing of  $0.2 \text{ \AA}$  and minimizing the residual forces without any symmetry constraints by  $0.05 \text{ eV \AA}^{-1}$ . The relative energies (REs) were calculated with respect to the most stable isomer. The binding energies of the cations to the cluster were calculated by subtracting the sum of the energies of the cluster  $[\text{Ag}_{29}(\text{BDT})_{12}]^{3-}$  and M ( $\text{M} = \text{H}$ ,  $\text{Na}$  etc.) from their respective complexes,  $[\text{Ag}_{29}(\text{BDT})_{12}\text{M}]^{2-}$ . The structures of the dimers have been optimized using the same level of theory as that used for the monomers.

## 3. Results and discussion

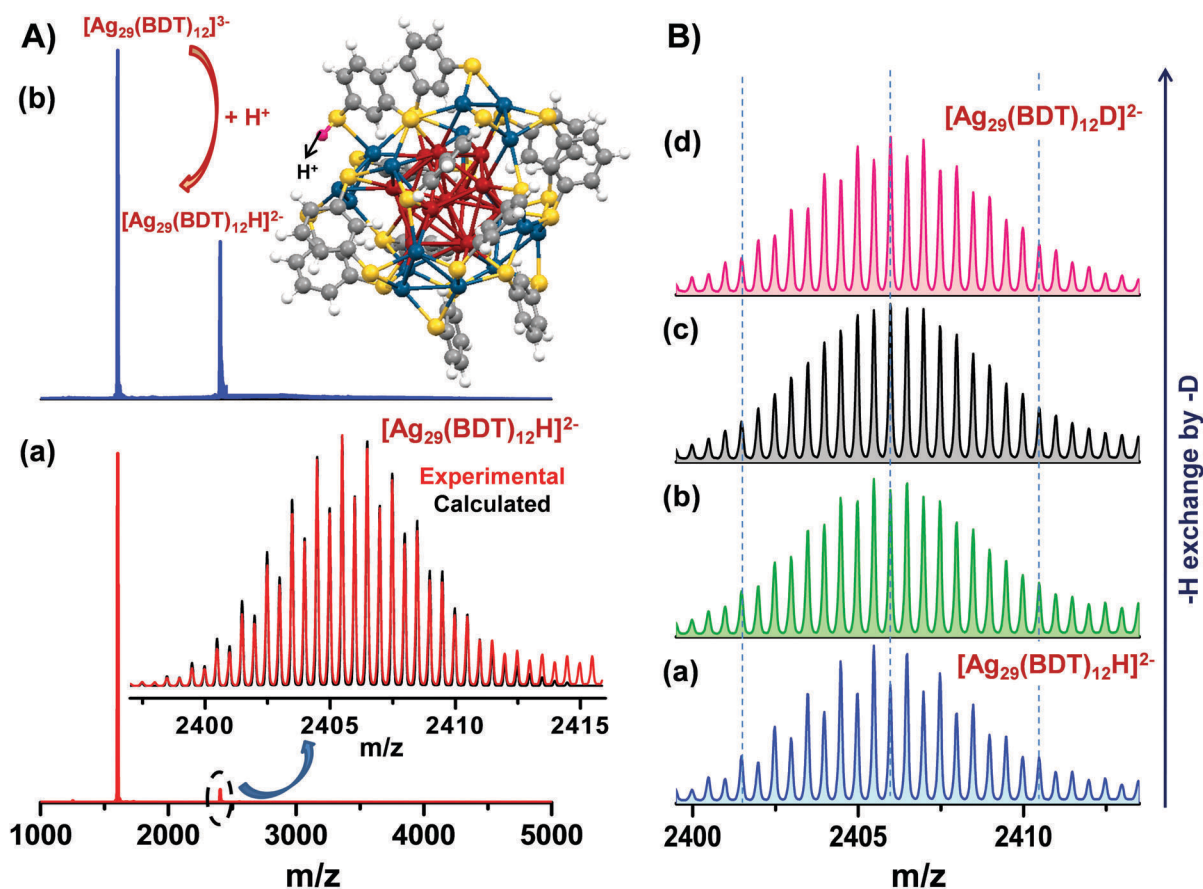
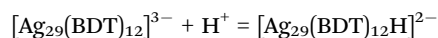
The  $[\text{Ag}_{29}(\text{BDT})_{12}(\text{TPP})_4]^{3-}$  cluster was synthesized by the method described above (see Experimental section 2.2) and characterized using UV-vis and ESI MS (see Fig. S1, ESI†).<sup>11</sup> The cluster was

well characterized by distinct molecule-like features at 447 nm and 513 nm in its optical absorption spectra. In ESI MS, an intense peak was observed at  $m/z$  1603, which corresponded to  $[\text{Ag}_{29}(\text{BDT})_{12}]^{3-}$ . The labile TPP ligands were lost during the ionization. The intact  $[\text{Ag}_{29}(\text{BDT})_{12}(\text{TPP})_4]^{3-}$  cluster could be observed only under soft ionization conditions (Fig. S1C, ESI†). So, the gas-phase measurements and the related theoretical calculations have been performed primarily with  $[\text{Ag}_{29}(\text{BDT})_{12}]^{3-}$  clusters.

### 3.1 Protonation of $[\text{Ag}_{29}(\text{BDT})_{12}(\text{TPP})_4]^{3-}$ clusters

It is known from previous reports that the  $[\text{Ag}_{29}(\text{BDT})_{12}(\text{TPP})_4]^{3-}$  cluster<sup>11</sup> consists of an icosahedral  $\text{Ag}_{13}$  core protected by staple motifs consisting of Ag and S atoms. Though the core remains highly protected, the Ag and S atoms in the exterior shells may exhibit some selective affinity towards specific binding groups. The delocalized negative charge density of the cluster also imparts an affinity for binding with suitable positively charged counterparts. In an attempt to explore such reactivity, we studied the effect of the addition of cations to the cluster. As there are numerous S atoms exposed in the outer staples, they may interact with protons and induce some specific structural changes in the

system. Experiments were carried out by adding formic acid (a well-known proton donor) to the cluster solution and its reactivity was monitored carefully using ESI MS. A solution of about 0.1 mM cluster solution was prepared, and in the presence of about 1 mM formic acid in DMF, a peak at  $m/z$  2406 started increasing in intensity. This is shown in Fig. 1A(a). The peak increased in intensity with increasing concentration of the acid (Fig. S2, ESI†) and became maximum when the formic acid concentration was around 12 mM (Fig. 1A(b)). However, the concentration of the acid could not be increased further to favor a complete conversion as, beyond this concentration of the acid, the cluster started to show degradation. Addition of formic acid changes the pH of the solution, it may also cause a change in the charge distribution of the cluster and all these factors can significantly affect the cluster stability. The new peak was assigned as  $[\text{Ag}_{29}(\text{BDT})_{12}\text{H}]^{2-}$ . The inset of Fig. 1A(a) shows the comparison between the experimental isotope patterns and the calculated patterns, which confirms its composition. The reactivity can be expressed in the form of the following chemical equation,



**Fig. 1** (A) ESI MS of (a)  $[\text{Ag}_{29}(\text{BDT})_{12}]^{3-}$  cluster in the presence of 1 mM formic acid and (b) maximum conversion of  $[\text{Ag}_{29}(\text{BDT})_{12}]^{3-}$  to  $[\text{Ag}_{29}(\text{BDT})_{12}\text{H}]^{2-}$  upon addition of formic acid. Inset of (a) shows the experimental and calculated isotope patterns of  $[\text{Ag}_{29}(\text{BDT})_{12}\text{H}]^{2-}$  and inset of (b) shows the lowest energy DFT optimized structure of  $[\text{Ag}_{29}(\text{BDT})_{12}\text{H}]^{2-}$ . The proton is marked in the figure. Experimental spectrum (inset of (a) extends beyond 2415 due to overlapping contribution from other ions). (B) Isotope patterns of (a)  $[\text{Ag}_{29}(\text{BDT})_{12}\text{H}]^{2-}$ , (b) and (c) gradual changes in the pattern upon replacement of H by D and (d)  $[\text{Ag}_{29}(\text{BDT})_{12}\text{D}]^{2-}$ . See the change in the intensities of the peaks on the dotted lines in relation to the nearby peaks from (a) to (d). Color codes: red: Ag of core; blue: Ag of staples; yellow: S; grey: C; white: H atoms; and purple: proton.

However, this species should not be confused with the 2− charge state of the parent cluster as that would have only a difference of  $m/z$  0.5 with respect to this protonated species. The isotope distribution of the species  $[\text{Ag}_{29}(\text{BDT})_{12}\text{H}]^{2-}$  was also compared with the theoretical pattern of  $[\text{Ag}_{29}(\text{BDT})_{12}]^{2-}$  to show the clear distinction between them (see Fig. S3, ESI†). As the cluster was sensitive to the presence of  $\text{H}^+$  in solution, a few other control studies were also carried out by varying the solvents and the proton sources in order to get more insights about its proton capture affinity. The cluster was dissolved in a 1:1 mixture of DMF:MeOH to enhance the polarity of the medium and its mass spectrum was measured without the addition of any formic acid. In this case also, the peak for  $[\text{Ag}_{29}(\text{BDT})_{12}\text{H}]^{2-}$  was observed, though at low intensity, as shown in Fig. S4A (ESI†). It was even sensitive to the proton concentration when one drop of water was added to the cluster solution in DMF (see Fig. S4B, ESI†). We also studied the feasibility of H/D exchange in the system by adding  $\text{D}_2\text{O}$  as the  $\text{D}^+$  source and within 2 min of  $\text{D}_2\text{O}$  addition, there was a complete exchange and  $[\text{Ag}_{29}(\text{BDT})_{12}\text{D}]^{2-}$  was formed. In Fig. 1B, where (a) represents the ESI MS of  $[\text{Ag}_{29}(\text{BDT})_{12}\text{H}]^{2-}$ , gradual changes in the distribution of the peaks of the isotope pattern start upon addition of  $\text{D}_2\text{O}$ , which is shown in (b) and (c). Finally, on complete conversion to  $[\text{Ag}_{29}(\text{BDT})_{12}\text{D}]^{2-}$ , there was a shift to higher mass by  $m/z$  0.5 and this is shown in (d). H/D exchange further confirmed the binding of a proton to the cluster and hence the assignment.

Again, the cluster solutions were prepared in  $\text{NH}_4\text{OAc}$  buffer solutions of varying concentrations (0.25 M, 0.5 M and 1 M) in a

1:1 mixture of DMF and MeOH and ESI MS was measured. The conversion of  $[\text{Ag}_{29}(\text{BDT})_{12}]^{3-}$  to  $[\text{Ag}_{29}(\text{BDT})_{12}\text{H}]^{2-}$  increased with an increase in the concentration of  $\text{NH}_4\text{OAc}$  and finally in a solution of 1 M  $\text{NH}_4\text{OAc}$ , there was a complete conversion of the cluster to  $[\text{Ag}_{29}(\text{BDT})_{12}\text{H}]^{2-}$ . This was monitored by ESI MS, as shown in Fig. 2A. The decay in the relative intensity of  $[\text{Ag}_{29}(\text{BDT})_{12}]^{3-}$  and the corresponding growth in the intensity of  $[\text{Ag}_{29}(\text{BDT})_{12}\text{H}]^{2-}$  with an increase in the concentration of  $\text{NH}_4\text{OAc}$  are shown in Fig. 2B. There was no complexation with  $\text{NH}_4^+$ , instead, proton transfer occurred from the reaction medium (pH of the medium was 6.8). This supports the strong proton capture tendency of the cluster. When a tertiary amine salt ( $\text{NMe}_4\text{Br}$ ), which has no transferable protons on the N atom, was added, the cluster showed complexation with the  $(\text{NMe}_4)^+$  group (Fig. S5, ESI†). However, in all such reactions, the absorption features of the cluster were not much affected (Fig. S6, ESI†). In the structure of the cluster, there are no free groups like  $-\text{OH}$ ,  $-\text{NH}_2$  or  $-\text{COO}^-$  in the ligands that can become easily protonated. So, the proton possibly interacts at some specific site of the cluster and that results in a change in the overall charge delocalization. MS/MS studies were also carried out to gain better insight into the structure and the binding interactions (Fig. S7, ESI†).<sup>27,48–50</sup> Upon increasing energy, the proton was lost and the cluster  $[\text{Ag}_{29}(\text{BDT})_{12}]^{3-}$  was reformed.  $[\text{Ag}_5(\text{BDT})_3]^-$  is a common fragment of  $[\text{Ag}_{29}(\text{BDT})_{12}]^{3-12}$  and the proton was found to be associated with the thiolates as  $[\text{Ag}_4(\text{BDT})_3\text{H}]^-$ . Further, by the use of soft ionization conditions, we have observed that proton capture can occur with the intact  $[\text{Ag}_{29}(\text{BDT})_{12}(\text{TPP})_4]^{3-}$  clusters that exist in solution,

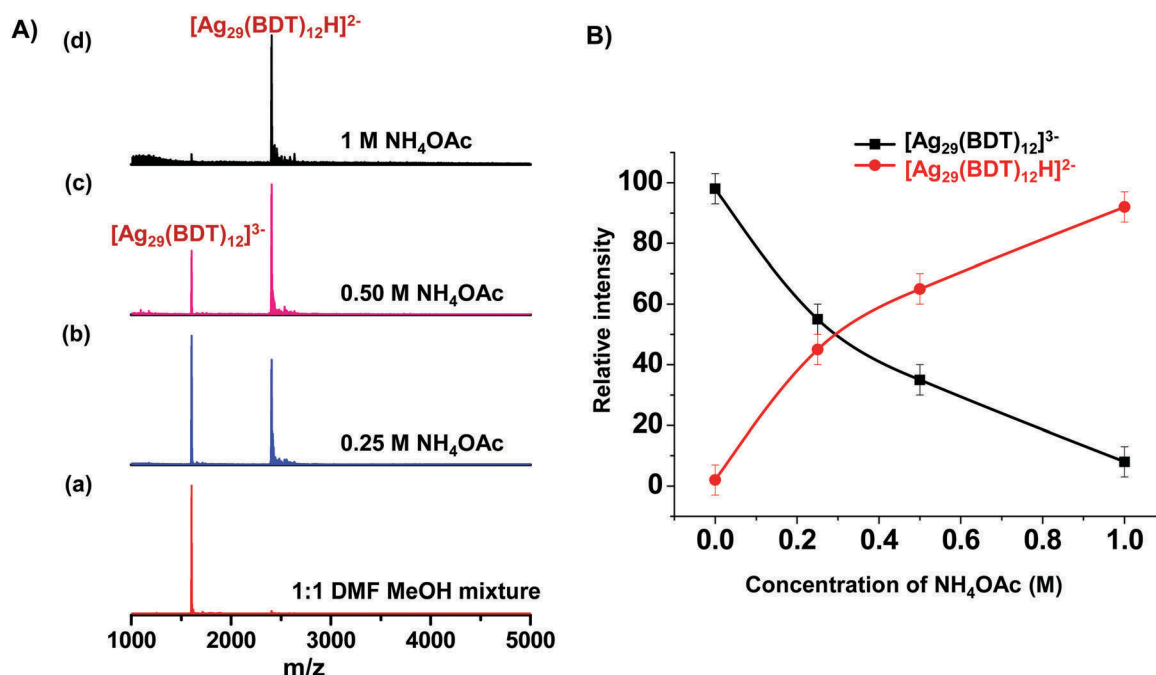


Fig. 2 (A) ESI MS of  $[\text{Ag}_{29}(\text{BDT})_{12}]^{3-}$  cluster in 1:1 DMF/MeOH solution of  $\text{NH}_4\text{OAc}$  at different concentrations: (a) 0 M, (b) 0.25 M, (c) 0.5 M and (d) 1 M. The spectra show that there is an increase in the conversion of  $[\text{Ag}_{29}(\text{BDT})_{12}]^{3-}$  to  $[\text{Ag}_{29}(\text{BDT})_{12}\text{H}]^{2-}$  with an increase in the concentration of  $\text{NH}_4\text{OAc}$ . (B) Plot showing the decay in the relative intensities of  $[\text{Ag}_{29}(\text{BDT})_{12}]^{3-}$  and growth in the relative intensities of  $[\text{Ag}_{29}(\text{BDT})_{12}\text{H}]^{2-}$ , respectively with an increase in the concentration of  $\text{NH}_4\text{OAc}$ .



leading to the formation of  $[\text{Ag}_{29}(\text{BDT})_{12}\text{H}(\text{TPP})_n]^{2-}$  ( $n = 1-4$ ) clusters, as shown in Fig. S8 (ESI†). To understand the possible structures of  $[\text{Ag}_{29}(\text{BDT})_{12}\text{H}]^{2-}$ , computational studies were carried out. The most stable structure is shown in the inset of Fig. 1A(b).

### 3.2 DFT optimized structure of $[\text{Ag}_{29}(\text{BDT})_{12}\text{H}]^{2-}$

The structure of  $[\text{Ag}_{29}(\text{BDT})_{12}]^{3-}$  was optimized using the coordinates of the crystal structure from previous reports.<sup>11</sup> A proton may interact with Ag and S atoms. In the exterior shell, two types of S atoms are present, S atoms that form the  $\text{Ag}_3\text{S}_3$  crown motifs are bonded only to Ag atoms of the staples and the other S atoms are bonded to both the core and staple Ag atoms (Fig. S9, ESI†). The possible structures of  $[\text{Ag}_{29}(\text{BDT})_{12}\text{H}]^{2-}$  were optimized using DFT calculations and the optimized geometries are shown in Fig. S10 (ESI†). We first started with the attachment of a proton onto the S atoms that are bonded only to the outer shell Ag atoms in the structure of  $[\text{Ag}_{29}(\text{BDT})_{12}]^{3-}$ . Initially, the proton was placed in the vicinity of three S atoms of one  $\text{Ag}_3\text{S}_3$  unit but during optimization, it was shifted towards one of them (Fig. S10A, ESI†) and forms a bond with S at a distance of 1.38 Å. This results in the cleavage of one of the Ag–S bonds and this Ag–S distance changes from 2.52 to 3.59 Å. The S atom retains its bonding with the other Ag atom. Next, the proton was interacted with the S atom that is connected to one of the core Ag atoms. DFT optimization suggests the formation of a bond in this case also (Fig. S10B, ESI†). However, the interaction of a proton at this position was less favorable. The relative energies for all the proton-bound clusters were calculated and are shown in Fig. S10 (ESI†). The proton attached to the S atom that is bonded only to the outer shell Ag atoms was the most stable structure. This optimized structure is shown in the inset of Fig. 1A(b) and also in the ESI.† The binding energy of the proton to the cluster in the most stable structure of  $[\text{Ag}_{29}(\text{BDT})_{12}\text{H}]^{2-}$  is  $-74.07 \text{ kcal mol}^{-1}$ . The H–S bond distance (1.38 Å) is slightly higher than the normal covalent H–S bond length (1.34 Å) and subsequently the binding energy is also slightly less than the average value reported for a covalent H–S bond energy ( $-86.8 \text{ kcal mol}^{-1}$ ).<sup>51</sup>

As the proton capture can occur with the intact  $[\text{Ag}_{29}(\text{BDT})_{12}(\text{TPP})_4]^{3-}$  clusters, we have further optimized the structure of  $[\text{Ag}_{29}(\text{BDT})_{12}\text{H}(\text{TPP})_4]^{2-}$  by using DFT calculations. In the presence of TPP ligands, the binding of a proton also occurs in a similar manner and the S–H bond distance (1.38 Å) is the same in both cases (Fig. S11, ESI†). Binding energy is also similar in both the structures  $[\text{Ag}_{29}(\text{BDT})_{12}\text{H}]^{2-}$  ( $-74.07 \text{ kcal mol}^{-1}$ ) and  $[\text{Ag}_{29}(\text{BDT})_{12}\text{H}(\text{TPP})_4]^{2-}$  ( $-73.92 \text{ kcal mol}^{-1}$ ), which suggests that the TPP ligands do not impart additional steric hindrance or play any major role in the stabilization of the proton addition to the cluster. Further, the reactivity of a cluster depends on the energy gap between its highest occupied molecular orbital (HOMO) and lowest unoccupied molecular orbital (LUMO). The interaction with the proton can alter the HOMO–LUMO energy gap. The calculated HOMO–LUMO gap decreases from 1.62 eV to 1.15 eV in the most stable structure of  $[\text{Ag}_{29}(\text{BDT})_{12}\text{H}]^{2-}$ . However, these HOMO–LUMO calculations are based on the ground state geometry of the clusters. Actual comparison with

the experimental optical absorption spectra requires further studies involving time dependent density functional theory (TDDFT) calculations that will consider the optical excitations.

We have not observed more than one proton binding to the cluster in our experiments. However, computationally, we have checked the effect of the addition of another proton to the structure of  $[\text{Ag}_{29}(\text{BDT})_{12}\text{H}]^{2-}$ . The structure of  $[\text{Ag}_{29}(\text{BDT})_{12}\text{H}_2]^{-}$  was constructed by adding a proton to another equivalent S atom in the structure of  $[\text{Ag}_{29}(\text{BDT})_{12}\text{H}]^{2-}$  and then optimizing it in DFT (see Fig. S12, ESI†). Binding energy of the second proton ( $-36.20 \text{ kcal mol}^{-1}$ ) decreases significantly compared to that of the first proton ( $-74.07 \text{ kcal mol}^{-1}$ ). The protons are likely to attach on the S atoms, which weakens the bonding of the –SR groups with the Ag atoms. Hence, if more protons are bound to the cluster, it might ultimately lead to degradation of the system due to significant weakening of the bonding of the thiol group with the metal core.<sup>52</sup> Further, as the interaction of the protons is mainly with the S atoms of the thiol groups, this indicates that such protonation might also be possible for free-standing Ag(I)SR oligomers.

### 3.3 Reactivity with alkali metal ions

The study was extended to a series of alkali metal ions ( $\text{Li}^+$ ,  $\text{Na}^+$ ,  $\text{K}^+$ ,  $\text{Rb}^+$  and  $\text{Cs}^+$ ). While moving down the periodic table, from  $\text{Li}^+$  to  $\text{Cs}^+$ , the ions show increasing atomic radius, decreasing electronegativity, and increasing reactivity. The  $\text{Li}^+$  ion is the smallest and it has a high hydration energy in the gas phase, its reduction potential is more negative than the others indicating it to be the most electropositive alkali metal. Due to such properties, there may be some difference in the reactivity of the cluster with the metal ions. However, the cluster reacted with each of these metal ions to form  $[\text{Ag}_{29}(\text{BDT})_{12}\text{Li}]^{2-}$ ,  $[\text{Ag}_{29}(\text{BDT})_{12}\text{Na}]^{2-}$ ,  $[\text{Ag}_{29}(\text{BDT})_{12}\text{K}]^{2-}$ ,  $[\text{Ag}_{29}(\text{BDT})_{12}\text{Rb}]^{2-}$ , and  $[\text{Ag}_{29}(\text{BDT})_{12}\text{Cs}]^{2-}$ , respectively. Fig. 3 shows the ESI MS of the cluster in the presence of about 1 mM solutions of the respective salts. The isotope patterns of each of these peaks have been matched with the calculated patterns to confirm their composition, as shown in the insets of Fig. 3. Each of these species was subjected to MS/MS studies. The fragmentation pattern was similar to the case of  $[\text{Ag}_{29}(\text{BDT})_{12}\text{H}]^{2-}$ . With the increase of energy, the metal ions were lost and the cluster ion  $[\text{Ag}_{29}(\text{BDT})_{12}]^{3-}$  was reformed. Along with the formation of the common fragment  $[\text{Ag}_5(\text{BDT})_3]^{-}$ , the alkali metal ions were found to be associated with the thiolates as  $[\text{Ag}_4(\text{BDT})_3\text{M}]^{-}$  ( $\text{M} = \text{Li}, \text{Na}, \text{K}, \text{Rb}, \text{Cs}$ ) (Fig. S13, ESI†). Though the dissociation pattern proposes a similarity between all these structures, significant differences are expected as compared to the structure of  $[\text{Ag}_{29}(\text{BDT})_{12}\text{H}]^{2-}$  as the proton is smaller in size and also has different properties. We have studied the possible structure of one of these species,  $[\text{Ag}_{29}(\text{BDT})_{12}\text{Na}]^{2-}$ , by DFT calculations. Similar to the case of the proton, the alkali metal ion capture can also occur with the intact  $[\text{Ag}_{29}(\text{BDT})_{12}(\text{TPP})_4]^{3-}$  clusters that exist in solution (Fig. S14, ESI†).

### 3.4 DFT optimized structure of $[\text{Ag}_{29}(\text{BDT})_{12}\text{Na}]^{2-}$

The structure of  $[\text{Ag}_{29}(\text{BDT})_{12}\text{Na}]^{2-}$  was optimized in a similar manner as in the case of the proton. Interestingly,  $\text{Na}^+$  sits



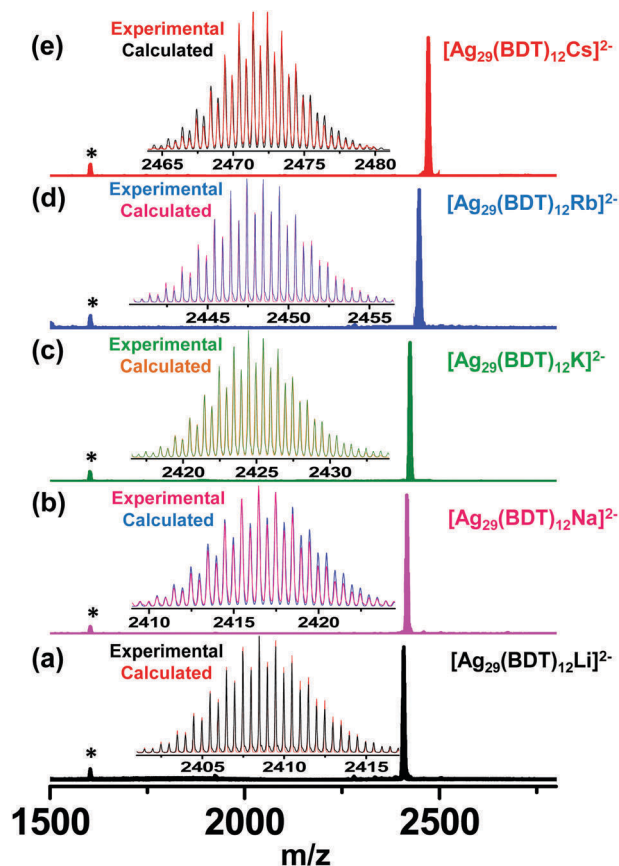


Fig. 3 ESI MS of (a)  $[\text{Ag}_{29}(\text{BDT})_{12}\text{Li}]^{2-}$ , (b)  $[\text{Ag}_{29}(\text{BDT})_{12}\text{Na}]^{2-}$ , (c)  $[\text{Ag}_{29}(\text{BDT})_{12}\text{K}]^{2-}$ , (d)  $[\text{Ag}_{29}(\text{BDT})_{12}\text{Rb}]^{2-}$ , and (e)  $[\text{Ag}_{29}(\text{BDT})_{12}\text{Cs}]^{2-}$ . Insets show their respective experimental and calculated isotope patterns. '\*' indicates the peak for  $[\text{Ag}_{29}(\text{BDT})_{12}]^{3-}$ .

above the plane of three S atoms, which is in contrast to the binding pattern of the proton. The optimized structures are shown in Fig. 4, where (A) represents the DFT optimized structure with  $\text{Na}^+$  sitting over the plane of three S atoms, one of which is connected to the core, and (B) represents the structure with  $\text{Na}^+$  sitting over the plane of three S atoms of a  $\text{Ag}_3\text{S}_3$  motif, all S atoms of which are bonded only to Ag atoms of the staples. The distances between Na and S range from 2.74 to 2.77 Å and 2.84 to 2.86 Å in the two cases, respectively.  $\text{Na}^+$  also interacts with the Ag atom that resides at the center of the three S atoms at a distance of 2.99 Å in the case of structure (A), whereas it has interactions with all three Ag atoms of the outer shell at a distance of 2.97–3.03 Å in the case of the second structure (B). The structure (A) is energetically more stable, which is reflected in its lower bonding distances and interaction energies. The interaction energies are  $-60.43 \text{ kcal mol}^{-1}$  and  $-45.51 \text{ kcal mol}^{-1}$  for the structures (A) and (B), respectively. The strength of the interaction is weaker when compared to the proton and in the case of  $\text{Na}^+$ , the interactions were mainly electrostatic in nature. To understand the interaction, bader charge analysis was performed on the complex, which shows that the charge on Na in the complex is  $0.86e$ . The interaction of a molecule with a metal ion can have several components such

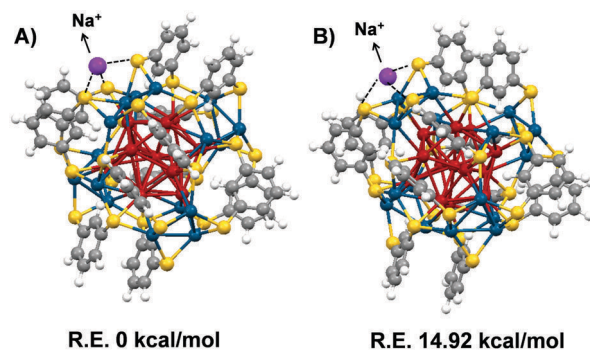


Fig. 4 DFT optimized structure of  $[\text{Ag}_{29}(\text{BDT})_{12}\text{Na}]^{2-}$  with  $\text{Na}^+$  atom sitting over the plane of three S atoms, (A) one of which is connected to a core Ag atom and (B) all of which are bonded only to Ag atoms of the staples.

as electrostatic, charge transfer and polarization. Here, the interactions were stabilized by both electrostatic and charge transfer contributions.<sup>53</sup> The calculated HOMO–LUMO gap for  $[\text{Ag}_{29}(\text{BDT})_{12}\text{Na}]^{2-}$  is 1.14 eV, which is less than the HOMO–LUMO gap for  $[\text{Ag}_{29}(\text{BDT})_{12}]^{3-}$  (1.62 eV), which implies that the electrostatic interaction changes the reactivity of the cluster.

A similar structure is expected for the clusters with the other alkali metal ions.  $\text{Cs}^+$  was interacted with the cluster in a similar fashion to understand the effect of the size of the ions. The structure is similar with  $\text{Cs}^+$  situated above the plane of three S atoms at a distance of 3.65 Å from the Ag atom, situated at the centre of the plane of the three S atoms, which is higher than that of  $\text{Na}^+$  (2.99 Å) and this is due to the larger size of  $\text{Cs}^+$  (Fig. S15, ESI†). The distances between  $\text{Cs}^+$  and the neighbouring three S atoms range between 3.31 and 3.40 Å, which is also higher compared to that of  $\text{Na}^+$ .

### 3.5 Separation of the dimers $[\text{Ag}_{29}(\text{BDT})_{12}\text{M}]_2^{4-}$ [ $\text{M} = \text{Na}, \text{K}, \text{Rb}, \text{Cs}$ ] by ion mobility mass spectrometry (IM MS)

Cation binding is known to induce conformational changes in proteins, amino acids, drugs, carbohydrates, *etc.*<sup>54–59</sup> Proton-bound and alkali-metal bound dimers<sup>60–64</sup> have also been observed in several cases. Similarly, on complexation with the alkali metal ions, new metal centers are introduced into the cluster system and new interactions originate at specific sites. The cation bound species were subjected to ion mobility studies by passing them through the mobility drift tube. The changes in their structures were reflected in their drift time values (Fig. 5A). With an increase in the size of the cations ( $\text{H}^+ < \text{Li}^+ < \text{Na}^+ < \text{K}^+ < \text{Rb}^+ < \text{Cs}^+$ ), there was a slight increase in the drift time of the monomeric species  $[\text{Ag}_{29}(\text{BDT})_{12}\text{M}]^{2-}$  [ $\text{M} = \text{H}, \text{Li}, \text{Na}, \text{K}, \text{Rb}, \text{Cs}$ ]. With appropriate optimization of the ion mobility conditions, dimerization was observed in some of these species. Dimers having a composition of  $[\text{Ag}_{29}(\text{BDT})_{12}\text{M}]_2^{4-}$  [ $\text{M} = \text{Na}, \text{K}, \text{Rb}, \text{Cs}$ ] were separated in the mobility cell and this phenomenon was selective to the nature of the cations (Fig. 5A). An optimised condition involving a trap gas flow of  $10 \text{ mL min}^{-1}$ , He gas flow of  $180 \text{ mL min}^{-1}$  and IMS gas flow of  $120 \text{ mL min}^{-1}$  was used for separating the dimers. The wave velocity and wave height were kept at  $650 \text{ m s}^{-1}$  and 35 V, respectively. The relative population of the respective monomers and dimers was

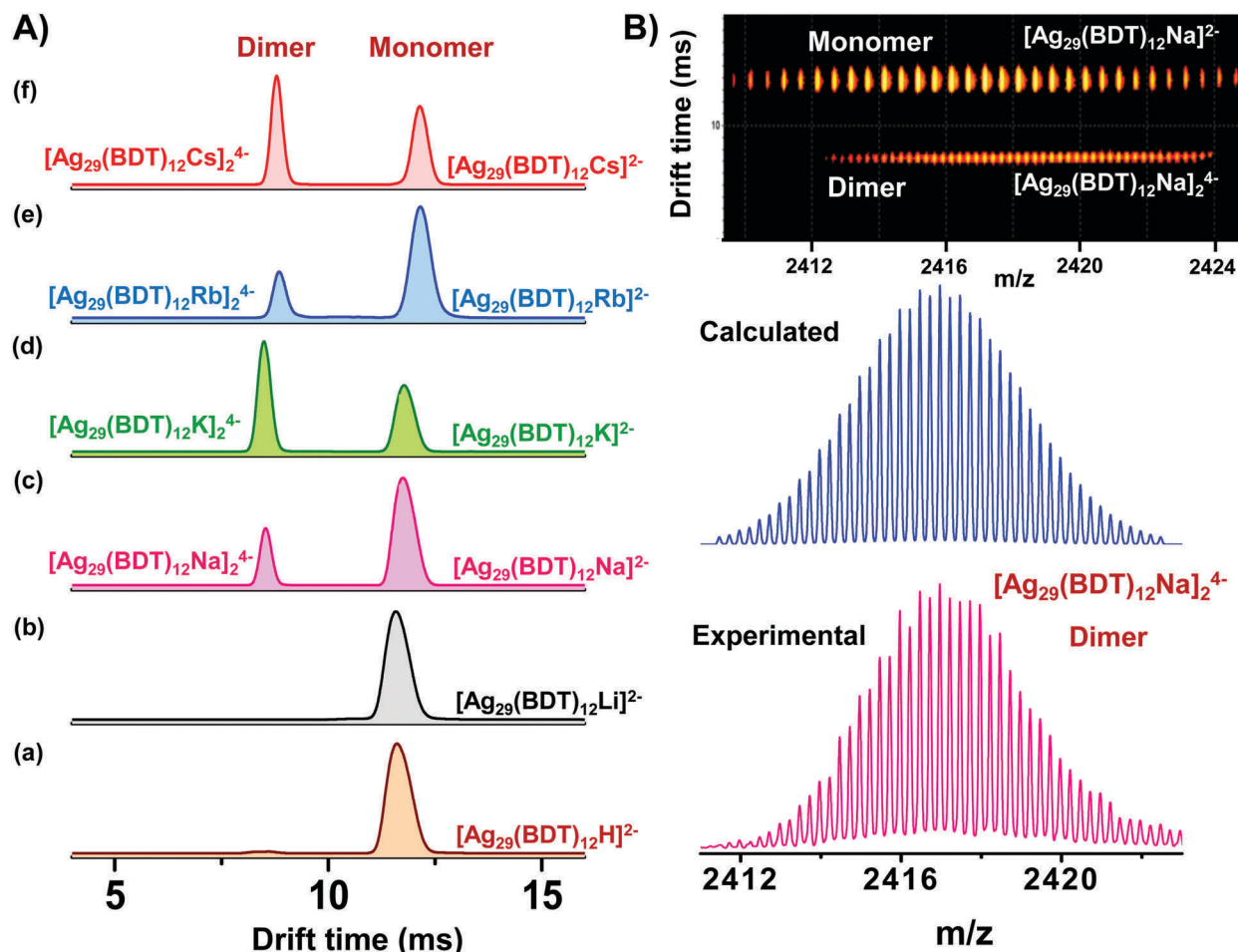


Fig. 5 (A) Drift time profile of (a)  $[Ag_{29}(BDT)_{12}H]^{2-}$ , (b)  $[Ag_{29}(BDT)_{12}Li]^{2-}$  and dimers and monomers of (c)  $[Ag_{29}(BDT)_{12}Na]^{2-}$ , (d)  $[Ag_{29}(BDT)_{12}K]^{2-}$ , (e)  $[Ag_{29}(BDT)_{12}Rb]^{2-}$  and (f)  $[Ag_{29}(BDT)_{12}Cs]^{2-}$ . (B) Experimental and calculated isotope patterns of the dimer  $[Ag_{29}(BDT)_{12}Na]^{2-}$  along with the plot of drift time vs.  $m/z$  showing the separation of monomers and dimers.

specific to the instrumental conditions used. Fig. 5B shows the calculated and experimental isotope patterns of the dimer of one such species,  $[Ag_{29}(BDT)_{12}Na]^{2-}$ , along with the drift scope view showing its separation. The isotope patterns of the other dimeric species are included in the ESI† (Fig. S16). Dimer formation was not observed for the species containing the smaller sized cations  $H^+$  and  $Li^+$ . From such phenomena, it is clear that specific metal ions are required for the dimerization process to be favorable. The size of the cations may be one such critical factor. The cluster itself does not dimerize (Fig. S17, ESI†), dimerization is induced by the presence of cations in this case. The interactions should be strong enough to hold the two clusters together. DFT calculations revealed some changes in the structure and binding interactions between  $H^+$  and  $Na^+$  bound clusters, and this was reflected in their tendency towards dimerization as well. In order to form dimers, a monomer of the cluster should interact with another monomer through  $H^+$  or  $Na^+$ . The proton resides inside the space between the three S atoms due to its smaller size. Hence, it is not available for interacting with another cluster.  $Na^+$  is more exposed as it is present over the plane of the three S atoms on the outer surface of the cluster. Therefore, it is available to

interact with another cluster. This explains the need for a critical size of the metal ions for forming the dimers.

A protonated benzene dimer with a sandwich like structure was reported by Jouvét *et al.*<sup>65</sup> In the structure of the  $[Ag_{29}(BDT)_{12}]^{3-}$  cluster, the benzene rings of two BDT ligands lie in parallel orientation. So, there are additional possibilities of such sandwich protonated structures and the fact that smaller cations like  $H^+$  and  $Li^+$  do not form dimers might also be due to such structures remaining in competition. To consider such possibilities, we have constructed a structure of  $[Ag_{29}(BDT)_{12}H]^{2-}$  with the proton sandwiched between the benzene rings of two BDT ligands and optimized it using DFT calculations. As an initial input, the proton was placed equidistant from the benzene rings of the two BDT ligands. However, in the final structure obtained after complete optimization, the proton was bound to a C atom of one of the benzene rings with a bond length of 1.13 Å, which is slightly higher than that of the usual C–H bond distance. The distance of the proton from the nearest C atom of the other benzene ring is 2.54 Å (Fig. S18, ESI†). This conformation with the proton sandwiched between the benzene rings of two BDT ligands is similar to that observed in the case of the protonated benzene dimer.<sup>65</sup> However, when compared to the structure of  $[Ag_{29}(BDT)_{12}H]^{2-}$  with the

proton attached at the staple S atoms, this sandwiched structure is energetically less favourable (the structure is 20.30 kcal mol<sup>-1</sup> higher in energy than the lowest energy structure). Thus, it is verified that structures with cations sandwiched between the benzene rings are less likely to be in competition.

### 3.6 DFT optimized structure of the dimer [Ag<sub>29</sub>(BDT)<sub>12</sub>Na]<sub>2</sub><sup>4-</sup>

Computational studies were extended to understand the structure of the dimers. Since dimerization is induced by the metal ions, Na<sup>+</sup> of one of the monomers can interact with another monomer in different ways and act as a bridge between the two clusters. The possible DFT optimized structures and the calculated relative energies are shown in Fig. 6. Na<sup>+</sup> interacts with the S atoms present in another monomer. The stability of these structures is attributed to Na–S interactions. In the lowest energy structure (A), two monomers are bonded with the help of two Na<sup>+</sup> ions. In another possible structure (B), only one Na<sup>+</sup> participates in the dimerization process. The energy difference between the two isomeric structures is 23.86 kcal mol<sup>-1</sup>. The Na–S bond distances are about 2.76–2.85 Å and 3.76 Å for structures (A) and (B), respectively. The greater number of Na–S interactions provides higher stability to structure (A). The structure of the dimers, [Ag<sub>29</sub>(BDT)<sub>12</sub>Na]<sub>2</sub><sup>4-</sup>, is very different to the structure of the dimers of Au<sub>25</sub>(SR)<sub>18</sub> clusters, reported recently.<sup>21</sup> While the dimerization of Au<sub>25</sub>(SR)<sub>18</sub> was favored by aurophilic interaction and inter-staple bonding, in this case, dimerization is due to the incorporation of the additional metal center linking the two clusters.

### 3.7 Structural correlation between the monomers and the dimers from IM MS and dissociation studies

Correlation between the structures of the monomeric species, [Ag<sub>29</sub>(BDT)<sub>12</sub>M]<sub>2</sub><sup>4-</sup> (M = H, Li, Na, K, Rb, Cs), as well as their

dimers, [Ag<sub>29</sub>(BDT)<sub>12</sub>M]<sub>2</sub><sup>4-</sup> (M = Na, K, Rb, Cs), was clearly reflected in their drift time values. Drift time (ms) of the species was studied as a function of *m/z* for all the monomeric as well as the dimeric species (see Fig. 7A and B). As discussed earlier, with an increase in the size of the metal ions, there was an elongation of the M–S bond length, which resulted in an increase in the overall size of the cluster, and this was reflected in the increasing drift time values for the monomers and their respective dimers. The collision cross section (CCS) values of the respective monomers and dimers, measured from IM MS studies, also suggested a similar increase in the overall size of the species with an increase in the size of the metal ions (Fig. S19, ESI†). Monomers and dimers containing larger sized cations show a significant increase in CCS values compared to those of the protonated species. This might also be due to the fact that larger cations like Rb<sup>+</sup> and Cs<sup>+</sup> are not buried into the ligands and are situated away from the surface of the cluster. Dissociation studies were also carried out on the dimers. Upon increasing the collision energy (CE, instrumental units), fragmentation of the dimers to their respective monomers occurred. Drift time profiles showing the CE dependent abundances of the monomers and the dimers with increasing energy are presented in Fig. S20 (ESI†). Relative abundance of the monomers and the dimers are plotted as a function of the applied CE in Fig. 7C. It was observed that all the dimeric species followed a similar trend in their dissociation. At CE 30, there was about 50% dissociation of the dimers to their respective monomers, whereas, after CE 50, there was complete dissociation to the monomers. The dissociation thresholds were similar in all cases, which suggests a similarity in the structure of the dimers formed by the different metal ions.

### 3.8 Possibilities of interaction with other metal ions, detection of [Ag<sub>29</sub>(BDT)<sub>12</sub>Ag]<sub>2</sub><sup>4-</sup>

Similar reactivity can be extended to a range of other metal ions also. Complexation of the cluster with Ag<sup>+</sup> was also observed, which leads to the formation of the cluster–metal ion adduct having a composition of [Ag<sub>29</sub>(BDT)<sub>12</sub>Ag]<sub>2</sub><sup>2-</sup>. When it was passed through the ion mobility cell, dimers of [Ag<sub>29</sub>(BDT)<sub>12</sub>Ag]<sub>2</sub><sup>2-</sup> were also separated under similar conditions, as shown in Fig. 8. The area under the peaks of the mobilogram reflects the relative abundance of the respective species. The experimental and calculated isotope patterns of the dimers and the monomers are shown in the insets of Fig. 8, which confirm their composition. The drift time of the [Ag<sub>29</sub>(BDT)<sub>12</sub>Ag]<sub>2</sub><sup>2-</sup> monomer is 11.40 ms and that of the [Ag<sub>29</sub>(BDT)<sub>12</sub>Ag]<sub>2</sub><sup>4-</sup> dimer is 8.57 ms, which are much lower drift time values than expected from the drift time vs. *m/z* correlation of the species [Ag<sub>29</sub>(BDT)<sub>12</sub>M]<sub>2</sub><sup>4-</sup>, as shown in Fig. 7A and B. Thus, it is evident that this correlation between drift time (ms) and *m/z* might not be valid in the case of Ag<sup>+</sup> or other monovalent cations. With an increase in the mass of the alkali metals, there is also an increase in their size from Li<sup>+</sup> to Cs<sup>+</sup>. The structures of [Ag<sub>29</sub>(BDT)<sub>12</sub>M]<sub>2</sub><sup>4-</sup> may vary depending on the nature of the metal. This implies that Ag cation capture may lead to a very different bonding scheme and incorporation of Ag within the Ag core can also occur. However, the exact structure of [Ag<sub>29</sub>(BDT)<sub>12</sub>Ag]<sub>2</sub><sup>2-</sup> cannot be predicted only from the drift

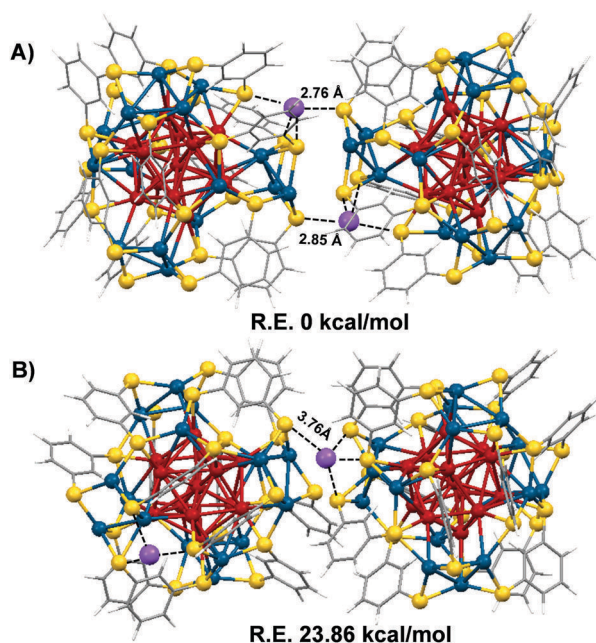


Fig. 6 DFT optimized structures of the dimer, [Ag<sub>29</sub>(BDT)<sub>12</sub>Na]<sub>2</sub><sup>4-</sup>, with two monomers bonded with (A) two Na<sup>+</sup> and (B) only one Na<sup>+</sup>.



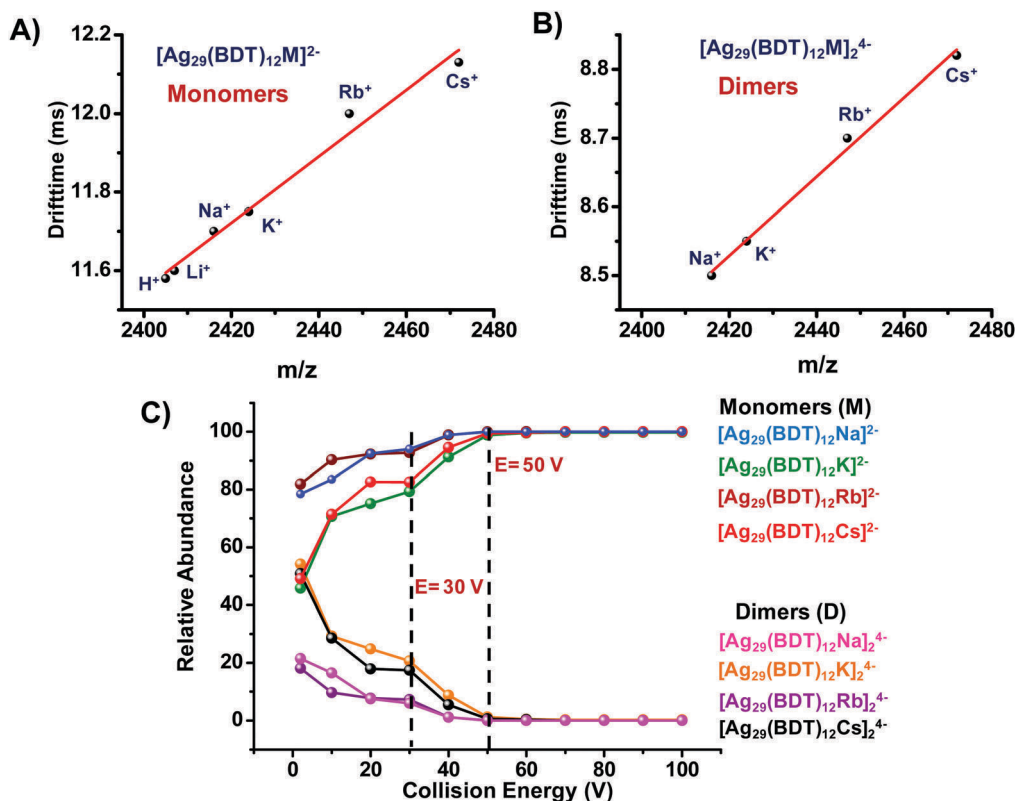


Fig. 7 Plot of drift time vs.  $m/z$  of (A) monomeric species  $[\text{Ag}_{29}(\text{BDT})_{12}\text{M}]^{2-}$  (M = H, Li, Na, K, Rb, Cs) and (B) dimeric species  $[\text{Ag}_{29}(\text{BDT})_{12}\text{M}]_2^{4-}$  (M = Na, K, Rb, Cs); (C) collision energy resolved fragmentation curves of the dimers and the monomers.

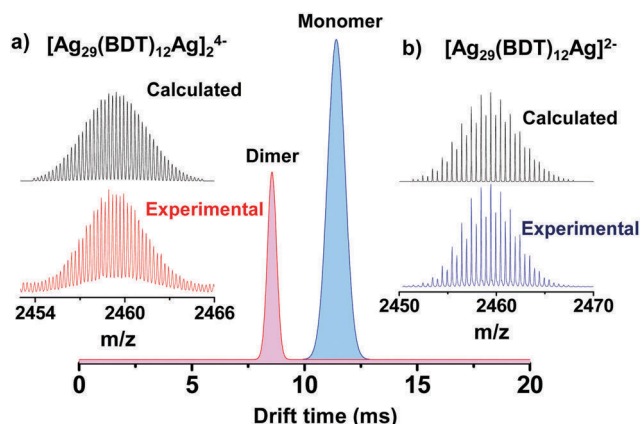


Fig. 8 Drift time profile showing the separation of the dimers and the monomers of  $[\text{Ag}_{29}(\text{BDT})_{12}\text{Ag}]^{2-}$ . Insets show the calculated and experimental isotope patterns of (a) the dimer  $[\text{Ag}_{29}(\text{BDT})_{12}\text{Ag}]_2^{4-}$  and (b) the monomer  $[\text{Ag}_{29}(\text{BDT})_{12}\text{Ag}]^{2-}$ .

time vs.  $m/z$  correlation. For complete structural elucidation, detailed studies are required, which are areas for further investigation.

## 4. Conclusions

In summary, we have explored the reactivity of a proton ( $\text{H}^+$ ) and alkali metal ions ( $\text{Li}^+$ ,  $\text{Na}^+$ ,  $\text{K}^+$ ,  $\text{Rb}^+$  and  $\text{Cs}^+$ ) with the

$[\text{Ag}_{29}(\text{BDT})_{12}]^{3-}$  cluster. The structural changes resulting from the binding of the ions have been studied and alkali metal-bound dimers of the cluster have been separated by IM MS. While this study helps to identify the structural changes and interactions that can favour the formation of cluster aggregates, such transient states can also be related to the chemical reactivity of the cluster. The sensitivity of the cluster towards  $\text{H}^+$  can be used to quantify the proton concentration in organic solvents. As affinity towards  $\text{H}^+$  gives an idea regarding the gas-phase basicity of a molecule, the acid base chemistry involving the cluster can be explored in more detail. Due to the strong tendency of the cluster to bind to cations, it may be used in the detection of alkali metal ions like  $\text{Na}^+$ ,  $\text{K}^+$ , etc.

## Conflicts of interest

There are no conflicts to declare.

## Acknowledgements

P. C. thanks the Council of Scientific and Industrial Research (CSIR) for a research fellowship. A. B. thanks IIT Madras for an Institute Postdoctoral fellowship. S. K. M. thanks DST-INSPIRE for his research fellowship. A. N. thanks IIT Madras for an Institute Doctoral fellowship. G. P. thanks IIT Madras for an Institute Post-Doctoral fellowship. We thank the Department of

Science and Technology, Government of India for continuous support of our research program.

## References

- 1 R. Jin, C. Zeng, M. Zhou and Y. Chen, *Chem. Rev.*, 2016, **116**, 10346–10413.
- 2 A. Mathew and T. Pradeep, *Part. Part. Syst. Charact.*, 2014, **31**, 1017–1053.
- 3 I. Chakraborty and T. Pradeep, *Chem. Rev.*, 2017, **117**, 8208–8271.
- 4 N. Goswami, Q. Yao, T. Chen and J. Xie, *Coord. Chem. Rev.*, 2016, **329**, 1–15.
- 5 J. Fang, B. Zhang, Q. Yao, Y. Yang, J. Xie and N. Yan, *Coord. Chem. Rev.*, 2016, **322**, 1–29.
- 6 M. Zhu, C. M. Aikens, F. J. Hollander, G. C. Schatz and R. Jin, *J. Am. Chem. Soc.*, 2008, **130**, 5883–5885.
- 7 H. Qian, W. T. Eckenhoff, Y. Zhu, T. Pintauer and R. Jin, *J. Am. Chem. Soc.*, 2010, **132**, 8280–8281.
- 8 Y. Levi-Kalisman, P. D. Jadzinsky, N. Kalisman, H. Tsunoyama, T. Tsukuda, D. A. Bushnell and R. D. Kornberg, *J. Am. Chem. Soc.*, 2011, **133**, 2976–2982.
- 9 H. Yang, Y. Wang, H. Huang, L. Gell, L. Lehtovaara, S. Malola, H. Hakkinen and N. Zheng, *Nat. Commun.*, 2013, **4**, 2422.
- 10 C. P. Joshi, M. S. Bootharaju, M. J. Alhilaly and O. M. Bakr, *J. Am. Chem. Soc.*, 2015, **137**, 11578–11581.
- 11 L. G. Abdul Halim, M. S. Bootharaju, Q. Tang, S. Del Gobbo, R. G. Abdul Halim, M. Eddaoudi, D.-E. Jiang and O. M. Bakr, *J. Am. Chem. Soc.*, 2015, **137**, 11970–11975.
- 12 P. Chakraborty, A. Baksi, E. Khatun, A. Nag, A. Ghosh and T. Pradeep, *J. Phys. Chem. C*, 2017, **121**, 10971–10981.
- 13 A. Baksi, S. R. Harvey, G. Natarajan, V. H. Wysocki and T. Pradeep, *Chem. Commun.*, 2016, **52**, 3805–3808.
- 14 A. Baksi, A. Ghosh, S. K. Mudedla, P. Chakraborty, S. Bhat, B. Mondal, K. R. Krishnadas, V. Subramanian and T. Pradeep, *J. Phys. Chem. C*, 2017, **121**, 13421–13427.
- 15 M. R. Ligare, E. S. Baker, J. Laskin and G. E. Johnson, *Chem. Commun.*, 2017, **53**, 7389–7392.
- 16 K. R. Krishnadas, A. Ghosh, A. Baksi, I. Chakraborty, G. Natarajan and T. Pradeep, *J. Am. Chem. Soc.*, 2016, **138**, 140–148.
- 17 K. R. Krishnadas, A. Baksi, A. Ghosh, G. Natarajan and T. Pradeep, *Nat. Commun.*, 2016, **7**, 13447.
- 18 B. Yoon, W. D. Luedtke, R. N. Barnett, J. Gao, A. Desiredy, B. E. Conn, T. Bigioni and U. Landman, *Nat. Mater.*, 2014, **13**, 807.
- 19 A. Som, I. Chakraborty, T. A. Maark, S. Bhat and T. Pradeep, *Adv. Mater.*, 2016, **28**, 2827–2833.
- 20 M. De Nardi, S. Antonello, D.-E. Jiang, F. Pan, K. Rissanen, M. Ruzzi, A. Venzo, A. Zoleo and F. Maran, *ACS Nano*, 2014, **8**, 8505–8512.
- 21 A. Baksi, P. Chakraborty, S. Bhat, G. Natarajan and T. Pradeep, *Chem. Commun.*, 2016, **52**, 8397–8400.
- 22 F. Lanucara, S. W. Holman, C. J. Gray and C. E. Eyers, *Nat. Chem.*, 2014, **6**, 281–294.
- 23 Y. Zhong, S.-J. Hyung and B. T. Ruotolo, *Expert Rev. Proteomics*, 2012, **9**, 47–58.
- 24 A. A. Shvartsburg, S. Y. Noskov, R. W. Purves and R. D. Smith, *Proc. Natl. Acad. Sci. U. S. A.*, 2009, **106**, 6495–6500.
- 25 M. Zhou, S. Dagan and V. H. Wysocki, *Angew. Chem., Int. Ed.*, 2012, **51**, 4336–4339.
- 26 R. S. Quintyn, M. Zhou, S. Dagan, J. Finke and V. H. Wysocki, *Int. J. Ion Mobility Spectrom.*, 2013, **16**, 133–143.
- 27 R. S. Quintyn, S. R. Harvey and V. H. Wysocki, *Analyst*, 2015, **140**, 7012–7019.
- 28 S. Daly, C. M. Choi, A. Zavras, M. Krstić, F. Chiro, T. U. Connell, S. J. Williams, P. S. Donnelly, R. Antoine, A. Giuliani, V. Bonačić-Koutecký, P. Dugourd and R. A. J. O'Hair, *J. Phys. Chem. C*, 2017, **121**, 10719–10727.
- 29 A. Soleilhac, F. Bertorelle, C. Comby-Zerbino, F. Chiro, N. Calin, P. Dugourd and R. Antoine, *J. Phys. Chem. C*, 2017, **121**, 27733–27740.
- 30 G. Hu, Q. Tang, D. Lee, Z. Wu and D.-E. Jiang, *Chem. Mater.*, 2017, **29**, 4840–4847.
- 31 R. Araake, K. Sakadani, M. Tada, Y. Sakai and Y. Ohki, *J. Am. Chem. Soc.*, 2017, **139**, 5596–5606.
- 32 M. S. Bootharaju, R. Dey, L. E. Gevers, M. N. Hedhili, J.-M. Basset and O. M. Bakr, *J. Am. Chem. Soc.*, 2016, **138**, 13770–13773.
- 33 R. S. Dhayal, W. E. van Zyl and C. W. Liu, *Acc. Chem. Res.*, 2016, **49**, 86–95.
- 34 A. Zavras, G. N. Khairallah, T. U. Connell, J. M. White, A. J. Edwards, R. J. Mulder, P. S. Donnelly and R. A. J. O'Hair, *Inorg. Chem.*, 2014, **53**, 7429–7437.
- 35 A. Moser, K. Range and D. M. York, *J. Phys. Chem. B*, 2010, **114**, 13911–13921.
- 36 E. P. L. Hunter and S. G. Lias, *J. Phys. Chem. Ref. Data*, 1998, **27**, 413–656.
- 37 S. G. Lias, J. F. Liebman and R. D. Levin, *J. Phys. Chem. Ref. Data*, 1984, **13**, 695–808.
- 38 F. Wang, S. Ma, D. Zhang and R. G. Cooks, *J. Phys. Chem. A*, 1998, **102**, 2988–2994.
- 39 Z. Wu, C. Fenselau and R. Graham Cooks, *Rapid Commun. Mass Spectrom.*, 1994, **8**, 777–780.
- 40 M. R. A. Blomberg and P. E. M. Siegbahn, *Biochim. Biophys. Acta*, 2006, **1757**, 969–980.
- 41 H. Ishikita and K. Saito, *J. R. Soc., Interface*, 2014, **11**, 20130518.
- 42 D. Jacquemin, J. Zuniga, A. Requena and J. P. Ceron-Carrasco, *Acc. Chem. Res.*, 2014, **47**, 2467–2474.
- 43 J. J. Warren and J. M. Mayer, *Biochemistry*, 2015, **54**, 1863–1878.
- 44 J. J. Mortensen, L. B. Hansen and K. W. Jacobsen, *Phys. Rev. B: Condens. Matter Mater. Phys.*, 2005, **71**, 035109.
- 45 J. Enkovaara, C. Rostgaard, J. J. Mortensen, J. Chen, M. Dulak, L. Ferrighi, J. Gavnholt, C. Glinsvad, V. Haikola, H. A. Hansen, H. H. Kristoffersen, M. Kuisma, A. H. Larsen, L. Lehtovaara, M. Ljungberg, O. Lopez-Acevedo, P. G. Moses, J. Ojanen, T. Olsen, V. Petzold, N. A. Romero, J. Stausholm-Møller, M. Strange, G. A. Tritsaridis, M. Vanin, M. Walter, B. Hammer, H. Häkkinen, G. K. H. Madsen, R. M. Nieminen, J. K. Nørskov, M. Puska, T. T. Rantala, J. Schiøtz,

- K. S. Thygesen and K. W. Jacobsen, *J. Phys.: Condens. Matter*, 2010, **22**, 253202.
- 46 J. P. Perdew, K. Burke and M. Ernzerhof, *Phys. Rev. Lett.*, 1996, **77**, 3865–3868.
- 47 A. H. Larsen, M. Vanin, J. J. Mortensen, K. S. Thygesen and K. W. Jacobsen, *Phys. Rev. B: Condens. Matter Mater. Phys.*, 2009, **80**, 195112.
- 48 R. G. Cooks, *J. Mass Spectrom.*, 1995, **30**, 1215–1221.
- 49 E. R. Williams, L. Fang and R. N. Zare, *Int. J. Mass Spectrom. Ion Processes*, 1993, **123**, 233–241.
- 50 G. E. Johnson, T. Priest and J. Laskin, *Chem. Sci.*, 2014, **5**, 3275–3286.
- 51 S. W. Benson, *J. Chem. Educ.*, 1965, **42**, 502.
- 52 L. Gell and H. Häkkinen, *J. Phys. Chem. C*, 2015, **119**, 10943–10948.
- 53 B. Sharma, Y. I. Neela and G. Narahari Sastry, *J. Comput. Chem.*, 2016, **37**, 992–1004.
- 54 T. G. Flick, I. D. G. Campuzano and M. D. Bartberger, *Anal. Chem.*, 2015, **87**, 3300–3307.
- 55 L. Chen, Y. Q. Gao and D. H. Russell, *J. Phys. Chem. A*, 2012, **116**, 689–696.
- 56 A. Memboeuf, K. Vekey and G. Lendvay, *Eur. J. Mass Spectrom.*, 2011, **17**, 33–46.
- 57 S. Lee, T. Wyttenbach, G. von Helden and M. T. Bowers, *J. Am. Chem. Soc.*, 1995, **117**, 10159–10160.
- 58 Y. Seo, M. R. Schenauer and J. A. Leary, *Int. J. Mass Spectrom.*, 2011, **303**, 191–198.
- 59 Y. Huang and E. D. Dodds, *Anal. Chem.*, 2013, **85**, 9728–9735.
- 60 W. Fu, J. Xiong, M. J. Lecours, P. J. J. Carr, R. A. Marta, E. Fillion, T. McMahon, V. Steinmetz and W. S. Hopkins, *J. Mol. Spectrosc.*, 2016, **330**, 194–199.
- 61 B. Yang, R. R. Wu and M. T. Rodgers, *J. Am. Soc. Mass Spectrom.*, 2015, **26**, 1469–1482.
- 62 M. Tsuge, J. Kalinowski, R. B. Gerber and Y.-P. Lee, *J. Phys. Chem. A*, 2015, **119**, 2651–2660.
- 63 B. Yang and M. T. Rodgers, *Phys. Chem. Chem. Phys.*, 2014, **16**, 16110–16120.
- 64 L. Wu, E. C. Meurer, B. Young, P. Yang, M. N. Eberlin and R. G. Cooks, *Int. J. Mass Spectrom.*, 2004, **231**, 103–111.
- 65 S. Chakraborty, R. Omidyan, I. Alata, I. B. Nielsen, C. Dedonder, M. Broquier and C. Jouvet, *J. Am. Chem. Soc.*, 2009, **131**, 11091–11097.

## Electronic Supplementary Information

### Understanding proton capture and cation-induced dimerization of $[\text{Ag}_{29}(\text{BDT})_{12}]^{3-}$ clusters by ion mobility mass spectrometry

Papri Chakraborty,<sup>a,\*</sup> Ananya Baksi,<sup>a,†,+</sup> Sathish Kumar Mudedla,<sup>b</sup> Abhijit Nag,<sup>a</sup> Ganesan Paramasivam,<sup>a</sup> Venkatesan Subramanian<sup>b</sup> and Thalappil Pradeep<sup>\*a</sup>

<sup>a</sup> DST Unit of Nanoscience (DST UNS) and Thematic Unit of Excellence, Department of Chemistry, Indian Institute of Technology Madras, Chennai 600036, India.

\*E-mail: pradeep@iitm.ac.in

<sup>b</sup>Chemical Laboratory, CSIR-Central Leather Research Institute, Adyar, Chennai 600020, India

#### Table of contents

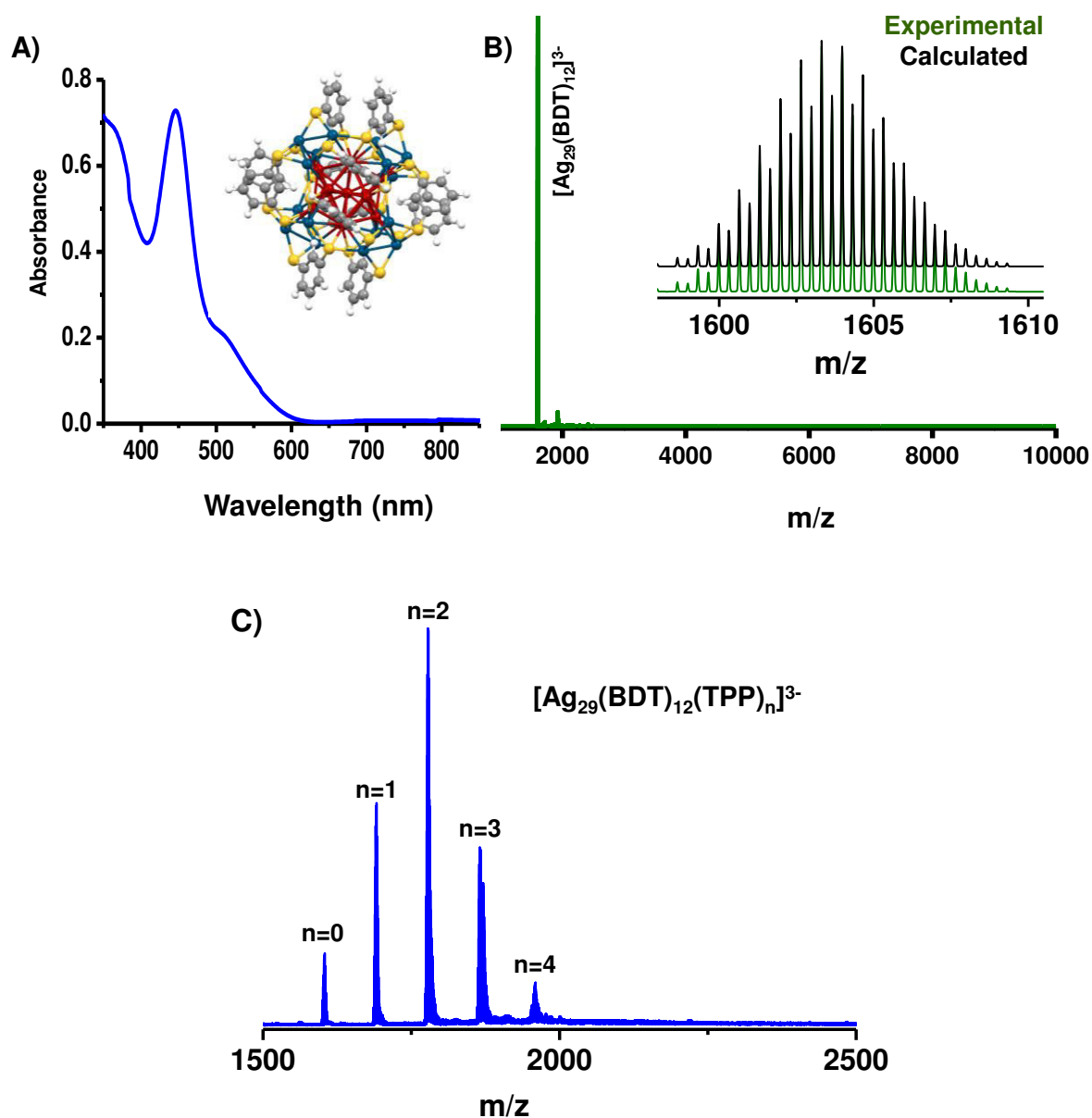
Name	Description	Page No.
Fig. S1	UV-vis and ESI MS characterization of $[\text{Ag}_{29}(\text{BDT})_{12}]^{3-}$ cluster	4
Fig. S2	ESI MS showing conversion of $[\text{Ag}_{29}(\text{BDT})_{12}]^{3-}$ to $[\text{Ag}_{29}(\text{BDT})_{12}\text{H}]^{2-}$ at different concentrations of formic acid	5
Fig. S3	Comparison of isotope patterns of $[\text{Ag}_{29}(\text{BDT})_{12}]^{2-}$ and $[\text{Ag}_{29}(\text{BDT})_{12}\text{H}]^{2-}$	6
Fig. S4	Detection of $[\text{Ag}_{29}(\text{BDT})_{12}\text{H}]^{2-}$ by increasing polarity of solvents	6
Fig. S5	Reactivity of $[\text{Ag}_{29}(\text{BDT})_{12}]^{3-}$ with $\text{NMe}_4\text{Br}$	7



Fig. S6	UV-vis spectra of $[\text{Ag}_{29}(\text{BDT})_{12}]^{3-}$ cluster in presence of different concentration of formic acid and $\text{NH}_4\text{OAc}$	7
Fig. S7	MS/MS of $[\text{Ag}_{29}(\text{BDT})_{12}\text{H}]^{2-}$	8
Fig. S8	ESI MS under soft ionization conditions showing the formation of intact $[\text{Ag}_{29}(\text{BDT})_{12}(\text{TPP})_n\text{H}]^{2-}$ ( $n=1-4$ ) clusters.	9
Fig. S9	Structure of $[\text{Ag}_{29}(\text{BDT})_{12}]^{3-}$ showing different types of S atoms in the outer shell of the cluster	9
Fig. S10	DFT optimized possible structures of $[\text{Ag}_{29}(\text{BDT})_{12}\text{H}]^{2-}$	10
Fig. S11	DFT optimized structure of $[\text{Ag}_{29}(\text{BDT})_{12}\text{H}(\text{TPP})_4]^{2-}$	11
Fig. S12	DFT optimized structure of $[\text{Ag}_{29}(\text{BDT})_{12}\text{H}_2]^{-}$	11
Fig. S13	MS/MS of $[\text{Ag}_{29}(\text{BDT})_{12}\text{M}]^{2-}$ ( $\text{M}=\text{Na}, \text{K}, \text{Cs}$ )	12
Fig. S14	ESI MS under soft ionization conditions showing the formation of intact $[\text{Ag}_{29}(\text{BDT})_{12}(\text{TPP})_n\text{K}]^{2-}$ ( $n=1-4$ ) clusters.	13
Fig. S15	DFT optimized possible structures of $[\text{Ag}_{29}(\text{BDT})_{12}\text{Cs}]^{2-}$	13
Fig. S16	Experimental and calculated isotope patterns of the dimers $[\text{Ag}_{29}(\text{BDT})_{12}\text{M}]_2^{4-}$ ( $\text{M}=\text{Na}, \text{K}, \text{Rb}, \text{Cs}$ )	14
Fig. S17	Drift time profile of $[\text{Ag}_{29}(\text{BDT})_{12}]^{3-}$	15
Fig. S18	DFT optimized structure of $[\text{Ag}_{29}(\text{BDT})_{12}\text{H}]^{2-}$ with H sandwiched between the two benzene rings of the BDT ligands.	15

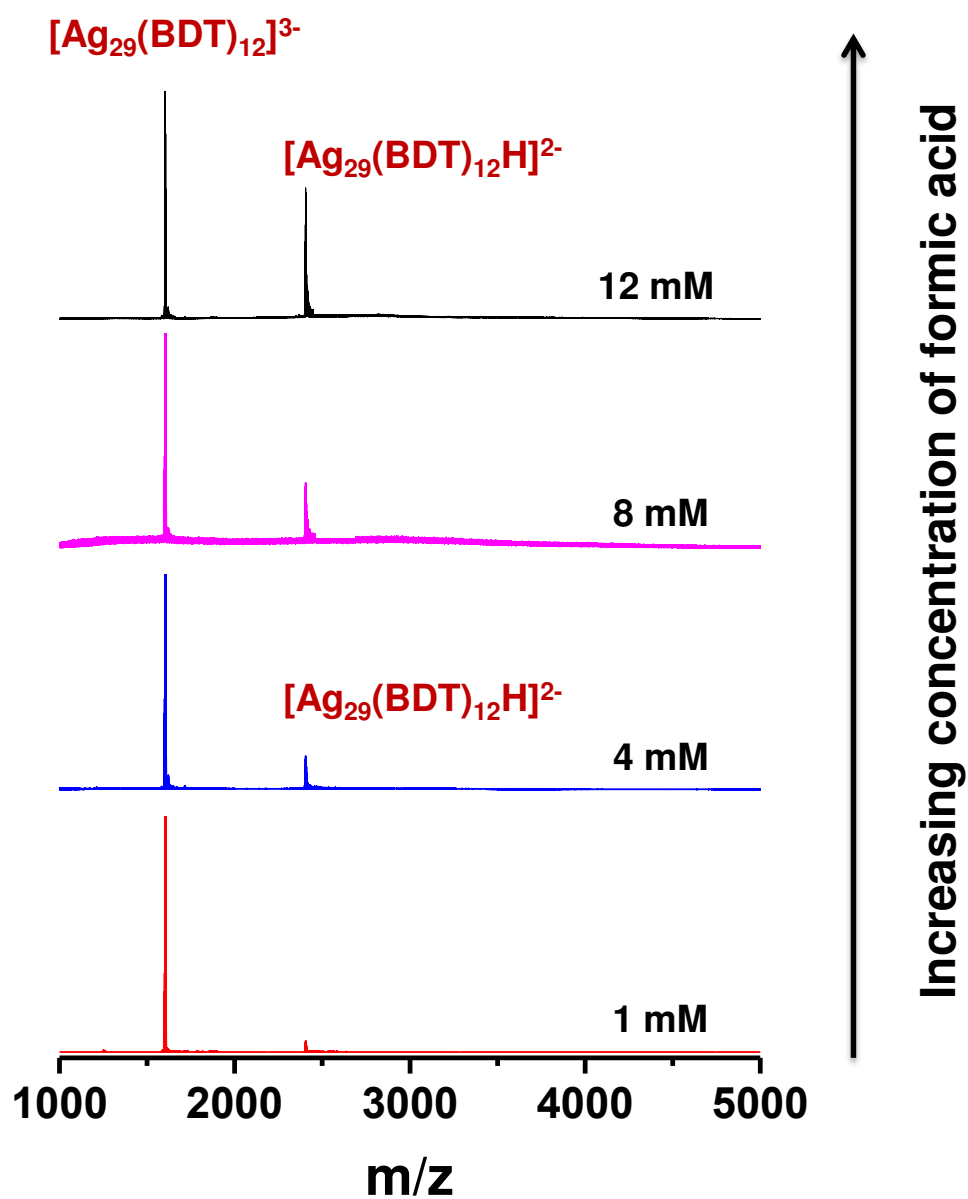
Fig. S19	Experimental CCS values of the monomers and the dimers	16
Fig. S20	CID of the dimers $[\text{Ag}_{29}(\text{BDT})_{12}\text{M}]_2^{4-}$ (M=Na, K, Rb, Cs)	17
	Cartesian co-ordinates of the DFT optimized lowest energy structures	18-34

## Supplementary Information 1



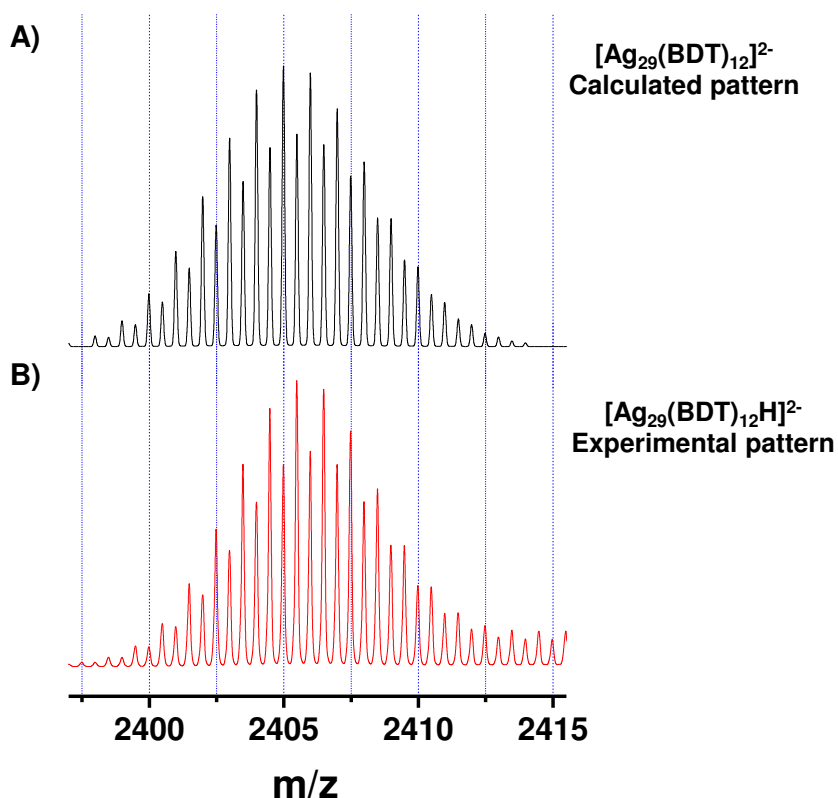
**Fig. S1** A) UV-vis of  $[\text{Ag}_{29}(\text{BDT})_{12}(\text{TPP})_4]^{3-}$  cluster, B) ESI MS of  $[\text{Ag}_{29}(\text{BDT})_{12}]^{3-}$ , the TPP ligands are lost during the ionization. Inset of B) shows the experimental and calculated isotope patterns of  $[\text{Ag}_{29}(\text{BDT})_{12}]^{3-}$ . The structure of  $[\text{Ag}_{29}(\text{BDT})_{12}]^{3-}$  is shown in the inset of A). C) ESI MS under the soft ionization conditions showing the intact  $[\text{Ag}_{29}(\text{BDT})_{12}(\text{TPP})_n]^{3-}$  ( $n=1-4$ ) clusters. Color codes: red: Ag atoms of the core; blue: Ag atoms of the staples; yellow: S; grey: C and white: H. The structure has been modelled taking the co-ordinates of its crystal structure.

## Supplementary Information 2



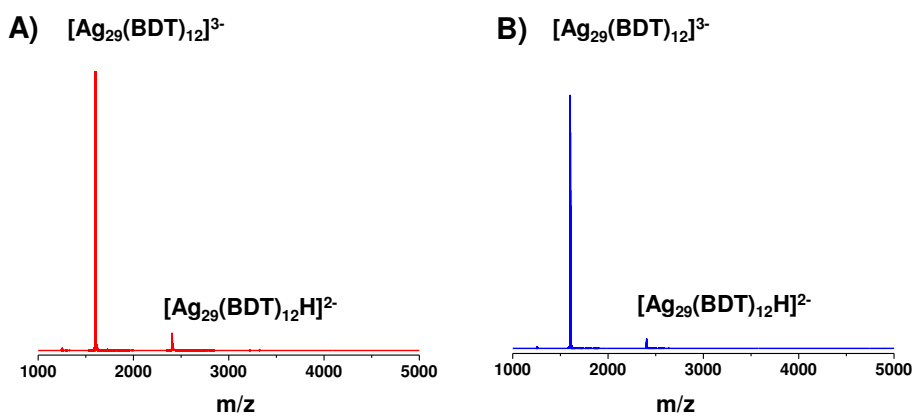
**Fig. S2** ESI MS showing increase in the peak of  $[Ag_{29}(BDT)_{12}H]^{2-}$  with increase in the concentration of formic acid. Formic acid concentration (mM) is indicated in the figure.

### Supplementary Information 3



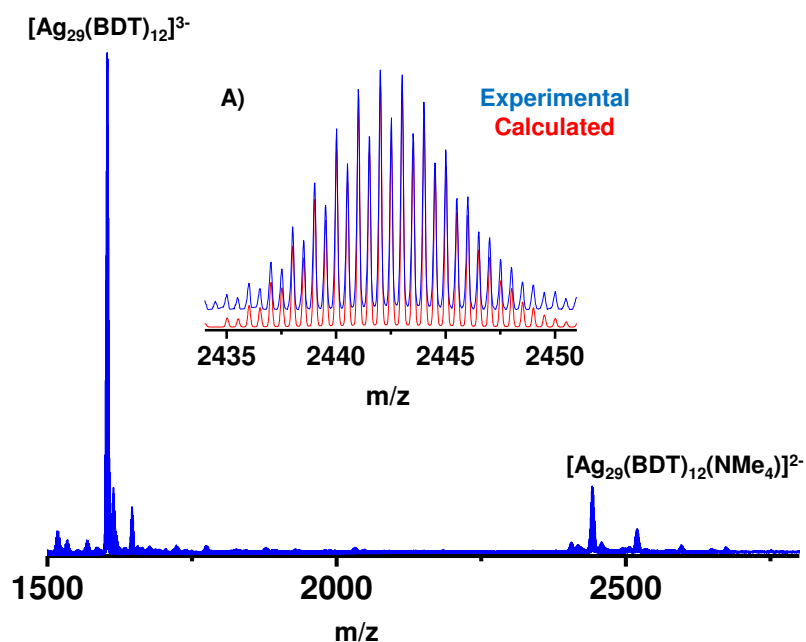
**Fig. S3** A) Calculated isotope patterns of  $[\text{Ag}_{29}(\text{BDT})_{12}]^{2-}$  and B) experimental isotope pattern of  $[\text{Ag}_{29}(\text{BDT})_{12}\text{H}]^{2-}$ . The isotope patterns show the difference between the two species. Experimental spectrum in the higher mass region overlaps with other features.

### Supplementary Information 4



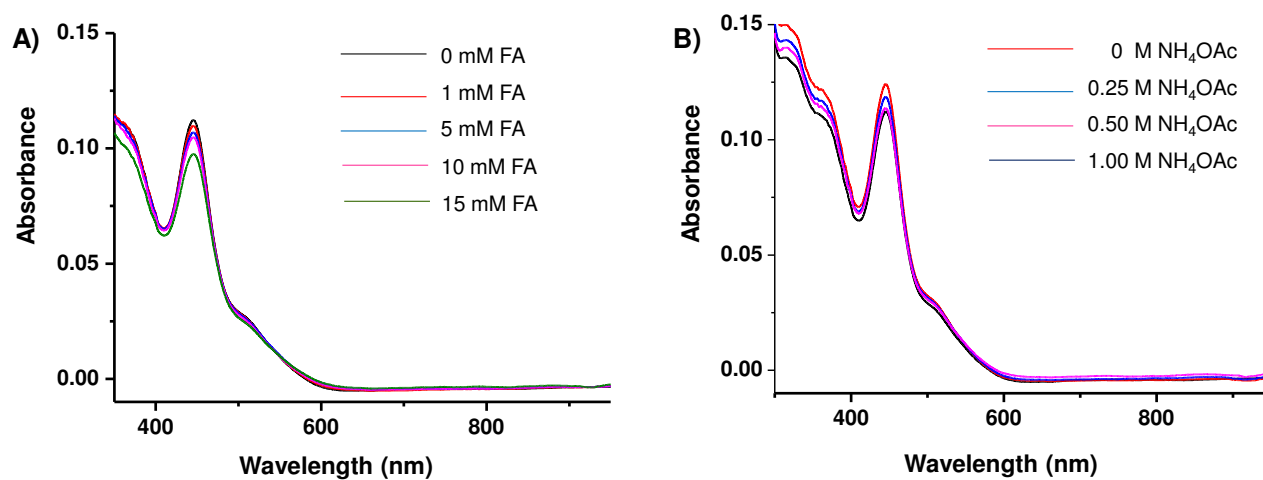
**Fig. S4** ESI MS of  $[\text{Ag}_{29}(\text{BDT})_{12}]^{3-}$  in A) 1:1 DMF/MeOH mixture and B) DMF with one drop of  $\text{H}_2\text{O}$  added as the  $\text{H}^+$  source. Peak for  $[\text{Ag}_{29}(\text{BDT})_{12}\text{H}]^{2-}$  was detected in both cases.

## Supplementary Information 5



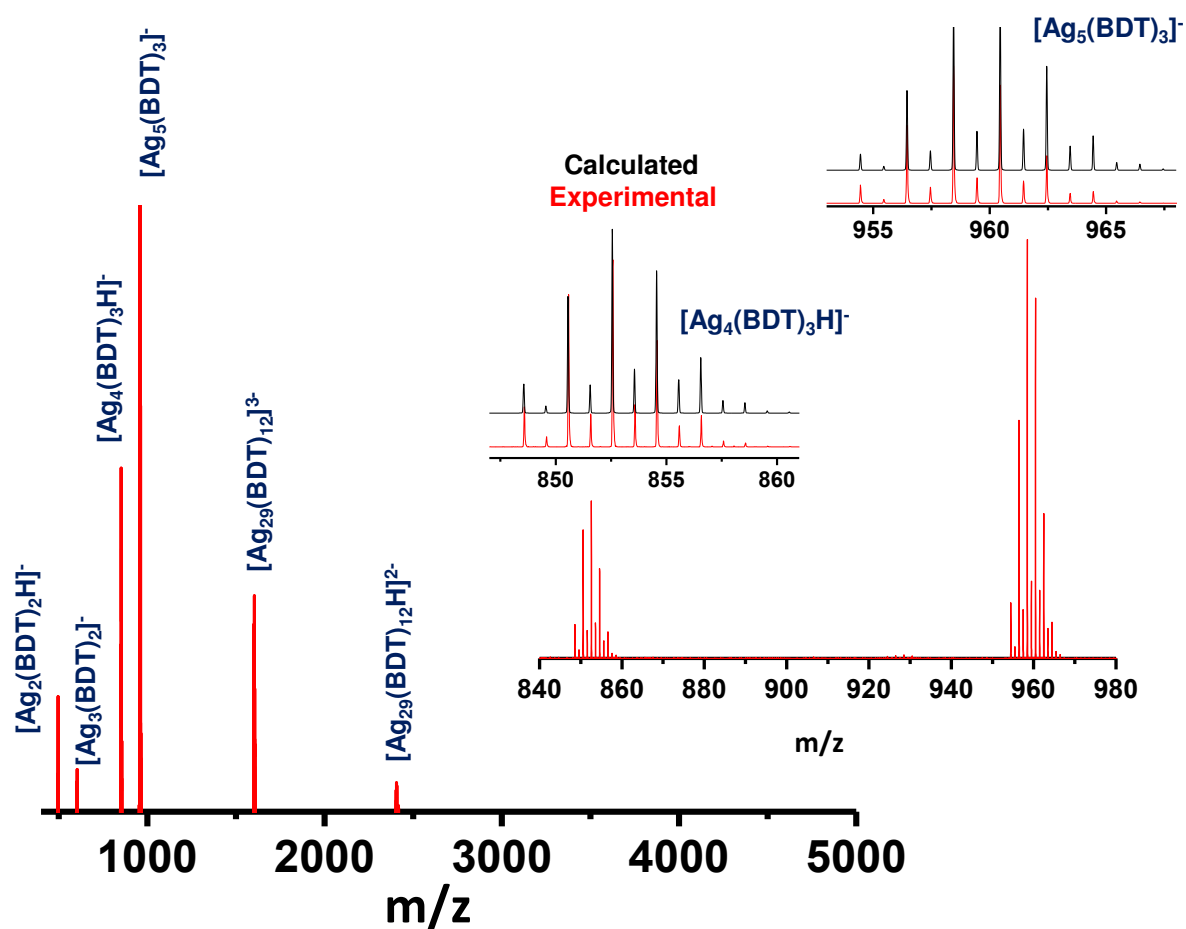
**Fig. S5** ESI MS of  $[\text{Ag}_{29}(\text{BDT})_{12}]^{3-}$  cluster in presence of  $\text{NMe}_4\text{Br}$ . The cluster shows complexation with  $\text{NMe}_4^+$  and hence a peak for the complex  $[\text{Ag}_{29}(\text{BDT})_{12}(\text{NMe}_4)]^{2-}$ . Inset A) shows the comparison of experimental and calculated isotope patterns of  $[\text{Ag}_{29}(\text{BDT})_{12}(\text{NMe}_4)]^{2-}$ .

## Supplementary Information 6



**Fig. S6** UV-vis spectra of  $[\text{Ag}_{29}(\text{BDT})_{12}]^{3-}$  cluster in presence of different concentration of A) formic acid (FA) and B)  $\text{NH}_4\text{OAc}$ .

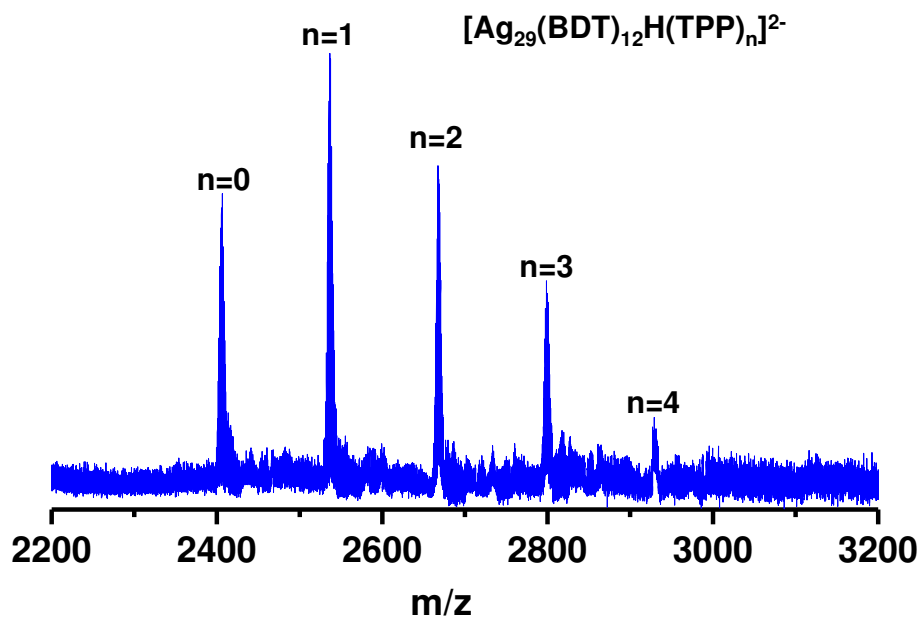
## Supplementary Information 7



**Fig. S7** MS/MS of  $[\text{Ag}_{29}(\text{BDT})_{12}\text{H}]^{2-}$ . Inset shows the expanded view of the region from  $m/z$  840 to 980 showing the fragments  $[\text{Ag}_4(\text{BDT})_3\text{H}]^-$  and  $[\text{Ag}_5(\text{BDT})_3]^-$ . The theoretical and experimental isotope patterns of the fragments are also shown.

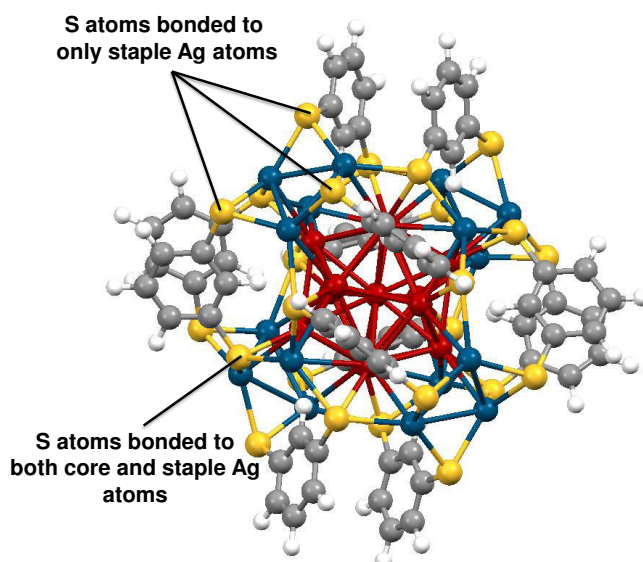


## Supplementary Information 8



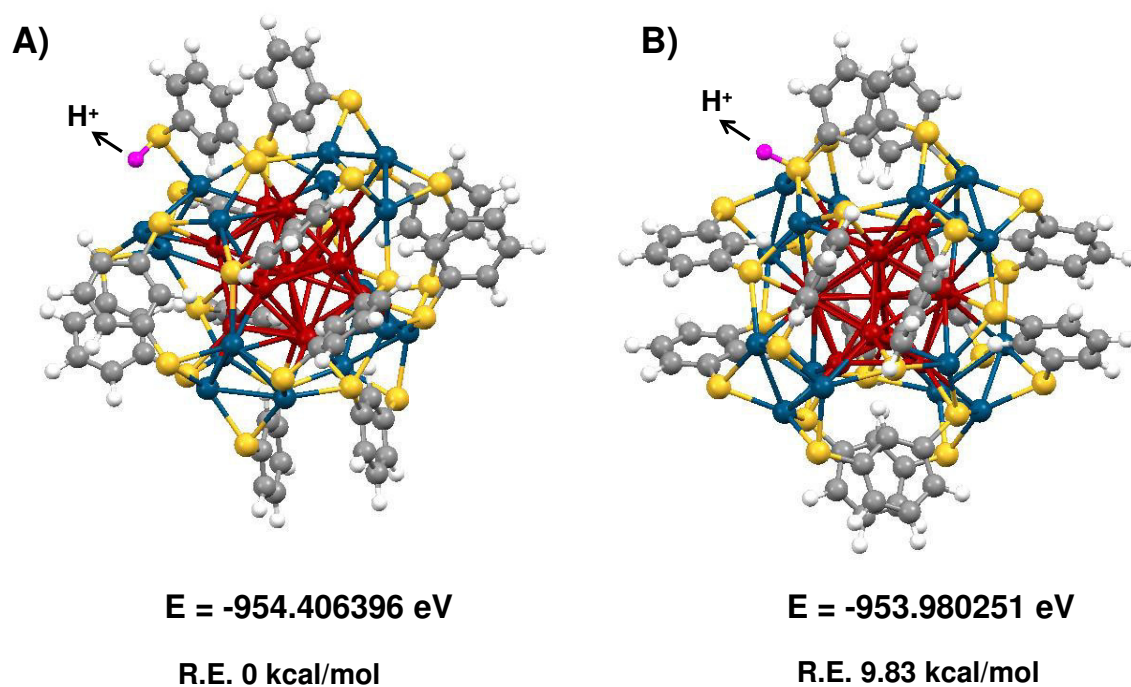
**Fig. S8** ESI MS under soft ionization conditions showing the formation of intact  $[\text{Ag}_{29}(\text{BDT})_{12}\text{H}(\text{TPP})_n]^{2-}$  ( $n=1-4$ ) clusters.

## Supplementary Information 9



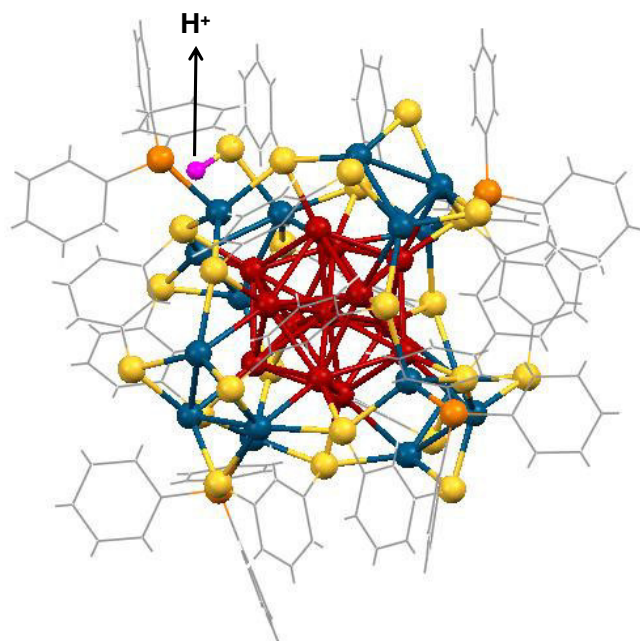
**Fig. S9** Structure of  $[\text{Ag}_{29}(\text{BDT})_{12}]^{3-}$  cluster showing two different types of S atoms in the exterior shell. Color codes: red: Ag atoms of the core; blue: Ag atoms of the staples; yellow: S; grey: C and white: H.

## Supplementary Information 10



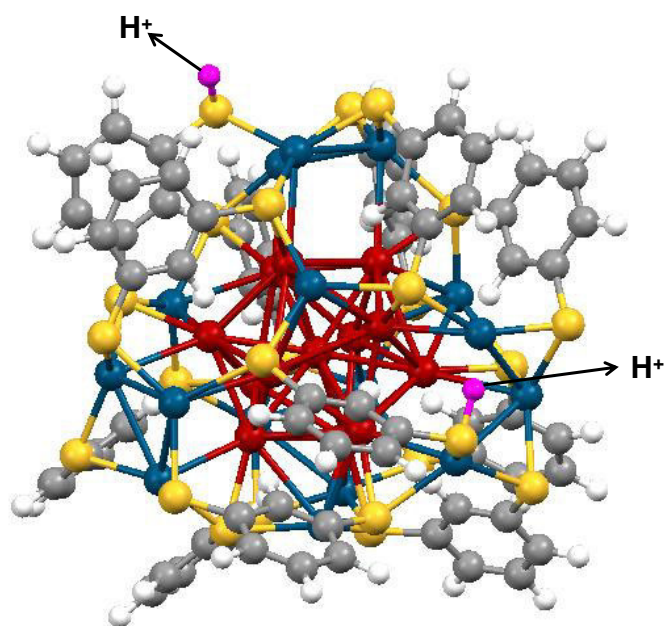
**Fig. S10** Structure of  $[\text{Ag}_{29}(\text{BDT})_{12}\text{H}]^{2-}$  with proton attached to S atom A) bonded to only Ag atoms of the staples and B) bonded to both staple and core Ag atoms. Color codes: red: Ag atoms of the core; blue: Ag atoms of the staples; yellow: S; grey: C, white: H and purple: proton.

## Supplementary Information 11



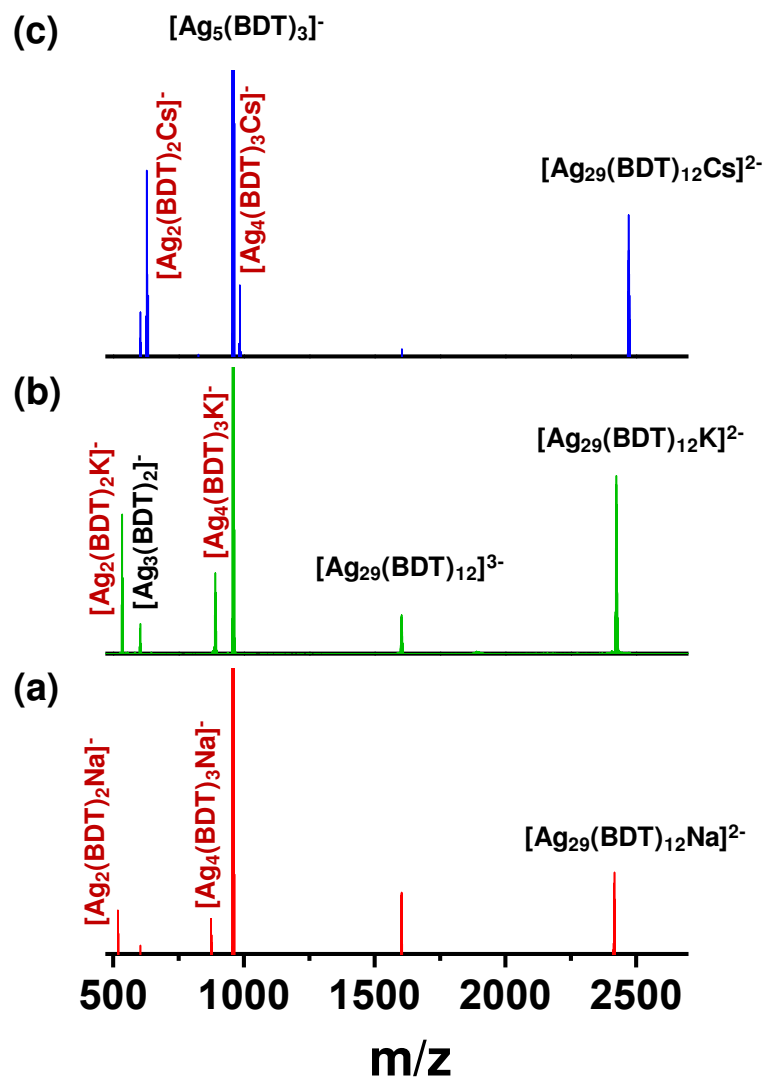
**Fig. S11** Structure of  $[\text{Ag}_{29}(\text{BDT})_{12}\text{H}(\text{TPP})_4]^{2-}$ . S-H bond distance is 1.38 Å and binding energy of proton is -73.92 kcal/mol. The P atoms are shown in orange color and thickness of the bonds in the ligands has been reduced for better clarity, proton is shown in purple color.

## Supplementary Information 12



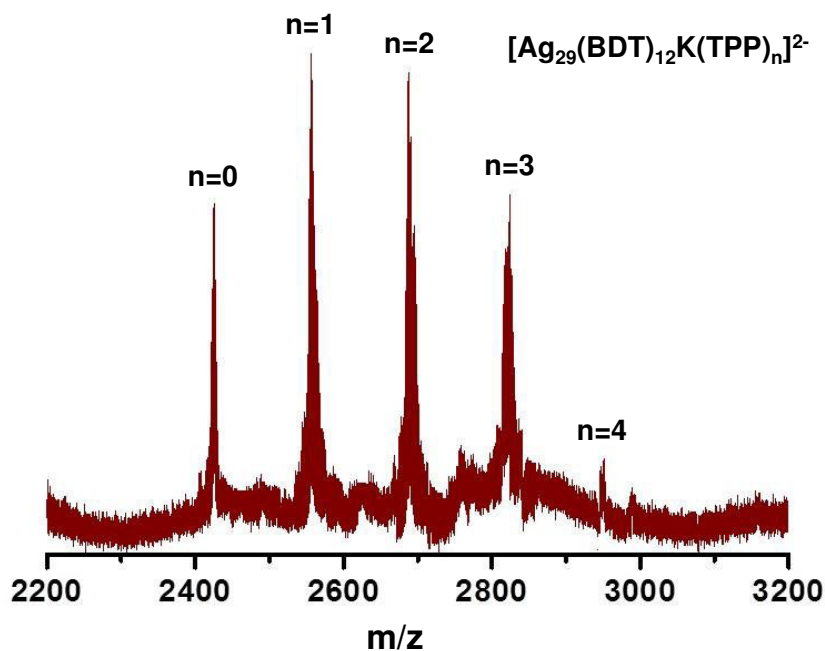
**Fig. S12** DFT optimized structure of  $[\text{Ag}_{29}(\text{BDT})_{12}\text{H}_2]^-$ . Proton is shown in purple color.

## Supplementary Information 13



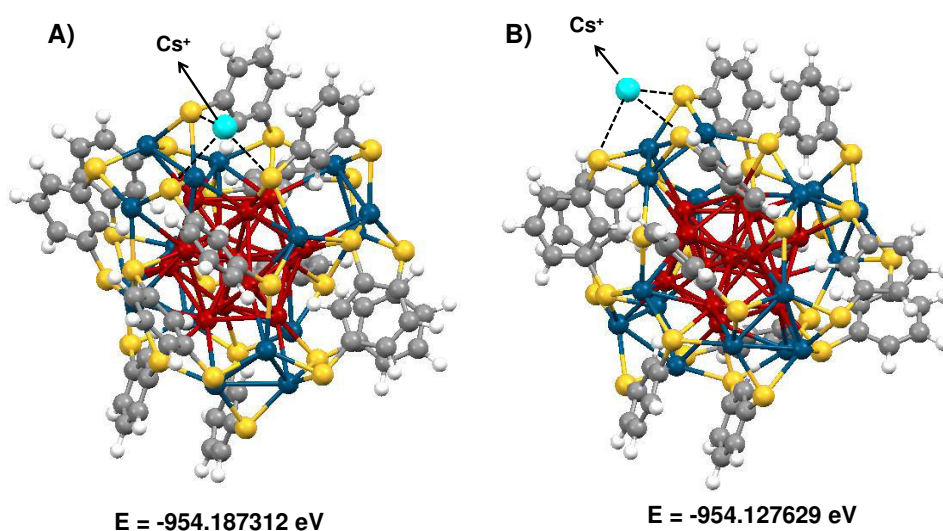
**Fig. S13** MS/MS of (a)  $[\text{Ag}_{29}(\text{BDT})_{12}\text{Na}]^{2-}$ , (b)  $[\text{Ag}_{29}(\text{BDT})_{12}\text{K}]^{2-}$  and (c)  $[\text{Ag}_{29}(\text{BDT})_{12}\text{Cs}]^{2-}$ .

## Supplementary Information 14



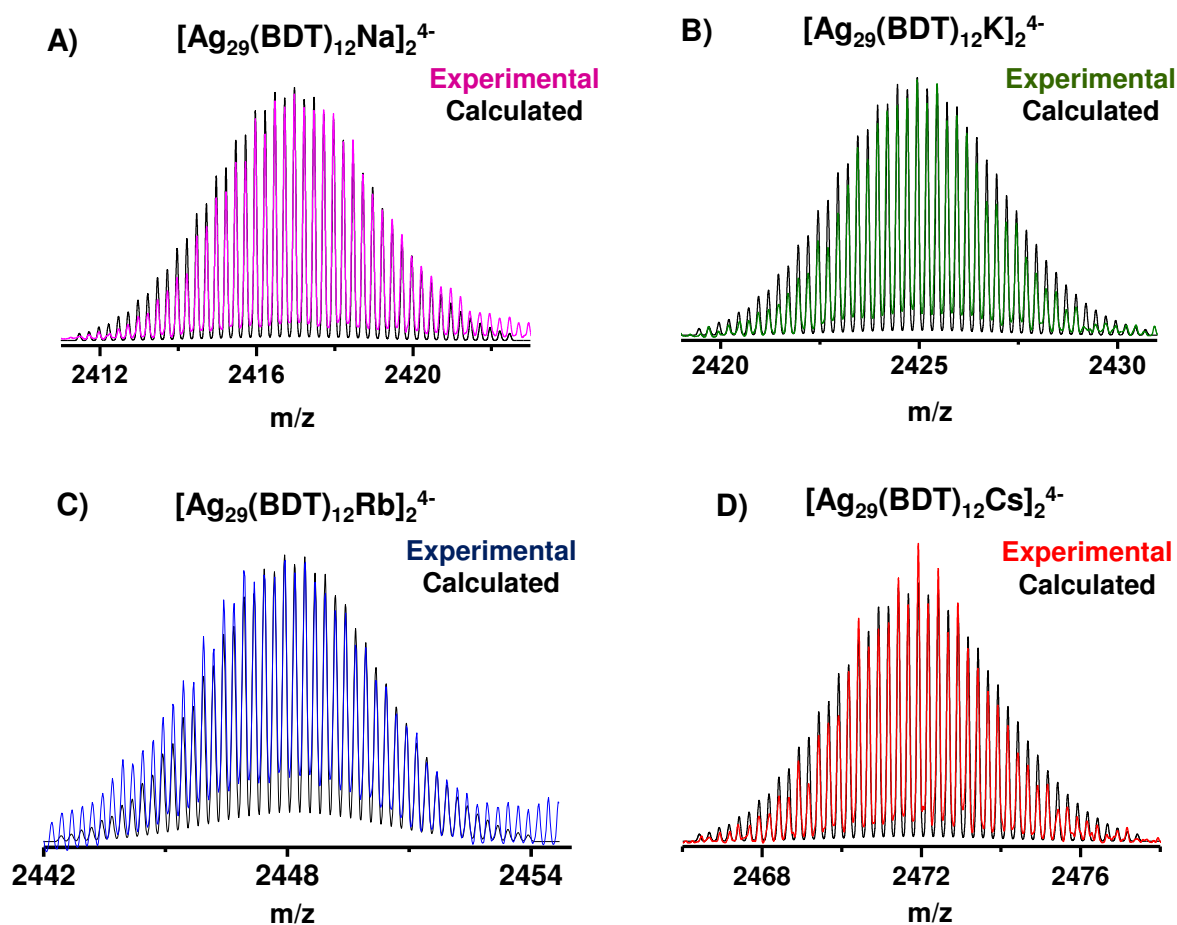
**Fig. S14.** ESI MS under soft ionization conditions showing the formation of intact  $[Ag_{29}(BDT)_{12}K(TPP)_n]^{2-}$  ( $n=1-4$ ) clusters.

## Supplementary Information 15



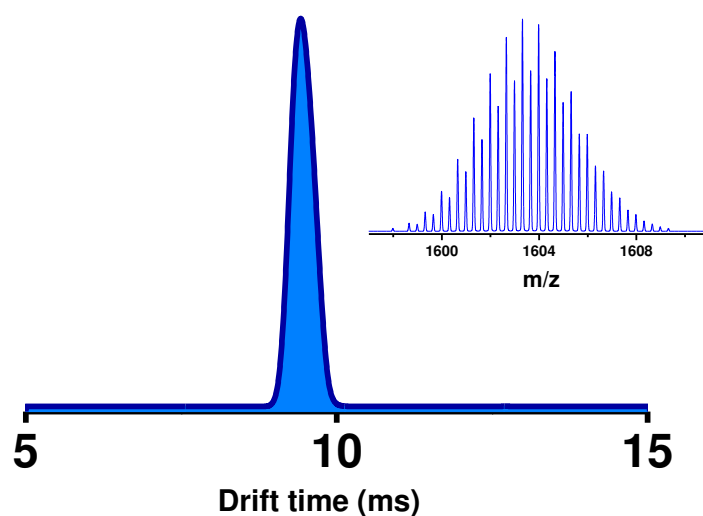
**Fig. S15** DFT optimized structure of  $[Ag_{29}(BDT)_{12}Cs]^{2-}$  with A)  $Cs^+$  attached to S atoms one of which is attached to a core Ag atom and B) all S atoms are attached only to staple Ag atoms. Relative energies of A) 0 kcal/mol and B) 1.38 kcal/mol.

## Supplementary Information 16



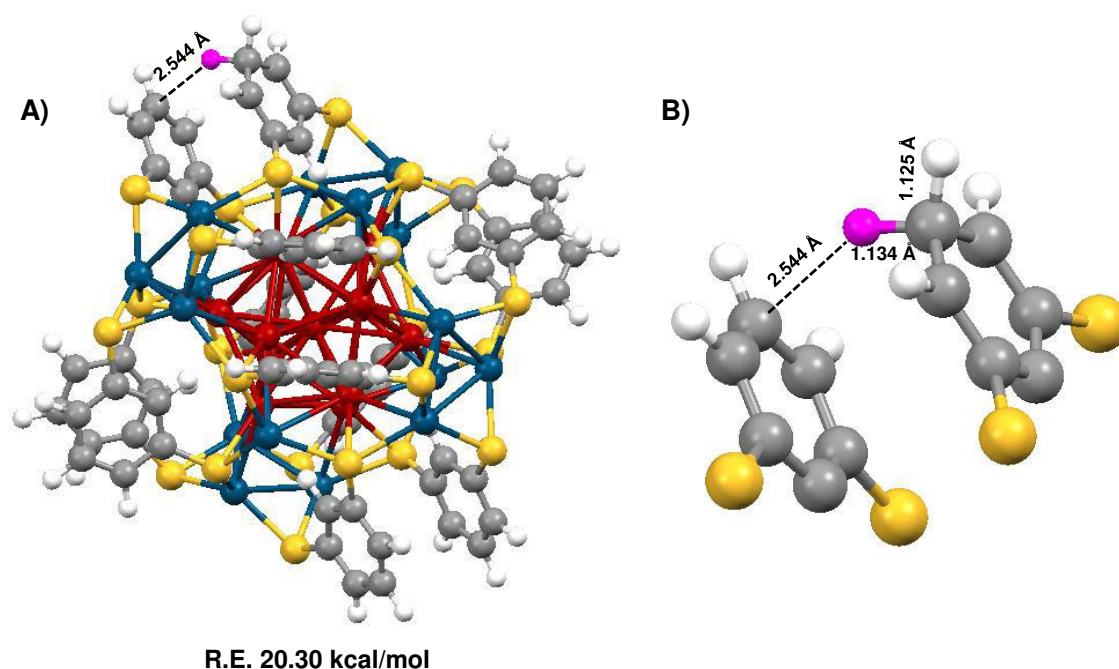
**Fig. S16** Experimental and calculated isotope patterns of the dimers A)  $[\text{Ag}_{29}(\text{BDT})_{12}\text{Na}]_2^{4-}$ , B)  $[\text{Ag}_{29}(\text{BDT})_{12}\text{K}]_2^{4-}$ , C)  $[\text{Ag}_{29}(\text{BDT})_{12}\text{Rb}]_2^{4-}$  and D)  $[\text{Ag}_{29}(\text{BDT})_{12}\text{Cs}]_2^{4-}$ .

## Supplementary Information 17



**Fig. S17** Drift time profile of  $[\text{Ag}_{29}(\text{BDT})_{12}]^{3-}$  showing only a single peak for the monomer. Inset shows the ESI MS corresponding to the mobilogram.

## Supplementary Information 18



**Fig. S18** A) DFT optimized structure of  $[\text{Ag}_{29}(\text{BDT})_{12}\text{H}]^{2-}$  with proton sandwiched between the two benzene rings of the BDT ligands. B) Expanded view showing the conformation of the proton sandwiched between the two benzene rings. Proton is colored in purple.



## Supplementary Information 19

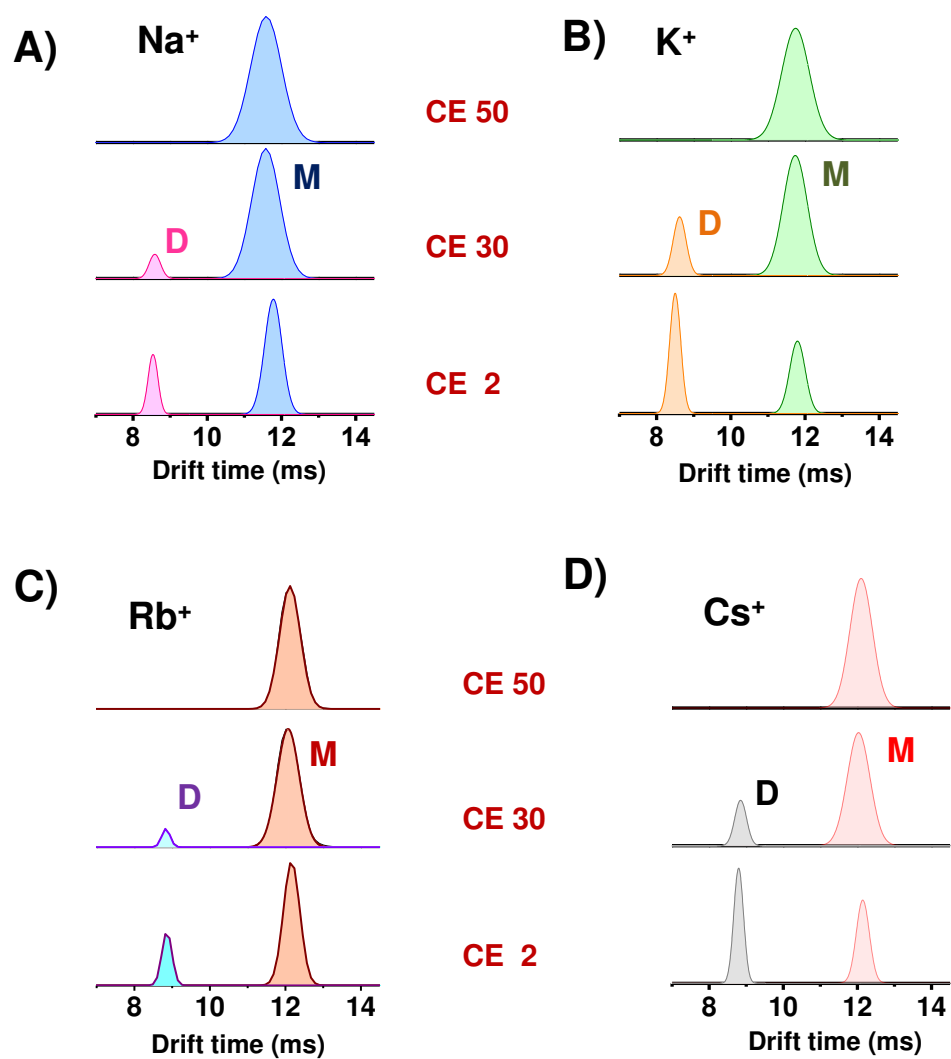
Species (Monomers)	CCS values ( $\text{\AA}^2$ )
$[\text{Ag}_{29}(\text{BDT})_{12}\text{H}]^{2-}$	535.57
$[\text{Ag}_{29}(\text{BDT})_{12}\text{Li}]^{2-}$	535.92
$[\text{Ag}_{29}(\text{BDT})_{12}\text{Na}]^{2-}$	537.52
$[\text{Ag}_{29}(\text{BDT})_{12}\text{K}]^{2-}$	539.78
$[\text{Ag}_{29}(\text{BDT})_{12}\text{Rb}]^{2-}$	543.67
$[\text{Ag}_{29}(\text{BDT})_{12}\text{Cs}]^{2-}$	547.92

Species (Dimers)	CCS values ( $\text{\AA}^2$ )
$[\text{Ag}_{29}(\text{BDT})_{12}\text{Na}]_2^{4-}$	877.31
$[\text{Ag}_{29}(\text{BDT})_{12}\text{K}]_2^{4-}$	880.51
$[\text{Ag}_{29}(\text{BDT})_{12}\text{Rb}]_2^{4-}$	887.30
$[\text{Ag}_{29}(\text{BDT})_{12}\text{Cs}]_2^{4-}$	894.72

**Fig. S19** CCS values of the monomers  $[\text{Ag}_{29}(\text{BDT})_{12}\text{M}]^{2-}$  ( $\text{M}=\text{H}, \text{Li}, \text{Na}, \text{K}, \text{Rb}, \text{Cs}$ ) and the dimers  $[\text{Ag}_{29}(\text{BDT})_{12}\text{M}]_2^{4-}$  ( $\text{M}=\text{Na}, \text{K}, \text{Rb}, \text{Cs}$ ) measured from IM MS.

## Supplementary Information 20



**Fig. S20** CID of the dimers  $[\text{Ag}_{29}(\text{BDT})_{12}\text{M}]_2^{4+}$ , A)  $\text{M}=\text{Na}$ , B)  $\text{M}=\text{K}$ , C)  $\text{M}=\text{Rb}$  and D)  $\text{M}=\text{Cs}$ .

## Supplementary Information 21

### Cartesian coordinates of the DFT optimized lowest energy structures

#### 1. Lowest energy structure of $[\text{Ag}_{29}(\text{BDT})_{12}\text{H}]^{2-}$

Ag	12.12766	11.84008	12.01999
Ag	14.14016	13.63322	10.95673
Ag	12.34732	14.27013	13.43560
Ag	11.08233	14.08635	10.69810
Ag	10.29240	9.92083	13.11112
Ag	17.18262	14.32407	10.82974
Ag	12.93858	16.30210	11.36363
Ag	11.06812	15.86380	15.53885
Ag	9.23988	15.12299	8.71579
Ag	8.46109	14.53151	15.48484
Ag	7.63643	11.04486	12.40879
S	16.08939	12.30479	15.49843
S	12.86353	16.76545	13.83854
S	10.78274	16.58668	9.95942
S	8.02919	9.03544	13.88296
S	18.15181	15.16647	12.97794
S	12.14824	15.40121	17.87582
S	8.85050	16.97962	15.22178
S	8.08747	13.24027	17.61022
C	15.59368	13.69200	16.50911
C	16.59040	14.38601	17.23824
H	17.65286	14.11403	17.09193
C	16.23151	15.40103	18.14352
H	17.02116	15.93002	18.71159
C	14.88287	15.73914	18.35886
H	14.60110	16.50926	19.10220
C	13.89528	15.07864	17.59741
C	14.24078	14.07569	16.67305
H	13.45302	13.58586	16.06329
C	14.60781	16.82307	14.25914
C	15.05527	17.83715	15.13709
H	14.32178	18.50916	15.62184
C	16.43800	17.99457	15.35534
H	16.79341	18.79078	16.03909
C	17.37381	17.17243	14.70391
H	18.45943	17.32342	14.85896
C	16.93277	16.14298	13.83048

C	15.54432	15.97269	13.63630
H	15.19288	15.16526	12.96043
C	9.60929	17.24053	11.16748
C	9.61463	16.79520	12.50615
H	10.27577	15.95500	12.80378
C	8.80624	17.41264	13.48813
C	7.95702	18.47721	13.09175
H	7.32747	18.97959	13.85091
C	7.92363	18.89241	11.74888
H	7.24797	19.71813	11.45076
C	8.74629	18.28882	10.77824
H	8.73373	18.63482	9.72757
C	7.65321	9.69823	15.50851
C	8.05005	10.99559	15.89582
H	8.72055	11.57489	15.22790
C	7.60650	11.57920	17.10436
C	6.75990	10.82524	17.95246
H	6.40093	11.26733	18.90178
C	6.38983	9.51734	17.58495
H	5.73328	8.93146	18.25821
C	6.82904	8.94286	16.37730
H	6.52651	7.91752	16.09219
Ag	14.57966	10.82296	11.01006
Ag	12.35392	12.03352	9.21788
Ag	11.78429	9.34962	10.72547
Ag	9.76635	13.01636	13.14855
Ag	17.56469	11.34773	10.57893
Ag	13.73919	9.55782	8.43322
Ag	10.88793	12.88166	6.76239
Ag	11.49647	6.34311	11.05050
Ag	8.09106	12.50804	7.97804
S	15.04959	15.86772	10.07581
S	13.17304	11.53739	6.87287
S	12.01254	7.74500	8.78677
S	7.22775	13.27529	13.55354
S	18.14799	13.12352	8.87991
S	11.39748	15.27926	5.85530
S	8.99678	11.49258	5.90386
S	6.89583	14.73342	8.16886
C	14.57902	16.02442	8.36027
C	15.45195	16.73082	7.49463
H	16.42739	17.08079	7.88379
C	15.07452	16.99663	6.16792
H	15.76233	17.55691	5.50612

C	13.82417	16.57575	5.67567
H	13.50721	16.81392	4.64354
C	12.97052	15.84497	6.52873
C	13.34886	15.54751	7.85119
H	12.67711	14.94316	8.49571
C	14.73133	12.40773	6.69305
C	15.09855	12.87808	5.41045
H	14.39502	12.77364	4.56244
C	16.37333	13.44858	5.22782
H	16.66655	13.81401	4.22390
C	17.28707	13.54368	6.29228
H	18.29365	13.97690	6.13577
C	16.92864	13.07249	7.58250
C	15.63995	12.52403	7.76474
H	15.35489	12.14634	8.76789
C	10.66735	8.15279	7.67189
C	10.33329	9.48971	7.36901
H	10.83763	10.31385	7.91409
C	9.38332	9.80701	6.37432
C	8.73953	8.74595	5.68867
H	7.99050	8.97370	4.90623
C	9.04627	7.41208	6.01529
H	8.52816	6.58827	5.48531
C	10.00392	7.10134	6.99885
H	10.24810	6.05179	7.24776
C	6.60158	14.35376	12.27004
C	6.99367	14.18743	10.92670
H	7.78341	13.44908	10.68059
C	6.39916	14.93337	9.88537
C	5.37908	15.86087	10.20973
H	4.89588	16.44781	9.40566
C	4.99605	16.03745	11.55319
H	4.19917	16.76670	11.80071
C	5.60119	15.30236	12.59019
H	5.29047	15.44558	13.64270
Ag	14.56979	12.31734	13.43863
Ag	13.11700	9.47201	13.24184
Ag	11.82524	11.81259	14.79417
Ag	9.78658	11.54266	10.40601
Ag	17.62538	12.73191	13.28901
Ag	14.29516	10.53575	15.79093
Ag	12.60453	6.52623	13.87518
Ag	10.43216	12.80926	17.13157
Ag	9.67755	6.90629	13.40637

S	16.04943	9.45337	9.47365
S	14.47761	8.17858	14.95007
S	12.30053	11.21372	17.29607
S	7.38451	10.85042	9.90927
S	18.89358	10.69739	12.59865
S	13.48891	5.15473	11.98646
S	10.75661	6.13345	15.52712
S	9.09064	5.70884	11.29863
C	16.09814	7.84543	10.27090
C	17.30764	7.11391	10.24960
H	18.22149	7.56964	9.82335
C	17.32703	5.80790	10.77653
H	18.27352	5.23247	10.76304
C	16.16864	5.22016	11.31443
H	16.19369	4.19029	11.71931
C	14.95243	5.95078	11.34997
C	14.94166	7.26386	10.83083
H	13.99323	7.83943	10.85647
C	16.15266	8.13582	14.30568
C	16.93547	6.98566	14.55504
H	16.47874	6.10569	15.04547
C	18.29481	6.98979	14.18767
H	18.91359	6.09185	14.38543
C	18.88372	8.11666	13.58741
H	19.95706	8.11591	13.31825
C	18.10124	9.26924	13.31756
C	16.73459	9.25170	13.67044
H	16.11713	10.14843	13.45400
C	11.32663	9.70691	17.49570
C	11.35053	8.69952	16.51074
H	11.90863	8.86542	15.56740
C	10.67758	7.47036	16.70072
C	9.95172	7.28277	17.90651
H	9.41343	6.32908	18.06885
C	9.91206	8.29810	18.87898
H	9.33453	8.13899	19.81164
C	10.59906	9.51287	18.69179
H	10.57252	10.30543	19.46323
C	7.41812	9.07941	9.61850
C	8.23874	8.22607	10.38330
H	8.96486	8.66164	11.10065
C	8.13085	6.82102	10.28752
C	7.18732	6.27594	9.37829
H	7.08354	5.17650	9.29813

C	6.39246	7.12809	8.59074
H	5.66289	6.69089	7.88024
C	6.49560	8.52847	8.69983
H	5.85629	9.19818	8.09399
H	10.57455	15.96614	6.73137
H	12.27233	16.73926	18.16195

## 2. Lowest energy structure of $[\text{Ag}_{29}(\text{BDT})_{12}\text{Na}]^{2-}$

Ag	11.95973	12.00974	11.99381
Ag	14.42864	12.16314	13.48003
Ag	13.40786	14.49236	12.14506
Ag	12.09081	13.43340	14.44515
Ag	11.94554	10.45090	14.36655
Ag	14.33432	12.18867	10.56967
Ag	10.41898	14.38335	11.91192
Ag	13.55040	9.62893	11.78774
Ag	11.77999	13.55548	9.57835
Ag	9.57844	11.78097	13.48966
Ag	9.52745	12.06769	10.49916
Ag	10.57998	9.52315	12.05734
Ag	12.10206	10.58496	9.50575
Ag	16.19958	13.77189	15.35536
Ag	15.37121	16.20265	13.78583
Ag	13.74582	15.34684	16.16968
Ag	14.69966	9.38179	14.54317
Ag	14.49618	14.81571	9.29519
Ag	9.34341	14.52767	14.68794
Ag	10.32328	8.49118	16.10779
Ag	14.94163	9.90605	9.16855
Ag	8.48787	16.10670	10.28548
Ag	15.32934	7.35410	10.26613
Ag	10.07172	15.38439	7.82215
Ag	7.85206	10.07064	15.37251
Ag	8.65487	7.70567	13.72820
Ag	13.49063	8.30243	7.38777
Ag	7.72666	13.71498	8.60723
Ag	9.35375	9.33302	9.35394
S	11.16450	14.67550	16.45022
S	16.48411	11.17366	14.63075
S	14.66867	16.47795	11.17308
S	12.91604	9.14432	16.32099



S	16.33432	13.02676	9.15979
S	9.10514	16.30832	12.89774
S	14.84744	7.58400	12.72365
S	12.68791	14.81746	7.54709
S	7.62468	12.66614	14.83224
S	7.56275	11.10249	9.19972
S	9.33784	7.52864	11.12029
S	11.12656	9.25240	7.53515
S	15.27676	14.03587	17.66339
S	17.70020	15.30960	14.05962
S	13.99251	17.67662	15.25721
S	8.82408	9.73855	17.67363
S	17.39804	8.85359	9.62873
S	9.74752	17.67823	8.79027
S	10.02551	6.17767	15.15436
S	15.18557	9.94835	6.42402
S	6.19649	15.10918	10.00273
S	6.32971	8.57785	14.04986
S	14.11212	6.15124	8.47441
S	8.60221	14.06242	6.27771
C	10.70824	13.40569	17.63373
C	17.60416	10.70399	13.31021
C	13.39936	17.65815	10.70702
C	10.81362	13.69938	19.01343
C	18.99939	10.79356	13.52646
C	13.68541	19.03831	10.81636
H	11.26396	14.65561	19.34043
H	19.38524	11.24525	14.45983
H	14.63608	19.36803	11.27652
C	10.33017	12.76632	19.95105
C	19.88059	10.29268	12.54917
C	12.75106	19.97076	10.32479
H	10.41350	12.99205	21.03308
H	20.97386	10.35553	12.72295
H	12.96784	21.05451	10.40952
C	9.74015	11.55808	19.53944
C	19.40261	9.70217	11.36442
C	11.55281	19.55257	9.71970
H	9.34821	10.83887	20.28416
H	20.10714	9.28891	10.61693
H	10.83119	20.29310	9.32440
C	9.63992	11.24797	18.15751
C	18.00539	9.62711	11.12552
C	11.25032	18.16917	9.61672

C	10.14598	12.17840	17.22375
C	17.13121	10.14569	12.10392
C	12.17959	17.24106	10.13359
H	10.07230	11.94360	16.14168
H	16.03799	10.09482	11.92406
H	11.95012	16.15718	10.06355
C	13.35315	10.39349	17.53094
C	17.56391	13.48371	10.37672
C	10.35272	17.52332	13.32867
C	13.19312	10.09202	18.90312
C	18.93789	13.31505	10.08249
C	10.05456	18.89416	13.15228
H	12.71184	9.14295	19.20591
H	19.25205	12.88251	9.11173
H	9.10949	19.19292	12.66106
C	13.66156	11.00741	19.86446
C	19.90432	13.72384	11.02055
C	10.97074	19.85988	13.61267
H	13.54092	10.77135	20.94054
H	20.97872	13.57863	10.78999
H	10.73912	20.93526	13.47599
C	14.28793	12.20753	19.48323
C	19.52432	14.31335	12.23818
C	12.16890	19.48461	14.24469
H	14.66819	12.91382	20.24584
H	20.29004	14.64581	12.96509
H	12.87346	20.25162	14.62021
C	14.43512	12.52856	18.10857
C	18.14912	14.49139	12.54563
C	12.48938	18.11093	14.40474
C	13.94877	11.61360	17.15019
C	17.18767	14.05439	11.60893
C	11.57231	17.14854	13.93024
H	14.05904	11.85847	16.07329
H	16.11111	14.17685	11.84740
H	11.81135	16.07273	14.05980
C	13.59261	6.36296	13.11132
C	13.13405	13.51925	6.39176
C	6.40684	13.07096	13.58044
C	12.42009	6.72548	13.80229
C	13.81585	12.35805	6.81199
C	6.76301	13.74751	12.39522
H	12.22345	7.79254	14.03114
H	13.99797	12.19744	7.89399

H	7.83102	13.95961	12.18416
C	11.47965	5.75606	14.21788
C	14.27142	11.39191	5.88942
C	5.78906	14.18096	11.46980
C	11.73329	4.39458	13.90712
C	14.02008	11.59964	4.50964
C	4.42550	13.90186	11.74710
H	11.00416	3.62495	14.22671
H	14.36821	10.84988	3.77357
H	3.65018	14.23474	11.03069
C	12.88967	4.03581	13.19152
C	13.30997	12.74023	4.09186
C	4.07114	13.20084	12.91306
H	13.06780	2.97089	12.94052
H	13.08799	12.88288	3.01574
H	3.00504	12.97060	13.10959
C	13.82677	5.00611	12.78757
C	12.86438	13.70430	5.01648
C	5.04732	12.78160	13.83745
H	14.73630	4.72219	12.22463
H	12.30906	14.60097	4.68176
H	4.76476	12.23175	14.75477
C	6.37642	10.55085	10.42900
C	10.52655	6.32515	10.53015
C	10.58826	10.45658	6.32640
C	6.78264	9.98692	11.65708
C	11.74895	6.69146	9.92581
C	10.02134	11.68327	6.72826
H	7.85856	9.98054	11.93282
H	12.05675	7.75764	9.90527
H	10.01918	11.96623	7.80206
C	5.85159	9.39776	12.54064
C	12.58419	5.72360	9.32071
C	9.42319	12.55783	5.79376
C	4.47745	9.41412	12.18500
C	12.19224	4.36413	9.34743
C	9.43338	12.19007	4.42175
H	3.73741	8.95302	12.86696
H	12.84130	3.60710	8.86630
H	8.95834	12.86027	3.67938
C	4.06799	10.00989	10.97959
C	10.98999	3.99482	9.97807
C	10.03523	10.98462	4.01734
H	2.99119	10.02579	10.71676

H	10.68985	2.92839	10.00078
H	10.04007	10.70936	2.94336
C	5.00269	10.57665	10.09179
C	10.15471	4.95945	10.56874
C	10.61246	10.10835	4.95625
H	4.67874	11.02790	9.13474
H	9.20208	4.66744	11.04919
H	11.06424	9.14840	4.64323
Na	17.40195	10.90581	7.78562

### 3. Lowest energy structure of $[\text{Ag}_{29}(\text{BDT})_{12}\text{Na}]_2^{4-}$

Ag	12.37740	11.69433	12.00183
Ag	13.09149	13.06790	14.42051
Ag	11.53374	14.41782	12.41534
Ag	10.40224	12.30024	13.97578
Ag	12.34086	10.04092	14.29241
Ag	14.35750	13.66263	11.85953
Ag	9.88713	12.46379	10.85814
Ag	15.01878	11.02061	12.90129
Ag	12.30643	13.24506	9.60731
Ag	10.40273	9.67892	12.22666
Ag	11.51317	10.50176	9.56700
Ag	13.13167	8.94680	11.78442
Ag	14.52717	11.29915	10.12577
Ag	12.26712	14.99767	16.62078
Ag	10.82666	16.55726	14.45720
Ag	9.38106	14.40261	15.97002
Ag	14.67471	10.97350	15.86698
Ag	13.30199	15.98868	10.47896
Ag	7.91855	11.27272	12.73833
Ag	11.84838	7.21985	15.36786
Ag	16.91182	12.75226	11.29963
Ag	8.30205	12.83292	8.28742
Ag	18.48773	10.88218	12.80063
Ag	10.83818	13.87899	7.00315
Ag	9.64728	6.89911	13.33812
Ag	12.39797	6.02333	12.63187
Ag	17.74090	10.95525	9.28824
Ag	10.14958	10.96003	6.82860
Ag	13.71213	8.62526	8.90180
S	8.10963	12.19000	15.09673
S	14.46873	13.41894	16.53441
S	11.38345	16.90917	11.85213

S	12.92725	9.28248	16.64680
S	15.67710	15.85016	11.48309
S	7.35730	12.82092	10.80429
S	16.72168	10.09668	14.55640
S	12.90730	15.19916	8.09438
S	8.02511	8.77476	12.34006
S	11.51281	8.81672	7.65645
S	13.97725	6.81907	10.64514
S	15.60005	10.09999	8.13240
S	10.50904	14.09873	18.18729
S	12.67388	17.37292	15.94728
S	8.36487	16.46284	14.93215
S	9.42015	6.78584	15.84298
S	18.79514	13.49845	13.00439
S	8.65507	15.11024	7.30455
S	13.56686	5.48007	14.76088
S	18.13240	13.42029	8.97476
S	7.66668	10.70472	7.09697
S	10.25072	5.11487	11.68481
S	18.92691	9.34769	10.76394
S	11.43821	12.31078	5.14117
C	8.15814	10.70698	16.10608
C	16.03690	14.10895	15.99861
C	10.03683	17.04414	10.67276
C	7.42946	10.69752	17.31908
C	16.70408	15.02430	16.84498
C	9.23650	18.21090	10.69193
H	6.94250	11.62662	17.67185
H	16.21065	15.37150	17.77228
H	9.38830	18.96561	11.48638
C	7.33117	9.49890	18.05166
C	18.00001	15.45803	16.50535
C	8.26974	18.39797	9.68532
H	6.75490	9.48696	18.99907
H	18.53167	16.16226	17.17588
H	7.64557	19.31453	9.69518
C	7.94012	8.31554	17.59833
C	18.64325	15.00055	15.34084
C	8.08969	17.44946	8.66294
H	7.84577	7.37357	18.17272
H	19.67156	15.33272	15.10292
H	7.34147	17.61377	7.86332
C	8.69489	8.31713	16.39565
C	17.97231	14.10084	14.47473

C	8.87328	16.26590	8.64444
C	8.80111	9.52732	15.67318
C	16.67225	13.67389	14.81690
C	9.83029	16.07736	9.66635
H	9.39141	9.53966	14.73341
H	16.14811	12.96339	14.14507
H	10.44810	15.15501	9.65719
C	11.82713	10.21879	17.71118
C	15.52210	16.74189	13.03049
C	7.11569	14.41985	11.57588
C	11.31170	9.58857	18.86784
C	16.56426	17.60118	13.45533
C	6.10874	15.27389	11.06672
H	11.51404	8.51534	19.04481
H	17.49013	17.70096	12.85459
H	5.55969	14.98769	10.14915
C	10.55944	10.34681	19.78494
C	16.40992	18.34731	14.63981
C	5.82015	16.47321	11.74538
H	10.15951	9.85556	20.69452
H	17.23062	19.01364	14.97326
H	5.03471	17.14612	11.34579
C	10.31375	11.71492	19.57169
C	15.23238	18.26202	15.40264
C	6.51005	16.83440	12.91602
H	9.73890	12.30868	20.30825
H	15.11836	18.85709	16.32946
H	6.26686	17.77380	13.44905
C	10.80417	12.35244	18.40234
C	14.17957	17.40401	14.99036
C	7.53695	15.99619	13.42463
C	11.54945	11.58236	17.48132
C	14.35197	16.64252	13.81437
C	7.83057	14.80150	12.73078
H	11.93848	12.07353	16.56515
H	13.53654	15.95964	13.49671
H	8.63196	14.14106	13.12222
C	16.55540	8.30966	14.55895
C	14.53765	14.77369	7.47249
C	7.55622	8.56818	10.62165
C	15.28830	7.69140	14.54038
C	15.53138	14.24633	8.32464
C	7.85128	9.54820	9.65036
H	14.37344	8.31043	14.43257

H	15.27157	14.00953	9.37596
H	8.46515	10.42882	9.93066
C	15.15079	6.29066	14.67141
C	16.85004	14.01900	7.87506
C	7.37922	9.44428	8.32324
C	16.32335	5.49930	14.78205
C	17.16952	14.32882	6.52850
C	6.60969	8.30480	7.96949
H	16.22724	4.39992	14.86834
H	18.19755	14.15617	6.15755
H	6.24064	8.20484	6.93023
C	17.58771	6.11252	14.77179
C	16.17351	14.83232	5.67089
C	6.33806	7.31258	8.92825
H	18.50070	5.48793	14.84131
H	16.42855	15.05484	4.61615
H	5.75133	6.41805	8.63601
C	17.71653	7.51040	14.67406
C	14.86009	15.05637	6.12584
C	6.79980	7.43078	10.25370
H	18.71533	7.98119	14.70443
H	14.08087	15.44810	5.44428
H	6.58736	6.64794	11.00639
C	10.60987	7.38911	8.25914
C	15.74949	6.75708	10.88700
C	15.00519	10.90244	6.64593
C	10.68458	6.96140	9.60270
C	16.53402	7.92673	10.81977
C	13.67534	11.35963	6.54812
H	11.23176	7.57693	10.34704
H	16.03953	8.91582	10.73005
H	13.01631	11.32403	7.44093
C	10.10323	5.74429	10.02431
C	17.94176	7.86262	10.84561
C	13.14848	11.83389	5.32676
C	9.41154	4.95835	9.06588
C	18.57047	6.59858	10.95731
C	14.00692	11.89053	4.19869
H	8.95624	4.00039	9.38361
H	19.67619	6.53264	10.97665
H	13.61043	12.26567	3.23589
C	9.30769	5.39862	7.73502
C	17.78674	5.43466	11.05321
C	15.34556	11.47068	4.30669



H	8.75451	4.78116	6.99888
H	18.28877	4.45174	11.14824
H	16.01148	11.53026	3.42317
C	9.90096	6.60520	7.31779
C	16.38168	5.49840	11.02094
C	15.85578	10.96793	5.51846
H	9.83344	6.94352	6.26669
H	15.76989	4.57848	11.08585
H	16.90058	10.61143	5.59503
Na	18.52227	15.41837	10.95586
Ag	27.85165	12.33035	11.93239
Ag	26.95021	10.71180	14.13698
Ag	28.44921	9.52188	11.98025
Ag	29.70018	11.30674	13.82961
Ag	27.95002	13.65727	14.44207
Ag	25.71956	10.58302	11.46362
Ag	30.30109	11.52281	10.73684
Ag	25.26700	13.11245	12.86596
Ag	27.87571	11.13843	9.32856
Ag	29.96942	14.13590	12.47516
Ag	28.88183	13.77843	9.71267
Ag	27.30637	15.13081	12.09205
Ag	25.83933	13.19603	10.07281
Ag	27.53116	8.44085	16.05378
Ag	28.89095	7.05943	13.73412
Ag	30.47590	8.88585	15.52789
Ag	25.49283	12.73667	15.82313
Ag	26.67981	8.41017	9.74762
Ag	32.30319	12.29241	12.78885
Ag	28.60067	16.28160	15.91409
Ag	23.33908	11.92684	10.94994
Ag	31.95919	11.38201	8.17248
Ag	21.77617	13.64367	12.71506
Ag	29.39867	10.76281	6.69364
Ag	30.88555	16.63952	13.97717
Ag	28.21509	17.83678	13.35100
Ag	22.56799	13.97161	9.15507
Ag	30.32311	13.59797	6.96312
Ag	26.85474	15.91778	9.26638
S	31.94782	11.08697	14.99704
S	25.50024	10.20892	16.18826
S	28.42737	7.14049	11.07149
S	27.34860	14.12906	16.87328
S	24.31371	8.55692	10.71665

S	32.78368	10.94774	10.68433
S	23.55373	13.90825	14.58951
S	27.18809	9.49442	7.50964
S	32.41709	14.82492	12.74611
S	29.07624	15.69659	8.05455
S	26.55441	17.42085	11.26779
S	24.87083	14.71892	8.24517
S	29.32261	8.97015	17.74612
S	26.93257	6.22233	15.05370
S	31.33543	6.88785	14.25612
S	31.04786	16.41347	16.48040
S	21.41001	11.08390	12.50418
S	31.44625	9.29702	6.87865
S	27.01307	18.19823	15.50647
S	22.10252	11.56588	8.56264
S	32.80485	13.59580	7.30234
S	30.44987	18.68759	12.59130
S	21.37389	15.33866	10.85651
S	28.96857	12.63367	5.07655
C	31.97602	12.40312	16.21575
C	23.91254	9.74689	15.48513
C	29.79871	7.04543	9.91675
C	32.65801	12.17589	17.43480
C	23.11082	8.78458	16.14005
C	30.50075	5.82294	9.79307
H	33.05990	11.16945	17.65940
H	23.50282	8.25555	17.02943
H	30.26185	4.98123	10.47061
C	32.82063	13.24320	18.33901
C	21.81447	8.52364	15.65268
C	31.48443	5.69584	8.79318
H	33.35479	13.06711	19.29498
H	21.18099	7.76969	16.16091
H	32.03427	4.73858	8.68851
C	32.32411	14.52649	18.04858
C	21.30061	9.21525	14.54170
C	31.77575	6.75620	7.91695
H	32.46636	15.36257	18.75999
H	20.28020	9.01573	14.16144
H	32.53928	6.63853	7.12375
C	31.61973	14.76186	16.83837
C	22.09818	10.18173	13.87972
C	31.08905	7.99269	8.04100
C	31.44254	13.68122	15.94573

C	23.40404	10.41482	14.35242
C	30.11611	8.11825	9.05658
H	30.88566	13.85684	15.00165
H	24.03777	11.15900	13.82918
H	29.57338	9.08046	9.16167
C	28.32979	12.96688	17.82446
C	24.30912	7.46166	12.13027
C	32.87020	9.24490	11.23909
C	28.84989	13.37889	19.07391
C	23.17398	6.65955	12.39796
C	33.82838	8.38537	10.65165
H	28.72291	14.42726	19.40427
H	22.27447	6.72751	11.75438
H	34.43660	8.74370	9.79925
C	29.51406	12.43795	19.88395
C	23.19929	5.76336	13.48360
C	33.99157	7.08578	11.16882
H	29.92388	12.75903	20.86268
H	22.30599	5.14309	13.69523
H	34.73805	6.40815	10.70739
C	29.66541	11.10101	19.47491
C	24.33779	5.64395	14.29967
C	33.22517	6.63050	12.25599
H	30.17479	10.36425	20.12586
H	24.35283	4.93063	15.14538
H	33.36678	5.60957	12.66019
C	29.16403	10.68234	18.21509
C	25.48164	6.44347	14.04316
C	32.24957	7.47792	12.84468
C	28.51175	11.63442	17.40217
C	25.44113	7.35177	12.96442
C	32.08072	8.77425	12.30997
H	28.11813	11.31204	16.41649
H	26.32945	7.98565	12.76495
H	31.31845	9.44113	12.76361
C	23.84335	15.65743	14.84141
C	25.60738	10.12837	6.94057
C	32.95146	15.23459	11.08276
C	25.14883	16.17001	14.97609
C	24.64095	10.61939	7.84441
C	32.61710	14.41977	9.98109
H	26.02055	15.49632	14.84432
H	24.88806	10.68527	8.92340
H	31.92610	13.56384	10.12508

C	25.37683	17.53034	15.27673
C	23.35879	11.02145	7.41084
C	33.15036	14.65409	8.69453
C	24.25941	18.39052	15.42803
C	23.04833	10.92792	6.02987
C	34.02849	15.75612	8.52215
H	24.42647	19.45984	15.65912
H	22.04910	11.24039	5.67153
H	34.45229	15.95694	7.51934
C	22.95755	17.88574	15.26415
C	24.01595	10.45275	5.12589
C	34.33522	16.59150	9.61086
H	22.08999	18.56698	15.36205
H	23.76945	10.39581	4.04742
H	35.00264	17.46366	9.45611
C	22.73616	16.52772	14.97121
C	25.29301	10.05360	5.56453
C	33.80675	16.34541	10.89294
H	21.70922	16.13756	14.83604
H	26.05183	9.68713	4.84724
H	34.04576	17.00806	11.74643
C	30.06702	16.94775	8.87248
C	24.77625	17.57365	11.45042
C	25.45512	14.08966	6.67165
C	29.96437	17.19553	10.25781
C	23.89081	16.50013	11.21472
C	26.75229	13.54948	6.54883
H	29.33290	16.53545	10.88842
H	24.29399	15.48472	11.01885
H	27.37497	13.40652	7.45654
C	30.62584	18.28573	10.86475
C	22.49067	16.69946	11.20392
C	27.29337	13.21239	5.28850
C	31.42687	19.12869	10.05072
C	21.97533	17.99277	11.45667
C	26.48395	13.39043	4.13671
H	31.94655	19.98782	10.51750
H	20.88043	18.16203	11.44001
H	26.89624	13.12979	3.14282
C	31.55333	18.86715	8.67510
C	22.85892	19.05596	11.72513
C	25.17605	13.89226	4.26278
H	32.18330	19.53021	8.04813
H	22.44971	20.06392	11.93526

H	24.55036	14.02066	3.35694
C	30.88220	17.78505	8.07438
C	24.25145	18.85980	11.72500
C	24.65051	14.24959	5.51944
H	30.97197	17.58540	6.98990
H	24.94307	19.69991	11.92544
H	23.63033	14.66710	5.61340
Na	21.64199	9.35531	10.27244

## Cluster Crystals

Probing the Mechanical Response of Luminescent Dithiol-Protected  $\text{Ag}_{29}(\text{BDT})_{12}(\text{TPP})_4$  Cluster CrystalsKorath Shivan Sugi,<sup>[a]</sup> Gangapuram Mallikarjunachari,<sup>[b]</sup> Anirban Som,<sup>[a]</sup> Pijush Ghosh,<sup>\*,[b]</sup> and Thalappil Pradeep<sup>\*,[a]</sup>

**Abstract:** Atomically precise clusters of noble metals are considered to be an important class of advanced materials. Crystals of these clusters composed of inorganic cores and organic ligands are fascinating owing to their tunable and unique properties. Understanding their mechanical properties can give more insight into the design of nanocluster-based devices. Here, we probe the mechanical response of single crystals of  $\text{Ag}_{29}(\text{BDT})_{12}(\text{TPP})_4$  cluster (BDT = 1,3 benzenedithiol, TPP = triphenylphosphine) under both quasi-static and dynamic loading conditions. Surprisingly, the measured reduced Young's modulus ( $E_r$ ) and hardness ( $H$ ) were 4.48 and

0.285 GPa, respectively, similar to those of polymers and much smaller than the values for bulk silver. These observations indicate a significant role of capping ligands on the physical properties of such materials. The observed storage modulus, loss modulus and loss factor were also found to be similar to those of polymers. The magnitude of loss factor suggested the ability of nanocrystals to absorb energy under dynamic loading. These studies of mechanical properties of cluster materials could be useful in developing their applications.

## Introduction

Atomically precise nanometer-sized pieces of noble metals, protected with ligands having well-defined crystal structures<sup>[1]</sup> belong to a new category of materials. They are distinctly different from nanoparticles in their spectroscopic properties, such as well-defined features in their optical absorption and emission spectra, just like molecules, which has been efficiently manipulated to create functional devices. Luminescent properties of these noble metal nanoclusters (NMNCs) have been used in the creation of sensors.<sup>[2]</sup> In contrast, nanoparticles of such metals composed of thousands of atoms exhibit strong surface plasmon resonance and nearly undetectable luminescence. Due to their pronounced luminescence, NMNCs are successfully conjugated with other functional materials for the creation of solar cells.<sup>[3]</sup> They are also used as cocatalysts in improving the performance of  $\text{MoS}_2$  towards hydrogen evolution reaction (HER).<sup>[4]</sup> Such exciting optical, electronic properties of these materials can be enhanced further by changing the size and shape of the metal core during synthesis or by alloying.<sup>[5]</sup>

These NMNCs, synthesized in solution, make crystals under controlled conditions. Total structures of many of these clusters have been solved by growing such single crystals. Kornberg group in 2007 reported the first crystal structure of the decahedral  $\text{Au}_{102}$ .<sup>[1d]</sup> Total structures of several other gold clusters like  $\text{Au}_{18}$ ,<sup>[6]</sup>  $\text{Au}_{20}$ ,<sup>[7]</sup>  $\text{Au}_{23}$ ,<sup>[8]</sup>  $\text{Au}_{24}$ ,<sup>[9]</sup>  $\text{Au}_{25}$ ,<sup>[10]</sup>  $\text{Au}_{28}$ ,<sup>[11]</sup>  $\text{Au}_{30}$ ,<sup>[12]</sup>  $\text{Au}_{36}$ ,<sup>[13]</sup>  $\text{Au}_{38}$ ,<sup>[14]</sup> and  $\text{Au}_{133}$ <sup>[15]</sup> of varying crystal systems have been reported till date. In the case of silver clusters, although the developments have been slower, some reports have become available in recent years which include  $\text{Ag}_{14}$ ,<sup>[16]</sup>  $\text{Ag}_{25}$ ,<sup>[17]</sup>  $\text{Ag}_{29}$ ,<sup>[18]</sup>  $\text{Ag}_{44}$ ,<sup>[1e]</sup> and  $\text{Ag}_{67}$ .<sup>[19]</sup> All the clusters are protected with ligands, often thiolates and have counter ion to compensate charges. For example,  $\text{Ag}_{44}$  exists as  $[\text{Ag}_{44}(\text{SR})_{30}]^{4-} \text{Na}_4$ . Functional groups present on the organic ligands of these NMNCs interact chemically between neighboring NMNCs and dictate the orientation and packing of the nanocluster (NC) in the crystal.<sup>[20]</sup> Controlling such ligand-ligand interactions open up possibilities to further tune and optimize the properties of NMNCs for applications in optical and electronic devices. In the recent past, physical properties such as hardness ( $H$ ) and Young's modulus ( $E_r$ ) have been correlated well with molecular properties.<sup>[21]</sup> Interesting observations have been made in the context of solubility and mechanical properties of pharmaceuticals which are relevant in the context of drug delivery.<sup>[22]</sup> Due to the presence of long-range order in the NC crystals, it is likely that physical properties of such crystals will be closely related to the molecular structure of the individual NC, much like fullerenes.<sup>[23]</sup>

Nanoindentation<sup>[24]</sup> is a reliable method to precisely understand bulk mechanical properties of materials. Recently, the nanoindentation technique has been widely used for evaluating the mechanical properties of various organic and inorganic

[a] K. S. Sugi, A. Som, Prof. T. Pradeep  
DST Unit of Nanoscience (DST UNS) and Thematic Unit of Excellence (TUE),  
Department of Chemistry, Indian Institute of Technology Madras, Chennai  
600 036, India  
E-mail: pradeep@iitm.ac.in

[b] G. Mallikarjunachari, Prof. P. Ghosh  
Department of Applied Mechanics & Soft Matter Center, Indian Institute of  
Technology Madras, Chennai 600 036, India  
E-mail: pijush@iitm.ac.in

Supporting information for this article is available on the WWW under  
<https://doi.org/10.1002/cnma.201700371>

crystals as well as metal-organic frameworks (MOFs).<sup>[25]</sup> Such studies indicate an important correlation between mechanical and molecular aspects of materials. Assembly of plasmonic metal or semiconductor nanoparticles, forming superlattice crystals, has been a subject of study.<sup>[26]</sup> Electronic properties of such materials from the context of origin of metallicity has been examined in detail.<sup>[26a]</sup> Nanocrystal superlattices exhibit superior mechanical strength and are capable of withstanding repeated indents.<sup>[26b,27]</sup> Such remarkable mechanical cohesion in the superlattices are due to the van der Waals interactions between ligands on neighboring nanocrystals.<sup>[28]</sup> Due to versatile properties of Au nanocrystals, considerable effort has been paid to understand their mechanical properties. Mueggenburg et al. had reported that the dodecanethiol-ligated gold nanocrystal monolayers, have Young's modulus of the order of several GPa and they remain intact and able to withstand tensile stresses up to temperatures around 370 K.<sup>[26b]</sup> Nanoindentation studies performed on oleic acid stabilized PbS nanoparticles by Tam et al. attributed the mechanical properties to the organic capping agents surrounding the inorganic core.<sup>[29]</sup> Similar studies by Podsiadlo et al. on both the shaped superlattice crystals and the evaporated, layer-by-layer superlattice crystals correlated the mechanical properties of PbS, CdSe, and CoPt<sub>3</sub> superlattice crystals with the nanocrystal size, capping ligands, and degree of ordering.<sup>[26c]</sup>

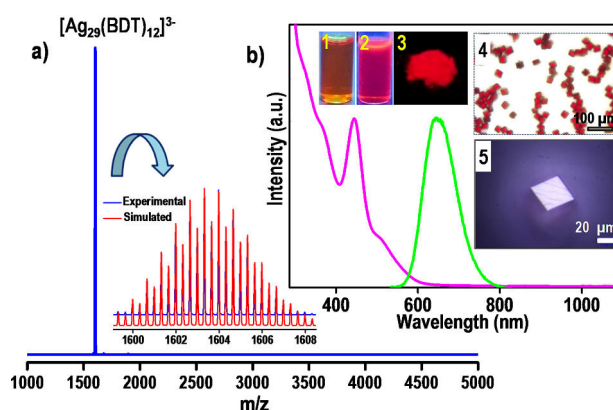
Single crystals of NMNCs are different from all these materials as in former case atomically precise NCs are assembled into macroscopically ordered crystals. While the optical and electronic properties of NMNCs are being intensely researched upon, mechanical properties of such materials are yet to receive significant attention. However, properties of NMNC-based devices would depend also on their mechanical properties (like hardness and modulus, etc.), which emphasizes the need to study and understand them in detail. Moreover, all of these properties of a NMNC-crystal will depend upon how strongly a NMNC interacts with its neighboring clusters. While such interactions are difficult to study experimentally at single NMNC level, bulk mechanical properties can be correlated to NC-NC interactions in the crystal.

Herein, we present an early investigation into the mechanical properties of one such silver NC system. The present study focuses on mechanical properties of crystals of bidentate thiol protected, highly stable<sup>[30]</sup> Ag<sub>29</sub>(BDT)<sub>12</sub>(TPP)<sub>4</sub> NCs (BDT – 1,3 benzenedithiol, TPP – triphenylphosphine), for which the light-harvesting capabilities and charge transfer dynamics<sup>[31]</sup> were well studied recently. The cluster crystal is referred to as **I** in the following discussion. This makes such systems promising candidates for NC-based devices. Nanomechanical characterization techniques, such as nanoindentation, nanoscratch, and nano-dynamic mechanical analysis (DMA) have been applied to understand the mechanical properties of **I**. Quasi-static nano-indentation was applied to determine the two fundamental properties, *E<sub>r</sub>* and *H* of the **I**. The storage modulus, loss modulus and loss factor at different frequencies were determined by applying dynamic loading. Nanoscratch technique was applied to examine the material heterogeneity, if any, along and across the depth. We find that the *E<sub>r</sub>* and *H* of **I** are 4.48 and 0.285 GPa,

respectively, far lower than the respective values of bulk silver (62.52 and 3.57 GPa). Interestingly, these properties are similar to commonly known polymers such as polymethyl methacrylate (PMMA). The clusters were found to be intact under experimental investigations and no change in electronic properties was observed.

## Results and Discussion

ESI MS was employed to confirm the composition and purity of the Ag<sub>29</sub>(BDT)<sub>12</sub>(TPP)<sub>4</sub> cluster. The negative ion mode mass spectrum of the purified cluster is shown in Figure 1a which



**Figure 1.** a) Negative ion mode SI-MS of Ag<sub>29</sub>(BDT)<sub>12</sub>(TPP)<sub>4</sub> clusters. The inset shows the comparison of experimental and simulated mass spectra of [Ag<sub>29</sub>(BDT)<sub>12</sub>]<sup>3-</sup> which match exactly. b) Optical absorption (pink) and emission spectra (green) of Ag<sub>29</sub>(BDT)<sub>12</sub>(TPP)<sub>4</sub> clusters. The excitation wavelength is 450 nm. Inset 1 and 2 are the photographs of the cluster solution under visible and UV light, respectively. Inset 3 is the photograph of the cluster powder under UV light. Inset 4 and 5 are the optical images of **I** collected in transmission and reflected modes, respectively.

agrees well with the reported spectrum of Ag<sub>29</sub>(BDT)<sub>12</sub>(TPP)<sub>4</sub>. The peak centered at 1603 corresponds to [Ag<sub>29</sub>(BDT)<sub>12</sub>]<sup>3-</sup> as the weakly bonded phosphines dissociate during ionization. Expansion of the peak centered at 1603 shows a characteristic isotropic distribution in which each peak separation corresponds to *m/z* = 0.33, which in turn corresponds to the –3 charge state. The optical characterization of clusters was done using UV-vis and photoluminescence (PL) measurements. Figure 1b shows the UV-vis absorption spectrum (pink trace) and emission spectrum (green trace) of the Ag<sub>29</sub>(BDT)<sub>12</sub>(TPP)<sub>4</sub> cluster solutions. Molecular transitions are observed at 447 and 513 nm. When excited at 450 nm, the emission maximum was observed around 670 nm. Inset 1 of Figure 1b is the photograph of cluster solution in visible light and inset 2 is the photograph under UV light. Inset 3 is the photograph of the cluster powder under UV light. The purified cluster was crystallized in a dark box for a period of 3–4 days. After four days, red square plate-shaped crystals were observed. Insets 4 and 5 of Figure 1b are the optical images of the **I** collected in the transmission and reflected modes, respectively. The cluster crystallizes in cubic Pa3 space group. The crystal structure of



the cluster is shown in Figure S1a (Supporting Information). The SEM image of the cluster crystals also confirms the formation of uniform cubical crystals (Figure S2).

Compared to other mechanical investigations, nanoindentation leaves only a small imprint on materials and can be considered as a non-destructive technique even though sharp indenters are used to penetrate the surface of the sample. A typical load-displacement curve during loading and unloading is shown in Figure S3. The label,  $h_{max}$  is the maximum penetration depth associated with the applied maximum load  $P_{max}$ ;  $h_p$  is the residual penetration depth at full unloading while  $h_e$  is the elastic penetration depth recovered at full unloading and  $h_c$  is the contact depth under the maximum indentation force. In our experiments with I, a holding time of 10 s before unloading was applied to reduce the effect of creep on the measured quantities. An optical microscope was used to position the indenter tip over nanocrystals. The  $E_r$  and  $H$  were determined from load-displacement curves by applying Oliver and Pharr analysis.<sup>[32]</sup> The Oliver–Pharr method is the most common method used for establishing the projected contact area and predicting the elastic modulus of ordinary materials. In this method, the unloading portion of indentation graph was fitted into the power-law,

$$P = B(h - h_p)^m \quad (1)$$

where,  $B$  and  $m$  are fitting parameters and  $h_p$  is the final indentation depth after complete unloading.

According to this method, in the absence of creep, the initial unloading of the sample is elastic and the contact area stays constant. Stiffness ( $S$ ) is the measure of the resistance offered by an elastic body to deformation. The slope of initial part of the unloading curve thus represents the stiffness of the indented material. From this data, the initial unloading slope, i.e., contact stiffness  $S$  is estimated by analytically differentiating Equation (1) and evaluating the result at the maximum indentation depth.

$$S = \left( \frac{dP}{dh} \right)_{h=h_{max}} = Bm(h_{max} - h_p)^{m-1} \quad (2)$$

where,  $P$  is the applied load and  $h$  is the displacement. Finally, in the case of a rigid indenter, the elastic modulus  $E_r$  is calculated by

$$E_r = \frac{1}{\beta} \frac{\sqrt{\pi}}{2} \frac{S}{\sqrt{A}} \quad (3)$$

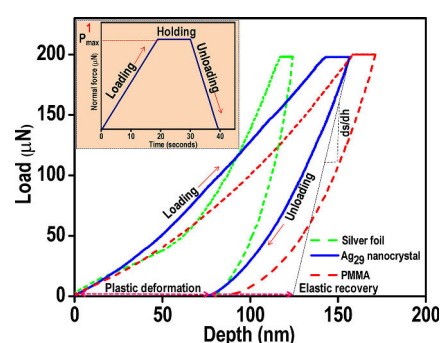
where,  $\beta$  is the correction factor.

The hardness of a material is the measure of its ability to resist plastic deformation and is given by the Equation (4).

$$H = \frac{P_{max}}{A} \quad (4)$$

where,  $P_{max}$  is the peak indentation load and  $A$  is the projected area of the impression. The nanocrystals are crystallized on a

glass microscope slide. To avoid the substrate effect, all the experiments were performed such that the maximum depth of penetration attained remained below 10% of the crystal size. We performed load dependent studies initially on I (Figure S4) by applying a series of loads, such as 50  $\mu$ N, 100  $\mu$ N, 150  $\mu$ N and 200  $\mu$ N and corresponding moduli were determined. The  $E_r$  depends mainly on  $S$  and the  $A$  of the residual imprint. As peak load increases, these two factors changes, thus affecting the Young's modulus. The variation of  $E_r$  and  $H$  with increasing load is shown in Figure S5. The modulus and hardness values corresponding to lower loads were disregarded since those represent more of the surface properties and not of the bulk. Also, due to low displacement in the normal directions at lower loads, the surface roughness influences the response of the true material. The load-displacement response of a single crystal at 200  $\mu$ N is shown in Figure 2. The schematic of



**Figure 2.** Load-displacement curves of silver foil (green dotted line), I (blue solid line) and PMMA (red dotted line) with Berkovich indenter. Inset 1 shows a schematic of the trapezoidal load function.

trapezoidal load function used for indentation is shown in the inset of Figure 2. The loading part of the curve is elastic-plastic in nature. The slope of the initial part of the unloading curve represents the elastic recovery of the material and thus is applied to estimate the elastic modulus of a material. For comparison, NI tests were also performed on a silver foil and PMMA. The values determined at 200  $\mu$ N load are shown in Table 1. The  $E_r$  and  $H$  values corresponding to 200  $\mu$ N can be considered as representative bulk values. These  $E_r$  and  $H$  values obtained for I were  $4.48 (\pm 0.115)$  GPa and  $0.285 (\pm 0.006)$  GPa, respectively.

It is to be noted that the elastic modulus of I is similar to that of some of the widely-used polymers such as PMMA and polystyrene<sup>[33]</sup> and is significantly different from silver metal, which constitutes the cluster core. The large Young's modulus in polymers is attributed to the entanglement of monomer

Table 1. Measured Young's modulus and hardness of the different materials		
Material	$E_r$ (GPa)	$H$ (GPa)
Silver foil	$62.52 \pm 1.8$	$3.57 \pm 0.250$
Ag <sub>29</sub> nanocrystal	$4.48 \pm 0.115$	$0.285 \pm 0.006$
PMMA	$3.90 \pm 0.155$	$0.187 \pm 0.030$

molecules.<sup>[34]</sup> In case of **I** the Young's modulus is presumably a consequence of the ligand confinement and associated interactions. This observation suggested that the protecting ligands not only act as spacers but also provide significant mechanical strength through ligand-ligand interactions.

The initial part of the unloading curve of the load-displacement plot indicates elastic recovery (Figure 2). The area under the respective elastic recovery region and plastic deformation region of load-displacement curve provides an insight into the elastic work done ( $W_E$ ) and the energy dissipated ( $W_P$ ) due to plastic deformation during the application of load (Figure S6).  $W_E$  is the amount of energy utilized in deforming a material which recovers when the load is removed and plastic work done  $W_P$  is the amount of energy dissipated while the material undergoes plastic deformation. The calculated ratio of  $W_P$  to  $W_E$  from the load-displacement curve of the crystal is 1.89 which further confirms the permanent deformation in the crystal. The permanent deformation in the nanocrystal possibly arises from the relative displacement of the clusters under the applied load.

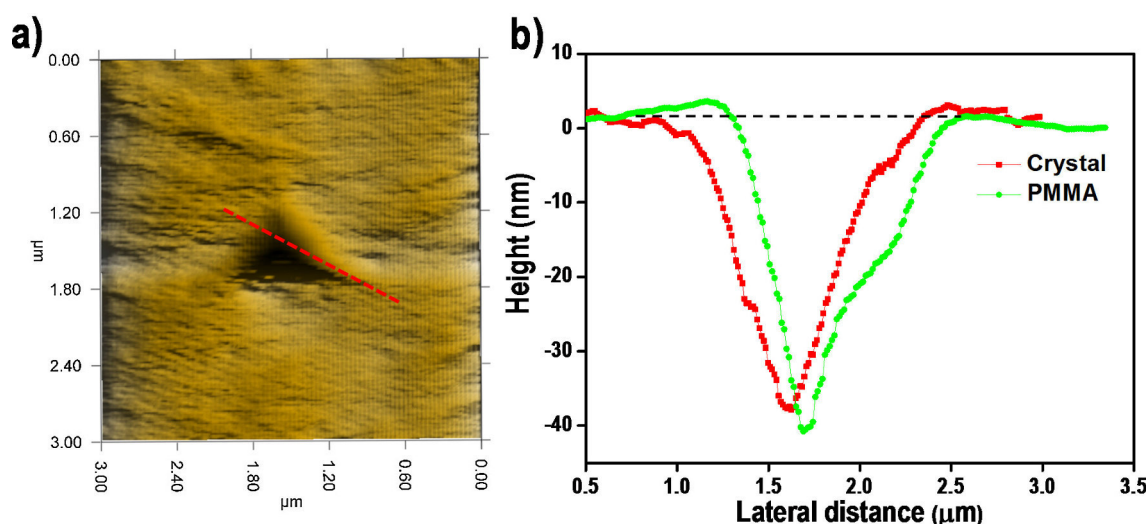
It is observed from the load-displacement plot that during the hold time of 10 s, the crystal underwent a creep displacement of about  $14 \pm 2$  nm. Creep<sup>[35]</sup> is a phenomenon where under a constant load; a visco-elastic material undergoes displacement. Under identical conditions, PMMA showed a comparable creep displacement of  $12 \pm 2$  nm. The presence of organic ligands, therefore, contributes to the time-dependent creep behavior of **I**.

The residual indentation impression of the indented surface of the nanocrystal is shown in Figure 3a. In the normal direction, the maximum depth of penetration of 170 nm was attained under the maximum load; whereas with the removal of the load, the nanocrystal recovered, leaving a residual depth of 40 nm. The number of unit cells subjected to direct load under the indenter was calculated by measuring the volume of residual impression from the piezo image. The volume of

indentation imprint is  $3.181 \times 10^{-21} \text{ m}^3$ . The volume of the molecular crystal unit cell is  $40006 \times 10^{-30} \text{ m}^3$ . Therefore, the number of unit cells subjected to direct load under the indenter is approximately  $7.952 \times 10^4$ . This translates to a number of  $6.362 \times 10^5$  clusters under the indented volume. These are also approximately the number of clusters which have undergone permanent deformation and thus contribute to the plastic energy ( $W_P$ ). The variation observed in the values of  $H$  for PMMA and the nanocrystal (Table 1) is due to the difference in maximum displacement (Figure 2). This is because the area of residual indentation imprint used for calculating hardness changes with the change in maximum displacement. The slightly higher value of hardness of the nanocrystal could be due to the even distribution of stress in **I** than a polymer network.

To investigate the strength of **I**, we have performed indentation with a higher load of 10000  $\mu\text{N}$  (Figure S7a). There was no evidence of fracture even at such high loads (Figure S7b and c). The indentation was also performed at higher loading rate, i.e., 10000  $\mu\text{N/s}$ ; however, still no fracture or crack propagation was observed in the SEM image of the residual indentation imprint (Figure S7d and e). The absence of any formation or propagation of cracks even at higher loads might be due to the ligand-ligand interactions in the nanocrystal which imparts such ductile (visco-elastic) nature to the material.

Pile-up is a phenomenon of accumulation of materials on the surface around the indenter tip resulting in plastic deformation due to the applied load. Since the elastic modulus of **I** is similar to that of PMMA and also the fact that it exhibits creep behavior, we have measured the pile-up of **I** during indentation. The section profiles of the nanocrystal and PMMA (Figure 3b) were taken along the indentation impression (dotted red line) as shown Figure 3a. The PMMA exhibits slight pile-up whereas no pile-up was observed in the case of **I** which might be due to its work hardening capacity. Work hardening in materials is induced normally when the density of disloca-

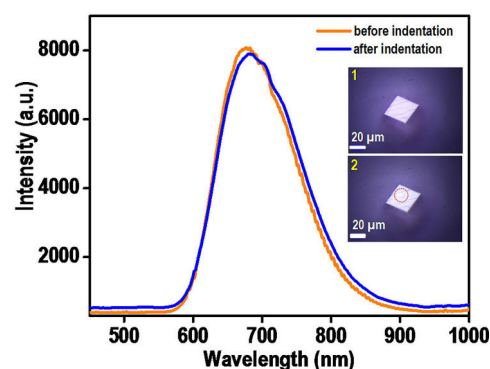


**Figure 3.** a) Piezo image of residual indentation imprint on **I**. b) Cross-sectional profile of the indentation imprint in **I** along with the dotted line (in red), is shown in comparison with that of PMMA (in green).

tions becomes sufficient that they begin to interact and hamper further deformation.<sup>[36]</sup> In general, the pile-up is greatest in materials with large  $E_r/H$  and thereby such systems will not have much work hardening capacity. The capacity for work hardening inhibits the pile-up because the hardening of material during deformation at the proximity of indenter tip constrains the upward flow of material to the surface. The value of  $E_r/H$  obtained for I was 15.71 and that of PMMA was 20.85, respectively. In case of I, the volume of material under the indenter tip could possibly be experiencing significant compaction thus preventing any pile-up. Under applied stress, the benzene rings in the cluster might have oriented by tipping of the planes in the direction of the load. This could result in the interdigitation of ligands in the proximity of the indenter (Figure S8).

In order to confirm that the electronic structure of the cluster remains intact before and after indentation, emission spectra were collected from the indentation spot before and after nanoindentation with a confocal Raman microscope. The emission spectra (Figure 4) remain essentially the same before and after indentation confirming the stability of the clusters. The observed shift in the spectra before and after indentation was found to be 6 nm. However, spectral shifts in nanoclusters due to structural changes are found to be significantly higher, to the extent of hundreds of nm. Therefore, we concluded that the nanoindentation did not affect the overall structures of the nanoclusters. The observed small shift in the spectra might stem from the slight reorientation of the ligands due to compaction caused by nanoindentation. Inset 1 and 2 of Figure 4 are the optical images of the nanocrystals before and after indentation.

Since the  $E_r$ ,  $H$  and creep behavior of the nanocrystals strongly resembled that of a polymer, DMA was performed to understand the frequency sensitivity of different polymeric properties, particularly the loss and storage modulus. The storage modulus (in-phase component) is an indication of the amount of energy restored as the dynamic load is removed, whereas, the loss modulus (out-of-phase component) is a measure of energy dissipated or lost in undergoing permanent changes. The storage modulus is the dynamic counterpart of elastic modulus. The ratio of loss to storage modulus of a material is quantified as  $\tan \delta$ , also known as damping or loss



**Figure 4.** Emission spectra of I before and after indentation collected from the indentation spot (red dotted circle). Insets 1 and 2 are the optical images of I before and after indentation.

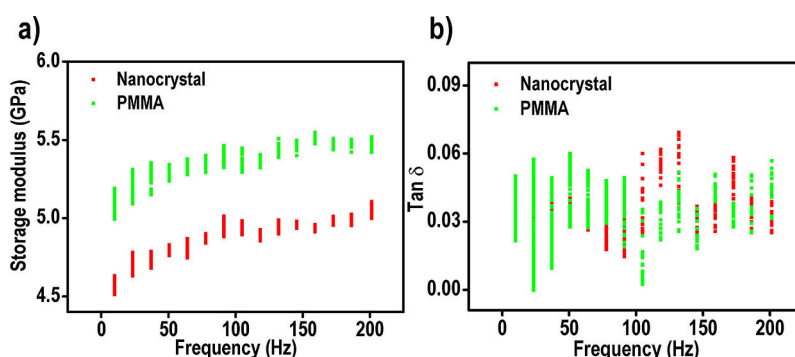
factor. This factor indicates the ability of a material to absorb energy through different internal mechanisms when subjected to dynamic loading. The  $\tan \delta$  values of  $0^\circ$  and  $90^\circ$  represent a purely elastic and viscous material, respectively. Sinusoidal (AC) load of  $10 \mu\text{N}$  was applied over a frequency range of 10 to 200 Hz. Assuming linear viscoelasticity, the frequency dependent dynamic response of the material can be determined using the following Equation 5 and 6, respectively.

$$E'(\text{storage}) = \frac{K_s \sqrt{\pi}}{2\sqrt{A_c}} \quad (5)$$

$$\tan \delta = \frac{\omega C_s}{K_s} \quad (6)$$

where,  $E'$  is the storage modulus and  $\omega$  is the frequency of the applied load and  $K_s$  and  $C_s$  are the sample stiffness and damping coefficients, respectively and  $A_c$  is the projected contact area of the indent on the surface of the specimen.

The variation of storage modulus with frequency for the I is shown in Figure 5a. The dynamic response of PMMA is also depicted in Figure 5a for comparison after necessary corrections. The nanocrystal shows increase in storage modulus at higher frequencies similar to that of a polymer. At higher frequencies, polymer network does not get sufficient time to



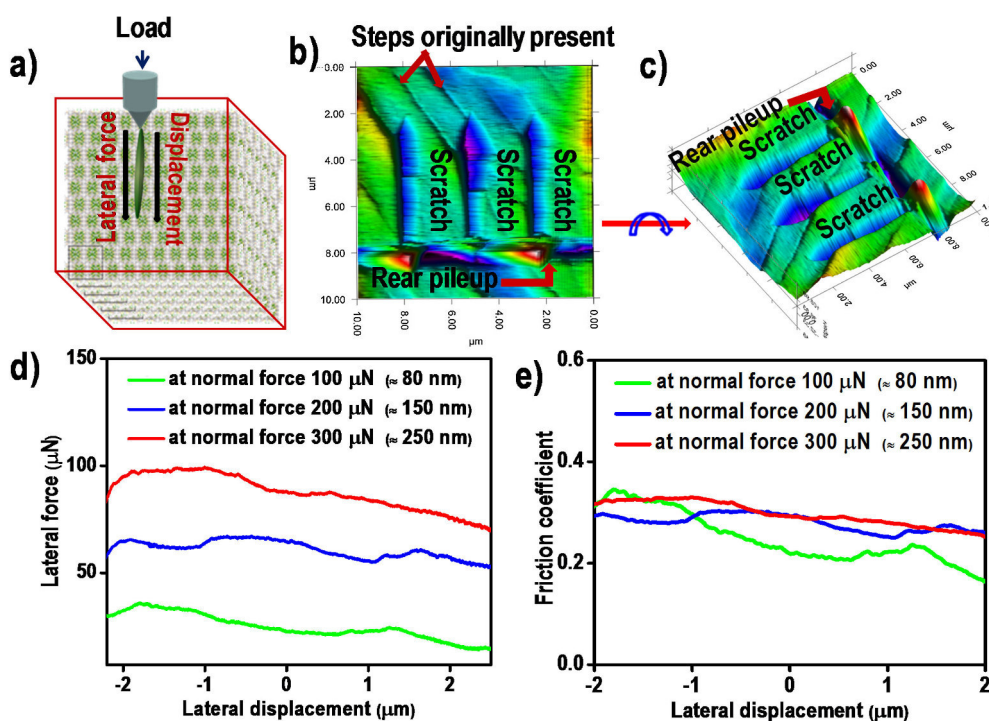
**Figure 5.** a) Variation of storage modulus with frequency for I (red) and PMMA (green). b) Variation of  $\tan \delta$  with frequency for I (red) and PMMA (green).

undergo the necessary relaxation and thus behave more like a stiffened mass, showing higher modulus. The storage modulus value for the nanocrystal ranges from 4.5 GPa to 5.5 GPa in the frequency range of 10 Hz to 200 Hz. Also, the value of storage modulus determined is in the range of the elastic modulus measured in quasi-static indentation test. The loss modulus varies from 0.1 to 0.3 GPa in the same frequency range (Figure S9). The variation of  $\tan \delta$  with frequency is shown in Figure 5b.

Any significant difference in the value of  $\tan \delta$  was not observed with the change in frequency. The magnitude of loss modulus and  $\tan \delta$  obtained for the nanocrystal indicates that it has the ability to absorb some energy under dynamic loading. Interdigitation of ligands and segmental motions of the clusters together could help in the energy dissipation in the nanocrystal. The characteristic  $\tan \delta$  of I is also very similar to that of PMMA (Figure 5b). However, the observed  $\tan \delta$  value is not as high as shock absorbing polymeric foams, where it's in the range of 0.6 to 0.7 at room temperature.<sup>[37]</sup>

Nanoscratch technique was applied to examine the homogeneity across the depth of I. In nanoscratch experiment, the indenter with constant load is glided through the surface of the nanocrystal. The lateral force experienced during scratching was recorded as a function of lateral displacement. Schematic representation of the nanoscratch technique is demonstrated in Figure 6a. Different sets of normal loads, 100  $\mu\text{N}$ , 200  $\mu\text{N}$  and 300  $\mu\text{N}$  were applied separately on three different crystals. Scratch length of 5  $\mu\text{m}$  was made with different penetration depths. The piezo images of the scratch made with 300  $\mu\text{N}$  load and a penetration depth of 250 nm are shown in Figure 6b and

6c. The rumpled structures observed at the end of the scratch is rear pile-up formed by the aggregation of wear debris. The lateral force-displacement plots (Figure 6d) reveal the slight uneven force experienced by the indenter tip which presumably is due to the steps or undulations present on the surface of I. The friction coefficient plots with different scratch depth are shown in Figure 6e. The coefficient of friction along the lateral length is calculated from the nanoscratch experiments. It is defined as the ratio of the lateral load over the normal load. The variations observed in the friction coefficient plots (Figure 6e) might be due to the steps or undulations in I. During nanoscratch, i.e. when the tip slides over the crystal surface, a sudden change in lateral load is expected due to the presence of the steps which may be resulted in the variation of the friction coefficient. Cluster crystals, being grown in solution may incorporate solvent molecules. There is a possibility that these molecules may be lost upon storage. While this may not change the electronic properties such as luminescence of the crystal as well as structural features, the appearance of the crystal may be affected. In view of these, we have measured the mechanical properties of as prepared and aged I which do not show much difference in the  $E_r$  value (Figure S10). The dimensions of the indenter are much below the separation between the surface defects and therefore the indenter probes a defect-free region, as has been noted earlier in case of PbS nanocrystals.<sup>[26c]</sup> Both the fresh and aged crystals have same unit cell parameters as that of cubic I. Also, the variation in the friction coefficient was observed mainly at lower depths but was not much prominent at a depth of 250 nm. This observation confirms that the steps or undulations are present



**Figure 6.** a) Schematic representation of the nanoscratch experiment on I. b) and c) are the 2D and 3D piezo images of I after 300  $\mu\text{N}$  load nanoscratch. d) Variation of lateral force along the scratch length at different loads on I. e) Friction coefficient plots at different scratch depths.



only at the surface of the crystal. No cracks due to experimental load were observed during scratch experiments.

## Conclusions

This work probed the mechanical properties of dithiol protected Ag<sub>29</sub> nanocrystals experimentally. Not only the observed Young's modulus and hardness values, 4.48 and 0.285 GPa, respectively, were similar to that of polymers, but the material also exhibited dynamic mechanical responses similar to polymeric materials. These experiments imply that the capping ligands play a significant role in the mechanical properties of nanocrystals. Moreover, this also indicates that such materials could be processed in very similar ways as polymers for device integration or could be easily incorporated into existing polymer-based devices to add extra functionality without any drastic changes in the mechanical properties of parent polymers. While these mechanical properties can be linked directly to the structure of the cluster and inter-cluster interactions in nanocrystals, unraveling those would require significant computational effort.

## Experimental section

**Chemicals:** All chemicals, including sodium borohydride (NaBH<sub>4</sub>, 99.99% metal basis), triphenylphosphine (TPP), benzene-1,3-dithiol (BDT) were purchased from Sigma-Aldrich. Silver nitrate (AgNO<sub>3</sub>, 99%), was purchased from Rankem. Solvents including methanol, dichloromethane (DCM), dimethylformamide (DMF) were of HPLC grade.

**Synthesis of Ag<sub>29</sub>(BDT)<sub>12</sub>(TPP)<sub>4</sub> nanoclusters:** Synthesis of Ag<sub>29</sub> nanoclusters (NCs) was performed by following a previously reported procedure.<sup>[18]</sup> Briefly, Ag<sub>29</sub>(BDT)<sub>12</sub> NCs were prepared by dissolving 25 mg of silver nitrate in 5 mL of methanol. To this solution, 10 mL of DCM and 15  $\mu$ L of BDT were added. After the addition of BDT, the solution changed to turbid yellow. The yellow colored solution became colorless by the addition of 200 mg of TPP (in 1 mL DCM). After 15 minutes, 10.5 mg of NaBH<sub>4</sub> in 500  $\mu$ L deionized (DI) water was added. The color of the solution changed to dark brown after the addition of NaBH<sub>4</sub>. After three hours of continuous stirring, the dark brown solution turned to orange. The orange solution was centrifuged and the supernatant was discarded. The residue was washed several times with methanol to remove excess thiols and thiolates and it was dispersed in DMF.

**Crystallization of Ag<sub>29</sub>(BDT)<sub>12</sub>(TPP)<sub>4</sub> nanoclusters:** The purified clusters were dispersed in DMF, and filtered using a syringe filter. The concentrated cluster solution was drop-casted on a microscope slide and kept undisturbed at room temperature. After 3–4 days luminescent red crystals were observed.

## Characterization

**UV-vis measurements:** The absorption spectrum of the cluster solution was measured with a Perkin-Elmer Lambda 25 UV-vis absorption spectrophotometer. Spectrum was measured in the range of 190–1100 nm. The cluster was dissolved in the respective solvents and the spectrum was recorded in quartz cuvettes with 10 mm path length.

**Luminescence measurements:** Luminescence measurements of solution were carried out using the HORIBA JOBIN VYON NanoLog instrument. The bandpass for excitation and emission was set at 3 nm. Diluted cluster solution was used for the measurement. Emission spectra of the nanocrystals, especially from the indentation spots were collected on a confocal Raman microscope, Alpha 300 S from WiTec GmbH, using a 633-nm laser and 150 g/mm grating.

**ESI-MS measurement:** Waters Synapt G2-Si High Definition mass spectrometer equipped with electrospray ionization, matrix-assisted laser desorption ionization and ion mobility separation was used. The sample was analyzed in the negative mode of electrospray ionization. The instrument was calibrated using CsI as the calibrant.

**SEM and EDAX measurements:** Scanning electron microscopy (SEM) and energy dispersive X-ray (EDAX) analysis were done using an FEI QUANTA-200 SEM.

**Nanoindentation measurements:** Nanoindentation (NI) experiments were conducted using a Hysitron TI Premier nanomechanical testing instrument. For measuring mechanical properties, a three-sided Berkovich indenter, of radius 150 nm was used. The indentation loads ranged from 50  $\mu$ N to 10,000  $\mu$ N and a trapezoidal load function was used, which includes three segments. In the first segment, the load was increased linearly to its maximum in 20 s, the second segment corresponds to a constant holding of 10 s and in the third segment, the load was linearly decreased to zero in 10 s. In-situ SPM was used to examine the surface topographies prior to and after indentation. The  $E_r$  and  $H$  were calculated by applying the Oliver and Pharr method.<sup>[32]</sup> According to this method,  $E_r$  and  $H$  were determined from the initial part of the unloading segment of the load-displacement curve.

**Nano DMA measurements:** DMA was performed by using load controlled frequency sweep mode of nano-DMA. In this mode, the oscillating dynamic load was superimposed on static load over a frequency range of 10–200 Hz. The applied static load for all the samples was 200  $\mu$ N and the dynamic load was 10  $\mu$ N. The tests were carried out using a Berkovich indenter. A time-dependent nanomechanical property was analyzed by applying a sinusoidal force signal and capturing the displacement response at the same applied frequency by the nanoindentation system. The resulting phase lag from applied and resultant signal will provide information about the storage and loss moduli.

**Nanoscratch measurements:** Nano-scratch measurements were conducted using the Berkovich probe. In this technique, a 5  $\mu$ m long scratch was made with three different loads (100, 200 and 300  $\mu$ N) on three different crystals. The image was taken after each scratch through the in-situ SPM imaging technique to analyze the scratch response of the nanocrystal. The lateral force experienced by the probe was recorded as a function of displacement.

## Supporting Information

Supporting Information is available from the Wiley Online Library or from the author.

## Acknowledgements

We thank the Department of Science and Technology, Government of India for constantly supporting our research program

on nanomaterials. K.S.S. thanks the University Grants Commission (UGC), Govt. of India for a research fellowship. She also thanks, Sowmiya Narayani, Jyoti Sarita Mohanty and Papri Chakraborty for their help and suggestions.

## Conflict of Interest

The authors declare no conflict of interest.

**Keywords:** cluster compounds • mechanical properties • nanoindentation • nanocrystals • single crystals

- [1] a) W. Kurashige, Y. Niihori, S. Sharma, Y. Negishi, *Coord. Chem. Rev.* **2016**, 320, 238–250; b) R. Jin, *Nanoscale* **2015**, 7, 1549–1565; c) I. Chakraborty, T. Pradeep, *Chem. Rev.* **2017**, 117, 8208–8271; d) P. D. Jadzinsky, G. Calero, C. J. Ackerson, D. A. Bushnell, R. D. Kornberg, *Science* **2007**, 318, 430–433; e) H. Yang, Y. Wang, H. Huang, L. Gell, L. Lehtovaara, S. Malola, H. Häkkinen, N. Zheng, *Nat. Commun.* **2013**, 4, 2422.
- [2] A. Ghosh, V. Jeseentharani, M. A. Ganayee, R. G. Hemalatha, K. Chaudhari, C. Vijayan, T. Pradeep, *Anal. Chem.* **2014**, 86, 10996–11001.
- [3] a) Y.-S. Chen, H. Choi, P. V. Kamat, *J. Am. Chem. Soc.* **2013**, 135, 8822–8825; b) V. Jeseentharani, N. Pugazhenthiran, A. Mathew, I. Chakraborty, A. Baksi, J. Ghosh, M. Jash, G. S. Anjusree, T. G. Deepak, A. S. Nair, T. Pradeep, *ChemistrySelect* **2017**, 2, 1454–1463.
- [4] S. Zhao, R. Jin, Y. Song, H. Zhang, S. D. House, J. C. Yang, R. Jin, *Small*, 1701519-n/a.
- [5] G. Soldan, M. A. Aljuhani, M. S. Bootharaju, L. G. AbdulHalim, M. R. Parida, A.-H. Emwas, O. F. Mohammed, O. M. Bakr, *Angew. Chem. Int. Ed.* **2016**, 55, 5749–5753.
- [6] S. Chen, S. Wang, J. Zhong, Y. Song, J. Zhang, H. Sheng, Y. Pei, M. Zhu, *Angew. Chem. Int. Ed.* **2015**, 54, 3145–3149.
- [7] C. Zeng, C. Liu, Y. Chen, N. L. Rosi, R. Jin, *J. Am. Chem. Soc.* **2014**, 136, 11922–11925.
- [8] A. Das, T. Li, K. Nobusada, C. Zeng, N. L. Rosi, R. Jin, *J. Am. Chem. Soc.* **2013**, 135, 18264–18267.
- [9] D. Crasto, G. Barcaro, M. Stener, L. Sementa, A. Fortunelli, A. Dass, *J. Am. Chem. Soc.* **2014**, 136, 14933–14940.
- [10] M. W. Heaven, A. Dass, P. S. White, K. M. Holt, R. W. Murray, *J. Am. Chem. Soc.* **2008**, 130, 3754–3755.
- [11] C. Zeng, T. Li, A. Das, N. L. Rosi, R. Jin, *J. Am. Chem. Soc.* **2013**, 135, 10011–10013.
- [12] D. Crasto, S. Malola, G. Brofsky, A. Dass, H. Häkkinen, *J. Am. Chem. Soc.* **2014**, 136, 5000–5005.
- [13] C. Zeng, H. Qian, T. Li, G. Li, N. L. Rosi, B. Yoon, R. N. Barnett, R. L. Whetten, U. Landman, R. Jin, *Angew. Chem. Int. Ed.* **2012**, 51, 13114–13118.
- [14] H. Qian, W. T. Eckenhoff, Y. Zhu, T. Pintauer, R. Jin, *J. Am. Chem. Soc.* **2010**, 132, 8280–8281.
- [15] A. Dass, S. Theivendran, P. R. Nimmala, C. Kumara, V. R. Jupally, A. Fortunelli, L. Sementa, G. Barcaro, X. Zuo, B. C. Noll, *J. Am. Chem. Soc.* **2015**, 137, 4610–4613.
- [16] H. Yang, J. Lei, B. Wu, Y. Wang, M. Zhou, A. Xia, L. Zheng, N. Zheng, *Chem. Commun.* **2013**, 49, 300–302.
- [17] C. P. Joshi, M. S. Bootharaju, M. J. Alhilaly, O. M. Bakr, *J. Am. Chem. Soc.* **2015**, 137, 11578–11581.
- [18] L. G. AbdulHalim, M. S. Bootharaju, Q. Tang, S. Del Gobbo, R. G. AbdulHalim, M. Eddaoudi, D.-e. Jiang, O. M. Bakr, *J. Am. Chem. Soc.* **2015**, 137, 11970–11975.
- [19] M. J. Alhilaly, M. S. Bootharaju, C. P. Joshi, T. M. Besong, A.-H. Emwas, R. Juarez-Mosqueda, S. Kaappa, S. Malola, K. Adil, A. Shkurenko, H. Häkkinen, M. Eddaoudi, O. M. Bakr, *J. Am. Chem. Soc.* **2016**, 138, 14727–14732.
- [20] a) C. Zeng, Y. Chen, K. Kirschbaum, K. J. Lambright, R. Jin, *Science* **2016**, 354, 1580–1584; b) B. Yoon, W. D. Luedtke, R. N. Barnett, J. Gao, A. Desiredy, B. E. Conn, T. Bigioni, U. Landman, *Nat. Mater.* **2014**, 13, 807–811.
- [21] S. Varughese, M. S. R. N. Kiran, U. Ramamurty, G. R. Desiraju, *Angew. Chem. Int. Ed.* **2013**, 52, 2701–2712.
- [22] C. Sun, D. J. W. Grant, *Pharm. Res.* **2001**, 18, 274–280.
- [23] A. Richter, R. Ries, R. Smith, M. Henkel, B. Wolf, *Diamond Relat. Mater.* **2000**, 9, 170–184.
- [24] a) M. R. VanLandingham, *J. Res. Natl. Inst. Stand. Technol.* **2003**, 108, 249–265; b) J. L. Loubet, J. M. Georges, O. Marchesini, G. Meille, *J. Tribol.* **1984**, 106, 43–48.
- [25] J. C. Tan, J. D. Furman, A. K. Cheetham, *J. Am. Chem. Soc.* **2009**, 131, 14252–14254.
- [26] a) K. Kimura, T. Pradeep, *Phys. Chem. Chem. Phys.* **2011**, 13, 19214–19225; b) K. E. Mueggenburg, X.-M. Lin, R. H. Goldsmith, H. M. Jaeger, *Nat. Mater.* **2007**, 6, 656; c) P. Podsiadlo, G. Krylova, B. Lee, K. Critchley, D. J. Gosztola, D. V. Talapin, P. D. Ashby, E. V. Shevchenko, *J. Am. Chem. Soc.* **2010**, 132, 8953–8960.
- [27] W. Cheng, M. J. Campolongo, J. J. Cha, S. J. Tan, C. C. Umbach, D. A. Muller, D. Luo, *Nat. Mater.* **2009**, 8, 519.
- [28] U. Landman, W. D. Luedtke, *Faraday Discuss.* **2004**, 125, 1–22; discussion 99–116.
- [29] E. Tam, P. Podsiadlo, E. Shevchenko, D. F. Ogletree, M.-P. Delplancke-Ogletree, P. D. Ashby, *Nano Lett.* **2010**, 10, 2363–2367.
- [30] A. Ghosh, D. Ghosh, E. Khatun, P. Chakraborty, T. Pradeep, *Nanoscale* **2017**, 9, 1068–1077.
- [31] a) G. H. Ahmed, M. R. Parida, A. Tosato, L. G. AbdulHalim, A. Usman, Q. A. Alsulami, B. Murali, E. Alarous, O. M. Bakr, O. F. Mohammed, *J. Mater. Chem. C* **2016**, 4, 2894–2900; b) S. M. Aly, L. G. AbdulHalim, T. M. D. Besong, G. Soldan, O. M. Bakr, O. F. Mohammed, *Nanoscale* **2016**, 8, 5412–5416.
- [32] W. C. Oliver, G. M. Pharr, *J. Mater. Res.* **2011**, 7, 1564–1583.
- [33] a) D. Ciprari, K. Jacob, R. Tannenbaum, *Macromolecules* **2006**, 39, 6565–6573; b) K. Komvopoulos, L. Pruitt, C. Klapperich, *J. Tribol.* **2001**, 123, 624–631; c) G. Mallikarjunachari, P. Ghosh, *Polymer* **2016**, 90, 53–66.
- [34] X. W. Gu, X. Ye, D. M. Koshy, S. Vachhani, P. Hosemann, A. P. Alivisatos, *Proc. Natl. Acad. Sci. U.S.A.* **2017**, 114, 2836–2841.
- [35] A. Zandiatashbar, C. R. Picu, N. Koratkar, *Small* **2012**, 8, 1675–1675.
- [36] W. Paul, D. Oliver, P. Grutter, *Phys. Chem. Chem. Phys.* **2014**, 16, 8201–8222.
- [37] L. Ugarte, S. Gómez-Fernández, C. Peña-Rodríguez, A. Prociak, M. A. Corcuera, A. Eceiza, *ACS Sustainable Chem. Eng.* **2015**, 3, 3382–3387.

Manuscript received: December 5, 2017  
Version of record online: March 6, 2018

# Supporting Information

## Probing the mechanical response of luminescent dithiol protected $\text{Ag}_{29}(\text{BDT})_{12}(\text{TPP})_4$ cluster crystals

*Korath Shivan Sugi, Gangapuram Mallikarjunachari, Anirban Som, Pijush Ghosh\* and*

*Thalappil Pradeep\**

K.S. Sugi, Anirban Som, Prof. Thalappil Pradeep

DST Unit of Nanoscience (DST UNS) and Thematic Unit of Excellence (TUE), Department of Chemistry, Indian Institute of Technology Madras, Chennai 600 036, India

E-mail: [pradeep@iitm.ac.in](mailto:pradeep@iitm.ac.in)

G. Mallikarjunachari, Prof. Pijush Ghosh

Department of Applied Mechanics & Soft Matter Center, Indian Institute of Technology Madras, Chennai 600 036, India

E-mail: [pijush@iitm.ac.in](mailto:pijush@iitm.ac.in)

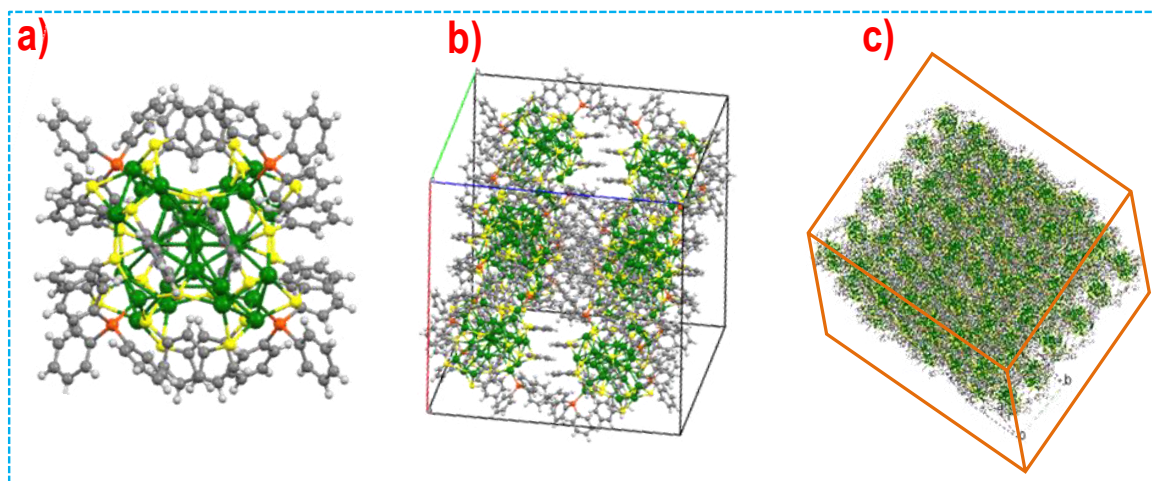
Keywords: atomically precise clusters, nanoindentation, single crystal, mechanical properties

### Table of contents

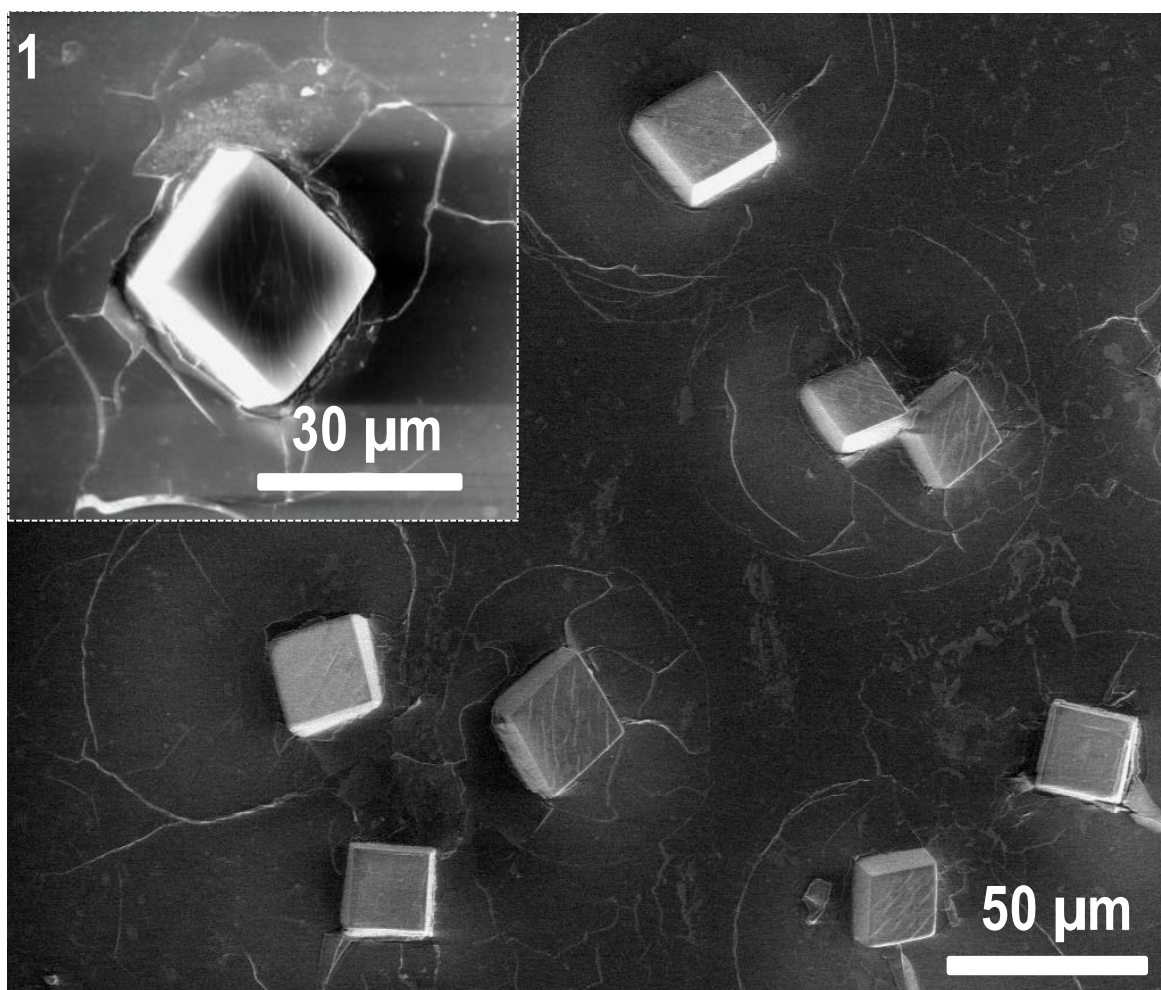
SL.No.	Description	Page No.
S1	Crystal structure of $\text{Ag}_{29}(\text{BDT})_{12}(\text{TPP})_4$ cluster	3
S2	SEM image of <b>I</b>	4
S3	Schematic of load displacement curve	5
S4	Load-displacement curves for multiple indentations by varying the load	6
S5	Variation of modulus and hardness as a function of load	7
S6	Schematic of elastic and plastic work done	8



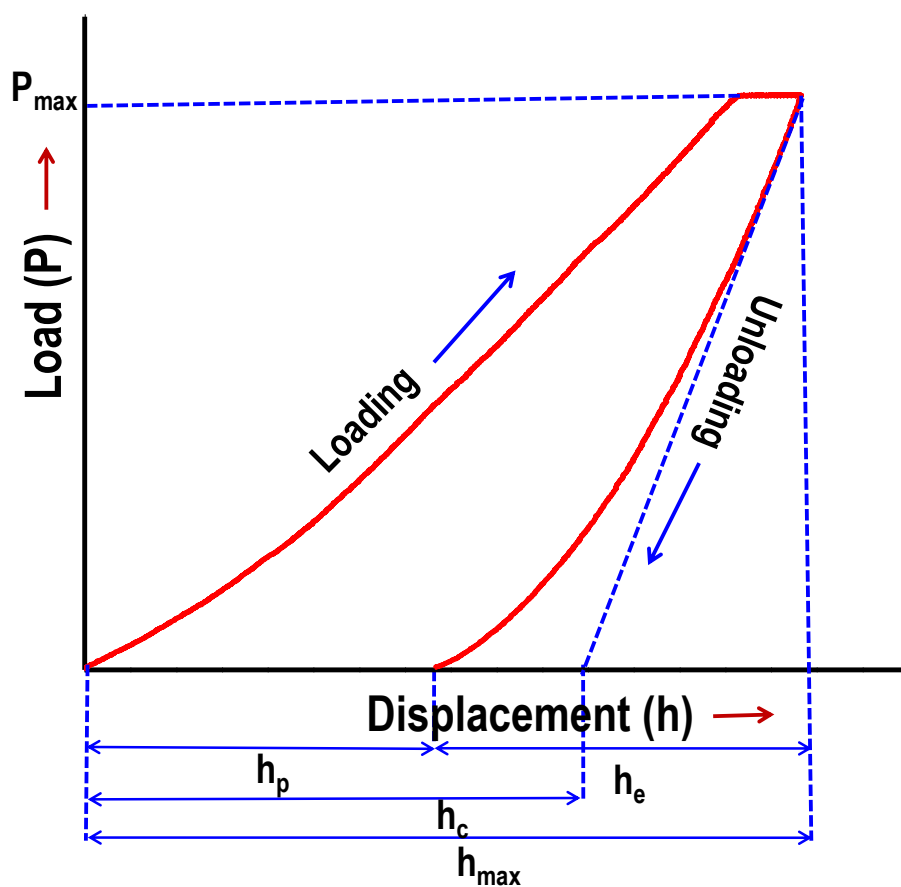
S7	Load-displacement curves with higher load and corresponding piezo and SEM images of indentation impression	8
S8	Packing of Ag <sub>29</sub> nanoclusters in crystal	9
S9	Variation of loss modulus with frequency	9
S10	Load-displacement curves for 200 $\mu$ N load on fresh and aged <b>I</b>	10



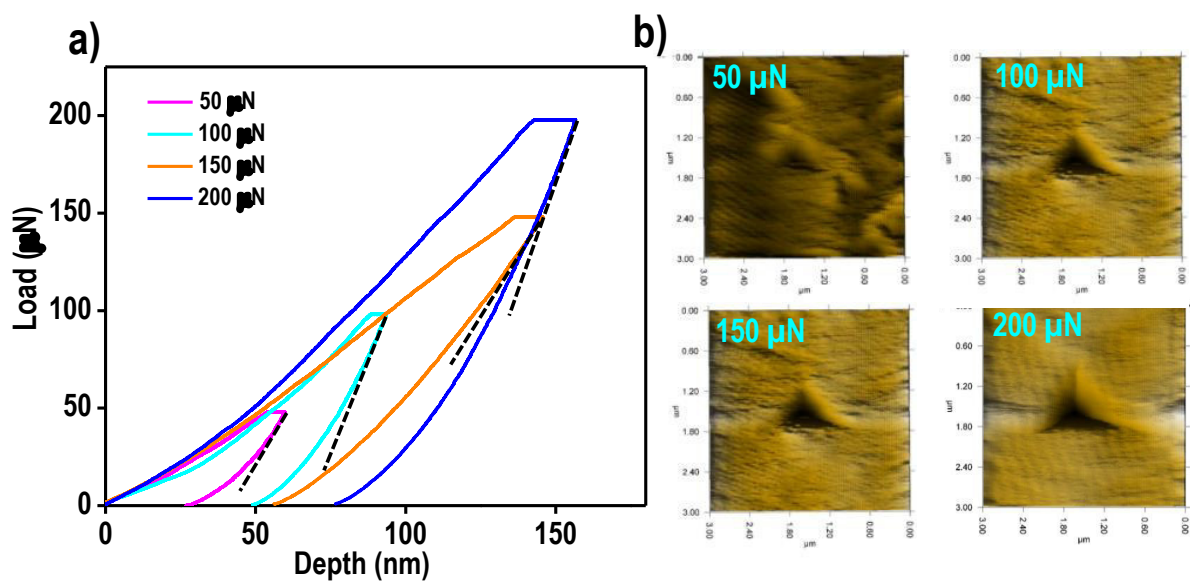
**Figure S1.** a) Crystal structure of  $\text{Ag}_{29}(\text{BDT})_{12}(\text{TPP})_4$  cluster. b) The 3D view of the cubic unit cell of **I**. c) The schematic of 2x2 cubic unit cell of **I**. Color legend: green, silver; yellow, sulphur; orange, phosphorous; grey, carbon; white, hydrogen.



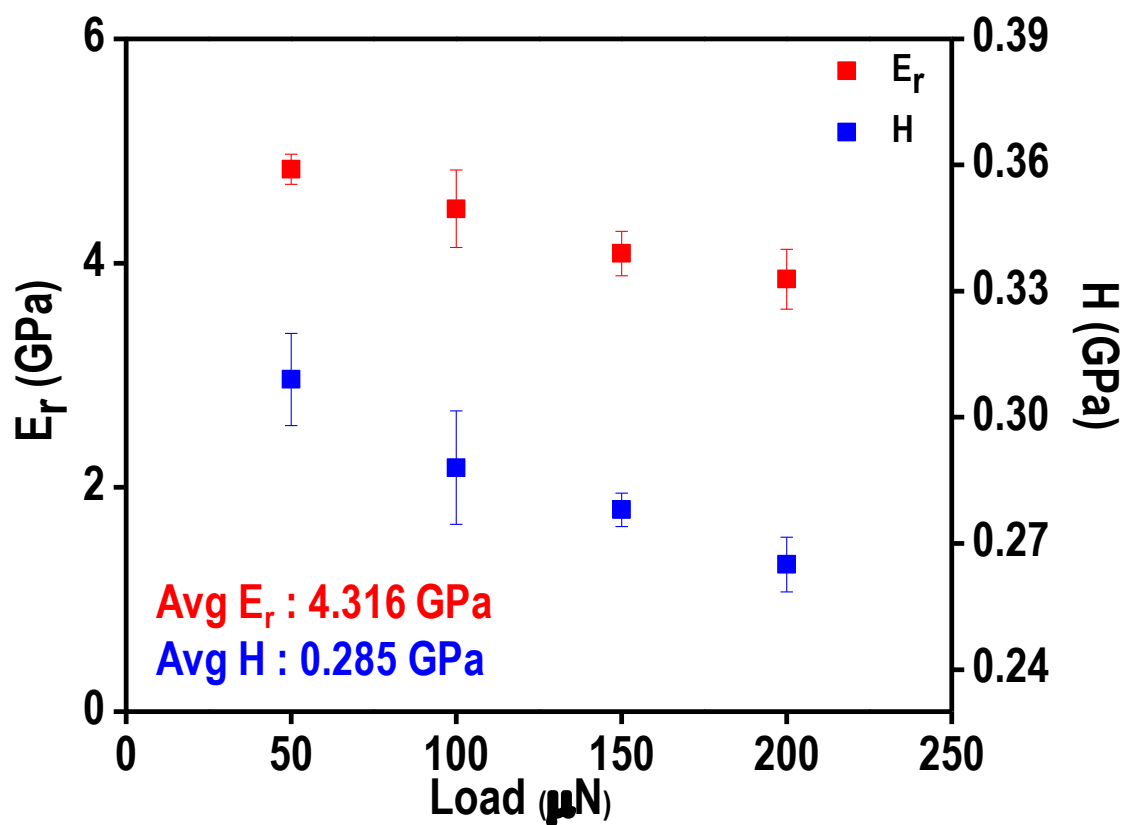
**Figure S2.** SEM image of **I**. Inset 1 shows a single **I**.



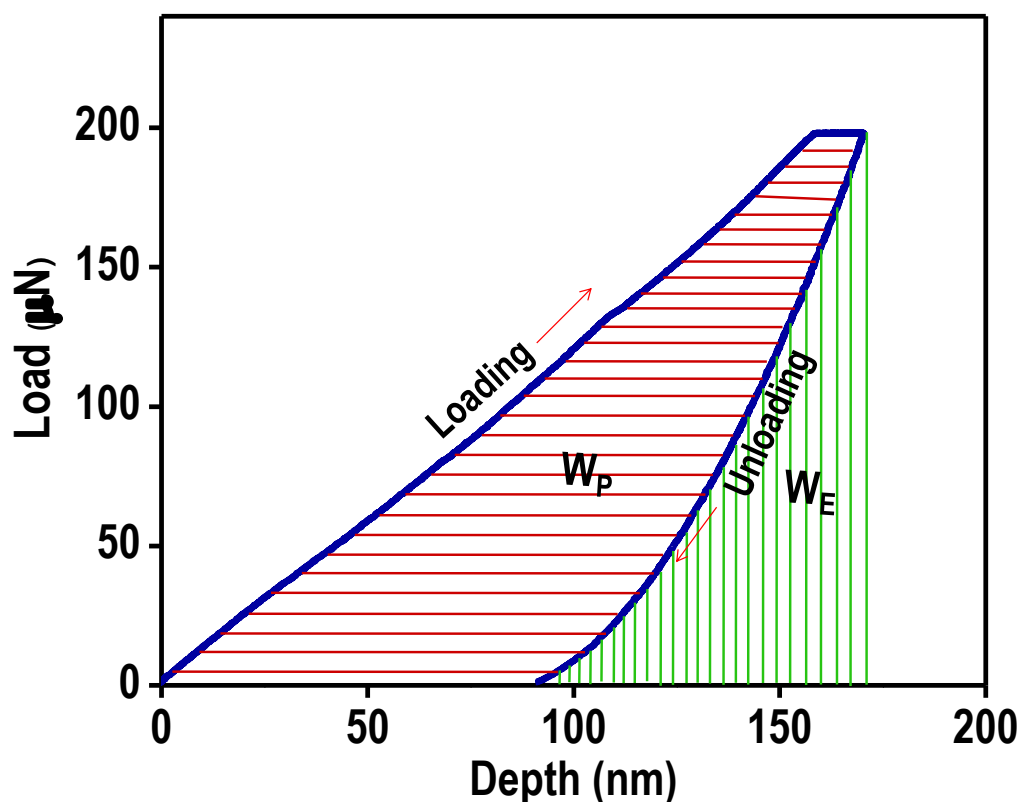
**Figure S3.** A typical load-displacement curve obtained in a nanoindentation experiment.



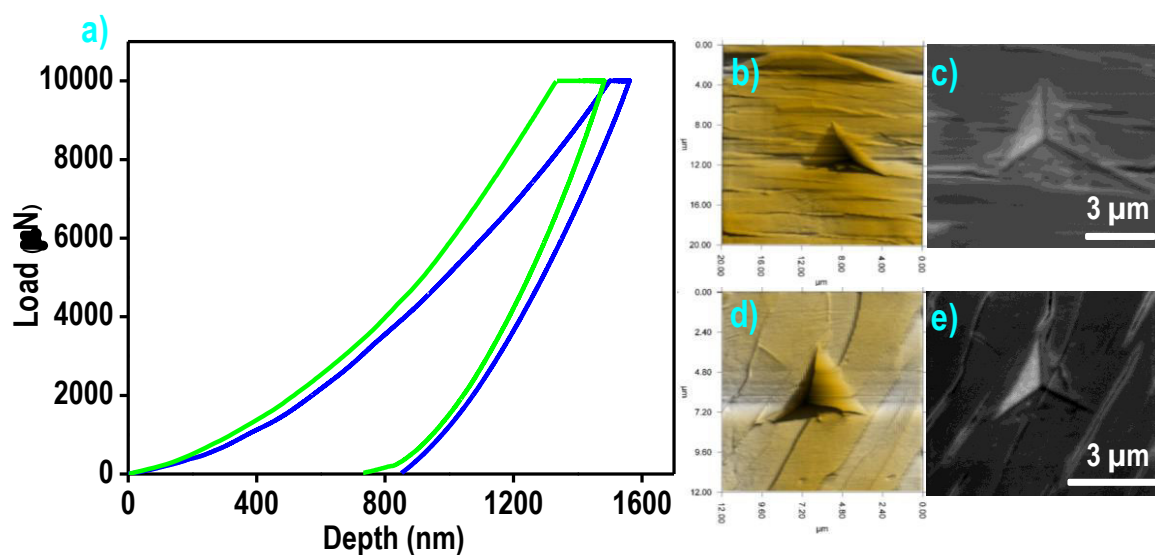
**Figure S4.** a) Load-displacement curves obtained from multiple indentations by varying the magnitude of load. For all loads, elastic recovery is observed. b) Residual indentation impressions on **I** at different loads.



**Figure S5.** Variation of modulus and hardness as a function of load.



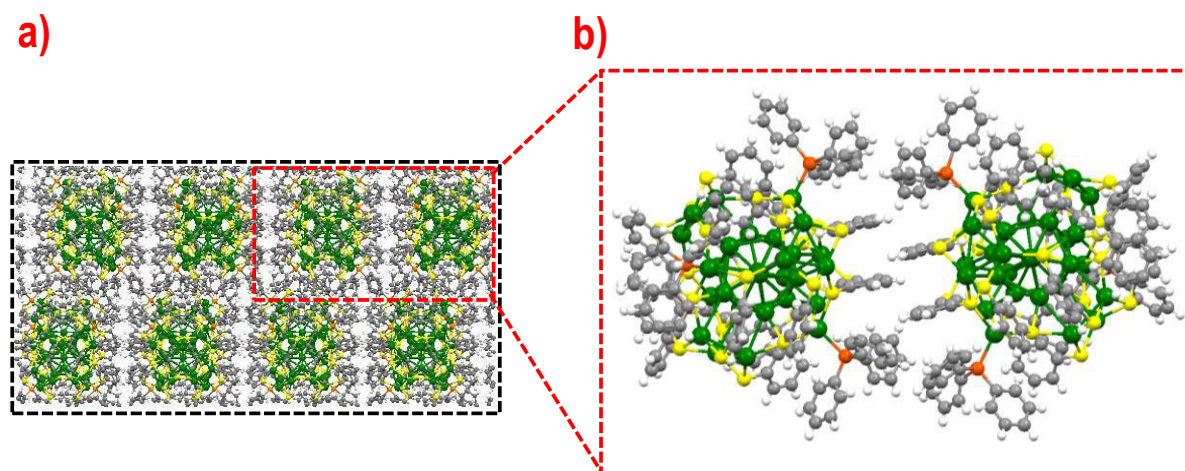
**Figure S6.** a) Load-displacement curve for 200  $\mu\text{N}$  load. The red shaded area represents the plastic work done and the green shaded area represents the elastic work done.



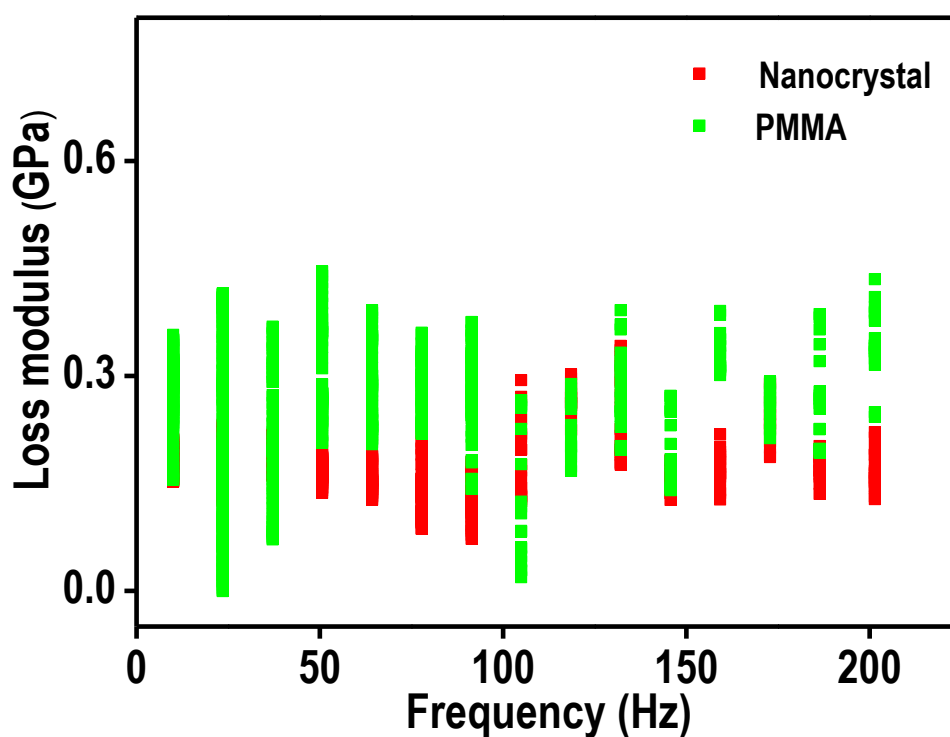
**Figure S7.** a) Load-displacement curves for 10000  $\mu\text{N}$  load with trapezoidal load function (blue color) and 10000  $\mu\text{N}$  load with higher load rate (i.e., 1000  $\mu\text{N/s}$ ) (green color). Image b and c are the piezo and SEM image of residual indentation impression with 10000  $\mu\text{N}$  load.



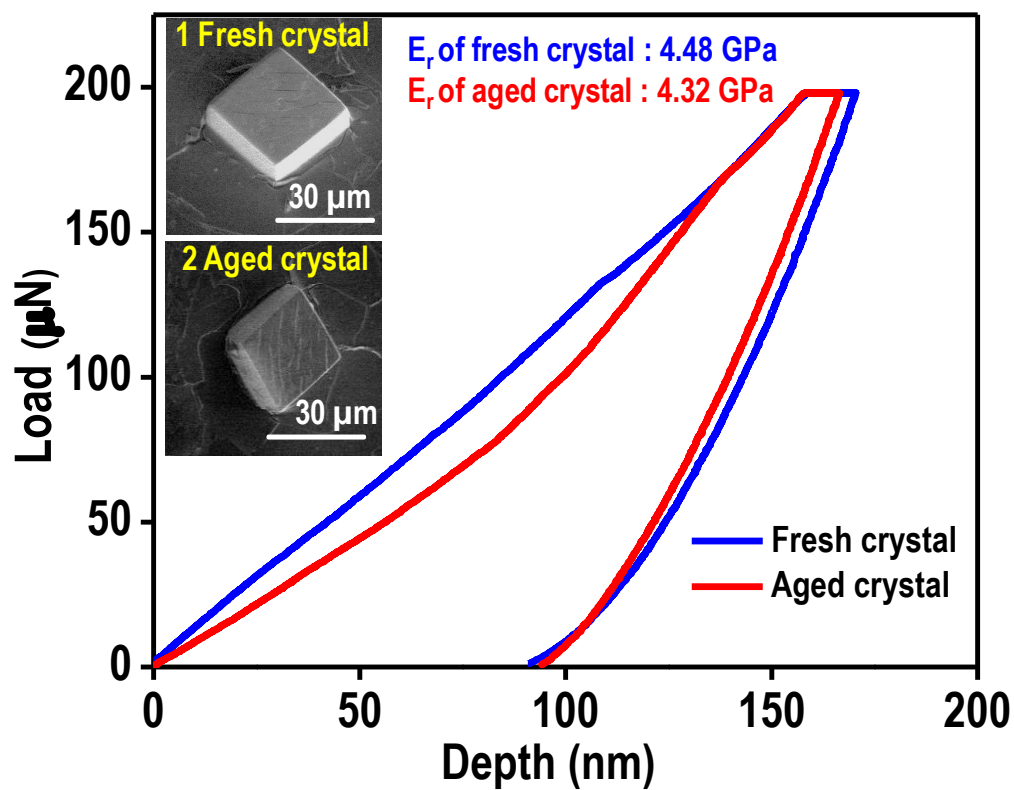
Image d and e are the piezo and SEM image of residual indentation impression with 10000  $\mu\text{N/s}$  load rate.



**Figure S8.** a) Packing of  $\text{Ag}_{29}$  cluster layers in **I**. b) Expanded view of the intercluster region. Color legend: green, silver; yellow, sulphur; orange, phosphorous; grey, carbon; white, hydrogen.



**Figure S9.** Variation of loss modulus with frequency for **I** (red) and PMMA (green).



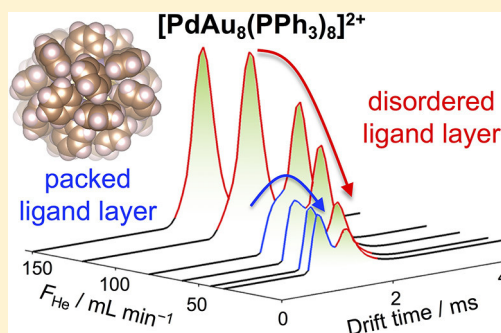
**Figure S10.** Load-displacement curves for 200  $\mu\text{N}$  load on fresh (blue color) and aged (red color) crystal. Inset 1 and 2 shows the SEM images of fresh and aged crystals.

# Publications with Other Groups

Interconversions of Structural Isomers of  $[\text{PdAu}_8(\text{PPh}_3)_8]^{2+}$  and  $[\text{Au}_9(\text{PPh}_3)_8]^{3+}$  Revealed by Ion Mobility Mass SpectrometryKeisuke Hirata,<sup>†</sup> Papri Chakraborty,<sup>‡</sup> Abhijit Nag,<sup>‡</sup> Shinjiro Takano,<sup>†</sup> Kiichirou Koyasu,<sup>†,§</sup> Thalappil Pradeep,<sup>\*,‡,§</sup> and Tatsuya Tsukuda<sup>\*,†,§</sup><sup>†</sup>Department of Chemistry, School of Science, The University of Tokyo, 7-3-1 Hongo, Bunkyo-ku, Tokyo 113-0033, Japan<sup>‡</sup>DST Unit of Nanoscience and Thematic Unit of Excellence, Department of Chemistry, Indian Institute of Technology Madras, Chennai, 600 036, India<sup>§</sup>Elements Strategy Initiative for Catalysts and Batteries (ESICB), Kyoto University, Katsura, Kyoto 615-8520, Japan

## S Supporting Information

**ABSTRACT:** Collision cross sections (CCSs) of ligand-protected metal clusters were evaluated using ion mobility mass spectrometry. The targets used in this study were phosphine-protected clusters  $[\text{PdAu}_8(\text{PPh}_3)_8]^{2+}$  and  $[\text{Au}_9(\text{PPh}_3)_8]^{3+}$ , for which the total structures have been resolved by single-crystal X-ray analysis. The arrival time distributions of  $[\text{PdAu}_8(\text{PPh}_3)_8]^{2+}$  as a function of the He flow rate in a cell located just in front of a traveling wave ion mobility cell filled with  $\text{N}_2$  buffer gas demonstrated that it got converted to another structural isomer having a smaller CCS, with the increase in the nominal collision energy. A similar phenomenon was observed for  $[\text{Au}_9(\text{PPh}_3)_8]^{3+}$ . These results were explained by the collisional excitation and cooling with the buffer gas inducing the conversion of the packing arrangement of the ligands rather than the atomic structure of the metallic core: the ligand layer was converted from disordered to the closely packed arrangement found in a single crystal during this process. This study showed that the ligand layer with a disordered arrangement in solution was retained during desolvation upon electrospray ionization and was annealed into the most stable closely packed arrangement by collisions.



## 1. INTRODUCTION

Ligand-protected metal clusters have extended the scope of materials science owing to their novel properties.<sup>1–9</sup> The key descriptors through which we can tune the properties and functions of protected metal clusters are the number (cluster size) and composition of metal atoms at the core. There are many examples illustrating how the optical, catalytic, and magnetic properties of protected metal clusters are affected by their size and composition.

However, the properties and functions of such clusters are decided not only by size and composition, but also by the geometric structure. Especially, the atomic packing of the metallic core is an important parameter because protected metal clusters can take a variety of structural isomers<sup>10,11</sup> and the electronic structures are strongly coupled with the core structures. For example, optical spectra of structural isomers  $\text{Au}_{28}(\text{SPh}^t\text{Bu})_{20}$  and  $\text{Au}_{28}(\text{S}-c\text{-C}_6\text{H}_{11})_{20}$  exhibit different profiles reflecting the difference in the core structures.<sup>11</sup> Another example is that the optical absorption spectrum is strongly dependent on temperature<sup>12</sup> due to thermal fluctuation of the metallic core.<sup>13</sup> The structure of the ligand layer is also an important parameter determining the physicochemical properties including chirality,<sup>14,15</sup> nonlinear optical activity,<sup>16</sup> and electron transfer reactions.<sup>17</sup> While the monolayer of alkanethiolates on an Au cluster exhibits a

disordered structure, that in the solid state forms a bundlelike structure.<sup>18</sup> The electron transfer reaction for an alkanethiolate ( $\text{C}_n\text{H}_{2n+1}\text{S}$ )-protected  $\text{Au}_{25}$  cluster is independent of  $n$  in the range 12–18 due to the formation of a bundlelike structure.<sup>18</sup>

Recently, several unique techniques have been used for the structural characterization of protected metal clusters isolated in a vacuum. The methods include ion mobility mass spectrometry (IM MS),<sup>19–21</sup> collision-induced dissociation mass spectrometry (CID MS),<sup>22–24</sup> and photoelectron spectroscopy (PES).<sup>25,26</sup> These methods provide essential information on the stability and structures without any influence from the solvents. For example, Ligare et al. reported IM MS of  $[\text{Au}_8(\text{PPh}_3)_{7-x}(\text{PPh}_2\text{Me})_x]^{2+}$  as a function of  $x$  and found that arrival times decrease abruptly from  $x = 3$  to 4.<sup>27</sup> This behavior was ascribed to the formation of a closely packed arrangement of the phosphine ligands due to dispersion interactions. However, several interesting questions remained unaddressed using IM MS: (1) Does the collision cross section (CCS) value determined by IM MS quantitatively reproduce those for the structures determined by X-ray crystallography? (2) Does the CCS value reflect the structure of the protected

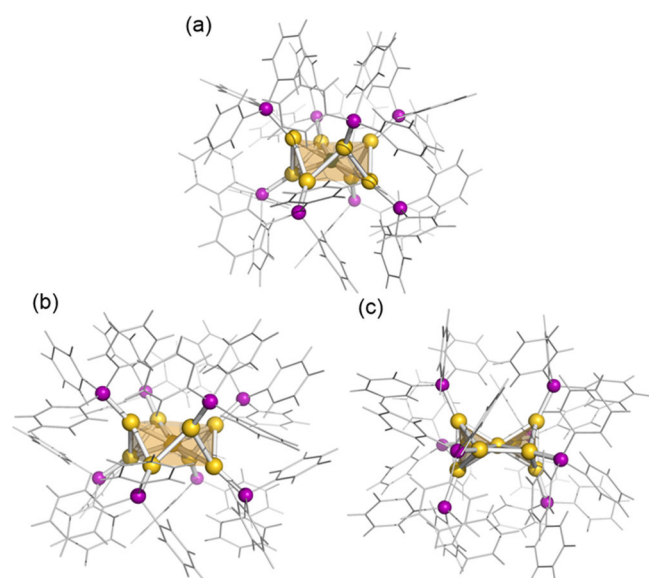
Received: May 18, 2018

Revised: September 13, 2018

Published: September 14, 2018

metal clusters in the solution? (3) Can we probe collision-induced isomerization by IM MS?

To address the above issues, we conducted IM MS measurements on  $[\text{PdAu}_8(\text{PPh}_3)_8]^{2+}$  and  $[\text{Au}_9(\text{PPh}_3)_8]^{3+}$ , the structures of which have been determined by single-crystal X-ray analysis (Figure 1).<sup>28–31</sup>  $[\text{PdAu}_8(\text{PPh}_3)_8]^{2+}$  takes a crown



**Figure 1.** Crystal structures of (a)  $[\text{PdAu}_8(\text{PPh}_3)_8]^{2+}$  with a crown motif and  $[\text{Au}_9(\text{PPh}_3)_8]^{3+}$  with (b) crown and (c) butterfly motifs. Yellow, gray, and purple colors indicate Au, Pd, and P atoms, respectively. Ph group is shown by wireframe.

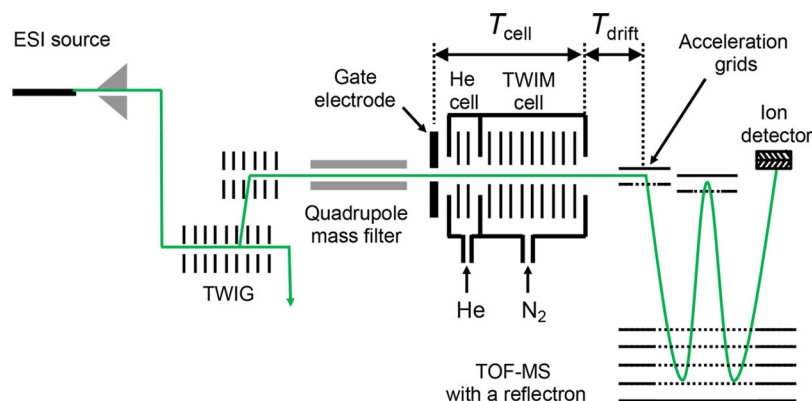
motif (Figure 1a), while  $[\text{Au}_9(\text{PPh}_3)_8]^{3+}$  can take two isomeric forms in the crystal phase, a crown (Cr) or a butterfly (Bt) motif, depending on the size of the counteranions (Figure 1b,c).<sup>32,33</sup> The single-crystal structures shown in parts a, b, and c of Figure 1 are hereafter referred to as  $\text{PdAu}_8(\text{Cr})$ ,  $\text{Au}_9(\text{Cr})$ , and  $\text{Au}_9(\text{Bt})$ , respectively. The absence of a butterfly motif in  $[\text{PdAu}_8(\text{PPh}_3)_8]^{2+}$  was ascribed to suppression of the core isomerization due to stiffening of the intracuster bonds by Pd doping.<sup>33</sup> Their metallic cores  $[\text{Au}_9]^{3+}$  and  $[\text{PdAu}_8]^{2+}$  can be viewed as oblate-shaped superatoms with an electron configuration of  $(1\text{S})^2(1\text{P})^4$ .<sup>31,33</sup> Close inspection of  $\text{PdAu}_8(\text{Cr})$  and  $\text{Au}_9(\text{Cr})$  reveals that the structures of the ligand layers are different although their cores have crown motifs;  $\text{CH}-\pi$  and  $\pi-\pi$  interactions between the phenyl rings

of adjacent  $\text{PPh}_3$  ligands, respectively, play a role in determining the structures of the ligand layers (Figure S1). We determined by IM MS the CCS values of electrosprayed  $[\text{PdAu}_8(\text{PPh}_3)_8]^{2+}$  and  $[\text{Au}_9(\text{PPh}_3)_8]^{3+}$  and compared them with those of the structures determined by X-ray crystallography. The results showed that the disordered ligand layers of  $[\text{PdAu}_8(\text{PPh}_3)_8]^{2+}$  and  $[\text{Au}_9(\text{PPh}_3)_8]^{3+}$  in solution are retained during desolvation by electrospray ionization (ESI), but can be converted to more compact structures found in single crystals via collisional excitation and cooling.

## 2. METHODS

**2.1. Ion Mobility Mass Spectrometry.** The synthesis procedure and characterization of  $[\text{PdAu}_8(\text{PPh}_3)_8](\text{NO}_3)_2$  or  $[\text{Au}_9(\text{PPh}_3)_8](\text{NO}_3)_3$  are described in the Supporting Information. Mass spectra and arrival time distributions (ATDs) were measured using an ion mobility mass spectrometer (Synapt G2-Si, Waters Corp., Manchester, U.K.) installed at Indian Institute of Technology Madras (IIT Madras) (Figure 2).<sup>21,34</sup> The apparatus consists of an ESI source, a traveling wave ion guide (TWIG), a quadrupole mass filter, a trapping TWIG (not shown in Figure 2), a helium cell, a traveling wave ion mobility (TWIM) cell, and a time-of-flight mass spectrometer (TOF MS) equipped with a reflectron.  $[\text{PdAu}_8(\text{PPh}_3)_8](\text{NO}_3)_2$  or  $[\text{Au}_9(\text{PPh}_3)_8](\text{NO}_3)_3$  dispersed in methanol was introduced into the mass spectrometer via the ESI source. After the elimination of neutral species by the TWIG, the ions of interest were mass-selected by the quadrupole mass filter. The mass-selected cationic clusters were stored in the trapping TWIG and injected periodically into the He and TWIM cells<sup>35</sup> by applying a pulsed voltage to the gate electrode. The pressures in the cells were changed by controlling the flow rates of He and  $\text{N}_2$  gases ( $F_{\text{He}}$  and  $F_{\text{N}_2}$ ) in the ranges 0–150 and 45–55  $\text{mL min}^{-1}$ , respectively. The ions in the TWIM cell were propelled by the continuous sequence of traveling waves with a triangular shape, but were unable to keep up with the wave front in the presence of the buffer gas. Compared with ions with a low mobility, ions with a large mobility slip behind the waves less often and so are ejected from the cell earlier than those of a low mobility.<sup>34</sup> The ions thus separated based on the mobility were orthogonally extracted by a pulsed electric field between the acceleration grids and were detected by the TOF MS.

The ATD was obtained by plotting the intensities of  $[\text{PdAu}_8(\text{PPh}_3)_8]^{2+}$  or  $[\text{Au}_9(\text{PPh}_3)_8]^{3+}$  as a function of the time



**Figure 2.** Schematic illustration of the experimental setup.



difference between the ion injection into the He cell and ion extraction into the TOF MS. Thus, the arrival time giving the peak of ATD ( $AT_{\max}$ ) is expressed by

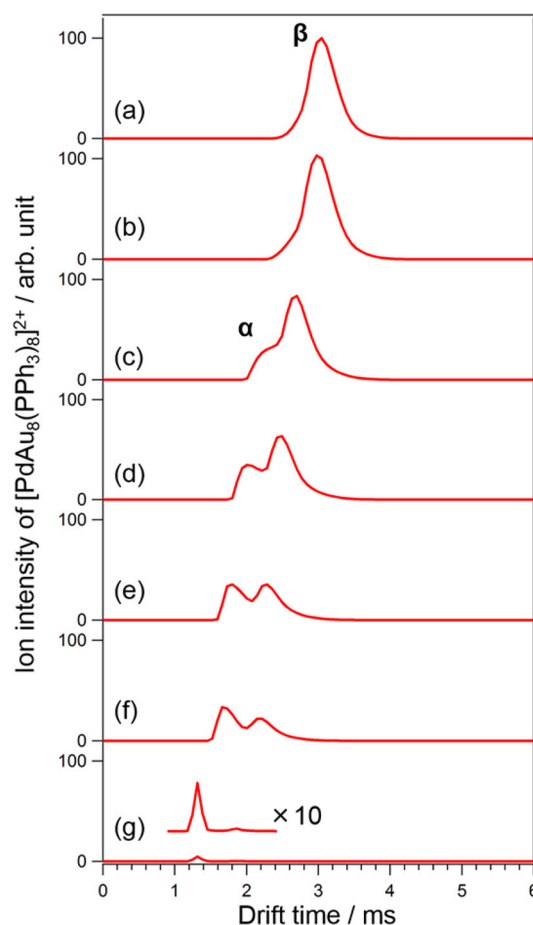
$$AT_{\max} = T_{\text{cell}} + T_{\text{drift}} = \frac{\sqrt{\mu}}{z} A \Omega_{\text{exp}}^B + c \sqrt{\frac{m}{z}} \quad (1)$$

where  $T_{\text{cell}}$  and  $T_{\text{drift}}$  represent the drift time spent in the cell and that spent from the exit of the cell to the acceleration region of the TOF MS.<sup>36</sup> The terms  $m$ ,  $z$ ,  $\mu$ , and  $\Omega_{\text{exp}}$  are the ion mass, the charge, the reduced mass of the clusters and the buffer gas, and the CCS, respectively.<sup>37</sup> The constants  $A$  and  $B$  were calibrated with the experimental data on myoglobin collected at  $F_{\text{He}}$  and  $F_{\text{N}_2}$  values of 43.2 and 55 mL min<sup>-1</sup>, respectively, and at room temperature.<sup>38</sup> The constant  $c$  was obtained from commercially available software. Key experimental parameters are listed in the [Supporting Information](#).

**2.2. Theoretical Calculation of CCS.** The CCS values of PdAu<sub>8</sub>(Cr), Au<sub>9</sub>(Cr), and Au<sub>9</sub>(Bt) were calculated by three methods: diffuse hard-sphere scattering (DHSS),<sup>38</sup> projection approximation (PA), and exact hard-sphere scattering (EHSS).<sup>39,40</sup> The DHSS method assumes that the cluster consists of hard-sphere atoms. According to ref 36, we assumed that 91% of the collisions between the buffer gas (N<sub>2</sub>) and the cluster are inelastic and diffusive and the remaining 9% of the collisions are elastic and specular. The atomic radii of Au, Pd, P, C, and H atoms were set to 1.66, 2.0, 1.8, 1.7, and 1.1 Å, respectively. A N<sub>2</sub> molecule was regarded as a sphere with a radius of 1.5 Å. The clusters were rotated three times in a surrounding environment of 30 000 N<sub>2</sub> molecules during the simulation for DHSS. The re-emission velocity of gas molecules after collision was assumed to have a Maxwell distribution. In the PA method, the CCS value was determined by projecting a three-dimensional ion geometry onto a two-dimensional plane and averaging all the possible geometries assuming a hard-sphere model. The clusters were rotated 100 times in a surrounding environment of 30 000 N<sub>2</sub> molecules during the simulation. In the EHSS method, all the collision events with N<sub>2</sub> gas were assumed to be completely elastic. The temperature and N<sub>2</sub> pressure used in these calculations were 300 K and 290 Pa, respectively. IMoS software<sup>37</sup> was used for calculations.

### 3. RESULTS AND DISCUSSION

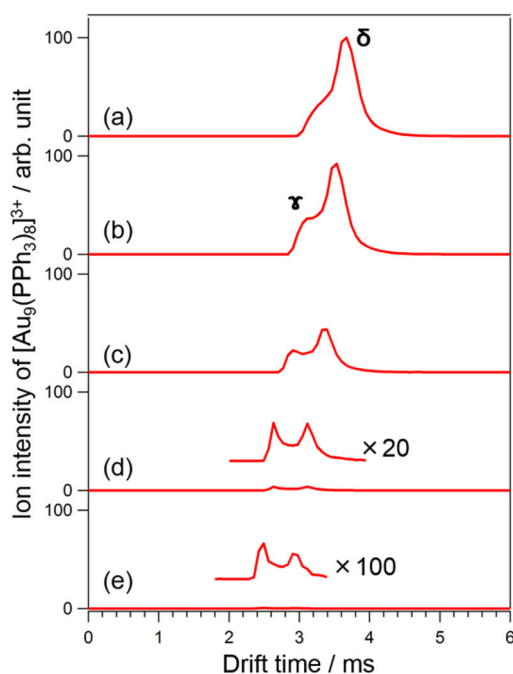
**3.1. Pressure-Dependent ATD.** The ATDs of [PdAu<sub>8</sub>(PPh<sub>3</sub>)<sub>8</sub>]<sup>2+</sup> are shown in Figure 3 as a function of  $F_{\text{He}}$ . The ATDs exhibit a single peak  $\beta$  when  $F_{\text{He}}$  is higher than 120 mL min<sup>-1</sup> (Figure 3a,b). When  $F_{\text{He}}$  is reduced to 80 mL min<sup>-1</sup>, a new peak  $\alpha$  appears as a hump at the shorter arrival time side of peak  $\beta$  (Figure 3c). The relative intensity of peak  $\alpha$  with respect to peak  $\beta$  increases with the decrease in  $F_{\text{He}}$  (Figure 3d–f), and peak  $\alpha$  dominates the ATD when  $F_{\text{He}}$  is reduced to 0 mL min<sup>-1</sup> (Figure 3g). The decrease in  $F_{\text{He}}$  leads to a decrease of collision frequency of the target cluster and to an increase in the mean free path. As a result, the ions in the He cell gain more kinetic energy from the traveling electric field, collide with the N<sub>2</sub> gas with a higher collision energy and exit the cell in shorter time under low pressure. Therefore, the transformation from peak  $\beta$  to peak  $\alpha$  in Figure 3 indicates that an isomer for peak  $\beta$  (PdAu<sub>8</sub>(B)) is “converted” to a more compact isomer for peak  $\alpha$  (PdAu<sub>8</sub>(A)) by collisional heating. The gradual decrease in the total ion intensities is due to the CID of [PdAu<sub>8</sub>(PPh<sub>3</sub>)<sub>8</sub>]<sup>2+</sup>.



**Figure 3.** Arrival time distributions of [PdAu<sub>8</sub>(PPh<sub>3</sub>)<sub>8</sub>]<sup>2+</sup> at  $F_{\text{N}_2}$  = 45 mL min<sup>-1</sup> and  $F_{\text{He}}$  = (a) 150, (b) 120, (c) 80, (d) 60, (e) 43, (f) 35, and (g) 0 mL min<sup>-1</sup>.

A similar behavior was observed in the ATD of [Au<sub>9</sub>(PPh<sub>3</sub>)<sub>8</sub>]<sup>3+</sup> recorded in the range of  $F_{\text{He}}$  = 35–80 mL min<sup>-1</sup> (Figure 4). Figure 4 clearly shows that the relative abundance of Au<sub>9</sub>(C) giving peak  $\gamma$  with respect to Au<sub>9</sub>(D) giving peak  $\delta$  increases with decrease of  $F_{\text{He}}$ . This result indicates that Au<sub>9</sub>(D) is converted into the more compact Au<sub>9</sub>(C) upon collisional excitation and cooling. The more rapid decrease in the intensity of [Au<sub>9</sub>(PPh<sub>3</sub>)<sub>8</sub>]<sup>3+</sup> than [PdAu<sub>8</sub>(PPh<sub>3</sub>)<sub>8</sub>]<sup>2+</sup> at lower  $F_{\text{He}}$  is associated with the fact that the former is more easily dissociated into fragment ions.

**3.2. Experimental and Theoretical CCS Values.** To help the assignment of structural isomers found in section 3.1, we compared the CCS values experimentally determined ( $\Omega_{\text{exp}}$ ) to those calculated for the single-crystal structures in Figure 1 ( $\Omega_{\text{calcn}}$ ). The ATDs of [PdAu<sub>8</sub>(PPh<sub>3</sub>)<sub>8</sub>]<sup>2+</sup> and [Au<sub>9</sub>(PPh<sub>3</sub>)<sub>8</sub>]<sup>3+</sup> were dominated by peaks  $\beta$  and  $\delta$  assigned to PdAu<sub>8</sub>(B) and Au<sub>9</sub>(D), respectively, at  $F_{\text{He}}$  = 43.2 and  $F_{\text{N}_2}$  = 55 mL min<sup>-1</sup> employed for calibration. The  $\Omega_{\text{exp}}$  values for PdAu<sub>8</sub>(B) and Au<sub>9</sub>(D) were determined to be 422 and 442 Å<sup>2</sup> using eq 1 (Table 1). Peak  $\alpha$  for PdAu<sub>8</sub>(A) and peak  $\gamma$  for Au<sub>9</sub>(C) emerged with slight alteration of  $F_{\text{N}_2}$ , wave velocity, and wave height as shown in Figure 5 (parameters are shown in the [Supporting Information](#)). The  $\Omega_{\text{exp}}$  values for PdAu<sub>8</sub>(A) and Au<sub>9</sub>(C) were determined to be 404 and 402 Å<sup>2</sup>, respectively, using that for PdAu<sub>8</sub>(B) as a reference. The

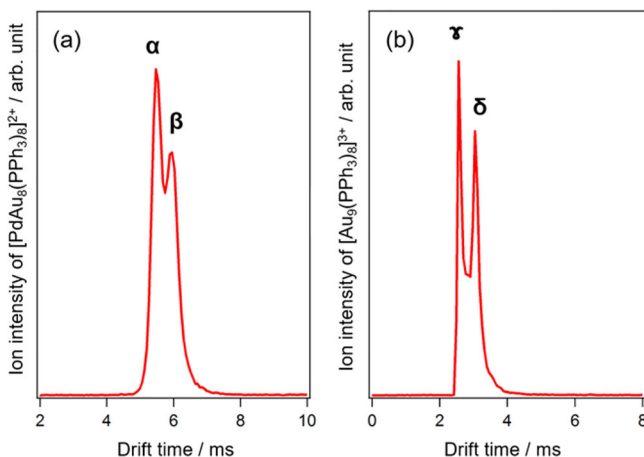


**Figure 4.** Arrival time distributions of  $[\text{Au}_9(\text{PPh}_3)_8]^{3+}$  at  $F_{\text{N}_2} = 55 \text{ mL min}^{-1}$  and  $F_{\text{He}} =$  (a) 80, (b) 70, (c) 60, (d) 45, and (e) 35  $\text{mL min}^{-1}$ .

**Table 1.** Experimental CCS Values

isomer	peak	$\Omega_{\text{exp}}^a (\text{\AA}^2)$
$\text{PdAu}_8(\text{A})$	$\alpha$	404
$\text{PdAu}_8(\text{B})$	$\beta$	422
$\text{Au}_9(\text{C})$	$\gamma$	402
$\text{Au}_9(\text{D})$	$\delta$	442

<sup>a</sup>CCS value experimentally determined.



**Figure 5.** Arrival time distributions of (a)  $[\text{PdAu}_8(\text{PPh}_3)_8]^{2+}$  and (b)  $[\text{Au}_9(\text{PPh}_3)_8]^{3+}$  recorded at  $F_{\text{He}} = 43.2 \text{ mL min}^{-1}$  and  $F_{\text{N}_2} = 47.2 \text{ mL min}^{-1}$ .

$\Omega_{\text{exp}}$  values for all the isomers were reproduced within the statistical error of  $\sim 1\%$ .

The  $\Omega_{\text{calcn}}$  values obtained by the DHSS, PA, and EHSS methods for  $\text{PdAu}_8(\text{Cr})$ ,  $\text{Au}_9(\text{Cr})$ , and  $\text{Au}_9(\text{Bt})$  are listed in Table 2. The  $\Omega_{\text{calcn}}$  values are strongly dependent on the calculation methods. Especially, the DHSS method overestimates the  $\Omega_{\text{exp}}$  values significantly, although it was reported

**Table 2.** Theoretical CCS Values

structure	$\Omega_{\text{calcn}}^a (\text{\AA}^2)$		
	DHSS	PA	EHSS
$\text{PdAu}_8(\text{Cr})$	514	367	420
$\text{Au}_9(\text{Cr})$	509	365	413
$\text{Au}_9(\text{Bt})$	514	366	416

<sup>a</sup>CCS value theoretically calculated.

that DHSS reproduced the  $\Omega_{\text{exp}}$  values determined using diatomic and polarizable molecules such as  $\text{N}_2$  as buffer gas better than other methods such as PA and EHSS.<sup>37</sup> This result suggests that  $\text{N}_2$  molecules collide with the clusters in an elastic manner. In addition, there was no appreciable difference in the  $\Omega_{\text{calcn}}$  values for the two isomers of  $\text{Au}_9(\text{Cr})$  and  $\text{Au}_9(\text{Bt})$ , indicating that IM MS cannot differentiate isomers having different core structures in the present case.

**3.3. Collision-Induced Isomerization.** Significant discrepancies between  $\Omega_{\text{exp}}$  and  $\Omega_{\text{calcn}}$  do not allow us to make a straightforward assignment of the isomers in Table 1. In  $\text{PdAu}_8(\text{Cr})$ , the  $\text{PPh}_3$  layer forms a densely packed structure around the core due to  $\text{CH}-\pi$  interactions between the phenyl rings of adjacent  $\text{PPh}_3$  ligands (Figure S1a). Because no other isomer having a more compact packing than  $\text{PdAu}_8(\text{Cr})$  is available, we assign  $\text{PdAu}_8(\text{A})$  to  $\text{PdAu}_8(\text{Cr})$ . Since no other isomer with a different core structure is known for  $[\text{PdAu}_8(\text{PPh}_3)_8]^{2+}$ , it is reasonable to assign  $\text{PdAu}_8(\text{B})$  to a less stable isomer having poorly packed ligand structures compared to  $\text{PdAu}_8(\text{Cr})$ . This assignment leads us to conclude that the structure of  $[\text{PdAu}_8(\text{PPh}_3)_8]^{2+}$  introduced into vacuum via the ESI source is different from  $\text{PdAu}_8(\text{Cr})$  in terms of the ligand packing. Probably, the structure of the ligand layer of  $\text{PdAu}_8(\text{B})$  introduced in the gas phase via the ESI source is similar to that in the solution, which is determined by the balance between the ligand-to-ligand and ligand-to-solvent interactions. During the desolvation process in the ESI source, the disordered packings of the ligand layer may be frozen at various metastable states. Upon the collisional activation and subsequent collisional cooling, the ligand layer of  $\text{PdAu}_8(\text{B})$  is annealed into the most stable, densely packed structure with the maximal ligand-to-ligand interaction similar to that in the crystal.

Given that the core of  $[\text{Au}_9(\text{PPh}_3)_8]^{3+}$  takes the crown motif in solution, it is reasonable to assign the final species  $\text{Au}_9(\text{C})$  to  $\text{Au}_9(\text{Cr})$  found in the crystalline phase.  $\text{Au}_9(\text{D})$  was assigned to an isomer having poorly packed ligand structures. Thus, the isomerization from  $\text{Au}_9(\text{D})$  to  $\text{Au}_9(\text{C})$  in Figure 4 can be explained by a collision-induced crystallization of the ligand layer. However, we cannot exclude the possibility that core isomerization from the crown to the butterfly also occurred because their  $\Omega_{\text{calcn}}$  values are very close (Table 2). Table 1 shows that the  $\Omega_{\text{calcn}}$  value of  $\text{Au}_9(\text{D})$  ( $442 \text{ \AA}^2$ ) is much larger than that of  $\text{PdAu}_8(\text{B})$  ( $422 \text{ \AA}^2$ ). This may suggest that  $\text{Au}_9(\text{D})$  takes a more expanded core than  $\text{Au}_9(\text{Cr})$  reflecting the softer Au–Au bonds than Pd–Au bonds in  $\text{PdAu}_8(\text{Cr})$ .<sup>33</sup>

## 4. CONCLUSIONS

The CCS values of  $[\text{PdAu}_8(\text{PPh}_3)_8]^{2+}$  and  $[\text{Au}_9(\text{PPh}_3)_8]^{3+}$ , electrosprayed into the gas phase, were determined by IM MS, and they were found to be 422 and  $442 \text{ \AA}^2$ , respectively. With the reduction of the flow rates of He into the cell,  $[\text{PdAu}_8(\text{PPh}_3)_8]^{2+}$  and  $[\text{Au}_9(\text{PPh}_3)_8]^{3+}$  underwent collision-



induced isomerization to smaller species with the CCS values of 404 and 402 Å<sup>2</sup>, respectively. However, the CCS values theoretically calculated for their single-crystal structures were in the range 360–520 Å<sup>2</sup> depending on the calculation methods. We interpret the experimental observations to conversion of the clusters with disordered ligand layers in the solution into their single-crystal structures with packed ligand layers. The present study illustrates that IM MS will be useful for structural characterization in ligand-protected metal clusters in solutions and for understanding their isomers in the gas phase.

## ■ ASSOCIATED CONTENT

### Supporting Information

The Supporting Information is available free of charge on the ACS Publications website at DOI: 10.1021/acs.jpcc.8b04722.

Synthesis procedure and geometric structures determined by single-crystal X-ray diffraction of [PdAu<sub>8</sub>(PPh<sub>3</sub>)<sub>8</sub>]<sup>2+</sup> and [Au<sub>9</sub>(PPh<sub>3</sub>)<sub>8</sub>]<sup>3+</sup> as well as experimental parameters for determining the CCS values and obtaining Figures 3–5 (PDF)

## ■ AUTHOR INFORMATION

### Corresponding Authors

\*E-mail: tsukuda@chem.s.u-tokyo.ac.jp.

\*E-mail: pradeep@iitm.ac.in.

### ORCID

Shinjiro Takano: 0000-0001-9262-5283

Kiichirou Koyasu: 0000-0002-9106-0054

Thalappil Pradeep: 0000-0003-3174-534X

Tatsuya Tsukuda: 0000-0002-0190-6379

### Notes

The authors declare no competing financial interest.

## ■ ACKNOWLEDGMENTS

K.H. thanks the Materials Education Program for the Future Leaders in Research, Industry, and Technology (MERIT) for the financial support of the research in India. This study was financially supported by the Elements Strategy Initiative for Catalysts & Batteries (ESICB) and by a Grant-in-Aid for Scientific Research (JP17H01182) from the Ministry of Education, Culture, Sports, Science and Technology (MEXT) of Japan. T.P. thanks the Department of Science and Technology, Government of India, for continuously supporting his research program on nanomaterials. P.C. thanks the Council of Scientific and Industrial Research (CSIR) for a research fellowship. A.N. thanks IIT Madras for a doctoral fellowship.

## ■ REFERENCES

- (1) Häkkinen, H. Atomic and Electronic Structure of Gold Clusters: Understanding Flake, Cages and Superatoms from Simple Concepts. *Chem. Soc. Rev.* **2008**, *37*, 1847–1859.
- (2) Jin, R. Quantum Sized, Thiolate-protected Gold Nanoclusters. *Nanoscale* **2010**, *2*, 343–362.
- (3) Maity, P.; Xie, S.; Yamauchi, M.; Tsukuda, T. Stabilized Gold Clusters: From Isolation Toward Controlled Synthesis. *Nanoscale* **2012**, *4*, 4027–4038.
- (4) Konishi, K. Phosphine-Coordinated Pure-Gold Clusters: Diverse Geometrical Structures and Unique Optical Properties/Responses. *Struct. Bonding (Berlin, Ger.)* **2014**, *161*, 49–86.
- (5) Tsukuda, T.; Häkkinen, H. *Protected Metal Clusters: From Fundamentals to Applications*, 1st ed.; Elsevier, B.V.: Amsterdam, The Netherlands, 2015.
- (6) Fernando, A.; Weerawardene, K. L. D.; Karimova, N.; Aikens, C. M. Quantum Mechanical Studies of Large Metal, Metal Oxide, and Metal Chalcogenide Nanoparticles and Clusters. *Chem. Rev.* **2015**, *115*, 6112–6216.
- (7) Jin, R.; Zeng, C.; Zhou, M.; Chen, X. Atomically Precise Colloidal Metal Nanoclusters and Nanoparticles: Fundamentals and Opportunities. *Chem. Rev.* **2016**, *116*, 10346–10413.
- (8) Kurashige, W.; Niihori, Y.; Sharma, S.; Negishi, Y. Precise Synthesis, Functionalization and Application of Thiolate-Protected Gold Clusters. *Coord. Chem. Rev.* **2016**, *320–321*, 238–250.
- (9) Chakraborty, I.; Pradeep, T. Atomically Precise Clusters of Noble Metals: Emerging Link between Atoms and Nanoparticles. *Chem. Rev.* **2017**, *117*, 8208–8271.
- (10) Jensen, K. M. Ø.; Juhas, P.; Tofanelli, M. A.; Heinecke, C. L.; Vaughan, G.; Ackerson, C. J.; Billinge, S. J. L. Polymorphism in Magic-Sized Au<sub>144</sub>(SR)<sub>60</sub> Clusters. *Nat. Commun.* **2016**, *7*, 11859.
- (11) Chen, Y.; Liu, C.; Tang, Q.; Zeng, C.; Higaki, T.; Das, A.; Jiang, D.; Rosi, L. N.; Jin, R. Isomerism in Au<sub>28</sub>(SR)<sub>20</sub> Nanocluster and Stable Structures. *J. Am. Chem. Soc.* **2016**, *138*, 1482–1485.
- (12) Devadas, M. S.; Bairu, S.; Qian, H.; Sinn, E.; Jin, R.; Ramakrishna, G. Temperature-Dependent Optical Absorption Properties of Monolayer-Protected Au<sub>25</sub> and Au<sub>38</sub> Clusters. *J. Phys. Chem. Lett.* **2011**, *2*, 2752–2758.
- (13) Yamazoe, S.; Takano, S.; Kurashige, W.; Yokoyama, T.; Nitta, K.; Negishi, Y.; Tsukuda, T. Hierarchy of bond stiffness within icosahedral-based gold clusters protected by thiolates. *Nat. Commun.* **2016**, *7*, 10414.
- (14) Knoppe, S.; Bürgi, T. Chirality in Thiolate-Protected Gold Clusters. *Acc. Chem. Res.* **2014**, *47*, 1318–1326.
- (15) Takano, S.; Tsukuda, T. Amplification of Optical Activity of Gold Clusters by the Proximity of BINAP. *J. Phys. Chem. Lett.* **2016**, *7*, 4509–4513.
- (16) Knoppe, S.; Verbiest, T. Resonance Enhancement of Nonlinear Optical Scattering in Monolayer-Protected Gold Clusters. *J. Am. Chem. Soc.* **2017**, *139*, 14853–14856.
- (17) Templeton, A. C.; Wuelfing, W. P.; Murray, R. W. Monolayer-Protected Cluster Molecules. *Acc. Chem. Res.* **2000**, *33*, 27–36.
- (18) Antonello, S.; Arrigoni, G.; Dainese, T.; De Nardi, M.; Parisio, G.; Perotti, L.; René, A.; Venzo, A.; Maran, F. Electron Transfer through 3D Monolayers on Au<sub>25</sub> Clusters. *ACS Nano* **2014**, *8*, 2788–2795.
- (19) Angel, L.; Majors, L.; Dharmaratne, A.; Dass, A. Ion Mobility Mass Spectrometry of Au<sub>25</sub>(SCH<sub>2</sub>CH<sub>2</sub>Ph)<sub>18</sub> Nanoclusters. *ACS Nano* **2010**, *4*, 4691–4700.
- (20) Baksi, A.; Harvey, S. R.; Natarajan, G.; Wysocki, V. H.; Pradeep, T. Possible Isomers in Ligand Protected Ag<sub>11</sub> Cluster Ions Identified by Ion Mobility Mass Spectrometry and Fragmented by Surface Induced Dissociation. *Chem. Commun.* **2016**, *52*, 3805–3808.
- (21) Baksi, A.; Chakraborty, P.; Bhat, S.; Natarajan, G.; Pradeep, T. Isomerism in Monolayer Protected Silver Cluster Ions: An Ion Mobility-Mass Spectrometry Approach. *Chem. Commun.* **2016**, *52*, 8397–8400.
- (22) Hamouda, R.; Bertorelle, F.; Rayane, D.; Antoine, R.; Broyer, M.; Dugourd, P. Glutathione Capped Gold Au<sub>N</sub>(SG)<sub>M</sub> Clusters Studied by Isotope-Resolved Mass Spectrometry. *Int. J. Mass Spectrom.* **2013**, *335*, 1–6.
- (23) Black, D. M.; Bhattarai, N.; Whetten, R. L.; Bach, S. B. H. Collision-Induced Dissociation of Monolayer Protected Clusters Au<sub>144</sub> and Au<sub>130</sub> in an Electrospray Time-of-Flight Mass Spectrometer. *J. Phys. Chem. A* **2014**, *118*, 10679–10687.
- (24) Johnson, G. E.; Olivares, A.; Hill, D.; Laskin, J. Cationic Gold Clusters Ligated with Differently Substituted Phosphines: Effect of Substitution on Ligand Reactivity and Binding. *Phys. Chem. Chem. Phys.* **2015**, *17*, 14636–14646.
- (25) Hamouda, R.; Bellina, B.; Bertorelle, F.; Compagnon, I.; Antoine, R.; Broyer, M.; Rayane, D.; Dugourd, P. Electron Emission

of Gas-Phase  $[\text{Au}_{25}(\text{SG})_{18}-6\text{H}]^{7-}$  Gold Cluster and Its Action Spectroscopy. *J. Phys. Chem. Lett.* **2010**, *1*, 3189–3194.

(26) Hirata, K.; Yamashita, K.; Muramatsu, S.; Takano, S.; Ohshimo, K.; Azuma, T.; Nakanishi, R.; Nagata, T.; Yamazoe, S.; Koyasu, K.; et al. Anion photoelectron spectroscopy of free  $[\text{Au}_{25}(\text{SC}_{12}\text{H}_{25})_{18}]^{-}$ . *Nanoscale* **2017**, *9*, 13409–13412.

(27) Ligare, M. R.; Baker, E. S.; Laskin, J.; Johnson, G. E. Ligand Induced Structural Isomerism in Phosphine Coordinated Gold Clusters Revealed by Ion Mobility Mass Spectrometry. *Chem. Commun.* **2017**, *53*, 7389–7392.

(28) Schulz-Dobrick, M.; Jansen, M. Supramolecular Intercluster Compounds Consisting of Gold Clusters and Keggin Anions. *Eur. J. Inorg. Chem.* **2006**, *2006*, 4498–4502.

(29) Wen, F.; Englert, U.; Gutrath, B.; Simon, U. Crystal Structure, Electrochemical and Optical Properties of  $[\text{Au}_9(\text{PPh}_3)_8](\text{NO}_3)_3$ . *Eur. J. Inorg. Chem.* **2008**, *2008*, 106–111.

(30) Ito, L. N.; Johnson, B. J.; Muetting, A. M.; Pignolet, L. H. Heterobimetallic Au–Pd Phosphine Cluster Complexes. X-ray Crystal and Molecular Structure of  $[\text{Au}_8\text{Pd}(\text{PPh}_3)_8](\text{NO}_3)_2$ . *Inorg. Chem.* **1989**, *28*, 2026–2028.

(31) Matsuo, S.; Takano, S.; Yamazoe, S.; Koyasu, K.; Tsukuda, T. Selective and High-Yield Synthesis of Oblate Superatom  $[\text{PdAu}_8(\text{PPh}_3)_8]^{2+}$ . *ChemElectroChem* **2016**, *3*, 1206–1211.

(32) Briant, C. E.; Hall, K. P.; Mingos, D. M. P. Structural Characterisation of Two Crystalline Modifications of  $[\text{Au}_9\{\text{P}(\text{C}_6\text{H}_4\text{OMe-}p)_3\}_8](\text{NO}_3)_3$ : The First Example of Skeletal Isomerism in Metal Cluster Chemistry. *J. Chem. Soc., Chem. Commun.* **1984**, 290–291.

(33) Yamazoe, S.; Matsuo, S.; Muramatsu, S.; Takano, S.; Nitta, K.; Tsukuda, T. Suppressing Isomerization of Phosphine-Protected  $\text{Au}_9$  Cluster by Bond Stiffening Induced by a Single Pd Atom Substitution. *Inorg. Chem.* **2017**, *56*, 8319–8325.

(34) Pringle, S. D.; Giles, K.; Wildgoose, J. L.; Williams, J. P.; Slade, S. E.; Thalassinou, K.; Bateman, R. H.; Bowers, M. T.; Scrivens, J. H. An Investigation of the Mobility Separation of Some Peptide and Protein Ions Using a New Hybrid Quadrupole/Travelling Wave IMS/oa-ToF Instrument. *Int. J. Mass Spectrom.* **2007**, *261*, 1–12.

(35) Giles, K.; Williams, J. P.; Campuzano, I. Enhancements in Travelling Wave Ion Mobility Resolution. *Rapid Commun. Mass Spectrom.* **2011**, *25*, 1559–1566.

(36) Bush, M. F.; Hall, Z.; Giles, K.; Hoyes, J.; Robinson, C. V.; Ruotolo, B. T. Collision Cross Sections of Proteins and Their Complexes: A Calibration Framework and Database for Gas-Phase Structural Biology. *Anal. Chem.* **2010**, *82*, 9557–9565.

(37) Shvartsburg, A. A.; Smith, R. D. Fundamentals of Traveling Wave Ion Mobility Spectrometry. *Anal. Chem.* **2008**, *80*, 9689–9699.

(38) Jurneczko, E.; Kalapothakis, J.; Campuzano, I. D. G.; Morris, M.; Barran, P. E. Effects of Drift Gas on Collision Cross Sections of a Protein Standard in Linear Drift Tube and Traveling Wave Ion Mobility Mass Spectrometry. *Anal. Chem.* **2012**, *84*, 8524–8531.

(39) Larriba, C.; Hogan, C. J. Ion Mobilities in Diatomic Gases: Measurement versus Prediction with Non-Specular Scattering Models. *J. Phys. Chem. A* **2013**, *117*, 3887–3901.

(40) Clemmer, D. E.; Jarrold, M. F. Ion Mobility Measurements and their Applications to Clusters and Biomolecules. *J. Mass Spectrom.* **1997**, *32*, 577–592.

## Supporting Information

---

### Interconversions of Structural Isomers of $[\text{PdAu}_8(\text{PPh}_3)_8]^{2+}$ and $[\text{Au}_9(\text{PPh}_3)_8]^{3+}$ Revealed by Ion Mobility Mass Spectrometry

Keisuke Hirata<sup>†</sup>, Papri Chakraborty<sup>‡</sup>, Abhijit Nag<sup>‡</sup>, Shinjiro Takano<sup>†</sup>, Kiichirou Koyasu<sup>†,§</sup>, Thalappil Pradeep<sup>\*,‡</sup> and Tatsuya Tsukuda<sup>\*,†,§</sup>

<sup>†</sup>Department of Chemistry, School of Science, The University of Tokyo, 7-3-1 Hongo, Bunkyo-ku, Tokyo 113-0033, Japan.

<sup>‡</sup>DST Unit of Nanoscience and Thematic Unit of Excellence, Department of Chemistry, Indian Institute of Technology Madras, Chennai, 600 036, India.

<sup>§</sup>Elements Strategy Initiative for Catalysts and Batteries (ESICB), Kyoto University, Katsura, Kyoto 615-8520, Japan.

\*E-mail: pradeep@iitm.ac.in, tsukuda@chem.s.u-tokyo.ac.jp

---

### Synthesis and characterization

$[\text{Au}_9(\text{PPh}_3)_8](\text{NO}_3)_3$  was synthesized by a method similar to that reported elsewhere.<sup>1</sup> First, ethanolic solution (13 mL) of  $\text{NaBH}_4$  (9.4 mg, 0.25 mmol) was added to that (13 mL) of  $\text{Au}(\text{NO}_3)(\text{PPh}_3)$  (521 mg, 1.0 mmol). The mixture was filtrated after stirring for 15 min at room temperature and the filtrate was evaporated. The residue was poured into tetrahydrofurane (THF) (35 mL) and made to standstill overnight. The precipitate was collected by filtration and washed with THF and hexane. The green solid (95 mg) was obtained by evaporating the residual solvent.

$[\text{PdAu}_8(\text{PPh}_3)_8](\text{NO}_3)_2$  was synthesized by a method similar to that reported elsewhere.<sup>1</sup> Dichloromethane solution (20 mL) of  $\text{Pd}(\text{PPh}_3)_4$  (115 mg, 0.10 mmol) was quickly added to that (20 mL) of  $\text{Au}(\text{NO}_3)(\text{PPh}_3)$  (421 mg, 0.81 mmol). After stirring for 1 min, ethanolic solution (15 mL) of  $\text{NaBH}_4$  (20 mg, 0.53 mmol) was quickly added into the mixture. The mixture was evaporated after stirring for 1 min. The residue was poured into methanol (10 mL). The precipitate was filtrated and mixed with acetone (5 mL). The precipitate was filtrated and poured into methanol (50 mL). Diethylether (70 mL) was slowly added into the solution to precipitate  $[\text{PdAu}_8(\text{PPh}_3)_8](\text{NO}_3)_2$ . The brownish solid (193 mg) was obtained by filtration followed by washing with diethylether and hexane. Both samples were characterized by UV-vis absorption spectroscopy.

Table S1. Apparatus parameters

	Calibration <sup>a)</sup>	Figure 3	Figure 4	Figure 5
Capillary bias (kV)	3.5	3.0	3.5	2.0
Source temp. (°C)	100	100	100	100
Sampling core (V)	40	20	0	0
Source offset (V)	60	20	0	0
Desolvation temp. (°C)	150	150	150	150
Cone gas flow (L hr <sup>-1</sup> )	0	0	0	0
Desolvation gas flow (L hr <sup>-1</sup> )	400	400	400	400
Nebulizer gas (bar)	2.5	2.5	2.5	2.5
Trap gas flow (mL min <sup>-1</sup> )	0	0	0	0
Helium cell flow rate $F_{\text{He}}$ (mL min <sup>-1</sup> )	43.2	0–150	35–80	43.2
TWIM cell flow rate $F_{\text{N}_2}$ (mL min <sup>-1</sup> )	55	45	55	47.3
Sample infusion flow rate (μL min <sup>-1</sup> )	10	10	10	20
Trap DC entrance (V)	0	0	0	0
Trap DC bias (V)	25.6	27.2	25.6	24.1
Trap DC exit (V)	0	3.0	0	0
Transfer voltage (V)	0	0	0	2
IMS wave velocity (m s <sup>-1</sup> )	650	700	650	658
IMS wave height (m s <sup>-1</sup> )	40	40	25	38.2

<sup>a)</sup>Acetonitrile/water mixed solution (1:1, v/v) containing myoglobin and 0.1% of formic acid was electrosprayed.

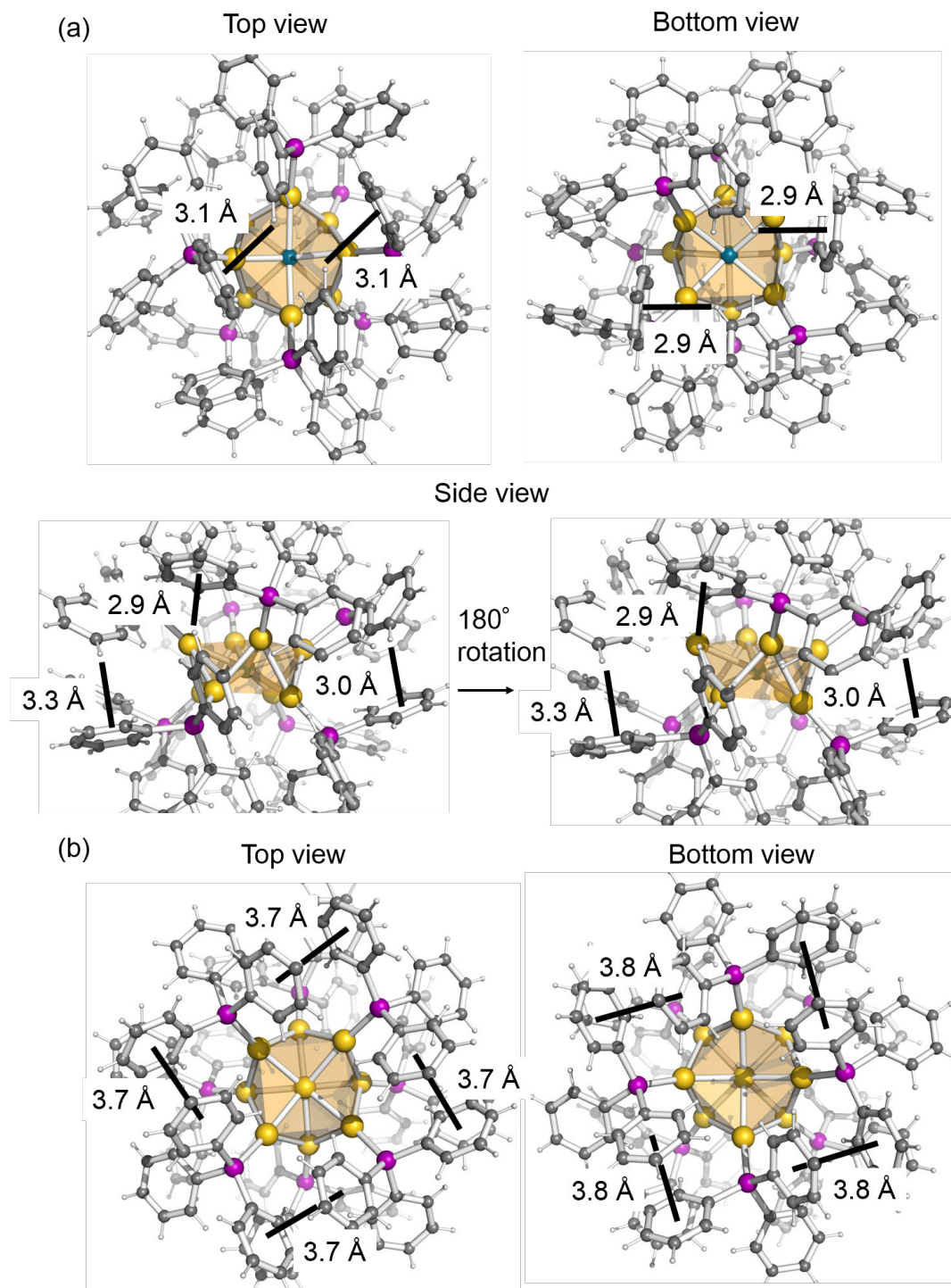


Figure S1. Ligand packing in the crown-shaped crystals of (a)  $[\text{PdAu}_8(\text{PPh}_3)_8](\text{NO}_3)_2$  and (b)  $[\text{Au}_9(\text{PPh}_3)_8](\text{PW}_{12}\text{O}_{40})$ .<sup>2,3</sup>

#### References:

1. Yamazoe, S.; Matsuo, S.; Muramatsu, S.; Takano, S.; Nitta, K.; Tsukuda, T. Suppressing Isomerization of Phosphine-Protected  $\text{Au}_9$  Cluster by Bond Stiffening Induced by Single Pd Atom Substitution *Inorg. Chem.* **2017**, 56, 8319–8325.
2. Matsuo, S.; Takano, S.; Yamazoe, S.; Koyasu, K.; Tsukuda, T. Selective and High-Yield Synthesis of Oblate Superautom  $[\text{PdAu}_8(\text{PPh}_3)_8]^{2+}$  *ChemElectroChem* **2016**, 3, 1206–1211.
3. Jansen, M.; Schulz-Dobrick, M. Supramolecular Intercluster Compounds Consisting of Gold Clusters and Keggin Anions *Eur. J. Inorg. Chem.* **2006**, 2006, 4498–4502.



Cite this: *Nanoscale*, 2018, **10**, 7581

# Self-propagated combustion synthesis of few-layered graphene: an optical properties perspective†

Manonmani Mohandoss,<sup>a</sup> Soujit Sen Gupta,<sup>b</sup> Ramesh Kumar,<sup>b</sup> Md Rabiul Islam,<sup>b</sup> Anirban Som,<sup>b</sup> Azhardin Ganayee Mohd,<sup>b</sup> T. Pradeep<sup>b</sup> and Shihabudheen M. Maliyekkal<sup>\*c</sup>

This paper describes a labour efficient and cost-effective strategy to prepare few-layered of reduced graphene oxide like (RGOL) sheets from graphite. The self-propagated combustion route enables the bulk production of RGOL sheets. Microscopic and spectroscopic analyses confirmed the formation of few-layer graphene sheets of an average thickness of  $\sim 3$  nm and the presence of some oxygen functional groups with a C/O ratio of 8.74. A possible mechanistic pathway for the formation of RGOL sheets is proposed. The optical properties of the RGOL sample were studied in detail by means of Spectroscopic Ellipsometry (SE). The experimental abilities of SE in relating the optical properties with the number of oxygen functionalities present in the samples are explored. The data were analysed by a double-layered optical model along with the Drude–Lorentz oscillatory dispersion relation. The refractive index ( $n = 2.24$ ), extinction coefficient ( $k = 2.03$ ), and dielectric functions are obtained using point-by-point analysis and are also checked for Kramers–Kronig (KK) consistency.

Received 9th December 2017,

Accepted 12th March 2018

DOI: 10.1039/c7nr09156g

rsc.li/nanoscale

## 1. Introduction

Over the last decade, since the invention of graphene by Geim and Novoselov in 2004,<sup>1</sup> graphene and its derivatives have gained unprecedented attention from the scientific and technological community. Its perfect 2D structure and extraordinary electronic, optical, mechanical, and thermal properties make graphene an ideal choice for diverse applications. Flexibility and transparency of the sheet along with high electrical conductivity make graphene an excellent candidate for roll-up and wearable electronic devices.<sup>2</sup> The remarkable optical properties of graphene have paved the way to its use as filler nanocomposites in photovoltaic<sup>3</sup> and optoelectronic devices.<sup>4</sup> Being anisotropic,<sup>5</sup> graphene exhibits optical birefringence, which finds wide applications in optical devices such as LCDs, modulators, colour filters and optical grating.<sup>6</sup> Other promising appli-

cations of graphene include its use in memory devices,<sup>7</sup> sensors,<sup>8</sup> biomedical devices,<sup>9</sup> hydrogen storage,<sup>10</sup> solar cells,<sup>11</sup> super-capacitors,<sup>12</sup> transparent electrodes<sup>13</sup> and environmental clean-up.<sup>14</sup> However, the ability to produce graphene at an affordable cost is the crux to make field level applications a reality.

Several strategies have been developed to produce graphene sheets by mechanical,<sup>1</sup> chemical,<sup>15</sup> and thermal<sup>16</sup> exfoliation methods. The first chemical exfoliation of graphite was performed in 1857 by vaporization of graphite intercalating compounds (GICs) such as bromine<sup>17</sup> and potassium.<sup>18</sup> Since then several attempts were made to produce few-layer graphene sheets in laboratories around the world. The isolation of a single sheet of graphene from a piece of highly oriented pyrolytic graphite (HOPG) using ‘scotch tape’ was achieved in 2004.<sup>1</sup> Though the technique is still practiced in laboratories, the low production yield and intensive labour requirements limit its practical use. Berger *et al.*<sup>19</sup> have demonstrated the epitaxial growth of few-layer graphene on SiC surface. The chemical vapour deposition (CVD) method was first reported by Somani *et al.* (2006)<sup>20</sup> with camphor as the precursor. Efforts have also been made to grow graphene on various metal substrates like Ni,<sup>21</sup> Ru,<sup>22</sup> Ir,<sup>23</sup> Cu,<sup>24</sup> dielectrics, and insulators<sup>25</sup> using methane as the carbon precursor.<sup>26</sup> Though the synthesis of graphene on a large-scale on Cu foil is performed through the CVD process, the cost and ease of production is still a major concern when it is required to be produced on an

<sup>a</sup>School of Electronics Engineering, Vellore Institute of Technology, Chennai Campus, Chennai – 600 127, India

<sup>b</sup>DST Unit on Nanoscience and Thematic Unit of Excellence (TUE), Department of Chemistry, Indian Institute of Technology Madras, Chennai 600 036, India

<sup>c</sup>Department of Civil Engineering, Indian Institute of Technology Tirupati, Tirupati-517506, India. E-mail: shihab@iittp.ac.in, sm.maliyekkal@gmail.com; Fax: +91-877-2500370; Tel: +91-877-2500369

†Electronic supplementary information (ESI) available. See DOI: 10.1039/c7nr09156g

industrial scale. Stankovich *et al.* (2006)<sup>27</sup> demonstrated an efficient solution-based route for the scalable synthesis of graphene by reducing graphene oxide (GO)<sup>28</sup> with hydrazine hydrate.<sup>29</sup> Reduction methods such as thermal,<sup>30</sup> microwave,<sup>31</sup> photo,<sup>32</sup> photocatalytic,<sup>33</sup> and solvothermal<sup>34</sup> are also reported. Aerosol pyrolysis,<sup>35</sup> ionic-liquid assisted electrochemical method,<sup>36</sup> electrolytic exfoliation,<sup>37</sup> unzipping of CNTs,<sup>38</sup> arc discharge method,<sup>39</sup> mechanical delamination,<sup>40</sup> and combustion<sup>41</sup> are other reported methods of synthesizing graphene.<sup>42</sup> Among these, chemical exfoliation of graphite by intercalation followed by the reduction of graphene oxide (GO) to reduced graphene oxide (RGO) is a widely practiced technique for bulk synthesis.<sup>29</sup> Though popular, this wet chemistry method is laborious, time-consuming and requires harsh chemicals for production. Various strategies followed for the synthesis of graphene is summarised in Table S1 of the ESI.†

This paper demonstrates a low-cost strategy to exfoliate graphite through a combustion route. The self-propagated combustion synthesis method proposed here is simple, reliable and quick. This method enables the production of few-layered graphene (RGOL) in bulk quantity compared to the other reported methods. The optical properties of RGOL sheets are explored by Spectroscopic Ellipsometry (SE). The first report on the optical functions of exfoliated single-layer graphene sheet on a silicon and amorphous quartz substrate was authored by Kravets and coworkers.<sup>43</sup> Weber *et al.*<sup>44</sup> have analysed exfoliated graphene fragments on a silicon substrate using B-splines parameterization. The ellipsometry of epitaxially grown graphene on Ni, Cu and SiC substrates,<sup>45</sup> and CVD grown graphene on Si substrates are explored.<sup>46</sup> The optical properties of the chemically and thermally reduced graphene oxides are also studied.<sup>47</sup> However, to the best of our knowledge, no studies have been performed to understand the optical properties of few-layered graphene synthesized through a combustion route. Efforts are also required to understand the effect of oxygen functionalities and defects on the optical properties of graphene.

## 2. Experimental sections

### 2.1. Chemicals

All chemicals were used as received without further purification. All solutions were prepared in de-ionized water (0.056  $\mu\text{S cm}^{-1}$ ). The graphite sample of particle size 2–5  $\mu\text{m}$  was procured from Tamil Nadu Minerals Ltd (TAMIN), India. Potassium persulfate was procured from Rankem Chemicals Pvt. Ltd, India. Glucose was sourced from a local grocery store in Chennai, India.

### 2.2. Synthesis

The RGOL sheet was synthesized from graphite through a self-propagated combustion route using glucose ( $\text{C}_6\text{H}_{12}\text{O}_6$ ) and potassium persulfate ( $\text{K}_2\text{S}_2\text{O}_8$ ) as a fuel and an oxidizer, respectively, in a ratio of 1 : 1 : 1. Graphite was taken as the carbon precursor and was mixed thoroughly with the fuel and the oxidizer using a mortar and pestle. The fuel to oxidizer ratio was fixed by

a trial and error method. The solid homogeneous mixture was compressed to a pellet and it was kept in a ceramic crucible and transferred to a temperature programmed furnace. The furnace temperature was elevated from an ambient condition to 350 °C at a heating rate of  $\sim 3\text{ }^\circ\text{C min}^{-1}$ . The temperature was held at 350 °C for 2 h and then gradually cooled to room temperature at the ambient rate. The obtained sample was washed several times with de-ionized water and stored after drying.

### 2.3. The proposed mechanism of formation of RGOL sheets

In reality, the mechanism of the combustion process is very complex. Several parameters including the fuel to oxidant ratio, the temperature of the reaction, ignition temperature, maximum flame temperature, chemical composition, and mass of the precursor reagent affect the process. A possible mechanism for the formation of RGOL by the proposed self-propagated combustion process is explained below.

When the temperature of the system reaches 60–100 °C, the oxidizer  $\text{K}_2\text{S}_2\text{O}_8$  starts to decompose to release oxygen. At this stage, the oxygen groups are expected to become attached to the edge of the graphite sheet to form partially expanded graphite oxide. When the temperature is at 146 °C and above (melting temperature of glucose is 146 °C), the glucose starts to melt, as the graphite sheets are partially expanded and exfoliated, and the fuel (*i.e.*, the melted glucose molecules) tends to intercalate into the partially oxidised graphite sheets. As the temperature increases to  $\sim 250\text{ }^\circ\text{C}$  (around the ignition temperature of the fuel), the combustion reaction starts, where the glucose reacts with oxygen to form  $\text{CO}_2$  and water as per the reaction (R1). The reaction is highly exothermic with the heat of combustion of  $-2801\text{ kJ mol}^{-1}$ . The pressure exerted due to the release of  $\text{CO}_2$  helps in further exfoliation of graphite oxide. Subsequently, as the temperature reaches 350–400 °C, auto-ignition of the fuel occurs with the release of excess energy and the actual temperature of the system is higher than the set value (called maximum flame temperature). The heat that is liberated is sufficient to trigger graphite oxide for its highly exothermic de-oxygenation reaction. At this temperature, the oxygen groups are mostly reduced and the sheets which are formed are almost similar to reduced graphene oxide (RGO). The combustion of intercalated graphite oxide may be vigorous and propagating. It is also reported that once the exfoliation process is initiated in graphite oxide, the multilayer is ruptured at an accelerating pace. The pressure that is generated by the release of  $\text{H}_2\text{O}$  and  $\text{CO}_2$  during combustion of the fuel is 60 MPa and 100 MPa, which exceeds the van der Waals attraction between two GO sheets (2.5 MPa).<sup>48</sup> This facilitates the exfoliation process.



## 3. Instrumentation

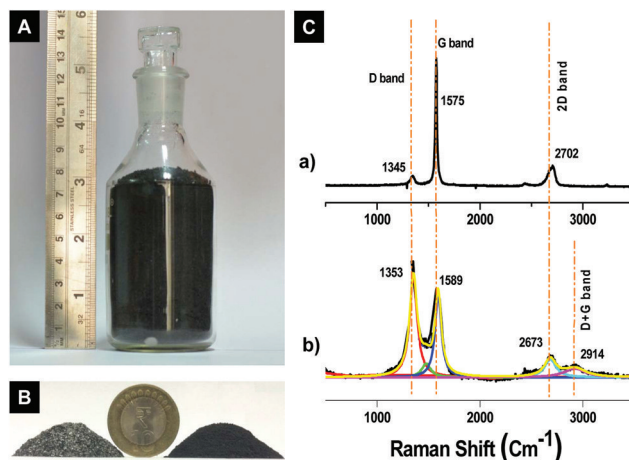
High-resolution transmission electron microscopy (HRTEM) images of the graphene sample were measured with a JEM



3010 (JEOL, Japan) transmission electron microscope. Dilute dispersion of the sample was spotted on amorphous carbon film supported on copper grids and dried under ambient conditions. The X-ray photoelectron spectroscopy (XPS) spectrum of the RGOL sheet sample was recorded using ESCA Probe TPD of Omicron Nanotechnology. Polychromatic Mg K $\alpha$  was used as the X-ray source ( $h\nu = 1253.6$  eV). The binding energy was calibrated with respect to C 1s at 284.5 eV. Fourier transform infrared (FT-IR) spectrum of the sample was collected using a Nicolet 6700 spectrometer. The spectrum was collected in the range of 650–4000  $\text{cm}^{-1}$ . The thermogravimetric analyser (TGA) unit of SEIKO model TG/DTA 6200 (Thermo Gravimetric/Differential Thermal Analysis) was used to measure high-temperature transitions and decomposition peak values. The initial weight of 5.014 mg of the sample was tested at a temperature ranging from 40–800  $^{\circ}\text{C}$  at a heating rate of 10  $^{\circ}\text{C min}^{-1}$  with  $\text{N}_2$  as the carrier gas. A confocal Raman microscope, CRM a300 S (WI Tec GmbH), coupled with an atomic force microscope (AFM) was used for collecting Raman spectra and AFM images. An UVISEL, HORIBA Jobin Yvon ellipsometry system was used to measure the refractive index, thickness and optical constants of the RGOL film. The RGOL film was obtained by vacuum filtration of the sample dispersion, through Whatman cellulose acetate filter paper of pore size 220 nm. Then the filtrate was transferred onto the surface of the glass substrate and dried. The measurements were performed at room temperature with a xenon lamp as the source of radiation. The spectra were obtained with a 0.01 eV resolution in the photon energy range of 0.5 eV to 6 eV using the sensitive photoelastic modulator (PEM) model of an ellipsometer. The instrument is driven by using the powerful and advanced DeltaPsi2 software, designed for accurate and flexible measurement and characterization of thin film structures.

## 4. Results and discussion

Fig. 1A shows RGOL prepared in bulk quantity ( $\sim 10$  g) and the difference in colour between the pristine graphite (left) and RGOL (right) is shown in Fig. 1B. The shiny texture of graphite is lost after the thermal exfoliation. A detailed characterization of RGOL was done by using various microscopic and spectroscopic techniques. The structural evolution of the graphene derivative, the presence of defects, edge and grain boundaries, and the number of layers can be learned from the Raman spectrum.<sup>49</sup> Fig. 1C shows the Raman spectrum of graphite and the RGOL sample. As expected, the Raman spectrum of graphite (Fig. 1Ca) displays a prominent G peak at 1575  $\text{cm}^{-1}$  corresponding to the primary in-plane vibrational mode and a less intense sharp 2D peak at 2707  $\text{cm}^{-1}$  is due to the second order overtone of in-plane vibration. The presence of defects and disorders in the crystal symmetries of the precursor graphite is indicated by the occurrence of a small D peak at 1345  $\text{cm}^{-1}$ . Fig. 1Cb shows the Raman spectrum of the RGOL sample. There is a red-shift in the G band position when compared to bulk graphite flakes



**Fig. 1** (A) Photograph of RGOL sample (10 g), (B) graphite (left) and RGOL sheets (right). (C) Raman spectrum of (a) graphite and (b) RGOL sheets.

and this shift is attributed to the transformation of the bulk graphite crystal to graphene sheets.<sup>50</sup> The RGOL sheet shows a prominent D peak ( $\sim 1353$   $\text{cm}^{-1}$ ) with intensity comparable to those of the G peaks ( $\sim 1589$   $\text{cm}^{-1}$ ). From the ratio of the peak intensities,  $I_D/I_G$  of the Raman spectrum, the levels of the disorders can be characterised.<sup>51</sup> The  $I_D/I_G$  ratio was calculated from the deconvoluted spectra with Lorentzian outlines and the ratios were found to increase from 0.19 for graphite to 1.21 for RGOL sheets. The G band broadens significantly with respect to that of graphite but there is no shift in its peak positions indicating that the thermal treatment has not affected the hexagonal carbon network. Generally, the position and shape of the 2D band define the number of layers stacked as sheets. The 2D band at 2673  $\text{cm}^{-1}$  originating from a two-phonon double resonance is indicative of the graphitic nature. The 2D peak appears to be shorter and broader, which is attributed to the destruction of the band structure by the introduction of defects on graphene sheets.<sup>52</sup> Close to the 2D peak, the sample exhibits a (D + G) peak at 2914  $\text{cm}^{-1}$ , which is induced by the presence of smaller disorders. Among the two types of crystal edges, namely armchair and zig-zag structures, only armchair edges have the capability of elastically scattering charge carriers that give rise to an intense D peak.<sup>53</sup> The very intense D peak of the Raman spectrum of the RGOL sheet suggests that the prepared sample has armchair crystal edges. Table 2 of the ESI† shows the comparison of the measured parameters of RGO synthesized through different approaches.

The UV-Vis absorption spectrum (see Fig. 2A) of the RGOL sheet exhibits a peak at 269 nm, which is attributed to the aromatic C=C bonds of the  $\pi$ -conjugation network similar to RGO prepared by the chemical route.<sup>54</sup> The inset of Fig. 2Aa shows the aqueous dispersion of 0.01 wt% of the RGOL sheet. The FT-IR spectrum in Fig. 2B shows a broad band in the range of 3200–3400  $\text{cm}^{-1}$  and is attributed to –OH stretching vibrations. The peaks centered at  $\sim 2924$   $\text{cm}^{-1}$  and 2854  $\text{cm}^{-1}$  correspond to the stretching vibrations of the asymmetric and

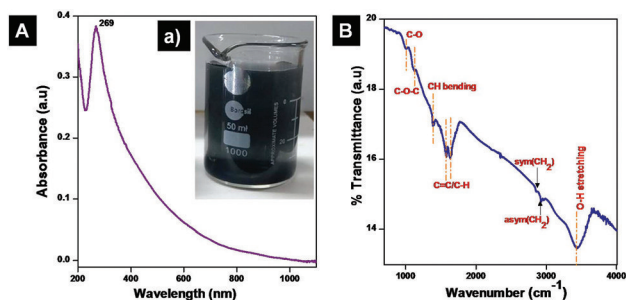


Fig. 2 (A) UV-Vis and (B) FT-IR spectrum of the RGOL sheet. The inset in (A) shows the aqueous dispersion of 0.01 wt% of RGOL sheets.

symmetric bands of the alkyl groups ( $-\text{CH}_2$ ), respectively. The small sharp peak observed at  $1389\text{ cm}^{-1}$  is due to the C-H vibration due to some defects arising from  $\text{sp}^3$  hybridization. The presence of defects was also seen in the Raman spectrum of the RGOL sheet in Fig. 1Cb. The C=C bond at  $\sim 1639\text{ cm}^{-1}$  is attributed to the skeletal vibrations of the un-disturbed graphitic domains. The prominent peak centered at  $1579\text{ cm}^{-1}$  corresponds to the aromatic C=C bonding. The absorption band intensities at C-O (epoxy) and C-O (alkoxy) groups at  $1125\text{ cm}^{-1}$  and  $1089\text{ cm}^{-1}$ , respectively, are weak, indicating that the oxygen groups are concentrated at the edges and not in the basal plane of graphene.<sup>55</sup>

Fig. S1 in the ESI† shows the TG plot of the RGOL sample. The TG curve shows the details of weight loss from room temperature to  $800^\circ\text{C}$ . The sample exhibits an initial weight loss of about 5.5% in the temperature range of  $30$  to  $180^\circ\text{C}$ . This can be attributed to the loss of adsorbed water. The decomposition of the mixture is displayed by a sharp mass loss of about 21.5% from  $330$  to  $430^\circ\text{C}$ . This is attributed to the loss of edge oxygen functionality in the RGOL sheet.

Fig. 3A shows the XPS survey spectrum of the RGOL sample. The spectrum shows the presence of carbon and oxygen as the only elements. The XPS peaks were fitted to Voigt functions having 80% Gaussian and 20% Lorentzian characteristics after performing Shirley background correction. In Fig. 3Ba, the  $\text{sp}^2$  peak of C 1s is centered at  $284.6\text{ eV}$  and has FWHM of  $1.72\text{ eV}$ . A small peak at  $286.4\text{ eV}$  is assigned to the epoxide group (C-O-C). The less intense peak at  $288.3\text{ eV}$  is attributed to the carbonyl (C=O) group that may occur due to the attachment of the oxygen group to the edges of graphite during the combustion process. In Fig. 3Bb, the peaks at  $531.1\text{ eV}$  and  $532.9\text{ eV}$  of the O 1s spectrum corresponding to C=O and C-O groups, respectively, are shown. The C/O ratio of the sample is calculated from the C 1s and O 1s regions of the survey spectrum and is found to be 8.74. The quantitative analysis of the individual components of carbon and oxygen groups obtained from the fitted results of C 1s and O 1s regions of the XPS spectra is tabulated in Table 1.

Fig. 3C shows the AFM topological image on which the height profile is taken, marked with a red line. The height measurements derived from the AFM image show that the

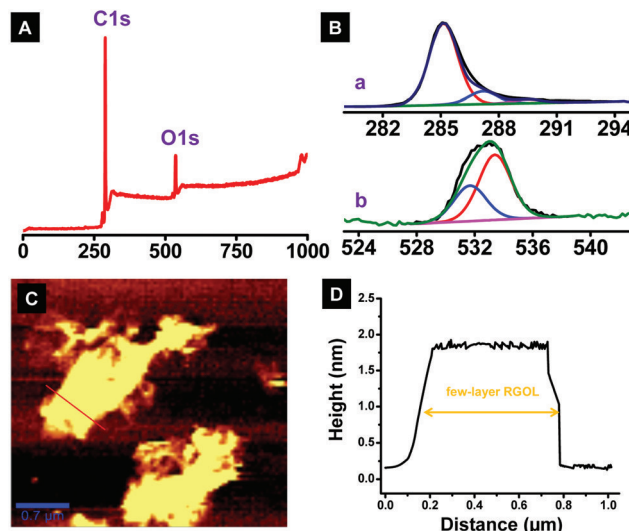


Fig. 3 (A) XPS survey spectrum of the RGOL sheets, (B) deconvoluted XPS spectrum of C 1s (a) and O 1s (b) (C) AFM image of the RGOL sheets along with the height profile and lateral dimension (D).

Table 1 Quantitative analysis of individual components obtained from fitted C 1s and O 1s regions of XPS spectra of the RGOL sheet

	C 1s			O 1s	
B.E (eV)	284.6	286.4	288.3	531.1	532.9
Assignment	Csp <sup>2</sup>	C-OH	C=O	C=O	C-O
RGOL sheets (%)	71.08	14.06	4.58	4.93	5.32

thickness of the sheet is around  $1.7\text{ nm}$  that corresponds to the presence of approximately 5 layers of graphene. The lateral dimension of the sheet was found to be  $\sim 0.7 \times 1.5\text{ }\mu\text{m}$ . Fig. 4 shows the HRTEM images of the RGOL sample. Fig. 4A shows

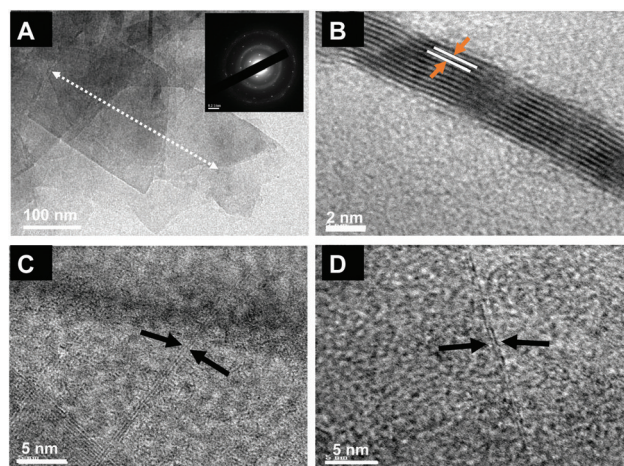


Fig. 4 (A) TEM image showing the lateral dimension of few-layered graphene sheet along with folds and wrinkles of RGO, the inset shows the SAED image of the same. (B) HRTEM image showing the lattice fringes of few-layered graphene. (C) and (D) show the presence of tri- and bi-layers of RGOL sheets.

the low magnification TEM image of the sample. The nanosheets are transparent, wrinkled, and folded at the edge, indicating the presence of few-layered graphene sheets (2–3 layers). The lateral dimension of the graphene sheet was found to be  $\sim 500$  nm, though, in some regions, some sheets are of micron size (shown in Fig. S2†). The inset in Fig. 4A shows the corresponding SAED pattern for the area shown in Fig. 4(A). Well-defined diffraction rings of (1 0 0) and (1 1 0) confirm the crystalline structure of graphene.<sup>56</sup> It is also worth noting that (1 0 0) spots are brighter than (1 1 0) spots indicating the formation of good quality graphene.<sup>57</sup> A bright spot can be seen owing to (0 0 2) planes because of defects in  $sp^2$  carbon. The ordered graphitic lattice fringes (shown by the white line and arrows) are evidently visible in the high-resolution TEM image of the graphene sheet (Fig. 4B). The interlayer spacing between the lattice fringes is found to be 0.34 nm. The HRTEM micrographs in Fig. 4C and D also show the presence of trilayers and bilayers of graphene sheets. The measured thicknesses of double, triple, and a few layers of graphene are 0.7 nm, 1.0 nm and 3.3 nm (Fig. 4B), respectively. This observation is in close agreement with the AFM and ellipsometry data as well. The RGOL layers can be further separated by performing ultra-centrifugation if required, as reported by Coleman *et al.*<sup>58</sup>

## 5. Optical properties

Spectroscopic ellipsometry is used to determine the film thickness, optical constants, surface roughness, porosity, composition, and uniformity on solid surfaces.<sup>56</sup> SE measures the amplitude change ( $\psi$ ) and the difference in the phase shift ( $\Delta$ ) between the incident and reflected light. Fig. 5A shows the measured  $\psi$  and  $\Delta$ , respectively, at the angle of incidence (AOI) of  $65^\circ$ . The optical parameterization technique is followed to obtain the optical constants  $n$  and  $k$  as a function of wavelength. The method involves (i) constructing a model, (ii) assigning the dispersion relation to each layer and (iii) modeling the parameter and optimising it through an iterative procedure until a good fit with the measured data is obtained. Using this model, the refractive index ( $n$ ), extinction coefficient

( $k$ ), and dielectric functions are derived using point-by-point analysis and are also checked for Kramers–Kronig (KK) consistency.<sup>59</sup>

The experimental data of the RGOL sample were studied using a Drude–Lorentz oscillatory dispersion relationship on the three-layered model consisting of the bottom glass substrate, a very thin Cauchy mid sublayer (4 nm) that represents the intercalated air or water between the layers and the top graphene layer. The model parameters were fitted for the lowest  $\chi^2$  value of 0.03.

Fig. 5B shows an intense peak of the refractive index ( $n$ ) and the extinction coefficient ( $k$ ) at 2.24 and 2.03, respectively. The presence of defects in the sample was assessed by analysing the variation of the amplitude of the imaginary part  $\langle \epsilon_2 \rangle$  of the pseudo-dielectric function,  $\langle \epsilon \rangle = \langle \epsilon_1 \rangle + i\langle \epsilon_2 \rangle$ . The variations in amplitude can give an indication of the defects caused by the oxidation of the sample. Losurdo *et al.*<sup>60</sup> have reported that the presence of oxygen functional groups like  $-C=O$  or  $-C-O$  can redshift the  $\langle \epsilon_2 \rangle$  peak from a normal value of 4.8 eV (for pristine graphene).<sup>46</sup> They observed a red-shift of 0.5 eV for every 10% increase in oxygen functionalities. The sample showed a  $\langle \epsilon_2 \rangle$  peak of 4.6 eV (Fig. 6B), with a shift of 0.2 eV from that of pristine graphene. This perhaps indicates the presence of around 4% of oxygen in the form of  $-C=O$  or  $-O-H$ . These data are also in close agreement with the % of oxygen groups calculated from XPS data. Fig. 6A shows the absorption spectra of the RGOL sheet at room temperature. The absorption peak at 4.9 eV arises due to the inter-band transition by the resonant excitons.<sup>61</sup> The apparent shift of about 0.4 meV from that of the absorption peak of graphene at 4.5 eV is due to the absence of electron–hole interactions.<sup>62</sup> These features of the absorption spectra confirm that the synthesized sample consists of few-layered graphene sheets.<sup>63</sup>

The good optical properties of RGOL sheets indicate its possible applications in photonic materials and in the development of optoelectronic devices such as LEDs and solar cells. Table 2 shows a comparative analysis of the optical constants of the RGOL sheet with those shown in the literature and the data are in close agreement with those in the literature.<sup>43,64</sup>

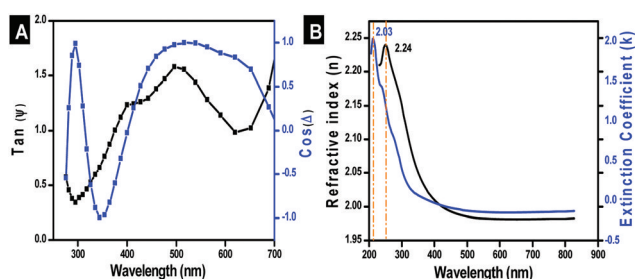


Fig. 5 (A) The experimental ellipsometric parameters of  $\tan(\psi)$  and  $\cos(\Delta)$  of the RGOL sheet. (B) The measured refractive index ( $n$ ) and the extinction coefficient ( $k$ ) of the RGOL sheet.

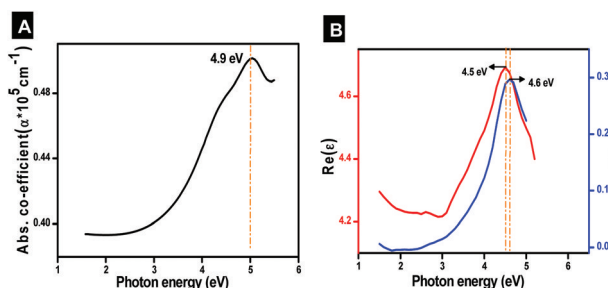


Fig. 6 (A) Spectra showing the measured absorption coefficient of the RGOL sheet. (B) Spectra of the real ( $\epsilon_1$ ) and imaginary ( $\epsilon_2$ ) parts of the complex dielectric function of the sample.



**Table 2** Comparative analysis of optical parameters of graphene samples

Author/Ref.	Thickness	<i>n</i>	<i>k</i>
Present work	0.846 nm	2.24	2.03
Nelson <i>et al.</i> <sup>5</sup>	4 layers	2.3	2.42
Jellison <i>et al.</i> <sup>65</sup>	Single layer	2.56	2.03
Kravets <i>et al.</i> <sup>43</sup>	0.335 nm	2.8	1.45
Matković <i>et al.</i> <sup>64</sup>	Single layer	2.7	1.35
Wurstbauer <i>et al.</i> <sup>66</sup>	Single layer	3.0	1.35
Weber <i>et al.</i> <sup>44</sup>	0.34 nm	3.4	3.42
Ochoa-Martínez <i>et al.</i> <sup>67</sup>	Multilayer	3.9	3.86

## 6. Conclusion

A single-pot combustion synthesis approach for the successful bulk production of a graphenic material from graphite is demonstrated, with a production efficiency of more than 90%. This method enables the production of few-layered graphene in a short period of time at an affordable cost (INR ~430 per kg). We believe that this is a significant step towards the bulk production of few-layered graphene from graphite. The process can be easily scaled up to produce kilograms of graphene in few hours. The data reveal that the as-produced graphene shows excellent optical properties comparable with that of RGO synthesized by the known conventional methods. Achieving the bulk production of dispersible graphene with good optical properties stimulates new research opportunities in developing low-cost filtration membranes, optoelectronics, and photovoltaic devices.

## Conflicts of interest

There are no conflicts of interest to declare.

## Acknowledgements

The authors thank IIT Madras, IIT Tirupati, and VIT Chennai for supporting this research work. XPS, Raman, AFM and HRTEM analyses were performed in the DST Unit of Nanoscience, Department of Chemistry, IIT Madras. The authors also thank Dr Prathiba Nalini from the School of Mechanical and Building Sciences, VIT Chennai, for support in spectroscopic ellipsometry measurements.

## References

- 1 K. S. Novoselov, A. K. Geim, S. V. Morozov, D. Jiang, Y. Zhang, S. V. Dubonos, I. V. Grigorieva and A. A. Firsov, Electric field effect in atomically thin carbon films, *science*, 2004, **306**(5696), 666–669.
- 2 Y. J. Yun, W. G. Hong, W. J. Kim, Y. Jun and B. H. Kim, A novel method for applying reduced graphene oxide directly to electronic textiles from yarns to fabrics, *Adv. Mater.*, 2013, **25**(40), 5701–5705.
- 3 F. Yu and V. K. Kuppala, Enhancement in the performance of organic photovoltaic devices with pristine graphene, *Mater. Lett.*, 2013, **99**, 72–75.
- 4 X. Wan, Y. Huang and Y. Chen, Focusing on energy and optoelectronic applications: a journey for graphene and graphene oxide at large scale, *Acc. Chem. Res.*, 2012, **45**(4), 598–607.
- 5 F. Nelson, V. Kamineni, T. Zhang, E. Comfort, J. Lee and A. Diebold, Optical properties of large-area polycrystalline chemical vapor deposited graphene by spectroscopic ellipsometry, *Appl. Phys. Lett.*, 2010, **97**(25), 253110.
- 6 J. E. Kim, T. H. Han, S. H. Lee, J. Y. Kim, C. W. Ahn, J. M. Yun and S. O. Kim, Graphene oxide liquid crystals, *Angew. Chem., Int. Ed.*, 2011, **50**(13), 3043–3047.
- 7 A. J. Hong, E. B. Song, H. S. Yu, M. J. Allen, J. Kim, J. D. Fowler, J. K. Wassei, Y. Park, Y. Wang, J. Zou, R. B. Kaner, B. H. Weiller and K. L. Wang, Graphene Flash Memory, *ACS Nano*, 2011, **5**(10), 7812–7817.
- 8 R. Arsat, M. Breedon, M. Shafiei, P. G. Spizziri, S. Gilje, R. B. Kaner, K. Kalantar-zadeh and W. Wlodarski, Graphene-like nano-sheets for surface acoustic wave gas sensor applications, *Chem. Phys. Lett.*, 2009, **467**(4–6), 344–347.
- 9 H. Shen, L. Zhang, M. Liu and Z. Zhang, Biomedical Applications of Graphene, *Theranostics*, 2012, **2**(3), 283–294.
- 10 V. Tozzini and V. Pellegrini, Prospects for hydrogen storage in graphene, *Phys. Chem. Chem. Phys.*, 2013, **15**(1), 80–89.
- 11 Z. Yin, J. Zhu, Q. He, X. Cao, C. Tan, H. Chen, Q. Yan and H. Zhang, Graphene-Based Materials for Solar Cell Applications, *Adv. Energy Mater.*, 2014, **4**(1), 1300574.
- 12 Y. B. Tan and J.-M. Lee, Graphene for supercapacitor applications, *J. Mater. Chem. A*, 2013, **1**(47), 14814–14843.
- 13 K. S. Kim, Y. Zhao, H. Jang, S. Y. Lee, J. M. Kim, K. S. Kim, J.-H. Ahn, P. Kim, J.-Y. Choi and B. H. Hong, Large-scale pattern growth of graphene films for stretchable transparent electrodes, *Nature*, 2009, **457**(7230), 706–710.
- 14 K. C. Kemp, H. Seema, M. Saleh, N. H. Le, K. Mahesh, V. Chandra and K. S. Kim, Environmental applications using graphene composites: water remediation and gas adsorption, *Nanoscale*, 2013, **5**(8), 3149–3171.
- 15 S. Eigler, M. Enzelberger-Heim, S. Grimm, P. Hofmann, W. Kroener, A. Geworski, C. Dotzer, M. Röckert, J. Xiao and C. Papp, Wet chemical synthesis of graphene, *Adv. Mater.*, 2013, **25**(26), 3583–3587.
- 16 C. Botas, P. Álvarez, C. Blanco, R. Santamaría, M. Granda, M. D. Gutiérrez, F. Rodríguez-Reinoso and R. Menéndez, Critical temperatures in the synthesis of graphene-like materials by thermal exfoliation–reduction of graphite oxide, *Carbon*, 2013, **52**, 476–485.
- 17 D. D. L. Chung, Exfoliation of graphite, *J. Mater. Sci.*, 1987, **22**(12), 4190–4198.
- 18 H. Shioyama, Cleavage of graphite to graphene, *J. Mater. Sci. Lett.*, 2001, **20**(6), 499–500.

- 19 C. Berger, Z. Song, T. Li, X. Li, A. Y. Ogbazghi, R. Feng, Z. Dai, A. N. Marchenkov, E. H. Conrad and P. N. First, Ultrathin epitaxial graphite: 2D electron gas properties and a route toward graphene-based nanoelectronics, *J. Phys. Chem. B*, 2004, **108**(52), 19912–19916.
- 20 P. R. Somani, S. P. Somani and M. Umeno, Planer nano-graphenes from camphor by CVD, *Chem. Phys. Lett.*, 2006, **430**(1–3), 56–59.
- 21 A. Reina, X. Jia, J. Ho, D. Nezich, H. Son, V. Bulovic, M. S. Dresselhaus and J. Kong, Layer Area, Few-Layer Graphene Films on Arbitrary Substrates by Chemical Vapor Deposition, *Nano Lett.*, 2009, **9**(8), 3087–3087.
- 22 Y. Pan, D.-X. Shi and H.-J. Gao, Formation of graphene on Ru(0001) surface, *Chin. Phys.*, 2007, **16**(11), 3151.
- 23 C. Vo-Van, A. Kimouche, A. Reserbat-Plantey, O. Fruchart, P. Bayle-Guillemaud, N. Bendiab and J. Coraux, Epitaxial graphene prepared by chemical vapor deposition on single crystal thin iridium films on sapphire, *Appl. Phys. Lett.*, 2011, **98**(18), 181903.
- 24 X. Li, W. Cai, J. An, S. Kim, J. Nah, D. Yang, R. Piner, A. Velamakanni, I. Jung and E. Tutuc, Large-area synthesis of high-quality and uniform graphene films on copper foils, *Science*, 2009, **324**(5932), 1312–1314.
- 25 C.-Y. Su, A.-Y. Lu, C.-Y. Wu, Y.-T. Li, K.-K. Liu, W. Zhang, S.-Y. Lin, Z.-Y. Juang, Y.-L. Zhong, F.-R. Chen and L.-J. Li, Direct Formation of Wafer Scale Graphene Thin Layers on Insulating Substrates by Chemical Vapor Deposition, *Nano Lett.*, 2011, **11**(9), 3612–3616.
- 26 I. N. Kholmanov, E. Cavaliere, C. Cepek and L. Gavioli, Catalytic chemical vapor deposition of methane on graphite to produce graphene structures, *Carbon*, 2010, **48**(5), 1619–1625.
- 27 S. Stankovich, R. D. Piner, X. Chen, N. Wu, S. T. Nguyen and R. S. Ruoff, Stable aqueous dispersions of graphitic nanoplatelets via the reduction of exfoliated graphite oxide in the presence of poly (sodium 4-styrenesulfonate), *J. Mater. Chem.*, 2006, **16**(2), 155–158.
- 28 B. C. Brodie, On the Atomic Weight of Graphite, *Philos. Collect. R. Soc. London*, 1859, **149**, 249–259.
- 29 S. Pei and H.-M. Cheng, The reduction of graphene oxide, *Carbon*, 2012, **50**(9), 3210–3228.
- 30 S. H. Huh, Thermal reduction of graphene oxide, in *Physics and Applications of Graphene-Experiments*, InTech, 2011.
- 31 W. Chen, L. Yan and P. R. Bangal, Preparation of graphene by the rapid and mild thermal reduction of graphene oxide induced by microwaves, *Carbon*, 2010, **48**(4), 1146–1152.
- 32 M. Mohandoss, S. S. Gupta, A. Nelleri, T. Pradeep and S. M. Maliyekkal, Solar mediated reduction of graphene oxide, *RSC Adv.*, 2017, **7**(2), 957–963.
- 33 W. Fan, Q. Lai, Q. Zhang and Y. Wang, Nanocomposites of TiO<sub>2</sub> and reduced graphene oxide as efficient photocatalysts for hydrogen evolution, *J. Phys. Chem. C*, 2011, **115**(21), 10694–10701.
- 34 S. Dubin, S. Gilje, K. Wang, V. C. Tung, K. Cha, A. S. Hall, J. Farrar, R. Varshneya, Y. Yang and R. B. Kaner, A one-step, solvothermal reduction method for producing reduced graphene oxide dispersions in organic solvents, *ACS Nano*, 2010, **4**(7), 3845–3852.
- 35 J. Campos-Delgado, J. M. Romo-Herrera, X. Jia, D. A. Cullen, H. Muramatsu, Y. A. Kim, T. Hayashi, Z. Ren, D. J. Smith, Y. Okuno, T. Ohba, H. Kanoh, K. Kaneko, M. Endo, H. Terrones, M. S. Dresselhaus and M. Terrones, Bulk Production of a New Form of sp<sup>2</sup> Carbon: Crystalline Graphene Nanoribbons, *Nano Lett.*, 2008, **8**(9), 2773–2778.
- 36 N. Liu, F. Luo, H. Wu, Y. Liu, C. Zhang and J. Chen, One-Step Ionic-Liquid-Assisted Electrochemical Synthesis of Ionic-Liquid-Functionalized Graphene Sheets Directly from Graphite, *Adv. Funct. Mater.*, 2008, **18**(10), 1518–1525.
- 37 G. Wang, B. Wang, J. Park, Y. Wang, B. Sun and J. Yao, Highly efficient and large-scale synthesis of graphene by electrolytic exfoliation, *Carbon*, 2009, **47**(14), 3242–3246.
- 38 D. V. Kosynkin, A. L. Higginbotham, A. Sinitskii, J. R. Lomeda, A. Dimiev, B. K. Price and J. M. Tour, Longitudinal unzipping of carbon nanotubes to form graphene nanoribbons, *Nature*, 2009, **458**(7240), 872–876.
- 39 K. S. Subrahmanyam, L. S. Panchakarla, A. Govindaraj and C. N. R. Rao, Simple Method of Preparing Graphene Flakes by an Arc-Discharge Method, *J. Phys. Chem. C*, 2009, **113**(11), 4257–4259.
- 40 C. Knieke, A. Berger, M. Voigt, R. N. K. Taylor, J. Röhl and W. Peukert, Scalable production of graphene sheets by mechanical delamination, *Carbon*, 2010, **48**(11), 3196–3204.
- 41 K. V. Manukyan, S. Rouvimov, E. E. Wolf and A. S. Mukasyan, Combustion synthesis of graphene materials, *Carbon*, 2013, **62**, 302–311.
- 42 R. S. Edwards and K. S. Coleman, Graphene synthesis: relationship to applications, *Nanoscale*, 2013, **5**(1), 38–51.
- 43 V. Kravets, A. Grigorenko, R. Nair, P. Blake, S. Anissimova, K. Novoselov and A. Geim, Spectroscopic ellipsometry of graphene and an exciton-shifted van Hove peak in absorption, *Phys. Rev. B: Condens. Matter Mater. Phys.*, 2010, **81**(15), 155413.
- 44 J. Weber, V. Calado and M. Van De Sanden, Optical constants of graphene measured by spectroscopic ellipsometry, *Appl. Phys. Lett.*, 2010, **97**(9), 091904.
- 45 M. Losurdo, M. M. Giangregorio, P. Capezzuto and G. Bruno, Ellipsometry as a real-time optical tool for monitoring and understanding graphene growth on metals, *J. Phys. Chem. C*, 2011, **115**(44), 21804–21812.
- 46 W. Li, G. Cheng, Y. Liang, B. Tian, X. Liang, L. Peng, A. H. Walker, D. J. Gundlach and N. V. Nguyen, Broadband optical properties of graphene by spectroscopic ellipsometry, *Carbon*, 2016, **99**, 348–353.
- 47 I. Jung, M. Vaupel, M. Pelton, R. Piner, D. A. Dikin, S. Stankovich, J. An and R. S. Ruoff, Characterization of thermally reduced graphene oxide by imaging ellipsometry, *J. Phys. Chem. C*, 2008, **112**(23), 8499–8506.
- 48 M. J. McAllister, J.-L. Li, D. H. Adamson, H. C. Schniepp, A. A. Abdala, J. Liu, M. Herrera-Alonso, D. L. Milius, R. Car and R. K. Prud'homme, Single sheet functionalized gra-

- phene by oxidation and thermal expansion of graphite, *Chem. Mater.*, 2007, **19**(18), 4396–4404.
- 49 G. Gouadec and P. Colombari, Raman spectroscopy of nanomaterials: how spectra relate to disorder, particle size and mechanical properties, *Prog. Cryst. Growth Charact. Mater.*, 2007, **53**(1), 1–56.
  - 50 A. Gupta, G. Chen, P. Joshi, S. Tadigadapa and P. Eklund, Raman scattering from high-frequency phonons in supported n-graphene layer films, *Nano Lett.*, 2006, **6**(12), 2667–2673.
  - 51 L. G. Cançado, A. Jorio, E. Martins Ferreira, F. Stavale, C. Achete, R. Capaz, M. Moutinho, A. Lombardo, T. Kulmala and A. Ferrari, Quantifying defects in graphene via Raman spectroscopy at different excitation energies, *Nano Lett.*, 2011, **11**(8), 3190–3196.
  - 52 A. C. Ferrari and D. M. Basko, Raman spectroscopy as a versatile tool for studying the properties of graphene, *Nat. Nanotechnol.*, 2013, **8**(4), 235–246.
  - 53 D. Zhan, L. Liu, Y. N. Xu, Z. H. Ni, J. X. Yan, C. Zhao and Z. X. Shen, Low temperature edge dynamics of AB-stacked bilayer graphene: Naturally favored closed zigzag edges, *Sci. Rep.*, 2011, **1**, 1–5.
  - 54 P.-G. Ren, D.-X. Yan, X. Ji, T. Chen and Z.-M. Li, Temperature dependence of graphene oxide reduced by hydrazine hydrate, *Nanotechnology*, 2010, **22**(5), 055705.
  - 55 B. Gupta, N. Kumar, K. Panda, V. Kanan, S. Joshi and I. Visoly-Fisher, Role of oxygen functional groups in reduced graphene oxide for lubrication, *Sci. Rep.*, 2017, **7**, 45030.
  - 56 G. Wang, J. Yang, J. Park, X. Gou, B. Wang, H. Liu and J. Yao, Facile synthesis and characterization of graphene nanosheets, *J. Phys. Chem. C*, 2008, **112**(22), 8192–8195.
  - 57 J. Cui, Z. Song, L. Xin, S. Zhao, Y. Yan and G. Liu, Exfoliation of graphite to few-layer graphene in aqueous media with vinylimidazole-based polymer as high-performance stabilizer, *Carbon*, 2016, **99**, 249–260.
  - 58 J. N. Coleman, Liquid exfoliation of defect-free graphene, *Acc. Chem. Res.*, 2012, **46**(1), 14–22.
  - 59 A. Kuzmenko, Kramers–Kronig constrained variational analysis of optical spectra, *Rev. Sci. Instrum.*, 2005, **76**(8), 083108.
  - 60 M. Losurdo, M. M. Giangregorio, G. V. Bianco, P. Capezzuto and G. Bruno, How spectroscopic ellipsometry can aid graphene technology?, *Thin Solid Films*, 2014, **571**, 389–394.
  - 61 D.-H. Chae, T. Utikal, S. Weisenburger, H. Giessen, K. v. Klitzing, M. Lippitz and J. Smet, Excitonic Fano Resonance in Free-Standing Graphene, *Nano Lett.*, 2011, **11**(3), 1379–1382.
  - 62 L. Yang, Excitons in intrinsic and bilayer graphene, *Phys. Rev. B: Condens. Matter Mater. Phys.*, 2011, **83**(8), 085405.
  - 63 L. Yang, J. Deslippe, C.-H. Park, M. L. Cohen and S. G. Louie, Excitonic Effects on the Optical Response of Graphene and Bilayer Graphene, *Phys. Rev. Lett.*, 2009, **103**(18), 186802.
  - 64 A. Matković, A. Beltaos, M. Milićević, U. Ralević, B. Vasić, D. Jovanović and R. Gajić, Spectroscopic imaging ellipsometry and Fano resonance modeling of graphene, *J. Appl. Phys.*, 2012, **112**(12), 123523.
  - 65 G. E. Jellison Jr., J. D. Hunn and H. N. Lee, Measurement of optical functions of highly oriented pyrolytic graphite in the visible, *Phys. Rev. B: Condens. Matter Mater. Phys.*, 2007, **76**(8), 085125.
  - 66 U. Wurstbauer, C. Röling, U. Wurstbauer, W. Wegscheider, M. Vaupel, P. H. Thiesen and D. Weiss, Imaging ellipsometry of graphene, *Appl. Phys. Lett.*, 2010, **97**(23), 231901.
  - 67 E. Ochoa-Martínez, M. Gabás, L. Barrutia, A. Pesquera, A. Centeno, S. Palanco, A. Zurutuza and C. Algorta, Determination of a refractive index and an extinction coefficient of standard production of CVD-graphene, *Nanoscale*, 2015, **7**(4), 1491–1500.

# Self-propagated combustion synthesis of a few layer graphene: An optical properties perspective

*Manonmani Mohandoss,<sup>a</sup> Soujit Sen Gupta,<sup>b</sup> Ramesh Kumar,<sup>b</sup> Rabiul Islam<sup>b</sup> Anirban Som,<sup>b</sup>  
Mohd Azhardin Ganayee<sup>b</sup>, T. Pradeep<sup>b</sup> and Shihabudheen M. Maliyekkal<sup>c,\*</sup>*

<sup>a</sup> School of Electronics Engineering, VIT University, Chennai Campus, Chennai – 600 127, India

<sup>b</sup> DST Unit on Nanoscience and Thematic Unit of Excellence (TUE), Department of Chemistry,  
Indian Institute of Technology Madras, Chennai 600 036, India

<sup>c</sup> Department of Civil Engineering, Indian Institute of Technology Tirupati, Tirupati-517506,  
India

\*Corresponding author: E-mail: shihab@iittp.ac.in; sm.maliyekkal@gmail.com

Tel: + 91-877 2500369, Fax: + 91-877 2500370

## Supporting Information

### Table of contents

Supporting Information	Description
S1	Table 1: Milestone in exfoliating graphite and graphene synthesis
S2	Table 2: Comparison of measured parameters of RGO synthesized through different approaches
S3	Figure S1: TG Plot of the as-synthesized RGOL sample
S4	Figure S2: TEM image of micron sized RGOL sheet



**Table 1: Milestones in exfoliating graphite and graphene synthesis**

Year	Precursor	Method of Exfoliation	Treatment	Applications	Ref
1958	Graphite	Chemical	Intercalation	-	1
1987	HOPG	Chemical	Intercalation	-	2
1993	Natural graphite	Laser assisted	Intercalation	-	3
2004	HOPG	Mechanical	Scotch-Tape	Logic circuits, p-n junctions and non-transistor	4
2004	SiC	Epitaxial growth	Sublimation	Electronics and Optoelectronics	5
2006	Camphor	CVD	Thermal pyrolysis	Large area electronic applications	6
2007	Graphite	Wet-chemical approach	Oxidation-Reduction	Hydrogen storage and electrically conducting filler in nanocomposites	7
2008	Ferrocene, Thiophene and ethanol	Aerosol pyrolysis	Ultra-sonication followed by thermal treatment	gas storage devices, electronic wires, sensors, catalytic substrates, field emission sources, batteries	8
2008	Graphite	Electro-chemical Exfoliation	Ionic-liquid assisted process	Biological labelling and imaging	9
2009	Graphite	Electrolytic Exfoliation	Electrolysis	Electronics, composite materials, molecular gas sensor, energy storage	10
2009	SWCNT/MWCNT	Unzipping of CNTs	Annealing	Electronics, Energy storage devices and batteries	11
2009	Graphite electrode	Arc-discharge method	Arc evaporation in the presence of H <sub>2</sub>	Electronics applications	12
2009	GO	Self-assembly	Electrostatic Interaction	Molecular sensor, transparent electronics	13
2010	Graphite	Sono-chemical Exfoliation	Ultra-sonication in highly reactive solvent	Preparation of graphene based nanocomposite materials	14
2012	Graphite	Combustion	Self-propagating flame method	Schottky solar cells and energy storage devices	15

**Supporting Information S1:**

**Table 2. Comparison of measured parameters of RGO synthesized through different approaches**

Precursor/Reduction method	C/O	I <sub>D</sub> /I <sub>G</sub>	Ref
GO/Hydrazine hydrate	10.3	>1	7
GO/Sulfonic acid groups	C/S=35	-	16
GO/NaBH <sub>4</sub>	5.3	>1	17
GO/Hydrothermal	5.6	0.90	18
GO/Solvothermal	6.4	1.16	19
GO/pre-reduction by NaBH <sub>4</sub> and heating in H <sub>2</sub> SO <sub>4</sub> at 200 °C	8.57	1.0	20
GO/Electrolytic exfoliation	-	>1	10
GO/Thermal Exfoliation (1000 °C- >2000 °C)	10.3	-	21-23
GO/Microwave	5.46	0.96	24
GO/Thermal treatment (DMF)	-	1.06	25
GO/photoreduction in H <sub>2</sub>	4.1	1.02	26
GO/ Photoreduction (sunlight)	3.54	1.06	27
GO/Fe	7.9	0.32	28
GO/Al powder	-	1.81	29
GO/Photocatalytic (ZnO)	33.5	>1	30
GO/organic solvents-DMF	2.8	-	31
DMSO	4.0		
NMP	4.4		
Self-propagating solid state reduction of GO	5.9	-	32

**Supporting Information S2:**

Propagative exfoliation of graphite	-	1.98	<sup>33</sup>
Self-propagating combustion based exfoliation of graphite	8.74	1.2	This Work

**Supporting Information S3:**

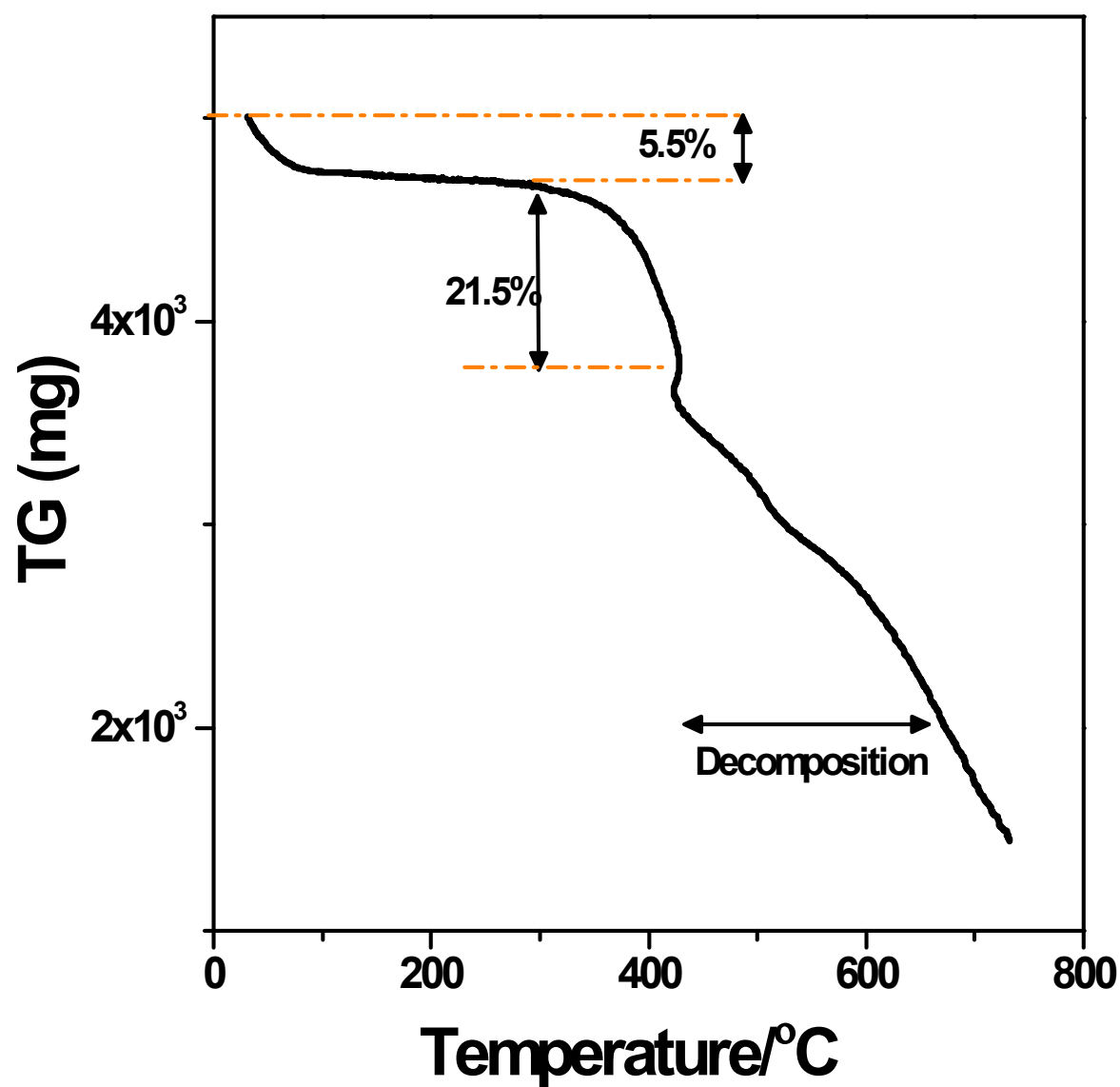


Figure S1: TG Plot of RGOL sample

Supporting Information S4:

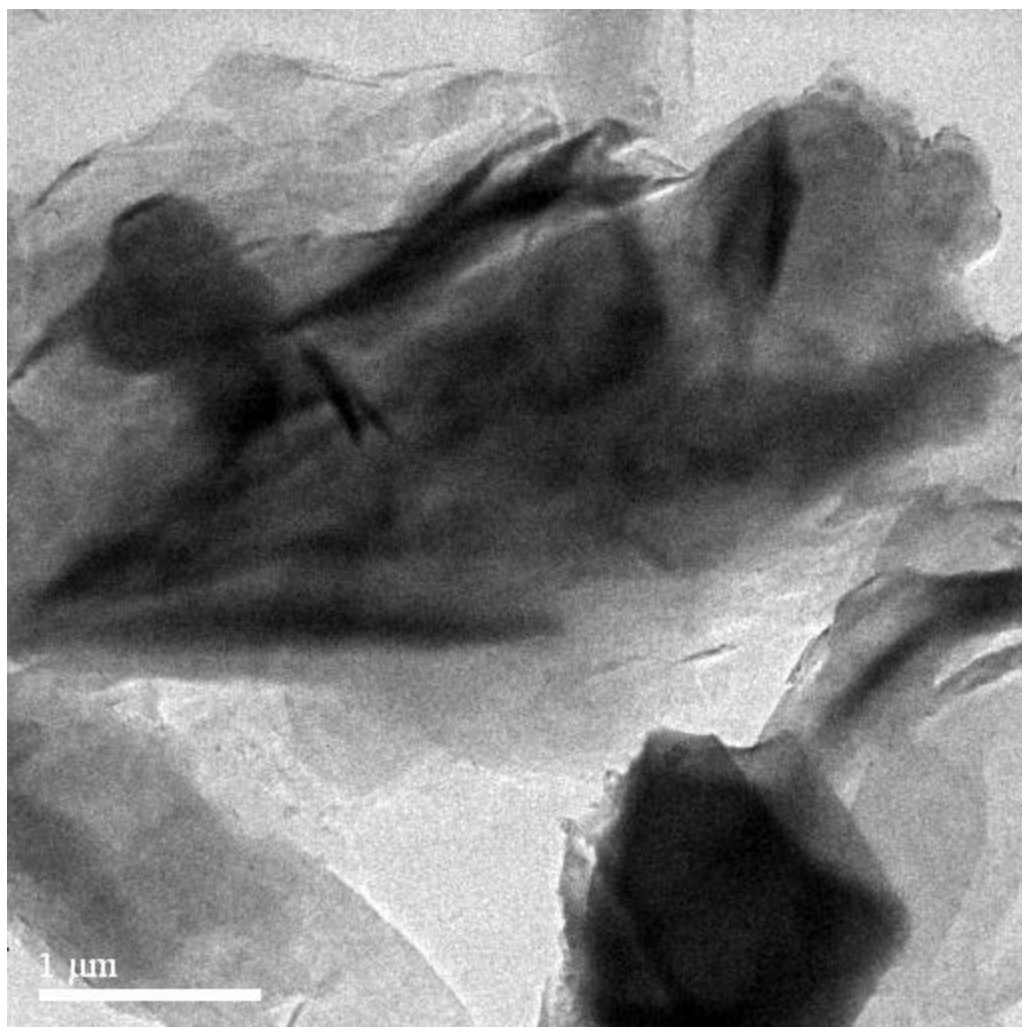


Figure S2: TEM image of micron sized RGOL sheet

## References

1. Hummers, W. S.; Offeman, R. E., Preparation of Graphitic Oxide. *Journal of the American Chemical Society* **1958**, *80* (6), 1339-1339.
2. Chung, D., Intercalate vaporization during the exfoliation of graphite intercalated with bromine. *Carbon* **1987**, *25* (3), 361-365.
3. Kuga, Y.; Oyama, T.; Wakabayashi, T.; Chiyoda, H.; Takeuchi, K., Laser-assisted exfoliation of potassium-ammonia-graphite intercalation compounds. *Carbon* **1993**, *31* (1), 201-204.
4. Novoselov, K. S.; Geim, A. K.; Morozov, S. V.; Jiang, D.; Zhang, Y.; Dubonos, S. V.; Grigorieva, I. V.; Firsov, A. A., Electric field effect in atomically thin carbon films. *science* **2004**, *306* (5696), 666-669.
5. Berger, C.; Song, Z.; Li, T.; Li, X.; Ogbazghi, A. Y.; Feng, R.; Dai, Z.; Marchenkov, A. N.; Conrad, E. H.; First, P. N., Ultrathin epitaxial graphite: 2D electron gas properties and a route toward graphene-based nanoelectronics. *arXiv preprint cond-mat/0410240* **2004**.
6. Somani, P. R.; Somani, S. P.; Umeno, M., Planer nano-graphenes from camphor by CVD. *Chemical Physics Letters* **2006**, *430* (1), 56-59.
7. Stankovich, S.; Dikin, D. A.; Piner, R. D.; Kohlhaas, K. A.; Kleinhammes, A.; Jia, Y.; Wu, Y.; Nguyen, S. T.; Ruoff, R. S., Synthesis of graphene-based nanosheets via chemical reduction of exfoliated graphite oxide. *carbon* **2007**, *45* (7), 1558-1565.
8. Campos-Delgado, J.; Romo-Herrera, J. M.; Jia, X.; Cullen, D. A.; Muramatsu, H.; Kim, Y. A.; Hayashi, T.; Ren, Z.; Smith, D. J.; Okuno, Y., Bulk production of a new form of sp<sup>2</sup> carbon: crystalline graphene nanoribbons. *Nano letters* **2008**, *8* (9), 2773-2778.
9. Liu, N.; Luo, F.; Wu, H.; Liu, Y.; Zhang, C.; Chen, J., One-step ionic-liquid-assisted electrochemical synthesis of ionic-liquid-functionalized graphene sheets directly from graphite. *Advanced Functional Materials* **2008**, *18* (10), 1518-1525.
10. Wang, G.; Wang, B.; Park, J.; Wang, Y.; Sun, B.; Yao, J., Highly efficient and large-scale synthesis of graphene by electrolytic exfoliation. *Carbon* **2009**, *47* (14), 3242-3246.
11. Kosynkin, D. V.; Higginbotham, A. L.; Sinitskii, A.; Lomeda, J. R.; Dimiev, A.; Price, B. K.; Tour, J. M., Longitudinal unzipping of carbon nanotubes to form graphene nanoribbons. *Nature* **2009**, *458* (7240), 872-876.
12. Subrahmanyam, K.; Panchakarla, L.; Govindaraj, A.; Rao, C., Simple method of preparing graphene flakes by an arc-discharge method. *The Journal of Physical Chemistry C* **2009**, *113* (11), 4257-4259.
13. Shen, J.; Hu, Y.; Li, C.; Qin, C.; Shi, M.; Ye, M., Layer-by-layer self-assembly of graphene nanoplatelets. *Langmuir* **2009**, *25* (11), 6122-6128.
14. Xu, H.; Suslick, K. S., Sonochemical preparation of functionalized graphenes. *Journal of the American Chemical Society* **2011**, *133* (24), 9148-9151.
15. Manukyan, K. V.; Rouvimov, S.; Wolf, E. E.; Mukasyan, A. S., Combustion synthesis of graphene materials. *Carbon* **2013**, *62*, 302-311.
16. Si, Y.; Samulski, E. T., Synthesis of Water Soluble Graphene. *Nano Letters* **2008**, *8* (6), 1679-1682.
17. Shin, H. J.; Kim, K. K.; Benayad, A.; Yoon, S. M.; Park, H. K.; Jung, I. S.; Jin, M. H.; Jeong, H. K.; Kim, J. M.; Choi, J. Y., Efficient reduction of graphite oxide by sodium borohydride and its effect on electrical conductance. *Advanced Functional Materials* **2009**, *19* (12), 1987-1992.
18. Zhou, Y.; Bao, Q.; Tang, L. A. L.; Zhong, Y.; Loh, K. P., Hydrothermal dehydration for the "green" reduction of exfoliated graphene oxide to graphene and demonstration of tunable optical limiting properties. *Chemistry of Materials* **2009**, *21* (13), 2950-2956.

19. Choucair, M.; Thordarson, P.; Stride, J. A., Gram-scale production of graphene based on solvothermal synthesis and sonication. *Nature nanotechnology* **2009**, *4* (1), 30-33.
20. Gao, W.; Alemany, L. B.; Ci, L.; Ajayan, P. M., New insights into the structure and reduction of graphite oxide. *Nature chemistry* **2009**, *1* (5), 403-408.
21. Wu, Z.-S.; Ren, W.; Gao, L.; Liu, B.; Jiang, C.; Cheng, H.-M., Synthesis of high-quality graphene with a pre-determined number of layers. *Carbon* **2009**, *47* (2), 493-499.
22. Schniepp, H. C.; Li, J.-L.; McAllister, M. J.; Sai, H.; Herrera-Alonso, M.; Adamson, D. H.; Prud'homme, R. K.; Car, R.; Saville, D. A.; Aksay, I. A., Functionalized single graphene sheets derived from splitting graphite oxide. *The Journal of Physical Chemistry B* **2006**, *110* (17), 8535-8539.
23. McAllister, M. J.; Li, J.-L.; Adamson, D. H.; Schniepp, H. C.; Abdala, A. A.; Liu, J.; Herrera-Alonso, M.; Milius, D. L.; Car, R.; Prud'homme, R. K., Single sheet functionalized graphene by oxidation and thermal expansion of graphite. *Chemistry of materials* **2007**, *19* (18), 4396-4404.
24. Chen, W.; Yan, L.; Bangal, P. R., Preparation of graphene by the rapid and mild thermal reduction of graphene oxide induced by microwaves. *Carbon* **2010**, *48* (4), 1146-1152.
25. Lin, Z.; Yao, Y.; Li, Z.; Liu, Y.; Li, Z.; Wong, C.-P., Solvent-assisted thermal reduction of graphite oxide. *The Journal of Physical Chemistry C* **2010**, *114* (35), 14819-14825.
26. Matsumoto, Y.; Koinuma, M.; Kim, S. Y.; Watanabe, Y.; Taniguchi, T.; Hatakeyama, K.; Tateishi, H.; Ida, S., Simple photoreduction of graphene oxide nanosheet under mild conditions. *ACS applied materials & interfaces* **2010**, *2* (12), 3461-3466.
27. Mohandoss, M.; Gupta, S. S.; Nelleri, A.; Pradeep, T.; Maliyekkal, S. M., Solar mediated reduction of graphene oxide. *RSC Advances* **2017**, *7* (2), 957-963.
28. Fan, Z.-J.; Kai, W.; Yan, J.; Wei, T.; Zhi, L.-J.; Feng, J.; Ren, Y.-m.; Song, L.-P.; Wei, F., Facile synthesis of graphene nanosheets via Fe reduction of exfoliated graphite oxide. *ACS nano* **2010**, *5* (1), 191-198.
29. Fan, Z.; Wang, K.; Wei, T.; Yan, J.; Song, L.; Shao, B., An environmentally friendly and efficient route for the reduction of graphene oxide by aluminum powder. *Carbon* **2010**, *48* (5), 1686-1689.
30. Mei, X.; Ouyang, J., Ultrasonication-assisted ultrafast reduction of graphene oxide by zinc powder at room temperature. *Carbon* **2011**, *49* (15), 5389-5397.
31. Compton, O. C.; Jain, B.; Dikin, D. A.; Abouimrane, A.; Amine, K.; Nguyen, S. T., Chemically active reduced graphene oxide with tunable C/O ratios. *ACS nano* **2011**, *5* (6), 4380-4391.
32. Kim, F.; Luo, J.; Cruz-Silva, R.; Cote, L. J.; Sohn, K.; Huang, J., Self-propagating domino-like reactions in oxidized graphite. *Advanced Functional Materials* **2010**, *20* (17), 2867-2873.
33. Feng, L.; Liu, Y.-W.; Tang, X.-Y.; Piao, Y.; Chen, S.-F.; Deng, S.-L.; Xie, S.-Y.; Wang, Y.; Zheng, L.-S., Propagative exfoliation of high quality graphene. *Chemistry of Materials* **2013**, *25* (22), 4487-4496.



# Book Chapters

# ***Capacitive Deionization (CDI): An Alternative Cost-Efficient Desalination Technique***

**Soujit Sen Gupta, Md Rabiul Islam, Thalappil Pradeep**

*DST Unit of Nanoscience (DST UNS), and Thematic Unit of Excellence (TUE), Department of Chemistry, Indian Institute of Technology Madras, Chennai, India*

## ***7.1 Introduction***

Availability of clean drinking water is a basic human right, according to the United Nations [1]. There is a shortage in the supply of clean drinking water because of the exponential growth of human population. Due to increased industrialization, agriculture, and climate change, the existing fresh water is also getting contaminated. For meeting the demand of safe drinking water globally, methods such as brackish and seawater desalination were introduced. Multiple water desalination techniques to accomplish this, such as distillation, reverse osmosis (RO), and electrodialysis have emerged successfully in the last few decades. These techniques produce clean water but are either cost or energy-inefficient. Capacitive deionization (CDI) is an emerging desalination technology in the 21st century. CDI has multiple advantages over other desalinating processes: (i) the technique works by the process of electroadsorption, and is even more energy-efficient, as it does not require any high-pressure pumps; (ii) as the module works in 0.8–2.0 V, it can be combined with solar/wind power and can work in remote areas, where availability of electricity is a major issue; (iii) water reject is much less as compared with other techniques such as RO; (iv) carbon particles can withstand much higher temperature than membranes, thereby can be used for wider applications; and (v) as, the device works like a capacitor and high-energy recovery is possible.

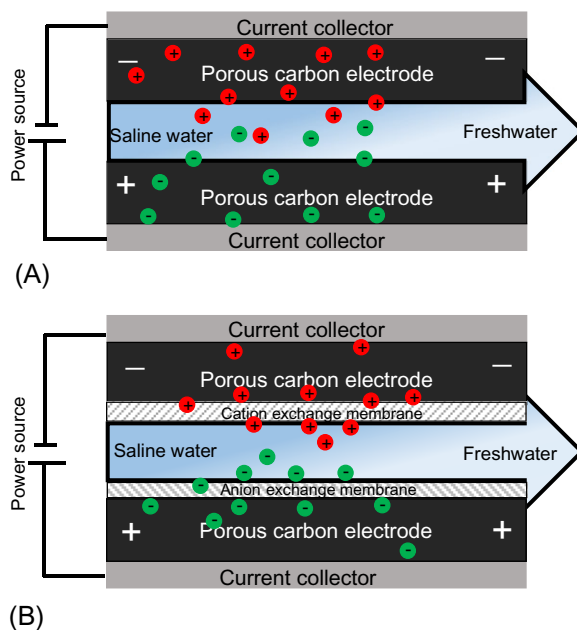
Although CDI has multiple advantages over other techniques, the limitation lies on the availability of sustainable electrode materials having high electroadsorption capacity and high average salt adsorption rate (ASAR). An appropriate material for CDI electrode should have the following characteristics: (i) large surface area; (ii) high porosity (both meso and micropores); (iii) high electrical conductivity; (iv) electrochemical stability; (v) bio-inertness; (vi) fast adsorption-desorption kinetics; (vii) good wetting behavior; (viii) low cost; and (ix) scalability.

Electrodes materials used for CDI are activated carbon, carbon cloth, ordered mesoporous carbon, carbon nanofibers, carbon nanotubes/multiwalled carbon nanotubes (CNTs/MWCNTs), and graphene and graphene-based composites.

A CDI cell comprises of a pair of porous electrodes (especially made of carbon), separated by a nonconducting membrane called a separator. When a potential difference is applied to the electrodes, the electrodes get charged (called as cell voltage or charging voltage). Typically, the cell voltage ranges from 0.8 to 2.0 V. The ions present in the feed water migrate to the electrical double layer (EDL) of the oppositely charged porous carbon electrodes. The ions are electrostatically held at the EDL until an equilibrium is reached when no more ions gets adsorbed. This step is known as electroadsorption and subsequently, desorption happens when the potential is reversed or the external power supply is shorted. During this step, the ions leave the electrodes as the brine stream thereby regenerating them and energy can be recovered from the charge, that is, leaving the cell.

A major problem of CDI lies in the regeneration step. When the electrodes are saturated with oppositely charged ions and reaches an equilibrium, the adsorption step is stopped and the terminals are reversed for desorption. During this step, the adsorbed ions will get desorbed in the bulk fluid but simultaneously the oppositely charged ions from the solution will get adsorbed on the electrodes. Actually, the adsorption and desorption occur at the same time during this step. Therefore, the amount of salt which is adsorbed in the first cycle is not desorbed completely during the desorption step. The residual ions in the electrodes decrease the adsorption efficiency of the material in the next adsorption step. An improvement in the efficiency was shown by the incorporation an ion-exchange (IEX) membrane on top of the porous carbon electrodes and the technique is called membrane capacitive deionization (MCDI) [2]. The membrane can be put in front of the electrodes either as a stand-alone film of 50–200  $\mu\text{m}$  or can be coated on to the electrode surface with a typical thickness of around 20  $\mu\text{m}$ .

In the case of MCDI, the cations penetrate freely through the cation-exchange (CEX) membrane and are held electrostatically in the vicinity of the EDL of the negatively charged electrode, that is, cathode. Similarly, the anions permeate through the anion-exchange (AEX) membrane to the positively charged electrode, that is, anode and get adsorbed. During the regeneration step, when the potential is reversed, the cations from the electrode are desorbed and permeate through the CEX to the bulk fluid, while the presence of CEX will block the anions to penetrate and get adsorbed on the electrode surface even while the electrodes are positively charged. Similarly, in the case of AEX, the cations will not permeate through in the desorption step. Thus, during the regeneration step, no adsorption occurs unlike that of the conventional CDI and all the ions which get adsorbed are desorbed. The next adsorption cycle happens again by reversing the polarity of the power supply, having a fresh electrode surface for adsorption. Thus, there is no loss of adsorption efficiency of the electrodes in the case of MCDI. Schematic in Fig. 7.1 shows the basic mechanism of CDI (Fig. 7.1A) and MCDI (Fig. 7.1B) process [3]. With this concept, Lee et al. in 2006 first developed an MCDI unit for desalinating power plant waste water [4].



**Fig. 7.1**

A schematic showing the working principle of (A) capacitive deionization (CDI) and (B) membrane capacitive deionization (MCDI) during the electroadsorption process. *Modified from Porada S, Zhao R, van der Wal A, Presser V, Biesheuvel PM, Review on the science and technology of water desalination by capacitive deionization. Prog. Mater. Sci. 58(8): 1388–1442, 2013.*

They claimed that the salt removal rate was 19% more than of conventional CDI and the salt removal capacity was 92% at an operational potential of 1.2 V using 1000 ppm of NaCl, the energy requirement was 1.96 Wh/L. Długoleć and van der Wal in 2013 showed that the energy recovery for MCDI [5] was 83% as compared with that of 62.1% in case of CDI [6]. They also suggested that by implementing energy recovery as an essential part of the MCDI operation, the overall energy consumption can be as low as 0.26 (kWh)/m<sup>3</sup> of produced water to reduce the salinity by 10 mM and this value is independent of feed water concentration.

In the 21st century, CDI has gone through various modifications than the early work started in the mid-20th century. The modifications include the flow-through electrodes where the water is directed from the top of electrodes, introduction of IEX, constant current operation, salt release at reverse voltage, energy recovery from the desorption cycles, and stop-flow operation during ion release. On the materials point of view, new materials and composites are still emerging in search of novel electrodes having high electroadsorption capacity.

## 7.2 History of CDI

Historically, the technique of desalination of water using porous “inert” carbon electrodes was reported by Blair and Murphy in the early 1960s and was termed as “electrochemical demineralization of water.” In those days, it was assumed that the ions from water were

removed by specific functional chemical groups present on the carbon surface by forming an ionic bond. Evans and Hamilton in 1966 studied the mechanism of demineralization and regeneration at carbon electrodes using Columbic and mass-balance analysis [7]. The efficiency of the salt removal capacity was assumed to be proportional to the concentration of the functional group present on the electrode surfaces. In 1968, Reid designed a 20 gallon/day desalination unit (named as DC-5 demineralization unit, shown in Fig. 7.2) and has shown its commercial relevance [8]. It was tested with natural saline water and the effect of flow rate, pH, cell potential, turbidity, bacteria, algae, and the deterioration of the electrodes were demonstrated. Removal efficiency of various ions like sodium, magnesium, calcium, chloride sulfate, nitrate, and phosphate in the context of drinking water was also mentioned.

The theory of EDL was proposed by Johnson et al. in 1970 as the actual mechanism responsible for reversible electrosorption of salt water using porous carbon electrodes [9]. The work stated that the adsorption capacity of the electrodes depends on the applied potential, available surface area, and the electrical capacity of the double layer. Multiple reports were published by the same group in the next few years but they have to discontinue the study because of the instability of electrodes [10]. A preliminary cost estimation was also presented where it was claimed that a cost-efficient desalination technique by this technology can be achieved only if stable high surface area electrodes are produced.

Electrode material development started from the 1990s, Adelmann used activated carbon electrodes and used as a flow-through capacitor in 1990. The major break-through came by the



**Fig. 7.2**

The photograph of DC-5, the first 20 gallon/day demineralization unit. *Data from G.W. Reid, A. Stevens, J. Abichandani, F. Townsend, M. Al-Awady, Field Operation of a 20 Gallons Per Day Pilot Plant Unit for Electrochemical Desalination of Brackish Water, U.S. Dept. of the Interior, Washington, DC, 1968.*

pioneering work of Farmer et al. in 1996 [11], where the term CDI was first used. They reported that deionization was performed using carbon aerogel (CA) electrodes and the ions were removed from water by applying electricity. When a potential difference was applied on the electrodes, the ions moved toward the oppositely charged electrodes and get adsorbed electrostatically in EDL formed at the surface of the electrodes. The methods and apparatus for CDI, effect of cell voltage, and regeneration of electrodes using CA electrodes were patented by Joseph Farmer in 1995. Since, then researchers have continuously looked at new and stable materials for CDI. The same group has consecutively published three patents which served as a stepping stone of the CDI technology in recent days [12]. Shiue et al. in 2001 introduced CNT as the electrode material and was first to use nanomaterials in the electrode system [13].

Welgemoed and Schutt in 2005 developed a bench-scale module of CDI unit and evaluated its performance with respect to other membrane technologies [14]. In all 12 pairs of CA electrodes were used having average density and total accessible area of  $0.78 \text{ g/cm}^3$  and  $2.29 \text{ m}^2$ , respectively. The electrodes were having Brunauer-Emmett-Teller (BET) surface area of  $600 \text{ m}^2/\text{g}$ , bulk resistivity of  $20 \text{ m}\Omega \text{ cm}$ , and specific capacitance of  $2 \text{ F/cm}^2$ . They have evaluated the cost requirement for treating  $800\text{--}10,000 \text{ mg/L}$  of brackish water to be  $0.5\text{--}2.25 \text{ Wh/gallon}$  for the CDI technology. Other membrane-based technologies such as RO and electrodialysis were found to be  $8.5$  and  $7.7 \text{ Wh/gallon}$ , respectively, at the same conditions. In addition, they have claimed that as CA electrodes are chemically resistant oxidizing agents and therefore the lifetime of the electrodes can be extended to 10 years with proper handling.

In 2004, Adelman in a US patent, first introduced “charge barrier flow-through capacitor,” popularly known as MCDI in recent days. The technique was used to desalinate waste water by a pilot plant in the work of Lee et al. [4] Theory and physical understanding of MCDI was given by a group of researcher in Wetsus and collaborators in 2010 [15]. Researchers have worked to enhance the maximum adsorption capacity of the electrode material using graphene and its composites, different composite materials such as nanomaterials, metal oxides, CNTs, carbon from biomass, etc., Kim and Choi in 2012 showed that it was possible to remove selective ions from a mixture by modifying the electrode surface and membrane in MCDI [16]. A great advancement in the field of CDI was made with the introduction of carbon flow electrodes which was able to desalinate sea water having total dissolved solids (TDS) of  $31 \text{ g/L}$ . [17] The use of ionic group derivitized nano-porous carbon electrodes for CDI was demonstrated by Adelman in 2014 as a proof of concept [18]. Different companies and start-ups have come with CDI products both community and domestic units are now in the market. An overview of CDI development and important milestones in the area is depicted in Fig. 7.3.

### **7.3 Patents in CDI**

After a gap of almost two decades, CDI was reborn with the introduction of CA by J.C. Farmer as a stable material for electrodes, in the early 1990s. He showed the method and apparatus for CDI, electrochemical purification, and regeneration of electrodes.

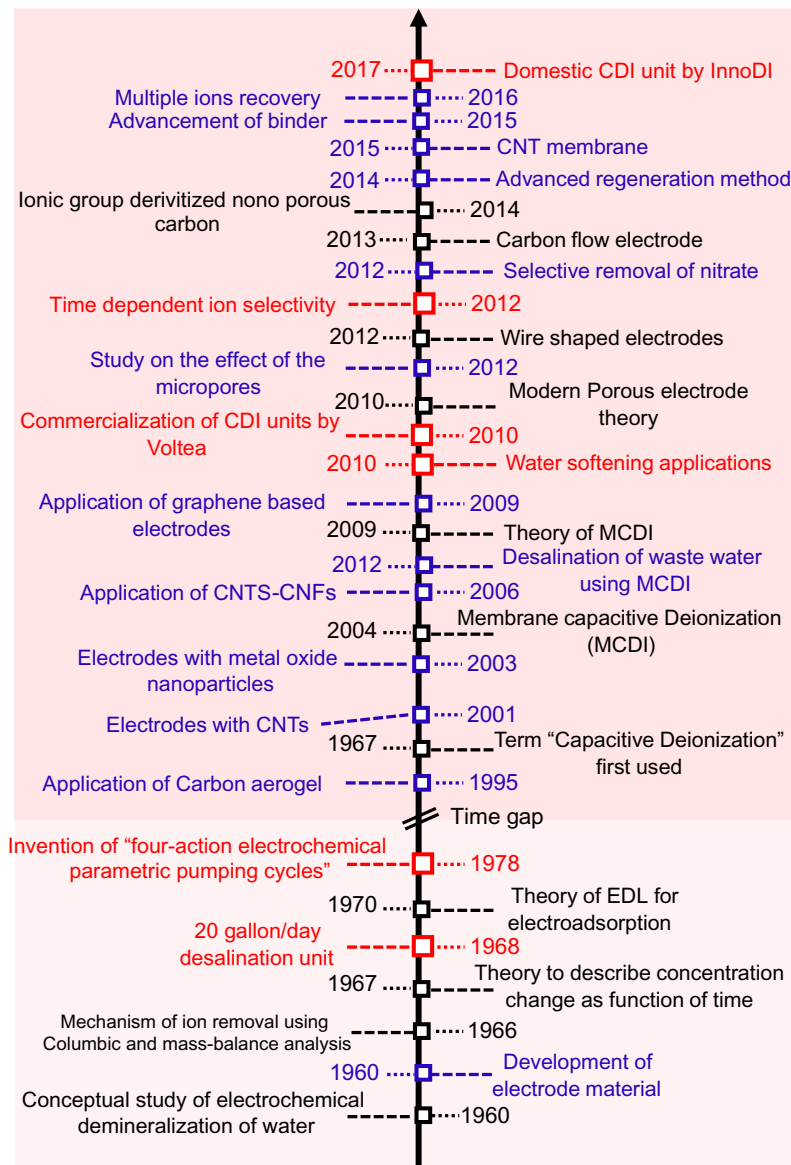


Fig. 7.3

Timeline of developments in CDI indicating the milestones. Modified from Porada S, Zhao R, van der Wal A, Presser V, Biesheuvel PM, Review on the science and technology of water desalination by capacitive deionization. *Prog. Mater. Sci.* 58(8): 1388–1442, 2013.

Eric D. Nyberg gave the idea of electrochemically assisted IEX for efficient CDI. An energy efficient flow-through capacitor, particularly for the concentration and/or separation of seawater was patented by Marc Andelman. He also introduced the concept of charge barrier flow-through capacitor, that is, the use of an IEX. Lih-Ren Shiue in 2002 showed that energy



can be recovered during the regeneration cycle, thereby reduce the overall energy consumption of the system. Ho-Jung Yang in 2009 used transition metals with CNT as an electrode material and introduced an integrated electrode-current collector sheet for CDI. Ali Altaee in the same year showed a process for separating organic compounds from an aqueous medium by using a surfactant. The surfactant reacts with the organic molecules and getting charged, which helps in removing it during the charging cycle. Sean Knapp in the same year showed a method of operating CDI cell using a regeneration cycle to increase pure flow rate and efficiency of the cell. Sundara Ramaprabhu in 2011 shows that ions such as arsenic can be efficiently removed from water using CDI technology. Marc Andelman again in 2012 introduced the concept of polarized electrode for flow-through CDI, where the carbon materials are functionalized and therefore the cells can work efficiently without any IEX. Matthew E. Suss in the same year showed an electrode “flow-through” capacitive desalination system wherein feed water is pumped through the pores of a pair of monolithic porous electrodes separated by an ultrathin nonconducting porous film. The feed water flows through the electrodes and the spacing between electrodes is of the order 10  $\mu\text{m}$ . Kyung-Seok Kang in 2013 has showed that selective ions can be removed from water using MCDI. Patrice Simon used flow electrode architecture for removal of ions from water. Muataz Ali Atieh in 2015 showed that CNT membrane can be used as an electrode for efficient salt removal at low cost. Different binders, composite materials, apparatus, cell architecture, and modified electrodes have been patented in subsequent years. Tae Gong Ryu in 2016 modified the system and showed that ions can be recovered selectively from the system having complex multiions. [Table 7.1](#) shows the list of patents in the course of development of CDI technologies over the years.

## **7.4 Theory of CDI**

The principle of ion removal mechanism in CDI is through physical adsorption on to the surface of the electrodes with the solution and not by oxidation/reduction reaction. It is believed that the Faradic reactions also take place with the carboxy and phenolic group of the electrodes to form a chemical bond with cations in the feed solution. Both these processes contribute to the overall removal efficiency in the CDI cell [\[53\]](#).

In an electrochemical processes when a potential difference is applied to the electrodes, the ions migrate toward the oppositely charged electrodes. This separation mechanism was first studied by Helmholtz in 1893 and described it as EDL model [\[54\]](#). Similar theory was also given by Perrin in 1904. They assumed that positively charged ions move toward cathode and the negatively charged ions move toward anode creating external Helmholtz layers, leaving a hydrated sheet in the middle consisting of water molecules called the inner Helmholtz layer as shown in [Fig. 7.4](#). This theory has certain limitations as it considered the electrodes to be rigid blocks and neglected the factors like diffusion, mixing, and adsorption of ions on the electrodes

**Table 7.1 List of patents in the course of development of CDI technology since, early 1990s**

Sl. No.	Inventor (Year of filing)	Patent No.	Title
1	Joseph Farmer (1994) [12a]	US5425858 A	Method and apparatus for capacitive deionization, electrochemical purification, and regeneration of electrodes
2	Joseph Farmer (1995)[12b]	US5954937 A	Method and apparatus for capacitive deionization and electrochemical purification and regeneration of electrodes
3	Eric D. Nyberg (1997) [19]	US5788826 A	Electrochemically assisted ion exchange
4	Tri D. Tran (1999)[12c]	US6309532 B1	Method and apparatus for capacitive deionization and electrochemical purification and regeneration of electrodes
5	Marc D. Andelman (2000) [20]	US6325907 B1	Energy and weight efficient flow-through capacitor, system and method
6	Marc D. Andelman (2001) [21]	WO2002086195 A1	Charge barrier flow-through capacitor
7	Hiroshi Inoue (2002) [22]	US20030189005 A1	Ion exchanger
8	Lih-Ren Shiue (2002) [23]	US6580598 B2	Deionizers with energy recovery
9	Marc Andelman (2004) [2]	US20040174657 A1	Charge barrier flow-through capacitor
10	Ho-Jung Yang (2009) [24]	US20100140096 A1	Electrode for capacitive deionization, capacitive deionization device and electric double-layer capacitor including the electrode
11	Ho-Jung Yang (2009) [25]	US20100181200 A1	Transition metal/carbon nanotube composite and method of preparing the same
12	Ho-Jung Yang (2009) [26]	US8518229 B2	Integrated electrode-current collector sheet for capacitive deionization, capacitive deionization device and electric double-layer capacitor having the same
13	Ali Altaee (2009) [27]	WO2010035004 A1	Capacitive deionization
14	Sean KNAPP (2009) [28]	US20100065511 A1	Method of Regenerating A Capacitive Deionization Cell
15	Kyung-Seok Kang (2010) [29]	US2012032519A1	Capacitive electrode for deionization, and electrolytic cell using same
16	Chang-Hyun Kim (2010) [30]	US20120132519 A1	Capacitive deionization device
17	Kyung Seok Kang (2010) [31]	US20110147212 A1	Ion selective capacitive deionization composite electrode, and method for manufacturing a module
18	Sundara Ramaprabhu (2011) [32]	EP2487278 A2	Methods and systems for separating ions from fluids

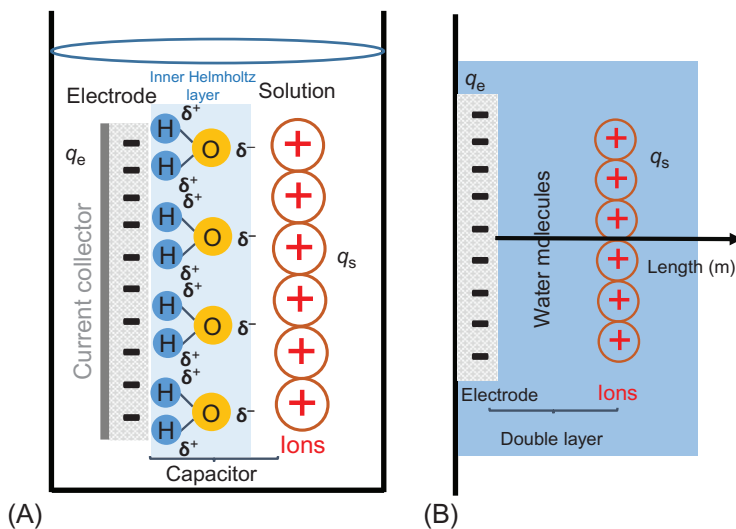
**Table 7.1 List of patents in the course of development of CDI technology since, early 1990s—Cont'd**

Sl. No.	Inventor (Year of filing)	Patent No.	Title
19	David J. Averbeck (2011) [33]	US20120186980 A1	Ion removal using a capacitive deionization system
20	David J. Averbeck (2011) [34]	US9637397 B2	Regeneration of a capacitive deionization system
21	Zhuo Sun (2011) [35]	US9695070 B2	Membrane enhanced deionization capacitor device
22	Marc D. Andelman (2012) [36]	US20130153426 A1	Polarized electrode for flow-through capacitive deionization
23	Matthew E. Suss (2012) [13]	WO2012129532 A1	Flow-through electrode capacitive desalination
24	Moon Il Jung (2012) [37]	S20120273359 A1	Capacitive deionization apparatus
25	Joon Seon JEONG (2013) [38]	US 20130206598 A1	Capacitive deionization apparatus and methods of treating fluid using the same
26	Kyung-Seok Kang (2013) [39]	US20140144779 A1	Method of manufacturing capacitive deionization electrode having ion selectivity and cdi electrode module including the same
27	Antonino ABRAMI (2013) [40]	WO2013183973 A1	Method and plant for the reduction of the concentration of pollutants and/or valuable elements in the water
28	Patrice Simon (2014) [41]	WO2014024110 A1	Method and device to remove ions from an electrolytic media, such as water desalination, using suspension of divided materials in a flow capacitor
29	Myung Dong Cho (2014) [42]	WO 2014195897 A1	Composition for electrode of capacitive deionization apparatus, and electrode including same
30	Yoo Seong Yang (2014) [43]	US5425858 A	Capacitive deionization electrodes, capacitive deionization apparatuses including the same, and production methods thereof
31	Joon Seon Jeong (2014) [44]	US5954937 A	Regeneration methods of capacitive deionization electrodes
32	Yeong Suk Choi (2014) [45]	US5788826 A	Composition for electrode of capacitive deionization apparatus, and electrode including same
33	Zhenxiao Cai (2015) [46]	US6309532 B1	Capacitive deionization system, electrode pack and method for operating the system
34	Muataz Ali Atieh (2015) [47]	US6325907 B1	Fabrication of carbon nanotube membranes

(Continued)

**Table 7.1 List of patents in the course of development of CDI technology since, early 1990s—Cont'd**

Sl. No.	Inventor (Year of filing)	Patent No.	Title
35	Po-I Liu (2015) [48]	WO2002086195 A1	Binder for capacitive deionization electrode and method for manufacturing the same
36	Yeong suk Choi (2015) [49]	US20030189005 A1	Electrode composition for capacitive deionization device, and electrode for capacitive deionization device containing the same
37	Hyun Sung Choi (2016) [50]	US6580598 B2	Capacitive deionization apparatus
38	Jency DANIEL (2016) [51]	US20040174657 A1	Electrode for capacitive deionization
39	Tae Gong Ryu (2016) [52]	US20100140096 A1	System for recovering multiple kinds of ions



**Fig. 7.4**

(A) The electrical double-layer (EDL) model of Helmholtz and Parrin and (B) the potential profile with distance across the electrode-solution interface. *Modified from AlMarzooqi FA, Al Ghaferi AA, Saadat I, Hilal N, Application of capacitive deionisation in water desalination: a review. Desalination 342: 2014, 3–15.*

in the solution. The model also suggested that the capacitance does not change with potential and follows the relation:

$$C = \frac{dq}{dV} = \frac{\epsilon \epsilon_0 A}{d} \quad (7.1)$$

Gouy and Chapman in 1913 observed that the electrochemical capacitance strongly depends on the applied potential and the ionic concentration of the feed water. To understand this effect,

they incorporated the parameters of the thermal effect and the gradient of electron density on the double-layer model leading to the so-called diffuse charge model. In this model, the authors applied Maxwell Boltzmann statistics. The charge distribution of the ions in the solution was taken as a function of distance utilizing Thomas Fermi screening distance from the electrodes. The thermal effect was also incorporated in the model using the Boltzmann constant  $k$ . The Gouy–Chapman developed a model for capacitance accounting the effect of potential difference  $\phi M$  and temperature  $T$ :

$$C = (\cosh(ze_0\phi M)/2kT) \left( \sqrt{2 \epsilon_0 z^2 e_0^2 c_0 / kT} \right) \quad (7.2)$$

where  $z$  is an integer,  $e_0$  is the ionic cloud charge,  $\phi M$  is the potential difference,  $k$  is the Boltzmann constant,  $T$  is the temperature of the solution, and  $c_0$  is the ionic concentration in the solution.

The limitation of Gouy–Chapman model arises from the assumption of point charge ions and neglected the ion-ion interaction in the solution, which become significant at higher ionic concentrations. They also assumed that at the interface between the electrode and the bulk solution the dielectric constant is constant. Therefore, the model fails for highly charged diffuse layers. In 1924, Stern combined the Helmholtz–Perrin and Gouy–Chapman models into one as two capacitors in series with the total capacitance expressed as

$$\frac{1}{C} = \frac{1}{C_H} + \frac{1}{C_G} \quad (7.3)$$

where  $C$  is the total capacitance and subscripts H and G denote the Helmholtz–Perrin and Gouy–Chapman capacitance, respectively.

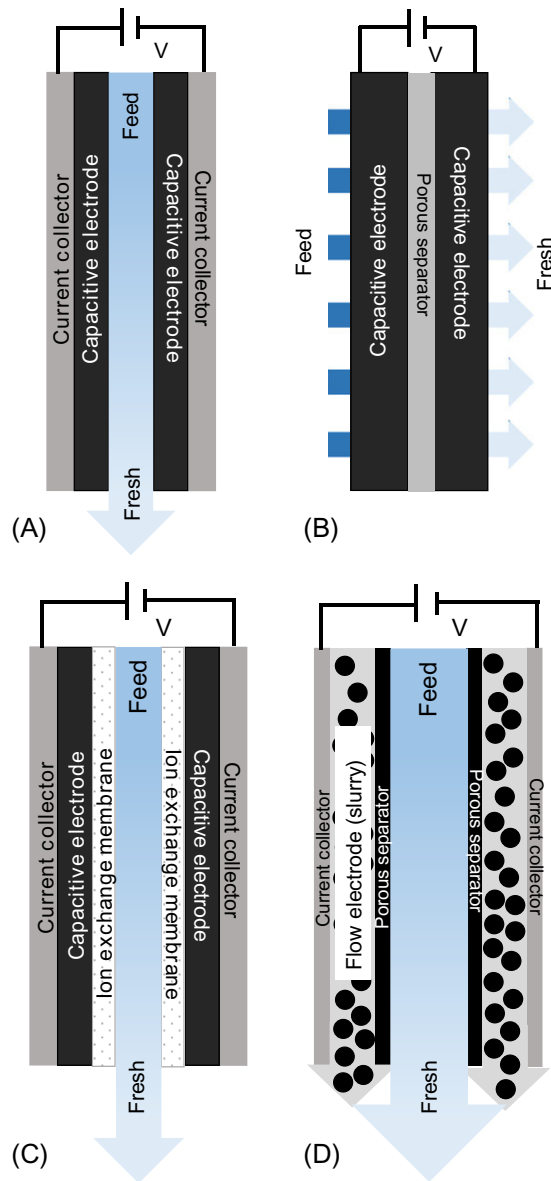
Stern's model, is a combination of the Helmholtz–Perrin and Gouy–Chapman model. He proposed that some ions adhere to the electrode in the internal layer as suggested by Helmholtz, giving an internal Stern layer, while some forms a Gouy–Chapman diffuse layer. Close to the electrodes, the Helmholtz–Perrin model dominates, while toward the bulk solution, Gouy–Chapman model dominates. The limitation in Stern's model was that he assumed that there is no interaction of ions and electrodes and therefore, it fails for metallic conductor and in application such as super-capacitors and Li ion battery. But in CDI, the mechanism of ion adsorption follows Stern's model, as the electrodes are inert toward the electrolytes. According to this model, if there are high Stern layer capacities, then it will allow for a high surface charge and, thereby, high salt adsorption capacity (SAC).

## 7.5 CDI Cell Architectures

The architectures of CDI cells have been a great interest of study in recent years. Two main types of electrode cell architectures are static and flow electrodes. Static electrode architecture includes flow between and flow-through electrodes and membrane CDI. Recent modification in

flow between electrode uses surface-modified anode called inverted CDI (i-CDI) [3]. Flow electrode architecture is feed in where a carbon slurry continuously flows to desalinate feed water [13]. Another new class of CDI architecture is electrostatic ion pumping and desalination through wires. The first and the most used CDI architecture till date is flow between electrodes and is also called flow by electrodes, introduced by Blair and Murphy in the early 1960, later by Oren and Soffer in the 1970s and Farmer et al. in 1996 [12a]. It consists of a pair of porous carbon electrodes, separated by a spacer and the saline water flows perpendicular to the applied potential as shown in Fig. 7.5A. This architecture is commonly used for fundamental studies to determine the maximum salt adsorption capacity (mSAC), to determine the performance of new and novel electrode materials and salt removal at various feed concentrations. Johnson et al. in the 1970s introduced the concept of flow-through electrodes, where the feed water is passed parallel to the applied electric potential and straight through the porous electrodes as shown in Fig. 7.5B. Avraham et al. in 2009 reintroduced the concept after almost 40 years, where they introduced the concept of charge efficiency [55]. Later, the same group compared the charging efficiency between flow-through and flow-between electrodes and claimed for faster cell charging for flow-through electrodes. Suss et al. in 2012 also claimed high efficiency and high rate of adsorption for CA as active electrode in the flow-through architecture [13]. The main advantage of this architecture over the other is the minimization of the spacer thickness from 200–500  $\mu\text{m}$  in flow between to 10  $\mu\text{m}$  in flow-through. As the spacer thickness is reduced, the ionic resistance of the cell is lowered with increased adsorption rate. This architecture requires the electrode material to be porous with both micropores (which enables fast mass transfer) and micropores (which helps in adsorption of ions).

One of the major developments in CDI cell architecture occurs with the introduction of IEX in front of the porous carbon electrodes called MCDI. The concept was first introduced by Andelman in 2004, where he called it as charge barrier flow capacitor [2]. Lee et al. in 2006 demonstrated the MCDI system for desalination of thermal power plant waste water [4], where they used an AEX on top of the anode and CEX on top of the cathode as shown in Fig. 7.5C. They claimed that the efficiency of MCDI was much higher than CDI (flow between) in the contest of salt removal capacity and rate. The membranes can be either placed as a free standing or can be coated over the electrodes. The thickness of the membrane while coating can be thinner and have higher salt removal efficiency with respect to stand-alone membranes [56]. The incorporation of membrane in front of the electrode has two advantages; first, the IEX blocks the co-ions to leave the electrode surface and thereby increases the SAC and second, during the desorption step, it fully flushes the counter-ions and therefore completely regenerated the electrode surface for the next adsorption cycle. In addition to this, membranes can be tuned for selective adsorption of ions having the same charge sign, which thereby, helps in selective removal of ions from a multiion system [16]. The architecture is most widely used in recent days and in the last one decade there have been a tremendous development of MCDI in its theoretical understanding [15, 57], membrane materials and in commercial applications.



**Fig. 7.5**

Different cell architectures used for CDI, (A) flow between, (B) flow-through, (C) MCDI, and (D) carbon flow electrodes.

A new class of cell architecture called carbon flow electrode/flow electrode capacitive deionization (FCDI) cell was introduced in 2013 by Jeon et al. [17] In this architecture, carbon slurry is passed through the electrode compartments having opposite charge as shown in Fig. 7.5D. The cations migrate toward the cathode and anions move toward the anode and get



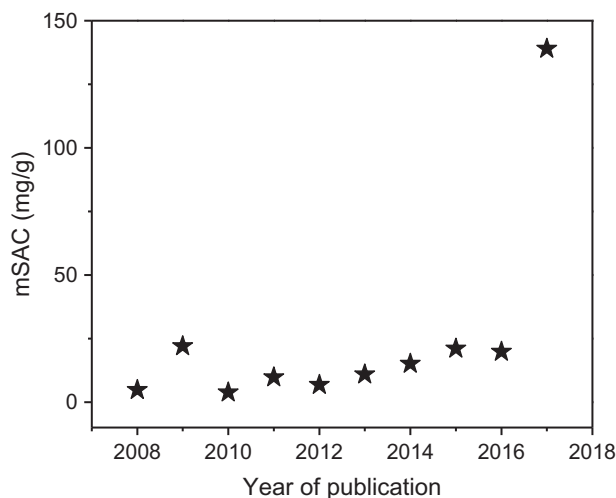
electroadsorbed. The main advantage of this architecture is that the carbon slurry is continuously passed through the compartment and the ions continuously get adsorbed and desorption happens in a different compartment downstream. In the case of static CDI, the ions are adsorbed until the electrodes get saturated and then the terminals have to be reversed to desorb the ions. The steps require complicated fluid handling and loss of efficiency as the adsorption and desorption cycle repeats at regular intervals. Another advantage of FCDI over static CDI is that the former introduces uncharged carbon particles continuously and thereby increases the desalination capacity as the effective capacitance increases. Therefore, FCDI can desalinate water of higher salinity and even sea water having TDS of 31 g/L with an efficiency of 95% and can overcome the limitation of conventional CDI as claimed by Jeon et al.

## 7.6 CDI Electrode Parameter Metrics

The field of CDI has enormously grown in the last one decade. Therefore, there is a need for the standardization of CDI cell performance. Different parameters which affect the efficiency of the electrodes are the active carbon materials having, porosity, pore size and pore volume, specific surface area, electrical conductivity, specific capacitance, and chemical inertness.

### 7.6.1 Maximum Salt Adsorption Capacity

In CDI, the most important parameter for defining the performance of a unit is the SAC. Soffer and Folman in 1972 first introduced SAC during a charge-discharge cycle [58]. The adsorption and desorption cycles can have different time duration, ranging from a few minutes, where the adsorption is fast but not complete and they can also be for a few hours where the saturation or equilibrium is reached for complete adsorption. For the latter, one can calculate the mSAC of an electrode, which is better known as equilibrium salt adsorption capacity (eqSAC). To reach the eqSAC, the cell potential and the salt concentration of the feed water should be constant throughout the adsorption cycle. At equilibrium, no more adsorption happens and can be calculated differently for batch mode and single-pass method. In batch mode, the salt removed is calculated by decrease in the salt concentration in the system multiplied with the total volume and is dependent on the initial salt concentration. For the single-pass method, the equilibrium concentration is reached when the input concentration of the feed water equals the output concentration over a time at a constant flow rate. The value of mSAC is calculated by the change in the effluent concentration over a time multiplied by the flow rate, that is, the total volume of water passed to reach the equilibrium. The SAC and mSAC is typically reported by calculating the total salt removal dividing with the total adsorbent weight and expressed in mg/g of the electrodes. Reports have been made either considering the total electrode weight (i.e., the carbon and the binder) or only with the active material (i.e., the porous carbon). Fig. 7.6 shows the maximum adsorption capacity of the electrode materials reported in years.



**Fig. 7.6**

The trend in maximum salt adsorption capacity (mSAC) of different materials over the last decade using different carbon-based electrode materials in batch study, at 500 mg/L of NaCl concentration.

Table 7.2 shows the adsorption capacity of different electrode materials at different concentrations of feed water at different modes of operation. It is important to note that the mSAC is only an electrode property and does not affect by any cell component when all other operational parameters are kept constant. This is an important and mostly used metrics in CDI community to assess the performance (electroadsorption of ions) of electrode material.

### 7.6.2 Average Salt Adsorption Rate (ASAR)

Another parameter which gives an insight into the performance of CDI cell is ASAR. The value of mSAC gives an indication for the amount of salt adsorbed by the CDI electrode but it gives no information for the adsorption kinetics. ASAR helps us to find the rate at which the salt is adsorbed on the electrodes and it is expressed in mg/g/min. Where, mg is the amount of salt adsorbed, g is the weight of the adsorbent, and min is the average time for the charging or discharging step. Unlike mSAC, ASAR depends on multiple external factors such as flow rate, applied potential, initial feed water concentration, and also the cell architecture. As, for example, if two systems have the same CDI electrode materials and also the thickness of the electrodes are equal then flow-through cell architecture have higher ASAR than flow-by electrode architecture. This is because in the flow-through system, the gap (i.e., the spacer distance) between the electrodes is smaller than that of flow-by system, thus lowering cell resistance and thus cell charging time. For the same electrode and at the same operational potential, ASAR will vary with the flow rate of the feed water. Applied potential plays an important role in deciding the ASAR value, ASAR will increase with the increase in the potential, reaches a maximum, and then decreases. The decrease later is due to the possibility of

Table 7.2 mSAC of different CDI electrode material at different initial salt concentration (mg/L)

Sl. No.	First Author (Year of Publication) [Ref.]	Journal	Materials	Initial Conc. (mg/L)	mSAC (mg/g)
1	J.C. Farmer (1996) [11]	J. Electrochem. Soc.	Carbon Aerogel (CA)	500	2.90
2	K. L. Yang (2001) [59]	Langmuir	CA	1000	2.00
3	K. Dai (2005) [60]	Mater. Lett.	MWCNTs	3000	1.70
4	S. Wang (2007) [61]	Sep. Purif. Technol.	MWCNTs	3500	9.35
5	P. Xu (2008) [62]	Water Res.	CA	2250	7.10
6	H. Li (2009) [63]	J. Mater. Chem.	Graphene	25	1.85
7	H. Li (2010) [64]	Environ. Sci. Technol.	Graphene-like nanoflakes	25	1.35
8	R. Zhao (2010) [65]	J. Phys. Chem. Lett.	Commercial activated carbon electrode	292	10.90
9	C. Tsouris (2011) [66]	Environ. Sci. Technol.	Resorsinol-based mesoporous carbon (MC)	5000	15.20
10	J. Landon (2012) [67]	J. Electrochem. Soc.	Carbon Xerogel	260	3.20
11	H. Wang (2012) [68]	J. Mater. Chem.	Graphene	86.9	0.88
12	Z. Wang (2012) [69]	Desalination	Graphene-CA	65	3.23
13	B. Jia (2012) [70]	Carbon	Sulfonated graphene Ns	250	8.60
14	M. E. Suss (2012) [71]	Energy Environ. Sci.	Microporous carbon aerogel monoliths	5800	10.20
15	D. Zhang (2012) [72]	Nanoscale	Graphene/mesoporous carbon	40	0.73
16	D. Zhang (2012) [73]	J. Mater. Chem.	Graphene/carbon nanotube	29	1.40
17	H. Li (2012) [74]	J. Mater. Chem.	RGO-AC	29	2.94
18	Z. Peng (2012) [75]	J. Mater. Chem.	Ordered mesoporous carbon-CNTs	46	0.63
19	X. Wen (2013) [76]	J. Mater. Chem. A	3D Graphene-based hierarchically porous carbon composites	25	6.18
20	G. Wang (2013) [77]	Sep. Purif. Technol.	Highly mesoporous AC	500	10.90
21	H Yin (2013) [78]	Adv. Mater.	Graphene-Aerogel	500	9.90
22	Z. Y. Yang (2014) [79]	Adv. Funct. Mater.	Sponge-templated graphene	106	4.95
23	Y. Liu (2014) [80]	J. Mater. Chem. A	CNRs	500	15.12
24	A. G. El-Deen (2014) [81]	Desalination	MnO <sub>2</sub> -Nanorods@graphene	~50	5.01
25	X. Xu (2015) [82]	Sci. Rep.	Graphene sponge	500	14.90
26	P. Nalenthiran (2015) [83]	ACS Appl. Mater. Interfaces	Cellulose-derived graphenic fibers	500	13.10
27	A. G. El-Deen (2015) [84]	Desalination	RGO/TiO <sub>2</sub>	300	9.10

**Table 7.2 mSAC of different CDI electrode material at different initial salt concentration (mg/L)—Cont'd**

Sl. No.	First Author (Year of Publication) [Ref.]	Journal	Materials	Initial Conc. (mg/L)	mSAC (mg/g)
28	G. Rasines (2015) [85]	Carbon	N-doped CA	1500	8.20
29	Xingtao Xu (2015) [86]	J. Mater. Chem. A	Graphene/CNT	500	18.70
30	R. Kumar (2016) [87]	Carbon	CA	800	10.54
31	A. S. Yasin (2016) [88]	Sep. Purif. Technol.	Graphene oxide/ZrO <sub>2</sub>	~50	4.55
32	H. Zhang (2016) [89]	RSC Adv.	Moderately oxidized graphene-CNT	500	8.45
33	S. Zhao (2016) [90]	Applied Surface Sci.	N-Doped porous hollow carbon spheres	500	12.95
34	W. Kong (2016) [91]	Nano Res.	Holey graphene hydrogel	5000	26.80
35	X. Xu (2016) [92]	J. Mater. Chem. A	hCNT/PCP	2000	20.50
36	T. Gao (2017) [93]	Desalination	Mesoporous carbons	250	4.80
37	D. Xu (2017) [94]	ACS Sustain. Chem. Eng.	N, P codoped meso-/microporous carbon	1000	20.78
38	S. Zhao (2017) [95]	RSC Adv.	micro/mesoporous carbon sheets	500	17.38
39	H. Wang (2017) [96]	ACS Sustain. Chem. Eng.	N-doped hollow multiyolk@shell carbon (HMYSC)	500	16.10
40	T. Wu (2017) [97]	Environ. Sci. Technol.	Porous carbon nanosheets (PCNSs)	500	15.60

Data after 1996 are given.

electrolysis above a certain potential for the electrode material. So, there is an optimum value where the ASAR is maximum. Also, the CDI electrode material can affect the value of measured ASAR, as for example, if the electrodes have larger mesopores than micropores, which allows higher salt sorption then the ASAR will be higher. Thus, ASAR is a combination of several factors and therefore it should be considered a cell component property rather than only electrode property.

### 7.6.3 Charge Storage Capacity

Along with mSAC and ASAR, the third metrics for CDI cell are the charge storage capacity, this metric is of a great importance in the super-capacitor community. This metric/parameter is obtained from the amount of current used vs. time during the charging and discharging cycles. Data for current are expressed in units of Amperes ( $A = C/s$ ), and it is integrated with respect to time to obtain the electric charge transfer between two oppositely charged electrodes of the cell

(in units of Coulombs, C). For obtaining the capacitance of a single electrode, the capacitive charge (i.e., C) is divided by the mass of a single electrode material and by half of the cell voltage (assuming cell symmetry), called as specific capacitance.

#### 7.6.4 Charge Efficiency

The electric charge accumulates on the electrodes during the adsorption cycle (i.e., charging) and is released during desorption cycle (i.e., discharging). To express the charge in moles, the accumulated electric charge is divided with Faraday ( $F = 96,485 \text{ C/mol}$ ) and is a measure of salt adsorption per cycle. Thus, charge efficiency can be defined as the ratio of adsorbed salt over charge. Avraham in 2009 [55] first used the term “charge efficiency” and Zhao et al. in 2009 [65] used the symbol  $\Lambda$  while describing charge efficiency.  $\Lambda$  depends on cell potential and feed water salt concentration. Generally,  $\Lambda$  increases when the charging voltage increases and decreases with decreasing salt concentration as shown in Fig. 7.7.

$\Lambda$  is an important parameter for evaluating the performance of the CDI cell. First, the energy requirement can be accounted from the value of  $\Lambda$ , a higher  $\Lambda$  means lower energy consumption. Zhao et al. in 2012 provided experimental data to compare the energy consumption in MCDI and CDI at constant voltage and constant current operation [57a]. For a constant charging voltage, MCDI has higher charge efficiency and therefore, consume lower energy than CDI. Second, during charging when the equilibrium is reached, equilibrium EDL theory can predict  $\Lambda$ , or vice versa [57a].

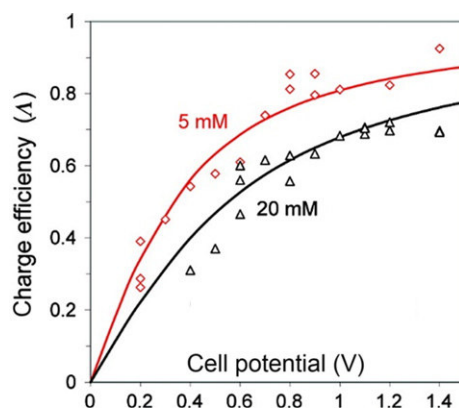


Fig. 7.7

Variation of charge efficiency  $\Lambda$  as a function of cell potential and feed water concentrations of 5 and 20 mM. Reproduced with permission from Zhao R, Biesheuvel PM, Miedema H, Bruning H, van der Wal A, Charge efficiency: a functional tool to probe the double-layer structure inside of porous electrodes and application in the modeling of capacitive deionization. *J. Phys. Chem. Lett.* 1(1): 2010, 205–210.

### 7.6.5 Porosity

Porosity is regarded as one of the most important factors for electrochemical capacitors and CDI electrodes. The efficiency of CDI electrodes, that is, the capacitance depends on the accessible pores and the pore sizes. According to the IUPAC, pores are classified into three types: macropores ( $>50\text{ nm}$ ), mesopores ( $2\text{--}50\text{ nm}$ ), and micropores ( $<2\text{ nm}$ ) [98]. Some reports suggest that the pore size less than  $0.5\text{ nm}$  [99] is not accessible for ion adsorption as the ions are in hydrated form in aqueous solutions. As per solvated ion adsorption theory, high energy of the order of kilojoules per mole is required to remove the hydrated shell [100]. Therefore, it was believed that a bimodal porosity containing both micro and mesopores is required in carbon material for enhanced capacitance and ion adsorption. Ion adsorption occurs in the micropores whereas the mesopores allows fast mass transport of electrolyte to the micropores. Depending upon the pore distribution, Hwang et al. proposed a theory of splitting of the capacitance in two different regimes of pores. For mesopores, a traditional EDL model was followed:

$$\frac{C}{A} = (\epsilon_r \epsilon_0) / \left( b^* \ln \left( \frac{b}{b-d} \right) \right) \quad (7.4)$$

where  $C$  is the capacitance,  $A$  is the specific surface area,  $b$  is the pore radius, and  $d$  is the distance of approach of the ions to the carbon electrodes. For micropores, it was assumed that the ions enter the pores gets desolvated and stack as a line, where cylindrical electrical wire model was followed:

$$\frac{C}{A} = \epsilon_r \epsilon_0 / b^* \ln \left( \frac{b}{a_0} \right) \quad (7.5)$$

where  $a_0$  is the desolvated ion size.

## 7.7 Emerging CDI Electrode Materials

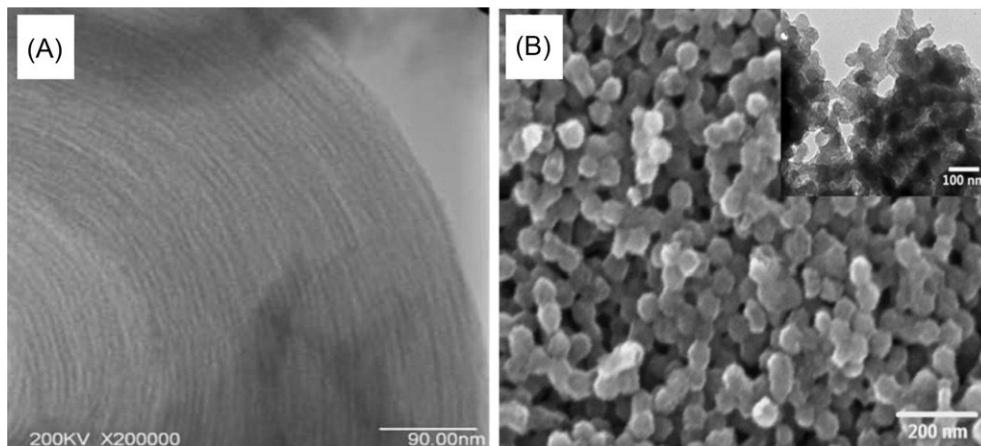
### 7.7.1 Activated Carbon

The most widely used material for CDI since the early 1970s is alternating current (AC). It is generally derived from raw materials such as petroleum, coconut shell, wood, rice husk, etc., having a surface area of  $500\text{--}2300\text{ m}^2/\text{g}$ , with tunable porosity and varying hardness [101]. Zou et al. in 2008 claimed that electrosorption capacity of activated carbon can be enhanced by chemical surface modification or by incorporating metal-oxide nanoparticles such as  $\text{TiO}_2$  [102]. Zeng et al. in 2017 reported that the electroadsorption capacity of commercially available AC can be increased 5.09 times by plasma treatment [using coupled plasma of Ar and  $10\% \text{ O}_2$ , at a pressure of  $4.0\text{ Torr}$ , resorsinol-formaldehyde (RF) power ranges from  $50$  to  $100\text{ W}$  for  $10\text{ min}$ ] [103]. Lado et al. in 2017 reported an abundant, low cost biowaste carbon material (Sugar Cane Bagasse Fly Ash) which after activation with  $\text{KOH}$  at  $800^\circ\text{C}$ , gave high

electrosorption capacity of 48%–74%. They claimed that the presence of small amounts of ether/alcohol functional groups increase the carbon hydrophilicity and hence, increase the SAC [104]. Alencherrya et al. in 2017 showed that the addition of silver and CNTs in AC enhances the electrical conductivity as well as the hydrophilicity, which in terms increase the electrosorption capacity by around twofolds [105]. Chen et al. in 2018 economically prepared ACs recycled from bitter-tea and palm shell wastes and was used for CDI electrodes and showed removal capacity up to 40% using 1000 ppm NaCl solution. They have modified the electrodes with Ag@C core shell nanoparticles to provide additional disinfection ability during desalination [106]. Yashin et al. in 2018 used N<sub>2</sub> and TiO<sub>2</sub>/ZrO<sub>2</sub> as a support for AC for enhancing the electrochemical performance [107].

### 7.7.2 Ordered Mesoporous Carbon

Zou et al. [108] in 2008 had prepared ordered mesoporous composite (OMC) and claimed that the CDI performance was better than AC. The pore size of the OMC material was found to be  $\sim 3.3$  nm which allows the salt ions to pass through the pores freely and the ordered mesostructure allows fast adsorption and desorption of Na<sup>+</sup> and Cl<sup>−</sup> ions. Li et al. in 2009 also found that the CDI efficiency of OMC doped with Ni salt is higher than that of AC. Transmission electron microscopy (TEM) image of OMC is shown in Fig. 7.8A [109]. In case of AC, some surfaces are unavailable for electroadsorption as the micropores are smaller than the hydrated radii of the ions. Tsouris et al. in 2011 prepared self-assembled mesoporous carbon



**Fig. 7.8**

(A) Transmission electron microscopy (TEM) image of ordered mesoporous composite (OMC) [109] and (B) scanning electron microscopy (SEM) image of MCs and the inset shows a TEM image of the same material [93]. Reproduced with permission from Gao T, Li H, Zhou F, Gao M, Liang S, Luo M, Mesoporous carbon derived from ZIF-8 for high efficient electrosorption. *Desalination* 108, 2017; Li L, Zou L, Song H, Morris G, Ordered mesoporous carbons synthesized by a modified sol–gel process for electrosorptive removal of sodium chloride. *Carbon* 47(3): 2009, 775–781.



using phenolic resins, such as resorcinol or phloroglucinol by sol-gel technique and then carbonization at 750°C [66]. They claimed that the performance of MC was superior to that of CA due to the fact that most of the pores in CA are micropores in the range of 10 Å which are not accessible for the adsorption of ions. Peng et al. in 2012 prepared OMC/CNT composites by the organic-inorganic self-assembly route. With a loading of 10% CNT, the material showed superior electroadsorption capacity and exhibits low energy consumption when compared with pristine OMC for CDI [75]. Wang et al. in 2013 had taken mesoporous activated carbon for CDI and showed that the electroadsorption capacity of the electrodes depended on the solution temperature. The capacity decreased with the increase in temperature [77]. Gao et al. in 2017 prepared MCs by direct carbonization of ZIF-8 at 1000°C in Ar/H<sub>2</sub> atmosphere. They got an adsorption capacity of 4.8 mg/g using 250 mg/L of NaCl solution but claimed that the theoretical mSAC can reach 17 mg/g according to the Langmuir adsorption isotherm. The scanning electron microscopy (SEM) image of MC is shown in Fig. 7.8B and the inset shows a TEM image [93].

### 7.7.3 Carbon Aerogel (CA)

The revolution of CDI electrodes came with the new class of carbon material called CAs in 1996 by Farmer et al. [11]. Traditionally, inorganic aerogels were prepared by hydrolysis and condensation of metal-alkoxides using sol-gel technique. Similar procedure was extended to form organic aerogels and xerogels using resorcinol (R) and formaldehyde (F)/melanin and formaldehyde to form cross-linked gels. These gels were dried and pyrolyzed in inert atmosphere at a temperature of 800–1500°C to form CA [110]. CA has high surface area (400–2600 m<sup>2</sup>/g), high electrical conductivity (~25–100 S/cm), high electrochemical stability in water and tunable porosity (the ratio of micro and mesopores).

Yang et al. in 2001 prepared CA electrodes and developed EDL model to predict the electroadsorption of ions. The adsorption largely depends on the pore size of the material. The smaller pores, that is, the micropores do not contribute to adsorption. As the feed water ion concentration increases, the cut-off pore width decreases. The cut-off pore width is found to decrease with increasing feed ion concentration and applied potential [59]. Jung et al. in 2007 prepared RF organic aerogel in a cost-effective route using acetone as a solvent exchanger and used ambient drying conditions. The solid was pyrolyzed after drying in N<sub>2</sub> atmosphere at 800°C. They have reported the material having high surface area of 610 m<sup>2</sup>/g, very high specific capacitance of 220 F/g, high electrical conductivity of 13.2 S/cm, high porosity of 80%, and low bulk density of 0.5 g/cm<sup>3</sup>. They have tested the CA electrodes at 50 mg/L NaCl solution at a flow rate of 400 mL/min at an applied potential difference of 1.5–1.7 V and claimed the removal efficiency was 92.8% and 97.6% at 1.5–1.7 V, respectively [111]. Xu et al. in 2008 had taken CA electrodes and showed the selectivity of I<sup>−</sup> is more in the presence of other ions like Br<sup>−</sup>, Cl<sup>−</sup>, etc. Therefore, they claimed that the technology can be used for iodine recovery from waste water [62].

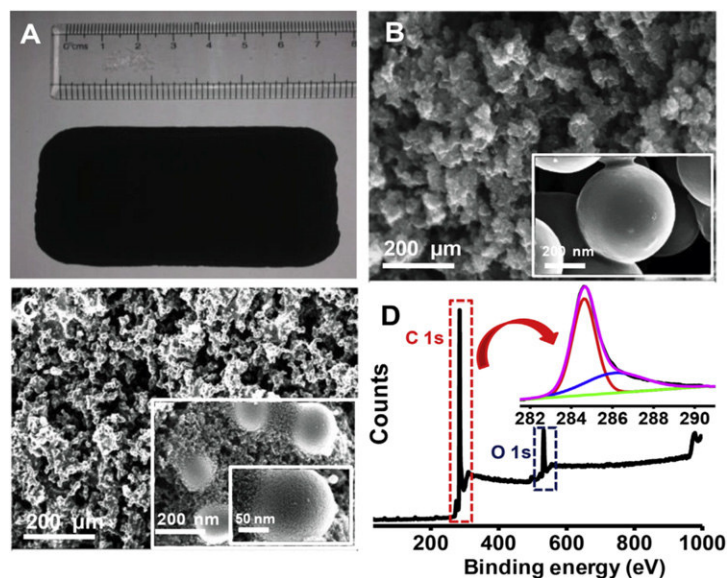


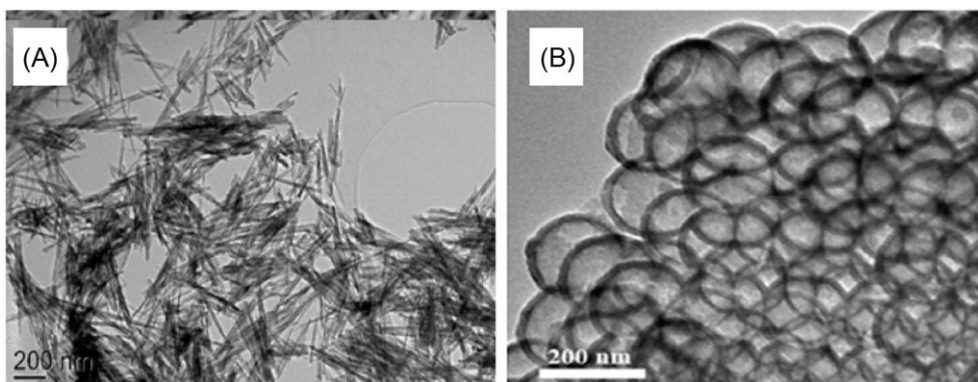
Fig. 7.9

(A) The photograph shows the as-prepared carbon aerogel (CA) block of dimension 7 cm (length)  $\times$  3 cm (width)  $\times$  1 cm (thick), field emission scanning electron microscopy (FESEM) images of (B) Si-CA and (C) CA, and (D) X-ray photoelectron spectroscopy (XPS) spectrum of CA showing the presence of carbon and oxygen. *Reproduced with permission from Kumar R, Gupta SS, Katiyar S, Raman VK, Varigala SK, Pradeep T., Sharma A, Carbon aerogels through organo-inorganic co-assembly and their application in water desalination by capacitive deionization. Carbon 99: 2016, 375–383.*

Rasines et al. in 2015 prepared N-doped CA polycondensation of resorcinol-formaldehyde-melamine mixtures [85]. Kumar et al. in 2016 prepared Si-CA using RF and tetraethyl orthosilicate (TEOS) as silica precursors. They dried the gel in ambient condition and carbonized it in inert atmosphere at 900°C. The carbonized product formed was Si-CA. CA was prepared subsequently by etching Si with 1 M KOH. Etching of Si enhances the porosity of the composites. Both Si-CA and CA were tested as CDI electrode materials and they showed high efficiency for salt removal with good regeneration property [87]. Spectroscopic and microscopic characterization data of the material are shown in Fig. 7.9.

#### 7.7.4 Other Carbon Derivatives

Poroda et al. in 2012 reported porous carbide-derived carbon material with tunable pore sizes as efficient CDI electrodes. The work emphasized that the adsorption capacity of any carbon material has a positive correlation with subnanometer pores (pore size less than 1 nm) [112]. Liu et al. in 2014 prepared carbon nanorods (CNRs) from nanocrystalline cellulose by heating at 1200°C under inert atmosphere [80]. TEM image of CNR is shown in Fig. 7.10A. CNRs shows high specific capacitance of 264.19 F/g, surface area of 864.10 m<sup>2</sup>/g and pore volume of



**Fig. 7.10**

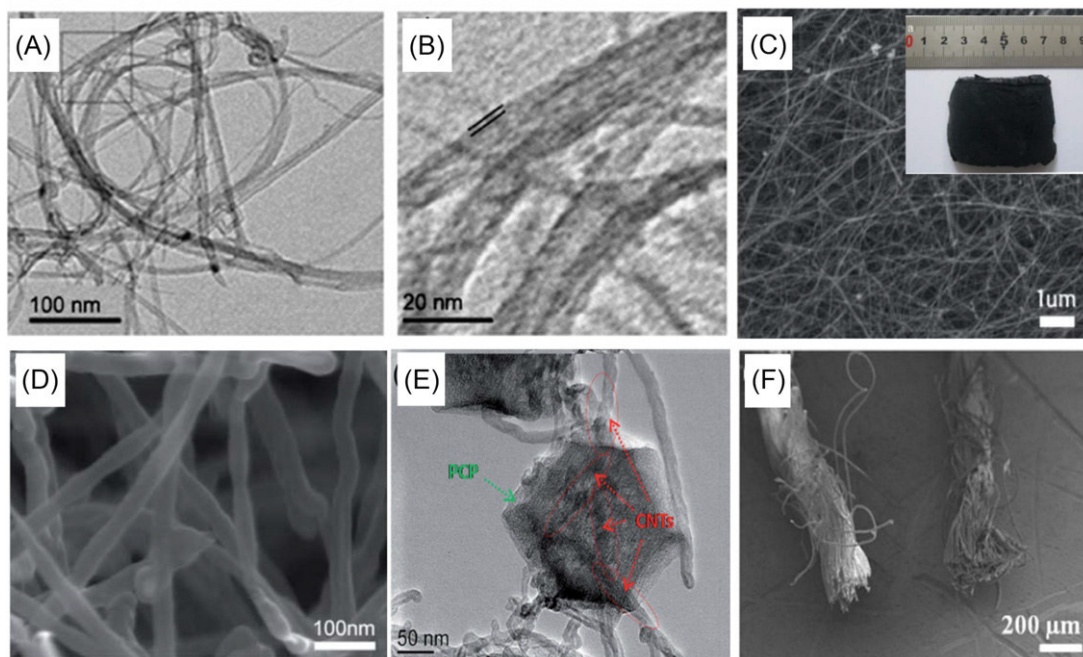
TEM image of (A) carbon nano rods [80] and (B) N-doped hollow carbon spheres [90]. Reproduced with permission from Liu Y, Pan L, Xu X, Lu T, Sun Z, Chua DH, Carbon nanorods derived from natural based nanocrystalline cellulose for highly efficient capacitive deionization. *J. Mater. Chem. A* 2(48): 2014, 20966–20972; Zhao S, Yan T, Wang H, Chen G, Huang L, Zhang J, Shi L, Zhang D, High capacity and high rate capability of nitrogen-doped porous hollow carbon spheres for capacitive deionization. *Appl. Surf. Sci.* 369: 2016, 460–469.

$0.47 \text{ cm}^3/\text{g}$ . The material shows high adsorption capacity of  $15.12 \text{ mg/g}$  due to large surface area and low charge transfer resistance. Zhao et al. prepared N-doped hollow carbon spheres as shown in TEM image in Fig. 7.10B. They used polystyrene (PS) spheres as hard templates and dopamine hydrochloride as carbon and nitrogen sources [90]. Recently, sustainable materials derived from biomass are of great interest because of low cost and abundance. The same group in 2017 prepared micro/mesoporous carbon sheets using watermelon peel as a carbon source [95], Wu et al. prepared porous carbon nanosheets using starch [97] and Xu et al. developed N and P co-doped carbon material from biomass with high specific surface area of  $2726 \text{ m}^2/\text{g}$  and 52% of mesopores [94].

### 7.7.5 Carbon Nanotubes (CNTs)

CNTs are a class of one-dimensional (1D) tubular carbon materials formed by rolling of graphene sheets. They are classified into single-walled carbon nanotubes (SWCNTs) and MWCNTs as per the number of layers. SWCNTs are formed by a single-layer graphene and MWCNTs are formed by multilayer graphitic carbon. CNTs can be metallic or semiconducting depending on how the sheets are rolled, which results in armchair, zig-zag, and chiral configuration [113]. The advantages of CNTs over other carbon materials are that they can carry high current density through the tubes without electronic scattering, that is, the charge transport occurs ballistically [113].

Yan et al. in 2012 prepared SWCNT and polyaniline (PANI) composites by in situ polymerization. The TEM images in Fig. 7.11A and B show that PANI forms a shell around SWCNT. The addition of PANI in SWCNT decreases the specific surface area due to the



**Fig. 7.11**

Microscopic characteristics of different carbon nanotube (CNT) composites. (A and B) TEM image of polyaniline (PANI)@CNT composite, PANI forms a shell over single-walled carbon nanotubes (SWCNTs) as shown in (B) [114]. (C) SEM image of CNT sponge [115], the inset shows a photograph of the same. (D) High-resolution scanning electron microscopy (HRSEM) image of CNT sponge showing network-like structure [115]. (E) HRTEM image of hierarchical porous CNT (hCNT)/porous carbon polyhedra (PCP) [92], both CNT and PCP are marked in the figure and (F) SEM image of pristine and CNT threads [116]. Reproduced with permission from Xu X, Wang M, Liu Y, Lu T, Pan L, Metal–organic framework-engaged formation of a hierarchical hybrid with carbon nanotube inserted porous carbon polyhedra for highly efficient capacitive deionization. *J. Mater. Chem. A* 4(15): 5467–5473, 2016. Yan C, Zou L, Short R, Single-walled carbon nanotubes and polyaniline composites for capacitive deionization. *Desalination* 290: 125–129, 2012. Wang L, Wang M, Huang Z-H, Cui T, Gui X, Kang F, Wang K, Wu D, Capacitive deionization of NaCl solutions using carbon nanotube sponge electrodes. *J. Mater. Chem.* 21(45): 2011, 18295–18299; Moronshing M, Subramaniam C, Scalable approach to highly efficient and rapid capacitive deionization with CNT-thread as electrodes. *ACS Appl. Mater. Interfaces* 9(46): 39907–39915, 2017.

removal of micropores but the mesopore volume increases appreciably, which in contrast increases the salt removal efficiency by 12% as compared with SWCNTs. They claimed that the improvement in the adsorption capacity is due to the pi-pi conjugation of the benzenoid chain of PANI and aromatic carbon skeleton of SWCNT [114]. Wang et al. in 2013 prepared CNT sponge electrodes by a chemical vapor deposition (CVD) process using 1,2 dichlorobenzene as carbon precursor and ferrocene as catalyst [115]. CDI cells were prepared using these CNT sponges without any use of binder. Fig. 7.11C shows the SEM image of CNT sponges.

High-resolution scanning electron microscopy (HRSEM) image in Fig. 7.11D shows continuous three-dimensional (3D) web structure and are randomly cross-linked with each other having 20–40 nm in diameter. The inset in Fig. 7.11C shows the photograph of a CNT sponge. They claimed the desalination capacity of the material to be 40 mg/g of electrodes, which was highest at that time.

Xu et al. prepared hierarchical porous CNT/porous carbon polyhedra (PCP) (hCNT/PCP) which is shown in Fig. 7.11E. Hybrid with CNTs and ZIF-8 showed that the material is a good candidate for effective CDI electrodes [92]. Moronshing et al. in 2017 had prepared CDI electrodes using CNT threads having specific surface area of 900 m<sup>2</sup>/g, electrical conductivity of 25 S/cm, specific capacitance of 27.2 F/g, and porosity of 0.7 and 3.0 nm with a hydrophilicity having contact angle of 25°. In a flow-through experiment using a single pair of electrodes, having the saline concentration of 50–1000 ppm, they have reported the highest electroadsorption capacity of 139 mg/g for the electrode [116]. SEM image of pristine thread (left) and CNT thread (right) is shown in Fig. 7.11F.

### 7.7.6 Graphene and Graphene-Based Composites

Since the discovery of graphene by Geim and Novoselev in 2004 [117], it has become subject of major interest. The one atom thick two-dimensional (2D) material with extraordinary electronic, thermal, and electrical properties made the material to be called as a “wonder” material. Graphene and its analogs due to its large surface area, high electrical conductivity, antibacterial property, and tuneable functionalization make the material a potential candidate in water purification applications. Overwhelming number of articles is published in the last decade using graphene as an adsorbent for water remediation.

Li et al. in 2010 first used graphene nano-flakes (GNFs) as a CDI electrode material and showed the electroadsorption capacity was better than that of AC. GNFs were prepared by modified Hummers’ method followed by reduction with hydrazine. They conducted CDI experiment with different cations and reported that the higher valence ions with smaller hydrated radii will be strongly adsorbed. The cations with same charge with smaller hydrated radii will be removed preferentially. They concluded that the electroadsorption capacity is in order  $\text{Fe}^{3+} > \text{Ca}^{2+} > \text{Mg}^{2+} > \text{Na}^+$  [118]. Till then many groups have worked with graphene and its composites for making novel and efficient electrode materials. Jia et al. in 2012 prepared graphene nanosheet (GN) from graphene oxide (GO) by a multistep process and used it as an electrode material for CDI. The TEM image of GNs is shown in Fig. 7.12A. The material has mean pore size of 3.3 nm, surface area of 464 m<sup>2</sup>/g, and specific capacitance of 149.8 F/g, the GNs electrodes show NaCl removal efficiency of 83.4% and electroadsorption capacity of 8.6 mg/g of electrode material [70]. Yin et al. in 2013 reported highly efficient CDI electrode materials using 3D graphene/metal oxide hybrid composites for the first time [78]. Wang et al. in same year prepared 3D macroporous graphene architecture (3DMGA), which shows high specific surface



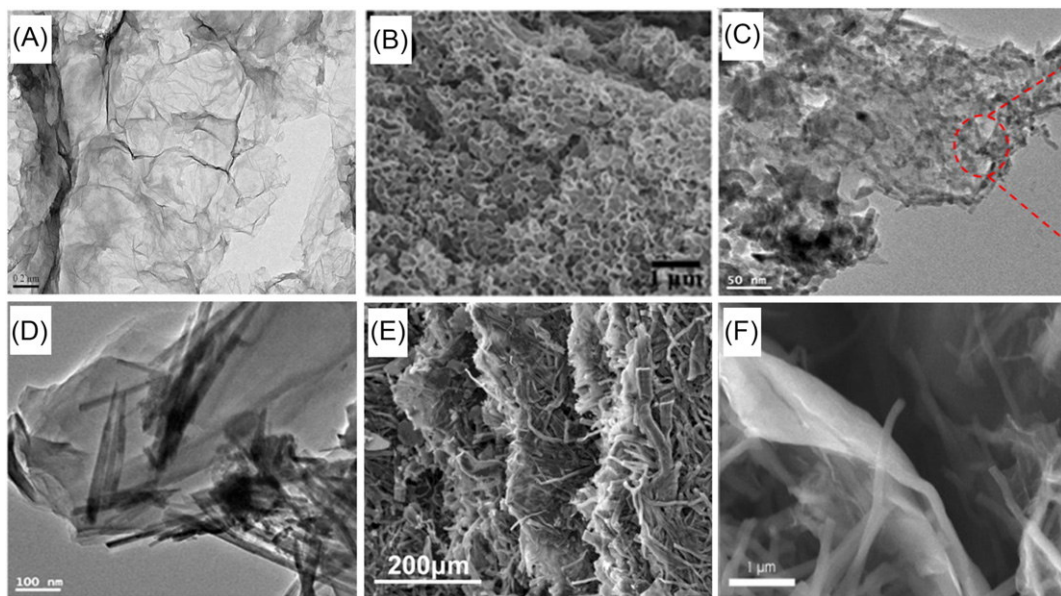


Fig. 7.12

Microscopic images of graphenic materials used for CDI electrodes: (A) TEM image graphene nanosheets (GNs) [70], (B) SEM image of three-dimensional (3D) macroporous graphene architecture [119], TEM images of (C) graphene@MnO<sub>2</sub> nanoparticles and (D) graphene@MnO<sub>2</sub> nanorods [81], (E) SEM image of cellulose-derived graphenic fibers [83], and (F) 3D composite of graphene@carbon fibers [120]. Reproduced with permission from Jia B, Zou L, Graphene nanosheets reduced by a multi-step process as high-performance electrode material for capacitive deionisation. *Carbon* 50(6):2315–2321, 2012; El-Deen AG, Barakat NAM, Kim HY, Graphene wrapped MnO<sub>2</sub>-nanostructures as effective and stable electrode materials for capacitive deionization desalination technology. *Desalination* 344:289–298, 2014; Pugazhenthiran N, Sen Gupta S, Prabhath A, Manikandan M, Swathy JR, Raman VK, Pradeep T, Cellulose derived graphenic fibers for capacitive desalination of brackish water. *ACS Appl. Mater. Interfaces* 7(36): 20156–20163, 2015. Luo G, Wang Y, Gao L, Zhang D, Lin T, Graphene bonded carbon nanofiber aerogels with high capacitive deionization capability. *Electrochim. Acta*; Li H, Liang S, Li J, He L, The capacitive deionization behaviour of a carbon nanotube and reduced graphene oxide composite. *J. Mater. Chem. A* 1(21): 6335–6341, 2013.

area and porosity for rapid ion and electron transport when used as CDI electrodes [119]. They prepared 3DMGA by mixing GO and PS, where PS was used as a sacrificial template, which was further dried and calcinized at elevated temperature in an inert atmosphere. The SEM image in Fig. 7.12B shows 3D nature of 3DMGA. Earlier the same group used pyridine to prepare graphene by thermal heating and showed its application in CDI electrodes [68].

El-Deen et al. in 2014 showed that the electroadsorption capacity of graphene increases when MnO<sub>2</sub> nanostructure was incorporate in it. Graphene-wrapped MnO<sub>2</sub> nanostructure was prepared by oxidation-reduction reaction using graphite and manganese sulfate as precursors. The oxidation graphite was done with ammonium peroxysulfate and hydrogen peroxide in the

presence of  $\text{MnSO}_4$  followed by reduction with piperidine under microwave irradiation. The morphology of graphene  $\text{MnO}_2$  nanostructure can be controlled by varying the microwave irradiation time from 15 to 30 min to form graphene@ $\text{MnO}_2$  nanorods and graphene@ $\text{MnO}_2$  nanorods, respectively, as shown in TEM images in Fig. 7.12C and D [81]. Pugazhentiran et al. in 2015 prepared cellulose-derived graphenic fibers using tissue paper. Tissue paper was taken along with graphite powder as a conducting agent and TEOS as a silica precursor and the mixture was pyrolyzed under  $\text{N}_2$  atmosphere at  $700^\circ\text{C}$ . Silica was then etched with aqueous KOH solution to enhance the porosity, especially the micropores in the carbon structure. The SEM image of graphite-reinforced carbon (GrC) is shown in Fig. 7.12E, fiber kind of nature of the material can be seen from the image. The as-prepared material was termed as GrC and was used as CDI electrodes without any kind of binder in a batch mode. GrC showed high electroadsorption property of 13.1 mg/g for 500 mg/L of NaCl solution with an excellent recyclability [83]. Hierarchical hole-enhanced 3D graphene assembly was prepared by Li et al. in 2017 [121] and showed the desalinating capacity of 8.0, 16.9, and 29.6 mg/g in aqueous NaCl concentrations of 80, 270, and 572 mg/L, respectively, at 2.0 V. Luo et al. in 2017 prepared a fascinating 3D porous structure consisting of 1D (i.e., nanofibers) and 2D (i.e., graphene) carbon nanomaterials as shown in Fig. 7.12F [120]. The composite was prepared by carbonization of electrospun polyacrylonitrile with GO sheets. The material showed an adsorption capacity of 15.7 mg/g in 500 mg/L NaCl solution and an electrochemical stability for 100 cycles.

## 7.8 Electrochemical Impedance Spectroscopy for CDI Electrodes

Impedance is the measure of the ability of a circuit to resist the flow of electrical current. The term impedance refers to the frequency dependence to current flow in a circuit. It assumes an AC of specific frequency in Hz. It can be expressed as

$$Z_\omega = \frac{E_\omega}{I_\omega} \quad (7.6)$$

where,  $Z_\omega$  is the impedance,  $E_\omega$  is the frequency-dependant potential, and  $I_\omega$  is the frequency dependant current.

Electrochemical impedance spectroscopy (EIS)/equivalent series resistance (ESR) is a great technique that uses a small amplitude AC signal to measure the impedance characteristics of electrodes or a cell. To measure the impedance spectrum of an electrochemical cell under test, the AC signal is scanned over a wide range of frequencies. EIS allows the study of capacitive, diffusion, and inductive processes which takes place in the electrochemical cell and even the electron transfer rate of a reaction unlike that of direct current (DC) techniques. EIS has multiple applications which includes in the area of coatings, batteries, fuel cells, photovoltaic, sensors, and biochemistry.



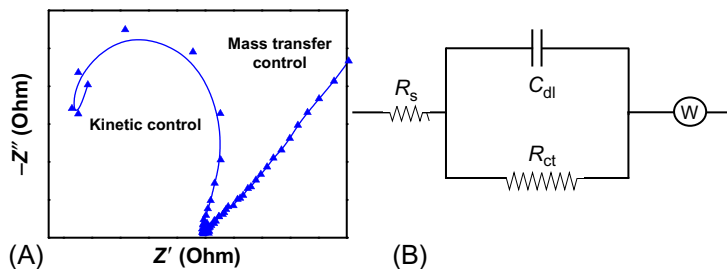


Fig. 7.13

(A) Nyquist plot of graphenic material prepared from cellulose and (B) the equivalent electrical circuit extracted from the plot in part (A). Unpublished data from the authors' laboratory.

EIS data can be represented as a complex plane (Nyquist) plot. Nyquist plot is defined as the “representation of the vector response of a feedback system (especially an amplifier) as a complex graphical plot showing the relationship between feedback and gain.” Nyquist plot is generally used for assessing the stability of the system with feedback. In the Cartesian coordinates, the real part is plotted in the X-axis ( $Z'$ ) and the imaginary part is plotted on the Y-axis ( $-Z''$ ).

A Nyquist plot for a graphenic material prepared from cellulose is shown in Fig. 7.13A. The Nyquist curve has two parts (i) head part (semicircle part) and (ii) tail (inclined line). A semicircle at high frequency and an inclined line at low frequency were found here.

Meng et al. [122] explained that from Nyquist plot we can know about the equivalent circuit of the electrodes as shown in Fig. 7.13B, where,  $R_s$  is the ohmic resistance,  $R_{ct}$  is the electrochemical charge transfer resistance,  $C_{dl}$  is the electrochemical double-layer capacitance, and  $W$  is the Warburg impedance.  $C_{dl}$  of the electrodes is given as follows:

$$C_{dl} = 1/T(j\omega)^\varphi \quad (7.7)$$

$$T = C_{dl}^\varphi (R_s^{-1} + R_{ct}^{-1})^{1-\varphi} \quad (7.8)$$

where  $\omega$  is the angular frequency (in rad/s) of the AC voltage and  $\varphi$  is the depression angle  $90(1 - \varphi)$  of the semicircle.  $T$  is a constant associated with the double-layer capacitance.

In the high-frequency region, the semicircle refers to the polarization resistance which includes the charge-transfer resistance between the electrodes and the salt solution interface. Wang et al. [123] in 2013 in the case of 3DMGAs electrode found a semicircle with small diameter which indicates the polarization resistance is relatively small. When the diameter of the semicircle is large as in the case of graphene, the charge transfer resistance is high.

Yang et al. [79] in 2014 showed Nyquist plot of sponge-templated graphene sheets (STGSs) displays a straight line which indicates a behavior characteristic of capacitive nature at the lower frequency region, which is attributed because of fast and easy diffusion of salt ions into

the 3D macropores. But in case of GNs an inclined line as compared with STGS, implies poor diffusion behavior of the ions. The intersecting point in the real axis (X-axis) of the Nyquist plots is referred to the value of the ESR, which includes the electrolyte resistance, electrical resistance between the current collector and the electrode material and the internal electrode. The ESR values obtained for STGS and for GN are 0.84 and 1.16  $\Omega$ , respectively. The ESR for STGS was quite small and is because of sufficient exfoliation due to sponge-templated strategy, indicating low internal resistance and fast charge/discharge rate which is appropriate for CDI application. Ahmed G. El-Deen et al. [124] in 2016 found that the carboxylic group ( $\text{COO}^{2-}$ ) rich 3D-activated porous graphene electrode (QC-3DAPGr) cell at high frequency (i.e., left side) shows lower intercepts with the X-axis and small semicircle diameter, indicating small intrinsic resistance of electrodes and low charge transfer resistance compared with all cell configurations. Hence, the asymmetric QC-3DAPGr electrode provides ideal capacitive behavior and lower internal resistances that can improve the desalination performance for CDI.

## 7.9 Energy Consumption of CDI in Comparison to RO

The current methods of desalinations are RO, electrodialysis, thermal evaporation, and CDI. Among these, RO is most popular, around 85% of desalination plants are based on this technique [125]. RO works on the principle to remove water from the dissolved solids using external pressure, whereas CDI removes ions producing clean water. The typical TDS in sea water is around 35,000 and 1000–4000 ppm for brackish water. Irrespective of the process, the minimum energy required (thermodynamically) for desalinating sea water and brackish water can be calculated theoretically. The minimum energy required for removing ions from a solution are 1.1 and 0.12 kWh/m<sup>3</sup>, respectively, for sea water and brackish water. In case of RO, the value depends on the input-output TDS concentration and water recovery [126]. If the ratio is 0.5 the minimum energy required will be 1.6 and 0.17 kWh/m<sup>3</sup>, respectively, and energy consumption increases to 2.0 and 0.21, respectively, if the ratio increases to 0.7. Zhao et al. listed out working RO plants in different parts of the world and seen that majority of the RO systems consumes energy around 2 kWh/m<sup>3</sup> with feed concentration below 3.5 g/L. If the feed concentration increases to 8 g/L, the energy consumption increases to 6.5 kWh/m<sup>3</sup> as listed for a RO plant in Lipari, Italy [127]. Besides energy requirement, the final cost of water depends on the size of the unit, operation, and maintenance. A smaller unit having a capacity to produce 1 million gallon of water per day (1 MGD), costs 1.3 \$/m<sup>3</sup>, whereas, a bigger unit of 10 MGD able to deliver water for 0.4 \$/m<sup>3</sup> [128]. Major operational cost related to RO is the replacement of the membranes too often.

As discussed earlier, CDI electroadsorb ions from the solution in the double layer formed at the electrodes when a potential difference is applied. For a parallel plate capacitor, the charge separation is electrostatic and depends on area of the plates and the distance of the separation as per the following equation:

$$C = \epsilon_0 \epsilon_r \frac{A}{d} \quad (7.9)$$

where  $C$  is the capacitance in F,  $\epsilon_0$  is the permittivity of free space ( $8.854 \times 10^{-12}$  F/m),  $\epsilon_r$  is the relative permittivity of the material between two plates,  $A$  is the area of each plates, and  $d$  is the distance of separation between the plates (in m).

The capacitors can be connected either parallel or in series and the equivalent capacitance ( $C_{eq}$ ) can be calculated by the following equations:

$$\text{Parallel: } C_{eq} = \sum C_n \quad (7.10)$$

$$\text{Series: } \left( \frac{1}{C_{eq}} \right) = \sum \frac{1}{C_n} \quad (7.11)$$

Therefore, the energy stored can be calculated as

$$E_{\text{stored}} = \frac{1}{2} CV^2 \quad (7.12)$$

where  $E$  is the energy (in J),  $C$  is the capacitance (in F), and  $V$  is the potential difference (in V).

Electrochemically, the capacitance can be calculated using cyclic voltammetry. The operational value is constrained to 1.2–1.5 V because of the redox potential of the water. Considering no Faradic reaction occurs, the capacitance can be directly calculated from the voltammogram and the sweep rate as per the following equation:

$$C = \int \frac{dq}{dV} = I \cdot \int \frac{dt}{dV} = \frac{I}{v} \quad (7.13)$$

where  $q$  is the charge (in C),  $V$  is the potential difference (in V),  $I$  is the current intensity (in A), and  $v$  is the sweep rate (V/s).

In case of CDI, as the energy can be easily recovered during the regeneration step. Thus, the net energy required is the difference between the charging (i.e., the adsorption step) and the discharging (i.e., the desorption step)

$$W_{\text{CDI}} = W_{\text{charging}} - W_{\text{discharging}} \quad (7.14)$$

The energy recovered during the discharging step makes the system more energetically favorable than other techniques. Still, much work is needed to develop in electronics and electrochemical methods to efficiently extract the regeneration energy. Since, this strategy can decrease the overall energy requirement of the system, it will be an essential and important part of CDI system in near future. Biesheuvel in 2009 gives a model for calculating maximum theoretical round-trip efficiency for CDI, which was 96% in the case [129]. The efficiency was independent of salt concentration and the regeneration cycle uses only 25% of water as that of

the adsorption cycle. Similarly, Anderson et al. in 2010 theoretically calculated the round-trip efficiency of CDI to produce  $1 \text{ m}^3$  of  $300 \text{ mg/L}$  of clean water from varying concentration ( $0.5\text{--}3.5 \text{ g/L}$ ) at  $1.2 \text{ V}$  was  $70\%\text{--}95\%$ .

In the experiments of Farmar et al. in the 1990s, the energy consumption was  $0.1 \text{ kWh/m}^3$  to desalinate brackish water. For brackish water (TDS less than  $2000 \text{ mg/L}$ ), CDI requires much less energy than that of RO even with a moderate efficiency of  $60\%\text{--}70\%$  as reported by Zhao et al. [127] If the efficiency of  $85\%$  can be attend then CDI will be much energy efficient than that of RO, not only for brackish water but also for sea water as well. Miller and Burke had reported that the round-trip efficiency for carbon-based super capacitor can be as high as  $95\%$  in cases [130].

## 7.10 CDI Technology in Market

The first recognized CDI company to be established was Voltea in 2008, situated in the United States and the Netherlands. They developed a tuneable water desalination technique using MCDI and named it as “CAPDI.” They have claimed that the water recovery rate was  $95\%$  and it lowers the waste water production by  $60\%$  as compared with other membrane-based technologies. They have different products ranging from industrial scale (Fig. 7.14) to a miniature version for domestic use named “DIUSE.” From then, different companies have come into existence and the most recognized ones are UR-WATER<sub>LLC</sub> in the United States



**Fig. 7.14**

A standard industrial-scale MCDI product developed by Voltea. Adapted from [voltea.com](http://voltea.com)

formed as a start up with Prof. Anderson, Atlantis Technologies in Canada, Idropan Dell'Orto in Italy, Ionic Engineering Technology Pvt. Ltd. in India, PowerTech Water in the United States and EcoloxTech, which came recently into the CDI market.

Atlantis Technologies claimed that their product removes impurities to 99% and can reduce salinity up to 100,000ppm with reduced maintenance. Idropan Dell'Orto formed by Tullio Servida have products named Plimmer 4G Alpha and Delta, where they claimed that a TDS of 2000 uS can be reduced to 70%–85% by a single pass and 85%–95% by double pass. They have different partners in countries such as EUROWATER in Denmark, ECOWATER in the United States, AquaSphere in India, and others in Russia, Tunasia, Australia, and Saudi Arabia. PowerTech Water founded in 2014 has just prepared the prototype and is ready for marketing. InnoDI is a new start-up from IIT Madras, established in 2017 and have launched their first domestic CDI product in the market in 2017. [Table 7.3](#) shows a list of CDI companies.

**Table 7.3 The leading CDI companies in market in 2018 and their location**

Sl. No.	Company	Inventors/MD	Technology	Year of Establish	Location
1	Voltea	Bryan Brister, Jonathan Hodes, Timothy Cavitt	MCDI/CAPDI	2008	Wasbeekerlaan 24, 2171 AE Sassenheim, The Netherlands
2	UR_WATER <sub>LLC</sub>	Mr. John Etter and Prof. Marc Anderson	Modified CDI	~2012	Madison, WI 53718, United States
3	Idropan Dell'Orto	Tullio Servida	MCDI	~2012	Via Valassina 19 20159 Milan, Italy
4	Atlantis Technologies	Patrick Curran, Brian Hill	Radial deionization	~2014	32932, Pacific Coast Hwy #14, Dana Point, CA 92629, United States
5	Current Water Technologies inc.	Dr. Gene S. Shelp	Electro-static deionization	~2016	70 Southgate Drive, Unit 4 Guelph, ON, Canada
6	Ionic Engineering Technology Pvt. Ltd.	K.V. Raman	CAPDI <sup>c</sup>	~2016	Ground Floor, B Wing, Mahalaxmi Heights, Mumbai, India
7	PowerTech Water, LLC	Dr. Cameron Lippert	Inverted-CDI	~2016	Lexington, KY, United States
8	InnoDI (An IITM incubated (company))	Tullio Servida, Vijay Sampath, Prof. T. Pradeep	MCDI	2017	Bangalore, India

## 7.11 Conclusions

The field of CDI has seen a tremendous growth in the last two decades. It has come out from the laboratories to commercial market as a product for water desalination. Different novel active carbon materials have come out in the last few years with high electroadsorption capacity with different cell architecture. Currently, it is possible to deliver water of any derived quality and quantity with CDI. Even the cost of clean water is comparable to RO. Thermodynamic energy requirement for desalination using capacitive electrodes is much less than the actual energy required. So, there is a scope for further improvement of thermodynamic efficiency in future [5].

## Acknowledgments

We acknowledge our colleagues who have contributed for the development of CDI technology in our laboratory. Department of Science and Technology for several grants, Government of India is thanked for the financial support.

## References

- [1] <http://www.un.org/News/Press/docs/2010/ga10967.doc.htm>.
- [2] Andelman, M.; Walker, G., Charge barrier flow-through capacitor. Google Patents 2004.
- [3] S. Porada, R. Zhao, A. van der Wal, V. Presser, P.M. Biesheuvel, Review on the science and technology of water desalination by capacitive deionization, *Prog. Mater. Sci.* 58 (8) (2013) 1388–1442.
- [4] J.-B. Lee, K.-K. Park, H.-M. Eum, C.-W. Lee, Desalination of a thermal power plant wastewater by membrane capacitive deionization, *Desalination* 196 (1) (2006) 125–134.
- [5] P. Długolecki, A. van der Wal, Energy recovery in membrane capacitive deionization, *Environ. Sci. Technol.* 47 (9) (2013) 4904–4910.
- [6] O.N. Demirel, R.M. Naylor, C.A. Rios Perez, E. Wilkes, C. Hidrovo, Energetic performance optimization of a capacitive deionization system operating with transient cycles and brackish water, *Desalination* 314 (2013) 130–138.
- [7] S. Evans, W. Hamilton, The mechanism of demineralization at carbon electrodes, *J. Electrochem. Soc.* 113 (12) (1966) 1314–1319.
- [8] G.W. Reid, A. Stevens, J. Abichandani, F. Townsend, M. Al-Awady, Field Operation of a 20 Gallons Per Day Pilot Plant Unit for Electrochemical Desalination of Brackish Water, U.S. Dept. of the Interior, Washington, DC, 1968.
- [9] J. Newman, R.G. Wilbourne, A.W. Venolia, A.M. Johnson, C. Marquardt, United States, The Electrosorb Process for Desalting Water, U.S. Dept. of the Interior, Washington, DC, 1970, p. iii 31 p.
- [10] A.M. Johnson, J. Newman, Desalting by means of porous carbon electrodes, *J. Electrochem. Soc.* 118 (3) (1971) 510–517.
- [11] J.C. Farmer, D.V. Fix, G.V. Mack, R.W. Pekala, J.F. Poco, Capacitive deionization of NaCl and NaNO<sub>3</sub> solutions with carbon aerogel electrodes, *J. Electrochem. Soc.* 143 (1) (1996) 159–169.
- [12] (a)Farmer, J., Method and apparatus for capacitive deionization, electrochemical purification, and regeneration of electrodes. Google Patents: 1995;(b)Farmer, J. C., Method and apparatus for capacitive deionization and electrochemical purification and regeneration of electrodes. Google Patents: 1999;(c)Tran, T. D.; Farmer, J. C.; Murguia, L., Method and apparatus for capacitive deionization and electrochemical purification and regeneration of electrodes. Google Patents: 2001.
- [13] Suss, M. E.; Baumann, T. F.; Bourcier, W. L.; Spadaccini, C.; Stadermann, M.; Rose, K.; Santiago, J. G., Flow-through electrode capacitive desalination. Google Patents 2012.

- 
- [14] T. Welgemoed, C. Schutte, Capacitive deionization technology: an alternative desalination solution, *Desalination* 183 (1–3) (2005) 327–340.
  - [15] P. Biesheuvel, A. Van der Wal, Membrane capacitive deionization, *J. Membr. Sci.* 346 (2) (2010) 256–262.
  - [16] Y.-J. Kim, J.-H. Choi, Selective removal of nitrate ion using a novel composite carbon electrode in capacitive deionization, *Water Res.* 46 (18) (2012) 6033–6039.
  - [17] S.-I. Jeon, H.-R. Park, J.-G. Yeo, S. Yang, C.H. Cho, M.H. Han, D.K. Kim, Desalination via a new membrane capacitive deionization process utilizing flow-electrodes, *Energy Environ. Sci.* 6 (5) (2013) 1471–1475.
  - [18] M. Andelman, Ionic group derivitized nano porous carbon electrodes for capacitive deionization, *J. Mater. Sci. Chem. Eng.* 02 (03) (2014) 7.
  - [19] Nyberg, E. D., Electrochemically assisted ion exchange. Google Patents 1998.
  - [20] Andelman, M. D., Energy and weight efficient flow-through capacitor, system and method. Google Patents 2001.
  - [21] Andelman, M. D., Charge barrier flow-through capacitor. Google Patents 2002.
  - [22] Inoue, H.; Yamanaka, K.; Tamura, M.; Yoshida, S.; Nakamura, H., Ion exchanger. Google Patents 2003.
  - [23] Shiue, L. R.; Sun, A.; Shiue, C. C.; Hsieh, F. C.; Hsieh, Y. H.; Jou, J. J., Deionizers with energy recovery. Google Patents 2003.
  - [24] Yang, H. J.; Kang, H.; Song, T.; Kim, C. H., Electrode for capacitive deionization, capacitive deionization device and electric double layer capacitor including the electrode. Google Patents 2010.
  - [25] Yang, H. J.; Kang, H.; KIM, K.; KIM, J., Transition metal/carbon nanotube composite and method of preparing the same. Google Patents 2010.
  - [26] Yang, H. J.; Kang, H.; Song, T.; Kim, C. H., Integrated electrode-current collector sheet for capacitive deionization, capacitive deionization device and electric double layer capacitor having the same. Google Patents 2013.
  - [27] Altaee, A., Capacitive deionization. Google Patents 2010.
  - [28] KNAPP, S.; Leffew, M., Method of regenerating a capacitive deionization cell. Google Patents 2010.
  - [29] Kang, K. S.; Choi, J. H., Capacitive electrode for deionization, and electrolytic cell using same. Google Patents 2012.
  - [30] Kim, C. H.; Kang, H.; Yang, H. J.; Kim, H., Capacitive deionization device. Google Patents 2011.
  - [31] Kang, K. S.; Son, W. K.; Choi, J. H.; Park, N. S.; Kim, T. I., Ion-selective capacitive deionization composite electrode, and method for manufacturing a module. Google Patents 2012.
  - [32] Ramaprabhu, S.; Mishra, A. K., Methods and systems for separating ions from fluids. Google Patents 2012.
  - [33] Averbek, D. J.; Tallon, R. M.; Boedeker, B. A., Ion removal using a capacitive deionization system. Google Patents 2017.
  - [34] Averbek, D. J.; Tallon, R. M.; Boedeker, B. A., Regeneration of a capacitive deionization system. Google Patents 2017.
  - [35] Sun, Z.; Pan, L.; Li, H.; Sun, Y., Membrane enhanced deionization capacitor device. Google Patents 2013.
  - [36] Andelman, M. D., Polarized electrode for flow-through capacitive deionization. Google Patents 2012.
  - [37] Jung, M. I. I.; Ko, Y. C.; JEONG, I. J.; Mingming, Y.; Yeo, H. S., Capacitive deionization apparatus. Google Patents 2013.
  - [38] Jeong, J. S.; Kim, H. S.; PARK, D. H.; Ham, D. J.; Kang, H. R., Capacitive deionization apparatus and methods of treating fluid using the same. Google Patents 2014.
  - [39] Kang, K. S.; Son, W. K.; Kim, T. I.; Kim, M. Y., Method of manufacturing capacitive deionization electrode having ion selectivity and CDI electrode module including the same. Google Patents 2013.
  - [40] ABRAMI, A.; TAMBURINI, F., Method and plant for the reduction of the concentration of pollutants and/or valuable elements in the water. Google Patents 2014.
  - [41] Simon, P.; Taberna, P. L.; Daffos, B.; Iwama, E.; Tzedakis, T.; Gogotsi, Y.; Hatzell, K.; Gogotsi, O., Method and device to remove ions from an electrolytic media, such as water desalination, using suspension of divided materials in a flow capacitor. Google Patents 2014.
  - [42] Cho, M. D.; Kim, H. S.; JEONG, J. S., Composition for electrode of capacitive deionization apparatus, and electrode including same. Google Patents 2017.
  - [43] Yang, Y. S.; Kim, J. E.; Kim, H. S.; Lee, S. J.; Kang, H. R.; JEONG, J. S., Capacitive deionization electrodes, capacitive deionization apparatuses including the same, and production methods thereof. Google Patents 2017.



- [44] Jeong, J. S.; Kim, H. S.; Cho, M. D.; Kang, H. R., Regeneration methods of capacitive deionization electrodes. Google Patents 2015.
- [45] Choi, Y. S.; Lee, S. J.; Jeong, J. S., Composition for electrode of capacitive deionization apparatus, and electrode including same. Google Patents 2015.
- [46] Cai, Z.; Schwannecke, J. K.; Anderson, D. J.; Taylor, R. M., Capacitive deionization system, electrode pack and method for operating the system. Google Patents 2015.
- [47] Atieh, M. A.; Laoui, T., Fabrication of carbon nanotube membranes. Google Patents 2017.
- [48] Liu, P. I.; Chung, L. C.; Liang, T. M.; Horng, R. Y.; Shao, H.; Chen, R. S.; Fan, H. T.; Fang, C. H.; Chang, M. C., Binder for capacitive deionization electrode and method for manufacturing the same. Google Patents 2017.
- [49] Choi, Y.; Lim, J. W., Electrode composition for capacitive deionization device, and electrode for capacitive deionization device containing the same. Google Patents 2017.
- [50] Choi, H. S.; Choi, S. H.; Hwang, S. H.; Choi, W.; Kim, S., Capacitive deionization apparatus. Google Patents 2017.
- [51] DANIEL, J.; Ghosh, S.; Rajanarayana, V., Electrode for capacitive deionization. Google Patents 2017.
- [52] Ryu, T. G.; Kim, B. G.; Ryu, J. H.; Park, I. S.; Hong, H. J.; Chung, K. S., System for recovering multiple kinds of ions. Google Patents 2017.
- [53] F.A. AlMarzooqi, A.A. Al Ghaferi, I. Saadat, N. Hilal, Application of capacitive deionisation in water desalination: a review, *Desalination* 342 (2014) 3–15.
- [54] H. Helmholtz, Helmholtz's theory of double electric layers, *J. Frankl. Inst.* 115 (4) (1883) 310.
- [55] E. Avraham, M. Noked, Y. Bouhadana, A. Soffer, D. Aurbach, Limitations of charge efficiency in capacitive deionization II. On the behavior of CDI cells comprising two activated carbon electrodes, *J. Electrochem. Soc.* 156 (10) (2009) 157–162.
- [56] Y.-J. Kim, J.-H. Choi, Improvement of desalination efficiency in capacitive deionization using a carbon electrode coated with an ion-exchange polymer, *Water Res.* 44 (3) (2010) 990–996.
- [57] (a) R. Zhao, P.M. Biesheuvel, A. van der Wal, Energy consumption and constant current operation in membrane capacitive deionization, *Energy Environ. Sci.* 5 (11) (2012) 9520–9527; (b) P. Biesheuvel, R. Zhao, S. Porada, A. Van der Wal, Theory of membrane capacitive deionization including the effect of the electrode pore space, *J. Colloid Interface Sci.* 360 (1) (2011) 239–248.
- [58] A. Soffer, M. Folman, The electrical double layer of high surface porous carbon electrode, *J. Electroanal. Chem. Interfacial Electrochem.* 38 (1) (1972) 25–43.
- [59] K.-L. Yang, T.-Y. Ying, S. Yiacoumi, C. Tsouris, E.S. Vittoratos, Electrosorption of ions from aqueous solutions by carbon aerogel: an electrical double-layer model, *Langmuir* 17 (6) (2001) 1961–1969.
- [60] K. Dai, L. Shi, J. Fang, D. Zhang, B. Yu, NaCl adsorption in multi-walled carbon nanotubes, *Mater. Lett.* 59 (16) (2005) 1989–1992.
- [61] S. Wang, D. Wang, L. Ji, Q. Gong, Y. Zhu, J. Liang, Equilibrium and kinetic studies on the removal of NaCl from aqueous solutions by electrosorption on carbon nanotube electrodes, *Sep. Purif. Technol.* 58 (1) (2007) 12–16.
- [62] P. Xu, J.E. Drewes, D. Heil, G. Wang, Treatment of brackish produced water using carbon aerogel-based capacitive deionization technology, *Water Res.* 42 (10) (2008) 2605–2617.
- [63] H. Li, T. Lu, L. Pan, Y. Zhang, Z. Sun, Electrosorption behavior of graphene in NaCl solutions, *J. Mater. Chem.* 19 (37) (2009) 6773–6779.
- [64] H. Li, L. Zou, L. Pan, Z. Sun, Novel graphene-like electrodes for capacitive deionization, *Environ. Sci. Technol.* 44 (22) (2010) 8692–8697.
- [65] R. Zhao, P.M. Biesheuvel, H. Miedema, H. Bruning, A. van der Wal, Charge efficiency: a functional tool to probe the double-layer structure inside of porous electrodes and application in the modeling of capacitive deionization, *J. Phys. Chem. Lett.* 1 (1) (2010) 205–210.
- [66] C. Tsouris, R. Mayes, J. Kiggans, K. Sharma, S. Yiacoumi, D. DePaoli, S. Dai, Mesoporous carbon for capacitive deionization of saline water, *Environ. Sci. Technol.* 45 (23) (2011) 10243–10249.
- [67] J. Landon, X. Gao, B. Kulengowski, J.K. Neathery, K. Liu, Impact of pore size characteristics on the electrosorption capacity of carbon xerogel electrodes for capacitive deionization, *J. Electrochem. Soc.* 159 (11) (2012) A1861–A1866.

- [68] H. Wang, D. Zhang, T. Yan, X. Wen, L. Shi, J. Zhang, Graphene prepared via a novel pyridine–thermal strategy for capacitive deionization, *J. Mater. Chem.* 22 (45) (2012) 23745–23748.
- [69] Z. Wang, B. Dou, L. Zheng, G. Zhang, Z. Liu, Z. Hao, Effective desalination by capacitive deionization with functional graphene nanocomposite as novel electrode material, *Desalination* 299 (2012) 96–102.
- [70] B. Jia, L. Zou, Graphene nanosheets reduced by a multi-step process as high-performance electrode material for capacitive deionisation, *Carbon* 50 (6) (2012) 2315–2321.
- [71] M.E. Suss, T.F. Baumann, W.L. Bourcier, C.M. Spadaccini, K.A. Rose, J.G. Santiago, M. Stadermann, Capacitive desalination with flow-through electrodes, *Energy Environ. Sci.* 5 (11) (2012) 9511–9519.
- [72] D. Zhang, X. Wen, L. Shi, T. Yan, J. Zhang, Enhanced capacitive deionization of graphene/mesoporous carbon composites, *Nanoscale* 4 (17) (2012) 5440–5446.
- [73] D. Zhang, T. Yan, L. Shi, Z. Peng, X. Wen, J. Zhang, Enhanced capacitive deionization performance of graphene/carbon nanotube composites, *J. Mater. Chem.* 22 (29) (2012) 14696–14704.
- [74] H. Li, L. Pan, C. Nie, Y. Liu, Z. Sun, Reduced graphene oxide and activated carbon composites for capacitive deionization, *J. Mater. Chem.* 22 (31) (2012) 15556–15561.
- [75] Z. Peng, D. Zhang, L. Shi, T. Yan, High performance ordered mesoporous carbon/carbon nanotube composite electrodes for capacitive deionization, *J. Mater. Chem.* 22 (14) (2012) 6603–6612.
- [76] X. Wen, D. Zhang, T. Yan, J. Zhang, L. Shi, Three-dimensional graphene-based hierarchically porous carbon composites prepared by a dual-template strategy for capacitive deionization, *J. Mater. Chem. A* 1 (39) (2013) 12334–12344.
- [77] G. Wang, B. Qian, Q. Dong, J. Yang, Z. Zhao, J. Qiu, Highly mesoporous activated carbon electrode for capacitive deionization, *Sep. Purif. Technol.* 103 (2013) 216–221.
- [78] H. Yin, S. Zhao, J. Wan, H. Tang, L. Chang, L. He, H. Zhao, Y. Gao, Z. Tang, Three-dimensional graphene/metal oxide nanoparticle hybrids for high-performance capacitive deionization of saline water, *Adv. Mater.* 25 (43) (2013) 6270–6276.
- [79] Z.Y. Yang, L.J. Jin, G.Q. Lu, Q.Q. Xiao, Y.X. Zhang, L. Jing, X.X. Zhang, Y.M. Yan, K.N. Sun, Sponge-templated preparation of high surface area graphene with ultrahigh capacitive deionization performance, *Adv. Funct. Mater.* 24 (25) (2014) 3917–3925.
- [80] Y. Liu, L. Pan, X. Xu, T. Lu, Z. Sun, D.H. Chua, Carbon nanorods derived from natural based nanocrystalline cellulose for highly efficient capacitive deionization, *J. Mater. Chem. A* 2 (48) (2014) 20966–20972.
- [81] A.G. El-Deen, N.A.M. Barakat, H.Y. Kim, Graphene wrapped MnO<sub>2</sub>-nanostructures as effective and stable electrode materials for capacitive deionization desalination technology, *Desalination* 344 (2014) 289–298.
- [82] X. Xu, L. Pan, Y. Liu, T. Lu, Z. Sun, D.H. Chua, Facile synthesis of novel graphene sponge for high performance capacitive deionization, *Sci. Rep.* (5) (2015). srep08458.
- [83] N. Pugazhenthiran, S. Sen Gupta, A. Prabhath, M. Manikandan, J.R. Swathy, V.K. Raman, T. Pradeep, Cellulose derived graphenic fibers for capacitive desalination of brackish water, *ACS Appl. Mater. Interfaces* 7 (36) (2015) 20156–20163.
- [84] A.G. El-Deen, J.-H. Choi, C.S. Kim, K.A. Khalil, A.A. Almajid, N.A. Barakat, TiO<sub>2</sub> nanorod-intercalated reduced graphene oxide as high performance electrode material for membrane capacitive deionization, *Desalination* 361 (2015) 53–64.
- [85] G. Rasines, P. Lavela, C. Macías, M.C. Zafra, J.L. Tirado, J.B. Parra, C.O. Ania, N-doped monolithic carbon aerogel electrodes with optimized features for the electrosorption of ions, *Carbon* 83 (2015) 262–274.
- [86] X. Xu, Y. Liu, T. Lu, Z. Sun, D.H. Chua, L. Pan, Rational design and fabrication of graphene/carbon nanotubes hybrid sponge for high-performance capacitive deionization, *J. Mater. Chem. A* 3 (25) (2015) 13418–13425.
- [87] R. Kumar, S.S. Gupta, S. Katiyar, V.K. Raman, S.K. Varigala, T. Pradeep, A. Sharma, Carbon aerogels through organo-inorganic co-assembly and their application in water desalination by capacitive deionization, *Carbon* 99 (2016) 375–383.
- [88] A.S. Yasin, H.O. Mohamed, I.M. Mohamed, H.M. Mousa, N.A. Barakat, Enhanced desalination performance of capacitive deionization using zirconium oxide nanoparticles-doped graphene oxide as a novel and effective electrode, *Sep. Purif. Technol.* 171 (2016) 34–43.
- [89] H. Zhang, P. Liang, Y. Bian, Y. Jiang, X. Sun, C. Zhang, X. Huang, F. Wei, Moderately oxidized graphene–carbon nanotubes hybrid for high performance capacitive deionization, *RSC Adv.* 6 (64) (2016) 58907–58915.

- [90] S. Zhao, T. Yan, H. Wang, G. Chen, L. Huang, J. Zhang, L. Shi, D. Zhang, High capacity and high rate capability of nitrogen-doped porous hollow carbon spheres for capacitive deionization, *Appl. Surf. Sci.* 369 (2016) 460–469.
- [91] W. Kong, X. Duan, Y. Ge, H. Liu, J. Hu, X. Duan, Holey graphene hydrogel with in-plane pores for high-performance capacitive desalination, *Nano Res.* 9 (8) (2016) 2458–2466.
- [92] X. Xu, M. Wang, Y. Liu, T. Lu, L. Pan, Metal–organic framework-engaged formation of a hierarchical hybrid with carbon nanotube inserted porous carbon polyhedra for highly efficient capacitive deionization, *J. Mater. Chem. A* 4 (15) (2016) 5467–5473.
- [93] T. Gao, H. Li, F. Zhou, M. Gao, S. Liang, M. Luo, Mesoporous carbon derived from ZIF-8 for high efficient electrosorption, *Desalination* (2017).
- [94] D. Xu, Y. Tong, T. Yan, L. Shi, D. Zhang, N. P-co-doped meso-/microporous carbon derived from biomass materials via a dual-activation strategy as high-performance electrodes for deionization capacitors, *ACS Sustain. Chem. Eng.* (2017).
- [95] S. Zhao, T. Yan, Z. Wang, J. Zhang, L. Shi, D. Zhang, Removal of NaCl from saltwater solutions using micro/mesoporous carbon sheets derived from watermelon peel via deionization capacitors, *RSC Adv.* 7 (8) (2017) 4297–4305.
- [96] H. Wang, T. Yan, L. Shi, G. Chen, J. Zhang, D. Zhang, Creating nitrogen-doped hollow multiyolk@ shell carbon as high performance electrodes for flow-through deionization capacitors, *ACS Sustain. Chem. Eng.* 5 (4) (2017) 3329–3338.
- [97] T. Wu, G. Wang, Q. Dong, F. Zhan, X. Zhang, S. Li, H. Qiao, J. Qiu, Starch derived porous carbon nanosheets for high-performance photovoltaic capacitive deionization, *Environ. Sci. Technol.* 51 (16) (2017) 9244–9251.
- [98] K.S.W. Sing, D.H. Everett, R.A.W. Haul, L. Moscou, R.A. Pierotti, J. Rouquerol, T. Siemieniowska, Reporting physisorption data for gas/solid systems, in: G. Ertl, H. Knözinger, F. Schüth, J. Weitkamp (Eds.), *Handbook of Heterogeneous Catalysis*, Wiley Online Library, 2008, <https://doi.org/10.1002/9783527610044.hetcat0065>.
- [99] H. Shi, Activated carbons and double layer capacitance, *Electrochim. Acta* 41 (10) (1996) 1633–1639.
- [100] Y. Marcus, Thermodynamics of solvation of ions. Part 5.—Gibbs free energy of hydration at 298.15 K, *J. Chem. Soc. Faraday Trans. 87* (18) (1991) 2995–2999.
- [101] J. Gamby, P.L. Taberna, P. Simon, J.F. Fauvarque, M. Chesneau, Studies and characterisations of various activated carbons used for carbon/carbon supercapacitors, *J. Power Sources* 101 (1) (2001) 109–116.
- [102] L. Zou, G. Morris, D. Qi, Using activated carbon electrode in electrosorptive deionisation of brackish water, *Desalination* 225 (1-3) (2008) 329–340.
- [103] A. Zeng, M. Shrestha, K. Wang, V.F. Neto, B. Gabriel, Q.H. Fan, Plasma treated active carbon for capacitive deionization of saline water, *J. Nanomater.* 2017 (2017) 8.
- [104] J.J. Lado, R.L. Zornitta, F.A. Calvi, M. Martins, M.A. Anderson, F.G.E. Nogueira, L.A.M. Ruotolo, Enhanced capacitive deionization desalination provided by chemical activation of sugar cane bagasse fly ash electrodes, *J. Anal. Appl. Pyrolysis* 126 (Suppl. C) (2017) 143–153.
- [105] T. Alencherry, A. Naveen, S. Ghosh, J. Daniel, R. Venkataraghavan, Effect of increasing electrical conductivity and hydrophilicity on the electrosorption capacity of activated carbon electrodes for capacitive deionization, *Desalination* 415 (2017) 14–19.
- [106] P.A. Chen, H.C. Cheng, H.P. Wang, Activated carbon recycled from bitter-tea and palm shell wastes for capacitive desalination of salt water, *J. Clean. Prod.* 174 (Suppl. C) (2018) 927–932.
- [107] A.S. Yasin, I.M. Mohamed, H.M. Mousa, C.H. Park, C.S. Kim, Facile synthesis of TiO<sub>2</sub>/ZrO<sub>2</sub> nanofibers/nitrogen co-doped activated carbon to enhance the desalination and bacterial inactivation via capacitive deionization, *Sci. Rep.* 8 (1) (2018) 541.
- [108] L. Zou, L. Li, H. Song, G. Morris, Using mesoporous carbon electrodes for brackish water desalination, *Water Res.* 42 (8) (2008) 2340–2348.
- [109] L. Li, L. Zou, H. Song, G. Morris, Ordered mesoporous carbons synthesized by a modified sol–gel process for electrosorptive removal of sodium chloride, *Carbon* 47 (3) (2009) 775–781.
- [110] R.W. Pekala, C.T. Alviso, F.M. Kong, S.S. Hulsey, Aerogels derived from multifunctional organic monomers, *J. Non-Cryst. Solids* 145 (1992) 90–98.

- [111] H.-H. Jung, S.-W. Hwang, S.-H. Hyun, K.-H. Lee, G.-T. Kim, Capacitive deionization characteristics of nanostructured carbon aerogel electrodes synthesized via ambient drying, *Desalination* 216 (1-3) (2007) 377–385.
- [112] S. Porada, L. Weinstein, R. Dash, A. van der Wal, M. Bryjak, Y. Gogotsi, P.M. Biesheuvel, Water desalination using capacitive deionization with microporous carbon electrodes, *ACS Appl. Mater. Interfaces* 4 (3) (2012) 1194–1199.
- [113] R.H. Baughman, A.A. Zakhidov, W.A. De Heer, Carbon nanotubes—the route toward applications, *Science* 297 (5582) (2002) 787–792.
- [114] C. Yan, L. Zou, R. Short, Single-walled carbon nanotubes and polyaniline composites for capacitive deionization, *Desalination* 290 (2012) 125–129.
- [115] L. Wang, M. Wang, Z.-H. Huang, T. Cui, X. Gui, F. Kang, K. Wang, D. Wu, Capacitive deionization of NaCl solutions using carbon nanotube sponge electrodes, *J. Mater. Chem.* 21 (45) (2011) 18295–18299.
- [116] M. Moronshing, C. Subramaniam, Scalable approach to highly efficient and rapid capacitive deionization with CNT-thread as electrodes, *ACS Appl. Mater. Interfaces* 9 (46) (2017) 39907–39915.
- [117] K.S. Novoselov, A.K. Geim, S.V. Morozov, D. Jiang, Y. Zhang, S.V. Dubonos, I.V. Grigorieva, A.A. Firsov, Electric field effect in atomically thin carbon films, *Science* 306 (5696) (2004) 666–669.
- [118] H. Li, L. Zou, L. Pan, Z. Sun, Using graphene nano-flakes as electrodes to remove ferric ions by capacitive deionization, *Sep. Purif. Technol.* 75 (1) (2010) 8–14.
- [119] H. Wang, D. Zhang, T. Yan, X. Wen, J. Zhang, L. Shi, Q. Zhong, Three-dimensional macroporous graphene architectures as high performance electrodes for capacitive deionization, *J. Mater. Chem. A* 1 (38) (2013) 11778–11789.
- [120] G. Luo, Y. Wang, L. Gao, D. Zhang, T. Lin, Graphene bonded carbon nanofiber aerogels with high capacitive deionization capability, *Electrochim. Acta* 260 (2018) 656–663.
- [121] J. Li, B. Ji, R. Jiang, P. Zhang, N. Chen, G. Zhang, L. Qu, Hierarchical hole-enhanced 3D graphene assembly for highly efficient capacitive deionization, *Carbon* 129 (2018) 95–103.
- [122] F. Meng, Q. Zhao, X. Na, Z. Zheng, J. Jiang, L. Wei, J. Zhang, Bioelectricity generation and dewatered sludge degradation in microbial capacitive desalination cell, *Environ. Sci. Pollut. Res.* 24 (6) (2017) 5159–5167.
- [123] H. Li, S. Liang, J. Li, L. He, The capacitive deionization behaviour of a carbon nanotube and reduced graphene oxide composite, *J. Mater. Chem. A* 1 (21) (2013) 6335–6341.
- [124] A.G. El-Deen, R.M. Boom, H.Y. Kim, H. Duan, M.B. Chan-Park, J.-H. Choi, Flexible 3D nanoporous graphene for desalination and bio-decontamination of brackish water via asymmetric capacitive deionization, *ACS Appl. Mater. Interfaces* 8 (38) (2016) 25313–25325.
- [125] R. Borsani, S. Rebagliati, Fundamentals and costing of MSF desalination plants and comparison with other technologies, *Desalination* 182 (1) (2005) 29–37.
- [126] M.A. Anderson, A.L. Cudero, J. Palma, Capacitive deionization as an electrochemical means of saving energy and delivering clean water. Comparison to present desalination practices: will it compete? *Electrochim. Acta* 55 (12) (2010) 3845–3856.
- [127] R. Zhao, S. Porada, P.M. Biesheuvel, A. van der Wal, Energy consumption in membrane capacitive deionization for different water recoveries and flow rates, and comparison with reverse osmosis, *Desalination* 330 (2013) 35–41.
- [128] I.C. Karagiannis, P.G. Soldatos, Water desalination cost literature: review and assessment, *Desalination* 223 (1-3) (2008) 448–456.
- [129] P. Biesheuvel, Thermodynamic cycle analysis for capacitive deionization, *J. Colloid Interface Sci.* 332 (1) (2009) 258–264.
- [130] J.R. Miller, A.F. Burke, Electrochemical capacitors: challenges and opportunities for real-world applications, *Electrochem. Soc. Interface* 17 (1) (2008) 53.

# Lectures Delivered

1. Reactions between nanoparticles, Conference on Advances in Catalysis for Energy and Environment – CACEE-2018 at TIFR, Mumbai, India, January 10-12, 2018.
2. Reactions between nanoparticles, ACS on Campus, the American Chemical Society's premier outreach program hosting professional development events at University of Delhi, India on Monday, February 5 and IIT Roorkee, India on Wednesday, February 7, 2018.
3. From ions to functional materials, 29<sup>th</sup> James Waters Symposium, Pittcon, Orlando, February 26, 2018.
4. Clean water using advanced materials: Science, technology, incubation and industry, RENEW Innovation Lecture, University at Buffalo, New York, USA, February 28, 2018.
5. Reactions between nanoparticles, International Conference on Nanoscience and Nanotechnology (ICONSAT), Bengaluru, India, March 23, 2018.
6. Materials to clean water: Science, technology, incubation and industry, NIT Calicut, India, March 28, 2018.
7. Infinite possibilities of the infinitesimal, Science Academies Refresher Course on Nanoscience and its Applications, K. S. Rangasamy College of Technology, Tiruchengode, India, April 16, 2018.
8. Reactions between nanoparticles, Science Academies Refresher Course on Nanoscience and its Applications, K. S. Rangasamy College of Technology, Tiruchengode, India, April 17, 2018.
9. Clusters: The interface of molecules and materials, Academy Refresher Course Saiva Bhanu Khsatriya College, Aruppukottai, Tamil Nadu, India, May 7, 2018.
10. Nanostructures for clean water: From science to devices, Academy Refresher Course Saiva Bhanu Khsatriya College, Aruppukottai, Tamil Nadu, India, May 8, 2018.

11. Molecular chemistry of monolayer protected noble metal clusters, Asian Symposium on Nanoscience & Nanotechnology, Plenary Lecture, University of Tokyo, Japan, May 12, 2018.
12. Molecular chemistry of monolayer protected noble metal clusters, Research Institute for Electronic Science, Hokkaido University, Japan, May 15, 2018.
13. Nanostructures for clean water: From science to devices, Centre for Interdisciplinary Studies, Kolkata, India, June 11, 2018.
14. Clean water using advanced materials: Science, technology, incubation and industry, CSIR-IMMT, India, June 27, 2018.
15. Reactions between noble metal clusters, International Conference on Chemical Bonding, Lihue, Hawaii, July 13-17, 2018.
16. Chair of a session - introductory remarks, Gordon Research Conference in Green Chemistry held at the Rey Don Jaime Grand Hotel Castelldefels, Spain, July 28 - August 3, 2018.
17. Reactions between noble metal clusters, Chemical Frontiers Goa @ 10, August 19-22, 2018.
18. Atomically precise nanoparticles of noble metals: Emerging frontiers, Tosoh Corporation R&D Center, Japan, August 27, 2018.
19. Reactions between nanoparticles, ACS On Campus, NIT Calicut, India, September 7, 2018.
20. Reactions between nanoparticles, Inorganic and Physical Chemistry, Indian Institute of Science, Bengaluru, India, September 13, 2018.
21. From materials to clean water: Growing companies from wet labs, IISER Tirupati, India, September 14, 2018.
22. Reactions between nanoparticles, One Day Symposium on Recent Advances in Nanoscience and Technology, Department of Atomic and Molecular Physics, MAHE, India, September 24, 2018.

23. Reactions between nanoparticles, CiHS - 2018, IIT Madras, Chennai, India, September 28, 2018.
24. Reactions between nanoparticles, International Conference on Recent Trends in Materials Science and Technology (ICMST-2018), IIST, Thiruvananthapuram, India, October 10-13, 2018.
25. Advanced materials for clean water, 9<sup>th</sup> MRS Trilateral Conference on Advances in Nanomaterials: Energy, Water & Healthcare (9<sup>th</sup> MRSTC), CeNS, Bengaluru, October 22-24, 2018.
26. Advanced materials for clean water, AICTE-QIP, Civil Engineering Department, IIT Madras, Chennai, India, November 13, 2018.
27. Atomically precise nanoparticles of noble metals: Emerging frontiers, HNB Garhwal University, Srinagar Garhwal, Uttarakhand, India, November 17, 2018.
28. Atomically precise materials, Emerging Frontiers in Chemical Sciences (EFCS) – 2018, organized by Farook College, November 23-24, 2018.
29. Reactions between nanoparticles, TWAS 14<sup>th</sup> General Conference & 28<sup>th</sup> General Meeting, Trieste, Italy, November 27-29, 2018.
30. Advanced materials for clean water, Dipartimento di Chimica, Politecnico di Milano, Milan, Italy, November 30, 2018.
31. Nanotechnologies for clean water, 10<sup>th</sup> Bengaluru India Nano, Bengaluru, India, December 5-7, 2018.
32. Water for Life – through materials, Industry academia collaboration for social impact, Mumbai, India, December 10, 2018.
33. Atomically precise nanoparticles, International conference on chemistry and physics of materials, St. Thomas College, Thrissur, India, December 19, 2018.



# Patents/Technology

## Patent Applications

1. Aqueous composition for durable and extremely efficient water repelling superhydrophobic materials at ambient condition thereof, T. Pradeep, Avijit Baidya, Azhar Ganayee and Jakka Ravindran Swathy, 201741036772, October 17, 2017, complete specification filed on October 16, 2018.
2. Method of making nanoparticles of precise isotopic composition by rapid isotopic exchange, T. Pradeep, Papri Chakraborty, Abhijit Nag, Esma Khatun, Ganapati Natarajan and Ganesan Paramasivam, 201741037349, October 23, 2017, complete specification filed on October 23, 2018.
3. Monolayer protected noble metal clusters as standards for negative ion mass spectrometry, T. Pradeep, Ananya Baksi, Papri Chakraborty, Abhijit Nag, Debasmita Ghosh and Shridevi Bhat, 201841029515, August 6, 2018.
4. An enhanced carbon dioxide sorbent nanofiber membrane and a device thereof, T. Pradeep, Anangha Yatheendran, Ramesh Kumar and Arun Karthik, 201841031076, August 20, 2018.
5. A process for low temperature, low pressure synthesis of gas hydrates, T. Pradeep, Jyotirmoy Ghosh, Rabin Rajan J. Methikkalam, Radha Gobinda Bhuin, Gopi Ragupathy, Nilesh Choudhary and Rajnish Kumar, 201841049836, December 29, 2018.
6. Synthesis of protein protected luminescent metal clusters and retaining the bioactivity of the protein, T. Pradeep, Debasmita Ghosh, Mohammad Bodiuzzaman, Anirban Som, Ananya Baksi, Atanu Ghosh, and Jyotirmoy Ghosh, 201841049925, December 31, 2018.

## **PCT applications**

1. Multilayer multifunctional nasal filter, T. Pradeep, Arun Karthick S, Srikrishnarka Pillalamarri, Vishal Kumar, Ramesh Kumar, Sathvik Ajay, IDF 1527, 201741007433, March 2, 2017. Filed as PCT/IN2017/50108, March 01, 2018.
2. Method of making nanometer thin sheets of metals in air, T. Pradeep, Depanjan Sarkar, Anirban Som, C. K. Manju, IDF 1594, 201741036233, October 12, 2017. Filed as PCT/IN2018/50654, October 10, 2018.
3. Method for creating nanopores in MoS<sub>2</sub> nanosheets by chemical drilling for disinfection of water under visible light, T. Pradeep, Depanjan Sarkar, Anirban Som, Biswajit Mondal and Jakka Ravindran Swathy, PCT/IN2018/050677, October 18, 2018.
4. Method of field induced photoionization of molecules using low power pointer laser in laser assisted paper spray ionization mass spectrometry (LAPSI MS), T. Pradeep, Pallab Basuri, Depanjan Sarkar, Ganesan Paramasivam, IDF 1614, 201741040383, November 13, 2017. Filed as PCT/IN2018/50734, November 13, 2018.
5. A method of identifying isomers of curcumin and preferential stabilization of one of them, T. Pradeep, Abhijit Nag, Papri Chakraborty, Ananya Baksi, Ganapati Natarajan, IDF 1609, 201741040570, November 14, 2017. Filed as PCT/IN2018/50749, November 14, 2018.
6. Removal of lead from waste water using nanoscale MoS<sub>2</sub>, T. Pradeep, Biswajit Mondal, Ananthu Mahendranath, Anirban Som, Sandeep Bose, Tripti Ahuja, Avula Anil Kumar, Jyotirmoy Ghosh, IDF 1584, 201741044447 filed on December 11, 2017. Filed as PCT/IN2018/50814, December 05, 2018.
7. A portable water filtration device for removing impurities from water using contaminant-specific purification cartridges, T Pradeep, Ramesh Kumar, IDF1638, 201741047404, December 30, 2017. Filed as PCT/IN2018/050895, December 29, 2018.
8. An integrated CDI electrode, T. Pradeep, Md. Rabiul Islam, Soujit Sengupta, Srikrishnarka Pillalamarri and Sourav Kanti Jana, filed as PCT/IN2018/050894, December 29, 2018.

## **Patents Granted**

### **Indian**

1. One container gravity fed storage water purifier, Indian patent application, T. Pradeep, Amrita Chaudhary, M. Udhaya Sankar and Anshup, 1522/CHE/2011, granted as patent no. 293515 dated February 28, 2018.
2. A method of preparing self-assembled manganese-zinc oxide nanosheet granular composite for pathogens and heavy metals free water, Amrita Chaudhary, T. Saraladevi, Shihabudheen M. Maliyekkal, M. Udhaya Sankar, Anshup and T. Pradeep, filed as 2433/CHE/2010 on August 23, 2010. Granted as patent number 300346 on August 28, 2018.
3. Removal of pesticides from water using graphenic materials, T. Pradeep, Shihabudeen Maliyekkal and T. S. Sreeprasad, filed as 3587/CHE/2011 on October 19, 2011. Granted as patent number 302262 on October 17, 2018.
4. Method of extraction of silver by glucose, T. Pradeep, Ananya Baksi, Mounika Gandhi, Swathi Chaudhari, Soumabha Bag, filed as 6730/CHE/2014 on December 30, 2014, full specification filed on December 28, 2015. Granted as patent number 302630 on October 30, 2018.
5. A method for preparing of monolayer protected silver clusters as antibacterial agents, T. Pradeep, Indranath Chakraborty, Udayabhaskararao Thumu and G. K. Deepesh, 485/CHE/2013, February 4, 2013. Patent No. 303077, granted on November 13, 2018.
6. Facile synthesis of highly anisotropic gold nanoflowers: a new class of infrared absorbing nanomaterials with applications in labeling and printing, P. R. Sajanlal and T. Pradeep, provisional application 2262/CHE/2008 dated September 17, 2008. Patent No. 304127, granted on December 6, 2018.
7. Dechlorination of lindane and its removal from water using graphene nanocomposites, T. Pradeep, Soujit Sengupta, Indranath Chakraborty and Shihabudheen M. Maliyekkal, 5988/CHE/2013 filed on December 20, 2013. Patent No. 304213, granted on December 7, 2018.

8. Water filled organic templated metal oxide/hydroxide/oxyhydroxide particle network for water purification and a device thereof, T. Pradeep, M. Udhaya Sankar, Amrita Chaudhary, A. Anil Kumar, Anshup, 525/CHE/2013 filed on February 17, 2013. Granted as patent number 304463, on December 14, 2018.
9. Application of nanoscale Zinc Oxide in peanut crop, T. Pradeep, T. N. V. K. V. Prasad, P. Sudhakar, T. S. Sreeprasad and P. R. Sajanlal, 3586/CHE/2011, October 19, 2011. Granted as 304588 on December 18, 2018.

### **PCT Patents Granted**

1. Coated mesoflowers for molecular detection and smart barcode materials, T. Pradeep, Ravindranathan Sajanlal Panikkanvalappil, PCT/IB2014/61096. April 30, 2014. Granted as US patent US9903821 B2 on February 27, 2018.
2. A sustained silver release composition for water purification, T. Pradeep, Anshup, Amrita Chaudhary, M. Udhaya Sankar, and S.Gayathri, PCT/IB2012/001079, filed on March 25, 2012. Granted as US patent US2018186667 A1 on July 05, 2018.
3. Multilayer organic-templated-boehmite-nanoarchitecture for fluoride removal, T. Pradeep, A. Leelavathi, Amrita Chaudhary, M. Udhaya Sankar and Anshup, PCT/IB2012/002885. Granted in Australia as patent number 2012342118 on April 26, 2018. In United states as patent no. US 10035131 B2 on July 31, 2018.
4. Detection of quantity of water flow using quantum clusters, T. Pradeep, Leelavathi A, M. Udhaya Sankar, Amrita Chaudhary, Anshup, T. Udayabhaskararao, Issued US patent no. US 10041925 B2, issued on August 7, 2018. Issued in Japan patent no. JP6367182 B2 on August 8, 2018.
5. Reduced graphene oxide-based-composites for the purification of water, T. Pradeep, M. M. Shihabudheen and T. S. Sreeprasad, PCT/IB2011/002740, September 2, 2011. Granted as US patent US2018221850 A1 on August 09, 2018.

## **Technology Development**

AquEasy is implementing a new technology based on sustainable materials for clean water. Arsenic and iron removal technologies are now delivering clean water to 900,000 people each day. In Punjab, the community purifier has crossed accumulative water output of 10 million liters each day.

## **Incubation**

1. Vayujal received funding of 1 crore INR for the development of atmospheric water capture from Engineers India Limited.
2. InnoDi received a tax holiday of 3 years.
3. InnoDi received govt. of Karnataka startup grant of 35 lacs.

## **A new initiative – ICCW**

A new initiative to build the International Centre for Clean Water (ICCW) has begun. It aims to be one of the best ecosystems of its kind in the world to ideate, nurture and translate disruptive technologies for sustainable clean water, with collective participation of the global community, delivering first rate science, leading to wealth and social good simultaneously, in the process building water professionals of tomorrow. Construction for the establishment of ICCW has started at the IITM Research Park.

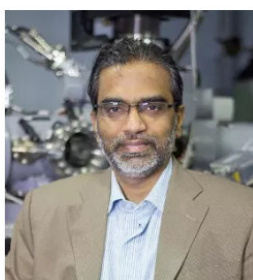
# Media Reports

# IIT Madras Professor T. Pradeep elected to Two Global Academies

BY EDITOR · DECEMBER 20, 2018

**He has developed technologies that deliver clean water to 9 million people in India every day with benefits crossing Rs. 500 cr.**

Indian Institute of Technology Madras Faculty and Prominent nanotechnologist Prof. Thalappil Pradeep has been elected to two global academies.



He is one of the Seven Fellows globally to be elected in the field of Chemistry to the Fellowship of The World Academy of Sciences (TWAS), based in Trieste, Italy. Prof Pradeep was also elected to American Association for the Advancement of Science (AAAS), based in Washington DC, U.S.A.

The AAAS, founded in 1848, elects Fellows from all areas of science, engineering, medicine and social sciences. Around 416 fellows were elected globally this year. TWAS, founded in 1983, is an academy of distinguished scientists and engineers, chosen mostly from developing nations and having a Fellowship base of about 1,200 from 90 countries. Around 46 fellows from across the world were elected this year.

Prof Pradeep, Institute Professor and Deepak Parekh Institute Chair Professor, Chemistry Department, IIT Madras, has been recognised for his distinguished contributions to the field of materials chemistry and for discovering, developing and implementing solutions for affordable clean water.

Speaking about the recognition, Prof Pradeep said, "Recognitions of this kind are important and they will enhance the quality and quantity of science."

His technologies are delivering drinking water to nine million people in the country each day. He has discovered new chemistry that are the basis of these technologies and has incubated multiple companies to convert such science to technologies and products.

He is an inventor of about 100 patents and technologies resulting from them have resulted in benefits over Rs. 500 crores for the nation. He has built laboratories housing sophisticated instrumentation to enable advanced science in materials. Some of those instruments were also built by him.

He has published 430 papers in journals, authored several books and is an inventor of close to 100 patents. He has trained over 250 researchers and has received several Indian and international recognitions and holds visiting positions across the world.

His research Interests include molecular and nanoscale materials, nanoscience and nanotechnology, molecular surfaces, ion scattering, instrumentation and water purification.



These six startups are making drinking water more accessible to Indians - Inventiva

## These six startups are making drinking water more accessible to Indians

By **inventiva** - September 15, 2018



India is facing the worst kind of water scarcity in its history. A recent report by WaterAid states that India has the lowest access to clean drinking water – close to 163 million Indians are said to be suffering from this scarcity.

Government data suggests the average annual per capita water availability fell drastically between 2001 and 2011, from 1.8 million litres to 1.5 million litres. With water becoming even more scarce, the Indian government expects annual per capita water availability to stand at 1.3 million litres and 1.1 million litres in the years 2025 and 2050 subsequently.

Luckily, not just the government but social impact businesses too have taken notice of this situation and have introduced technological products and services to battle this rising shortage in the country.

From Internet of Things (IoT) to solar power, **YourStory** lists six startups that are leveraging technology to provide clean drinking water solutions to the masses.

### AMRIT

Developed in 2013 by a group of researchers at IIT Madras and headed by Professor T Pradeep, AMRIT is a nanoparticle-based water technology that is making arsenic-free water a reality in India.

The AMRIT (Arsenic and Metal Removal by Indian Technology) water purifier is in use in several places in West Bengal and the Union Ministry of Drinking Water and Sanitation is now recommending its usage in all states that are affected by arsenic contamination.

With an investment of \$18 million, it is able to provide a litre of purified water for just five paise in 900 locations, serving more than six lakh people and has given patent rights to consumer goods company Eureka Forbes to use this technology.

<https://www.inventiva.co.in/2018/09/15/these-six-startups-are-making-drinking-water-more-accessible-to-indians/>

## EDUCATION

## Research for change



R.Sujatha

SEPTEMBER 29, 2018 13:43 IST  
 UPDATED: SEPTEMBER 29, 2018 13:43 IST

### A student-driven project at the IIT-M is being widely used to eliminate arsenic from water

A professor and his students at the Indian Institute of Technology - Madras (IIT-M) have developed a technology to remove arsenic from water and make it potable. Over a period of 10 years since the project began in 2008, the researchers have finally seen the benefits of their work on the ground. The technology developed by the Institute is being used widely in West Bengal and Punjab to eliminate arsenic from water.

In as many as eight to 10 states in the country, the groundwater contains a large amount of arsenic – a chemical that is a major health hazard causing an increase in cancer mortality

rate. States such as West Bengal, Assam, Bihar, Chhattisgarh, Jharkhand, Nagaland, portions of Uttar Pradesh, Manipur and Punjab bear the brunt of arsenic deposits in water. In these states, the concentration of arsenic is as high as 200 parts per billion litres (ppb) when the permissible limit is only 10 ppb. Until recently, the only solution was installing reverse osmosis plants, which were expensive.

#### Cost effective

IIT-M's solution was to develop a material that can selectively absorb arsenic from water. "Over nine lakh units have been installed benefitting 70 lakh people," says T. Pradeep, professor of chemistry at the Institute, who leads the research. In Punjab, using the same technology, around 10 million litres of clean water are currently being provided.

The cost of removing arsenic is less than two to five paise per litre of water, which is far less compared to the budget governments must allocate to put up reverse osmosis plants.

"What is clear from this data is that all forms of water quality situations spread across the country, in arsenic affected areas can be tackled by this technology.

In places where there is a genuine desire to solve this menace, this solution is being implemented. We can confidently say that the arsenic menace can be wiped out from the country," says Pradeep.

#### Way forward

"Right now, we have only community scale units, but we are still developing the technology that would make it viable for domestic use," says Ramesh Kumar Soni, an M.Tech student who is now involved in the project.

The material developed by the IIT-M uses no chemicals and is "by the water, for the water", according to him. Ramesh is excited about the project which won the Millennium Alliance Award. He is now improving upon the material that can be installed for domestic use.

A native of Rajasthan, Ramesh says that in his state the problem is fluoride in water. He would get to that issue at a later date as his specialisation is understanding contamination of groundwater.

Printable version | Oct 4, 2018 12:33:29 PM |

<https://www.thehindu.com/education/research-for-change/article25079450.ece>

© The Hindu

## SCIENCE

# Novel technique to detect paraffin oil contamination in coconut oil

**IIT Madras team found paraffin oil contamination was as high as 10%**

Using a novel approach, researchers at Indian Institute of Technology (IIT) Madras have for the first time been able to use mass spectrometry to analyse various saturated and unsaturated hydrocarbons directly from solutions. Ionising the constituent molecules of a hydrocarbon sample for detection using mass spectrometry has not been easy till date as hydrocarbons do not tend to lose or gain electrons to form ions.

Using the novel technique — laser-assisted paper spray ionisation mass spectrometry — the research team led by Prof. T. Pradeep from the institute's Department of Chemistry could detect various hydrocarbons, importantly, paraffin oil contamination in coconut oil samples. Though it is common knowledge that vegetable oils are adulterated, the extent of contamination with paraffin oil was as much as 10%. "It was shocking to see such high levels of mineral oil contamination in coconut oil meant for cooking," says Prof. Pradeep. "We could detect down to 1% paraffin oil present in coconut oil."

The results were published in the journal *Analytical Chemistry*.

Detecting ions using paper spray ionisation mass spectrometry is known already. In this method, a regular filter paper containing the sample is subjected to high electrical potential and the charged droplets and the ions derived from them are analysed using a mass spectrometry. But this method cannot be used for detecting hydrocarbons.

**Humble but handy**

So the researchers turned to the humble laser pointer used commonly during presentations to turn the stubborn hydrocarbons to emit ions for the measurement. Tiny amounts of the sample to be analysed were added to the filter paper kept at about 10 mm from the mass spectrometer and subjected to an electrical potential of 1 kV. Ionisation of hydrocarbon molecules began the moment the tip of the paper containing the sample was exposed to the laser.

The hydrocarbons molecules present in the sample get trapped between the cellulose fibres that make up the paper. "And when an electrical potential is applied, the molecules experience an intense electric field. This is because the molecules are trapped between the fibres which are about 10 microns apart," says Prof. Pradeep.

"When 1 kV potential is applied, the electric field experienced by the molecule is comparable to the field experienced by electrons moving around the nucleus, but not sufficient enough for them to jump out. When we shine the laser, the small energy supplied is enough to cause ionisation," explains Prof. Pradeep.

**R. Prasad**APRIL 28, 2018 17:06 IST  
UPDATED: APRIL 28, 2018 17:07 IST

Different potentials had to be applied to cause different hydrocarbons to get ionised for the same laser. "If we modify the filter paper by coating it with carbon nanotubes, then the fibres will be in the nanometer range and the applied potential can be reduced to even 1 volt," says Pallab Basuri from the Department of Chemistry, IIT Madras and first author of the paper. "This throws open new possibilities for detecting food adulteration, water quality and environmental contamination." The detection limit of the analytes is in the range of nanogram quantities.

According to Basuri, the paper strips containing the samples can be shipped to the place of analysis from remote locations. By varying the composition of the paper and structure of the fibres, it may be possible to store the paper strip containing the sample for future analysis.

Printable version | Apr 29, 2018 9:38:18 PM | <http://www.thehindu.com/sci-tech/science/novel-technique-to-detect-paraffin-oil-contamination-in-coconut-oil/article23710451.ece>



# IIT rolls out water purifier

Published: 📅 Apr 18, 2018 ⌚ 01:59 AM

Updated: 📅 May 10, 2018 ⌚ 08:10 PM

[f Share](#) [🐦 Tweet](#) [🌐](#) [💬 Comments \(0\)](#)

[✉ Mail](#) [🖨 Print](#)

[A](#) [A](#)

***IIT Madras Researchers have developed a water purification system called Roll Pure to help people who don't have access to clean water.***



IIT Madras

**Chennai:** According to a survey by “National Sample Survey Office (NSSO)”, about 54% of the Indian women from rural areas travel between 200 meters to five kilometres daily to get drinking water.

Thus, a water carrier with inbuilt water purification system is essential in rural India to solve this problem. In the project “Roll Pure”, IIT Madras researchers have used 1,000 times efficient biocidal nano materials to perform in-situ disinfection, and nano composite materials to remove soluble geo-specific contaminants.

The project lead Ramesh Kumar Soni said that in order to use the unit, water volume up to 40 litres is filled inside the polybag from open water bodies and unit is rolled to the point of end use. During rolling, biocidal material kills available biological contaminants and dead debris of same is filtered. Pressure differential required for filtration of dead debris and chemical contaminants is developed by a bellow pump.

## COMMENT

## How far does a PhD go?



T. Pradeep

SEPTEMBER 20, 2018 00:15 IST  
UPDATED: SEPTEMBER 19, 2018 22:30 IST**As the job market is tight for those with PhDs in science, it is important that they develop other skill sets**

The number of PhD graduates has proliferated over the decades — while there were only a dozen doctorates till 1920 in India (the first was awarded in 1904), there were 24,000 in all disciplines from about 900 institutions in 2017. While the number may not be surprising, what is disquieting is that of the 6,000 people granted science PhDs annually, [not even 2,000 find decent employment today](#).

**More doctorates, less positions**

Let's look at the numbers. There were 326 PhD-awarding institutions in 2000; this rose to 912 in 2017. According to the University Grants Commission and the Department of Science and Technology, the number of science PhD holders tripled in the same period. With the number of PhD holders surpassing the number of opportunities created, many are left without jobs.

The top-ranked universities in India grant around 2,500 science PhDs each year. In chemistry alone, Indian Institute of Technology (IIT)-Madras grants over 25 PhDs every year. The number is similar in the older IITs, which means that there are 150 chemistry PhDs from these IITs every year. The remaining 11 newer IITs (the latest six are not being considered) add another 100 PhDs. The National Institutes of Technology (NITs) account for about 150, the Indian Institute of Science (IISc) for about 25, the older Indian Institutes of Science Education and Research (IISER) for about 60. The Council of Scientific and Industrial Research (CSIR) labs and institutions of the Department of Atomic Energy (DAE) add another 100 PhDs. Top universities produce about 250. In all, we have more than 800 chemistry PhDs a year.

Get a PhD in India

However, our capacity to employ them is dismal. On average, the IITs and the IISc together recruit only about 25 chemists to their faculty in a year. The older IITs are saturated, so recruitment is rare. Another 50 are recruited in the CSIR, the DAE and the NITs. Overall, the annual intake is not more than 75. If other research labs, the IISERs, and top universities employ about 100 PhDs, that still leaves over 600 chemists without reasonable employment. Options for them include recruitment into State universities, colleges and private institutions, but it is important to remember that these institutions also produce PhDs, whom we have not counted. This has led to a situation where there are over 300 applicants for one faculty position alone. The situation is nearly similar for physics, and worse for biology. Those with PhDs in mathematics fare better. Engineers have not faced this challenge yet.

Thus, after earning a PhD and completing one or two postdoctoral stints, a scientist often stands at a crossroads after the age of 30. This unfortunately happens even to those who have published papers in respected journals and have obtained globally renowned fellowships. The only reasonable option for those with science PhDs seems to be the position of a permanent postdoc in foreign labs. Finding underemployed PhDs who have completed four postdoctoral fellowships is not uncommon. After 40, they are not accepted in entry-level positions.

**Science, funding and productivity**

The vicious cycle continues because a scientist's performance is evaluated largely based on some standard criteria: in order to get the first promotion, he/ she has to publish five to 10 papers, and at least one PhD student should graduate under his/ her supervision. Awards and fellowships are also given based on such criteria. As a result, scientists end up training more scientists.

ALSO READ

Job seekers beware!

A big problem for scientists is funding, which is mostly provided by the government. Funding is crucial for good scientific research. Further woes for scientists include the fact that available resources are not distributed properly, funds are pruned, delayed, or stopped altogether.

While the government pays well, an Assistant Professor in a self-financed college in southern Tamil Nadu is paid just ₹8,000 a month. Many private colleges in and around Chennai pay about ₹30,000 for a

person who holds a science PhD with postdoctoral training. In established private companies, barring exceptions, a postdoctorate is paid ₹70,000. There is indeed an oversupply of candidates.

A job in academia is the most desired, as many industries have not developed adequately to absorb highly trained personnel. While employment opportunities do exist in corporate research and consultancy, about 60% of IIT-Madras' PhDs are in academia. Corporate research and development provide employment to only 10%. It is important for PhDs and postdoctorates to have other skill sets to be employed in business incubators, industry, journalism, and patenting offices. Available positions must be filled quickly in academia. It is crucial for the PhD to regain its respectability.

*T. Pradeep is an Institute Professor at IIT Madras. Email: [pradeep@iitm.ac.in](mailto:pradeep@iitm.ac.in)*

Printable version | Sep 25, 2018 11:18:33 AM | <https://www.thehindu.com/opinion/op-ed/how-far-does-a-phd-go/article24988294.ece>

© The Hindu





During the visit of Prof. Graham Cooks, Purdue University, December 14, 2018

## **Acknowledgements**

### **Students and Collaborators**

## **Funding**



सत्यमेव जयते

**Department of Science and Technology**  
**Government of India**